BESSY - Annual Report

2004

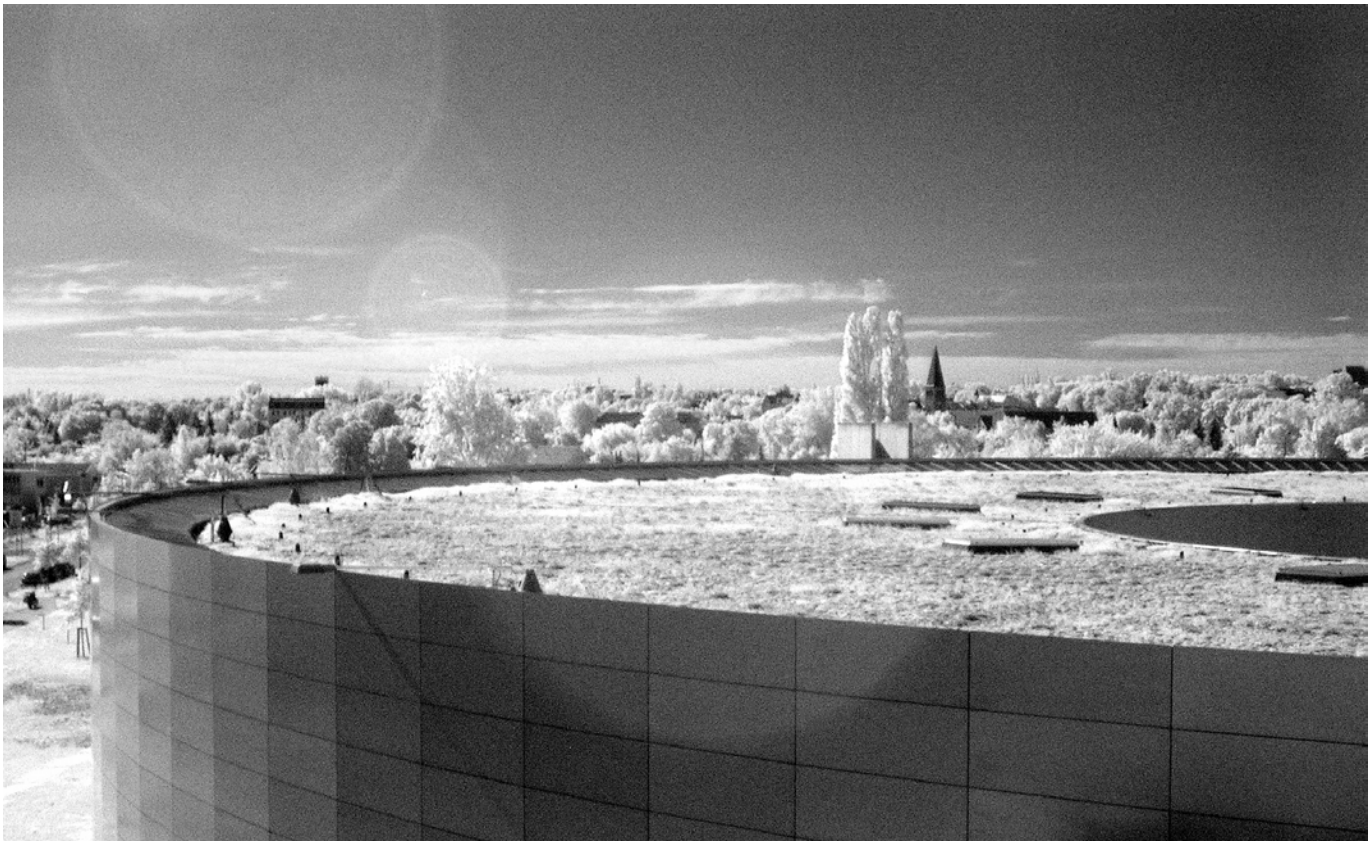

Berliner Elektronenspeicherring-Gesellschaft für Synchrotronstrahlung m.b.H.

Published by:
Berliner Elektronenspeicherring-Gesellschaft
für Synchrotronstrahlung m.b.H. (BESSY)

Albert-Einstein-Str.15
12489 Berlin
Tel. +49 30 6392 2999
Fax +49 30 6392 2990
info@bessy.de
www.bessy.de

Edited by :
Dr. Kai Godehusen

BESSY GmbH • Mitglied der Leibniz-Gemeinschaft (WGL) • Vorsitzender des Aufsichtsrates: Prof. Dr. Joachim Treusch, Jülich
Geschäftsführer : Prof. Dr. Dr. h. c. Wolfgang Eberhardt, Prof. Dr. Eberhard Jaeschke • Sitz der Gesellschaft : Berlin •
Handelsregister : Amtsgericht Charlottenburg HRB 14 635 • Bankkonto: Deutsche Bank AG, Filiale Berlin, Konto-Nr. 4 173 001 01, Bankleitzahl 100 700 00

Dear user and friends,

the activities of a new and exciting year often supersede the events of the past year very quickly. However, 2004 was truly a memorable year. Not only due to the 25th anniversary of BESSY but also due to several outstanding events concerning BESSY's future.

In early summer, BESSY was evaluated by Leibniz-Gemeinschaft for the first time since BESSY II went into operation and we all await the results with great interest. Almost in parallel the FEL team finalised the Technical Design Report for our second generation Free Electron Laser Facility and handed it over to Staatssekretär Dr. Husung from the Berlin government. Shortly thereafter the Standing Committee for Science and Technology of the Berlin State Assembly (Abgeordnetenhaus) met at BESSY to discuss this project. Across all party boundaries the BESSY-FEL project received the full support of all committee members and the Berlin Senate asked the German Science Council (Wissenschaftsrat) for an evaluation of the technical design of this facility, which will take place in 2005.

The 25th anniversary celebration was a great success (except for the weather and most regrettably the cream). Alex Bradshaw reflected on the past quarter century: the "good old days" when BESSY was established as the first dedicated SR source in Germany, the "wavy" times during the planning and decision making process leading to the funding of BESSY II, as well as the realisation and growth of BESSY II and its user community into one of the worlds foremost synchrotron radiation centres for the VUV and soft X-ray spectral region. Additionally, the festivities included a glance into the future with the ground breaking of the Willy-Wien-Laboratory, the new Metrology Light Source of the PTB, which is realised in collaboration with BESSY, and with Joe Stöhr's exciting lecture on femtosecond research in magnetism which will be enabled by Free Electron Lasers delivering controlled and synchronised fs-pulses in the soft X-ray spectral region.

Talking about exciting research... Alltogether five user groups were able to publish their results in high-ranking journals such as Science and Nature in 2004 (see for example the Highlights of Erdélyi et al. and Sørensen et al.). The variety of research taking place at BESSY is still expanding and we have chosen fifteen articles for the Highlights to represent a truly diverse range of topics from atomic physics to life sciences and archaeometry. Since the creation of the "BESSY-Highlights" in 2001, we have encouraged authors to introduce their special field of research to a more general public. This approach seems to be successful since non-scientists keep us asking for a "German Highlights" version. We have not abandoned this idea but for the present we had to postpone it.

Among some 2,500 visitors in 2004, we have had the honour to welcome the German Chancellor Gerhard Schröder, the Federal Minister of Commerce and Labour Wolfgang Clement, and the Federal Minister of Research and Education Edelgard Bulmahn together with several prominent CEO's of leading German industries (BASF, Bertelsmann, BMW, Celon, IBM, EnBW, Schering, ThyssenKrupp, Telekom, and others) during a meeting of the initiative "Partner für Innovation".

Finally, thanks to more than 1,000 scientists, who came to BESSY in 2004 in pursuit of their research programmes and who made our facility a lively and successful site for research and for cultural and scientific exchange.

Enjoy reading the Annual Report and the Highlights 2004.

Instrument Characterization for Solar Observations

M. Richter, A. Gottwald, U. Kroth, W. Paustian, H. Schöppe, R. Thornagel
Physikalisch-Technische Bundesanstalt, Berlin, Germany

B. Kent
Rutherford Appleton Laboratory, Chilton, UK

U. Schühle
Max Planck Institute for Solar System Research, Katlenburg-Lindau, Germany

For many years, radiometric testing and calibration of space instrumentation in the spectral range of vacuum-UV (VUV) radiation and X-rays has been one of the major activities in the PTB laboratories at BESSY I and BESSY II. Outstanding examples are the calibration of the SUMER (*Solar Ultraviolet Measurements of Emitted Radiation*) and CDS (*Coronal Diagnostic Spectrometer*) telescopes of the *Solar and Heliospheric Observatory* (SOHO) and X-ray detector calibrations for the X-ray observatories *Chandra* and XMM-*Newton*. The measurements were based on so-called source based radiometry operating the storage ring as a primary source standard of calculable synchrotron radiation and calibrating radiation sources or energy dispersive X-ray detectors as the transfer standards. The latter then are brought to the instrument test facilities for further measurements. The CDS instrument, e.g., was characterized at the *Rutherford Appleton Laboratory* (RAL) in Chilton (UK) with the help of a hollow cathode rare gas plasma source with collimating optics (Fig. 1) calibrated by PTB at BESSY I.

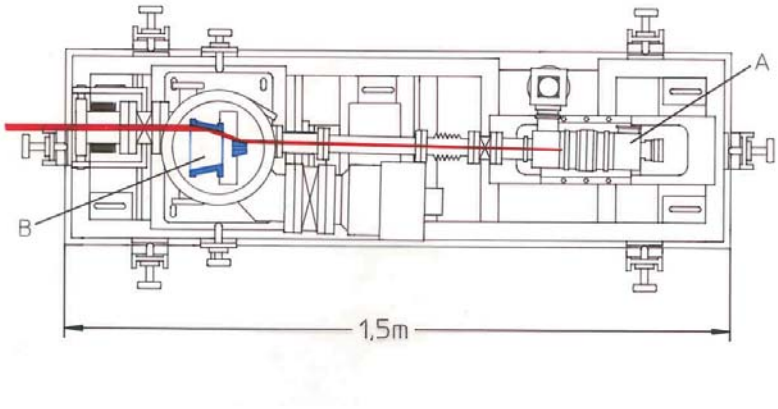

Fig. 1. *Schematic diagram of the CDS calibration source. The diverging radiation from the hollow cathode (A) is collimated by a back-side illuminated Wolter type II telescope (B) [1].*

Later, within a scientific cooperation between PTB and RAL, the CDS calibration source has been operated for the radiometric characterization of the SERTS (*Solar EUV Research Telescope and Spectrograph*) instrument (NASA) and, recently, the *EUV Imaging Spectrometer* (EIS) for the *Solar B* mission. Fig. 2 shows the VUV emission spectrum of neon in the spectral range from 18.5 to 21.0 nm as emitted by the source and measured with the EIS instrument during its calibration campaign in May 2004. In 2005, characterization of the EUNIS (*Extreme Ultraviolet Normal Incidence Spectrometer*) and MOSES (*Multi-Order Solar EUV Spectrograph*) instruments is scheduled. Future projects refer to the *Solar Orbiter* mission of ESA.

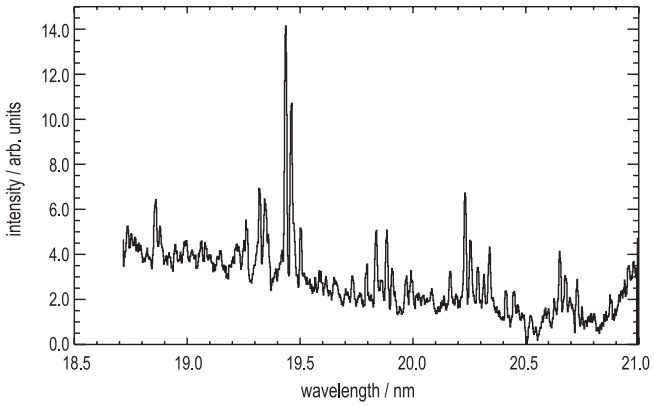

Fig. 2. *VUV emission spectrum of neon as emitted by the CDS calibration source and measured with the EUV Imaging Spectrometer (EIS) of the Solar B mission.*

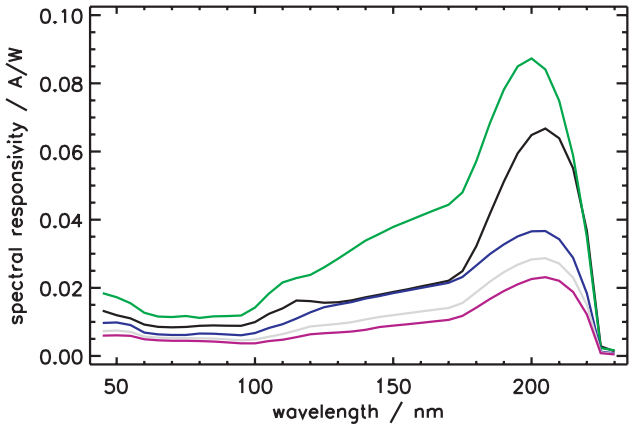

Fig. 3. *Spectral responsivity of diamond detectors [2,3].*

For reliable calibration of VUV space telescopes, their optics and photodetectors must be of high stability and fulfill further specific requirements. For future solar instrumentation in space, the development of new detectors has been pursued under the BOLD (Blind to Optical Light Diamond) project. Fig. 3 shows spectral responsivity curves of different diamond detectors measured within the framework of the BOLD project and a scientific cooperation between PTB and the *Max Planck Institute for Solar System Resarch* (MPS). Due to the wide band gap of diamond of 5.4 eV, optical radiation above 230 nm is strongly suppressed on the photodetection. First application of these detectors is scheduled for the *Lyman-alpha Radiometer* LYRA and the SWAP (*Sun Watcher using APS detectors and image Processing*) instrument of the PROBA II (*Project for On Board Autonomy*) mission (ESA).

[1] J. Hollandt, M.C.E. Huber, M. Kühne, Metrologia **30**, 381-388 (1993).
[2] U. Schühle et al., Proc. SPIE **5171**, 231-238 (2004).
[3] A. BenMoussa et al., Exp. Astron. (2005), in press.

Quantitative Characterization and Monitoring of VUV Free-Electron Laser Radiation

M. Richter, A. Gottwald, A. Hoehl, U. Kroth, H. Schöppe, A. Sorokin
Physikalisch-Technische Bundesanstalt, Berlin, Germany

U. Hahn, K. Tiedtke
Deutsches Elektronensynchrotron, Hamburg, Germany

S. Bobashev
Ioffe Physico-Technical Institute, St. Petersburg, Russia

In the near future, completely new and fascinating experiments in many fields of research will be feasible by the development of vacuum-UV (VUV) and X-ray free electron lasers (FELs). However, the extreme characteristics of FEL radiation, compared to bending magnet or undulator radiation, also imply a serious challenge for any type of signal detection. In the case of photodetection with the direct FEL beam, e.g., peak radiant power values of more than 1 GW are expected to degrade, saturate, or even destroy solid state photodetectors commonly used in the VUV and X-ray spectral ranges. In order to overcome these difficulties, PTB has developed, within a close cooperation with the *Deutsches Elektronensynchrotron* (DESY) in Hamburg and the *Ioffe Physico-Technical Institute* in St. Petersburg, a stable, linear, and almost transparent monitor detector which is based on the photoionization of a rare gas at low particle density [1-3]. Recently, four upgraded versions of this device have been constructed, tested, and calibrated in the PTB laboratory at BESSY II for use as permanently and online operating monitor detector systems for pulse resolved intensity and beam position measurements at DESY's VUV-FEL in Hamburg.

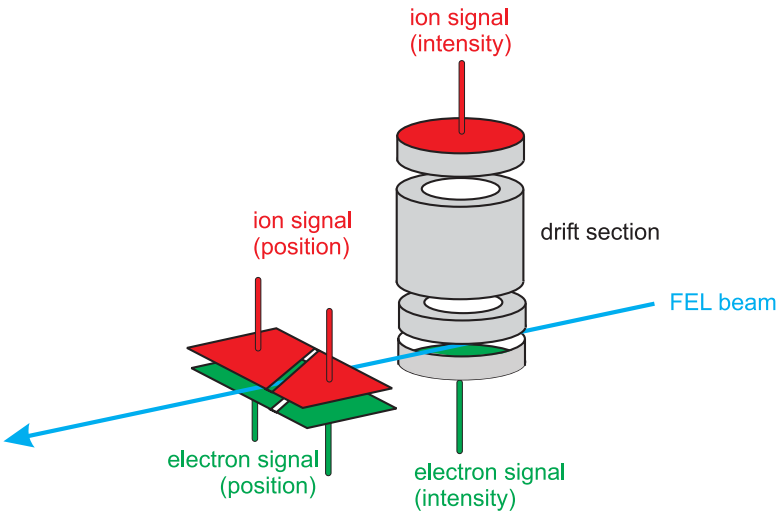

Fig. 1. *Gas monitor detector for VUV-FEL intensity and beam position measurements [4].*

Fig. 1 demonstrates the measurement principle. Electrons and ions created by photo-ionization are extracted by an almost homogenous electric field. Their charge is detected by metallic electrodes, respectively. A drift section within the ion path of the intensity monitor part of the detector allows for ion time-of-flight (TOF) measurements for additional diagnostics. All charge signals may be recorded in a pulse resolving mode, the ion signals alternatively in a RC-smoothed current mode. The latter is sensitive enough for calibration with dispersed synchrotron radiation at low photon intensities. Fig. 2 shows the normalized quantum efficiency of the ion current signal as determined recently in the PTB laboratory at BESSY II.

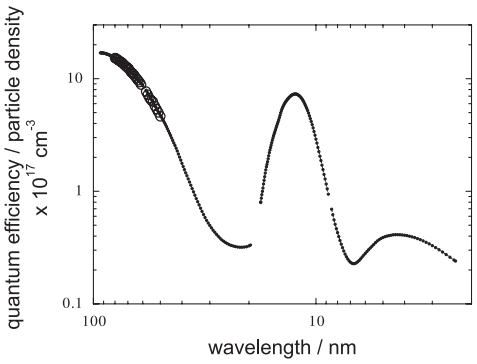

Fig. 2. *Quantum efficiency of the ion-current signal of one of the four gas-monitor detector systems operated with xenon, normalized to particle density. The dots, using xenon cross section data [5], stand for an extrapolation of the calibration values (open circles) which were measured in the PTB laboratory at BESSY II.*

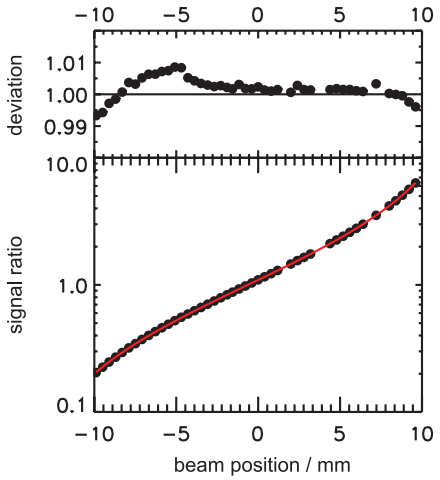

Fig. 3. *Bottom: Measured (black symbols) and calculated (red line) ratio between the two ion-current signals of one of the four beam position detectors as a function of the beam position. Top: Relative deviation between the measured and calculated signal ratio.*

For beam position measurements, the respective rectangular electrodes are split diagonally into two parts so that the corresponding signal ratio is a measure for the respective beam position coordinate. Corresponding tests have been performed in the PTB laboratory at BESSY II as demonstrated in Fig. 3. As a result, the uncertainties for beam position measurements are well below 50 µm. At the VUV-FEL in Hamburg, the four detection systems will be used to measure horizontal and vertical beam positions at two different positions of about 15 m distance along the FEL beam, respectively, which also allows horizontal and vertical beam angle measurements with an accuracy in the µrad regime.

The detection systems will start operation at the VUV-FEL in March 2005 for photon diagnostics purposes as well as for user support. The detection principle is best suited also for the scheduled BESSY-FEL. Extension into the X-ray regime where the atomic photoionization cross sections are by orders of magnitude lower requires further design studies which have been started within the framework of the XFEL project in Hamburg and a close cooperation between PTB and DESY.

[1] M. Richter et al., Appl. Phys. Lett. **83**, 2970-2972 (2003).
[2] M. Richter et al., Deutsches Patent- und Markenamt, No. 102 44 303, München (2004).
[3] A.A. Sorokin et al., AIP Conference Proceedings **705**, 557-560 (2004).
[4] A. Gottwald et al., Proc. SPIE **5534**, 13-21 (2004).
[5] M. Richter et al., AIP Conference Proceedings **652**, 165-171 (2003).

Layer thickness determination in the nanometer region – a comparison of X-ray reflectometry (XRR) and reference free X-ray fluorescence analysis (XRF)

M. Kolbe, B. Beckhoff, M. Krumrey, G. Ulm
Physikalisch-Technische Bundesanstalt, Abbestraße 2-12, 10587 Berlin, Germany

Abstract Two methods employing X-rays for the non-destructive investigation of thin layered materials have been compared by the Physikalisch-Technische Bundesanstalt (PTB). The measurements were performed by use of synchrotron radiation at the electron storage ring BESSY II. For this purpose copper and nickel layers as well as double layers of both metals on silicon have been studied. The thickness of the layers varied between 5 nm and 50 nm. All samples have been investigated with X-ray reflectometry (XRR) and X-ray fluorescence (XRF) analysis. The fundamental parameter approach was used to analyze the fluorescence spectra. Due to the absolutely calibrated instrumentation of the PTB all experimental values have been obtained reference and standard free.
Both methods showed within the frame of their respective uncertainties the same results for the determined layer thicknesses.

Introduction The developments in the semiconductor industry call for better and accurate thickness determination of thin films and layers in the nanometer range. X-ray reflectometry is an approved method for this task. But inhomogeneities and very thin layers increase the uncertainties of the determined thicknesses. On the other side X-ray fluorescence analysis determines the mass deposition of an element. Knowing the density a thickness can be calculated. Normally this methods needs a reference standard for the determination due to the mostly imprecise knowledge of experimental parameters like the solid angle of detection and detector efficiencies. Due to the calibration of our detectors in the PTB laboratory all relevant experimental parameter are known and a fundamental parameter based analysis without any reference is applied.

Experimental For the comparison of both methods layers of copper and nickel on silicon have been investigated. In a first attempt single one-elemental layers of both elements with thicknesses from 5 to 50 nm have been analyzed. In a second step our investigations have been extended to double layered systems containing both metals on silicon. The measurements have been carried out in the laboratory of the PTB, where experimental stations for XRR as well as for XRF are provided. Both methods have been performed at the four crystal monochromator beamline providing monochromatized X-ray radiation in the energy range from 1.75 to 10.5 keV.
For the X-ray reflectometry investigations the samples were mounted inside a reflectometer. The reflectivity of the layered systems in dependence on the grazing incidence angle has been taken in a theta-two theta scan rotating the sample and the detector around an axis in the sample surface. The energy of the incident radiation was 8048 eV, the energy of the copper Kα fluorescence line, to be comparable to the energy typically used in table top devices.
For the investigated double layered systems 8048 eV is not convenient due to the similarity of the optical constants of nickel and copper at this energy. The optical constants change at the absorption edge of the respective element. For this reason 8400 eV, an energy between the K absorption edges of both elements, has been used.
The chamber for the X-ray fluorescence analysis is equipped with calibrated diaphragms in fixed but changeable positions to define the geometry between the incident radiation, the sample surface, and the fluorescence radiation. Due to the calibration the solid angle of detection is well known. The flux of the incident radiation is determined by calibrated photodiodes. The fluorescence radiation is measured with a Si(Li) detector, which was

calibrated with respect to its efficiency and its response function. Due to this equipment all data for a reference-free fundamental parameter based evaluation of the fluorescence analysis are available. The excitation energy was chosen above the K absorption edge of the respective layer. Thus the systems with nickel layers have been excited at 8900 eV and the systems with copper at 9500 eV. The double layered systems were investigated with the latter energy to excite both elements in the sample.

Data evaluation The reflectivity in dependence on the grazing angle was simulated with the common IMD program using the layer thickness and roughness as parameters. The best fit based on a the minimization of χ^2 led to the data of the involved layers. These data were compared with the data provided by the manufacturer using a table top device for the XRR measurements of the same samples. The values agree very well. The layer roughness determined by XRR did not exceed 0.5 nm.
The count rates of relevant fluorescence lines were determined from the XRF spectra employing experimentally based detector response functions. The incident photon flux was monitored during the spectra exposure by a calibrated transmission photodiode. Using these data in the fundamental parameter approach for primary and secondary excitation the thickness of the layers could be determined. The results were compared to the XRR results. The uncertainties of the XRF are combined from the experimental uncertainties and the uncertainties of the fundamental parameter. The latter are not exactly known and the data from different data bases differ. Thus the relative uncertainty of the XRF results is about 6% assuming a relative uncertainty of 5 % of the fluorescence cross section of the transition metals of interest here. The standard-free fundamental parameter based XRF showed, within the combined uncertainties, the same results as the XRR, e.g. for the nominal 50 nm thick copper layer the XRR determined thickness is (49.7±0.5) nm and the thickness determined from fundamental parameter based XRF is (48.4±2.9) nm. Also the homogeneity of the samples has been investigated by mapping with XRF. The deviation from the mean value did not exceed 1 %.

Conclusion We have shown, that the thicknesses determined by both methods agree very well within their respective uncertainties. The reference free fundamental parameter based X-ray fluorescence analysis is able to supplement thickness determination of thin layers in view of the increasing uncertainties of X-ray reflectometry for very thin or inhomogeneous layers.

References

[1] P. Thomsen-Schmidt, K. Hasche, G. Ulm, K. Herrmann, M. Krumrey, G. Ade, J. Stümpel, I. Busch, S. Schädlich, A. Schindler, W. Frank, D. Hirsch, M. Procop, U. Beck, Realisation and metrological characterisation of thickness standards below 100 nm, Appl. Phys. A 78 (2004) 645 – 649

[2] M. Krumrey, M. Hoffmann, G. Ulm, K. Hasche, P. Thomsen-Schmidt, Thickness determination for SiO_2 films on Si by X-ray reflectometry at the Si K edge, Thin Solid Films 459 (2004) 241 –244

[3] B. Beckhoff, M. Mantler, M. Bavdaz, G. Fraser, M. Kolbe, M. Krumrey, a: Owens; A. Peacock, D. Pullan, F. Scholze, G. Ulm, Evaluation of complete standardless quantitation for synchrotron radiation induced X-ray fluorescence analysis, BESSY Annual report (2003) 31-34

[4] M. Kolbe, B. Beckhoff, M. Krumrey, G. Ulm, X-ray fluorescence analysis for the quantitative investigation of nanolayered systems, Appl. Surf. Sci., in print (2005)

ULTRA-TRACE NITROGEN SPECIATION IN SIZE FRACTIONATED ATMOSPHERIC AEROSOLS EMPLOYING TXRF-EXAFS

S. TÖRÖK[1], J. OSÁN[1], E. CURIS[1,2], B. BECKHOFF[3], G. ULM[3]

[1]KFKI Atomic Energy Research Institute, P.O. Box 49, Budapest, H-1525, Hungary

[2]Faculté de Pharmacie, Univesité de Paris V, Paris, France

[3]Physikalisch-Technische Bundesanstalt, Berlin, Germany

Keywords: atmospheric aerosols, chemical speciation, TXRF, NEXAFS.

INTRODUCTION

Nitrogen compounds play a very important role in the atmosphere's chemical conversion processes (Harrison & Van Grieken, 1998). Most oxidized nitrous compounds have a relatively short residence time in the atmosphere and interact with the available radicals or aerosols. While compounds in the gas phase can be measured by high temporal and spatial resolution using optical and remote sensing methods it is crucial to have analytical methods that enable to measure the aerosols from a short sampling period while retaining the information on the size distribution of the particles. Satellite-borne sensors provide a synoptic view of environmental condition and this objective information is an ideal support for transboundary pollution because there is no legal limitation on the data. From the processed images the estimation of the rate of atmospheric turbidity due to aerosols, namely particulate optical thickness is possible (Masuda *et al.*, 2003). A near edge X-ray absorption fine structure (NEXAFS) investigation in conjunction with total reflection X-ray fluorescence (TXRF) analysis is able to contribute to the speciation of the atmospherically important low-*Z* elements (C, N and O) on wafer surfaces. TXRF using high flux synchrotron radiation (SR) for the specimen excitation is a powerful technique for the non-destructive analysis of nanoscopic (10^{-9} g) amounts of solid material collected on silicon wafer surfaces (Beckhoff et *al.*, 2001).

METHODS

Aerosol samples were collected at two locations in Hungary, a rural (Szatmárcseke, close to Ukrainian border) and a suburban (KFKI campus, Budapest) site. Particles were sampled on silicon wafers using a seven-stage May cascade impactor. Aerosol collection was performed only at stages 5, 6 and 7, with aerodynamic cut-off diameters of 1, 0.5 and 0.25 μm, respectively. As standards of known nitrogen speciation, thin layers of submicrometer particles were prepared on silicon wafer substrates from suspensions containing pro analysis grade $NaNO_3$ and $(NH_4)_2SO_4$. The TXRF-NEXAFS measurements were carried out at the PGM monochromator beamline at the electron storage ring BESSY II using undulator radiation. The samples were investigated under UHV conditions. The beam profile was 140 × 40 μm² resulting in an illuminated area of 3.2 mm × 40 μm at an angle of incidence of 2.5°. N-Kα fluorescence count rates were recorded by a Si(Li) detector equipped with an ultra-thin polymer window. The incident radiant power was recorded by means of a reference measurement employing a calibrated photo diode allowing for a normalization procedure. For a typical energetic scan at the N-K edge the incident photon energy was varied from 395 eV to 415 eV in steps of 125 meV. At each point of the scan a TXRF spectrum was recorded during 20 s.

RESULTS

The N K-edge NEXAFS spectra of the submicrometer aerosol fractions showed multiplet π* resonances similar to that of ammonium sulfate. No significant difference was found in the spectra of the suburban and rural aerosol samples (Török et al., 2004). The spectra of the 1 μm to 2 μm aerosol fraction were more

similar to that of nitrate, but the π* resonance peaks at 400.3 and 400.5 eV indicate the presence of ammonium in significant amount. Similar results were obtained by Mészáros *et al.* (1997) from wet chemical analyses of size-fractionated high volume samples where ammonium was dominating the smaller particle size fractions. Semi-quantitative evaluation of a spectrum of the 1 µm to 2 µm fraction was performed using linear combination of the ammonium sulfate and sodium nitrate standard spectra. The result of the fitting is shown in Fig. 1, giving a nitrate–ammonium ratio of 70%/30%. Looking at the fitting residuals in Fig. 1, minor π* resonances at 399.3 eV could not be described with ammonium and nitrate, that can be due to the presence of organic nitrogen compounds. The presence of biogenic particles containing significant amount of nitrogen was verified using electron-probe microanalysis (EPMA).

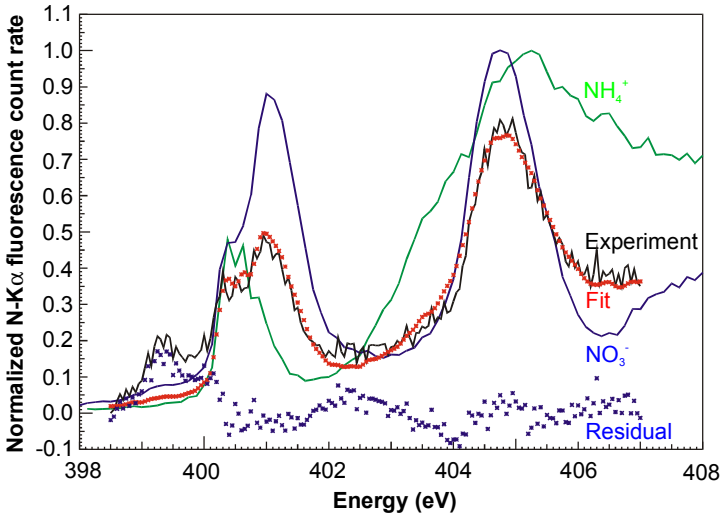

Fig. 1. Calculated evaluation (red) of the measured N K-edge TXRF-NEXAFS spectrum (black) of the 1 µm to 2 µm aerosol fraction collected at Szatmárcseke, using linear combination of standard spectra of ammonium (green) and nitrate (blue). The residual curve (dotted) demonstrates the good agreement of this linear combination above 400 eV.

CONCLUSION

The TXRF-NEXAFS experiments showed that the sensitivity of the technique enables to carry out nitrogen speciation studies on nanoscopic amounts of aerosols, or potentially even of an individual nanoscaled particle using a few µm broad beam. For atmospheric research this implies that the analytical method enables high time resolution (1 min to 10 min) or sampling in areas with very low aerosol mass concentration.

ACKNOWLEDGEMENTS

The present research was supported by the Hungarian National Science Foundation (OTKA) through Contract No. T034195. The János Bolyai Research Fellowship for J. Osán is also appreciated. The authors would like to thank R. Fliegauf, M. Kolbe and J. Weser for supporting the TXRF-NEXAFS experiments at the PGM-U49 beamline of the PTB.

REFERENCES

Harrison, R.M., and Van Grieken, R.E., Atmospheric Particles (John Wiley & Sons, 1998) p. 120.

Masuda, K., Ishimoto, H., and Takashima, T., *Int. J. Remote Sensing* **23** (2003) 3835–3851.

Mészáros, E., Barcza, T., Gelencsér, A., Hlavay, J., Kiss, Gy., Krivácsy, Z., Molnár A., and Polyák, K., *J. Aerosol Sci.* **28** (1997) 1163–1175.

Beckhoff, B., Fliegauf, R., Ulm, G., Pepponi, G., Streli, C., Wobrauschek, P., Fabry, L., and Pahlke, S., *Spectrochim. Acta B* **56** (2001) 2073-2083.

Török, S., Osán, J., Beckhoff, B., and Ulm, G., *Powder Diffr.* **19** (2004) 81-86.

Investigation of the morphology of solid-state interfaces by diffuse X-ray scattering

I. Busch [1], M. Krumrey [2] and J. Stümpel [1]

[1] Physikalisch-Technische Bundesanstalt, Bundesallee 100, 38116 Braunschweig, Germany
[2] Physikalisch-Technische Bundesanstalt, Abbestraße 2-12, 10587 Berlin, Germany

The investigation of solid-state interfaces is of main interest for both: basic research and R&D. With the shrinking of the dimensions of solid-state systems its physical properties become more and more influenced by the structure of the interface. Diffuse X-ray scattering (DXRS) is sensitive to the morphological aspects of the interfaces in thin film systems. In the vicinity of the critical angle of reflection the intensity of X-rays is detected, which are diffusely scattered by the rough interfaces. Because of the small incident (α_i) and exit angles (α_f) the resulting scattering vector **q** is very small, and the Laue condition for constructive interference is only fulfilled for the interfaces of the superlattice, i.e. the films can be crystalline, amorphous, polycrystalline, etc. The coplanar scattering geometry (cf. fig. 1) used in this experiment causes a zero q_y component of the scattering vector **q**. The q_x- and q_z-components are adjusted by the two angles α_i and α_f with respect to the sample surface. These two components create the reciprocal space as it is shown in fig. 1 (right). Only the area white marked is accessible for measurements, in the grey-shaded areas on the left and right side, one of the angles is below zero. The reflected X-ray intensity measured at the different points of the reciprocal space generates the scattering image of the interface (space map). The structure of this space map is basically generated by the morphology of the interface.

X-ray reflectometry (XRR) is a special case of the general DXRS. In fig. 1 (right), the XRR is equivalent to the sketched θ/2θ-scan. In this case, the specular reflected X-rays are measured while the condition $\alpha_i = \alpha_f$ is fulfilled. The scattering vector **q** has only a component perpendicular to the surface (q_z). The simultaneously measured diffuse scattered intensity already provides access to the rms-roughness of the interface. For an advanced analysis of the lateral structure of the interface topography, the measurement of the off-specular reflections is required, because in this case **q** has an additional component parallel to the interface (q_x).

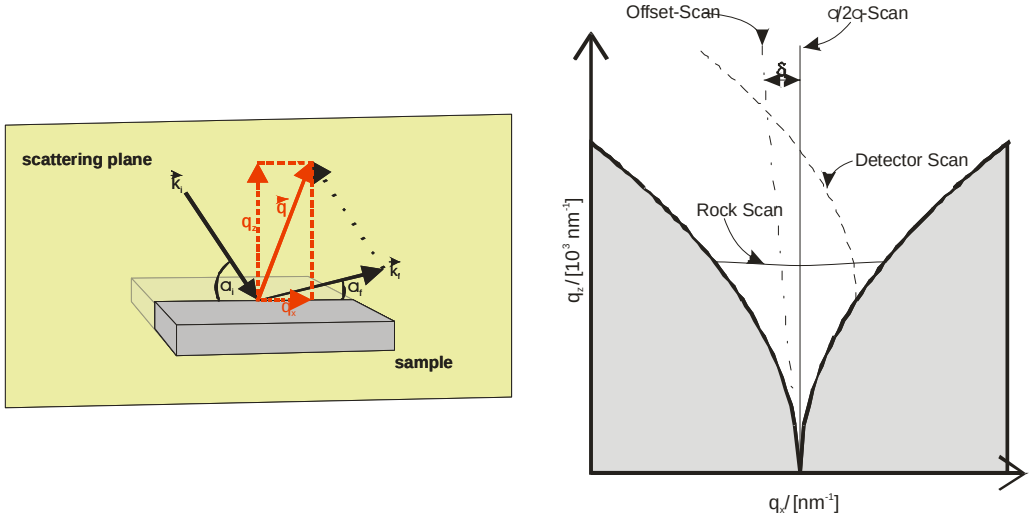

Figure 1 Sketch of the coplanar scattering geometry and the construction of the reciprocal scattering vector **q**. Incident beam, reflected beam, and the normal to the surface are within the same (scattering) plane (left side). The resulting reciprocal scattering plane and the path of the different scan modi are pictured on the right side.

The measurements of the diffuse scattered X-rays over the complete reciprocal space are carried out with a series of rock scans to produce the space map of the system (cf. Fig. 1, right side and Fig. 3). The simulation of the scattering process with structure models for the multilayer system are done on the basis of the Distorted Wave Born Approximation (DWBA) and fractal models for the rough interfaces [2,3]. This simulation provides the critical parameters for the morphology of the interface, like rms-roughness σ, lateral $\xi_{\parallel}$, and vertical correlation length $\xi_{\perp}$ etc.

In a first series of measurements, the influence of growth interruptions on the formation of solid- state interfaces is investigated. For this reason, three GaAs/AlAs multilayer systems are produced by molecular beam epitaxy (MBE). Each system consists of 50 double layers of AlAs and GaAs which are grown on a (100) GaAs substrate. The nominal layer thicknesses for the MBE process are 2.65 nm and 1.73 nm, respectively. Finally, the system is covered by a 10 nm cap layer of GaAs. One of the samples (P90-12) is grown in a continuous mode, i.e. the new layer is grown immediately after the deposition of the preceding layer. The other samples have a growth interruption of 50 s after the deposition of each GaAs layer (P92-13) and after the deposition of AlAs (P91-11), respectively. Due to the growth interruption, an enlarged diffusion along the interface occurs which results in a change of the morphology. The DXRS measurements serve to determine the morphological parameter of these three samples and the comparison of the different growth conditions.

The measurements are carried out at the four-crystal monochromator (FCM) beamline of the PTB at BESSY II at a photon energy of E=8048 eV (Cu-K_{α} radiation). At first, the reflectograms of the samples are measured to determine the correct thickness of the multilayer films. These values are used as necessary input data for the simulation models (cf. fig. 2). To achieve a large dynamical range of approx. nine orders of magnitude, two detectors were used: a silicon photodiode and a photon-counting silicon drift detector (SDD). The SDD is indispensable for the low intensities of the diffuse-scattered radiation. The analysis of the reflectogram delivers a thickness of a single GaAs/AlAs double layer (d_{MBE} = 4.38 nm) of $d_{P90\text{-}12}$ = 4.17 nm for the continuously grown multilayer and $d_{P92\text{-}13}$ = 4.29 nm for the sample with growth interruption after the GaAs layer. The reproduction of the layer thickness during the production of the multilayer with MBE is by far better. This is proved by high resolution scans ($\Delta\theta$ = 0.001 °) of the samples which also resolves the small side maxima.

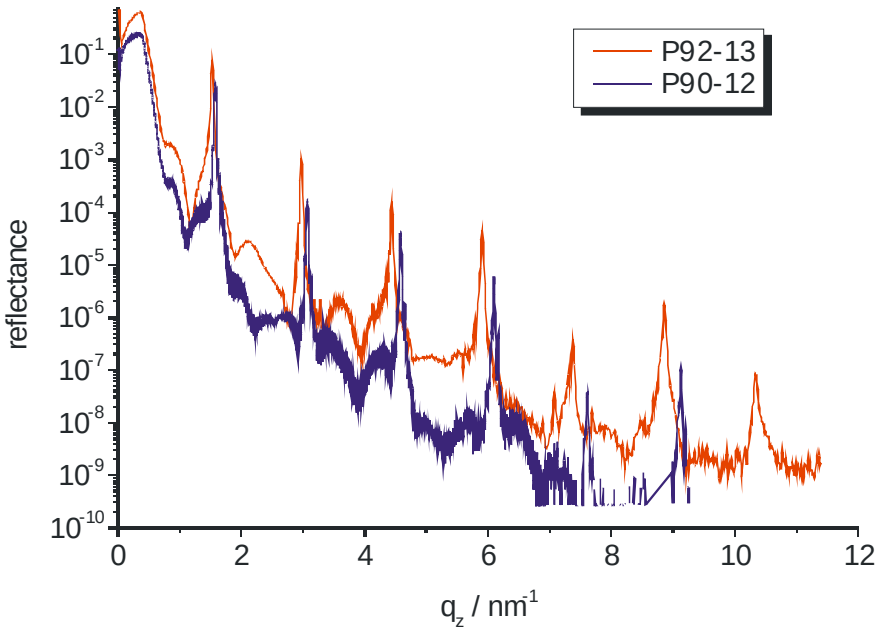

Figure 2 Reflectogram of two multilayers with an identical setup of 50 double layers of GaAs/AlAs. The sample P90-12 is produced by MBE in the continuous-growth mode. The sample P92-13 has a growth interruption of 50 s after deposition of each GaAs layer. The blue scan has been measured with a higher angular resolution, so that the side maxima are also resolved. This leads to an apparent broadening of the blue diagram.

The value of the rms-roughness of both multilayers is almost identical ($\sigma \approx 0.5$ nm), but the shape of the reflectograms and thus the lateral structure of the interfaces varies significantly. This is documented by the difference in the space maps of the systems, particularly in the changes of the shape of the intensity maxima in the diffuse part.

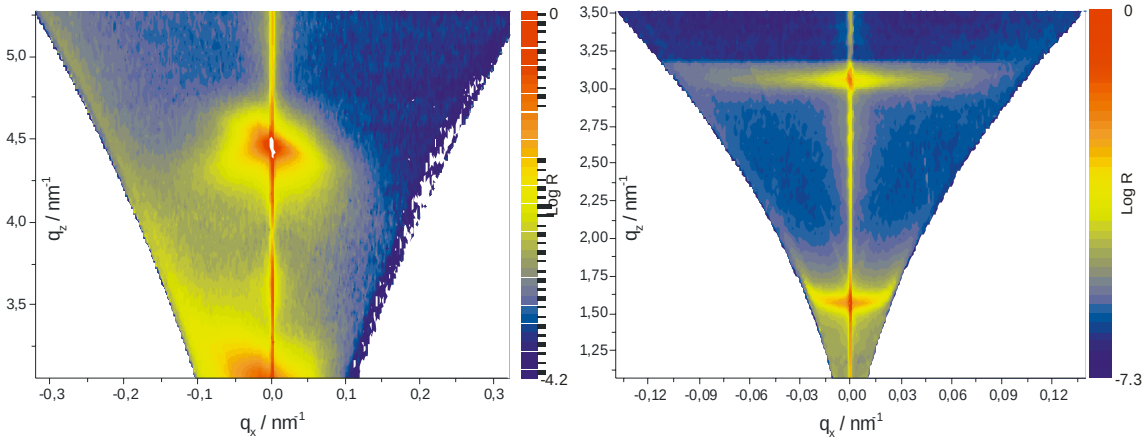

Figure 3 Space maps of the samples P90-12 (right) with continuous growth and P92-13 (left) with a growth interruption of 50 s after deposition of each GaAs layer. The obvious difference in the distribution of the scattered intensity is a result of the change of the interface morphology due to the growth interruption.

In the case of the continuously grown sample (P90-12, the space map on the right side of Fig. 3), the lateral correlation length $\xi_{\parallel}$ has a value of some ten nanometers (the large extend of the 'banana' in q_x direction), the vertical correlation length $\xi_{\perp}$ is in the region of some hundred nanometers (the concentration of the maximum in q_z direction), i.e. the replication of surface features through the next layer, is almost perfect.

The sample P92-13 with a growth interruption of 50 s shows a high concentration of the coherent scattered radiation in a small area of the reciprocal space (cf. fig. 3, left). The lateral correlation length of this sample is greatly extended in comparison with the first sample. It is in the region of some hundred nanometers. The replication of the interface topography stays on the same high level as before. The value of $\xi_{\perp}$ is again some hundred nanometers.

The preliminary analysis of the measured DXRS data clearly indicates the emergence of long-range structures at the solid state-interfaces as a result of the enlarged two-dimensional diffusion during the growth interruptions in the MBE process. After the detailed analysis of all measurements of the three samples und the modelling of the multilayer systems in computer simulations on the basis of DWBA, more precise and quantitative data with respect to the roughness and correlation length will be available. These data will be the starting point for investigations of the transport processes in comparable systems.

References

[1] G. Bernatz; S. Nau; R. Rettig; H. Jänsch; W. Stolz, *J. Appl. Phys.* **86** (1999) 6752

[2] S.K. Sinha et al., *Phys. Rev. B* **38** (1988) 2297

[3] I. Busch and J. Stümpel, *J. Appl. Surf. Sci.* **212-213** (2003) 201

Irradiation Stability of VUV Optical Materials and Material Surfaces

A. Gottwald, H. Schöppe, U. Kroth, M. Letz[1], M. Richter
Physikalisch-Technische Bundesanstalt, Abbestr. 2-12, 10587 Berlin, Germany
[1]Schott Glas, Research and Development, 55014 Mainz, Germany

Degradation of reflecting optics irradiated by EUV and soft X-ray radiation is known to be mainly caused by surface processes due to contaminations present in the residual gas or as adsorbates on the optical surfaces. Bulk effects usually play a secondary role compared to the surface due to the short penetration depths of the radiation. At VUV wavelengths above 120 nm, where optical components (e. g. lenses, filters) are used in transmission, however, both contributions to degradation must be taken into account. By measuring the reflectance and transmission of optical materials, radiation induced changes can be separated into bulk and surface effects. In cooperation with Schott as a major manufacturer of optical materials, we investigated radiation-induced damages of optical components by measurements of optical properties in the VUV range between 90 nm and 220 nm. The selected samples had been partially irradiated with high doses of 193 nm-laser radiation.

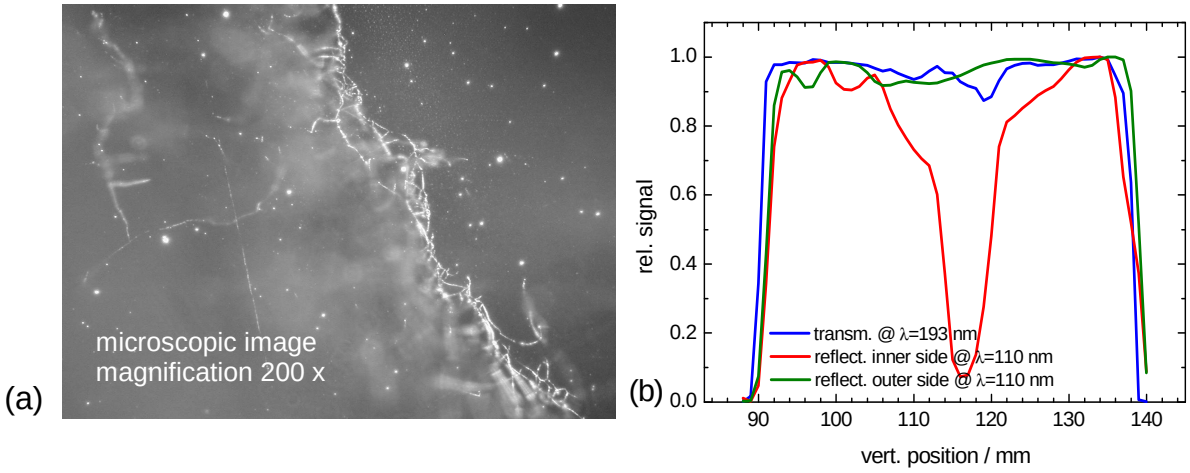

Figure 1 (a) Microscopic image of a CaF_2 laser window surface in the border region between laser irradiated and non-irradiated areas. (b) Vertical reflectance and transmittance profile of the same window sample. The inner window side pointed towards the laser tube during irradiation.

Figure 1(a) shows a microscopic image (magnification 200) of a CaF_2 sample surface in the border region between irradiated and non-irradiated areas. The sample has a size of several centimetres and a thickness of 6 mm and has a central irradiated area of a few mm. The sample was highly irradiated with 193 nm VUV radiation. The microscopic image reveals a blurring of the material in the irradiated area.

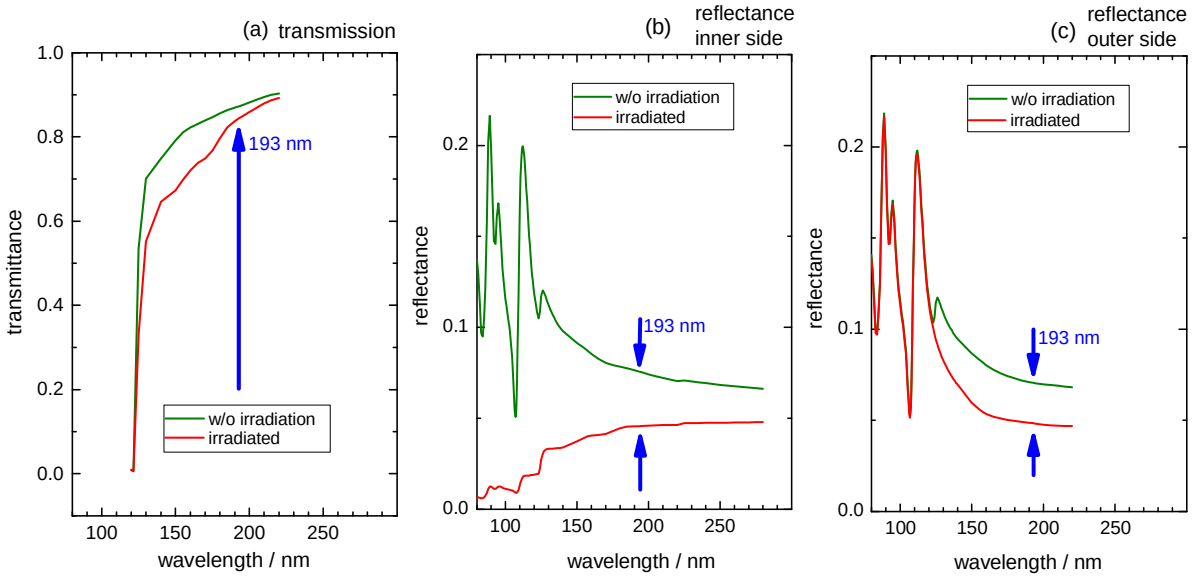

Figure 2 Transmittance (a) and reflectance (b,c) of the CaF_2 laser window with strong surface damage.

Figure 1 (b) shows a normalized vertical profile of the sample transmission at a wavelength of 193 nm and reflectance at 110 nm. The sample side, which was pointing towards an ArF atmosphere during irradiation (inner side), shows a strong decrease in reflectance, while the other side (outer side) as well as the total transmittance only shows minor changes.

Figure 2 shows the spectral dependence of the window transmittance (a). The change in transmittance alone does not allow to judge whether a surface or a bulk effect of material degradation is present. The reflectance for the inner side (b) and outer (c) side clearly reveal that a surface degradation is present. Below the transmittance edge around 120 nm, the reflectance is dominated by the resonance of the CaF_2 Γ-exciton at 112 nm. As already seen in figure 1, the inner window side shows a very strong degradation in reflectance while the other shows much less. Moreover, the characteristic resonance structures from CaF_2 are strongly suppressed, indicating a chemical change of the surface on a depth which is larger than the wavelength of the radiation, e.g. several 10^{th} of lattice constants. Otherwise the bulk material and the outer window side are not strongly affected. This indicates that the damage caused by strong laser irradiation is mainly a surface effect which depends on atmospheric conditions and the surface treatment (polishing, coating). Additional experiments using sliced cuts from an irradiated CaF_2 rod confirm this assumption: the cut surface which had been inside the rod during irradiation showed almost no degradation while the outlying surfaces of the rod changed.

Linearity of photodiodes under EUV radiation

R. Müller, F. Scholze, R. Klein, S. Plöger, G. Ulm

Physikalisch-Technische Bundesanstalt, Abbestr. 2-12, 10587 Berlin, Germany

Photodiodes are used as easy-to-operate detectors in the extreme ultraviolet spectral range. The Physikalisch-Technische Bundesanstalt calibrates photodiodes in the EUV spectral range with a relative uncertainty of the spectral responsivity of 0.3 % or better. These calibrations are based on the comparison of the photodiodes to a cryogenic radiometer as primary detector standard using monochromatized synchrotron radiation, a quasi DC-radiation with a rather low radiant power of about 1 µW [1]. At the customer, these diodes may be used for strongly pulsed radiation and very different radiant power. Therefore, the saturation behavior of the diode signal with incident power of EUV radiation at about 13 nm has to be known. Previously we have investigated the influence of the photon beam spot size on the diode responsivity at high radiant power [2]. In this contribution we show the strong influence of the measurement position at the diode on the linearity of the photodiode.

The measurements were performed at the EUV system metrology beamline at the undulator U49 of PTB at BESSY II [3, 4]. To achieve sufficiently high levels of photon flux to saturate the photodiode, direct undulator radiation was used. For details of the beamline and the EUV radiant power see references 3, 4 and 5.

As a reference of the diode linearity, the photon flux from the storage ring was used. The photon flux scales linear with the stored electron current. Therefore we measured the photocurrent of the photodiode as a function of the stored electron current. For each value of the stored electron current, we measured the photocurrent for various apertures which were successively placed in front of the diode. The photodiode was moved behind the aperture in order to get a position dependent information about the responsivity. This measurement was repeated for stepwise decreased electron current until the photocurrent and electron current ratio was constant. As the total power incident on the photodiode scales with the aperture size, the photocurrent differs for the different aperture sizes. The measurements were done for different apertures, having diameters of 0.25mm to 6 mm. Here we present the results for two apertures, namely 1 mm and 4 mm.

In figure 1, the ratio between photodiode current and stored electron current in relation to the spot-position on the photodiode is shown for different electron currents of the storage ring. For higher currents the diode is in saturation showing an relative enhancement of the responsivity at the edge of the active area. If the ring current is lowered the shape of the responsivity shows a linear behavior (“plateau-behavior”) over the whole area of the photodiode. From our previous measurements taken at the center of the diode we derived the electron current (irradiance power) which is necessary to operate the diode in a linear regime [2]. The values of these currents are equal to the currents were the diode responsivity crosses over to the “plateau-behavior“ (see figure 1). For smaller apertures the linearity regime of the

diode is reached at higher electron currents [2]. The same results could be derived from our measurements of the position dependent relative responsivity (see figure 1).

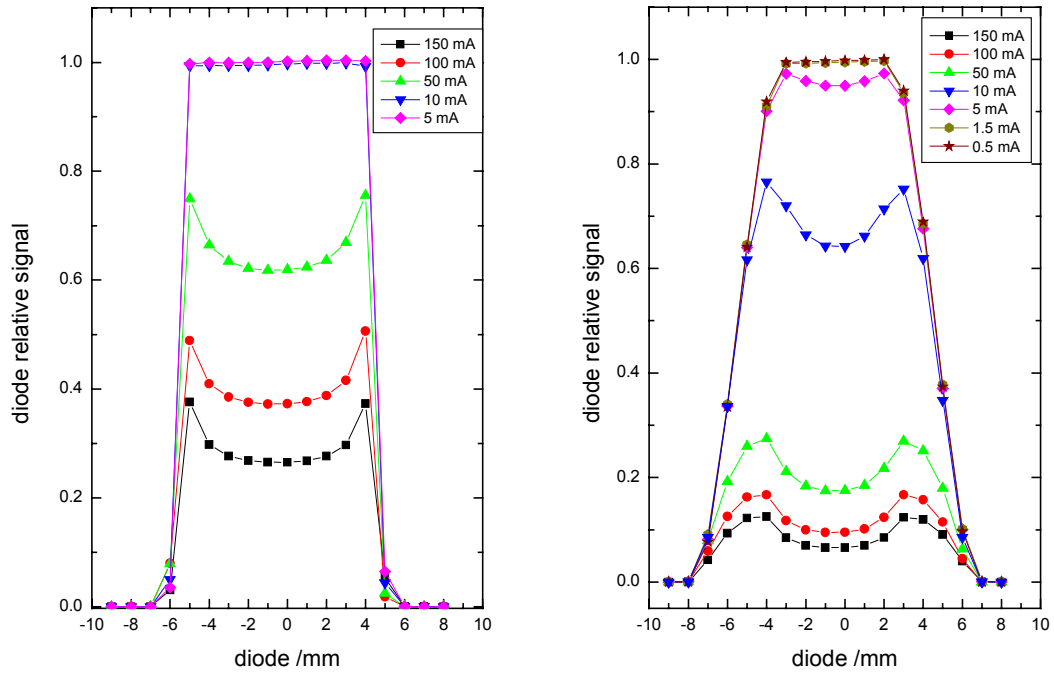

Figure 1. Diode photocurrent normalized to input power as a function of the position of the photodiode measured for different stored electron currents (see insets). Shown are measurements for aperture sizes of 1 mm (left) and 4 mm (right).

Recently, we have shown that the maximum irradiance for a linear operation of the photodiode (1 % relative saturation) increases from 30 mW/cm² for the 6 mm aperture to about 2 W/cm² for a 0.25 mm aperture. The behavior was explained by a change in the effective serial resistance with photon beam size. This effect can be attributed to the finite conductivity of the thin front contact layer carrying the current to the electrode [2]. This result was derived from a simple model for the diode based on an equivalent electrical circuit with an electrometer. In this circuit the photodiode is characterized mainly by its equivalent serial resistance (for details see reference 2). A detailed comparison of our new position dependent data with this model is under way.

[1] H. Rabus, V. Persch, G. Ulm, Appl. Opt. **36**, 5421 (1997)

[2] F. Scholze, R. Klein, R. Müller, Proc. SPIE **5374**, 926 (2004)

[3] F. Scholze et al., Proc. SPIE **4344**, 402 (1998)

[4] R. Klein et al., Synchrotron Radiation News **15**, 23 (2002)

[5] A. Gottwald, R. Müller, A.A. Sorokin, M. Richter, G. Ulm, Meas. Sci. Technol. **15**, 437 (2004)

Status and Improvements of the Reflectometer for Large EUVL Optics at PTB

C. Laubis, F. Scholze, G. Brandt, A. Fischer, S. Plöger, F. Scholz, H. Wagner and G. Ulm.

Physikalisch-Technische Bundesanstalt, Abbestraße 2-12, 10587 Berlin, Germany

The EUV reflectometer for large optics[1] of up to 550 mm and 50 kg went into its second year of operation. Now lithography in the extreme ultraviolet (EUVL) is entering the next stage towards industry implementation[2]. The first tools are actually being built[3]. To ensure that all mirrors are in spec metrology is ever-important. In 2004 we did 2269 hours of measurement at the PTB soft X-ray beamline and added new capabilities to the EUV reflectometer[4]: Simultaneous photocurrent measurements and improved reproducibility of wavelength using the Kr $3d_{5/2}$–5_p resonance of a gas-filter as wavelength reference.

The simultaneous measurement of reflectance and photocurrent offers new analytical capabilities for the multilayer characterization. The simple model for wavelength-dependent photocurrent of normal incidence EUV-mirrors is a standing wave created by the incident and the reflected beam. As the penetration depth of the light depends on the wavelength, the phase of the standing wave at the surface of the mirror will change with the wavelength. Thus the photocurrent is a sensitive means to get information on surface layers[4,5]. Figure 1 shows measurements for one 65(Mo/Si) mirror in March 2002 and August 2004. The spectral reflectance curves are nearly identical. It was, however, recently demonstrated that the photoelectron current from the mirror surface can be used to determine the thickness of surface layers, e.g. the build-up of carbon contamination. The phase-shift of the photocurrent curve clearly indicates an increase in top layer thickness by about 0.2 nm only.

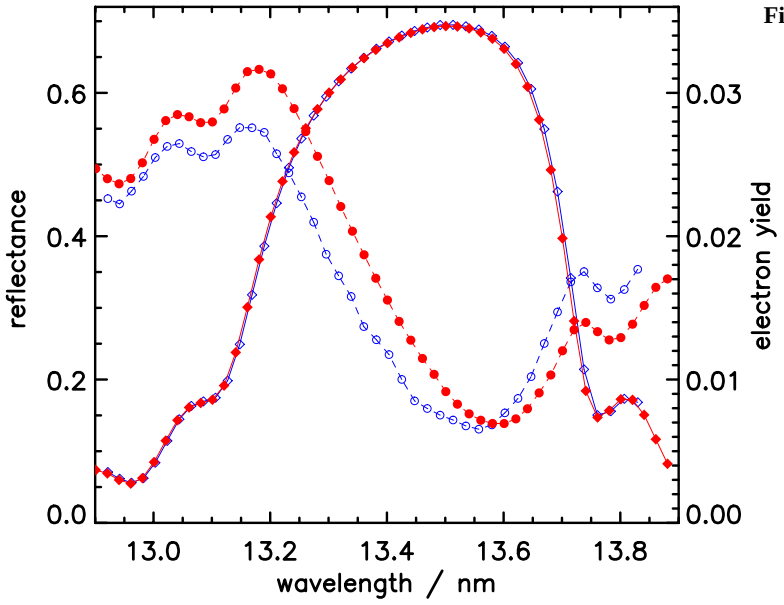

Figure 1 Reflectance of a mirror measured in March 2002 (open diamonds) and August 2004 (closed diamonds). The diamonds are the spectral reflectance, left scale. The circles (open and closed respectively) are the photocurrent signal, right scale. The reflectance curve is almost identical; the phase-shift of the photocurrent curve indicates an increase in top layer thickness by about 0.2 nm.

The repeatability of the wavelength measurement is only determined by the statistical fluctuations of the measured reflectance which influence the determination of the centre wavelength[4]. The dominating contribution for the reproducibility comes from drifts in the over-all beamline alignment. We therefore routinely check the wavelength by measuring the absorption edge of the Be-filter. If the measured wavelength differs by more than 1.9 pm from

the value of 11.080(1) nm, the monochromator is re-aligned[6]. This hard boundary corresponds to a 1-σ value of 1.1 pm. In 2004 we introduced a gas filter into the beamline to enhance our reproducibility of wavelength. The main difference between the wavelength measurement for the mirrors and the Be-edge is that the edge is an asymmetric feature. The determination of the edge position is compromised by offsets in the signal, e.g. changes in the dark current. For an almost symmetric feature like the multilayer reflectance curve, an offset in the signal would influence both sides of the peak in a similar way such that the centre remains the same. Therefore, we tried to replace the Be-edge by another wavelength reference. It would be much better to have a symmetric feature for the wavelength-reference as well. The most direct way is to use the Kr $3d_{5/2}$-5_p absorption resonance at 13.5947(15) nm[7], which is used as the absolute wavelength reference. To be able to introduce this new feature into the beamline without compromising any of our standard procedures we built a gas filter, see Figure 2, which can be moved in and out of the beam. Figure 3 shows a wavelength scan of the Kr gas filter.

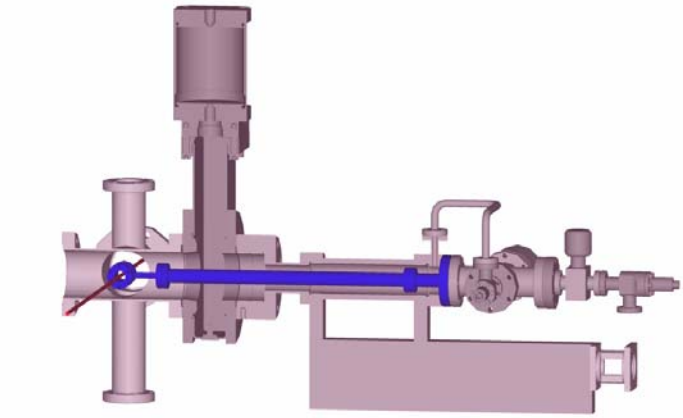

Figure 2 Retractable gas filter for the PTB EUV beamline. Beamposition is indicated in dark red on the left side, movable arm of the gas filter is shown in blue. The movable part can be retracted and shut off from the beamline vacuum.

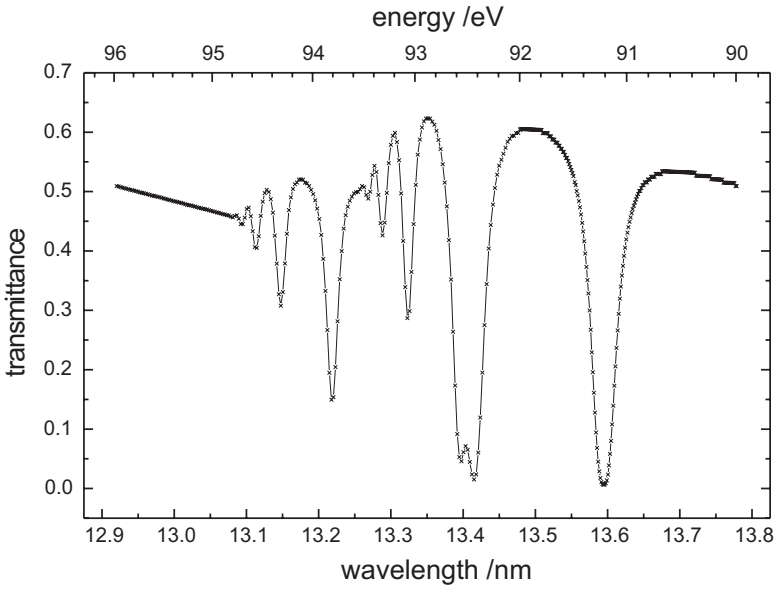

Figure 3 Scan of the Kr $3d_{5/2}$-5_p absorption. The Kr $3d_{5/2}$-5_p resonance can be seen at 13.595 nm.

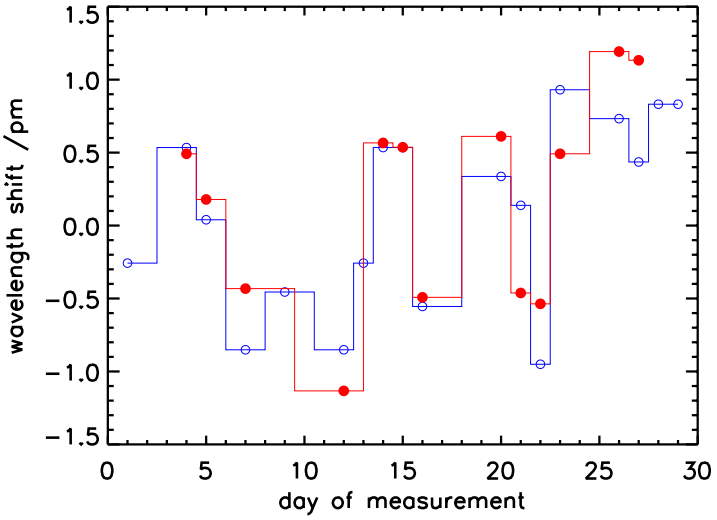

Figure 4 Comparison of the measured wavelength shift of the monochromator using the Kr 3d5/2-5p absorption resonance at 13.5947(15) nm (closed circles) and the Be K-edge at 11.080(1) nm (open circles).

Figure 4 shows the comparison of measurements of the Be K-edge wavelength and Kr $3d_{5/2}$-5_p. Both measurements with respect to the Kr resonance and the Be- edge wavelength show the same trends. The measurement using the Kr-resonance, however, seems to have less noise. The good agreement of the absolute numbers only reflects that we traced the absorption wavelength of our filter foils to the rare gas absorption resonances since there were no reliable data with low uncertainty available in the literature and the metal foils might suffer from chemical shifts of the absorption edges in the oxide layers.

Acknowledgement

The authors gratefully acknowledge the help of Alexander Glatz for construction of the mechanical and vacuum system of the gas filter during his practicum. We thank the BESSY staff for reliable operation of the storage ring as an essential prerequisite for high-accuracy measurements.

References

1 J. Tümmler, F. Scholze, G. Brandt, B. Meyer, F. Scholz, K. Vogel, G. Ulm, M. Poier, U. Klein and W. Diete, "New PTB reflectometer for the characterization of large optics for the extreme ultraviolet spectral region", Proc. SPIE **4688**, 338 – 347 (2002)

2 E. Zoethout, P. Suter, R.W.E. van de Kruijs, A.E. Yakshin, E. Louis, F. Bijkerk, H. Enkisch, S. Müllender, "Subatomic accuracy in EUVL multilayer coatings", Proc. SPIE **5374**, 892 – 896 (2004)

3 H. Enkisch and J. Trenkler, "EUV lithography: technology for the semiconductor industry in 2010", Europhysics News **9/10**, 149-152 (2004)

4 F. Scholze, C. Laubis, C. Buchholz, A. Fischer, S. Plöger, F. Scholz, H. Wagner and G. Ulm, "High accuracy EUV reflectometry at PTB", 3rd EUVL Symposium, 1. – 4. November 2004 , Miyazaki, Japan

5 R. van de Kruijs, E. Zoethout, E. Louis, A. Yakshin, I. Nedelcu, F. Bijkerk, S. Mullender, H. Enkisch, G. Sipos, M. Wedowski, M. Weiss, "Mo/Si multilayers for EUVL", PXRMS 2004: 7th International Conference on the Physics of X-Ray Multilayer structures, Sapporo 2004

6 F. Scholze, J. Tümmler, and G. Ulm, "High-accuracy radiometry in the EUV range at the PTB soft x-ray beamline", Metrologia **40**, S224 – S228 (2003)

7 G. King, M. Tronc, F. Read, R. Bradford, "An investigation of the structure near the L2,3 edges of Argon, the M4,5 edges of Krypton and the N4,5 edges of Xenon using electron impact with high resolution", J. Phys. B **10**, 2479-2495 (1977)

Micro-focus reflectometry at the PTB-PGM at the U49

Andreas Fischer, Frank Scholz, and Frank Scholze

Physikalisch-Technische Bundesanstalt, Abbestraße 2-12, 10587 Berlin, Germany

PTB's soft X-ray radiometry bending magnet beamline[1] was designed first of all for a parallel beam with reasonably low size. This was driven by the demand for high angular resolution also in the reflected beam for scatterometry applications. Also detector calibration using PTB's cryogenic radiometer requires a parallel beam[2]. For measurements at structured substrates and small detectors, however, a photon beam much smaller than 1 mm is needed. At the soft X-ray beamline, the practical lower limit for the photon spot size is about 0.2 mm (FWHM)[3].

A small focal spot can only be achieved with a rather short focal length. This is mechanically not compatible with the large EUV reflectometer[4]. Therefore, the refocusing unit was designed to be used at PTB's plane grating monochromator[1] with a smaller reflectometer. This smaller reflectometer can be used for samples up to 6" square, i.e. photomasks. To achieve a broad spectral band pass for the EUV range down to 5 nm, gold coated mirrors at 10° grazing incidence are used. Ray tracing showed that 10° is a sufficiently large angle to use toriodal mirrors for imaging. The double mirror system as shown in Figure 1 does not only provide an exit beam parallel to the input beam but also corrects for most of the aberrations. Ray trace simulation showed a nearly perfect image of the primary focus of the undulator beamline.

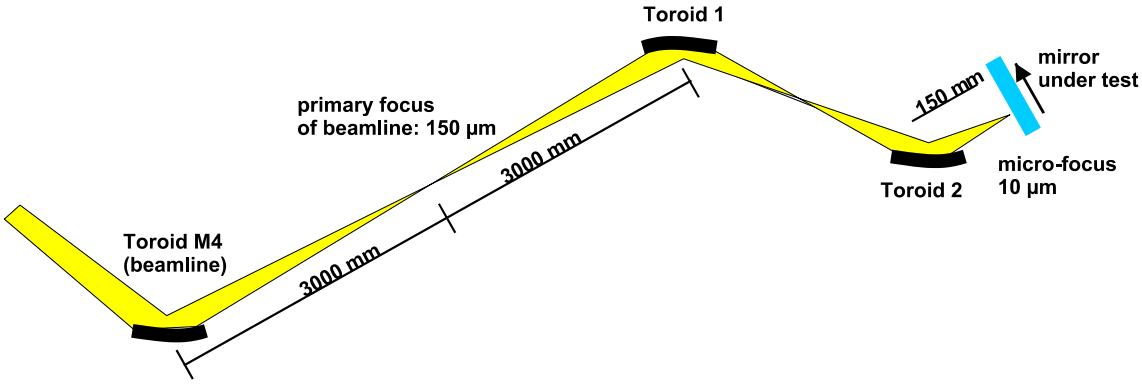

Figure 1 Refocusing unit with 20-fold demagnification installed behind the primary focus of the undulator beamline of PTB. A 10 µm focal spot is achieved.

The beam width was experimentally verified using the knife-edge method (see Figure 2). A FWHM of 10 µm is achieved as predicted by ray tracing. The broader background distribution is possibly caused by mirror aberrations and small angle scattering (flare). Most probably, however, it is an image of all the aberrations in the beamline already present in the primary focus. In our first attempt we omitted any small apertures to cut off the aberrations at the primary focus, because this would induce instabilities in the transmitted intensity in the case of any minor vibration or drift. Figure 3 shows the reflectance mapped for a reference mark at an EUV mask. The 25 µm wide lines are clearly resolved. The contours, however, are slightly distorted and the measured reflectance in the bright region is not completely flat. The reflectance cross sections also shown indicate that this is caused by the wings of the beam profile. Although this measurement is not yet perfect, it clearly indicates that bright or dark structures of about 50 µm to 100 µm square are sufficiently large to measure the local reflectance. This is substantially smaller than the 1 mm^2 size required at the radiometry

beamline and would allow to measure representative processing parameters for EUV mask production.

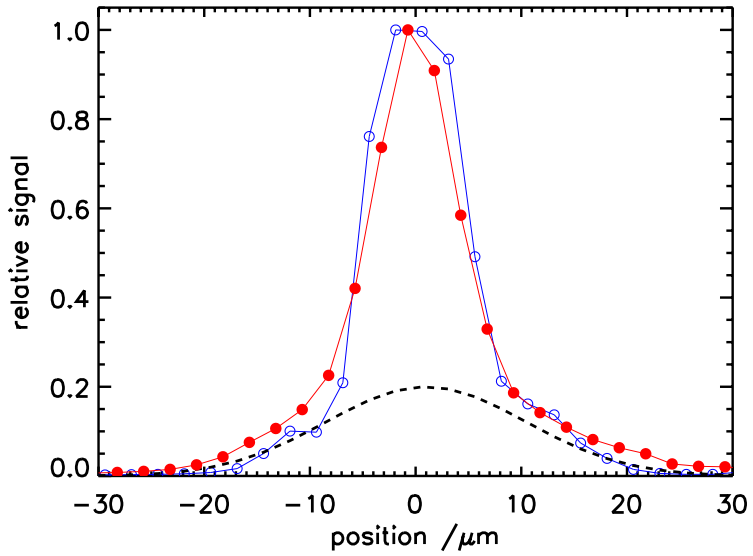

Figure 2 Knife-edge scans at the focal position. Shown is the derivated signal for a horizontal (closed circles) and vertical (open circles) scan. The FWHM is 10 µm for both measurements. A background component twice as wide is indicated by the dashed line.

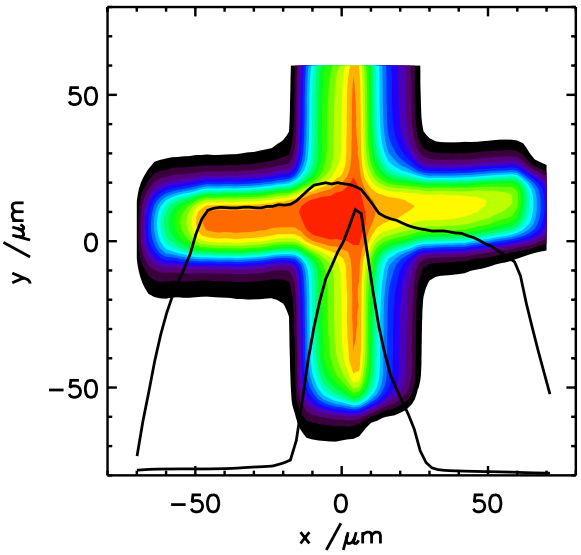

Figure 3 Mapping of the reflectance for a reference mark at an EUV mask. The bars of the cross are 25 µm wide. The contours are in steps of 5% relative reflectance. The lines show the reflectance profile at y-positions of -30 µm and 10 µm respectively. Here, the influence of the non-gaussian beam profile is clearly seen.

Another application of the micro-reflectometry option is the investigation of multilayer coatings close to the edge of the substrate. Figure 4 shows reflectance profiles at different wavelengths close to the edge of an EUV mirror coated by magnetron sputtering. It was known that differences in electrical potential between substrate and holder influence the sputtering process. With the mico-reflectometry we measured in detail the coating profile close to the edge. The double layer thickness decreases by 1 nm within about 0.5 mm from the edge.

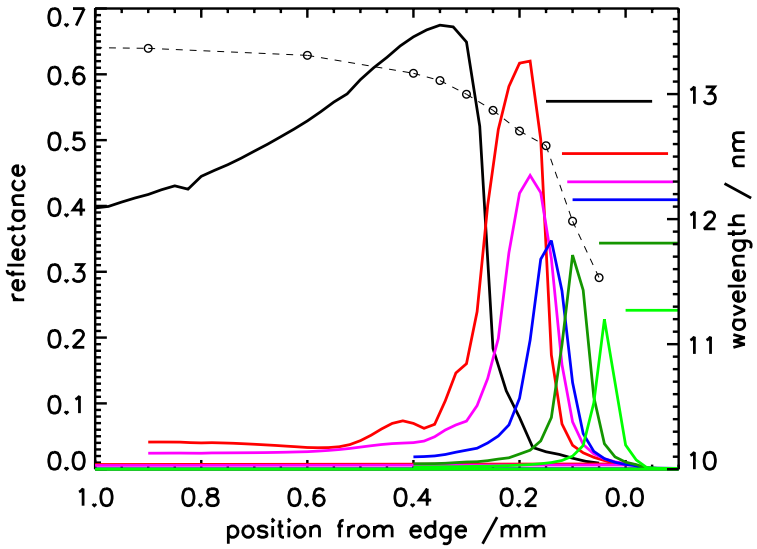

Figure 4 Reflectance (solid lines, left scale) close to the edge of the substrate measured at the wavelengths (right scale) indicated by the horizontal lines. The circles show the measured peak wavelength as function of position.

For spatially resolved reflectometry at structured or small samples, a new refocusing unit is installed at the PTB undulator beamline. A beam size of 10 µm FWHM was measured with the knife-edge test. The new facility enables, e.g., the characterization of processed EUV masks with representative size of bright or dark test fields.

Acknowledgement

The authors gratefully acknowledge the help of Tillmann Berg for the optical pre-alignment of the refocusing double mirror unit during his practicum.

References

1 F. Scholze, B. Beckhoff, G. Brandt, R. Fliegauf, A. Gottwald, R. Klein, B. Meyer, U. Schwarz, R. Thornagel, J. Tümmler, K. Vogel, J. Weser, and G. Ulm, “High-accuracy EUV metrology of PTB using synchrotron radiation,” Proc. SPIE 4344, 402 – 413 (2001)

2 F. Scholze, J. Tümmler, G. Ulm, "High-accuracy radiometry in the EUV range at the PTB soft X-ray radiometry beamline," Metrologia **40**, S224-S228 (2003)

3 J. Tümmler, G. Brandt, J. Eden, H. Scherr, F. Scholze, G. Ulm, “Characterization of the PTB EUV reflectometry facility for large EUVL optical components,” Proc. SPIE 5037, 265-273 (2003)

4 J. Tümmler, F. Scholze, G. Brandt, B. Meyer, F. Scholz, K. Vogel, G. Ulm, M. Poier, U. Klein, W. Diete, "New PTB reflectometer fort he characterization of large optics fort he extreme ultraviolet spectral region," Proc. SPIE 4588, 338 – 347 (2002)

Long-term reproducibility of reflectance measurements at Mo/Si-multilayer mirrors

Christian Laubis, Christian Buchholz, Andreas Fischer, Sven Plöger, Frank Scholz, Heike Wagner, Frank Scholze

Physikalisch-Technische Bundesanstalt, Abbestraße 2-12, 10587 Berlin, Germany

Long term stability of optical components is one of the key issues for the development of EUV lithography systems. For investigations of irradiation stability, the reflectance of a mirror is measured before and after irradiation. The time scale of these investigations is a few weeks. To detect changes that are small enough to extrapolate the measurements to a system lifetime of several thousands of hours requires a high reproducibility of the measurement and a high stability of the (un-illuminated) mirrors themselves. Therefore, PTB regularly measures the reflectance of a set of reference mirrors to detect any drifts in the measurements. Two mirrors without diffusion barriers 65(Mo/Si) bi-layers and six mirrors with diffusion barriers 60(Mo/B4C/Si/C) were coated by magnetron sputtering by Fraunhofer IWS in 2001. The peak reflectance and centre wavelength of these mirrors were measured for a period of 40 months.

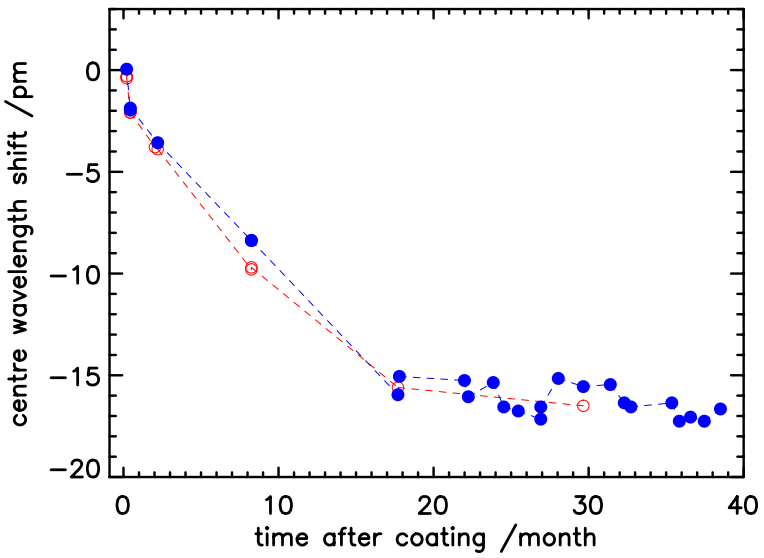

Figure 1 Measured shift of centre wavelength of two EUV mirrors with 65 (Mo/Si) bi-layers coated in June 2001. The standard deviation of the last points from month 18 on is 0.75 pm.

The measured wavelength (50% centre) for the reference mirrors is shown as function of time from coating in Figure 1 and Figure 2. For the two mirrors without diffusion barrier a significant shift of the wavelength was observed during the first 20 months. For the following time, the mirrors stabilized and the standard deviation of the wavelength for all measurements from month 18 on is 0.75 pm. The situation is different for the mirrors with diffusion barrier. Here, no significant shift in wavelength could be observed and the standard deviation of the wavelength measurements from month 18 on for all but two mirrors is 0.8 pm. The measurements always included the full cycle of mounting and alignment. All additional uncertainties from angle and temperature and also coating thickness inhomogeneities are thus included in the standard deviation of 0.8 pm derived here. This number is lower than the value of 1.1 pm used as criterion for the stability of the wavelength measurement at the Be K-edge[1].

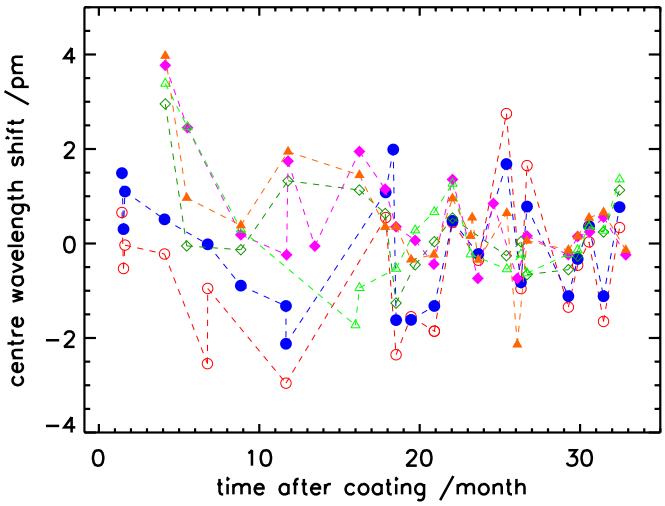

Figure 2 Measured shift of centre wavelength of six EUV mirrors coated with 60(Mo/B4C/Si/C) layers in December 2001. Data are normalized to the mean, because no significant shift is observed. The standard deviation for measurements after month 18 is 0.8 pm for all but two mirrors (open and closed circles).

The repeatability of the wavelength measurement is only determined by the statistical fluctuations of the measured reflectance which influence the determination of the centre wavelength[2]. The dominating contribution for the reproducibility comes from drifts in the over-all beamline alignment. We therefore routinely check the wavelength by measuring the absorption edge of the Be-filter. If the measured wavelength differs by more than 1.9 pm from the value of 11.080(1) nm, the monochromator is re-aligned[1]. This hard boundary corresponds to a 1-σ value of 1.1 pm.

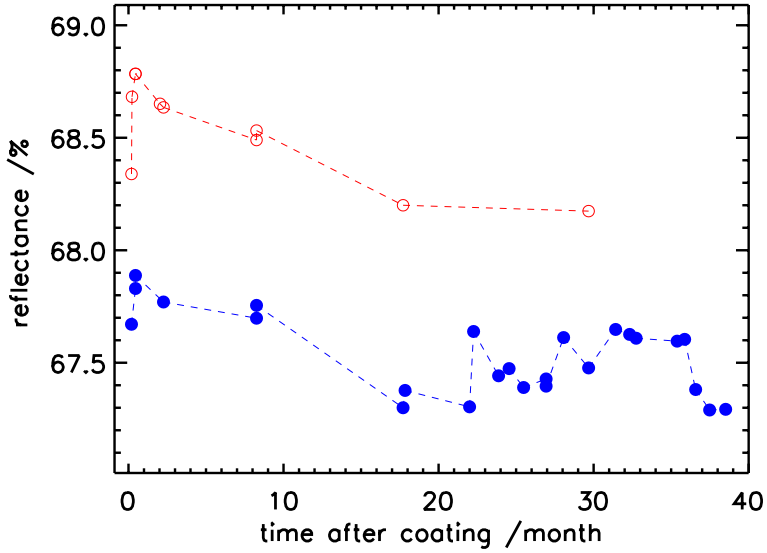

Figure 3 Measured peak reflectance of two EUV mirrors coated with 65 (Mo/Si) bi-layers in June 2001. The step in month 36 is caused by replacement of the detector photodiode. The values measured just before are too high due to increasing inhomogeneities of the old diode. The standard deviation for the data after month 18 is 0.18 %.

In Figure 3 and Figure 4, the measured peak reflectance is shown over a period of 40 months. The symbols used for the mirrors are the same as for Figure 1 and Figure 2. Here, the mirrors without diffusion barrier also show an initial degradation which stabilizes after 20 months. In the case of the mirrors with diffusion barrier, no significant drop in reflectance is observed for all but one mirror. The lower stability and homogeneity also reflects in the numbers for the standard variation of the measured reflectance.

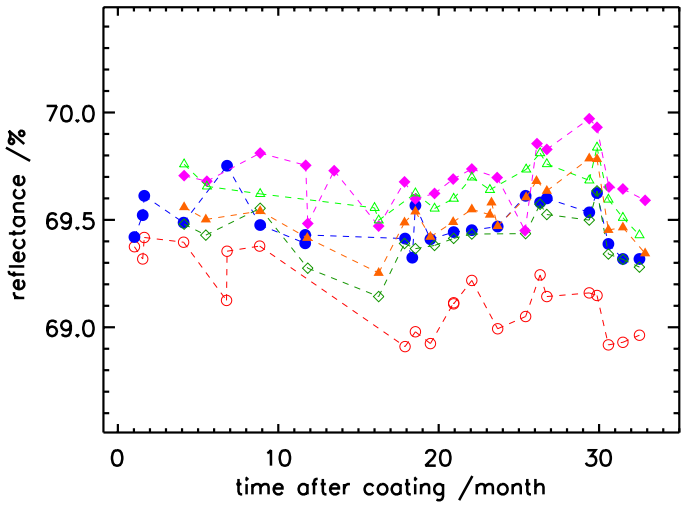

Figure 4 Measured peak reflectance of six EUV mirrors coated with 60(Mo/B4C/Si/C) layers in December 2001. The step in month 30 is caused by replacement of the detector photodiode. The values measured just before are too high due to increasing inhomogeneities of the detector diode. The standard deviation for all but one mirror (open circles) is between 0.11 % and 0.14 %.

For the mirrors with diffusion barrier this number varies between 0.11 % and 0.14 % while it is 0.18 % for the mirror without the barrier. The different reproducibility for the individual mirrors can be correlated to the mirror homogeneity. The absolute position of the mirrors in the sample holder is only reproduced within about 1 mm. Therefore, inhomogeneities of the mirrors influence the measured reflectance. This must be kept in mind if comparing these numbers with the value of 0.05 % given in ref.[1]. There is, however, a simultaneous significant drop in reflectance by about 0.25 % observed for all mirrors in month 30. This is caused by an increased uncertainty due to the inhomogeneity of the detector in the months before. There was increasing radiation damage in the centre of the detector. Due to our measurement geometry, the incident photon beam is smaller at the detector than the reflected beam. Thus our measured incident signal was too low with the incoming photon beam well aligned to the centre of the detector and correspondingly the measured reflectance increased. After observing this effect with our reference mirrors we figured out the reason, replaced the detector and reduced the interval for detector homogeneity tests.

A detailed analysis of measurements with a set of reference mirrors over a 40-month period showed that we reproduced the measured centre wavelength even better than suspected from our monitor measurements with the Be K-edge. For the measurement of the reflectance it turned out that a tighter control of the beam profile and detector homogeneity is needed to assure the reproducibility over long periods of time. The observed variation of the measured reflectance was, however, within our claimed total uncertainty, which actually is dominated by the contribution of scattered radiation.

References

1 F. Scholze, J. Tümmler, G. Ulm, "High-accuracy radiometry in the EUV range at the PTB soft X-ray radiometry beamline", Metrologia **40**, S224-S228 (2003)

2 F. Scholze, C. Laubis, C. Buchholz, A. Fischer, S. Plöger, F. Scholz, H. Wagner and G. Ulm, "High-accuracy EUV reflectometry at PTB", 3rd EUVL Symposium, Miyazaki Japan (2004)

Design and fabrication of diffractive X-ray optics at BESSY.

Alexandre Firsov[a], Alexei Erko[a], Bernd Loechel[a], Daniel Schondelmaier[a], Ingrid Wichert[a],
Thomas Blume[a],Alexandre Svintsov[b],
[a]BESSY GmbH, Albert-Einstein-Str. 15, D-12489, Berlin, Germany.
[b]Institute of Microelectronics Technology (IMT) RAS, 142432, Chernogolovka, Moscow distr., Russia.

The concept of the design and fabrication of X-ray diffraction focusing elements for the new BESSY beamlines is discussed. This concept includes both reflection types of optics as well as equipment necessary for their fabrication.

The project closely connected with the construction of new beamlines at BESSY. These are: the Microfocus Beamline with down to sub-micron spatial resolution in the energy range of 1.9 keV - 30 keV and the 'slicing' time-resolved beamline for the energy range of 700 eV – 900 eV, were only one optical element, reflection zone plate, is used for focusing and energy dispersion simultaneously. Surface structure variations of diffractive optical elements for different energy ranges require specific technologies. The IMT RAS - BESSY project on advanced diffraction X-ray optics based on the long-time experience of the IMT RAS in diffraction optics developments and technological potential and laboratory equipment of the BESSY Application Center for Microtechniques, which started its operation in November 2001.

At the new-designed BESSY Microfocus Beamline, the horizontal beam focusing is achieved with the help of a sagittal Bragg-Fresnel lens for micro small angle x-ray scattering (μSAXS) experiments (figure 1). Several Bragg-Fresnel lenses are placed on the second monochromator crystal, in our case Ge (111), which provides about 30% higher flux in comparison with a Si (111) crystal.

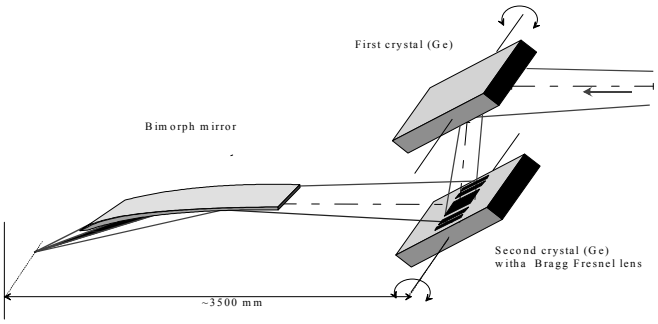

Figure 1. μSAXS focusing system employing a Bragg-Fresnel lens and bimorph mirror.

A linear Bragg-Fresnel lens on a crystal substrate was suggested and tested several years ago [1]. The first tests were done on the structures etched in a Si crystal to produce a π phase shift, necessary for an effective diffraction focusing [2]. The main problem in using such a structure for microfocusing was a very large depth of profile necessary to achieve the optimal phase shift. For Ge (111) at 10 keV the depth reaches 0.6 μm. One needs to use an etching technology with a very high aspect ratio to obtain a reasonable lens aperture, which is defined by the minimum zone width. Several attempts were made to produce a special "incline" profile to improve zone plate acceptance and resolution. Recently this problem has been solved using metal coating technology [3].

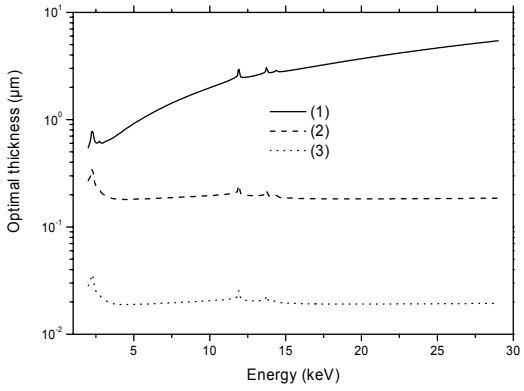

Figure 2. Optimal thickness of a gold layer vs. photon energy for a transmission zone plate (1) and two Bragg-Fresnel lenses on a Si (111) (2)and a multilayer substrate (3).

A Fresnel structure was fabricated using a metal coating on a perfect Si (111) crystal in the shape of a Fresnel zone plate. In the case of such a coated zone plate the beam is transmitted twice through the thickness of a metal coating at the Bragg grazing angle θ_B. In comparison with transmission zone plates the value of the optimal thickness is reduced by the factor of $0.5\sin(\theta_B)$.

The difference in optimal thickness is most considerable for high energies. A comparison of the theoretical value of the optimal thickness for the transmission zone plate and two types of Bragg Fresnel lens is shown in figure 2. As the Bragg-Fresnel lens substrate we chose a Si (111) crystal with the lattice period of 0.31 nm and a multilayer mirror with a period of 3 nm. According to figure 3 even with the technology with an aspect ratio of about 1:1 (layer thickness equal to a groove width) an outer zone width of the Bragg-Fresnel lens at 30 keV can reach 0.2 μm. It can be easily fabricated for the photon energies as high as 100-200 keV, which is a great problem for conventional zone plates due to the very high material thickness required.

The combination of the linear BFL and bimorph mirror in meridional direction allows a small-range energy scan without a loss in spatial resolution. Several lenses fabricated on the same substrate will cover the entire operational energy range of the beamline. Special attention must be paid to beam position stabilisation for the microfocus experiments.

Figure 3 shows a Ge (111) single crystal monochromator with and gold structure of reflection zone plates.

Elliptical zone plates fabricated on a mirror surface, so-called "reflection zone plate" (RZP), can be effectively used for an x-ray monochromatizsation and beam focusing at the photon energies below 1000 eV. This element can be applied in the beamlines with a specific beam conditions such as very high thermal and radiation load or very low flux and necessity to use only one optical element in an optical design to reduce a loss.

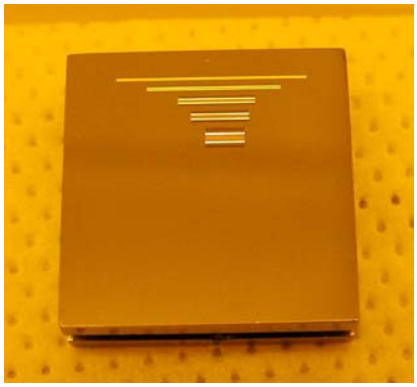

Figure 3. Lenses for energy 24.34 keV, 16.11 keV, 8.98 keV, 7.11 keV, 4.04 keV. Focus distance is 310 centimeters. Last zone size is 300 nanometers.

It is important, that the RZP must be off-axis, to provide best energy and spatial resolution. Development of an off-axis RZP at BESSY closely connected with a new project of the BESSY low-energy free-electron laser and ultra-high time resolved experimental beamline at the "time-slicing" undulator. In figure 5 an optical scheme of a focusing monochromator exploring off-axis RZP is shown. The lens with the size of 86 mm x 10 mm has a focal length of 9 m. Variable groove period in the central part of the lens is on the order of 18 μm and in the outer part about 1.3 μm.

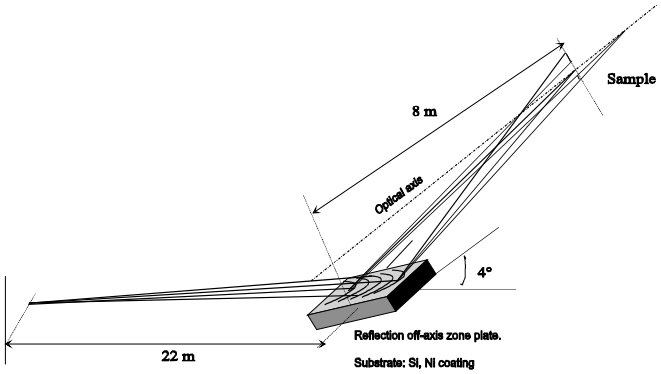

Figure 4. Optical layout of the reflection zone plate monochromator.

The lens is designed using the same software, as a Bragg-Fresnel lens. A silicon substrate is covered by a gold layer with a thickness of 50 nm, the depth profile 10 nm. The technology of the lens fabrication includes e-beam lithography for photo-mask, photo-lithography, and ion etching. A substrate is mono-crystalline silicon with a slope error of 0.2 arcsec and roughness of 0.2 nm RMS. The monochromator for the slicing beamline is shown in figure 5.

All the above mentioned optical elements have been fabricated at the BESSY Application Center for Microtechnology. Electron beam writing was done with an electron scanning microscope LEO 1560 equipped with a pattern generator and software from "Interface ltd", Moscow. The magnetron sputtering system BESTEC was used for metal coating. The system Plasmalab 80 Plus by OXFORD Instruments consists of plasma etching installation based on ICP source and plasma deposition installation based on ICP source and was used for etching in oxygen plasma before metal coating and Si_3N_4 membrane creation. A Kaufman ion source was used for ion milling processes to transfer pattern via resist mask. Resist coating technique as well as photolithography installations and electron scanning microscope LEO 1560 are placed in a clean room.

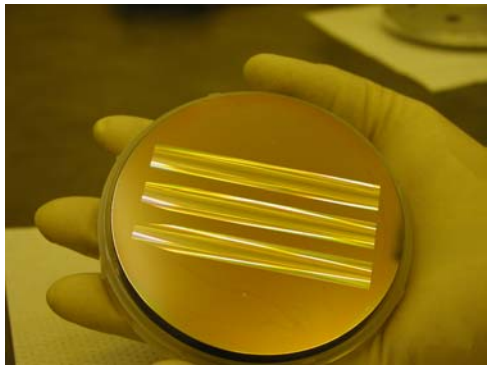

Figure 5. Lenses for energy 715 eV, 785 eV, 861 eV. Focus distance is 902 centimeters. Last zone size is 1 μm.

1. V. V. Aristov, A. A. Snigirev, Yu. A. Basov, and A. Yu. Nikulin, X-ray Bragg optics, AIP Conference Proceedings, **147(1),** (1986), 253-259

2. V. V. Aristov, Yu. A. Basov, S. V. Redkin, A. A. Snigirev and V. A. Yunkin, Bragg zone plates for hard X-ray focusing, Nuclear Instruments and Methods in Physics Research, **B261(1)**, (1987)**,** 72-74

3. A. Firsov, V. Aristov, A. Asryan, A. Erko, M. Ferstl, W. Gudat, S. Shapoval, A. Svintsov "Crystal-based diffraction focusing elements for third-generation synchrotron radiation sources", Nuclear Instruments and Methods in Physics Research **A 467-468** (2001) 366-369.

Determination of GBL content in SU-8 layers using FTIR microspectroscopy

JOSEF KOUBA, MARTIN SCHMIDT, ULRICH SCHADE, DANIEL SCHONDELMAIER

BESSY GmbH, Albert-Einstein-Strasse 15, 12489 Berlin, Germany
E-mail: josef.kouba@bessy.de, Tel: +49-30-6392-3125

Introduction

SU-8 is an epoxy-based, chemically amplified, negative resist suitable for fabrication of microstructures using UV- and X-Ray lithography [1] especially for fabrication of high aspect ratio structures. In order to fabricate these structures, a thick layer (up to several millimeters) of SU-8 resist is exposed to X-Ray radiation through a mask. In the exposed regions, photo-initiator present in the resist decomposes and forms free radicals causing the epoxy to cross-link and become chemically insoluble. In the subsequent step, the non-exposed resist is dissolved using a proper developer leaving the exposed structures intact.

In order to prepare thick layers of SU-8, solid SU-8 epoxy is dissolved in GBL (gammabutyrolacton), spin-coated on the substrate and baked in order to evaporate the solvent. After the baking step, solvent concentration ranges from 0 to 10 % depending on baking conditions. Furthermore, the distribution of solvent over the resist height is not constant since the solvent can only evaporate in the topmost layer.

Remaining solvent concentration is an important factor for the further fabrication process of microstructures since it has a strong impact on the diffusion of decomposed radicals. Due to high complexity of the exposure process and related chemistry, it is crucial to know the exact remaining solvent concentration, especially the distribution. This information is one of the key parameters for further improvement of the lithographical process using SU-8.

Experimental setup

To determine the solvent distribution over the height of the resist, Fourier Transfer Infrared (FTIR) microspectroscopy was used. The measurements were carried out at the IRIS Beamline which provides brilliant synchrotron IR radiation and which is equipped with a Nicolet Nexus 870 FT-IR spectrometer and a SpectraTech Continuμm microscope allowing IR vibrational microspectroscopy with a diffraction-limited spatial resolution [2].

Measurements were performed in transmission with the samples placed on a CaF_2 substrate using the bare CaF_2 as reference. For initial tests the conventional globar source was used and spectra of single sample points were recorded at a spatial resolution of 70 μm, a spectral resolution of 4 cm^{-1} and co-adding 128 scans each. For mapping of areas, the brilliant synchrotron IR radiation was used to obtain a spatial resolution of 15μm. A step size of 15 μm was chosen, for each sample point 64 scans were co-added and spectra were recorded with a spectral resolution of 16 cm^{-1}. Background spectra for normalization of beam current and instrumental drift were collected after every 3rd sample spectrum.

Experimental results

In order to evaluate the possibility to determine GBL solvent in SU-8 resist, absorption spectra of fully dry SU-8 resist and not completely dry film were taken. SU-8 films were prepared by spin-coating the SU-8 resist and baking it under different conditions. The amount of remaining GBL was evaluated by weighing the samples before and after bake. Figure 1 shows the spectra of 15 μm thick (a) fully dried resist film and (b) film containing approximately 15 % (wt.) of GBL. A characteristic band at 1775 cm^{-1} corresponding to the C=O stretching vibration of GBL is clearly visible in the chart (b). Since

there is no corresponding band in the spectra of dried SU-8, this band can be used as a marker to evaluate GBL concentration in the film. Also, it was tested for possible solvent evaporation and spectra for single points were recorded repeatedly over several hours and were found to be reproducible.

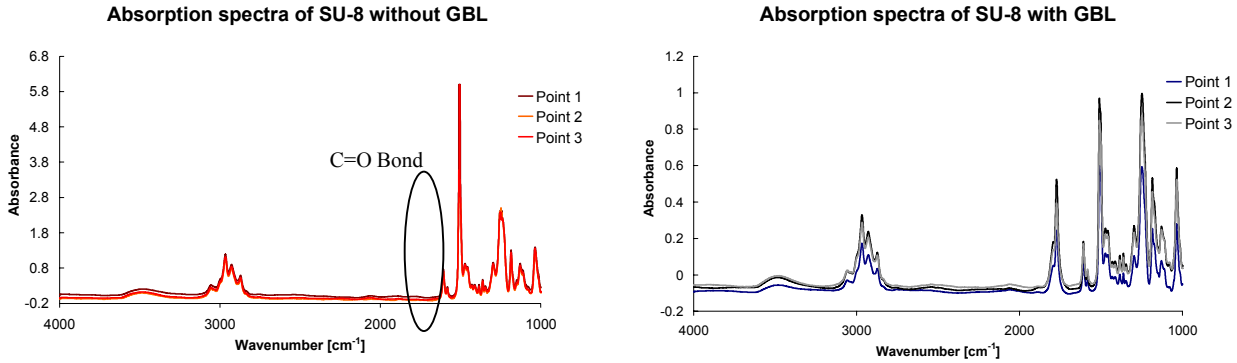

(a) **(b)**

FIGURE 1 – Absorption spectra of SU-8 resist (a) without and (b) with GBL. Spectra in (b) have a clear absorption band at 1775 cm^{-1} showing the possibility to determine the presence of GBL in SU-8 resist

In order to evaluate the distribution of GBL solvent in the resist film over its height, 1 mm thick layers of SU-8 were prepared on Kapton films and sliced using a microtome. In such a way, 10 – 20 µm thick slices were prepared. To evaluate the remaining GBL concentration maps showing to the integrated signal intensity between 1700 and 1850 cm^{-1} corresponding to the GBL C=O bond stretching were obtained. Figure 2 shows the map of remaining GBL concentration in a 10 µm thick, 50 µm wide slice prepared out of 500 µm thick resist film. One can clearly recognize an increase in the signal closer to the Kapton substrate indicating expected behavior that the solvent concentration is not constant over the resist film thickness.

FIGURE 2 – Baseline-corrected map of integrated band intensity between 1700 and 1850 cm^{-1} showing distribution of GBL concentration over the height of a 500 µm thick SU-8 film; higher concentration towards the substrate can be clearly observed

Conclusion

Synchrotron-based IR transmission microspectroscopy showed to be a suitable tool for investigation of GBL concentration in dried SU-8 resist films. The C=O stretching vibration of GBL could be used as a distinct marker for the detection of GBL in the resist film. Using this method, GBL distribution map over the entire thickness of a SU-8 resist film could be evaluated. Practical limitations for prepared samples were found to be the required thickness, which needs to be restricted to below 20 µm, and possibly sample thickness inhomogeneity.

References

1. Jian, L., et al. *SU-8 based deep X-ray lithography/LIGA*. in *SPIE*. 2003.
2. Schade, U., et al., Review of Scientific Instruments, 2002. **73**.

A Microfluidic System of a New Biosensor Chip for Measuring Antioxidative Capacity of Anti-Aging Products

A. Walter[a], N. Beisser[a], B. Loechel[a], A. Krylov[b], F. Lisdat[b], H. Adamzig[c], O. Pulz[d]
[a] Berliner Elektronenspeicherring-Gesellschaft für Synchrotronstrahlung mbH, Application Center for Microengineering, Berlin, Germany
[b] Universität Potsdam, Institut für Biochemie und Biologie, Potsdam, Germany
[c] Elbau GmbH, Berlin, Germany
[d] Institut für Getreideverarbeitung, Bergholz-Rehbrücke, Germany
e-mail: antje.walter@bessy.de, Tel.: +49-30-6392-4601, Fax: +49-30-6392-4682

Presently anti-aging products are an intensely discussed subject. Free radicals generated by UV-radiation in skin are the main reason of aging. These aggressive oxygen compounds affect healthy molecules in body and contribute to development of diseases. Substances with antioxidative activity in cosmetics and novel food products protect against attacks of free oxygen radicals. Antioxidants delay aging processes, decrease the risk of arteriosclerosis and are supportive of detoxication of carcinogenic agents in body [1]. Thus, detection of antioxidative substances becomes more important for the characterization of cosmetics and food products.
BESSY is partner in the BMBF InnoRegio project "Measurement of the antioxidative effectiveness of polydispersive systems in food and beauty treatment". In co-operation with the other project partners we have developed and fabricated a microfluidic system for an amperiometric biosensor chip. Main focus of our work was set on the mixer and on distances, in which flowing media including oxygen radicals were mixed with dissolved samples.
We have designed the mixer for manufactoring with methods of precision engineering and for the special requirements of the bioanalytic chip. The cosmetics and food products have to be dissolve before measurement of antioxidative activity can take place. Only a few solvents like dimethylsulfoxid and butandiole are usably for various composition of analyzing substances and custom-designed needs. High viscose flowing medium with low flow rates can adversely affect mixing. Therefore, we have engineered different mixer structures which fulfill our demands of good mixing.
Flowing medium and sample channel were brought together to one serpentine narrowed channel, in which free radicals and antioxidants were mixed. Two different mixers designs were tested: a two-dimensional acting meandering structure and a three-dimensional acting zigzag structure (see Figs. 1a and 1b). These mixers were formed in synthetic material by precision mechanics. The microfluidic system was milled in two base plates, which were adjusted and bonded together. The material of the whole biosensor chip was polymethylmetacrylate. Its advantages are transparency, reusableness and compatibility with used chemicals.
After testing the mixers by using various solvents and different flow rates we have integrated the structures in an analytic chip containing channels of different form and length (see Figs. 1c and 2). The two access channels, one for the flowing medium with oxygen radicals and one for dissolved sample, merge in the mixer. After leaving the mixer the liquids pass a measurement chamber containing special electrodes for detection of antioxidative activity. A final waste drain connects the measurement chamber with the outer supply system.

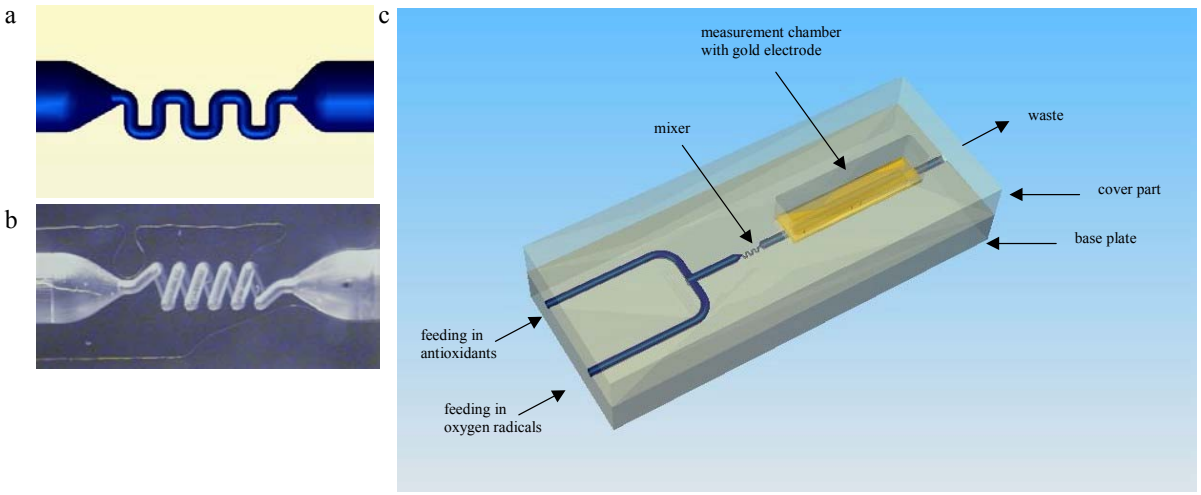

Fig. 1 Design of a) a two-dimensional acting meandering mixer and b) a three-dimensional acting zigzag mixer. c) Scheme of the biosensor chip for measurement of antioxidative activity

The basis for the measurement is the reaction of antioxidants with superoxid radicals generating by xanthine oxidase, which catalyzed conversion of hypoxanthine to uric acid. For the amperiometric radicale determination, a cytochrome *c* modified electrode was used [2, 3].
The described mixers have proved to be usable in biosensor chip for measuring the antioxidative activity of polydispersive systems like novel food products and beauty treatment.
Due to its simple designs the mixers are best qualified for use in various application systems. They are easy to manufacture also in different materials and can be used for mixing aqueous and high viscous liquids and can easily be integrated in other microfluidic systems.

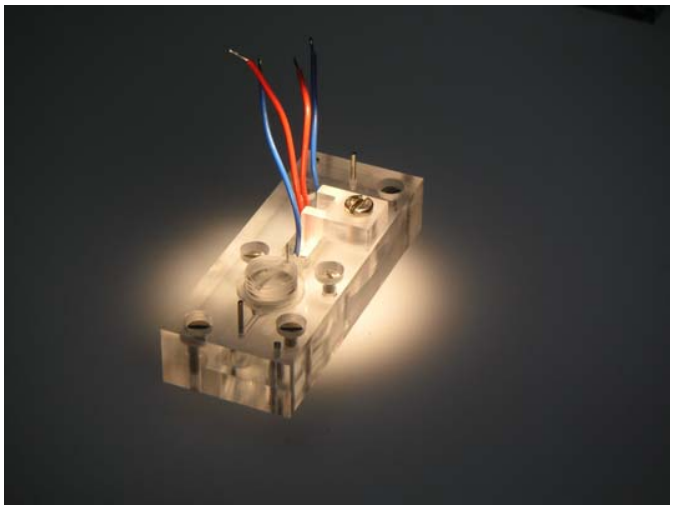

Fig. 2 Top view of the assembled biochip

References

1. Cooke M.S., Evans M.D., Mistry N., Lunec J., Nutrition Research Reviews 15 (2002): 19-41(23)
2. Lisdat F., Ge B., Reszka R., Kozniewka E., Fresenius J Anal Chem 365 (1999): 494-498
3. Ignatov S., Shishniashvili D., Ge B., Scheller F.W., Lisdat F., Biosensors and Bioelectronics 17 (2002): 191-199

Herstellen von Mikroschlitzplatten aus Nickel/Eisen

Martin Bednarzik und Ivo Rudolph

Bessy GmbH, Anwenderzentrum für Mikrotechnik, A. - Einstein - Str. 15, D - 12489 Berlin

Im ersten Quartal 2004 wurde aufgrund von Umstrukturierungen im Projekt MICROCOMP für Bessy eine Ni/Fe Galvanikanlage von der Firma Technotrans AG angeschafft (microform.100). Sie zeichnet sich insbesondere durch eine rotierende Kathode, eine Pulsstromquelle, eine automatische pH-Regulierung und durch eine automatische Eisenzudosiereinheit aus. Sie erlaubt das galvanisieren von Proben auf unterschiedlichen Substraten mit einem Durchmesser von 4 und 6 Zoll.
Die Maschine wurde im Reinraum des Anwenderzentrums für Mikrotechnik installiert. Nach einigen Folgearbeiten wurde der Testbetrieb aufgenommen. Er konzentriert sich vorerst auf Ganzflächenabscheidungen von 4 Zoll Siliziumwafern mit einer Ti/Au-Platingbase bzw. auf Stahlplatte. Dadurch konnten Aufwachsraten bestimmt und Stressmessungen bzw. die Durchbiegung des Wafers gemessen werden. In Abb. 1 sind zwei Graphen dargestellt, die die Aufwachsraten und die Durchbiegung des Wafers bei unterschiedlichen Stromdichten zeigen. Vorzugsweise wurden Schichten bis zu 300 µm galvanisiert.

Abb. 2 zeigt Bilder der im Reinraum des Anwenderzentrums für Mikrotechnik installierten Maschine. Das Labor verfügt jetzt unter anderem über zwei Anlagen zur Abscheidung von Kupfer, eine Anlage zur Abscheidung von Nickel und zwei Anlagen zur Abscheidung von Nickel/Eisen Legierungen. Die integrierte Pulsstromquelle erlaubt das schnelle Abscheiden unter minimalem Stress der aufwachsenden Ni/Fe Legierung. Erste gepulste Abscheidungen mit einem zusätzlichen Negativimpuls von nur wenigen Millisekunden sind vielversprechend.

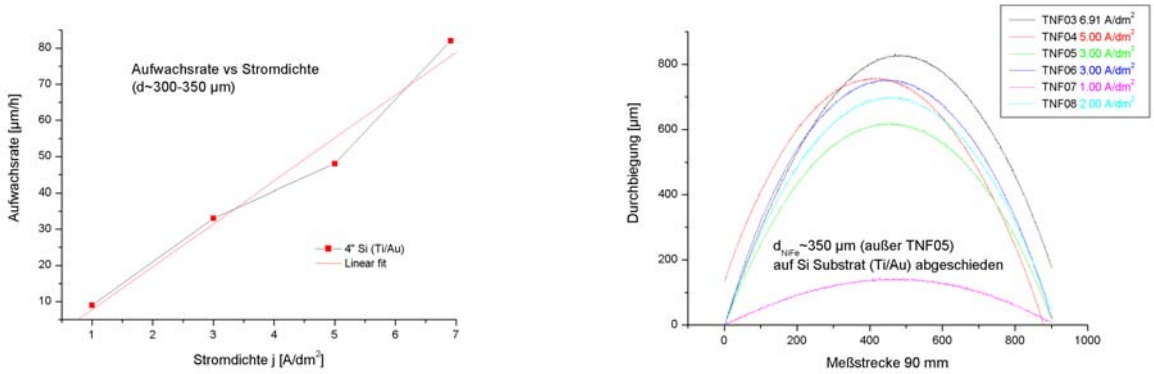

Abbildung 1: Bild links: Aufwachsrate in Abhängigkeit von der Stromdichte experimentell ermittelt, Bild rechts: Stressmessungen bzw. maximale Durchbiegung des Wafers in Abhängigkeit der Stromdichte

Abbildung 2: Fotos der im Reinraum installierten Technotrans Galvanikanlage microform.100

Im Rahmen des Projekts MICROCOMP sollen LIGA- Mischplatten für Schlitzplattenmischer hergestellt werden. Diese bestehen aus Nickel/Eisen und sollen 300 µm hoch sein. Die kleinsten zu galvanisierenden Strukturweiten betragen 10 µm. Der Projektpartner Ehrfeld AG lässt seine Schlitzplatten bei einem Zulieferer herstellen, der mit einem Laserschneidverfahren Metallplatten strukturiert und schneidet. Die kleinste realisierbare Schlitzbreite beträgt jedoch nur 100-200 µm. Um die Mischer effizienter zu machen sind kleinere Schlitzbreiten notwendig. An der Stelle bietet sich das direkt LIGA Verfahren an (Aspektverhältnis 30:1).

Der in Abb. 3 rechts abgebildete Wafer zeigt die ersten hergestellten Schlitzplatten vor der Vereinzelung. Die Probe ist mit einem Läppschritt auf 300 µm planarisiert worden. Nach der Belichtung eines photoempfindlichen Polymers durch eine Maske mit Synchrotronstrahlung wird die Probe entwickelt und kann galvanisiert werden. Das elektrochemische Abscheiden erfolgte mit der Pulsplating-Anlage, nachdem ein geeigneter Prozess gefunden wurde, der ein schnelles und stressfreies Galvanisieren erlaubt. Die Rate beträgt ~70 µm/h bei einer relativ großen zu galvanisierenden Fläche von 0.29 dm².

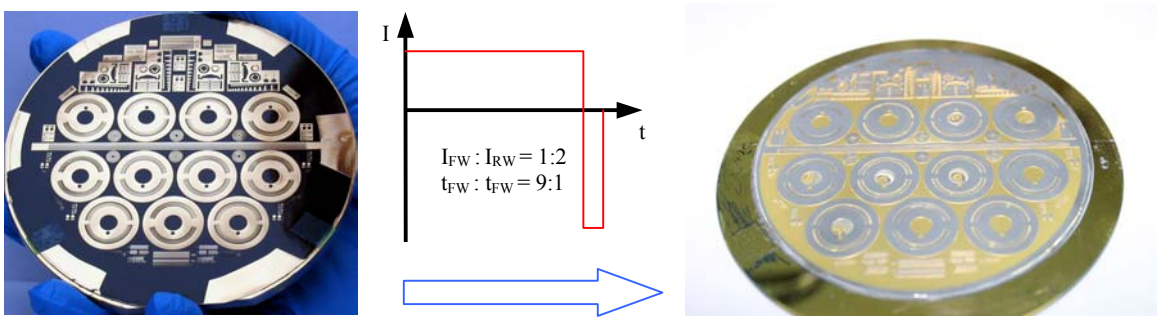

Abbildung 2: Das linke Bild zeigt die Röntgenmaske der Mischerplatten, die auch im Anwenderzentrum für Mikrotechnik hergestellt wurde. Im rechten Bild ist das Abbild mit den mit NiFe aufgefüllten Strukturen zu sehen. In der Mitte ist ein Pulsmuster angedeutet, welches zu sehr guten Resultaten führte.

THE VACUUM -UV PHOTOABSORPTION SPECTROSCOPY OF THE THREE-MEMBERED RING SYSTEMS C_3H_6, C_2H_4O and C_2H_4S AND THEIR OPEN CHAIN ISOMERS.

R. Locht[1], B. Leyh[1], H.W. Jochims[2] and H. Baumgärtel[2].

[1]Laboratoire de Dynamique Moleculaire, Départment de Chimie, Université de Liège, Institut de Chimie, Bât. B6c, Sart-Tilman par B-4000 Liège 1, Belgium.
[2]Institute für Physikalische Chemie, Freie Universität Berlin, Takustrasse 3, D-14195 Berlin, Germany.

During several years we investigated the vacuum UV photoabsorption, the He(I)- and threshold photoelectron spectra and the photoionization mass spectrometry of many halogenated derivatives of methane [1] and ethylene [2-4]. A very large amount of data has been obtained and their publication are in progress. These data were completed by laboratory work performed in Liège on the translational energy distribution measurements of most of the fragment ions appearing in the mass spectra recorded with He(I), Ne(I) and Ar(II) resonance lines.

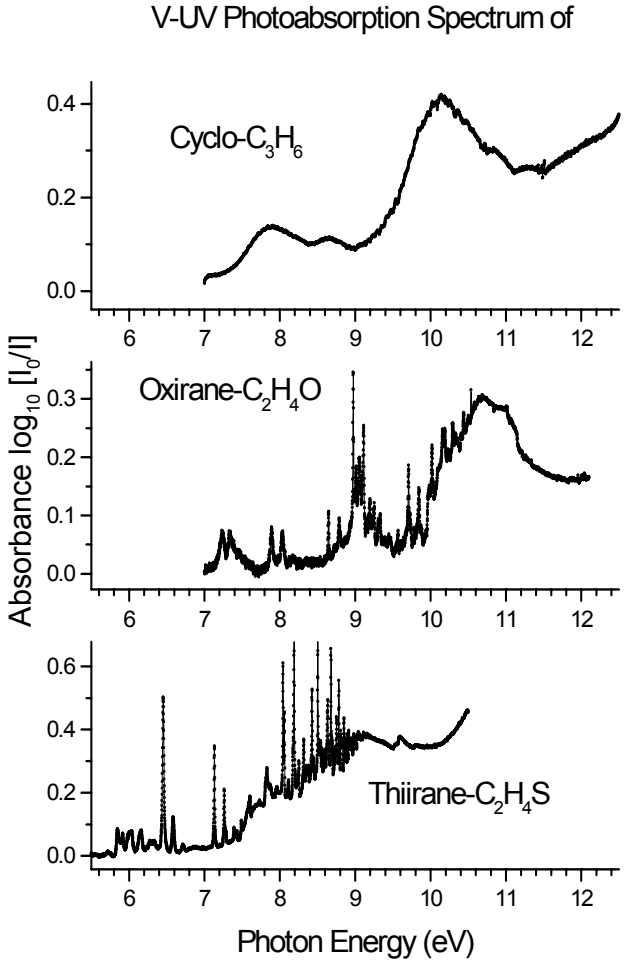

Fig. 1: Vacuum UV absorption spectra of cyclo-propane, oxirane and thiirane.

Another class of interesting small molecular systems are the three-membered rings: C_3H_6 or cyclo-propane, C_2H_4O or oxirane, C_2H_4S or thiirane and C_2H_5N or aziridine. Spectroscopic data related to these systems are very scarce in the literature. No high level quantum mechanical calculations are available. When stable, the open structured isomers are also worth being reinvestigated at higher resolution.

These are a few reasons of a thorough investtigation of the photoabsorption and mass spectrometric photoionization of these compounds. The data obtained at BESSY II were completed by laboratory experiments of He(I)-, Ne(I)- and Ar(II)-resonance line photoelectron and photoion kinetic energy spectroscopy of the fragments.

A 3m-NIM monochromator (on the 3m-NIM-2

beamline) was used, equipped with a 600 ℓ/mm Al-grating. A major disadvantage of this material, however, is its reflectivity gap between 16-18 eV. Entrance and exits slits were adjusted at 10-30 µm allowing a resolution of about 5 000. The photon energy was scanned between 5-25 eV.

Fig.1 shows typical exemples of photoabsorption spectra recorded between 5.5-12.5 eV for cyclopropane, oxirane and thiirane respectively. The high toxicity of aziridine prevent to introduce it in the experimental hall.

Excepting that of cyclopropane, the spectrum of the two other compounds show very sharp and strong features corresponding to Rydberg transitions accompanied by well resolved vibrational fine structure. A close examination of the broad absorption band peaking at about 10.12 eV in cyclopropane reveals also a vibrational progression. The detailed examination and interpretation of the experimental results and the assignment of all these features are in progress.

The photoabsorption spectra have been measured under the same conditions for the stable open chain isomers of C_3H_6 and C_2H_4O, i.e. propene and acetaldehyde.

Ackowledgments.

We gratefully acknowledge the European Community for a financial support through the Contract N° R II 33-CT-2004-506008. R.L. and B.L. wish to thank the Communauté Française de Belgique for an “Actions de Recherche Concertée” (A.R.C.) contract.

References.

[1]. R. Locht, B. Leyh, A. Hoxha, D. Dehareng, H.W. Jochims, H. Baumgärtel, Chem.Phys. **257** (2000) 283; ibid. **272** (2001) 259; **272** (2001) 277.
[2]. R. Locht, B. Leyh, K. Hottmann, H. Baumgärtel, Chem.Phys. **220** (1997) 217.
[3]. R. Locht, A. Hoxha, B.Leyh, K. Hottmann, H.W. Jochims, H. Baumgärtel, BESSY Jahresbericht (**1996**) 160.
[3]. A. Hoxha, R. Locht, B. Leyh, D. Dehareng, K. Hottmann, H. Baumgärtel, Chem.Phys. **256** (2000) 239.
[4]. R. Locht, B. Leyh, H.W. Jochims, H. Baumgärtel, BESSY Jahresbericht (**1996**) 156 ; ibid. (**1999**) 251; ibid. (**2003**) 49.

THE PHOTOIONZATION MASS SPECTROMETRIC STUDY OF THE THREE-MEMBERED RING SYSTEMS C_3H_6, C_2H_4O and C_2H_4S AND THEIR OPEN CHAIN ISOMERS.

R. Locht[1], B. Leyh[1], H.W. Jochims[2] and H. Baumgärtel[2].

[1]Laboratoire de Dynamique Moleculaire, Départment de Chimie, Université de Liège, Institut de Chimie, Bât. B6c, Sart-Tilman par B-4000 Liège 1, Belgium.
[2]Institute für Physikalische Chemie, Freie Universität Berlin, Takustrasse 3, D-14195 Berlin, Germany.

A previous contribution to this volume [1] reported about a the investigation of three-membered ring systems, i.e. Cyclopropane, Oxirane and Thiirane. We briefly described their V-UV photoabsorption spectra. These are essential tools for the understanding of the photoionization of these molecules which will briefly be reported here. The same work has been performed for the open chain isomers, i.e. propene and acetaldehyde. The thio-derivative corresponding to the latter compound is very unstable and therefore could not be investigated here.

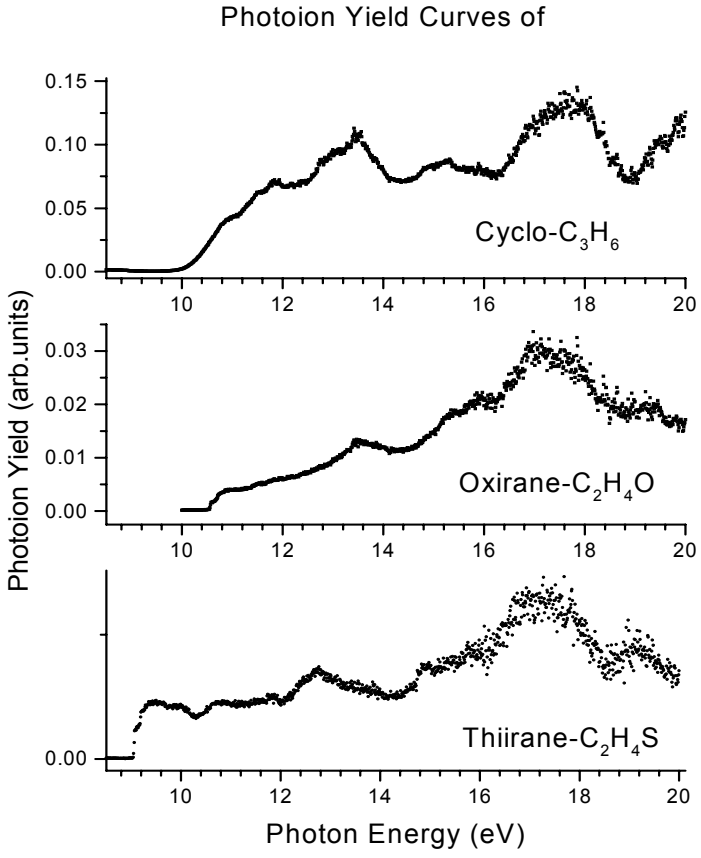

Fig.1: Photoionization efficiency curves of the Cyclopropane, Oxirane and Thiirane molecular ions.

The most extensive photoionization study dedicated to two of these molecules, i.e. C_3H_6 and C_2H_4O (ring and open chain isomers), has been published by Kraessig et al. [2] using synchrotron radiation. Most of the fragmentation pathways were considered. More recently, a low resolution dissociative photoionization study of Oxirane by synchrotron radiation has been reported [3], completed by quantum mechanical calculations. The threshold energy for almost all dissociation channels was measured.

For Thiirane the literature data are very scarce. Only one dissociative photoionization work, restricted to the molecular ion and two fragments, i.e. m/z=59 and m/z=45, has to be mentioned [4].

The present dissociative photoionization study has been performed on the 3m-NIM monochromator, equipped with a 600 ℓ/mm Al-grating and slit

widths adjusted at 20µm (resolution about 5 000).

Fig.1 shows the ionization efficiency curve for the three parent ions, i.e. of Cyclopropane, oxirane and thiirane respectively. Up to about 15 eV the signal/noise ratio is satisfactory. Above this energy this ratio decreases dramatically owing to the 90% reflectivity loss of the grating installed on the monochromator. However, the main and usually structureless features remain measurable. Fig. 2 displays the threshold region of the ion yield curve of $C_2H_4O^+$ and $C_2H_4S^+$ near threshold. The crude numerical first differential is inserted in this figure to compare the vibrational intensity distribution with that observed in the He(I) photoelectron spectrum measured in the laboratory. The modifications have to be ascribed to the contribution of vibrational autoionization to the population of the individual vibrational levels.

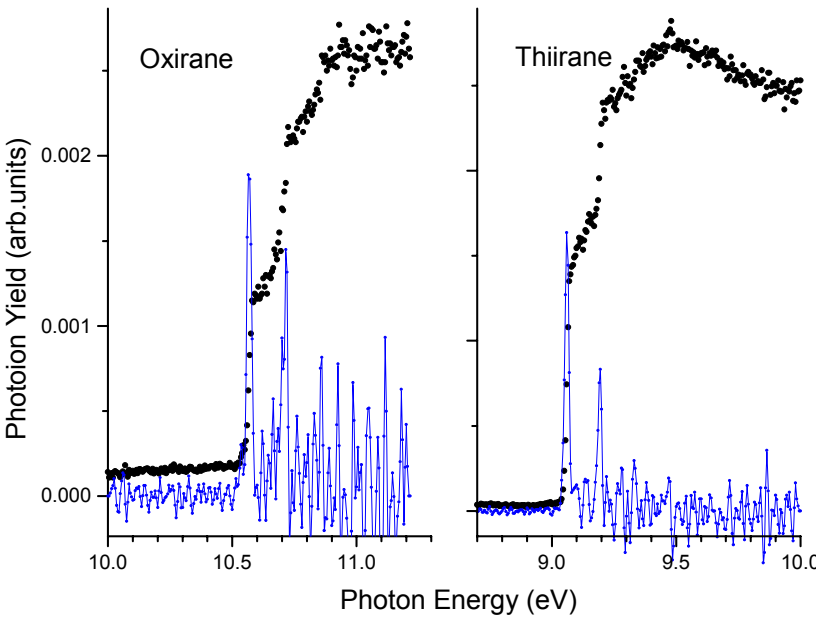

Fig.2: Direct (black) and numerically first differentiated (blue) photoion yield curves of $C_2H_4O^+$ and $C_2H_4S^+$ near threshold.

The ionization efficiency of all the fragment ions have been recorded as far as their intensity is larger than 1% of the total ionization. This work has been completed by the measurement of the kinetic energy distribution of these fragment ions at photon energies of 21.22 eV (HeI), 16.85 eV (NeI) and 13.47 eV (ArII).

Ackowledgments.

We gratefully acknowledge the European Community for a financial support grant through the Contract N° R II 33-CT-2004-506008. R.L. and B.L. wish to thank the Communauté Française de Belgique for an "Actions de Recherche Concertée" (A.R.C.) contract.

References.

[1]. R. Locht, B. Leyh, H.W. Jochims, H. Baumgärtel, BESSY Jahresbericht (**2004**).
[2]. R. Kraessig, D. Reinke, H. Baumgärtel, Ber.Bunsenges.Phys.Chem. 78 (**1974**) 116.
[3]. F. Liu, F. Qi, H. Gao, L. Sheng, Y. Zhang, S. Yu, K.C. Lau, W.K. Li, J.Phys.Chem. A (**1999**) 4155.
[4]. J.J. Butler, T. Baer, Org.Mass Spectrom. 18 (**1983**) 248.

Isotope Effect and Core Hole Localization in Homonuclear Molecules

D. Rolles, M. Braune, R. Hentges, S. Korica, A. Reinköster, J. Viefhaus, and U. Becker

Fritz-Haber-Institut der Max-Planck-Gesellschaft, Faradayweg 4-6, 14195 Berlin, Germany

The emission of core photoelectrons from homonuclear diatomic molecules can be interpreted as a molecular two-slit experiment. This was shown experimentally for the first time by our measurements of the laboratory and molecule frame angular distributions of the $1\sigma_g$ and $1\sigma_u$ photoelectrons in N_2 [1]. The indistinguishability of the two nuclei expressed in the inversion symmetry of the molecule leads to coherent emission of photoelectron waves from both molecular centers and to the resulting characteristic interference patterns in the $1\sigma_g$ and $1\sigma_u$ molecule frame photoelectron angular distributions reflecting the pure l-odd or l-even character of the gerade and ungerade core hole state (Fig. 1). This result can also be interpreted as a proof for the complete quantum mechanical *non-localization* of the remaining core hole in the molecule.

However, the question arises whether the coherent photoelectron emission and the core hole non-localization can be affected if the indistinguishability of the nuclei is destroyed. We therefore investigated the transition to the symmetry-broken system by comparing the natural $^{14,14}N_2$ nitrogen molecule to two different isotope substituted species, singly substituted $^{14,15}N_2$ and doubly substituted $^{15,15}N_2$. Using five rotatable electron time-of-flight (TOF) analyzers in the single bunch mode of BESSY at beamline UE56/2-PGM1 and UE56/1-PGM, we studied our sample gases by means of high-resolution angle-resolved photoelectron spectroscopy. Since the N($1s$)-doublet (Fig. 2a and b) with a splitting of less than 100 meV [2] had to be resolved while data was acquired over several days, the experiment required extremely high energy resolution of both the beamline and our setup as well as a very high photon beam stability.

The effects of the isotope substitution are best illustrated in the *ratio* of the photoelectron spectra of normal and substituted nitrogen (Fig. 2c and d) and can be grouped into two categories: The most obvious difference is a smaller vibrational constant in the isotope-substituted species (both experiment and model calculations yield a difference of about 5 meV in $^{14,15}N_2$ and 10 meV in $^{15,15}N_2$) due to an increased reduced mass. This leads to pronounced oscillations in the intensity ratios, which coincide with the position of the vibrational progression. A simulation of the vibrational effect (dashed line) reproduces those oscillations very well, but fails to explain the additional "wiggle" (shaded areas) at the high-energy end of the N_2/$^{14,15}N_2$ ratio, which is visible both in the ratio at the "magic angle" (Fig. 2c) as well as under 0 degree to the light polarization (Fig. 2d). This second effect, which does *not* appear in the N_2/$^{15,15}N_2$ ratio, can only be explained by a change in both relative intensity as well as angular distribution of the g and u components in $^{14,15}N_2$ compared to the two other species. A simulation including these changes (solid lines) reproduces the experimental data even at the high-energy end of the N_2:N($1s$) photo line.

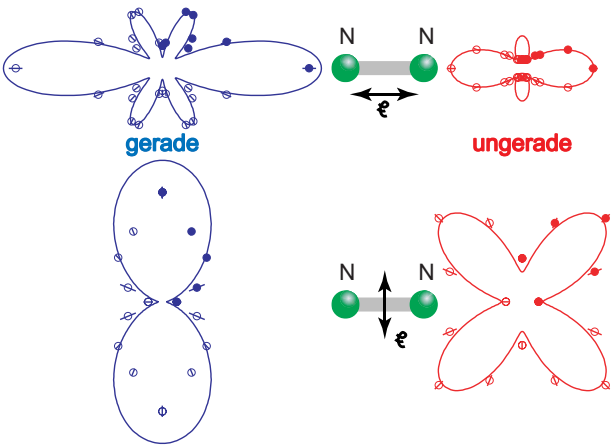

Figure 1: Molecule-frame photoelectron angular distributions of the gerade (blue) and ungerade (red) symmetry components of the N_2:N($1s$) photoline for molecules oriented parallel and perpendicular to the light polarization. Solid lines are predictions for coherent emission calculated in the MSNSP approach [3].

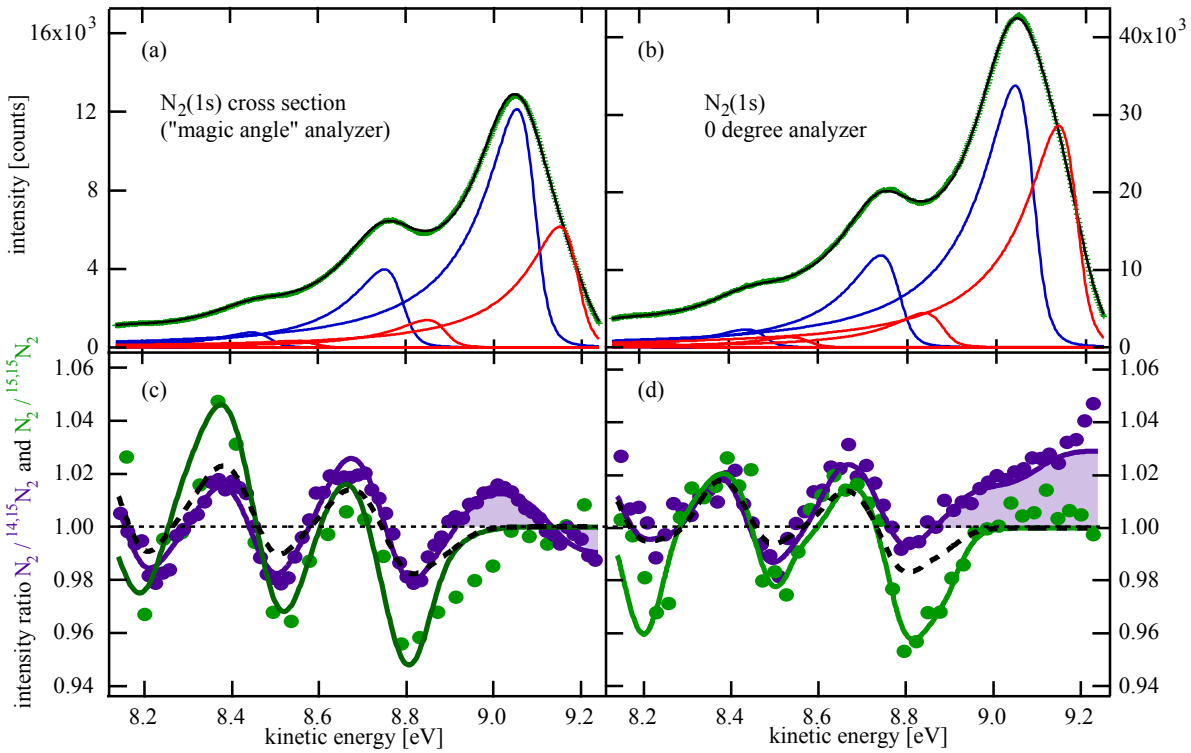

Figure 2: N_2:N($1s$) photoelectron spectrum measured at UE56/2-PGM1 (a) at the ”magic angle” and (b) under 0 degree to the light polarization and fitted with a doublet of PCI-deformed peaks including vibrational progression. (c) Ratio between normal N_2 and isotope-substituted $^{14,15}N_2$ (purple) respectively $^{15,15}N_2$ (green) for the photoelectron intensity at the magic angle and (d) under 0 degree to the light polarization. The solid lines are model calculations which include the vibrational effect and, for $^{14,15}N_2$, also the effect of the symmetry-breaking (shaded areas). For $^{14,15}N_2$, the dashed line shows a modeling of the vibrational effect only.

We attribute this cross section and angular distribution effect to the broken inversion symmetry in the singly substituted species leading to a partial localization of the core hole. While the inversion symmetry of N_2 is maintained in the doubly substituted species $^{15,15}N_2$, the electron wave function in $^{14,15}N_2$ is slightly modified due to the broken symmetry of the singly substituted molecule, where the (still remaining) symmetry center of the molecular potential no longer coincides with the shifted center of mass. As g and u lose their character as parity eigenfunctions in the molecule with broken inversion symmetry, they mix and consequently become more similar in their cross section and angular distribution, leading to an overall effect in the percentage range.
In summary, it was shown that the symmetry breaking through isotope substitution leads to a partial localization of the core hole reflected by the parity mixing of the outgoing photoelectron waves. This effect does neither exist for the non-substituted nor the doubly substituted molecule which both have a non-broken symmetry. This unexpected isotope effect on the electronic structure of a diatomic molecule is the first experimentally observed effect of its kind.
This project has been supported by the Deutsche Forschungsgemeinschaft (Be 860/18-2) and the Bundesminister für Bildung und Forschung (BMBF-05KS1EB12).

[1] D. Rolles *et al.*, BESSY Annual Report 2003.
[2] U. Hergenhahn *et al.*, J. Phys. Chem. A **105**, 5704 (2001).
[3] R. Díez Muiño *et al.*, J. Phys. B. **35**, L359 (2002).

X-ray Raman scattering with Bragg diffraction in a La-based superlattice

J.-M. André, P. Jonnard, C. Bonnelle

Laboratoire de Chimie Physique - Matière et Rayonnement, Université Pierre et Marie Curie, UMR-CNRS 7614, 11 rue Pierre et Marie Curie, 75231 Paris Cedex 05, France ; andrejm@ccr.jussieu.fr

E. O. Filatova

Institute of Physics, St Petersburg University, Ulianovskaya 1, St Petersburg, 198904, Russia

Periodic multilayer structures with layer thicknesses in the nanometer range, labelled hereafter superlattices offer the possibility to observe atomic processes in combination with optical phenomena such as Bragg reflection. Enhancement of x-ray fluorescence observed in the Bragg conditions from a W/C superlattice has been recently reported [1].

In this work, we study the interaction of a La-based superlattice with a monochromatic radiation in the La 4d threshold region. The intensity of the non-dispersed scattered radiation is recorded as a function of the incident photon energy and of the scattering angle. We have observed that the energy dependence of the scattered radiation clearly changes with the scattering angle. We propose to account for such a behaviour by a combination of Raman scattering with the Bragg reflection by the planes of the periodic structure.

A La/B_4C superlattice with 20 bilayers was fabricated using a diode sputtering technique [2]. The thickness of the La and B_4C layers are respectively 4.69 nm and 4.87 nm. The superlattice was irradiated by the monochromatic radiation supplied by the 1200 lines/mm plane grating monochromator associated with the undulator of the UE56/1-PGM-b beamline. The spectral bandwidth of the quasi-monochromatic radiation delivered by the monochromatic is close to 100 meV and the radiation is circularly polarized. The geometry of the experiment is given in Figure 1. To carry out our measurements, we used the polarimeter-goniometer developed by Schäfers et al. [3]. The glancing angle θ_{in} is equal to 31°.

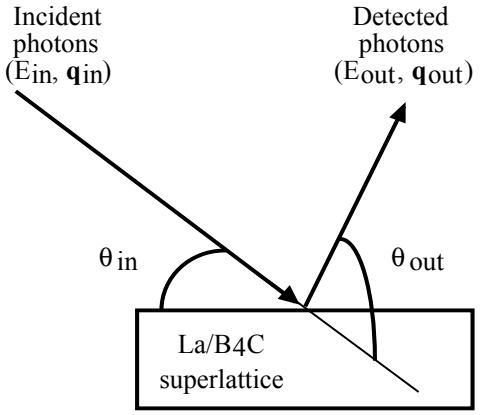

Fig. 1: Geometry of the experiment

The scattering angle θ_{out} is defined as the angle between the direction of the incident beam and the direction of observation. For different values of θ_{out}, the non-dispersed emitted intensity was measured versus the incident energy E_{in} by means of a GaAs diode with a

100 µm entrance slit located at 140 mm from the superlattice. The results of these measurements are called hereafter « excitation spectra ». The incident energy E_{in} has been varied in a spectral domain above the La 4d excitation transitions and the ionization threshold (125-200 eV).

The curves giving the emitted intensity from the superlattice versus the incident energy, that is the excitation spectra, are shown in Figure 2 for different scattering angles θ_{out} ranging from 43 to 67°. One observes a peak which shifts towards the low-energy side as the value of the scattering angle θ_{out} increases and then remains around 120 eV for θ_{out} greater than 85°. The amplitude of this peak is maximum when the scattering angle θ_{out} is equal to the specular angle, that is θ_{out}= 62°. We do not observe such a peak with homogeneous films of lanthanum compounds such as LaF_3 and La_2O_3.

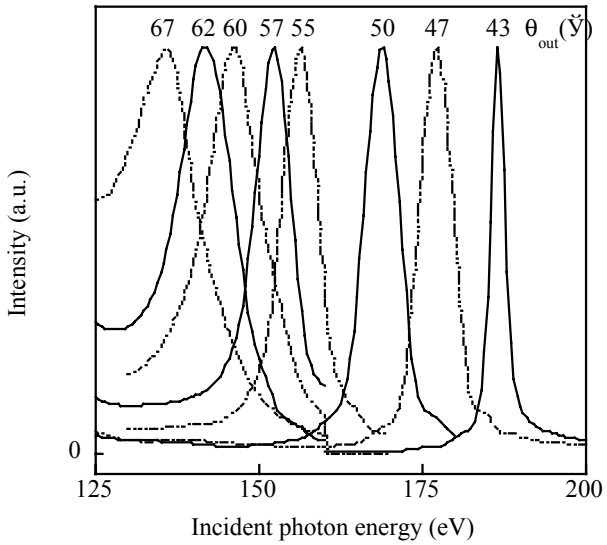

Figure 2 : Excitation spectra of the La/B_4C superlattice for different scattering angles ranging from 43 to 67 degrees. The spectra are normalized with respect to their maximum.

We propose to explain this peak by an x-ray Raman scattering process associated with Bragg diffraction by the superlattice. In a x-ray Raman process, the difference between the incident and scattered photon energies is equal to the difference between the initial and final states of the atoms. Here the initial state is the ground state and the final state has the La $5p^5$ configuration. Indeed, the transition 4d-5p is the most probable one following a 4d ionization. The energy difference, labelled E_x, is estimated to be about 20 eV in the superlattice [4].

To describe from a kinematical point of view the Raman process associated with Bragg diffraction, we write the laws of energy and momentum conservation for the whole system : photons, atoms and multilayer structure. Combining the equations expliciting these two laws leads to the following relationship which links the value of the resonant excitation energy $E_{in,max}$ to the scattering angle θ□□□:

$$E_{in,max} = \frac{E_X}{2} + \frac{\sqrt{2\,c^2\,q^2\,(1-\cos\theta_{out}) - E_X^2\,\sin^2\theta_{out}}}{2\,(1-\cos\theta_{out})} \qquad (1)$$

with

$$q^2 = (\mathbf{q}_x + \hbar\,\mathbf{G})^2 = q^2{}_x + (\hbar\,G)^2 + 2\,q_x\,\hbar\,G\cos(\theta_X)\ , \qquad (2)$$

where θ_x is the angle between the direction of **G**, the reciprocical wavevector, and $\mathbf{q}_X$, the momentum associated with the atomic state X of energy E_x.

The above equation can be regarded as a Bragg law generalized to the case of inelastic (Raman) scattering. Agreement exists between our experimental results and the values computed from Eqs. (1) and (2) by taking E_x = 19.5 eV and θ_x in such a way that the direction of $\mathbf{q}_x$ is the direction of observation, i.e. $\theta_x = \frac{\pi}{2} + \theta_{out} - \theta_{in}$. (See Figure 3).

Let us emphasize that our simple model does not allow to justify the above assumption concerning the angle θ_x. It is interesting to compare the excitation energy $E_{in,max}$ with the Bragg energy computed in the specular condition from a dynamical calculation of reflectivity [5]. This is done in Figure 3. It appears that neither the data of the above model neither the experimental results agree with the Bragg energy calculated in the framework of the standard Bragg diffraction. A dynamical model using a theoretical approach similar to the one given in [1] but extended to the inelastic scattering should be implemented to account more accurately for our experimental results. This work is in progress.

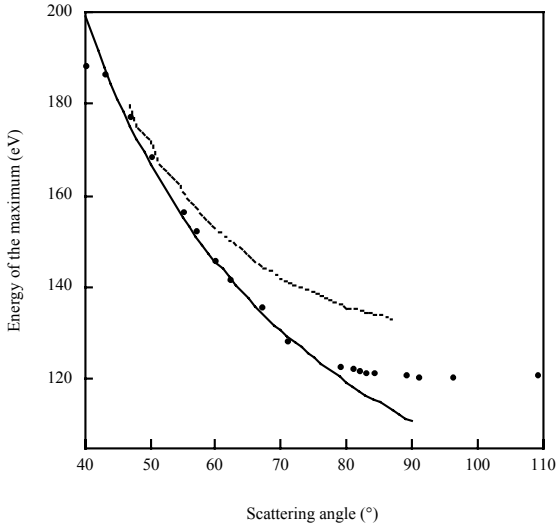

Figure 3: Peak position of the "resonant" excitation energy $E_{in,max}$ versus scattering angle : experiment (dots), our model (solid line), Bragg energy (dotted line).

Acknowledgments : This work was partly carried out at BESSY in the framework of the project Number BI3A-21/300804 and supported through the European Commission under I 3 Contract 3-CT-2004-506008. The authors are indebted to C. Michaelsen and J. Wiesmann at Incoatec (Germany) for supplying the superlattice. A. Gaupp and F. Schäfers from BESSY are warmly thanked for their help during the measurements.

[1] P. Jonnard, J.-M. André, C. Bonnelle, F. Bridou, B .Pardo, Phys. Rev. A **68** (2003)032505
[2] C. Michaelsen, J. Wiesmann, R. Bormann, C. Nowak, C. Dieker, S. Hollensteiner and W. Jäger, Optics Lett. **26** (2001)792-794
[3] F. Schäfers, H.-C. Mertins, A. Gaupp, W. Gudat, M. Mertin, I. Packe, F. Schmolla, S. Di Fonzo, G. Soullié, W. Jark, R. Walker, X. Le Cann, R. Nyholm and M. Eriksson, Appl. Opt. **38** (1999) 4074-4088
[4] J.-E. Rubensson, J. Lüning, S. Eisebitt and W. Eberhardt, Appl. Phys. A **65** (1997) 91-96
[5] B. Pardo, T. Megademini and J.-M. André, Rev. Phys. Appl. **23** (1988)1579-1597

Hydrogen absorption spectrum: determination of the transition moments

M. Glass-Maujean, L. Werner, S. Lucht*, S. Klumpp*, A.Ehresmann* and H. Schmoranzer**
Laboratoire de Physique Moléculaire pour l'Atmosphère et l'Astrophysique Université P et M. Curie /CNRS, 4, pl Jussieu, F-75252 Paris Cedex 05, France
* Fachbereich Physik, Technische Universität Kaiserslautern, D-67653 Kaiserslautern, Germany
HPP contract: HPP13/506008

Molecular hydrogen emission is an important astrophysical process. Since Voyager and IUE flights and later on with the Hubble Space Telescope and the Galileo spacecraft, it has been known that H_2 emission is the primary VUV and EUV emission process in the atmospheres of outer planets [1,2]. The understanding of such spectra needs a good knowledge of the absorption spectrum in this energy range. Surprisingly, the absorption spectrum of molecular hydrogen has not been interpreted for wavelengths below 78 nm. In this energy range, the molecular hydrogen spectrum is dense, full of narrow rotational lines of numbers of Rydberg vibrational series overlapped. In the previous recordings, the resolution is not high enough to isolate most of the lines.

The determination of the lines' positions and of the transition moments is an important tool for the computation of simulated spectra used in astrophysical studies [3]. On another part, the understanding of the simplest molecule in its refinements is of interest for molecular models of more complicated molecules.

The new 10-meter normal-incidence spectrometer gives us a wonderful opportunity to get this information. During the two experimental periods, we were able to record the absorption spectrum of H_2, for the first time, at very high resolution, in the 72 to 78 nm spectral range, at low pressure and room temperature. With 15-μ slits and a 1200 l/mm grating, the observed line widths are of 0.00014nm giving a resolution of 65000, very near the theoretical resolution (67000). (The Doppler width of the lines may be the origin of the small difference).

Simultaneously with the absorption spectrum, atomic Ly-α fluorescence and ions were detected, monitoring the dissociation and the ionization channels. These three spectra recorded over the whole 71.9-80.6 spectral range give us quantitative dynamic data. The absorption spectrum can be calibrated, knowing the optical path, and tested on lines with known intensities. The fluorescence and ion detection efficiencies can be calibrated versus the incident light, using lines known either to be fully dissociated or to be fully ionized presenting Beutler-Fano profiles.

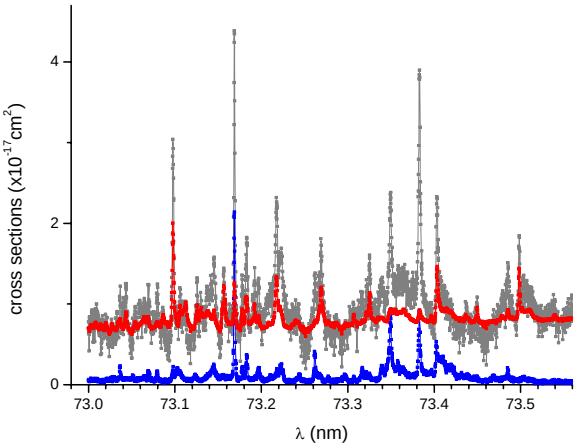

fig. 1

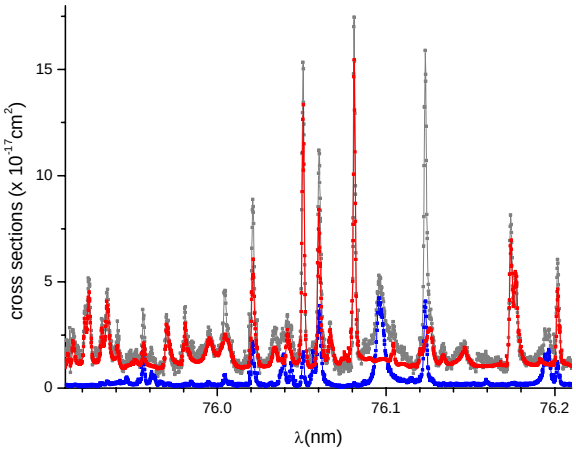

fig. 2

Figures 1 and 2 present a part of the spectra: absorption (grey line), ionisation (red line) and dissociation spectra (blue line).

Cross sections of the observed absorbed lines lie between 10 and 600 Mb. The sensitivity is higher for the dissociation or ionisation cross sections of the order of 1Mb. Absorption is no more linear for strong lines, corrections have to be applied on the three spectra. Special care was taken of the continua, in order to get quantitative results, which is not easy in absorption.

The main encountered problem remains the uncertainty on the line position. The wavelength scan is not perfectly linear. It has been greatly improved between June and August, but there was still some uncertainty left on the position of the lines. This uncertainty has to be worked on further as it represents some handicap to the interpretation of the results.

The recorded spectra present hundreds of lines for which the absorption cross section, the dissociation cross section and the ionisation cross section will be determined for the first time. In order to obtain the oscillator strengths we need to assign the rotational lines. A model spectrum will be computed with ab inito computed line positions and fitted absorption intensities, dissociation widths and ionisation widths.

The full processing of these data will be long.

Acknowledgements. The authors are grateful to the BESSYstaff, particularly to Dr. G. Reichardt and Andreas Balzer, for their help. Financial support by EC (HPP13/506008) is gratefully acknowledged.

[1] A.L. Broadfoot et al. Science, 204 709 (1979)
[2] J.T. Clarke, H.W. Moos, S.K. Atreya and A.L. Lane, **ApJ 241**, 179 (1980)
[3] X. Liu, D.E. Shemansky, J.M. Ajello, D.L. Hansen, C. Jonin and G.K. James **ApJS 129**, 267 (2000)

Publication:

M. Glass-Maujean, S. Klumpp, L. Werner, A.Ehresmann and H. Schmoranzer, “Photodissociation of doubly excited states of H_2 into H(2s) ans H(2p) fragments” J. Phys.B **37**, 2677 (2004)

Rotational Structure of Dissociation Products from Inner-Shell Excited Molecules

M. Meyer[1], P. O'Keeffe[1], R. Flesch[2], and E. Rühl[2]

[1] L.U.R.E,, Centre Universitaire Paris-Sud, Bâtiment 209D, F-91898 Orsay cedex, France

[2] Institut für Physikalische Chemie, Universität Würzburg, Am Hubland, 97074 Würzburg, Germany

The internal energy of dissociation products formed upon resonant core level excitation has been studied by means of high-resolution dispersed fluorescence spectroscopy in the UV/Visible wavelength regime. The present work has focused on fragmentation of H_2S induced by resonant S 2p excitation at photon energies around 165-170 eV. The H_2S molecule has already been studied extensively by means of electron and ion spectroscopy [1, 2] and fast dissociation processes are established to occur upon resonant S 2p excitation. In addition, symmetry-resolved ion yield spectra have shown a strong variation of the molecular geometry for the different resonant states that are reached upon S 2p excitation [3]. The aim of the present study, which relies in particular on the analysis of the rotational structure of the emission bands of the HS^+ fragments, is to obtain direct insight into the fragmentation processes of 2p-excited H_2S.

The experiments have been performed at the U49-1-SGM beamline of BESSY II using monochromatic synchrotron radiation with high energy resolving power ($E/\Delta E > 5000$) in order to excite selectively different S 2p near-edge resonances. A typical total ion yield spectrum is displayed in Fig. 1, which is similar to the absorption cross section of H_2S. The spectrum is dominated by a broad resonance feature around $h\nu = 165$ eV arising from transitions of the S 2p electron into the unoccupied a_1 and b_2 molecular orbitals and a series of narrow structures attributed to S $2p \rightarrow n\ell$ Rydberg resonances [4]. The UV/Visible fluorescence is collected by a set of optical elements. It is analyzed with respect to its wavelength using a high-resolution spectrometer (Jobin Yvon HR460) [5] providing an ultimate wavelength resolution of $\Delta\lambda = 0.03$ nm.

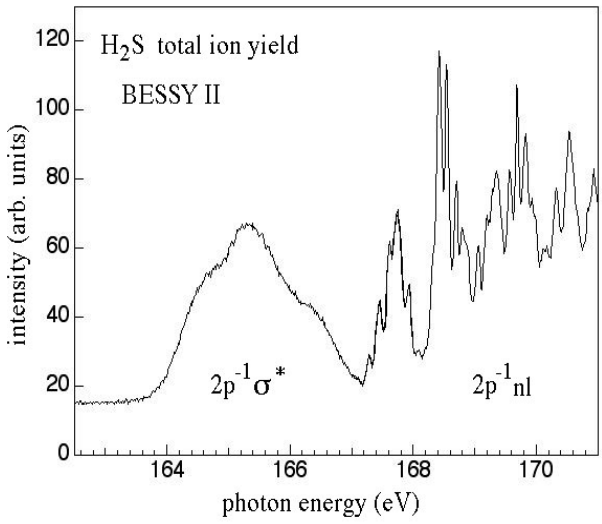

Fig. 1: Total ion yield of H_2S in the S 2p excitation regime. The bandwidth of the exciting synchrotron radiation was set to $\Delta E = 30$ meV.

The dispersed fluorescence spectra show, besides a huge number of fluorescence lines that are attributed to excited, neutral, and singly charged atomic fragments (H^*, S^* and S^{+*}), fluorescence emission from molecular species in the spectral regime between 330 and 340 nm (see Fig. 2). These lines are assigned to the rotational structure of the HS^+ ($A\ ^3\Pi$, v' = 0) - ($X\ ^3\Sigma$, v = 0) transition [6]. The spectrum is rather complicated due to the different fine structure terms of the triplet states involved in the $^3\Pi$-$^3\Sigma$ transition, which gives rise to a total of 27 rotational branches. Already a qualitative analysis of the fluorescence spectra recorded upon S 2p excitation to the σ^*-resonance (165 eV) and to a Rydberg resonance of strong $2p^{-1}3d$ character (168.40 eV), respectively, shows clearly strong differences in the relative line intensities and indicates that the population of the rotational levels depends on the primary excitation energy. This behavior can be related to pronounced differences between the geometry of the molecular σ^*-state and the $2p^{-1}3d$ Rydberg state. The latter should have a geometry that is close to that of the molecular ion. This implies that the Rydberg electron does not interact with the ionic core. A detailed analysis of the rotational profiles and the relaxation and dissociation dynamics is currently in progress, partially with N. Kosugi (Okasaki, Japan).

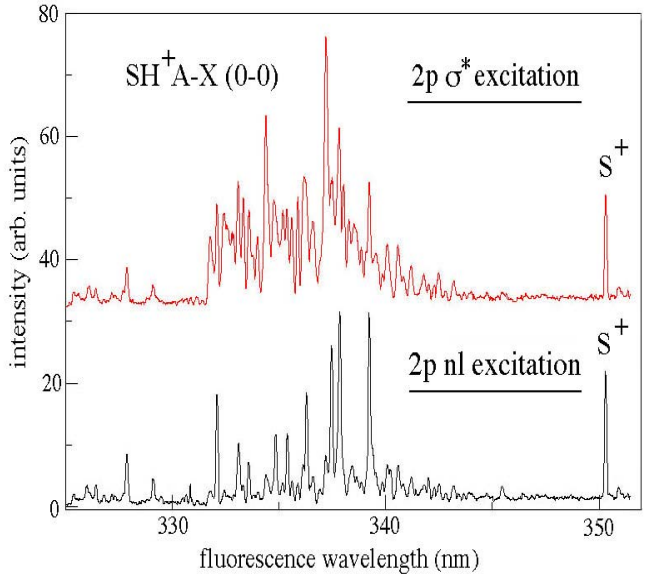

Fig. 2: Dispersed fluorescence spectrum of HS^+ formed after dissociation of H_2S, which is resonantly excited to the S $2p^{-1}\sigma^*$ (top) and S $2p^{-1}3d$ Rydberg resonance (bottom).

Financial support by a Franco-German PROCOPE project and the Deutsche Forschungsgemeinschaft is gratefully acknowledged.

References

[1] H. Aksela et al., Phys. Rev. A **45**, 7948 (1992); A. Naves de Brito, H. Agren, Phys. Rev. A **45**, 7953 (1992); Naves de Brito et al., J. Chem Phys. **106**, 18 (1997).

[2] P. Morin, M. Lavollée, M. Simon, VUV-10 Conf. Proc., World Scientific, p. 211 (1993).
[3] E. Shigemasa and N. Kosugi, private communication (2004).
[4] E. Hudson, D.A. Shirley, M. Domke, G. Remmers, G. Kaindl, Phys. Rev. A **49**, 161 (1994).
[5] A. Marquette, M. Gisselbrecht, W. Benten, M. Meyer, Phys. Rev. A **62**, 022513 (2000).
[6] J. Rostas, M. Horani, J. Brion, D. Daumont, and J. Malicet, Mol. Phys. **52**, 1431 (1984).

Photoexcitation and Photofragmentation of the 3d-transition metal compounds $FeCl_2$ and $FeBr_2$

M. Al-Hada, T. Richter, P. Zimmermann
Institut für Atomare Physik und Fachdidaktik, Technische Universität Berlin

M. Martins
Institut für Experimentalphysik, Universität Hamburg

Ö. Gergülüler, M. Yalcinkaya, A. Tutay
Science Faculty, Istanbul University

The atomic absorption spectrum of the 3d element Fe in the region of the 3p excitation is dominated by strong resonances (giant resonances) due to discrete transitions $3p^6 3d^6 \rightarrow 3p^5 3d^7$ [1]. This is caused by the large overlap of the 3p and 3d wave functions. The atomic Fe 3p photoelectron spectrum in a similar way is determined by the 3p-3d interaction resulting in a large splitting of the $3p^{-1}$ multiplet [2]. This interaction of the Fe (3p) hole with the valence electrons can also be used to study the influence of the interatomic interaction in Fe compounds like $FeCl_2$ and $FeBr_2$.
3p photoabsorption and photoelectron spectra of molecular $FeCl_2$ and $FeBr_2$ are investigated by photoion and photoelectron spectroscopy using molecular beam technique by thermal evaporation of the metal compounds at a temperature of approx. 700 K from a stainless steel crucible and monochromatized synchrotron radiation at the BESSY beam line U125/2-SGM in the range of 50-120 eV. For the absorption spectra, photoions are produced in the excitation energy range of 50-70 eV and detected by a time-of-flight (TOF) spectrometer used in pulsed voltage mode. The photoelectrons are created by photons of 100 eV and 120 eV for $FeCl_2$ and $FeBr_2$ respectively and analysed using a hemispherical electron spectrometer (Scienta SES-2002).

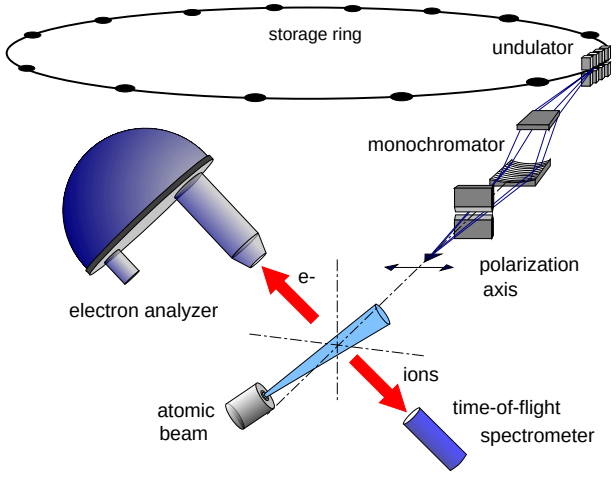

Figure 1: *Experimental Setup*

Experimental results of in the partial ion yield of Fe, FeCl and FeBr ions in the region between 50-70 eV are shown in (Fig. 2a) and (Fig. 2b). The main features of the partial ion yield for the molecules $FeCl_2$ and $FeBr_2$ are two broad resonances at 54.0 eV and 56.1 eV looking very similar to the results (53.3 and 56.2 eV) of the atomic Fe measurements [1]. These resonances are due to the discrete transitions Fe $3p^6 3d^6 \rightarrow 3p^5 3d^7$ and a consequent rapid autoionization process to $3p^6 3d^5 + \varepsilon\ell$. In the case of the molecular spectra similar resonances were found.

For the photoelectron spectra in the atomic case (Fig. 3a) the line structure is governed by the

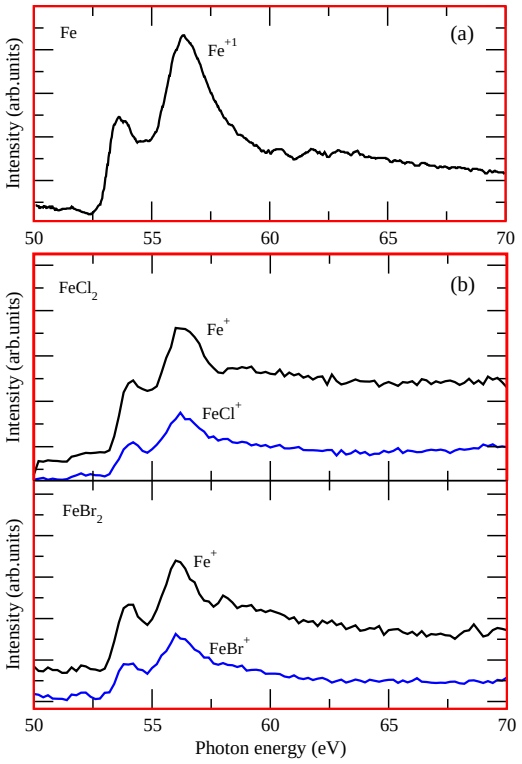

Figure 2: *(a)Partial ion yield spectra of the atomic Fe in the region of the 3p excitation and ionization between 50 and 70 eV[1] (b) Partial ion yield spectra of the $FeCl_2$ and $FeBr_2$ molecules in the energy range 50-70 eV*

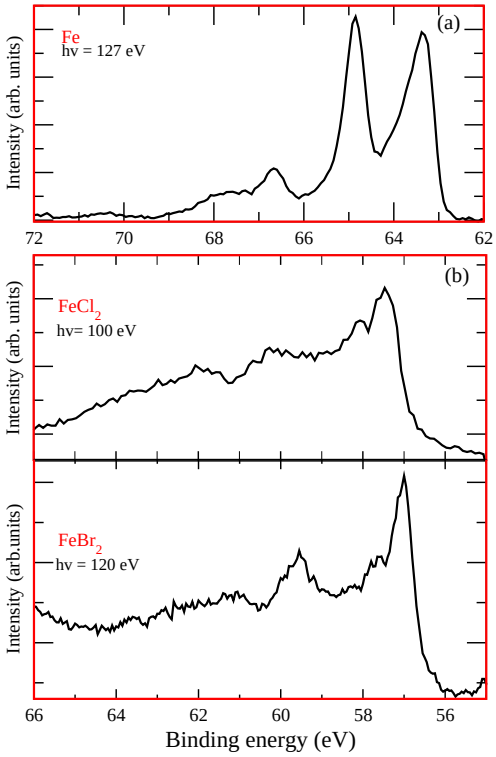

Figure 3: *(a)Experimental 3p photoelectron spectrum of atomic Fe (b) 3p photoelectron spectra of $FeCl_2$ and $FeBr_2$ taken at a photon energy of 100 and 120 eV respectively*

intensive multiplet splitting due to the Coulomb interaction of the Fe 3p hole state with the 3d valence shell. For the molecular spectra (Fig. 3b) the interpretation is more complicated due to the influence of the molecular binding in the 3d valence shell. A charge transfer model by introducing an additional $3d^7$ configuration has been used to interpret the molecular structure of $FeCl_2$ in the 2p photoelectron region [3].This model maybe also useful to describe the 3p photoelectron spectra of the $FeCl_2$ and $FeBr_2$.

[1] H. Feist, M. Feldt, Ch. Gerth, M. Martins, P. Zimmermann Phys. Rev. A 53 760 (1995)
[2] K. Tiedtke, Ch. Gerth, M. Martins, P. Zimmermann Phys. Rev. A 64 022705 (2001)
[3] T. Richter, K. Godehusen, T. Wolf, M. Martins, P. Zimmermann Phys. Rev. Lett. 93 023002 (2004)

Cross Sections and Branching Ratios of Radiative Transitions from Doubly Excited Helium Determined by Photon Induced Fluorescence Spectroscopy

S. Mickat, K.-H. Schartner, S. Kammer, R. Schill
I. Physikalisches Institut der Justus-Liebig-Universität Giessen

S. Klumpp, L. Werner, A. Ehresmann, H. Schmoranzer
Fachbereich Physik der Universität Kaiserslautern

V. Sukhorukov
Rostov State University

1. Introduction

Single photon absorption of helium leading to the population of doubly excited states was reported by Madden and Codling in pioneering absorption experiments using synchrotron radiation [1]. Doubly excited states have regained increased interest during the last decade since nowadays experiments with undulator radiation allow to resolve absorption resonances with high n values of the Rydberg electron [2] and to apply electron spectroscopy to identify autoionization channels with large values of N, the main quantum number of the inner electron [3]. A sequence of experiments were initiated by the first description of the radiative decay of doubly excited states on photoabsorption resonances, observed through the detection of metastable helium atoms and undispersed VUV photons [4,5]. These experiments revised the earlier assumption that the radiative decay of the doubly excited states is negligible in relation to a dominating autoionization channel.

With respect to calculations of the characteristics and behaviour of doubly excited states , the contribution by Zitnik et al [6] contains the most detailed prediction of the photoabsorption cross sections and radiative cascading transitions of the seven series of ^1P,^3P and ^3D symmetry with values of A = +1, -1 and 0 as indicators of the radial correlation of the two electrons. In [6], the doubly excited states of the series converging to the N = 2 treshold of helium are treated. They display different decay patterns with respect to the relative population of 1sns,nd states of singly excited helium. The latter are populated under the emission of photons with energies of about 40 eV and decay into lower 1snp states and finally into the $1s^2$ helium ground state or to 1s2s metastable states. These patterns reflect the composition of the wave function of the doubly excited states.

Our experiments presented in the following were carried out with the intention to analyze the cascade patterns spectroscopically resolved and to provide absolute cross sections for the product of resonance excitation and radiative transition into the 1snd or 1sns levels. Moreover the angular distribution of the 1snd $\rightarrow$ 1s2p fluorescence intensity was measured. The experimental method of photon induced fluorescence spectroscopy (PIFS) was applied [7]. Preliminary data were published in [8]. The results test the calculations by Zitnik et al [6] on an absolute scale, and with respect to branching ratios on a relative scale. So far only relative intensities of metastable atoms or of undispersed photons in the spectral range of the VUV were compared with the calculations [6].

Exemplary, Zitnik et al. display the fluorescence rates for the n = 5 resonances to decay into the 1sms and 1smd states as function of m in a bar diagram. In fig. 1 we display a corresponding bar diagram for the measured cross section σ_{ij} in comparison with the calculated values. The bars without hatching mark the experimental data, the hatched ones the calculated values. The cross sections hold for the absorption and radiative decay into the level j on the peak energy of the resonance i measured with a bandwidth of 4 meV which is also folded into the calculation.

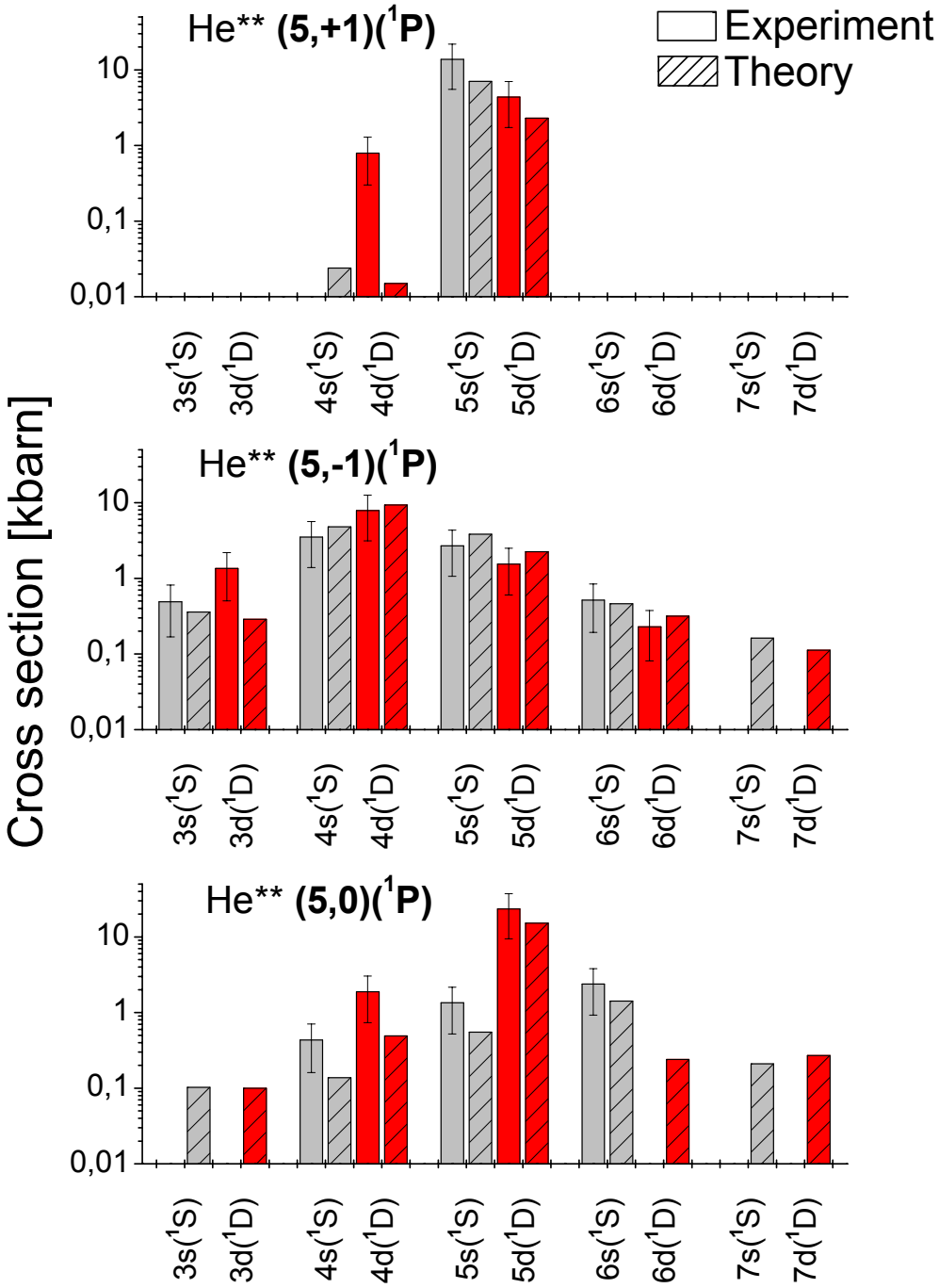

Figure 1: Comparison between measured and calculated cross sections for populating 1sms(^{1}S) and 1smd(^{1}D) states of singly excited helium on the maxima of the absorption resonances (5,+1)(^{1}P), (5,-1)(^{1}P) and (5,0)(^{1}P). Calculated values from [6] folded with 4 meV experimental bandwidth of the exciting synchrotron radiation.

The lower limit of the experimental cross sections is 0.1 kbarn, determined by the signal rate which is acceptable with respect to signal/noise ratio and also with respect to the available beam time. A good overall agreement within the error bars between experiment and calculation is observed. There are differences outside the uncertainty especially for weak transitions within a decay scheme, e.g. for the population of the 1s4d(^{1}D) state on the (5,+1)(^{1}P) resonance.

For he (5,-1)^{1}P resonances the dominant decay channel populates the 1s5d(^{1}D) state of singly excited helium. The (5,-)^{1}P state presents a broad decay pattern with the 1s4d(^{1}D) state dominating and the (5,+1)^{1}P state decays with comparable contribution into the 1s5s(^{1}S) and the 1s5d(^{1}D) states. The broad decay pattern of the (5,-1)^{1}P state, reflects the stronger electron correlation with respect to the two other states. It shifts with n as predicted in [6].

For the *ß*-parameter of the 1s4d(^{1}D)-1s2p(^{1}P)-transition, values very close to the prediction of -0.35 were measured [6]. Finally, the observation of transitions within the triplet system, observed also on the ^{1}P-resonances, shows their weak but existing triplet component caused by the spin-orbit interaction.

The presented experimental study complements the preceding investigations of the radiative decay of resonantly doubly excited states of helium [4,5] by the first spectroscopically resolved analysis of the photon induced fluorescence. The comparison with the calculated product of excitation cross section and fluorescence yield with the measured cross sections results in a good overall agreement. Disagreement is observed for weak channels.

References

[1] R.P. Madden and K. Codling, Phys. Rev. Lett. **10** (1963) 516

[2] M. Domke, K. Schulz, G. Remmers, and G. Kaindl, Phys.Rev.A **53** (1996) 1424

[3] Y. H. Jiang, R. Püttner, R. Hentges, J. Viefhaus, M. Poiguine, U. Becker, J. M. Rost, and G. Kaindl, Phys. Rev.A. **69** (2004) 042706

[4] J.-E.Rubenson, C. Sathe, S. Cramm, B. Kessler, S. Stranges , R. Richter, M. Alagia, M.Coreno, Phys. Rev. Lett. **83** (1999) 947

[5] M.K. Odling-Smee, E. Sokell, P. Hammond, and M.A. MacDonald. Phys.Rev.Lett. **84** (2000) 2598

[6] M. Zitnik, K. Bucar, M. Stuhec, F. Penent, R.I. Hall, and P. Lablanquie, Phys.Rev.A **65** (2002) 032520-1

[7] B. Zimmermann, K.-H. Schartner, O. Wilhelmi, S. Kammer, H. Liebel, A. Ehresmann, and H. Schmoranzer, J. Phys.B : At. Mol. Opt. Phys. **37** (2004) 511

[8] K.-H. Schartner, B. Zimmermann, S. Kammer, S. Mickat, H. Schmoranzer, A. Ehresmann, H. Liebel, R. Follath, and G. Reichardt, Phys.Rev.A **64** (2001) 040501(R)

Vibrational cascades in the C-X fluorescence of N_2^+ after resonant $1s^{-1}\ \pi_g^*$ excitation of N_2

L Werner†, S Lucht†, S Klumpp†, H Schmoranzer†, A Ehresmann†, S Mickat§, R H Schill§ , K-H Schartner§, Ph V Demekhin‡, M P Lemeshko‡, V L Sukhorukov‡

† Fachbereich Physik, Technische Universität Kaiserslautern, D-67653 Kaiserslautern, Germany
§ I Physikalisches Institut, Justus-Liebig-Universität, D-35392 Giessen, Germany
‡ Rostov State University of Transport Communications, 344038 Rostov-on-Don, Russia

E-mail: arnauld@rhrk.uni-kl.de

The interaction between synchrotron radiation and molecules offers an excellent basis for investigations of photon-induced molecular processes, like (resonant) photo-excitation, photo-ionisation and photo-dissocation. If this excitation is combined with fluorescence spectroscopy it is possible to measure partly on a quantative basis state selective cross sections when excited particles are formed.
Fluorescence spectroscopy experiments in combination with synchrotron radiation were mainly focused on outer-shell excitations of molecules (e.g. (Liebel *et al* 2002), (Hatano 1999), (Poliakoff 1991)), whereas the decay of inner shell excitations was investigated only scarcely (see e.g. (Marquette *et al* 2000)). The excitation of an inner shell electron in a molecule induces very complex relaxation processes, which are governed by the competition between autoionization and fragmentation of the molecule. In the present work we investigated aspects of the decay of the $1s^{-1}\pi_g^*$ resonance of N_2 by fluorescence spectroscopy, measuring dispersed VUV-fluorescence intensities (135 nm$\leq \lambda_{fl} \leq$190 nm) as complementary experiments to the ones performed by (Marquette *et al* 2000).
Synchrotron radiation from the storage ring BESSY II (Berlin) has been used for the vibrationally selective inner-shell photoexcitation of the $N_2(1s^{-1}\pi_g^*)(v)$-resonances. The subsequent autoionization into different vibrational levels of the N_2^+ C $^2\Sigma_u^+$ electronic state and the double autoionization into the N_2^{2+} D $^1\Sigma_u^+$ state were investigated using photon-induced dispersed fluorescence spectroscopy (PIFS) (Schmoranzer *et al* 2001), which has proven to be a powerful tool for molecular spectroscopy (e.g. (Ehresmann *et al* 2004), (Liebel *et al* 2002)), by measuring the fluorescence intensities of N_2^+ C $-$ X and N_2^{2+} D $-$ X bands as functions of the exciting-photon energy. Simultaneously to the dispersed fluorescence intensities the photoabsorption and the photoion signal were measured.
The monochromatized synchrotron radiation, from the UE 56/2 PGM beamline, has been focused into a differentially pumped target cell filled with molecular nitrogen at room temperature and at a pressure of 27.6 μbar. The pressure has been chosen to be in the linear regime of the fluorescence-intensity pressure function, to avoid artifacts, such as photoelectron impact induced fluorescence. The exciting-photon energy has been varied in the region between 400 eV to 402 eV in steps of 20 meV. A bandwidth of the exciting radiation of about 75 meV FWHM at 400 eV has been determined mainly by a reasonable signal to noise ratio for the observed fluorescence intensities. The exciting photon energy was calibrated to the energetic positions of the vibrational levels of the $N_2(1s^{-1}\pi_g^*)$ $(v = 0, 1, ...)$-resonances (Hitchcock and Brion 1980) using the measured total photoion yield. Fluorescence radiation has been observed perpendicularly to the exciting-photon beam and parallel to the $\overrightarrow{E}-$ vector of the exciting radiation, dispersed by a 1 m normal incidence monochromator equipped with a 1200 lines/mm grating and recorded by a position-sensitive CsI microchannel-plate detector. The resolution of this 'monochromator-detector' combination was about $\lambda_{fl} = 0.3$ nm. The transmitted flux of the exciting photons has been monitored using a GaAs photodiode. Within the target cell two electrodes have been used to measure simultaneously the photo-ion yield. A two-dimensional fluorescence yield spectrum in the exciting-photon energy region between 400 and 402 eV and in the fluorescence wavelength range from 135 nm to 190 nm is displayed in figure 1, assignments of the fluorescence lines are tabulated in table 1. The recorded N_2^+ and N_2^{2+} fluorescence lines are overlaps of bands with fixed $\Delta v = v'' - v'$.
The investigated exciting-photon energy range is dominated by some transitions in atomic nitrogen which result from dissociative spectator Auger decays of the $N_2^*(1s^{-1}\pi_g^*(v))$ resonance (see equation 2) and C $^2\Sigma_u^+(v') \rightarrow$ X $^2\Sigma_g^+(v'')$ transitions in the N_2^+ molecular ion resulting from participator Auger decays (see equation 3). The corresponding processes are schematicaly depicted as follows:

$$N_2\ 1\sigma_g^2 1\sigma_u^2 2\sigma_g^2 2\sigma_u^2 1\pi_u^4 3\sigma_g^2 \left(X\ ^1\Sigma_g^+\right)(v_0 = 0) + \hbar\omega_{ex} \quad \rightarrow \quad 1s^{-1}\pi_g^*(v) \quad \pi^*\text{resonance excitation} \qquad (1)$$

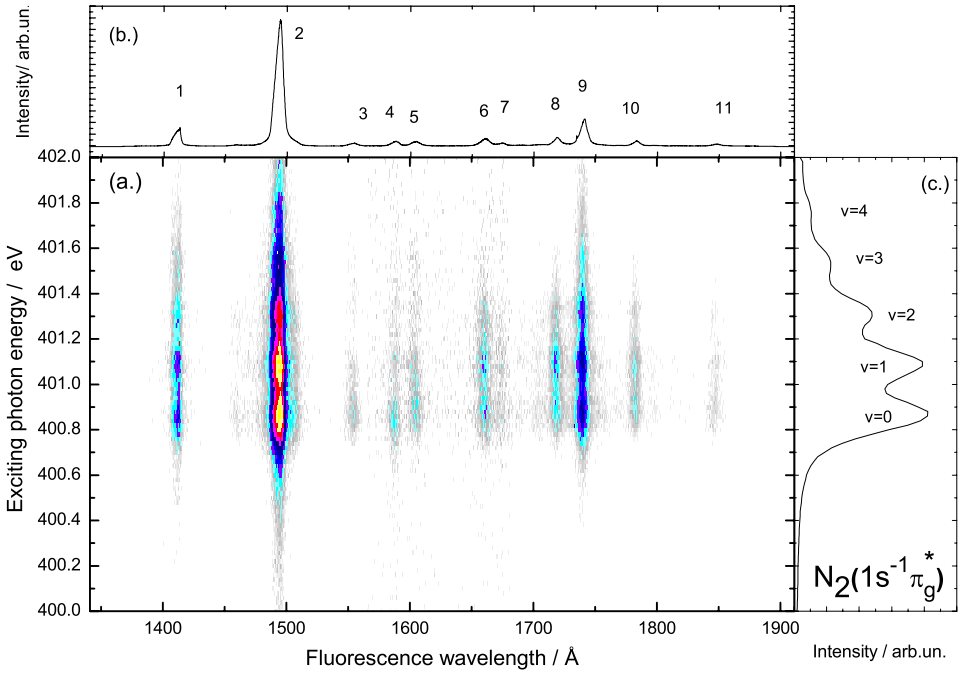

Figure 1. (a) Two-dimensional fluorescence yield spectrum. Top panel (b) fluorescence intensities integrated over the exciting-photon energies between 400 and 402 eV. Line numbers see table 1. Right panel (c) represents exciting-photon energy intensities integrated over all fluorescence wavelengths.

$$
\begin{array}{lcll}
1\mathrm{s}^{-1}\pi_g^*\left(v\right) & \rightarrow & \mathrm{N}_2^+\left(n_1\lambda_1^{-1}n_2\lambda_2^{-1}\left(\Lambda S\right)\right)\pi^*\left(v'\right)+\varepsilon\lambda & \text{spectator Auger decay} \\
& \hookrightarrow & \mathrm{N}^*\left(2\mathrm{p}^2\left(^3\mathrm{P}\right)3\mathrm{s}\ ^2\mathrm{P}_J\right)+\mathrm{N}^+\left(2\mathrm{p}^2\left(LS\right)\right) & \text{predissociation} \\
& & \hookleftarrow & \\
& \hookrightarrow & \mathrm{N}^*\left(2\mathrm{p}^2\left(^3\mathrm{P}\right)3\mathrm{s}\ ^2\mathrm{P}\right)\rightarrow\mathrm{N}^*\left(2\mathrm{p}^3\ ^2\mathrm{P},^2\mathrm{D}\right)+\hbar\omega_{fl}^{at} & \text{fluorescence}
\end{array}
\tag{2}
$$

$$
\begin{array}{lcll}
1\mathrm{s}^{-1}\pi_g^*\left(v\right) & \rightarrow & \mathrm{N}_2^+\left(2\sigma_u^1 1\pi_u^4 3\sigma_g^2\left(C\ ^2\Sigma_u^+\right)\right)\left(v'\right)+\varepsilon\lambda & \text{participator Auger decay} \\
& & \hookleftarrow & \\
& \hookrightarrow & \mathrm{N}_2^+\left(2\sigma_u^2 1\pi_u^4 3\sigma_g^1\left(X\ ^2\Sigma_g^+\right)\left(v''\right)\right)+\hbar\omega_{fl}^{mol} & \text{fluorescence}
\end{array}
\tag{3}
$$

Measured intensities of the N_2^+ C-X fluorescence lines as functions of the exciting-photon energy are shown in figure 2.2, in comparison to the absorption and photoion signal. The relative intensities of the N_2^+ $\mathrm{C}-\mathrm{X}$ fluorescence transitions as functions of the exciting-photon energy are strongly affected by the participator Auger decay. This directly reflects the coupling of the final ionic vibronic levels to the $\mathrm{N}_2(1\mathrm{s}^{-1}\pi_\mathrm{g}^*)(\mathrm{v})$ vibronic levels. As is obvious from there the intensity functions are quite different from each other.

Line	Wavelength[Å]	Assignment			
1	1410	NI $2\mathrm{s}^2 2\mathrm{p}^3\ ^2\mathrm{P}_\mathrm{J}$	-	$2\mathrm{s}^2 2\mathrm{p}^2(^1\mathrm{D})3\mathrm{s}\ ^2\mathrm{D}_\mathrm{J}$	
2	1490	NI $2\mathrm{s}^2 2\mathrm{p}^3\ ^2\mathrm{D}_\mathrm{J}$	-	$2\mathrm{s}^2 2\mathrm{p}^2(^1\mathrm{D})3\mathrm{s}\ ^2\mathrm{P}_\mathrm{J}$	
3	1553	N_2^+ C $^2\Sigma_\mathrm{u}^+$	-	N_2^+ X $^2\Sigma_\mathrm{g}^+$	$v''-v'=0$
4	1587	N_2^{2+} D $^1\Sigma_\mathrm{u}^+$	-	N_2^{2+} X $^1\Sigma_\mathrm{g}^+$	$v''-v'=0$
5	1603	N_2^+ C $^2\Sigma_\mathrm{u}^+$	-	N_2^+ X $^2\Sigma_\mathrm{g}^+$	$v''-v'=1$
6	1660	N_2^+ C $^2\Sigma_\mathrm{u}^+$	-	N_2^+ X $^2\Sigma_\mathrm{g}^+$	$v''-v'=2$
7	1674	NII $2\mathrm{s}^2 2\mathrm{p}^3\ ^3\mathrm{P}_\mathrm{J}$	-	$2\mathrm{s}^2 2\mathrm{p}^2(^2\mathrm{P})3\mathrm{p}\ ^3\mathrm{S}_\mathrm{J}$	
8	1718	N_2^+ C $^2\Sigma_\mathrm{u}^+$	-	N_2^+ X $^2\Sigma_\mathrm{g}^+$	$v''-v'=3$
9	1740	NII $2\mathrm{s}^2 2\mathrm{p}^3\ ^3\mathrm{P}_\mathrm{J}$	-	$2\mathrm{s}^2 2\mathrm{p}^2(2\mathrm{P})3\mathrm{p}\ ^3\mathrm{D}_\mathrm{J}$	
		NI $2\mathrm{s}^2 2\mathrm{p}^3\ ^2\mathrm{P}_\mathrm{J}$	-	$2\mathrm{s}^2 2\mathrm{p}^2(2\mathrm{P})3\mathrm{s}\ ^2\mathrm{P}_\mathrm{J}$	
10	1783	N_2^+ C $^2\Sigma_\mathrm{u}^+$	-	N_2^+ X $^2\Sigma_\mathrm{g}^+$	$v''-v'=4$
11	1848	N_2^+ C $^2\Sigma_\mathrm{u}^+$	-	N_2^+ X $^2\Sigma_\mathrm{g}^+$	$v''-v'=5$

Table 1. Observed fluorescence transitions after resonant $1\mathrm{s}^{-1}\pi_\mathrm{g}^*$ excitation of N_2.

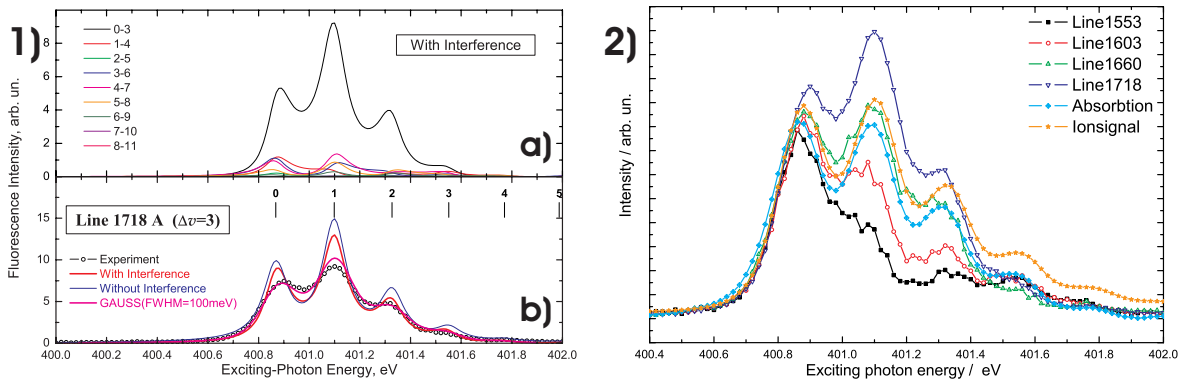

Figure 2. (1): (a) Calculated fluorescence intensities for N_2^+ $C-X$-transition with $\Delta v = v'' - v' = 3$ at 1718 Å. Note that interference effects for the different fluorescing vibrational states are taken into account. (b) Comparison between the calculated total fluorescence intensities of the N_2^+ $C-X$ transitions and measured fluorescence intensity. Blue line represent the total fluorescence intensity of the C-X transitions without interference effects between the N_2 $(1s^{-1}\pi_g^*)$ resonances, red line considering interference effects between the N_2 $(1s^{-1}\pi_g^*)(v)$ resonances and magenta line also considering the broadenig of the line width due to the apparatus resolution due to convolution with a 100 meV (FWHM) Gauss function. , Energetic positions of the N_2 $(1s^{-1}\pi_g^*)(v)$ resonances are indicated with vertical bars. (2): Comparison of the measured fluorescence intensities of N_2^+ $C \rightarrow X$ transitions (line numbers 3,5,6 and 8 (at 1553 Å , 1603 Å, 1660 Å and 1718 Å)), the photoion yield and the absorption signal in respect to the exciting photon energy.

In order to explain the differences in these functions *ab-initio* calculations of the corresponding potential curves and transition probabilities have been performed. The results for the calculated N_2^+ C-X band intensities with $\Delta v = 3$ (line number 8 in figure 1b at 1718 Å) are displayed in figure 2.1. As it is evident from the calculations in figure 2.1a the main influence in the N_2^+ $C-X$ fluorescence line stems from the $(v'' = 3;\ v' = 0)$ transition. In figure 2.1b the integrated fluorescence intensities of the N_2^+ $C-X$ transitions are displayed as the blue line, where a maximum intensity is observed after the decay of the $N_2(1s^{-1}\pi_g^*)(v = 1)$ vibronic level. The influence of interferences (Lagutin *et al* 2003) between decays of overlapping $N_2(1s^{-1}\pi_g^*)(v)$ resonances have been taken into account, red line in figure 2.1b. For this specific example the influence of interferences on the intensity functions are not very large. Measured and calculated total fluorescence intensities, considering the line broadening due to the finite excitig-photon energy band width, are in very good agreement. As is obvious from the calculations of the individual N_2^+ C-X $v' - v''$ band intensities´, no obvious correlation between the v' of the N_2^+ C state and the v of the $N_2(1s^{-1}\pi_g^*)(v)$ resonance can be drawn. This is in contrast to observations of the population at N_2^+ A $^2\Pi_u$ states, showing that the excitation of a particular vibrational level of the $N_2(1s^{-1}\pi_g^*)(v)$ resonances clearly favours the population of that v'-level of the N_2^+ A $^2\Pi_u$ state which has the same vibrational quantum number as the core-excited state (Marquette *et al* 1999).

The authors gratefully acknowledge the valuable help of Dr. G. Reichardt during beamtime at BESSY II.

References

Ehresmann A, Liebel H, von Kröger M and Schmoranzer H 2001 *J. Phys. B: At. Mol. Opt. Phys.* **34**, 3119-31.

Ehresmann A, Werner L, Klumpp S, Schmoranzer H, Demekhin Ph V, Lagutin B M, Sukhorukov V L, Mickat S, Kammer S, Zimmermann B and Schartner K-H 2004 *J. Phys. B: At. Mol. Opt. Phys.* **37**, 4405-4422.

Hatano Y *Phys. Rep.* 1999 **313**, 109.

Hitchcock A P and Brion C E*J. Electron Spectrosc. Relat. Phenom.* 1980 **18**, 1-12.

Lagutin B M, Demekhin Ph V, Sukhorukov V L, Ehresmann A and Schmoranzer H 2003 *J. Phys. B: At. Mol. Opt. Phys.* **36**, L163-L168.

Liebel H, Ehresmann A, Schmoranzer H, Demekhin Ph V, Lagutin B M and Sukhorukov V L 2002 *J. Phys. B: At. Mol. Opt. Phys.* **35**, 895-905.

Marquette A, Meyer M, Sirotti F and Fink R F 1999 *J. Phys. B: At. Mol. Opt. Phys.* **32**, L325-L333.

Marquette A, Gisselbrecht M, Benten W and Meyer M 2000 *Phys. Rev. A* **62**.

Poliakoff E D *Vacuum Ultraviolet Photoionization and Photodissociation of Molecules and Clusters*, edited by Ng C Y (World Scientific, Singapore, 1991).

Schmoranzer H, Liebel H, Vollweiler F, Müller-Albrecht R, Ehresmann A, Schartner K H and Zimmermann B 2001 *Nucl. Instrum. Methods in Phys. Res. A* **467-468**, 1526-1528.

Channel-resolved decay of doubly excited helium below the ionization threshold I_8 and I_9

Y. H. Jiang,[1,2] R. Püttner,[1] R. Hentges,[3] J. Viefhaus,[3] M. Braune,[3] M. Poiguine,[1] U. Becker,[3] J. M. Rost,[2] and G. Kaindl[1]

[1]*Institut für Experimentalphysik, Freie Universität Berlin, Arnimallee 14, D-14195 Berlin-Dahlem, Germany*

[2]*Max-Planck-Institut für Physik Komplexer Systeme, Nöthnitzer Strasse 38, D-01187 Dresden, Germany*

[3]*Fritz-Haber-Institut Berlin, Faradayweg 4-6, D-14195 Berlin-Dahlem, Germany*

Double-excitation states in helium have been considered to be prototypical for two-electron systems with strong correlation. In the region extremely close to the double ionization threshold, the interferences due to the intense overlap of pertubers with different Rydberg series render the observed spectra highly complicated. The approximate quantum numbers begin to lose their meaning, and the regularities in the two-electron resonance spectrum start to dissolve. Statistical nearest-neighbor spacing studies based on the total cross section (TCS) [1] have shown a transition from integrability to chaos in the region of the ionization threshold I_9. For partial cross sections (PCSs), the correlation and coupling effects of the outgoing channels are included individually and thus one expect to observe additional resonances due to stronger variations in the PCSs than in the TCS. For these reasons, the last eV below the double ionization threshold has drawn considerable attention in both, experimental and theoretical studies. With one time-of-flight (TOF) electron spectrometer we measured in our previous studies the PCSs up to the threshold I_7 [2]. In this report, we present state-of-the-art measurements of PCSs below I_8 and I_9.

Modern high-resolution monochromators in combination with TOF photoelectron spectrometers allow one to explore the autoionization of resonances in the region close to the double-ionization threshold of helium. The experiments were performed at the undulator beamline U125/2-SGM (BUS-beamline) of the Berliner Elektronenspeicherring für Synchrotronstrahlung (BESSY) using a photon energy resolution of $\Omega \cong 6$ meV (FWHM). The TOF spectrometer was mounted at the magic angle, i.e. in the dipole plane at an angle of $\theta = 55^o$ relative to the polarization direction of the incoming light. A needle (10 cm long, less than 500 μm inner diameter) directs an effusive jet of gas to the interaction region; the background pressure in the chamber was $\cong 10^{-4}$ mbar. TOF spectra were taken for different photon energies using a

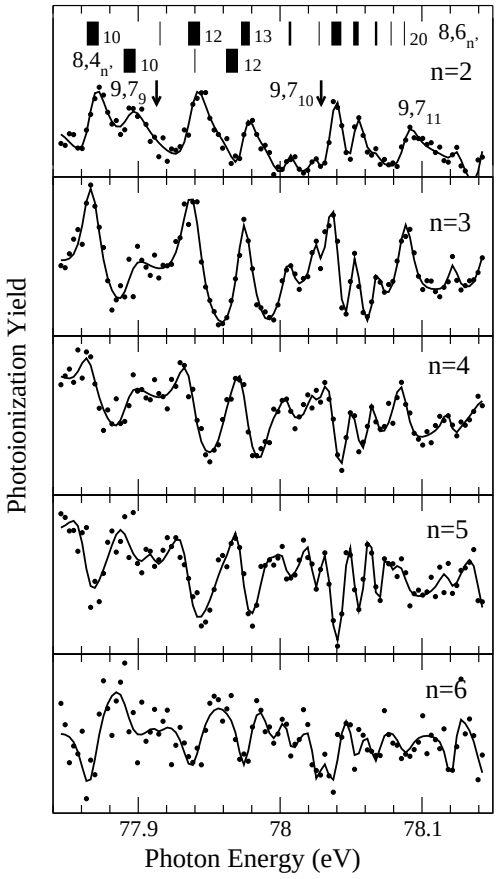

FIG. 1: Experimental partial cross sections, σ_n^8, leading to the final states $He^+(n)$ with $n = 2-6$. The two vertical-bar diagrams in the upper part of the figure give the assignments of the double-excitation resonances by specifying n'; with the widths of bars being proportional to the linewidths of the corresponding resonances [5]. The vertical arrows mark the calculated energies of the pertuber. The filled data points are the present experimental results, with the solid curves through the data points representing the fit results.

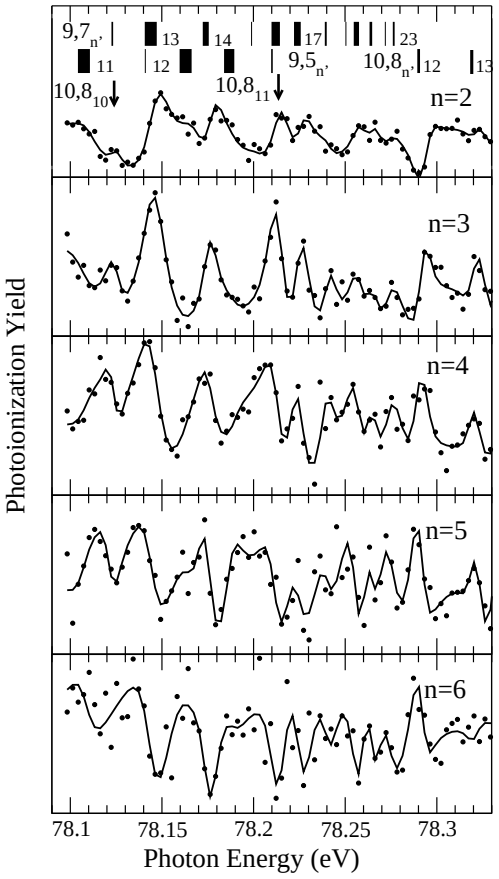

FIG. 2: Experimental partial cross sections, σ_n^9, leading to the final states $He^+(n)$ with $n = 2-6$. For details, see Fig. 1

step-width of 1 meV and converted into photoemission spectra (PES) by the well-known time-to-energy conversion procedure. In order to eliminate the influences caused by the decrease of the ring current and fluctuations of the gas pressure in the interaction region during data acquisition, the spectra were normalized to the intensity of the n=1 line (For details see [2]).

The measured double-excitation $^1P^o$ resonances of helium can be identified in a simplfied

classification scheme $N, [K_{n'}\ 3,4]$, with N and n' standing for the ionization threshold of a given channel and the running index of the considered Rydberg series, respectively; K represents the angular-correlation quantum number. In an independent particle picture, N (n') can be understood as the quantum number of the inner (outer) electron. Note that for convenience we employ in our discussion the notation σ_n^N to label various PCSs, where the lower index n refers to the principal quantum number of the remained electron in the ion.

Figs. 1 and 2 display our results for the PCSs σ_n^8 and σ_n^9 (with $n = 2-6$), respectively, along with the results of a least-squares fit analysis (filled data points and solid curves). In the PCSs σ_n^8 the resonance $^1P_1^o$ is resolved for the first time using an experimental resolution of $\cong$6 meV. This observation is in contrast to previous measurements [6] of total cross section with a much high resolution of $\cong$2 meV and is due to the fact that the PCSs include additional electron-coupling information between various outgoing channels. As a result, this resonance becomes more pronounced in the various PCSs. A more detailed analysis and in particular a comparison with theoretical results is subject to future work.

This work was supported by the Bundesministerium für Bildung und Forschung, project no. 05 KS1EB1/2, and the Deutsche Forschnungsgemeinschaft, project no. PU 180/1-1.

---

[1] R. Püttner, B. Grémaud, D. Delande, M. Domke, M. Martins, A. Schlachter, and G. Kaindl, Phys. Rev. Lett. **86**, 3747 (2001).

[2] Y. H. Jiang, R. Püttner, R. Hentges, J. Viefhaus, M. Poiguine, E. Becker, J. M. Rost, and G. Kaindl, Phys. Rev. A **69**, 2706 (2004).

[3] D. R. Herrick and O. Sinanoğlu, Phys. Rev. A **11**, 97 (1975).

[4] C. D. Lin, Phys. Rev. A **29**, 1019 (1984).

[5] J. M. Rost, K. Schulz, M. Domke, and G. Kaindl, J. Phys. B **30**, 4663 (1997).

[6] M. Domke, K. Schulz, G. Remmers, G. Kaindl, and D. Wintgen, Phys. Rev. A **54**, 1424 (1996).

Atom-specific identification of adsorbed chiral molecules by photoemission

J. W. Kim,[1] M. Carbone, [2] J. H. Dil, [1] M. Tallarida, [1] R. Flammini, [3] M. P. Casaletto, [4] K. Horn, [1] and M. N. Piancastelli[2]

[1]*Fritz-Haber-Institut der Max-Planck-Gesellschaft, D-14195 Berlin, Germany*

[2]*Department of Chemical Sciences and Technologies, University "Tor Vergata",I-00133 Rome, Italy*

[3]*CNR-IMIP, Area della Ricerca di Roma 1, I-00010 Monterotondo Scalo, Italy*

[4]*CNR-ISMN, Area della Ricerca di Palermo, I-90146 Palermo, Italy*

The identification of chiral centers in adsorbed species is a desirable goal in view of the importance of adsorbed chiral molecules as modifiers in heterogenous catalytic processes. Here we show that the chiral character of adsorbed stereoisomers of 2,3 butanediol molecules adsorbed on Si(100) can be detected using circularly polarized x-rays, through a circular dichroism (CD) in carbon 1s core level photoemission. The CD measurements were performed using right and left circularly-polarized (RCP and LCP) light at the UE56/2-PGM1 beam line at BESSY II. 2,3-butanediol was adsorbed on the Si(100) surface to a saturated amount at room temperature (RT) and its coverage is estimated to be about 0.25 monolayer [1]. Data were recorded under a few different azimuthal directions of the emitted photoelectrons.

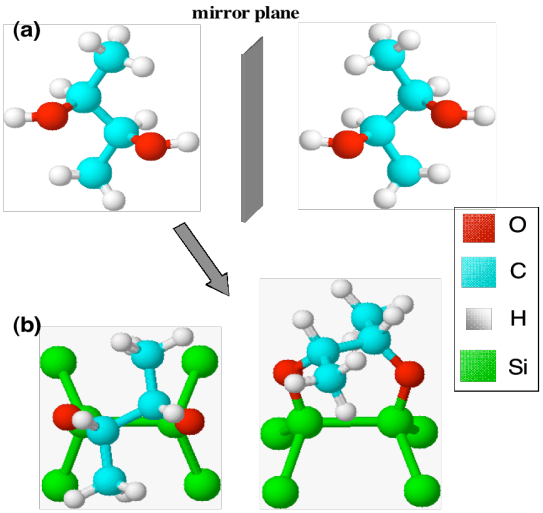

Fig. 1 *Structural models before and after the adsorption. (a) the enantiomers of (S,S): left and (R,R): right- forms of 2,3-butanediol. (b) adsorption geometry for the (S,S)-2,3-butanediol on a Si(100) surface as inferred from core and valence level photoemission (ref. [1])*

It is advantageous to use 2,3-butanediol for such a study, since this molecule has both chiral and achiral carbon atoms in the molecule, as evident from Fig. 1(a) which shows two enantiomers [(*S,S*)- and (*R,R*)- forms] of the molecule; moreover, an achiral (*R,S*) stereoisomer molecule exists. Upon adsorption on Si(100) at RT, the O-H bonds are spontaneously broken, and the molecule is supposed to take a bridging position on the Si(100) surface as shown in Fig. 1(b) [1]. The "chiral" carbon atom bonded to the oxygen atom, and the "achiral" one in the CH3 group are separated by 1.3 eV, on account of their different chemical environment. This provides the opportunity to measure an atom-specific CD effect. The data for the C 1*s* core level from (*R,R*)-2,3-butanediol under RCP (blue) and LCP (red) light are shown in the topmost spectra of Fig. 2. A sizeable dichroic effect occurs in the peak arising from the carbon atom in the chiral center. An asymmetry of equal magnitude but opposite sign occurs when the (*S,S*) enantiomer, the mirror image of the (*R,R*)-form, is investigated. Finally, no asymmetry occurs when the achiral (*R,S*) isomer is adsorbed on the surface as shown in the bottom spectra. These observations are a clear proof that this dichroic signal is caused by the chiral nature of the environment of the respective carbon atom.

The C 1*s* core level is unlikely to "feel" the chiral nature of its molecular environment; the asymmetry then arises from a transition of the photoexcited electron from the core level into an

unoccupied or continuum state. The influence of the latter determines the sign and magnitude of the circular dichroism [2]. Considering the matrix element governing the photoemission intensity, the strongest transitions will occur into those unoccupied levels that are localized near the core-ionized carbon atom, *i.e.* those that exhibit chirality as a result of the electronic charge distribution around them. The effect is proportional to the interference of pairs of dipole matrix elements which differ by the signs of all projections of orbital momenta. For non-chiral molecules having a plane of symmetry, these differences are equal to zero. In fact, no dichroism is found in the achiral enantiomer (bottom spectra of Fig. 2) where the emission from the *R* and *S* forms of carbon atoms in a molecule cancels.

In an analysis of CD in core level photoemission, one has to take into account an effect arising from the experimental geometry, however. Schönhense and co-workers have demonstrated that strong circular dichroism can be observed even in adsorbed achiral molecules, e.g. linear ones, such as CO/Pd(111) [3,4], because of the handedness in the combined system of incoming photons, emitted photoelectrons and the orientation of the molecule. We conclude that the asymmetries in Fig. 2 indeed arise from the chiral centers in the molecule because CDAD in an emission direction **k** in the plane defined by the incident light vector **q** and the surface normal **n** will vanish, since no handedness is present in the experimental geometry [4]. This is the reason for the choice of our measurement geometry. In view of the increasing importance of an analysis of biologically active surface species, our observation may provide a path to analyzing chiral centers in complex adsorbed molecules using photoemission spectroscopy.

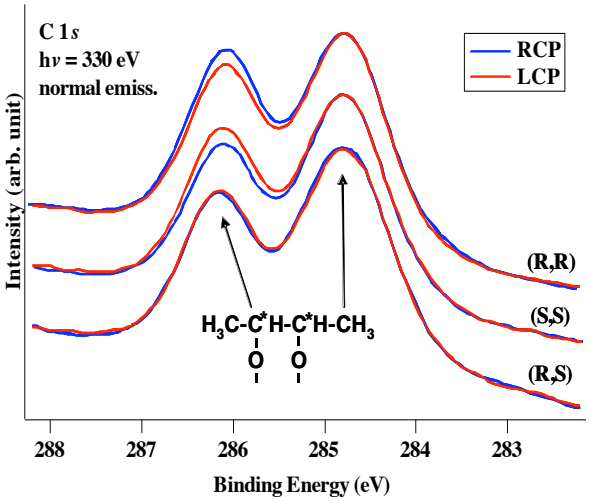

Fig. 2 *Photoelectron spectra of the C 1s core levels for the adsorbed stereoisomers of 2,3-butanediol excited by right (blue) and left-circularly polarized (red) light at hν = 330 eV. Dichroism is observed on the higher-binding energy component attributed to emission from the carbon atoms in the chiral center from the (R,R) and (S,S) forms. The dichroic effect changes sign either with photon polarization or molecular handedness. No dichroism is observed in the achiral (R,S) form.*

Acknowledgement

This work is supported by EU under the ARI program. J.W.K. acknowledges support by the Alexander von Humboldt Foundation.

Literature references

[1] J. W. Kim, M. Carbone, M. Tallarida, J. H. Dil, K. Horn, M. P. Casaletto, R.Flammini, and M. N. Piancastelli. Surf. Sci. **559**, 179 (2004).
[2] N. Chandra, Phys. Rev. A **39**, 2256 (1989).
[3] J. Bansmann, Ch. Ostertag, G. Schönhense, F. Fegel, C. Westphal, M. Getzlaff, F.Schäfers, and H. Petersen, Phys. Rev. B **46**, 13496 (1982).
[4] G. Schönhense, Physica Scripta T **31**, 255 (1990).

Photoelectron circular dichroism in the angular distribution: Investigating the Carvone molecule

CJ Harding, EA Mikajlo, I Powis
School of Chemistry, University of Nottingham, Nottingham, NG7 2RD, UK.
S Barth, U Hergenhahn
Max-Planck-Institute for Plasma Physics, EURATOM Association, Boltzmannstr. 2, 85748 Garching.
EU BI3A-11/160604

Introduction

Carvone is a natural substance used in everyday consumer products, such as toothpaste, to provide flavour and fragrance. Carvone exists in two enantiomeric forms; R-Carvone giving a spearmint flavour and the S-Carvone a caraway flavour. Enantiomers are chemically identical but the configuration of the chemical groups around one or more carbon centers in the molecule, such that the two enantiomers are non-superimposable mirror images of each other. It has been predicted that the electric dipole transition amplitude for circularly polarized light irradiating an enantiomerically pure, randomly oriented sample can produce a dichroic effect in the order of several percent [1, 2, 3]. This effect would manifest itself as a difference in the angle- and energy-resolved photoelectron yield (Circular Dichroism in the Angular Distribution, CDAD). Very recently, CDAD in valence and core level photoionization of chiral molecules has been demonstrated experimentally [4, 5]. A dichroic effect of this size would be several orders of magnitude larger than dichroic effects measured using traditional adsorption techniques.

Measurements reported here involve the use of the UE56/2-PGM1 beamline operating in dual-beam mode. This beamline facilitates the rapid interchange of left and right circularly polarised light and turned out to be crucial for measuring the dichroic effect of interest without introducing artificial asymmetries due to beam drift and sample density fluctuations. The final outcome from measurements made in this way provides dichroism signals that can be calculated per photoline and also on a per atom basis. These dichroic signals should be seen to be of equal magnitude and opposite sign on the change of enantiomer form.

Photoline dichroism signals

Typical results for the photoline dichroism of Carvone recorded at a photon energy of 300 eV are shown in figure 1. The C 1s photoelectron spectra were measured using rapid switching between right and left circularly polarised light. The CDAD is calculated from the measured spectra using the following relation:

$$A_{CDAD} = \frac{R-L}{R+L}, \tag{1}$$

where R and L represent C 1s spectra of a single enantiomer of Carvone, recorded using right and left circularly polarised light respectively. Since there is a small intensity difference between up- and downstream undulator, R and L have to be calculated as $R = (R_d R_u)^{1/2}$, and analogously for L. Here, R_u and R_d designate spectra measured with the upstream (downstream) undulator. The photoelectron spectra are measured at an angle of 54.7° between the direction of propagation of the light and the photoelectron momentum. This results in a cancellation of the anisotropy parameter β from the denominator of equation 1, allowing normalisation to the

count rate without modulation from the anisotropy parameter.

Computationally predicted photoline dichroism signals are presented in figure 2. In the upper pane of figure 2 the experimental photoelectron spectrum is shown together with stick spectra resulting from a highly accurate computational technique for the calculation of core electron binding energies. Two sets of stick spectra are shown to represent the conformers of Carvone that are present at room temperature. Theoretical predictions show that the peak at a binding energy of 293 eV is given by the single carbonyl carbon of the Carvone molecule, the peak at 290 eV gives the $=\mathbf{C}H_2$ of the molecule and the band at approximately 290 eV gives the remaining carbon atoms. Using these predicted binding energies multiple scattering calculations are used in an attempt to provide a simulation for the photoline dichroism signal. It can be seen that the prediction for the carbonyl peak is correct, while for the remaining lines a higher degree of fine structure is predicted than could be experimentally observed.

Dichroism signal for single carbon atoms

As the multiple scattering calculation provides a very reasonable description of the photoelectron spectrum resulting from the carbonyl carbon, we can use it to predict the dichroism originating from this one carbon atom over a range of kinetic energies. The resulting plot is shown in figure 3. The theoretical predictions for the carbonyl carbon photoelectron line are plotted against experimental points for the dichroism extracted at different photon energies. As can be seen there is a good correlation between the theoretical predictions and the measured circular dichroism, and the experimental data for the two enantiomers show the equal and opposite trend as would be expected from symmetry arguments.

The fact that the dichroism occurs and that the C 1s orbital from which the photoelectrons are ionised in our experiment is spherically symmetric, implies that the dichroism measured in this system is a final state effect and is caused by the scattering of outgoing photoelectrons from the chiral molecular potential.

References

[1] B. Ritchie, Physical Review A **13**, 1411 (1976).

[2] I. Powis, Journal of Chemical Physics **112**, 301 (2000).

[3] I. Powis, Journal of Physical Chemistry A **104**, 878 (2000).

[4] N. Böwering *et al.*, Physical Review Letters **86**, 1187 (2001).

[5] U. Hergenhahn *et al.*, Journal of Chemical Physics **120**, 4553 (2004).

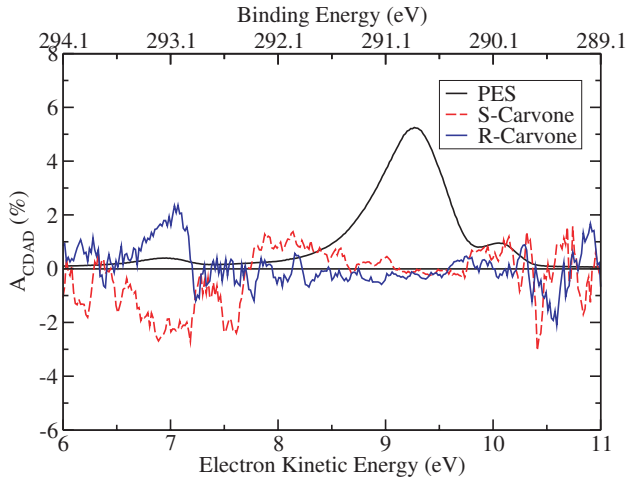

Figure 1: A plot showing the high resolution C 1s photoelectron spectrum, and the dichroism signal calculated on a photoline basis for both R- and S-Carvone

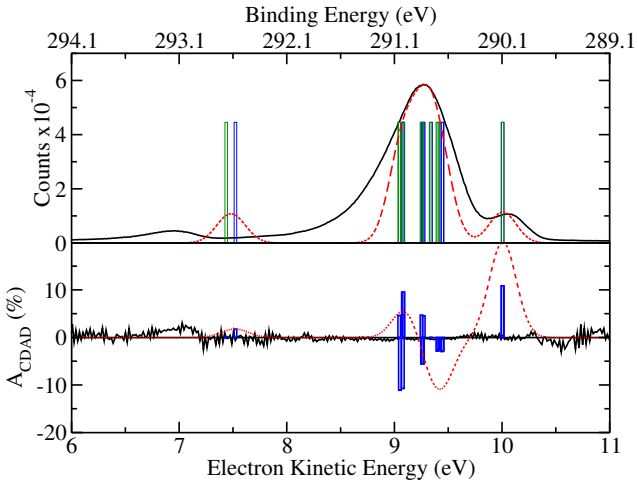

Figure 2: A plot showing a C 1s high resolution photoelectron spectrum together with a stick spectrum representing calculated binding energies (upper) and the experimental and calculated photoline dichroism signal (lower panel).

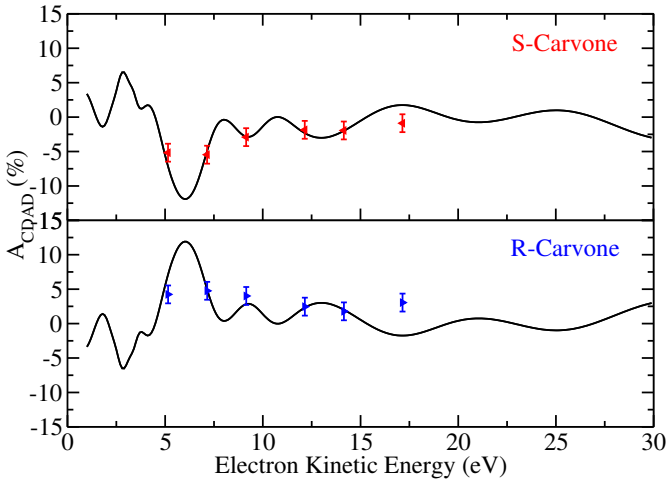

Figure 3: Experimental and calculated asymmetry of the carbonyl C 1s photoelectron line of carvone, given as $100 A_{CDAD}/cos(54.7°)$. The cosine factor arising from our experimental geometry is removed from the data for easier comparison with other experiments.

Investigation of Trapped Nano- and Micro-Particles using Soft X-Rays

C. Graf, [a] B. Langer,[a,b] S. Dembski,[a] R. Lewinski,[a] E. Rühl [a]

[a] Institut für Physikalische Chemie, Universität Würzburg, Am Hubland, 97074 Würzburg

[b] Max-Born-Institut Berlin, Max-Born-Str. 2a, 12489 Berlin

Progress on investigations of single, trapped nano- and micro-particles is reported, which is based on previous work [1]. The aim of this research is to investigate electronic, structural, and dynamic properties of variable size and composition II-VI semiconductor nanoparticles in different environments. This also requires methodological developments in order to facilitate investigations on trapped solid and as well as liquid particles. The particles are prepared by chemical syntheses, where neat or coated II-VI semiconductor nanoparticles are synthesized [2]. Moreover, sophisticated test systems for core-shell particles, such as silica nanoparticles that have been coated by a thin metallic layer, are accessible by chemical approaches [3].
We have performed first test experiments on trapped liquid microparticles. These are prepared using a liquid microdroplet piezo injector, where a mixture of water and dimethyl siloxane - (60% propylene oxide - 40% ethylene oxide) - block/graft-copolymer (polyalkylene oxide modified silicone oil) obtained from ABCR is used (cf. formula shown in Fig. 1). When the micro droplet with an initial diameter of 70 μm leaves the droplet generator it is charged by an external voltage due to electrostatic induction. Subsequently, it is stored in an electrodynamic trap, similar to previous experiments [1,4,5]. After evaporation of the water a single, liquid droplet with diameters between 200 nm up to 10 μm remains up to several hours in the three dimensional electrodynamic trap [1,4,5]. Typical diameters range between 5 and 10 μm. First experiments on liquid particles focused on the charging behavior of liquid polymers, which can easily be stored in the high vacuum environment of the trap.

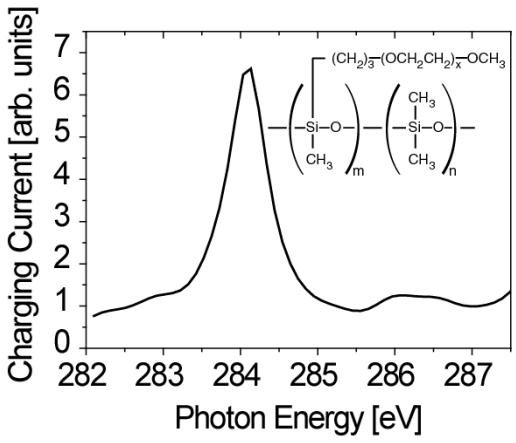

Fig. 1: Charging current of a trapped, single 8 μm dimethylsiloxane - (60% propyleneoxide - 40% ethyleneoxide) - block/graft-copolymer droplet in the C 1s-excitation regime.

The trapped particle is illuminated by a frequency doubled Nd:YAG laser (P < 50 mW, λ = 532 nm). The scattered light is collected by a lens and is detected by an avalanche photodiode. The scattered light is modulated by the eigenfrequencies of the trapped particle due to its motion through the Gaussian laser beam. These frequencies can be obtained from a fast Fourier transform of the photodiode signal. The charge-to-mass ratio Q/M of the particle is very precisely derived, once the parameters of the electrodynamic trap are known. The experiments were carried out at the following beamlines: UE-52-SGM and U 41-PGM.

The C 1s- and the O 1s-edges of liquid particles were investigated. Charging curves are obtained from measuring changes in particle charge as a function of photon energy. The first derivative of these charging curves provides the charging current as a function of photon energy, which gives information on the electronic structure of the trapped species, similar to previous work [1,3,4]. Fig. 1 shows the charging current of a stored liquid droplet in the C 1s-excitation regime. A single sharp resonance is observed, which indicates the occurrence of a C 1s $\rightarrow \sigma^*$-resonance in the near-edge regime. This result shows for the first time that trapped, liquid particles can be investigated using soft X-rays and that information on the electronic structure of the particles can be derived from these experiments. It appears also possible to investigate aqueous droplets at ambient pressure as well as II-VI seminconductor nanoparticles or other systems, which are dispersed in trapped liquid droplets.
First charging experiments on trapped, solid ZnS nanoparticles have been performed in the Zn 2p-regime (1010-1050 eV), which have radius of 531 nm [2]. They are trapped at low charge

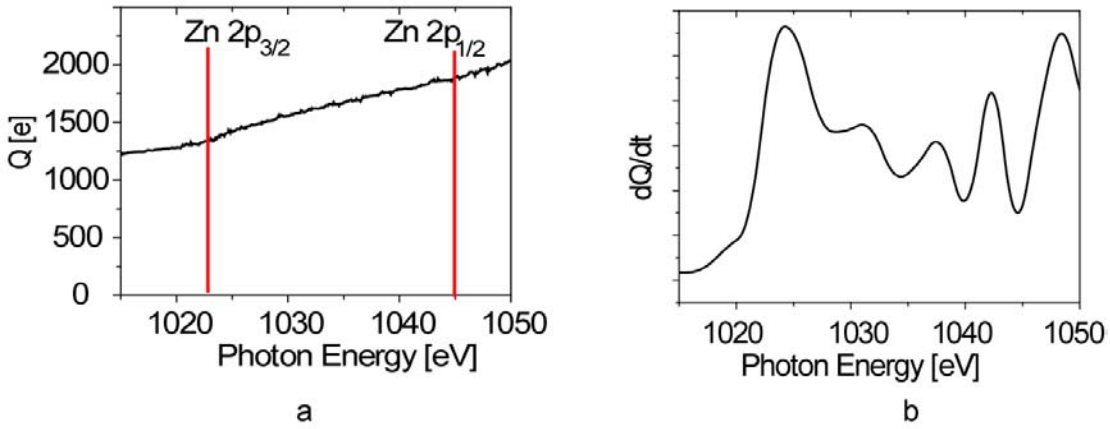

Fig. 2: (a) Charging curve of a single, trapped ZnS nanoparticle (radius: 531 nm) recorded in the Zn 2p-regime: (a) charging curve, (b) first derivative of spectrum (a) corresponding to the charging current of the particle.

state, i.e. 1200 < Q < 2000 e. The charging current shows a clear onset above 1020 eV and a dominant maximum near 1024 eV, which is also found in near-edge spectra of solid ZnS samples [6]. Besides weaker features, there is another dominant one near 1048 eV. Both dominant features are explained by the substantial spin-orbit splitting of the near-edge fine structure (cf. Fig. 2 (vertical lines in (a))). The shape of the near-edge spectrum is consistent with a zinc blende structure, as communicated in ref. [6]. This structural assignment is also consistent with additional work on the crystal structural using X-ray diffraction [2].
Charging of neat Silica particles (250 nm radius) has been studied before [1]. New experiments focus on smaller silica particles, where changes in particle charging and electronic structure are observed as a result of coating the particles with a thin gold shell (39 nm - see Fig. 3(a)). Such experiments have prototype character for later work on core-shell systems containing e.g. II-VI semiconductors. The density of colloidal gold (ρ = 18.9 g/cm³) and the low surface charge of these particles lead to a low charge-to-mass ratio, so that they cannot be easily stored in the trap by using the simple injection approach via a vibrating membrane [1]. This problem is overcome by charging the particles by synchrotron radiation before they are trapped. At low charge states (Q < 1000 e) and low photon flux in the soft X-ray regime the charge state of the particle increases stepwise, similar to previous work [1].

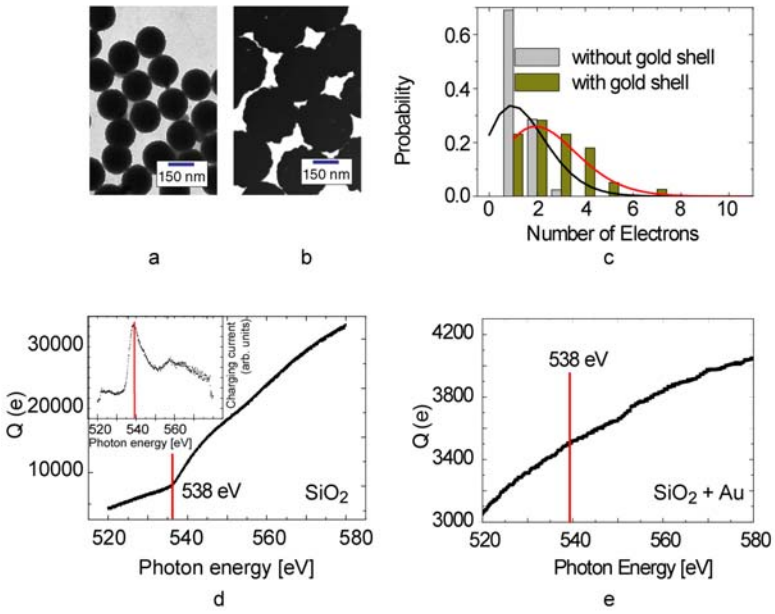

Fig. 3: Silica particles with and without a gold shell: TEM micrograph of silica particles (158 nm radius) before (a) and after coating with a gold shell of 39 nm thickness (b). (c) Probability of the electron emission per absorbed 84 eV photon. Charging in the O 1s regime of uncoated (d) and Au-coated silica particles (e). The inset in Fig. 1(d) shows the first derivative of curve (d) which corresponds to the charging current.

Charging at low flux using 84 eV photons shows a significant change due to the metal coating (cf. Fig. 3(c)). Pure silica colloids emit per absorbed photon predominantly one or two electrons. In contrast, gold coated silica particles emit up to 7 electrons per absorbed photons. This can be explained by the lower work function of gold, where the thin film has evidently already metallic properties. There are also significant changes in the charging current. The neat silica particle shows a distinct near-edge feature in the O 1s-regime (cf. Fig. 3(d)). In contrast, the gold coated particle does not show any evidence for changes in particle charge due to resonant O 1s-absorption. This implies that properties of thin films in core-shell particles can be sensitively probed by single, trapped nanoparticles. Furthermore, the thin metal film is evidently closed, so that the silica core does not contribute to particle charging (cf. Fig. 3(e)).

We thank Melanie Grom for the preparation of nanoparticle samples and R. Neder for providing the XRD results on ZnS nanoparticles. Finanical support by the Deutsche Forschungsgemeinschaft (Sonderforschungsbereich 410 (TP C8)) is gratefully acknowledged.

References

1 M. Grimm, B. Langer, S. Schlemmer, T. Lischke, W. Widdra, D. Gerlich, U. Becker, E. Rühl, AIP Conf. Proc. **705**, 1062 (2004).
2 R. Lewinski, Diplomarbeit, Universität Würzburg (2004).
3 C. Graf, D.L.J. Vossen, A. Imhof, A. van Blaaderen, Langmuir **19**, 6693 (2003).
4 M. Grimm, B. Langer, S. Schlemmer, T. Lischke U. Becker, W. Widdra, D. Gerlich, E. Rühl, manuscript in preparation (2005).
5 M.A. Hamza, B. Berge, W. Mikosch, E. Rühl, Phys. Chem. Chem. Phys. **6**, 3484 (2004).
6 B. Gilbert, B.H. Fraser, H. Zhang, F. Huang, J.F. Banfield, D. Haskel, J.C. Lang, G. Scrajer, G. de Stasio, Phys. Rev. B **66**, 245205 (2002).

Radiative Relaxation of 2p-Excited Argon Clusters

R. Flesch[1], I.L. Bradeanu[1], M. Meyer[2], E. Rühl[1]

[1] Institut für Physikalische Chemie, Universität Würzburg, Am Hubland, 97074 Würzburg, Germany

[2] LURE, Centre Universitaire Paris-Sud, Bât.209d, F-91898 Orsay Cedex, France

The emission of ultraviolet fluorescence radiation from variable size argon clusters is investigated at high spectral resolution in the Ar 2p excitation regime. This radiative process has been observed before in numerous experiments on gaseous and solid rare gases and is often termed '*third continuum*' fluorescence [1-3]. The origin and mechanisms leading to the emission of these fluorescence photons is still not fully known. This is the primary motivation for the present work, which follows preliminary low resolution experiments [4].

The experimental setup consists of a continuous supersonic jet that is used for variable size argon cluster preparation. The average cluster size <N> is varied by changing the stagnation conditions (cf. [4]). The total fluorescence in the ultraviolet regime is detected by a cooled photomultiplier tube, which is mounted behind a quartz window (EMI 9789QB). This setup is also used to measure fluorescence excitation spectra at the U49/2-PGM1-beamline. The fluorescence in the ultraviolet/visible regime is dispersed by a secondary monochromator (HR-460, Jobin-Yvon), which is equipped with a CCD-camera [5] The spectra are recorded by setting the undulator to the nominal photon energy and tuning the monochromator to zeroth order. The results from fluorescence excitation spectra are compared to the photoion yield of the atom and clusters as well as the atomic fluorescence (see Fig. 1). There is strong fluorescence intensity from clusters in the Ar 2p-continuum, but no evidence for the occurrence of discrete core-exciton states in the near-edge regime. This is unlike the absorption and photoionization cross section of argon clusters and the solid. The dispersed fluorescence shows a broad molecular band which is centered near 280 nm, as shown in Fig. 2.

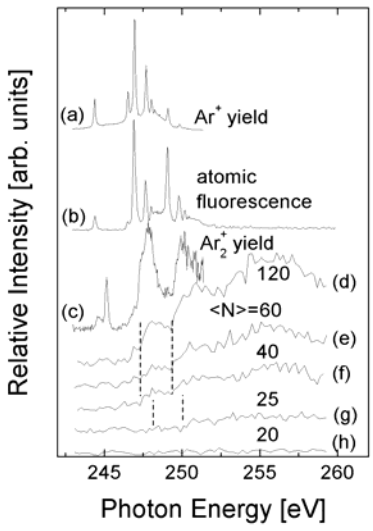

Fig. 1: Fluorescence excitation spectra of variable size argon clusters ((d)-(h)) in comparison with the photoion yield of Ar^+ (a), the atomic fluorescence (b), the Ar_2^+ yield (c). Note that a variable contribution of the fluorescence of atomic argon has been subtracted from the spectra shown in (d)-(h). The vertical dashed lines indicate the step-like increase of the fluorescence yield at the Ar 2p-edge.

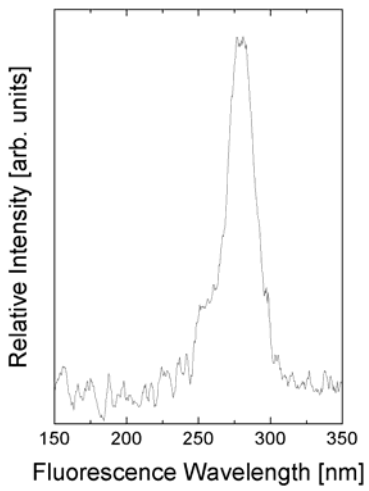

The appropriate mechanism of this radiative decay can be developed together with results from related work, indicating that double or even multiple ionization in the Ar 2p continuum initiates the fluorescence process in clusters. This assignment is due to the occurrence of ultraviolet fluorescence in the 2p-continnum, with a step-like onset at the 2p-ionization energies in variable size clusters (cf. vertical dashed lines in Fig. 1).

Fig. 2: Dispersed fluorescence spectrum recorded upon excitation of argon clusters at <N> = 80 at a photon energy of 263 eV.

After creation of the core hole and electronic relaxation via the normal or double Auger decay, there is subsequently ultrafast charge-delocalization. This is a result of an interatomic energy transfer (intramolecular Coulomb decay (ICD) [6]) to the neighboring sites of the core-excited center, which occurs in the femtosecond time regime. This leads to the formation of singly charged moieties within the cluster. On the other hand, it is known that fluorescence in the 250 nm regime occurs in the nanosecond time regime [3]. Thus, it appears unlikely that doubly charged moieties have such a long lifetime in clusters, so that charge transfer excimers between a dication and surrounding neutrals can be formed, as proposed before to rationalize the '*third continuum*' fluorescence in gaseous Ar [2]. The cluster size dependence of the fluorescence yield indicates that radiative relaxation occurs preferably from clusters that are stable with respect to fission, i.e. containing more than 90 atoms per cluster. This also explains why there is only little fluorescence yield in the regime of small clusters. Consistently, the spectra shown in Fig. 1 (d)-(f) give evidence for a broad continuum resonance between 254 and 259 eV, which occurs primarily from the excitation of bulk sites.

We thank H.-W. Jochims for his help in preparation of the experiments. This work is supported by the Franco-German Procope Program and the Deutsche Forschungsgemeinschaft.

References

1 T.D. Strickler, E.T. Arakawa, J. Chem. Phys. **41** 1783 (1964); G. Klein, M.J. Carvalho, J. Phys. B **14**, 1283 (1981).
2 H. Langhoff, Opt. Commun. **68**, 31 (1988); H. Langhoff, J. Phys. B **27**, L709 (1994).
3 E. Robert, A. Khacef, C. Cachoncinlle, J.M. Pouvesle, Opt. Commun. **117**, 179 (1995); J. Wieser, A. Ulrich, A. Fedenev, M. Salvermoser, Opt. Commun. **173**, 233 (2000).
4 E. Rühl, C. Heinzel, H.-W. Jochims, Chem. Phys. Lett. **211**, 403 (1993).
5 A. Marquette, M. Gisselbrecht, W. Benten, M. Meyer, Phys. Rev. A **62**, 022513 (2000).
6 L. S. Cederbaum, J. Zobeley, F. Tarantelli, Phys. Rev. Lett. **79**, 4778 (1997).

Size Dependence of the Near Edge X-ray Absorption of Small Deposited Chromium Clusters

M. Reif, L. Glaser, M. Martins, and W. Wurth
Universität Hamburg, Institut für Experimentalphysik
Luruper Chaussee 149, D-22761 Hamburg

BMBF KS1GUB/5

Small metal clusters show a strong size dependence of their physical properties. Element specificity and the ability to investigate low target densities makes x-ray absorption spectroscopy (XAS) an ideal tool for the exploration of low coverage cluster systems. It has been shown previously using XPS and XAS, that core level binding energies and line widths are sensitive to changes in the electronic structure of cluster systems [1–3].

We have recently investigated chromium clusters deposited on a ∼4ML Fe/Cu(100) film in a size range of one to thirteen atoms per cluster. A detailed description of the experimental setup and the capability of the cluster source is given elsewhere [4]. In short, clusters are generated by high energy ion bombardment (Xe^+) of a chromium target. After mass separation using a magnetic dipole field, the clusters are decelerated and deposited onto a Fe/Cu(100) surface utilizing argon as buffer gas in a soft landing scheme. XAS measurements have been performed under UHV conditions at a base pressure below $3 \cdot 10^{-10}$mbar. The samples have been prepared in situ under UHV conditions and the absorption spectra have been recorded using the total electron yield (TEY), i.e. the sample current. Measurements have been performed at beamline UE56/1-PGM in a normal incidence geometry. The absorption spectra are taken as the sum of spectra measured with right and left circular polarized light.

A detailed description of the data treatment and an elaborate discussion of the results can be found in [5].

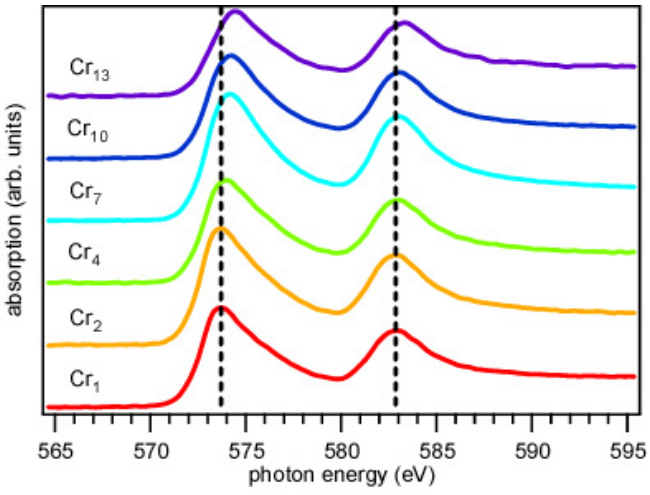

Figure 1: X-ray absorption spectra of selected Chromium clusters. Dashed vertical lines are a guideline for the eye.

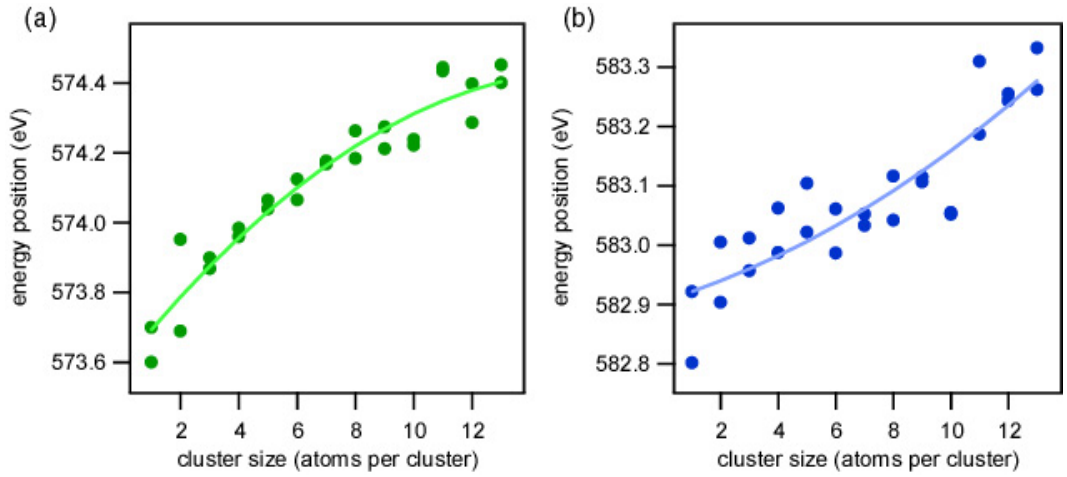

Figure 2: Position of the absorption peak maximum versus cluster size. (a) L_3 edge (b) L_2 edge. Maximum positions of all preparations are shown.

The spectra have been normalized to the incident photon flux using the current of the refocussing mirror. The mirror signal contains a chromium oxide contamination which is too small to affect the normalization of the spectra, but can be used for energy calibration purposes. According to Ito et al. [6], the position of the chromium $2p_{3/2}$ absorption maximum can be found at 575.8eV for Cr_2O_3. Thus, all spectra have been calibrated, so that the maximum of the chromium $2p_{3/2}$ peak in the current from the mirror is at 575.8eV. For all graphs presented in this paper the division of the spectra by the bare substrate spectra has been used for normalization.

The positions of the $2p_{3/2}$ and $2p_{1/2}$ absorption resonances of the clusters have been determined very accurately by analyzing the smoothed first and second derivatives of the spectra. The results of this evaluation are displayed in figure 2(a) and 2(b). The resonance position shifts towards higher photon energies with increasing cluster size for both, the $2p_{3/2}$ and $2p_{1/2}$ absorption lines. Compared to the energy position of the 2p absorption resonance for chromium bulk which is located at 576.5eV [7] for the $2p_{3/2}$ line, the values for the clusters are much smaller. The chromium monomer deposited onto the iron surface has a maximum position of the $2p_{3/2}$ line at an energy of 573.7eV, taking the average value of the two cluster preparations. Interestingly, this is approximately the same resonance position as for the free chromium atom which is found at 573.5eV [8]. We attribute the size dependence mainly to a change in core level binding energy resulting from the size dependence of the valence electronic structure [5].

In figure 3 the difference of the maximum positions of the $2p_{3/2}$ and $2p_{1/2}$ lines is plotted versus cluster size. A decreasing difference of the maximum positions with increasing cluster size is obtained. There are two possible contributions to a relative change of the energetic difference between the L3 and L2 maxima. Firstly, a size dependent change in the shape of the unoccupied valence density of states could result in a change of the peak shape and a shift of the maximum position. This could be different for the spin-orbit split core levels through symmetry induced coupling to different empty valence states. However, since we discuss sum spectra obtained by averaging left and right circular polarization this should be a minor effect. Secondly, the spin-orbit splitting can change with cluster size. A change in

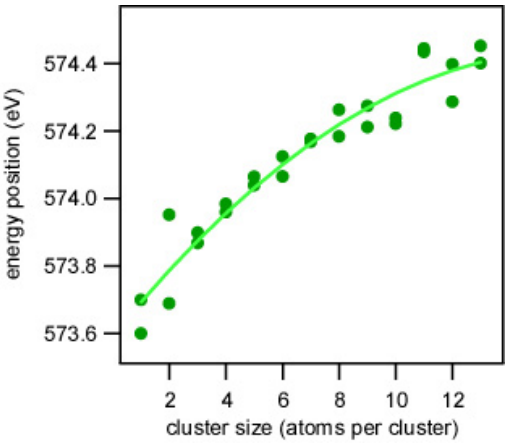

Figure 3: Difference of maximum positions of the L_3 and L_2 absorption peaks, i.e. spin-orbit splitting versus cluster size. Results of all preparations are shown.

the spin-orbit splitting is reasonable, because the spin-orbit splitting Δ_{SO} is to first order proportional to a change in the potential $\Delta_{SO} \propto \partial V/\partial r$. The effective potential V seen by the core levels is expected to change with cluster size as discussed above. Therefore, the spin-orbit coupling should depend on the cluster size.

In conclusion, a pronounced size dependence for the energetic position of the L_3 and L_2 absorption resonances of deposited chromium clusters is observed.

We gratefully acknowledge the traditionally great support of the BESSY staff during beamtime. Special thanks go to A. Föhlisch for fruitful discussions and for technical support to H. Meyer and S. Gieschen.
This work was supported by the German ministry for education and research (BMBF) under grant KS1 GUB/5.

References

[1] W. Eberhardt, P. Fayet, D. M. Cox, Z. Fu, A. Kaldor, R. Sherwood, and D. Sondericker, Phys. Rev. Lett. **64**, 780 (1990).

[2] H.-V. Roy, P. Fayet, F. Patthey, W.-D. Schneider, B. Delley, and C. Massobrio, Phys. Rev. B **49**, 5611 (1994).

[3] J. T. Lau, A. Achleitner, and W. Wurth, Chem. Phys. Lett. **317**, 269 (2000).

[4] J. T. Lau, A. Achleitner, H.-U. Ehrke, U. Langenbuch, M. Reif, and W. Wurth, Rev. Sci. Instr. (2004), submitted.

[5] M. Reif, L. Glaser, M. Martins, and W. Wurth, Phys. Rev. B (2005), submitted.

[6] Y. Ito, T. Tochio, A. M. Vlaicu, D. Ohsawa, T. Mukoyama, Y. Muramatsu, R. C. C. Perera, M. M. Grush, T. A. Callcott, and E. Sherman, J. Electron Spectrosc. Relat. Phenom. **101-103**, 851 (1999).

[7] J. Fink, T. Müller-Heinzerling, B. Scheerer, W. Speier, F. U. Hillebrecht, J. C. Fuggle, J. Zaanen, and G. A. Sawatzky, Phys. Rev. B **32**, 4899 (1985).

[8] U. Arp, K. Iemura, G. Kutluk, T. Nagata, S. Yagi, and A. Yagishita, J. Phys. B: At. Mol. Opt. Phys. **28**, 225 (1995).

Magic numbers in self-assembled two-dimensional nanoclusters of C_{60}

A. Varykhalov[1], O. Rader[1], V. K. Adamchuk[2], W. Gudat[1]
[1] *BESSY, Albert-Einstein-Str. 15, D-12489, Berlin, Germany*
[2] *St.Petersburg State University, 198904, St. Petersburg, Russia*

The observation of magic numbers is among the most intriguing issues of self-organization phenomena. Their existance has been revealed in many systems of different nature. A very prominent example of such self-organization are fullerenes. Fullerenes are spherical hollow clusters with n atoms of carbon, where n is a magic number: in stable clusters only particular values like 26, 28, 60, 70 etc. [1] are allowed. Magic numbers have been observed for many metal cluster systems and were recently observed for gases. It has been show that He atoms tend to produce He_n clusters with n=0, 14, 22, 44 [2]. Similar phenomena were observed also in two-dimensional systems, where the formation of perfectly uniform metallic nanoclusters on Si(111)-(7×7) template was achieved [3]. So far, such effects on atoms are widely studied and generally understood while only a few reports on self-organization of molecules have been published, and no study at all on cluster formation of fullerenes (except for cases of anisotropic or large-scale lateral superstructures). In the following the first observation of perfectly uniform two-dimensional nanoclusters of C_{60} is presented.

In the experiment a carbon passivated W(110), the famous two-dimensional surface carbide R(15×3) [4], has been used as a template. The preparation of this surface is reported elsewhere [5]. Sub-monolayer amounts of C_{60} were deposited *in situ* at very low arrival rate on the substrate held at room temperature. Self-organization of uniform clusters was systematically studied at BESSY using an in-house scanning tunneling microscope (STM) and the HiRes chamber at beamline UE52-SGM for photoemission.

Figure 1 shows the STM observation of several phases of self-organization which take place in dependence of fullerene coverage and deposition rate. Although we did not succeed to resolve individual molecules in the topographic channel, the modulation of the tunneling current reveals that clusters consist of C_{60} chains aligned to rows of surface carbide i.e. to $V_{\parallel}$-direction of carbon superstructure (Fig. 1(c)). Careful analysis of cluster dimensions has shown that the allowed number of fullerene molecules n can either be n=6 (in K_{low} configuration, Fig. 1(a)) or n=9 (K_{high} configuration, Fig. 1(b)). At elevated coverage and particular deposition rate even more complicated effect of „macro“ self-organization has been observed. Figure 1(d) demonstrates cluster chains which are ca. 15 nm long and consist of arranged K_{low} and K_{high} nanoclusters.

Photoemission measurement of valence band have been performed in order to clarify the nature of the observed self-organization as well as the electronic properties of molecular nanoclusters. Results of comparative study of C_{60} on W(110)/C-R(15×3) and W(110) are reported in Figure 2. Photoelectron spectra measured for different amounts of deposited molecules (0.3 – 2 ML) are presented. While solid line denotes photoemission from fullerenes arranged on surface carbide, the dashed one represents C_{60} on clean tungsten, where STM has shown no pronounced self-organization. A notable point is strong charge transfer from clean W to C_{60}, which appears as energy shift of whole electronic structure by δE=0.45 eV (see Fig. 2, note that the solid- and dashed-line spectra are aligned to the energy of molecular orbital HOMO-1). Since this shift is due to covalent bonding C_{60}-W, it is assured that no strong chemical interaction happens between adsorbed fullerenes and carbon passivated W(110)/C-R(15×3). The weak electrostatic bonding to the substrate is therefore the straightforward explanation for the increased molecule mobility at room temperature. Considering the strongly anisotripoic charge distribution in the surface carbide (see [5]) one can assume an induced polarization of adsorbed C_{60} which causes Van-der-Waals interaction. These

assumptions lead us to the model of a two-dimensional fullerene gas, the properties of which are determined by the geometry and electronic structure of the W(110)/C-R(15×3) template.

Another notable feature is the internal energy shift δH=0.52 eV in the electronic structure of HOMO which appears only for sub-monolayer coverage of C_{60} deposited on the surface cabide (Fig. 3). It vanishes for the multilayer and is not observed at all in photoemission from fullerenes on clean W(110). This effect can unambigously be attributed to modification of C_{60} electronic structure upon cluster formation and, in particular, to the formation of a joint electronic structure of extended π-states. This last point is confirmed by voltage-dependent STM measurements. Based on these observations, the occurrence of the magic numbers can be explained by energy minimization in the electron subsystem of C_{60} adsorbed on W(110)/C-R(15×3).

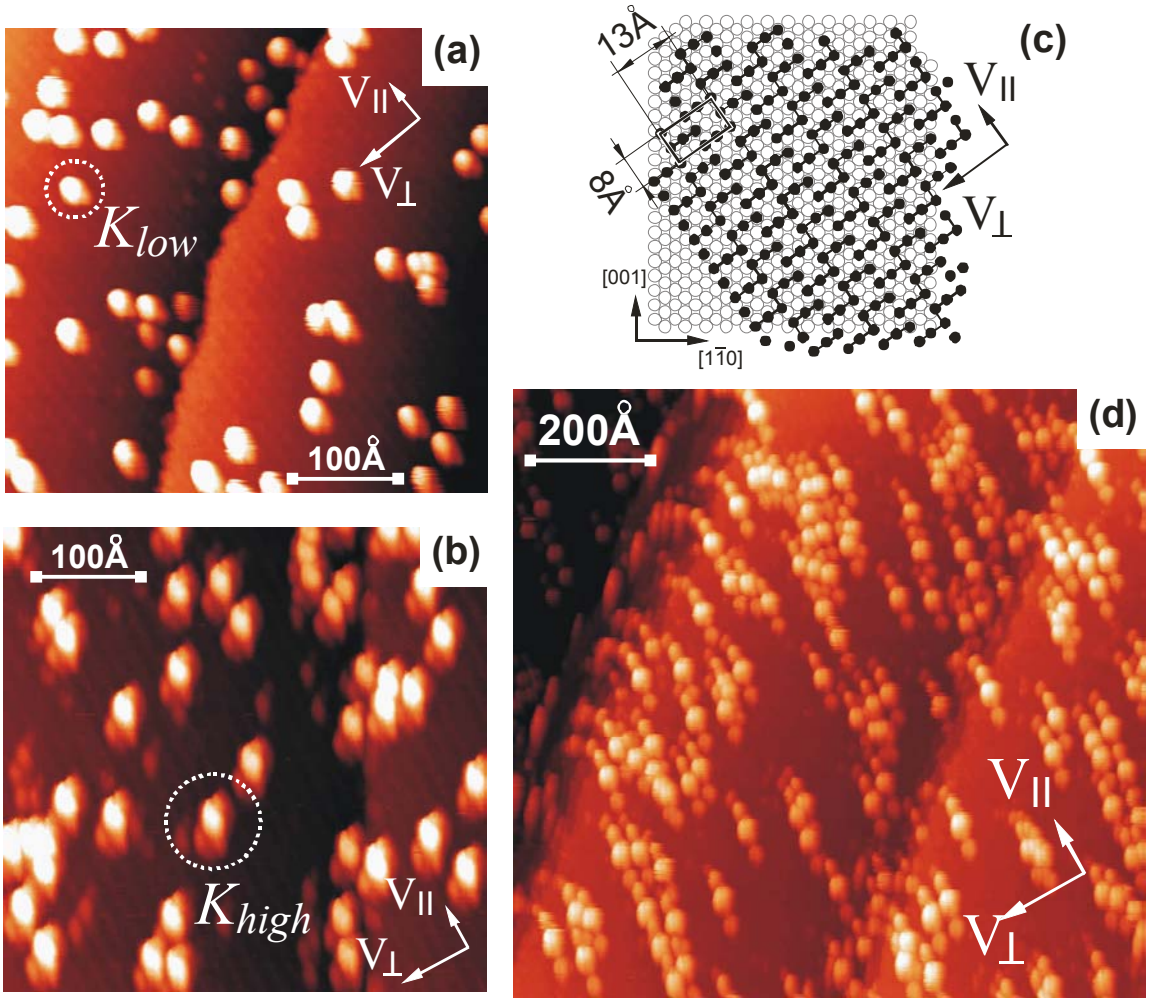

Fig. 1. STM study of fullerene molecular nanoclusters on the surface carbide W(110)/C-R(15×3); (a) K_{low} cluster configuration with n=6 molecules in each cluster produced at low coverage and low deposition speed; (b) K_{high} configuration (n=9) appears at elevated deposition rate; (c) atomic structure of the two-dimensional surface carbide R(15×3); (d) „macro“ self-organization of cluster chains.

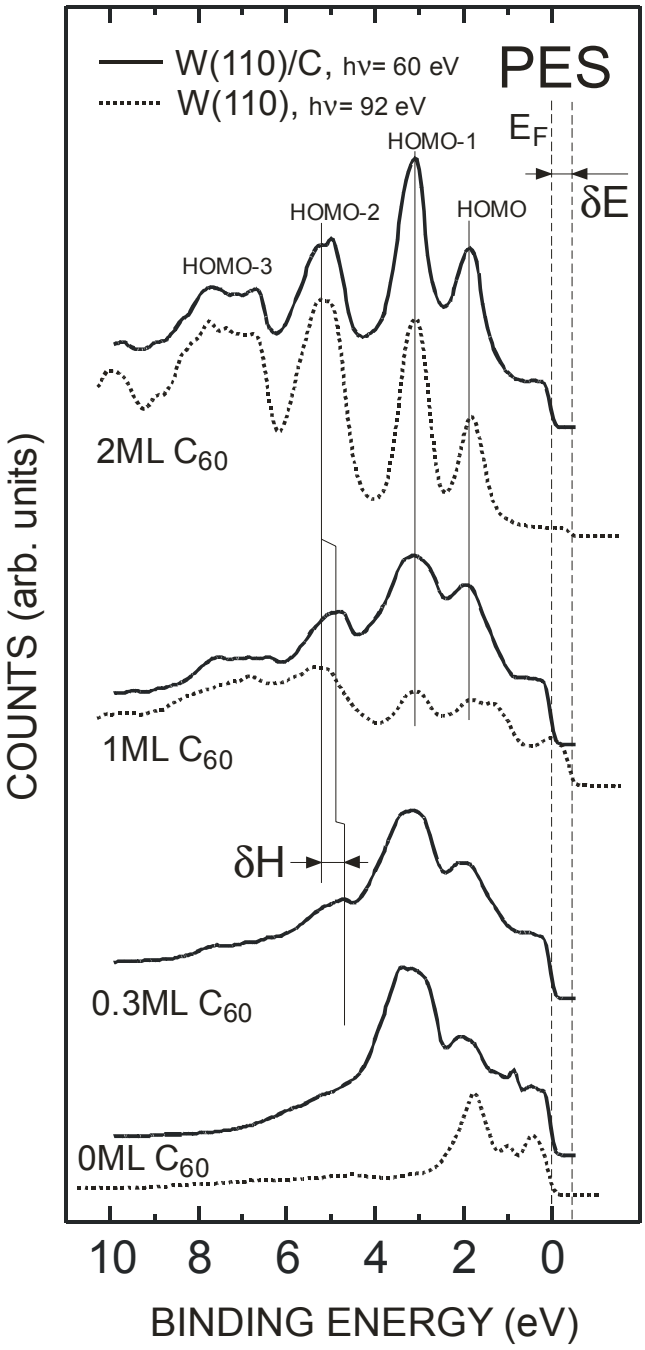

Fig. 2. Results of the photoemission experiment. The comparative study shows that 1ML and 2ML of C_{60} on *clean* W(110) have the same valence band (dotted spectra) and reveal only a general charge transfer which appears as energy shift δE. As opposed to that, photoemission from sub-monolayer amount of C_{60} on the surface carbide (solid line) reveals an internal modification of electronic structure with an energy shift δH observed for the HOMO-2 peak. This effect is assigned to the formation of a joint electronic structure in the cluster assembly.

References:

1. M. Knupfer, Surf. Sci. Rep. **41**, 1 (2001).
2. R. Brühl et. al, Phys. Rev. Lett. **92**, 185301 (2004).
3. S.-C. Li et. al, Phys. Rev. Lett. **93**, 116103 (2004)
4. M. Bode, R. Pascal, R. Wiesendanger, Surf. Sci. **344**, 185 (1995);
   Z. Phys. B: Cond. Matt. **101**, 103 (1996).
5. A. Varykhalov et al. „Quantum-size effects in a surface carbide: W(110)/C-R(15×3)“, published in the present BESSY Annual Report.

Mass-filtered cobalt nanoparticles on ferromagnetic surfaces

J. Bansmann, A. Kleibert, F. Bulut[1], R.K. Gebhardt[1], M. Getzlaff[1], E. Holub-Krappe[2], D. Schmitz[2], H. Maletta[2], K.H. Meiwes-Broer

Institute of Physics, University of Rostock, D-18051 Rostock
[1] Institute of Applied Physics, University of Düsseldorf, D-40225 Düsseldorf
[2] Hahn-Meitner-Institut, D-14109 Berlin

supported by DFG via BA 1612/3-1 (in the DFG priority call 1153).

The reduced atomic coordination number of magnetic nanoparticles gives rise to properties being different from the respective bulk behaviour. Especially the large surface - to - volume ratio of clusters leads to an enhancement of the orbital moment as observed for iron nanoparticles over a large size regime [1-4]. Here, we will focus on investigations related to the magnetic behaviour of cobalt clusters on ferromagnetic surfaces. For our experiments we

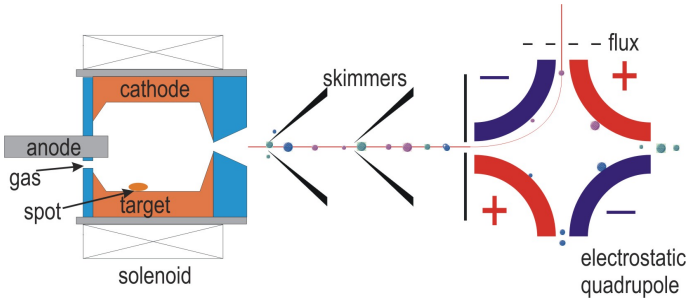

Figure 1: Schematic drawing of the arc cluster ion source ACIS and the mass-filtering unit (electrostatic quadrupole deflector) [5].

have produced mass-filtered cobalt clusters with sizes of 5 nm and 12 nm from a high-purity Co rod. The clusters have been created using the arc cluster ion source and mass filtered in an electrostatic quadrupole deflector, cf. fig. 1 [5]. Finally, the clusters were deposited under UHV and soft-landing conditions onto epitaxially ordered thin films. In order to magnetize these clusters remanently without additional external magnetic fields, ferromagnetic thin Fe(110) and Ni(111) films on W(110) with uniaxial in-plane anisotropies have been chosen as support. Additionally, TEM measurements were carried out in our laboratories [6]. The spin and orbital moments of these cobalt nanoparticles and the underlying ferromagnetic films have been investigated in-situ using the element-specific X-ray Magnetic Circular Dichroism (XMCD) technique at the UE46-beamline at BESSY. The corresponding absorption spectra are shown in fig. 2 for Fe(110) films on W(110) in the left part and cobalt clusters on Fe(110) in the right part. The Fe(110) data (left) clearly display strong XMCD effects close to the Fe 2p absorption edge (i.e., different intensities when reversing

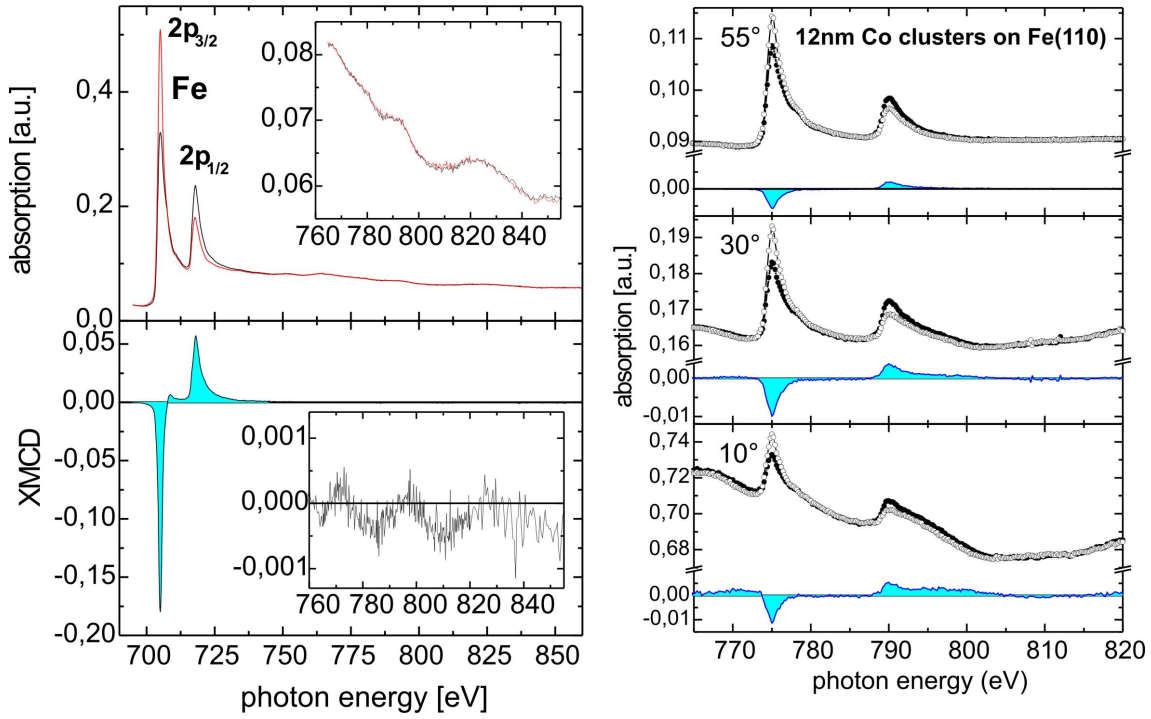

Figure 2: Left: photoabsorption (upper part) and XMCD spectra (lower part) from an Fe(110) film on W(110) close to the Fe 2p levels. The insets show the energetic regime from 760 to 850 eV enlarged. Right: respective spectra taken from mass-filtered cobalt nanoparticles deposited on Fe(110) films at different angles of incidence [7].

the magnetization of the film, see also lower part). The NEXAFS oscillations visible in the upper inset (angle of incidence: 30° grazing) significantly disturb the XMCD data analysis of cobalt clusters on these surfaces, cf. right part of this figure. Especially at grazing incidence with less than 30°, NEXAFS oscillations modulate the absorption signals recorded from the Co 2p core levels and disturb a careful data analysis. Furthermore, as shown in the lower inset in the right part, different photoabsorption intensities may also appear in the NEXAFS energy range well above the absorption edge. Thus, we choose an angle of 55° where, on the one hand, the NEXAFS oszillation vanish, and, on the other hand, the XMCD signal still has a good signal to noise ratio. In XMCD, the photon spin has to be aligned to the magnetization direction, cf. magnitude of the XMCD signals (shaded areas) in the right part. Investigations on mass-filtered cobalt clusters have also been carried out on Ni(111) films on W(110). Here, NEXAFS oscillations of the underlying nickel film ($h\nu \geq 850\,eV$) to not interfere with the absorption signal from cobalt clusters. The experimental results for cobalt clusters are displayed in fig. 3 as a function of cluster size, the upper part shows the ratio of orbital to spin moment, the lower part the corresponding spin moment.

Cobalt cluster do not show significantly enhanced orbital moments as in the case of iron clusters on a hcp(0001) cobalt film [3,4]. Especially in the case of cobalt clusters on Ni(111), the ratio of orbital to spin moment is clearly below the corresponding bulk value. Moreover, most of the spin moments are smaller than the bulk value of $1.55\mu_B$.

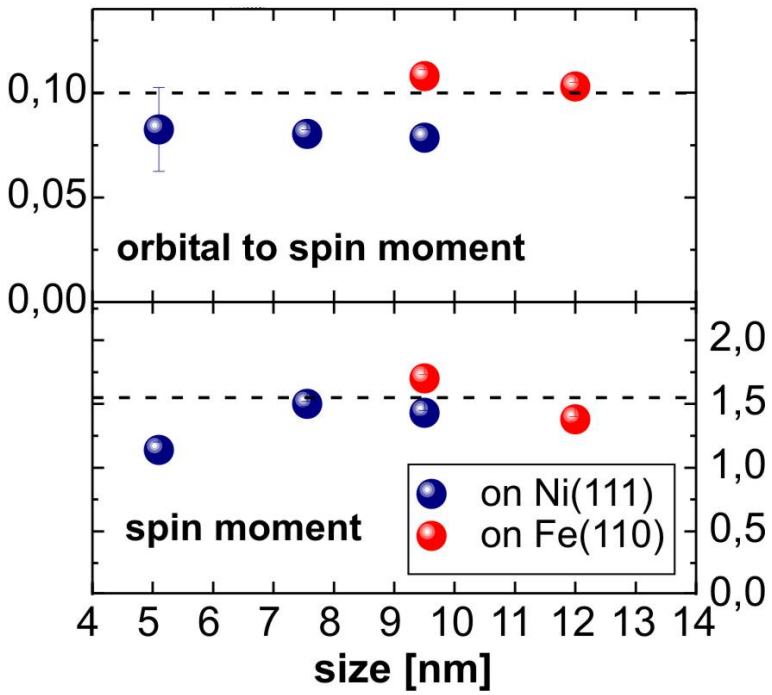

Figure 3: Magnetic properties of Co nanoparticles on Fe(110) (red dots) and on Ni(111) (blue dots) as a function of cluster size. Top: ratio of orbital to spin moment, bottom: spin moment in μ_B [7]. Dashed lines denote bulk cobalt values.

It should be mentioned that the ferromagnetic films are always saturated as observed by XMCD. However, the saturation magnetization of nickel is much smaller ($M_s = 0.6\,T$) than iron ($M_s = 2.2\,T$), which could lead to a non-saturated magnetization in cobalt clusters on nickel surfaces.

These results clearly reveal that the chemical nature of the underlying ferromagnetic film and its physical properties strongly influence the magnetic properties of clusters on surfaces. Detailed investigations on the geometric structure should give further insight into the origin of these interesting results.

References:

[1] K.W. Edmonds et al., J. Magn. Magn. Mat. **220**, (2000).
[2] J.T. Lau et al., Phys. Rev. Lett. **89**, 057201 (2002).
[3] J. Bansmann and A. Kleibert, Appl. Phys. A **80**, in press (2005).
[4] J. Bansmann et al., Surface Science Reports **56**, 189 (2005).
[5] R.P. Methling et al., Europ. Phys. J. D **16**, 173 (2001).
[6] R.P. Methling et al., PhD thesis, University of Rostock (2005).
[7] J. Bansmann et al., Appl. Phys. A, submitted (2005).

X-ray absorption spectroscopy of Co/CoO core/shell nanoparticles Ar^+ and H^+ sputtered: a comparison

P. Imperia[1], D. Schmitz[1], H. Maletta[1], N.S. Sobal[2] and M. Giersig[2]
[1]Hahn Meitner Institut, Glienicker Strasse 100, 14109 Berlin, Germany
[2]CESAR Research Center, Ludwig-Erhard-Allee 2, 53175 Bonn, Germany

To cast cobalt nanoparticles (NPs) prepared *ex-situ* by chemical synthesis on a Si substrate is easy, fast and cost effective. The particles prepared by chemical synthesis have a regular spherical shape, are arranged in two-dimensional self assembled arrays and posses a sharp size distribution [1]. The ability to easily tailor and strictly control the particles diameter allows, in principle, to fine tune the final magnetic properties of the samples by engineering the anisotropy. However, NPs chemically prepared are coated with organic surfactants (oleic acid) and a thin CoO shell. Argon ion (Ar^+) sputtering is often used to remove the surfactant and the oxide shell. We investigated the NPs as function of the sputtering time by means of soft x-ray absorption spectroscopy (XAS) at the C and O K-edges and at the Co $L_{2,3}$-edges. Previous works on Ar^+ ion etched NPs found that the Co/CoO interface plays a crucial role in a dramatically enhanced spin to orbital magnetic moment ratio μ_l/μ_s^{eff} [2]. According to ferromagnetic resonance (FMR) measurements, non sputtered NPs do not show any enhanced μ_l/μ_s^{eff} ratio [2]. FMR is sensitive to the whole ferromagnetic (FM) core of NPs and is not influenced by the antiferromagnetic (AF) CoO layer. The enhanced μ_l/μ_s^{eff} ratio was measured by means of magnetic circular X-ray dichroism (XMCD) that is especially sensitive to the magnetic properties of the surface and near-surface interfaces when measured recording the total electron yield by the sample drain current. The discrepancy between the XMCD measurements, the FMR results and unanswered questions connected with the NPs surface properties are challenging to be clarified. Therefore, we started to study the effect of Ar^+ and H^+ ion etching and the magnetic properties of such *ex-situ* chemically synthesised nano-dimensional crystals.

The Co/CoO core/shell NPs were prepared following the synthetic route described in [3]. The final result was a film of regularly spaced particles of 9.7 nm diameter having a very narrow size distribution with a standard deviation of about 5 %. The samples were studied after *in-situ* Ar^+ or H^+ ion etching. The surface sensitive and material selective XAS technique allowed us to investigate the progress of the sample properties after each etching step. The measurements were performed at the beam line UE46 PGM, BESSY (Berlin). The XMCD signal was measured by reversing the photon helicity, indicated as σ^+ and σ^-, of two successive energy scans of the circularly polarised incoming beam in the case of the Ar^+ etched samples or reversing the magnetic applied field in the case of the H^+ etched ones. The energy resolution of the beamline monochromator during the XAS spectra was better than 0.2 eV. The base pressure in the UHV chamber during the measurements was better than $4x10^{-10}$ mbar. The XAS spectra were recorded measuring the sample drain current in grazing incidence at an angle of 20° with respect to the substrate plane. All the curves were normalised by means of the last mirror current.

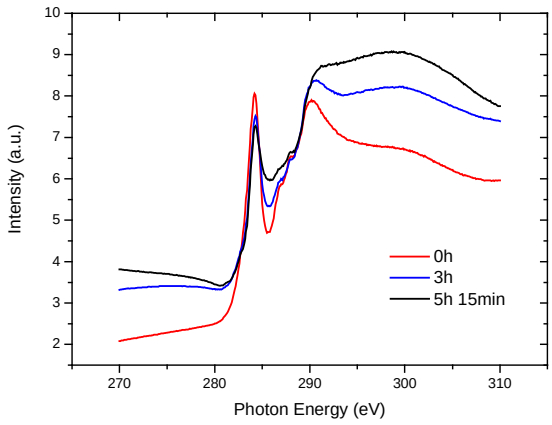

Fig. 1: Co nanoparticles at C K-edge under X-ray illumination. The spectra are normalised at 284.7 eV and with a cleaned Si substrate.

The question about the stability of the NPs sample under the high photon flux of the beam was the first addressed. Under illumination the spectra taken at the Co $L_{2,3}$ absorption edges exhibited a rising background. The increase was nearly linear during the first hour of measurement, until it saturated after a few hours. At the Co $L_{2,3}$ edges this effect influenced only the spectra background without any change of the shape. The spectra in fig. 1, show how the shape of C K-edge typically changes over time. The background rise was not observed for samples with the organic coating layer removed. Under synchrotron radiation illumination the organic coating material gets damaged. Low energy

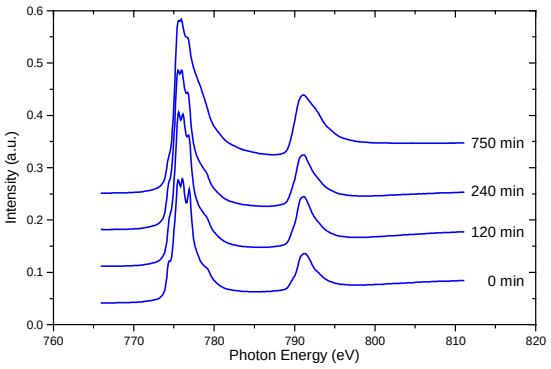

Fig. 2 Co nanoparticles (9.7nm) at Co $L_{2,3}$ edges at increasing Ar^+ etching time (500 eV, last 350 minutes at 900 eV). A vertical offset is used for clarity.

Ar^+ ion etching is an effective and simple way to remove the organic layer.

In Fig. 2 the spectrum labelled with time 0 shows the Co $L_{2,3}$ absorption edges as the sample is introduced in the UHV chamber. The presence of CoO on the surface of the NPs can be immediately recognised by the typical splitting of the main peak. After 120 minutes of etching at 500 eV there are not substantial changes. After 240 minutes of sputtering the typical multiplet structure of CoO is less defined. By only increasing the sputtering energy to 900 eV and etching for further 350 minutes at this higher energy, we started to observe the metallic Co single peak. Simultaneously, at the O K-edge a considerable change in the line shape was recorded. The *ex-situ* prepared NPs have an "onion" like structure. Our XAS experiments indicate that it is possible to remove the organic surfactant on the surface by means of Ar^+ ion etching at moderate energy without significantly affect the NPs oxide shell. Only by high Ar^+ etching energies (over 900 eV) and long sputtering time it was possible to partially remove the metal oxide composed of a mixture of CoO and Co_2O_3 [4]. However, only when the sample was further etched with Ar^+ at 1.5 keV for 240 minutes and then at 3.5 keV for further 180 minutes it was possible to record a small magnetic dichroic signal.

After each sputtering step at 180, 240 and 300 minutes, at 3.5 keV, the sample was cooled to 15 K. During cooling a pulsed magnetic field of about 0.4 T was applied. The upper panel of Fig. 4 shows the isotropic spectra for two etching times resulting from the sum of two subsequently measured spectra with reversed helicity ($\sigma^+ + \sigma^-$). The corresponding XMCD signals ($\sigma^+ - \sigma^-$) are displayed in the lower panels. The most relevant value that can be extracted from this data is the the spin to orbital magnetic moment ratio μ_l/μ_s^{eff} determined, according to the sum rules [5, 6 and 7], directly using the ratio of the values of the integral calculated from the XMCD signal at the L_3 and L_2 edges. The ratio is independent from the geometrical conditions of the experiment and it does not need an a priori knowledge of the number of 3d holes in the ground state. We observed a significant enhancement of μ_l/μ_s^{eff} with respect to bulk Co and in function of the Ar^+ etching time. This is in good agreement with previous measurements of NPs of the same size [2]. The value of μ_l/μ_s^{eff} increases with the sputtering time from μ_l/μ_s^{eff} = 0.14 after 180 minutes to μ_l/μ_s^{eff} = 0.18 after 240 minutes. A larger ratio μ_l/μ_s^{eff} = 0.3 obtained after 300 minutes of high energy (3.5 keV) Ar^+ etching, was calculated using a dichroic spectrum of low quality. In such a case the application of the sum rules results difficult and leads to a large error of about 33%. The observed enhancement could be essentially attributed to an increase of the orbital magnetic moment μ_l, while the spin values μ_s^{eff} stay almost constant when considering the error bars [4]. The surface and the Co/CoO interface of the NPs play a crucial role; they are the essential factor that enhances the orbital moment [4].

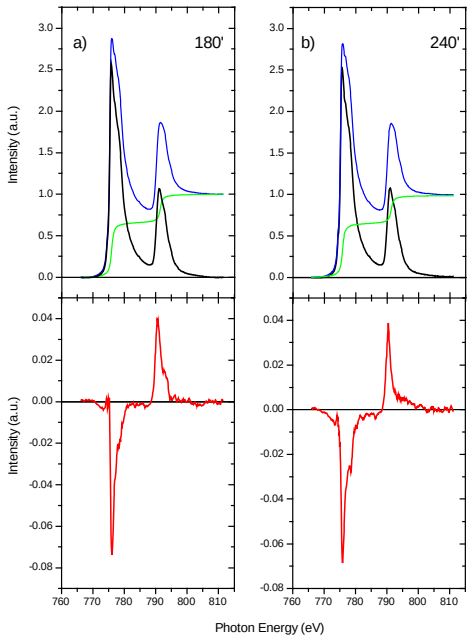

Fig. 4 NPs (9.7nm) at Co $L_{3,2}$ edges after a) 180 minutes and b) 240 minutes Ar^+ etching (3.5 keV). Upper panel: blue, isotropic spectra ($\sigma^- + \sigma^+$); red, step function; black, isotropic spectrum minus step function. Lower panel: dichroism spectra ($\sigma^- - \sigma^+$).

Samples etched with Hydrogen ions show a completely different behaviour. Opposite to the Ar^+ etched NPs, they do not have any dramatic increase of the moments ratio. With respect to argon, low energy H^+ etching (500 eV) seems to be extremely effective in reducing

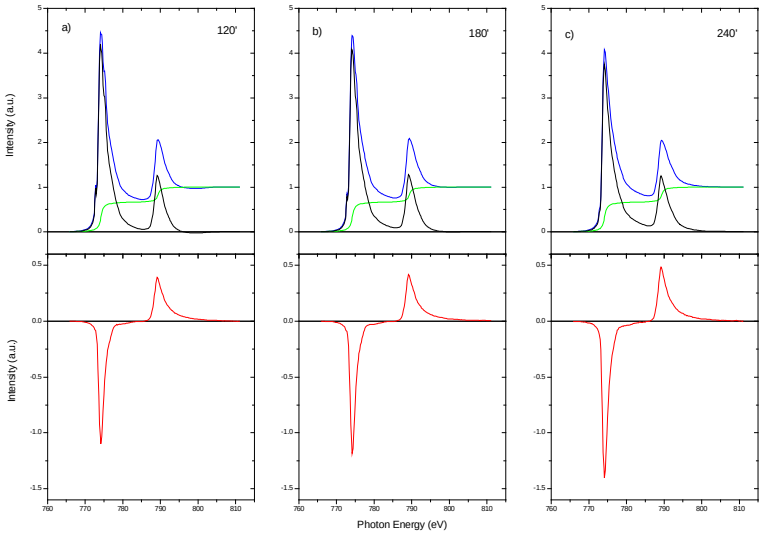

Fig. 5: NPs (9.7nm) at Co $L_{3,2}$ edges after a) 120 minutes, b) 280 minutes and c) 240 minutes H^+ etching (500 eV).Upper panel: blue, isotropic spectra; green, step function; black, isotropic spectrum minus step function. Lower panel: dichroism spectra.

the CoO layer. The value of the ratio μ_l/μ_s^{eff} we calculated after 240 minutes of etching is just slightly higher than for the Co bulk (μ_l/μ_s^{eff} = 0.095 [7]). As shown in figure 5 after 240 minutes of etching there is no more trace of CoO on the XAS signal. The μ_l/μ_s^{eff} ratio remains constant at about μ_l/μ_s^{eff} = 0.10 and increases to μ_l/μ_s^{eff} = 0.12 only after 240 minutes of H^+ sputtering. The CoO shell was entirely reduced by means of the H^+ etching procedure within a sputtering time that could be estimated between 180 and 240 minutes. The dichroism, in this case, was calculated subtracting two subsequent XAS scans measured applying a constant 3 T magnetic field and reversing its direction after each scan at room temperature. The high quality of the data, opposite to the Ar^+ etched samples, allows a more extensive analysis of the magnetic properties of the H^+ reduced NPs. To obtain the values of the orbital and spin moments, μ_l and μ_s^{eff}, it's necessary to subtract the contribution of the s states and to know the amount of 3d holes in the ground state [7]. The NPs under study do not have a regular crystallographic structure. Using the $\mathbf{n}_{3d}$ value normally attributed to Co bulk, $\mathbf{n}_{3d}$ = 7.5 [7], and only for comparative purpose, we found that for H^+ etched samples the orbital moment remains stable between 120 and 180 minutes of sputtering and only after 240 minutes it reaches the value of μ_l = 0.10 (μ_B /atom). The spin moment increases constantly passing from μ_s^{eff} = 0.67 (μ_B /atom) after 120 minutes to 0.69 (μ_B /atom) after 180 minutes and reach the value of μ_s^{eff} = 0.79 (μ_B /atom) after 180 minutes. With respect to the Ar^+ sputtered samples the situation is dramatically different. While there the estimated increase of the orbital magnetic moment can be easily attributed to the presence of a Co/CoO interface and to a disruption of the surface, in the H^+ etched samples case an almost constant orbital moment points in the direction of a much less aggressive action of the H^+ etching on the NPs.

The effect of the light H^+ ions is less devastating on the surface of the NPs than the heavy Ar^+ bombardment. Long time Ar^+ sputtering at high energies induces a progressive and significant enhancement in the orbital to spin magnetic moment ratio that can be attributed mainly to the Co/CoO interface and to the surface disruption of the NPs, while low energy and short time H^+ ion etching gives values of the moments ratio very similar to the bulk values of Co.

We thank S. Rudorff for his invaluable technical support. We are also deeply in debt with Dr. E. Goering and Dr. K. Fauth for the stimulating scientific discussions and technical help.

References

1 M. Spasova, U.Wiedwald, R. Ramchal, M. Farle, M. Hilgendorff and M. Giersig, J. Magn. Magn. Mater. **240**, 40 (2002).

2 U. Wiedwald, M. Spasova, E. L. Salabas, M. Ulmeanu, M. Farle, Z. Frait, A. Fraile Rodriguez, D. Arvanitis, N. S. Sobal, M. Hilgendorff and M. Giersig, Phys. Rev. B **68**, 064424 (2003).

3 C. B. Murray, Shouheng Sun, W. Gaschler, H. Doyle, T. A. Betley, and C. R. Kagan IBM J. Res. & Dev. **45**, 47 (2001).

4 P. Imperia, D. Schmitz, H. Maletta, N. Sobal and M. Giersig, submitted to Phys Rev. B (2004)

5 B. T. Thole, P. Carra, F. Sette, G. van der Laan, Phys Rev. Lett. **68**, 1943 (1992).

6 P. Carra, B. T. Thole, M. Altarelli, Xindong Wang, Phys Rev. Lett. **70**, 694 (1993).

7 C. T. Chen, Y. U. Idzerda, H.-J. Lin, N. V. Smith, G. Meigs, E. Chaban, G. H. Ho, E. Pellegrin, F. Sette, Phys Rev. Lett. **75**, 152 (1995).

Near edge X-ray absorption fine structure spectroscopy on chemically prepared lanthanide phosphate nanoclusters

E. Suljoti, A. Pietzsch, A. Föhlisch, M. Nagasono, and W. Wurth

Institut für Experimentalphysik, Universität Hamburg,
Luruper Chaussee 149, 22761 Hamburg, Germany

Lanthanide phosphate nanocrystals ($LaPO_4$ – $YbPO_4$), capped by organic ligands were chemically prepared in liquid-phase synthesis[1]. These nanocrystals have a mean-size of 5-6 nm, high crystallinity and a good solubility in different organic solutions as well as a high luminescence quantum yield, which makes them useful in a variety of applications. As a consequence, it is interesting to study their electronic structure, as a function of lanthanide-ion, cluster size and interface between cluster and ligands. In order to investigate the unoccupied density of states of these clusters we have recently performed near edge x-ray absorption fine structure spectroscopy (NEXAFS).
The Lanthanide nanoclusters were dissolved in 1% solutions of Methanol, and spin-coated on p-type (100) silicon wafers. The Si surfaces were hydrogen-passivated by HF etching to remove the surface oxide. Scanning electron micrographs (SEM) of the spin coated layers showed an uniform size distribution of the nanoclusters in a densely packed layer on the Si surface.

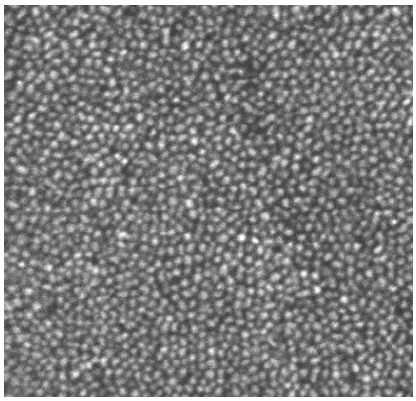

In Figure 1, the SEM micrograph ($300x300nm^2$) of $LaPO_4$ nanoparticles spin coated on a Si wafer is shown.
The NEXAFS measurements on lanthanide phosphate nanocrystals were performed at BESSY II, beam line UE52-SGM, and U41. The photon beam was incident at an angle of 7° with respect to the sample surface.

Figure1. SEM micrograph ($300x300nm^2$) of $LaPO_4$ colloidal clusters spin coated on a Si (100) wafer.

The NEXAFS spectra of the lanthanide phosphate nanocrystals, in particularly the $3d^{10}4f^n \rightarrow 3d^9 4f^{n+1}$ transitions of lanthanide ions, were measured in the total electron yield mode (TEY) by monitoring sample current and in the partial electron yield mode (PEY) by monitoring the lanthanide *MNN* auger lines. They are shown in Figure 2. The spectra are characterized by two well separated groups of lines: $3d_{5/2}(M_5)$ to $4f$ transitions (lower energy region), and $3d_{3/2}(M_4)$ to $4f$ transitions (higher energy region) with distinct fine structures. Across the lanthanide series, a change in the relative intensity between M_4 and

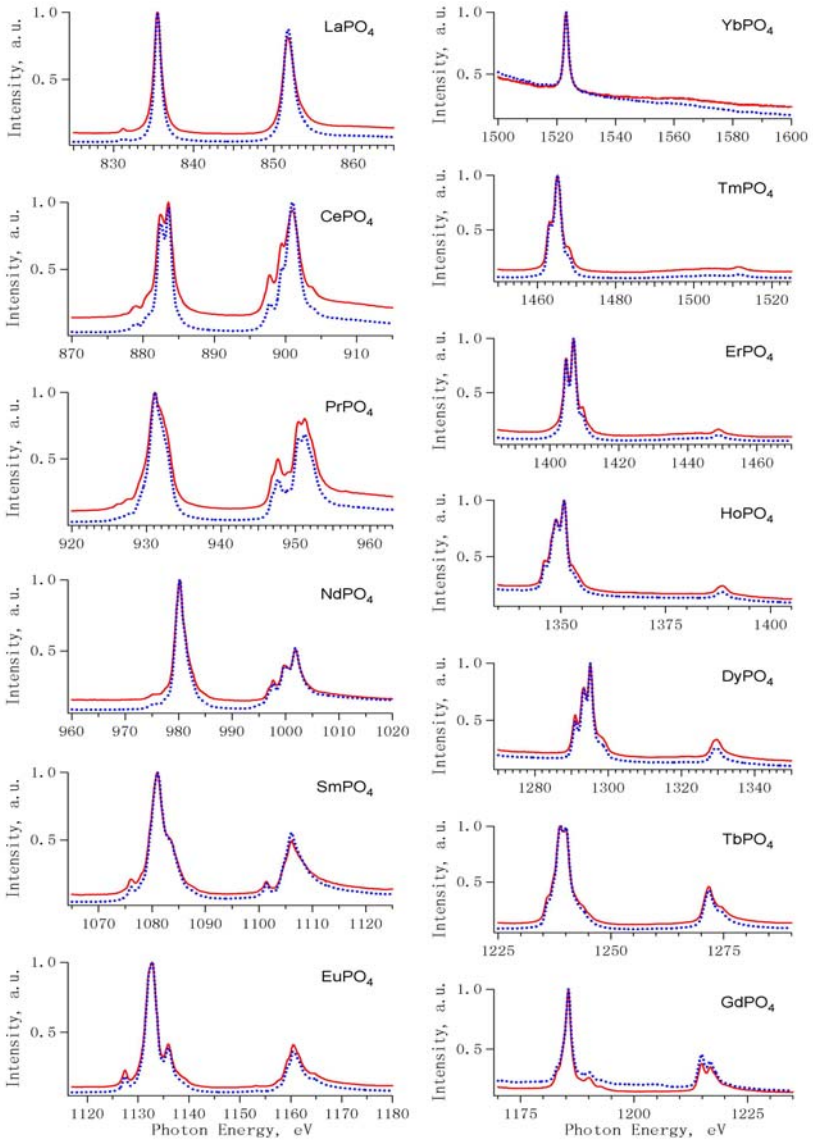

Figure 2. NEXAFS spectra of the $3d^{10}4f^{n} \rightarrow 3d^{9}4f^{n+1}$ Lanthanide transitions in the lanthanide phosphate nanoparticles. Solid red line: TEY and dotted blue line: PEY.

M_5 absorption lines is observed. The relative intensity is similar in the early lanthanides, but it decreases in the heavier lanthanides, which is due to the selection rules[3]. For Yb^{3+} a single line is observed because the 3d to 4f dipole transition is only allowed for the $3d_{5/2}$ state.

We also observe a life time broadening for M_4 absorption lines in comparison to the M_5 lines due to Coster-Kronig decay. Detailed analysis of the data is under way.

Acknowledgment: This work was supported by the Graduiertenkolleg project: “Spektroskopie an lokalisierten atomaren Systemen, Felder und lokalisierte Atome - Atome und lokalisierte Felder”, and the DFG Sonderforschungsbereich 508 – Quantenmaterialien-laterale und hybride Strukturen, Hamburg. Especially, we would like to thank Prof. M. Haase who provided the nanocrystals.

References:

[1] O.Lehmann, H. Meyssamy, K.Kömpe, H. Schnablegger, and M. Haase, J. Phys. Chem. B 107 (2003) 7449.
[2] Sergei M. Butorin, J. El. Spec. Rel. Phen., 110-111, (2000) 213.
[3] B.T. Thole, G. van der Laan, J.C.Fuggle, G.A. Sawatzky, R.C. Karnatak and J.M. Esteva, Phys. Rew. B Vol. 32, Nr. 8, (1985).

Electronic Structure of TiO_2 Nanoparticles as Observed by X-ray Absorption Spectroscopy (XAS)

I. Preda [a], L. Soriano [a], A. Gutiérrez [a], S. Palacín [a], M. Fernández-García [b], C. Belver [b], N. González-Díaz [c], P.R. Bressler [d], J.M. Sanz [a]

[a] Departamento de Física Aplicada, Instituto de Ciencia de Materiales Nicolás Cabrera, Universidad Autónoma de Madrid, 28049 Madrid, Spain
[b] Instituto de Catálisis y Petroleoquímica (CSIC), c/ Marie Curie s/n, Campus Cantoblanco, 28049 Madrid, Spain
[c] Servicio Interdepartamental de Investigación, Universidad Autónoma de Madrid, 28049 Madrid, Spain
[d] BESSY GmbH, Albert-Einstein-Straβe 15, 12489 Berlin, Germany

It is well known that when materials are arranged in nanometric dimensions, their physical and chemical properties could change with respect to those of the same bulk materials. These changes are produced by changes in their electronic structure induced by size effects. So that, the study of the electronic structure of nanoparticles materials is a hot topic in nanotechnology nowadays. Questions like why do the materials change their properties or what is the critical size at which their properties change, are of enormous interest.

In this work we study the electronic structure of TiO_2 nanoparticles by means of X-ray Absorption Spectroscopy (XAS). The large variety of properties of Titanium oxides gives this family of oxides relevant importance in many technological applications such as catalysis and photocatalysis, sensors, optical coatings, paintings, etc. On the other hand, the sensitivity of XAS to the local order range makes this technique suitable for such analysis.

TiO_2 nanoparticles have been grown by the inverse micro-emulsion of water and oil method[1]. The powder obtained was analyzed by X-Ray Diffraction giving the pattern of the anatase structure and a particle size of 10 nm was derived from the width of the diffraction lines. For XAS measurements, the powders were pressed into a suitable sample holder of dimensions according to the manipulator in the spectrometer. The Ti K edge was measured at the KMC1 beam-line in both, total electron yield and fluorescence yield. The Ti $L_{2,3}$ and O K edges were measured at the PM3 beam-line in near-total electron yield, that means by tuning the electron analyzer at the kinetic energy of the main secondary electron bump (10 eV). In the case of the Ti 2*p* edge, it was also measured in the partial yield detection mode. This means that the electron analyzer was tuned at the kinetic energy of the Ti LMM Auger peaks. It is known that partial yield spectra are more surface sensitive than those obtained in the total yield mode. The experimental spectra were corrected with the I_0 current taken from a gold grid. Other spectra of rutile and anatase measured in a different beam-line at BESSY (VLS-PGM) are shown for comparison.

The Ti K edges of the TiO_2 nanoparticle sample in both, total electron yield (a) and fluorescence yield (b), are shown in Fig. 1. Also the same spectra of a rutile single crystal are shown for comparison. In general, the spectra of the TiO_2 nanoparticles are very similar to those of rutile, except for the small peaks at the edge. The spectra of the TiO_2 nanoparticles show clearly three peaks whereas those of rutile show only two. This

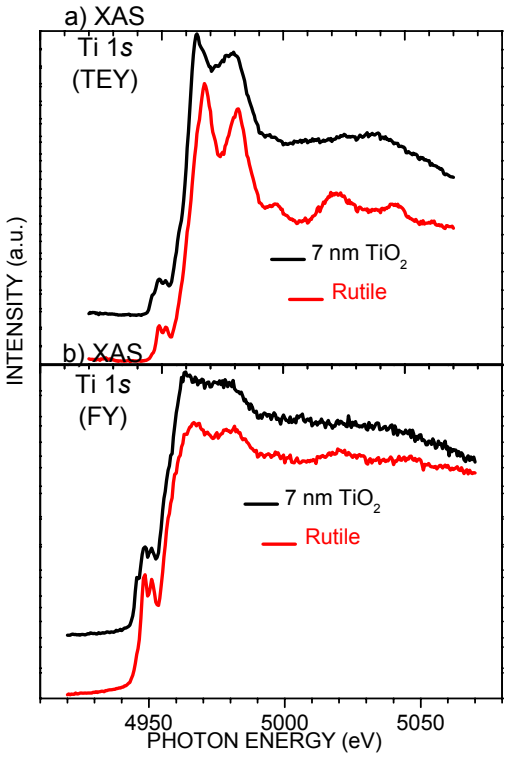

is more clearly observed in the spectra of fluorescence yield which presents the absorption edge more resolved than in the total yield spectra. On the other hand, it is clearly seen that both, total yield and fluorescence spectra, coincide for each sample. The spectrum of the nanoparticles agrees with other published spectra for the Ti K edge in anatase[2].

So that, these results confirm that the nanoparticles show the anatase structure in agreement with XRD data of the nanoparticles. It is worthy to note here that FY spectra are volume sensitive whereas TEY spectra are more surface sensitive, although the probing depth of XAS in TEY mode at these energies (5 KeV) is probably larger than the size of the nanoparticles.

The Ti 2p XAS spectra of the TiO_2 nanoparticles are shown in Fig. 2. We show the spectra taken in total yield and in partial yield by tuning the electron analyzer at the kinetic energy of the Ti LMM Auger peak. The reason is that, even though the total Ti 2p XAS spectra taken in total yield are more surface sensitive than those of the Ti 1s edge because the lower incident photon energy, the partial yield spectra are even more surface sensitive since the Auger electrons are only collected from the outer most region of the sample. By comparing both, total and partial yield spectra they show exactly the same structures although the partial yield spectra has a lower background as the secondary electrons are not collected. This indicates that at the depth of these techniques, the Ti atoms have the same local structure.

The main point now is to assign these spectra to a Ti oxide. We also show in Fig. 2 the corresponding spectra of rutile and anatase samples. As it is seen, the spectrum of the nanoparticles does not agree with the reference rutile and anatase spectra. However, if one compare this spectrum with that measured by Lusvardi *et al.*[3] in FY for TiO (Ti^{2+}), the agreement is excellent.

The O 1s XAS spectrum of the nanoparticles is shown in Fig.3. The spectra of the reference rutile and anatase samples are also depicted. It is seen that, as in the case of the Ti 2p spectra, the nanoparticles do not seem to be associated to rutile nor to anatase. In this case the higher photon energy region of the spectrum agrees in some way with that of anatase but the lower photon energy region of the spectra differs from that of anatase. The splitting of the two sub-bands (2.6 eV for anatase and rutile)[4], associated with the t_{2g} and e_g states via hybridization does not appear in the spectrum of the nanoparticles. An extra peak centered between the t_{2g} and e_g bands arises to dominate the spectrum. This extra peak can be associated to the O 1s spectrum of TiO shown in the literature[3].

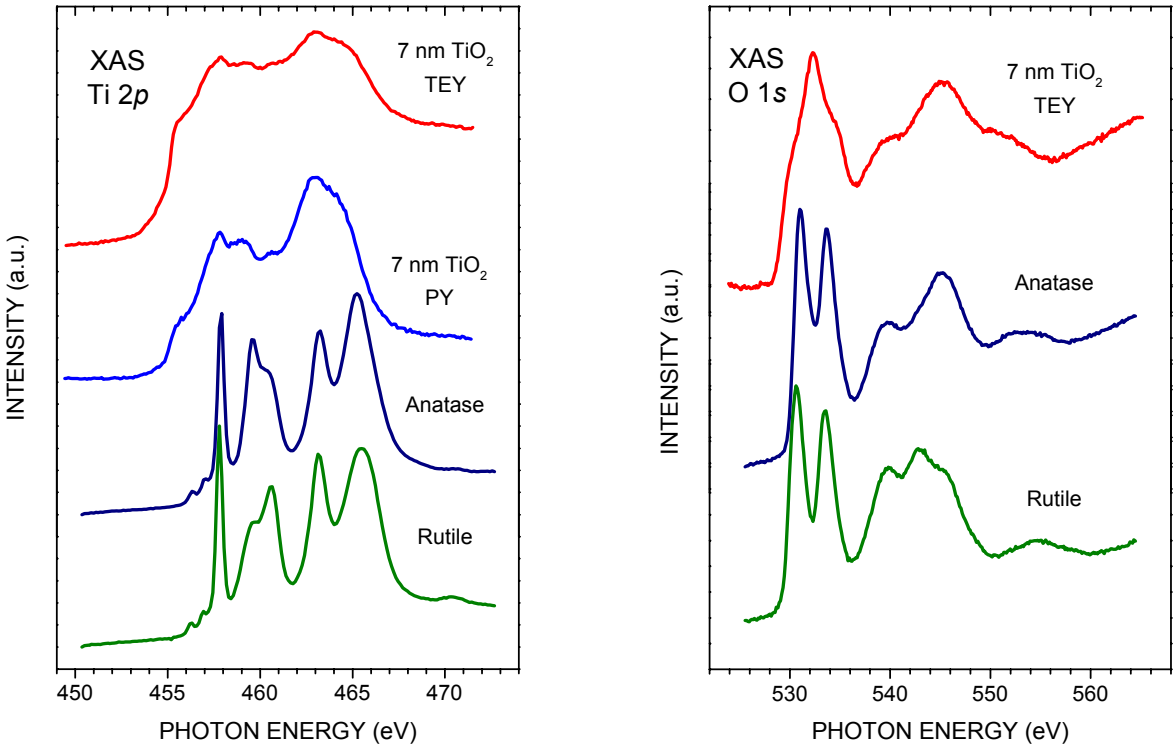

In summary, the above results seem to indicate that whereas the bulk of the nanoparticles remains as TiO_2 in the anatase form, the surface of the nanoparticles seems to be strongly reduced to TiO (Ti^{2+}). Of course, the existence of some amount of Ti^{3+} species at the surface cannot be neglected. However, and what it is more important, this result is contradictory with respect to Ti oxides surfaces. It is well known that the surfaces of the lower oxidation state oxides in contact with atmosphere tend to oxidize up to the larger oxidation state, i.e. Ti^{4+} but here the process is just the contrary: the surface of a higher oxidation state Ti oxide (Ti^{4+}) is strongly reduced.

This preliminary result require more investigation by using surface sensitive characterization techniques.

Acknowledgements:

This work was supported by the EU - Research Infrastructure Action under the FP6 *Structuring the European Research Area* Programme, through the contract R II 3-CT-2004-506008; and by the Spanish CICYT through the contract BFM2003-03277. A.G. thanks the Spanish *Ministerio de Educación y Ciencia* for financial support through the *"Ramón y Cajal"* Program.

References:

[1] A. Fuerte, M.D. Hernández-Alonso, A.J. Maira, A. Martínez-Arias, M. fernández-García, J.C. Conesa, J. Soria, G. Munuera, *J. of Catálisis* **212**, 1 (2002).
[2] F. Farges, G.E. Brown Jr., J.J. Rehr, *Phys. Rev. B* **56**, 1809 (1997).
[3] V.S. Lusvardi, M.A. Barteau,, J.G. Chen, J. Eng Jr., B. Frühberger, A. Teplyakov, *Surface Science* **397**, 237 (1998).
[4] F.M.F. de Groot, J. faber, J.J.M. Michiels, M.T. Czyzyk, M. Abbate, J. C. Fuggle, *Phys. Rev. B* **48**, 2074 (1993).

Size Related Electron Structure Transformation of Isolated Silver Supported Clusters

V.M. Mikoushkin, S.Yu. Nikonov, Yu.S. Gordeev,
Ioffe Physical-Technical Institute, Russian Academy of Sciences, 194021,St.-Petersburg, Russia
S.L.Molodsov, Yu.S. Dedkov
Institut für Oberflächen- und Mikrostrukturphysik, Technische Universität Dresden, D-01062 Dresden, Germany

Abstract. New technique of fabrication of quasi-isolated supported clusters and of variation of their sizes was developed using soft etching of thin silver film deposited on the oxidized silicon surface. Size-related core level binding energy increase, Auger-energy decrease and transformation of the valence photoelectron spectrum of the clusters were observed in decreasing the cluster size. The conclusion was made that the observed line-shifts are caused by change of the inter-atomic relaxation energy and that the created cluster systems can be interesting from the point of view of fabrication of electrostatic single electron memory devices.

Introduction

Clusters supported by surfaces have been an object of fundamental research for a long time because of special properties being intermediate between solid state and atom. Recently supported clusters have prompt additional interest due to the problem of quantum dots (QDs), which are created on the basis of systems of supported clusters by their burying with semiconductor materials. A lot of electronic devices are already designed and fabricated on the bases of this new physical object [1,2]. Electronic properties of the cluster- and QD-systems are well known to strongly depend on the average cluster size. At the same time knowledge about transformation of cluster properties due to variation of their sizes seems to be not entire [3-5]. Typically supported clusters or QDs of certain sizes are studied. There is a lack of researches devoted to variation of cluster sizes in a wide range. The conducted research applied to the problem of the size-transformation of electronic properties of supported clusters, namely to the transformation of the energy electron structure of clusters in a wide range of cluster sizes. One of the main objectives of the research was fabrication of quasi-isolated supported clusters whose properties look like those of free clusters. To study properties of a single cluster by electron spectroscopy using synchrotron radiation (SR), a system of clusters of close sizes has to be fabricated. Therefore a new technique of fabrication of quasi-isolated supported clusters and of variation of theirs sizes was developed.

Fabrication of quasi-isolated supported Ag-clusters and variation of theirs sizes

The technique of fabrication of quasi-isolated supported Ag-clusters is based on the assumption that thin metallic films (< 10÷20 ML) are characterized by a hilly relief even being grown at room temperature. These hills can be considered as Ag-clusters superimposed on thin Ag-layer. The technique includes fabrication of such film and the uniform etching of the film by low energy (1 keV) Ar^+ ion beam at normal direction. This uniform etching makes Ag-clusters smaller and Ag-layer thinner

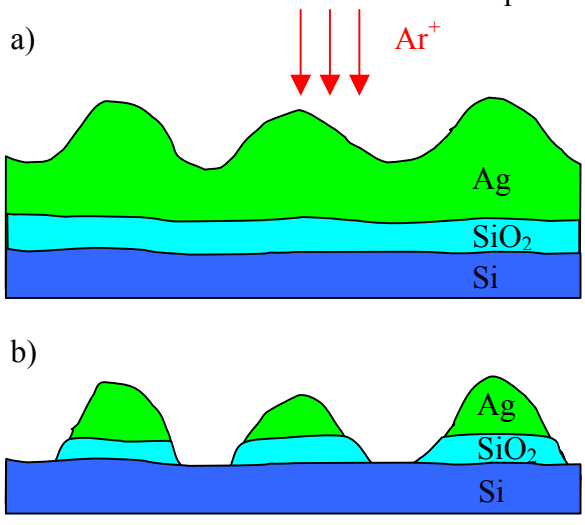

Fig.1. a). Ag-thin film on the SiO_2/Si surface being under Ar^+ ion bombardment.
b). System of Ag-clusters on Si surface.Clusters are isolated from the conductive Si- surface by dielectric SiO_2- disks.

(Fig.1a). At some stage of the etching, Ag-layer disappears in the region between clusters and a system of separated clusters is originated on the supporting surface. Thus, systems of clusters of different average sizes were available for study. To diminish the cluster-surface interaction and to make a hilly relief more prominent, the surface of native silicon oxide being relatively inert was chosen as a supported one. SiO_2 surface is also characterized by some relief, which can be a reason of the lake-like Ag-cluster formation. The typical thickness of native silicon oxide layer is known to be 1-2 nm. Etching of this layer in the region between Ag-clusters creates on the Si- surface an original system of Ag-clusters, which are isolated from this conductive surface by dielectric and chemically inert SiO_2- disks (Fig.1b). Each of the clusters has got a low capacity, can be charged up to essential potential by one or several electrons and can keep the electric charge for a long time. The created cluster systems can be interesting from the point of view of fabrication of electrostatic single electron memory devices. Thus, variation of the average cluster size was achieved by sequential ion beam etching the sample. The total amount of silver n_s was estimated by monitoring the intensities of Ag 3d photoelectron lines. Observation of the photoelectron line shift (Ag 3d electron binding energy) was considered as an indication of the modification of the cluster electron structure due to size confinement.

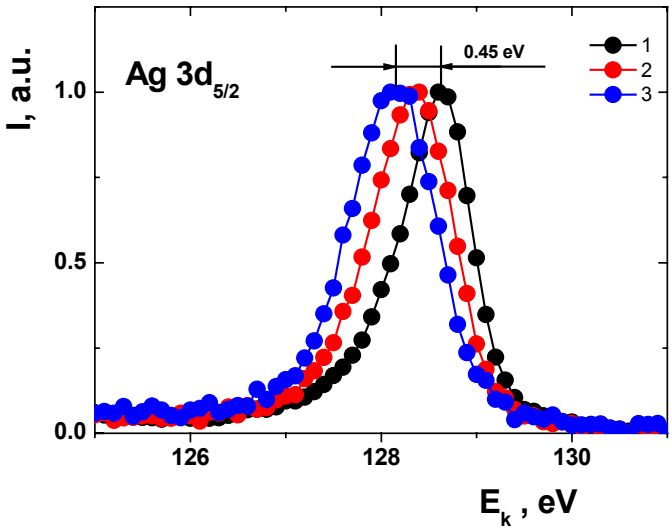

Fig.2. Ag3d photoelectron spectra of $Ag/SiO_2/Si$ system at different stages of ion etching. Photon energy is hν = 550 eV.

Size related Ag3d core photoelectron line shift.

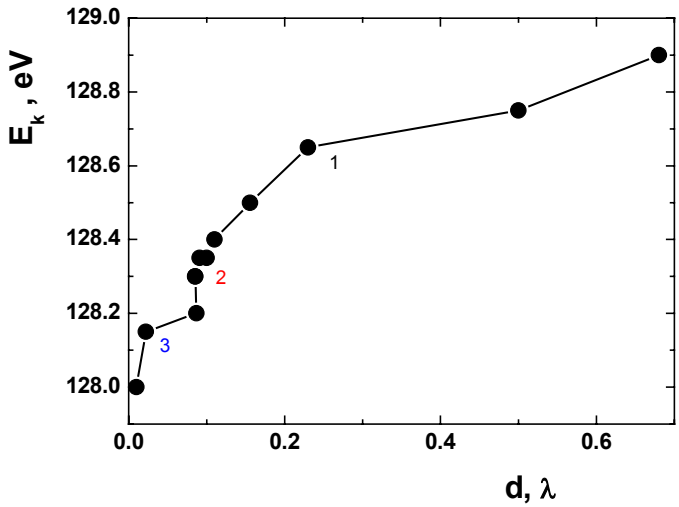

Fig.3. Dependence of the Ag3d core level binding energy on the silver amount or the average number of atoms in the system of silver clusters on the Si/SiO_2 surface.

Fig.2 shows a sequence of $Ag3d_{5/2}$ photoelectron spectra of the $Ag/SiO_2/Si$ system measured at different stages of ion etching. The photon energy was hν = 550 eV. The figure demonstrates diminishing of the kinetic energy E_k (n_s) of $Ag3d_{5/2}$ photoelectron in the course of etching and reducing of the total amount of silver n_s. Dependence of the $Ag3d_{5/2}$ electron binding energy $E_B(n_s) = h\nu - E_k(n_s) - e\varphi$ on the total amount of silver is shown in Fig.3. The total amount of silver was supposed to be connected with cluster size. This dependence is a monotonous function like that previously obtained for silver clusters grown on graphite [3] and Si(100) [4,5] by sequential deposition of Ag atoms. The observed scale of the core level binding energy shift (ΔE_b~0.9 eV) proved to be practically the same as in the former research

in which the shift was caused by cluster size related effects. Ag MVV Auger-energy shift obtained in this work also turned out to be an order of former one.

The conclusion was made in the former research for clusters consisting of more then several atoms that the dominant role in the observed binding and Auger energy shifts belong to the variation of the relaxation energy. The increasing role of the relaxation energy in the cluster size increasing is physically caused by enlargement of the density of states near the Fermi level and of the degree of collectivization of valence electrons, which lead to an increase in the extra-atomic relaxation energy. In present study the relaxation energy diminishes in the course of cluster size decreasing due to etching of the $Ag/SiO_2/Si$ system.

Conclusions

1. New technique of fabrication of supported clusters and variation of theirs sizes was suggested and developed. Systems of quasi-isolated clusters of different average sizes were available for study in the course of ion etching.

2. Ag3d core level binding energy increase, Ag MVV Auger-energy decrease and transformation of the valence photoelectron spectrum of quasi-isolated Ag-clusters were observed in the cluster size decreasing. The observed scale of the Ag 3d core level binding energy shift ($\Delta E_b \sim 0.9$ eV) proved to be practically the same as in the former research of the Ag cluster grown on the surfaces of pyrolytic graphite and Si(100) when the line-shifts were caused by change of the inter-atomic relaxation energy.

3. A system of small silver clusters on the silicon surface was created. A unique feature of the system is that the metallic clusters are isolated from the surface by the SiO_2 sub-layer, have got a low capacity, can be essentially charged by single or several electrons and can save the charge for a long time. The conclusion was made that the cluster system can be interesting from the point of view of fabrication of an electrostatic single electron memory devices or/and a single electron transistor.

Acknowledgements

The project was supported by BESSY-II, by the Russian Academy of Sciences. (program “Low-Dimensional Quantum Structures”) and by the Russian Ministry of Education and Science (program “Physics of Solid-State Nanostructures”).

References:

1. Grundmann et al., Phys. Rev. Lett., 74, 4043 (1995); Phys. Rev. B, **56** (1997), 506.
2. N. A. Cherkashin, M. V. Maksimov, A. G. Makarov, V. A. Shchukin, V. M. Ustinov, N. V. Lukovskaya, Yu. G. Musikhin, G. E. Cirlin, N. A. Bert, Zh. I. Alferov, N. N. Ledentsov, and D. Bimberg, Semiconductors, **37** (2003), 861.
3. Yu.S.Gordeev, M.V.Gomoyunova, V.M.Mikoushkin, I.I.Pronin, and S.E.Sysoev, Size relaxation effect in silver clusters on graphite, *Tech.Phys.Lett.* **20** (1994), 142.
4. V.M.Mikoushkin, *Technical Physsics* **44** (1999), 1077.
5. V.M. Mikoushkin, Atomic Cluster Collisions» (ISACC 2003), St.Petersburg, 18-21 July 2003, *Europhysics Conference Abstracts*, **27D**, Inv. Mo-III-2, p.76.

Destruction of Solid C_{60} by Synchrotron Radiation

V.M. Mikoushkin, V.V. Shnitov, V.V. Bryzgalov, and Yu.S. Gordeev
Ioffe Physical-Technical Institute, Russian Academy of Sciences, 194021, St.-Petersburg, Russia
S. L. Molodtsov, S. Danzenbächer
Institut für Oberflächen- und Mikrostrukturphysik, Technische Universität Dresden, D-01062 Dresden, Germany

Abstract. Destruction of condensed fullerenes C_{60} by Synchrotron radiation (SR) has been revealed. This process is accompanied by photoemission line shifts and by the raise of the spectra features typical for amorphous carbon. Mechanism of the modification includes generation of photo- and secondary electrons, excitation of valence electrons and formation of the large number of intermolecular bonds, which finally transform fullerenes into amorphous carbon. Non-evaporable image of the SR beam has been created demonstrating a possibility of dry x-ray lithography with using solid C_{60} as a photo-resist.

Introduction

Many efforts have been put to study of processes induced in solid C_{60} (fullerite) by radiation and by electrons. It has been discovered that ultraviolet radiation and electron bombardment lead to forming chemical bonds between neighboring fullerenes and to the creation of polymeric chains in fullerite [1-2]. The question about the possibility of fullerite modification by x-rays and by non-monochromatic SR has been remained open. Study of interaction of free fullerenes in the gas phase with SR-photons in the energy region of the maximal photoadsorption cross sections ($h\nu < 35$ eV) showed no fragmentation [3]. Therefore clarification of the question about the possibility of SR induced modification of solid C_{60} remains an actual task. There is also a practical importance of this question. Polymerized fullerite is thermally reversible, but it is characterized by low solubility in toluene, and this property is used in lithography with fullerite as a photo- or electron-resist. Revealing the analogous process under x-rays could enhance the lithography resolution. Recently a new process of fullerite amorphyzation due to destruction of fullerenes by electrons has been revealed, and the idea of "dry" lithography based on this process has been suggested [4]. In this extremely clean technology, non-evaporable picture drown by electron nanoprobe is displayed by heating and evaporation in vacuum of unirradiated fullerenes. Revealing the analogous process induced by x-rays could be very promising for dry x-ray lithography. The aim of the research was revealing these processes and clarification of their mechanisms.

Experimental Details

The experiment has been carried out at BESSY-II using the PGM beamline and the experimental facilities of the Russian-German laboratory. Thin fullerite C_{60} films with thickness of about 5-10 ML were *in situ* deposited on a silicon wafer both with the layer of native oxide and without it. C_{60} powder of 99.5 % purity was used. The films were repeatedly exposed to different doses of non-monochromatic SR provided by a "zero order" mode of the PGM or of monochromatic SR with photon energy $h\nu$=120 and 530 eV. Values of exposure dose Q were measured in arbitrary units refereed to the unit dose gained during 1 min at 100 mA electron current in the storage ring.

Modification of fullerite C_{60} by "zero order" SR

Strong polymerization and destruction of fullerite C_{60} under "zero order" SR has been revealed for the first time. The fullerite modification manifests itself in smearing of the molecular photoemission peaks and in a rise of quasi-continuous background of the valence band photoemission spectra [5,6]. It has been already shown in [5] that the raise of the quasi-continuous background is caused by the increasing contribution of the phase of amorphous carbon. Here we consider additional characteristics of the revealed effect. The modification is also accompanied by a red shift of the C1s core-level photoelectron line (Fig.1), by smearing

of the shake-up satellite features of this line (Fig.2), by blue shift of Auger peak, and by other manifestations [6]. Fig.1 shows that the C1s photoelectron line of pristine fullerite shifts by ~0.5 eV approaching to the position of amorphous carbon. Small line broadening indicates domination of single carbon phase – the phase of gradually modified fullerite.

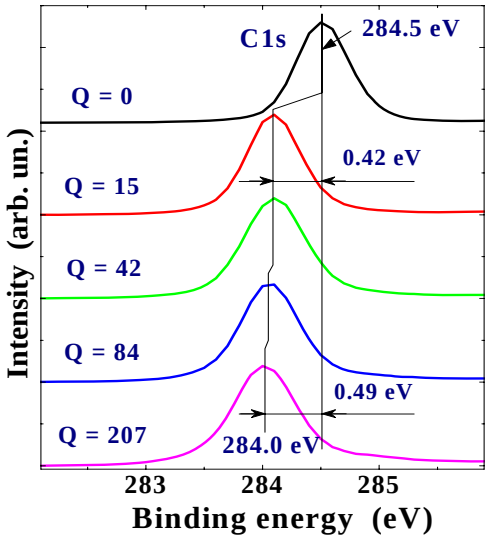

FIG. 1. C1s core-level photoemission spectra measured in the course of "zero order" SR irradiation. The spectra were recorded at the photon energy hν= 530 eV.

To clarify the nature of the fullerite modification, the evolution of shake-up satellite structure of C1s photoemission line was studied. Prominent peaks are seen in the spectrum of pristine C_{60} film (Fig.2, Q=0). Broad peak at the energy loss ΔE=6 eV corresponds to the intrinsic excitation of π-plasmon while others originate from the excitation of intermolecular π→π* transitions. Fig.2 (Q>0) shows that all molecular peaks gradually disappear and π-plasmon undergo noticeable red shift (from 6.0 to 5.7 eV) under irradiation. The observed shake-up structure transformation evidences for redistribution of the density of π-electron states. It can be explained by removing of molecular state degeneracy due to serious violations of the symmetry of the fullerene cages that is by their destruction. Thus, we may come to the conclusion that intense "zero order" SR irradiation of C_{60} film leads to gradual destruction of individual fullerenes C_{60} and, thereby, to gradual amorphization of fullerite.

It is known that polymerization of fullerite is thermally reversible process. To prove that fullerite can be destructed by SR, a thermal irreversibility of the revealed modification was experimentally demonstrated. Two different areas of thin fullerite film, pristine and irradiated with "zero order" SR, were studied before and after heating of the sample at T= 430 °C during Δt = 30 s (Fig.3). Drastic decrease in the intensity of C1s line for the unirradiated area indicates the practically complete evaporation of the fullerite film, whereas the high intensity of C1s line for the modified area evidences the conversion of fullerite into nearly non-evaporable carbon phase. Thus, thermally irreversible process of SR induced transformation of fullerite into amorphous non-evaporable phase has been revealed. This process can be used in "dry" lithography with fullerite as a photoresist.

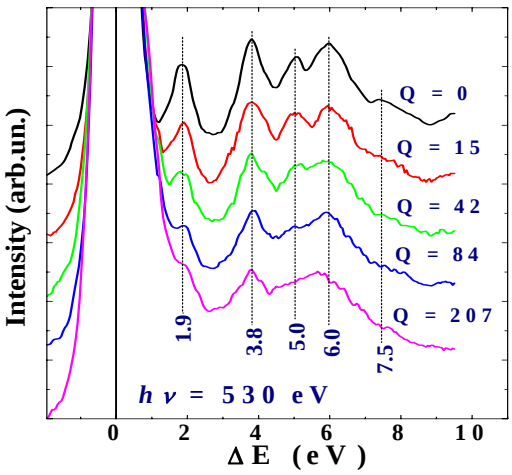

FIG. 2. Photoelectron C1s shake-up spectra of solid C_{60} recorded in the course of "zero order" SR irradiation. Spectra were measured at hν= 530 eV.

Modification of fullerite C_{60} by monochromatic SR and mechanism of this modification

Zero order" SR contains a VUV spectral region which is known to polymerize fullerite. To show that fullerite can be modifired by x-rays, fullerite films were irradiated by photons with energies $h\nu$=120 and 530 eV. Fig.4 shows valence bant spectra of pristine fullerite (1, Q = 0) and of that modified by x-rays (2 and 3, Q>0). As in the case of "zero order" SR, the molecular peaks undergo red shift under x-rays, their intensities diminish and continuous

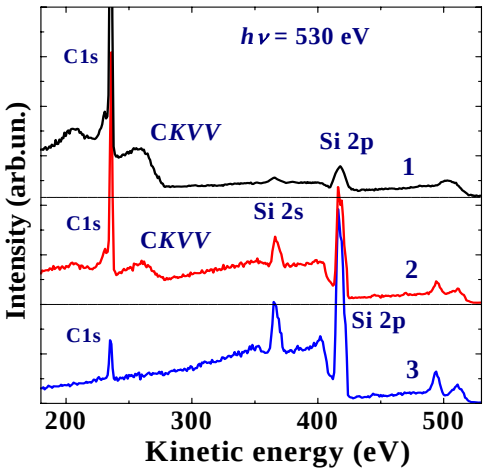

FIG.3. C1s and Si2p photoelectron spectra collected at different areas of C_{60} film: pristine-(1) and irradiated with "zero order" SR-(2,3). Spectrum (1) was recorded before heating and spectra (2,3) – after heating the sample.

background increases towards the spectrum of amorphous carbon. The revealed transformation of the spectra of valence electrons evidences the transformation of electronic and atomic structure of fullerenes towards that of amorphous carbon. Analogous transformation of loss spectra, red shift of the C1s binding energy, blue shift of Auger electrons under x-rays confirm this conclusion. The mechanism of the revealed modification includes an excitation of valence electrons, creation of intermolecular chemical bounds, loosing small fragments and decreasing high symmetry of large fragments [6]. Excitation of valence electrons is induced by photoelectrons and by a swarm of secondary electrons. As a result, the density of the electronic states near the Fermi-level increases resulting into the relaxation energy raise. This raise is known to be the reason of decrease of the binding energy (red shift) and of increase of the Auger electron energy (blue shift).

Conclusion

Modification including polymerization and destruction of solid C_{60} by "white" SR and by monochromatic soft and hard x-rays has been revealed for the first time. This process manifests itself in transformation of fullerite electron structure towards that of amorphous carbon. The mechanism of the fullerite modification is a stepwise one. It includes generation of photoelectrons and a swarm of secondary electrons, which excite valence electrons and stimulate formation of interatomic bonds between neighboring molecules. Creation of a large number of intermolecular bonds finally destroys fullerenes. Non-evaporable image of the SR beam in the form of a spot has been created demonstrating a principle possibility of dry x-ray lithography with fullerite as a photo-resist.

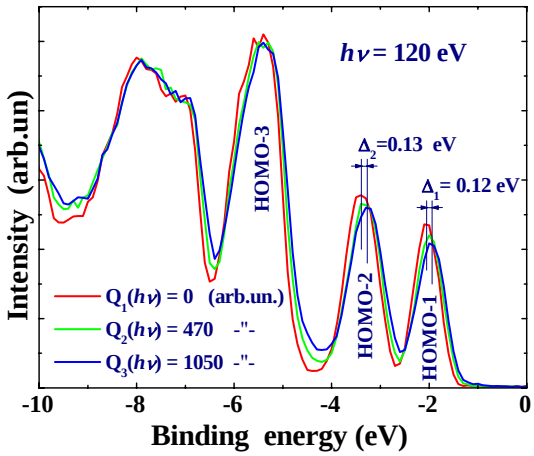

Fig.4. Photoelectron spectra of fullerite C_{60} valence band measured in the course of irradiation by monochromatic SR.

Acknowledgements

The project was supported by BESSY-II, by the Russian Academy of Sciences (program "Low-Dimensional Quantum Structures") and by the Russian Ministry of Education and Science (program "Physics of Solid-State Nanostructures").

References:

1. A. Ito, T. Morikawa, T. Takahashi. *Chem. Phys. Lett.*, **211** (1993), 333.
2. Y. Wang, J.M. Holden, A.M. Rao, et al., *Phys. Rev.* **B51** (1995), 7, 4547.
3. I.V.Hertel, H.Steger, J.de Vries, B.Weisser, et al., *Phys.Rev.Lett.*, **68**, 784 (1992).
4. V.V.Shnitov, V.M.Mikoushkin, Yu.S.Gordeev, *Microelectronic Engineering*, **69** (2003), 429.
5. Yu.S.Gordeev, V.M. Mikoushkin, V.V.Shnitov, S.L. Molodtsov, XXIII Int. Conf. on the Phys. of Electronic and Atomic Collisions (XXIII ICPEAC), Stockholm, 2003, We 187.
6. V.M.Mikoushkin, V.V.Shnitov, et al., *Physics of the Solid State*, **46** (2004), N12, 2311.

Photoionization and ICD in van-der-Waals clusters

S. Barth[1], S. Joshi[1], S. Marburger[1], V. Ulrich[1], A. Lindblad[2], O. Björneholm[2], and U. Hergenhahn[1]
[1]Max-Planck-Institut für Plasmaphysik, EURATOM Assoziation, Boltzmannstraße 2, 85748 Garching, Germany
[2]Department of Physics, Uppsala University, Box 530, S-751 21 Uppsala, Sweden

Resonant ICD-like processes

In most atoms and molecules the amount of energy deposed in the system by ionization of an inner valence state lies energetically below the first double ionization potential (DIP). Thus, relaxation of this state by autoionization is not possible. However, the Coulomb repulsion of the two positive charges in a doubly ionized state can be effectively screened if they can be distributed to two different centres, which is possible in weakly bound extended systems. Examples are van-der-Waals clusters or hydrogen bridge bonded systems, like water.

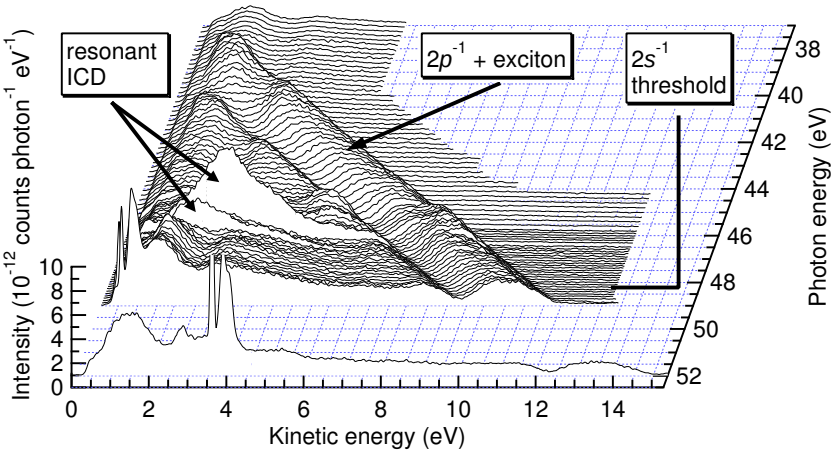

Figure 1: Low kinetic energy electron spectra of Ne clusters excited with photon energies around the Ne 2*s* threshold. Two resonantly enhanced, ICD-like features can be identified below the 2*s* threshold. 2*p* photoelectrons experiencing inelastic energy losses by intracluster creation of excitonic states can be seen in roughly the same energy region [her02].

In these systems, direct autoionization of an inner valence vacancy into a delocalized two hole state is possible. This process was termed ICD (Interatomic/Intermolecular Coulombic Decay) [ced97] and was demonstrated experimentally by some of the authors [mar03]. ICD proceeds by relaxation of an outer valence electron at the ionized site going along with an energy transfer, which causes outer valence ionization of a neighbouring atom or molecule.

ICD is an ultrafast process, the lifetime of $2s^{-1}$ states in Ne clusters has been measured as 6±1 fs for bulk atoms [oeh04]. This should make it the dominant relaxation mode whenever it can occur.

By tuning the excitation energy below the ionization threshold of an inner valence state, at some energies this inner valence electron will be excited to a discrete bound state. In analogy to the resonant Auger decay, one can speculate whether in a cluster the positive hole then relaxes by transmitting its energy to a neighbouring atom causing its autoionization.

We have therefore carried out an experiment to search for ICD-like electrons below the Ne 2*s* threshold in Ne clusters, and to determine whether their yield function reflects the sub-threshold resonances of the 2*s* shell.

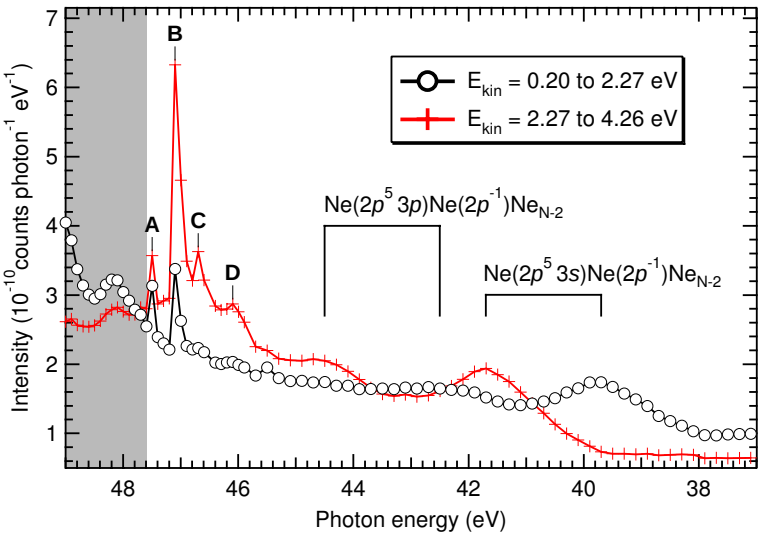

Figure 2: Integrated total electron intensity in two kinetic energy intervals versus photon energy. See text for explanation of the features.

Neon was expanded under conditions which facilitated cluster production (~63% condensation) and photoelectron spectra at different photon energies were recorded, figure 1. The photon energy was varied from roughly 52 to 37 eV, while the Ne 2*s* cluster threshold is at 48.04 eV for bulk and at 48.23 eV for surface atoms [oeh04].

Variations of the photon flux were normalized, a correction of the transmission curve of

the detector was not applied. For better clarity the values in only this figure are smoothed. The total intensity of each spectrum integrated over two different kinetic energy intervals (0.2-2.27 eV, and 2.27-4.26 eV) is plotted versus the excitation energy in figure 2. In the first interval at photon energies above the Ne 2*s* threshold the normal ICD signal shows up. Four obvious resonance structures labelled A to D at photon energies of 47.5 eV, 47.1 eV, 46.7 eV, and 46.1 eV can be observed. Comparing these results to published work on the 2*s* excitations in bulk condensed Ne [wie95], we assign resonances A, B to the bulk and surface components of the $2s \rightarrow 3p$ Rydberg excitation, observed at 46.9 and 46.4 eV in the solid [wie95]. Consequently, signals C and D have to be identified as bulk and surface $2s^2\ 2p^4\ 3s\ 3p$ doubly excited states. In the gray shaded area in figure 2, the Ne photoelectron signals are overlapping the low kinetic energy region. These have not been subtracted from the presented data points.

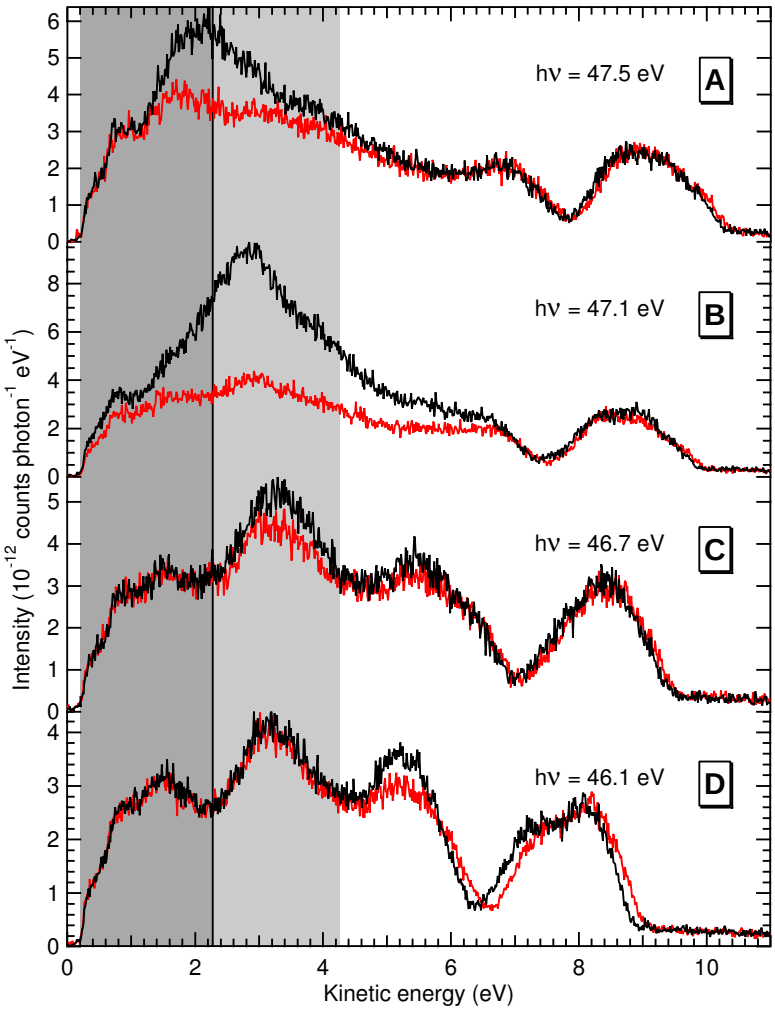

Figure 3: Electron spectra of Ne clusters at the photon energies of the resonances A to D (black), each together with a spectrum at a photon energy about 0.25 eV higher than the resonance (red).

Figure 3 again demonstrates the surplus of low kinetic energy electrons on resonances A and B. Since the kinetic energy of electrons from ICD of the 2*s* state above threshold is around 1.2 eV [mar03], it seems evident that the electrons observed below threshold result from resonant ICD-like processes of the type

$Ne_N + h\nu \rightarrow (Ne\ 2s^{-1}\ 3p)Ne_{N-1} \rightarrow (Ne\ 2p^{-1}\ 3p)(Ne\ 2p^{-1})Ne_{N-2} + e^-$,

which create electrons of somewhat higher energy due to better shielding of one of the final state holes.

Cluster Satellites

Quite generally, the photoionization lines due to single electron interaction are associated with weaker satellite lines as a consequence of multi-electron processes. A wealth of information has been gathered about satellite lines in atomic Neon, but apart from a recent work on excitonic satellites in Ne and Ar [her02] to the best of our knowledge no studies of photoionization satellites in clusters have been reported. Here, we have investigated the 2*p* correlation satellites in Ne clusters produced by supersonic expansion [mar03].

Figure 4 shows Ne photoemission spectra for a series of cluster sizes. The series was recorded by variation of nozzle temperature and stagnation pressure. The spectra show the 2*s* main line together with some 2*p* correlation satellite lines for the monomers and clusters. The cluster 2*s* photoline is split into contributions of bulk and surface atoms (see the inset). The bulk contribution increases as the cluster size is increased. Moreover, the atomic satellite lines are associated with cluster satellites lines, which show similar size dependence. The monomer and the cluster 2*s* photolines were fitted using Voigt line shapes for different cluster sizes. The results of these preliminary fits are plotted in figure 5 (a) and (b) for a series of cluster sizes. It is interesting to note that the percentage of satellite peak area (figure 5 (a), blue solid line) develops proportionally to the sum of the percentage of surface and bulk peak areas of the photoline (fig. 5 (b), green and red solid lines, respectively). A high-resolution (35 meV) Ne 2*s*

satellite spectrum (figure 6) shows only one component (yellow), to which therefore both the surface and the bulk atoms of the cluster contribute.

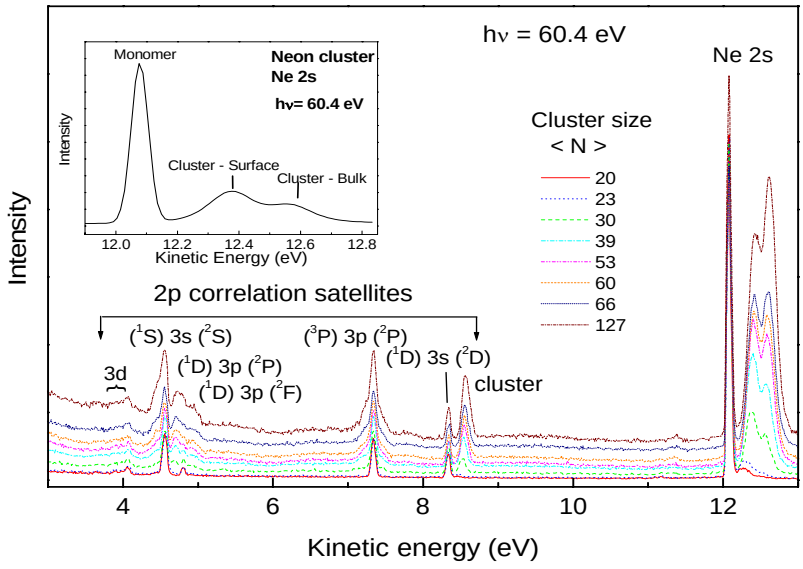

Figure 4: Photoelectron spectra of Ne clusters with a range of sizes. The 2*s* main line and the 2*p* correlation satellites are marked in the figure. The inset shows the cluster surface and bulk component of the 2*s* photoline.

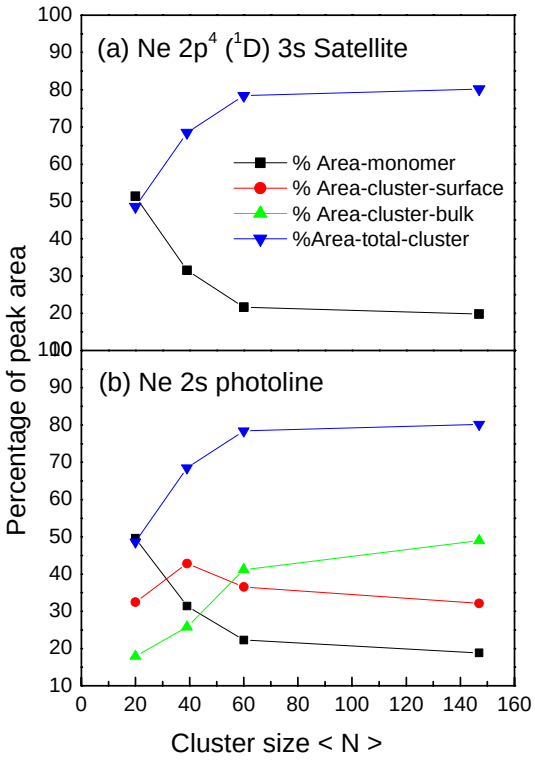

Figure 5: Percentage of peak area for the Ne 2*s* photoline (a) and the lowest satellite (b) as a function of cluster size <N>. Percentage of satellite peak area is a sum of percentage of surface and bulk peak areas of the photoline.

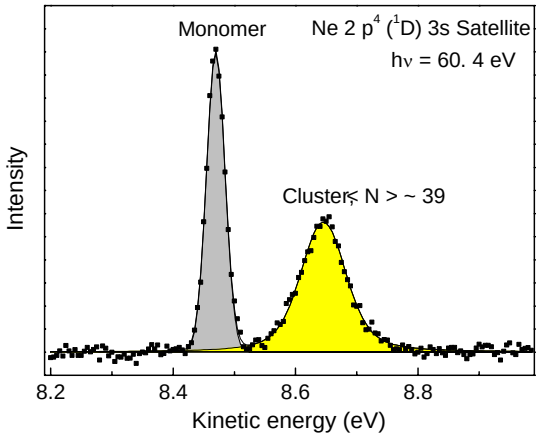

Figure 6: A high-resolution Ne 2*s* satellite spectrum for a cluster of size < N >~ 39. The experimental data is shown by solid squares and the solid lines represent fits.

References

[ced97] L.S. Cederbaum, J. Zobeley, and F. Tarantelli, Phys. Rev. Lett. **79**, 4778 (1997).

[her02] U. Hergenhahn, A. Kolmakov, M. Riedler, A.R.B. de Castro, O. Löfken, and T. Möller, Chem. Phys. Lett. **351**, 235 (2002).

[mar03] S. Marburger, O. Kugeler, U. Hergenhahn, and T. Möller, Phys. Rev. Lett. **90**, 203401 (2003).

[oeh04] G. Öhrwall, M. Tchaplyguine, M. Lundwall, R. Feifel, H. Bergersen,T. Rander, A. Lindblad, J. Schulz, S. Peredkov, S.L. Sorensen, S. Barth, S. Marburger, U. Hergenhahn, S. Svensson, and O. Björneholm, Phys. Rev. Lett. **93**, 173401 (2004).

[wie95] P. Wiethoff, H.-U. Ehrke, D. Menzel, and P. Feulner, Phys. Rev. Lett. **74**, 3792 (1995).

Photoelectron correlation spectroscopy (γ,2e) on Xe/Cu(111)

C. Winkler, K. Hünlich and J. Kirschner
Max-Planck-Institut für Mikrostrukturphysik, Weinberg 2, D-06120 Halle

1 Introduction

Correlation between electrons is a fundamental characteristics of systems containing many electrons. The influence of correlation on the electronic structure of solids manifests itself in enhanced or suppressed magnetic susceptibilities of paramagnetic metals, large electronic coefficients of the heat capacity, or in differences between experimental and theoretical one-electron band widths, to name only a few examples. A quite promising way to investigate these correlation effects is to study the double photoemission (DPE), where the absorption of a single photon leads to the simultaneous excitation and emission of two (correlated) electrons. This simultaneous two-orbital excitation following the absorption of one VUV photon is exclusively caused by the interelectronic interaction because in the case of exitations by electron dipole transitions, a photon can only interact with one electron at a time[1],[2]. Recent theoretical calculations, carried out by Fominykh et al[3] on Cu(001) at a photon energy of $h\nu = 21.2$ eV, yield a striking structure in the angular distribution of photoemission from a surface, namely zones of strongly reduced intensity when distribution of the momenta parallel to the surface of one electron with a certain energy is mapped while the second electron is fixed in its momentum at the same energy. This observation can be understood from electron-electron repulsion, where the exchange interaction prevents two electrons from escaping with comparable wave vectors within a proximity determined by the screening lenght. Therefore, this so-called *exchange correlation hole* can be seen as a direct manifestation of exchange and correlation between two photoelectrons, where the size of the hole reflects the strength of the interaction between two electrons.

In the present work, the energy- and angular-distributions of correlated photoelectrons

ejected from solid Xe were studied experimentally. A rare-gas solid was chosen because it is known that double photoemission is a very efficient process in the gas phase[4]. Since solid rare-gases are formed by weak Van-der-Waals interaction, double photoemission should be comparable to the gas phase, leading to reasonable measuring times.

The work was finally carried out at the dipole beamline CP-NIM of the BESSY II synchrotron radiation source in Berlin in the single-bunch-mode with photon energies of $h\nu \leq 50$ eV.

2 Experimental details

In the present experiment, the time-of-flight technique was utilised to determine the energy of the electrons released from the surface by an incoming photon. The momentum of one electron is determined by using a microchannelplate (MCP) in combination with a position sensitive resistive anode. The corresponding coincident electron is detected with a central collector. With a distance of $l \simeq 55$ mm between sample and detector, the flight time of the electrons is typically about a couple of tens ns, and the solid angle covered with this set up is $\Omega \simeq 1$ steradian. The experiments were carried out under UHV conditions at a base pressure of $p_b \leq 10^{-10}$ mbar. In order to increase the energy resolution of the TOF-spectrometer, external magnetic distortions were compensated. The sample was prepared by dosing 20 L Xe onto a Cu(111) single crystal surface,which was held continously at a temperature of $T_s \simeq 30$ K during the measurement. The Xe film was refreshed every eight hours. A schematic view of the experimental set up is given in fig. 1.

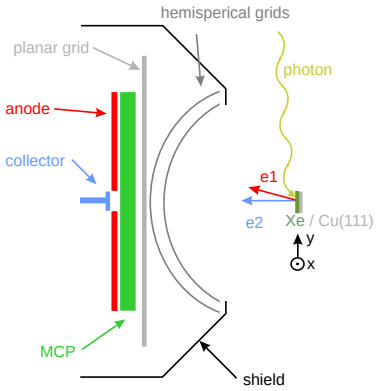

Figure 1: Schematic view of the experimental set up. e1, e2: photoelectrons, MCP: multichannelplate.

The flight times of the two electrons were measured with a set of time-to-amplitude converters (TAC) and the signals of the resistive anode were recorded with digitizers, while the bunchmarker of the beamline was taken to synchronise the system. Finally, an

additional electronic coincidence unit extensively suppresses the background and selects events due to time-correlated electrons.

3 Results

The present photoelectron coincidence spectroscopy experiments were actually carried out at a photon energy of $h\nu = 33$ eV with non-polarised synchrotron light. The surface normal of the probe was pointing to the center of the detector, marking the 0° polar angle of the emission direction. The very first results show that the current setup could be brought to the point from were it is worth to go into more detailed studies. Actually, the data are quite promising with respect to the coincidence rate, as expected from the gas phase data. However, for this synchrotron run the statistics of our data is unfortunately still insufficient to extract reliable data. On the basis of this encouraging work there is no doubt that these experiments will be resumed in one of the next single bunch synchrotron runs.

References

[1] J. Berakdar, *Phys. Rev B* **58** (1998) 9808

[2] J. Berakdar, *Appl. Phys. A* **69** (1999) 497

[3] N. Fominykh, J. Berakdar, J. Henk and P. Bruno, *Phys. Rev. Lett.* **89**, 086402 (2002)

[4] H.W. Biester, M.J. Besnard, G. Dujardin, L. Hellner and E.E. Koch, *Phys. Rev. Lett.* **59** (1987) 1277

Spectroscopic (NEXAFS, XPS) Characterization of Single-walled Carbon Nanotubes Carrier Doped by Encapsulation of Organic Molecules (TCNQ)

W. E.S. Unger[1], M. Shiraishi[2], S. Swaraj[1], M. Ata[3]

[1] Bundesanstalt für Materialforschung und -prüfung (BAM), Labor VIII.23, 12200 Berlin, Germany

[2] Graduate School of Engineering Science, Osaka University, Osaka 560-8531, Japan

[3] AIST Tokyo HQ, Kasumigaseki 1-3-1, Chiyoda-ku 100-8921, Tokyo, Japan

Single-walled carbon nanotubes (SWNTs) are a material characterized by a high potential for applications in molecular electronics. Semiconductive SWNTs have been investigated vigorously from the point of molecular electronics device applications, such as field effect transistors or diodes. For these device fabrications, carrier doping is one of the most important technique for constructing complementary electronics. Takenobu et al.[1] succeeded in doping of SWNTs by encapsulation of organic molecules, for example Tetracyano-p-quinodimethane (TCNQ) for p-type doping. The encapsulation of the organic molecules was observed by transmission electron microscopy, and the occurrence of charge transfer was also confirmed from observations by optical absorption and Raman spectroscopy. The goal of the present study was to provide direct evidence of a charge transfer by measuring π- and π^*-band structures in the molecular systems where TNCQs are encapsulated into SWNTs.

After purification, the SWNTs were deposited on Si substrates and the organic molecule encapsulation by a sublimation method was carried out. For details of this process see Ref. 1. For comparison, a pristine SWNT film without carrier doping as well as TCNQ films, deposited individually on Si substrates, were prepared. An Kratos AXIS Ultra instrument was used for XPS analysis. NEXAFS spectroscopy at the C K-edge was carried out at BESSY's HE-SGM monochromator dipole magnet CRG beam line 8.1B-1.

From the C/N XPS intensity ratio measured with TCQN@SWNT the number of TCNQ molecules related to the SWNT carbon atoms can be estimated. The result

was that one TCNQ molecule exists per 28 SWNT carbon atoms. The analysis of the TCNQ@SWNT N 1s photopeak (a single peak at BE = 398.0 eV) provides the rather important result that the encapsulated TNCQ molecules are negatively charged and these electrons are most probably transferred from the SWNT host material. Fig. 1 shows an overlay of the XPS valence bands measured with pristine SWNTs and the TCNQ@SWNT sample. A depletion of the density of states (DOS) in the π-band region was clearly observed.

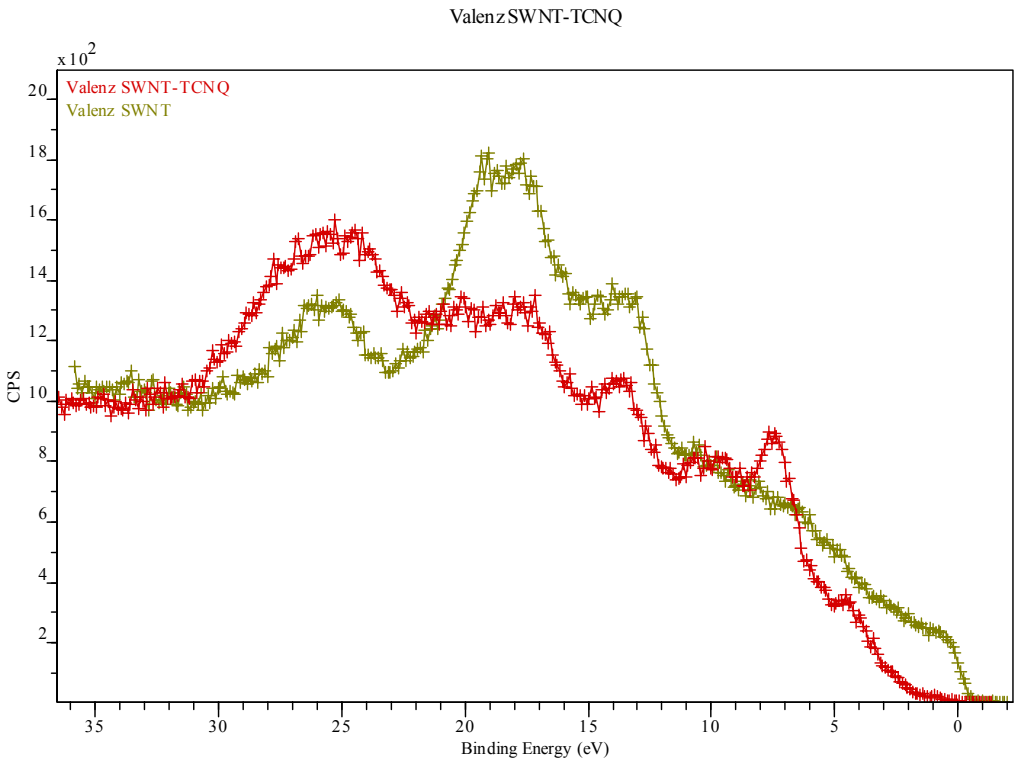

Fig. 1: VB spectra of pristine SWNTs (green) and the TCNQ@SWNT sample (red). Note the π DOS depletion in between 0 and ≈ 5 eV.

Considering the C K-edge NEXAFS of TCNQ@SWNT overlaid with that of the pristine SWNT sample differences become evident: The intensity of the π* resonance at 284.8 eV was slightly increased, an intense π* resonance at 286.3 eV occurred due to the nitrile group carbons, the spectral shape of the π* character region up to hν ≈ 290 eV is clearly changed and also the region of σ* resonances was strongly altered. Detailed π* related information can be derived from a comparison of the expanded C K-edge NEXAFS of TCNQ@SWNT (Fig. 2a) pure TCNQ (Fig. 2b) and a quantum-chemical simulation by the Fink group (University of Erlangen). In the

pure TCNQ C K-edge NEXAFS low energy π^* character resonances were observed (A and B) which are not found in the TCNQ@SWNT NEXAFS. From the gscf3 simulation it can be concluded that these low energy π^* character resonances are probably due to resonant excitations from the substituted and non-substituted cyclohexadiene carbons as well as from the carbene carbons of TCQN. Charge transfer from the SWNTs to the TCQN dopant will change the state of its original cyclohexadiene carbon species to substituted or non-substituted benzene carbons and also that of its involved carbene carbons. A disappearance of the resonances A and B is a strong indication of a chemical reaction between the SWNTs and the TCQN molecules which is accompanied by a charge transfer.

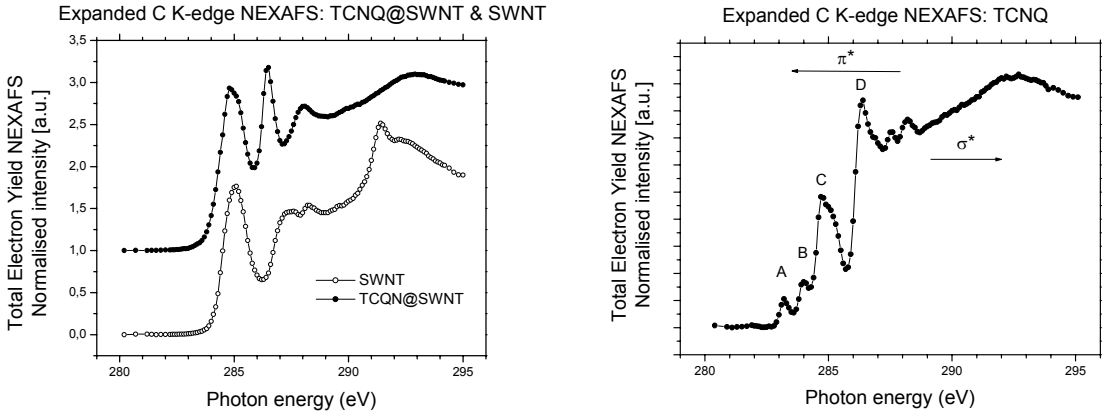

Fig. 2: a) Expanded C K-edge NEXAFS of pristine SWNTs, TCNQ@SWNT (left) and b) TCNQ (right).

Acknowledgements

Thanks are due to A. Lippitz (BAM), Dr. O. Schwarzkopf, M. Mast and Dr. W. Braun (BESSY) for support during experiments at BESSY. Special thanks are due to Prof. R. Fink (University of Erlangen, Germany) for providing TCQN C K-edge NEXAFS *gscf3* simulation results prior to publication.

References

1. T. Takenobu, T. Takano, M. Shiraishi, Y. Murakami, M. Ata, H. Kataura, Y. Achiba and Y. Iwasa, Nature Materials **2**, 683 (2003).

The Effect of Oxygen Exposure on Pentacene Electronic Structure

A. Vollmer - *BESSY G.m.b.H., Albert-Einstein-Str. 15, D-12489 Berlin, Germany*
O. D. Jurchescu, I. Arfaoui, T. T. M. Palstra, and P. Rudolf - *Materials Science Center, Rijksuniversiteit Groningen, NL-9747 AG Groningen, Netherlands*
I. Salzmann, J. P. Rabe, and N. Koch - *Humboldt-Universität zu Berlin, Institut f. Physik, Newtonstr. 15, D-12489 Berlin,*

Introduction and Experimental

Pentacene is the prototypical conjugated organic molecule for use as active material in novel electronic devices, such as thin film field effect transistors [1,2]. The interplay between thin film structure/morphology and measured charge carrier mobility as well as long term stability is of particular interest, as oxidation is believed to be a major reason for early device failure [3,4]. It has been observed that the measured conductivity of pentacene thin films and single crystal surfaces depends on the residual oxygen or air pressure and that oxygen can diffuse into pentacene, however it readily diffuses out again after re-evacuation [5]. Oxygen-induced changes in charge transport properties and possible new (chemical) species in pentacene films shall be addressed in this study by using ultraviolet photoelectron spectroscopy (UPS) performed at the end-station SurICat (beamline PM4) at BESSY with a Scienta SES 100 analyser. Changes in the EF-position of pentacene single crystals and thin films before and after exposure to oxygen and to air were of particular interest. Pentacene single crystals were grown ex situ and cleaved in situ. Pentacene evaporation was realized from a resistively heated pinhole source.

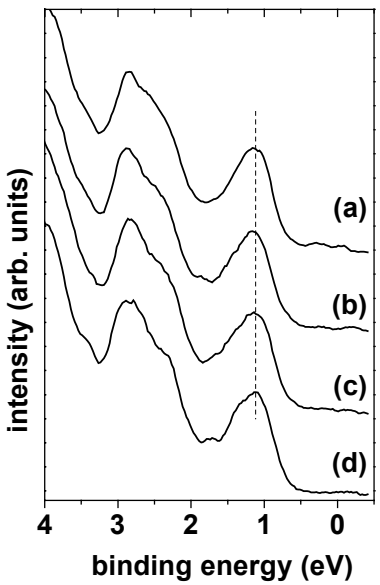

Figure 1. . UPS spectra of a pentacene single crystal: (a) 3×10^{-8} mbar partial O_2 pressure, (b) 2×10^{-9} mbar total residual pressure, (c) 3×10^{-8} mbar partial O_2 pressure after exposure to 5×10^{-6} mbar O_2 for 30 min., and (d) again at 2×10^{-9} mbar total residual pressure

Results and Discussion

The valence region UPS spectra (Fig. 1) recorded on a pentacene single crystal under different residual oxygen pressure during the measurement and total oxygen exposure clearly show that there is no influence of molecular oxygen on the position of the energy levels. If "doping" (*i.e.*, p-type) of pentacene by O_2 was the case, a clear shift of all levels towards lower binding energy (BE) would be observed [6,7]. Therefore, we have continued on *in situ* deposited thin films of pentacene. A pentacene film of 12 nm nominal thickness was deposited onto *in situ* sputtered polycrystalline Au. The corresponding UPS spectrum is shown on a wide energy range in Fig. 2 (bottom curve), and as a close-up in the figure inset. After exposure to O_2 at atmospheric pressure for one hour, the entire UPS spectrum was shifted 0.25 eV towards lower BE (Fig. 2, upper spectrum, and inset) but the lineshape remained unchanged. This result would be consistent with p-type doping of pentacene by oxygen that remains intercalated within the organic layer after re-evacuation.

However, it has been suggested[8] that oxygen adsorption below the organic film on the metal substrate surface changes its work function (Φ). Therefore, the shift seen in Fig. 2 may be related to this change of substrate Φ and/or a shift of the pentacene molecular levels due to doping. The only way to differentiate between the two mechanisms is the use of substrates which are not influenced by oxygen such as (SiO_2) and HOPG.

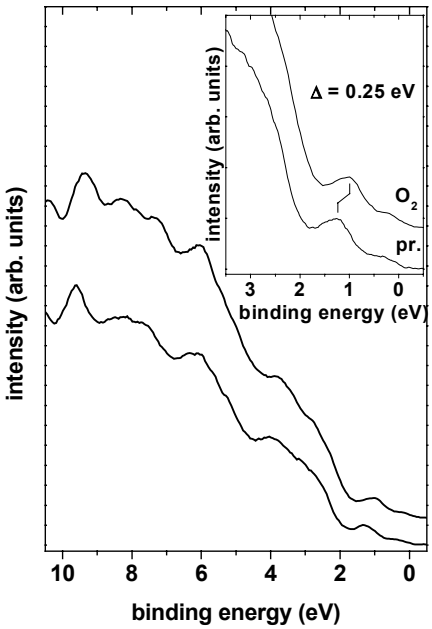

Figure 2. Extended BE scale UPS spectra of 12 nm pentacene on Au before (*pr*istine; bottom curve) and after (upper curve) exposure to one atmosphere of O_2 for 60 min. Inset: Close-up of the near-E_F region.

Fig. 3 shows UPS spectra of nominally 12 nm thick, pristine pentacene films on SiO_2 (a) and HOPG (e). These two spectra differ in the relative photoemission intensities from some molecular levels, as one can see clearly for the feature at ca. 3 eV BE. This is due to the fact that the long molecular axis of pentacene is oriented almost vertically on SiO_2 (grown at room temperature[9]), and parallel to the surface of HOPG [10]. The energy spacing of emission features in both films are identical, indicating intact pentacene on both surfaces. These two films were exposed to one atmosphere of pure oxygen in dark for 30 min. [Fig. 3 (b) and (f)]. Subsequently, the samples were exposed to one atmosphere of pure oxygen for 120 min. [Fig. 3 (c) and (g)], this time irradiated with visible light (to test the influence of pentacene optical excitation during exposure). In the next step, both samples were exposed to ambient air for 60 min. [Fig. 3 (d) and (h)], again with visible light irradiation. Finally, exposure to ambient air for 15 min. proceeded, with the samples being additionally exposed to ultraviolet (UV) light (inset of Fig. 3) (low-pressure Hg-lamp 10 cm away from the samples). After each exposure the samples were brought back to UHV conditions for the UPS measurements.

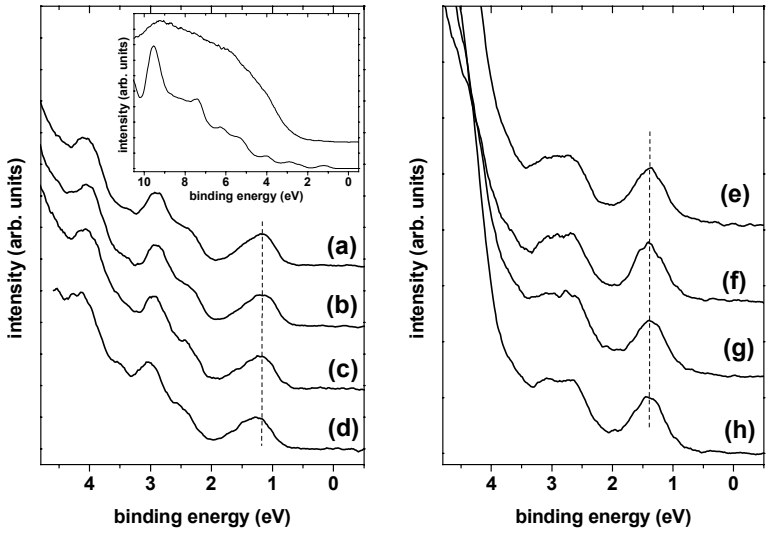

Figure 3. UPS spectra of 12 nm pentacene films on SiO_2 (left hand side) and HOPG (right hand side). (a) and (e): pristine. (b) and (f) after exposure to one atmosphere O_2 for 30 min. (in dark). (c) and (g) after additional exposure to one atmosphere O_2 for 120 min. (with visible light). (d) and (h) after additional exposure to ambient air for 60 min. (with visible light). Inset: Extended BE scale UPS spectra of the pristine pentacene film on SiO_2 (bottom curve), and after exposure to ambient air for 15 min. with UV irradiation (top curve

Most notably, spectra (a) – (d) and (e) – (h) of Fig. 3 are virtually identical in both energy position and lineshape, regardless of treatment. The essence of these results is that molecular oxygen and also water (from air) do not react with pentacene in dark or under visible light. The surface sensitivity of UPS would unmistakably allow for the identification of such a reaction. Furthermore optically excited pentacene (the optical gap 1.85 eV) is not sufficient to promote a reaction. Oxygen possibly diffused into pentacene at atmospheric pressure and out again after re-evacuation does not lead to irreversible changes. In contrast, the inset of Fig. 3 demonstrates that the exposure of pentacene to air in the presence of UV light leads to a rapid reaction of pentacene, most probably an oxidation by ozone (produced by the UV light). By the comparison of our results obtained on three different substrates we can clearly differentiate between doping of pentacene (*not observed* under the present experimental conditions) and a modification of the substrate properties (*observed* for the Au substrate) due to oxygen exposure. The implication for devices comprising pentacene and Au contacts is that upon exposure of the devices to oxygen/air a considerable lowering (increase) of the hole (electron) injection barrier from Au into pentacene, which is not caused by doping.

Conclusion

In extensive tests we have observed no reaction of pentacene with molecular oxygen and water, even if pentacene is optically excited. More importantly, it is found that oxygen diffusion through pentacene thin films (and single crystals) is reversible, and does not leave behind – after re-evacuation – electrically active electronic states that would lead to doping of the organic bulk material. However, it was found that the hole injection barrier at the Au/pentacene interface is lowered by oxygen exposure. Finally, it was demonstrated that rapid oxidation of pentacene occurs in air only in the presence of UV light, due to the formation of highly reactive ozone.

This work is supported by the *Sonderforschungsbereich 448* and by the *Schwerpunktprojekt Organische Feldeffekt-Transistoren* (Project No. Ka427/8), both sponsored by the DFG.

References

1. C. D. Dimitrakopoulos and P. R. L. Malenfant, Adv. Mater. **14**, 99 (2002).
2. M. Halik, H. Klauk, U. Zschieschang, T. Kriem, G. Schmid, W. Radlik, and K. Wussow, Appl. Phys. Lett. **81**, 289 (2002).
3. Ch. Pannemann, T. Diekmann, and U. Hilleringmann, J. Mater. Res. **19**, 1999 (2004).
4. J. E. Northrup and M. L. Chabinyc, Phys. Rev. B **68**, 041202 (2003).
5. O. D. Jurchescu, J. Baas, and T. T. M. Palstra, Appl. Phys. Lett. **84**, 3061 (2004).
6. J. Jo, J. J. Heremans, F. Bradbury, H. Chen, and V. Soghomonian, Nanotechnol. **15**, 1023 (2004)
7. W. Y. Gao and A. Kahn, Appl. Phys. Lett. **79**, 4040 (2001).
8. K. Seki and H. Ishii, J. Electron Spectrosc. Relat. Phenom. **88**, 821 (1998).
9. C. C. Mattheus, A. B. Dros, J. Baas, G. T. Oostergetel, A. Meetsma, J. L. de Boer, and T. T. M. Palstra, Synth. Met. **138**, 475 (2003).
10. Y. Harada, H. Ozaki, and K. Ohno, Phys. Rev. Lett. **52**, 2269 (2004).

Molecular Structure of Surface-Active Salt Solutions

Bernd Winter[1], Ramona Weber[1], Philipp M. Schmidt[1], Ingolf V. Hertel[1], Manfred Faubel[2], Lubos Vrbka[3], and Pavel Jungwirth[3]

[1]Max-Born-Institut, Berlin, Germany; [2]Max-Planck-Institut für Dynamik und Selbstorganisation, Göttingen, Germany; [3]Institute of Organic Chemistry and Biochemistry, Academy of Sciences and Center for Complex Molecular Systems and Biomolecules, Prague, Czech Republic

Solvation of surface-active tetrabutyl-ammonium iodide (TBAI) in pure liquid water was investigated by photoelectron (PE) spectroscopy and by molecular dynamics (MD) simulations. The interactions between water molecules and dissolved ions are of crucial importance for many physical and chemical processes in biological systems, in the atmosphere, and in technological applications. Recent experimental and theoretical studies of the interfacial structure of aqueous solutions suggest that certain hydrophilic aqueous ions are located within the solution surface [1-5], which would contrast the commonly assumed thermodynamic picture of an interface depleted of ions [6]. Non-polarizable ions, such as alkali metal cations or fluoride, have been shown by MD simulations, using polarizable force fields, to be repelled from the interface [1]. Contrarily, soft, polarizable simple ions, such as the heavier halides Cl^-, Br^-, and I^-, exhibit surface affinity. The effect scales with the anion polarizability and size, and is different from the hydrophobic interactions for ionic surfactants, containing for instance aliphatic chains, which also lead to the accumulation at the aqueous surface [1,2]. Thus, for the prototype ionic surfactant TBAI anionic and cationic surface propensity is of entirely different origin.

Photoelectron spectroscopy was combined with the liquid microjet technique (6μm diameter water jet) [7]. MD simulations were carried out using the AMBER7 software package with polarizable potentials. We used the parm99.dat force field with a slight modification of the iodide anion polarizability. A water slab consisting of 863 POL3 water molecules was used for the construction of the following two systems [8,9]. The first system contained in addition a single TBAI ion pair with the cation and anion initially located on the same side of the aqueous slab. The second system contained initially 8 TBAI ion pairs on each side of the water slab, i.e., 16 TBAI pairs in total. Both systems were placed in rectangular boxes with dimensions of 31×31×100 $Å^3$. Periodic boundary conditions were applied in all three dimensions to produce an infinite water slab in the xy-plane with two air-water interfaces perpendicular to the z-direction.

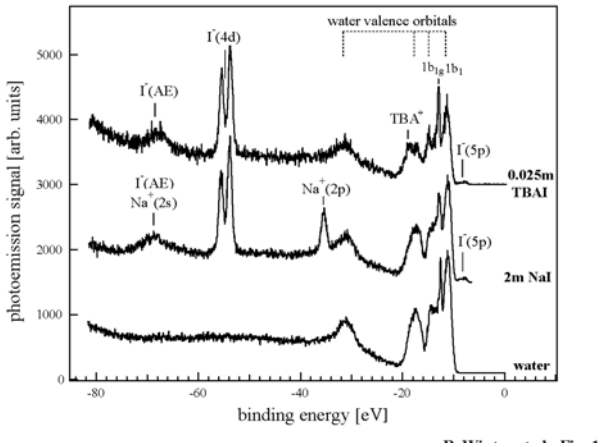

Figure 1 PE spectra of pure water, 2m NaI (molal), and 0.0025m TBAI aqueous solutions measured at 100 eV photon energy.

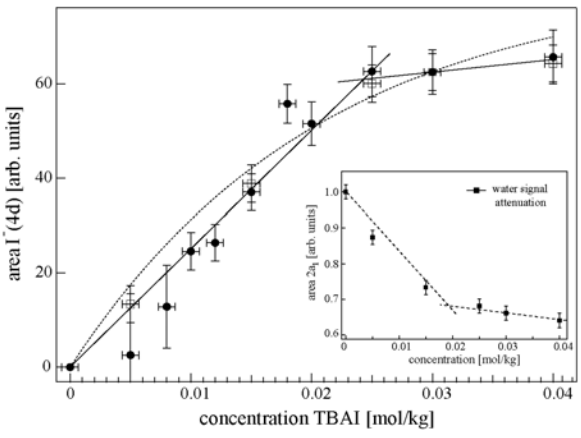

Figure 2 I^-(4d) PE signal as a function of the TBAI concentration. Squares and dots refer to two different sets of measurements. Inset: water signal attenuation. For the lines see text.

Photoemission spectra of pure liquid water, of a 0.025m TBAI aqueous solution and, for comparison, of 2m NaI aqueous solution are presented in Figure 1, respectively. The experiments were

performed at the U125/1 beamline. In the figure electron binding energies are presented with respect to vacuum, and relative intensities of the three traces are scaled to the ring current. The decreasing water feature intensity, from bottom to top, reflects the attenuation of the water signal for the respective salt solutions. The characteristic valence photoemission features of liquid water and the various emissions from Na^+ and I^- are labeled. Almost no TBA^+ signal is detectable due to low photoionization cross section. In the TBAI spectrum (top) the prominent iodide signal, I^-(4d) at 53.8/55.3 eV, is nearly as intense as for the NaI solution, even though the concentration of the former solution is 80 times lower. This immediately confirms substantial surface segregation (yielding segregation factor 70). Despite the different molecular structures for the two solutions identical iodide binding energies are observed, which can be attributed to the fact that a partial loss of the solvation shell is more than compensated at the surface by polarization interactions [10].

The iodide photoemission signal, I^-(4d), and the water signal evolution as a function of the TBAI concentration, is displayed in Figure 2. The steeper linear rise of the iodide signal for lower concentrations identifies sub-monolayer coverage, and the smooth intensity increase beyond 0.020m is attributed to the completed segregation monolayer. Two linear lines (solid) have been drawn to guide the eye. The dashed line is a fit that is proportional to $1- e^{-c/co}$, which is commonly used to model layer-by-layer film growth. It describes the envelope of consecutive linear segments, reflecting the sequential monolayers that have been built up. The fit parameter $c_o = 0.21$ corresponds to the salt concentration for saturation in the layer-by-layer model. Obviously, this is a poor fit, as expected if only one single monolayer is being formed. The break near 0.024m identifies the completed monolayer.

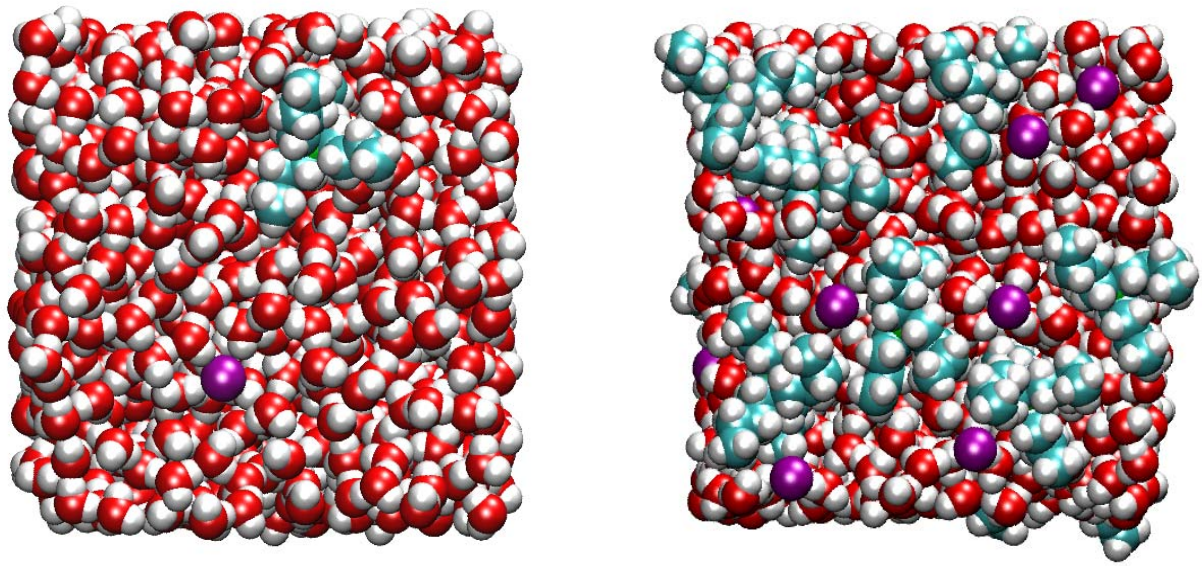

Figure 3 Snapshots from MD simulations showing the TBAI surface coverage (top view) for an aqueous slab containing (left) 1 TBAI ion pair and (right) 16 TBAI ion pairs and 863 water molecules. Color coding: TBA^+ - light blue and white, iodide – purple, water – red.

A qualitative picture of the surface molecular structure of TBAI can be obtained from simulation snapshots of one of the two vacuum/solution interfaces of the slab. Figure 3 shows such typical snapshots displaying the surface coverage of the water slabs with 1 or 16 (saturation) TBAI ion pairs, respectively. Note that both TBA^+ cations and I^- anions are present at the surface. The numerical values of the surface coverage for the two systems are 0.1×10^{13} cm^{-2} and 0.9×10^{14} cm^{-2}, respectively, which compares with 1.0×10^{14} cm^{-2}, the experimentally predicted value for the completed TBAI monolayer [11]. It can be seen in Figure 3 (right) that any additional cation is unlikely to fit on the surface; the available space is occupied by I^- anions. Density profiles for O, N, and I atoms for the systems with a single TBAI ion pair or 16 TBAI ion pairs are presented in Figure 4.

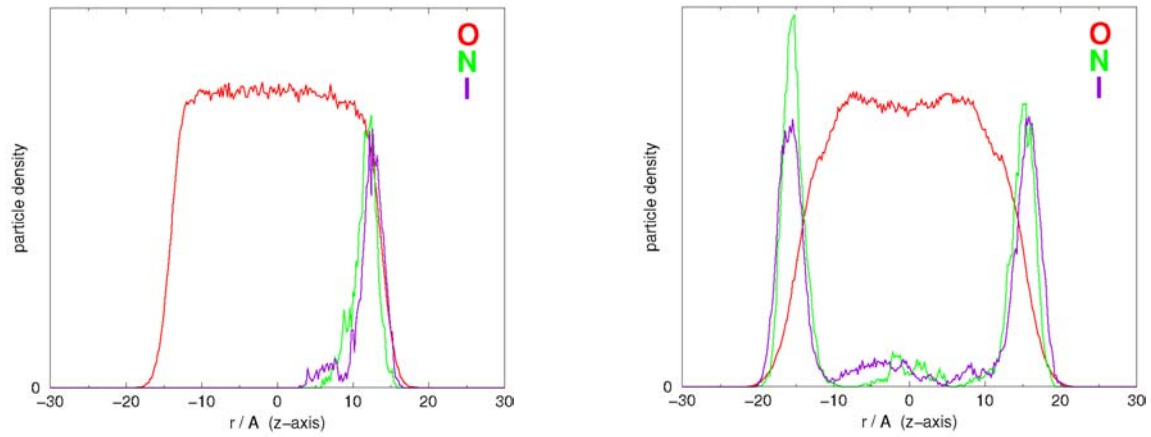

Figure 4 Density profiles of a dilute TBAI (single ion pair), left, and concentrated TBAI (16 ion pairs), right, solution across the aqueous slab.

The interfacial region for the latter system is largely affected by the high concentration of ions, leading to a decrease of the density of water oxygens. In all simulations both cations and anions clearly prefer positions at the surface, as expected for the reasons mentioned. The importance of the anion's polarizability is in fact confirmed by our test simulations, which show that iodide anions immediately disappear from the surface and prefer full solvation inside the bulk phase once the polarizability part of the force field is switched off. The cations remain at the interface even for the non-polarizable force field, since the surface driving force here is the hydrophobic interaction between the butyl groups and water. The corresponding charge profiles (not shown) are consistent with the non-existence of any appreciable charge segregation perpendicular to the interface, i.e., both cations and anions reside in the interfacial layer. This is in agreement with the experimentally observed constant low-energy cutoff (no changes in work function) when comparing the photoemission spectra of pure water and TBAI solutions of any concentration [8]. Hence the present results would be inconsistent with the formation of a strong electric double layer at the surface. One also notices from Figure 4 that the non-zero signal from the cation inside the aqueous bulk for the more concentrated system (Figure 4, right) confirms the completion of the surface monolayer. Indeed, since there is no space left at the surface, and surfactants do not tend to form more than one layer, one particular cation immerses into the bulk where it travels almost freely, accompanied by charge compensating iodide.

The analysis of the geometries of the flexible TBA cations shows that the butyl chains are preferentially orientated parallel to the surface and, particularly at higher salt concentrations, the chains point toward the aqueous bulk.

Support from the Czech Ministry of Education via a grant No. LN00A032 is gratefully acknowledged.

(1) Jungwirth, P.; Tobias, D. J. *Journal of Physical Chemistry B* **2001**, *105*, 10468.
(2) Jungwirth, P.; Tobias, D. J. *Journal of Physical Chemistry B* **2002**, *106*, 6361.
(3) Vrbka, L.; Mucha, M.; Minofar, B.; Jungwirth, P.; Brown, E. C. *Curr. Opn. Coll. Int. Sci.* **2004**, *9*, 67.
(4) Petersen, P. B.; Saykally, R. J. *Chemical Physics Letters* **2004**, *397*, 51.
(5) Dang, L. X.; Chang, T. M. *Journal of Physical Chemistry B* **2002**, *106*, 235.
(6) Adamson, A. W. *Physical Chemsitry of Surfaces*; Wiley: New York, 1990.
(7) Winter, B.; Weber, R.; Widdra, W.; Dittmar, M.; Faubel, M.; Hertel, I. V. *Journal of Physical Chemistry A* **2004**, *108*, 2625.
(8) Winter, B.; Weber, R.; Schmidt, P. M.; Hertel, I. V.; Faubel, M.; Vrbka, L.; Jungwirth, P. *J. Phys. Chem.* **2004**, *108*, 14558
(9) Vrbka, L.; Jungwirth, P. *Australian Journal of Chemistry* **2004**, *57*, 1.
(10) Bradforth, S. E.; Jungwirth, P. *Journal of Physical Chemistry A* **2002**, *106*, 1286.
(11) S. Holmberg; R. Moberg; Z. C. Yuan; Siegbahn, H. *J. Electron Spectrosc. Relat. Phenom.* **1988**, *47*, 27.

Photoemission Investigation on $Fe_{1-x}Co_xSi$ Single Crystals

D. Menzel, D. Zur, I. Jursic, and J. Schoenes
Institut für Physik der Kondensierten Materie, Technische Universität Braunschweig, Mendelssohnstraße 3, 38106 Braunschweig

Introduction

While FeSi is known for several decades, its narrow-gap-semiconductor behavior has led to a renewed interest due to the similarities with some rare-earth compounds known as Kondo insulators [1]. The magnetic susceptibility exhibits a maximum at 500 K and decreases according to a magnetic excitation across a narrow gap [2]. Doping with Co makes the gap disappear leading to a metallic character. The alloy $Fe_{1-x}Co_xSi$ is remarkable in that it is ferromagnetic for almost all compositions although the end members FeSi and CoSi are a paramagnetic semiconductor and a diamagnetic metal, respectively [3].

Experimental

$Fe_{1-x}Co_xSi$ single crystals have been prepared by tri-arc Czochralski crystal growth and are magnetically characterized by SQUID magnetometry. In Braunschweig, the photo-emission experiment was performed using a He spectral lamp at 21.2 eV with an energy reso-lution of 150 eV. High-resolution photoemission spectroscopy was done at BESSY II using the PHOENEXS chamber at U125/2-SGM. In order to clean the sample surface the crystals were sputtered by an Ar gun and subsequently annealed at 600°C.

Magnetic Properties

Below a Co concentration of 5% $Fe_{1-x}Co_xSi$ is paramagnetic. Fig. 1 (a) shows the susceptibility of $Fe_{1-x}Co_xSi$ single crystals for $x < 0.05$ as a function of temperature. The applied magnetic field was 1000 Oe. The susceptibiliy follows a Curie law with an effective magnetic moment of 1 μ_B per Co atom.

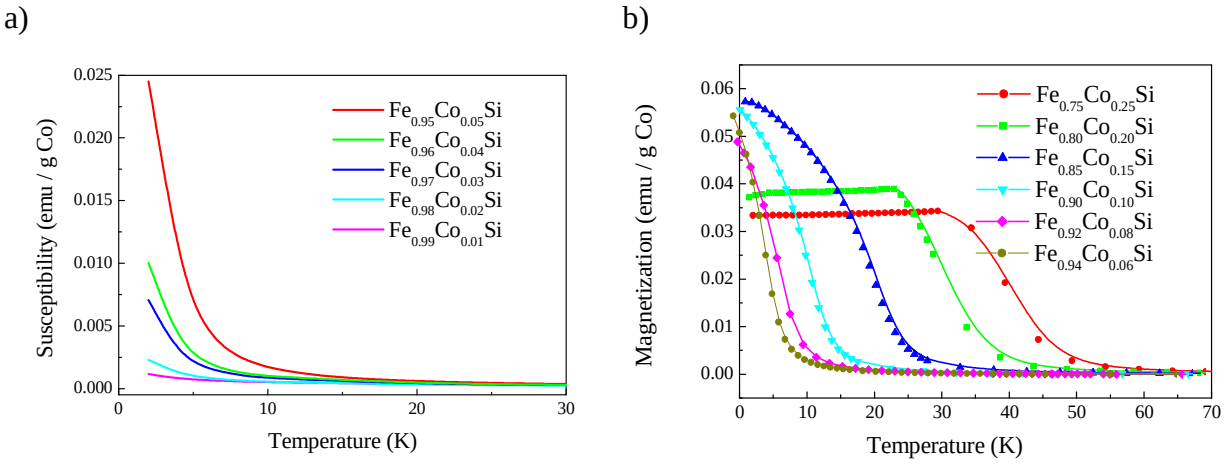

Fig. 1: *Paramagnetic susceptibility (a) and magnetization (b) of $Fe_{1-x}Co_xSi$ single crystals for various Co concentrations x as a function of temperature. The applied magnetic field was 1000 Oe.*

Above 5% Co, the alloy orders ferromagnetically and displays an increase of the Curie temperature with growing Co concentration. The magnetization of $Fe_{1-x}Co_xSi$ single crystals for a Co concentration x > 0.06 as a function of temperature in an applied magnetic field of 1000 Oe is shown in Fig. 1 (b).
The ratio of the effective moment calculated from the Curie-Weiss law and the saturation moment is greater than unity for Co concentrations in the ferromagnetic regime. This may be considered to be an indication of the nonlocalized nature of these moments according to the Rhodes-Wohlfarth criterion [4].

Photoemission spectroscopy

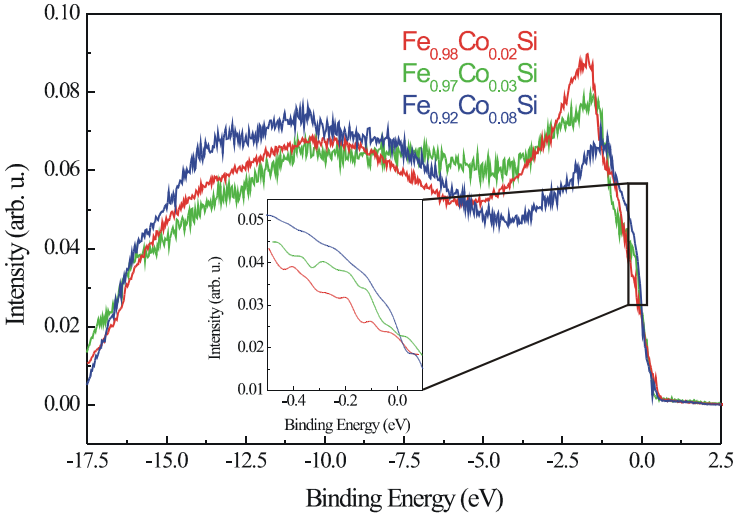

Fig. 2: *UV-Photoemission spectra of $Fe_{1-x}Co_xSi$ crystal surfaces with various Co concentrations x = 0.02; 0.03; 0.08 at room temperature. The experiment was performed using a He spectral lamp at 21.2 eV with an energy resolution of 150 meV.*

a) b)

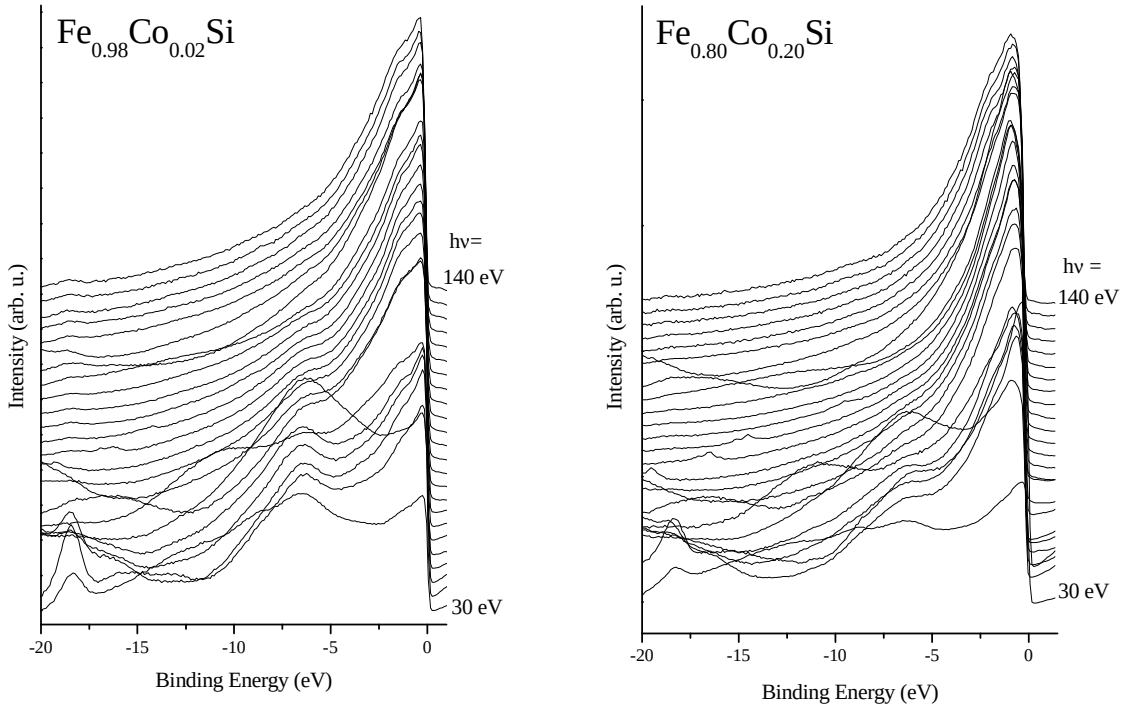

Fig. 3: *High-resolution photoemission spectroscopy of (a) $Fe_{0.98}Co_{0.02}Si$ (paramagnetic regime) and (b) $Fe_{0.80}Co_{0.20}Si$ (ferromagnetic regime) performed at BESSY II using the PHOENEXS chamber at U125/2-SGM.*

Photoemission spectra of $Fe_{1-x}Co_xSi$ crystal surfaces with various Co concentrations were measured at room temperature [5]. The experiments were performed in Braunschweig (He spectral lamp at 21.2 eV, Fig. 2) and at BESSY II using the PHOENEXS chamber at U125/2-SGM (Fig. 3). The spectra show a sharp maximum in the valence band. Photoemission spectra of pure FeSi are similar in shape [6] and linear augmented-plane-wave band calculations for FeSi also show a sharp peak in the density of states below the Fermi energy [7]. With increasing Co concentration the maximum in the density of states shifts towards the Fermi energy while the intensity decreases (Fig. 2). This suggests the closing of the band gap when doping FeSi with Co.
The comparison of the spectra of $Fe_{0.98}Co_{0.02}Si$ and $Fe_{0.80}Co_{0.20}Si$ shows that the density of states close to the Fermi energy (A, B) is higher for the Co rich sample than for that with low Co content (Fig. 4). The high density of states supports the ferromagnetic order according to the Stoner criterion.

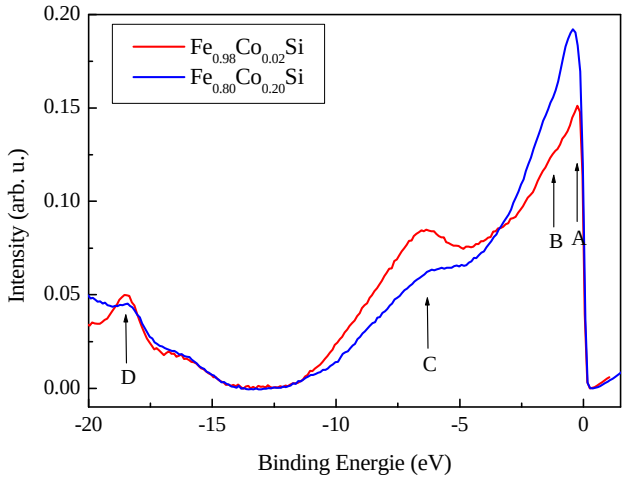

Fig. 4: *Comparison of the high-resolution photoemission spectra of $Fe_{0.98}Co_{0.02}Si$ and $Fe_{0.80}Co_{0.20}Si$ at a photon energy of 40 eV.*

The results presented so far indicate an intinerant model of the magnetism in the system $Fe_{1-x}Co_xSi$. However, a two-band Hubbard theory [8] as well as a periodic Anderson model [9] are a good approach to the optical and magnetic experimental findings. Thus, a Kondo-like description with localized moments cannot be excluded. A decisive experiment to manifest this correlated picture is to prove a sharp Kondo resonance at the Fermi energy. Therefore, highly-resolved photoemission measurements with a resolution better than 40 meV are mandatory.

Literature

[1] V. I. Anisimov et al., Phys. Rev. Lett. **89**, 257203 (2002)
[2] V. Jaccarino et al., Phys. Rev. **160**, 476 (1967)
[3] J. H. Wernick et al., Mater. Res. Bull. **7**, 1431 (1972)
[4] P. Rhodes and E. P. Wohlfarth, Proc. Roy. Soc. London Ser. A **273**, 247 (1963)
[5] D. Menzel et al., J. Magn. Magn. Mater. **272-276**, 130 (2004)
[6] C. H. Park et al., Phys. Rev. B **52**, R16981 (1995)
[7] L. F. Mattheiss et al., Phys. Rev. B **47**, 13114 (1993)
[8] C. Fu and S. Doniach, Phys. Rev. B **51**, 17439 (1995)
[9] M. E. Foglio and M. S. Figueria, Phys. Rev. B **62**, 7882 (2000)

We are indebted to the BESSY staff for the technical help. The financial support of BESSY is gratefully acknowledged.

Electronic Structure of Photochromic Compounds

D. Schulze, D. Wett, K. H. Hallmeier, A. Demund, R. Szargan

Wilhelm-Ostwald-Institut für Physikalische und Theoretische Chemie, Universität Leipzig, 04103 Leipzig, Germany

Recently there is an increasing interest on the preparation and investigation of photochromic compounds [1]. These are substances occurring in two isomeric forms and having the property of colour change after the absorption of light of specific wavelengths. It is required that this change can also be reversed by exposure to light and/or heat, yielding again the original substance. Applications that are envisaged for photochromism include optical data storage and optically controlled molecular switching, that ultimately may drive developments in molecular nanotechnology.

On the basis of 2*H*-1-benzopyrans there were synthesized novel 2,4,6-Triaryl-1-(spiro[2*H*-1-benzopyran-2,2´-indoline]-6-yl) pyridinium perchlorates [2]. The changing molecular structure of the investigated compound is shown in figure 1.

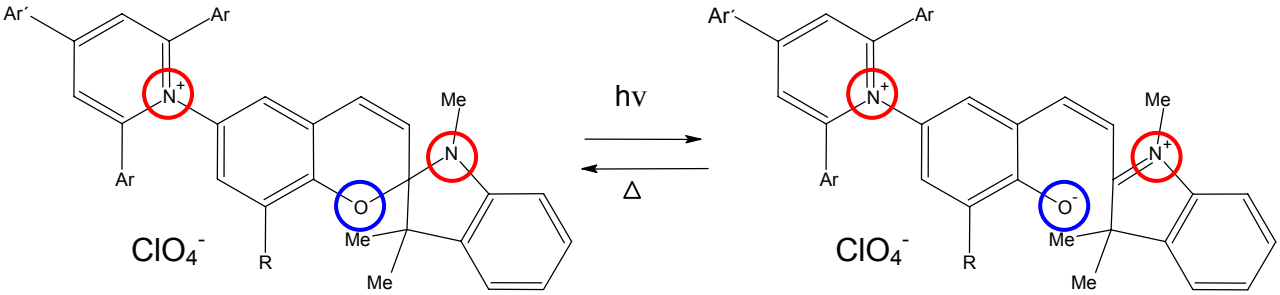

Fig. 1: 2,4,6-Triaryl-1-(spiro[2*H*-1-benzopyran-2´-indoline]-6-yl) pyridinium perchlorate (spiro-H)

Our special interest is the characterization of the electronic structure (electron density, influence of symmetry and probability of excitation states). Therefore we carried out examination with fluorescence spectroscopy both in the absorption and the emission mode. X-ray emission spectra were measured using the X-ray spectrometer XES 300 at the ROSA station (rotatable spectroscopy apparatus) by means of synchrotron radiation of the U41-PGM undulator beam-line at BESSY II . X-ray absorption (XANES) measurements were done in the fluorescence yield detection mode at ROSA.

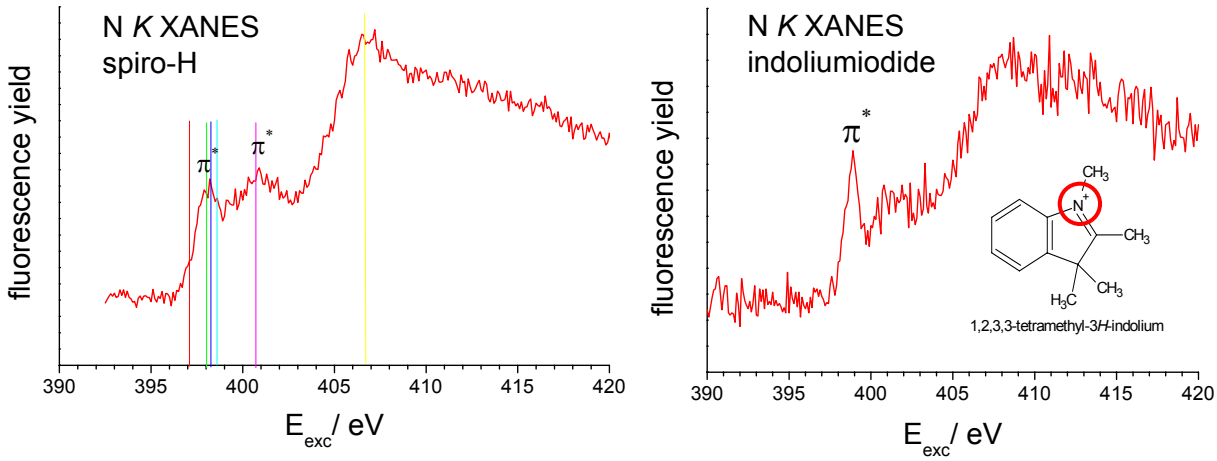

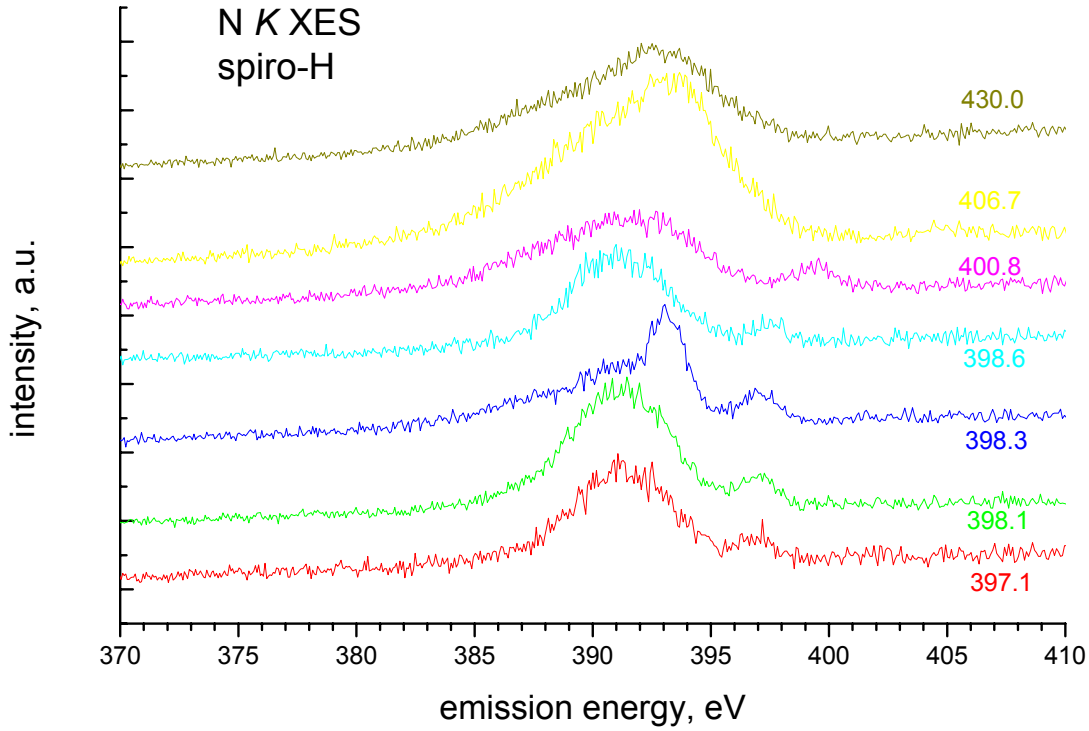

Fig. 2: N *K* XANES and N *K* RIXS spectra of photochromic compound (for comparison N *K* XANES indoliumiodide)

The N *K* XANES absorption edge (fluorescence yield) and the corresponding resonant emission spectra are shown in figure 2. The structures around 398.3 and 400.6 eV, resp., in the absorption spectrum of spiro-H are resonant π*-components ($1s^{-1}$ 2pπ* excitation) of the differently bound nitrogen in this molecule. In contrast the spectra of indoliumiodide indicate the fourfold bound nitrogen-ion only. Therefore we conclude a mixture of 3- and 4-fold bound nitrogen of the two isomers for the photochromic compound as indicated in the structure formula given above.

The RIXS spectra start with a nearly symmetrical shape reflecting transitions from predominantly π states (397.1, 398.1 eV). At an excitation energy of 398.3 eV a high-energy resonance appears in the emission spectrum indicating transitions from localized valence states. At higher excitation energies the low-energy shoulder of the emission spectra reflects additional transitions from σ states.

Acknowledgement:

This work was supported by the BMBF, grant number 05KS1OL1/3. We are grateful to the BESSY staff especially for technical assistance by C. Jung and M. Mast at the U41-PGM beamline.

References:

[1] Organic Photochromic and Thermochromic Compounds, C. Crano and R. Guglielmetti, eds., Vol 1, Plenum Press, New York, London, 1999, Vol 2, Kluwer Academic, Plenum Publishers, New York, Boston, Dordrecht, London, Moscow, 1999, and literature cited therein

[2] T. Zimmermann, O. Brede , J. Heterocyclic Chem., 40, 611 (2003)

Investigations of electron structure specificity and the nature of photoluminescence in porous materials and quantum points for indirect band-gap and direct-gap semiconductors (Si, GaP, InP, GaAs).

E.P. Domashevskaya, V.M. Kashkarov, V.A. Terekhov, S.Yu. Turishchev
Voronezh State University, Universitetskaya pl.1, 394006 Voronezh, Russia
S.L. Molodtsov[1], D.V. Vyalikh[2]
[1] *Institut für Oberflächen- und Mikrostrukturphysik, TU Dresden, Germany*
[2] *Instutut für Experimentalphysik, Freie Universität Berlin, Arnimallee 14, Berlin, Germany*

Crystalline and amorphous materials containing nano-size clusters draw a serious attention due to their unique physical properties. These clusters are characterized by quasi-atomic energy structure of the valence electron states, high adsorption capability and chemical activity. However, the main regularities of transformation of the electron and other physical properties under transition from the bulk crystalline materials to the nano-size objects have not yet been investigated in details. Specific features of the interactions between clusters and material of the ambient matrix, which is used for passivation of the cluster surface and stabilization of their properties in time, are not studied as well.

The aim of this work is to investigate electron yield spectra of the samples containing nanometer-scale clusters and quantum dots applying synchrotron radiation (SR). Electron yield spectra correspond to X-ray absorption near-edge spectra (XANES) and they allow to determine local partial density of states with certain symmetry into unoccupied states of the conduction band of different materials.

Two groups of the samples were investigated – the first one included samples on the basis of crystalline silicon, the second group was based on III-V compounds. The first group contained porous silicon samples obtained by standard electrochemical etching on silicon substrates of n-types as well as those ones subjected to post-etch treatment. We have also performed investigations of Ge quantum dots on silicon and $Ge_{1-x}Si_x$ alloys.

Second group of the investigated samples included porous InP obtained in different etching agents, containing HF, HCl or HBr and quantum dots of InP grown by MBE technique and buried in $In_{1-x}Ga_xP$ (x=0.5) film grown on GaAs substrate.

All the investigations were made at Russian-German beamline of BESSY synchrotron radiation facility. Experimental spectra of the investigated samples as well as the spectra of the reference samples are presented in Figs. 1-5. Energy resolution in the obtained spectra was less than 0.03 eV.

Let us now discuss the obtained results for porous silicon (fig. 1). Previously, we have found that according to our USXES and XPS data the surface layers of por-Si with a thickness of ~ 50 nm contain the phases of c-Si, SiO_x, SiO_2 and a-Si:H [1].

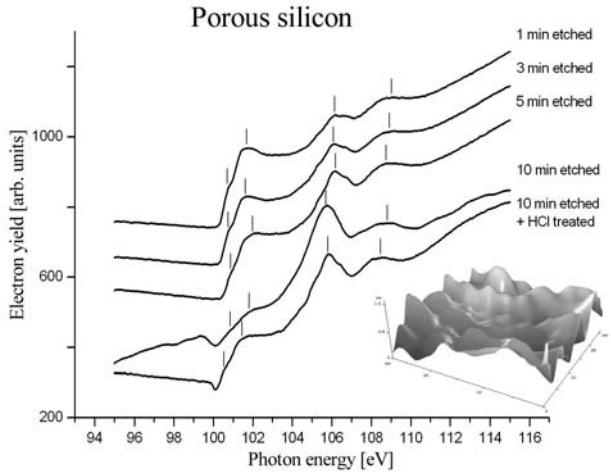

Fig.1. Electron yield spectra near Si $L_{2,3}$ absorption edge of porous silicon grown on c-Si <111> substrate with different etching time.

It is assumed that visible photoluminescence in porous silicon can be explained by the presence of quantum wires in the bulk of the material or, possibly, by the formation of oxide layer on the surface of these wires or pores. Since por-Si is characterized by a highly-developed surface and complicated phase composition, then a detailed analysis of electron yield spectra of porous silicon was performed with the use of some reference spectra of SiO_2

(α-quartz and natural oxide of SiO_2/Si [2]) as well as a-Si:H (amorphous hydrogenated silicon) spectrum (fig. 2).

One should immediately note the presence of rather sharp absorption edge in the range of 100 – 102 eV (fig. 1) which corresponds to the edges of crystalline and amorphous silicon. Besides, under increase of the etching time and, hence, an increase of the thickness of porous layer the peak at about 101.5 eV which is characteristic of amorphous hydrogenated silicon gradually disappears. At the same time an increase of the relative intensity of the spectral structure takes place in the range of 104 – 109 eV characteristic of silicon oxides. Under increase of the etching time up to 10 minutes the investigated spectrum is considerably transformed. Noticeable shift (by approximately 0.5 eV) of the peak at 105.5 eV takes place. All the observed changes of spectrum are connected with a considerable oxidation of surface por-Si layers.

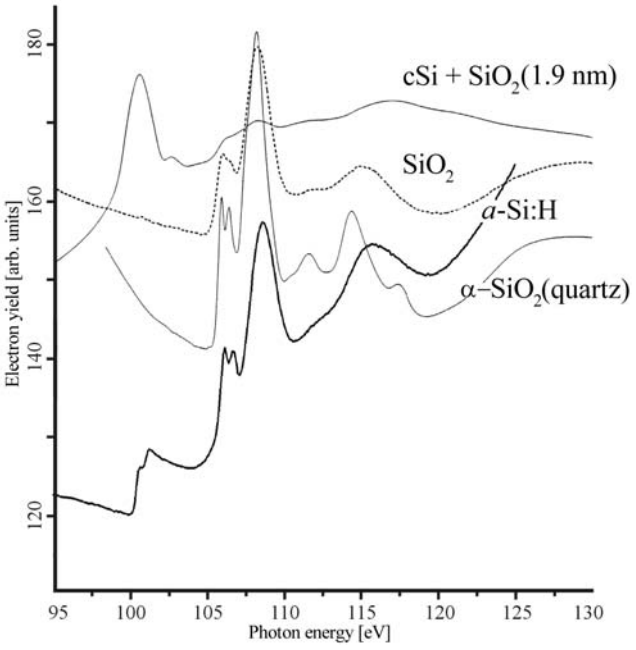

Fig.2. Si $L_{2,3}$ absorption edges of reference samples: cSi + SiO_2, SiO_2, α- SiO_2 (quatrz) [2] and electron yield spectrum near Si $L_{2,3}$ absorption edge of *a*-Si:H with inclusions of Si-nanocrystals.

Moreover, silicon edge at 100-102 eV becomes less distinguished and more flat. It can be the evidence that silicon particles of various nanometer sizes are present in the surface layer of this material and, hence, they are characterized by different positions of silicon absorption edge [3]. This statement is in agreement with the presence of a wide photoluminescence band in porous silicon [1].

The treatment of porous silicon in hydrochloric acid results in more distinct silicon edge of absorption. Moreover, a fine structure in the absorption spectrum of silicon oxide phase is revealed unlike of the spectrum of non-treated sample. According to the data in scientific literature under the treatment of porous silicon in hydrochloric acid dissolution of small-size silicon particles on the surface takes place if only these particles are weakly passivated by atmospheric oxygen [4]. Under etching in HCl the number of these particle in porous layer is reduced and silicon absorption edge becomes more sharp.

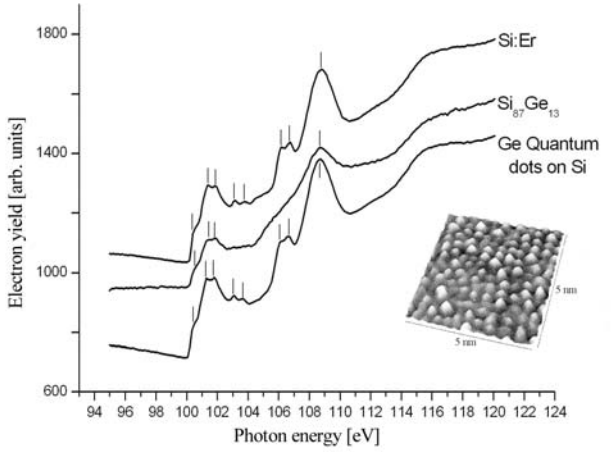

Fig.3. Electron yield spectra near Si $L_{2,3}$ absorption edge for erbium-doped silicon (Si:Er), $Si_{1-x}Ge_x$ alloy (x = 0.13) and germanium quantum dots on silicon.

Fig. 3 represents electron yield spectra near Si $L_{2,3}$-absorption edge for erbium-doped silicon, $Si_{1-x}Ge_x$ alloy (x=0.13) and germanium quantum dots on silicon substrate. Atomic force microscope image of quantum dots on Si surface is inserted to figure 3. One can see the appearance of fine structure in the spectra near Si $L_{2,3}$-absorption edge. It is assumed that this structure is due to the formation of nano-size particles of silicon which results in release of degeneration for the states in conduction band.

Now we consider the results of investigations of indium phosphide in different III-V materials. Unlike of silicon no one still could obtain X-ray P $L_{2,3}$ quantum yield spectra in single-crystalline III-V phosphides. It is assumed that this is connected with zinc-blend crystalline structure of these compounds. However, we have managed for the first time to obtain a distinct electron yield spectra of phosphorus in porous indium phosphide (fig. 4) and in $In_{0.5}Ga_{0.5}P$ alloy and InP quantum dots (fig. 5).

The sample obtained by InP etching in chlorine-containing ambient (fig. 4) demonstrates very sharp peaks that can be associated with the presence of quasimolecular structures in the porous layers. Analysis of the composition of porous InP by USXES-spectra shows that no any disproportionation of InP into components takes place [5]. Therefore, one can assume that under etching formation of very small InP particles takes place. As a result, relaxation of chemical bonds in these particles occurs causing distortion of symmetry in the structure net as compared with single crystal. This can be the reason of arising of rather contrast electron yield P $L_{2,3}$-spectra in porous InP.

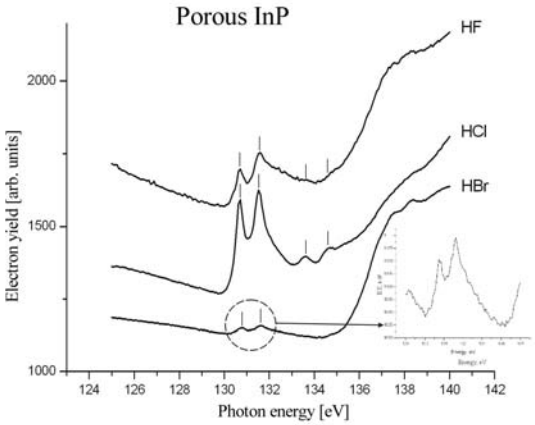

Fig.4 Electron yield spectra near P $L_{2,3}$ absorption edge of porous InP obtained in different etching agents, containing HF, HCl or HBr.

Similar situation is realized in $In_{0.5}Ga_{0.5}P$ alloy (spectrum in the bottom of fig. 5). Crystal lattice of the alloy is stressed. Elastic stresses in the lattice just the same result in distortions of local symmetry of interatomic bonds, thus resulting in appearance of electron quantum yield spectra.

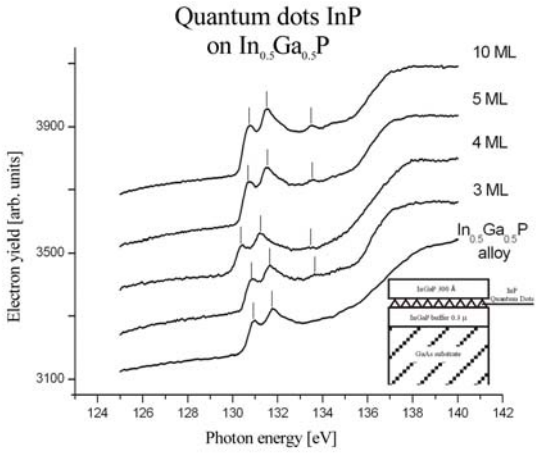

Fig.5. Electron yield spectra near P $L_{2,3}$ absorption edge of InP different size quantum dots on $In_{0.5}Ga_{0.5}P$ and $In_{0.5}Ga_{0.5}P$ alloy.

One should note that the spectra are characterized by two main peaks just as in the case of porous indium phosphide. However, the peaks are more smeared. The latter is caused by formation of various low-dimension cluster structures.

Analysis of electron yield spectra for quantum dots of InP in the matrix of $In_{0.5}Ga_{0.5}P$ alloy (cross-section of the structure is presented in the insertion to fig. 5) demonstrates that with an increase of efficient thickness of InP film which in fact characterizess the mean size of quantum dots, phosphorus absorption edge becomes more abrupt. Fine structure in the spectra becomes clearly expressed as well as the peak at approximately 133.5 eV. The presence of this peak can be due to the appearance of localized states in conduction band of the structure with InP quantum dots.

Thus, when executing the research it was shown that X-ray spectroscopy with the use of synchrotron radiation proved to be a powerful mean for the investigations of low-dimensional structures where some quantum properties can be observed.

[1] V.A. Terekhov, V.M. Kashkarov, E.Yu. Manukovskii, A.V. Shchukarev, E.P. Domashevskaya. J.Electr.Spectr. and Rel.Phen. 114-116 (2001) 895-900.

[2] E.O. Filatova Doctor Thesis. S - Petersburg. 2000. 374 p.

[3] T.van Buuren, L.N. Dinh, L.L. Chase, L.J. Terminello, M. Grush, T.A. Calcott, D.L. Ederer, J.A. Carlisle. Compendium of User Abstr. And Techn.Reps. Berkley, California, 1997. p.254

[4] J.I. Gole, J.A. DeVincentic, L. Seals, P.T. Lillehei, S.M. Prokes. Phys.Rev. B. 61. N 8. p.5615-5631.

[5] E.P. Domashevskaya, V.A. Terekhov, V.M. Kashkarov, I.N. Arsentyev, L.S. Vavilova, V.P. Ulin. Abstracts of V-th Russian Conf. on semiconductors, N-Novgorod, 2001, p.383.

XANES investigations of electron structure and phase composition in nanostructures SnO_x/Si(100).

E.P. Domashevskaya, V.M. Kashkarov, V.A. Terekhov, S.Yu. Turishchev, S.V. Ryabtsev
Voronezh State University, Universitetskaya pl.1, 394006 Voronezh, Russia
e-mail: root@ftt.vsu.ru

S.L. Molodtsov[1], D.V. Vyalikh[2]
[1] Institut für Oberflächen- und Mikrostrukturphysik, TU Dresden, Germany
[2] Instutut für Experimentalphysik, Freie Universität Berlin, Arnimallee 14, Berlin, Germany

Thin films of wide band-gap semiconductor SnO_2 are used as materials for gas sensors in ecology and analytical chemistry and also as antireflecting coatings, especially in combination with PbO_2. Tin dioxide can be doped with impurities of both n-type and p-type and this allows to apply it for detection of a wide range of gases in a dependence of their nature. At the same time electron structure even of the bulk crystals of SnO_2 has been studied to the insufficient extent. Besides, morphology and crystal structure of the films of tin dioxide was found to depend considerably on the technology of their preparation while their electrical and optical properties – on the type of doping impurity and the way of its introducing into the film. Moreover, there are certain assumptions that thin films of SnO_2 can contain inclusions of metallic tin with nanometer size due to disproportionation of tin dioxide according to the reaction $SnO_2 \rightarrow Sn + SnO$. While doping of the films with noble metals atoms Au, Pd, Pt can form clusters on the surface of the film thus having a considerable effect on the film conductivity and its changes under interaction with the gas ambient.

In our work we investigated thin films of SnO_2, obtained by magnetron sputtering and the following deposition of tin on the substrates of single crystalline silicon. Next, the 100 nm and 300 nm thickness films were oxidized in the atmosphere at different temperatures. Nanostructures SnO_x/Si obtained in this way were investigated at RGBL channel of BESSY II synchrotron radiation facility.

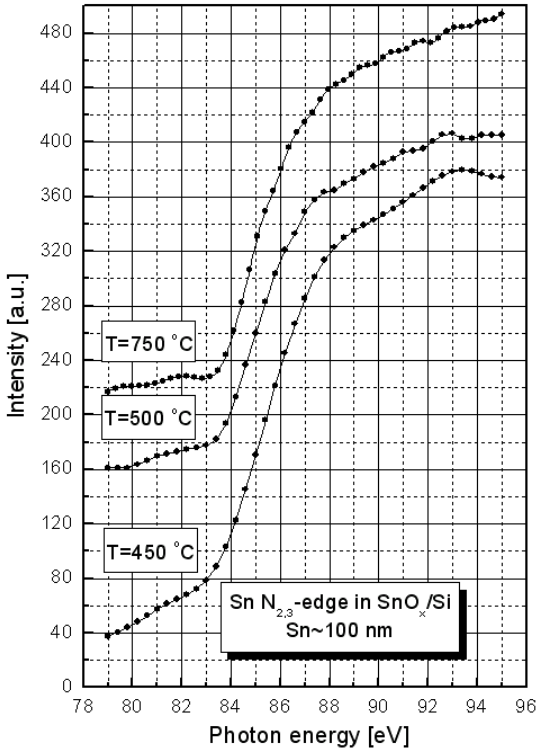

Figure 1 XANES $N_{2,3}$-spectra of tin in SnO_x/Si nanostructures obtained at different temperatures of anneal. Thickness of films – 100 nm.

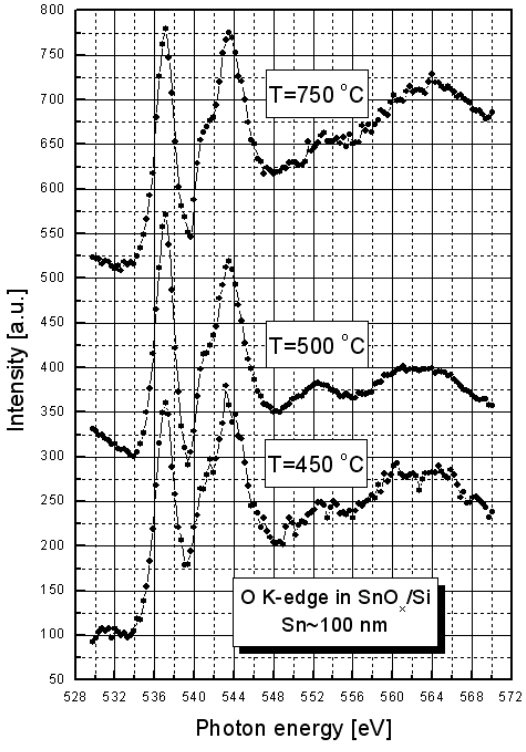

Figure 2 XANES O K_α-spectra of oxygen in SnO_x/Si nanostructures obtained at different temperatures of anneal. Thickness of films – 100 nm.

$N_{2,3}$-spectra of tin in SnO_x/Si nanostructures annealed at different temperatures in the range 450 °C – 750 °C are presented in Fig. 1. However, these spectra proved to be rather tailed without any distinct spectral features since they are strongly diffused due to very broad core levels N_3 and N_2 [1] as well as due to a high probability of electron Auger transitions between these levels.

O K_α-spectra XANES of the same nanostructures are given in Fig. 2. It is known that the these spectra represents distribution of non-occupied electron states of oxygen in conduction band. Analysis of oxygen XANES spectra demonstrates that all of them, have similar structure with a clearly expressed single peak at the energy of 536.9 eV and the second three-component peak with the energy of the largest peak in this group equal to 543.7 eV. The most distinct feature for the second peak is the left "shoulder" with the energy of approximately 540.7 eV. Next, following these two main peaks two more or less spectral features can be observed at the energies of 552 eV and 562 eV. Similar spectra were obtained for the films with a thickness of 300 nm presented in Fig.3.

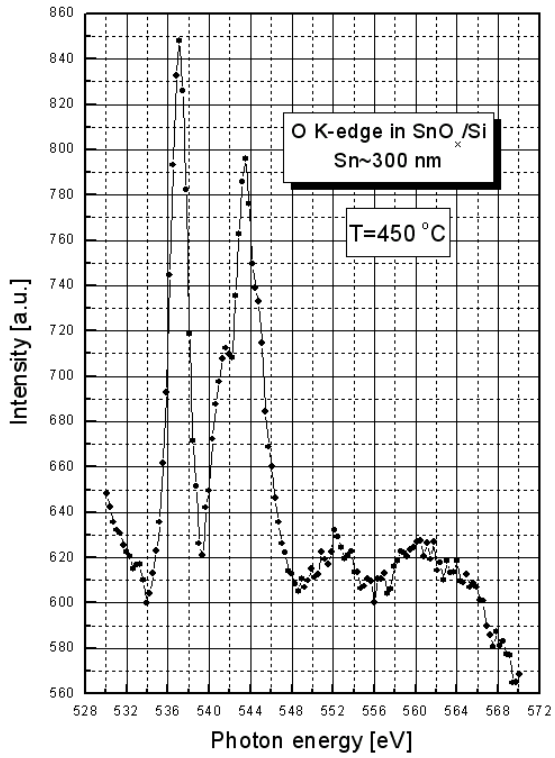

Figure 3 XANES O K_α-spectra of oxygen in SnO_x/Si nanostructure. Thickness of the film – 300 nm.

The presence of intensive narrow peak in the spectra of oxygen near X-ray absorption edge is obviously due to the presence of anti-bonding π^* orbital of oxygen in SnO_2 compound. Similar maximum was observed in [2] for lead dioxide, which is a crystallo-chemical analogue of tin dioxide and it can be connected with the bridge-type oxygen atoms in these compounds. On the other hand, according to the data of [3], conduction band bottom in SnO_2 can be formed with 5s-states of tin, therefore, the second peak in X-ray absorption spectra of oxygen can be due to the formation of hybrid non-occupied orbitals of Sn s^* and O p^* type.

Thus, oxygen X-ray absorption spectra indicate at the fact that the surface layer of SnO_x/Si nanostructures includes the phase of the higher tin oxide SnO_2 independent on the temperature of anneal in the range of 450 – 750 °C and thickness of the films.

[1] Masahide Ohno, Grant A. van Riessen. Journal of Electron Spectroscopy and Related Phenomena, v. 128 (2003), p. 1 - 31

[2] M. Uda, T. Yamamoto, H. Osawa, T. Tatebayashi, A. Kanai, H. Wakita, K. Taniguchi, J.H. Underwood, R.C.C. Perera. Advanced Light Source, Compendium of User Abstracts and Technical Reports, 1997. P. 79-81 (1997).

[3] Jean-Marc Themlin, Mohammed Chtaib, Luc Henrard, Philippe Lambin, Jacques Darville, Jean-Marie Gilles. Phys. Rev. B46, N 4, (1992), p. 2460-2466.

Interfacial interactions in iron/vanadiumoxide bilayers studied by x-ray absorption spectroscopy

B. Sass, S. Buschhorn, and W. Felsch
I. Physikalisches Institut, Universität Göttingen,
Friedrich-Hund-Platz 1, D-37077 Göttingen

V_2O_3 is a highly correlated oxide with a complex phase diagram [1]. In bulk stoichiometric form, for example, it undergoes a first order transition from a paramagnetic metallic (PM) to an antiferromagnetic insulating (AFI) phase at $T_{MI} = T_N \approx 150$ K. The lattice symmetry transforms from rhombohedral to monoclinic. Thin films of Fe deposited on single crystalline layers of V_2O_3 with different orientations (epitaxially grown on sapphire [2]) show a remarkable difference in their macroscopic magnetic behavior: the hysteresis loops are exchange biased on V_2O_3(0001) in the AFI phase of the oxide but not on V_2O_3(11-20). First results of X-ray magnetic circular dichroism (XMCD) obtained at LURE in Orsay indicated that this might be related to a magnetically 'dead' interfacial layer of Fe on the latter surface [3]. We have used X-ray absorption spectroscopy (XAS) together with measurements of XMCD at the undulator beamline UE46-PGM of BESSY on both bilayer systems Fe/V_2O_3(11-20) and Fe/V_2O_3(0001) to further explore the impact of the interfacial interaction effects (hybridization, exchange, oxidation of Fe) on the electronic structure and local magnetic properties of the constituent elements.

XMCD spectra were recorded by total electron yield (TEY) detection at room temperature and 120 K at the Fe-$L_{2,3}$ edges of ultrathin Fe layers. They were deposited, with thickness between nominally 2 and 12 monolayers (ML), in situ on the previously ion-etched and annealed V_2O_3 surface. The results are: (i) Ferromagnetic long-range order in Fe on V_2O_3(0001) appears only above 3 ML(Fig. 1). This is consistent with an island-like growth mode. (ii) The previous results for the V_2O_3(11-20) surface are confirmed: the first ML of Fe is magnetically dead. Further Fe growth proceeds layer by layer with the bulk-like magnetic moment of the bcc phase on top of the dead layer. (iii) The formation of iron oxide at interfaces can be excluded.

Due to the high energy resolution of the spectrometer and the high polarization rate of the beam linear dichroism known for bulk V_2O_3 single crystals [4] could be confirmed for the bare oxide layers by angular dependent XA measurements. This is a nice result and confirms their high quality. The Fe overlayers on both surfaces induce the insulating phase (PI) of V_2O_3 at the interface. For both bilayers systems Fe(8ML)/V_2O_3(11-20) and Fe(8ML/V_2O_3(0001), XMCD signals of ~0.5% at the V-$L_{2,3}$

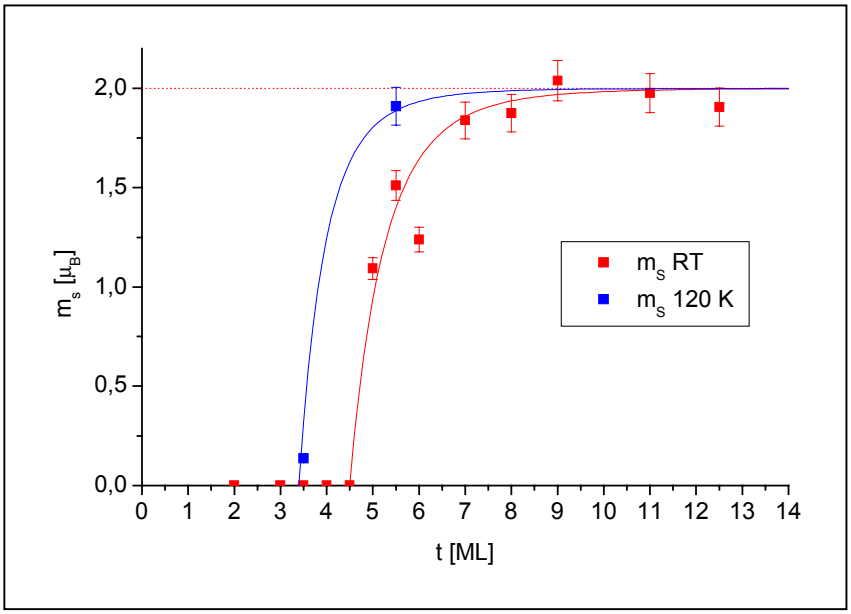

Fig. 1: Average magnetic spin moment per Fe atom, m_S, of ultrathin Fe layers on V_2O_3(0001) as a function of coverage t at room temperature (red squares) and 120 K (blue squares). The solid curves are guides to the eye. Dotted horizatal line: value of the spin moment of bulk bcc Fe.

and O-K edges were observed at room temperature (Fig. 2), indicating a small magnetic polarization of the V-3d and O-2p derived states at the interface induced by the

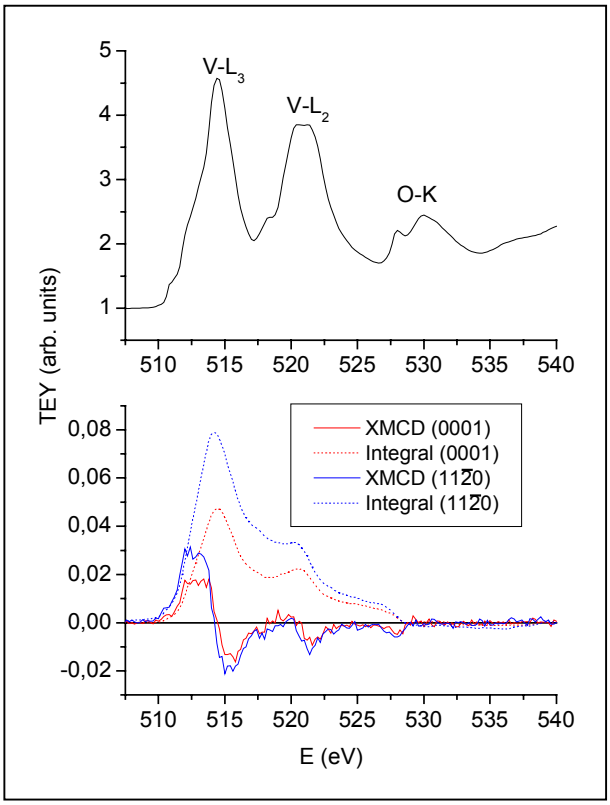

Fig. 2: XA spectrum (top) and XMCD signal (bottom, solid curves) at the V-$L_{2,3}$ and O-K edges of V_2O_3(0001) and V_2O_3(11-20) layers covered with 8 ML Fe, at room temperature. Dotted curves: integrated XMCD signals.

Fe overlayers. The V dichroism reveals a complex shape due to the small spin-orbit splitting of the initial 2p core levels. This precludes a simple application of the dichroism sum rules for deriving an estimate of the V magnetic moment. The dichroic signal of V reveals an opposite onset in sign as that compared to that of Fe, suggesting an antiparallel orientation of the V and Fe magnetic moments. Unfortunately, cryogenic limitations at the beamline did not permit to persue the evolution of these spectra to low temperature into the AFI phase of V_2O_3. This important point remains to be investigated.

To conclude, the XAS and XMCD experiments reveal a strong electronic interaction at the interface of Fe/V_2O_3 bilayers; it is very different for the two surfaces of the oxide. For an explanation theoretical support is mandatory. This is a difficult task in view of the challenge inherent to the theory dealing with the pure oxide itself [5].

We are indebted to the crew of beamline UE46-PGM for technical support. Funding was provided by the Deutsche Forschungsgemeinschaft within SFB 602 TPA1.

References

[1] M. Imada *et al*., Rev. Mod. Phys. **70**, 1039 (1998).
[2] B. Sass *et al.*, J. Phys.: Condens. Matter **16**, 77 (2004).
[3] B. Sass *et al.*, Phys. Rev B **71**, 014415 (2005).
[4] J.H. Park *et al*., Phys. Rev. B **61**, 11506 (2000).
[5] see, e.g., K. Held *et al.*, Phys. Rev. Lett. **86**, 5345 (2002).

Optical properties of DyS and DyAs

A. Navratil, U. Barkow, M. Marutzky, D, Menzel, H. Schröter, S. Weber, and J. Schoenes

Institut für Physik der Kondensierten Materie, formerly Institut für Halbleiterphysik und Optik, TU Braunschweig, Mendelssohnstr. 3, D-38106 Braunschweig, www.iho.tu-bs.de

Ellipsometric spectroscopy has various advantages in comparison to many other forms of optical spectroscopy. It provides simultaneous the real and the imaginary part of the optical functions without requiring a Kramers-Kronig-Transformation which is necessary when only the reflectivity is measured. Data obtained from ellipsometric investigations do not depend on surface properties as much as simple reflectivity measurements because the polarisation state of the reflected light is detected and not the intensity.
Quantitative information about the effective electron mass or electronic transitions, for example, can be extracted from the complex optical functions. So optical spectroscopy is a powerfull instrument to examine the electronic structure of solids, and whereas the optical data of LaS, CeS, NdS, SmS, GdS and TmS are known, the optical properties of DyS have not been investigated to our knowledge. The monopnictides of trivalent rare earths are semimetallic and the additional electron in the monochalcogenides modifies the chemical bonds, the crystal fields, the magnetic interactions and transforms the compound in a colored metal. So, the optical constants of DyAs were determined, additionally.
Both the monopnictides and the chalcogenides of the lanthanides and the actinides crystallize in rocksalt structure. DyS orders antiferromagnetically at $T_N = 40$ K, DyAs orders at $T_N = 8.5$ K in a HoP type structure. DyS executes a remarkable transition from cubic symmetry to a pseudo-tetragonal distorted NaCl structure while going from the paramagnetic into the antiferromagnetic state [1].

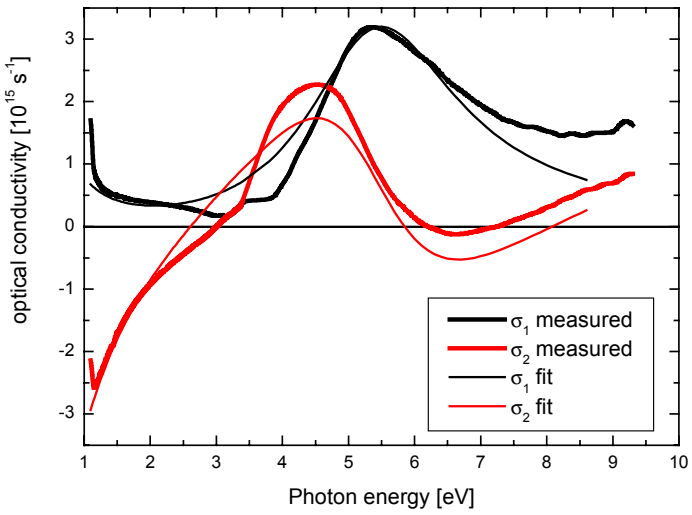

Fig. 1: Optical conductivity of DyS, as measured and a fit with a Drude Lorenz model

For energies between 1 and 4.5 eV the ellipsometric measurements where performed with our home-made spectrometer in Braunschweig. The measurements for higher energies were collected at the VUV-ellipsometer at BESSY II in Berlin. Fig. 1 shows the optical

conductivity for DyS. Whereas the imaginary part σ_2 is the dispersive part, the real part σ_1 is the absorptive part of the optical conductivity which must always be positive. The slope of the spectrum in Fig. 1 from 3 eV to lower energies is according to the Drude-theory the contribution of the free electrons and typicall for metals. This is also seen in Fig. 2 where the reflectivity is presented. For small energies the reflectivity is high, reaching nearly 100 % at the lowest energies. At the screened plasma frequency at 3.2 eV where σ_2 changes its sign with positive slope the reflectivity reaches a minimum (5 %). The drop in reflectivity in the blue part and near UV part of the electromagnetic spectrum causes the golden colour of the DyS crystal.

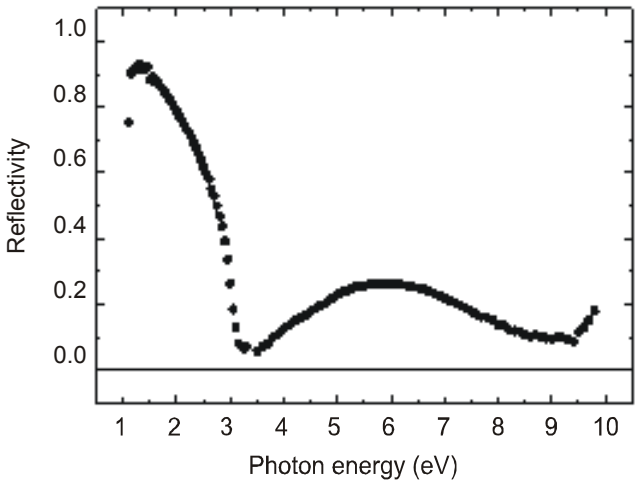

Fig. 2: Reflectivity of DyS obtained from ellipsometric spectroscopy

The large structure between 5 and 6 eV in σ_1 can be identified with *p-d* transitions. Because the structure is very broad, no crystal field effects can be resolved. These results are similar to other trivalent rare earth monochalcogenides. Supplementary to this qualitative discusion we have performed a quantitative analysis by fitting the spectra with a Drude Lorentz model (Fig. 1):

$$\sigma_1 = \sum_j \omega \varepsilon_0 f_j \omega_P^2 \frac{\omega \gamma_j}{\left(\omega_j^2 - \omega^2\right) + \omega^2 \gamma_j^2}$$

$$\sigma_2 = \omega \varepsilon_0 \varepsilon_{\text{opt}} + \sum_j \varepsilon_0 f_j \omega_P^2 \frac{\omega\left(\omega_j^2 - \omega^2\right)}{\left(\omega_j^2 - \omega^2\right) + \omega^2 \gamma_j^2}$$

Here $\omega_P = \sqrt{Ne^2 / \varepsilon_0 m^*}$, m^* is the effective electron mass, N is the number of electrons per unit cell which can contribute to optical transitions, ω_j is the excitation frequency, f_j is the phenomelogical oscillator strength, γ_j the damping constant of the jth oscillator and ε_{opt} takes into account excitations at higher energies. For the fit a Drude oscillator with $\omega_0 = 0$ and a Lorentz oscillator ω_1 representing the free electrons and the *p-d* transition, respectively, are assumed. The results are collected in Table 1. The deviations from the measurement suggest further optical transitions which should be taken into account, especially at energies above 10 eV where no experimental data are available.

ω_P [eV]	f_0	γ_0 [eV]	ω_1 [eV]	f_1 [eV]	γ_1 [eV]	ε_{opt}
2.25	6.55	1.99	5.5	14.5	2.8	1.99

Table 1.: Drude Lorentz fit of the measurement in Fig.1

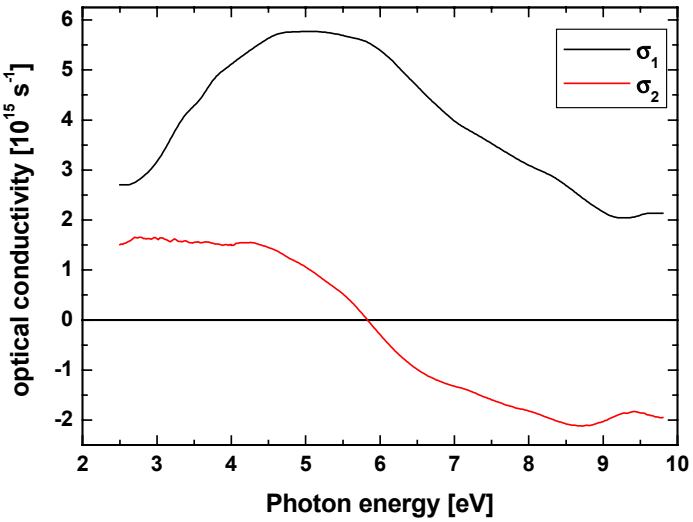

Fig. 3: Optical conductivity of DyAs

In Fig. 3 the optical conductivity of DyAs is shown. The real part σ_1 exhibits a huge structure around 5 eV. The position of this maximum and the magnitude of σ_1 is in good agreement with theoretic calculations [2]. Furthermore shoulders at 8.5 and 7.5 eV can be noticed. Whereas the energy dependence of optical conductivity of DyS below 3 eV is dominated by free electron contributions, that of DyAs is not which shows its semimetallic behaviour.
We have determined the optical properties of DyS and DyAs between 1 and 10 eV. These results are completed by magneto-optical investigations [3].

Acknowledgments

We would like to tank the research group of Dr. N. Esser for the possibility to use the VUV ellipsometer and the BESSY company for beam time and BMBF for financial support (Förderkennzeichen 05 ES3XBA/5).

[1] F. Hulliger, M. Landolt, and R. Schmelcer *The Rare Earths in Modern Science and Technology,* Vol. 3, eds. McCarthy, Silber and Rhyne, Plenum (1982), p. 455
[2] J. Schoenes, P. Repond, F. Hulliger, D.B. Ghosh, S.K. De, J. Kuneš, and P.M. Oppeneer, Phys. Rev. B **68** (2003), 085102
[3] A. Navratil, diploma thesis

X-ray absorption spectroscopy on layered cobaltates

T. Kroll[1], J. Geck[1], C. Hess[1], T. Schwieger[1], G. Krabbes[1], C. Sekar[1], D. Batchelor[2], M. Knupfer[1], J. Fink[1], and B. Büchner[1]

[1]Leibniz Institut für Festkörper- und Werkstoffforschung Dresden, P.O. Box 270016, 01171 Dresden, Germany
[2]BESSY, 12489 Berlin, Germany

Introduction:

The recent discovery of superconductivity in $Na_{0.35}CoO_2*1.3H_2O$ with a critical temperature T_c=5 Kelvin [1] has attracted much attention because it might exhibit unconventional superconductivity with a triplet pairing state. Similar to the doped cuprates the sodium cobaltates display a layered structure containing CoO_2-sheets. However, these layers consist of edge sharing CoO_6-octrahedra where, in contrast to the cuprates, the Co atoms form a triangular (hexagonal) lattice rather than a square lattice. The trigonal coordination of the Co-site results in geometric frustration that favours unconventional electronic ground states. The geometrically frustrated CoO_2-sublattice also exists in the non-hydrated parent compounds Na_xCoO_2, which have been examined in the near edge x-ray absorption fine structure (NEXAFS) study at hand. Also these materials caused high interest, due to their unusually high thermopower and an intriguing coexistence of Curie magnetism and itinerancy [2].

Experimental details:

Using NEXAFS one can probe the unoccupied energy levels close to the Fermi surface. The absorption has been measured via the drain current as the total electron yield. All measurements have been performed at the UE52-PGM beamline at BESSY, Berlin, providing an energy resolution of about 100 meV at the requested energies. We performed measurements on different single crystals with various sodium contents. All crystals were grown using the travelling solvent floating zone method, all of them of the same size of about 3x3 mm area and 1mm thickness. After cleaving the samples in-situ clean and shiny surfaces have been obtained. For the temperature dependent measurements between 25 and 372 Kelvin a Janis cryostat has been used.

Results:

In order to examine the electronic structure of Na_xCoO_2, samples with different sodium contents have been investigated at various temperatures. The NEXAFS spectra at the oxygen K-, cobalt $L_{2,3}$-, and sodium K-edge have been measured with the polarization of the incident beam perpendicular and parallel to the CoO_2-layers. A most important aspect concerning the measurements on Na_xCoO_2 is the sample treatment. The sample surface is very sensitive to any pollution and the samples have to be cleaved and to be measured in a pressure of around $2*10^{-10}$ mbar or less. Bad pressures and contaminated surfaces immediately result in pronounced spectral weight changes. In order to investigate this behaviour in more detail a $Na_{0.7+\varepsilon}CoO_2$ sample has been cooled down to 25 Kelvin and cleaved in-situ at a pressure of $2*10^{-10}$ mbar. With increasing temperature nothing changes at the oxygen K-edge as long as the pressure remains good. However, between 150 Kelvin and 300 Kelvin the pressure increases by one order of magnitude due to desorption from the cryostat, resulting in pronounced spectral weight changes. This behaviour is irreversible upon cooling down to 25 K again. A comparison to the temperature dependent behaviour of the Co $L_{2,3}$-edge proofs that the origin of this irreversible effect is due to surface contamination and not due to a change or a transition of the whole sample, since the Co $L_{2,3}$-edge remains unchanged with temperature (c.f. Fig.1 (c)). The spin state of the system is a low spin state, in agreement with the results reported by Wu *et al.* [3]. At the oxygen K-edge, core hole effects do not influence the NEXAFS results significantly, i.e. a direct interpretation of the results in terms of the unoccupied density of states is possible.

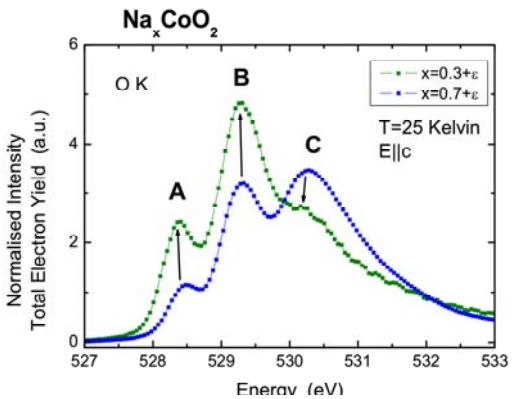

(a)

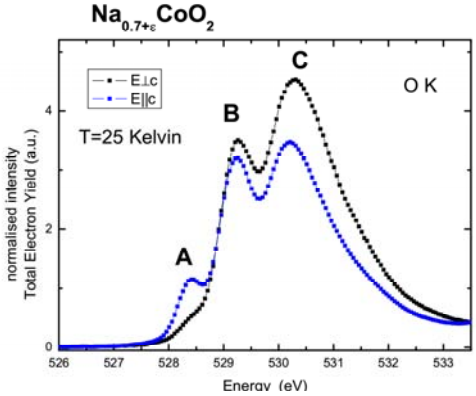

(b)

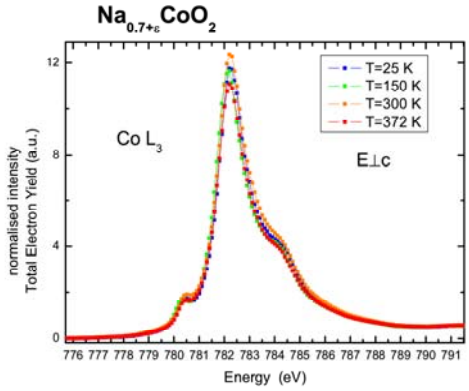

(c)

Fig.1: NEXAS measurements on Na_xCoO_2 (x=0.3,0.7). (a): Doping dependence of the O K-edge at 25 K. (b): Polarization dependence of the O K-edge at 25 K. (c): Temperature dependence of the Co L_3-edge for x=0.7.

For both stoichiometries x=0.3 and x=0.7, we observed three pronounced O 1s peaks, implying a strong hybridisation between O 2p and Co 3d ions. Referring to formal valences, the ratio between Co^{3+}- and Co^{4+}-ions increases with increasing sodium content x. As shown by the data given in Figure 1(a), the first two peaks A and B increase in intensity, while peak C decreases upon decreasing x. According to the local picture of Co^{3+}- and Co^{4+}-ions the two peaks A and B are related to transitions into unoccupied a_{1g}- and e_g^{σ}-levels of Co^{4+}, whereas peak C corresponds to transitions into e_g^{σ}-levels of Co^{4+}. Note, that the a_{1g}-level of Co^{3+} is filled.

From polarisation dependent measurements information about the orientation of the corresponding orbitals is obtained. The a_{1g} orbital in a trigonal symmetry can be written as $a_{1g}= 1/\sqrt{3}\ (d_{xy}+d_{yz}+d_{zx})$. This state points along the (1 1 1) direction of the distorted octahedra, i.e. parallel to the crystal c-axis. This is consistent with our data (Fig.1(b)): the first peak (denoted as A in Fig.1(a) and (b)) is strong for E||c, while it is almost gone for E⊥c. Thus, the low energy excitations have predominantly a_{1g} symmetry. In addition, the doping dependence of both the O K-edge and the Co L-edge reveals that the holes are located to a substantial amount at the oxygen sites. One also observes a polarisation dependence for the excitations into the e_g^{σ} orbitals, which can be explained by the distortion of the octahedra.

Previously, it was suggested that a spin state transition takes place at 280 Kelvin (c.f. [4]), which has been discussed in terms of charge ordering and formation of magnetopolarons due to a charge-induced spin-state transition of adjacent Co^{3+} ions. In contrast to this, no temperature dependence neither for $Na_{0.3+\varepsilon}CoO_2$ nor for $Na_{0.7+\varepsilon}CoO_2$ has been found between 25 Kelvin and 370 Kelvin in the present NEXAFS studies. This implies that the spin-state of Co as well as the electronic structure in this energy range is not affected by temperature (Figure 1 (c)).

Bibliography:

[1] K. Takada *et al.*, Nature **422**, 53 (2003)
[2] Terakasi *et al.*, Phys. Rev. B **69**, 180508 (2004)
[3] W.B. Wu *et al.*, cond-mat/0408467 (2004)
[4] C. Bernhard *et al.*, Phys. Rev. Lett. **93**, 1670023 (2004)

Hole localization and phase separation in cobaltites Li_xCoO_2: X-ray absorption and photoelectron study

V. R. Galakhov[1]*, A. S. Shkvarin[1], S. N. Shamin[1], K. Kuepper[2], A. F. Takács[2], M. Raekers[2], S. Robin[2], M. Neumann[2], G.-N. Gavrilă[3], A. S. Semenova[4], and D. G. Kellerman[4]

[1] *Institute of Metal Physics, Russian Academy of Sciences — Ural Division, 620219 Yekaterinburg GSP-170, Russia*
[2] *Universität Osnabrück — Fachbereich Physik, D-49069 Osnabrück, Germany*
[3] *Technische Universität Chemnitz — Institut für Physik, D-09107 Chemnitz, Germany*
[4] *Institute of Solid State Chemistry, Russian Academy of Sciences — Ural Division, 620219 Yekaterinburg GSP-145, Russia*

Oxides Li_xCoO have served as cathode materials for Li batteries [1]. $LiCoO_2$ is a semiconductor with the band gap of 2.7 eV [2] while Li_xCoO_2 at concentrations below $x = 0.75$ is metallic [3], implying that a metal-insulator transition occurs at intermediate Li concentrations. Defect cobaltites Li_xCoO_2 can be expected to contain both Co^{3+} and Co^{4+} ions. On the base of the study of Co $2p$ and O $1s$ X-ray absorption spectra of Li_xCoO_2 defect oxides Montoro *et al.* [4] have concluded that the trivalent Co ions remain unaffected by Li de-intercalation, i.e. in Li_xCoO_2 oxides, doped holes are localized in O $2p$ states. The Co ions in defect cobaltites can be regarded as being in the d^6 configuration, as it was shown by the Co $2p$ X-ray measurements of $NaCo_2O_4$ [5]. On the other hand side, Yoon *et al.* [6] have proposed that the charge compensation for the electron exchange in the Li-ion de-intercalated process could be achieved in both the oxygen sites and cobalt sites simultaneously.

A single-phase, homogeneous sample of $LiCoO_2$ was prepared by sintering a mixture of Co_3O_4 and Li_2CO_3. The synthesis was carried aut in air at a temperature of 700 °C for 20 h and after that at a temperature of 850 °C for 25 h, following by slow cooling. Samples of the Li_xCoO_2 ($x = 0.60$ – 0.96) oxides were obtained by chemical de-intercalation in 0.7 N H_2SO_4. A de-intercalation time of $\tau = 20$ min corresponds to the oxide with $x = 0.96$, and $\tau = 1.5$ h corresponds to $x = 0.6$. Li concentrations were estimated by means of atom-absorption analysis. The phase composition was checked by X-ray diffraction analysis. The core-level and valence-band X-ray photoelectron spectra

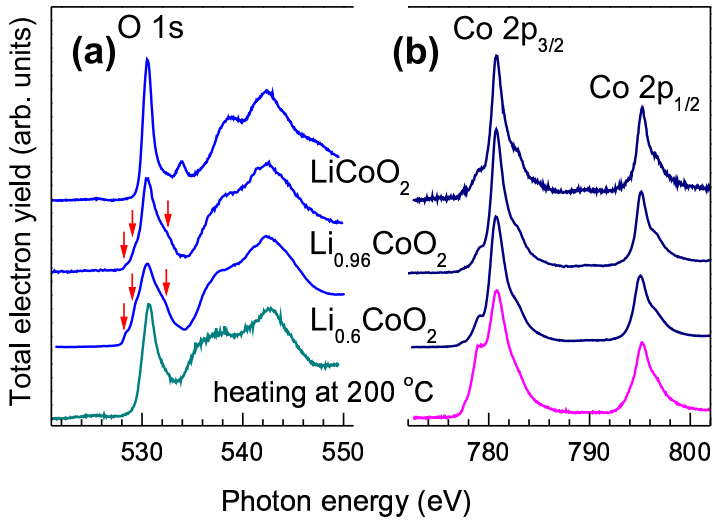

Figure 1: O $1s$ (a) and Co $2p$ (b) X-ray absorption spectra of Li_xCoO_2. The spectra labelled with 200 °C have been measured on the $Li_{0.6}CoO_2$ sample which has been heated at 200 °C for about 20 h.

*e-mail: galakhov@ifmlrs.uran.ru

of the Li_xCoO_2 oxides were obtained with a PHI 5600 CI Multitechnique System XPS spectrometer using monochromatized Al $K\alpha$ radiation. The Co $2p$ and O $1s$ X-ray absorption spectra (XAS) and valence-band photoelectron spectra (VB PS) excited at 150 and 200 eV were measured at BESSY II, at the Russian-German Beam Line.

The electric dipole-allowed $1s \rightarrow 2p$ transition of oxygen $1s$ X-ray absorption spectra provides direct information of the oxygen charge state and Co–O bonding interaction, since the $2p$ orbitals of oxygen ligand are involved in bonding configuration with Co metal ions (see Fig. 1 (a)). The sharp peak at 530.5 eV corresponds to the transition of oxygen $1s$ electrons to the hybridized state of Co $3d$ (e_g^*) and oxygen $2p\sigma$ orbitals whereas the broad bumps at energies of 538 eV and 542–544 eV reveal O $2p$ states mixed in the Co $4sp$ bands. The small feature at 534 eV in the spectrum of $LiCoO_2$ is formed by Li_2CO_3 contaminations.

As an alkali ion removed from $LiCoO_2$, the O $1s$ XAS spectra of the deintercalated Li_xCoO_2 compounds show significant changes: the spectra are broadened and three extra features are appeared (marked by lines). In alkali-ion de-intercalated cobaltites, an extra electron holes should be created in the upper t_{2g} valence band. For formally Co^{4+} ions the trigonal field splits the three t_{2g} orbitals into a a_{1g} orbital (with one electron) and two e_g' orbitals (with four electrons). The band structure calculations of the similar compound $NaCo_2O_4$ predict electronic holes introduced by alkali defects have mainly a_{1g} character [7]. Therefore, the features below the threshold in the O $1s$ X-ray absorption spectra of defect cobaltites are formed by hybridized Co a_{1g}–O $2p\pi$ states. These spectral features indicate additional unocuppied O $2p$ states.

Lithium de-intercalation does not change Co $2p_{3/2,1/2}$ X-ray absorption spectra. This means that cobalt ions remain in Co^{3+} state and electronic holes in defect Li_xCoO_2 cobaltites are mainly of the O $2p$ character. Heating in vacuum at 200 °C for about 20 h of defect cobaltites leads to dramatic change of X-ray absorption spectra. One can suggest degradation of these compounds due to the appearance of Co^{3+} and also some Co^{2+} ions as a result of transition of Li_xCoO_2 into $LiCoO_2$ with Co_3O_4 admixtures.

Figure 2 presents valence band photoelectron (VB PS) and O $1s$ X-ray absorption (XAS) spectra of $LiCoO_2$, $Li_{0.96}CoO_2$, and $Li_{0.6}CoO_2$. The XAS spectra have been brought to a common energy scale based on the O $1s$ binding energies obtained from our X-ray photoelectron experiment. The photoelectron spectrum of $LiCoO_2$ and O $1s$ X-ray absorption spectra of Li_xCoO_2 are deconvoluted.

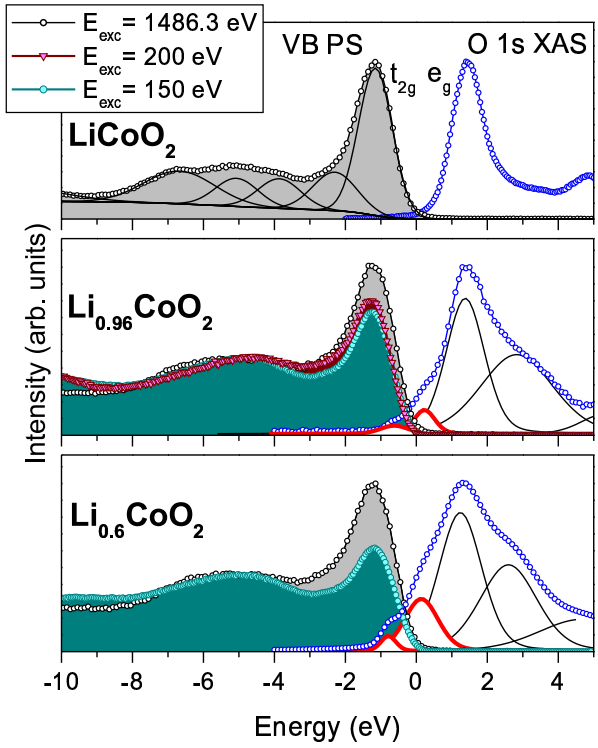

Figure 2: Valence-band photoelectron (VB PS) and O $1s$ X-ray absorption (XAS) spectra of Li_xCoO_2. The valence-band photoelectron spectra are measured at excitation energies of 1486.3, 200, and 150 eV. Shaded areas show occupied states determined from the valence-band photoelectron spectra.

Although the defect cobaltites Li_xCoO_2 are expected to be hole doped, the Co t_{2g} peak remains sharp. Therefore, one can suggest that the Co^{3+} state remains in the low-spin t_{2g} configuration and that the spectral weight near the Fermi level is dominated by the t_{2g} states.

A combination of the VB PS and O $1s$ XAS spectra shown in Fig. 2 yields clearly the band gap for $LiCoO_2$ and demonstrates metallic properties of de-intercalated cobaltites. The distance between t_{2g} and e_g peaks for $LiCoO_2$ is about 2.6 ± 0.2 eV that corresponds to the band gap

determined in Ref. [2] by a combination of X-ray photoelectron and bremsstrahlung isochromat spectra. For defect cobaltites Li_xCoO_2, the distance between the t_{2g} peak and the first feature (red curve) is about 0.5 ± 0.2 eV. One can suggest that these levels are overlapped. It is an evidence of metallic properties of de-intercalated oxides. Complex impedance measurements [3] show that Li_xCoO_2 becomes an electronic conductor for $x \leq 0.9$. According to the results presented in Fig. 2, the $Li_{0.96}CoO_2$ compound should be a metal. To our opinion, this discrepancy may be explained suggesting a so-called *phase separation effect*. A similar effect has been found in manganites [8]. A lithium de-intercalation leads to the appearance of small metallic islands with small Li concentrations surrounded by the insulating host material. The decrease in Li-content leads to the increase of sizes and the quantity of these islands, their overlapping and, as a result, to the appearance of metallic properties of the Li-deintercalated cobaltites.

In conclusion, we have studied the change in the electronic structure of defect oxides Li_xCoO_2 ($x = 0.6$, 0.96, and 1.0) by means of photoelectron and X-ray absorption spectroscopy. It was established that in defect cobaltites, electronic holes are localized mainly in O $2p$ states. Metallic character of defect cobaltites Li_xCoO_2 is confirmed by combination of X-ray photoelectron and O $1s$ X-ray absorption spectral measurements. An evidence of the phase-separation effect in defect cobaltites was found.

This work was supported by the Russian Foundation for Basic Research (Grant No 04-03-96092-Ural). One of the authors (V. R. G.) gratefully acknowledges fellowship support from the Deutscher Akademischer Austauschdienst (DAAD) Program. K. K. and A. F. T. acknowledge financial support by the Ph.D. program of Lower Saxony, Germany. The authors would like to thank D. V. Vyalikh, Yu. Dedkov, and M. Sperling for technical supports at BESSY.

---

[1] K. Mizushima, P. C. Jones, P. J. Wiseman, and J. B. Goodenough, Mater. Res. Bull. **15**, 783 (1980).

[2] J. van Elp, J. L. Wieland, H. Eskes, P. Kuiper, G. A. Sawatzky, F. M. F. de Groot, and T. S. Turner, Phys. Rev. B **44**, 6090 (1991).

[3] J. Molenda, A. Stoklosa, and T. Bak, Solid State Ionics **36**, 53 (1989).

[4] L. A. Montoro, M. Abbate, and J. M. Rosolen, Electrochem. Solid-State Letter **3**, 410 (2000).

[5] T. Matsushita, M. Mizumaki, N. Ikeda, M. Nakazawa, A. Agui, Y. Saitoh, T. Nakatani, A. Yoshigoe, and S. Nakamura, Surf. Rev. Letters **9**, 1327 (2002).

[6] W.-S. Yoon, K.-B. Kim, M.-G. Kim, M.-K. Lee, H.-J. Shin, and J.-M. Lee, J. Electrochem. Society **149**, A1305 (2002); W.-S. Yoon, K.-B. Kim, M.-G. Kim, M.-K. Lee, H.-J. Shin, J.-M. Lee and C.-H. Yo, J. Phys. Chem. B **106**, 2526 (2002).

[7] D. J. Singh, Phys. Rev. B **61**, 13397 (2000).

[8] J. M. De Teresa, M. R. Ibarra, P. A. Algarabel, C. Ritter, C. Marquina, J. Blasco, J. Garcia, A. Del Moral, and Z. Arnold, Nature (London) **386**, 256 (1997)

The hole density of Bi2201 superconductors determined by XAS at the Cu-L_3 edge.

L.Lasogga, R.Mitdank, A.Krapf, H.Dwelk, C.Janowitz and R.Manzke
Humboldt University Berlin, Department of Physics, Newtonstrasse 15, 12489 Berlin, Germany
A.Wojciechowski
Jagiellonian University, Institute of Physics, ul. Reymonta 4, 30-059 Krakow, Poland

1 Introduction.

Since the discovery of the High-T_c-superconductivity of the bismut cuprates great efforts are made to understand the mechanism. We know, that this mechanism is due to holes in the CuO_2 planes. Therefore it is essential to investigate these holes and their dependence on oxygen-content and substitution with other elements of different valence. In our case we studied the hole density by using x-ray absorption spectroscopy in the system $Bi_2Sr_{2-x}La_xCuO_{6+\delta}$ with series of variable content of lanthanum (x=0,1 ... 0,74). These investigations include both ceramics and single crystals.

2 Sample Preparation.

The change into the diamagnetic state with a suszeptibility of minus one is charakteristic for superconductivity. The temperature gradient of the phase transition from normal conductivity to superconductivity is a direct measure of the sample quality and indicates phase purity. By annealing the samples in vacuum or oxygen it is possible to get sharp transitions and optimize the superconducting phase (max. $\Delta T = 5K$, corresponding to maximum *La*-concentration). In our experiment we only used samples with a sharp transition. The content of lanthanum was determined by EDX.

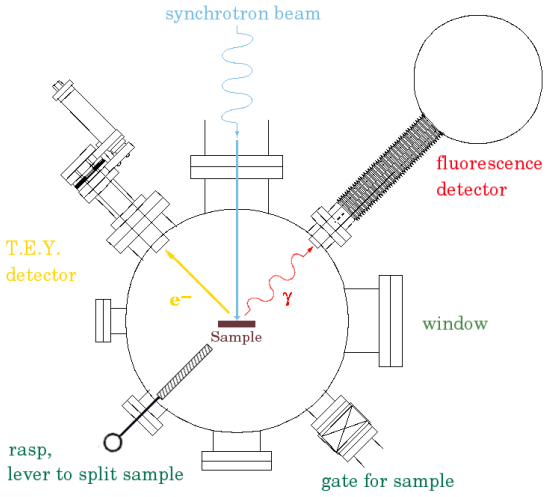

Figure 1: The fluorescence chamber.

3 Experimental Setup.

For our XAS experiments we used the BESSY fluorescence chamber as seen in figure 1. It consists of a fluorescence germanium detector and a total electron yield detector (T.E.Y.). The pressure in the chamber is about 10^{-9} mbar. The T.E.Y. measurements requires a clean surface. Therefore the surface of the ceramics is cleaned by a rasp. The single crystals were cleaved in the vacuum. The samples themselves are fixed on aluminium holders as seen in figure 2.

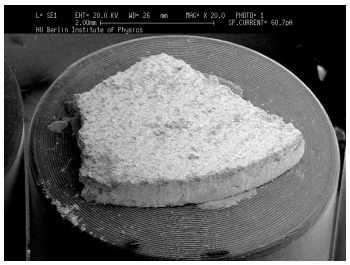

Figure 2: A ceramic sample on aluminium holder, seen in SEM.

4 Results.

The figures 3 and 4 below show the measured spectra at the Cu-L_3 edge in dependence on content of lanthanum.

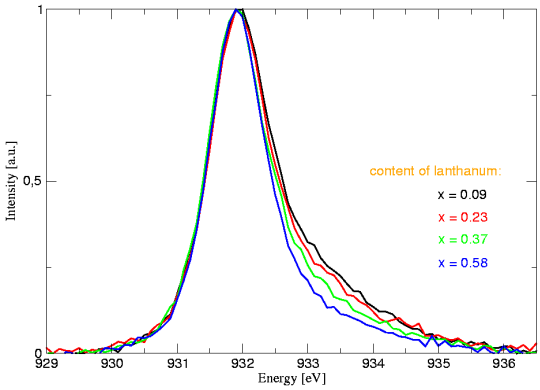

Figure 3: Measured spectra in ceramics.

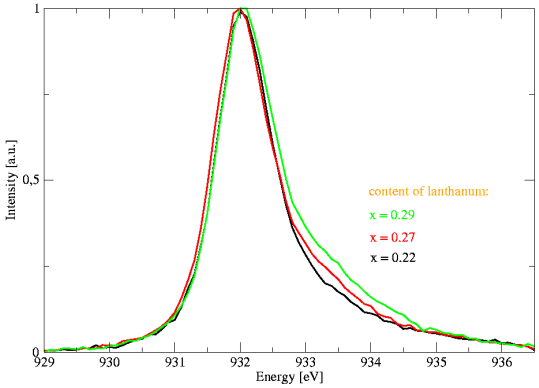

Figure 4: Measured spectra in single crystals.

In case of ceramics, the fit function for the measured spectra is a pseudo-voigt profil with three peaks, see figure 5. The intensity of the satellite peak decreases with increasing content of lanthanum, as it is shown in figure 6. Using [1, 2, 3], the density of holes can be calculated by the formula

$$n_h = \frac{I_{satellite}}{I_{satellite} + I_{whiteline}} \tag{1}$$

were $I_{satellite}$ denotes the intensity of the satellite peak and $I_{whiteline}$ denotes the intensity of the white line peak.

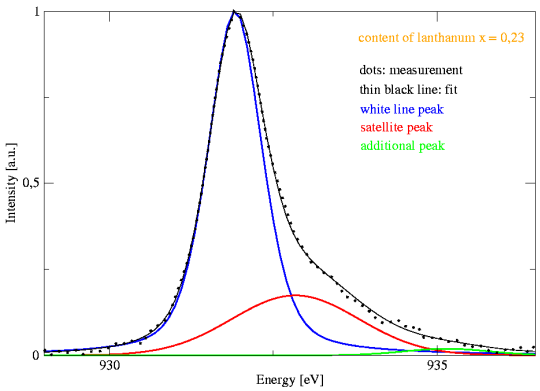

Figure 5: Example of a fit of a ceramic sample with x=0,23.

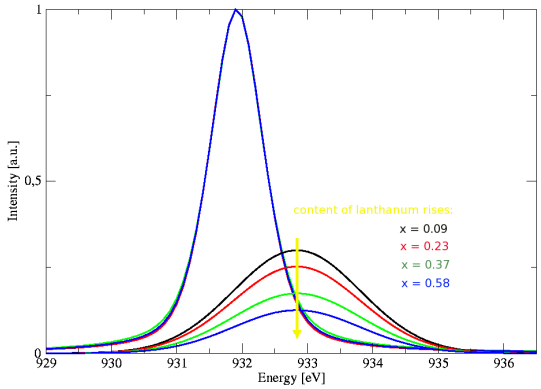

Figure 6: White line and satellite for different ceramic samples obtained by fitting.

Figure 7 shows the results based on the pseudo-voigt profil fit and the calculation [6] of the hole density by this equation.

As written above the satellite indicates the hole density in the CuO_2 planes. In the case of ceramics the shoulder gets smaller with rising content of lanthanum. In the case of single crystals the measured spectra refer to a maximum of the hole density at $x = 0{,}3$.

For ceramics the dependence between hole density and content of lanthanum is given by the equation

$$n_h = 0{,}26 - 0{,}27\,x \qquad (2)$$

Furthermore we get the dependence of the critical temperature on the hole density and on the content of lanthanum, figures 8 and 9. The critical temperature was determined by AC suszeptibility measurements (T_c onset). For purpose of comparation the results of [4] [5] are within the plot (dashed blue curve). For our work (the red function) we get the equations

$$\frac{T_c}{T_{c,max}} = 1 - 131\,(n_h - 0{,}17)^2 \qquad (3)$$

$$= 1 - 131\,(0{,}09 - 0{,}27x)^2 \qquad (4)$$

with a $T_{c,max}$ of 18 K. So the optimum of the density of holes in ceramics is

$$n_{h,opt} = 0{,}17 \pm 0{,}01$$

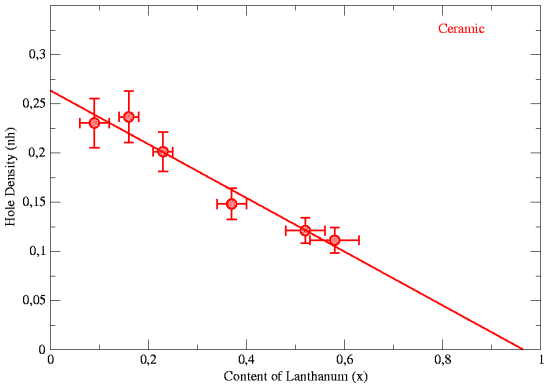

Figure 7: Dependence between content of lanthanum and hole density in case of ceramics.

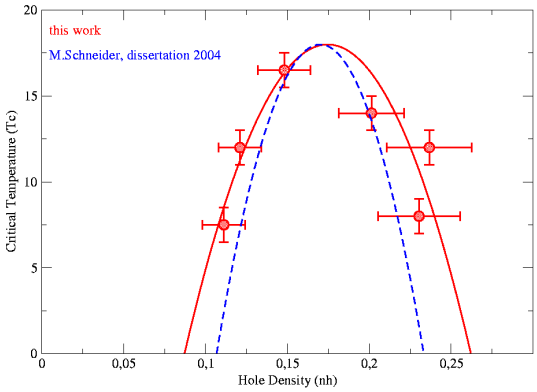

Figure 8: Dependence between critical temperature and density of holes.

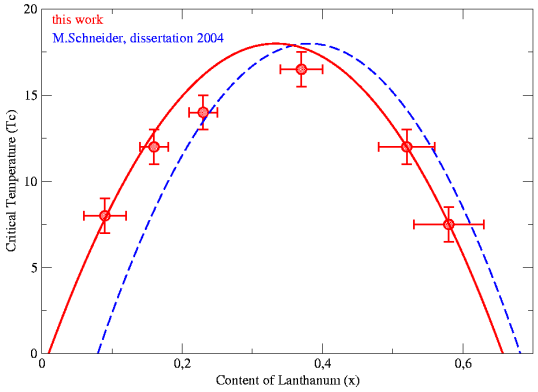

Figure 9: Dependence bewteen critical temperature and content of lanthanum.

By these detailed investigations it is now possible to relate the *La*-content directly to an absolute hole density in the CuO_2 planes.

5 Acknowledgment.

The authors thank Dr.T.Kachel from the BESSY Berlin GmbH for the support at the beamline PM3, Dr.S.Rogaschewski for performing EDX/SEM measurements.

References

[1] M.Ronay et al. *Solid State Comm. 77, 699 (1991)*

[2] A.Q.Pham et al. *Phys.Rev B 48, 1249 (1993)*

[3] N.L.Saini et al. *J.Phys.Soc.Japan 67, 393 (1995)*

[4] M.Schneider *dissertation 2004*

[5] M.Schneider, R.-St.Unger, R.Mitdank, A.Krapf, C.Janowitz, R.Manzke *Phys. Rev. B (2004)*, submitted

[6] ESRF *program xop/xplot 2004*

NEXAFS and XMCD of ultrathin Ni films grown with O surfactant

C. Sorg, N. Ponpandian, A. Scherz, M. Bernien, R. Nünthel,
T. Gleitsmann, K. Baberschke, and H. Wende

Institut für Experimentalphysik, Freie Universität Berlin,
Arnimallee 14, D-14195 Berlin-Dahlem, Germany.

Ultrathin ferromagnetic films on metallic substrates have become the subject of many investigations. One of the most famous systems in that field is Ni on the Cu(100) surface. Furthermore, it was shown that using surfactants during growth improves the structural properties of many different systems. Surfactants are adsorbed on the surface of the substrate prior to deposition of the film. They float on top of the deposited layers and thereby reduce the surface free energy. This has been studied for Ni on Cu(100) [1] and Cu(110) [2] with oxygen as the surfactant. Moreover, the spin reorientation transition (SRT) for Ni on Cu(100) is shifted to a lower Ni thickness due to a reduction of the magnetic surface anisotropy by the O surfactant [3, 4]. The magnetization of clean Ni/Cu(110) is always in the film plane up to a Ni thickness of at least 35 ML [5]. Only if the Ni films are grown with O as a surfactant, they show an out-of-plane magnetization at low temperatures at a Ni thickness larger than 5–6 ML.

In this work we investigate Ni films grown epitaxially on Cu(110) and Cu(100) both with and without oxygen surfactant. For our purpose near-edge X-ray absorption fine structure (NEXAFS)and X-ray magnetic circular dichroism (XMCD) both at the Ni $L_{2,3}$ edges and at the O K edge are the techniques of choice. We give final evidence that no bulk-like NiO is formed and that the O stays always on top when Ni is deposited. We study the influence of O as a surfactant on the Ni magnetism. Furthermore, we investigate the induced magnetic moment at the O site. Our results including the full detailed analysis has recently been published in Ref. [6], which is accompained by a Perspective on this subject [7].

The X-ray absorption measurements were carried out in remanence using circularly polarized light from the insertion device beamline UE56/1-PGM at BESSY. The absorption spectra were taken at low temperature (T = 30 K) in the gap-scan mode which drives the undulator and the monochromator simultaneously to provide a high photon flux together with a constant and high degree of circular polarization. For experimental details see [6].

Clear evidence that the oxygen flows at the surface of the Ni film is provided by the angular dependence of XAS at the O K edge. In Fig. 1 we display angular-dependent XAS of a bulk-like Ni film grown on the O/Cu(110) surface. These spectra were recorded with linearly polarized light at an angle $\varphi = 90°$ (normal incidence, solid line) and $\varphi = 20°$ (grazing incidence, dashed line) between the incident X-rays and the surface of the sample. Both spectra are normalized to the absorption of a clean bulk-like Ni film measured at $\varphi = 90°$ and $\varphi = 20°$, respectively. Only if the O is located at the surface and not embedded in the bulk of the sample, XAS will show such a strong angular dependence. In addition, the edge jump at the O K edge is the same for

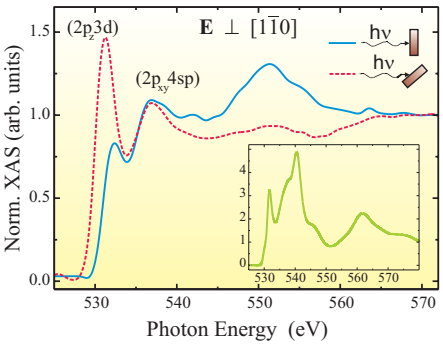

Figure 1: Angular-dependent XAS at the O K edge of a bulk-like Ni film on O/Cu(110) measured at an angle $\varphi = 90°$ (solid line) and $\varphi = 20°$ (dashed line) between the incident X-rays and the surface of the sample.

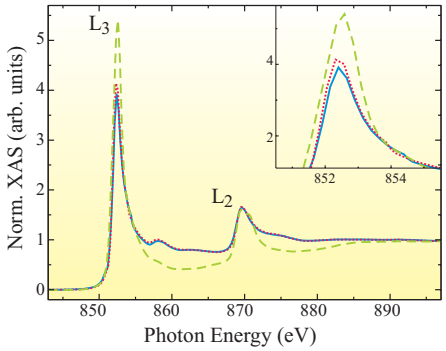

Figure 2: Normalized XAS at the Ni $L_{2,3}$ edges of 18 ML Ni/Cu(110)(solid line) and 6.5 ML (dotted line) Ni on O/Cu(110). For comparision a spectrum of NiO is also included (dashed line). The inset shows the variation of the intensity of the spectra at the L_3 edge due to the charge transfer from Ni to O.

the O/Cu(110) crystal and Ni films grown on O/Cu(110). This means the oxygen coverage stays constant upon Ni deposition. Since NEXAFS yields the electronic structure of the unoccupied density of states, it is possible to conclude simply from the line shape of the XAS that the O surfactant and the topmost Ni layer on O/Cu(110) do not form bulk-like NiO. For comparison, a spectrum of NiO at the O K edge is included in the inset of Fig. 1.

Figure 2 shows the normalized XAS at the Ni $L_{2,3}$ edges of 6.5 ML epitaxially grown Ni on the O/Cu(110) surface (dotted line) and 18 ML Ni on clean Cu(110) (solid line). Additionally, a spectrum of NiO is included (dashed line). The intensity of the XAS at the Ni $L_{2,3}$ edges is increased for NiO and the Ni film on the preoxidized substrate compared to clean Ni. In the same way as it is discussed for Ni films grown on the O reconstructed Cu(100) surface the increase of the XAS intensity follows from a charge transfer from Ni to O. The transitions from the initial $2p$ states at the Ni $L_{2,3}$ edges occur into $3d$ states just above the Fermi level. Hence, the larger XAS intensity evidences an enhancement of the number of Ni d holes. Furthermore, like at the O K edge, the line shape excludes the formation of bulk-like NiO.

Magnetic properties of ferromagnetic samples can be extracted from spin-dependent X-ray absorption spectra. Figure 3 shows the XMCD spectra for different Ni films. The XMCD signal is reduced for 5.5 ML Ni on O/Cu(100) (dashed line) compared to the thick Ni film (solid line). In contrast, on O/Cu(110) 6.5 ML Ni (dotted line) show an enhanced XMCD signal. Compared to the bulk, the Ni magnetization is reduced by $\sim$ 18% for 5.5 ML Ni on O/Cu(100). It is known that the magnetic moment of Ni at an interface to Cu is reduced [8,9]. On the other hand, the surface layer of a clean Ni/Cu(100) shows an enhanced magnetic moment. No change in the magnetization is observed for thin films of Ni/Cu(100) compared to bulk Ni, since the reduction at the interface is compensated by the enhancement at the surface [8]. Here, 5.5 ML Ni on O/Cu(100) show a reduction of the magnetization signal compared to bulk Ni. This means effectively that the O surfactant lowers the surface magnetic moment. Looking at the Ni films on O/Cu(110) one observes just the opposite compared to Ni on O/Cu(100): the total magnetization increases with decreasing Ni thickness. For 6.5 ML Ni on O/Cu(110) it is enhanced by $\sim$ 9% compared to the bulk value, although a reduction of similar size as on Cu(100) is also expected for the Ni moment at an interface to Cu(110) [9]. This means that

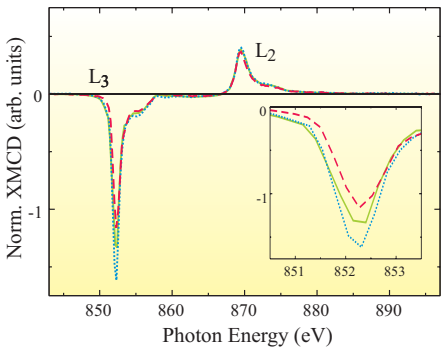

Figure 3: Normalized XMCD spectra at the Ni $L_{2,3}$ edges of 18 ML Ni/Cu(110) (solid line), 6.5 ML Ni on O/Cu(110) (dotted line), and 5.5 ML Ni on O/Cu(100) (dashed line)at $T = 30$ K.

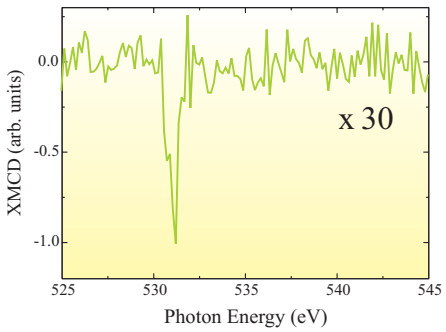

Figure 4: Dichroic signal at the oxygen K edge for bulk-like Ni on O/Cu(110). The scaling factor is given with respect to the edge jump.

Ni films on O/Cu(110) show an enhanced surface magnetization.

To separate spin and orbital contributions to the Ni magnetization, we have carried out a complete sum-rule analysis that we present in full detail in Ref. [6]. It turns out that on the O/Cu(100) surface both the spin and the orbital moment become smaller for the thinner Ni film. Their relative change is identical and their relative contribution to the total magnetization does not change. On the other hand, on O/Cu(110) a large relative increase of the orbital moment is observed for thinner Ni films whereas the spin moment stays more or less constant within the error. Hence, the increase of the magnetization of ultrathin Ni films on O/Cu(110) stems mainly from a raised orbital moment at the surface of these films.

Finally, we turn to the discussion of the induced orbital magnetism at the oxygen site. At the K edge transitions occur from $1s$ initial states to $2p$ final states. Thus, XMCD at the K edge provides *only* information on the *orbital* moment. At the same energy where we identify transitions to $(2p_z 3d)$-states a dichroic signal can be detected. Apart from that, no other significant features can be observed in the spectrum. This signal is shown in fig. 4. The scaling factor is given with respect to the edge jump at the O K edge. In principle, XMCD spectra at K edges can be analyzed with the help of the orbital sum rule. Despite the lack of sufficient statistics, which makes an application of the sum rule questionable, we can conclude from the negative sign of the signal that the orbital moment of the oxygen is aligned parallel to both spin and orbital moments of the nickel. The orientation of spin and orbital moments of both Ni and O is not straightforward evident. Since we do not have access to the O spin moment, we cannot answer the question whether the coupling of the Ni and O spin moments is ferromagnetic or antiferromagnetic from the experiment. Recent theoretical investigations predict a parallel alignment of the induced O spin moment to the Ni spin moment [4].

This work was supported by the BMBF (05 KS1 KEB/4, and 05 KS4 KEB/5).

References

[1] R. Nünthel et al., Surf. Sci. **531**, 53 (2003).

[2] R. Nünthel et al., Surf. Sci. **566-568**, 100 (2004).

[3] J. Lindner et al., Surf. Sci. **523**, L65 (2003).

[4] J. Hong et al., PRL **92**, 147202 (2004).

[5] M. Sacchi et al., Surf. Sci. **442**, 349 (1999).

[6] C. Sorg et al., Surf. Sci. **565**, 197 (2004).

[7] M. Farle, Surf. Sci. **575** 1 (2005).

[8] A. Ney et al. Phys. Rev. B **65**, 024411 (2002).

[9] A. M. N. Niklasson et al., Phys. Rev. B **59**, 6373 (1999).

RESONANT SOFT X-RAY EMISSION SPECTROSCOPY AND NEAR-EDGE X-RAY ABSORPTION FINE STRUCTURE OF V_2O_5

O.Yu. Khyzhun, T. Strunskus, Ch. Wöll

Lehrstuhl für Physikalische Chemie I, Ruhr-Universität Bochum,
Universitätsstraβe 150, D-44780 Bochum, Germany

1. Introduction

In recent papers Schmitt et al. [1-3] have investigated several vanadium oxides (V_2O_3, VO_2 and V_6O_{13}) by resonant soft X-ray emission (SXE) spectroscopy. In these works, strong hybridization of the O 2p- and V 3d-like states was observed for the vanadium oxides under study, and spectral features, which could be assigned to dd- and charge-transfer excitations, were found to be resolved in the resonant SXE spectra excited at V L emission band threshold of V_6O_{13}. A similar feature is also expected for the electronic structure of the highest vanadium oxide, V_2O_5. In order to continue the series for the different vanadium oxides, we have measured the resonant SXE spectra for polycrystalline V_2O_5 across the V 2p and O 1s absorption edges. In the present report also results of a study of V_2O_5 by near-edge X-ray absorption fine structure (NEXAFS) are presented.

2. Experimental

For the present resonant SXE and NEXAFS studies we have used powder divanadium pentoxide, V_2O_5, provided by Aldrich Chem. Co., with purity of 99.99%. This V_2O_5 powder was a single-phase material as confirmed by X-ray diffraction analysis. The present resonant SXE and NEXAFS measurements were carried out using undulator beam-line U41-PGM at the synchrotron facility BESSY II (Berlin). The resonant SXE spectra in the energy region corresponding to positions of the V Lα and O Kα bands were recorded using the apparatus ROSA. The spectra were measured with a high-resolution Rowland-mount grazing-incidence grating X-ray emission spectrometer Scienta XES 300 (Gammadata, Sweden) equipped with a two-dimensional detector. During the present investigation the spectrometer was mounted in a vertical position, perpendicular to the incoming synchrotron beam. The resonant SXE spectra were measured in the second order of diffraction using a spherical grating with radius of curvature of 5 m and with 1200 lines/mm. The NEXAFS spectrum was recorded in the fluorescence yield (FY) mode.

3. Results and discussion

Figure 1 shows a NEXAFS spectrum recorded for the divanadium pentoxide powder. In the energy region between 512 and 528.5 eV the data reveal two broad structures associated with the absorption at the V L_{III} and V L_{II} thresholds. The absorption band in the energy region from 512 to 521.5 eV is assigned to the V $2p_{3/2} \rightarrow$ V 3d transition (V L_{III}) whereas that in the energy region from 521.5 to 528.5 eV is related mainly to the V $2p_{1/2} \rightarrow$ V 3d transition (V L_{II}). Just above the broad structure assosiated with the absorption at the V L_{II} threshold (ca. 528.5 eV) the O 1s $\rightarrow$ O 2p transition (O K) starts to contribute. The superposition of the three absorption spectra leads to a rather complex spectrum with a variety of fine structure features.

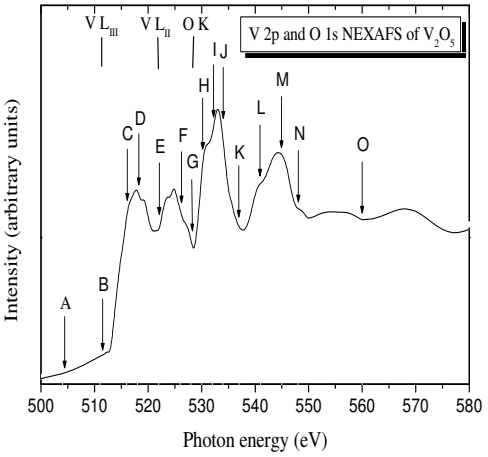

Figure 1. NEXAFS V 2p and O 1s spectrum of V_2O_5. Energies of photons employed for excitation of the resonant soft X-ray emission spectra in Fig. 2 are marked by arrows above the spectrum.

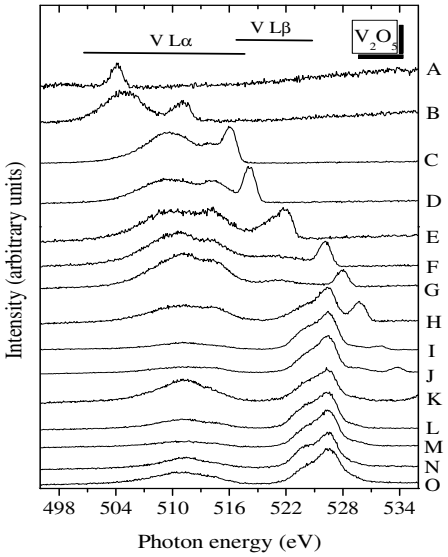

Figure 2. Resonant soft X-ray emission spectra of V_2O_5 excited with photon energies indicated by the arrows A–O in the NEXAFS spectrum presented in Fig. 1.

In Fig. 2 we present a series of SXE spectra recorded for divanadium pentoxide using different photon excitation energies. As can be observed from Fig. 2, there are significant changes of the spectra when turning the energy above the O K edge which is obscured by the V L edges (curves O – H). It is aparent that significant changes of the relative intensities of the O Kα and V Lα bands occur when turning the photon energy above the O K edge. If one compares the relative intensity of the V Lα band (with respect to the intensity of the O Kα band) on the SXE spectra presented in Fig.2, one could see that it decreases when turning the photon excitation energy towards the top of the two broad absorption bands positioned above the O K threshold (sequences N → M and K → J) and, further, the relative intensity of the V Lα band increases when the energy of photon excitation turns from the top of the absorption bands to the bottom (sequences M → L → K and I → H → G).

Evolution of the V Lα (transition V 3d → V $2p_{3/2}$) and V Lβ (V 3d → V $2p_{1/2}$) bands when changing the excitation energy across the V L_{III} and V L_{II} edges is presented in Fig. 2 by curves G to B. If one compares the spectra recorded above (curves O – G) and below (curves G – A) the O K edge, one finds that for the present V_2O_5 powder the V Lβ band can be detected in the SXE spectra only for photon energies just above the maximum of the V L_{II} absorption band (points F and G on the NEXAFS spectrum presented in Fig.1). As can be seen from curves F and G in Fig.2, the relative intensity of the V Lβ band positioned at energies about 521.5 eV is rather small in V_2O_5 and the band, due to superposition with the more intense O Kα band, is not visible on the SXE spectra excited with higher photon energies (curves H – O). When exciting the SXE spectra with photon energies corresponding to point E just above the V L_{II} edge, the V Lβ band overlaps the line produced by the elastic peak.

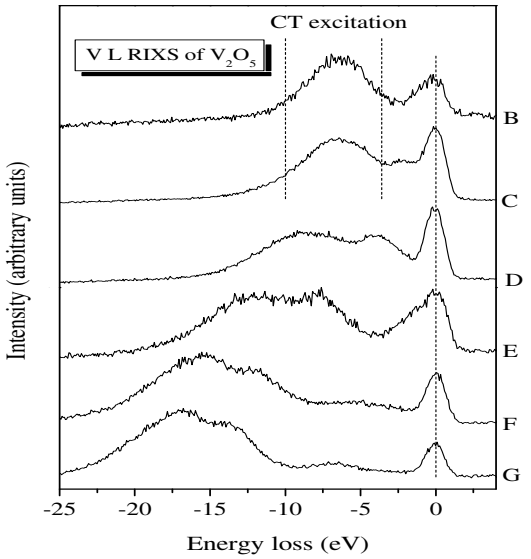

Figure 3. Resonant inelastic X-ray scattering spectra of V_2O_5 excited at the V L thresholds with photon energies indicated by the arrows B–G in the NEXAFS spectrum presented in Fig.1.

In Fig. 3 we have plotted the resonant SXE spectra that were recorded at the V L thresholds for divanadium pentoxide against an energy loss scale relative to the elastic peaks in the resonant SXE spectra of Fig. 2 (curves B to G). Similar to that observed in Ref. 3 for the resonant inelastic X-ray scattering (RIXS) spectra of V_6O_{13}, the analogous spectra recorded for V_2O_5 reveals the existence of the sub-band of the charge transfer (CT) states on the spectra recorded at energies marked by B and C (cf. Figs. 2 and 3). As one can see from Fig. 3, the sub-band of CT states in V_2O_5 is centered at ca. -7 eV with respect to the position of the elastic peak, being in excellent agreement with the results of analogous studies of V_6O_{13} by Schmitt et al. [3]. Nevertheless, our RIXS spectra presented in Fig. 3 do not reveal the existence of the sub-band of the local dd-excitations originating from the transition $e_g \rightarrow t_{2g}$. As it has been already mentioned above, according to the results by Schmitt et al. [3], the sub-band of the dd-excitations was detected at energies ca. -1.6 eV with respect to the position of the elastic peak on the resonant SXE spectra of V_6O_{13}. This difference we can explain by smaller occupation of the V $3dt_{2g}$ orbitals in V_2O_5 as compared with that in V_6O_{13}.

Acknowledgements

The authors gratefully acknowledge support by the group of Prof. R. Szargan (University of Leipzig) and the BESSY staff. Travelling costs for synchrotron measurements provided by BMBF through grant 05 ES3XBA/5 is also acknowledged.

References

[1] T. Schmitt, L.-C. Duda, A. Augustsson, J.-H. Guo, J. Nordgren, J.E. Downes, C. McGuinness, K.E. Smith, G. Dhalenne, A. Revcolevschi, M. Klemm, S. Horn, *Surf. Rev. Lett*. 9 (2002) 1369.

[2] T. Schmitt, L.-C. Duda, M. Matsubara, A. Augustsson, F. Trif, J.-H. Guo, L. Gridneva, T. Uozumi, A. Kotani, J. Nordgren, *J. Alloys Comp*. 362 (2004) 143.

[3] T. Schmitt, L.-C. Duda, M. Matsubara, M. Mattesini, M. Klemm, A. Augustsson, J.-H. Guo, T. Uozumi, S. Horn, R. Ahuja, A. Kotani, J. Nordgren, *Phys. Rev. B* 69 (2004) 125103.

Fermi Surface mapping by photoemission: The importance of indirect transitions

A. Tadich[a], L. Broekman[a], J.Riley[a], R.Leckey[a] ,T. Seyller[b], K.Emtsev[b], L.Ley[b]

[a]*School Of Physics, Latrobe University, Bundoora, Victoria 3083, Australia.*
[b]*Institut fur Technische Physik II, Universitat Erlangen Nurnberg, 91058 Erlangen, Germany.*

Using a recently developed toroidal spectrometer[1], we have been able to make relatively rapid surveys of full hemisphere emission from the Fermi Surface (FS) of both Cu and the binary alloy Cu_3Au covering a wide range of incident photon energies. A selection of such maps from Cu(111), transformed into momentum space in the usual way, is shown below in Fig.1. These display behaviour that is unexpected on the basis of most previous interpretations.

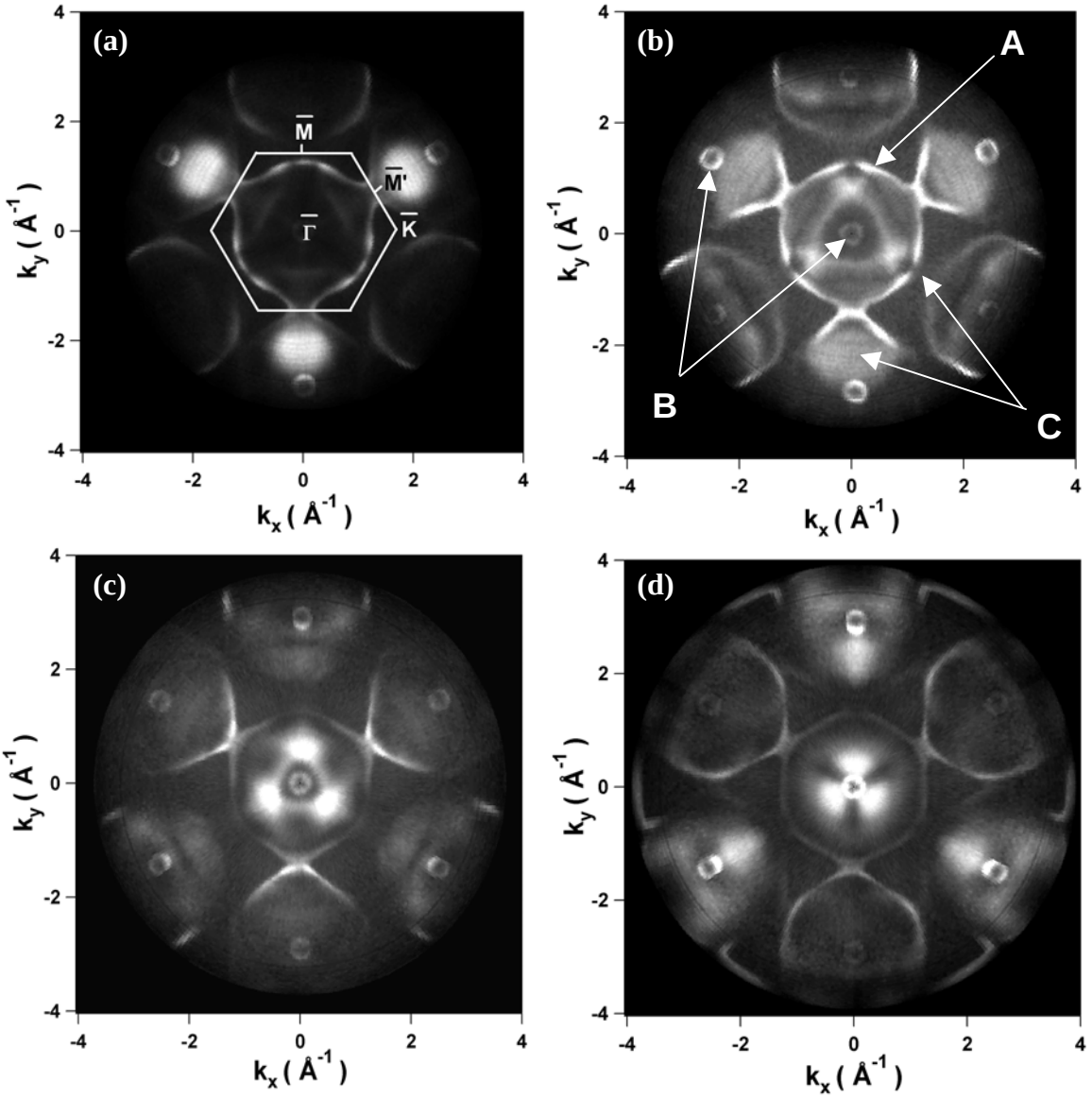

Fig. 1 Full hemisphere angle scanned photoemission results from the Fermi Surface of Cu. (a) hν = 46eV (b) hν = 52eV (c) hν = 58eV (d) hν = 64eV. Surface symmetry directions for the (111) face are indicated in (a). Important features common to all scans are indicated in (b) and are described within the text.

The most obvious feature is a relatively sharp outline (A), visible at all photon energies within each Brillouin zone and which exhibits the "expected" neck features along {111} directions. Although variations in intensity occur, the dimensions of this feature are remarkably constant as opposed to the expected effect of an increasing radius of the final state circle within a free electron model. It can also be noted that all six necks are generally visible, indicating that emission from regions of both hemispheres of the FS is evident. In addition to clear evidence of the well known Shockley surface state [2] surface state at the centre of each zone (B), diffuse structures may be seen to move within each zone with photon energy (C).

We have been able to identify the structures described above by performing swept photon energy constant initial state (CIS) experiments. Fig 2 relates to emission from the $\bar{\Gamma}\bar{K}$ azimuth covering the photon energy range 30 eV to 120 eV. Using a free electron model for the final state (V_o = 12eV), the data has been converted into absolute k. It is overlaid with the loci of expected direct transitions calculated using an empirical model of the FS based upon de-Haas Van Alphen data [3, 4](white dots).

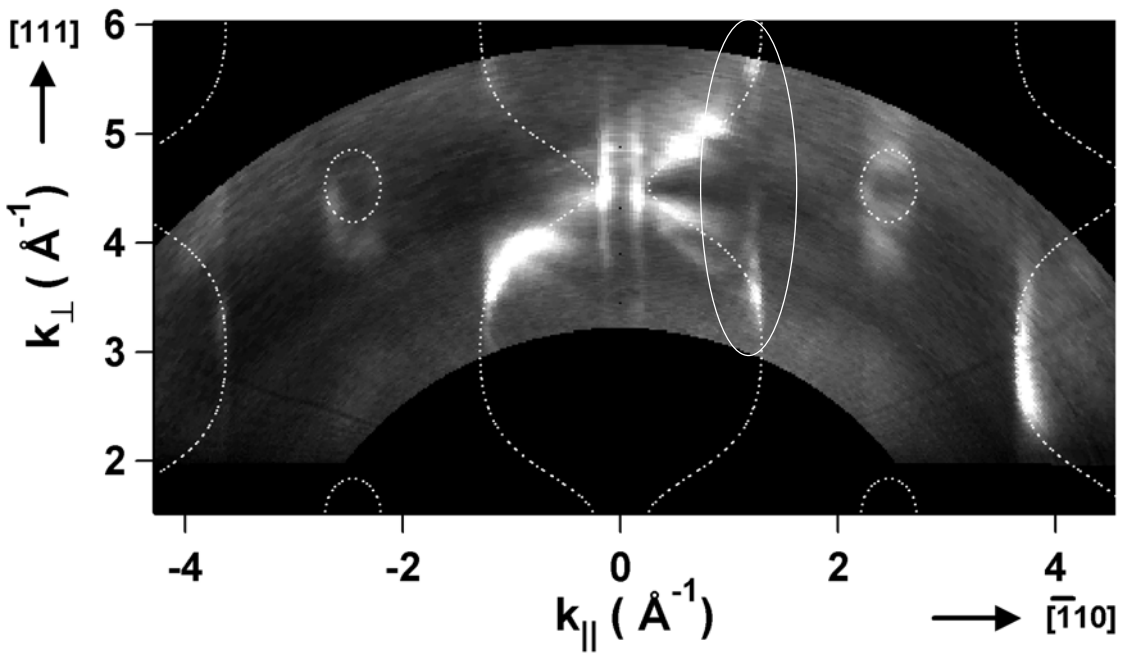

Fig 2. CIS measurement for the $\bar{\Gamma}\bar{K}$ plane. White dots illustrate the predicted FS contours considering only direct transitions from the FS (matrix elements neglected). Circled area indicates region of significant $k_\perp$ broadening.

Diffuse structures in the data follow the theoretical lines rather well, but it is clear that significant broadening occurs at many k-space locations, being most extreme for those regions (such as the "equator") where $dE/dk_\perp = 0$ (see circled region). From Fig. 2 it is clear that it is the diffuse features in Fig.1 which track direct transitions from the Fermi surface as the photon energy is varied, whereas the relatively well defined FS "outline" visible in a rather similar manner at all photon energies examined is a result of lifetime ($k_\perp$) broadening. The precise projection from the 3-dimensional Fermi surface which is observed at each photon energy is consequently a rather complex one which depends on the details of the $k_\perp$ dispersion at each k-space location. Such density of states (DOS) type indirect transitions have previously been predicted to occur in CIS experiments by Lindroos and Bansil[5] who performed first principles calculations of the photoemission intensity distribution from various faces of Cu for a photon energy of 21.21eV. Their calculations were later confirmed in an experimental study using 21.21eV light[6], leading to speculation that such indirect transitions could provide a more reliable source of FS data. Here the

effect is observed for the first time over many photon energies. These results indicate that in utilising photoemission to map the FS, one should take care to distinguish contributions from both direct transitions and DOS type indirect transitions.

We conclude by remarking that we have observed comparable effects from Cu(100) and significantly stronger evidence of indirect transitions from the alloy Cu_3Au. This may in part be due to the effect of band broadening in disordering alloys such as Cu_3Au[7]

Acknowledgements

We would like to thank the staff of BESSY for their invaluable help, as well as Dr C. Pettenkofer (Hahn-Meitner Institute Berlin) for providing the Cu crystal used in this study. This work was supported by the BMBF under grant # 05ES3XBA/5 and by the Australian Research Council.

References

[1] http://www.tp2.unierlangen.de/Englische_homepage/framedocu_Forschungsverbund_eng.html.
[2] S. D. Kevan, *et al.*, Physical Review B **36**, 5809 (1987).
[3] M. R. Halse, Phil. Trans. R.Soc. Lond. A **265**, 507 (1969).
[4] D. J. Roaf, Phil. Trans. R.Soc. Lond. A, 135 (1962).
[5] M. Lindroos, *et al.*, Phys. Rev. Lett. **77**, 2985 (1996).
[6] M. Lindroos, *et al.*, Surface Science **482-485**, 718 (2001).
[7] B. Ginatempo, Physical Review B. **42**, 2761 (1990).

Transition metal chalcogenide thin films and hetero structures - X-ray absorption (XANES) and resonant X-ray emisson (XES) of Fe thin films on ZnO(0001) substrates

D. Wett, D. Schulze, K. H. Hallmeier, A. Demund and R. Szargan

Wilhelm-Ostwald-Institut für Physikalische und Theoretische Chemie, Universität Leipzig, D-04103 Leipzig, Germany

The chemical, electronic as well as mechanical properties of materials like semiconductors, catalysts or composites are commonly linked to the interactions at metal/oxide interfaces. In many cases these interactions are chemical reactions and/or diffusion, which take place at least when the material is heated up to several hundreds of Kelvin. Also the formation of defined new phases has been observed previously [1,2,3,4].

The combination of the materials Zinc oxide and iron has been chosen because of its principle applicability as tunnelling barrier ($Fe/Zn_xMg_{1-x}O/Fe$) as well as because of the lack of information concerning this interface and its thermal stability. ZnO itself a transparent semiconducting material of a quite low price and is used in semiconductor and sensor technology, photo catalysis and as transparent, conductive material for solar cell caps.

Within this experiment Fe films has been prepared on (0001)-oriented ZnO pulsed laser deposited substrates applying an electron beam evaporator, which has the capability of film preparation from sub-monolayer up to 100s of nanometer film thickness range. To investigate the thermal stability of the prepared films the samples have been annealed up to 650°C. Furthermore, the samples have been sputtered by 3 kV Ar^+ ions after heating. The XANES (total electron yield mode) and X-ray emission measurements have been carried out at beamline U41-PGM by using the rotatable spectroscopy apparatus (ROSA).

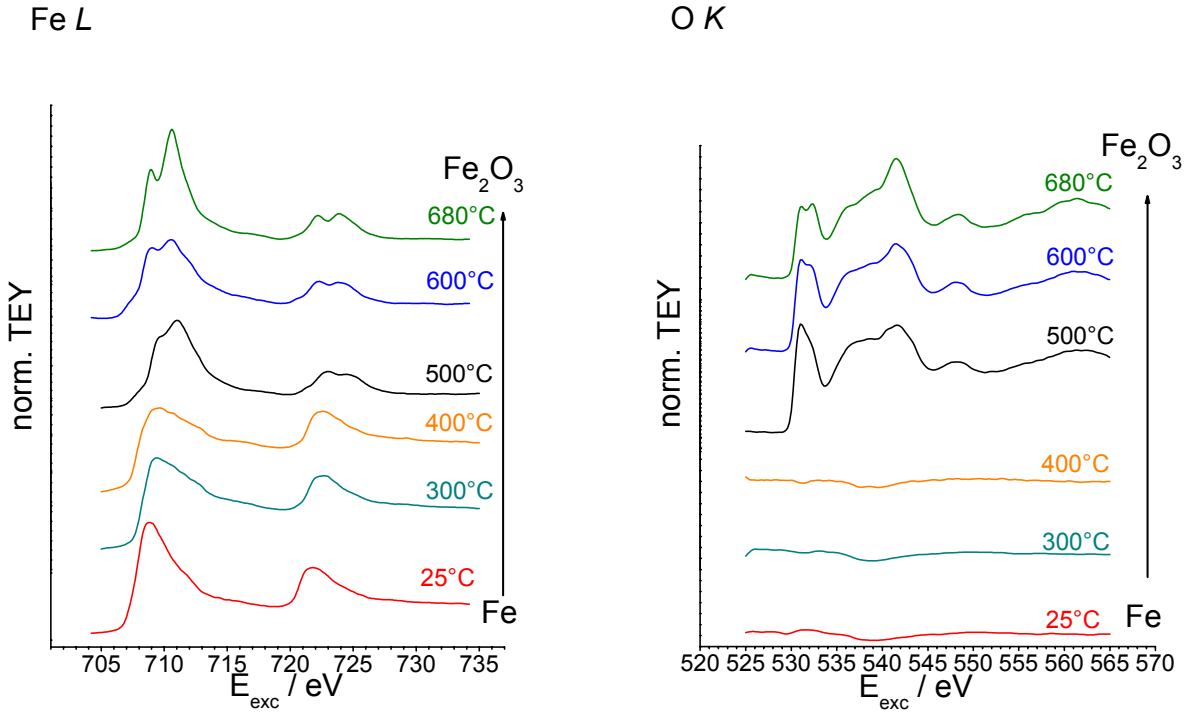

Fig. 1: Fe *L* (left) and O *K* XAS (right) of 12 nm Fe/ZnO(0001) after annealing at temperatures as noted in the right part of the spectra

Figure 1 shows the Fe *L* und O *K* X-ray absorption spectra measured in the total electron yield mode of a 12 nm thick Fe film. One can clearly see the successive conversion of the metal into trivalent iron oxide, which has finished at 680°C. Sputtering with 3 kV Ar^+ ions leads to the complete reduction of the Fe_2O_3 to FeO (fig. 2).

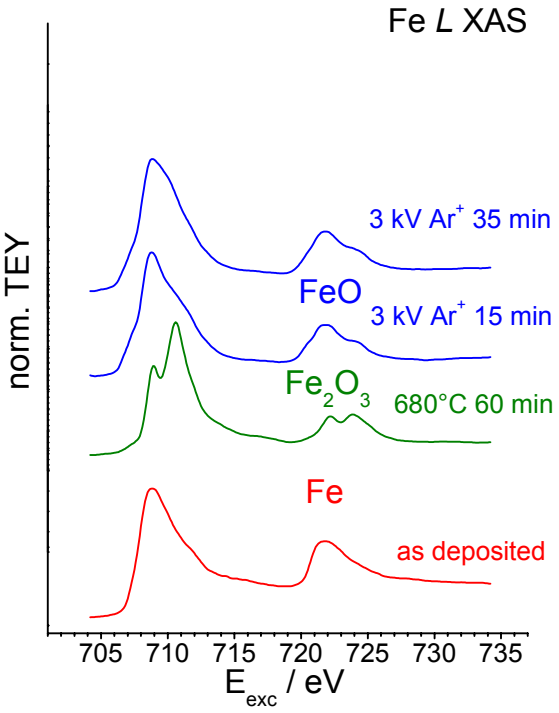

Fig. 2: Fe *L* XAS of the Fe film before (red) and after (green) the oxidation to Fe_2O_3 and after 3kV Ar^+ sputtering (blue)

The fine structure of the Fe L and O K spectra of the Fe_2O_3 agree well with experimental and calculated spectra found in the literature [5,6]. We should remark that during sputtering under the same conditions absolutely no metallic iron could be detected by XPS. So we can exclude a superposition of Fe^0 and Fe^{2+} components. Because only atoms of the first and the second coordination sphere around the probed atom are involved in the XANES and XES process, it is not clear, whether the iron oxides form real phases or the iron atoms are somehow "diluted" into the zinc oxide film.

Also resonantly excited X-ray emission spectra of the oxidized as well as of the reduced films were recorded (fig. 3).
The energy loss structures in the range of 2...5 eV originate from indirect excited d-d transitions, whereas at an energy position of about 7...11 eV charge transfer and Mott-Hubbard transitions (CT and MHT) are expected to appear. Because of the different strength of the Fe3d-O2p hybridization (larger bond length in the monoxide) and the differences in the charge transfer and Mott-Hubbard energies [5] the influences of these individual effects on particular intensity variations are difficult to separate yet.

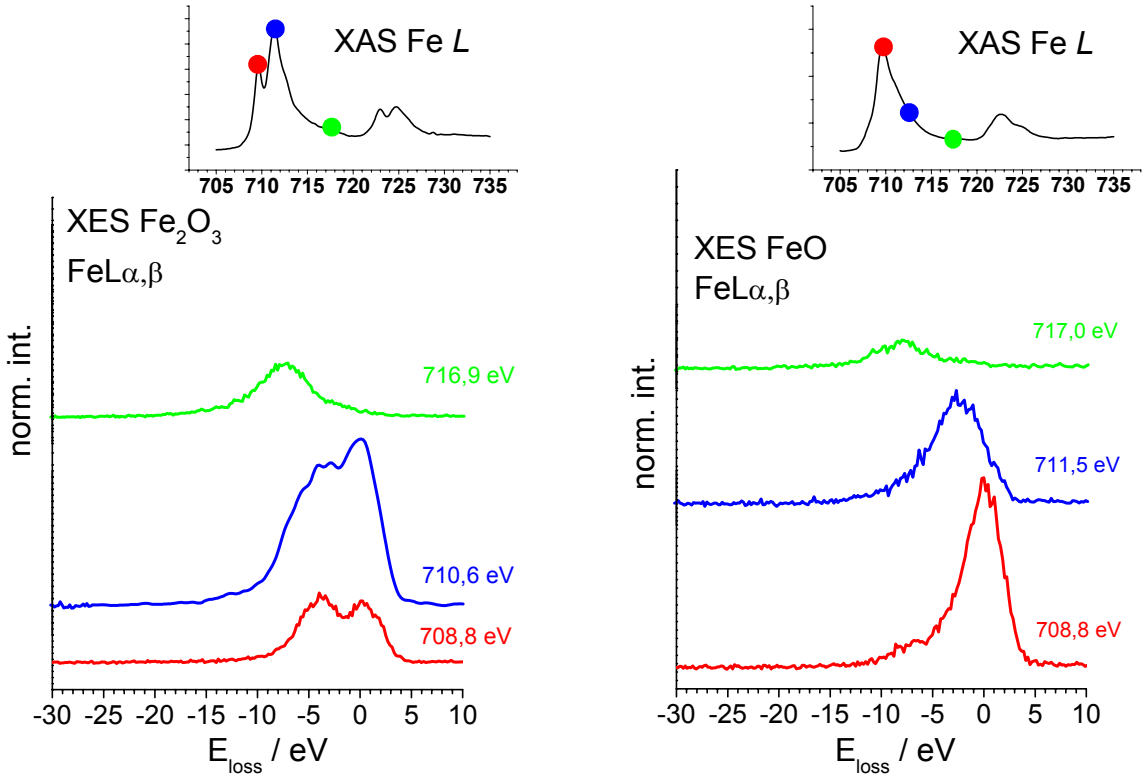

Fig. 3: Resonant Fe L_α X-ray emission of Fe_2O_3- and FeO, energy loss scale: $E_{loss} = E_{emission} - E_{excitation}$

Acknowledgement:

This work was financed by DFG FOR 404-SZ58/15 and BMBF, grant number 05KS1OL1/3. We are grateful for technical support by C. Jung and M. Mast at the U41-PGM beamline, BESSY.

References:

[1] L. Zhang, D. Wett, D. Schulze, and R. Szargan, M. Nagel, H. Peisert, and T. Chassé: Chemical reactions at Cu/ZnS(001) and In/ZnS(001) heterojunctions: A comparison of photoelectron and S L2,3 x-ray emission spectroscopy, Applied Physics Letters 86 (2005) 012108

[2] A. Arranz, V. Perez-Dieste and C. Palacio: Growth, electronic properties and thermal stability of the Fe/Al_2O_3 interface, Surface Science 521 (2002) 77–83

[3] P. Luches, M. Liberati and S. Valeri: Oxidation–reduction reactions at as-grown Fe/NiO interface, Surface Science 532–535 (2003) 409–414

[4] Irene Spolveri, Andrea Atrei, Brunetto Cortigiani, Ugo Bardi, Alessandro Santucci and Danila Ghisletti: Surface composition of the phases formed by solid state reaction at the Cr/ZnO(000$\bar{1}$) interface studied by low energy ion scattering and X-ray photoelectron spectroscopy, Surface Science 412/413 (1998) 631–638

[5] J. P. Crocombette, M. Pollack, F. Jollet, N. Thromat and M. Gautier-Soyer: X-ray-absorption spectroscopy at the Fe $L_{2,3}$ threshold in iron oxides, Physical Review B 52 (1995) 3143

[6] Z. Y. Wu, S. Gota, F. Jollet, M. Pollak, and M. Gautier-Soyer and C. R. Natoli: Characterization of iron oxides by x-ray absorption at the oxygen *K* edge using a full multiple-scattering approach, Physical Review B 55 (1997) 2570

Electron spectroscopy study of graphite layers grown on SiC(0001) surfaces

Th. Seyller[1], K.V. Emtsev[1], K. Gao[1], F. Speck[1], L. Ley[1], A. Tadich[2], L. Broekman[2], J.D. Riley[2], R.C.G. Leckey[2], O. Rader[3], A. Varykhalov[3], A.M. Shikin[3]

[1] *Institut für Technische Physik II, Universität Erlangen-Nürnberg, Germany*
[2] *Department of Physics, La Trobe University, Bundoora, Vic 3083 Australia*
[3] *BESSY, Berlin, Germany*

The observation of graphitic carbon in a number of ohmic metal/SiC structures [1,2] subjected to annealing and the ohmic behavior of graphite/SiC interfaces [3,4] suggests that graphitic carbon may play an important role in the formation of ohmic contacts on SiC. Consequently, the structural and electronic properties of graphitic layers on SiC surfaces are of great interest.

We have recently started to investigate the structural and electronic properties of graphitic layers grown on SiC(0001) surfaces following a recipe provided by Forbeaux et al. [5,6]. Different types of samples were investigated as discussed below. In all cases the surfaces were cleaned by ex-situ wet-chemical treatments followed by a dip in HF solution.

After load-locking the samples into the UHV system they were annealed at 950°C in a flux of Si. This procedure results in the formation of a Si-rich (3×3) reconstruction. The excess Si was then removed from the surface by further annealing steps at 1050°C, 1150°C and 1400°C leading to the Si-rich ($\sqrt{3}\times\sqrt{3}$)R30° structure, the carbon rich ($6\sqrt{3}\times6\sqrt{3}$)R30° structure and finally the graphitized surface, respectively.

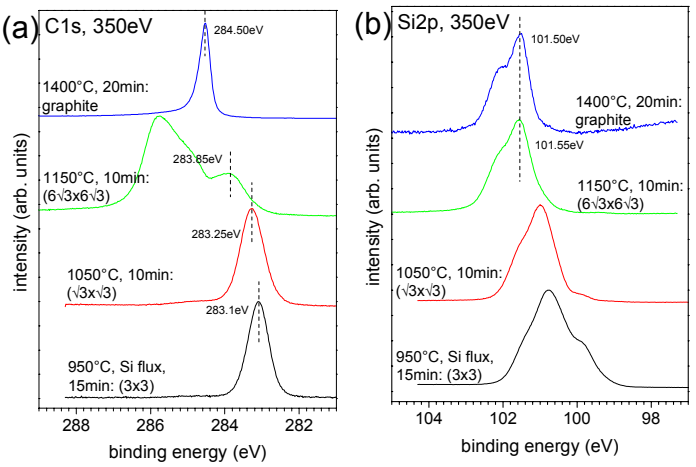

Fig. 1: C1s (a) and Si2p (b) core level spectra taken after subsequent preparation steps as described in the text. Spectra are normalized to the same height. The dashed lines indicate the position of the bulk contribution to each core line.

The process was monitored by core level spectroscopy (SXPS) at beamline U49/2-PGM 1 using the MUSTANG end station and low-energy electron diffraction (LEED). Results obtained for an n-type 6H-SiC(0001) polished substrate are shown in figure 1. The C1s and So2p core level line shapes observed after the individual stages of preparation agree excellently with the literature [7]. From the absolute intensities of the core level spectra we determine a graphite layer thickness of 20 Å. It is worth mentioning that the graphite layers exhibit a well defined (1×1) LEED pattern with sharp spots which indicate that they are rotated against the substrate lattice by 30°. AFM measurements (not shown here) show the presence of large (few 100 nm) graphite flakes with hexagonal and trigonal shapes.

The vertical dashed lines in figure 1 indicate the positions of the bulk contribution to each core line. The observed shift of the bulk line positions to higher binding energy is due to a change in surface band bending. The Si rich (3×3) and ($\sqrt{3}\times\sqrt{3}$)R30° structures are known to possess surface states in the fundamental band gap of the SiC substrate due to the presence of dangling bonds. These dangling bond states undergo a Mott-Hubbard metal-insulator transition leading to a filled lower Hubbard band and an unfilled upper Hubbard band which lie above the valence band maximum (VBM) and below the conduction band minimum (CBM), respectively. The upper Hubbard band will be partially filled by electrons from the conduction band of the n-type sample and therefore the surface Fermi level position is observed deeper in the gap than the bulk Fermi level.

Upon formation of the ($6\sqrt{3}\times6\sqrt{3}$)R30° structure a shift of the bulk core levels by 0.6 ± 0.1 eV to higher binding energy indicates that the Fermi level moves upwards in the gap closer to the CBM. The C1s core level binding energy observed for this structure amounts to 283.8 ± 0.05 eV (average over several measurements). The energy difference between the C1s core level and the VBM of SiC is 281.0 ± 0.1 eV [8]. Thus the surface Fermi level of the ($6\sqrt{3}\times6\sqrt{3}$)R30° structure is located at 2.8 ± 0.1 eV above the VBM. The theoretical bulk Fermi level position for this n-type 6H-SiC sample is 2.9 eV above the VBM [8]. Thus we can conclude that within the error of our measurement the ($6\sqrt{3}\times6\sqrt{3}$)R30° structure corresponds to a flat band situation.

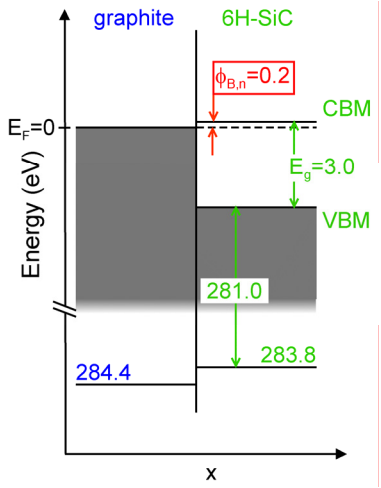

Fig. 2: Band diagram of the graphite/6H-SiC(0001) interface determined from the core level data. A possible small band bending (≤ 0.1 eV) in the SiC has been neglected.

The bulk Si2p core level binding energy of the $(6\sqrt{3}\times6\sqrt{3})R30°$ structure amounts to 101.50 ± 0.05 eV (average over several spectra) which is virtually identical with the value observed on the graphitized surface. Thus the flat band situation is conserved when the graphite layer is grown. In addition, since we know the energy separation between the SiC C1s core level and VBM, we are able to determine the Schottky barrier height of the graphite/n-type 6H-SiC(0001) layer system. This is demonstrated in figure 2. We obtain a value of $\phi_{B,n}$= 0.2 ± 0.1 eV which is a rather small value for a Schottky barrier and which may explain the observed ohmic behavior of graphitic contacts on n-type 6H-SiC(0001) [3].

In addition to core level measurements, we also carried out angle-resolved valence band measurements (ARUPS) using a newly developed toroidal electron analyzer (TEA) [9]. This apparatus allows us to simultaneously collect ARUPS spectra for emission angles between -90 and +90 degree within one azimuthal plane. In addition, it has multi-energy detection capability which reduces the data acquisition time and improves the signal to noise ratio.

Figure 3 shows ARUPS spectra of graphite grown on on-axis 6H-SiC(0001). Spectra are shown which were taken in *ΓM* direction and in *ΓK* direction. The band structure of graphite [10] with its characteristic σ and π bands is clearly discernable. The σ bands lie well below the Fermi level due to the strong σ bond of the sp^2 orbitals of graphite. The latter leads to a σ-σ^* band gap energy of 11 eV, which is twice as large as the band gap energy of sp^3 bonded diamond. The π bands reach the Fermi level only at the *K* points of the 1st Brillouin zone. The degeneracy of the occupied π and unoccupied π^* bands makes graphite a semi metal.

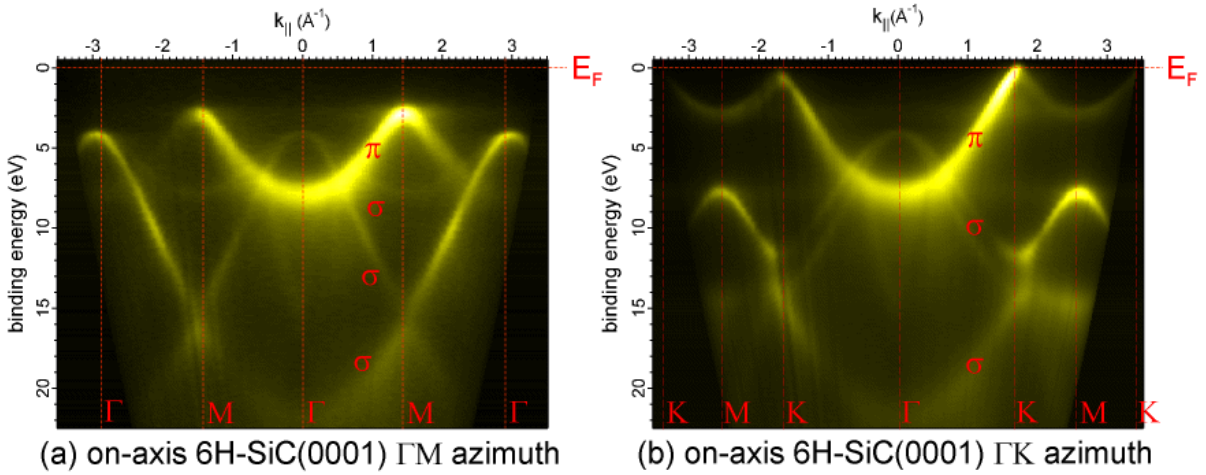

Figure 3: ARUPS spectra of graphite grown on on-axis 6H-SiC(0001) taken along the ΓM direction (a) and the ΓK direction (b) at a photon energy of 50 eV. Binding energies are given with respect to the Fermi level. The dashed lines indicate high symmetry points in reciprocal space. The Brillouin zone of hexagonal graphite is shown on the right hand side.

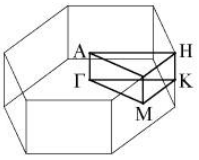

Recently the observation of stepped graphite on 3.5° off-axis oriented 6H-SiC(0001) was reported [11]. Although the LEED pattern of the graphite layer showed indications for a spot splitting due to a step structure, no step induced features were observed in the ARUPS spectra. In order to clarify this issue, we have used 8° off-axis oriented 4H-SiC(0001). The advantage of this surface is that it should provide shorter terrace widths thus making step induced features more prominent.

Figure 4 depicts an ARUPS spectrum of graphite grown on 8°off-axis 4H-SiC(0001) together with a sketch of the sample surface. The spectrum was taken along the $\Gamma\bar{M}$ direction as indicated in the sketch. The misalignment of the macroscopic surface normal is towards the $[11\bar{2}0]$ direction of the SiC substrate, i.e. the step edges are running parallel to the $[10\bar{1}0]$ direction. LEED patterns of the sample taken directly after load-locking the sample into the UHV chamber showed split spots due to the step structure of the surface in agreement with that misorientation. Analysis of the spot splitting yields a step width of 36 ± 2 Å. With an off-axis angle of 8° this corresponds to a step height of 5 Å which is equivalent to one half of the 4H-SiC unit cell or two bilayers. The graphite layer formed as described above is rotated by 30° with respect to the substrate. The 1st BZ of the resulting graphite layer is shown in figure 4. As can be seen the substrate steps are running in a direction perpendicular to the *ΓM* direction of the graphite overlayer.

The ARUPS spectra in figure 4 show a graphite band structure as observed with on-axis 6H-SiC(0001) [see figure 3(a)]. In addition, several ghost structures are observed in the spectrum. These ghost structures are replicas of the graphite band structure as indicated by the horizontal arrows. The first explanation that comes into one's mind is an *umklapp* process due to a regular array of steps on the surface. However, the apparent *g* vector is too large. From the terrace width of 36 Å one would expect $g = 0.18$ Å^{-1}. According to figure 4 the replicas appear at $g = 1 - 1.5$ Å^{-1} which is not possible. After a second glance at the data it becomes obvious that the replicas do not appear at a constant *g* but at a constant angle shift of around 28° independent on kinetic energy. Furthermore, no spot splitting is observed in LEED. Hence another explanation has to be sought.

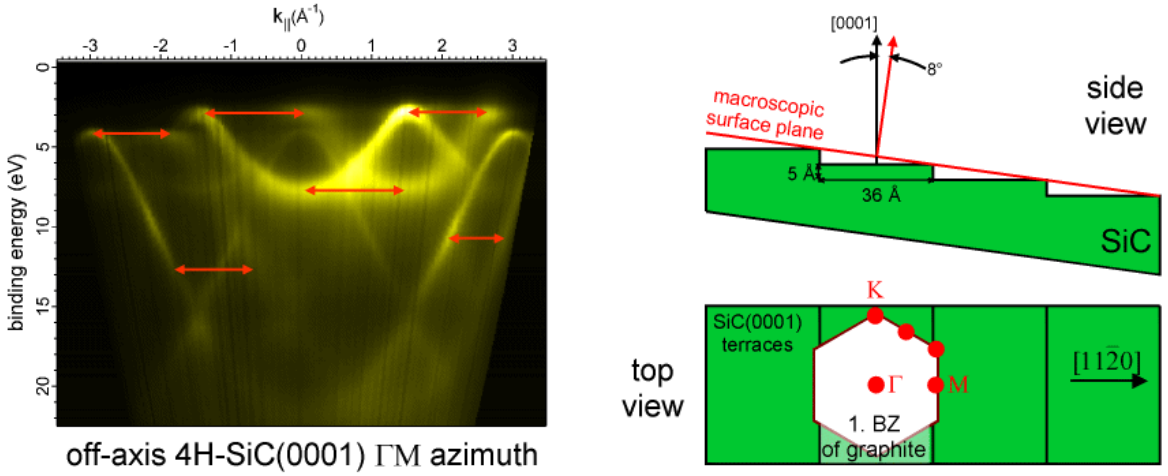

Figure 3: ARUPS spectrum of graphite grown on 8° off-axis 4H-SiC(0001) taken along the ΓM direction. The arrows indicate the position of and origin of some of the ghost structures described in the text. The sketch on the right had side shows the step structure of the SiC sample and the orientation of the graphite layers 1st BZ with respect to the steps.

An important hint for the explanation comes from STM images. Examples are shown in figure 5(a) and (b). Figure 5(a) displays the topography of a larger area (3670 Å × 3500 Å) of the sample. The surface consists of large terraces with varying terrace widths. The step height is typically around 20 Å, i.e. four times the original step height. Apparently step bunching occurs during the preparation of the graphite layer, although we cannot say explicitly during which of the different preparation steps. This needs further experiments.

The apparent step bunching by itself still cannot explain the ghost features in the ARUPS spectra. The solution comes from figure 5(b) where an atomically resolved image from a step edge is displayed. The structure of graphite on an atomic scale is clearly visible. Apparently, the graphite layer covers the step like a carpet, as also shown in the sketch in figure 5. Therefore the ghost features in the ARUPS spectra are most likely from facets that are present due to the carpet-like growth mode of the graphite. This is further supported by ARUPS spectra taken in ΓK direction, i.e. parallel to the steps. In this case the ghost features are absent.

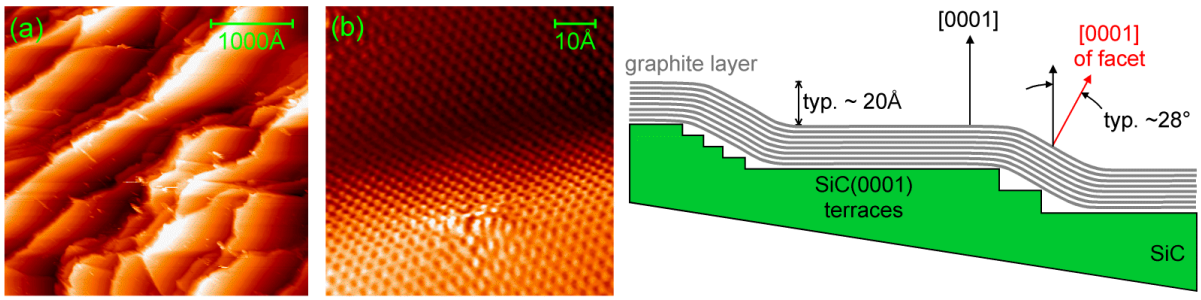

Figure 5: STM images of the graphite layer grown on 8° off-axis 4H-SiC(0001). (a) Topography of a large area (3670 Å × 3500 Å) of the sample. (b) Atomically resolved image (72 Å × 72 Å) of a 20Å high step.

In conclusion, we have investigated interesting aspects of graphite layers grown on SiC(0001) surfaces by solid state graphitization. The combination of SXPS, ARUPS, AFM, and STM provides detailed insight into structural properties of the graphite layers, their growth, and the electronic properties of the interface. In particular we benefit from the use of the toroidal analyzer which enables us to acquire large ARUPS data sets in a reasonably short time. Without the use of this analyzer the intriguing structural properties of the graphite layer grown on off-axis 4H-SiC would not have been recognized as easily.

The authors thank W. Braun, H. Pfau, and M. Sperling for their ongoing support. This work was supported by the BMBF through grant # 05 ES3XBA/5 and by the Australian Research Council.

[1] J. Crofton, P.G. McMullin, J.R. Williams, and M.J. Bozack: J. Appl. Phys. Vol. **77** (1995), p. 1317.
[2] E. Kurimoto, H. Harima, T. Toda, M. Sawada, M. Iwami, and S. Nakashima: J. Appl. Phys. Vol. **91** (2002), p. 10215.
[3] W. Lu, W.C. Mitchel, C.A. Thornton, G.R. Landis, and W.E. Collins: J. Electron. Mat. Vol. **32** (2003), p. 426.
[4] W. Lu, W.C. Mitchel, G.R. Landis, T.R. Crenshaw, and W.E. Collins: J. Appl. Phys. Vol. **93** (2003), p. 5397.
[5] I. Forbeaux, J.M. Themlin, and J.M. Debever: Phys. Rev. B Vol. **58** (1998), p. 16396.
[6] I. Forbeaux, J.M. Themlin, and J.M. Debever: Surf. Sci. Vol. **442** (1999), p. 9.
[7] L.I. Johansson, F. Owman, and P. Mårtensson: Phys. Rev. B Vol. **53** (1996), p. 13793.
[8] N. Sieber, Thesis, University of Erlangen-Nürnberg (2002).
[9] A. Tadich, L. Broekman, E. Huwald, R.G.C. Leckey, J.D. Riley, T. Seyller, and L. Ley: BESSY Annual Report 2003, p. 515.
[10] R. Ahuja, S. Auluck, J. Trygg, J.M. Wills, O. Eriksson, and B. Johansson: Phys. Rev. B Vol. **51** (1995), p. 4813.
[11] A. Varykhalov, A.M. Shikin, O. Rader, W. Gudat, A. Loza, M. Poiguine, V.K. Adamchuk, and D. Vyalikh: BESSY Annual Report 2002, p. 197.

Electronic properties of clean unreconstructed 6H-SiC{0001} surfaces studied by angle resolved photoelectron spectroscopy

K.V. Emtsev[1], Th.Seyller[1], L. Ley[1]
A.Tadich[2], L. Broekman[2], J.D. Riley[2], and R.C.G. Leckey[2]
[1] *Institut für Technische Physik II, Universität Erlangen-Nürnberg, Germany*
[2] *School of Physics, La Trobe Universtity, Bundoora, Vic 3083 Australia*

Hexagonal SiC surfaces exhibit a great variety of reconstructions depending on surface stoichiometry and preparation conditions. These reconstructions were studied intensively [1,2] over the last years on account of their technological importance. The properties of the 1×1 clean (0001)-Si-face and $(000\bar{1})$-C-face unreconstructed SiC surfaces, however, remained unexplored experimentally so far. Only theoretical considerations of such bulk truncated surfaces exist [3].

The possibility to obtain 1×1 unreconstructed surfaces from initially hydrogenated surfaces by non-thermal, photon-induced desorption of hydrogen was investigated earlier in our group [4,5]. Desorption of hydrogen occurs upon exposure of surfaces to a high flux of synchrotron radiation. During desorption the 1×1 periodicity is preserved. In contrast, thermal desorption activates the formation of the (√3×√3)R30° reconstruction on the (0001) surface or results in a 1×1 disordered surface with graphitic patches on $(000\bar{1})$ surface [6].

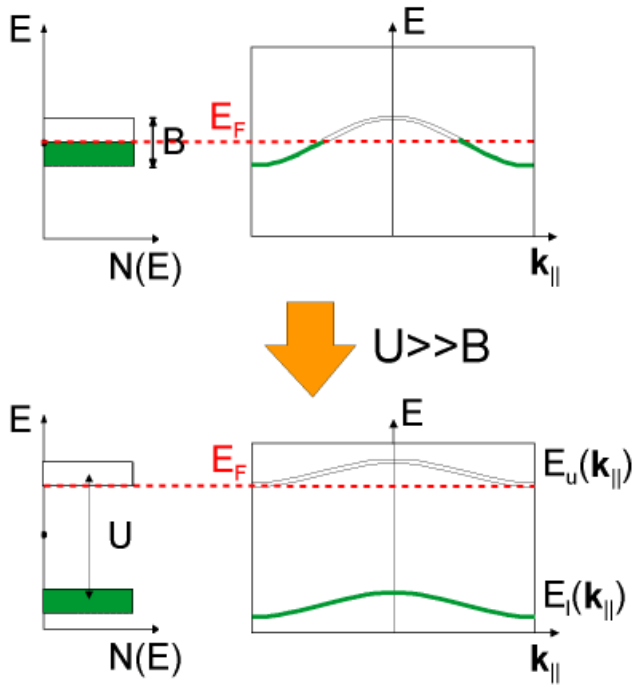

Fig. 1. Schematic representation of the Mott-Hubbard metal-insulator transition.

A number of the reconstructed hexagonal surfaces show an interesting behavior in that the dangling bond surface bands undergo a Mott-Hubbard metal-insulator transition [1, and references therein]. For all of these reconstructions there is one dangling bond per unit cell. Therefore, a half filled band crossing the Fermi level (E_F) is expected. Due to strong electron correlation this band splits into one filled band and one empty band which are separated by the correlation energy U (Fig.1). The transition is expected to take place if the parameter U, which is the energy required to put a second electron into a singly occupied orbital, is larger than the band width of this state (U>>B). This condition is well satisfied for the 3×3 and (√3×√3)R30° reconstructions (for example, U=2.0eV and B=0.2eV on the (√3x√3)R30° surface). By reducing the distance between the neighboring dangling bonds on the surface from 5.31 Å on the (√3x√3)R30° surface to 3.08 Å on the 1×1 surface the interaction between them increases which should be reflected in a larger band width. Therefore, the question addressed in this report is whether 1×1 unreconstructed SiC{0001} surfaces are still in the Mott-Hubbard regime or if they show the metallic behavior suggested by the theoretical calculations [3].

We have carried out experiments using synchrotron radiation at the beamlines TGM4 and UE56-2/PGM1. The unreconstructed SiC(0001) and SiC$(000\bar{1})$ surfaces were prepared by exposing hydrogen terminated surfaces to undispersed light ("0-order" of the monochromator). Angle-resolved photoemission spectra were taken by means of a newly designed toroidal electron analyser allowing us to collect all emission angles in one azimuthal plane simultaneously.

Fig. 2(a) and (b) show valence band spectra of the initial, H-terminated $(000\bar{1})$ surface and spectra taken after irradiation with "0-order" light, respectively. First of all, there are no states at the Fermi level before and after irradiation. Second, desorption of hydrogen is manifested by the appearance of the carbon dangling bond state (C_{db}) after irradiation. This state is best seen in the gap of the projected bulk band structure along the $\overline{\Gamma M K}$ line of the surface Brillouin zone and nearly coincides with the valence band maximum (VBM). C_{db} disperses downwards from Γ point and follows periodicity of the 1×1 unreconstructed surface. The dispersion of the band amounts to 0.6 eV. Another state (S) which lies within the ionic gap is seen in the proximity of the M point. A surface state at a similar position was obtained in the calculations as well [3].

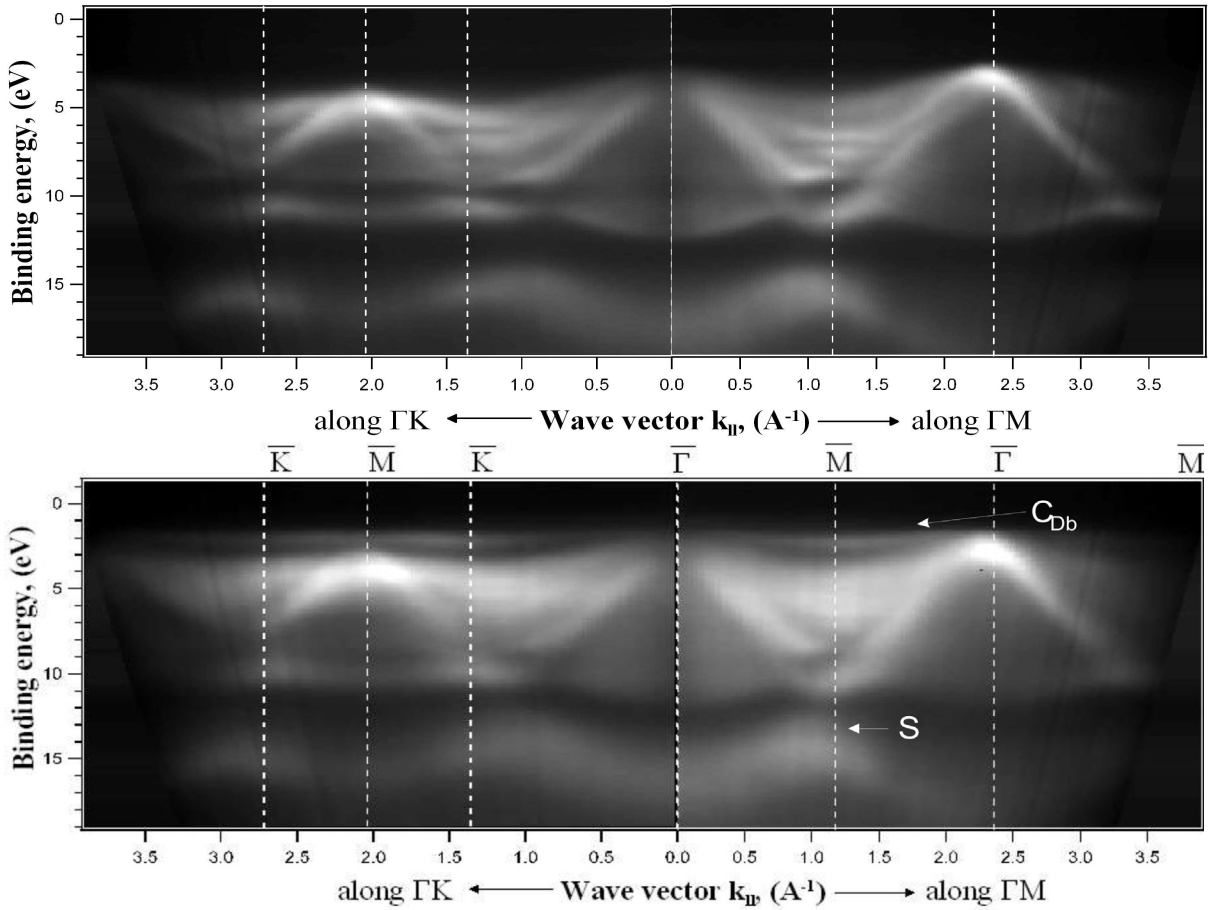

Fig. 2. ARUPS spectra of 6H-SiC($000\bar{1}$) surface. (a) The initial (H terminated) surface; (b) H-free unreconstructed surface obtained after irradiation with "0-order" light. Binding energies are given wit respect to E_F.

After irradiation an upward band bending of 0.85eV is observed on 6H-SiC($000\bar{1}$). This is consistent with the Mott-Hubbard picture taking into account the fact that on clean unreconstructed surface the Fermi level becomes pinned by the empty upper Hubbard band. In this way, we estimate a lower limit of 1.7 eV for the U parameter.

On the (0001) surface (results not shown) irradiation also gives rise to a Si dangling bond state (Si_{db}). The resulting band which follows the periodicity of the 1×1 unreconstructed surface is located 0.6eV above VBM but still below E_F and its dispersion amounts to 0.2 eV. The fact that the C dangling bond lies lower in energy than the Si dangling bond is attributed to the stronger potential of the carbon atom.

In conclusion, we have prepared clean unreconstructed Si- and C-truncated surfaces of 6H-SiC by light induced desorption of hydrogen. These surfaces represent further examples of a Mott-Hubbard insulating surface despite a separation of the dangling bonds that is markedly reduced in comparison with the reconstructed surfaces.

We like to acknowledge support by the BESSY staff as well as by W. Mahler and B. Zada from the FHI. This work was supported by the BMBF through grant # 05 ES3XBA/5 and by the Australian Research Council.

[1] J. Pollmann and P. Krüger, J. Phys.: Condens. Matter, Vol. **16** (2004) S1659.

[2] K. Heinz, J. Bernhardt, J. Schardt, U. Starke, J. Phys.: Condens. Matter, Vol. **16** (2004) S1705.

[3] M. Sabisch, P. Krüger, J. Pollmann, Phys. Rev B, Vol. **55** (1997) 10561.

[4] Th. Seyller, J. Phys.: Condens.Matter, Vol. **16** (2004) S1755.

[5] N. Sieber, Th. Seyller, L. Ley, M. Polcik, D. James, J.D. Riley, and R.C.G. Leckey, Mater.Sci.Forum, Vol. **389-393** (2003) 713.

[6] N. Sieber, Th. Seyller, L. Ley, M. Polcik, D. James, J. Riley, R. Leckey, Phys. Rev. B **67** (2003) 205304.

[7] A. Tadich, L. Broekman, E. Huwald, R.G.C. Leckey, J.D. Riley, T. Seyller, and L. Ley: BESSY Annual Report 2003, p. 515.

Local partial density of states in $CuInS_2$ determined by soft x-ray emission spectroscopy

L. Zhang[1], I. Konovalov[2], D. Wett[2], M. Nagel[1], D. Schulze[2], R. Szargan[2], and T. Chassé[1]

[1]*Institut für Physikalische und Theoretische Chemie, Universität Tübingen, Auf der Morgenstelle 8, 72076 Tübingen, Germany*
[2]*Wilhelm-Ostwald-Institut für Physikalische und Theoretische Chemie, Universität Leipzig, Linnéstrasse 2, 04103 Leipzig, Germany*

Thin-film Cu-III-VI_2 chalcopyrite ternary compounds are promising solar cell absorber materials due to their direct band gaps, high absorption coefficients and low material consumption for the thin film fabrication. The valence band structures of the $CuInS_2$ and $CuInSe_2$ are of fundamental importance and have been extensively investigated both theoretically and experimentally. Theoretical calculations by Jaffe and Zunger indicate that the valence bands of the chalcopyrite compounds consist of four distinct regions. Taking $CuInS_2$ as an example, the four regions are, in the sequence of increasing binding energy, (1) the upper valence band mostly composed of Cu 3d and S 3p states; (2) a band due to In 5s and S 3p mixture; (3) S 3s states and (4) In 4d level.[1]

A decomposition of the $CuInS_2$ and $CuInSe_2$ upper valence bands into Cu 3d, S 3p and Cu 3d, Se 4p local partial density of states (LPDOS), respectively, has been performed through analysis of sets of valence band photoelectron spectra obtained with variable excitation energy.[2,3] This attempt is based on the fact that the photoionisation cross section dependence on the excitation energy is significantly different for chalcogen p and Cu 3d levels. This method provides an indirect way to divide the total density of states into partial densities of states of the constituents.

On the other hand, x-ray emission spectroscopy is well known for its ability to detect directly the local partial density of states. Fluorescence yields for the L or M shells are generally much smaller than those of K shells, with a high photon-flux synchrotron radiation source the L or M emission spectra are detectable. Although limitations regarding resolution have sometimes to be accepted in order to compensate for the low intensity, the resolution is generally superior compared to the more conventional K spectra. In $CuInS_2$ or $CuInSe_2$, the Cu 3d, S 3p and Se 4p LPDOS, which are anticipated to form the upper valence bands, can be directly probed in soft x-ray range by exciting, e.g. Cu 2p, S 2s and Se 3s or 3d core levels, respectively.

A single crystalline $CuInS_2$ sample grown by the iodine transport technique has been used for the investigation. Cu $L_{2,3}$ ($3d \rightarrow 2p$), In $M_{4,5}$ ($5p \rightarrow 3d$) and S L_1 ($3p \rightarrow 2s$) x-ray emission spectra were measured at the ROSA endstation (with a SCIENTA XES 300 spectrometer) of the U41 PGM beamline at BESSY. The spectrometer resolution of the Cu $L_{2,3}$, In $M_{4,5}$ and S L_1 emission spectra is 3.6, 2.0 and 1.5 eV, respectively. X-ray photoelectron spectra of the Cu $2p_{3/2}$, In $3d_{5/2}$, S 2s core levels and the valence band were measured with an ESCALAB 220iXL (Fisons Instruments) using monochromatised Al Kα radiation (1486.6 eV). The calibration of the energy scale of the emission spectra is very important in order to plot the emission and the photoelectron spectra on a common binding energy scale. Here we used the Cu L_3 ($3d \rightarrow 2p_{3/2}$)

emission line (929.7 eV) of a pure Cu foil as the calibration line. Fortunately, the second and fourth order of the Cu L_3 line (464.9 and 232.4 eV, respectively) can be measured with high intensity in the same measuring window under the same settings as those of the In $M_{4,5}$ and S L_1 spectra, respectively, thus facilitating the calibration of the In $M_{4,5}$ and S L_1 spectra. The uncertainty of the peak position is estimated to be about 0.5 eV. The emission spectra were fitted employing the Unifit software in order to obtain the peak positions.

Figure 1(a) shows the Cu $L_{2,3}$ emission spectrum of the $CuInS_2$. The spectrum was fitted with two features corresponding to the L_3 and the L_2 transition, respectively. The binding energy of the Cu 3d maximum is calculated as 2.0 eV from the Cu $2p_{3/2}$ binding energy and the L_3 emission energy.

The In $M_{4,5}$ emission spectrum in the energy range around 440 eV represents the transition from the In 5p valence states to In 3d core holes. Although its intensity is much lower than the In 4p $\rightarrow$ 3d (core $\rightarrow$ core) transition intensity, it can still be clearly detected and is displayed in Fig. 1(b). The spectrum includes two main features originating from the M_5 and M_4 transitions, respectively. Each feature consists of a main component and a shoulder at the high photon energy side. The distances between the two main components as well as the two shoulders are in agreement with the In 3d spin-orbital splitting. No shoulders occurred in the In $M_{4,5}$ spectrum of a pure In metal using primary electrons as excitation source.[4] Therefore, the shoulders in Fig. 1(b) should be caused by In-S and/or In-Cu bonds in $CuInS_2$. The binding energies of the main component and the shoulder of the M_5 feature (In 5p valence states) are estimated to be 3.6 and 0.9 eV, respectively.

The S L_1 emission spectrum is shown in Fig. 1(c). It also contains a main component and a shoulder at the high photon energy side. These two components correspond to a binding energy of 3.7 and 0.9 eV, respectively. A previously reported Se $M_{4,5}$ emission spectrum (4p $\rightarrow$ 3d) of $CuInSe_2$ excited by an x-ray tube exhibited a similar shape to the S L_1 spectrum, with a main component at about 4.0 eV and a relatively higher shoulder at about 1.8 eV (the energy scale was calibrated by C 1s = 285.0 eV).[5]

The Cu $L_{2,3}$, In $M_{4,5}$ and S L_1 emission spectra, which represent the LPDOS of the Cu 3d, In 5p and S 3p valence states, respectively, and the valence band x-ray photoelectron spectrum, which represents the total density of states of $CuInS_2$, were plotted on a common binding energy scale, displayed in Fig. 2. Three features can be seen in the upper valence band (0 – 6 eV) of the photoelectron spectrum, and their origins may be deduced by comparing with the LPDOS revealed in the x-ray emission spectra. The dominant feature in the upper valence band at 1.9 eV should originate from Cu 3d states. The feature at 3.6 eV was considered attributed mainly to S 3p and marginally to Cu 3d states in the previous theoretical calculations,[1] but from our In $M_{4,5}$ emission spectrum, a contribution of In 5p states to this feature is evident. Similarly, the In 5p states can also be clearly seen to contribute to the feature close to the valence band edge at about 0.9 eV, whereas the previous theoretical calculations assign this feature to Cu 3d and S 3p antibonding states only.[1] The similarity of both the positions and the intensity ratios of the two components in the S 3p and In 5p LPDOS suggests that the S 3p and In 5p states mix in the upper valence band of $CuInS_2$. The participation of In 5p valence states in the bonds in $CuInS_2$ should be considered in the future electronic structure calculation.

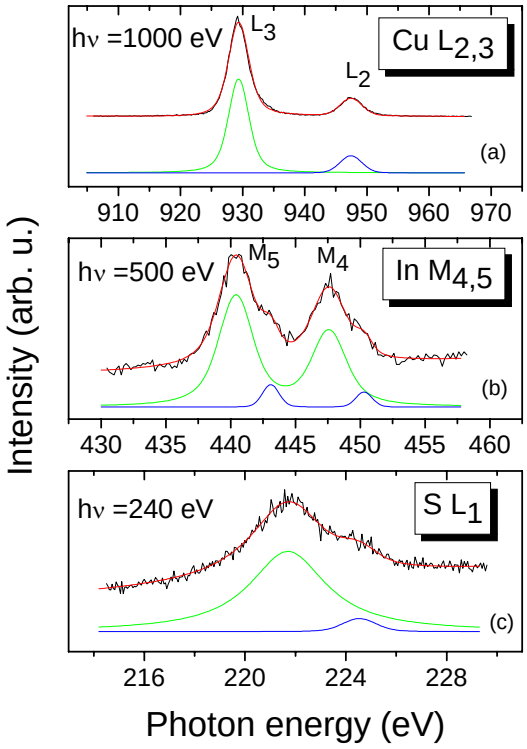

Fig. 1 (a) Cu $L_{2,3}$, (b) In $M_{4,5}$ and (c) S L_1 x-ray emission spectrum of $CuInS_2$

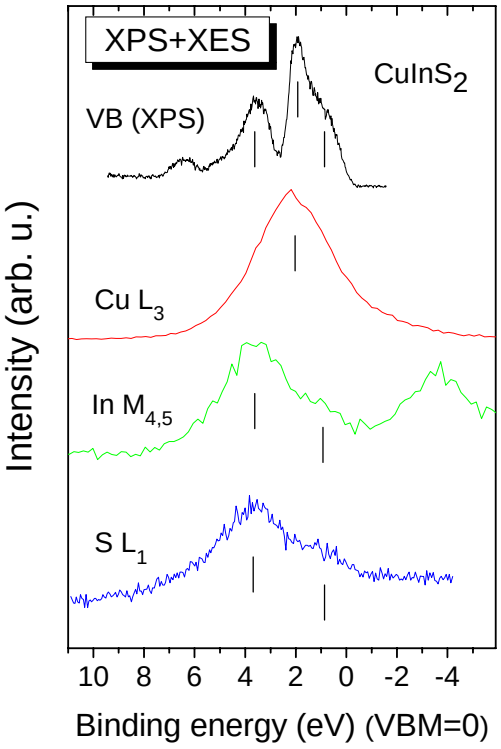

Fig. 2 Cu $L_{2,3}$, In $M_{4,5}$ and S L_1 x-ray emission spectra (XES) and valence band x-ray photoelectron spectrum (XPS) of $CuInS_2$ on a common binding energy scale

Acknowledgements:
The authors would like to thank Y. Tomm for providing the $CuInS_2$ single crystal. The financial support from the BMBF 05KS1OL1/3, 05KS1BLA/9, DFG Sz58/13 and BESSY is gratefully acknowledged.

References:

[1] J. E. Jaffe and A. Zunger, Phys. Rev. B **28**, 5822 (1983).
[2] T. Löher, A. Klein, C. Pettenkofer, and W. Jaegermann, J. Appl. Phys. **81**, 7806 (1997).
[3] W. Braun, A. Goldmann, and M. Cardona, Phys. Rev. B **10**, 5069 (1974).
[4] R. S. Crisp, D. Haneman, and J. W. Chu, Solid State Commun. **78**, 465 (1991).
[5] E. P. Domashevskaya, V. V. Gorbachev, V. A. Terekhov, V. M. Kashkarov, E. V. Panfilova, and A. V. Shchukarev, J. Electr. Spectr. Relat. Pheno. **114-116**, 901 (2001).

Thermal and chemical stability of Al_2O_3 on 4H-SiC(0001)

K.Y. Gao, Th. Seyller, K. Emtsev, and L. Ley

Institut für Technische Physik II, Universität Erlangen-Nürnberg, Germany

Silicon carbide SiC is a wide band gap semiconductor with properties that make it an outstanding candidate for high frequency power electronics [1]. This is due to the compared to conventional semiconductors large break-down field (~ 3 MV/cm), the high thermal conductivity at room temperature (5 W/cmK), and the large saturated electron drift velocity (2.7×10^7 cm/s).

Despite these promising properties the only device available on the market today is a Schottky diode. Due to the poor properties of the SiO_2/SiC interface, power MOSFETs which would be beneficial for many applications where switching of voltages in the kV range is required are currently not available. A high density of electrically active interface states (D_{it}) degrades the channel mobility and thus hampers the development of SiC-based MOSFET devices [2]. Several possible ways to solve this problem are currently being pursued. One of them is the use of alternative gate dielectrics such as AlN or Al_2O_3 deposited on SiC surfaces [3-5]. Recently, we reported on the interface properties of Al_2O_3/6H-SiC(0001) [5]. This interface exhibits a density of interface traps of around 5×10^{11} $cm^{-2}eV^{-1}$ just below the conduction band of 6H-SiC, which is almost an order of magnitude lower than that of thermally grown SiO_2. An abrupt interface free of Si-suboxide was proposed based on photoelectron spectroscopy measurements. Furthermore, Al_2O_3 provides energy barriers in excess of 1.5eV for both electrons and holes [5]. However, in order for Al_2O_3 to become a real competitor for SiO_2, the thermal and chemical stability of the interface between Al_2O_3 and SiC is an inevitable issue. In order to gain insight into the thermal behavior of Al_2O_3 on SiC, we have performed SXPS measurements on a 1.5 nm thick Al_2O_3 layer grown by atomic layer deposition (ALD) on H-terminated 4H-SiC(0001) before and after annealing in UHV. Details about the sample preparation can be found elsewhere [5].

Figure 1 shows the Si2p core-level spectra of the as prepared sample taken with photon energies of 200 eV, 380 eV, and 510 eV. At normal emission, this corresponds to inelastic mean free paths of photoelectrons (λ) of 3.1 Å, 4.9 Å and 7.0 Å, respectively. Using a standard peak fitting routine, the Si2p spectra are deconvoluted into three doublets corresponding to the Si atoms from the bulk SiC substrate and Si atoms in the formal oxidation state Si^+ and Si^{4+}, respectively. The considerable change of Si^{4+} with λ indicates that Si^{4+} is located on top of the Al_2O_3. The variation in the relative intensities of Si^+ and bulk components at 380eV and 510eV indicates a monolayer of Si^+ atoms formed at the interface of Al_2O_3 and SiC.

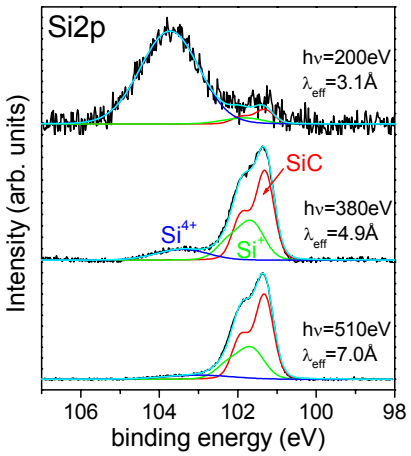

Figure 1: Si2p core level spectra taken at different photon energies from the as-deposited Al_2O_3 layer on H-terminated 4H-SiC(0001). λ refers to the electron mean free path.

The as deposited sample was then annealed in vacuum at different temperature from 350°C to 850°C. After each annealing temperature, the sample was probed by SXPS at different photon energies and emission angles. Figure 2 shows Si2p spectra at a photon energy of 380eV after subsequent annealing at different temperatures. The spectra are normalized and aligned with respect to the bulk line. The spectra show a clear variation of the relative intensities and chemical shifts of both Si^+ and Si^{4+} upon annealing in vacuum.

The Si spectra in figure 2 were analyzed similar to what is displayed in figure 1. In figure 3(a) the relative intensities of Si^{4+} and Si^+ are plotted as a function of annealing temperature. The intensity of Si^{4+} rises rapidly with temperature and reaches a maximum at 700°C indicating the formation of additional Si-O bonds. On the other hand, the Si^+ signal strength remains rather constant up to 600°C and increases somewhat.

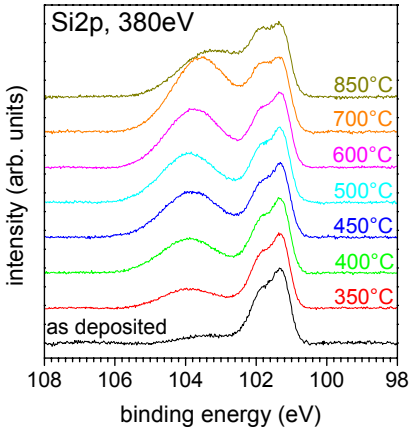

Figure 2: Si2p spectra taken at a photon energy of 380 eV from Al_2O_3/4H-SiC(0001) after annealing in vacuum at different temperatures.

The chemical shift of the Si^{4+} component (ΔE^{4+}) thereafter is shown in figure 3(b). It is evident that ΔE^{4+} is becoming smaller after annealing at temperatures higher than 500°C by up to 0.6 eV. Since Si-O bonds are more ionic than Al-O bonds (50% and 60-

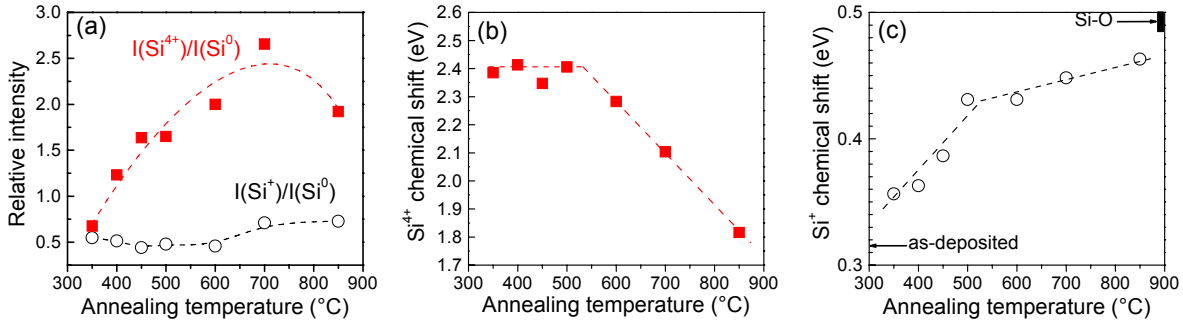

Figure 3: The dependence of (a) the Si^{4+} and Si^{+} intensities, (b) the chemical shift of Si^{4+}, and (c) the chemical shift of Si^{+} on the annealing temperature. The data shown were obtained by fitting the Si2p core level spectra shown in figure 2.

70%, respectively) the formation of an aluminum silicate is expected to lower the chemical shift of the Si^{4+} component.

Since the Si^{+} component is due to Si atom connected to three carbon atoms of the SiC substrate, the variation of its properties points towards a change in the interface structure. In figure 3(c) the chemical shift of Si^{+} (ΔE^{4+}) is shown to increase continuously from 0.31 to 0.46 eV with annealing temperature. If all the Si^{+} atoms are from C_3Si-O-Al configuration, its shift should be similar to what is observed for SiO_2/SiC, i.e. around 0.5 eV. Our data were well below, and approaching this value only when increasing the annealing temperature. Note that the substrate surface was H-terminated by annealing in ultra-pure hydrogen [6] before Al_2O_3 was deposited. A chemically shifted component in the Si2p core level spectra of H-terminated 6H-SiC(0001) at 0.22 eV was interpreted as Si-H bonds [7]. Therefore, the component assigned to Si^{+} could include both Si-O and Si-H bonds in the as-deposited sample. The shift of the Si^{+} component shown in figure 3(c) towards the a value close to what is observed with SiO_2/SiC would then be due to a temperature induced transformation of Si-H bonds into Si-O bonds under desorption of hydrogen.

In summary, the stability of ALD-deposited Al_2O_3 on H-terminated 4H-SiC(0001) was investigated by high resolution XPS measurement using synchrotron radiation. The evaluation of Si^{4+} demonstrated that the annealing process induces the information of a thin layer of SiO_2 and/or aluminum silicate on top of Al_2O_3 layer. In addition, a temperature dependence of the chemical shift of the Si^{+} component indicates that residual Si-H bonds might be present at the interface after deposition. They are transformed into Si-O bonds upon annealing in vacuum. The results are very valuable to understand and to try improving the interface between the deposited oxide and SiC.

The authors thank W. Braun, H. Pfau, and M. Sperling for their ongoing support. This work was supported by the BMBF through grant # 05 ES3XBA/5 and by the Bayerisches Staatsministerium für Wissenschaft, Forschung und Kunst within the Bayerisches Langzeitprogramm "Neue Werkstoffe".

References:

[1] G. Pensl and R. Helbig, Festkörperprobleme **30**, 133 (1990).
[2] V. V. Afanas'ev, F. Ciobanu, G. Pensl, and A. Stesmans, in *Silicon Carbide - Recent Major Advances*, edited by W. J. Choyke, H. Matsunami and G. Pensl (Springer, 2003), p. 343.
[3] C. I. Harris, M. O. Aboelfotoh, R. S. Kern, S. Tanaka, and R. F. Davis, Inst. Physc. Conf. Ser. **142**, 777 (1995).
[4] M. O. Aboelfotoh, R. S. Kern, S. Tanaka, R. F. Davis, and C. I. Harris, Appl. Phys. Lett. **69**, 2873 (1996).
[5] K. Y. Gao, T. Seyller, L. Ley, F. Ciobanu, G. Pensl, A. Taddich, J. D. Riley, and R. G. C. Leckey, Appl. Phys. Lett. **83**, 1830 (2003).
[6] N. Sieber, T. Seyller, B. F. Mantel, J. Ristein, and L. Ley, Mater. Sci. Forum **353-356**, 223 (2001).
[7] N. Sieber, T. Seyller, L. Ley, D. James, J. D. Riley, R. G. C. Leckey, and M. Polcik, Phys. Rev. B **67**, 205304 (2003).

EXAFS and XANES studies of polycrystalline $LiCoO_2$ thin films

D.Ensling[a], F.J.Fernandez-Madrigal[a], R.Hunger[a], C.Pettenkofer[b], A.Thißen[a], W.Jaegermann[a]

Fachbereich Materialwissenschaften - Oberflächenforschung der TU Darmstadt [a]
Hahn-Meitner-Institut, Abteilung SE6, Berlin [b]

Transition metal oxides with layered crystal structures like V_2O_5, $LiCoO_2$, $LiNiO_2$, $LiCo_xNi_{1-x}O_2$ and $LiMn_2O_4$ can be used as cathode materials in thin film Na- or Li-intercalation batteries. In an all-solid-state device the thin film cathode is deposited onto a thin film solid electrolyte that had been deposited before onto the anode material. The battery can be charged by an external voltage, leading to deintercalation of the alkaline metals from the cathode, transport through the ionic conducting electrolyte and insertion into the anode material. The discharge process leads to an intercalation of alkaline metal ions into the transition metal oxides. The electrochemical data of the cell are mostly determined by the change of the electronic structure of the cathode material during intercalation or deintercalation. For materials with complicated electronic structures like transition metal oxides these changes can not be described by a simple filling of rigid bands by electrons. Therefore, the valence band structure has been studied by Resonant Photoemission (ResPES) in an earlier work [1].

In this study x-ray absorption fine structure spectroscopy (EXAFS, XANES) has been carried out at the U49/II PGM2 beamline using the PHOIBOS electron analyser of the integrated Solid-Liquid-Analysis System (SoLiAS) at a fixed kinetic energy around 11eV detecting the secondary electrons giving an equivalent to the total photoelectron yield. Data analysis has been done using the FEFF program package. Polycrystalline $LiCoO_2$ thin film samples have been prepared by RF magnetron sputter deposition from a ceramic $LiCoO_2$ target on oxidized Si(111) substrates. Fig. 1 shows a survey XAF spectrum of a well ordered $LiCoO_2$ film in the energy range of $h\nu$=450…1250eV, indicating the XANES and EXAFS regimes of the O-K- and Co-L_{32}-edge. The EXAFS region of the O-K-edge has been carefully analysed by FEFF. In Fig. 2a a comparison of the Fourier transform of the EXAF spectrum (red line) and the radial distribution function from the FEFF analysis (blue line) is shown. The interatomic distances are well reproduced and give the correct values for the first 3 coordination shells. The deviation can be explained by the structure model, not including Co-Li interchange in the metal ion layers of the material. In Fig. 2b the XANES region of the O-K-edge is shown for films deposited at different substrate temperatures. The sharpening of the absorption features with increasing substrate temperatures indicates the increase of the structural ordering of the films. For sample S6, deposited at T_{sub}=440°C the partial local density of unoccupied states has been calculated from the spectrum using FEFF (Fig. 2c). While the lower energy states show mainly p-character the higher energy states are clearly d-type. Fig. 3a shows Co-L_{32}-edge XANE spectra of those $LiCoO_2$ films. With higher ordering of the films (e.g. higher substrate temperatures) the high energy shoulder gets more prominent. Due to the spin-orbit splitting of the L-edge and the energetic superposition of the 3/2 and 1/2 absorption a detailed analysis with FEFF in respect to short range order and LDOS of the unoccupied states is complicated. But ligand field multiplet anaylsis (Fig. 3b) of the $3d^6(^1A_1) \rightarrow 2p^5 3d^7$ transition (Co-L-edge) indicates the low spin state of the trivalent Co ions. The imperfection of the theoretical and experimental data is due to the occurrence of charge transfer effects in the ground state giving an overall transition reaction of $3d^6[^1A_1] + 3d^7[^2E]L(e) \rightarrow 2p^5 3d^7 + 2p^5 3d^8 L$ [2]. The resulting energy diagram of the valence states of $LiCoO_2$ (Fig. 3c) has already been discussed in literature [2].

Acknowledgement:
This work was supported by the DFG (SFB595) and the BMBF.

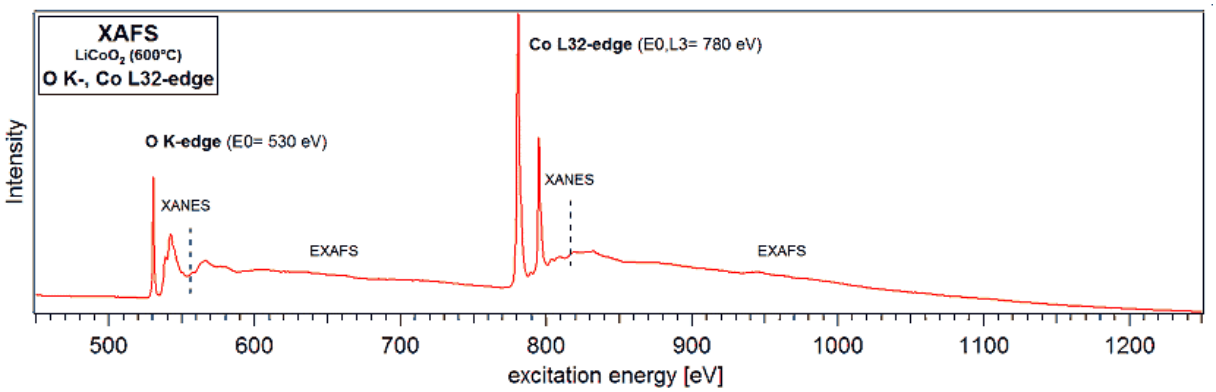

Figure 1: *XAFS O-K- and Co-L_{32}-edge survey spectrum of a thin polycrystalline $LiCoO_2$ film.*

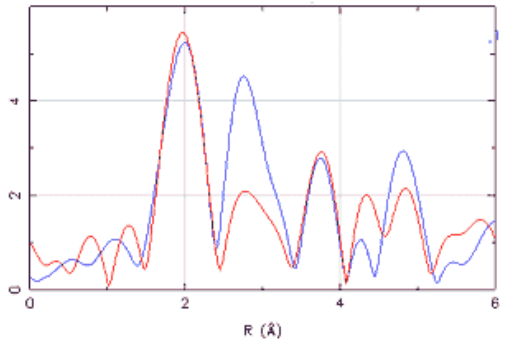

Figure 2a: *FEFF atomic distance analysis*

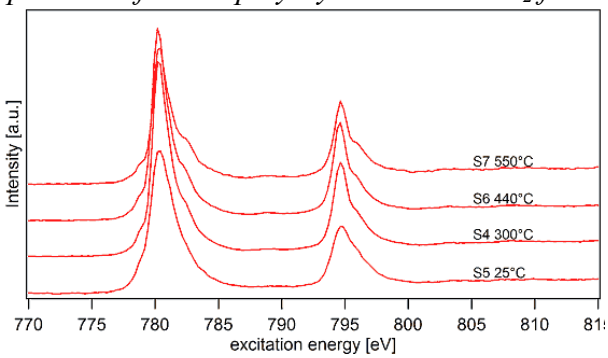

Figure 3a: *XANES data of Co-L_{32}-edge*

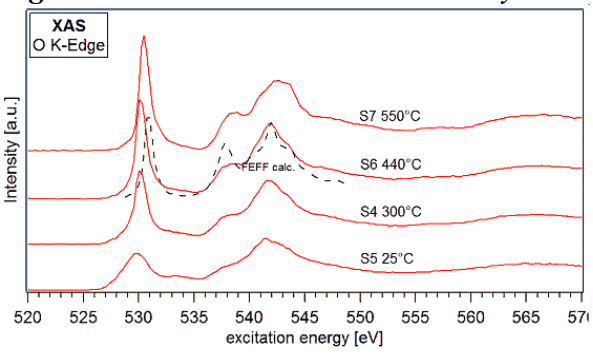

Figure 2b: *XANES data of O-K-edge*

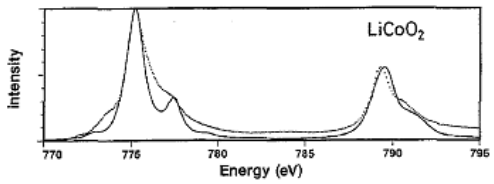

Figure 3b: *Co-L-edge data from [2]*

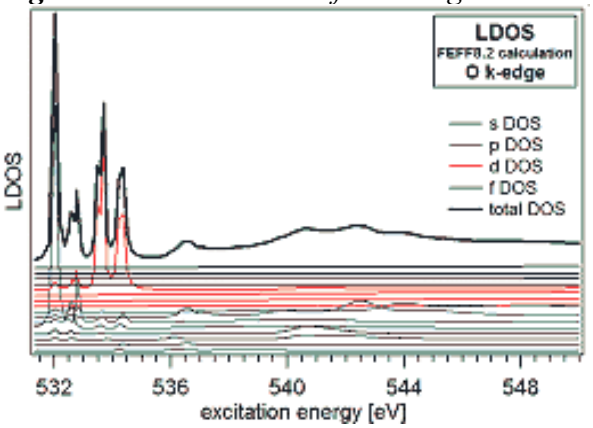

Figure 2c: *LDOS calculated from NEXAFS*

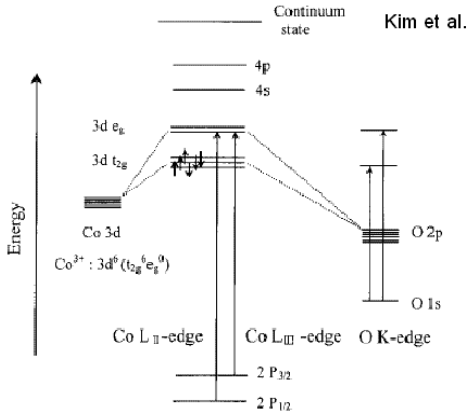

Figure 3c: *$LiCoO_2$ valence states [3]*

References:

[1] Ensling, Fernandez, Hunger, Pettenkofer, Thißen, Jaegermann, BESSY Ann. Rep. 2003
[2] de Groot, Abbate, van Elp, Sawatzky, Ma, Chen, Sette, J. Phys. Cond. Mat. 5 (1993) 2277
[3] Yoon, Kim, Kim, Lee, Shin, Lee, Lee, Yo, J. Phys. Chem. B106 (2002) 2526

Interface-formation of Ag with a GaSe van der Waals terminated Si(111)-surface – morphology and electronic properties

B. Jaeckel, R. Fritsche, A. Klein and W. Jaegermann
Materials Science - Surface Science Division
Petersenstr. 23, 64287 Darmstadt

The hetero-interface formation on silicon, as the base material in microelectronics, is an ongoing research subject in semiconductor science and technology. The use of buffer and passivation-layers is also important for controlling surface reactions and growth morphology. A GaSe passivation layer is used in this study as passivation layer, which provides a van der Waals type surface and saturates all dangling bonds of the Si(111)-surface. This results in nearly flatband conditions for the bare GaSe:Si(111) surface [1,2].
We use this passivated surface as substrate to study the interface formation and its properties with metals as e. g. silver. For that reason Ag was deposited in an homemade MBE-chamber on the Si-substrate hold at room-temperature. The SXPS investigations were performed at BESSY II-TGM-7–SoLiAS. In Darmstadt the STM and LEED measurements were made at DAISY-FUN.
In Figure 1 the STM and LEED results are presented. Ag nucleates at step-edges preferentially. The first islands are 3-5nm in height with a plane top-layer. With increasing amount of Ag on the surface the islands grow mostly in lateral size. The height remains nearly constant and flat terraces are formed on top of the Ag-islands which are orientated towards (111), parallel to the Si(111):GaSe surface. As follows from the LEED-pattern the Ag-film epitaxially grows on the GaSe:Si(111)-surface. At the end a Ag(111) surface is formed containing large flat areas, but also deep canyons as presented in Fig. 1 in the right image. The formation of (111) orientated islands can be understood by looking at surface energies of the possibly involved planes. For Ag (fcc: a=b=c=4,09Å) the surface energies of (111) and (110)-planes are 0.55 and 0.65eV/atom respectively [3]. This should lead to triangular and hexagonal islands. These shapes are not visible so well, but at some islands these orientations can be seen (marked in Fig. 1). The STM-images and LEED-pattern also show the formation of an epitaxial Ag(111)-film onto the GaSe:Si(111) substrate, at very high coverages (depostion time higher then 6h).

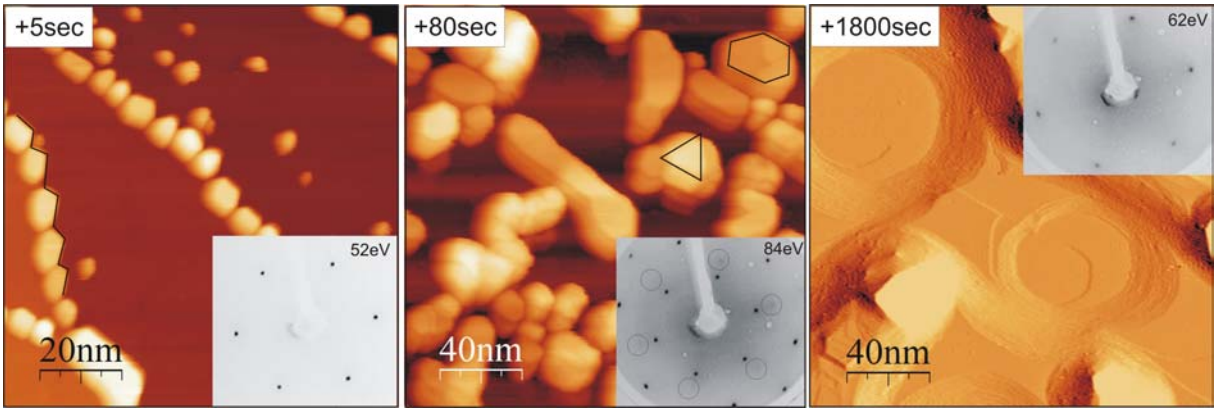

Figure 1: STM-images (U_{tip}=+2V) during the interface formation process of Ag with the GaSe:Si(111)-surface.

The electronic-properties of the interface to the Ag-film are studied with synchrotron induced XPS with a photon-energy of 80eV. A study of the core-levels and of valence-bands is performed. The measured spectra are given in Figure 2a-2c. In the beginning a strong energy-shift could be observed in all substrate emissions. The emissions show only one component during the Ag deposition. Therefore an interface reaction can be excluded. This fact is confirmed by the observations during an annealing step. A closed Ag-layers is heated up to

300°C and after the heating step the GaSe passivated surface was measurable again. This observeration points out that no interface reaction has taken place under the islands during the deposition and annealing (T≈300°C). Another feature in the spectra which confirm the stability of the GaSe passivation-layer is the presence of the Se p_z-states in the valence band at 2.5eV binding energy. Here the shift due to the band bending is also visible. So the valenceband remains and is not modified by the Ag-layer due to an interface-reaction.
The Ag 4d valence-band-signal increases rapidly, whereas the substrate emissions decrease (see Fig. 2d). No steps are visible in the intensity-plot indicating a homogeneous Ag-cluster growth onto the GaSe:Si(111) surface. A closer look to the Fermi-energy show a small photovoltage, induced by the synchrotron light. For the calculation of the distance valence-band-maximum (VBM) to the Fermi-level (E_{VBM}-E_F) this photovoltage must be taken into account. E_{VBM}-E_F is calculated from the Se3d and Ga3d-core levels using literature-values for the differences Se3d-VBM (54.04eV) and Ga3d-VBM (19.21eV) and is shown in Fig.2d. A Schottky-barrier $\Phi_{B,p}$ of 0.83eV is formed for a p-type Si(111)-sample. Similar results can be achived by using a n-type Si-substrate.

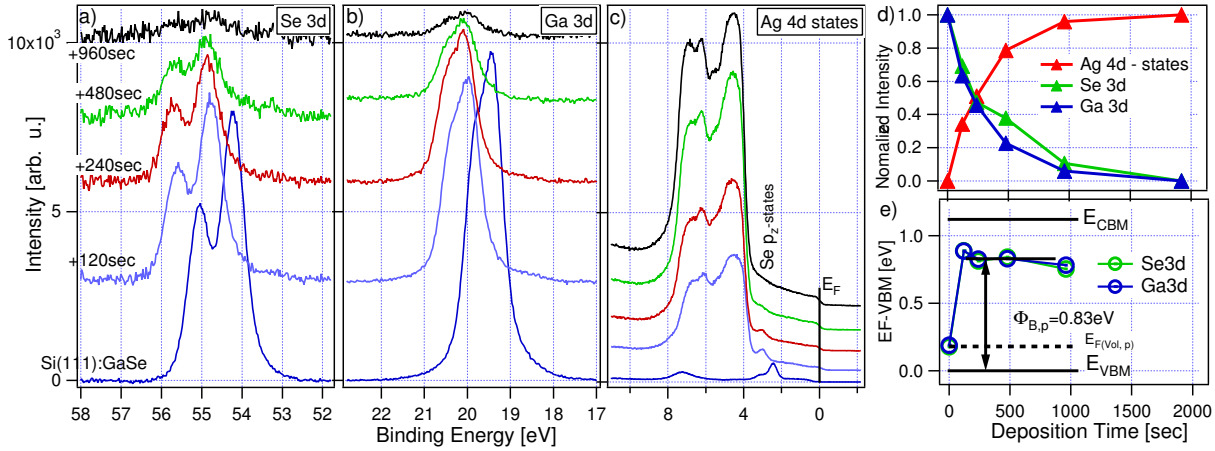

Figure 2: SXPS measurements with hν=80eV during the stepwise deposition of Ag onto the GaSe passivated Si(111) surface. Se 3d (a), Ga 3d (b) and Ag 4d states (c) are given representing the substrate and the growing film; normalized intensities (d) and the shift of the Fermi-level in the band-gap (e) are given.

A comparision of the measured barrier-height with literature-values [4] show a modification of about 500meV. In contrast the deposition of Au onto the GaSe:Si(111) surface leads to no modification of the barrier-height [5]. During the deposition of gold an interface reactions takes place forming an alloy (Au-Ga), selenide (Au-Se) and a silicide (Au-Si). During the deposition of Ag no indication of any kind of reaction were detected. This leads to the conclusion that the Schottky-barrier (Si-metal) can be dramatically modified with the GaSe half-sheet when the passivation layer is stable.
In summary SXPS, STM and LEED-measurements were performed to investigate the electronic properties as well as the morphology of a growing Ag-film onto a GaSe passivated Si(111)-surface. We have shown the the Schottky-barrier is modified by 500meV by inserting the GaSe half-sheet. During the growth no interface reactions takes place between the orientated growing Ag(111)-film onto the GaSe:Si(111)-surface.

[1] R. Fritsche et al., Appl. Phys. Lett. 80, 1388 (2002).
[2] R. Fritsche et al., Surface Science 515, 296 (2002).
[3] L. Vitos et al., Surface Science 411, 186 (1998).
[4] W. Mönch, *Electronic Properties of Semiconductor Interfaces*, Springer Verlag, Heidelberg, 2004
[5] R. Fritsche et al., Appl. Surf. Sci. 234, 321 (2004)

Interaction of Fe atoms with Si(100)2×1 surface

M.V.Gomoyunova [1], I.I.Pronin [1], D.E.Malygin [1], S.M.Soloviev [1], D.V.Vyalikh [2], S.L.Molodtsov [2]

[1] A.F.Ioffe Physico-Technical Institute, 194021, St.Petersburg, Russia
[2] Institut für Oberflächenphysik und Mikrostrukturphysik Fachrichtung Physik Technische Universität Dresden, D-01062 Dresden, Germany

The interaction of Fe atoms with single crystalline silicon is of great fundamental and technological interest due to potentialities of the epitaxial layers of β-$FeSi_2$ in silicon-integrated optoelectronic devices. The initial stages of the process reveal rather complex behavior even at room temperature, and the problem is still under discussion [1-5]. The aim of the present work was to study the interaction using high-resolution photoelectron spectroscopy with synchrotron radiation.

The experiments were carried out in vacuum ~5×10^{-11} mBar using the beams with the energy of 110÷540 eV. The overall energy resolution of the electron energy analyser and the monochromator was 130 meV. The substrates used were Si(100) wafers with a misorientation of less than 0.1°. Before introduction into UHV they were prepared by wet chemical treatment according to the method of Shiraki [6]. For final preparation, the samples were flashed up to 1200°C and cooled slowly, that ensured the sharp 2×1 LEED pattern and the absence of C and O contaminations. Iron was deposited from an electron bombardment evaporator at a rate of ~ 1 ML/min. Ultrathin Fe layers of increasing thickness up to 6 ML were deposited onto the clean silicon surface at room temperature and the sets of Si 2p and valence-band spectra were taken after each deposition. The spectra were recorded in a wide solid angle oriented around the normal to the surface of the sample. The Si 2p spectra were measured at two photon energies (hν = 130 eV and 112 eV) to ensure the highest surface and bulk sensitivity respectively.

The results obtained are illustrated in Fig.1 and 2. The Si 2p spectrum of the Si(100)2x1 surface reveals at the energy of 130 eV the well-known spin orbit splitting of the $2p_{1/2}$ and $2p_{3/2}$ levels and the shoulder at higher kinetic energy associated with the upper atoms in asymmetric dimers of the reconstructed surface. Deposition of 0.5 ML of Fe results in disappearance of the shoulder. As in the case of the Co/Si(100)2x1 system [7] this fact is the evidence for the loss of the initial reconstruction due to adsorption of Fe. Further deposition of iron gives rise to both the energy shift of the spectra to higher kinetic energy and the remarkable change of their line shape. Considerable modification of the valence-band spectra is observed during Fe deposition as well (Fig. 2). At Fe doses ≤ 1 ML the main effect manifests itself in gradual weakening and disappearance of the features typical to the substrate. Simultaneously a new peak arises at binding energy of 0.6 eV. At greater Fe doses the peak becomes dominant in the spectra and its shape is very similar to the Fe 3d spectrum of the clean iron sample. After deposition of 6 ML the valence band spectrum changes considerably again and becomes similar to the reference spectrum of Fe_3Si.

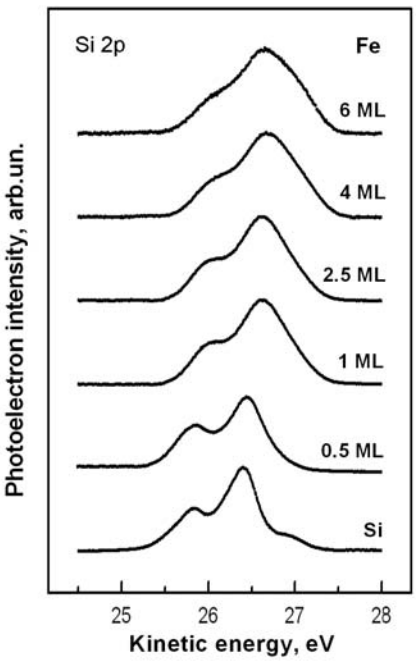

Fig. 1

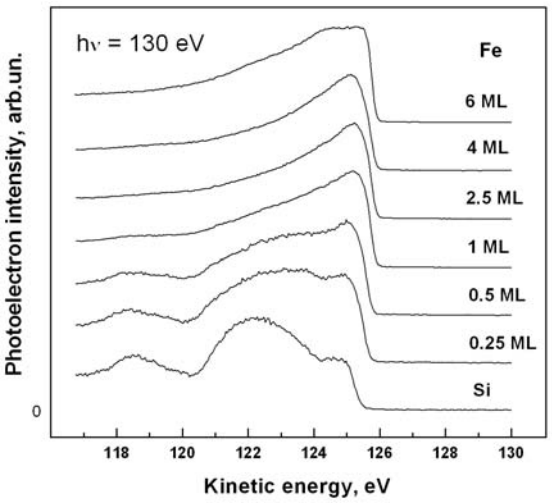

Fig. 2

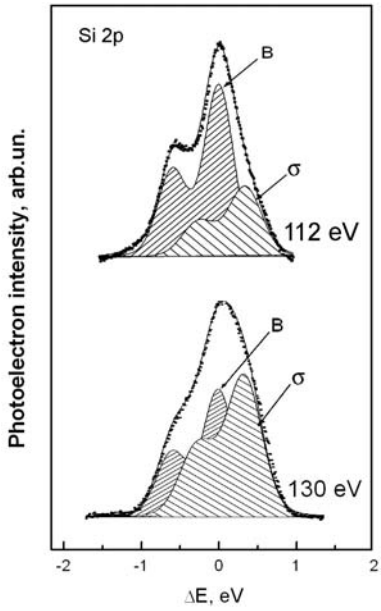

Fig. 3

To obtain the more detailed information about atomic processes under investigation, Si 2p spectra were decomposed into their elementary spectral modes. It was found, that all of them can be considered as a superposition of two components: the bulk mode B, which decreases with the growth of the coverage, and a new mode σ with a negative energy shift of – 0.32 eV, which on the contrary increases with the coverage and becomes greater than the mode B after deposition of 6 ML of Fe at hν=130 eV. As it follows from comparison of the surface- and bulk-sensitive spectra shown in Fig. 3 for the dose of 6 ML, Si atoms responsible for the mode σ are localized in the near-surface region. This is the evidence for intermixing of Fe and Si atoms at the Fe/Si interface and clearly demonstrates the reactive nature of the interface at room temperature. The mentioned large contribution of Fe 3d-states in valence electron emission from the sample with deposited 2.5 ÷ 4 ML of Fe allows us to consider the phase characterized by mode σ as a Fe-Si solid solution. The conclusion is supported by the fact, that the energy shift of the mode σ is very close to that for Co-Si solid solution [7]. At coverages higher than ~ 5 ML the Fe_3Si silicide is formed in the system as it follows from valence band spectra. Thus, the process of silicide formation requires a critical Fe dose at room temperature.

The work was supported by RFBR (grant № 04-02-17651) and the Russian-German laboratory at BESSY II.

References

1. J. Alvarez, J.J. Hinarejos, E.G. Michel et al. Surf. Sci. **251/252**, 59 (1991).
2. J. Alvarez, J.J. Hinarejos, E.G. Michel et al. Phys. Rev. B. **45**, 14042 (1992).
3. R.K. Kläsges, C. Carbone, W. Everhardt et al. Phys. Rev. B. **56**, 10801 (1997).
4. P. Bertoncini, P. Wetzel, D. Berling et al. Phys. Rev. B. **60**, 11123 (1997).
5. M. Hasegama, N. Kobayeshi, N.Hayashi et al. Surf. Sci. **357-358**, 931 (1996).
6. A. Ishizaka and Y. Shiraki. J. Electrochim. Soc. **133**, 666 (1986).
7. M.V. Gonoyunova, I.I. Pronin, N.R.Gall et al. Physics of the Solid State **45**, 1596 (2003).

O-K-edge shift at the Verwey transition of magnetite

E. Goering, S. Gold, M. Lafkioti, and G. Schütz
Max-Planck-Institut für Metallforschung, Heisenbergstrasse 3, 70569 Stuttgart, Germany

The temperature dependence of the X-ray absorption O K-edge threshold has been investigated along the Verwey transition of magnetite. A very small energy shift of 13meV has been found, in accordance with a more continuous shift above and below the transition temperature. A comparison of our results to published low and high energy photoemission experiments clearly exhibit the presence of an asymmetric gap shift. This explains remaining differences between photoemission and infrared derived gap energies, and supports the polaronic picture of the electrical conductivity of Fe_3O_4 above the Verwey transition temperature.

Magnetite (Fe_3O_4), which has been investigated since the last 2000 years, has recently attracted enormous interest. This is clearly related to its proposed half metallic behavior and a corresponding spin polarization at the Fermi level of 100% [1,2]. This transforms Fe_3O_4 into a promising candidate for spintronic applications [3,4]. Fe_3O_4 crystallizes at room temperature in the antiferromagnetic cubic inverse spinel structure ($Fd\bar{3}m$), formally written as Fe(A) Fe(B)$_2$O$_4$ [5,6]. The first *A*-type ions are tetrahedrally coordinated, while the *B*-site ions are located on octahedral sites. The *A* cations are nominally in a Fe^{3+} configuration, while the *B*-site cations have a mixed valence with equal distributed Fe^{3+} and Fe^{2+} ions. The magnetic moments of the *A* and *B* sites are aligned antiparallel to each other with a resulting magnetization per formula unit of 4.07μ_B [7]. At $T_V \approx 123$K Magnetite exhibits a first order phase transition, called "Verwey-transition" [8-10], with a jump in the electrical conductivity of about two orders of magnitude (see [11]and [12] and references therein). Verwey has explained this behavior by charge localization-delocalization of the conducting *B*-site electrons. Only recently an average charge of 2.5 has been observed at the *B*-site, with a charge ordering below T_V. This has been confirmed by recent theoretical band structure calculations [13,14]. Photoemission spectroscopy (PES) experiments have been performed above and below the Verwey transition, to verify the metallic behavior and higher temperatures and to observe variations near the chemical potential. Chainani et al. [15] and J. H. Park et al. [16] recognized a shift in energy, but nearly no spectral weight at the chemical potential has been found (near T_V). More recently a shift in energy of about 50meV has been found at T_V [17], where the energy position exhibits a clear jump at T_V and an additional continuous shift as a function of temperature [17]. From the photoemission data full energy gaps of 200meV ($T<T_V$) and 300meV ($T>T_V$) have been estimated, assuming a gap center position of the chemical potential [16]. This is in contrast to the infrared derived optical gap information, which suggest a full gap of about 140meV below T_V [18,19].

In this report we show high resolution X-ray absorption results at the O K-edge of magnetite, monitoring the unoccupied part of the band structure. We found a much smaller gap variation during the Verwey transition compared to the reported PES results. This suggests an asymmetric gap formation, which explains the discrepancies between IR and PES results.

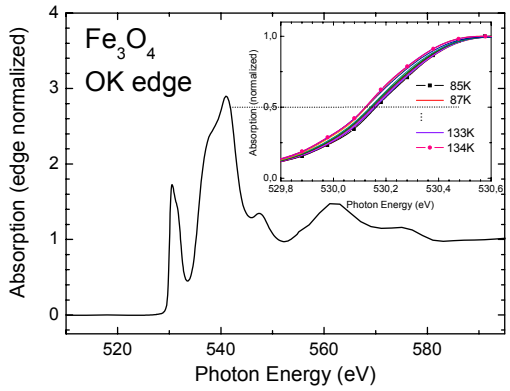

Figure 1: X-ray absorption spectrum at the O K edge of Fe_3O_4 (T=300K). Inset: Temperature dependence of the O K edge pre edge in the vicinity of the Verwey transition temperature region.

O-K edge spectra of a non magnetized high quality synthetic single crystalline sample were recorded in total electron yield mode (TEY) at the improved bending-magnet-beamline PM III at BESSY II with an energy resolution of about E/ΔE = 6000, utilizing circular polarized light. The sample has been cleaved at room temperature and in situ in UHV conditions. The ambient pressure during the measurement was better than $8*10^{-10}$ mBar. To prevent small possible energy variations related to synchrotron beam shifts, all spectra have been taken at the end of a single injection run. The step width and temperature slope have been chosen to obtain the best compromise between thermalization, necessary measurement time, and beam intensity variations.

Figure 1 shows the room temperature (RT) O K edge spectrum of the freshly cleaved Fe_3O_4 single crystal. The shape of the spectrum is in excellent agreement to previously published X-ray absorption data [16,20,21], where the "pre-edge" region between 528-534eV has been identified to O 2p states, which are strongly hybridized with unoccupied Fe 3d t_{2g}- and e_g- orbitals. The observable splitting originated by a mixture of crystal field splitting and the different chemical environment of *A* and *B* site Fe ions [21]. The features at higher energies are related to transitions into O 2p states hybridized with O 4s and 4p states (534-550eV).

The inset in Fig.1 shows the background subtracted and peak-height-normalized region of the O K edge pre-edge as a function of the sample temperature. A continuous shift of the near threshold region from 85K up to the 120K is observable, followed by a step like jump to lower excitation energies. We would like to emphasize that these shifts are only visible in this expanded view. To quantify this variation the half height position of the shown spline-extrapolated curves have been extracted and plotted in Fig. 2 as a function of temperature. The continuous regime is characterized by a linear variation of about 20meV. Between 120k and 125K a clear step of about 13meV width is observable, followed again by a linear variation. In the whole temperature range from 85-134k the half height position is shifted by 40meV. We could reproduce gap shifts in other separated injection runs.

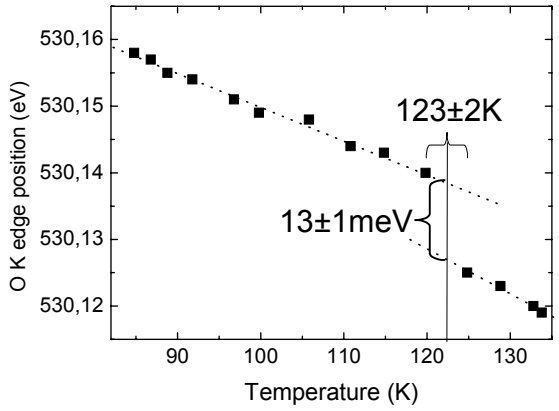

Figure 2: Temperature dependency of the half height position of the O K edge threshold, extracted from Fig. 1.

To verify this behavior, we have performed SQUID measurements (not shown). The related Verwey transition temperature was clearly observable at 123.7K, which is located at the same temperature of the energy position jump in Fig. 2. This demonstrates that the observed position shift is indeed related to the Verwey transition.

Comparing these results to the photoemission data demonstrates that the energy position variation of the conduction band states is much smaller as monitored by PES spectroscopy for the occupied states. If we compare our XAS shifts with the PES results corresponding to a similar sampling depth (from [17]) we found that the jump at T_V and the total shift in a wider temperature range are both reduced in XAS by the same factor of about 4-5.

This asymmetry suggests a pinning of the chemical potential more close to the conduction band, and a non-symmetric variation due to the Verwey transition. We would like to mention, that this behavior could also be explained (in principle) by strong modifications of the O K edge core hole screening behavior of the conduction electrons, but from our knowledge, this has not been reported so far. Comparable systems exhibiting even stronger metal to insulator transitions, for example VO_2, have shown comparable shifts of the occupied (PES [22]) and unoccupied states (O K edge [23]). If one assumes that the reduction is in fact related to differences in the core-hole screening behavior one would expect stronger screening variations at the Verwey transition, due to changed conductivity, but as mentioned above a similar reduced energy shift has been observed over the whole temperature range. Therefore, we believe that the observed asymmetric behavior is truly originated by an anisotropic gap shift.

XAS is not absolute in energy, related to the chemical potential, and no absolute gap could be determined. But the observations discussed above suggest an asymmetry of the gap. If we add the difference in the energy positions from XAS (13meV) and PES (50meV) a total gap change of 65±10meV could be estimated. This can explain present gap inconsistencies mentioned by Gasparov et al. [18].

In conclusion, we have investigated a Verwey transition related very small energy shift of 13meV at the O K edge of Fe_3O_4. This shift is much smaller, compared to photoemission results, and suggests the presence of an asymmetric gap present in magnetite.

We want to thank V.A.M. Brabers for supply of the excellent Fe_3O_4 single crystal, and T. Kachel and D. Herrendörfer for the excellent support at BESSY II. In addition, we thank the Max-Planck-Society for financial support of this project.

References

1. A. Yanase and K. Siratori, J.Phys.Soc.Jpn. **53**, 312 (1984).
2. Ze. Zhang and S. Satpathy, Phys.Rev.B **44**, 13319 (1991).
3. J. M. D. Coey, J. J. Versluijs, and M. Venkatesan, J.Phys.D: Appl.Phys. **35**, 2457 (2002).
4. J. M. D. Coey and C. L. Chien, Mrs Bulletin **28**, 720 (2003).
5. J. P. Wright, J. P. Attfield, and P. G. Radaelli, Phys.Rev.Lett. **87** (2001).
6. J. P. Wright, J. P. Attfield, and P. G. Radaelli, Phys.Rev.B **66** (2002).
7. P. Weiss and R. Forrer, Ann.Phys. **12**, 279 (1929).
8. E. J. W. Verwey, Nature **144**, 327 (1939).
9. E. J. W. Verwey and P. W. Haayman, Physica **8**, 979 (1941).
10. E. J. W. Verwey, P. W. Haayman, and F. C. Romeijn, J.Chem.Phys. **15**, 181 (1947).
11. J. Garcia and G. Subias, J.Phys.: Condens.Matter **16**, R145 (2004).
12. F. Walz, J.Phys.: Condens.Matter **14**, R285 (2002).
13. H. T. Jeng, G. Y. Guo, and D. J. Huang, Phys.Rev.Lett. **93** (2004).
14. I. Leonov *et al.*, Phys.Rev.Lett. **93** (2004).
15. A. Chainani *et al.*, Phys.Rev.B **51**, 17976 (1995).
16. J. H. Park *et al.*, Phys.Rev.B **55**, 12813 (1997).
17. D. Schrupp *et al.*, cond-mat , /0405623 (2004).
18. L. V. Gasparov *et al.*, Phys.Rev.B **62**, 7939 (2000).
19. S. K. Park, T. Ishikawa, and Y. Tokura, Phys.Rev.B **58**, 3717 (1998).
20. Y. Ma *et al.*, Phys.Rev.B **48**, 2109 (1993).
21. Z. Y. Wu *et al.*, Phys.Rev.B **55**, 2570 (1997).
22. E. Goering *et al.*, Phys.Rev.B **55**, 4225 (1997).
23. O. Müller *et al.*, J.Phys.IV **7**, 533 (1997).

Orientation of Perfluorinated Phthalocyanines: from Ultra-low Coverages on Hydrogen Passivated Silicon to Thick Layers

M. Gorgoi, G. Gavrila, D.R.T.Zahn

Institut für Physik, Technische Universität Chemnitz, D-09107 Chemnitz, Germany

W. Michaelis

IAPC, Universität Bremen, D-28334 Bremen, Germany

D. Schlettwein

Institut für Angewandte Physik, Justus-Liebig-Universität Gießen, D-35392 Gießen, Germany

W. Braun

BESSY GmbH, Albert-Einstein-Str. 15, D-12489 Berlin, Germany

Hybrid devices such as organic light emitting diodes, solar cells or thin film transistors, based on phthalocyanine (Pc) materials and silicon receive special attention nowadays. Pcs have a tendency to form ordered layers, however the growth mode may vary significantly on different substrates [1]. Moreover the first layers near the interface seem to have a structure distinct from the thick films. Consequently the present work was directed towards determining the molecular orientation of phthalocyanine monolayers and thin films using polarization dependent X-ray absorption spectroscopy. The organic materials involved are the copper phthalocyanine (CuPc) and its fluorine derivatives: F_4CuPc and F_{16}CuPc. Hydrogen passivated p-type (111) oriented silicon provided by Siltronic AG with a doping concentration of approximately $1.5x10^{15}$ cm^{-3} was used as the substrate. The passivation process consists of a wet chemical etching in a solution containing HF 40%. After the passivation process the samples were transferred into UHV. All measurements were performed on freshly evaporated organic layers. Their thickness was monitored by a quartz microbalance. The experiments were performed on the MUSTANG spectroscopy chamber at the Russian-German beamline at BESSY II. The NEXAFS spectra were acquired with a PHOIBOS 150 (SPECS) analyzer. The N1s NEXAFS raw data were divided by the spectra of the H-Si(111), background was subtracted and normalized to the absorption step at 425eV photon energy. A series of NEXAFS measurements were performed as a function of thickness and angle of incidence of the synchrotron radiation.

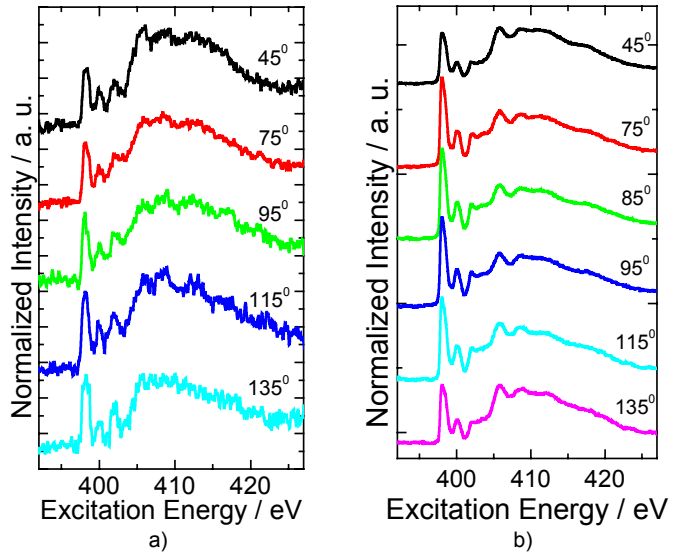

Figure 1. N1s excitation spectra of CuPc 2 monolayers a) and CuPc 20 nm b) as a function of θ the angle of incidence; The lower energy features (398-403 eV) represent the π* resonances, whereas those features above 403 eV are related to the σ* resonances.

Figure 1 displays the CuPc N1s excitation spectra for 2 monolayers a) and 20 nm thickness b) as a function of the angle of incidence θ (normal incidence θ = 90^0) of the synchrotron radiation. The intensity of the π* (relative to the σ^* one) resonances has a maximum at θ=135^0 Fig. 1 a) and θ=85^0 Fig.1 b). However, the intensity and features of σ^* resonance are still visible at the given incidence

angles. This suggests the presence of short range ordering in both cases. This behaviour is similar to F_4CuPc but opposite of F_{16}CuPc which is rather well ordered.

The quantitative analysis of the NEXAFS excitation spectra for CuPc, F_4CuPc and F_{16}CuPc is provided in figure 2. Figure 2 exhibits the normalized resonance intensity of the π^* orbitals as a function of the incidence angle of the synchrotron radiation for the three phthalocyanines. The normalized resonance intensity of the π^* orbitals is fitted [2] and the average tilt-angle for each case is calculated. The 3-fold symmetry of the silicon substrate is lifted by the surface roughness and as a consequence the model used for the fit contains an azimuthal dependence as well.

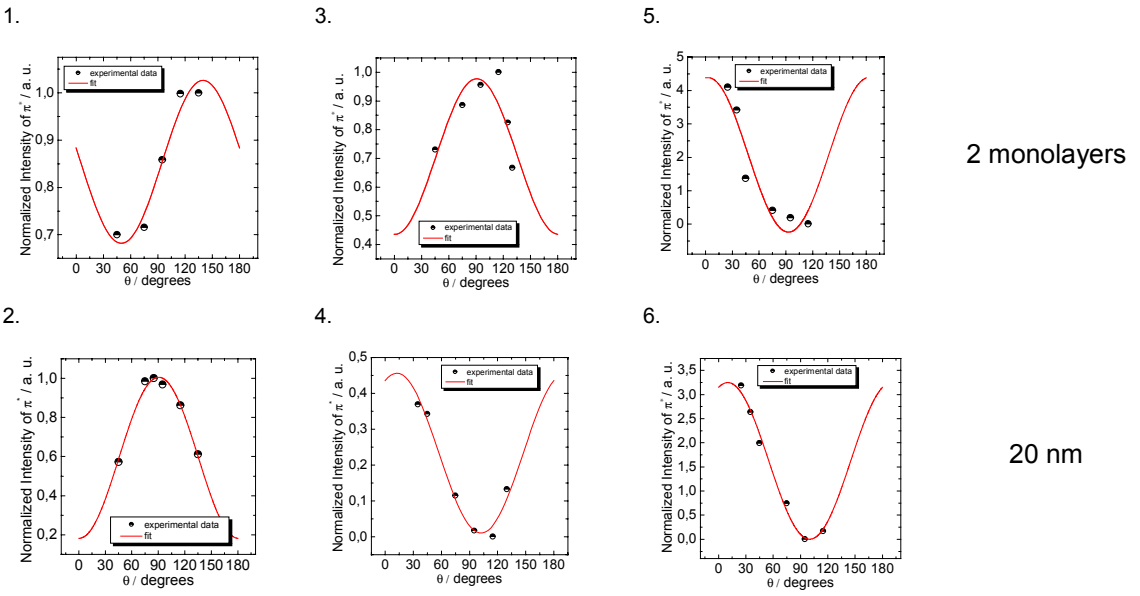

Figure 2. Normalized resonance intensity of the π^* orbitals as a function of the incidence angle θ of the synchrotron radiation – experimental data and fit.

Table 1 summarises the results in terms of tilt angles α and azimuthal angles Φ obtained from the fits as well as the average orientation of the molecules. While CuPc and F_4CuPc behave in a similar way in terms of adsorbate geometry with a tilt-angle of the molecular plane higher than 50^0, the F_{16}CuPc molecule behaves differently. Regarding the two measured thicknesses it is important to point out the different molecular orientations found in 2 monolayers and in a thin film of 20 nm for each phthalocyanine. This finding confirms previous results for CuPc [3] and represents a new step in describing the F_4CuPc and F_{16}CuPc molecules.

Table 1. Determined molecular orientation

	CuPc	F_4CuPc	F_{16}CuPc
2 ML	**$\alpha=70^0\pm2^0$** **$\Phi=108^0\pm3^0$** tilted	**$\alpha=90^0\pm3^0$** **$\Phi=55^0\pm5^0$** standing	**$\alpha=26^0\pm2^0$** **$\Phi=84^0\pm5^0$** almost lying
20 nm	**$\alpha=90^0\pm1^0$** **$\Phi=45^0\pm2^0$** standing	**$\alpha=60^0\pm2^0$** **$\Phi=82^0\pm4^0$** tilted	**$\alpha=10^0\pm2^\circ$** **$\Phi=0^\circ\pm0.3^\circ$** lying

The authors acknowledge the BMBF (FK MUSTANG 05KS40C1/3, OS ES3XBA/5) for the financial support and Mike Sperling for his assistance during the beam time.

References

[1] H. Peisert, T. Schwieger, J. M. Auerhammer, M. Knupfer, M. S. Golden, J. Fink, P. R. Bressler M. Mast, J. Appl. Phys. 90 (2001) 466;

[2] J. Stöhr, NEXAFS Spectroscopy, Surface Science Series, Springer, 1996.

[3] K. K. Okudaira, S. Hasegawa, H. Ishii, K. Seki, Y. Harada, N. Ueno, J. Appl. Phys. 85 (1999) 6453;

Absolute oscillator strength measurements for electron transitions in N 1*s* absorption spectrum of solid $NaNO_3$

V.N. Sivkov[a], A.S. Vinogradov[b], S.B. Nekipelov[a], D.V. Sivkov[a], D.V. Vyalikh[b,c], S.L. Molodtsov[b,c,d]

[a] Syktyvkar State University, Syktyvkar 167001, Russia; [b] V.A. Fock Institute of Physics, St.Petersburg State University, St.Petersburg 198504, Russia; [c]Russian-German Laboratory at BESSY,D-12489 Berlin-Adlershof, Germany; [d]Institut für Festkörperphysik, Tehnische Universität Dresden, D-01062 Dresden, Germany.

The complete distribution of dipole oscillator strength of a polyatomic system over the entire spectral range is very important from many points of view, both basic and applied. This distribution characterizes most of the ordinary optical properties related to absorption, refraction, dispersion, and reflection [1]. It governs interactions of the system with a charged particle or with another polyatomic system and is also highly pertinent to the inelastic collisions of fast charged particles with the polyatomic system [2]. A wealth of information contained in the complete oscillator strength distribution is commonly accessed through the sum rules which relate the distribution moments to various physical properties [1,2]. Among the complete distribution, the oscillator strengths for individual electron transitions are of considerable fundamental and practical interest since they characterize quantitatively the interaction processes of photons or particles of certain energy with matter and allow one to test results of theoretical calculations.

In the past two decades great experimental progress has been achieved in the field of soft-x-ray absorption spectroscopy and x-ray absorption near-edge spectra came into wide use to determine local electron structure and chemical environment of an absorbing atom [3,4]. In these spectra core excitations which are strongly localized within small polyatomic groups (an absorbing atom along with nearest-neighbor atoms) are of most interest because a number of these excitations (also known as "shape resonances") as well as their relative intensities, symmetry and energy positions characterize properties of unoccupied electron states and geometrical structure of the above polyatomic groups. At the same time, no consideration is commonly given to absolute transition intensities (oscillator strengths) which are also very useful spectroscopic parameters not only for the similar structure investigations, but for new experimental techniques such as resonant photoemission and resonant fluorescence.

The lack of information about oscillator for core electron transitions in polyatomic systems is caused by the fact that direct measurements of photoabsorption cross sections (oscillator strengths) over soft-x-ray range present considerable experimental difficulties. Long-wave stray radiation and short-wave higher-order light from monochromator gratings normally hinder direct transmission measurements of absolute cross sections. Measurements near the 1*s* absorption edges of C, N, and O ($h\nu$~250 – 600 eV) are particularly difficult on soft-x-ray beamlines, since there are significant second- and third-order components and contaminations on optical elements can introduce additional structures. To make absolute cross-section measurements, these extraneous contributions to photoabsorption must be well characterized, or removed entirely. The most straightforward and reliable way of the high-order light suppression is based on the use of the two-mirror suppressor [5,6] which has been used successfully in absolute cross-section measurements for simple low-Z gas-phase molecules [7,8]. However this method does not enable to allow for an effect long-wave stray radiation, what is necessary for the absolute measurements of the cross section for the samples with a small optical density. Recently we have found that the absolute cross-section measurements at the N 1*s* edge can be performed with a high accuracy using titanium absorption filters in combination with an one-mirror suppressor for an effective suppression of the high-order light and the VUV stray radiation [9]. This titanium filter method has been used successfully for the absolute cross-section measurements on solid $NaNO_3$ with an RSM-500 laboratory spectrometer [10].

The absolute measurements of photoabsorption cross section for solid $NaNO_3$ were performed with the direct transmission method over a wide interval of the sample thickness in the vicinity of the N 1s edge ($h\nu$=380 – 450 eV) using the Russian – Geman soft-x-ray beamline at BESSY-II [11]. The samples were polycrystalline films prepared *ex*

situ by thermal vacuum evaporation onto free ~ 150 nm thick titanium films calibrated within 1%. The Ti films were picked up on holders having a hole of 1.5 mm in diameter. Thicknesses of the samples (34 – 180 nm) were measured with a multiple wave interferometer. The Ti films were used for the effective suppression of the second-order light and the VUV stray radiation simultaneously. The incident and transmitted photon fluxes were alternately measured using a TEY detector recording electron yield from a CsI photocathode. The CsI photocathode has a high electron yield (~ 40%) in the range of the N 1s edge (~ 400 eV). The near-edge X-ray absorption

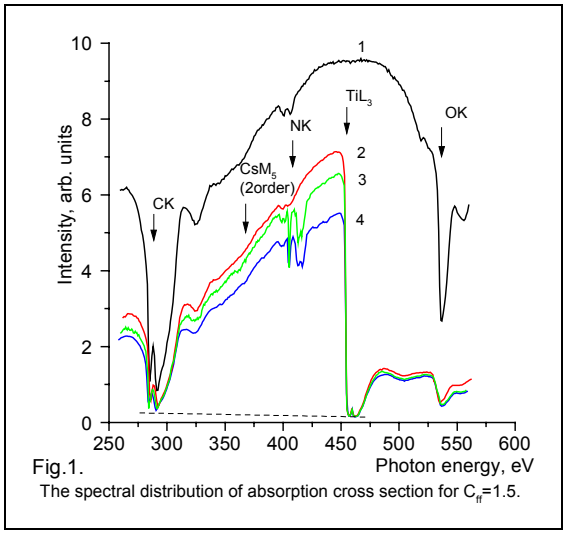

Fig.1.
The spectral distribution of absorption cross section for C_{ff}=1.5.

fine structure (NEXAFS) at the Cs $M_{4,5}$ edge (~ 741-726 eV) recorded in the second order of diffraction can be used for the control of the second-order light suppression. The spectral distributions of the photoabsorption cross section were studied at the N1s edge $NaNO_3$ for the fix-focus rations C_{ff} =1.5 and C_{ff} =2.25 since the calculation [12] has shown the nearly total higher-order suppression for $C_{ff}\leq 1.6$. It has shown that the ratio of the higher-order (second plus third order) to the first-order light transmission at N 1s edge is about 6% for C_{ff} =2.25 and at C 1s edge is about 1% for $C_{ff}\leq 1.6$ and about 10% for C_{ff}=2.25.

The spectral distributions x-ray radiation intensity incident on a sample (1) and transmitted through the Ti - film (2), the Ti – film plus $NaNO_3$ layer 110 nm (3) and 180 nm (4) thick were measured over a wide photon-energy range from 260 to 560 eV and are presented in Figs. 1 and 2 for C_{ff} =1.5 and C_{ff} =2.25, respectively. The arrows mark the energy positions of the C K, N K, O K, Ti L_3- and Cs M_5 (2. order) - edges. The dash lines mark the background level. Recently we have found that the carbon contaminations on optical elements can lead to the total suppression of the monochromatic radiation in the vicinity of the C K absorption edge (~290 eV) [9]. Therefore the minimal intensity of the radiation transmitted at the C K edge shows for C_{ff}=1.5 the intensity of the VUV stray radiation, which comprises about 8-10% of the intensity in the vicinity of the N 1s edge. Curve 2 in Fig. 1 shows a strong suppression of the short-wave radiation above the TiL_3 edge (454eV) and especially in the vicinity of the Ti L_3- and Ti L_2- absorption bands. This intensity averages less than 1% of the incident radiation

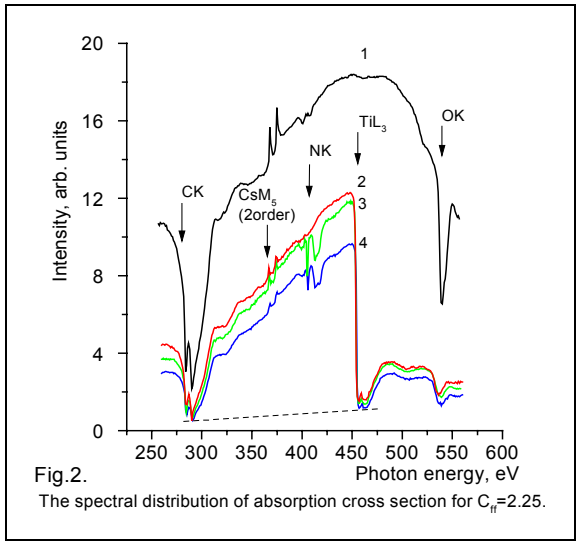

Fig.2.
The spectral distribution of absorption cross section for C_{ff}=2.25.

intensity and correlates well with the calculated value of the ratio of higher-orders to the first-order light transmission [12]. The $CsM_{4,5}$ NEXAFS spectra is not observed in the second-order of the diffraction, what confirms the low intensity higher-order light. The close minimal intensities at the C K and Ti $L_{2,3}$ edges are indicative of the full suppression of the VUV stray radiation by the Ti film.

The similar investigations at C_{ff} =2.25 (Fig.2) give the ratio of the intensity in the vicinity of the Ti L_3 and Ti L_2 absorption bands to the intensity of the incident radiation equal to 10-12%, which correlates well with the calculated ratio of the higher-order light to the first-order light transmission. Curves 1 and 2 in the Fig. 2 demonstrate two intense absorption bands at the $CsM_{4,5}$ threshold in the second-order of diffraction because of the strong short - wave background. It is essential that the Ti film decreases the intensity of these bands by four times, what is in good agreement with a transmission coefficient of the 150 nm thick Ti film at the photon energy of 740 eV. In this case the level of the short-wave background at the Ti L_3 edge is higher then that at the C K edge by

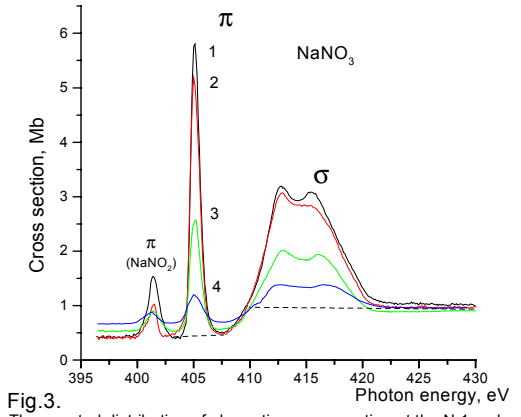

Fig.3.
The spectral distribution of absorption cross section at the N 1s edge for $NaNO_3$ layers of the varied thikness.

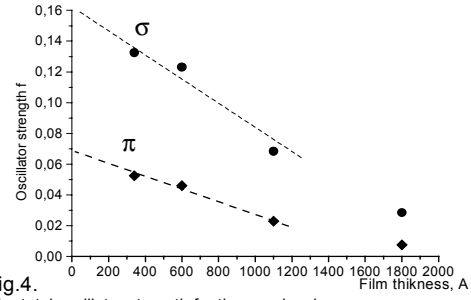

Fig.4.
The total oscillator strength for the π and σ shape resonances.

factor of 2. This can be explained by a fast decrease of the absorption cross section for the Ti metal with increasing the photon energy from 580 eV to 740 eV. Thus Ti-film cannot ensure the total suppression of the higher-order light for the high values of C_{ff}. It is quite possible that there is a need to use the two-mirror or one-mirror suppressor [9,10]. In Fig. 3 we compare the spectral distributions of the absorption cross section at the N 1s edge for the $NaNO_3$ layers of the varied thickness: 34 nm (1), 60 nm (2), 110 nm (3) and 180 nm (4). A narrow peak (405.3eV) and a broad band (~416eV), which are dominant in these spectra can be attributed to transitions of the N 1s electrons to empty electron states of the anion NO_3, which are described by molecular orbitals of $\boldsymbol{\pi}(a_{2u})$ and $\boldsymbol{\sigma}(a_{1g}, e_u)$ symmetry ($\boldsymbol{\pi}$ and $\boldsymbol{\sigma}$ shape resonances) [13]. It is essentially that the measurement cross sections measured before and above the N 1s edge, at the photon energy of 398 and 430 eV correlate with the data obtained with the use of x-ray charcteristic emission lines TiL_ℓ (0,5 Mb) and TiL_α(0.9 Mb) [10]. It can be seen from close examination of the curves 1- 4 (Fig.3) that areas of the $\boldsymbol{\pi}$ and $\boldsymbol{\sigma}$ shape resonances decrease with the increased thickness of the $NaNO_3$ layers. We associated this observation phenomena with the influence the remote tails of the spectral window of the spectrometer [9,10], which is well known as the "thickness effect" [14]. In Fig. 4 the thickness dependences of the total oscillator strength **f** of the $\boldsymbol{\pi}$ and $\boldsymbol{\sigma}$ shape resonances are presented. The values of **f** were obtained using the known relation between the absorption cross section σ (in Mb) and the spectral density of the oscillator strength df/dE: $\sigma(E)=(\pi e^2 h/mc)(df/dE)=109.8$ Mb·eV (df/dE) [1]. In Fig.4 the obtained total oscillator strength for the $\boldsymbol{\pi}$ and $\boldsymbol{\sigma}$ shape resonances are shown and they are extrapolated to the "zero" thickness. These values are equal to 0.07 and 0.162 for the $\boldsymbol{\pi}$ and $\boldsymbol{\sigma}$ shape resonances, respectively. Recently we have found that the oscillator strength extrapolated to the "zero" optical density gives its true value [9].

Acknowledgements:

This work was supported by RFBR (Grant No 04-02-17216) and the bilateral program "Russian-German Laboratory at BESSY II". We wish to thank the staff of BESSY for valuable technical assistance. V.N. Sivkov and A.S. Vinogradov gratefully acknowledge the financial support by BESSY and by the Technische Universitat Dresden.

References

1. U. Fano, J.W. Cooper, Rev. Mod. Phys. **40**, 441 (1968); **41**, 724 (1969).
2. M. Inokutti, Rev. Mod. Phys. **43**, 297 (1971).
3. J. Stöhr, *NEXAFS Spectroscopy*, Springer, Berlin, 1992.
4. J.C. Fuggle, J.E. Inglesfield, eds. Unoccupied electronic states. Fundamentals for XANES, EELS, IPS and BIS. Springer, Berlin, 1992.
5. E.S. Gluskin, E.M. Trachtenberg, A.S. Vinogradov, Nucl. Instrum. and Meth. **152**, 133 (1978).
6. W.B.Peatman, BESSY Technical Report TB Nr.160/90.
7. B.S. Itchkawitz, B. Kempgens, H.M. Köppe, et al., Rev. Sci. Instrum. **66**, 1531 (1995).
8. E.E. Rennie, B. Kempgens, H.M. Köppe, et al., J. Chem. Phys. **113**, 7362 (2000).
9. V.N. Sivkov, A.S. Vinogradov, Optika i Spektroskopiya **63**, 431 (2002) [Optics & Spectroscopy **63**, 395 (2002)].
10. V.N. Sivkov, A.S. Vinogradov, Poverkhnost' (in Russian) N11, 51(2002)..
11. S.I. Fedoseenko, D.V. Vyalikh, I.E. Iossifov, et al., Nucl. Instrum. and Meth. A **505**, 718 (2003)
12. S.A. Gorodovikov, S.L. Molodtsov,R. Follath, Nucl. Instrum. and Meth. **A 411**, 506 (1998).
13. A.S.Vinogradov, V.N.Akimov, Phys.Low.-Dim. Struct., **4/5**, 63 (1994).
14. L.G.Parratt, C.F.Hempstead, E.L. Jossem Phys. Rev., **105**, 1228(1957).

Sub-Monolayer Sensitivity in VUV Ellipsometry Investigations of Organic Thin Films

O. D. Gordan, C. Himcinschi, Yu J. Suzuki, G. Salvan,
D. R. T. Zahn
Institut für Physik, TU Chemnitz, 09107 Chemnitz, Germany
C. Cobet, N. Esser, W. Richter
Institut für Festkörperphysik, TU Berlin, 10623 Berlin, Germany
W. Braun
BESSY GmbH, 12489 Berlin, Germany

Vacuum Ultraviolet (VUV) Spectroscopic Ellipsometry (SE) measurements were performed *in situ* for the optical characterization of ultra-thin organic films on H-passivated Si(111).
With the reduced size of future devices the effects of dimensionality are becoming more and more important. Ellipsometry is a non-destructive and very sensitive surface and thin film measurement technique which can detect the changes in the optical response produced by an overlayer on a smooth surface. However, interpreting the ellipsometry spectra for very low coverages (below few nanometers) down to a monolayer or even submonolayer regime remains a challenging task as the optical path of the light through the material is much smaller than the wavelength [1]. In this case the light has a reduced sensitivity to the refractive index of the film which is strongly correlated with the film thickness. Consequently only the product of these parameters can be uniquely determined [1].
The smaller wavelength of the UV light accessible at BESSY is more sensitive to low coverages. The organic materials used in the investigations are *tris*-(8-hydroxyquinoline)-aluminum(III) (Alq_3) and N,N'–Di-[(1-naphthyl)-N,N'-diphenyl]-(1,1'-biphenyl)-4,4'-diamine (NPD) (fig 1). These materials are among the most commonly used as electron-transport (Alq_3) and hole-transport (α-NPD) materials in light emitting applications OLEDs [2-6].

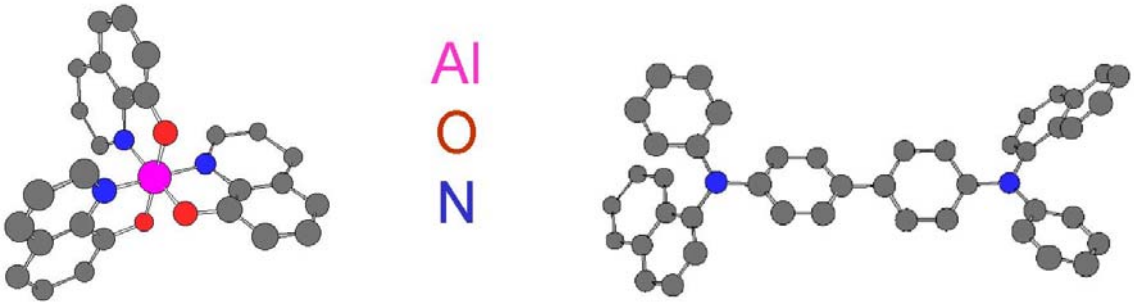

Figure 1. Molecular structures of Alq_3 and α-NPD

As can be seen in fig. 2 the changes in the optical response induced by the overlayer when compared to the H-Si(111) substrate are significant even for very low coverage. In the inset the thicknesses calculated from a quartz microbalance calibration are compared with the ones from the ellipsometry evaluation. The "ellipsometry" thicknesses are in very good agreement with those calculated from the frequency shifts indicating that ellipsometry is also an excellent tool for thickness monitoring.

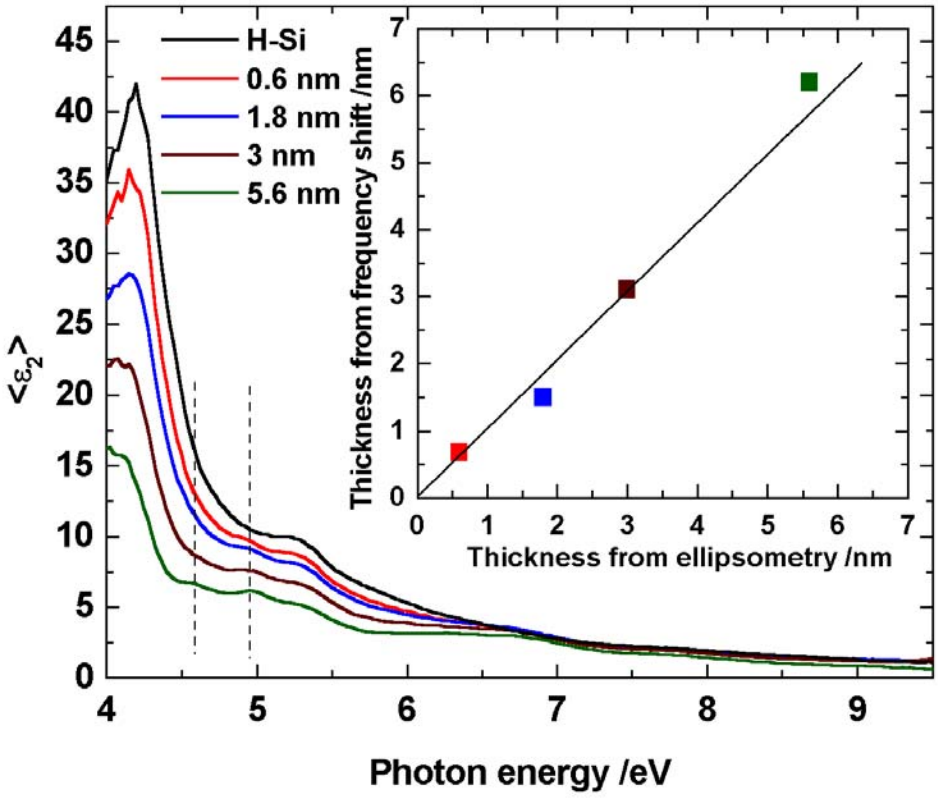

Figure 2. The effective $<\varepsilon_2>$ of the Alq_3 samples compared with the $<\varepsilon_2>$ of the H-Si(111) substrate. Vertical dashed lines mark the positions of strong Alq_3 induced features.

The strong changes in the experimental spectra indicate that for strongly absorbing organic materials a numerical fit for the optical constants can be performed even for very low coverages. Figure 3 shows for comparison the imaginary part of the dielectric function ε_2 of bulk Alq_3 compared with the one of a submonolayer deduced from a three phase model [1] substrate\film\ambient.

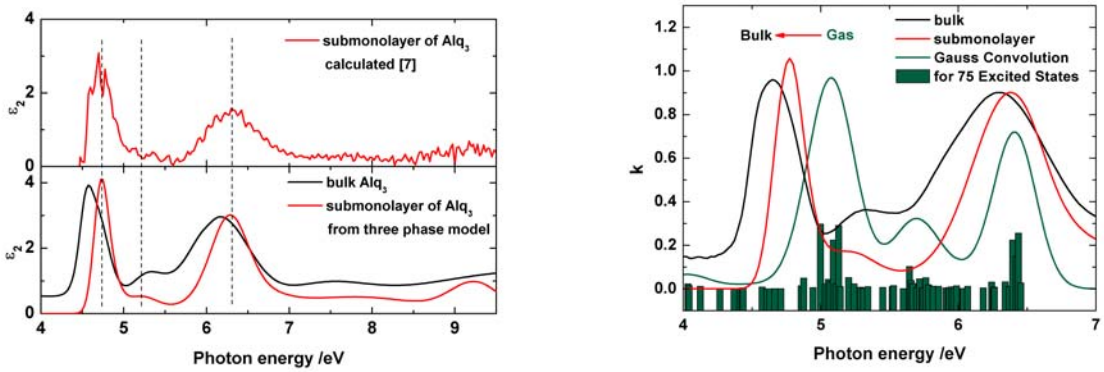

Figure 3. Left - comparison between the imaginary part of the dielectric function for a submonolayer of Alq_3 obtained from a three phase model and calculated [7]. The imaginary part of the dielectric function for bulk Alq_3 is also plotted.
Right – Comparison with theoretical calculation for 75 excited states.

The validity of the solution was checked using a direct calculation method [7]. In this case the calculated ε_2 is affected by the experimental noise of two different measurements, namely that of the H-Si(111) substrate and of the ultra-thin Alq_3.
The dominant features of the dielectric function in fig. 3 were assigned by comparison with the singlet-singlet transitions calculated using the Gaussian 98 software [8]. The molecular geometry of the *meridional*-isomer [9] was optimised using the Kohn-Sham density functional theory (DFT) with the 3-21G basis set and the Becke three-parameter hybrid exchange correlation functional (B3LYP). The time-dependent density functional theory (TD-DFT) was subsequently employed to calculate the excitation energies, oscillator strengths, and excited-state compositions in terms of excitations between occupied and unoccupied orbitals.
The differences between the calculated spectra for single molecule, submonolayers and bulk can be explained by a change in either electronic coupling or due to a molecular ordering of the Alq_3 molecules in the bulk.
A similar blue shift was obtained for ultra-thin NPD films. Further investigation are necessary in order to see how is correlated the amplitude of the shift the film thickness. This will provide valuable information not only about the electronic transitions in ultra-thin films, but also about the growth mode of the organic layers.

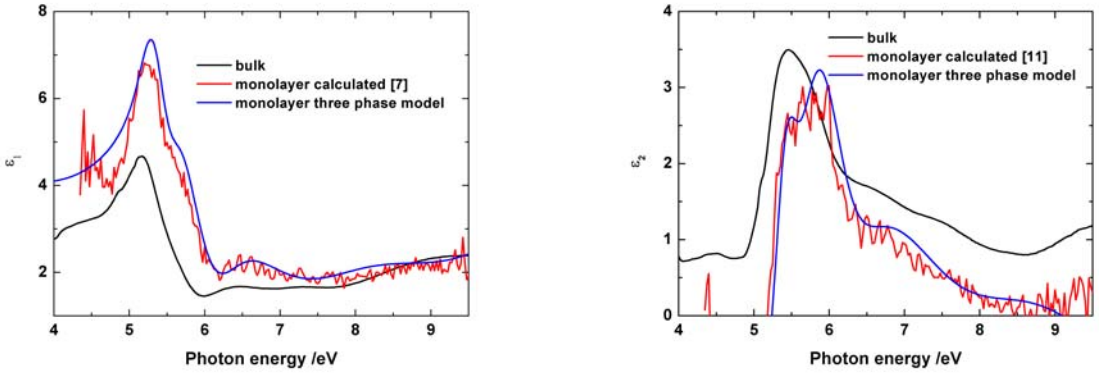

Figure 4. Comparison between the dielectric functions of the bulk NPD and monolayer. Left – real part. Right – imaginary part.

The authors gratefully acknowledge the Deutsche Forschungsgemeinschaft, Graduiertenkolleg 829 “Akkumulation von einzelnen Molekülen zu Nanostrukturen“, BMBF project 05 KS4KTB/3 and BMBF project 05 ES3XBA/5.
[1] R.M.A. Azzam, N.M. Bashara – Ellipsometry and Polarized Light, Elsevier, Amsterdam 1992
[2] L.C. Palilis, A.J. Mäkinen, M. Uchida, Z.H. Kafafi – Appl. Phys. Lett. 82, 2209, (2003)
[3] W. Gao, A. Kahn - J. Appl. Phys. 94, 359, (2003)
[4] L.S. Hung, C.H. Chen - Mat. Sci. Eng. R39, 143, (2002)
[5] C.H. Kim, J. Shinar - Appl. Phys. Lett. 80, 2201, (2002)
[6] T. Mori, H.G. Kim, T. Mizutani, D.C. Lee - Jpn. J. Appl. Phys. 40, 5346, (2001)
[7] D. Aspnes – Spectroscopic Ellipsometry of Solids, Chap 15, Optical Properties of Solids-New Developments, ed B.Seraphin, North Holland 1976
[8] M. J. Frisch *et al.* - *Gaussian 98*, Version 5.2; Gaussian, Inc.: Pittsburgh, PA, 2001.
[9] M. Cölle, and W. Brütting, phys. Stat. sol. (a) 201, 1095, (2004).

Quantum-size effects in a surface carbide: W(110)/C-R(15×3)

A. Varykhalov, O. Rader, W. Gudat
BESSY, Albert-Einstein-Str. 15, D-12489, Berlin, Germany

Usually, the electronic structure of surfaces is described in terms of two- and three-dimensional behavior of electrons. In order to lower the dimensionality further and confine the electrons into one dimension, it is a straightforward concept to modify the two-dimensional surface of a solid by placing obstructions on this surface. In order to reach the necessary area density of such nanoscale structures and to be able to study the electronic structure as a function of crystal momentum, a periodic array of nanostructures must be produced.

We have performed a combined study of atomic and electronic structure of the two-dimensional surface carbide W(110)/C-R(15×3) using LEED, STM, and core-level and valence-band photoemission. This system is mainly known as being the result of surface segregation of carbon on W(110), occurs in the initial stages of cleaning of a W(110) crystal, and has been characterized structurally before [1]. In Ref. [2], we have reported about the use of this system as template for the growth of one-dimensional Au nanostructures. In the present report, we focus on perspectives for electron confinement of the surface carbide itself. We prepare the structure starting out with an atomically clean W(110) surface by heating the crystal at 500-500°C in a propylene atmosphere (5×10^{-8}mbar, 5 min).

Figure 1 shows the geometrical model of the carbon nanostructure as a result of our STM investigation. It consists of C chains interconnected by a zigzag structure of C atoms. The unit cell represented by the rectangle is of dimensions (1.3×0.8) nm^2 according to our STM analysis and the periodicity along the [001]-direction of W is 0.633 nm. Angle-resolved photoemission spectra taken with the HiRes spectrometer at 110 eV photon energy at UE56/1-PGM and UE52-SGM monochromators are shown in Fig. 2. Part (a) and (b) show the results for W(110)/C-R(15×3) along the linear C chains (along basis vector $V_{\parallel}$ of R(15×3)) and perpendicular, i. e., along the zigzag structure (vector $V_{\perp}$). Each figure displays an energy range near the Fermi level highlighting the dispersion of a W(110) surface resonance with 0.7 eV binding energy in normal emission. This structure shows a parabolic dispersion along the $V_{\parallel}$-direction but is split up into two peaks along $V_{\perp}$. This behavior proves one-dimensional electron confinement and, in particular, the behavior in the $V_{\perp}$-direction is reminiscent of a lateral quantization as it has recently been achieved for surface states on stepped Au(111) [3]. Figs. 2(d) and (d) show, for comparison, the behavior of the surface state on clean W(110). (Note that the directions are the same as for the W(110)/C-R(15×3), i. e., they are not high-symmetry directions of the W(110) surface.) Along both directions the surface resonance displays a strong parabolic dispersion showing that the wave function we have probed is in fact initially spread out in two dimensions on the W surface.

Returning to the structure in Fig. 1, we note that confinement of W surface state electrons to the open W areas in between C atoms appears possible but conditions for the one-dimensional confinement seen in the photoemission spectra are not immediately apparent. This notion changes when STM data is analyzed as a function of the vertical tip distance probing the charge density as a function of the distance above the surface (Fig. 3). For certain distance (Fig. 3(d)), the symmetry apparently lowers with respect to the geometry given in Fig. 1. This superstructure in the charge density may be related to a lateral buckling reconstruction suggested by Bode et al. [1]. We cannot decide at present whether a geometrical reconstruction is indeed present or the effect is purely electronic. A buckling reconstruction could be the reason for the one-dimensional confinement of electrons seen in Fig. 2. The symmetry in our STM data is consistent with such an interpretation.

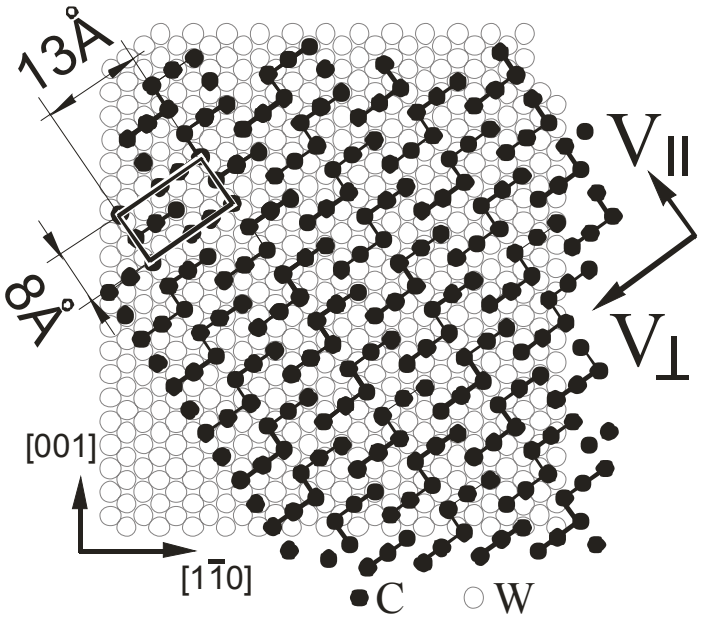

Fig. 1. Arrangement of the C atoms (dark) on the W(110) surface (light atoms). The structure is rotated by 14° relative to the in-plane [001]-direction. high symmetry directions $V_{\parallel}$ and $V_{\perp}$ of carbon superstructure are shown.

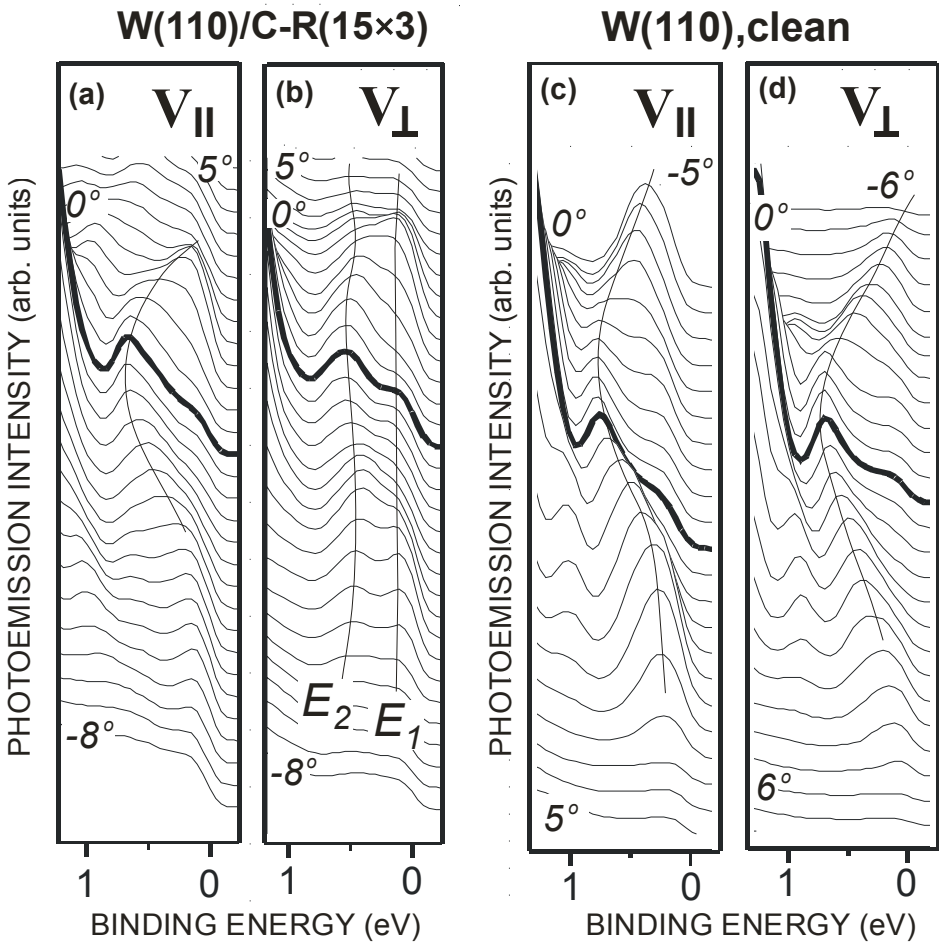

Fig. 2. Collection of angle-resolved photoemission spectra for the surface carbide (a,b) and the clean W(110) (c,d) for comparison. Only the energy range near E_F is shown where electron confinement and quantization occur for a W surface resonance.

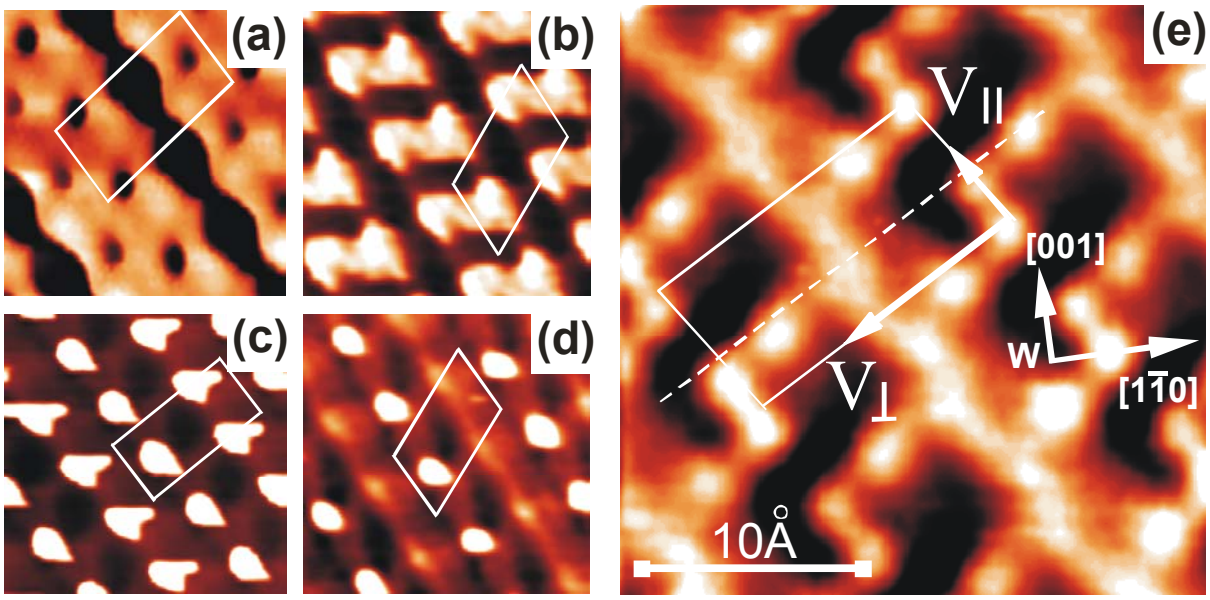

Fig. 3. Distance-dependent STM study of W(110)/C-R(15×3). Evolution of the image morphology with decreasing tunneling-gap resistance: (a) tunneling resistance Ω=1 GOhm, striped pattern; (b) Ω=770 MOhm, cluster-like sequence; (c) Ω=620 MOhm, array of double spots; (d) Ω=540 MOhm, strongly localized single spot likely manifest substrate lateral buckling; (e) Ω=170 MOhm, atomic resolution at low tip-surface separation.

References:

1. M. Bode, R. Pascal, R. Wiesendanger, Surf. Sci. **344**, 185 (1995); Z. Phys. B: Cond. Matt. **101**, 103 (1996).
2. A. Varykhalov, O. Rader, W. Gudat, BESSY Annual Report 2002, p. 142.
3. A. Mugarza, A. Mascaraque, V. Pérez-Dieste, V. Repain, S. Rousset, F. J. García de Abajo, and J. E. Ortega, Phys. Rev. Lett. **87**, 107601 (2001).

Linear chain approximation in extended phase accumulation model: Quantum well states in the Ag/W(100) system in the atomic limit

A.M. Shikin, M.B.Visman, G.G. Vladimirov, V.K. Adamchuk
St. Petersburg State University, St. Petersburg, 198504 Russia

O. Rader
BESSY, Albert-Einstein-Str. 15, D-12489 Berlin, Germany.

At present, quite a number of studies have reported the appearance of quantum well states (QWS's) in different kinds of overlayer systems. As to the theoretical description of these observations, two main approaches exist in the literature that describe the behavior of the energies of QWS's on the film thickness. The first approach is based on the nearly free electron approximation and is widely used in the "phase accumulation model" [1]. This approximation describes the experiment well when relatively thick films are studied, where the wave length of the QWS's is large compared to the interatomic distance. However, upon decreasing the film thickness towards the monolayer limit this approach shows significant differences from experiment. The second approach is based on the tight binding model in its simplest expression – the linear chain approximation, where the variable length of a linear chain of atoms is associated with the thickness of the deposited film in monolayers [2]. In order to include the influence of the substrate electron structure in this model, this approach can also used in the framework of the "phase accumulation model" by using the atomic wave functions instead of plane waves [3].

The aim of the present work is to test such approach for analysis of QWS's which develop in ultrathin films (in particular approaching the monolayer limit) of Ag on the W(100) surface. The electronic structure of Ag along [100] is characterized by Ag(d)-bands located lower than the middle of the Ag(sp)-band that allows to analyze the behavior of sp-QWS's in the lower part of the valence band, where the nearly-free-electron and linear-chain approximations predict different behaviors. Fig. 1 displays the changes of normal emission photoelectron spectra measured at the Russian-German beamline at $h\nu$ =65 eV under deposition of Ag on W(100). The changes show clearly the formation of Ag-derived QWS's, which are marked and labeled in Fig. 1. The corresponding changes of energies and intensities of the QWS-peaks are presented in Figs. 2 a,b, respectively. The thickness of the Ag-film in monolayers is shown in the upper part of Fig.2 b. The theoretical estimates of the QWS energies on the basis of the "extended phase accumulation model" using atomic wave functions are shown by open squares connected by straight lines. From the comparison we can correlate experimental results and theoretical estimations very well which confirms the validity of our approach even in the monolayer-like limit of the adsorbed film thickness. Moreover, in the present dependencies we can clearly distinguish in the lower part of the valence band (E_b > 2.5 eV) the parts of QWS-branches which are shifting under Ag deposition towards higher binding energies, i. e., opposite to the other parts of QWS-branches which shift towards the Fermi level). Such type of behavior can be explained only in the framework of the linear chain approximation and this could indicate that tight-binding approach is superior in the atomic limit of thickness than the one based on the nearly-free-electron approximation.

References.

1. N.V. Smith, Phys. Rev. **B 32**, 3549 (1985); N.V. Smith, N.B. Brookes, Y. Chang, P.D. Johnson, Phys. Rev. **B 49**, 332 (1994).
2. M. Grüne, J. Peltzer, K. Wandelt, I.J. Steinberger, J. Electron Spectrosc. Relat. Phenom. 98-99, 121 (1999).
3. A.M. Shikin, O. Rader, G.V. Prudnikova, V.K. Adamchuk, W. Gudat, Phys. Rev. **B65**, 075403 (2002); A.M. Shikin, D.V. Vyalikh, G.V. Prudnikova, V.K. Adamchuk, Surf. Sci., **487**, 135 (2001).

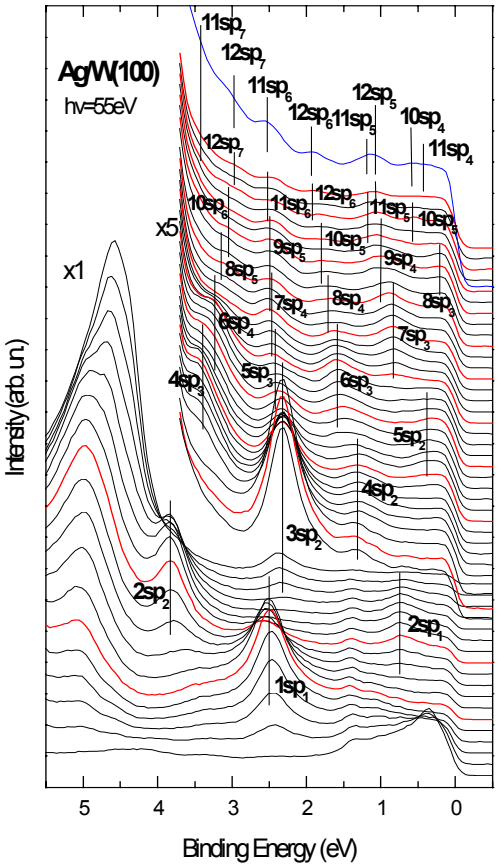

Fig.1. Series of normal emission valence band spectra under deposition of Ag on W(100). Notations of the formed QWS's are shown near each feature.

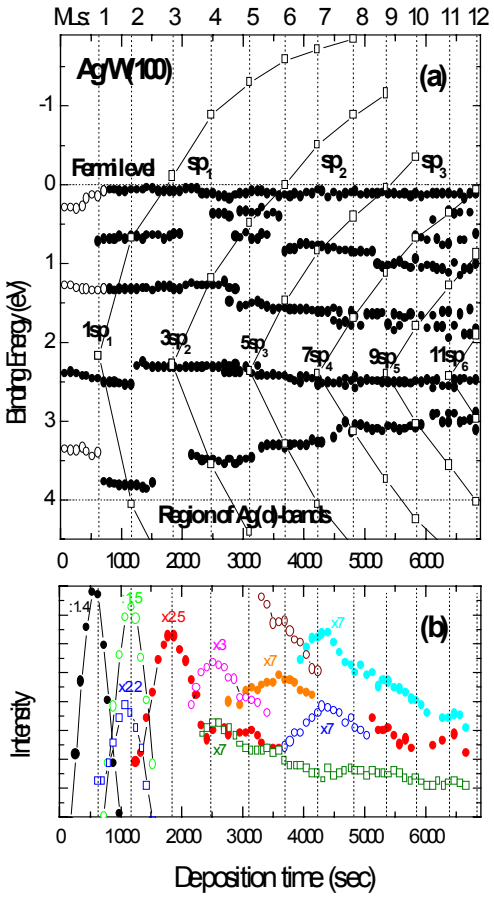

Fig. 2. Binding energies (a) and intensities (b) of sp-derived quantum-well states.

Resonant Photoemission Study of Diluted Magnetic Semiconductor $Ge_{1-x}Mn_x$

M. Fonin,[1] Yu. S. Dedkov,[2] E. Biegger,[1] D.V. Vyalikh,[2] and U. Rüdiger[1]

[1] *Fachbereich Physik, Universität Konstanz, D-78457, Konstanz, Germany*
[2]*Institut für Festkörperphysik, Technische Universität Dresden, D-01062 Dresden, Germany*

Since two decades diluted magnetic semiconductors (DMS's) attract extensive attention due to their unique magneto-optical and magnetotransport properties such as giant negative magnetoresistance, extremely large electronic *g* factor, large Faraday rotation, etc.[1] Recently the interest has surged again because of their possible applications to *spintronics* based on the semiconductor technology.[2] The coexistence of semiconductor properties and spontaneous long-range ferromagnetic order observed in DMS's, which are made by substitution of small amount of late 3*d* magnetic transition-metal (TM) atoms such as Cr, Mn, Fe, Co, and Ni ions into cation sites in the II-VI or III-V compound semiconductors, provides opportunity for fundamental studies as well as a variety of magnetic and spin-dependent transport devices. Although much effort has focused on DMS materials, the nature of ferromagnetic order remains unclear, particularly the precise role played by dopants and the semiconductor host. Ge provides a simple host lattice to explore the fundamental origins of ferromagnetic order, and it is lattice matched to the AlGaAs/GaAs family, facilitating incorporation into semiconductor based heterostructures. Recently, ferromagnetism in the $Ge_{1-x}Mn_x$ system was reported with T_C=116 K in epitaxial thin films[3] and 285 K in bulk single crystals.[4] Recent band structure calculations based on local spin density approximation to the density functional theory (LSDA-DFT) showed that the magnetically ordered phase arises from a long-range ferromagnetic interaction that dominates a short-range antiferromagnetic interaction.[3] The calculated density-of-states show a clear half-metallic feature, i.e. a metallic Fermi cut-off for the majority spin, with the disappearance of spectral weight near E_F - reflecting the energy gap - for the minority spin.[5,6]

In order to understand the electronic structure of $Ge_{1-x}Mn_x$ photoemission spectroscopy measurements were performed utilizing 3*p*-3*d* resonance near the Mn 3*p* absorption edge. This technique enables the investigation of the Mn 3*d* contribution to the electronic structure. As a result a sort of the 3*d* partial spectral weight can be extracted from the experimental spectra.

The single crystal samples were grown by a Bridgman crystal growth technique. The growth procedure is described elswere.[4] Samples with a Mn concentration of x=0.02, 0.04, 0.06, and 0.08 were prepared. The crystals were cut and polished to improve sample surface quality for the photoemission experiments. The crystallographic quality of the $Ge_{1-x}Mn_x$ crystals was investigated by θ–2θ x-ray powder diffraction (XRD). As an example, a XRD pattern of $Ge_{0.94}Mn_{0.06}$ is presented in Fig. 1. The lattice constants were determined from the positions of the Ge peaks for all samples. The lattice constant increases linearly with an increasing Mn concentration which is due to the larger atomic radius of Mn. The increase of the lattice constant with Mn concentration gives a clear evidence of the Mn incorporation into the Ge lattice.

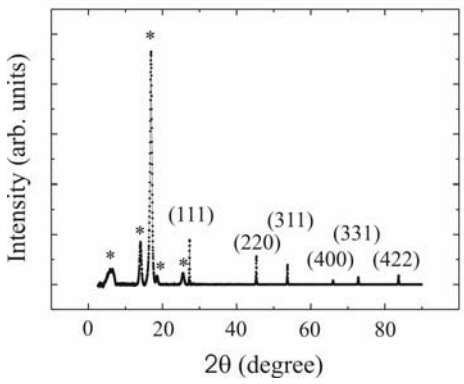

Fig.1. A XRD pattern of the $Ge_{0.94}Mn_{0.06}$ sample. Peaks labled with an asterisk (*) are due to the underlaying sample holder.

Magnetic properties of the $Ge_{1-x}Mn_x$ single crystals were investigated in a superconducting quantum interference device (SQUID)

magnetometer. Fig.2 shows the temperature-dependent magnetization of the $Ge_{0.98}Mn_{0.02}$ sample recorded from 5 to 350 K. The magnetization curve, which is typical for all prepared $Ge_{1-x}Mn_x$ samples, shows two pronounced transitions at about 150 K and 275 K. In the range of 150-275 K the samples display a clear hysteresis, indicating a ferromagnetic state (FM). Below 150 K the samples show antiferromagnetic ordering. Paramgnetic ordering results above 275 K.

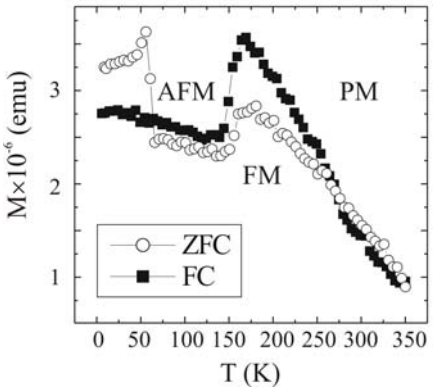

Fig.2. Magnetization as a function of temperature of the $Ge_{0.98}Mn_{0.02}$ sample recorded from 5 to 350 K. Zero field cooled (open circles) together with field cooled (black squares) measurements are presented.

Resonant photoemission (ResPES) experiments were carried out at the U125/1-PGM beam-line. The photon energy resolution was set to 100 meV. ResPES spectra were collected in the angle-integrated mode with the total energy resolution of 150 meV. The photoemission spectra were normalized to the incident photon flux, which was monitored by detecting the photocurrent from a last gold-covered mirror of the beamline. After introducing the sample into the UHV chamber at BESSY II its surface was cleaned by moderate Ar^+ ion sputtering. XPS analysis carried out after such treatment does not show any presence of carbon contaminations.

Figure 3 shows representative valence-band photoemission spectra of $Ge_{0.98}Mn_{0.02}$ sample measured with photon energies around the Mn 3*p* absorption edges. All spectra show a pronounced shoulder in the region between 2 and 12 eV, which correspond to the emission from the valence band of Ge. When the photoelectron spectra cross the Mn 3*p* absorption threshold (which is about 47 eV) the small shoulder at the right side of the spectra (3-4 eV) appears. To resolve this feature in the photoelctron spectra more clearly the off-resonance spectrum obtained at 45 eV and the photoelectron spectrum recoded just after resonance at 47.5 eV were substracted from each other. The obtained difference is shown in the inset of Fig.3 and corresponds to the partial contribution of the Mn 3*d* states in the valence band of $Ge_{0.98}Mn_{0.02}$. The important result of these measurements is the evidence that none of the samples presents any density of states within the forbidden band gap region. The binding energy of the Mn 3*d* band was found to be about 3.1 eV which is in good agreement with theoretical calculations for the $Ge_{0.97}Mn_{0.03}$ compound where the binding energy of Mn 3*d* band was determined to be around 2.5-3 eV.[6]

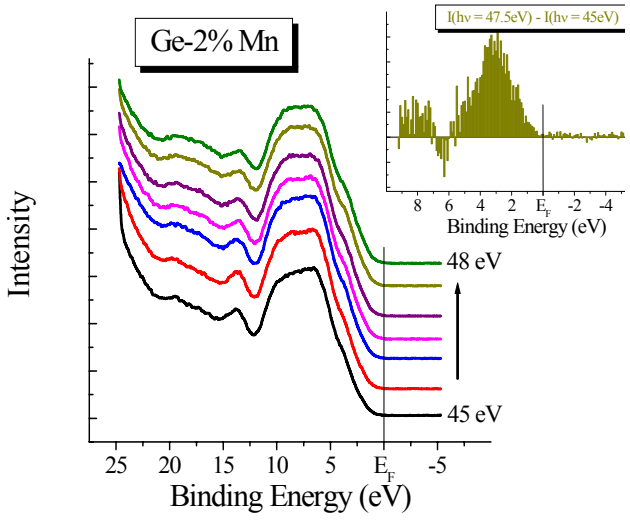

Fig.3. Resonant photoemission spectra of $Ge_{0.98}Mn_{0.02}$ sample at the Mn 3*p* adsorption edge.

Acknowledgements

This work was supported by the bilateral Project Russian-German Laboratory at BESSY II and by a grant from the Ministry of Science, Research and the Arts of Baden-Württemberg.

References

1. *Diluted Magnetic Semiconductors, Semiconductors and Semimetals*, edited by J. K. Furdyna and J. Kossut (Academic, New York, 1988), Vol. 25; *Diluted Magnetic Semiconductors*, edited by M. Jain (World Scientific, Singapore, 1991).
2. R. Fiederling et al., Nature (London) **402**, 787 (1999); Y. Ohno, D. K. Young, B. Beschoten, F. Matsukura, H. Ohno, and D. D. Awschalom, *ibid.* **402**, 790 (1999); T. Dietl, H. Ohno, F. Matsukura, J. Cibert, and D. Ferrand, Science **287**, 1019 (2000).
3. Y. D. Park *et al*., Science **295**, 651 (2002).
4. S. Cho *et al.*, Phys. Rev. B **66**, 033303 (2002).
5. T. C. Schulthess and W. H. Butler, J. Appl. Phys. **89**, 7021 (2001).
6. A. Stroppa *et al.*, Phys. Rev. B **68**, 155203 (2003).

Photoelectron spectroscopy of the dye sensitized nano-crystalline TiO_2 / electrolyte interface: adsorption of (Ru(dcbpy)2(NCS)2) and coadsorption of acetonitrile

***Konrad Schwanitz*, Thomas Mayer, and Wolfram Jaegermann**
TU-Darmstadt, FB Material- und Geowissenschaften, FG Oberflächenforschung, Petersenstraße 23, 64287 Darmstadt, Germany

Introduction

Wide band gap semiconductors can be sensitized to visible light by the adsorption of molecular dyes to their surface. Technological applications are found in dye-sensitized solar cells. The function of such devices is based upon the injection of an electron from a photoexcited state of the sensitizer dye into the conduction band of the semiconductor. Nanoporous oxide films are used particularly due to their high surface area available to dye sensitization. Films of sintered TiO_2 anatase nanocrystallites, sensitized by the dye RuII(2,2′-bipyridyl-4,4′- dicarboxy-late)2(NCS)2 (Ru-dye N^3), have yielded the most efficient cells reported to date. Most such devices employ a liquid electrolyte comprising, typically, an iodide/triiodide redox active couple dissolved in acetonitrile CH_3CN. The function of the redox couple is to rereduce the dye cation, following electron injection, and transport of the resulting positive charge to the counter electrode.

The complex interplay of TiO_2 bulk and surface states, dye HOMO-LUMO states and solute states in the solvent ambient is crucial for the photovoltaic efficiency and is subject of ongoing research. In this study we analyze the dye frontier orbital alignment and the influence of the solvent acetonitrile on this alignment (and on substrate surface states). The experiments have been performed at beamlines TGM7 and U49/2 using the endstation SoLiAS, which is especially designed for the analysis of solid liquid interfaces. Original materials as used for production of state of the art photovoltaic devices delivered by Solaronix are analyzed. Nanocrystalline nc-TiO_2 films have been prepared ex situ by sintering TiO_2 paste films at 450°C. Ru dye N^3 was adsorbed from ethanol solution in an UHV-integrated electrochemical cell under pure N_2 atmosphere that allows for transfer of wet chemically prepared interfaces to vacuum without contact to ambient air. Acetonitrile was adsorbed from gas phase onto LN_2 cooled samples. In future studies also the redox couple iodide/triiodide will be added.

Results

Valence band spectra as measured with 50eV photon energy near the Ti 3p→3d resonance (at 47 eV) are displayed in Fig.1a normalized to the O 2p emission at 6.18 eV binding energy E_B. Due to resonant excitation Ti^{3+} 3d gap states appear with exaggerated intensity with a maximum at 1.36 eV binding energy. Detailed spectra of the gap region have been measured and are displayed in Fig.1b after background subtraction taking across the normalization factors used in Fig.1a. Additional gap states extending up to the Fermi level show a similar resonance behaviour and are therefore also identified with Ti 3d states. The spectra of the as prepared sample look very similar as observed before by [1]. The gap states at 1.36 eV E_B have been discussed as localized Ti^{3+} states due to oxygen deficiency at the TiO_2 surface. The origin of the states just below the Fermi level is not jet clear. They are discussed as conduction band electrons interacting with codeposited e.g. alkali cations [1], which are not present in our case, or as interface states of the sintered nanocrystallites or as polaronic filled conduction band states. Recombination of the injected electrons with the dye hole may proceed via these surface gap states as competing loss mechanism in photovoltaic devices. The HOMO level of the adsorbed dye is found 1.15 eV above the valence band edge of nc-TiO_2 at 3.2eV. With an energy gap of 3.2 eV the conduction band minimum just coincides with the Fermi level.

Coadsorption of acetonitrile induces a shift of the dye HOMO by 160 meV to higher E_B which is completely reversed after desorption. The shift to higher binding energy opposes an expected stabilisation of the final state cation by solvation with the dipolar solvent acetonitrile.

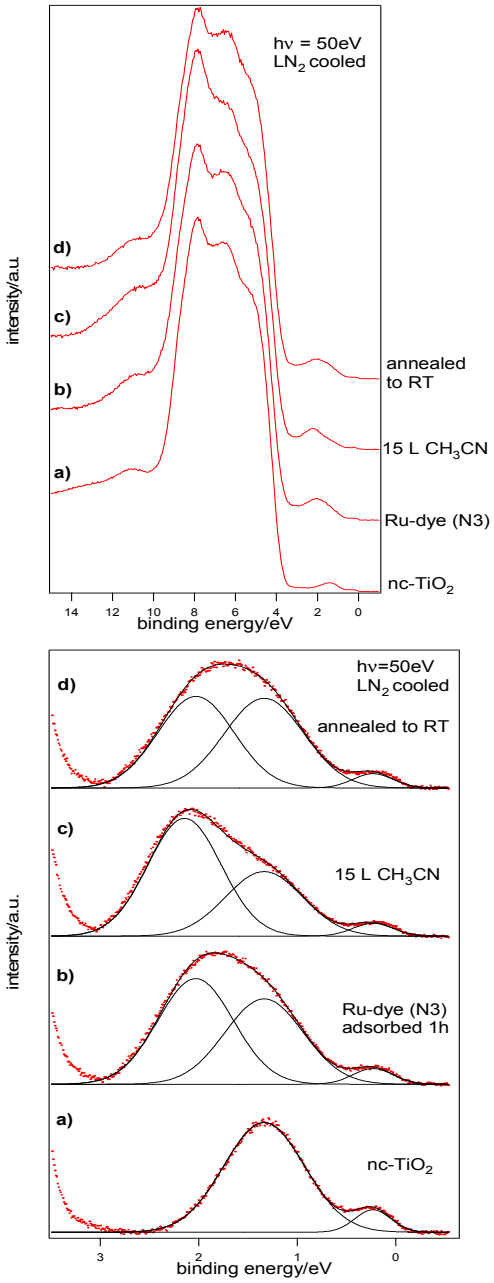

Fig. 1a): Valence band spectra of nc-TiO_2 as prepared a), after Ru-dye N3 adsorption from solution b), after 15 L acetonitrile coadsorption c) after annealing to room temperature d). hν=50 eV, close to Ti3d resonance.

Fig. 1b): Detail of the nc-TiO_2 gap states and the Ru-dye N^3 HOMO in the same conditions as in Fig.1a). The spectra have been normalized to the O2p emission at 6.18 eV.

All spectra taken on LN_2 cooled samples

The observed shift is therefore tentatively addressed to a dipole induced by the solvent between TiO_2 and the dye molecules. The measured HOMO corresponds to the position of the lowest energy hole-state created by the photoemission of an electron i.e. the HOMO of the molecular

cation. Except for a Frank Condon shift due to vibrational excitation in the photoemission process of approximately 0.1 eV away from the Fermi level, this is the relevant energy position for the rereduction by the redox system. For the injection process the line up of the LUMO to the conduction band edge is crucial. The positioning of the LUMO state of the neutral excited dye molecule can not be calculated by simply adding the energy of the optical absorption maximum (535nm=2.32eV) to the cation HOMO level as measured with PES because optical absorption creates a Frenkel exciton on the neutral molecule. Due to low dielectric ε in organic semiconductors exciton binding energies are found in the range of 0.4-1.0 eV. Sharing the exciton binding energy equally between hole and electron would lead to an upward shift of the hole by half the exciton binding energy. But the difference between the measured final state cation HOMO and the optically excited neutral molecule HOMO is unkonown. In Fig. 2 (d) we use an approximate value of 300meV for half the exciton binding energy. By adding the optical absorption energy we find the position of the LUMO of the excited molecule. Fig. 2 shows the HOMO alignment of the adsorbed dye, the HOMO shifted down with coadsorbed acetonitrile and the optical absorption gap positioned with the exciton HOMO shifted up again by 300meV, half of the assumed exciton binding energy. As a result the LUMO position of the dye in the excitonic state is found 400 meV above the conduction band edge.

Adsorption of the dye as well as of acetonitrile is accompanied by quenching of the Ti^{3+} 3d gap state emission. This is more clearly seen in valence band spectra of parallel experiments on single crystalline TiO_2 rutile (not displayed) than on the nanoporous anatase film. On the nc-films the Ti2p core orbital spectra displayed in Fig. 3 show quenching of the gap state emission as reduction of the Ti^{3+} low binding energy shoulder of the Ti^{4+} bulk emission. After desorption of CH_3CN the Ti^{3+} states emission is restored.

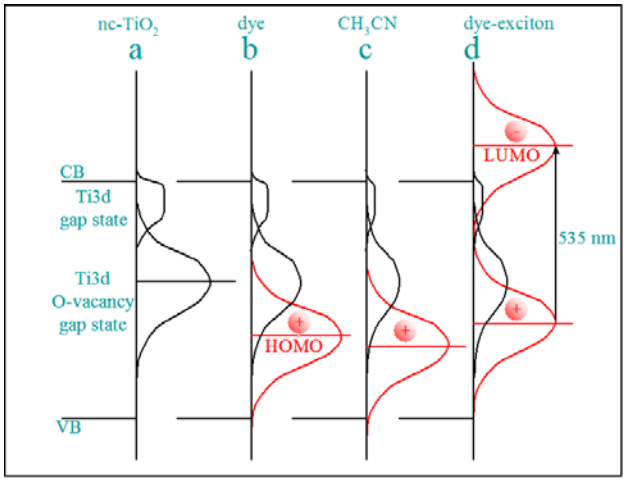

Fig. 2: Schematic of the photovoltaic relevant valence band states as measured on the as prepared nanocrystalline TiO_2 anatase film a), after adsorption from ethanol solution with the Ru dye N^3 HOMO of the final cation b), after coadsorption of the solvent acetonitrile with the HOMO shifted by 160meV to higher E_B c), the HOMO position corrected by an unknown value for the neutral excitonic state using half of an assumed exciton binding energy (300 meV). The dye LUMO is the found 400 meV above the conduction band. The figures are drawn to scale.

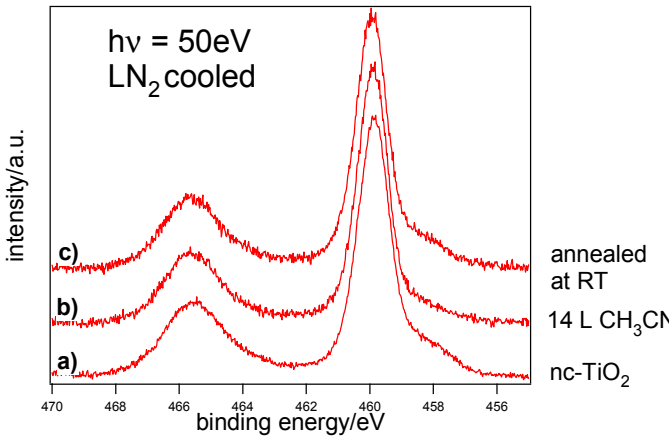

Fig.3: Ti 2p core level spectra of nc-TiO_2 as prepared a), after acetonitrile adsorption b), after annealing to room temperature c). hν=500 eV.

Summary
Nanocrystalline films of anatase TiO_2 show the valence band edge at 3.2 eV E_B implying that the conduction band edge just coincides with the Fermi level. Gap states are found with a maximum at 1.36 eV E_B and additional states extending up to the Fermi level. The intensity of these states decreases with adsorption of the dye as well as with acetonitrile. The HOMO of the sensitizer is found at 2.05eV binding energy before and at 2.17 eV after coadsorption of acetonitrile. Using the energy value of the optical absorption maximum and assuming that the hole state is stabilized in the optical excited Frenkel exciton by half the exciton binding energy of approximately 300 meV the LUMO is found at 450 meV above the conduction band edge.

Acknowledgement
Funding of the project by DFG under no. JA 859/3-3, of SoLiAS by BMBF under project no. 05KSIRD1/0, and of travel expenses by BMBF under no. 05 ES3XBA/5 is gratefully acknowledged.

[1] K. Westermark, A. Henningson, H. Rensmo, S. Södergren, H. Siegbahn, A. Hagfeldt
Chem. Phys. 285 (2002) 157

Direct observation of the hole ordering in a $La_{1-x}Sr_xMnO_3$ (x~1/8) single crystal by soft X-ray resonant scattering

Y. Su[1], H.F. Li[1], A. Nefedov[2], J. Grabis[2], H. Zabel[2], D. Wermeille[3], J. Persson[1], P. Meuffels[4], V. Kaiser[5] and Th. Brueckel[1]

[1]*Institute for Scattering Methods, IFF, Forschungszentrum Juelich,Germany*
[2]*Institut für Experimentalphysik/Festkörperphysik, Ruhr-Universität Bochum, Germany*
[3]*MuCAT, Advanced Photon Source, Argonne National Lab., U.S.A.*
[4]*Institute for Electronic Materials, IFF, Forschungszentrum Juelich, Germany*
[5]*Institut für Kristallographie, RWTH-Aachen, Germany*

1. Introduction

Lightly doped $La_{1-x}Sr_xMnO_3$ (x~1/8) compound exhibits a very intriguing ferromagnetic insulating (FMI) phase at low temperatures. The exact nature of this FMI behavior is still being strongly debated in spite of intensive investigations carried out during last couple of years [1-4]. Nevertheless, the consensus on the importance of charge and orbital degrees of freedom has been reached. The central argument is now focused on how charge and orbital ordering take place. The latest suggestion is that the localized holes and surrounding e_g orbitals in adjacent Mn cation sites are organized in the form of so-called orbital polarons, the ordering of such orbital polarons would lead to a FMI phase [2-3]. There are several alternative charge/orbital ordering models existing [4-5]. The charge ordering in this compound is among the most puzzling. Up to now, no hard experimental evidence concerning the occurrence of charge ordering has ever been obtained. Therefore, this compound still remains an outstanding example to tackle complex ordering phenomena in highly correlated transition-metal oxides (TMO). In the following parts, we will report the first direct observation of the hole ordering in this compound obtained via the soft X-ray resonant scattering technique.

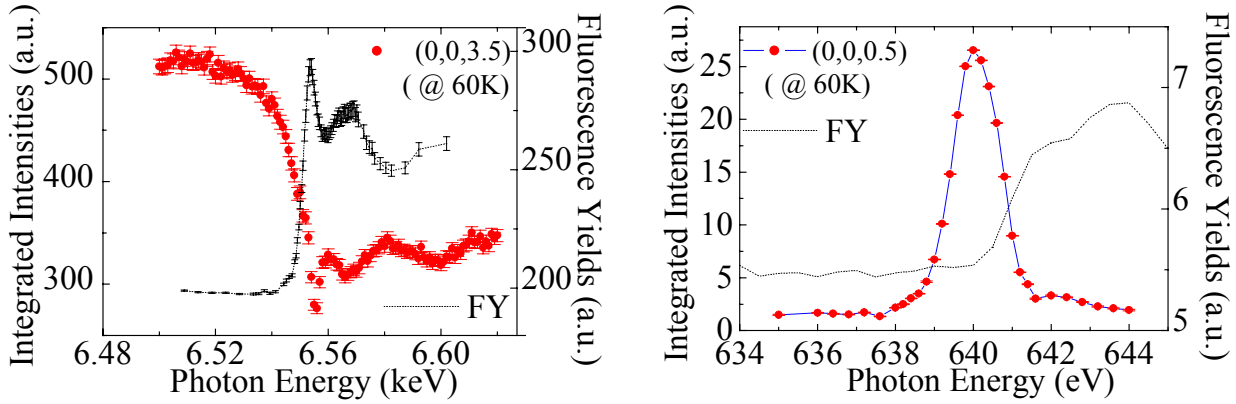

Fig. 1 Hugely different sensitivity of resonant X-ray scattering to charge ordering in manganites, (a) at the Mn K-edge, where no resonant enhancement can be observed (the energy dependence of the integrated intensities of superstructure reflections was measured at MuCAT, Advanced Photon Source (APS), U.S.A.); (b) at the Mn L_3-edge, where significant resonant enhancement is clearly seen (data taken at UE56/1-PGM-b, BESSY-II)

2. Results and Discussions

According to the classic ionic charge-ordering scenario in which Mn^{3+} and Mn^{4+} order periodically, and they can be distinguished via the chemical shift of the 1s core level. This chemical shift will lead to the occurrence of resonant enhancement of a charge-ordering reflection at the Mn K-edge via a 1s→4p dipolar transition. However, as shown in Fig. 1(a), no resonance at the charge-ordering reflection with $\boldsymbol{q}$ = (0,0,0.5) is observed

in our RXS experiment carried out at the Mn K-edge (~ 6.554 KeV), despite the proposed models predicted that the charge ordering should take place at $\boldsymbol{q}$ = (0,0,0.5) [4-5]. To clarify this issue, soft X-ray resonant scattering experiments were carried out in a UHV scattering chamber [7] at the beamline UE56/1-PGM-b of BESSY-II. This technique has hugely enhanced sensitivity to the charge ordering of 3*d* electrons via a dipolar transition to an unoccupied 3*d* sub-band, instead of via indirect chemical shift effects. As shown in Fig. 1(b), a significant resonant enhancement of $\boldsymbol{q}$ = (0,0,0.5) can be observed near the Mn L_3-edge i.e. at ~ 640 eV. A comparison of the longitudinal scans of $\boldsymbol{q}$ = (0,0,0.5) at and off the resonant energy is shown in Fig. 2.

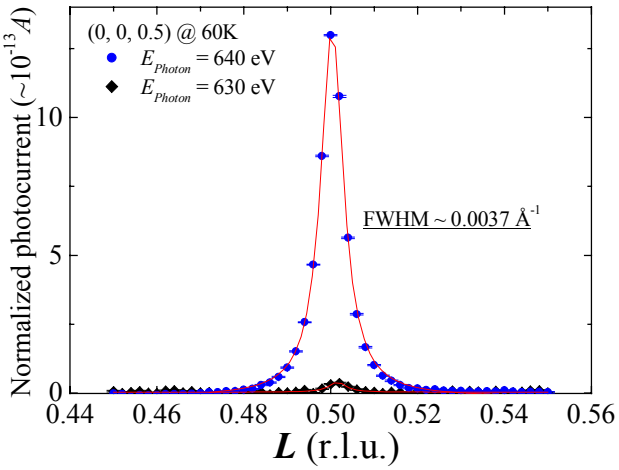

Fig. 2 Longitudinal scans of (0, 0, 0.5) at different incident photon energy, the red solid lines are the Lorentzian fittings to the data points

Furthermore, an extraordinary resonance was also observed near the O K-edge. These observations by soft X-ray resonant scattering enable us to finally confirm that the ordering of doped holes does take place in this compound, however, in a quite different fashion comparing to that in the classic ionic ordering scenario, in which integer $3d^n$ configurations of Mn ions and fully filled oxygen 2*p* shells are assumed. A detailed analysis on the observation and its implication will be published elsewhere [8].

Acknowledgements

We would like to thank the technical staffs at IFF (Juelich) for excellent supports on growing and characterizing single crystals. The authors also gratefully acknowledge the help from Dr. Olaf Hellwig (BESSY). This project was partly funded by the BMBF grant O3ZA6BC2. Use of the APS was supported by the U.S. Department of Energy (DOE), Office of Science, Office of Basic Energy Sciences (BES), under Contract No. W-31-109-ENG-38. The MUCAT sector at the APS and the research activity are supported by the U.S. DOE Basic Energy Sciences, Office of Science, through Ames Laboratory under contract no. W-7405-Eng-82.

References

[1] Y. Endoh, *et al.*, Phys. Rev. Lett. **82**, 4328 (1999)
[2] J. Geck, *et al.*, New Journal of Physics **6**, 152 (2004)
[3] R. Kilian and G. Khaliullin, Phys. Rev. B **58**, R11841 (1998)
[4] T. Mizokawa, *et al.*, Phys. Rev. B **61**, R3776 (2000)
[5] M. Korotin, *et al.*, Phys. Rev. B **62**, 5696 (2000)
[6] S. Ishihara and S. Maekawa, Rep. Prog. Phys. **65**, 561 (2002)
[7] J. Grabis, A. Nefedov, H. Zabel, Rev. Sci. Instr. **74**, 4048 (2003)
[8] Y. Su, *et al.*, (to be submitted)

PEEM imaging contrast in an operating organic electronic device

K. Müller, Y. Burkov, D. Schmeißer, Brandenburgische Technische Universität Cottbus, Angewandte Physik-Sensorik, 03013 Cottbus, P.O.Box 101344, Germany

Photoemission electron microscopy (PEEM) is used to image the active channel in an organic electronic devices. We study the hetero-atomic polymer Poly(3-hexylthiophene) (P3HT) which is an important semiconducting material for organic electronics. Field effect transistors (OFET) [1], [2] or solar cells [3] are processed as low-cost processing of this soluble conducting polymer results in a relatively high charge mobilities (typical value: $1x10^{-3}cm^2/Vs$ [4]). For our studies we use OFET structures which consist of source-drain-electrode structures of different organic materials like carbon-black or graphite plotted on a printing foil (Polyethylene Terephthalate, PET) [2].

Regio-regular P3HT (Aldrich) dissolved in dried chloroform is used. Thin films with thickness of around 100nm are prepared by a spin-coating procedure on the plotted source-drain structures for PEEM at applied voltages and stainless steel substrates for PES. The preparation was performed in argon atmosphere, film thickness and handling conditions are comparable with those applied for organic field effect transistors [2]. Samples are contacted in UHV to allow imaging in the channel while voltages (±10V) at the source and drain electrode are applied. We operate the PEEM (Focus) by illumination with a Hg lamp (4.9eV) or a D_2 lamp (continuum, max. 6.5eV). Using synchrotron radiation at the BESSY U49/2 beam line we record μ-XAS spectra with the PEEM and collect resonant PES data using a HA125 (Omicron) analyser [5].

In figure 1 we show three PEEM images taken with D_2 excitation. The channel is visible as a broad stripe in between the left electrode (with voltage applied) and the right electrode (at ground potential). With applied voltage the whole region of the channel becomes darker, independent of the polarity of the voltage applied. Also, the PEEM intensity of the channel, which is the yield of photoelectrons, appears to be homogeneous without any significant distributions or gradients. These findings are in striking contrast to our measurements of the surface potential. On the same sample we performed μ-PES at selected positions in the channel and are able to find a linear shift of the PES spectra due to the local potential. It represents the work function or surface potential of the selected areas and is in excellent agreement with our findings revealed by scanning Kelvin probe microscopy [6, 7]**.**
In order to explain the PEEM contrast of the organic structures we focus on the electronic structure of P3HT and show in Figure 2 a combined spectrum of the occupied and the empty valence states, all energies are referred to the Fermi level.
The occupied states are derived from energy distribution curves (EDC), we present the photoelectron spectra (PES) at resonant excitation energies at the C1s (285eV, black), the S2p (165eV, red) ionization thresholds, compared to spectra taken off resonance. These valence band data are dominated by two broad features, which are due to the C2s and S3s derived states and the C2p and S3p states. In the upper of these two bands the carbon derived (H_C) and sulphur derived (H_S) HOMOs of the thiophene monomer, respectively, are still dominating as marked by the dashed lines. The weaker emission of the highest band at –3.1eV is attributed to emission from electrons out of the delocalized π band, see also [8].
The empty states are derived from X-ray absorption spectra (μ-XAS) and the constant-initial-state (CIS) spectra again recorded in the range of the absorption edges of C1s (black) and S2p (red). The CIS spectrum at the C1s edge is taken at a binding energy close to the valence band

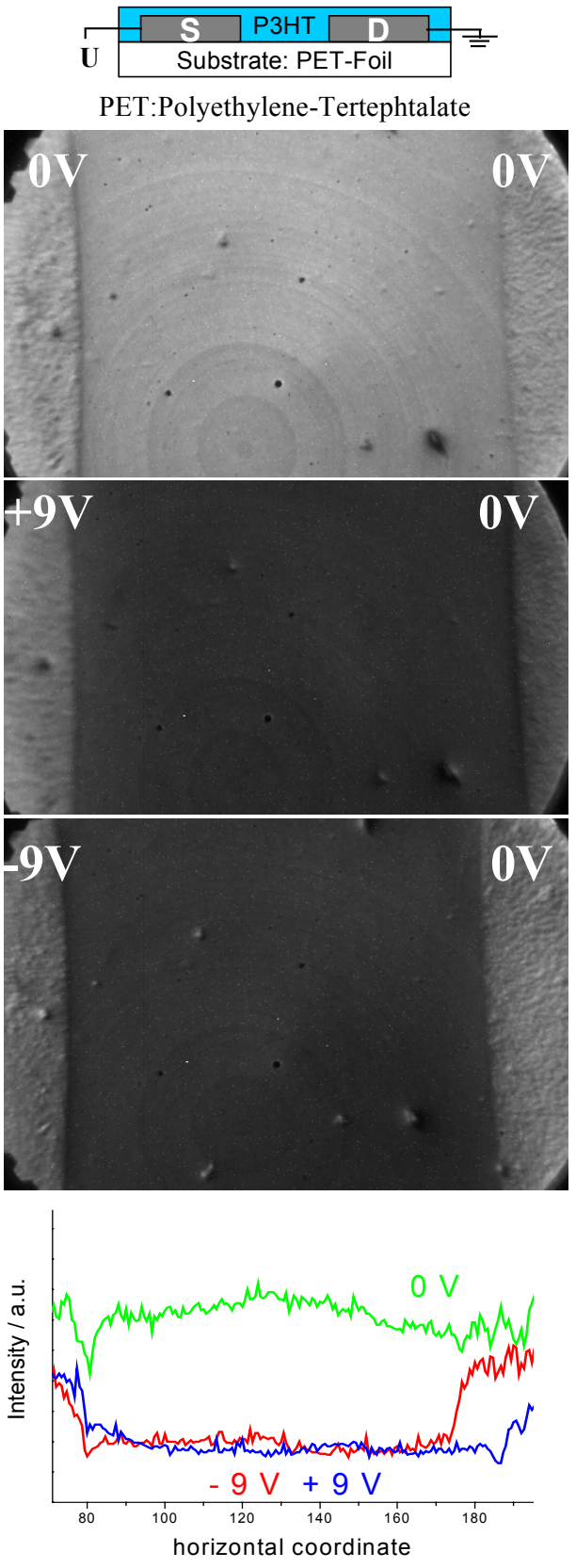

***Figure 1**: Schematic presentation of the device structure used (top).PEEM-images with D_2-excitation of the channel visible as a broad stripe, with 0V, +9V, and -9V applied at the left electrode. The lower diagram shows the intensity profiles across the channel for the three images shown above. Different channel lengths are due to strains.*

maximum. The CIS spectrum at the S2p edge is taken for the binding energy at the S3p HOMO (H_S). For both excitations (C1s or S2p) a pronounced peak occurs at energies just above the Fermi energy. It coincides with the excitonic feature in the μ-XAS curves.

These data elucidate that within the π band both, the C2p and the S3p derived states contribute. In the occupied part both appear in the resonant PES spectra. In the CIS data we learn that also both the C1s and the S2p wave functions contribute. It should be pointed out that there is a significant difference between the two. While the C2p derived states come out of the delocalized π band, those from the hetero-atom arise out of the S3p HOMO states. Here it indicates that in the empty π* band the contribution of the S3p states is even lower in excitation energy than the contribution from the C2p states. This is evident from both, the μ-XAS and the CIS data.

Coming back to the PEEM images, these are taken with an excitation energy of 4.9eV/E≤6.5eV. With these low excitation energies just electrons out of the π band can be excited, evidently. As the electrons in the π band are the only electrons that can be involved in the transport properties it is quite evident that the number of these charge carriers depend on the applied voltage within the channel of our devices. Any voltage, independent on the polarity, will cause the charge carriers to move out of the channel towards one of the two electrodes. Therefore, we do not find any dependence on the polarity in our PEEM data.

Finally, we like to address the fact that we do not observe the surface potential which is linear declining within the two electrodes, as it is found in our complementary μ-PES and Kelvin

probe studies. We learn from the µ-PES EDC curves that in the energy distribution we have a rather strong contribution close to the Fermi energy while the intensity at the secondary onset appears to be much weaker.

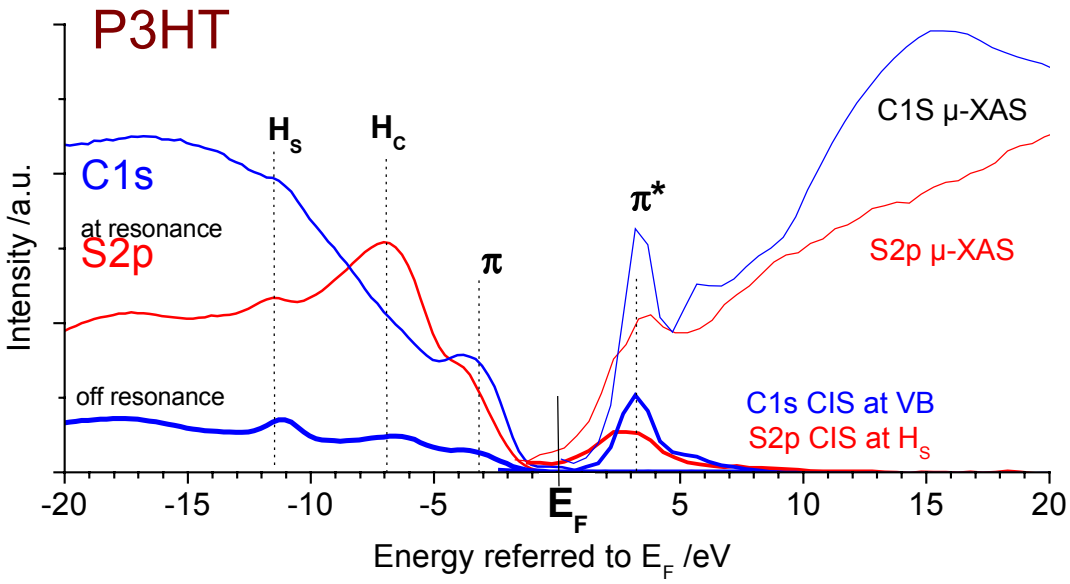

Figure 2: Electronic structure of P3HT. The valence band states are derived from UPS-EDC taken with resonant excitation (285eV, C1s black), (165eV, S2p red). The empty conduction band states show up in the µ-XAS and CIS- spectra as recorded around the C1s and S2p threshold. All data are referred to the Fermi level.

Obviously the intensity in our PEEM images is not determined by the secondaries but it is dominated by the contributions of the true photo electrons mostly. As a result of the low excitation energies these appear only at kinetic energies of a few eV. As a consequence, these electrons arise only out of the uppermost delocalized π-band, however, because of that they are extremely sensitive to the charge carrier concentration causing the conduction within the gate.
In summary, the combination of measuring the surface potential with the µ-PES mode and the density of charge carriers with the imaging mode offers a new analytical method for the characterization of active layers in operating polymeric devices.

References

[1] Z. Bao, A. Dodabalapur, A. Lovinger, Appl. Phys. Lett. 69 (1996) 4108.
[2] K. Müller, I. Paloumpa, D. Schmeißer, Synth. Metals 138 (2003) 271.
[3] D. Chirvase, J. Parisi., J.C. Hummelen, D. Dyakonov, Nanotechnology 15 (2004) 1317.
[4] H. Sirringhaus, H. Tessler, R. H. Friend, Synth. Metals 102 (1990) 857.
[5] D. Schmeißer, P. Hoffmann, G. Beuckert, Materials for Information Technology, Springer Verlag, submitted
[6] K. Müller, A. Goryachko, Y. Burkov, C. Schwiertz, M. Razke, J. Köble, J. Reif, D. Schmeißer Synthetic Metals 146 (2004) 377-382
[7] M. Geuss, K. Müller, D. Schmeißer, to be published
[8] D. Schmeißer, Synth. Metals 138 (2003) 135.

Chemistry of Metal/Organic Interfaces Revealed by High Resolution Photoemission Spectroscopy

G. Gavrila, M.Gorgoi, D.R.T Zahn

Institut für Physik, Technische Universität Chemnitz, D-09107, Chemnitz, Germany

W. Braun

BESSY GmbH, Albert-Einstein-Straße 15, D-12489 Berlin, Germany.

The chemical and electronic properties of interfaces in organic devices are decisive for charge carrier injection and transport. Metal/organic interfaces can undergo complex and spatially extended chemical interaction. We present here an overview of a detailed study of the interface formation between perylene derivatives (i.e. PTCDA and PTCDI) and low work function metals (i.e. Mg and In). The aim of this study is to understand whether a variation of the molecular structure by different functional endgroups result in different interface properties. The differences are explored via high resolution photoemission spectroscopy followed by a peak fitting procedure of the core levels as a function of metal deposition.

The organic layers were evaporated onto sulphur passivated GaAs substrates followed by metal evaporation with thicknesses monitored by a quartz microbalance. The experiments were performed at the Russian-German beamline at BESSY II using the MUSTANG experimental station. The photoelectron spectra were detected with a PHOIBOS 150 (SPECS) analyser.

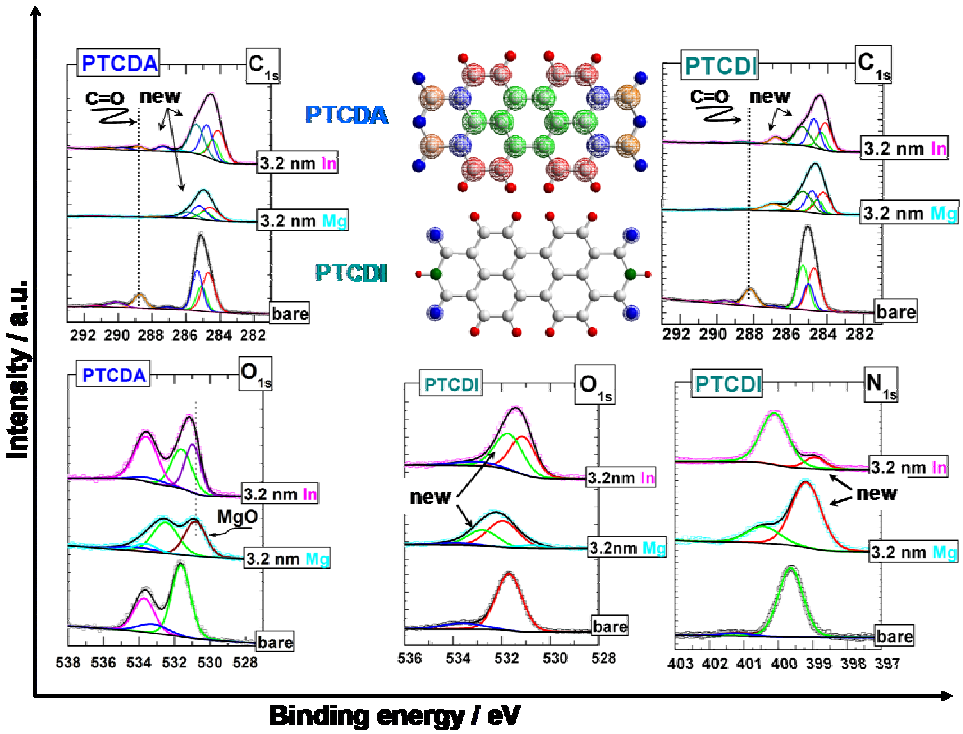

Fig.1.Contribution of the individual peaks to the overall intensities of the C_{1s}, O_{1s} and N_{1s} for bare organic and upon 3.2nm of metal deposition. The individual components for the C_{1s} of PTCDA are assigned according to the colour coding.

Fig.1. shows the C_{1s}, O_{1s} and N_{1s} spectra of about 15nm of PTCDA (left) and PTCDI (middle+right). The C_{1s} spectra consist of two well separated features. The main peak with maxima at about 285.3 eV is resulting from different carbon atoms of the aromatic part while the second peak situated at 288.9 eV and 288.3 eV stems from the carbon atoms of the anhydride and imide

endgroups, respectively. The O_{1s} spectra of PTCDA exhibit a double peak structures with energy separation of about 2.0eV. The low energy peak results from the carboxylic oxygen atoms (C=O) while the high energy peak is derived form the central oxygen atoms (C-O-C). In PTCDI this central atom is replaced by a NH group thus the O_{1s} spectrum will exhibit only the carboxylic contribution.

Strong changes are observed in all the core level emission spectra after 3.2 nm metal deposition. These changes include binding energy shifts, which differ for the various core levels and metals, and appearance of new components. We can conclude that each metal/organic interface has a distinct chemisorptive nature.

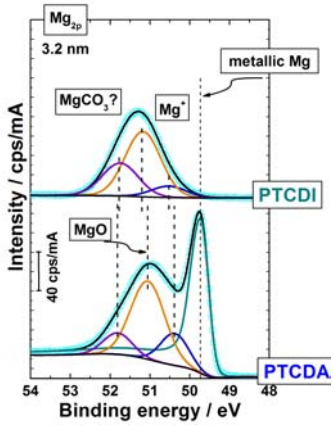

Fig.2. The individual components of Mg_{2p} core level emission at a thickness of 3.2nm on the two distinctive perylenes.

Mg case: In the C_{1s} and O_{1s} spectra of Fig. 1 for the molecules new components are present. In the PTCDA case we observe the following: vanishing of the C=O component, new component at a lower binding energy, and a ratio of the peaks 8:12:4. In the O_{1s} spectra the C-O-C peak vanishes and a new component corresponding to MgO is present. Presence of MgO is observed in the Mg_{2p} core level as well (see Fig.2). These findings are consistent with a strong chemical interaction between Mg and the single bonded oxygen atoms of PTCDA, resulting in MgO detached from the molecule. In the PTCDI case Mg affects again the side group of the molecule (imide group). The new components in the C_{1s}, O_{1s} , N_{1s} and Mg_{2p} spectra indicate that Mg is likely to be involved in "bridging" the carboxylic oxygen with the nitrogen. The main differences between the two molecules are that the oxidation (MgO formation) prevents diffusion of Mg into the organic film. Strong metallic Mg components are observed beyond 1.6nm Mg covarage onto PTCDA while for PTCDI the metallic component only appears at thicknesses larger than 33 nm. In both cases the perylene core retains its aromatic structure.

In case: In the C_{1s} and O_{1s} spectra of Fig. 1 the changes in the core levels upon In deposition are very similar for PTCDA and PTCDI. The changes observed strongly indicate that In atoms are placed in the neighbourhood of the aromatic rings and/or of the carboxylic oxygen atoms. The new components present in all the core level spectra, including In_{4d} (see Fig.3.) are related with an electron transfer from the metal to the π electron system of the molecule. Again large differences are observed in the degree of the diffusion of the In metal into the organic film.

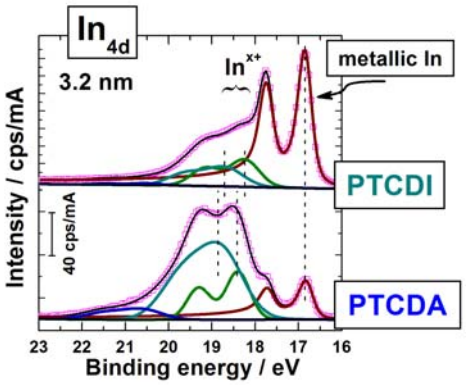

Fig.3. The individual components of In_{4d} core level emission at a thickness of 3.2nm on the two distinctive perylenes.

Acknowledgements

The authors acknowledge the BMBF (FK MUSTANG 05 KS40C1/3, 05 ES3XBA/5, 05 KS1OCA/1) for the financial support and Mike Sperling for his assistance during the beam time.

Pr4f occupancy and origin of gap states at the Pr_2O_3 / Si(001) interface

Dieter Schmeißer and H.J. Muessig
Angewandte Physik - Sensorik, BTU Cottbus, Postfach 10 13 44, 03044 Cottbus, Germany
ihp, Im Technologiepark 25, 15236 Frankfurt/Oder, Germany.

Resonant photoelectron spectroscopy (PES) at the Pr4d and O1s absorption edges is used to study the electronic properties at the interface of epitaxial grown Pr_2O_3 on Si(001) /1, 2/. In this contribution we focus on the Pr4f occupancy in the occupied VB states and in the empty CB states and on the origin of gap states which we derive from the O1s XAS data.

Experiments are performed at the U49/2 beam line at BESSY equipped with a PEEM used to record the XAS data and a hemispherical electron energy analyzer for the photoelectron spectra /3/. Pr_2O_3 is evaporated from an e-beam evaporator with the Si(001) surface kept at 600°C after removing the native SiO_2 layer by flashing.

At the Si(001) interface in-situ prepared epitaxial layers (d<5nm) enable us to study the contribution of the Pr4f electronic states in the valence band population as a function of layer thickness. We find a silicate intermediate which is deduced from the core level shift of the Si2p and the O1s levels /2, 4/. The offset in the VB maxima has been determined from the relative position of the valence band spectra in coverage dependent data /4/. Here we focus first on the population of the Pr4f states which can be studied at resonant excitation around the Pr4d-Pr4f resonance at around 125eV. The emission of the Pr4f states is identified to appear at –3eV in the bulk phase of Pr_2O_3 as it is significantly enhanced at resonance and appears as a pronounced contribution for all energies above the threshold /4/. These states reflect the existence of CT excitations which in the ground state of Pr_2O_3 cause f^0, f^1, and f^2 multiplets.

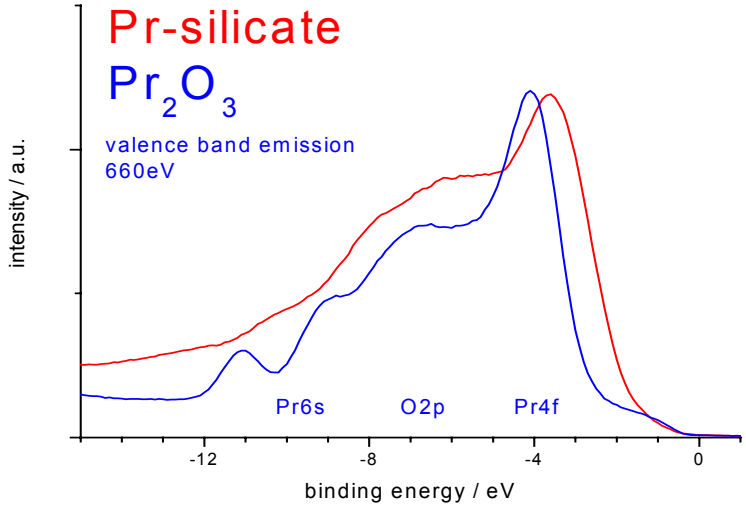

Fig.1: Valence band regime of Pr-silicate and of bulk Pr_2O_3 as recorded for photon energies around the Pr4d-Pr4f resonance.

In Fig.1 we show such data and focus on the differences between the silicate and the bulk Pr_2O_3 phase. We show valence band spectra recorded at 660eV in which the relative contributions of the Pr6s, O2p and Pr4f levels are indicated. In the Pr-silicate range (d<1nm) the Pr4f states ap-

pears considerable broadened and extends from –2eV down to –4eV. It clearly is above the bulk Pr4f emission and below the valence band maximum (VBM). Now the Pr4f emission in total has increased in width to amount about 2.5eV. The increase of the O2p emission in these data reflects the fact that there is an increase in the covalent interaction. It is caused by the silicate formation and the O2p and Pr4f/Pr5d states show a stronger mixing than in the bulk Pr_2O_3 phase, consequently. In the spectrum of the thicker Pr_2O_3 layer we notice the pronounced shoulder of the underlying Si substrate which becomes evident because of the rather high electron mean free path of the photoelectrons at that particular photon energy. The thickness of the Pr-silicate layer amounts to 1nm, that of the Pr_2O_3 layer is 2nm.

Next we focus on the X-ray absorption spectra which again are displayed for the bulk Pr_2O_3 phase and the silicate phase in Fig.2. The O1s XAS signal of the bulk Pr_2O_3 phase looks very complicated with its four significant maxima. Also, the changes that occur when going from Pr_2O_3 to the silicate phase are huge. To understand the spectral features in detail we have analyzed the shape of the O1s XAS signal in the related systems of CeO_2 and Ce_2O_3 as well. That comparison has the number of 4f states as a parameter which increases from 0 to 3 when going from CeO_2 to Pr_2O_3 /5/.

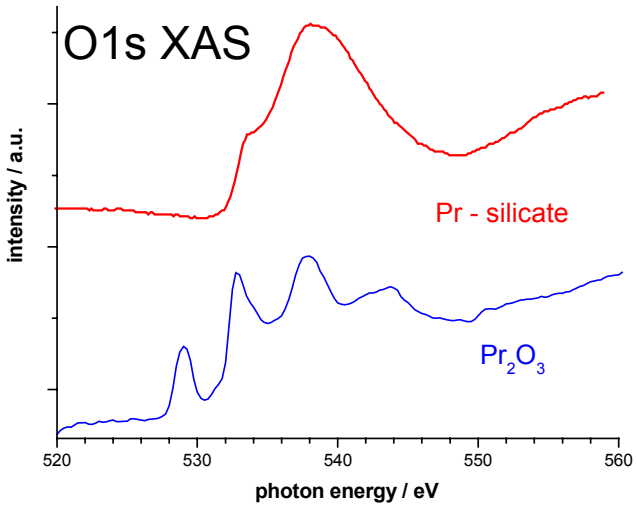

Fig.2: Oxygen 1s X-ray absorption spectra of Pr-silicate and Pr_2O_3.

The resonant contributions in the XAS data of Fig.2 must be assigned to a resonant Auger Raman scattering process /5, 6/. In our data for Pr_2O_3 we identify three resonant contributions as we do in the CeO_2 and Ce_2O_3 phases /4, 5/. The first two features are due to a scattering process involving CT complexes. These CT complexes represent electron hole excitations between the valence states (the O2p (Ligand) states) and the empty 4f states (529eV) as well as into the states of the upper Hubbard band (532.5eV). The third contribution at 537eV is due to scattering at electron-hole pairs created by band-to-band excitations. In our comparative study we learned that the first two resonant structures are much more pronounced in CeO_2 and are reduced in Ce_2O_3 /5/ in a similar way as those shown here for Pr_2O_3. We explain that reduced contribution by an enhancement of the covalent bonding which occurs between the O2p states and the Pr4f states, in agreement with theoretical studies /6-8/ and in agreement with the valence band spectra of Fig.1. Focusing now on the changes that occur in the Pr-silicate we notice that the third contribution is still pronounced in the Pr-silicate spectra while the former two resonant features are tremendously quenched. This behavior is consistent in the series CeO_2, Ce_2O_3, Pr_2O_3 which indicates an

increase in the covalent contributions /4, 5/. Again, we explain that reduced contribution by an enhancement of the covalent bonding which occurs between the O2p states and the Pr4f states but now – in the Pr-silicate - with additional contributions from the Si valence states. Awaiting theoretical confirmation we propose that the formation of Pr – O – Si bonds enables the formation of CT excitations by an additional charge transfer from a Si 3p electron into the Pr4f or Pr5d empty conduction band states.
The covalent contributions form a covalent (O2p, Pr4f) band at the top of the valence band which shows up as an additional feature at the VBM in the corresponding photoemission data (Fig.1). In addition, at the interface the charge transfer complexes from the Si3p states cause a broadening of the CT states which are located within the gap. Therefore they are no longer localized but act as gap states which because of their large concentration form a band of defects states. The band of defect states causes an almost continuous density of states and consequently, also the unoccupied states must have a similar distribution. The steep rise at 531eV indicates transitions into these band-like empty states.

In summary, resonant photoelectron spectroscopy (PES) with synchrotron radiation is used to study the electronic properties at the interface of epitaxial grown Pr_2O_3 on Si(001) surfaces. In the electronic structure of bulk Pr_2O_3 the valence band (VB) states are predominantly of Pr6s and O2p atomic parentage. Weak contributions from Pr4f states are identified from the strong increase the VB features at the Pr4d and Pr3d ionization thresholds. They are the consequence of mixed valency caused by ligand-to-Pr4f charge transfer states. We use in-situ prepared epitaxial layers ($d<5nm$) to study the contribution of the Pr4f electronic states in the valence band population as a function of layer thickness. We find for the silicate intermediate that the weak occupancy of the Pr4f states in the bulk phase of Pr_2O_3 is significantly enhanced. There is an additional 4f state which appears right at the valence band maximum (VBM). In x-ray absorption at the O1s edge we find the features of localized Pr4f states to be quenched. We conclude that the Pr-silicate causes an enhanced hybridization (covalent bonding) of the Pr4f states into the valence band. Consequently, our data indicate that the Pr-silicate has a metallic –like DOS. Indeed, such a metallic-like state is not favorable for the MOS architecture. Even if we consider that the defect states sill will have a low mobility because of the 4f contribution and the thereby associated effective mass. Currently, we undertake investigations on alloyed oxides such as $La_xPr_{2-x}O_3$ in order to avoid that formation of a continuous density of states within the gap. Our data are a step towards a full description of the interface properties of that high K material, a prerequisite for its possible application in storage, logic, and power electronic devices.

The assistance of Dr.P.Hoffmann and the support of the Bessy staff is acknowledged. This work is supported by DFG (Schm 745 / 9 - 1).

/1/ G.D.Wilk. R.M.Wallace, J.M.Anthony, J.Appl.Phys. 89 (2001) 5243.
/2/ D.Schmeißer, Materials Science in Semiconductor Processing 6 (2003)59.
/3/ D.R.Batchelor, R.Follath, D.Schmeißer, Nucl. Inst. Methods in Physics Research A 467 (2001) 470.
/4/ D.Schmeißer, H.-J.Müssig, J. Physics: Condensed Matter 16 (2004) S153.
/5/ D.Schmeißer, submitted to PRB.
/6/ A.Kotani and S.Shin, Rev.Mod.Phys. 73 (2001) 203.
/7/ G.Wendin, Phys.Rev.Lett. 53 (1984) 724; O.Gunnarson, K.Schönhammer, Phys.Rev.B28(1983)4315.
/8/ B.T.Thole, G.vanderLaan, J.C.Fuggle, G.A.Sawatzky, R.C.Karnatak, J.M.Esteva, Phys.Rev.B32 (1985) 5107.
/9/ A.Goryachko, I.Paloumpa, G.Beuckert, Y.Burkov, D.Schmeißer,
Physica Status Solidi C1 (2004) 265.

Photoelectron spectroscopy and microscopy on Cr nano particles embedded into block copolymers

O. Seifarth, Y. Burkov, A. Goryachko, D. Schmeißer,
A. Sydorenko*, R. Krenek*, M. Stamm*

Brandenburgische Technische Universität, Konrad Wachsmann Allee 17, 03046 Cottbus

*Leibniz-Institut für Polymerforschung, Hohe Straße 6, 01069 Dresden

In the last decades special interest arose in materials with reduced dimensions or diameters. Outstanding and unique physical properties are associated to materials exhibiting well defined structures in the nano-meter range [1]. But creating ordered arrays of nano structures up to centimetres is by far not trivial [2] [3]. In this report we present an approach using self assembled Cr_2O_3 related nano wires deposited on a well ordered block copolymer (BCP) template. These nano wire arrays form domain like areas on top of the block copolymer ranging from tens of nanometres to microns.

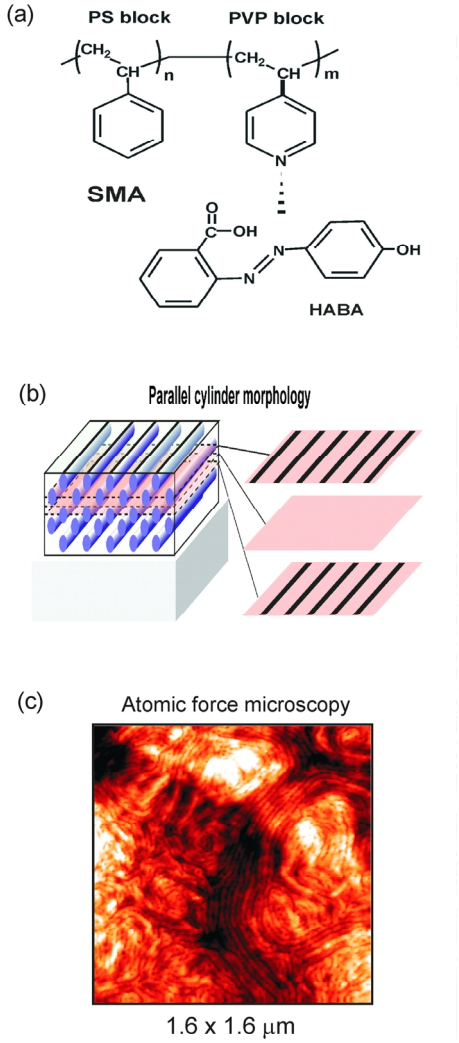

Fig.1. The SMA based approach for metal nanowire fabrication, chemical composition (a), microphase separation in thin films of SMA forming nanotemplates with in plane channels (b), atomic force microscopy image of Cr_2O_3 nanowires on the template.

To understand how Cr_2O_3 nano structures behave when embedded into block copolymers we evaluate the local distribution by means of Photoelectron emission microscopy (PEEM) and analyse the electronic and geometric changes of Cr_2O_3 with X-ray absorption spectroscopy (XAS).
Nano structured thin polymer films have been fabricated from the supramolecular assembly (SMA) of poly(styrene-block-4-vinylpyridine) (PS-PVP)(figure 1 (a)) and 2(4'hydoxybenzeneazo)-benzoic consisting of cylindrical in plane nano channels [4]. Extracting of HABA results in hollow channels which can now be filled with functional materials like Chromium or Chromium oxides in our case (b). There are different possible orientations for these nano-structures. It is also possible to produce nanometer sized spheres, perpendicular cylinders or even lamellars. Figure 1(c) presents the resulting surface of BCP covered with Cr_2O_3, which is arranged in self organized wires.

In figure 2. PEEM images depict formation of Cr_2O_3 related nanowire composed domains ranging from few nanometers to microns. These self organized structures have variable shapes and their arrangements changes within micrometers, as can be seen in the images (a) and (b). Despite this, areas composed of domains can also be found on the samples (c-d), indicating that it is possible to produce high quality samples with nano structure arrays over hundreds of microns.
Part (e) presents XAS data on the Cr L edge derived from the Chromium nano structured area shown in (b) in the total electron yield (TEY). The resulting characteristic double structure constituted by the L_{III} and L_{II} edges is compared with bulk Cr_2O_3. We can clearly identify significant variations in particular in the $L_{||}$ edge around 587 eV. The spectral intensity decreases by a factor of three. This scenario was recently observed in familiar manganese oxides and reflects different valence and oxidation states [5]. In the nano structured case the conduction electron density of states decays in a triplet with a weak transition in the center, surrounded by two stronger emissions. For bulk Cr_2O_3 the $L_{||}$ split appears to be favoured into a doublet state.

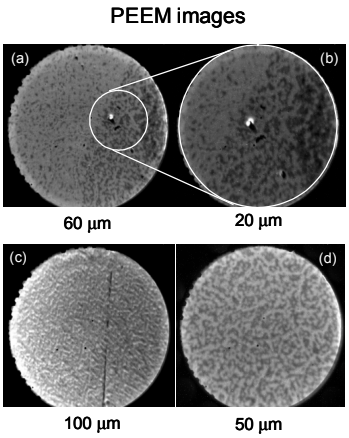

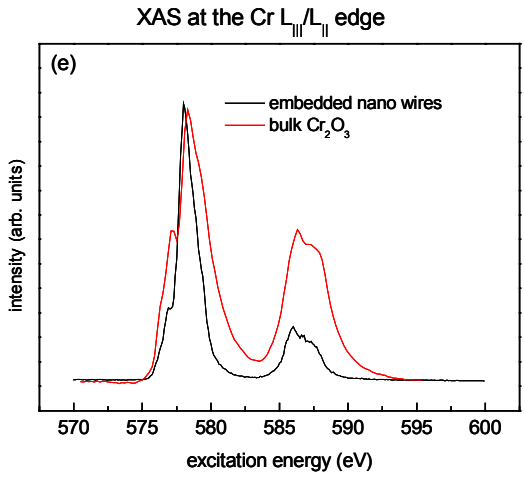

Fig.2. PEEM images from domains, composed of Cr derived nano wires on top of BCP in (a),(b),(c) and (d). The photon energy was set to 579 eV. Comparision of XAS spectra from the Chromium L edge taken of the nanowire arrays shown picture (b) and bulk Cr_2O_3 in (e) . Bulk data taken from [8].

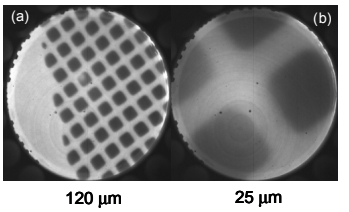

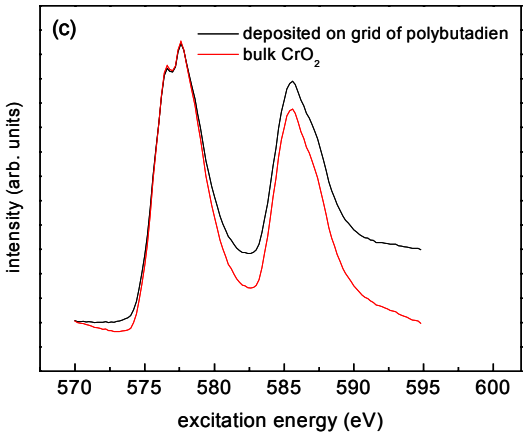

Fig.3. PEEM images from grid of polybutadien, to be riddled of Cr related nanoclusters in (a),(b). The photon energy was set to 579 eV. Comparision of XAS spectra from the Chromium L edge taken from the area depicted in (b) and shown in (c). Bulk data taken from [8].

Different peak intensities and shapes can also be observed in the $L_{|||}$ adsorption edge. First, the main emission at 578 eV seems to be much sharper contrasting to the reference data. This is intimately related with the oxidation state of the Cr ions in the BCP. It is generally believed, that (semi)metallic compounds exhibit narrower emissions in their XAS data compared to semiconducting or insulating materials. Together with the spectral features observed in the $L_{||}$ edge, we found evidence that our XAS data is derived from Cr nano particles in an intermediate state between metallic and insulating and not simple Cr_2O_3.
The lowest excitation around 577 eV in the nano template shifts about 0.2 eV towards lower energies. This indicates that nano structured Chromium oxides prefer a more metallic state by a total shift of conduction band density of states towards the Fermi energy or that additional band gap states are constituted by the nano pattering. The latter was recently observed in thin films of Cr_2O_3 experimentally [6] and confirmed with *ab initio* calculations [7].
In fig. 3 we present storing of different Chromium oxidation states is possible in polymers. In the PEEM images (a-b) a grid of polybutadien is shown, earlier exposed to deposition of Chromium. The corresponding XAS spectra in (c) reveals that the favoured oxidation state seems to be CrO_2 . Similar to fig.2 the photoemission intensity in the $L_{||}$ edge differs, now with higher intensity in the nano particles case.
Both L edges show a significant broader spectral shape than in bulk CrO_2, and the dip in between seems to be completed compared to the high energy tailed background. This is generally believed to play a significant role in understanding conducting or insulating properties within the metallic oxides and was recently observed in the case of copper [9]. Also in the case of Cr nano particles in polybutadien the oxidation state of the particles differ from the pure metallic CrO_2 state. This seems to be characteristic for stored Cr related clusters on and inside polymer samples.

In summary we demonstrated that Cr related particles can be stored in self organized nano structures in and on top of block copolymers. We found that domains composed of these structures regularly cover the complete sample. In particular we found characteristic features in the Cr L edges with XAS, which are related to Chromium oxide nanowires on top of BCP. Very remarkable however is the fact, that Cr nano particles in the wires prefer a different oxidation state than that of the most common Cr_2O_3 oxide.

The experiment was performed with the BTU ASAM endstation [10] and synchrotron radiation was delivered from U49/2 PGM 2 [11].
The support of P. Hoffmann, G. Beukert (both BTU) and the BESSY staff is gratefully acknowledged.

References:

[1] D. Schmeißer, O. Böhme, A. Yfantis, T. Heller, D.R. Batchelor, I. Lundstrom, and A.L. Spetz,
Phys. Rev. Lett. (1999), 83, 380-383

[2] J. Spatz, S. Mößmer, M. Möller, M. Kocher, D. Neher, and G. Wegner,
Adv. Mater. (1998), 10, 473-476

[3] T. Thurn-Albrecht, J. Schotter, G.A. Kästle, N. Emley, T. Shibauchi, L. Krusin-Elbaum, K. Guarni,
C.T. Black, M.T. Tuominen, and T.P. Russell, Science (2000), 290, 2126-2129

[4] A. Sydorenko, I. Tokarev, S. Minko, and M. Stamm,
J. Am. Chem. Soc. (2003), 125, 12211-12216

[5] B. Gilbert, B.H. Frazer, A. Belz, P.G. Conrad, K.H. Nealson, D. Haskel, J.C. Lang, G. Srajer,
and G. De Stasio, J. Phys. Chem. A (2003), 107, 2839-2847

[6] M. Bender, D. Ehrlich, I.N. Yakovkin, F. Rohr, M. Bäumer, H. Kuhlenbeck, H.J. Freund, V. Staemmler,
J. Phys. : Condens. Matter (1995), 7, 5289-5296

[7] J.A. Mejias, V. Staemmler, and H.J. Freund,
J. Phys. : Condens. Matter (1999), 11, 7881-7891

[8] Data courtesy of F. Himpsel, Univers. of Madison, WI, USA

[9] D. Schmeißer, unpublished

[10] D. Schmeißer, P. Hoffmann, G. Beuckert,
Materials for Information, Springer, submitted

[11] D.R. Batchelor, R. Follath, D. Schmeißer,
Nucl. Instrum. Methods Phys. Res., Sect. A (2001), 470, 467-468

High-resolution metal 2p x-ray absorption spectra of transition-metal acetylacetonate complexes, $M(acac)_3$.

A.S. Vinogradov [1], A.B. Preobrajenski [1,2], S.A. Krasnikov [1,3], E.V. Nikolaeva [1], Yu.S. Dedkov [4], S. L. Molodtsov [1,4] and R. Szargan [3]

[1] *V.A. Fock Institute of Physics, St. Petersburg State University, St. Petersburg, 198504 Russia;*
[2] *MAX-lab, Lund University, S-22100 Lund, Sweden;*
[3] *W. Ostwald-Institut für Physikalische und Theoretische Chemie, Universität Leipzig, D-04103, Leipzig, Germany;*
[4] *Institut für Festkörperphysik, Technische Universität Dresden, D-01062 Dresden, Germany*

The deep insight into the nature of electronic structure and chemical bonding in the transition metal (TM) compounds can be provided in the most straightforward and reliable way by the high-resolution x-ray absorption and photoelectron spectroscopy. Therefore, the metal atom 2*p* absorption spectra are widely used at the moment for characterizing electronic and structural properties of various TM compounds, including TM oxides which are of considerable technological importance [1]. However, these spectra are commonly very complicated because the absorption structures are affected by many such parameters as number of the empty 3*d* electron states of the TM atom, 3*d* – 3*d* and 2*p* – 3*d* exchange interactions in its partially filled electron shells, kind of surroundings atoms, shape and symmetry of the TM atom surroundings, interatomic distances, degree of covalency of the bonding between the central TM atoms and the ligands, etc. Thus, the proper understanding and interpretation of the spectroscopic data can be hardly obtained for a particular compound and additional spectroscopic investigations of related compounds are required. In particular, it is highly desirable to exclude at least some of these factors and reduce the real complex situation to a simplified one.

The TM acetylacetonates, $M(acac)_3$, are likely more appropriate model compounds for most of the TM oxides. These acetylacetonates (chemical formula $M(C_5H_7O_2)_3$, M=Sc, V, Cr, Mn, Fe, Co) are chelates that contain three heterocyclic rings with a central metal atom connected to the rings through six oxygen atoms. The key feature of their atomic structure is that the six oxygen atoms form an isolated and almost ideal octahedron around the TM atom, without any considerable distortions and of the nearly same size [2]. Thus, the comparison of the x-ray absorption in the TM acetylacetonates with that of the corresponding TM oxides, most of which have distorted octahedral environment of the TM atoms by six oxygen atoms, will allow us to reveal the effect of the octahedron distortion on the absorption spectrum and then on the electronic structure of the corresponding oxides. This is possible, because the fine structure in the x-ray absorption spectra of TM oxides is determined mainly by the first coordination shell around the TM ion, i.e., by the MO_6^{n-} quasi-molecule [3]. In addition, a close inspection of the spectral changes along the series of the metal 2*p* absorption spectra for $M(acac)_3$ should reveal the effects of the 3*d* electron number and the exchange interaction on the fine structure of the spectra under consideration.

The near-edge x-ray absorption fine structure (NEXAFS) at the TM atom 2*p* threshold was studied for a series of TM acetylacetonates, including $Sc(acac)_3$, $V(acac)_3$, $Cr(acac)_3$, $Mn(acac)_3$, $Fe(acac)_3$, $Co(acac)_3$, as well as for some oxides and other reference compounds, Sc_2O_3, VF_3, V_2O_5, Cr_2O_3, CrF_3, Fe_2O_3. All measurements were performed during the single-bunch beamtime at the Russian-German beamline. The NEXAFS spectra of these TM compounds were recorded via the total electron yield. All the samples were prepared by rubbing powders of these materials into the scratched surface of a clean tantalum plate. The photon-energy resolution varied between 70 meV at the Sc 2*p* edge (~400 eV) and 140 meV at the Co 2*p* edge (~780 eV). The absorption spectra were normalized to the incident photon flux, which was monitored by detecting the photocurrent from a gold mesh placed at the outlet of the beamline. The photon energy in the region of the TM atom 2*p* absorption spectra

(400 – 900 eV) was calibrated using the known energy position of the first narrow peak in the Ne 1*s* absorption spectrum of the gas-phase neon (867.13 eV [4]) and in the F 1*s* and Ti 2*p* absorption spectra of solid K_2TiF_6 (683.9 eV and 459.0 eV, respectively [5]).

An examination of the NEXAFS spectra obtained should be started with a consideration of changes in absorption structure, which are observed with increasing the 3*d*-electron number for the TM atom along the Sc-V-Cr-Mn-Fe-Co series (Fig. 1). The compared NEXAFS spectra at the metal $2p_{3/2}$ edge show substantial changes in the number and relative intensities of

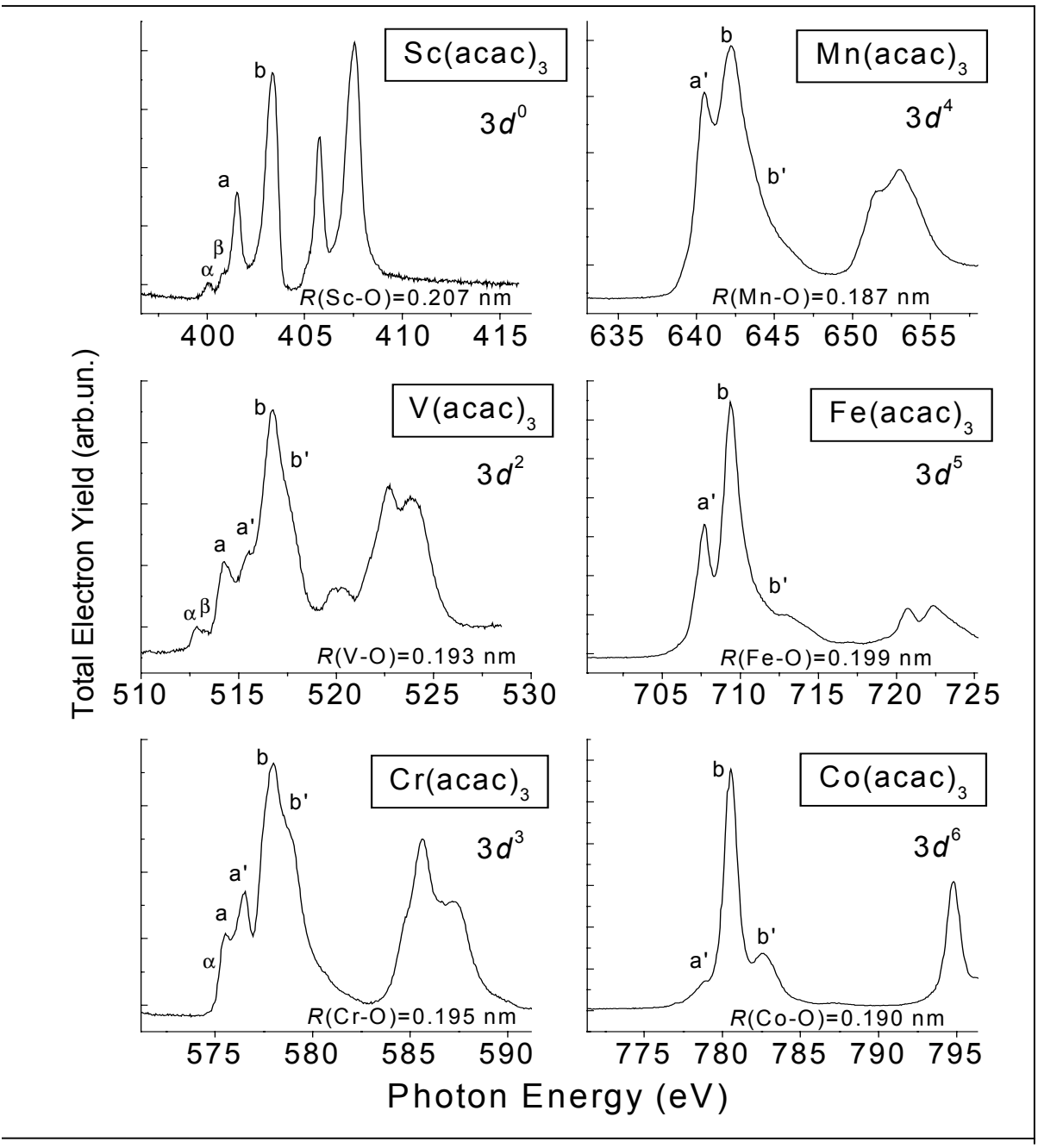

Fig. 1. *High-resolution metal atom 2p absorption spectra of 3d TM acetylacetonates, $M(acac)_3$.. Absorption structures only for the $2p_{3/2}$ spectra are marked.*

the absorption resonances. These changes are likely caused by (i) the decreasing number of the unoccupied 3*d* electron states of the TM atom accompanied by an increasing localization of these states along the series; and (ii) different exchange interaction between the 3*d* electrons in partially filled electron shells. Based on the formal valence, one may assume that

scandium (with a $3d4s^2$ valence-electron atomic configuration) has the electronic configuration of the Sc^{3+} cation in $Sc(acac)_3$ with no $3d$ electrons. In this case, the $3d - 3d$ exchange interaction is absent and the main absorption peaks *a* and *b* in the spectrum of $Sc(acac)_3$ can be related to $2p$ electron transitions to empty molecular orbitals (MO's) of the ScO_6 quasi-molecule, which have mainly the scandium $3dt_{2g}$ and $3de_g$ character, respectively, and are not split by the $3d$-$3d$ exchange interaction. We assume that the exchange interaction between the excited $3d$ electron and the $2p$ hole has no strong effect on absorption structures and it is only responsible for weak low-energy structures α and β associated with the electron transitions to the triplet excited states and for discrepancies between the relative intensities of the corresponding structures observed in the $2p_{3/2}$ and $2p_{1/2}$ spectra and those expected from the statistical ratios for the $2p_{3/2}$ and $2p_{1/2}$ core levels (2:1) and for the $3dt_{2g}$ and $3de_g$ states. In going to $V(acac)_3$ additional structures *a*' and *b*' appear in the absorption spectrum and the energy separation between the main peaks *a* and *b* increases: 1.83 eV for $Sc(acac)_3$ and 2.43 eV for $V(acac)_3$. In contrast to $Sc(acac)_3$ in the vanadium acetylacetonate with the $3d^2$ electron configuration for V^{3+}, the $3dt_{2g}$ and $3de_g$ states are additionally split due to exchange interaction between the $3d$ electrons into $t_{2g}\uparrow$, $t_{2g}\downarrow$, $e_g\uparrow$, and $e_g\downarrow$ components. In this case two available $3d$ electrons of the V^{3+} cation partly fill the lowest $3dt_{2g}\uparrow$ state. The increase of the ligand-field splitting of the $3d$ states in the MO_6 octahedron ($10D_q$) observed in the NEXAFS of $V(acac)_3$ results from the corresponding decrease of the interatomic distance R(M-O): 0.207 nm in $Sc(acac)_3$ and 0.193 nm in $V(acac)_3$. The NEXAFS spectra at the metal $2p$ edge for other TM acetylacetonates can be treated in the same way, taking into account the successive filling of the unoccupied $t_{2g}\uparrow$, $t_{2g}\downarrow$, $e_g\uparrow$, and $e_g\downarrow$ electronic states by the $3d$ electrons. We also assume that additional weak structures should appear owing to a multiplet splitting of the excited states.

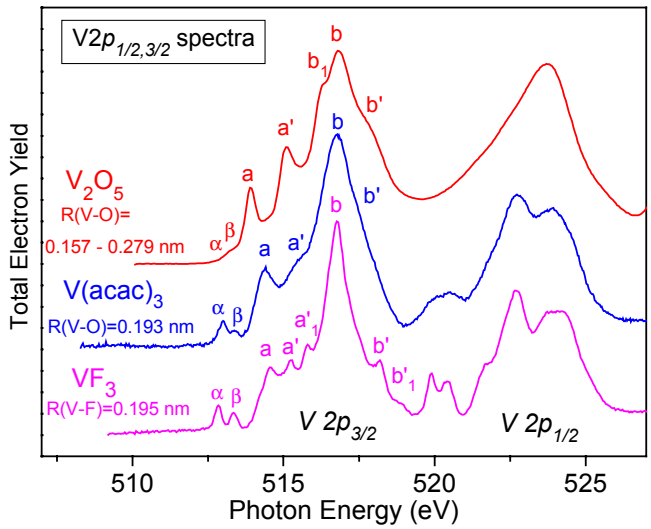

Fig. 2. *V 2p absorption spectra of VF_3, $V(acac)_3$, and V_2O_5 aligned in energy at the energy position of the peak b in $V(acac)_3$.*

This quasi-molecular assignment of the spectra obtained is confirmed by the direct comparison between the metal $2p$ spectra of $M(acac)_3$ and TM oxides and other reference compounds. Figure 2 illustrates this comparison for V $2p$ spectra: the spectra of VF_3 and $V(acac)_3$, which are characterized by the ideal VF_6 and VO_6 octahedral quasi-molecules of the close size, are in good agreement, while the similarity between the spectra of $V(acac)_3$ and V_2O_5 is clearly worse since the oxide has a strongly distorted VO_6 octahedron.

Acknowledgements

This work was supported by RFBR (Project No. 05-03-33254) and the bilateral program "Russian-German Laboratory at BESSY II". A.S. Vinogradov gratefully acknowledges the financial support by BESSY.

References

1. J.G. Chen, Surf. Sci. Reports **30**, 1-152 (1997).
2. E.C. Lingafelter, *J. Amer. Chem.Soc.* **88** (1966) 2951; Coord. Chem. Rev. 1966, N1,151-155; C.J. Hawkins. *Absolute configuration of metal complexes.* N-Y: Wiley-Interscience, 1971, ch.1; L.H. Pignolet, *Topics in Current Chem*. **56** (1975) 93.
3. A.S. Vinogradov, A.B. Preobrajenski, S.A. Krasnikov, et al., Surface Rev. & Lett. **9**, 359-364 (2002); A.S. Vinogradov, S.I. Fedoseenko, S.A. Krasnikov, A.B. Preobrajenski, et al., Phys. Rev. B **71**, in print (2005).
4. R.N.S. Sodhi, C.E. Brion, J. Electron Spectrosc. Relat. Phenom. **34**, 363-372 (1984).
5. A.S. Vinogradov, A.Yu. Dukhnyakov, V.M. Ipatov, et al., Sov. Phys. Solid State **24**, 803-806 (1982).

Electronic structure features of nickel phthalocyanine NiPc observed by x-ray absorption and resonant photoemission

A.S. Vinogradov [1], A.B. Preobrajenski [1,2], D.A. Zverev [1], E.V. Nikolaeva [1], D.V. Vyalikh[1,3], and S. L. Molodtsov [1,3]

[1] *V.A. Fock Institute of Physics, St. Petersburg State University, St. Petersburg, 198504 Russia;*
[2] *MAX-lab, Lund University, S-22100 Lund, Sweden;*
[3] *Institut für Festkörperphysik, Technische Universität Dresden,D-01062 Dresden, Germany*

The 3*d*-metal phthalocyanines (3*d*-MPc's), among them NiPc, Ni($N_8C_{32}H_{16}$), are very stable planar complexes that show various interesting properties and have extensive applications in the areas of catalysis, pigments, semiconductors and sensors [1]. The central part of the 3*d*-MPc's (including the 3*d*-atom and its nearest surroundings) is believed to be their most reactive part and to determine the most important applications of these compounds. The occupied and empty 3*d* electron states of the metal atom, which are located near the Fermi level, are essentially responsible for the unique properties of the 3*d*-MPc's. Since the practical application of 3*d*-metal phthalocyanines is based on the understanding their electronic structure, its investigation remains a subject of intense research over several decades. In particular, the occupied electronic states of 3*d*-MPc's were investigated by photoemission (PE) spectroscopy [2,3], while x-ray absorption (XA) and inverse photoemission spectroscopy were used for studying the unoccupied states [4-6]. However, the energy resolution of the spectra reported so far seems to be insufficient for identifying those spectral features, which result from the chemical bonding between the 3*d*-atom and the Pc macrocyclic ring, as well as for obtaining detailed information on the highest filled and lowest unfilled electronic states of 3*d*-MPc's. Reliable electronic structure calculations are not easy to perform for such complex systems and therefore they are few in number [7]. Therefore the metal 3*d* derived electronic states of MPc's are usually regarded, up to now, as the nearly pure atomic 3*d* components split by a square-planar (D_{4h}) molecular field of the complex [8].

Here we present high-resolution XA and PE measurements, including ResPE at the Ni 2*p* edge, made on NiPc in order to investigate the interaction between the central nickel atom and the ligand atoms as well as to characterize the electronic structure of nickel phthalocyanine in more detail.

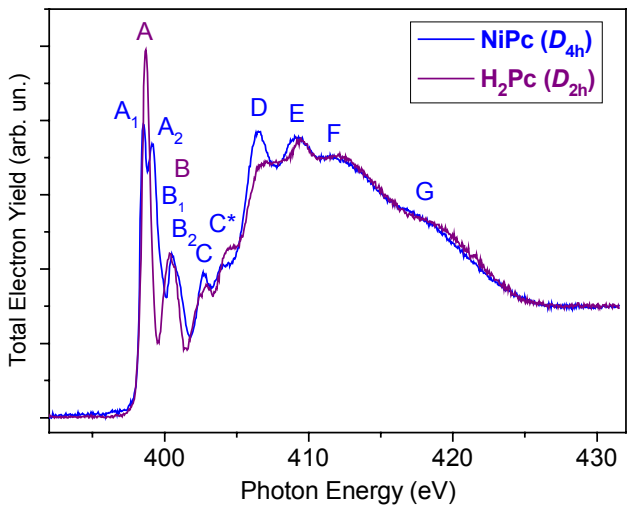

Fig. 1. *High-resolution N1s absorption spectra of NiPc and metal-free phthalocyanine, H_2Pc.*

All measurements on NiPc were performed at the Russian-German beamline at BESSY II. Thin films of NiPc and reference metal-free H_2Pc, in which the Ni atom is replaced with two H atoms, were prepared by thermal evaporation *in situ* onto Cu substrate. The XA spectra were recorded in the total electron yield detection mode at the photon-energy resolution of 144 meV (Ni 2*p*), and 70 meV (N1*s*). Photon energies in the range of the fine structure of absorption spectra were calibrated using the known positions of the 1*s*-3*p* transition (867.13 eV) in the absorption spectrum of Ne, the 1*s*-π*,*v*=0 transition (400.88 eV) in the spectrum of N_2. Valence-band PE spectra were collected in the angle-integrated mode with a VG CLAM 4 electron analyzer. The total energy resolution was about 400 meV for the PE spectra at the photon energies of 100-170 eV and ≥800 meV for the Res PE spectra at the Ni $2p_{1/2, 3/2}$ edges (hν~850-885 eV). The absorption and photoemission spectra were normalized to the incident photon flux, which was monitored by detecting the photocurrent from a gold mesh placed at the beam-line exit.

Fig. 1 presents the N 1*s* absorption spectra for NiPc and H_2Pc that are normalized to the same continuum absorption intensity at the photon energy of 430 eV. The spectra under comparison are quite similar in the photon energy range from 408 to 430 eV, but show considerable changes in the low-energy range. The most strong change is the splitting (0.65 eV) of the lowest absorption peak A in NiPc into two components A_1 and A_2. Evidently, this and other changes must be assigned to the manifestation of chemical bonding between the Ni atom and the Pc macrocyclic ring in NiPc. This chemical bonding is primarily defined by the covalent mixing of the valence Ni 3*d*, 4*s* electronic states with the valence 2*p* states of the ligating (bonding) N atoms of the four pyrrole rings in this planar molecular complex. This bonding can be described in terms of the formation of the σ and π bonds and the valence electronic structure of the complex can be characterized by the set of occupied and unoccupied molecular orbitals (MO's) of the σ and π type. The bonding π- and σ- MO's usually correspond to the occupied electronic states, while the antibonding π*- and σ*- MO's are unoccupied. The π bonding is generally weaker than the σ one, therefore the higher occupied and lower unoccupied electronic states are primarily associated with the MO's of the π type. Thus, we can assign the low-energy peaks in the N 1*s* absorption spectrum of NiPc to the 1*s* electron transitions to the low-energy empty π-MO's of the complex with the N 2*p* contributions. There are however two problems that do not allow us to identify unambiguously these transitions without the additional measurements or detailed MO calculations for NiPc. Firstly, the N 1*s* absorption spectra the MPc's are complicated by the fact that MPc's possess two sets of four equivalent nitrogen atoms (ligating and bridging). Secondly, the π-MO's can be split by the planar molecular field into two components which are parallel and perpendicular to the molecular plane. As a result of a qualitative consideration, we assume that structures A_1 and A_2 are caused by the 1*s* electron transitions of the ligating N atoms to the lowest π-MO which is split by the D_{4h} molecular field into two components (the similar transitions for the bridging N atoms are hidden under the above structures).

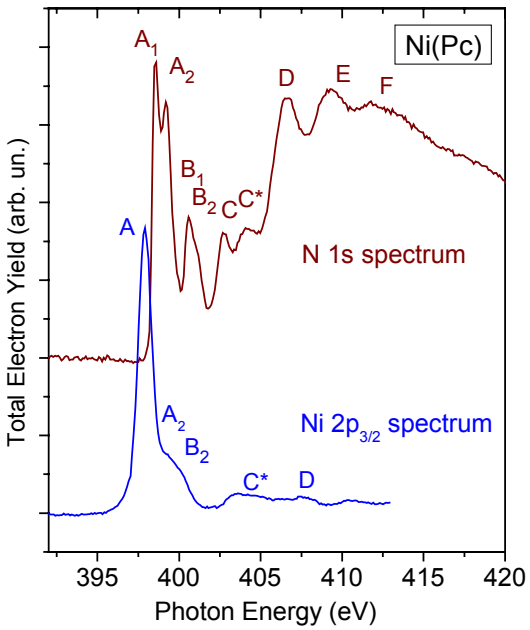

Fig. 2. *N 1s and Ni $2p_{3/2}$ absorption spectra of NiPc aligned in energy with the use of ΔE(Ni $2p_{3/2}$ - N1s)=456.8 eV.*

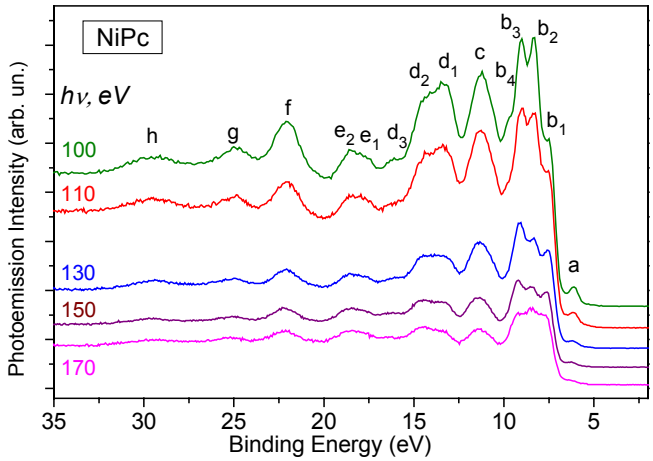

Fig. 3. *Valence-band photoemission spectra of NiPc taken with excitation photon energy of 100 - 170 eV.*

In Fig. 2 the N 1*s* and Ni $2p_{3/2}$ absorption spectra of NiPc aligned energetically on the scale of the N 1*s* spectrum are compared. As one can see from Fig. 2, the unoccupied electronic states of NiPc with the Ni 3*d* contribution are located not only near the Fermi level (peak A) but also up to 10 eV above it (structures A_2 – D). Based on the comparison between the energy positions of the absorption structures in the energetically aligned N 1*s* and Ni $2p_{3/2}$ spectra, we can state that, among the Ni 3*d* derived states, there are one unoccupied MO with the pure Ni $3d_{x^2-y^2}$ character (peak A) and several MO with the hybridized Ni 3*d* – N 2*p* composition. The first conclusion is in good agreement with the calculation of Ref. 7, while no hybridized Ni 3*d* – N 2*p* states are available among the unfilled MO's in this calculation.

In Fig. 3 the valence-band PE spectra for NiPc measured in the range of photon energies between 100 eV and 170 eV are presented. The binding energy scale is referred to the vacuum level E_V=0. From the spectra in Fig. 3 it is evident that the valence band *b* composed of separated subbands

b_1-b_4 undergoes the most strong changes when the exciting photon energy decreases from 170 eV to 100 eV. The subbands b_1, b_2 and b_3 are enhanced to a variable extent and thus change considerably their relative intensities. Band d_1-d_2 shows similar behavior. Taking into account the known Ni 3*d*-absorption cross section dependence, we associate the structures b_1, b_2, b_3, and d_1-d_2 with the occupied electronic states with the dominant Ni 3*d* character. According to the calculation [7] the highest occupied MO in NiPc is the $2a_{1u}$ MO, which is composed primarily of $2p_z$ orbitals on the pyrrole carbon atoms bound to the ligating nitrogen atoms. Below it, at the higher binding energies, three MO's ($12a_{1g}$, $6e_g$, and $8b_{2g}$) with the Ni 3*d* character are located. Based on this calculation, the bands *a*, b_1, b_2, and b_3 can be associated with these occupied MO's. At the same time, in the calculation there are no MO's with the Ni 3*d* contributions, which could be responsible for the band d_1-d_2.

The valence-band PE spectra of NiPc excited by photons of various energies in vicinity of the Ni $2p_{3/2}$ and $2p_{1/2}$ edges (as marked in the Ni 2*p* absorption spectrum, Fig. 4 a) are shown in Fig. 4 b. As the photon energy is scanned across the Ni $2p_{3/2}$ – $3d_{x^2-y^2}$ absorption resonance (curves 3 - 6), signal *b* gains in intensity, and a strong satellite band *s* appears. This observation can be regarded as an additional evidence for a large contribution of the Ni 3*d* states to the occupied electronic states of the band *b*. Finally, it should be noted that the intensity of the satellite relative to the valence signals is significantly higher at the Ni 2*p* – 3*d* resonance than at the Ni 3*p* – 3*d* one [3].

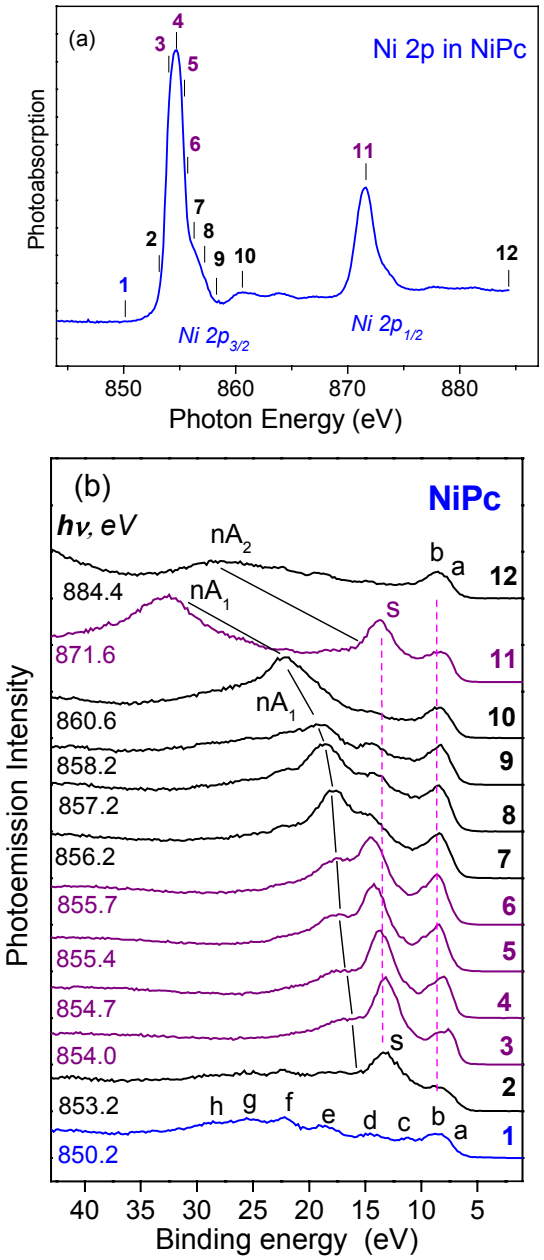

Fig.4. *X-ray absorption (a),valence-band PE and Auger spectra (b)of NiPc taken with photon energies at the Ni $2p_{3/2}$ and $2p_{1/2}$ edges.*

Acknowledgements

This work was supported by RFBR (Project Nos. 04-02-17646 and 05-03-33254) and the bilateral program "Russian-German Laboratory at BESSY II". A.S. Vinogradov and D.A. Zverev gratefully acknowledge the financial support by BESSY and by the Technische Universität Dresden.

References

1. C.C. Leznoff, A.B.P. Lever, *Phthalocyanines, Properties and Applications.* Vol. 3, VCH Publishers, Inc., NY, 1993.
2. W.D. Grobman, E.E. Koch, in: L.Ley, M. Cardona (Eds.), *Photoemission in Solids II,* Springer-Verlag, Berlin 1979, Chapter 5.; E.E. Koch, in: P. Reineker, H. Haken, H.C. Wolf (Eds.), *Organic Molecular Aggregates,* Springer-Verlag, Berlin 1983, p.35.
3. M. Iwan and E.E. Koch, Solid State Commun. **31**, 261 (1979).
4. E.E. Koch, Y. Jugnet, and F.J. Himpsel, Chem. Phys. Lett. **116**, 7 (1985).
5. M.L.M. Rocco, K.-H. Frank, P. Yannoulis, and E.E. Koch, J. Chem. Phys. **93**, 6859 (1990).
6. H. Yoshida, K. Tsutsumi, N. Sato, J. Electron Spectrosc. Relat. Phenom. **121**, 83 (2001).
7. F.W. Kutzler and D.E. Ellis, J. Chem. Phys. **84**, 1033 (1986).
8. H. Höchst, A. Goldmann, S. Hüfner, and H. Malter, Phys. Stat. Sol. (b) **76**, 559 (1976).

Photoelectron Diffraction on Transition Metal Oxide Ultrathin Films

K.-M. Schindler, Ch. Hagendorf, J. Wang, M. Huth, R. Börner, W. Widdra
FB Physik, Martin-Luther-Universität Halle-Wittenberg, D-06099 Halle, Germany

F. Allegretti, M. Polcik
Fritz-Haber-Institut der MPG, Faradayweg 4-6, D-14195 Berlin, Germany

The particular physical properties of transition metal oxides make them promising candidates in applications such as nonvolatile computer memory. Therefore, there is much interest in the growth mode, structure and properties of ultrathin films. This investigation aims at the determination of their structure with photoelectron diffraction (PED) in energy scanned mode. Furthermore, the feasability of PED to study their magnetic structure is investigated. Their elemental composition, reactions and electronic structure is probed with XPS and NEXAFS as necessary.

In a first run, ultrathin films of MnO were studied on a Ag(001) substrate. The films were prepared by reactive metal evaporation in an oxygen atmosphere with the substrate heated to 400 K. Former studies have shown that these conditions lead to a mostly layer-by-layer mode with the smallest roughness of the film.

Previous investigations have shown, that the films possess bulk properties as soon as their thick ness exceeds 3-4 atomic layers. NEXAFS spectra (fig. 1) of the O K edge however show a considerable difference between normal and grazing incidence spectra. The resonances A, C, F and H are clearly stronger in normal incidence, whereas the resonances B and E are stronger in grazing incidence. The resonances D and G are too weak for an unambiguos assignment. The conduction band of MnO is mainly composed of Mn 3d states. The obvious difference between normal and grazing incedence indicates that the resonances A and B relates to Mn 3d states oriented parallel and perpendicular to the surface, respectively. Further insights are expected from comparisons with theoretical investigations.

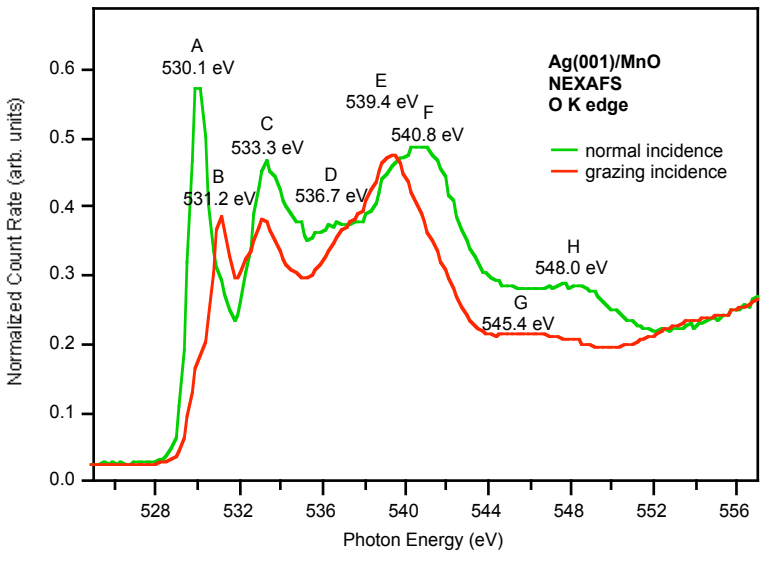

Fig. 1: NEXAFS O 1s spectra of Ag(001)/MnO

In addition to NEXAFS spectra photoelectron diffraction data in energy scan mode have been recorded for several emission directions. Fig. 2 shows one of the basic series of the O 1s photoemission spectra and the resulting intensity modulation.

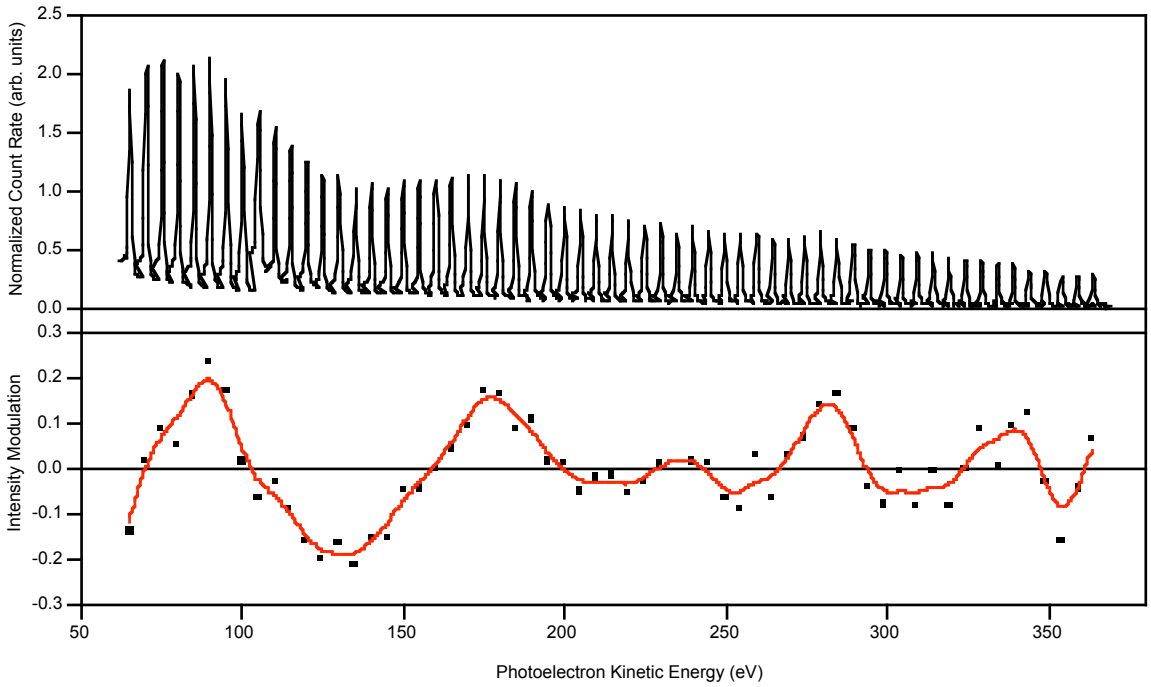

Fig. 2: O 1s spectra and photoelectron diffraction intensity modulations of Ag(001)/MnO .

In the energy range below 200 eV the intensity modulations are up to 20%. Together with other emission directions this yields a sufficient large basis of experimental data to investigate the geometric structure of the film, in particular the Mn-O bond length. Corresponding theoretical simulations of the photoelectron diffraction intensity modulations have been started.

The third topic of this investigation in probing magnetic properties of the film with photoelectron diffraction. For this purpose, photoelectron diffraction data were taken for the main and the satellite Mn 3s emission lines as shown in figure 3. The data analysis shows differences at certain energies, although the sample was at room temperature, where it is in its paramagnetic state. In the light of the insufficient S/N ratio further experimental and theoretical analyses are being carried out to verify the effect.

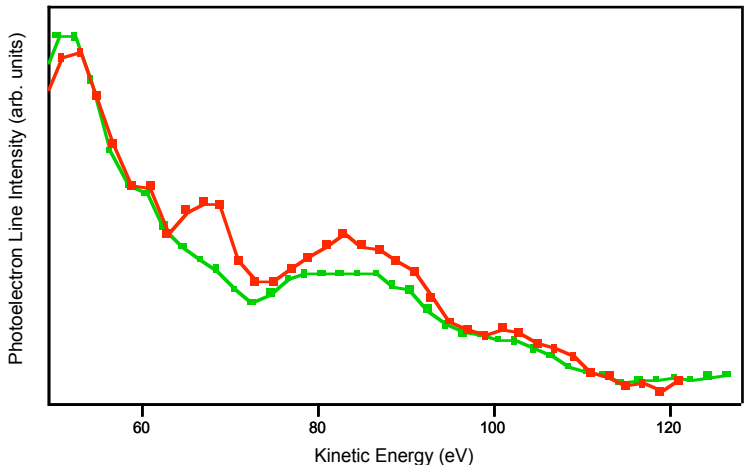

Fig. 3: Mn 3s photoelectron intensity of main and satellite lines of Ag(001)/MnO

Dielectric function and critical points of the band structure for hexagonal and cubic GaN and AlN

R. Goldhahn[1], C. Buchheim[2], V. Lebedev[2], V. Cimalla[2], O. Ambacher[2], C. Cobet[3], M. Rakel[3], N. Esser[3], U. Rossow[4], D. Fuhrmann[4], A. Hangleiter[4], S. Potthast[5], and D.J. As[5]

[1]Inst. f. Physik, [2]Zentrum f. Mikro- und Nanotechnologien, TU Ilmenau, PF 100565, 98684 Ilmenau, Germany
[3]Institute for Analytical Sciences, Department Berlin-Adlershof, Albert-Einstein-Str. 9, 12489 Berlin, Germany
[4]Institut für Technische Physik, TU Braunschweig, Mendelssohnstr. 2, 38106 Braunschweig, Germany
[5]Department Physik, Universität Paderborn, Warburger Str. 100, 33098 Paderborn, Germany

Funding: BMBF grants 05KS4KTB/3 and 05ES3XBA/5
Ministry of Science, Research and Art of Thuringia (B609-02004)

Over the past 10 years, the group-III nitride semiconductor alloy system (In,Ga)N was intensively studied because its unique properties allows the fabrication of very efficient light emitting and laser diodes for the blue/green spectral regions. The development of deep-UV lasers however can only be achieved if GaN, AlN, and their related alloys are used. Recently, deep-ultraviolet lasing at 241 nm was reported [1]. Other applications of AlN/GaN are the development of short period superlattices as Bloch oscillators [2] or distributed Bragg mirrors with very high reflectivity [3]. For the design of such heterostructures and for the evaluation of the achieved properties detailed knowledge of the complex dielectric function (DF) over an extended energy range is essential. It turns out, however, that the current knowledge of the DF for (Al,Ga)N is rather poor. Either the studies are restricted to the transparent region below the band gap [4], or only pseudo-dielectric functions were reported [5]. Here, we report for the first time DF's for GaN and AlN with both wurtzite and zincblende crystal structure as obtained from spectroscopic ellipsometry (SE) measurements. From the data the transition energies at critical points of the band structure are extracted. Preliminary studies of hexagonal AlGaN alloys with various Al concentrations allow in addition the determination of the bowing parameters (b) characterising the deviation of the peak shifts from linear behaviour.

Hexagonal GaN (thickness 1800 nm) and AlGaN films (400 nm on a 400 nm thick GaN buffer) were grown by MOVPE on sapphire substrates. Growth details can be found elsewhere [6]. The investigated AlN layers (200 nm) were deposited by plasma-induced MBE on Si(111). Either hexagonal or cubic films were obtained depending on the carbonisation conditions prior to growth (formation of approximately 3 nm thick in 3C-SiC coverage of Si) [7]. The cubic GaN under investigation is 600 nm thick and was grown by MBE on a 3C-SiC(100) substrate. For the VUV measurements (3 to 9.5 eV), the **3m**-**N**ormal-**I**ncidence-**M**onochromator **1** at BESSYII was used as light source. The ellipsometric parameters Ψ and Δ were recorded at an angle of incidence of 68°. Prior to the final measurements the samples were heated up to 400 °C for 10 minutes which removes residual organic contamination as monitored by a mass spectrometer and emphasised by a comparison of the pseudo DF's. For the determination of the DF in the low-energy range we used a commercial ellipsometer (J.A. Wollam Co., Inc.).

In order to obtain 'true' DF's and not only pseudo-dielectric functions, Ψ and Δ were fitted by taking in to account the rms surface roughness (for most films below ~1 nm) as well as the interface layers. Results for the real (ε_1) and imaginary parts (ε_2) of hexagonal GaN and

AlN are shown in Fig. 1. Due to (0001) orientation of the films, the data correspond nearly to the ordinary DF. First of all, the excellent matching of the data recorded by both ellipsometers should be noted. Taking into account the exciton binding energies, we obtain at the Γ-point of the Brillouin zone values for E_0 (splitting between Γ_9^V valence and Γ_7^C conduction band) of 3.45 eV (6.25 eV) for GaN (AlN). The other critical point are found at 6.95 (7.96) eV, 7.89 (8.95) eV, and 9.08 eV. Although theoretical calculations [8] yield qualitatively the same spectral dependency, the magnitudes or peak positions differ still.

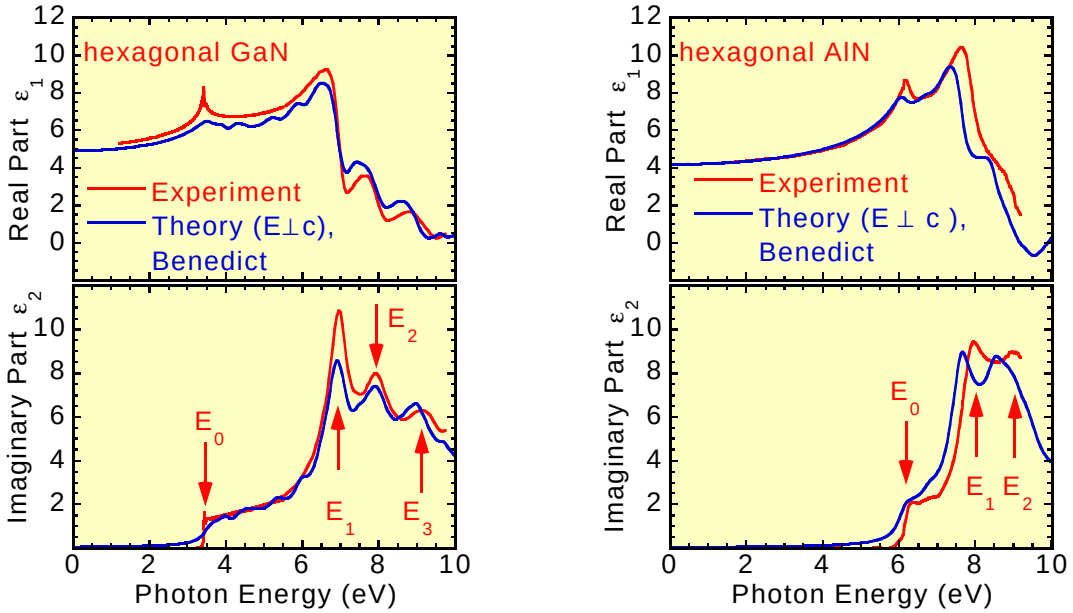

Fig. 1: Comparison of experimentally determined DF's (red) of hexagonal GaN (left) and AlN (right) with the results of theoretical calculations (blue) [8]. Critical point energies are indicated by arrows.

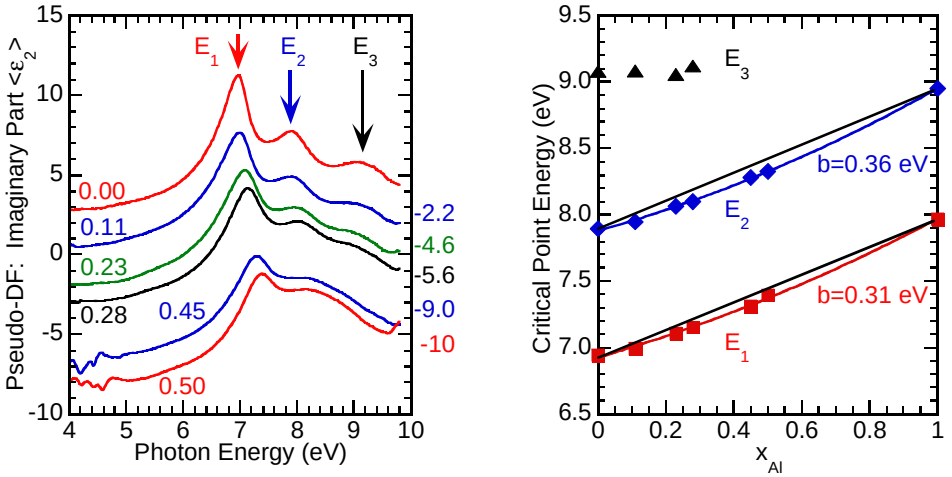

Fig. 2: Imaginary part (left) of the pseudo-dielectric functions for hexagonal $Al_xGa_{1-x}N$ alloy. Dependency of the critical point energies on the alloy composition and the fit results for the determination of the bowing parameter b are shown on the right.

Figure 2 (left) shows the imaginary part of pseudo DF's for AlGaN alloys with Al content up to 50%. Compared to previous studies [5], the critical points are much better resolved emphasising the excellent structural and surface properties of the films. In contrast to the analysis presented in Ref. 5, we find a clear deviation from linear increase of the E_1 and E_2 critical point energies with Al content (Fig. 2 right). A fit yields bowing parameters of b=0.31 eV and 0.36 eV for E_1 and E_2, respectively, while the E_0 band gap is well represented by

b=0.9 eV (not shown here). In the next step, the ellipsometric data has to be fitted in order to get the full DF's over the whole energy range.

Figure 3 shows for the first time DF's for cubic GaN (left) and AlN (right) up to 9.5 eV. Beside the E_0 band gap at 3.22 eV we determine the E_1 and E_2 critical point energies with 7.28 eV and 7.59 eV. An additional shoulder is found between 8 eV and 9 eV which is also predicted by the theoretical calculations. For cubic AlN the onset of strong absorption is found at 5.74 eV which corresponds to the valence band conduction band splitting at the Γ point of the Brillouin zone. The value is approximately 700 meV higher than reported in Ref. 9. Due to the small layer thickness it is not possible to determine the indirect band gap of cubic AlN. The other two critical points are resolved at 7.42 eV and 8.02 eV. They are only slightly shifted with respect to GaN which might be expected if previous results of low-Al content cubic layers [10] are taken into account.

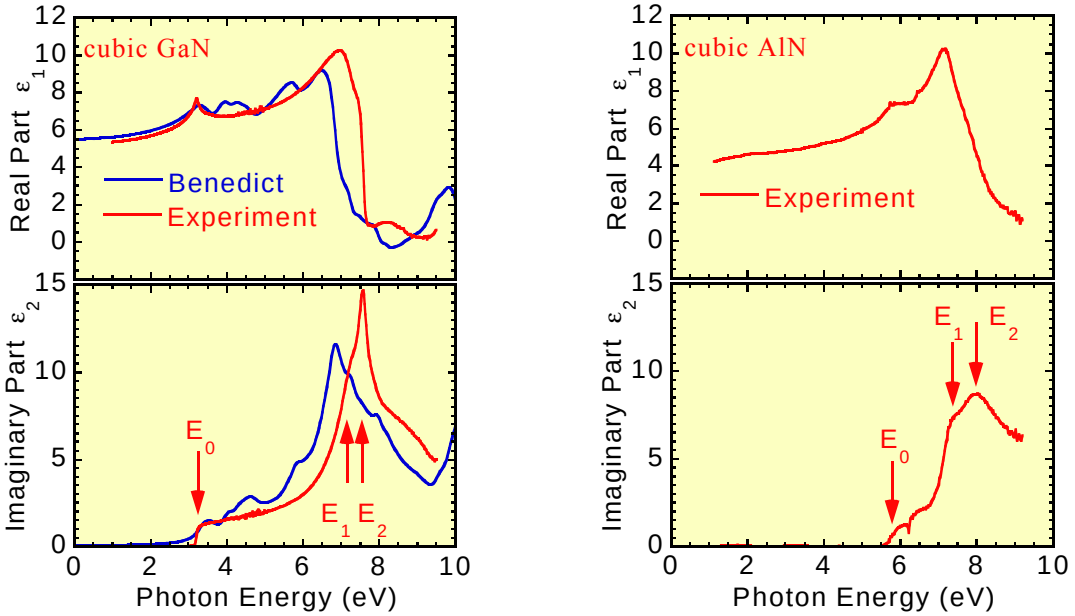

Fig. 3: Comparison of experimentally determined DF's (red) of cubic GaN (left) and AlN (right) with the results of theoretical calculations (blue) [8].

In summary, we have presented dielectric functions of hexagonal and cubic GaN and AlN as fitted from spectroscopic ellipsometry data. A large number of critical points of the band structure has been resolved. For hexagonal AlGaN alloys, the shift of the E_1 and E_2 transition energies with increasing Al content is characterised by a small bowing parameter. The direct absorption edge for cubic AlN is found at 5.74 eV which is much higher than previously reported.

References

[1] T. Takano *et al.*, Appl. Phys. Lett. **84**, 3567 (2004).
[2] V.I. Litvinov *et al.*, Appl. Phys. Lett. **85**, 600 (2004).
[3] T. Ive *et al.*, Appl. Phys. Lett. **85**, 1970 (2004).
[4] S. Shokhovets *et al.*, J. Appl. Phys. **94**, 307 (2003).
[5] T. Wethkamp *et al.*, Thin Solid Films **313-314**, 745 (1998).
[6] U. Rossow *et al.*, J. Cryst. Growth **272**, 506 (2004).
[7] V. Cimalla *et al.*, phys. stat. sol., in press.
[8] L.X. Benedict *et al.*, Solid State Commun. **112**, 129 (1999).
[9] T. Suzuki *et al.*, Jpn. J. Appl. Phys. Part2 **39**, L497 (2000).
[10] A. Kasic *et al.*, Phys. Rev. B **65**, 184302 (2002).

Thickness dependence of the transverse magneto-optical Kerr-effect at the 2p edges of ultrathin Co films on W(110)

A. Kleibert, P. Oppeneer*, V. Senz and J. Bansmann
Institut für Physik, Universität Rostock, D-18051 Rostock
Department of Physics, Uppsala University, Box 530, S-75121 Uppsala, Sweden
Supported by BMBF 05KS4HRA2/4.

X-ray magnetic resonant scattering (XMRS) is a powerful and elementspecific tool for investigations on complex, nanoscaled magnetic samples [1,2]. In the past these studies involved mainly ex-situ prepared samples or multilayers, where the capping layer has not been taken into account. In this contribution we present recently obtained results on the thickness dependence of the transverse magneto-optical Kerr-effect (T-MOKE) on *in situ* prepared Co(0001) films on W(110) with thicknesses ranging from several monolayers down to the submonolayer regime. We observe strong interference effects in the reflectivity, that are nicely reproduced by magneto-optical calculations based on independently determined optical constants and a matrix formalism [3].

Cobalt layers on W(110) have been extensively investigated by several groups during the last decades (see e.g., Refs. [4,5]). Thus, the magnetic, electronic and structural properties are well known. With respect to magneto-optics in the soft X-ray regime two features of these samples are of special interest. First, Co layer can be prepared as atomically smooth films with nearly perfect interfaces. Thus, they can be treated as ideal mirrors. Second, the uniaxial magnetic in-plane anisotropy enables an easy study of anisotropies in the magneto-optical response. In this contribution we will concentrate on the reflectivity, absorption, and T-MOKE measured in a fixed geometry with the magnetization being reversed parallel/antiparallel to the magnetic easy axis, i.e. the W[1$\bar{1}$0] direction.

T-MOKE and X-ray absorption spectra (XAS) have been recorded using soft X-rays impinging at a grazing angle of incidence of 22°. The sample was magnetized perpendicular to the plane of incidence by an external magnetic field. The optical constants used for the calculations have independently been determined by X-ray circular dichroism (XMCD) experiments carried out via total electron yield detection at the UE46 beamline. All films have been prepared *in-situ* by means of molecular beam epitaxy (MBE) at room temperature under UHV conditions. The base pressure during the preparation did not exceed $5 \cdot 10^{-10}$ mbar at an evaporation rate of 0.7 ML/min.

In Fig. 1 we show a set of absorption and reflectivity spectra in the T-MOKE geometry obtained for Cobalt films of several nominal thicknesses (0.6 ML up to 12ML) denoted in the left column. As expected the XAS signal rises monotonically with increasing thickness. In contrast to the absorption spectra, the reflectivity (middle column of Fig. 1) shows a more complex behaviour. Starting with pronounced dips near the absorption edges of an incomplete monolayer (a) strong peaks evolve when increasing the thickness up to 4 ML

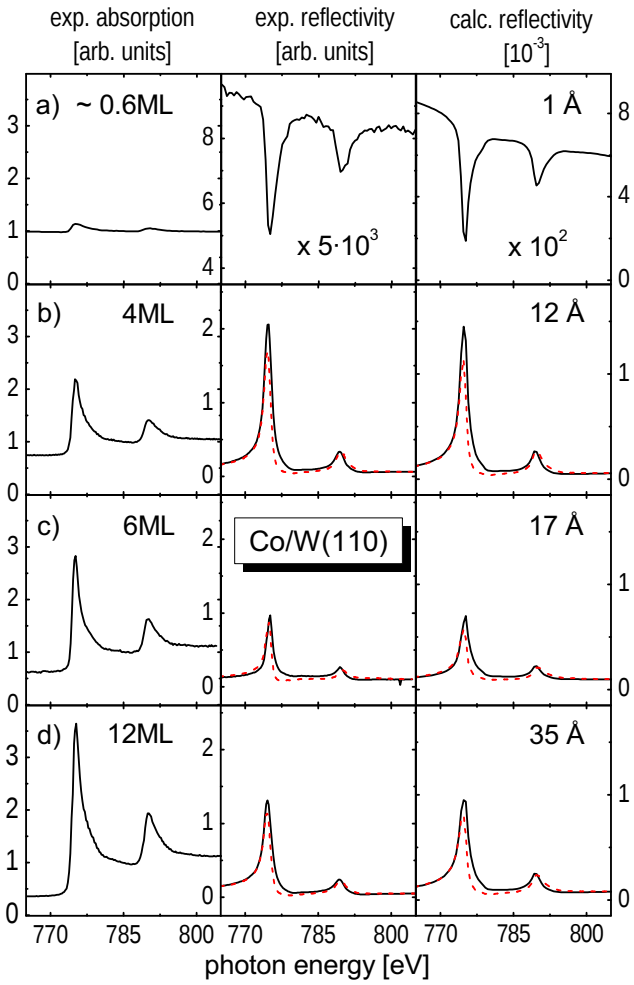

Figure 1: Thickness dependent XAS and T-MOKE spectra of Co /W(110) (left and middle column, respectively). For comparison calculated T-MOKE spectra are shown in the right column. T-MOKE spectra are denoted as solid and dashed red lines for opposite magnetization.

(b). Further increasing up to 6 ML temporary reduces the peak heights being nearly restored upon further Co deposition (12 ML), cf. Fig. 1(d), respectively. These changes in the reflectance are obviously due to strong interference effects and are nicely reproduced by calculations shown in the right column of Fig. 1 with the given parameters. Note, that the dashed and solid lines denote the reflectivity for opposite magnetization states perpendicularly to the plane of incidence. The submonolayer in (a) does not show any magnetic signal as expected at room temperature.

In order to demonstrate the importance of interference effects on the reflectance of ultrathin films in the soft X-ray regime we show in Fig. 2 calculated thickness-dependent *non-magnetic* p-polarized reflectivities at the Co 2p edges. The calculation shows a strong modulation of the intensity with increasing thickness. As a consequence one may expect that even one additional atomic layer could strongly reduce/enhance the observable reflected intensity. Moreover, it has been mentioned already in Ref. [6], that the remarkable changes in the shape of reflectivity spectra after adding/removing an atomic layer may serve as a

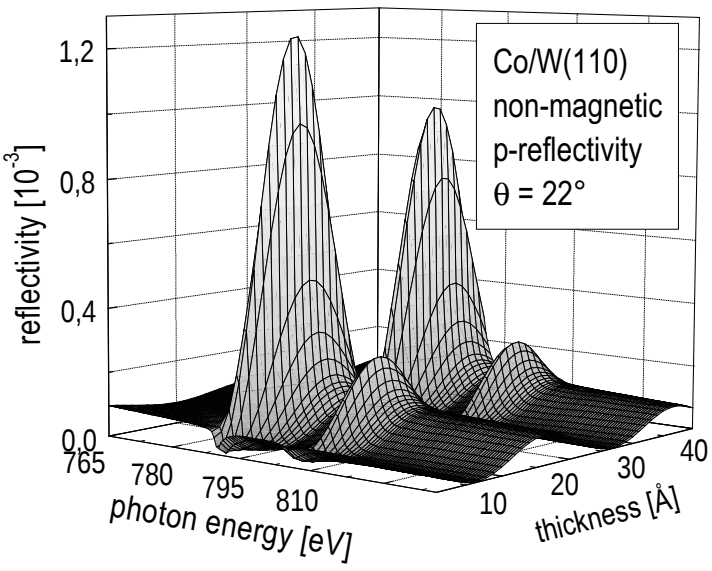

Figure 2: Calculated thickness dependence of the non-magnetic p-polarized reflectivity of Co/W(110) using data obtained from XMCD experiments and tabulated optical constants [7] for the tungsten substrate.

characteristic 'fingerprint' of the actual film thickness. Beyond these effects on the intensity we found that also the T-MOKE response is nicely reproduced by respective calculations if using reliable sets of optical constants (not shown here). These promising results underline the possibility to obtain detailed information from complex magnetic samples using T-MOKE.

References:

[1] C. Kao et al., Phys. Rev. Lett. **65**, 373 (1990).
[2] J. B. Korthright et al., Phys. Rev **B**. **62**, 12216 (2000).
[3] J. Zak et al., Phys. Rev. **B 43**, 6423 (1990).
[4] M. Pratzer et al., Phys. Rev. **B 64**, 153405 (2003).
[5] H. Fritzsche et al., Phys. Rev. **B 51**, 15933 (1995).
[6] M. Sacchi et al., Surf. Sci. **442**, 349 (1999).
[7] B. L. Henke et al., Atomic Data and Nuclear Data Tables **54**, 181 (1993).

Absence of Surface Core Level Shifts in organic thin films

M. B. Casu, Y. Zou, S. Kera, D. Batchelor, Th. Schmidt, and E. Umbach

Experimentelle Physik II, Universität Würzburg, Am Hubland, D-97074 Würzburg, Germany

Studies of the morphology, growth and structure of organic thin films are the subject of very intense investigations. Although there are still many open questions regarding their behaviour in the solid state, their importance in electronics grows day by day. They offer an interesting alternative to inorganic semiconductor electronics due to low-cost deposition methods, flexible substrates, and simple packaging [1, 2]. Their use ranges from Organic Field Effect Transistors (OFETs) [3], to Organic Light Emitting Devices (OLEDs) [4] or Photovoltaic Cells (PVs) [5] with a real market perspective [6]. The efficiency of a device depends on each single component and on how all they match together. The most important nucleus of this device is the organic medium. Organic solids are commonly considered governed by van der Waals interactions. The main characteristics of van der Waals solids are strong intramolecular bonds, weak intermolecular forces due to limited overlap, high polarisation energies for electron and holes. The charges are localised on individual molecules and charge transport is via hopping. However, this picture is insufficient to correctly explain the complete physics of organic materials.
In a photoemission process, a photon is absorbed and a charge is created. The energy necessary to remove the charge from the material depends on the ability of the surrounding to react, i. e. to screen in a poor or very efficient way the created charge. According to the van der Waals description, a weak interaction of the neighbouring molecules is expected in organic materials and the screening effects (essentially polarisation of the neighbourhood) are believed to be rather small in comparison with those occurring in covalent inorganic semiconductors.
Surface core level shifts (SCLS) are defined as the shift in the photoemission binding energy between the signal from the bulk and that from the surface. This has been related to various effects like narrowing of the valence band at the surface of metals [7], surface charge transfer different from the bulk [8], the difference between surface and bulk Madelung potential [9], change in the screening of the core photoemission of the core hole [10], or a combination of these effects [11]. From the experimental point of view, the improved resolution of analysers and the use of synchrotron radiation has increased the possibility to determine also very small shifts below 0.1 eV.

In this report, we present high resolved X-ray photoemission (XPS) measurements taken at different photon energies and at different take off angles in order to investigate the SCLS on various different organic systems. Thin films of perylenetetracarboxylic acid dianhydride (PTCDA), coronene, and metal free phthalocyanine (H_2Pc) were deposited on a Ag(111) single crystal. The organic molecules were chosen to represent systems with different interaction degrees: ranging from a strong reactive system like PTCDA films on Ag(111) to a less interacting one like coronene. The presented results are of paramount importance to answer some of the key points previously depicted. One of the fundamental questions is whether the surrounding of a generated charge is really different for interface, bulk, and surface. Answering this question will give a deeper insight in the screening process occurring in organic thin films.

The measurements were performed at the beamline UE52-PGM at BESSY (Berlin, Germany). This beamline is characterized by a plane grating monochromator. The photon energy ranges from 100 to 1500 eV, with an energy resolving power of $E/\Delta E$= 10500 at 401 eV (c_{ff}=10, 10 μm exit slit). The main chamber (base pressure $2x10^{-10}$ mbar) is equipped with a standard twin anode X-ray source, a SCIENTA SES200 electron energy analyser, and a home-made partial electron yield detector. For all XPS data a pass energy of 40 eV was used corresponding to an analyser nominal resolution of 50 meV. The Ag(111) single-crystal was cleaned in UHV by means of repeated cycles of Ar-sputtering and subsequent annealing. The organic materials were purified by using thermal gradient sublimation and deposited in UHV conditions on Ag(111) by using organic molecular deposition (OMBD) in-situ. The deposition was monitored with a quadrupole mass spectrometer and the nominal thickness was determined by using the attenuation of the XPS substrate signals (Ag3d). The nominal thickness was 10 monolayers for PTCDA and coronene, and 20 monolayers for H_2Pc. The homogeneity of the

samples was checked on micro and global scale by using XPS in situ and correlated to previous experiments. The XPS spectra were recorded in normal emission (0°) for incident photon energies of 335 and 700 eV and under an angle of 40°, 65° and 75° for PTCDA, coronene and H_2Pc, for a photon energy of 335 eV. By changing the kinetic energy and the emission angle of the emitted electrons the inelastic mean free path and hence the surface sensitivity was varied. The energies have been carefully calibrated according to reference 12. All samples were carefully checked for radiation damage during beam exposure. In addition, the experiment was carefully performed in order to avoid non-linearity effects due to the detection system (including the low count rate regime) that could be important in measuring the peak intensities and shapes. The sum of an exponential and a Shirley background were subtracted and the spectra were normalised for allowing their comparison.

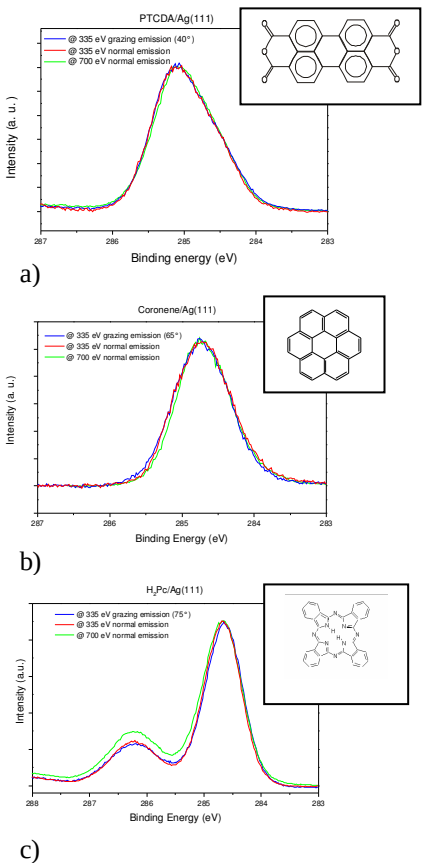

Fig. 1. C1s XPS spectra of multilayer of PTCDA, corone and H2Pc. The spectra were taken at different photon energies of 700 (a) and 335 eV in normal emission and off normal emission, as indicated.

Fig. 1 shows the photoemission spectra of the C_{1s} core levels for PTCDA, coronene, and H_2Pc thin films on Ag(111). The spectra were taken at photon energies of 700 (green curves) and 335 eV (red curves) in normal emission and at 335 eV in off normal emission (blue curves). The spectra at 700 eV in normal emission are the most bulk sensitive while those one at 335 eV in grazing incident are the most surface sensitive ones. At first glance, no changes are visible in peak position or shape for the three different results. This would indicate that there is no occurrence of any SCLS in the organic thin films here investigated.
The growth in intensity of the satellites in the higher binding energy range in the H_2Pc spectra (Fig. 1c, green curve) is a phenomenon not connected with the occurrence of SCLS but related to different atoms in the molecule a and to an inclined molecular orientation.

To support the observation of SCLS absence we performed a fit on the results assuming the presence of two components, surface and bulk. The obtained fit is given for PTCDA in Fig. 2 confirming the absence of SCLS: the intensities of the two contributions do not change significantly (changes are less than 2 %) in the two cases (Fig. 2a and 2b). This result rules out a different bulk/surface nature of the two features according to a different bulk sensitivity of the experimental conditions. The two components present in the fit in Fig. 2 actually originate from different C species [13].

As mentioned above, SCLS may have different causes, that can be attributed to initial or final state effects as well as by a mixture of both. It has been shown that SCLS can be also due to a change in the screening of the core photoemission of the core hole [14]. In systems like rare gas layers the changes in core level binding energies arise only from final state effects, and initial state contributions are negligible. This is due to the weak interaction of the rare gas atoms, which is essentially of van der Waals type, with the substrate and with their neighbours. Screening effects have been used in the explanation of the photoemission data of rare gas layers that show the occurrence of SCLS. In Xe multilayers deposited on Pd(111) the experimental SCLS has been found to be 0.26 eV, exactly reproduced by theoretical calculations [15]. This theoretical approach, in which the photoemission final states of the adsorbed Xe are fully charged rather than neutral, is based on the idea that the dominant contribution to the shift is the hole screening energy, calculated for the rare gas layers by using a dielectric continuum model. The discussion of this SCLS origin in van der Waals turns our attention back to the results presented in this report. The key to understand SCLS in organic materials is given by the final state effects. This is in agreement with the fact that organic materials are characterised by moderate values of the dielectric constant.. We can reasonably exclude all other contributions because of their inadequateness to the case here investigated. At this point, it is worth to underline the deep difference in SCLS between

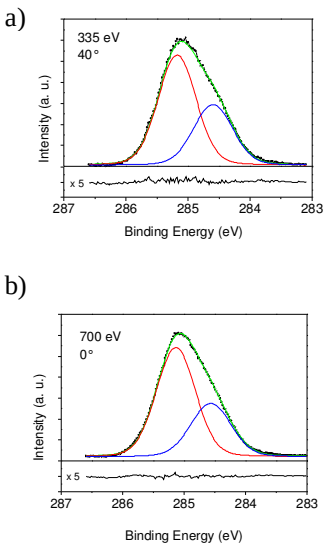

Fig. 2. C1s core level spectra of PTCDA measured at 700 eV in normal emission (a, black curve), and at 335 eV at 40° (b, black curve), together with their relative fit (green curve) using two components (blue and red curves).

organic thin films and real van der Waals solids. The latter show significant shifts due to different polarisation screening at the surface as compared to the bulk, while in organic thin films surface core level binding energies do not show any difference, within the present experimental resolution, with respect to the bulk.

In summary, the present experimental result indicates that the screening in organic material is much more efficient than thought. The creation of a hole at the surface or the creation of the same photoemission event in the bulk does not result in any difference in XPS spectra. If the molecular interaction is sufficiently strong, the screening by rapid delocalisation of the created charge may be quite efficient. Thus, the idea of a localised charge and of the electronic polarisation playing a major role in the electronic properties of organic materials has to be rediscussed. For example, the usual values considered for the polarisation energy are too high [16, 17] and not supported by the present SCLS investigation. This also implies that the influence of polarization on the determination of orbitals and gaps and on the electronic and transport properties of organics must be reconsidered taking this efficient delocalization process into account. This finding should have a strong implication for the characterisation in electronic devices, where concepts like band offsets or charge injection should be reconsidered under this new aspect.

Acknowledgements

The authors would like to thank the BESSY staff, in particular Dr. Ch. Jung, Stephan Pohl and Helder Marchetto, Fritz-Haber-Institut, Berlin, for the beamline support, Dr. A. Schöll for valuable technical suggestions, Dr. Paolo Imperia, Hahn-Meitner-Institut, Berlin, for technical support while measuring at BESSY. Financial support by the DFG through the OFET-Schwerpunktprogramm Um 6/8-1 + Um 6/8-2 and by the BMBF under contract 05KS1WWA/5 is gratefully acknowledged.

References

[1] C. J. Drury, C. M. J. Mutsaers, C. M. Hart, M. Matters, and D. M. de Leeuw, Appl. Phys. Lett. 73 (1998) 108.
[2] A. Bonfiglio, F. Mameli, and O. Sanna, Appl. Phys. Lett. 82 (2003) 3550.
[3] G. Horowitz, J. Mater. Res. 19 (2004) 1946.
[4] M. Pfeiffer, K. Leo, X. Zhou, J. S. Huang, M. Hofmann, A. Werner, J. Blochwitz-Nimoth, Org. Electron. 4 (2003) 89.
[5] H. Spanggaard and F. C. Krebs, Sol. Energy Mat. Sol. Cells 83 (2004) 125.
[6] J. R. Sheats, J. Mater. Res. 19 (2004) 1974.
[7] S. F. Alvarado, M. Campagna and W. Gudat, J. Electron. Spectrosc. 18 (1980) 43.
[8] D. E. Eastman, T.-C. Chiang, P. Heimann, and F. J. Himpsel, Phys. Rev. Lett. 45 (1980) 656.
[9] R. E. Watson, J. W. Davenport, M. L. Perlman, and T. K. Sham, Phys. Rev. B 24 (1981) 1791.
[10] W. F. Egelhoff, Jr., Surf. Sci. Rep. 6 (1987) 253.
[11] R. E. Watson and J. W. Davenport, Phys. Rev. B 27 (1983) 6418.
[12] A. Schöll, Y. Zou, Th. Schmidt, R. Fink, and E. Umbach, J. Electron. Spectrosc. 129 (2003) 1.
[13] Y. Zou, Doctoral Thesis, Universität Würzburg, 2003.
[14] W. F. Egelhoff, Jr., Surf. Sci. Rep. 6 (1987) 253.
[15] T. C. Chiang, G. Kaindl, T. Mandel, Phys. Rev. B. 33 (1986) 695.
[16] W. R. Salaneck, Phys. Rev. Lett. 40 (1978) 60.
[17] E. V. Tsiper, Z. G. Soos, W. Gao, A. Kahn, Chem. Phys. Lett 360 (2002) 47

Laser-induced phase transition at the Si(100) surface revealed by time-resolved photoelectron spectroscopy in the BESSY low-α mode

T. Gießel[1], D. Bröcker[1,4], H. Prima-Garcia[1], R. Schmidt[1], R. Weber[1], M. Weinelt[1,2], W. Widdra[3]

[1] *Max-Born-Institut, Berlin, Germany*, [1,2] *Freie Universität Berlin, Berlin, Germany* [3] *Martin-Luther-Universität Halle-Wittenberg, Halle (Saale), Germany* [4] *Infineon Technologies, München, Germany*

We report on the successful setup of a pump-probe experiment with combined laser and synchrotron radiation (SR) at the U125/1-PGM beamline. First measurements in the low-α mode demonstrate a time-resolution below 20 ps. Reversible spectral changes of the valence band and Si 2p core level upon laser excitation are interpreted in terms of a phase transition at the Si(100) surface.

For the optical excitation of the sample we use a Ti:sapphire regenerative amplifier system (Coherent, RegA 9050) producing pulses of 70 fs duration at 208,3 kHz repetition rate (pulse energy: 6 μJ at the fundamental wavelength of 800 nm). The laser beam is focused to a diameter of <100 μm in order to access the full intensity range up to the damage threshold of the sample. The laser-excited state of the sample is probed by valence band and core level photoelectron spectroscopy at the U125/1-PGM beamline. For this purpose the refocussing optics of the beamline were modified in March 2004 (R. Follath, J. Schmidt, BESSY) resulting in a focal diameter of the SR beam of $< 30\mu$m (FWHM). Figure 1 shows images of the fluorescence and stray light of the synchrotron and laser radiation, respectively. The position of the laser focal spot on the sample can be adjusted with a precision of 2 μm.

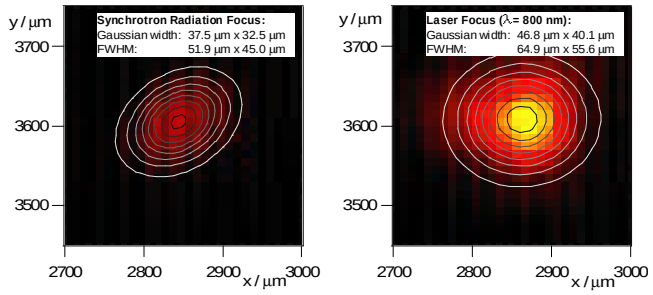

Fig. 1: Images of the fluorescence and stray light from the synchrotron and laser radiation, respectively.

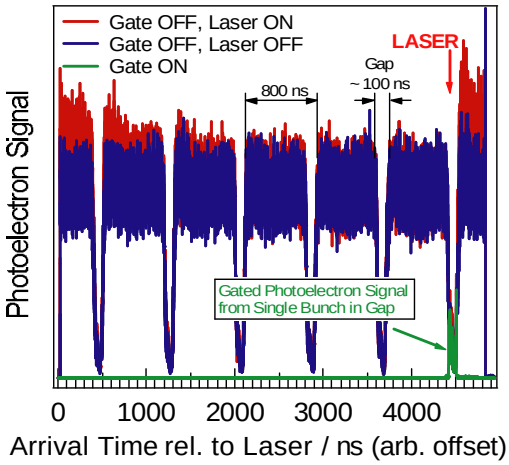

Fig. 2: Photoelectron intensity as a function of arrival time at the detector relative to the laser pulses for hybrid mode with (green) and without electronic gate (red and blue). Analyzer parameters are set for high transmission and energy resolution leading to a low time-resolution of about 40 ns as can be seen from the broad distribution of the electron signal caused by the single SR bunch in the gap between the multi bunch sequences.

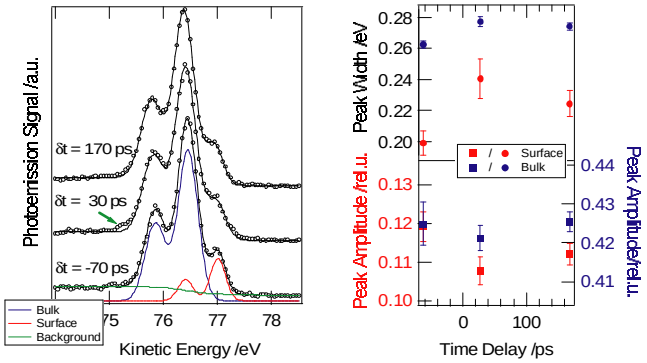

Fig. 3: Si 2p spectra for three different time delays between laser and SR: upon laser irradiation both the Gaussian width and amplitude of the surface component are changing significantly more than width and amplitude of the bulk component.

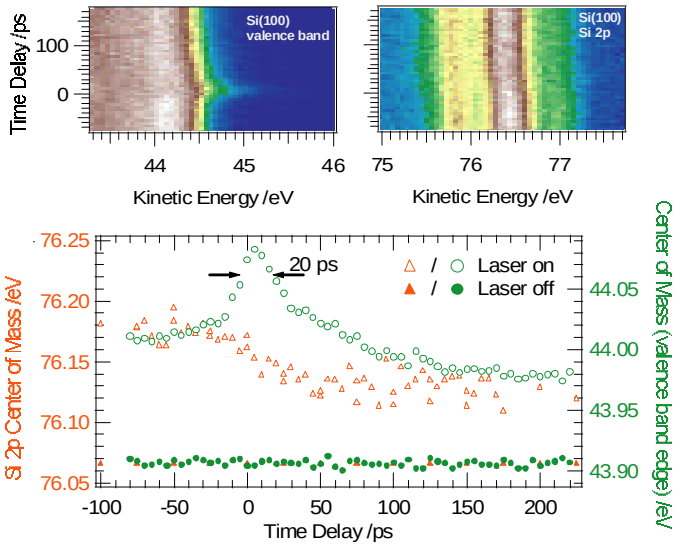

Fig. 4: Top: Si 2p spectra (right) and the Si(100) valence band edge (left) as a function of delay time between laser and SR: The shift of the valence band edge towards lower binding energies is considerably larger than that of the Si 2p spectrum. Bottom: Center of mass of the Si 2p (orange) and of the valence band edge spectra (green).

The laser pulses are synchronized (I. Will, MBI) to the 500 MHz BESSY master clock with a jitter < 10 ps, thereby matching the SR pulse length in the low-α mode (< 10 ps, November 2004). The delay between laser-pump and SR-probe pulses is monitored using a fast XUV sensitive photodiode and controlled electronically with an accuracy of 5 ps.

The electronics for time-resolved photoelectron counting was modified for two distinct detection schemes. For the investigation of the dynamics in the nanosecond to microsecond regime we developed a pump - multiple-probe detection scheme [1]. In this scheme the laser-excited state is probed in a parallel fashion by consecutive SR pulses in multi bunch mode. To assign the photoelectrons to individual synchrotron bunches requires a time-resolution of <2 ns. This limits the transmission and energy resolution of the electron analyzer. If the relevant time scale of the processes to be investigated is smaller than a few nanoseconds, it is more efficient to use an electronic gate for detecting exclusively photoelectrons caused by one particular SR pulse following the laser excitation. For a reasonably high transmission and energy resolution of the analyzer the time spread of the photoelectrons in the analyzer is ~ 40 ns. Hence, photoelectrons from one particular SR pulse can be discriminated only in single bunch mode or in the so-called hybrid mode. For the latter Fig. 2 shows the time-resolved photoelectron signal with (green) and without electronic gate (red and blue are with and without laser). All data shown in this report were measured in low-α hybrid mode gating the photoelectron signal.

The left panel of Fig. 3 shows Si 2p core level spectra measured at a photon energy of 170 eV 70 ps before as well as 30 ps and 170 ps after laser excitation. The fluence of the exciting laser pulse was set to 70 mJ/cm^2, which is well below the melting threshold of silicon of 170 mJ/cm^2 at 625 nm [2] (this work: 200 mJ/cm^2 at 800 nm). The spectra are analyzed distinguishing only between a spin-orbit split bulk (blue) and surface component (red). Upon laser irradiation peaks broaden and decrease in amplitude (see right panel of Fig. 3). The Gaussian width and amplitude of the surface component change significantly upon laser excitation while the bulk component is less affected. Furthermore, a new component at higher binding energy (green arrow in the left panel of Fig. 3), which has not been accounted for in the fitting procedure, appears in the Si 2p spectrum recorded at 30 ps after laser excitation. These laser-induced transient changes in the Si 2p spectrum cannot be assigned to surface photovoltage (SPV). SPV leads to a shift or (in case the SPV changes faster than the time resolution) to a broadening of the whole spectrum.

Figure 4 shows in the upper two panels the Si(100) valence band edge (left) and Si 2p spectra (right) as a function of delay time between laser and SR. The shift of the valence band edge towards lower binding energies is considerably larger than that of the Si 2p spectrum and occurs on a faster time scale. This is again evidenced in the lower panel, which shows the center of mass of the corresponding spectra. The slight shift of the Si 2p spectra is assigned to SPV. In contrast, the shift of the center of mass of the valence band edge (which is accompanied by a considerable change of the shape of the edge) can only be interpreted in terms of a change of the electronic structure due to the high concentration of electron-hole pairs in the near-surface region.

References

[1] T. Gießel, D. Bröcker, P. Schmidt and W. Widdra, Rev. Sci. Instrum. **74**, 4620 (2003).

[2] K. Sokolowski and D. von der Linde, Phys. Rev. B **61**, 2643 (2000).

Electronic Structure of Si Nanoparticles in SiO_2 Matrices studied by Soft X-ray Fluorescence Spectroscopy.

A. Zimina, S. Eisebitt, W. Eberhardt
BESSY m.b.H., Albert-Einstein-Str., 15, 12489, Berlin, Germany
J. Heitmann, M. Zacharias
Max-Planck- Institut für Mikrostrukturphysik, Halle, Germany

Nanoscaled structures play an important role in optoelectronic technologies. After the discovery of the strong, size dependent photoluminiscence (PL) in the visible spectral range of porous silicon [1], further research focused on Si nanoparticles which are more stable under ambient conditions.

A synthesis technique providing both the nanoparticle size distribution below 0.5 nm and the control over the spacing between the particles has been developed in Max Planck Institute for Microstructure Physics (Halle) [2]. The process is based on the growth of a SiO/SiO2 superlattice with subsequent high temperature annealing in N2 atmosphere, which leads to the formation of Si particles in a SiO2 matrix. Si nanoparticles as small as 1.5 nm in diameter can be produced with a narrow size distribution in this way. Resonant and low temperature photoluminescence (PL) measurements indicate the existence of electronic quantum confinement with a strongly enhanced ratio of direct to phonon assisted transitions at low temperature due to momentum broadened band edge states [3]. An increase of the PL peak energy up to 0.5 eV compared to bulk crystalline Si (c-Si) has been observed [2].

As c-Si is an indirect semiconductor, the strong photoluminescence observed in the nanosized Si particles a remarkable behavior for this material. The generally believed that indirect transitions from the bottom of the conduction band (CB) to the top of the valence band (VB) become probable due to the changes in the electronic structure when the size of the material gets smaller. It is still not clear if the material becomes a real direct band gap semiconductor under these conditions or if electronic states at the respective band edges get less well defined in momentum space, resulting in an increased overlap of the corresponding wave functions.

The PL measurements on the presented samples demonstrated not only the strong PL, but also size dependence of the maximum of the PL signal: it moves to the higher energies with the decreasing of the initial thickness of the SiO layer. This observation can be explained in terms of the quantum confinement theory. As the size of the material decreases, the electronic states have to fulfill new boundary conditions in the modified quantum wall. For decreasing size, this results in a larger energy spacing of the electronic states, so that the energy gap between VB maximum and CB minimum should increase. Furthermore, the entire shape of the bands as given by the density of states can change under the quantum confinement conditions. The information about the total opening of the band gap with the decreasing of the particle size can be obtained from the PL measurements. More detailed information concerning any size induced changes in the top occupied and lowest unoccupied bands of the Si can be obtained by Soft X-ray Spectroscopy (SXS) [4], as by this technique we were able to probe electronic states in these bands separately from each other.

In our previous work [5] we investigated the structure of the interface region between a Si nanoparticle and the surrounding SiO2 matrix (annealed samples initially consisting of 45 periods of SiO(n)/SiO2(5nm), n=5, 4, 3, 2nm on a quartz substrate). By analyzing the obtained data we were able to estimate the thickness of the sub-oxide shell around the Si-core. The results are summarized in the Table1 together with uncertainties originating from the experimental errors. From this measurements we can see, that the final size of the Si-core is smaller then the initial SiO thickness, but the sub-oxide layer is small relative to the Si-core diameter.

The sub-oxide shell influence the potential well acting as a confinement potential for the Si-core. Knowledge of this potential shape would enable quantitative models of the confinement energy as a function of particle size and interface structure. Detailed information about the core structure and sub-oxide layer is important not only as a feedback for the synthesis process, but also as input for theoretical calculations trying to describe the effects of confinement by the oxide

shell.

D_{SiO}, nm	Sub-oxide content, relative to the initial size of SiO layer, %	D_{Sicore} ± 20%, nm	$D_{sub-oxide}$ ±20%, nm
5,0	37	4,0	0,5
4,0	35	3,2	0,4
3,0	37	2,4	0,3
2,0	30	1,6	0,2

Table 1. Characteristics of the samples, evaluated from the SXF measurements [5].

In the present study we investigate the electronic structure of the Si-core by tuning the incoming photon energy to the absorption threshold of bulk c-Si.

As the samples are not conductive and diffuse reflection of the incident x-rays is strong, the Si 2p soft x-ray absorption (SXA) was recorded by chemically resolved partial fluorescence yield (PFY), accepting only characteristic soft x-ray fluorescence (SXF) from non-oxidized Si in a secondary Rowland spectrometer as a yield signal for SXA. Due to the inherently low x-ray fluorescence yield and the limited solid angle acceptance of the Rowland spectrometer, the counting rate of this signal is low in both SXA and SXF measurements. Nevertheless, a good signal to noise ratio can be achieved by long integration times (8 hours for a SXF spectrum, for instance). Our spectroscopic results on annealed samples with 5, 4, 3 and 2 nm initial SiO layer are presented in Fig.2 in comparison with c-Si spectra.

The PFY-SXA spectra are presented in Fig.2(b). The 2p3/2-2p1/2 spin orbit splitting of 0.6eV which is clearly visible in bulk crystalline silicon (edge inflection points at 99.8eV and 100.4eV) can be observed in the Si nanoparticle samples down to the smallest size. This indicates that inhomogeneous broadening *e.g.* due to particle size variation is small. At the same time, the unoccupied (s+d)-DOS is not dramatically different from bulk crystalline Si. In particular, the peak at 101.0eV with its spin-orbit partner at 101.6 eV produced by a LPDOS typical for crystalline Si [6] can be located in the nanoparticle spectra. In comparison, bulk amorphous silicon (a-Si:H) SXA spectra do not exhibit such a structure [7]. These observations are consistent with the formation of Si nanoparticles containing a core of crystalline silicon from our previous studies. We note changes of the spectral shape compared with the c-Si and as a function of the particle size. The slope of the CB edge becomes shallower when the particle size decreases. We cannot detect strong quantum confinement shift of the CB minimum with decreasing particle size. Based on effective mass theory and experimental findings for porous silicon [8], one would expect about 40% of the increase in band gap to be due to a shift of the CB. For the 2 nm Si particle PL measurements indicate a band gap increase compared to bulk crystalline Si of 0.35eV, which would amount to a CB fraction of 0.14eV, which should be detectable by this method. Moreover, the CB edge for the 3 and 2 nm samples is slightly extended to the *lower* photon energies.

SXF spectra excited at 100.5eV incident photon energy were measured for all samples and are compared with spectrum of bulk crystalline Si in Fig.1(a). At this excitation energy only 2p core levels of the c-Si are exited and thus the observed spectra reflect the (s+d)-DOS in the VB of the Si nanoparticle *core*. The (s+d)-DOS observed for the 3 nm, 4 nm and 5 nm sample indicated the presence of crystalline Si, with its characteristic three-peak structure. These findings are in agreement with our conclusions from the PFY-SXA spectra. The shape of the spectra differs from the c-Si spectrum, similar to the SXA measurements, and changes with the particle size. The peak at 96 eV emission energy is more “step-like” in the Si nanoparticles as compared to the “peak-like” shape in bulk crystalline Si. Similar changes in the SXF spectral shape have been observed for nanoporous silicon (p-Si) in the past, where they could be attributed to a changes in the (s+d)-

DOS due to quantum confinement [9,10]. The position of the VB maximum moves to the lower energies with decreasing particle size. Combining our results obtained by the SXA and SXF methods for the Si nanoparticles in the SiO_2 matrix, we estimated the total band gap opening to be 0.3±0.2 eV for the 5,4 and 3 nm particles and 0.5±0.2eV for the 2nm.

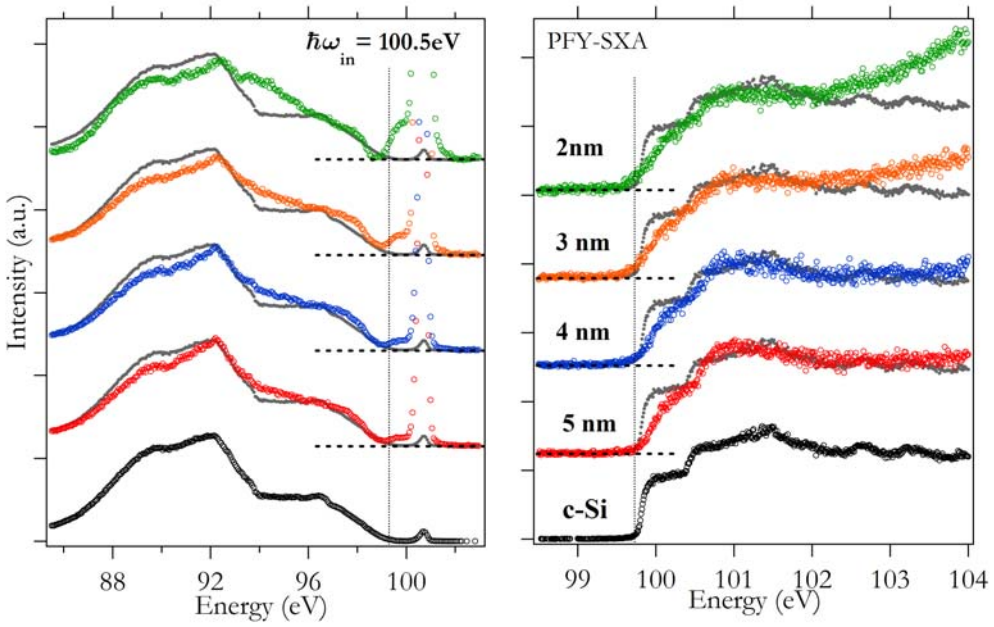

Fig. 1. SXF and SXA spectra measured on samples with 5,4,3 and 2 nm initial SiO layer.

The relative movement of the VB and CB edges for Si was calculated earlier with the effective mass approximation [8]. The experimental data on p-Si are in a good agreement with theoretical predictions. In contrast, the values obtained for the nanoparticles in this study clearly are smaller than the theoretical expectations. The most obvious difference between p-Si and presented material is that the Si nanoparticles are embedded in the glass matrix. We speculate that the electronic structure of the nanoparticles may be influenced by the surrounding glass matrix; potentially by exerting a strain on the particle. Measurements on strained model systems are currently under way.

[1] T.Canham, Appl. Phys. Lett. **57**, 1046 (1900), V.Lehmann, U. Goesele, Appl. Phys. Lett. **58**, 856 (1919)
[2] M. Zacharias, J. Heitmann, R. Scholz, *et al.*, Applied Physics Letters **80**, 661 (2002)
[3] J. Heitmann, D. Kovalev, F. Eichhorn, L.X. Yi, F. Müller, M. Zacharias, submitted for publication
[4] S. Eisebitt and W. Eberhardt, *Soft x-ray spectroscopy as a probe of nanostructured solids* in Frontiers of Nano-Optoelectronic Systems, Ed. L. Pavesi and E. Buzaneva, NATO Science Series II **6**, 347 (Kluwer, Dordrecht,2000)
[5] A. Zimina et al., BESSY Annual Report, p. 240 (2003)
[6] Bianconi, R. Delsole, A. Selloni, *et al.*, Solid State Communications **64**, 1313 (1987)
[7] L. Yang, B. Abeles, W. Eberhardt *et al.*, Physical Review B **39**, 3801 (1989)
[8] T. van Buuren, T. Tiedje, J. R. Dahn, *et al.*, Appl. Phys. Letters **63**, 2911 (1993)
[9] S. Eisebitt, J. Luning, J. E. Rubensson *et al.*, Solid State Communications **97**, 549 (1996)
[10] S. Eisebitt, S. N. Patitsas, J. Lüning et al., Europhysics Letters **37**, 133 (1997)

Adsorption geometry and molecule/metal interaction of ordered pentacene layers grown on Cu(119) studied by NEXAFS and XPS

Chiara Baldacchini

Dipartimento di Fisica, Istituto Nazionale per la Fisica della Materia, Università di Roma "La Sapienza", Piazzale Aldo Moro 2, I-00185 Roma, Italy and
SOFT-INFM, Dipartimento di Fisica, Piazzale Aldo Moro 2, I-00185 Roma, Italy.

Francesco Allegretti

Physics Department, University of Warwick, CV4 7AL Coventry, United Kingdom

Roberto Gunnella

Dipartimento di Fisica, Istituto Nazionale di Fisica della Materis, Università di Camerino, Via Madonna delle Carceri, I-62032 Camerino (MC), Italy

Maria Grazia Betti

Dipartimento di Fisica, Istituto Nazionale per la Fisica della Materia, Università di Roma "La Sapienza", Piazzale Aldo Moro 2, I-00185 Roma, Italy and
SOFT-INFM, Dipartimento di Fisica, Piazzale Aldo Moro 2, I-00185 Roma, Italy.

The adsorption geometry and the nature of the interactions of π-conjugated organic molecules on metal substrates are subjects of increasing research interest. Pentacene ($C_{22}H_{14}$) has often been used as prototype molecule in the study of molecule/metal interaction and adsorption mechanism, thanks to its π-conjugated orbitals, its linear shape and its interesting electronic properties when used as semi-conductive organic system in the electronic devices [1,2]. The long range ordering of the pentacene molecular structures can be obtained on suitable templates like the Cu(119) vicinal surface. A long-range ordered pentacene chain structure has been observed by Low Energy Electron Diffraction (LEED) [3] and Scanning Tunnelling Microscopy (STM) [4] with the molecule lying flat along the step terraces. This ordered molecular structure can be observed up to a saturation coverage (Θ_{HT} in the following) when the pentacene is deposited on the Cu(119) kept at 400K. It is possible to grow a thicker pentacene film on Cu(119) substrate kept at room temperature, but in this case long range order of the thick film is not detectable by LEED.
A detailed analysis of the local structure and the adsorption mechanism has been performed at the UE56/2-PGM2 beamline of the Bessy Synchrotron Radiation Facility. We have studied the evolution of molecule/substrate interaction and of molecular adsorption geometry as a function of pentacene deposition on the Cu(119) surface by means of and x-ray photoemission spectroscopy (XPS) and near-edge x-rays absorption spectroscopy (NEXAFS) experiments.
Pentacene molecules has been deposited on the Cu(119) surface keeping the substrate at 400 K. In the figure 1 is reported the spectral evolution of the C 1s photoemission structure for dilute layers of pentacene, up to the saturation coverage Θ_{HT}. At the first pentacene deposition the spectral shape shows two main features and it does not change at increasing pentacene coverage. In figure 2, the saturation coverage C 1s photoemission spectrum is compared with higher pentacene coverage grown on Cu(119) substrate kept at room temperature (300K) and at low temperature (80K).

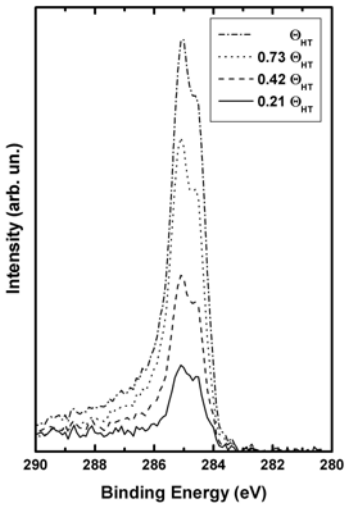

Figure 1: X-ray photoemission spectra evolution (hv=320eV) as a function of pentacene coverage on the Cu(119) surface from pentacene C 1s energy level at 400K.

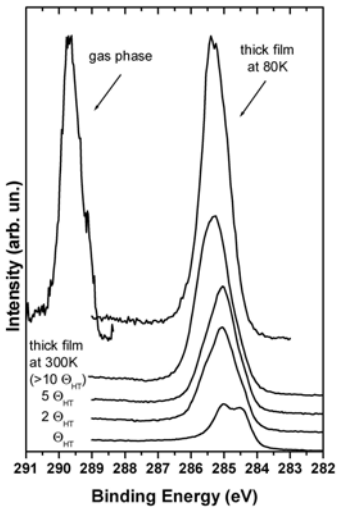

Figure 2: X-ray photoemission spectra evolution (hv=320eV) as a function of pentacene coverage on the Cu(119) surface from pentacene C 1s energy level at room temperature.

We have previously studied free pentacene molecule by means of NEXAFS at the C 1s edge and XPS at the Gas Phase beamline at ELETTRA Synchrotron Radiation Facility [5]. Below the Θ_{HT} coverage, when molecules are interacting with the metallic substrate [3], C 1s photoemission spectrum is different in shape and binding energy from the gas phase spectrum and from the molecular film spectrum, confirming a π-*d* interaction between pentacene and Cu metal substrate. At higher coverage the spectrum is characterized by the six components corresponding to the six unequivalent C atoms in the pentacene molecule, reflecting the lineshape of the C1s gas phase components previously experimentally and theoretically investigated [5].

The evolution as a function of pentacene deposition on the Cu(119) surface has been studied by NEXAFS, recording spectra at normal (θ=90°) and grazing (θ=10°) incidence in Auger electron yield mode. The experimental results are reported in figure 3, where NEXAFS spectrum of the Θ_{HT} coverage and higher coverage are compared with the gas phase NEXAFS spectrum. The energy region below 290eV is characterized by transition to the π^* molecular orbitals, while above 290eV is extending the *continuum* region of transition to the σ^* molecular orbitals [5]. We observe a simultaneous decreasing of resonance intensities corresponding to transitions to the π^* molecular states and increasing of those corresponding to transition to the σ^* molecular states changing the polarization of the incident photon from normal to igrazing incidence, suggesting an almost flat-lying adsorption geometry. Generally for thick pentacene films grown on inert substrates standing-on molecules are reported [6]. An ordered pentacene film grown on a metal substrate with molecules lying down on the surface, slightly tilted to reproduce pentacene crystal structure, has been previously obtained using supersonic molecular beam deposition [7].

Comparing NEXAFS spectra for pentacene adsorbed on Cu(119) and pentacene in the gas phase in the region with the three characteristic σ^* resonances (294, 300 and 306 eV) we do not observe clear differences except for a shift of the main structures towards higher photon energies at increasing pentacene coverage indicating a slight distortion of C-C bonding in the pentacene molecule. The π^* region is strongly different from solid to gaseous pentacene phase. The thick molecular layer shows sharper features with respect to the first stages of growth but with the same intensity behaviour of the π^* components. This confirms that the π^*statess are mainly involved in the interaction with the metal substrate and that the structure of the molecule is only slight distorted by the adsorption process.

An accurate theoretical approach will enlighten the

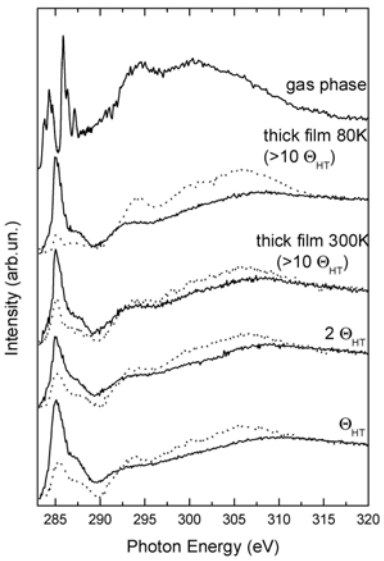

Figure 3: NEXAFS spectra evolution as a function of pentacene coverage on the Cu(119) surface at the C 1s edge, recorded at normal (dashed) and grazing (solid) incidence.

adsorption geometry using multiple scattering calculations, assisted by self-consistent procedure to mimic the charge transfer due to hybridisation with the substrate. In order to solve the complicate structure, an automated approach to the " try and error" procedure, using an efficient recently developed method of calculation [8] will be used.

Authors would like to acknowledge Prof.Woodruff and his staff for the use of their experimental chamber and spectrometer at the beamline UE56/2-PGM2 at Bessy.

[1] C.D. Dimitrakopoulos, P.R.L. Malefant, Adv. Mater. **14**, (2002) 99.
[2] S.F. Nelson, Y. Lin, D.J. Gudlach, T.N. Jackson, Appl. Phys. Lett. **72**, (1998) 1854.
[3] C. Baldacchini, M. G. Betti, V. Corradini, and C. Mariani, Surf. Sci. **566-568**, 613 (2004).
[4] L. Gavioli, M. Fanetti, D. Pasca, M. Padovani, M. Sancrotti, and M. G. Betti, Surf. Sci. **566-568**, 624 (2004).
[5] M. Alagia, C. Baldacchini, M. G. Betti, F. Bussolotti, V. Carravetta, U. Ekström, C. Mariani, S. Stranges, J. Chem. Phys.(2005) *in press*.
[6] S. Söhnchen, S. Lukas, and G. Witte, J. Chem. Phys. **121**, 525 (2004).
[7] L. Casalis, M. F. Danisman, B. Nickel, G. Bracco, T. Toccoli, S. Iannotta, and G. Scoles, Phys. Rev. Lett. **90**, 206101 (2005).
[8] M. Benfatto, A. Congiu-Castellano, A. Daniele and S. Della Longa, J. Sinchrotron Rad **8**, 267 (2001).

Electronical properties of Cyclopentene on Si(001)

M. Wahl[3], P. Vogt[1], R. Paßmann[3], R. Hunger[4] , W. Braun[2], W. Richter[1], N. Esser[3]

[1]*Technische Universität Berlin, Institut für Festkörperphysik, Berlin, Germany*
[2]*BESSY GmbH, Berlin, Germany*
[3]*Institute of Analytical Sciences, Department Berlin-Adlershof, Germany*
[4] *TU Darmstadt, Darmstadt*

The chemisorption of small organic molecules on the Si(001)-2x1 surface was subject of many studies in recent years. This surface shows a unique structure, because the top-most atoms are paired to form asymetric dimers. Due to this so-called “buckling” these dimers form bonding partners to unsaturated hydrocarbons like Cyclopentene. These molecular monolayers were mostly studied by STM and Photoemission.
We have shown recently that it is also possible to obtain information about the bonding geometry by Reflectance Anisotropy Spectroscopy (RAS) [1]. RAS requires a highly ordered molecular layer which can be obtained by preparing single-domain Si(001)-2x1 surfaces.
Here we used 4° offcut Silicon (001) as substrates. To obtain a clean, single domain (2x1) surface reconstruction the samples were degased at 600 °C overnight and heated with direct current stepwise up to 850 °C.
RAS spectra taken after preparation however, showed differences to single-domain Si(2x1) surfaces. The differences are also confirmed by SXPS measurements shown in Figure 1. Silicon 2p core-level spectra taken after preparation differ significantly from measurements found in literature. Still, most of the structures can be assigned in comparison to published data: Apart from the bulk related component B, one can see a structure S slightly shifted to higher binding energies as a dominant feature. This component was previously assigned to a monohydride phase, where the Si dimers stay intact, but are saturated by hydrogen [2]. On the other hand it is clear, that any structures related to the asymmetry of the dimers are missing. These core-level components are easy to assign, since due to the charge transfer within the dimer pairs the contribution of the upper Silicon atoms is significantly shifted to lower binding energies (about 500 meV [3]). In contrast we find a surface sensitive contribution shifted only about 300 meV to lower energies. Also this component was observed previously, yet not clearly assigned. (Either it stems from symmetric dimers or is defect related [3]). It should be also mentioned, that we found no contamination of the surface by other species after the preparation. It is also assumed that the asymmetry of the Silicon dimers vanishes upon hydrogen passivation. Therefore we conclude that our Si(001)-(2x1) surface refers to a (partly) H-terminated surface. The hydrogen originates from the residual gas in UHV maintained only by mechanical pumping (Turbo molecular pumps). Figure 2 show the Si 2p and C 1s core-level spectra of the Si(001) surface after exposure of about 37 Langmuir Cyclopentene. There are no new features in the Si 2p spectrum in comparison to the clean

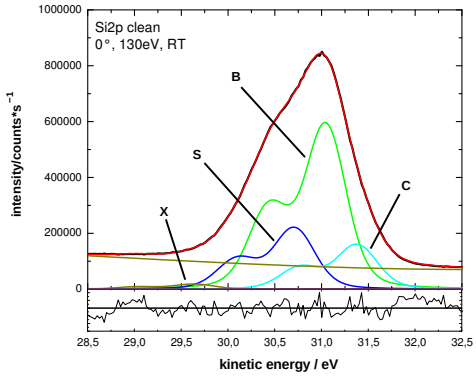

Fig.1: Si 2p core-level spectrum and “best-fit” decomposition after preparation. Spectrum differs significantly from literature.

spectrum. But from literature it is found, that the C-Si contribution (in case of a chemisorbed molecule) lies at 240-320 meV shifted to higher binding energies. In our case it is obvious that we would not be able to distinguish such a component from the one shifted about 400 meV still dominating the spectrum. The decomposition is easier for the carbon C 1s core-level shown in Fig. 2b. One can clearly see three contributions to the spectrum. In comparison to literature these components can be assigned to single and double bondings of carbon and a third component which was assigned to the Silicon-carbon bond [3]. Interesting is the fact that there are still carbon double-bondings visible, since at room temperature the molecule should bond to the silicon via the unsatured C=C carbons leaving an alkane like molecule.

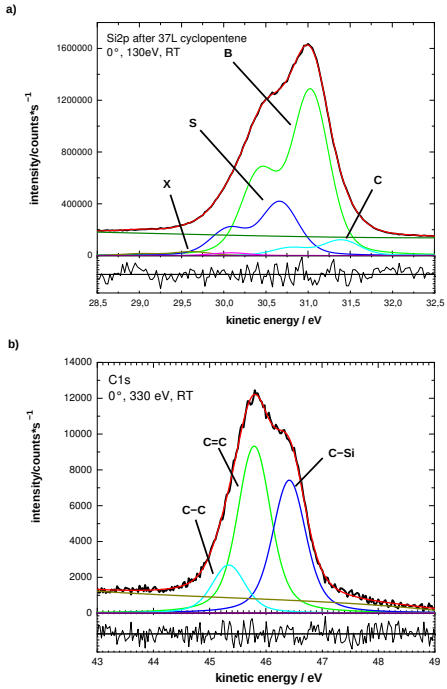

Fig. 2: core-level spectra and "best-fit" decomposition of 37 L Cyclopentene on Si(001). a) Si 2p core-level. b) C 1s core-level

Figure 3 compares the valence band spectra of the clean with the cyclopentene covered surface.

From the additional structures at binding energies higher than 5 eV one can conclude that the molecules stay intact upon adsorption at the surface. For comparison, the inset shows photoemission data of gas-phase cyclopentane taken from [2]. The peak positions of the measured spectrum lie at similar energies. The peak in the clean spectrum at about 300 meV below E_F is quenched upon adsorption of the molecule. We assume that this state is related to the dimers on the surface. A partly physisorption of the molecule is supported by the component at about 4 eV below E_F which is assigned to the HOMO of Cyclopentene [2].

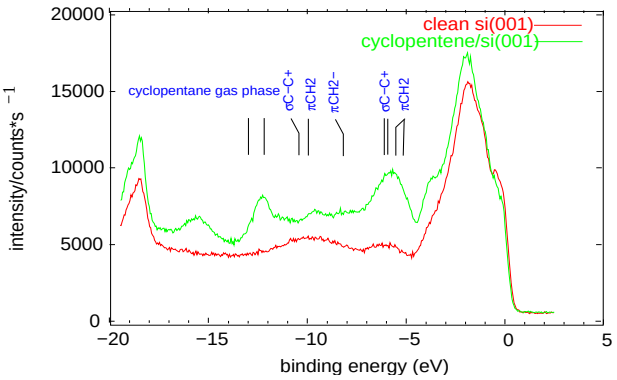

Fig. 3: Valenceband spectra of clean and Cyclopentene covered Si(001). A photon energy of 80 eV was used. Inset shows gas-phase PES data of Cyclopentane (taken from [2]).

To summarize, we performed SXPS measurements of Cyclopentene on Si(001). Possibly due to residual hydrogen it was not possible to prepare the asymmetric dimerized surface. Still, spectra of the C1s core-level and Valenceband suggest that the molecule is chemisorbed and stays intact.

[1] W.G. Schmidt et al, J. Phys. Condens. Matter 16, 4323 (2004).
[2] K. Yamamoto, J. Vac. Sci. Technol. B **12(4)**, 2493 (1994)
[3] S. Machida et al, J. Phys. Chem. B **106**, 1691 (2002).
[4] H. Liu et al, Surf. Science **416**, 354 (1998).

The methyl-terminated Si(111)-CH_3 surface: High-resolution synchrotron photoelectron spectroscopy of a prototypical silicon/organic interface

Ralf Hunger*, Rainer Fritsche, Bengt Jaeckel, Taek Lim, Wolfram Jaegermann

Fachgebiet Oberflächenforschung, Institut für Materialwissenschaft, TU Darmstadt, Petersenstr. 23, 64287 Darmstadt

in collaboration with:

Lauren J. Webb, Nathan S. Lewis

Division of Chemistry and Chemical Engineering, California Institute of Technology, 210 Noyes Laboratory, 127-72, Pasadena, CA 91125, USA

(funding by BMBF contract 05 KS4RDA/0)

Thin organic films for "plastic electronics", and metal/organic and semiconductor/organic interfaces are attracting increasing interest. We have re-examined the methyl-terminated Si(111)-CH_3 surface as we consider it as an interesting, prototypical system which represents one of the simplest possible silicon/organic interface structures. A ball-and-stick model of this surface structure is shown in Figure 1. The dangling bonds of the silicon(111) surface atom binds to a methyl group and are thereby electronically passivated.

Figure 1: Ball-and-stick model of the methyl-terminated Si(111)-CH_3 surface.

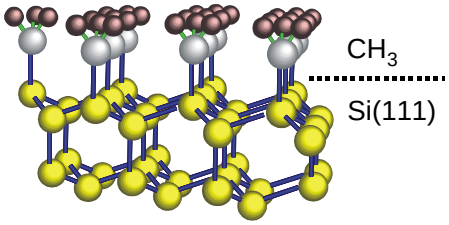

Methyl-termination of Si(111) can be achieved by various wet chemical processes [1]. The methyl-terminated surfaces that we analysed were prepared in a two-step chlorination/ alkylation process using a Grignard reaction with CH_3MgCl [2]. The preparation process is illustrated in more detail in Figure 2.

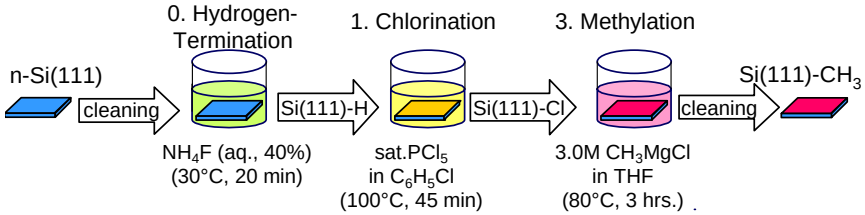

Figure 2: Schematics of the wet-chemical two-step chlorination/alkylation process using a Grignard reagent CH_3MgCl for the prepartion of methyl-terminated Si(111)-CH_3.

After introduction of such Si(111)-CH_3 samples into the vacuum system, a clear (1x1) LEED pattern with sharp spots and a low background intensity was obtained (Figure 3). A (1x1) symmetry is expected from the structural model in Figure 1. The well-defined LEED pattern

* hunger@surface.tu-darmstadt.de

indicates a highly ordered Si(111) surface with only few structural defects. Recently, it was also possible to measure STM images of such surfaces [3].

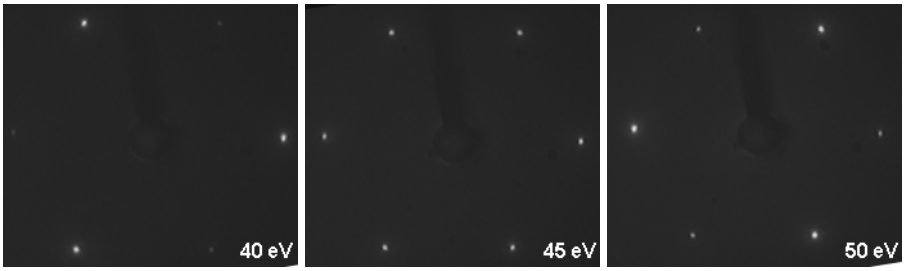

Figure 3: LEED patterns of Si(111)-CH_3. The (1x1) symmetry is consistent with a methyl-termination.

These surfaces were analysed by photoelectron spectroscopy at the U49/2-PGM2 beamline of the CRG BTU Cottbus, Hahn-Meitner-Institut and TU Darmstadt. The SoLiAS experimental station of the TU Darmstadt is dedicated to the analysis of solid/liquid interfaces (SoLiAS = Solid/Liquid Interface Analysis) by means of synchrotron photoelectron spectroscopy [4] and is equipped with a Phoibos 150-MCD9 analyser. Photoelectron spectra were acquired in normal emission.

The C1s core level emission of a methyl-terminated Si(111) surface before and after a vacuum anneal to 500°C are shown in Figure 3. The annealing step leads to the reduction of the component C^3 which is assigned to adventitious, non-methyl hydrocarbon compounds adsorbed on the methylated surface [5]. This adventitious hydrocarbon is largely desorbed from the surface during annealing. The methyl-related C1s emission (C^0, C^1, C^2) as a whole remains unchanged with the annealing step, indicating that the methyl-termination withstands an annealing to 500°C.

The carbon 1s emission related to the silicon-bound methyl groups shows an interesting fine structure: it consists of a main component C^0 and two equidistant satellite components C^1 and C^2, shifted to higher binding energies. C^1 and C^2 are caused by vibrational losses, where the first and second excited states of C-H stretch vibrations are generated on the photoionized methyl group. Such vibrational loss structures are well-known for gas phase core level spectra [6], but only lately have been identified for organic adsorbates on metals [7] or silicon (001) [8].

The line shape of the Si2p emission of methylated Si(111) remains essentially unaltered with the annealing step. Figure 4 displays the Si 2p spectra of an annealed Si(111)-CH_3 surface, excited with different photon energies. Apart from the bulk component B a surface component S is clearly identified by its dependence on excitation energy. The highest relative intensity of the carbon-bound surface silicon species is found for excitation with hν = 150 eV, where the surface sensitivity is highest. Curve fits to the Si2p spectrum are shown in Figure 5. The

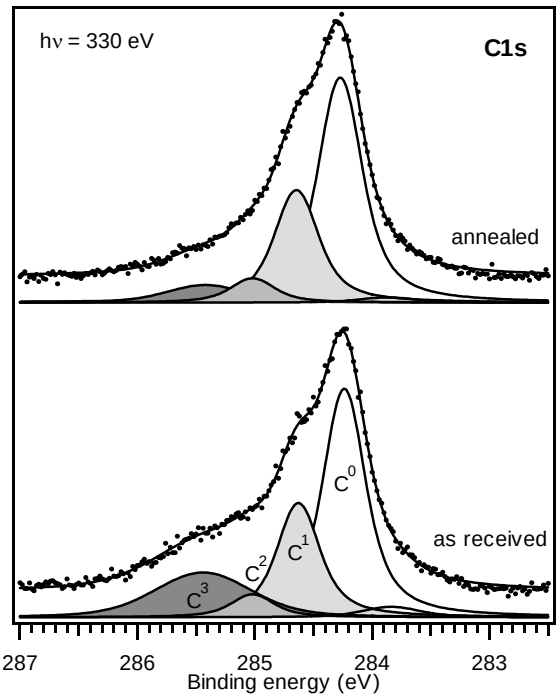

Figure 3:

Carbon 1s emission of Si(111)-CH_3 before and after vacuum annealing to 500°C. C^0 is the methyl-component, C^1 and C^2 are vibrational loss satellites, shifted to higher binding energies by n × 0.38(1) eV (n=1,2). C^3 is assigned to adventitious hydrocarbons which are largely desorbed by the anneal.

surface component exhibits a chemical shift of +0.30±0.01 eV with respect to the silicon bulk environment. A detailed account of the chemical and electronic characterisation of wet-chemically prepared Si(111)-CH_3 surfaces will be given in [2].

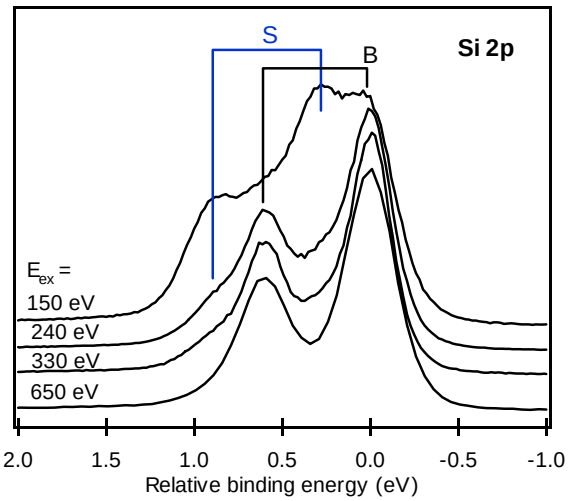

Figure 4:

Si2p spectra of methyl-terminated Si(111)-CH_3. By the variation of the excitation energy and hence the surface sensitivity, the surface component S arising from carbon-bound silicon surface atoms is clearly identified and distinguished from the bulk component B.

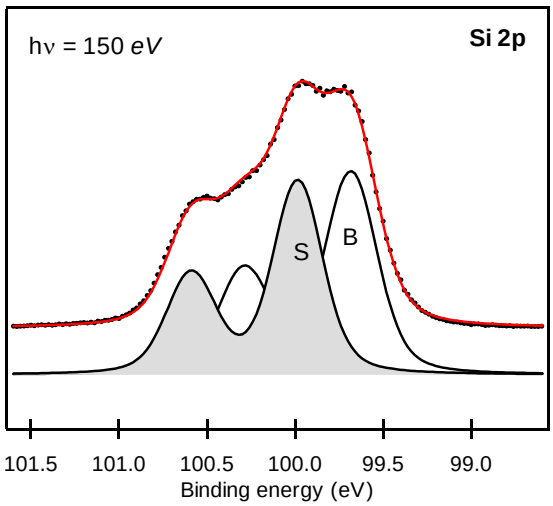

Figure 5:

Deconvolution of the Si2p emission by Voigt profiles. A chemical shift between carbon-bound surface silicon (S) and bulk silicon (B) of +0.30(1) eV is obtained.

Apart from being an interesting model system in terms of fundamental surface science, we consider the methyl-terminated Si(111)-CH_3 surface as well as promising substrate for the formation of silicon/organic heterostructures and hybrid devices. Future studies are planned to develop along this line.

Acknowledgements

This work was supported by the BMBF, contract numbers 05 KS1RD1/0 and 05 KS4RDA/0 (SoLiAS). Travel grants by the DFG (W.J.: JA 85910-1) and BMBF (R.F.: 05 ES3XBA/5) are gratefully acknowledged.

References

[1] L.J. Webb and N.S. Lewis, J. Phys. Chem. B **107** (2003) 5404.

[2] R. Hunger, R. Fritsche, B. Jaeckel, W. Jaegermann, L.J. Webb and N.S. Lewis, Phys. Rev. B (2005) submitted.

[3] H. Yu, L.J. Webb, R.S. Ries, S.D. Solares, W.A.G. III, J.R. Heath and N.S. Lewis, J. Phys. Chem. B (2005) 671.

[4] T. Mayer, M.V. Lebedev, R. Hunger and W. Jaegermann, Appl. Surf. Sci. (2005) in press.

[5] J. Terry, M.R. Linford, C. Wigren, R. Cao, P. Pianetta and C.E.D. Chidsey, J. Appl. Phys. **85** (1999) 213.

[6] H.M. Köppe, B.S. Itchkawitz, A.L.D. Kilcoyne, J. Feldhaus, B. Kempgens, A. Kivimäki, M. Neeb and A.M. Bradshaw, Phys. Rev. A **53** (1996) 4120.

[7] J.N. Andersen, A. Beutler, S.L. Sorensen, R. Nyholm, B. Setlik and D. Heskett, Chem. Phys. Lett. **269** (1997) 371.

[8] H.W. Yeom, S.Y. Baek, J.W. Kim, H.S. Lee and H. Koh, Phys. Rev. B **66** (2002) 115308.

Chemical bonding effects in soft X-ray absorption and fluorescence spectra of Sc compounds.

A. Zimina[1] and A. S. Vinogradov[2]
[1]BESSY GmbH, Albert-Einstein-Str. 15, 12489 Berlin, Germany
[2] V.A. Fock Institute of Physics, St. Petersburg State University, St. Petersburg 198504, Russia

The nature of the electronic structure and chemical bonding in 3*d* transition metal (TM) compounds is currently of great fundamental and technological interest because these compounds show many unique electronic and magnetic properties. The latter are usually analyzed taking into account the correlations between the highly localized 3*d* electrons, the charge transfer and covalent bonding (hybridization) between the TM atom and its nearest-neighbor atoms [1]. All of these effects are directly reflected in characteristics of the energy distribution of the filled and unfilled TM 3*d* states in a compound. Therefore, detailed information on the 3*d* electronic configuration is required for a better understanding of relationship between these factors**.** These electronic states can be well probed in an X-ray absorption experiment by excitation of metal 2*p* core electrons to unfilled 3*d* electron states. Up to now, the 2*p* excitations of the 3*d* atoms are usually considered as intra-atomic excitations. Those are strongly localized within the TM ions with formal [Ar]3d^n ground-state electronic configurations, and are mainly described in various ionic multiplet approaches [2] taking effects of chemical bonding implicitly into account. At the same time it is apparent that the TM 3*d* electrons participate in covalent bonding to an extent which depends strongly on ligand electronic structure. This hybridization between the TM 3*d* electrons and ligand valence electrons leads to delocalization of the 3*d* states and a decrease of the 3*d* electron density on the TM atoms, thus lowering the dominant role of the 3*d* electron correlations.

Here we report on a systematic study of different Sc compounds by soft X-ray absorption (SXA) and soft X-ray fluorescence (SXF) spectroscopy. Scandium is located at the beginning of the series of the 3*d* TM's and the ground state electronic configuration of its atom is [Ar] 3d4s^2. The Sc atom has usually a valence of three in its compounds and, therefore, in a simple ionic model there are no 3*d* electrons nominally in the ground state electronic configuration for these compounds. This leads to the expextation that the role of 3*d* electron correlations is not large for Sc compounds and, consequently, spectral changes along the above series will be mainly caused by changes in the character (ionicity) of the chemical bonding between the scandium and ligand atoms as well as by those in the metal atom coordination and the Sc-ligand atom distances (the latter are essentially chemical bonding effects, too). This investigation aimes at clarifying the subtle interplay between hybridization and 3*d* correlations in the electronic structure of the compounds of the Sc metal and other early TM's.

We studied several Sc compounds (among them ScF_3, $ScCl_3$, Sc_2O_3, $Sc(acac)_3$, $Sc_3N@C_{80}$, and Sc metal) which are supposed to have different valence charge on Sc and different surrounding geometry originating from different chemical bonding between the Sc and ligand atoms. Materials which were suspected to oxidize/decomposed in air were evaporated *in situ* on the sample-holder and transported into the experimental chamber in the vacuum. Particular attention was given to the consideration of the endohedral fullerene $Sc_3N@C_{80}$. The chemical state of the Sc in this metallofullerene is determined by its interactions with the nitrogen atom and the C_{80} cage [3] and characterized on the basis of the comparison between its Sc 2*p* spectrum and those of other Sc compounds.

The local partial density of the electronic states (LPDOS) in the valence band (VB) and conduction band (CB) is probed independently by SXF and SXA. The basic process involved in both techniques is the excitation of a core electron (in our study Sc 2p) into empty

states in the CB (SXA) and the subsequent relaxation when an electron from the VB or 3s core electron recombines with the core hole (SXF).

The study was performed at the BESSY U49/2-PGM1 beamline. The beamline energy bandwidth was set to 70 meV. Sc $L_{2,3}$-band and $L_{l,\eta}$ lines ($3s$- $2p_{3/2,1/2}$ transitions) were recorded using a Rowland-type soft x-ray fluorescence spectrometer [4] with 1200 l/mm spherical grating of 5000 mm radius and 2D-detection at an appropriate off-Rowland angle to obtain the entire spectrum in a parallel mode. With the entrance slit of 25μm the SXF energy resolution was 1.5eV as measured by the energy width of the primary x-rays elastically scattered from the sample. The SXA spectra were taken both in the total electron yield (TEY) mode and in the total fluorescence yield (FY) mode using a photodiode as detector.

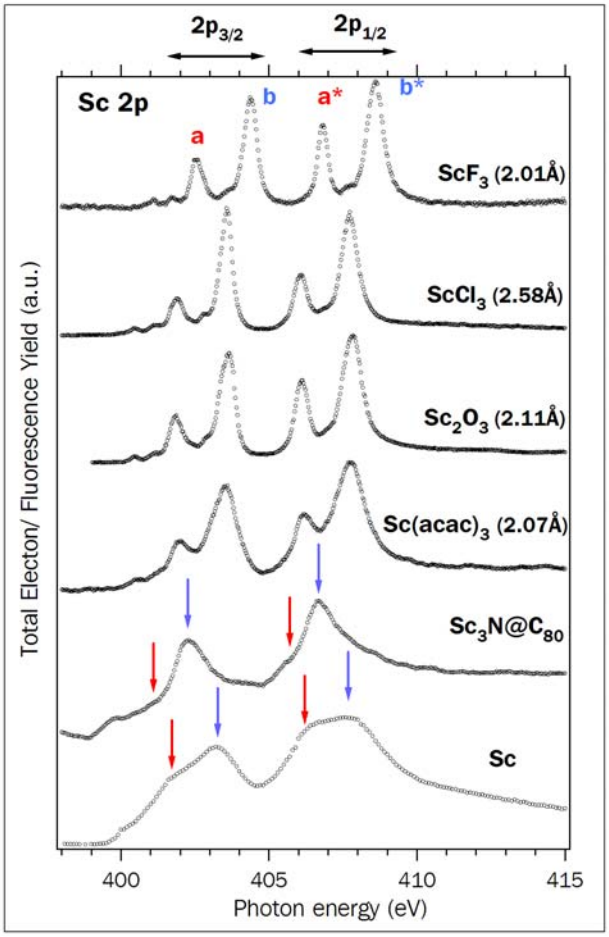

Fig. 1. SXA spectra for different Sc compounds. In brackets Sc-ligand distances are noted.

We observe strong correlation between the chemical state of Sc atom and the shape and energy position of the SXA spectra (Fig.1). Going from the Sc metal to the most ionic ScF_3 the main Sc $2p_{3/2}$ absorption band is split into two narrow and intense resonances *a* and *b* with additional weak low-energy structures, the whole spectrum moves to higher photon energies and the width of the absorption peaks decreases. These tendencies reflect the increase of charge transferred to the ligand from the Sc atom and changes in the local surrounding of the Sc atom.

As the exchange interaction of $3d$ electrons and core electrons is influenced by the hybridization between the Sc and ligand, we expected that the L fluorescence spectra would exhibit strong excitation energy dependence for the compounds with ionic bond. In contrast, compounds with covalent bonding character should show normal 'non-resonant' behavior. In Fig. 2 our spectra of resonant excited x-ray fluorescence resulting from electronic dipole transitions from the VB and 3s level to the 2p core hole on the Sc metal and Sc_2O_3 are shown. One can see that the fluorescence spectra behave as expected from the general consideration above. Similar sets of spectra were obtained also from $Sc(acac)_3$ and $Sc_3N@C_{80}$. The character of the excitation energy dependence of the SXF spectra from $Sc_3N@C_{80}$ is closer to the metal than to the oxide.

We expect to extract details of the electronic structure in $Sc_3N@C_{80}$ on the basis of the systematic comparison with the reference compounds. This work is currently in progress.

A.S. Vinogradov gratefully acknowledges the financial support by BESSY.

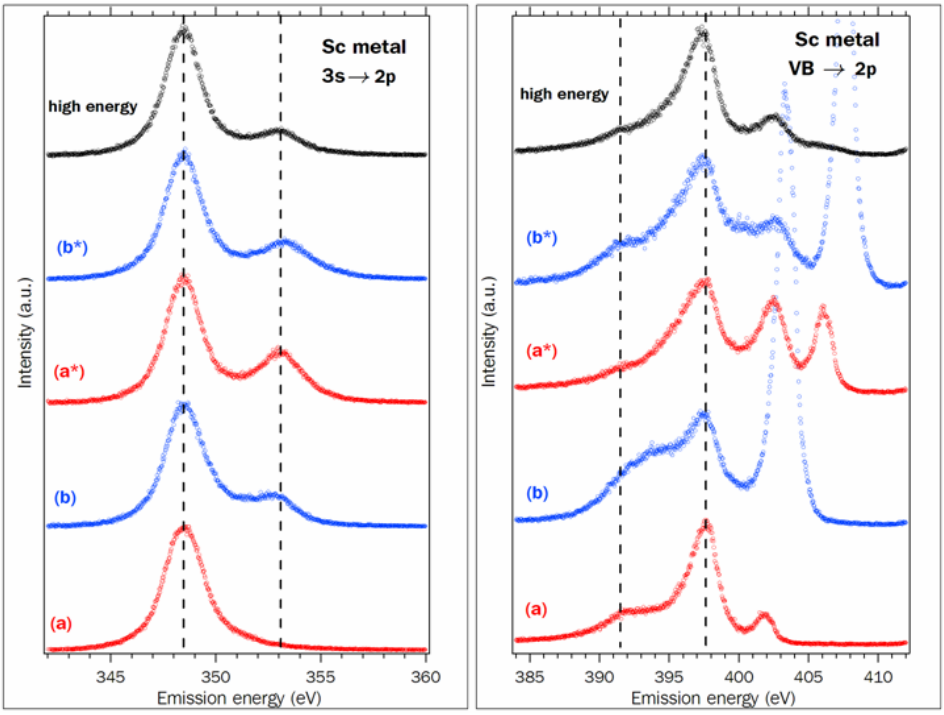

Fig. 2 (a). SXF spectra for Sc metal.

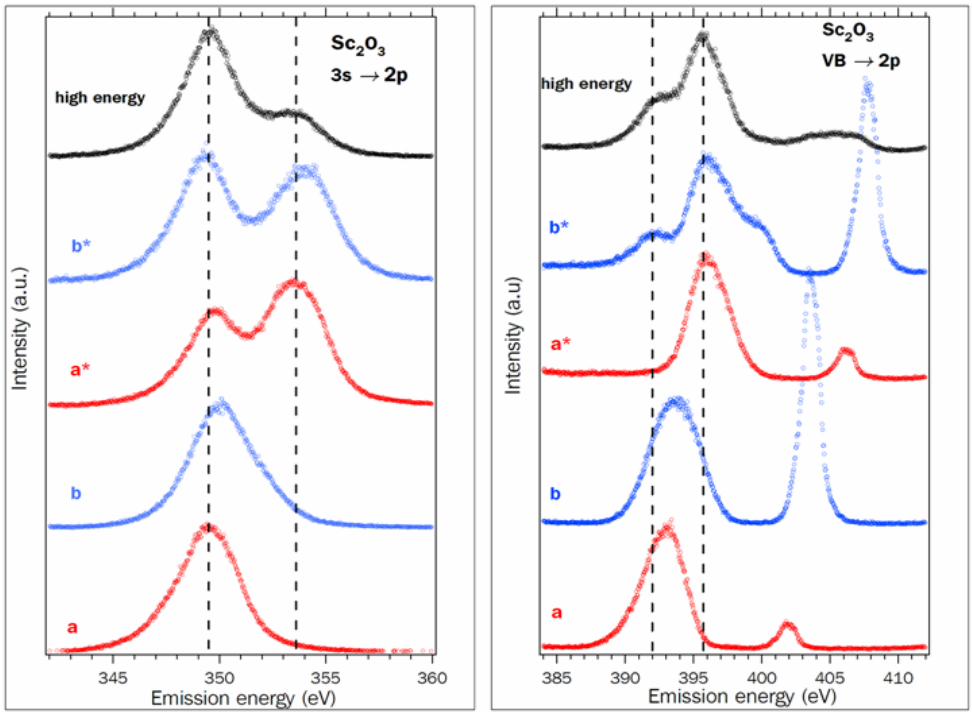

Fig. 2 (b). SXF spectra on Sc_2O_3.

[1] J. Zaanen, G. A. Sawatzky, and J. W. Allen, Phys. Rev. Lett. **55**, 418 (1985).

[2] F. M. F. de Groot et al., PRB, **41,** 928 (1990); **42**, 5459 (1990); G. van der Laan and L.W. Kirkman , J. Phys.: Condens. Matter **4**, 4189 (1992).

[3] S. Stevenson et al., Nature, **401**, 55 (1999)

[4] J. Lüning, J.-E. Rubensson, C. Ellmers, S. Eisebitt and W. Eberhardt, Phys. Rev. B **59**, 10573 (1999)

Band structure investigation of chalcopyrite $CuInSe_2$(001) by angle-resolved photoelectron spectroscopy (ARPES)

Ralf Hunger*, Wolfram Jaegermann

Fachgebiet Oberflächenforschung, Institut für Materialwissenschaft, TU Darmstadt, Petersenstr. 23, 64287 Darmstadt

(funding by BMBF contract 05 KS4RDA/0)

Keiichiro Sakurai, Shigeru Niki

Research Center for Photovoltaics, Advanced Institutes of Industrial Science and Technology, Tukuba Central #2,Umezono 1-1-1, Tsukuba, Ibaraki, Japan

Wolfram Calvet, Carsten Lehmann, Christian Pettenkofer

Abteilung SE 6, Bereich Solarenergieforschung, Hahn-Meitner-Insitut Berlin GmbH, c/o BESSY, Albert-Einstein-Str. 12, 12489 Berlin

The copper chalcopyrite semiconductors $CuInSe_2$, $CuGaSe_2$ and $CuInS_2$, and their solid solutions are widely investigated for their application in thin film solar cells [1, 2]. Even though angle-resolved photoelectron spectroscopy (ARPES) is the method of choice for the determination of such a fundamental material property as the valence electronic band structure, ARPES studies of $CuInSe_2$, $CuGaSe_2$, or $CuInS_2$, have not been reported, yet.

The presumable reason for the lack of experimental data is the difficulty of the preparation of clean, ordered (single crystalline) and oriented surfaces of these materials [3]. Recently, we could however demonstrate the possibility of the preparation of UHV-clean and ordered $CuInSe_2$(001) surfaces by a selenium capping and decapping process [3]. We employed this new technique for our ARPES study presented here.

The chalcopyrite structure is characterised by an ordering of the cations on the (021) planes of the cation fcc sublattice, giving rise to an uniaxial distortion of the crystal lattice along the c-axis and a resulting tetragonal crystal symmetry (space group No. 122, I-42d). The relation between the zincblende lattice and the chalcopyrite lattice is illustrated by the unit cells in Figure 1. For $CuInSe_2$, $c_{CIS}/2 > a_{CIS} > a_{GaAs}$, and hence in the heteroepitaxial growth of $CuInSe_2$ on GaAs(100), the so-called c-axis orientation with $CuInSe_2$(001) as epilayer growth surface is established by lattice strain minimization [4].

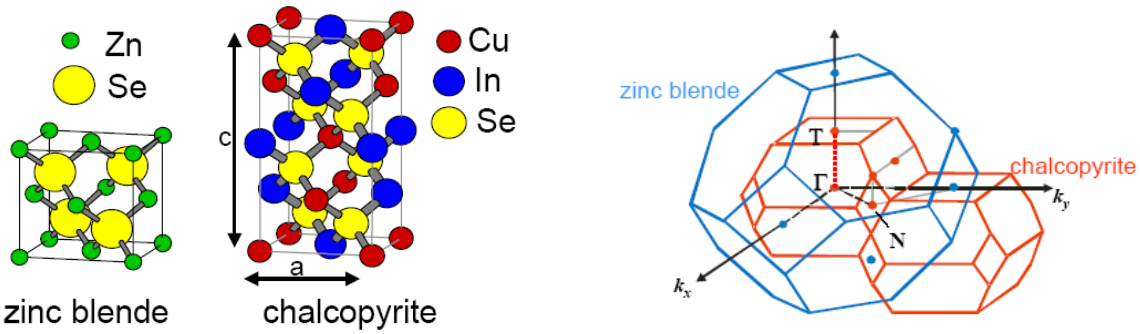

Figure 1: Comparison of the zinc blende and chalcopyrite unit cells in real space and the first Brillouin zones in reciprocal space. A doubling of the unit cell along the c-axis is caused by the ordering of the Cu and In atoms on the $(021)_{fcc}$ planes of the cation fcc sublattice. Due to the lower symmetry of the chalcopyrite lattice, the Brillouin zone of the chalcopyrite is much smaller.

* hunger@surface.tu-darmstadt.de

After growth of an $CuInSe_2$(001)/GaAs epilayer with near-stoichiometric film composition by molecular beam epitaxy and selenium capping at the AIST [3, 4], the samples were transported to BESSY, and introduced in the SoLiAS experimental station [5]. After thermal desorption of the protective selenium cap layer by a vacuum anneal to ~350°C, the $CuInSe_2$(001) surface showed a low-energy-electron-diffraction pattern with a (4x2) superstructure[1]. As first step of the ARPES study, the band structure along the ΓT line, i.e. the [001] direction was analysed. Electron distribution curves (EDC) were collected in normal emission with a VG ADES 500 analyser for excitation energies from 9.6 eV to 40 eV, employing both gratings of the TGM 7 monochromator.

An EDC series from E_{ex} = 10 eV to 27 eV is plotted in Figure 2. An exemplary EDC is compared to the literature data of a cleaved $CuInSe_2$ crystal, that was measured on the same instrument (E_{ex} = 21 eV [6]). The valence band features are very similar, proving again the validity of the selenium capping and decapping approach for the preparation of single crystalline surfaces.

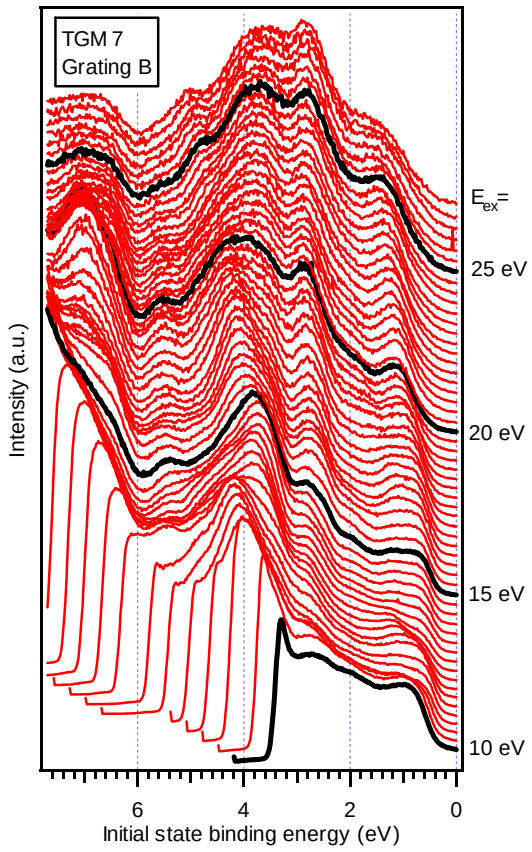

Figure 2: EDCs of a $CuInSe_2$(001)-(4x2) surface measured in normal emission with excitation energies from 10 eV to 27 eV.

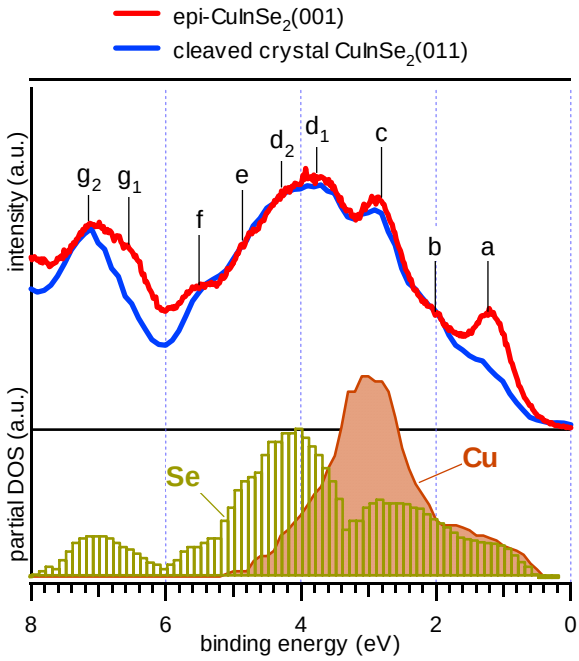

Figure 3: Comparison of the valence band emissions of a decapped $CuInSe_2$(001)-epilayer with a cleaved single crystal with (011) face (Ref [6]). The labels a to g denote the different emission bands. In the bottom, the partial density of states (pDOS) of selenium and copper as determined in [6] are included.

The dispersion of the emission bands labelled a to g becomes obvious from the structure plot in Figure 4. It is a grey-scale representation of the second derivatives of the data in Figure 2, where white contrast corresponds to prominent emission features. The white diagonal lines represent the assumed position of transitions at the centre (Γ) or boundary (T) of the Brillouin zone (inner potential of –14.8 eV w.r.t. vacuum). Hence, the stretch between the Γ and T lines corresponds to the band dispersion along ΓT. For comparison, the band structure of $CuInSe_2$ calculated by [7] is reproduced to the right of Figure 4. The agreement between measured and calculated bands is generally very good: The energetic position and non-dispersive character of the emission band c, which is derived from non-bonding Cu3d orbitals is well reproduced. The bandwidth of the topmost valence band a, derived from Se4p-Cu3d hybrid orbitals with

dominant Se4p-character is experimentally with ~0.7 eV somewhat smaller than the calculated one of 1.0 eV. The bonding p-d orbitals (dominant Cu3d) can be resolved as structures d_1,d_2,e, and f. As well, the splitting of the In-Se bond-derived band g_1/g_2 is measured.

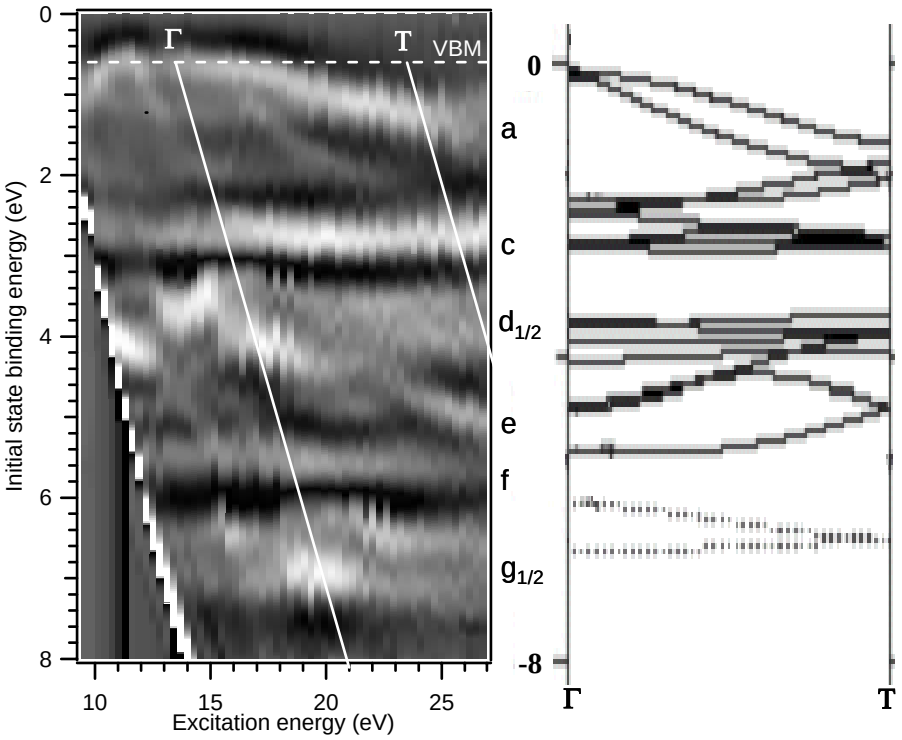

Figure 3: "Structure plot" derived from the data in Figure 2 (left). The white parameter lines mark the transitions at the Brillouin zone boundaries, Γ and T. The calculated band structure along ΓT to the right is reproduced from [7].

This assignment of the emission features is consistent with earlier synchrotron studies of $CuInSe_2$ crystals [6, 8], however, for the first time we could establish the band dispersion of a copper chalcopyrite by photoelectron spectroscopy. In future, these studies shall be extended to other sections of the Brillouin zone and other copper chalcopyrite materials.

Acknowledgements

Discussions and helpful advice by Andreas Klein are gratefully acknowledged. We also would like to thank Karsten Horn for the proliferation of Igor procedures.

References

[1] U. Rau and W. Schock, Appl. Phys. A **69** (1999) 131.

[2] R. Hunger, K. Sakurai, A. Yamada, P. Fons, K. Iwata, K. Matsubara and S. Niki, Thin Solid Films **431-432** (2003) 16.

[3] R. Hunger, T. Schulmeyer, A. Klein, W. Jaegermann, K. Sakurai, A. Yamada, P. Fons, K. Matsubara and S. Niki, Surf. Sci. **557** (2004) 263.

[4] S. Niki, Y. Makita, A. Yamada, O. Hellman, P.J. Fons, A. Obara, Y. Okada, R. shioda, H. Oyanagi, T. Kurafuji, S. Chichibu, H. Nakanishi, J. Cryst. Growth **150** (1995) 1201.

[5] T. Mayer, M.V. Lebedev, R. Hunger and W. Jaegermann, Appl. Surf. Sci. (2004) in press.

[6] T. Löher, A. Klein, C. Pettenkofer and W. Jaegermann, J. Appl. Phys. **81** (1997) 7806.

[7] M. Belhadj, A. Tadjer, B. Abbar, Z. Bousahla, B. Bouhafs and H. Aourag, phys. stat. sol. (b) **241** (2004) 2516.

[8] K. Takarabe, K. Kawai, S. Minomura, T. Irie and M. Taniguchi, J. Appl. Phys. **71** (1992) 441.

[1] Presented elsewhere in this volume: *"A study of the (4x2) surface reconstruction of $CuInSe_2$(001) by LEED and synchrotron X-ray photoelectron spectroscopy"* by T. Deniozou, N. Esser, K. Sakurai, S. Niki, R. Hunger.

Photoelectron Diffraction from Cu Surfaces Using a New High Resolution Toroidal Electron Energy Analyser.

L. Broekman[1], A. Tadich[1], J. Riley[1], R. Leckey[1]
Th. Seyller[2], K.V. Emtsev[2], L. Ley[2], A. Winkelmann[3]

[1]*Department Of Physics, Latrobe University, Australia.*
[2]*Institut fur Technische Physik, Universitat Erlangen, Germany.*
[3]*Max-Planck-Institut für Mikrostrukturphysik, Weinberg 2, D-06120 Halle, Germany*

Photoelectron diffraction has been used in either angle scan mode at one energy or energy scan mode at one angle to determine surface structures. Mostly a single line of data is fitted to a multiple scattering calculation to achieve an R factor fit of the surface structure to the diffraction pattern. Diffraction patterns covering 2π steradians have often been performed using single scattering calculations.

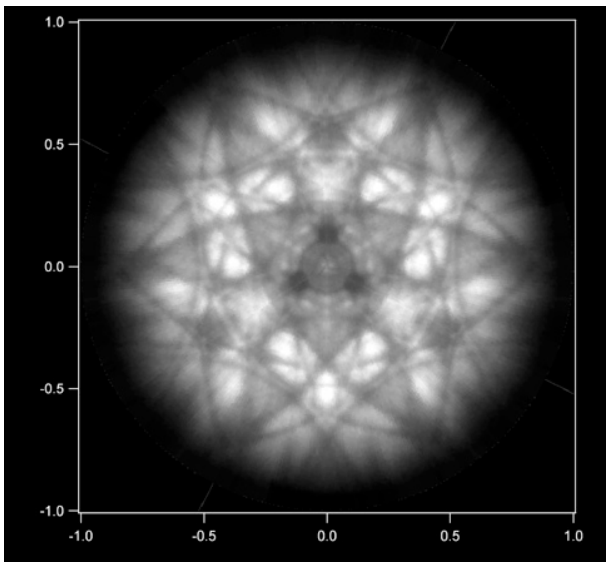

Fig 1 Full hemisphere diffraction pattern from Cu(111) using Cu 2p core level with kinetic energy of 520 eV.

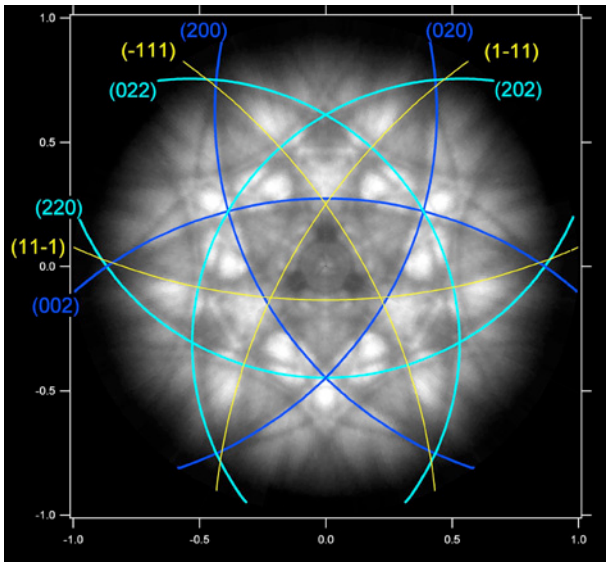

Fig 2 Calculated Bragg lines for some low index planes showing both the agreement and the small separations from the observed lines.

Our new toroidal analyser is able to obtain a diffraction image of 2π steradians by data collection over emission angles of ± 90˚ in a plane and by the rotation of the sample through 390˚ or an angle determined by the symmetry of the surface.. Collection times range from 20 to 60 minutes. An image obtained from Cu(111) using Cu 2p with kinetic energies of 520 eV is shown in Fig 1.

The relative intensities of the forward scattering along the principle planes is comparable to previously published work. However the improved resolution of the toroidal analyser permits the Kikuchi related cancellations to be observed with clarity. These lines, called Kossel lines in x-ray diffraction, are the result of interference between a directly emitted ray and a Bragg reflected ray.

Calculations based on this geometry give agreement with the observed cancellations as shown in Fig 2. Calculated lines show a shift from the observed Bragg lines which may be due to the extra phase shift associated with the interaction of the scattered electron wave with the atomic potential relative to the direct wave. [3,4]

Simulation of diffraction patterns is complicated by the need to include multiple scattering. Two approaches recommend themselves; the multiple scattering processes of low energy electrons represented by the program “mscd” [1] and the Kikuchi band calculations [2] derived from high energy electron scattering with the inclusion of multiple forward scattering.

In the first simulation the intensities of the forward scattering Kikuchi bands are similar to the observations. The formation of circles around the low index directions show that the calculation gives more significant interference along the atom chains than is observed. It is not clear whether the limited cluster size or shifts in the outer layers of the crystal is the cause. However it is likely that the limited cluster size reduces the resolution of the Bragg cancellations in this calculation.

Fig 4 shows the Kikuchi band calculation in which an infinite crystal is assumed. In this case the Bragg cancellations are reproduced rather well. The forward scattering along the principle planes still dominates but the calculated intensities differ from those observed. Each calculation has inbuilt limitations but attempts are being made to improve both.

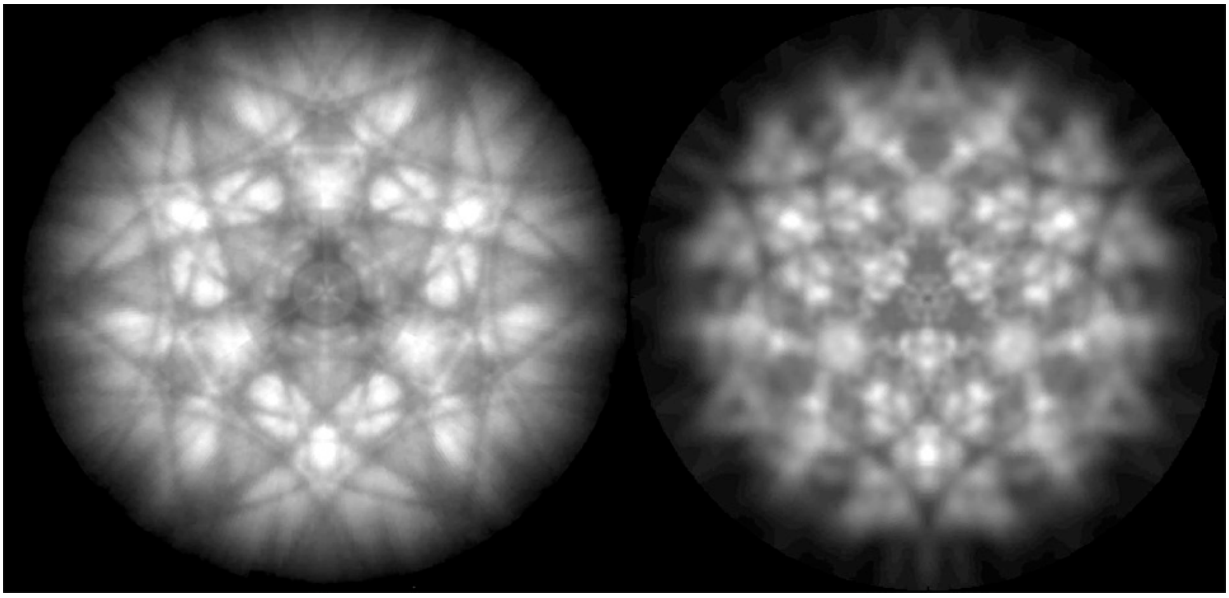

Fig 3 Experimental result and the theoretical diffraction pattern calculated using "mscd" with a cluster size of 10x10x10 atoms.

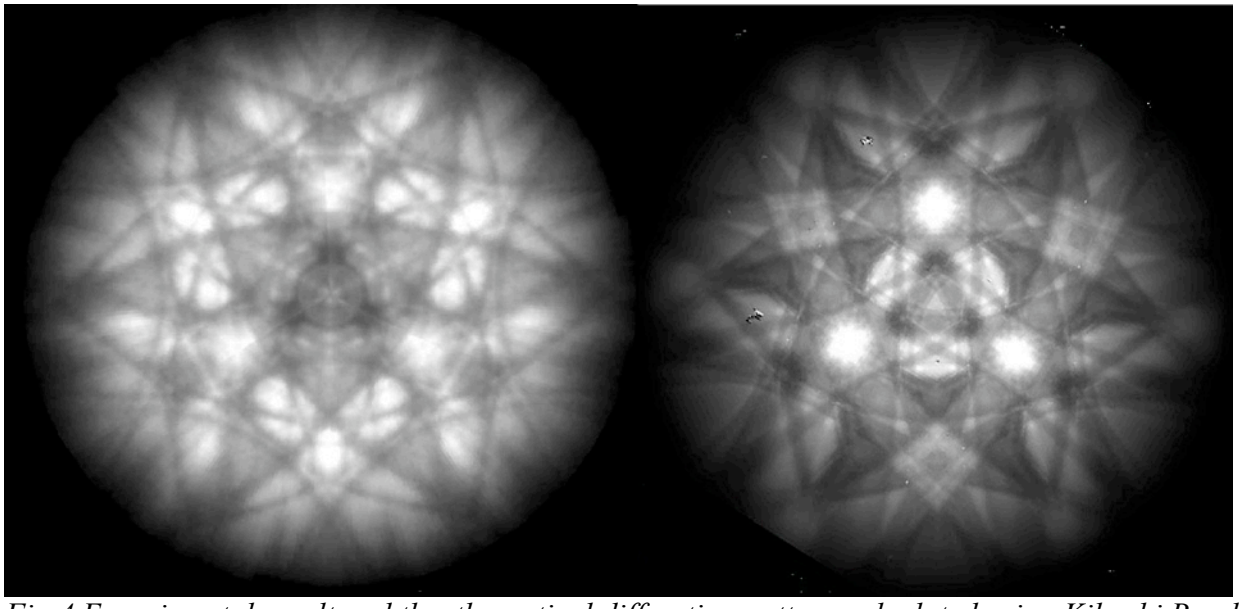

Fig 4 Experimental result and the theoretical diffraction pattern calculated using Kikuchi Band theory.

[1] F. J. Garcı´a de Abajo, M. A. Van Hove, C. S. Fadley. Phys. Rev. B, **63**, 075404 (2001)
[2] A. Winkelmann *et al*. Phys. Rev. B **69**, 245417 (2004)
[3] S. Omori *et al*. Jap.J Appl. Phys. **37**, 4076 (1998)
[4] Y. Ichinohe *et al*. J. Vac. Sci Technol. A **13**, 1489 (1995)

Observing an unobservable Bragg peak: Resonant soft x-ray diffraction from magnetite thin films

J. Schlappa, C.-F. Chang, C. Schüßler-Langeheine, H. Ott, and L. H. Tjeng
II. Physikalisches Institut der Universität zu Köln, Zülpicher Str. 77, 50937 Köln
E. Schierle, E. Weschke, and G. Kaindl
Institut für Experimentalphysik. Freie Universität Berlin, Arnimallee 14, 14195 Berlin

Funded by the DFG through SFB 608, TP C4.

Magnetite (Fe_3O_4) is one of the longest known magnetic materials, whose properties have been described already around 800 B.C. by Greek writers. Magnetite crystallizes in the inverse spinel structure (Fig. 1) with Fe^{3+} ions on tetrahedrally coordinated A sites (yellow balls in Fig. 1) and Fe ions with a formal oxidation state 2.5+ (red balls) on octahedrally coordinated B sites. The room temperature conductivity of magnetite is explained by the hopping of electrons along the linear rows of B-site Fe ions (sticks in Fig. 1). Verwey noticed in 1939 that when cooled below ≈120 K the resistivity of magnetite increases in a sharp first-order transition by two orders of magnitude and that the structure distorts from cubic symmetry [1]; he explained the transition by a formation of a charge-ordered arrangement of 2+ and 3+ ions on B sites, which hinders the electron hopping. Despite continuos experimental and theoretical efforts since then, the details of the low temperature phase are still a puzzle [2]: not only the character of the charge-ordered phase is unclear, but some results question the existence of charge order all together. A very recent resonant diffraction study at the Fe *K*-edge in the conventional x-ray range found no difference in the resonant behavior between fundamental Bragg peaks and those superstructure peaks with wave vector **q** = (001) and **q** = (00½), which appear below the Verwey transition and were assigned to the formation of charge order [3]. From this result it was concluded that a charge modulation on B-sites, if it exists, has to be smaller than the detection limit for *K*-edge resonant diffraction, which is 0.1 electron charges. This detection limit is determined by the character of the intermediate states involved in the resonance process, which at the Fe *K* edge are predominantly the Fe 4*p* states; they are forming bands and are hence sensitive to the lattice symmetry rather than to the 3*d* occupation, which is, however, the quantity of interest that should vary from site to site.

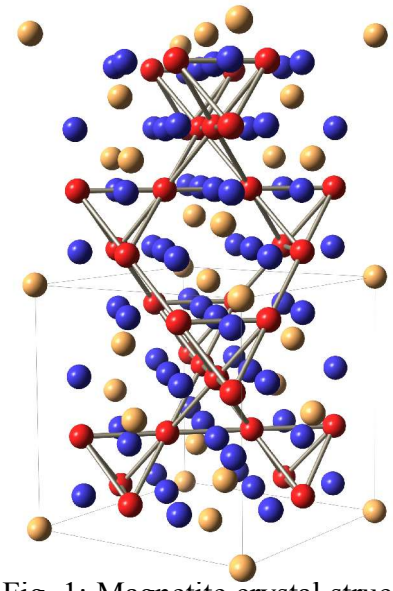

Fig. 1: Magnetite crystal structure: Oxygen ions are marked in blue, A-site Fe ions in yellow, and B-site Fe ions in red. Shown is the unit cell doubled along the c-axis.

Resonant diffraction at the Fe $L_{2,3}$ resonance in the soft x-ray range, on the other hand, is probing the 3*d* occupation directly and turns out to be very sensitive to even small variations of the oxidation state [4]. One major limitation of the technique is the rather long photon wavelength (λ) at resonance, which limits the accessible **q**-space. At the Fe L_3 resonance at 710 eV, λ is 17.5 Å. From the Bragg equation, $2d \sin\Theta = n\lambda$, one sees that the shortest possible periodicity, *d*, can be probed in backscattering geometry (incidence angle $\Theta = 90°$) and amounts to $\lambda/2$ = 8.73 Å. This is

unfortunately still longer than the magnetite unit cell extension of 8.396 Å, which corresponds to the (001) reflection, making this peak apparently unobservable.

We now found a way to observe this peak by studying a 40-nm thin film of magnetite grown on MgO. Bragg peaks in thin films are broadened in reciprocal space along the surface normal, which leads to some intensity in that part of momentum space that can be accessed at the Fe resonance. In Fig. 2 we present a scan along the [001] (L) direction taken at 708.5 eV, showing the superstructure peak at (00½) and a rise of intensity towards (001). The vertical line denotes the maximum possible momentum transfer, which is about 0.96 r.l.u.; the red line shows the result of a simulation consisting of the Fresnel-reflectivity, which causes the rise towards smaller L-values, and both superstructure peaks, which are assumed to have the same line shape. From the agreement between experimental data and the simulation it is clear that the intensity we observe at high L values is indeed coming from the (001) Bragg peak.

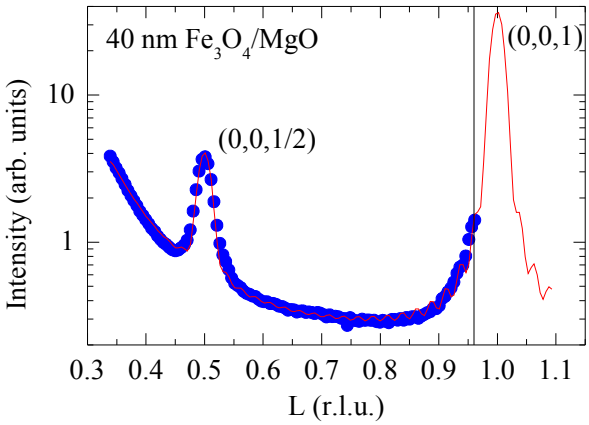

Fig. 2: Scan along the [001] (L) direction in reciprocal space using 708.5-eV photons (blue dots). The vertical line denotes the maximum possible momentum transfer at this energy, the red line is the result of a simulation as described in the text.

We are now able to perform spectroscopy on both superstructure peaks and do find a significant difference in the resonance between them. Furthermore both peak resonances differ strongly from the x-ray absorption (XAS) signal (Fig. 3). Using the same powerful microscopic modeling of the superstructure resonances as we used for the case of $La_{1.8}Sr_{0.2}NiO_4$ [4], we expect to obtain a comprehensive understanding of the character of the observed superstructures, which has been missing since more than 60 years.

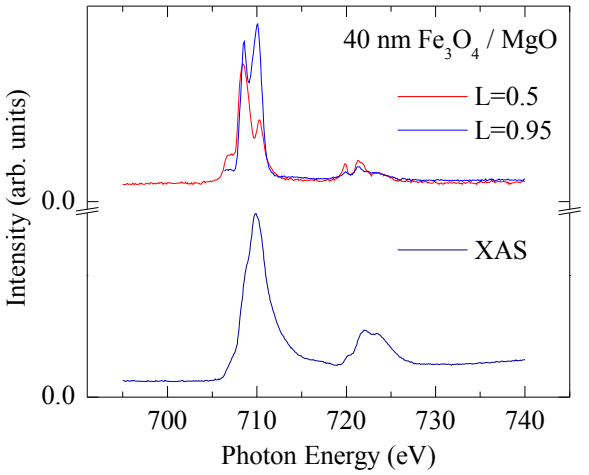

Fig. 3: Resonant behavior of the diffraction signal at L = 0.5, at L = 0.95, and of the XAS signal.

Experiments were carried out at U49/2-PGM1 and UE52-SGM; we gratefully acknowledge the experimental support from the BESSY staff and the excellent working conditions there.

[1] E. J. M. Verwey, Nature **144**, 327 (1939).
[2] For a review see: F. Walz, J. Phys. Condens. Matter **14**, R285 (2002).
[3] G. Subias et al., Phys. Rev. Lett. **93**, 156408 (2004).
[4] J. Schlappa et al., "Spectroscopy from stripe order in $La_{1.8}Sr_{0.2}NiO_4$" in this volume.

Spectroscopy from stripe order in $La_{1.8}Sr_{0.2}NiO_4$

J. Schlappa, C. Schüßler-Langeheine, Z. Hu, C.-F. Chang, M. Benomar, H. Ott, O. Friedt, M. Braden, and L. H. Tjeng

II. Physikalisches Institut der Universität zu Köln, Zülpicher Str. 77, 50937 Köln

E. Schierle, G. Kaindl, and E. Weschke

Institut für Experimentalphysik, Freie Universität Berlin, Arnimallee 14, 14195 Berlin

A. Tanaka

Department of Quantum Matter, ADSM, Hiroshima University, Higashi-Hiroshima 739-8530, Japan

Hole-doped La_2NiO_4 is the first system where a stripe-like superstructure, assigned to charge ordering, was observed by scattering techniques [1, 2]. From the appearance of superstructure peaks in the diffraction pattern it was concluded that hole-rich stripes form antiphase domain walls for the antiferromagnetic order on the Ni^{2+}sites. Since the standard neutron and x-ray scattering techniques are not directly sensitive to charge, and therefore cannot reveal the electronic structure behind the superstructure formation, the physics of the phenomenon has remained unclear so far; in particular the local symmetry of the doped holes has been a puzzle. Here we used the novel technique of resonant diffraction in the soft x-ray range at the Ni $L_{2,3}$ and La $M_{4,5}$ thresholds, which probes superstructures with a very high sensitivity to the electronic state [3].

We carried out resonant diffraction experiments at the spin-order and charge-order superstructure peaks. We observed a pronounced photon-energy and polarization dependence of the intensities, which allows us to critically determine the local symmetry of the ordered spin and charge carriers. Furthermore we performed microscopic modelling calculations of the system that confirms the results of our data.

A single crystal of $La_{1.8}Sr_{0.2}NiO_4$ was grown by a traveling solvent method in the laboratory in Cologne and characterized by neutron diffraction at the Orphée reactor. The sample was cut and polished with a (103) surface orientation and mounted with the [100] and [001] directions in the diffraction plane. The x-ray scattering experiment was performed at U49/2-PGM and UE52-SGM using the UHV soft x-ray diffractometer built by Eugen Weschke and coworkers. The incoming light was linearly polarized either parallel (π polarization) or perpendicular (σ polarization) to the scattering plane.

The position of the superstructure peaks in reciprocal space depends on the doping level and is described by an incommensurability parameter ε. For our sample the charge order peak is located at $(2\varepsilon,0,1)$ and the spin order peak at $(1-\varepsilon,0,0)$, with $\varepsilon = 0.278$. The energy dependence of the superstructure intensities across the La $M_{4,5}$ and Ni $L_{2,3}$ edges for the two different polarizations is displayed in Fig. 1. For both superstructure peaks the intensity shows a resonant enhancement in the vicinity of the Ni L_3 white line (851.6 eV), which is in striking contrast to the shape of the XAS data (Fig. 1c), which is dominated by the La M_4 and M_5 resonances at 849.2 and 833 eV.

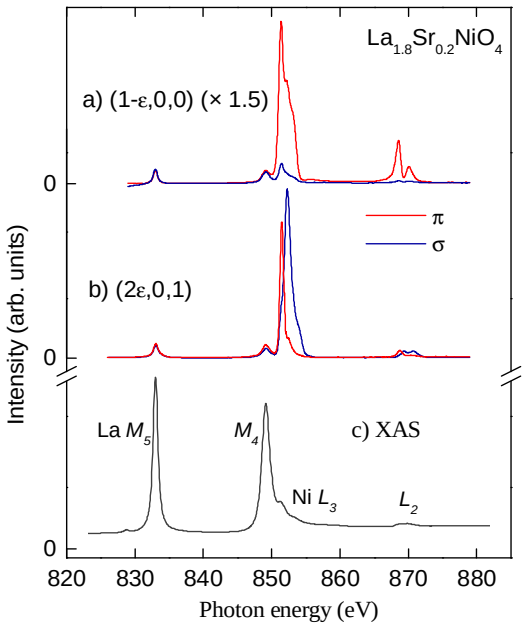

Fig. 1: Intensities of the a) spin-order and b) charge order superstructures at 60 K. c) x-ray absorption signal

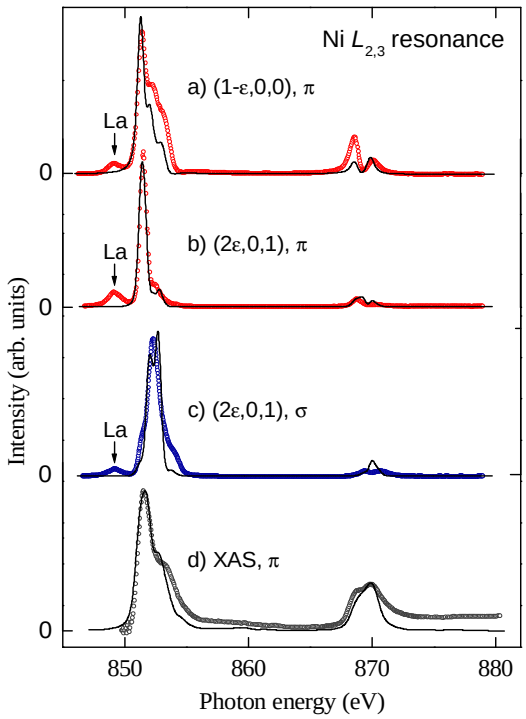

Fig. 2: Comparison between measured data (symbols) and the cluster calculation (solid line). a) spin order b), c) charge order d) x-ray absorption signal. The La M_4 peaks, marked by arrows, are not included in the simulation.

This strong enhancement at the Ni resonance shows directly that both orders, spin and charge, reside mainly within the NiO_2 layers.

Both superstructures show a dramatic polarization dependence. For the spin order peak the signal for σ polarization is about 10 times weaker than that for π polarization. In the resonance of the charge order peak there is a shift of 1 eV towards higher energies for σ-polarized light in respect to π polarization at the L_3 and L_2 edges, while the intensity is almost the same. From the weakness of the spin order signal observed with σ-polarized light, where in our scattering geometry the electric field of the incoming beam is parallel to the charge stripes, one can conclude that the Ni spins are essentially (but not perfectly) collinear with the stripes.

While some qualitative information can be obtained from the spectra directly, the full power of the technique is developed in combination with a realistic microscopic modelling. We performed cluster configuration interaction calculations assuming diagonal stripes of hole-rich Ni sites in a Ni^{2+} background. This model reproduces correctly the diffraction signals, as well as the Ni contribution to the XAS signal (which was determined by substracting out the La contribution as obtained from $LaTiO_3$: Fig. 2d).

As can be infered from Fig. 2, also the polarization effects are well reproduced by the model. The agreement for π-polarized data is particularly good for all spectra. For σ polarization the agreement is less accurate, but the model reproduces correctly the polarization-dependent 1 eV energy shift in the charge-order resonance.

The model calculations turned out to be very sensitive to the choice of parameters. The good agreement with the experimental data was obtained by the assumption that the doped holes at the Ni^{3+} sites reside mainly at the surrounding in-plane oxygen ions in a molecular orbital with $x^2 - y^2$ symmetry, and that the hole spin couples antiferromagnetically with the Ni spin. The 3*d* electron number at the Ni^{3+} ions is as high as 7.9, which is surprisingly not much smaller than the value of 8.2 for the Ni^{2+} sites. This scenario is analogous to the Zhang-Rice singlet state in cuprates [4] and is further supported by the observed polarisation dependence of the charge order resonance: The 1-eV shift indicates a large energy splitting of the unoccupied Ni $x^2 - y^2$ and $3z^2 - r^2$ levels, since the transition probability into the $x^2 - y^2$ level for σ polarization is much higher than into the $3z^2 - r^2$ level. With such a strong level splitting, the doped holes can be considered to be well confined within the in-plane oxygens and the system posseses strong two-dimensionality like cuprates.

We gratefully acknowledge the experimental support from the BESSY staff and the excellent working conditions there.
This work has been supported by the DFG through SFB 608 TPC4.

[1] C. H. Chen, S.-W. Cheong, and A. S. Cooper, Phys. Rev. Lett. 71, 2461 (1993).
[2] J. M. Tranquada, J. D. Buttrey, V. Sachan ,and J. E. Lorenzo, Phys. Rev. Lett. 73, 1003 (1994).
[3] C. Schüßler-Langeheine et al., Bessy Highlights 2003, 16 (2004)
[4] F. C. Zhang and T. M. Rice, Phys. Rev. B 37, 3759 (1988).

Photoemission of isolated V adatoms on alkali surfaces

M. Veronese[1], P. Moras[1], P. Gambardella[2], H. Brune[2], O. Rader[3]

A. Varykhalov[3], A. Vollmer[3], S. Gardonio[1], C. Carbone[1]

[1] CNR Trieste , [2] EPFL Lausanne, [3] BESSY

Alkali metals, with their simple electronic structure, are considered to be ideal hosts for studying the interaction between localized *d* states and a free-electron Fermi gas. It is known that 3*d* metal impurities dissolved in alkali metals possess surprisingly large magnetic moments, which have been attributed to the survival of localized *d*-orbitals at the impurity sites with correspondingly large, atomic-like magnetic moments given by Hund's rules. The case of V, however, seems to be different, since a total magnetic moment of 7 μ_B has been reported for V impurities on the surface of K and Na [1], which cannot be reconciled with a simple atomic picture of the V electronic states. We have performed a photoemission spectroscopy experiment to investigate the electronic structure of V impurities on K films. One of the experimental goals was also to assess the capability of photoemission to provide information on diluted surface impurities, and to establish under which conditions the best sensitivity could be achieved. To this purpose, photoemission measurements have been performed in different photon energy regimes at beamlines UE52-SGM and UE56/1-PGM. Resonant photoemission and Auger spectra have been acquired at the V 2p→3d threshold, and direct photoemission data were obtained at lower photon energy (50 - 120 eV). Resonant photoemission from the V states and the related Auger spectral feauture could be observed clearly for diluted V concentration. However, the most detailed spectral feature could be observed at photon energies below 100 eV (Fig. 1a). The V 3d states of the isolated impurity display two pronounced structures (coverage $\delta \leq 0.03$ monoatomic layers, ML) which evolve into a bandlike lineshape as interactions between the adatoms increase at higher impurity concentration. Also, preliminary data were obtained as a test on Fe on Cu(100), indicating that the interaction with a substrate of high sp-electron density effectively quenches the fine spectral structure characteristic of atomic-like states (Fig. 1b). The data display more details and a few features contrasting with respect to the Fe on Cu(111) case, which has been recently studied a with laboratory light source [2]. These results demonstrate that photoemission is capable of providing detailed information on highly diluted impurity systems, to a degree that appears to have been largely underestimated until now, and that can be efficiently exploited with intense synchrotron sources.

[1] F. Song and G. Bergmann, Phys. Rev. Lett. 88, 167202 (2002)

[2] T. Susaki et al., Phys. Rev. Lett. 88, 187602 (2002)

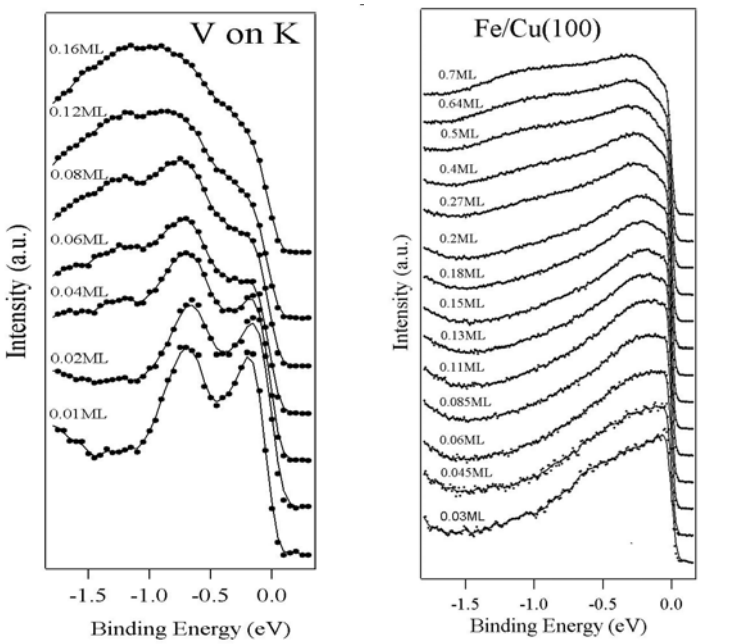

Fig. 1 (a) (left) Photoemission spectra measured with 90 eV photon energy from V impurities deposited on a K film. (b) (right) Photoemission spectra measured at 70 eV photon energy from Fe impurities and higher coverages deposited on Cu(100). All of the depositions and measurements were performed at 15 K in order to suppress adatom surface diffusion and clustering.

Determination of the magnetization depth profile of Fe on V(110) by combining X-Ray Magnetic Circular Dichroism with X-Ray Resonant Magnetic Reflectometry

D. Schmitz, P. Imperia, H. Maletta
Hahn-Meitner-Institut Berlin, Glienicker Str. 100, 14109 Berlin

U. Grüner, M. Harlander, S. Macke, E. Goering
MPI für Metallforschung, Heisenbergstr. 3, 70569 Stuttgart

The magnetization depth profile of ultrathin Fe on a V(110) single crystal has been studied by combining X-Ray Magnetic Circular Dichroism (XMCD) with X-Ray Resonant Magnetic Reflectance (XRMR) measurements at the $L_{2,3}$ absorption edges of Fe and V using two different approaches. In the first approach the average magnetic Fe moment per atom was determined with XMCD measurements as a function of the Fe film thickness. In this way we achieved that the measured average magnetic moments are consistent with a reduced Fe moment at the interface to V and an enhanced Fe moment at the surface [1].
In the second approach [2] we intend to determine the magnetization depth profile from specular reflectance measurements as a function of the angle of incidence. For this purpose our spectroscopy chamber was operated as a reflectometer. The samples were magnetized to remanence and the magnetic signal was measured reversing the helicity of the incoming elliptically polarized radiation. The magnetic measurements were performed in resonance, *i.e.*, the photon energy was tuned to the L_3 absorption edges of Fe and V in order to utilize that the magnetic cross section is resonantly enhanced by orders of magnitude near an absorption threshold [3].
The helicity-averaged reflectances and asymmetries measured at the Fe L_3 edge for Fe/V and V/Fe/V are shown as dashed lines in Fig. 1a-b and Fig. 1c-d, respectively, as a function of the momentum transfer along the surface normal. The measurements were performed in a momentum transfer range from 0 $Å^{-1}$ to 0.7 $Å^{-1}$ which corresponds to a grazing incidence angle range from 0° to 80°. The reflectances contain the information about the chemical and the asymmetries about the magnetic depth profile.
In order to determine the magnetization depth profile the measured asymmetry has to be compared with a simulated asymmetry. The simulation was performed with a computer program [4] which is based on the kinematic approximation and the Parratt algorithm. The program takes into account the non-magnetic and magnetic contributions to the index of refraction and the elliptical polarization of the radiation. Moreover, it is possible to vary the magnetization at interfaces by convoluting the chemical depth profile with a Gaussian for the magnetic part. Since the magnetic reflection measurements were performed with resonant excitation at the L_3 absorption edge, the index of refraction of the corresponding material could not be taken from tables. Instead, the imaginary part of the index of refraction of the same samples which were measured in reflection was determined by XMCD measurements, and the real part of the index of refraction was determined by Kramers-Kronig transformation.
The simulated asymmetries are shown in Fig. 1 as solid lines. For all simulated curves the thicknesses and roughnesses determined from the isotropic reflectance measurement were used and kept constant. For each sample two simulated asymmetries are shown: one for homogeneous Fe magnetization (red lines) and one for modified Fe magnetization at both interfaces (green lines). For Fe/V (Fig. 1c) the assumption of a homogeneous Fe magnetization results in a simulated asymmetry (red line) which does not agree with the measurement, *i.e.*, the peak at 0.5 $Å^{-1}$ is too high in momentum transfer as compared with the measurement. This peak moves to lower momentum transfer if the Fe magnetization at the interface to V and at the surface is reduced in the simulation. Therefore one can conclude that the information about the Fe magnetization at the interfaces is contained in the peak at a momentum transfer of 0.4 $Å^{-1}$. Another Fe film which was covered as fast as possible with V

was also measured in reflection after covering with V. The resulting asymmetry is shown in Fig. 1d. Also for this sample the measured asymmetry is described better if the Fe magnetization is modified at the interfaces.

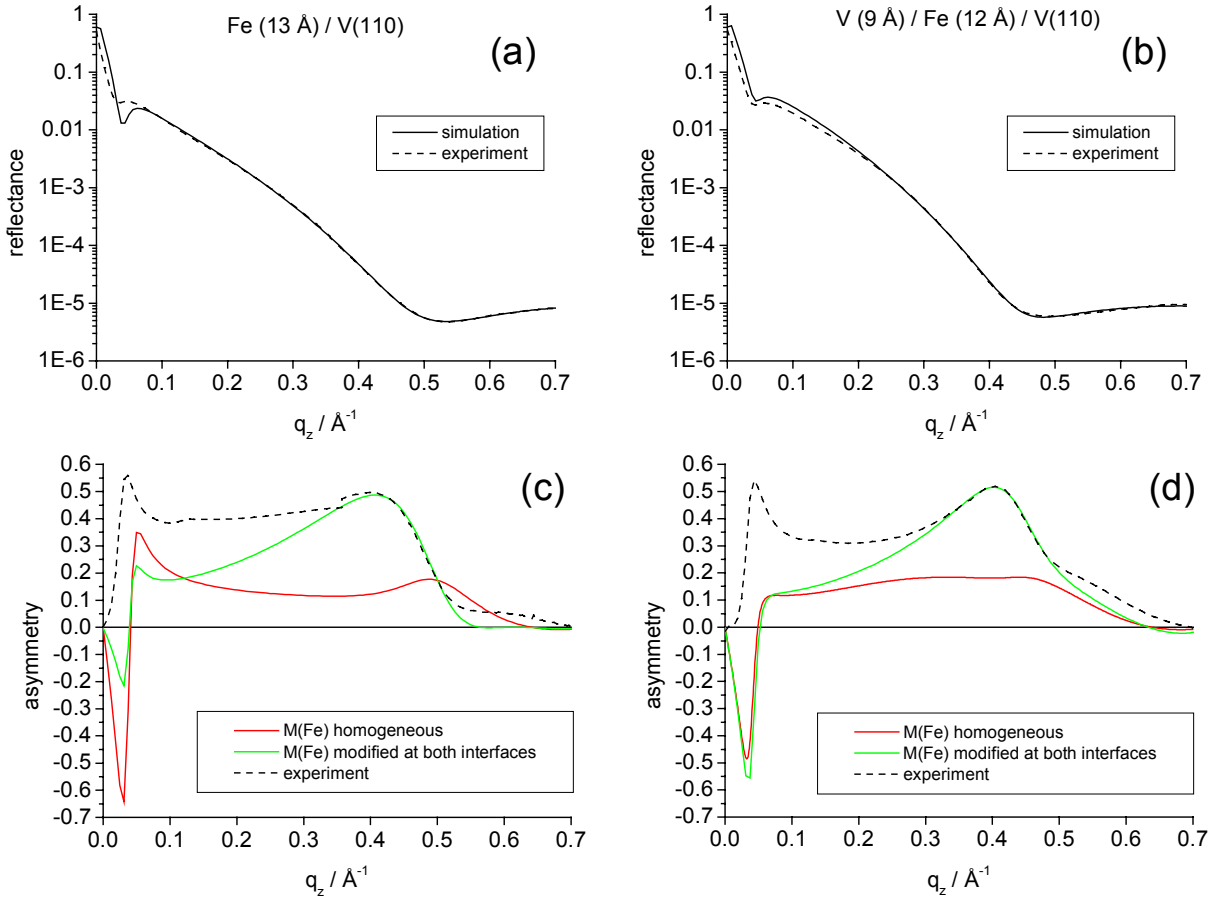

Fig.1: Measured (dashed lines) and simulated (solid lines) reflectances and asymmetries for Fe/V (a, c) and V/Fe/V (b, d) as a function of the momentum transfer along the surface normal. The photon energy was tuned to the L_3 absorption edge of Fe.

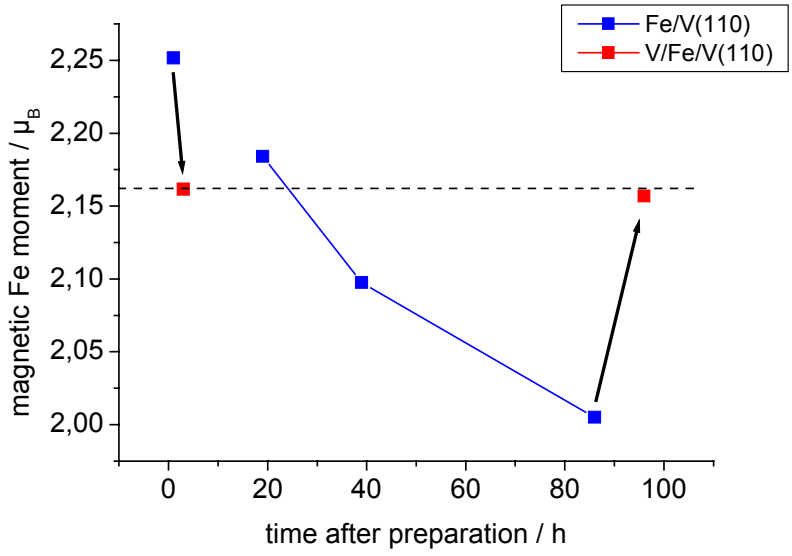

Fig.2: Average magnetic Fe moment per atom before (blue squares) and after (red squares) covering the Fe film with V.

The finding that the Fe magnetization is reduced also at the surface of the uncovered Fe film is consistent with the observation measured with XMCD that the average magnetization decreased as a function of time due to oxidation (blue squares in Fig. 2). Indeed, the peak at 0.4 $Å^{-1}$ in Fig. 1a was measured about 80 hours after preparation.
In addition we studied the change of the Fe magnetization when covering the Fe film with V as shown by the red squares in Fig. 2. One can distinguish two cases. In the first case the uncovered Fe film was measured as fast as possible after the Fe deposition and then directly covered with V. Under these conditions the experimental value of the Fe moment indeed decreased because the enhanced Fe surface moment [5] was replaced by a reduced Fe moment at the interface to the V top layer [6]. In the second case the uncovered Fe film was measured for 90 hours before covering it with V. During this time the Fe moment decreased due to the starting oxidation of the surface. Covering then with V results in an increase of the Fe moment due to an increase of the number of Fe 3d holes as indicated by an increase of the area under the isotropic spectrum. In other words, there is a charge transfer from Fe to V which in the presence of oxygen causes an increase of the Fe moment.
A remaining problem is the negative asymmetry of the simulation below 0.05 $Å^{-1}$. This may be due to the breakdown of the kinematical single-scattering approximation at small grazing incidence angles where the reflectance is large. Therefore further development and tests are under way in order to be able to quantify the magnetization depth profile for Fe/V and V/Fe/V in the near future.

We would like to thank S. Rudorff and S. Miemietz for technical support.

[1] D. Schmitz, J. Hauschild, P. Imperia, Y.T. Liu, H. Maletta, J. Magn. Magn. Mater. 269/1, 89 (2003)
[2] J. Geissler, E. Goering, M. Justen, F. Weigand, G. Schütz, J. Langer, D. Schmitz, H. Maletta, R. Mattheis, Phys. Rev. B 65, 020405(R) (2001)
[3] M. Blume, J. Appl. Phys. 57, 3615 (1985); D. Gibbs, D.R. Harshman, E.D. Isaacs, D.B. McWhan, D. Mills, C. Vettier, Phys. Rev. Lett. 61, 1241 (1988); E.D. Isaacs, D.B. McWhan, C. Peters, G.E. Ice, D.P. Siddons, J.B. Hastings, C. Vettier, O. Vogt, Phys. Rev. Lett. 62, 1672 (1989)
[4] E. Goering, J. Geissler, S. Gold, G. Schütz, D. Schmitz, H. Maletta, submitted
[5] R. Wu, A.J. Freeman, Phys. Rev. Lett. 73, 1994 (1994)
[6] J. Izquierdo, R. Robles, A. Vega, M. Talanana, C. Demangeat, Phys. Rev. B 64, 060404 (2001)

Photoemission study of Ag and Au oxide films formed by microwave-excited oxygen

A.I. Boronin[1], S.V. Koscheev[1], A.I. Stadnichenko[1], M.V. Poyguin[2], D.V. Vyalikh[3], S.L. Molodtsov[3]

[1] – Boreskov Institute of Catalysis SB RAS, Novosibirsk 630090, Russia
[2] – Institut für Experimentalphysik, FU Berlin, D-14195 Berlin-Dahlem, Germany
[3] – Institut für Festkörperphysik, TU Dresden, D-01062 Dresden, Germany

The interaction of oxygen with metal surfaces has both fundamental and applied industrial aspects. Silver is of particular interest because of the unique catalytic ability to oxidize selectively some organic molecules. In catalysis, the reaction pathways are largely determined by surface oxygen species [1]. The catalytic process occurs under real conditions when high pressure of the reaction media is used. Therefore, the oxygen states on the silver surface undergo some transformation beginning from the formation of the physisorbed and chemisorbed molecular states. Then, at the increasing temperature, there is the dissociation process resulting in the surface atomic oxygen, which is an intermediate to form some oxidized silver phases. In contrast to the O_2 adsorption mechanisms on the metallic silver surfaces, the mechanism of the following deep silver oxidation has not yet been investigated in detail.

Recently we assumed that as the surface and subsurface region are saturated with oxygen, the Ag-O bonds become weaker and oxygen atoms are stimulated to associate into stable quasimolecular species (species characterized by O-O bonding) [2,3] located inside the surface (and subsurface) lattice space like vacancies or empty sites on the silver defects [2]. It was proposed that such oxygen species could be responsible for the selective oxidation of some organic molecules.

In order to check this idea it was necessary to carry out the oxidation silver surface in the vacuum chambers of electron spectrometer immediately. However, because of thermodynamic reasons, the oxidation requires the high-pressure conditions of O_2 treatment at elevated temperatures to increase the rate of oxidation.

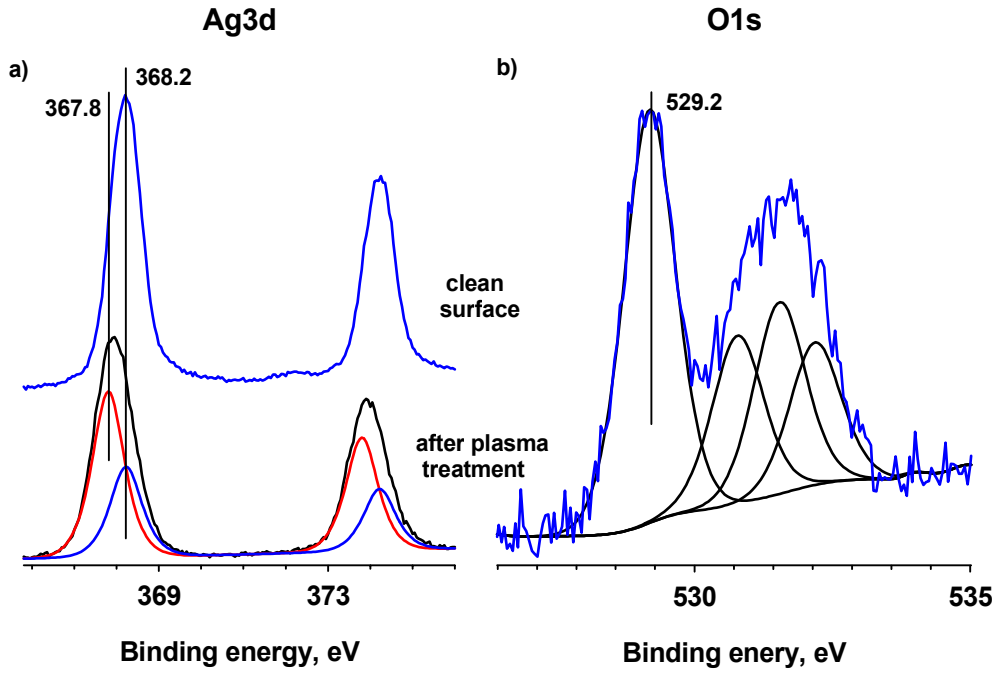

Fig. 1. Ag3d (a) and O1s (b) spectra recorded before (Ag3d) and after the plasma treatment of silver foil during 5 minutes.

This effect imposes a substantial limitation regarding the UHV equipment. To solve this problem, the silver surface was subjected by microwave O_2 discharge at moderate conditions (T = 300 K, P(O_2) ~ 10-30 Pa). Such oxygen treatment provides a strong oxidation of silver surface at low temperatures [3,4].

The spectra were recorded at the Russian-German beamline with a photoemission spectrometer operating with CLAM4 (Thermo VG Scientific) analyzer. The base pressure in the analyzer chamber was less than $5*10^{-10}$ mbar. O1s and Ag3d spectra were recorded at 650 eV photon energy that provided a good surface sensitivity. The valence band spectra were obtained with 100 eV photon energy at the take-off-angle close at right angle to the sample plane.

In Figure 1 Ag3d and O1s spectra obtained after the plasma treatment are presented. Fig. 1(b) shows that O1s spectrum consists of two main peaks, namely peak at 529.2 eV and broad peak around 532 eV. Peak with E_b = 529.2 eV can be reliably attributed to the silver oxide Ag_2O [3-5]. It is also confirmed by the appearance of a new component with $E_b(Ag3d_{5/2})$ = 367.8 eV in Ag3d spectrum after plasma treatment. This peak corresponds to Ag(1+), while the state of metallic silver is characterized by $E_b(Ag3d_{5/2})$ = 368.2 eV [6]. O1s peak at the application of curve fitting analysis shows that broad peak around 532 eV is decomposed on three peaks with $E_b(Ag3d_{5/2})$ = 530.8 eV, 531.6 and 532.2 eV, respectively. These peaks can not be attributed to oxygen states located within the silver oxide lattice like AgO because O1s line position of AgO oxide is equal to ~ 528-529 eV [7-9].

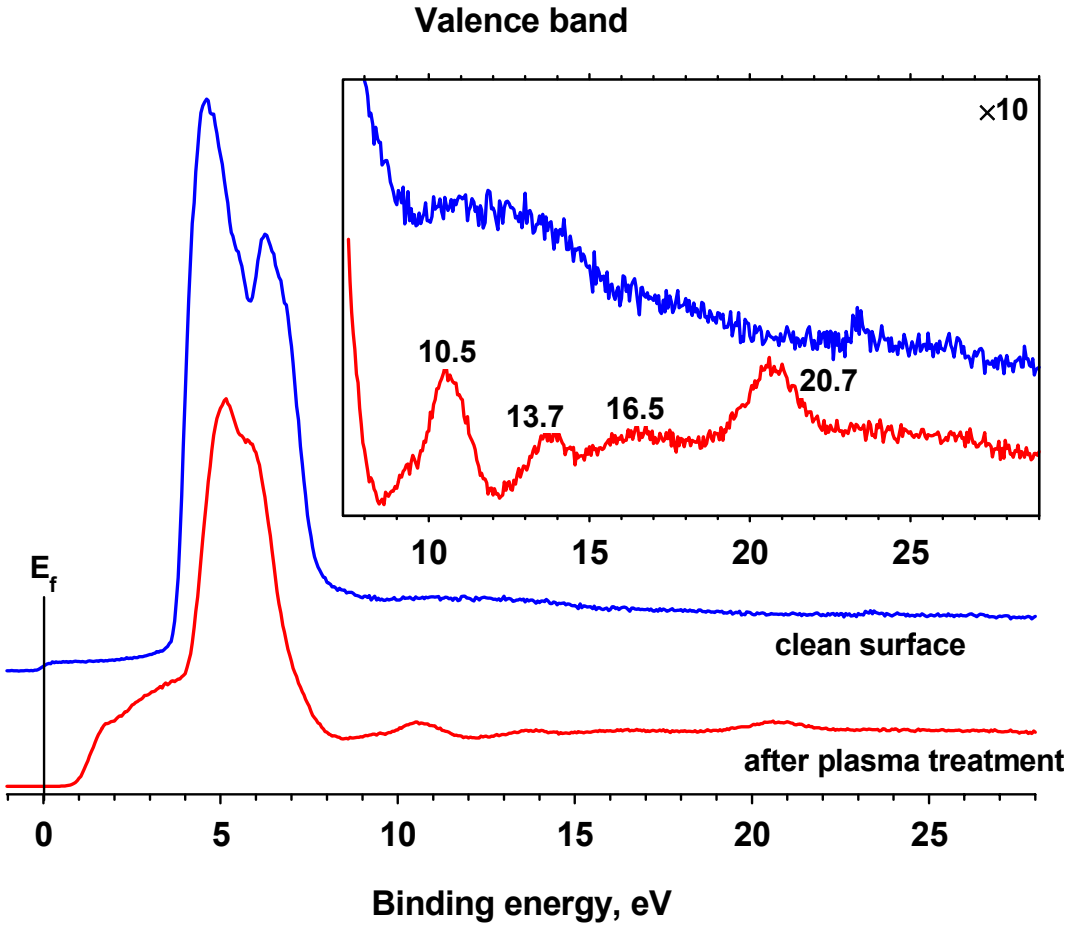

Fig. 2. VB photoemission spectra recorded before and after the plasma treatment of silver foil during 5 minutes.

Based on our previous papers we propose that the oxidation process is accompanied by the defect surface formation, so an additional oxygen species can be formed. In order to

understand the nature of these oxygen species observed in O1s spectra the investigation of the valence band before and after the oxygen plasma treatment has been carried out.

In Figure 2, the photoemission spectra of the valence band of silver surface before and after O_2 plasma treatment are presented. This figure shows that plasma treatment results in a strong redistribution of Density of States in the valence band. The redistribution is mainly bound with 5sp and 4d bands. The narrowing of 4d band (region 4-8 eV) and the appearance of a new band between 4d band and Fermi level (region 1-4 eV) implies definitely the formation of the oxidized silver surface [3,5]. Apparently, the valence band redistribution corresponds to the observation of O1s peak with E_b = 529.2 eV. Thus, the data of Fig.2 are in a good accord with the results obtained from the core level spectra.

Concerning other peaks with high binding energies in O1s spectra there is a set of the valence band features in the E_b range 8-23 eV. Four peaks are clearly seen in this energy range after the intensity scale magnification. Peak with E_b = 20.7 eV belongs to O2s level of atomic oxygen in the silver oxide phase. Other features can not be attributed to the silver oxide phase. These three features is a reliable evidence for the O-O bond formation [2,3].

We propose that the formation of O-O bonds takes place due to the existence of some special or defect sites within the interface metal-oxide layer stabilizing such quasimolecular oxygen species. Quasimolecularity of the observed oxygen species implies its electrophilic properties, that is, the charge on an oxygen atom is not high and bond Ag-O is covalent and weakly polarized. The revealed quasimolecular oxygen species is proposed to play an important role since the oxygen states, which are active in the selective catalysis, is known to have electrophilic properties.

References

[1] R.A. van Santen and H.P.C.E. Kuipers, Adv. Catal. **35** (1987) 265.

[2] V.I. Avdeev, A.I. Boronin, S.V.Koscheev, G.M. Zhidomirov. J. Molec. Catal. A: Chemical 154 (2000) 257.

[3] A.I. Boronin, S. V. Koscheev, K. T Murzakhmetov, V. I. Avdeev, G.M. Zhidomirov, App. Surface Science 165 (2000) 9.

[4] M. Bowker, Surf. Sci. **155** (1983) L276.

[5] L.H. Tjeng, M.B.J. Meinders, J. Vanelp, J. Ghijsen, G.A. Sawatzky, R.L. Johnson, Phys. Rev. **B 41** (1990) 3190.

[6] Moulder J.F., Stickle W.F., Sobol P.E., Bomben K.D., Handbook of X-Ray Photoelectron Spectroscopy. - Perkin - Elmer, Eden Prairie, MN, 1992.

[7] G. Schon, Acta Chem. Scand. **27**, 2623 (1973).

[8] J.S. Hammond, S.W. Gaarestroom, and N. Winograd, Anal. Chem. **47**, 2193 (1975).

[9] M. Bielmann, P. Schwaller, P. Ruffieux, O. Groning, L. Schlapbach and P. Groning. Phys. Rev. B, **65**, (2002) 235431.

Valence electron photoemission in ThO_2 and UO_2 near the Th(U) 5d→5f resonant excitation

Yu.A.Teterin[1], I.O.Utkin[1], A.Yu.Teterin[1], T.Reich[2], F.U.Hillebrecht[3], S.L.Molodtsov[4], A.Yu.Varykhalov[5], and W.Gudat[5]

[1] *Russian Research Centre "Kurchatov Institute", 1,Kurchatov sq. 123182, Moscow, Russia*
[2] *Johannes Gutenberg-Universität Mainz, Institut für Kernchemie, D-55128 Mainz, Germany*
[3] *Institute for Transuranium Elements, P.O.Box 2340, D-76125 Karlsruhe, Germany*
[4] *Technische Universität Dresden, FR Physik, Institut für Festkörperphysik, D-01062 Dresden, Germany*
[5] *BESSY GmbH, D-12489, Berlin, Germany*

An overlap between the partially and completely filled electronic shells of the close actinide (An) and ligand (L) ions in the range of binding energies (BE) from 0 to 50 eV leads to formation of the outer valence molecular orbital (OVMO): 0 - ~15 eV from the An 6p, 6d, 7s, 5f and O 2p atomic orbitals (AOs), and inner valence molecular orbital (IVMO): ~ 15 - 40 eV from the An 6s, 6p and O 2p, 2s Aos, in compounds [1-3]. As a result, x-ray photoelectron spectra (XPS) in the binding energy range 0 – 50 eV exhibit fine complex structure. Interpretation of this structure will enable to understand the role of the An 6p, 5f electrons in the chemical bonding and to establish a correlation of the fine spectral structure parameters with physical and chemical properties of actinide compounds. The present work, which was performed at the Russian-German beamline, examines the electron photoemission from thin films of UO_2 and ThO_2 deposited on metal surfaces, as well as from UO_3 and U_3O_8 embedded in indium on copper substrates under excitation by x-ray radiation close to the Th(U) 5d – 5f excitation threshold (Fig.1). The samples were not extra cleaned in the spectrometer preparation chamber. An oxide like U_3O_{8+x} was formed on the surface of UO_3 sample due to the loss of oxygen in the spectrometer chamber. As a result, a jump of intensity around the resonance energy was observed for all samples (Fig. 2). Earlier [4] for UO_2 single crystals, a similar behavior was observed for the OVMO electrons (0 - ~13 eV BEs). The following excitation-decay processes can describe this spectral structure at the resonance edge to a first approximation:

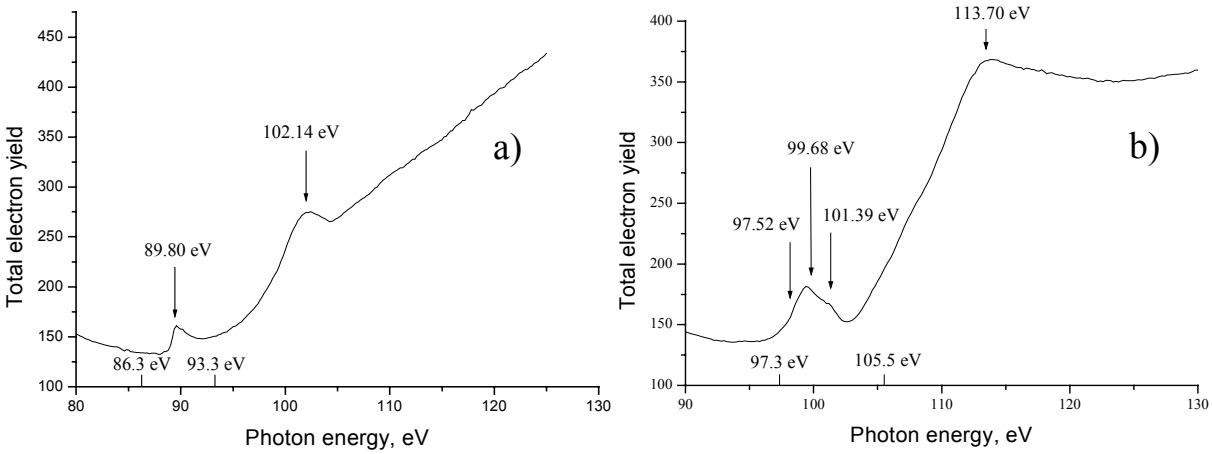

Fig. 1. Total electron yield spectra from: a) ThO_2 on the surface of thorium plate, b) UO_2 on the surface of uranium plate. The spectra were normalized to the photon flux. Electron BEs for ThO_2 a) and UO_2 b) embedded in indium on titanium substrates are given [1-3].

$$An5d^{10}(IVMO)^{k}(OVMO)^{m}5f^{n} + h\nu \rightarrow An5d^{9}(IVMO)^{k}(OVMO)^{m}5f^{n+1}, \quad (1)$$

$$An5d^{9}(IVMO)^{k}(OVMO)^{m}5f^{n+1} + (e^{2}/r) \rightarrow An5d^{10}(IVMO)^{k}(OVMO)^{m}5f^{n-1} + e, \quad (2)$$

$$An5d^{9}(IVMO)^{k}(OVMO)^{m}5f^{n+1} + (e^{2}/r) \rightarrow An5d^{10}(IVMO)^{m-1}5f^{n} + e, \quad (3)$$

$$An5d^{9}(IVMO)^{k}(OVMO)^{m}5f^{n+1} + (e^{2}/r) \rightarrow An5d^{10}(IVMO)^{k-1}(OVMO)^{m}5f^{n} + e. \quad (4)$$

It has to be noted that also direct photoemission takes place together with these processes. However, due to large probability of the autoionization decays (2), (3), and (4) of the intermediate state (1) the resonance spectra to a greater extent reflect the partial An np and An 5f electronic state densities. The observed smearing of the structure in the range ~15 - 40 eV BEs can be explained by the IVMO formation in the studied compounds [1-3]. These results agree with the data for U_3O_8 and UO_3.

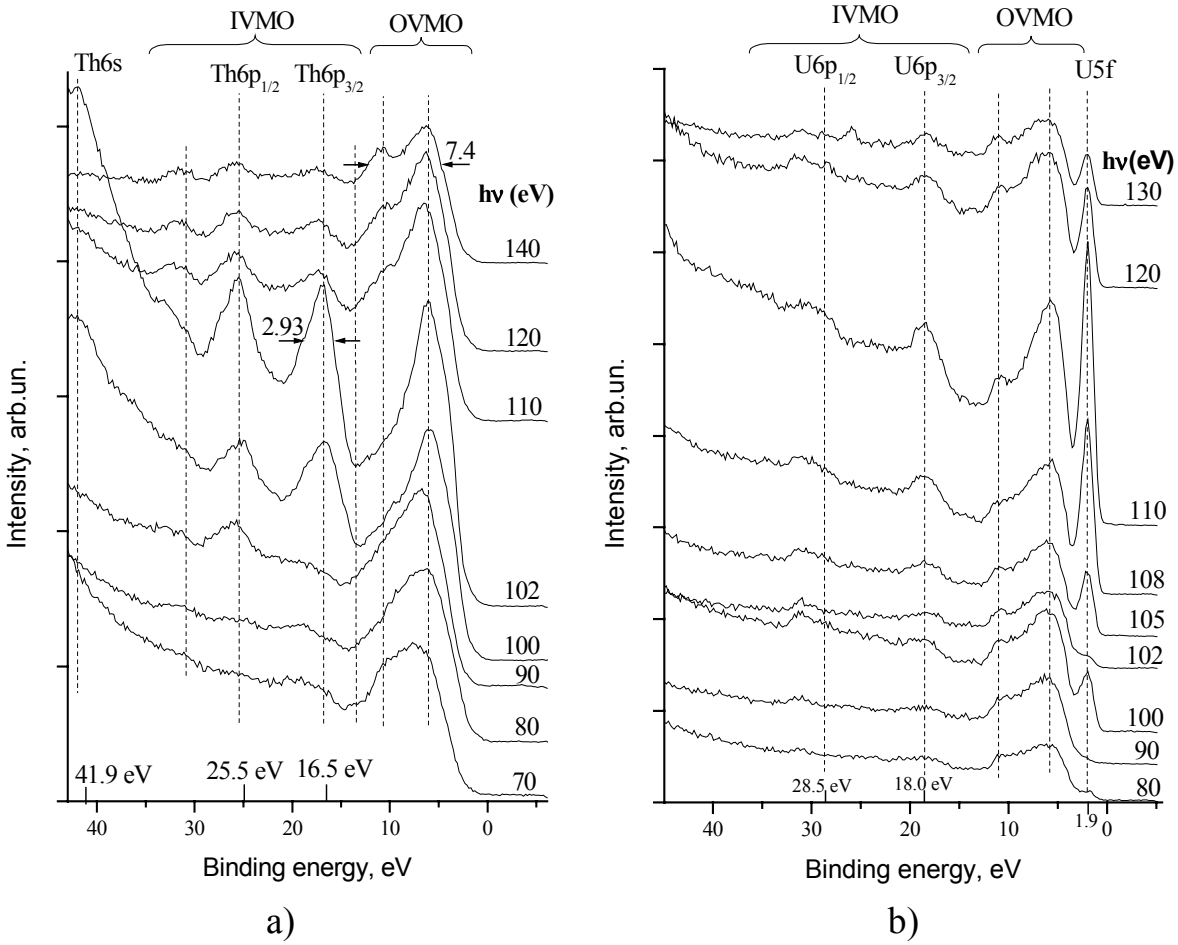

Fig. 2. Photoemission from: a) ThO_2 on the surface of thorium plate, b) UO_2 on the surface of uranium plate taken with different excitation energies hν. The spectral intensities were normalized to the ring current. Electron binding energies for ThO_2 a) and UO_2 b) embedded in indium on titanium substrates are given [1-3]. The C 1s binding energy from hydrocarbons on the sample surfaces was assumed to be 285.0 eV.

References:

[1] Yu.A.Teterin, A.S.Baev. Rentgenovskaya Fotoelektronnaya Spektroskopiya Soedinenii Legkikh Aktinoidov (X-Ray Photoelectron Spectroscopy of Light Actinide Compounds) (Moscow: Ts:NIIatominform, 1987, 102 p.)(in Russian).(see in Russian Chemical Reviews.2004).

[2] Yu.A Teterin., S.G. Gagarin. Russian Chemical Reviews. 1996. Vol 65(10). P.825-847.

[3] Yu.A., Teterin, A.Yu. Teterin. Russian Chemical Reviews. 2002.Vol.71(5).P.347-381.
[4] L.E.Cox, W.P.Ellis, R.D.Cowan, J.W.Allen, S.-J.Oh, I.Lindau, B.B.Pate, A.J.Arko. Phys.Rev. B. 1987. Vol.35(11). P.5761-5765.

Electronic properties of potassium doped CuPc

O.V. Molodtsova[1], T. Schwieger[1], V.M. Zhilin[2], D.V. Vyalikh[3], V.Yu. Aristov[2], M. Knupfer[1]

[1]*Leibniz Institute for Solid State and Materials Research, D-01069 Dresden, Germany*
[2]*Institute of Solid State Physics, Russian Academy of Sciences, Chernogolovka, Moscow Distr., 142432, Russia*
[3]*Institute of Solid State Physics, TU Dresden, D-01069 Dresden, Germany*

Organic molecular thin films (OMTF's) have been intensively studied since about twenty years because of their potential applications in various devices such as organic light-emitting diodes, organic field effect transistors and organic solid state injection lasers. Among OMTF's, the family of the phthalocyanines (Pc's) (which are archetypal organic molecular semiconductors) play an important role. They have attracted considerable interest because of their biological significance, catalytic properties and potential technological applications. In addition, Pc's demonstrate a good compatibility with ultra-high vacuum (UHV) and can be successfully grown as thin, ultra-clean, well ordered films on a substrate in standard UHV spectrometers. These films therefore possess excellent and well defined electronic structures. Consequently, for the family of the phthalocyanines the structural and electronic characterization via standard modern UHV techniques is possible. The information about their electronic properties, obtained by such techniques, is of vital importance both for understanding of underlying physics and numerous applications.

It is worth to mention the ability of molecular crystals to incorporate electron acceptors and donors and thus the possibility to control electronic properties of the material by introducing charge carriers. This special aptitude represents a promising route for technology as well as to study the fundamental properties of molecular crystals. In particular such knowledge can help to develop optoelectronic devices as well as lead to fascinating and surprising physical properties.

The purpose of the investigation presented in our report was to study evolution of the electronic structure of metal-phthalocianine (MPc) film at different levels of doping by alkali metal by example of CuPC as organic semiconductor and potassium as alkali metal. We have performed intensive investigation of core levels and top of the valence band for pristine CuPc and set of doses of potassium doping by means of high-resolution photoemission electron spectroscopy (HR-PES). The bottom of the conduction band was studied by NEXAFS (near edge x-ray absorption fine structure) spectroscopy at the same experimental conditions. All experiments were performed at the Russian-German beamline of the BESSY synchrotron radiation facility.

Figure 1 shows a set of PE C 1*s* core level spectra recorded during deposition of potassium metal. Decomposition of PE C 1*s* the spectrum for clean CuPc (not shown here) confirms the conclusion (see [1-3]) that C1s has 2 components: C-1 which corresponds to carbon in benzene rings of CuPc molecules (aromatic carbon) and C-2 shifted by 1.4 eV toward higher binding energy which correspond to the carbon linked to nitrogen (pyrolle carbon). This energy shift results from the charge redistribution between carbon and nitrogen atoms. In addition each component has a satellite. In the same diagram the evolution of the spectrum with increasing potassium doping is shown. One can see the appearance and rapid growing of a K 2*p* spin-orbit doublet at kinetic energies of 288 eV and 293 eV. The energy position of the doublet gives grounds for assumption that K atoms give over the valence *s*-electrons to CuPc molecules and intercalate into the molecular solid [2,3]. The shape of K 2*p* doublet does basically not change with the doping. So it seems that one deals with only one component in the entire range of potassium concentrations studied in the present investigation. Therefore we can conclude that K atoms intercalated into CuPc solid occupy essentially similar positions.

Evolution of PE C 1*s* core level spectrum with potassium doping results in a strong and continuous broadening of the C-2 component. On the other hand the lineshape of C-1 component on the whole persists. In particular, the decomposition of C 1s core-level at different potassium concentrations confirms this observation. This behavior of C 1*s* and K 2*p* core levels of molecular CuPc film with potassium doping indicates that most probably intercalation sites of K ions could be found in equivalent positions connected to pyrolle carbons.

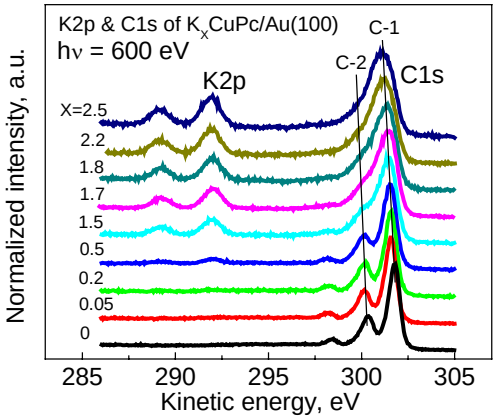

Fig. 1.C 1*s* and K 2p core levels as a function of K deposition on CuPc.

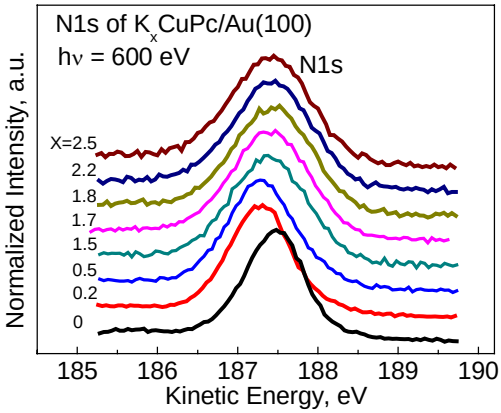

Fig. 2. Same as in Fig. 1 for N 1s core level.

More precise conclusions could be elaborated from the evolution of N 1s core level with K doping which is drawn in Fig. 2. N 1s core level of pristine CuPc solid is shown in the bottom spectrum of the figure. It looks like a single narrow peak. With increasing potassium intercalation the N 1s peak became broader. The results of N 1s peak decomposition for selected potassium intercalations are shown in Fig. 3. The parameters of each peak were taken from the N1s core level spectrum of pure solid and were kept unchanged at all potassium doping. It is clear, that with the doping the component A of the spectrum shows a shift to the higher binding energy and as a result of the first K deposition one more component B appears being shifted to lower binding energy as compared to component A. With the doping one observes a rapid attenuation of the component A and at the same time – growth of component B which saturates at B/A ≈ 1 at high doping (see inset in the Fig. 3). However, the total intensity of N 1s core level does not change. Thus we have found different chemical bonding conditions for two inequivalent types of nitrogen sites in CuPc molecules (it is worth to remark, that in pristine films the two inequivalent types of nitrogen sites in CuPc have the same energy positions). From our point of view the component A could be attributed to nitrogen atoms, connected to Cu. The fact that Cu 2p core level shows small changes with potassium doping (not shown here) in the range studied supports this conclusion. The second B component of the N 1s core-level must be attributed to the rest of N atoms which are linked to pyrolle carbon. A schematic diagram of possible K ions positions is presented in the Fig.4 where the concentration of K atoms corresponds to two K atoms per CuPc molecule. According to the simple approach the K atoms transfer a negative charge to nearest N atoms and as a consequence the energy position of N 1s core level shifts to lower BE (component B). Relative intensity A/B ≈ 1 corresponds to the fact that in CuPc molecule the number of N atoms linked to Cu is equal to that linked to pyrolle carbon. Thus we suppose that due to the relatively low first ionization energy of K atoms they give over electrons to the CuPc matrix. Such an ionization of the potassium atoms leads to repulsion between positively charged K ions and diffusion along interstitial sites of molecular solid.

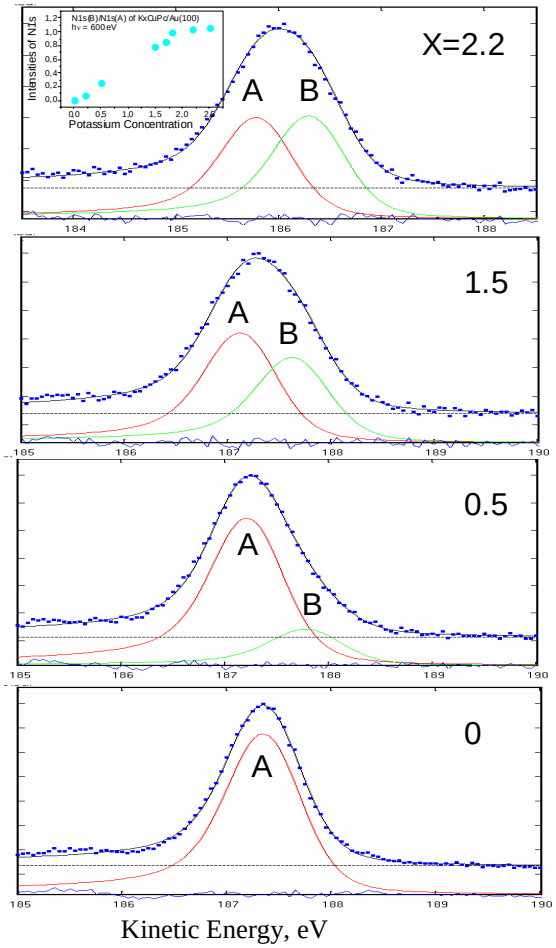

Fig. 3. Decomposition of N 1s core level for selected potassium doping.

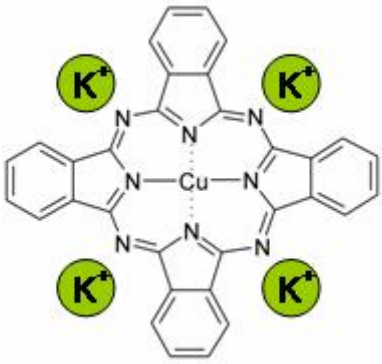

Fig. 4. Supposed K ions positions in CuPc film.

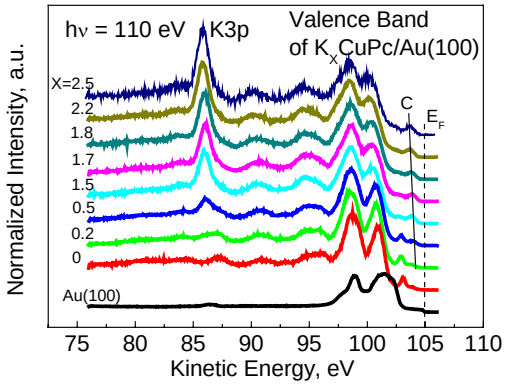

Fig. 5. Valence band and K 3p core level spectra as a function of K deposition on CuPc.

In this investigation some other interesting effects were observed. Among them we would like to mention an electronic state "C" which appears in the CuPc gap as a result of the first K deposition. The state growths with doping (see Fig. 5). One can propose a least two possible mechanisms of the state formation. According to the first one, we deal with appearance of K atom induced state. According to other point of view the potassium intercalation leads to splitting of an empty carbon-derived band into two and filling of one of the bands by electrons.

References

[1] O.V. Molodtsova, *Electronic properties of based and potassium doped CuPc/C60 and C60/CuPc interfaces (Oral)*, PHD Seminar of Institute for Solid State Physics of IFW Dresden, Raten, Germany, October 28-30, 2004.

[2]. O.V. Molodtsova, T. Schwieger, V.M. Zhilin, D.V. Vyalikh, V.Yu. Aristov, M. Knupfer, *Electronic properties of potassium doped CuPc (Poster)*, 23rd BESSY Users' Meeting 2004, Berlin, Germany, December 2/3, 2004.

[3] T. Schwieger, H. Peisert, M.S. Golden, M. Knupfer, and J. Fink, Phys.Rev. **B66** (2002) 155207.

Determining the natural line width of Au $4f_{7/2}$ by volume-sensitive high resolution photoelectron spectroscopy at high kinetic energies

Patrick Bressler, Thomas Owens, Marcel Mertin, Franz Schäfers

BESSY GmbH

HIKE is a new BESSY end station for highest-resolution-photoelectron spectroscopy at high kinetic energies. It was set-up this year on the double crystal monochromator KMC-1 (hv: 2-12 keV) for performance tests. Major components of the HIKE endstation are a Gammadata Scienta R-4000 hemispherical analyzer specifically modified for high transmission and highest-resolution at kinetic energies up to 10 keV, an analysis chamber, a liquid helium manipulator (T_{min} [sample] < 25 K) and a rapid entry load lock. The UHV-compatible station is dedicated to PES at high kinetic energies. Volume-sensitive photoemission (PE) data can now be obtained.

The inelastic mean free path (IMFP) for (photo-)electrons in condensed matter increases with the electron kinetic energy from a few Ångströms at E_{kin}~ 50 eV to over 80 Å at E_{kin}~10000 eV. Consequently, the bulk valence state contribution in a photoelectron spectrum increases to over 95% at 6-10 keV final state kinetic energy. This straight-forward method to derive bulk valence states by PES used to be almost impossible to realize because of the drastic decline in excitation cross-section for valence electrons at higher excitation energies. PE count rates were severely reduced and very long acquisition times (e.g.: over 24 hours) were necessary. Nowadays, such experiments are becoming feasible due to "third-generation" source brightness and new electron spectrometers optimized for high performance operation.

At KMC-1 photoemission spectra were taken on polycrystalline Au films at photon energies ranging from 2400 eV to 8000 eV. Prior to experiments all samples had been exposed to ambient atmosphere for unspecified periods of time and no attempt was made to prepare "clean" surfaces. To test surface-insensitivity the station was not baked out. Pressure at room temperature was ~ 4×10^{-8} mbar and equivalent to a rest gas exposition of roughly 0.2 monolayers per second. Acquisition times ranged from 3 to 7 hours per spectra. No surface interference was detected.

A full width at half maximum (FWHM) of 312 meV was obtained for the Au 4f core level with photon energy of 5670 eV and pass energy of 100 eV (figure 1) using Si(422) crystals in the KMC-1 monochromator. This is a significant improvement over ealier measurements /1/ and also confirms the assumption that Au 4f peaks are significantly sharper in bulk than at the surface due to the lack of broadening induced by structural disorder and loss of symmetry at the surface.

Calculated KMC-1 resolution ($E/\Delta E$) and measured values are presented in figure 2. Green line and dots show the results for Si(422) crystals. Measured resolution (monochromator only) at 5900 eV is 300 meV (solid green circle). Moving towards lower energies the energy resolution increases to ~ 100 meV at 5600 eV. At 5670 eV we estimate the monochromator resolution to be at least 250 meV. The experimental spectrometer resolution (0.3 mm entrance slit) is safely better than 100 meV. For Au $4f_{7/2}$ this yields a lower limit of 155 meV for the natural line width. Assuming near theoretical instrument values give an upper limit of 230 meV. Previous PE studies had suggested a natural line width between 100-150 meV /1/.

Finally, we wish to thank Gunnar Öhrwall (Physics Department, Uppsala University, Uppsala, Sweden & GAMMADATA, Uppsala, Sweden) and Gunnar Vegerfors (GAMMADATA, Uppsala, Sweden) for the great support and excellent job during set-up.

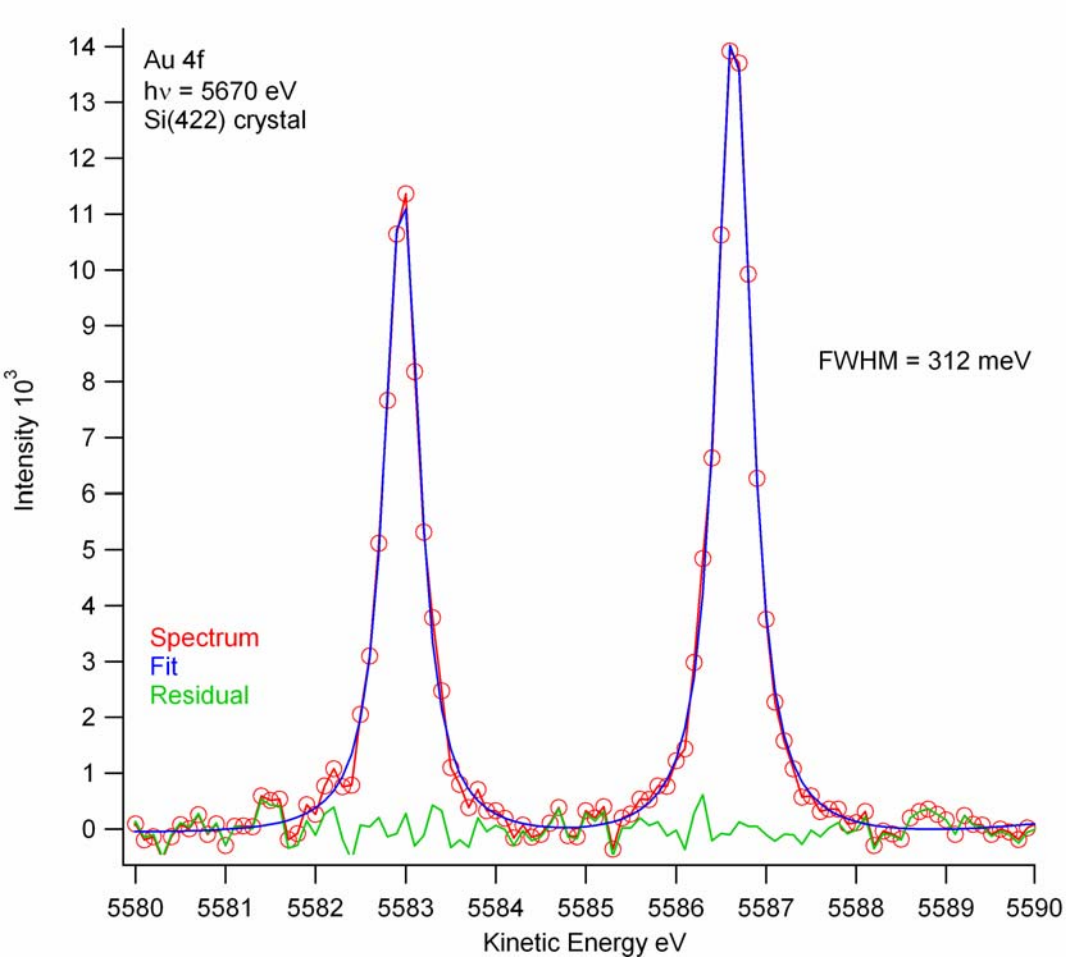

Figure 1.: Photoelectron spectrum of Au $4f_{5/2}$ and Au $4f_{7/2}$ at 5670 eV excitation after background subtraction. Voigt profile fit yields FWHM (Au $4f_{7/2}$) of 312 meV.

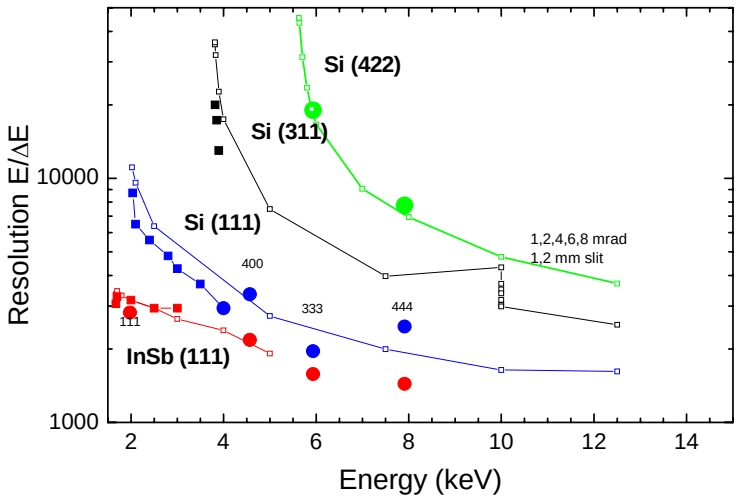

Figure 2.: Calculated (lines) and experimentally determined (solid circles) resolutional power for KMC-1 InSb(111) (red), Si(111) (blue), Si(333) (black) and Si(422) (green).

/1/ see e.g.: I. Lindau et al. Nature **250**, 214, 1974, or

K. Kobayashi et al., Appl.Phys. Lett. 83, 1005, (2003) and refs. therein.

Electron localisation in metallic quantum wells

J.H. Dil, J.W. Kim, Th. Kampen, K. Horn and A.R.H.F. Ettema*

Department of Molecular Physics, Fritz-Haber-Institut der Max-Planck-Gesellschaft, Germany

**Department of Nanoscience, Delft University of Technology, The Netherlands*

The physical properties of ultrathin epitaxial metallic films exhibit marked differences compared to those of the bulk, through the effect of electron confinement in the film, and the influence of the boundary between film and substrate. Electron confinement leads to the formation of discrete quantum well states[1], which may play a decisive role in growth morphology[2], and may lead to "magic" or "critical" thicknesses[3], oscillations in the magnitude of the superconducting transition temperature[4], and oscillations in direction and magnitude of the Hall effect[5,6]. In extended metal films, electron motion is only confined in the (z-) direction normal to the film. Hence quantum well states are expected to exhibit a dispersion relation E ($k_{||x}$, $k_{||y}$) for the component of electron wave vector $k_{||}$ along the x and y directions parallel to the film, that is similar to the bulk band from which they are derived. Effective masses m* are used to describe the dispersion with the parallel component of the wave vector $k_{||}$ in these s-p-derived bands, $E = \hbar^2 k_{||}^{\ 2}/2m^*$. As determined experimentally from angle-resolved photoemission studies, they generally agree well with those from theoretical calculations based on free-standing films. This indicates that the influence of interface structure and confinement on this aspect of electron dynamics is negligible. Here we show that in the Pb/Si(111) system, the effective mass m* of the Pb $6p_z$ band is enhanced dramatically in Pb quantum wells. We interpret this observation as due to electron localisation, and present arguments for its occurrence in this particular system.

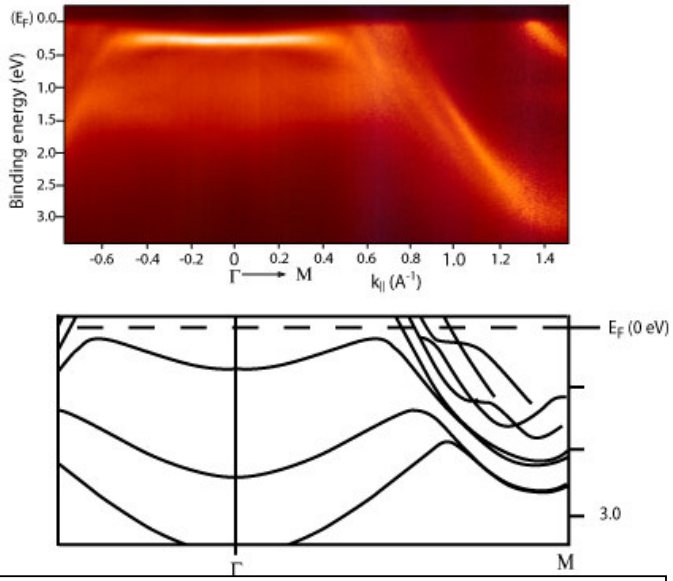

Figure 1: Top: Distribution of photoemission intensity for a 6 ML Pb film on Si(111):Pb √3x√3 of a cut through the Brillouin zone along the Γ-M direction. The effective mass for the QWS is fitted to be 8.1 m_e. Bottom: Calculated band structure for a 6 ML thick freestanding Pb slab.

Angle-resolved photoemission is ideally suited to determine electronic band dispersions in a wide variety of systems, and in electron energy analyzers which permit a display of E(k) in an imaging mode, patterns due to emission from band states can be directly observed. In Figure 1 the photoemission intensity distribution for a 6 ML Pb film on Si(111) along the $\overline{\Gamma} - \overline{M}$ direction is shown. To allow for a good comparison to theory slab calculations for a free-standing Pb films are shown at the bottom. The bright feature around $\overline{\Gamma}$ is the topmost quantum well state, while the features dispersing downward beyond $k_{||}$ = 0.6 Å^{-1} arise from the $6p_{x-y}$ band.

When comparing theory and experiment the most striking difference is the dispersion of the quantum well state around the center of the Brillouin zone. The calculated QWS has an effective mass close to the free electron mass, whereas the measured QWS hardly shows any dispersion at all and can be fitted with an effective mass of 8 times the free electron mass. The splitting of the downwards turning bands is fully reproduced as is the backfolding of these bands towards the edge of the Brillouin zone, indicating the good correspondence between theory and experiment.

The effective mass should decrease with coverage since in the limit of thick films, approaching the bulk regime, m* should reach the corresponding value for the bulk band. Figure 2 shows the in-plane dispersion close to the Brillouin zone center for films of 14, and 18 ML thickness on Si(111). It can be seen m* has decreased compared to the 6 ML film, however even for 18 ML the effective mass is still 5.2 m_e for the highest occupied quantum well state. Effective mass values were obtained by taking slices through the image every 0.023 $Å^{-1}$, which results in a set of electron distribution curves similar to those measured with a single channel angle resolved electron energy analyzer. These spectra were then fitted to obtain peak positions for the QWS as a function of in-plane momentum. By accurately analysing the features in the images, spectra and fits, the QWS can be distinguished from any substrate features that are in the same region.

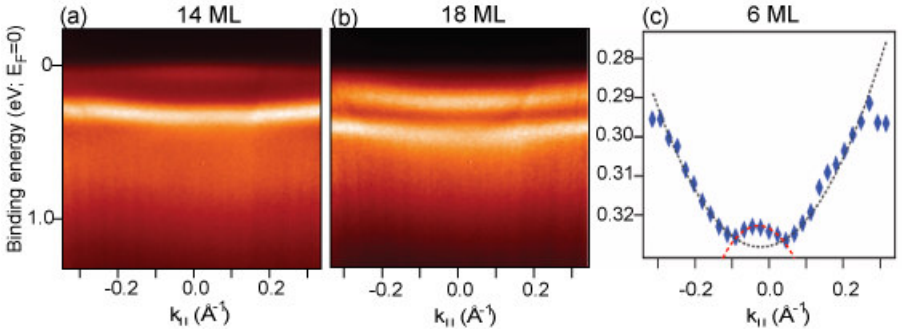

Figure 2: In-plane dispersion for (a) 14 and (b) 18 ML of Pb on Si(111):Pb √3x√3. (c) Data points for the position of the QWS in 6 ML of Pb on Si(111):Pb √3x√3

Figure 2 (c) shows the result of a fit performed in this manner for the 6 ML film, where the binding energy range is magnified compared to the other images. Here the upward parabola of the QWS can be clearly distinguished from the downward parabola from the topmost valence band edge of the Si(111) substrate (red dashed line). The black dashed line indicates the fit performed to extract the effective mass for the Pb quantum well state from the data.

The magnitude of the effective mass is a measure of the localisation of electrons in a specific state. The observation of larger m* hence suggests that electron correlation processes are at work in the thin Pb film. In order to determine the strength of these electron correlation effects one should compare the bandwidth *W* with the electron-electron interaction parameter *U* from the Hubbard model, i.e. compare the kinetic and thermal energy of the electrons with their exchange energy. This competition between kinetic and interaction energies is also known to be the driving force behind the Kondo effect. In contradiction to other quantum well systems the electron interaction energy is larger for Pb/Si(111) then the bandwidth of the quantum well states, therefore indicating a prevalence of electron correlation effects.

*[1] T.-C. Chiang, Surf.Sci. Reports **39**, 181-235 (2000). [2] K. Budde, E. Abram, V. Yeh, and M.C. Tringides, Phys.Rev. B **61**, 10602 (2000). [3] Z. Zhang, Q. Niu, and C.K. Shih, Phys.Rev.Lett. **80**, 5381 (1998). [4] B.G. Orr, H.M. Jaeger, and A.M. Goldman, Phys.Rev.Lett. **53**, 2046 (1984). [5] M. Jalochowski, M. Hoffmann, and E. Bauer, Phys.Rev.Lett. **76**, 4227 (1996). [6] I. Vilfan, M. Henzler, O. Pfennigstorf, and H. Pfnür, Phys.Rev. B **66**, 241306 (2002).*

Circular dichroism in core-level photoelectrons from tartaric acid adsorbed on Cu(110)

Jeong Won Kim, J. Hugo Dil, Thorsten U. Kampen, and Karsten Horn*

Fritz-Haber-Institut der Max-Planck-Gesellschaft, Faradayweg 4-6, Berlin 14195, Germany
* Nano-Surface Group, Korea Research Institute of Standards and Science,
PO box 102, Yuseong, 305-600 Daejon, Korea.

In search of heterogeneous catalysis for enantioselective reactions, recent interest has focused on the properties of chiral molecules in the adsorbed phase. It was found that these may arrange into well-ordered structures which are strongly influenced by the handedness of the molecule.[1] Among such systems, the adsorption properties of tartaric acid have been investigated by means of scanning tunneling microscopy (STM), low energy electron diffraction (LEED), reflection absorption infrared spectroscopy (RAIRS), and x-ray photoelectron diffraction (XPD)[2] and the interpretation is supported in part by a theoretical calculation.[3] Here we report on a study of different isomers of tartaric acid on Cu(110) using the method of circular dichroism in C 1s core level photoemission upon irradiation of circularly-polarized x-ray. We demonstrate that the chiral nature of different enantiomers of tartaric acid adsorbed on Cu(110) can be identified by means of circular dichroism in core level photoemission.

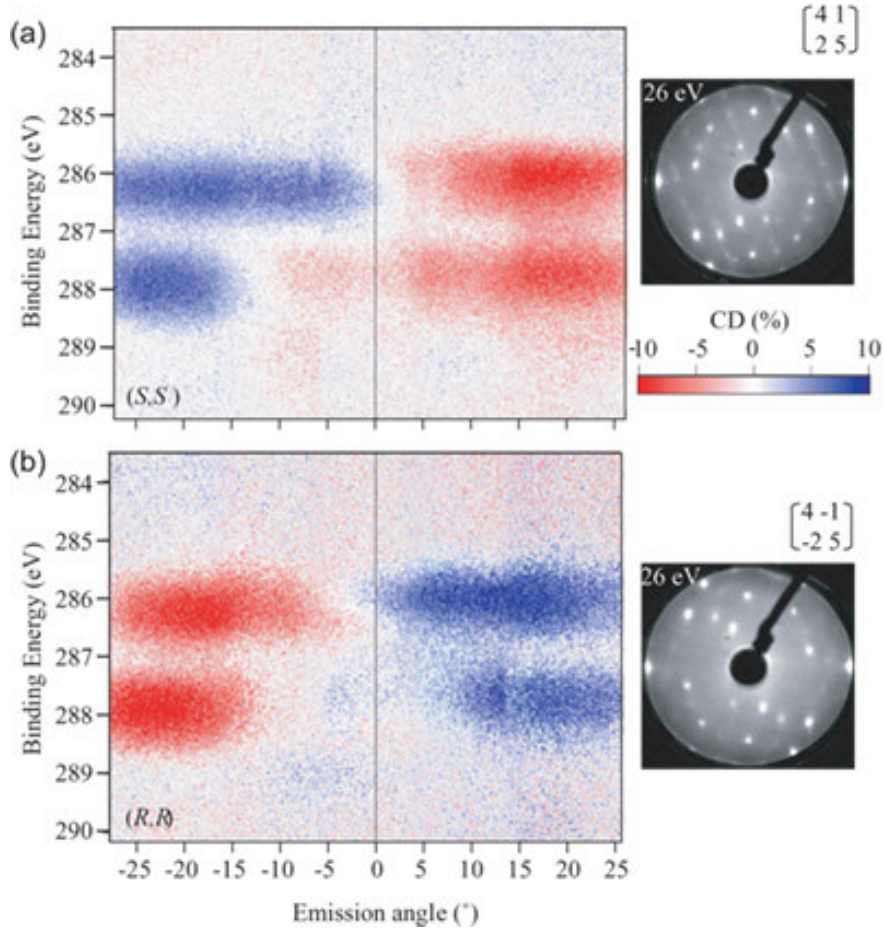

Figure 1:

Circular dichroism images from the C 1s region along the substrate [001] direction, from the high coverage monotartrate phase, for (*R,R*) and (*S,S*) tartaric acid. The respective LEED patterns for the (4 1, 2 5) (*R,R*) (a) and (4 -1, -2 5) (*S,S*) (b) are shown on the right-hand side.

A Cu(110) crystal was cleaned by repeated cycles of Ar^+ sputtering (800 eV) and annealing to 200 °C. Different optical isomers of tartaric acids (Chiron AS, 99 %) were evaporated from a home-made Knudsen cell at 80 °C in ultrahigh vacuum onto the clean Cu(110) surface held at around 100 °C. Two kinds of stable phases are made to compare with each other: a low coverage bitartrate phase ({9 0, 1 2} structure in matrix notation of low energy electron diffraction), and a high coverage monotartrate phase with {4 1, 2 5} structure. In this report only results for the high coverage phase are presented.

All measurements were performed at beamline UE56/2 PGM 1. Carbon 1s photoelectrons were recorded at a photon energy of 380 eV with the sample at room temperature using left- and right-circularly polarized (LCP and RCP) light. Photoelectron spectra were recorded with a PHOIBOS 100 electron energy analyzer equipped with a 2D CCD detector (Specs GmbH), permitting to record photoelectrons over a 14° angular range with about 0.1° angular resolution. Special attention was paid to the influence of the geometrical CDAD effect, which occurs when the direction of the photon beam, surface normal and electron emission are not coplanar, i.e. have an "experimental handedness". All data were collected only in a coplanar geometry within an error of 0.5°, along different azimuths of the copper sample. The angle between photon beam and electron emission was 54 ± 7°.

In the tartaric acid molecule, there are two different types of carbon atom from a chemical point of view: one in the carboxylic group, and one in the alcohol group. Structural studies have demonstrated that tartaric acid is bound to the Cu surface atoms through the carboxylic oxygen atoms after deprotonation. The different carbon atoms in the adsorbed molecule can be readily identified in core level photoemission. Two peaks are observed, at 286.60 (C1) and 288.15 eV (C2), respectively, similar to a previous study of the related molecule glycine adsorbed on Cu(110).[4]

By utilizing the parallel detection capabilities of our photoelectron energy analyzer, we obtain images of photoelectron intensity rather than separate spectra. This provides a graphic representation of changes induced by a reversal of photon helicity (Figure 1). The magnitude of circular dichroism is defined as the asymmetry $A = (I^{RCP} - I^{LCP})/I^{RCP} + I^{LCP})$, where I is the measured intensity under the respective light helicity. Photoemission images in an angular range of ± 7° were recorded with RCP and LCP light and were subtracted from one another after a background normalization. From a set of images at different angle settings, images such as in Figure 1 were assembled, where blue means a positive and red a negative value as indicated in the color table bar. The binding energy range encompasses the C1 and C2 features mentioned above, clearly seen by the two horizontal bars of intensity. In Figure 1 we compare the asymmetry values in the two C 1s components for the (*R,R*) and (*S,S*) enantiomers of tartaric acid in the high coverage monotartrate (4 1, 2 5) phase (upper and lower panel, respectively). This structure gives rise to the LEED patterns shown on the right-hand side of each asymmetry plot; they are mirror images of one another, brought about by the interplay between the molecular structure of the adsorbate and the Cu(110) surface geometry as demonstrated through STM. Two effects are immediately evident: emission from both carbon atoms exhibits circu lichroism, and the asymmetry reverses sign with emission angle in the plane spanned by the light a he surface normal. The asymmetry is rather small in normal emission, but reaches values of up to 10 % at emission angles around 20° and beyond. A striking observation comes from a comparison of circular dichroism from the (*R,R*) and (*S,S*)-forms, however. A comparison of circular dichroism from the (R,R) and (S,S) forms of tartaric acid adsorbed on Cu(110) yields the clear result that, within a good approximation, the intensity patterns (blue and red contrast) of Figures 1(a) and (b) are mirror images of one another with respect to the 0° emission angle line. This is a most important result since it demonstrates that the observed dichroism is due to the chiral nature of the adsorbed molecule, and is not related to the geometrical CDAD. This is because in our experiment, in which the incident radiation, the surface normal and the detector are all coplanar, the CDAD will be zero if that plane coincides with a mirror plane of the (nonchiral) surface as stated in the previous section. Within this mirror plane, the observed dichroism is therefore a **direct consequence** of the chirality of the adsorbed molecule. This is also clear from the reversal of asymmetry between the (*R,R*) and (*S,S*) forms of tartaric acid. The above results are readily understood if one considers that in optical transitions at low photon energies, parity-violating processes are negligible. The result of an experiment involving chiral molecules must therefore be invariant upon an application of the parity operation which changes both the photon helicity and the handedness of the molecule. This invariance causes the interaction of RCP light with a"right-handed" enantiomer to yield an identical results as LCP light wit a "left-handed" enantiomer.

[1](a) Fang, H. B.; Giancarlo, L. C.; Flynn, G. W. J. *Phys. Chem. B* **1998,** 102, 7311–7315. (b) Fasel, R.; Parschau, M.; Ernst, K.-H. *Angew. Chem. Int. Ed.* **2003**, 42, 5177–5181. (c) Barlow, S. M; Raval, R. *Surf. Sci. Rep.* **2003**, 50, 201–341. (d) Kühnle, A., Linderoth, T. R., Hammer, B. & Besenbacher, F. *Nature* **2002**, 415, 891–893. (e) Ortega Lorenzo, M., Baddeley, C. J., Muryn, C. & Raval, R. *Naure* **2000**, 404, 376–379.

[2] (a) Lorenzo, M. O.; Haq, S.; Bertrams, T.; Murray, P.; Raval, R.; Baddeley, C. J. J. *Phys. Chem. B* **1999**, 103, 10661–10669. (b) Fasel, R.; Wider, J.; Quitmann, C.; Ernst, K.-H.; Greber, T. *Angew. Chem. Int. Ed.* **2004**, 43, 2853–2856.

[3] Barbosa, L. A. M. M.; Sautet, P. *J. Am. Chem. Soc.* **2001**, 123, 6639–6648.

[4] Hasselström, J.; Karis, O.; Weinelt, M.; Wassdahl, N.; Nilsson, A.; Nyberg, M.; Pettersson, L. G. M.; Samant, M. G.; Stöhr, J. *Surf. Sci.* **1998**, 407, 221–236.

Confinement width of Ag quantum well states

J. Cordón[1], M. Ruiz-Osés[1], D. Vyalikh[2], J. E. Ortega[1], F. Schiller[1]

[1]*Donostia International Physics Center, Manuel Lardizabal 4, E-20018 Donostia/San Sebastián, Spain*
[2]*Institut für Festkörperphysik, TU- Dresden, D-01062 Dresden, Germany*

The photon energy dependence in metallic quantum wells provides useful information about both electron wave functions in the well and photoemission final states. Spectra are characterized by peaks around vertical transitions, with total width determined from the sum of final state and initial state wave vector broadening. For ultrathin films and low excitation energies, the initial state broadening due to confinement in the well dominates. In this work we have examined the case of a well-defined, ultrathin quantum well system with a sharp interface, namely Ag/W(110).

Angle resolved photoemission spectroscopy (ARPES) experiments were carried out at the U125/2-10m-NIM beamline of BESSY II (Berlin, Germany) using a spherical electron analyser working at 1° angular and 50-100 meV (photon and electron) energy resolution in a vacuum of 2×10^{-10} mbar. Ag was deposited in-situ by thermal deposition onto a clean W(110) substrate hold at room temperature. A clean substrate was achieved by cycles of thermal treatments consisting in W(110) heating at 1300 K for 20 minutes in 2×10^{-7} mbar oxygen partial pressure followed by short sample flashs at 2300 K until a sharp (1×1) low energy electron diffraction (LEED) pattern was observed. Crystalline quality of the growing Ag film was checked by LEED and photoemission indicating well resolved quantum well states (see below).

The electronic structure of W(110) consists of a large Σ_1 symmetry band gap along the perpendicular ΓN direction. Λ_1 states of a fcc or hcp thin film grown on top of W(110) an located at the same energy region as the band gap are likely to be confined within the film [1]. The scattering at the edges of the quantum well may be qualitatively described by phase shifts Φ_B and Φ_C of the electron wave on both sides of the well, the vacuum and the interface, respectively. Using the Bohr-Sommerfeldt quantisation rule, a full round trip inside the quantum well is a multiple of 2π:

$$k_\perp d + \Phi_B + \Phi_C = 2\pi n \qquad (1)$$

where $k_\perp$ is the wave vector perpendicular to the film and d the layer thickness.
Figure 1 shows the PE spectrum of approx. 2.5 ML Ag/W(110). The two well resolved structures at 3.1 and 2.4 eV binding energy are emissions located inside the W(110) substrate band gap and recognised as Ag *sp*-like quantum wells characteristic for Ag films of 2.5 atomic layers [2]. The intensity enhancement below the Fermi level is assigned to the Ag surface state, the strong peaks between 4 and 8 eV binding energy are due to emission from Ag 4*d* bands, and the other (small) features belong to the substrate. The two *sp*-like quantum well states originate from the first quantum level (n=1) in patches of 2 and 3 ML thick Ag films, respectively [2].

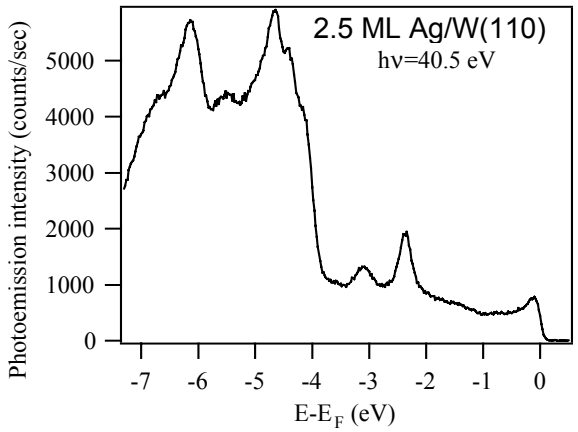

Figure 1: Photoemission spectrum of 2.5 ML Ag/W(110).

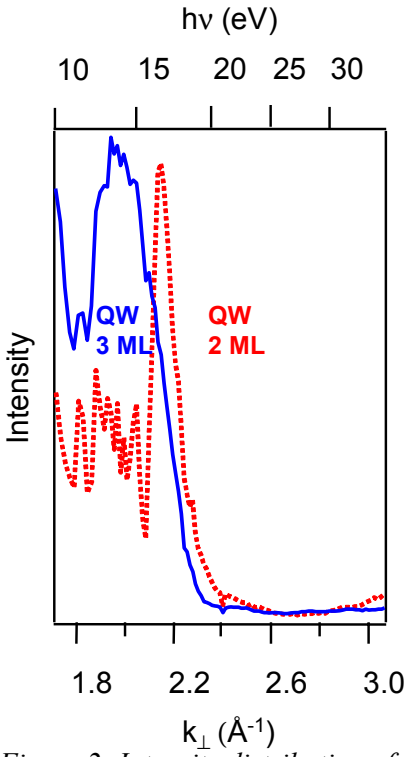

Figure 2: Intensity distribution of the two Ag quantum well states as a function of $k_\perp$ and hν. Surprisingly, the transition gets wider for the thicker film.

A whole series of photoemission spectra was taken for this film varying the photon energy between 10 and 50 eV in steps of 200 meV. Every spectrum was fitted using Lorentzian functions for all peak features. Figure 2 shows the intensity of the two Ag *sp* quantum wells as a function of photon energy and wave vector perpendicular to the film using

$$k_\perp = 0.512 \cdot \sqrt{h\nu - E_B + V_0} \qquad (2)$$

where V_0=8 eV is used for the Ag inner potential. The two curves peak at 16.8 and 13.6 eV photon energies, respectively. Two main points may be observed: (i) the maximum position of the two curves and (ii) the transition width of the peaks are different. Figure 3 describes schematically the observation: The photoemission process may be described as a transition from an initial (occupied) to a final (unoccupied) state within the Ag band structure. Due to the back-folding of the band at the Brillouin zone boundary and the different energy positions of the quantum well states, the transition should result in two different energies (two vertical solid arrows). Photon energy dependent mappings carried out for quantum well states with several *n* of different Ag film thicknesses can therefore used to determine the final state wavefunction [3]. A further possibility for the analysis of the data is a comparison to theory. Band structure calculations of Ag reveal the transition of the first quantum level (*n*=1) for a two and three layer film at 16.0 and 12.2 eV, respectively, in good agreement with the experimental data.

The experimental width Γ_{exp} of the transitions in Fig. 2 is related to the sum of the initial and final state width by [4]

$$\frac{\Gamma_{exp}}{\hbar v_f} = \left(\Delta k_i + \Delta k_f\right), \qquad (3)$$

where v_f is the group velocity of the final state. The initial and final states are assumed to be linear in *k*, an approximation valid for the small momentum range concerning the convolution. The initial state momentum broadening Δk_i is related to the photohole lifetime and the effective confinement of the states. The broadening of the final state momentum is determined by the escape depth $\lambda_f = |v_f| / \Gamma_f$, which in turn is linked to the momentum broadening by the uncertainty principle, $\Delta k_f = 1/\hbar\lambda_f = \Gamma_f / \hbar|v_f|$, and it is an order of magnitude smaller than Δk_i. Hence, the confinement length δ of a quantum well in three and two Ag layers may be extracted almost directly from the curves shown in Figure 2. Obviously, we expect a narrower transition in the quantum well state representative for the 3 ML

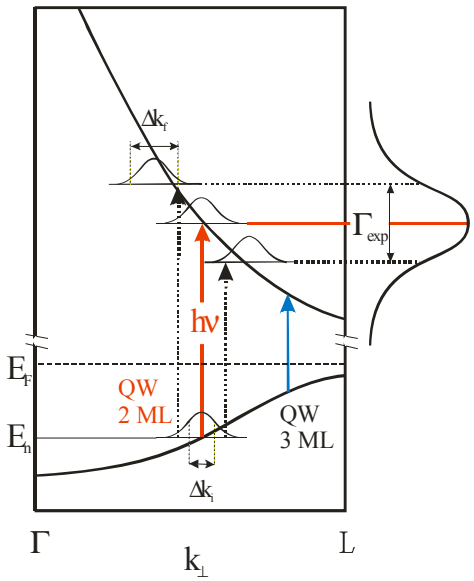

Figure 3: Schematic description of the electronic transition from two Ag quantum wells (vertical solid arrows) affected by initial and final state broadening leading to the experimentally observed width.

patch, but this is contrary to the observations. For the above described analysis, however, the special band structure of the photoemission final state (including tungsten final states) was not taken into account and may be responsible for the different finding.

This work was supported by the European Community I 3 Contract (RII 3-CT-2004-506008). We further acknowledge technical help from Dr. G. Reichardt, Dr. O. Rader, A. Varykhalov, and Dr. A. M. Shikin.

References:
[1] H. Knoppe and E. Bauer, Phys. Rev. B **48**, 5621 (1993)
[2] D. Vyalikh *et al.*, Surf. Sci. **540**, L638 (2003)
[3] A. Mugarza and J. E. Ortega, J. Phys. Cond. Mat. **15**, S3281, (2003)
[4] N. V. Smith, P. Thiry and Y. Petroff, Phys Rev. B **47**, 15476 (1993)

Spectroscopy of niobium oxide films on $Cu_3Au(100)$

D. Starr, F. Mendes, S. Guimond, H. Kuhlenbeck, S. Shaikhutdinov, H.-J. Freund
Fritz Haber Institute of the Max Planck Society, Chemical Physics Department
Faradayweg 4-6, 14195 Berlin

This work has been funded by the Deutsche Forschungsgemeinschaft via its Sonderforschungsbereich 546

Ordered niobium oxide films grown on $Cu_3Au(100)$ have been investigated with angularly resolved XPS using light from the UE52-PGM1 monochromator. The oxide layers were grown by deposition of niobium onto an oxygen pre-covered $Cu_3Au(100)$ surface followed by annealing in an oxygen atmosphere according to a method originally proposed by the group of Horst Niehus (Humboldt University, Berlin) and further modified by us. The investigated films had a thickness in the Angstrøm range. Niobium oxide may act as a catalyst for oxidation reactions similar to vanadium oxide which we investigated in some depth in the framework of the Sonderforschungsbereich 546 of the Deutsche Forschungsgemeinschaft.

A LEED pattern of a film obtained after deposition of 1.6 Å of niobium, oxidized as described above is shown in Fig. 1. The oxide exhibits two domains of a (2×7) unit cell which does not correspond to the common NbO_2 and Nb_2O_5 lattices. This result is not too surprising since the oxide layers consist mainly of interface and surface atoms which means that a structure different from the known bulk structures may be energetically favorable. The aim of the XPS studies was to learn about the oxidation state of the niobium atoms and the electronic structure of the film.

Fig. 2 compares valence band spectra of the oxide film with spectra of NbO_2 and Nb_2O_5 (reproduced from ref 1). The structure near to about 1.3 eV binding energy in the spectrum of NbO_2 is due to niobium 4d electrons which do not exist in the case of Nb_2O_5. The data of the thin film do not exhibit intensity near to E_F indicating that the oxide is non-conducting. There is also no structure at 1.3 eV binding energy which would mean that the oxide film does not consist of NbO_2. However, this conclusion is not unambiguous since there is some intensity near to the onset of the substrate d levels which may be attributed to modified substrate valence band states as well as to emission of Nb4d electrons.

Additional information comes from Nb3d spectra (see Fig. 3). The energy of the Nb3d level depends significantly on the niobium oxidation state. An overview of literature data is given in Table 1. From the data in this table it is clear that the $Nb3d_{5/2}$ binding energy observed for the 2.6 Å thick film fits reasonably well to literature data reported for Nb_2O_5 whereas for the 0.5 and 1.6 Å layers the $Nb3d_{5/2}$ binding energy is nearer to that observed for NbO_2. However, for these very thin layers the screening of the XPS final state core hole by the Cu_3Au substrate electrons will pull the Nb3d levels to lower binding energy. Thus the binding energies observed for the thin layers could also be compatible with niobium in a 5+ oxidation state. A definite

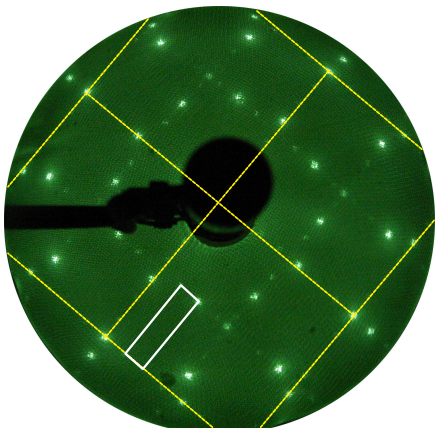

Figure 1: LEED pattern of a niobium oxide layer on $Cu_3Au(100)$ obtained after deposition of 1.6 Å niobium onto oxygen pre-covered $Cu_3Au(100)$ and subsequent oxygen treatment. The oxide (solid line) and substrate (dashed line) surface unit cells in reciprocal space are indicated, assuming substrate surface termination by only one type of atoms. E_p=70.2 eV.

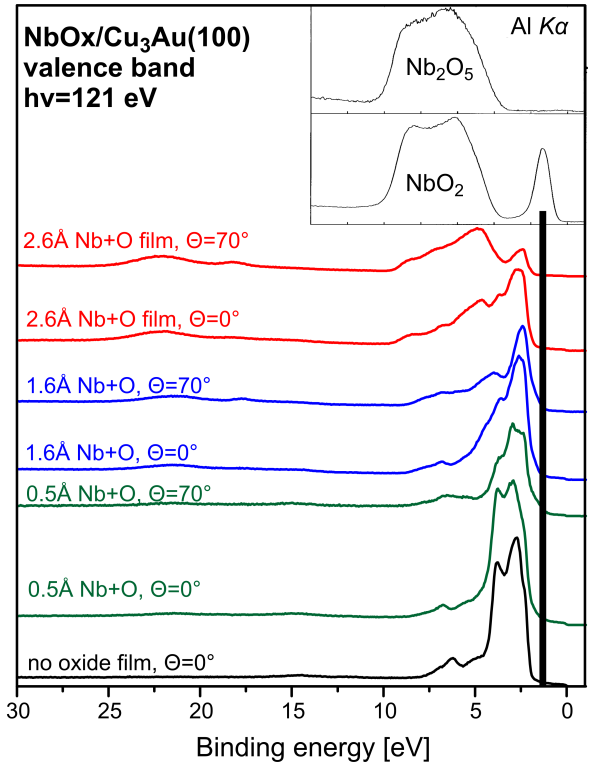

Figure 2: Valence band spectra of niobium oxide layers obtained after deposition of different amounts of niobium onto oxygen-precovered $Cu_3Au(100)$ followed by annealing in oxygen. The electron exit angles Θ with respect to the surface normal are given at the spectra. In the inset spectra of NbO_2 and Nb_2O_5 powder samples are shown (reproduced from ref 1).

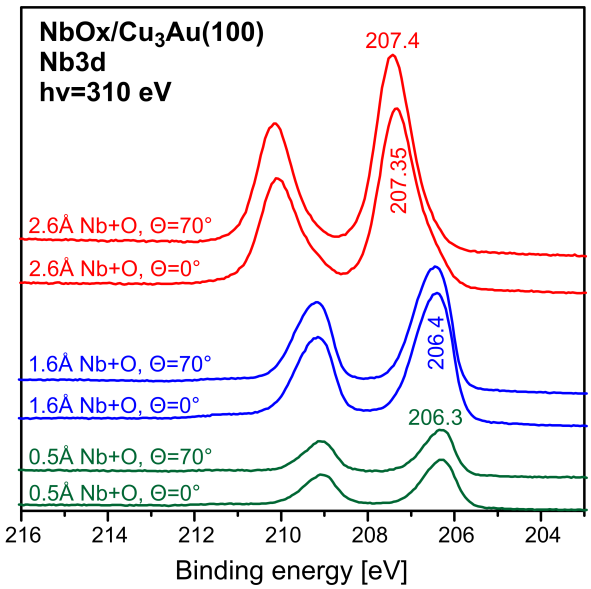

Figure 3: Nb3d XPS spectra of niobium oxide layers obtained after deposition of different amounts of niobium onto oxygen pre-covered $Cu_3Au(100)$ followed by annealing in oxygen. Spectra were taken at two different electron exit angles Θ with respect to the surface normal.

assignment is currently not possible.

Nb_2O_5	NbO_2	NbO	Nb	this work
powder: 207.8 [1]	powder: ≈205.9* and ≈206.7* [1]	on Pt(111): 203.8 [2]	202.3 [3]	206.3-206.4 and 207.35-207.4
on Pt(111): 207.5 [2]	on Pt(111): 205.8 [2]	on Nb foil: 202.9 [4]	202.2 [4]	
on Nb foil: 207.5 [4]	on Nb(110): 206.4±0.1 [5]			
	on Nb foil: 206 [4]			

*: estimated from a figure in the publication.

Table 1: Overview of literature data for $Nb3d_{5/2}$ binding energies (in eV) of niobium in different oxidation states.

References

[1] D. Morris, Y. Dou, J. Rebane, C. E. J. Mitchell, R. G. Egdell, D. S. L. Law, A. Vittadini, and M. Casarin, Phys. Rev. B **61**, 13445 (2000).

[2] L. Xie, D. Wang, C. Zhong, X. Guo, T. Ushikubo, and K. Wada, Surf. Sci. **320**, 62 (1994).

[3] J. C. Fuggle and N. Mårtensson, J. Eletron Spectrosc. Relat. Phenom. **21**, 275 (1980).

[4] M. M. Thiam and Z. Bastl, Surf. Sci. **507-510**, 678 (2002).

[5] I. Arfaoui, J. Cousty, and C. Guillot, Surf. Sci. **557**, 119 (2004).

Circular dichroism in core level photoemission from an adsorbed chiral molecule

M. Polcik[1], F. Allegretti[2], D.I. Sayago[1], G. Nisbet[3] , C.L.A. Lamont[3] and D.P. Woodruff[2]

[1] ***Fritz-Haber-Institut der MPG, Faradayweg 4-6, D 14195 Berlin, Germany***
[2]*Physics Department, University of Warwick, Coventry CV4 7AL, UK*
[3]*Centre for Applied Catalysis, Department of Chemical and Biological Sciences, University of Huddersfield, Queensgate, Huddersfield, HD1 3DH, UK*

There has been growing interest in the last few years in the properties of chiral molecules adsorbed on surfaces, motivated in part by the potential importance of producing molecular products of a single 'handedness' (enantioselective) by heterogeneous catalysis. In such studies a simple spectroscopic measurement, which could establish if the surface species (which may be unknown reaction intermediates) are predominantly of a single chirality, would be of great value. Conventional optical absorption measurements on sub-monolayer coverages of adsorbed molecules which exploit the circular dichroism (a difference in absorption for left- and right-circularly polarised radiation) are unlikely to be fruitful. However, spatially oriented chiral molecules, such as those adsorbed on a surface, should show circular dichroism in the angular distribution (CDAD) of photoelectrons emitted from these species [1, 2]. Indeed, such an effect has recently been observed [3] even for randomly oriented chiral molecules in the gas phase. We have therefore undertaken a CDAD investigation of the model system of alanine, or more strictly, alaninate, $NH_2CH_3HC^*COO^-$, (where the asterisk marks the chiral C centre) on Cu(110) to characterise this effect. Fig. 1 shows a schematic diagram of the local structure which this species is believed to adopt on this surface, while fig. 2 shows that photoemission from the 1s states of the three chemically-distinct C can be distinguished by chemical shifts. The inset shows the effect on this spectrum of opposite senses of circular polarisation of the incident radiation, recorded in a geometry which shows a large CDAD effect.

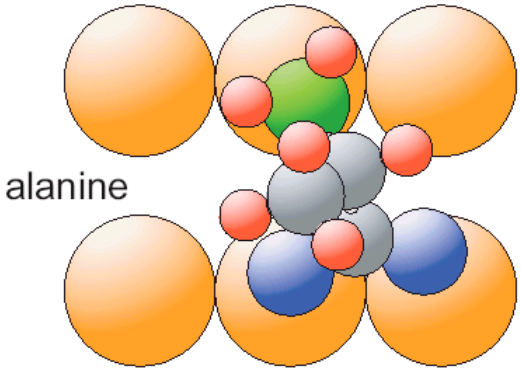

Fig. 1 Schematic plan view of the local structure of alanine on Cu(110) based on DFT calculations [4]

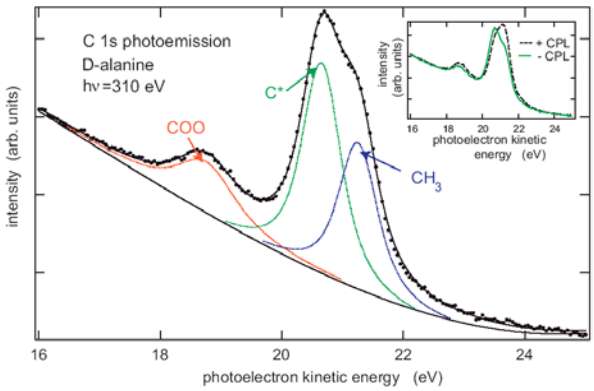

Fig. 2 C 1s photoelectron energy spectrum from alanine on Cu(110) showing the chemically shifted component peaks

One important complication in the CDAD experiment is that it is well known that dichroism is seen even for non-chiral samples if the experimental geometry is chiral. If the incident (circularly polarised) radiation and the electron detection are in a mirror plane of the substrate of the sample, however, the detected CDAD must arise only from the surface chirality. In order to distinguish these effects, therefore, measurements were made as a function of the azimuthal orientation of plane, defined by the incident and detection directions, relative to the crystal surface [5]. Fig. 3 shows the results for each of the two enantiomers of alanine.

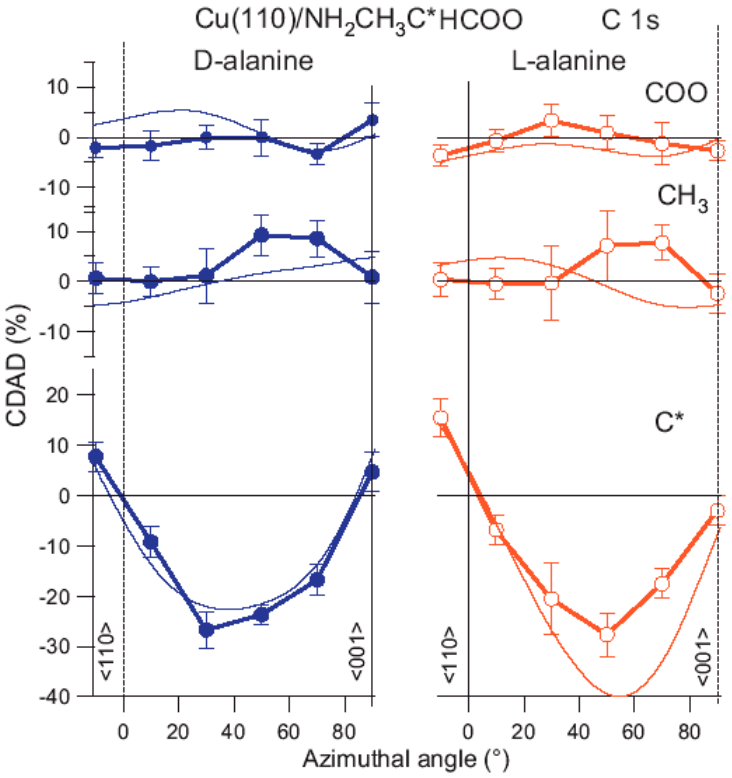

Fig. 3 Measured CDAD from the three chemically-distinct C 1s photoemission peaks of the two enantiomers of alanine adsorbed on Cu(110) as a function of azimuthal plane. The thin lines are the results of theoretical calculations.

The results of fig. 3 show clearly that the largest CDAD is for chiral experimental geometries out of the substrate mirror planes, an effect reasonably well described by model calculations. However, there is some weak residual CDAD in the substrate mirror planes which shows the expected sign reversal between the two enantiomers, for example in the <001> azimuth for both the C* and carboxyl (COO) emission. Further measurements show residual chiral-induced CDAD for both the N and O 1s photoemission, confirming the expectation that adsorption of the chiral molecule on the surface creates a situation in which *all* atoms are in a chiral environment. However, the effect due to the surface chirality is clearly weak, so it is far from clear that this effect can be used as a routine spectral fingerprint of surface chirality.

1 B. Ritchie, *Phys. Rev. A* **12**, 567 (1975); **13**, 1411 (1976)

2 N.A Cherepkov, *Chem. Phys. Lett*. **87**, 344 (1982)

3 U. Hergenhahn, E.E. Rennie, O. Kugeler, S Marburger, T. Lischke, I. Powis and G. Garcia, *J. Chem. Phys*. **120**, 4553 (2004)

4 R.B. Rankin and D.S. Sholl *Surf. Sci,* **574** (2005) L1

5 M. Polcik, F. Allegretti, D.I. Sayago, G. Nisbet , C.L.A. Lamont and D.P. Woodruff, ***Phys. Rev. Lett.* 92** (2004) 236103

Structure determination of formic acid reaction products on TiO_2(110)

D.I. Sayago[1], M. Polcik[1], R. Lindsay[2], R.L. Toomes[3], J.T. Hoeft[1], M. Kittel[1] and D.P. Woodruff[3]

[1] ***Fritz-Haber-Institut der MPG, Faradayweg 4-6, D 14195 Berlin, Germany***
[2]*Chemistry Department, Manchester University, Manchester M13 9PL, UK*
[3]***Physics Department, University of Warwick, Coventry CV4 7AL, UK***

The interaction of formic acid, HCOOH, with rutile TiO_2(110) surfaces has been studied extensively by a range of experimental and theoretical methods, and it well-established that dehydrogenation occurs to produce an adsorbed formate, HCOO-, species. The fate of the H atom removed in this process has been discussed rather little, but it seems that this probably bonds to a outermost layer O atom of the substrate to produce a hydroxyl, OH-, species, and there are theoretical studies which support this view. X-ray photoelectron diffraction (XPD) studies indicate the formate species is bonded with its molecular plane perpendicular to the surface in the [001] azimuth. A single O 1s chemical-state specific scanned-energy mode photoelectron diffraction (PhD) spectrum recorded in early experiments at the ALS was shown to be consistent with the results of a total-energy cluster calculation which indicated the formate bridges a pair of adjacent five-fold coordinated surface Ti atoms such that the O atoms are off-atop these Ti atoms [1]. However, this structure investigation was far from complete, and there is some evidence from NEXAFS [2] and vibrational spectroscopy [3] that a second formate geometry, azimuthally rotated by 90°, is co-occupied

.

We have now undertaken a true structure determination of this surface using chemical-state specific PhD from both the O 1s and C 1s photoemission, including measurements in a range of emission directions. The chemical shift in the O 1s photoelectron binding energy of the formate O atoms relative, to the substrate O atoms, allows us to extract structural information specific to the O atoms in the adsorbate species. Extensive tests of the possibility of two azimuthally-rotated formate geometries were made, but no evidence for any significant occupation of a second site was found, the results strongly favouring the same local site found in several total energy calculations and supported by the early PhD measurement. C 1s PhD spectra provide the most unambiguous evidence that there is only one azimuthally-oriented adsorbed formate species. However, we note that the O 1s chemical shift associated with the adsorbed formate species is essentially identical to that for a surface hydroxyl species, so the chemical-state specific adsorbate O 1s PhD spectra represent an incoherent sum of the PhD modulations of these two coadsorbed species. Based on this interpretation of the data we find a much-improved fit to the PhD spectra using our multiple scattering model calculations, which then allows us to determine the local adsorption geometry of both the adsorbed formate and adsorbed hydroxyl species [4]. Fig. 1 shows a side view of these local geometries. The formate species is aligned along the [001] bridging an adjacent pair of surface 5-fold-coordinated Ti atoms with the formate O atoms near-atop the Ti atoms and a Ti-O bondlength of 2.08±0.03 Å. The hydroxyl species are formed by H attachment to the

surface bridging O atoms and have a Ti-O bondlength of 2.02±0.05 Å, significantly longer than for the bridging oxygen atoms on a bulk-terminated surface or as previously reported for the clean surface.

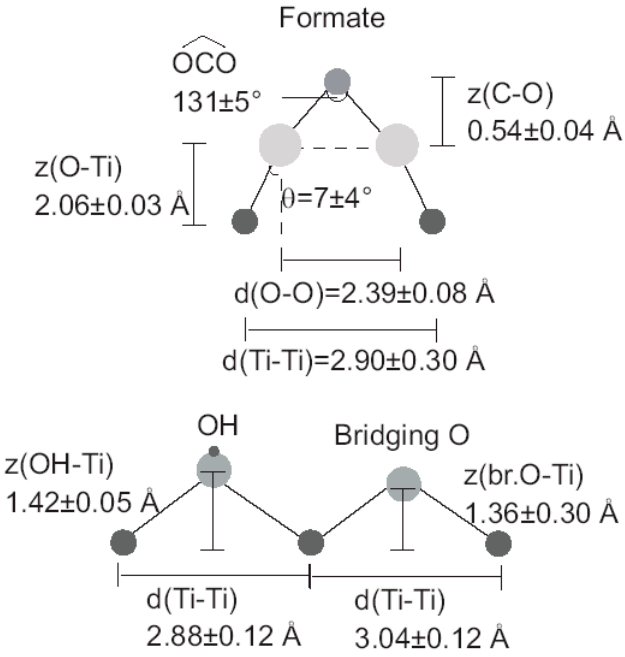

Fig. 1 Side views, in the [001] azimuth, of the local geometry of the adsorbed formate, HCOO-, and hydroxyl, OH-, species found in this study. The dark-shaded circles represent 5-coordinated Ti atoms in the TiO_2(110) surface. The larger circles represent O atoms. The small light-shaded circle is the C atom of the formate species. The H atom locations are unknown. Note that the poor precision for the height of the bridging O atoms, which are not bonded to H atoms, arises because the O 1s photoemission signal from these O atoms cannot be distinguished from that of sub-surface O atoms. The location of these atoms can therefore only be obtained from their weak influence on the scattering of photoelectrons emitted from the formate and hydroxyl O atoms.

1 S.A. Chambers, S. Thevuthasan, Y.J. Kim, G.S. Herman, Z. Wang, E.D. Tober, R.X. Ynzunza, J. Morais, C.H.F. Peden, K. Ferris and C.S. Fadley, *Chem. Phys. Lett.***267** (1997) 51

2 A. Gutiérrez-Sosa, P. Martínez-Escolano, H. Raza, R. Lindsay, P.L. Wincott and G. Thornton, *Surf. Sci.* **471** (2001) 163

3 B.E. Hayden, A. King and M.A. Newton, *J. Phys. Chem. B* **103** (1999) 203

4 D.I. Sayago, M. Polcik, R. Lindsay, J.T. Hoeft, M. Kittel, R.L.Toomes and D.P.Woodruff *J. Phys. Chem. B* **108** (2004) 14316

CO adsorption on Pt(355) and Pt(644) investigated by in-situ high resolution XPS – similarities and differences

B. Tränkenschuh, T. Fuhrmann, C. Papp, R. Denecke and H.-P. Steinrück
Lehrstuhl für Physikalische Chemie II, Universität Erlangen-Nürnberg,
Egerlandstr. 3, 91058 Erlangen

The CO adsorption on differently stepped platinum surfaces was studied in-situ using a combination of supersonic molecular beam and high-resolution x-ray photoelectron spectroscopy (HRXPS). The Pt(355) and Pt(644) surfaces are vicinal surfaces with five atom rows wide (111) terraces. The structural difference of the two surfaces is the orientation of the monatomic steps ((111) and (100), respectively). Due to the different step orientations the effective terrace width available for adsorbates is 4.33 and 4.66 rows, respectively.
The experiments were performed at beamline U49/2-PGM1, using a transportable apparatus described elsewhere[1]. It combines HRXPS with a supersonic molecular beam for gas dosing at varying pressures. C 1s spectra were acquired in-situ within 4 s, using synchrotron radiation of 380 eV with a resolution of 170 meV, while adsorbing CO.

Fig. 1 shows C 1s XP spectra of the CO background adsorption experiment ($p=1.8*10^{-9}$ mbar) on Pt(355) (panel b) and Pt(644) (panel c) at 130 K, until saturation is reached; for comparison the spectra for Pt(111) are shown in Fig. 1a. On both stepped surfaces, the peaks at 286.1 and 286.8 eV are assigned to bridge and on-top bound species on terraces, respectively; they have the same binding energy as on Pt(111)[2]. The smaller peak at 286.4 eV for Pt(355) is allocated to step adsorption[3]. In the case of Pt(644) there are two step sites distinguishable: step 1 at 285.8 eV and step 2 at 286.4 eV. Quantitative analysis by fitting an asymmetric Doniac-Sunjic function to each contribution shows that for both stepped surfaces the step adsorption sites are occupied first, followed by on-top and bridge bonded species. As thermal equilibrium in the site occupation is reached at 130 K [2], this indicates a higher molecular binding energy on the steps as compared to the terrace sites. In both cases, the step adsorption amounts to about 1/5 of the total coverage, as expected from surface geometry.

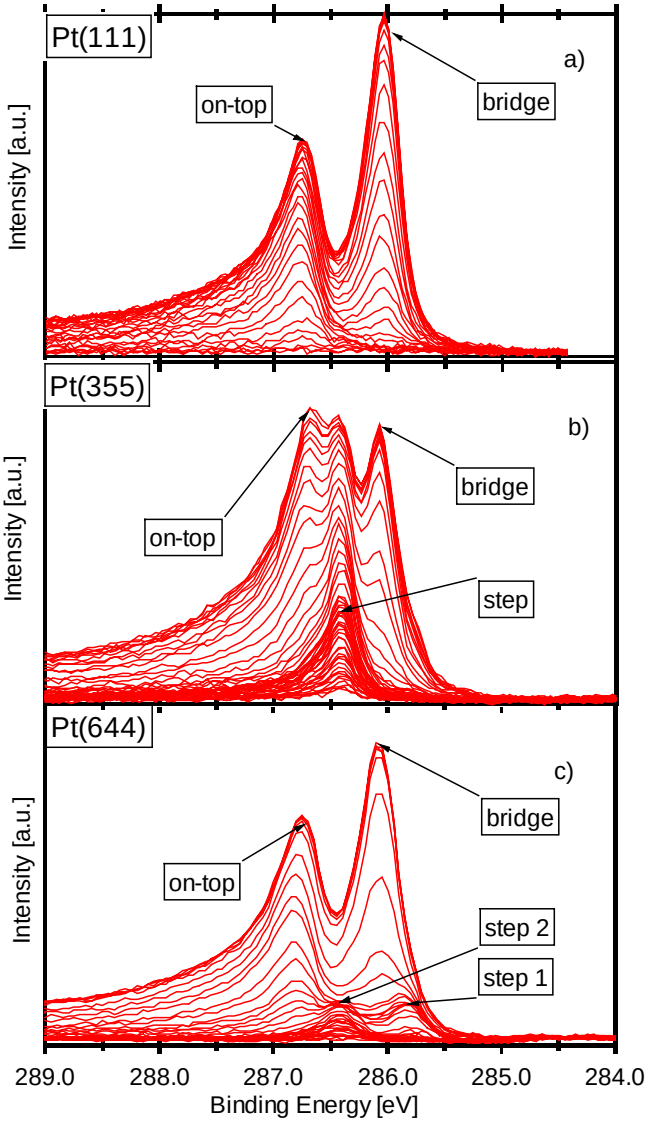

Fig. 1: C 1s XP-spectra of CO background uptake at low temperatures (109 – 130 K) with p = $1.8*10^{-9}$ mbar on (a) Pt(111), (b) Pt(355) and (c) Pt(644).

Despite a naively expected similarity in the behavior of the adsorption sites on the terraces and on Pt(111), it seems interesting to study the terrace adsorption behavior in detail.

In Fig. 2, the partial coverages of on-top and bridge bonded species are plotted versus normalized total coverage (a) and normalized terrace coverage (b,c), for better comparison. In all three cases the on-top sites are occupied first, but the shapes of the curves are quite different. For Pt(111), occupation of bridge sites starts at the highest coverage of all three surfaces, and for high relative coverages ($\theta_{Total}/\theta_{Total*}$ ~0.9) the ratio of on-top/bridge reaches one. At a surface temperature of 200 K the total absolute coverage of CO is 0.5 ML, with on-top and bridge sites both having a coverage of 0.25 ML, which corresponds to a c(4x2) LEED pattern. For Pt(644), the ratio of one for on-top to bridge occupation was also reached at about the same $\theta_{Total}/\theta_{Total*}$ -value; for this surface at 200 K a very similar LEED pattern was observed. In contrast, no LEED pattern could be found for Pt(355), in agreement with the fact that no 1:1 site distribution is observed. The variations in the coverage-dependent behaviour are attributed to the effective differences in molecular binding energy of these two adsorption sites, being different due to changed adsorbate-adsorbate interactions. Thus, the CO adsorption behavior on Pt(644) is closer to Pt(111) than that on Pt(355), although the stepped surfaces have nominally a very similar terrace width. This is also reflected in the absolute value of the total coverage, being similar for Pt(644) and Pt(111) (both reaching about 0.5 ML at 200 K), but smaller for Pt(355).

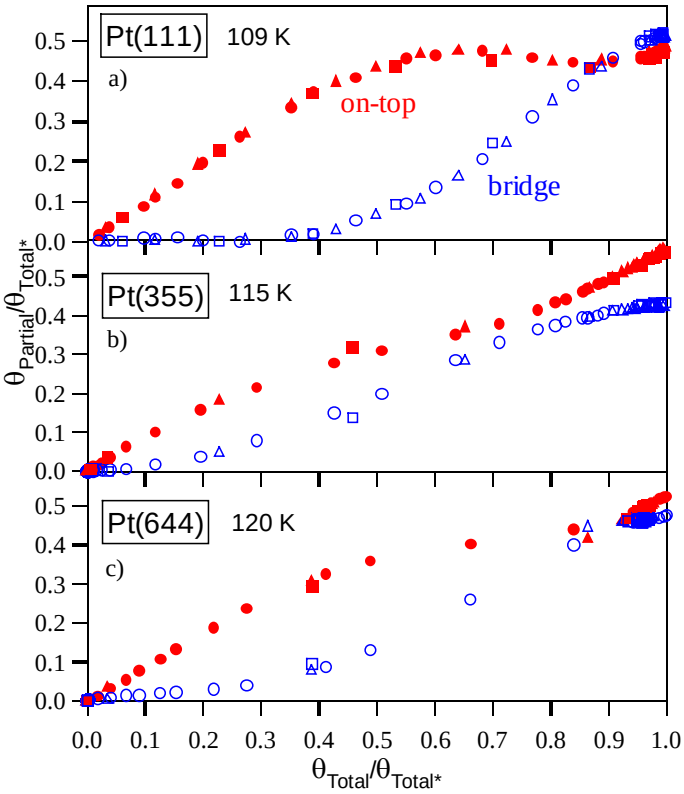

*Fig. 2:.Coverages of on-top (red symbol) and bridge (blue symbol) are plotted vs. the normalized total coverage for pressures of 1.8*10^{-9} (●○), 5.3*10^{-8} (▲△) and 4*10^{-7} mbar (■□) in a) for Pt(111), in b) for Pt(355) and in c) for Pt(644).*

As can be seen in Fig. 2 for all surfaces, the curve shapes obtained for all investigated CO pressures are the same, showing thermal equilibrium in the site occupation, even at low temperatures.

This work was supported by DFG (STE 620/4-2).

[1] R. Denecke, M. Kinne, C. M. Whelan, H.-P. Steinrück, *Surface Review and Letters* **2002**, 9, 797.

[2] M. Kinne, T. Fuhrmann, C. M. Whelan, J. F. Zhu, J. Pantförder, M. Probst, G. Held, R. Denecke, H.-P. Steinrück, *Journal of Chemical Physics* **2002**, 117, 23.

[3] J. S. Luo, R. G. Tobin, D. K. Lambert, G. B. Fisher, C. L. DiMaggio, *Surface Science* **1992**, 274, 53.

Ethane on Pt(111)- An investigation using in-situ XPS combined with a molecular beam

T. Fuhrmann, M. Kinne, B. Tränkenschuh, J.F. Zhu, R. Denecke and H.-P. Steinrück
Lehrstuhl für Physikalische Chemie II, Universität Erlangen-Nürnberg

The investigation of the adsorption process as the initial step in heterogeneous catalysis is expected to lead to deeper insight into surface reactions. For the smaller saturated hydrocarbons, like methane and ethane, dissociative adsorption is well known at temperatures, where no physisorption occurs. To study this dissociative adsorption process for ethane, only integral methods have been used in the past. By combining a supersonic molecular beam and high resolution XPS, we were now able to not only follow the adsorption behaviour of ethane on Pt(111) in situ, but also to determine the chemical nature of the adsorbed species. In order to study the thermal evolution of the adsorbed species, continuous data aquisition has been performed while heating the crystal with a linear heating ramp (TPXPS).

The experimental setup has been described elsewhere [1]. A seeded beam of ethane in helium, generated by a heatable nozzle (Mo, Ø=100 µm), is impinging normal to the surface. Using a photon energy of 380 eV at the beamline U49/2-PGM1 and an aquisition time of 8 s per spectrum, an overall resolution of ~160 meV was achieved in the XPS measurements.

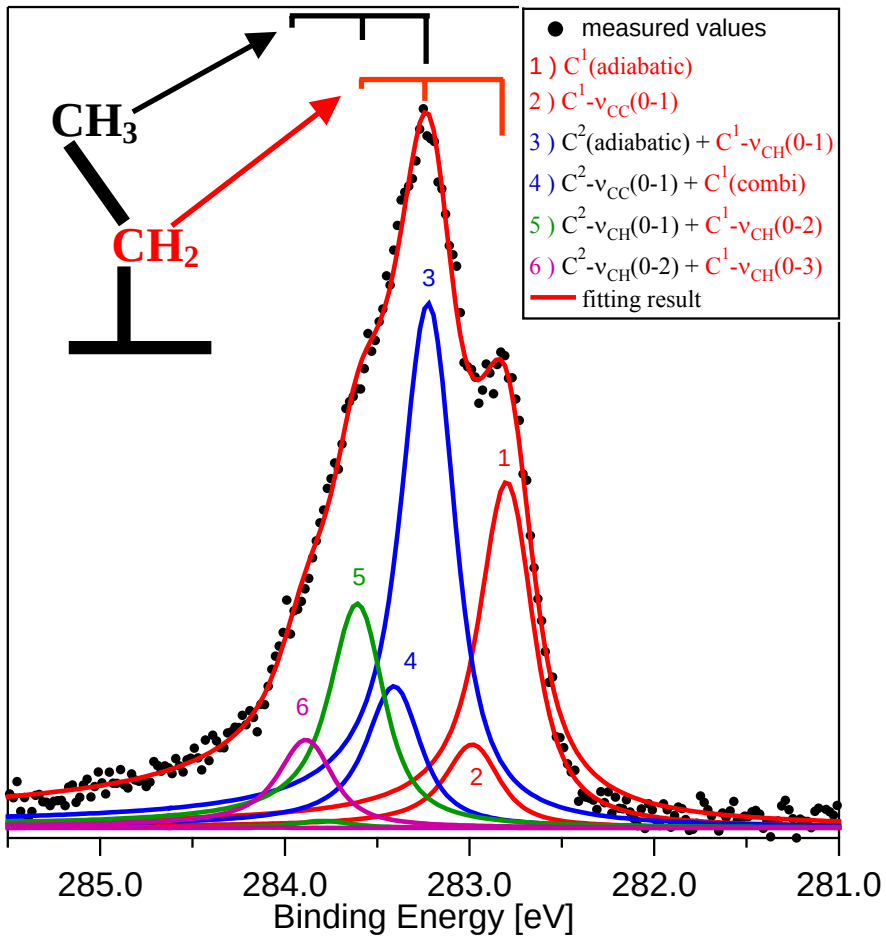

Fig. 1: C 1s spectrum of ethyl on Pt(111) at 140 K. The kinetic energy of 0.54 eV was generated by seeding 7% ethane in helium at 773 K nozzle temperature. Included is the deconvolution into vibrationally splitted components.

Measurements with different kinetic and vibrational energy of the molecules impinging on the surface show no change in the chemical nature of the adsorbed species. A typical C 1s spectrum, which was obtained using a nozzle temperature of 773 K and 7% ethane seeded in helium, resulting in a kinetic energy of 0.54 eV, is shown in Fig. 1. A surface temperature of 140 K has been used to avoid physisorption, that is observed at 100 K due to the high local pressure of the molecular beam. The adsorbed species is identified as ethyl (C_2H_5). For the two non-equivalent C-atoms (C^1 and C^2) a superposition of two distinct carbon signals, each including vibra-

tional splitting is expected. Gas phase measurements of ethane show a vibrational splitting of 404 meV for the C-H stretching mode and 185 meV for the C-C stretching mode [2]. Each main peak in Fig. 1 is, therefore, accompanied by two peaks due to C-H excitation, $\nu_{CH}(0\text{-}1)$ and $\nu_{CH}(0\text{-}2)$, one due to C-C excitation, $\nu_{CC}(0\text{-}1)$, and a combination mode. All peaks are fitted using Doniach-Sunjic line shapes with parameters from gas phase data [2]. The higher intensity of the second main peak is explained by the superposition of the adiabatic peak of the CH_3 group (C^2) and the first excited peak of the CH_2 group (C^1), which appear at the same binding energy in the spectrum. This leads to a peak separation of 425 ± 10 meV for the two main peaks, which are found at 282.79 and 283.21 eV.

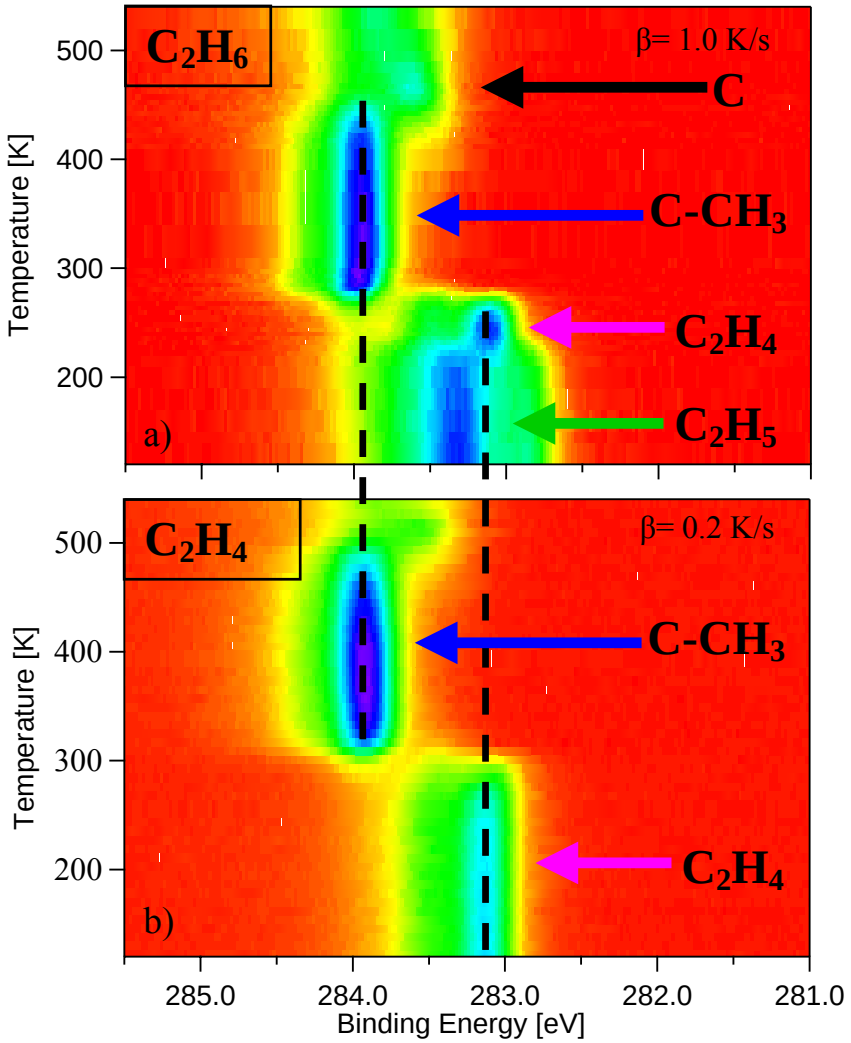

Fig. 2: Colour-coded TPXPS density plots of (a) ethyl and (b) ethylene. Blue shows high intensity, red low intensity.

Evaluating the adsorption behaviour shows a strong dependence of the initial sticking coefficient and the saturation coverage on the kinetic energy, as was also observed for methane on Pt(111) [3].

To study the thermal evolution of the adsorbed ethyl species, TPXPS has been performed, by taking a spectrum about every 10 K. The result is shown as colour-coded density plot in Fig. 2a. In order to identify the formed intermediates, we performed a comparable experiment also for ethylene, were ethylidyne is known as an intermediate [4] - see Fig. 2b. The comparison shows that the first intermediate in the decomposition of ethyl is ethylene (C_2H_4), which is observed at around 240 K. The small temperature range of its existence requires (continuous) TPXPS instead of measurements after stepwise annealing. As the next step in the thermal evolution of ethyl, the formation of ethylidyne (CCH_3), appearing at 260 K, can be noticed. Thereafter, starting at about 350 K, the complete dehydrogenation to carbon takes place. Due to the high resolution in XPS, the various intermediates are additionally identified by their vibrational fine structure.

This work was supported by DFG (Ste620/4-2).

[1] R. Denecke, M. Kinne, C.M. Whelan, H.P. Steinrück, Surf. Rev. Lett. 9 (2002) 797.
[2] S.J. Osborne, S. Sundin, A. Ausmees, S. Svensson, L.J. Saethre, O. Svaeren, S.L. Sorensen, J. Vegh, J. Karvonen, S. Aksela, A. Kikas, J. Chem. Phys. 106 (1997) 1661.
[3] T. Fuhrmann, M. Kinne, B. Tränkenschuh, C. Papp, J.F. Zhu, R. Denecke, H.-P. Steinrück, New J. Phys., submitted.
[4] N. Sheppard, C. De La Cruz, Adv. Catal. 41 (1996) 1.

Selective gas-phase hydrogenation of C-5 hydrocarbons using palladium and nickel based catalysts

D. Teschner, A. Knop-Gericke, E. Vass, S. Zafeiratos, A. Pestryakov, E. Kleimenov, M. Hävecker, H. Bluhm, R. Schlögl
Fritz-Haber-Institut der Max-Planck-Gesellschaft, Faradayweg 4-6, D-14195 Berlin

Aim of the work and scientific background:

Heterogeneous catalysis plays an essential role in the field of chemistry and in chemical manufacturing. The complexity of a catalytic process usually requires that chemistry and engineering intimately mix to deliver the desired effect. The research project Athena (Advanced technology in catalytic chemistry and engineering for novel application) is a joint collaboration of Fritz-Haber-Institute and several British and American institutions presenting a multi-disciplinary approach to investigate heterogeneous catalytic reactions. The aim of *this* project is to investigate Pd and Ni based catalysts in the hydrogenation of C5 molecules containing different functionalities. A focal point of the activities concerns the relationship between selectivity and catalyst properties like structure, shape, carbonaceous deposits and possible support induced effects. Our group attempts to identify the electronic structure of the catalytic system, the role of carbon (deposit and/or incorporated in the bulk) as selectivity inducing co-catalyst [1] and recognizes the role of subsurface hydrogen [2,3] as modifier for chemisorption/electronic structure. For these purpose single crystals, foils and supported catalysts are used and studied by surface sensitive techniques like XPS and NEXAFS. These measurements are performed *in-situ* as this is the only way to gain information about a catalyst in the working state. Our novel *in-situ* XPS (and NEXAFS) set-up based on differentially pumped electrostatic lens-system is well suited for the experiments. This report summarizes the results obtained during the measurements at BESSY.

Results

Hydrogenation of trans-2-pentene (t-2-p) was observed on polycrystalline Pd foil (RT and 100 °C), but not on Pd(111) single crystal [4]. We observed the reaction in the presence of a significant amount of carbon (more than 60 %) in the information depth of ~ 1 nm. On Pd(111) mainly graphite was present while other components, *C–H* (chemisorbed species) and *C–Pd* (interface carbon), were also formed on the foil to a greater extent. The d-band of the foil showed a remarkable up-shift towards E_{FERMI} as compared to Pd(111). The palladium foil lost its activity at elevated temperature (250 °C), most probably due to desorption of hydrogen. Using additional UPS measurements on adsorbed trans-2-pentene we concluded that t-2-p reacts with hydrogen in σ-bonded chemisorption modus, at least in UHV conditions.

In the hydrogenation of 1-pentyne the palladium samples were examined by XPS and an industrial nickel/alumina catalyst by XAS (because of charging no XPS was possible). On the palladium samples the selectivity towards single hydrogenation is high. Lower temperature enhances the total hydrogenation selectivity on the supported samples. Very low total hydrogenation was found on Pd foil, and no pentane was observed on Pd(111). Bulk palladium tends to hinder total hydrogenation. The single crystal was not inactive in single hydrogenation, as in the t-2-pentene case, however its activity was at least three times lower than that of polycrystalline foil. Palladium 3d (5/2) core level of a 5% Pd/carbon-nanotubes shows an adsorbate induced state (BE: ~335.5-335.6 eV) evolving at the high-BE side of the bulk Pd3d after introducing the reaction mixture (*Figure 1*). Its intensity increases with increasing temperature to 85 °C, at which temperature maximum activity is observed. A similar trend was found with the polycrystalline foil sample, as well. Depth-profiling experiment with the planar foil sample using different photon energies clearly indicates that this new state is surface related (*Figure 2*). With the single crystal this signal was weak. The Pd3d surface state correlates well with the catalytic activity. Heating up the foil to 250 °C, the catalytic activity, as well as this Pd 3d feature diminished. By the heating, the carbon content is not significantly altered, thus the loss of the Pd3d component cannot be correlated with the total carbon content. Desorption of surface hydrogen at higher T is the reason of the loss of activity.

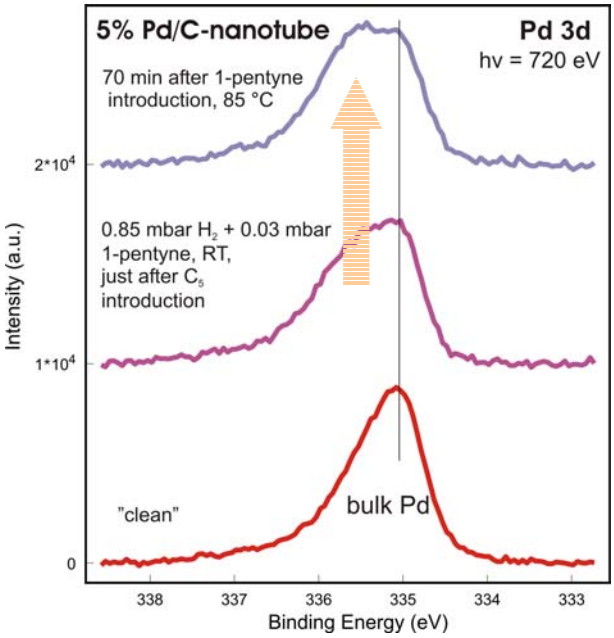

Figure 1: Pd3d of 5% Pd/CNT at different conditions

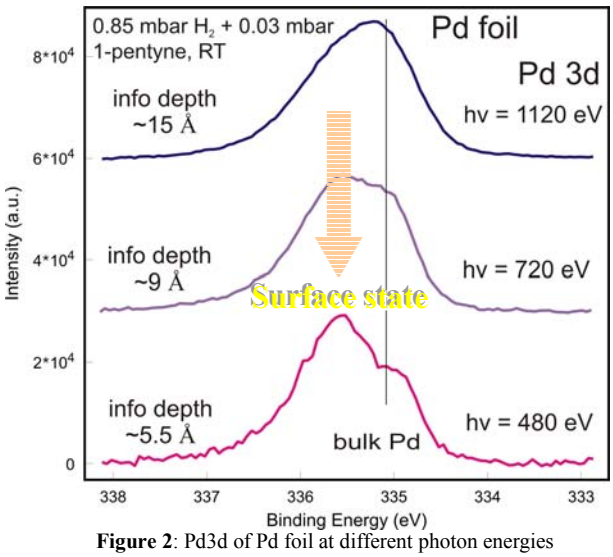

Figure 2: Pd3d of Pd foil at different photon energies

A significant amount of subsurface carbon was found from the depth profiling experiments (*Figure 3*) as the carbon content showed a maximum curve as a function of photoelectron kinetic energy (i.e. inelastic mean free path). Carbon in subsurface position blocks the way of

hydrogen entering the surface from the bulk. This hydrogen has a higher energy compared to surface hydrogen [2] therefore it is less selective. The lower total hydrogenation thus is in good accord with the blocking role of subsurface carbon species.

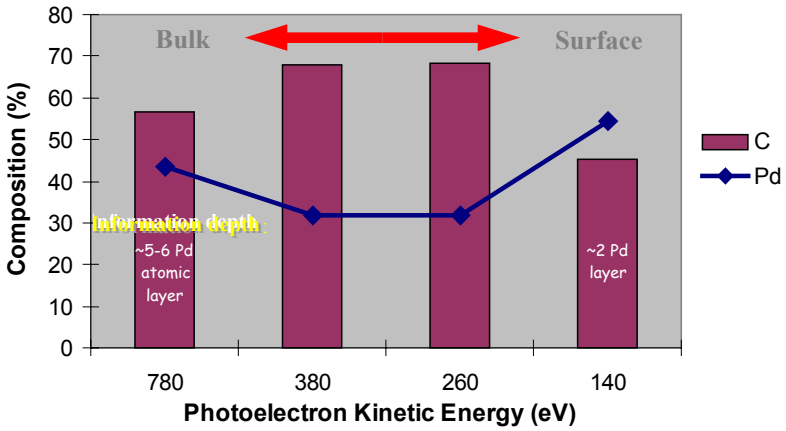

Figure 3: Elemental composition during depth-profiling experiment on Pd foil

The palladium β-hydride state was also investigated [5]. The palladium 3d core level is changed compared to clean Pd; the peak is shifted slightly (~ +0.15 eV) to higher binding energy and the asymmetry of the peak is much less. Therefore the palladium surface state (335.5 eV Pd3d component) during the catalytic experiment is not a hydride-induced state. The valence band measured at 150 eV photon energy reveals a broad hydrogen induced band between ~ 4-9 eV.

The nickel sample was active (mainly single hydrogenation) after low T redox (O_2 followed by H_2) treatment, although the Ni $L_{3,2}$ edge revealed clearly oxidic Ni (NiO). As the information depth of XAS is approx. the same as the mean particle size and as the reaction is not expected to proceed on oxides, the top surface layer of the NiO is most probably metallic. After high T redox treatment (500 °C) the sample was approx. twice as active and Ni was metallic. Moreover, the selectivity towards total hydrogenation increased as well. Hydrogen is known to readily dissolve in the bulk of metallic Ni particles. As a consequence, the NiO core of the particles played a similar role as subsurface carbon in Pd, namely avoiding the participation of high-energy hydrogen in the hydrogenation, thus increasing selectivity.

Acknowledgement

The authors thank the BESSY staff for their continual support during the measurements. The work was supported by the Athena Consortium.

References

1 N. Keller, N. Maksimova, V. V. Roddatis, M. Schur, G. Mestl, Y. V. Butenko, V.L. Kuznetsov, R. Schlögl, *Angew. Chem. Int. Ed.* **41** (2002) 1885.
2 S. T. Ceyer, *Acc. Chem. Res.* **34** (2001) 737.
3 Sh. Shaikhutdinov, M. Heemeier, M. Bäumer, T. Lear, D. Lennon, R. J. Oldman, S. D. Jackson, H.-J. Freund, *J. Catal.*, **200** (2001) 330.
4 D. Teschner, A. Pestryakov, E. Kleimenov, M. Hävecker, H. Bluhm, H. Sauer, A. Knop-Gericke, R. Schlögl, *J. Catal.*, (Part II) **in press**
5 D. Teschner, A. Pestryakov, E. Kleimenov, M. Hävecker, H. Bluhm, H. Sauer, A. Knop-Gericke, R. Schlögl, *J. Catal.*, (Part I) **in press**

Deprotonation-driven phase transformations in terephthalic acid self-assembly on Cu(100)

S. Stepanow[1], M. Lingenfelder[1], A. Dmitriev[1], N. Lin[1], J.V. Barth[2,3], K. Kern[1,2]

[1]Max-Planck-Institut für Festkörperforschung, Stuttgart, [2]Institut de Physique des Nanostructures, Ecole Polytechnique Fédérale de Lausanne, [3]Advanced Materials and Process Engineering Laboratory, University of British Columbia

Th. Strunskus, Ch. Wöll

Lehrstuhl für Physikalische Chemie I , Ruhr-Universität Bochum

Self-assembled terephthalic acid adlayers on a Cu(100) surface have been studied by X-ray photoelectron spectroscopy, near-edge X-ray absorption fine structure and scanning tunneling microscopy in the temperature range 190 - 400 K under ultra-high vacuum conditions. We observed three distinct well-ordered phases evolving with increasing temperature. The combined data analysis reveals that thermally activated deprotonation of molecular carboxyl groups is decisive in the irreversible transformation of the respective structures. Their self-assembly is mediated by changing intermolecular hydrogen bond configurations, whereby a flat adsorption geometry is retained.

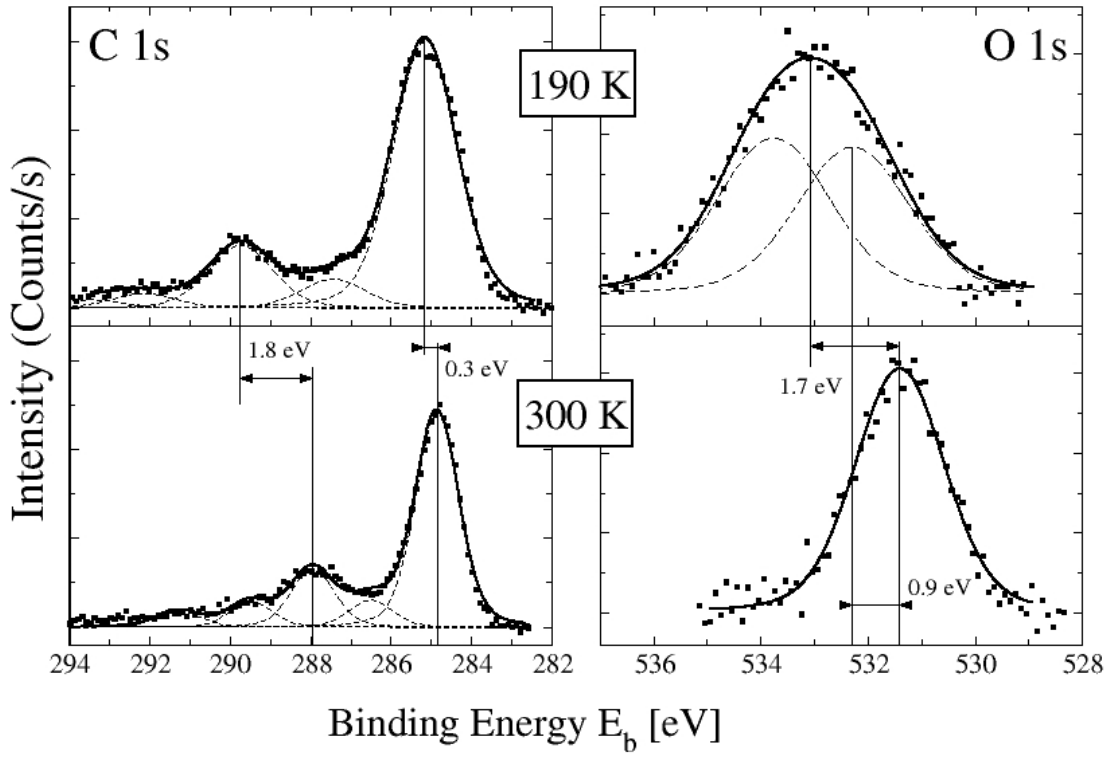

XP spectra of the C 1s and O 1s for a TPA layer prepared at 190 K (upper graphs) and following annealing at 400 K for 30 min (measured at room temperature, lower graphs). The data (squares) have been fittet by a set of one to six Voigt-type curves. The fwhm parameters for the Voigt-curves in the O 1s region are 2.47 eV and 1.98 eV for the substrate at low and room temperature, respectively. Peak positions are marked by vertical lines. The deconvolution of the broad low-temperature oxygen peak reflects the two chemically different carboxyl oxygen, while the sharpened peak appearing upon annealing is associated with equivalent oxygen in the diterephthalate species. The larger low-energy peaks in C 1s are from aromatic carbon and the smaller high-energy peaks are attributed to carbon of carboxyl and carboxylate side groups, respectively.

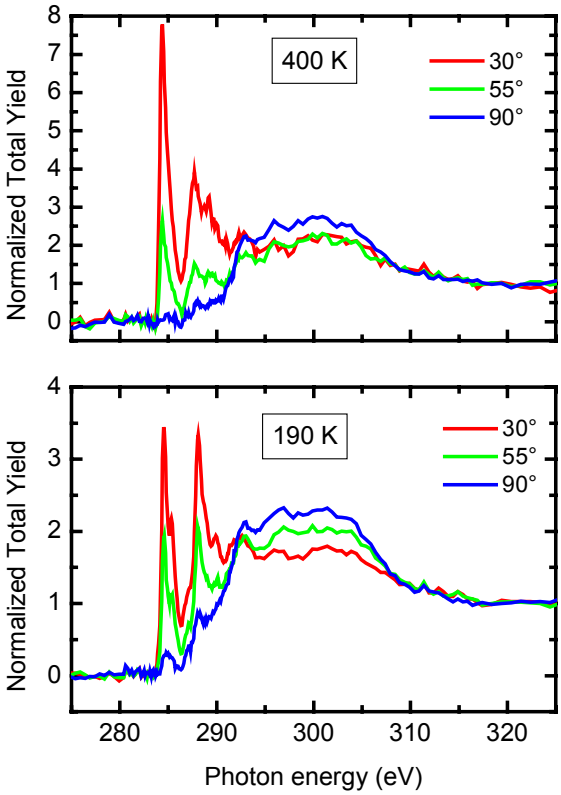

NEXAFS spectra recorded at the C K-edge for a TPA monolayer prepared at 190 K (lower graph) and after annealing at 400 K for 30 min (measured at room temperature, upper graph). Solid and dashed lines indicate spectra obtained at different angles of incidence of the synchrotron light (90° means normal incidence to the Cu(100) surface). These data show furthermore unambiguously that both the integral molecule and the terephthalate species adsorb essentially in a flat-lying geometry. The deprotonation of the carboxylic groups upon changing the temperature from 190 K to 300 K leads to the pronounced changes of the C1s->π*-resonances located around 288 eV. Whereas the phenyl C1s->π*-resonances at around 285 eV remain essentially unchanged.

Investigation of styrene production over carbon catalysts using high-pressure XPS.

J.A. Maciá-Agulló, D. Cazorla-Amorós, A. Linares-Solano, M. Hävecker*, D. Teschner*, E. Kleimenov*, A. Knop-Gericke*, R. Schlögl*.
Dpto. Química Inorgánica, Universidad de Alicante, Apartado 99, E-03080 Alicante, Spain.
**Fritz-Haber-Institut der Max Planck Gesellschaft, Abteilung Anorganische Chemie, Faradayweg 4-6, D-14195 Berlin, Germany.*
Project number: BESSY-ID.04.1.015 User contract: BI3A-15/210604

Introduction.

High-pressure in situ X-ray photoelectron spectroscopy is a useful technique for the elucidation of active phases under reaction conditions [1]. Our reaction of interest was the oxidative dehydrogenation (ODH) of ethylbenzene to styrene:

$$C_6H_5C_2H_5 \text{ (ethylbenzene)} + ½\ O_2 \rightarrow C_6H_5C_2H_3 \text{ (styrene)} + H_2O$$

This is an important process in the petrochemical industry. It is well known that carbon materials such as activated carbons [2], activated carbon fibres, carbon blacks and more recently carbon nanotubes and onion-like carbons are good catalysts in the oxidative dehydrogenation of ethylbenzene to styrene. In the literature, it is speculated that carbonyl and quinone groups play the role of active phase in the oxidative dehydrogenation [3,4] and recent results at a pressure of 1 atm [5] support this idea. The previously mentioned experiments [5] (quasi in-situ) are not real in-situ experiments because the sample was analyzed after reaction but no during reaction. The goal of the proposed experiments was to obtain photoemission spectra of a catalyst's surface under working conditions and it must be pointed out the novelty of the experiments performed, it is the first time that this type of experiments has been applied to the oxidative dehydrogenation of ethylbenzene to styrene.

Experimental.

In the present study, we employed different carbon materials to study changes on the surface during oxidative dehydrogenation of ethylbenzene to styrene by high pressure XPS. The samples used were: a graphite (DFP-1, Poco Graphite), DFP-1 oxidized by HNO_3 (65%), carbon fibres (Donacarbo S-241, Osaka gas Co., Ltd) oxidized by nitric acid, activated carbon fibres and activated carbon fibres oxidized by nitric acid. The catalytic activity of the different samples was measured by a quadrupole mass spectrometer and a proton-transfer reaction mass spectrometer (PTR) coupled to the XPS equipment. Temperature ranged from 325 to 500ºC, being 325ºC the most widely-used temperature. A stoichiometric molar ratio of ethylbenzene/O_2 = 2 and a total pressure of 0.25mbar were employed. The energies of the photons were calibrated by calculation of the Fermi level of a gold film. Samples mainly contained carbon and oxygen, and some of them contained also nitrogen. In order to separate the gas phase and surface contributions to the C1s and O1s peaks, a potential of 150V was applied to the nozzle.

Results and discussion.

In spite of the high pressure employed (0.25mbar) and the subsequent attenuation of the XPS signal, XPS spectra with a good intensity were obtained.

All the above-mentioned samples showed some styrene production, the higher the surface area and oxygen functional groups content, the higher was the styrene production. Results for the graphite DFP-1 oxidized by HNO_3 are shown as a representative example of the experiments carried out. Sample was mounted in the reaction chamber and it was heated up to 400ºC in vacuum losing an important amount of oxygen on the surface.
Figure 1 shows the response of the quadrupole mass spectrometer for the m/e = 104 (related to styrene) versus time and at different temperatures (400 and 500ºC). Oxidative dehydrogenation starts at around 320ºC and increases with reaction temperature. Therefore styrene production at 0.25mbar is proved.

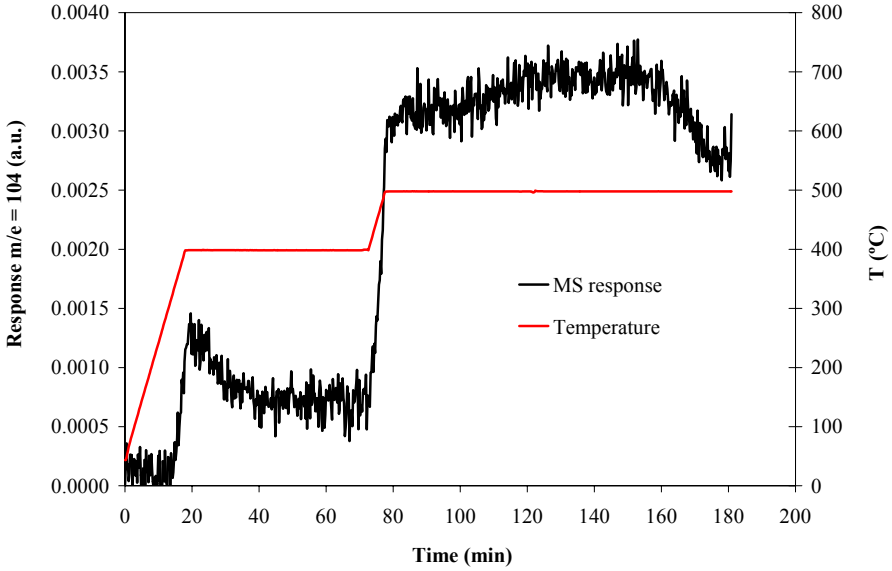

Figure 1. MS response for m/e = 104 with time and temperature.

Figures 2a and 2b contain O1s spectra of the sample under different reaction conditions. A Shirley type background has been used and the intensity has been normalized to the beam intensity. XPS spectra areas have been corrected considering that C1s peaks have the same area in order to compare O1s peaks directly.

It can be observed that the sample under an atmosphere of ethylbenzene (Eb) and O_2 at 70ºC (orange line) has a high amount of oxygen groups on the surface. After, heating the sample up to 400ºC (black line), oxidative dehydrogenation of ethylbenzene to styrene takes place and a pronounced decrease in the O1s peak is observed. Oxygen groups at around 530eV are practically not affected and, on the contrary, the rest of the groups decrease considerably. This fact can be explained by desorption of oxygen groups and by chemical transformation of oxygen groups in presence of O_2. When the temperature of the ODH reaction is increased until 500ºC and kept constant for a period of time (blue and red lines), the peak at around 533eV decreases, the peak at around 530eV is shifted to lower binding energies and the intensity increases with increasing the reaction time. The decrease of the peak at 533eV can be ascribed to a stronger oxidation of groups C-O towards C=O (530eV). In the same way, long reaction time (red line) favours oxidation of oxygen groups and increases the peak at 530eV at the expense of the peak at 533eV. After that, the sample was heated in vacuum at 500ºC for several minutes and, then, O_2 was introduced at 500ºC (grey line). As it can be observed, O_2 atmosphere produces a higher amount of oxygen groups at around 533eV than ODH at the same temperature but after a shorter period of time. It seems that the aforesaid groups (carbonyl) are involved in the ODH reaction. In agreement with previous results at 1 atm [5], there are mainly two peaks involved (530 and 533eV) in the ODH.

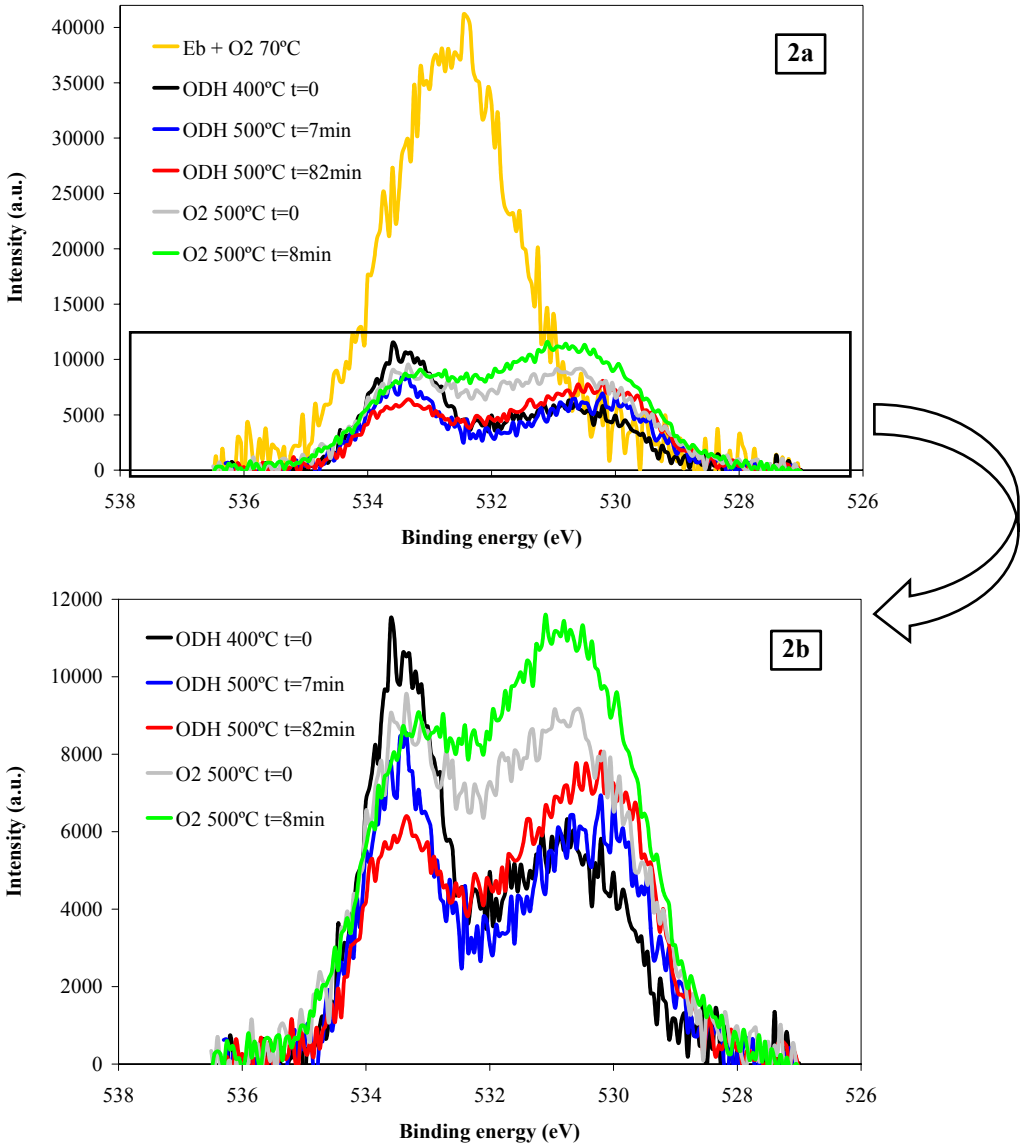

Figures 2a & 2b. XPS O1s spectra under different atmospheres and temperatures of the graphite DFP-1 oxidized by HNO_3.

Acknowledgements.

The authors gratefully acknowledge the financial support through the BESSY-EC-I3 Contract No. RII 3-CT-2004-506008.

References.

[1] M. Haevecker, R. W. Mayer, A. Knop-Gericke, H. Bluhm, E. Kleimenov, A. Liskowski, D. Su, R. Follath, F. G. Requejo, D. F. Ogletree, M. Salmeron, J. A. Lopez-Sanchez, J. K. Bartley, G. J. Hutchings, R. Schloegl. Journal of Physical Chemistry B. 2003;107(19): 4587-4596.

[2] M. F. R. Pereira, J. J. M. Órfão, J. L. Figueiredo, Appl. Catal. A. 1999;184:153-160.

[3] Y. Iwasawa, H. Nobe, S. Ogasawara. Journal of Catalysis 1973;31:444-449.

[4] L. E. Cadus, L. A. Arrua, O. F. Gorriz, J. B. Rivarola, Ind. Eng. Chem. Res. 1988;27:2241-2246.

[5] J. A. Maciá-Agulló, D. Cazorla-Amorós, A. Linares-Solano, U. Wild, D. S. Su, R. Schlögl. Catalysis Today, accepted.

Combined *in situ* XPS and *in situ* soft XAS study of Cu/ZnO catalysts for methanol steam reforming

M. Hävecker, B.L. Kniep, E. Kleimenov, P. Schnörch, D. Teschner, S. Zafeiratos,
H. Bluhm, A. Knop-Gericke, T. Ressler, R. Schlögl
Fritz-Haber-Institut der MPG, Faradayweg 4-6, D-14195 Berlin (Dahlem), Germany

Introduction

Copper-zinc oxide (alumina) catalysts have found industrial use for the low temperature methanol synthesis, for the low temperature water-gas shift reaction, and for the steam reforming of methanol following the reaction [1]: $CH_3OH + H_2O \rightarrow 3H_2 + CO_2$. An important application could be the onboard production of hydrogen for fuel cell application. It is the proposed synergistic effect in the binary copper/zinc oxide that makes this system interesting for investigation [2]. The knowledge of the relationship between the catalytic activity, surface structure, and bulk structure is necessary in order to elucidate synthesis pathways to new and improved catalysts. Obviously, the surface properties play a decisive role for the understanding of a catalyst. Here, we report on a combined *in situ* X-ray photoelectron spectroscopy (XPS) and *in situ* soft X-ray absorption spectroscopy (XAS) study of the surface of differently prepared Cu/ZnO catalysts under activation conditions (H_2, 250 °C) and under methanol steam reforming reaction conditions (H_2O/CH_3OH, 250 °C), i.e. under the presence of a reactive environment. Using the unique properties of synchrotron radiation, the depth sensitivity of XPS was tuned from the outermost surface layer to deeper layers without destruction of the material. Furthermore, the dynamics of the surface were studied by taking fast, single scans, i.e. temperature programmed reduction/reaction (TPR)-XPS (see Fig. 3).

Experimental

Cu/ZnO catalysts (molar ratio Cu:Zn = 70:30) were prepared by co-precipitation of mixed copper zinc hydroxy carbonates at constant pH = 7 (denoted CAT). Additionally, material was synthesized by separate precipitation of the hydroxy carbonates for comparison (denoted MIX). The precipitates were aged under constant stirring in their mother liquor for different times (0 min – 120 min). The resulting precursors were washed (80 °C, 80 ml H_2O), dried (110 °C, 20 h) and calcined (330 °C, 3 h, static air) under the same conditions. Zn2p/3p, Cu2p/3p, O1s, C1s XP core level spectra were taken in a temperature range of 25 °C – 250 °C in the presence of 0.25 mbar H_2 and in the H_2O/CH_3OH reaction mixture (p_{tot}=0.25 mbar), respectively. Cu $L_{2,3}$ - and Zn $L_{2,3}$ - near edge X-ray absorption fine structure (NEXAFS)

spectra were taken under these conditions as well. Synchrotron radiation delivered by the undulator U49/2 at the storage ring BESSY was used. Changes in the gas phase composition were monitored by on-line mass spectrometry simultaneously to the spectroscopic characterization of the catalyst surface (compare to Fig. 3).

Results

We found that the reduction process of the catalyst is crucial for its structure under methanol steam reforming conditions. A sequential two-step reduction process at the surface ($CuO \rightarrow Cu_2O \rightarrow Cu$) was observed. The Zn3p/Cu3p core level intensity ratio altered strongly during the reduction in H_2. In the first reduction step ($CuO \rightarrow Cu_2O$), an increase was observed. Further reduction caused a decrease of this intensity ratio. This observation stresses the dynamic behavior of the surface and the presence of strong surface modifications during the activation process.

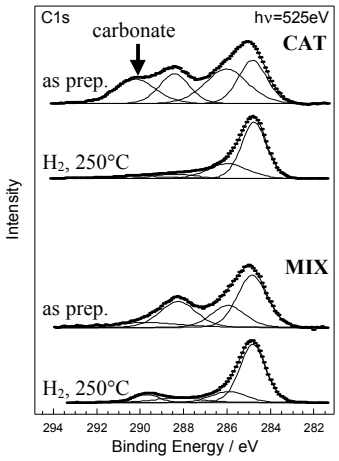

Fig. 1: C1s core level spectra of the co-precipitated material (CAT) and the separate precipitated material (MIX) before the activation in H_2 and after the treatment.

Residual carbon species (carbonates and others) were observed on the surface even after prolonged calcination in air (Fig. 1). The Zn L_3-NEXAFS indicates the presence of a zinc species different to ZnO by the occurrence of a resonance at the onset of the absorption edge ("A" in Fig. 2). This modification is likely caused by the residual carbonates. These carbonate species decomposed during the reduction of the catalyst in H_2 and a NEXAFS typical for ZnO was obtained. The decomposition of the carbonates caused the CO_2 trace in the mass spectrum (Fig. 3a) while the H_2O signal is the result of the reduction of CuO to Cu. Consequentially, the reduction process was accompanied by the disappearance of the CuO peak in the O1s XP spectra shown in Fig. 3a.

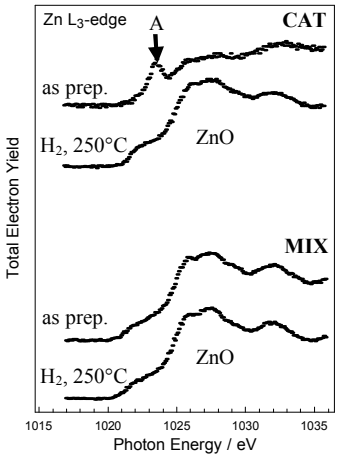

Fig. 2: Zn L_3-NEXAFS of the co-precipitated material (CAT) and the separate precipitated material (MIX) before the activation in H_2 and after the treatment.

The material synthesized by separate precipitation (MIX) instead of co-precipitation of copper/zinc hydroxyl carbonates (CAT) did not show this carbonate species (Fig. 1). The Zn L_3-NEXAFS indicates solely ZnO (Fig. 2). This material was much less active in the methanol steam reforming reaction than the co-precipitated catalyst.

Furthermore, a surface oxygen species was found

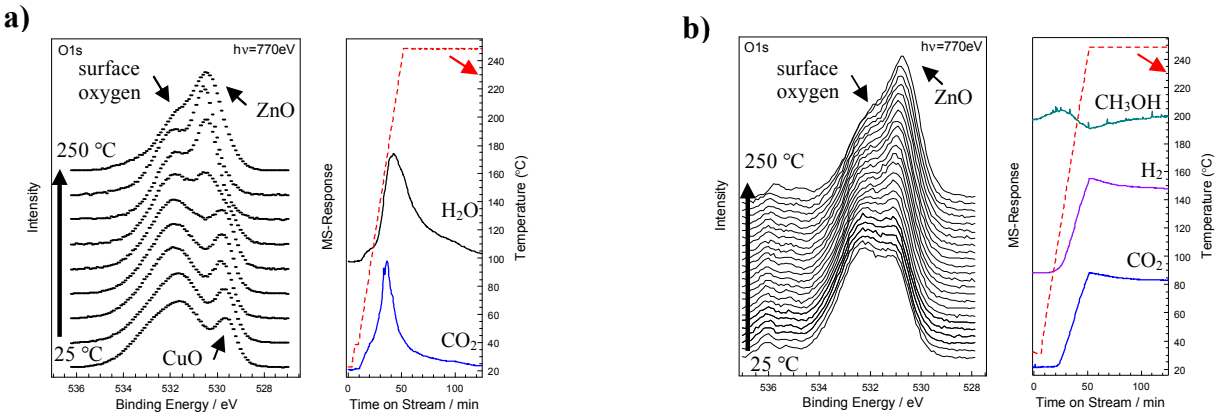

Fig. 3: O1s core level spectra of the co-precipitated catalyst (CAT) during the activation in 0.5 mbar H_2 (a) and in the reaction mixture of CH_3OH and H_2O (b). XP spectra were taken while the temperature was ramped from 25°C to 250°C (TPR-XPS). Simultaneously, the gas phase composition was monitored by on-line mass spectrometry.

after activation and under methanol steam reforming reaction conditions that is primarily located in the outermost surface layers of the reduced catalyst (Fig. 3). This fact was verified by taking O1s XP spectra at different incident photon energies (Fig. 4). Comparison to reference compounds and literature data suggests the assignment to OH-species that are known to create a modified, defective surface on single phase ZnO [3]. The activity of the catalyst was proven by the detection of the reaction products H_2 and CO_2 in the gas phase and the consumption of methanol when the catalyst was heated in the reaction mixture. The methanol conversion was approx. 5% at 250°C (Fig. 3b). Gas phase peaks of CH_3OH and H_2O were observed under methanol steam reforming reaction conditions in the O1s spectra at high binding energies (BE > 534 eV, Fig. 3b and 4).

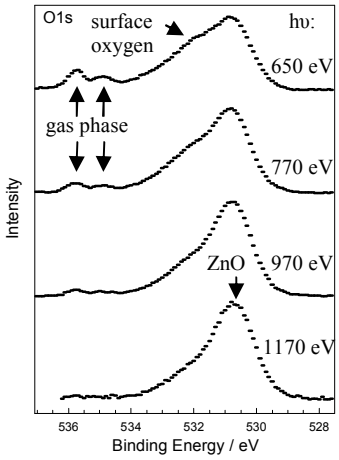

Fig. 4: O1s core level spectra of the catalyst under methanol steam reforming reaction conditions. The photon energy was varied as indicated. Thus, the surface sensitivity increases from down to up.

This investigation highlights the potential of surface sensitive in situ methods like high pressure XPS and high pressure soft XAS in material science in general and catalysis research in particular.

References

[1] P.J. Wild, M.J.F.M. Verhaak, Catal. Today 60 (2000) 3.

[2] B.L. Kniep, T. Ressler, A. Rabis, F. Girgsdies, M. Baenitz, F. Steglich, Angew. Chemie 116 (2004) 114.

[3] M. Kunat, St. Gil Girol, U. Burghaus, Ch. Wöll, J. Phys. Chem. B 107 (2003) 14350.

High–pressure oxidation of the Ru(0001) surface at elevated temperatures investigated by in situ X-ray photoelectron spectroscopy

R. Blume, H. Niehus

Institut für Physik der Humboldt-Universität, Newtonstr. 15, 12489 Berlin, Germany

H. Bluhm, M. Hävecker, A. Knop-Guericke, R. Schlögl, H. Conrad

Fritz-Haber-Institut der Max-Planck-Gesellschaft, Faradayweg 4-6, 14195 Berlin, Germany

Introduction

The most disputable issue regarding the oxidation of the Ru(0001) surface is the morphology and the active phase on the Ru surface under realistic catalytic oxidation conditions. According to the model, based on the investigations of oxidation reactions on Ru(0001) at T > 600 K, the surface under reaction conditions consists of islands of inactive (1x1) chemisorbed phase with 1 ML oxygen, and a catalytically active rutile RuO_2 surface, the latter exposing coordinatively unsaturated sites (cus-Ru), where CO can adsorb and react.[1,2] This model does not exclude coexisting phases, as buried oxide and subsurface oxygen but they are considered of minor importance. Extensive experimental spectroscopic and structural studies showed no evidence of bulk oxide formation below 550 K, although up to ~ 4 ML of oxygen can be accumulated if the Ru(0001) surface is disordered.[3,4,5] Despite that, this 'non-oxide' phase, which is supposed to be a disordered precursor, also appears active in CO titration experiments under UHV conditions.[3] The tentative explanation is that the distortion of the lattice by the incorporated oxygen between the first and second Ru layers weakens the O adsorption bond, converting the adsorbed O into active species. The ex-situ studies also showed that the Ru 3d and O 1s core level spectra are excellent fingerprints for identification of the adsorption, adsorption, subsurface and RuO_2 phases (see table 1), which provide a solid base for verifying their actual role in catalytic oxidation reactions. [5, 6, 7]

Results and discussion

The Ru $3d_{5/2}$ spectra, measured during the high pressure XPS experiments at P_{O2} = 2 mbar and temperatures 330-850 K confirmed the existence of the two different phases, the low temperature (LT), containing up to 4 ML adsorbed and incorporated oxygen, and the high temperature (HT) one, containing the rutile RuO_2 phase. The Ru 3d spectra are almost identical to those measured in the ex-

[1] Over, H.; Kim, Y.D.; Seitsonen, A.P.; Lundgren, E.; Schmid, M.; Varga, P.; Morgante, A.; Ertl, G. Science, 287, 1474 (2000).
[2] Over, H., and Muhler, M., Prog. Surf. Sci. 72, 3, 2003 and references therein.
[3] R. Blume, A. Böttcher, H. Conrad, H. Niehus, J.Chem.Phys. 120 (2004) 3871
[4] Blume, R.; Niehus, H.; Conrad, H.; Böttcher,. J. Phys. Chem. B 108 (2004) 14332 and references therein.
[5] R. Blume, H. Conrad, A. Böttcher, H. Niehus, L. Aballe, A. Barinov, L. Gregoriatti , M. Kiskinova, J. Chem. Phys. Submitted.
[6] Over, H., Seitsonen, A.P; Lundgren, E.; Wiklund, M.; Andersen, J.N. Chem. Phys. Lett. 342, 467 (2001).
[7] Lizzit, S.; Baraldi, A.; Groso, A.; Reuter, K.; Ganduglia-Pirovano, M.V.; Stampfl, C.; Scheffler M.; Stichler, M.; C. Keller, C.; Wurth, W.; Menzel, D. Phys. Rev. B **2001**, 63, 205419.

situ experiments. They are deconvoluted, using the already established cus-Ru and lattice-Ru components of the RuO_2 rutile phase, Ru_{cus} and Ru_{ox}, and the components of the precursor phase, corresponding to differently O-coordinated Ru atoms from the first and second layer. [5-7] Further on the activity of the RuO_2 formed at 575 K and the LT-phase formed at 525 K in the CO oxidation reaction is monitored following the evolution of the Ru $3d_{5/2}$ spectra in the ambient of CO and O_2 in the pressure range 2 – $9x10^{-3}$ mbars. The results are summarised in Figs. 1 and 2. Fig. 1 illustrates the evolution of the Ru $3d_{5/2}$ spectra starting from a surface, with coexisting RuO_2 and non-oxide phases, representing the morphology of the catalyst surface under CO oxidation conditions. The deconvolution of the initial spectrum requires the bulk Ru component, Ru_b, Ru_{ox} and Ru_{cus} for the RuO_2, and two more components. Note that the intensity of the Ru_{cus} is rather small: the cus-Ru atoms are a fraction of the RuO_2 surface and also depends on the degree of the structural order of the oxide. The extra two components account for the coexisting 'precursor' phase with subsurface oxygen, resembling the LT phase with ~ 3 ML oxygen.[8] The experiments were carried out at constant P_{O2} and by varying the CO pressure we are switching from oxidation to reduction conditions. The initial reaction conditions were slightly oxidising leading to a small gain in the intensity of the Ru_{ox}, and Ru_{cus} at the expense of those of the coexisting precursor phase. Increasing the P_{CO} leads to fast reduction of the Ru_{ox} component, accompanied by reduction of the components of the 'precursor' phase and an increase of the Ru_b until a steady state is achieved. The Ru $3d_{5/2}$ spectrum of the steady state still has a Ru_{ox} component, but its intensity is substantially reduced. The other two components are characteristic for the coexisting adsorption phase with triple, Ru(I)-3O and double-coordinated Ru atomsm Ru(I)-2O. The Ru(I)-2O almost overlaps with the Ru_{cus}, the latter should have become negligibly weak after such substantial reduction of the RuO_2 phase. Complete consumption of the oxide is possible by further increase of the CO pressure, which leaves a diluted adsorption state with only singly coordinated Ru atoms, Ru(I)-1O.
The evolution of the Ru 3d spectra of the LT phase with subsurface oxygen is illustrated in Fig. 2. The first spectrum represents a steady-state condition obtained at 525 K in $CO+O_2$ ambient ($P_{CO}=10^{-3}$ mbar, $P_{O2}=7x10^{-3}$ mbar). According to our previous studies the components that are required reflect the presence of adsorbed and subsurface oxygen with total oxygen load of ~ 2 ML.[5] By changing the P_{O2} we switched from oxidation to reduction conditions. The titration of the oxygen is well represented by the changes of the Ru $3d_{5/2}$ spectra under reduction conditions: they loose the subsurface components and convert to a spectrum characteristic for the adsorption phase with 0.5 – 0.6 ML of oxygen. The initial state can be reversibly restored by increasing the oxygen pressure.

In conclusion the in-situ XPS experiments provide direct evidence that oxygen from both the LT precursor phase and the HT RuO_2 phase can be easily titrated under reducing conditions during the CO oxidation. The RuO_2 should play decisive role at reaction temperatures higher than 600 K, which favour its formation. Under these reaction conditions also a disordered precursor can be present, and undergoes reduction with a comparable rate. The surface of the precursor formed at T < 550 K, when the oxygen load is limited to the top few layers, also appears active under reduction conditions.

---

[8] Böttcher, A.; Starke, U.; Conrad, H.; Blume, R.; Gregoriatti, L.; Kaulich, B.; Barinov, A.; Kiskinova, M. J. Chem. Phys. **2002,** 117 8104.

However, further studies, monitoring in-situ the CO_2 production under steady state conditions at the same reaction temperature are necessary in order to prove the catalytic activity of the LT phase.

Binding Energy [eV]	oxygen coordination
0	bulk
-0.3	Ru(I)
0.02	Ru(II)
0.36	Ru(I)-2O
0.96	Ru(I)-3O
1.36	Ru(I)-4O
0.125	Ru(II)-1O
0.56	Ru(II)-2O
0.78	Ru(II)-2O
0.35	Ru-cus
0.63	RuO_2(110) bulk

Table 1:
Ru3d5/2 Binding Energy positions with respect to bulk peak (280.1 eV); Ru(I): first Ruthenium layer, Ru(II): second Ruthenium layer.

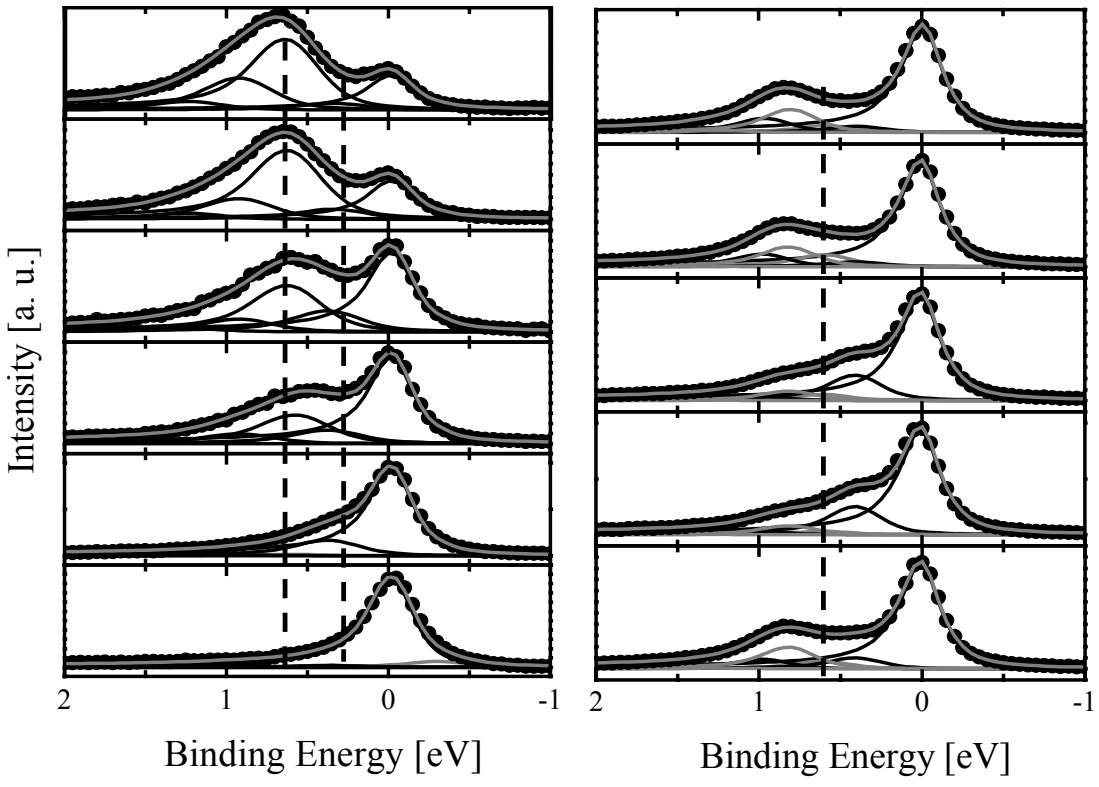

Fig. 1:
Ru3d5/2 spectra during reaction of an oxide surface with CO and O_2 at T=575K; the O_2-pressure was kept constant at $2x10^{-3}$ mbar; CO-pressure was held at 10^{-3}, $2.4x10^{-3}$, $4.4x10^{-4}$ and $5*10^{-2}$ mbar.

Fig. 2:
Ru3d5/2 spectra taken during reaction of a subsurface surface with CO and O_2 at T=525K; CO-pressure was kept constant; O_2-pressure was changed from $7x10^{-3}$, $2x10^{-3}$ and $4x10^{-3}$ mbar.

Oxygen dissolution: *in situ XPS investigation of Pd(111) oxidation*

Balazs Aszalos-Kiss and Dmitry Zemlyanov*

Materials and Surface Science Institute and Physics Department, University of Limerick, Limerick, Ireland

Harald Gabasch, Werner Unterberger and Bernhard Klötzer

Intitut für Physicalische Chemie, Universität Innsbruck, A-6020, Innsbruck, Austria

Evgueni Kleimenov, Detre Teschner, Spiros Zafeiratos Michael Hävecker, Axel Knop-Gericke and Robert Schlögl

Abteilung Anorganische Chemie, Fritz-Haber-Institut der Max-Planck-Gesellschaft, Faradayweg 4-6, D-14195 Berlin, Germany

1. Introduction

Palladium is considered as the best catalyst for the catalytic combustion of methane, which is an environmentally benign process for power generation with low NOx emissions and to remove residual methane from the emission gases of methane-powered vehicles [1].Catalytic combustion is carried out in stages varying from low temperature, where PdO is the thermodynamically stable phase, to high temperature, where Pd metal is the stable phase. Therefore, the oxidation of metallic Pd is critical for the understanding of catalytic combustion. One important phenomenon is the hysteresis in the oxidation/decomposition cycle; the sample reoxidizes only at a much lower temperature than the one predicted by thermodynamics. Salomonsson *et al.* [2] explained the hysteresis in term of a three-phase system: gas phase O_2, oxygen dissolved the palladium bulk and PdO_x. However, no experimental evidences were proposed.

There are number of 'surface science' studies of oxygen/palladium system [3-8]. The question is can the surface species characterised in great detail under high-vacuum conditions adequately

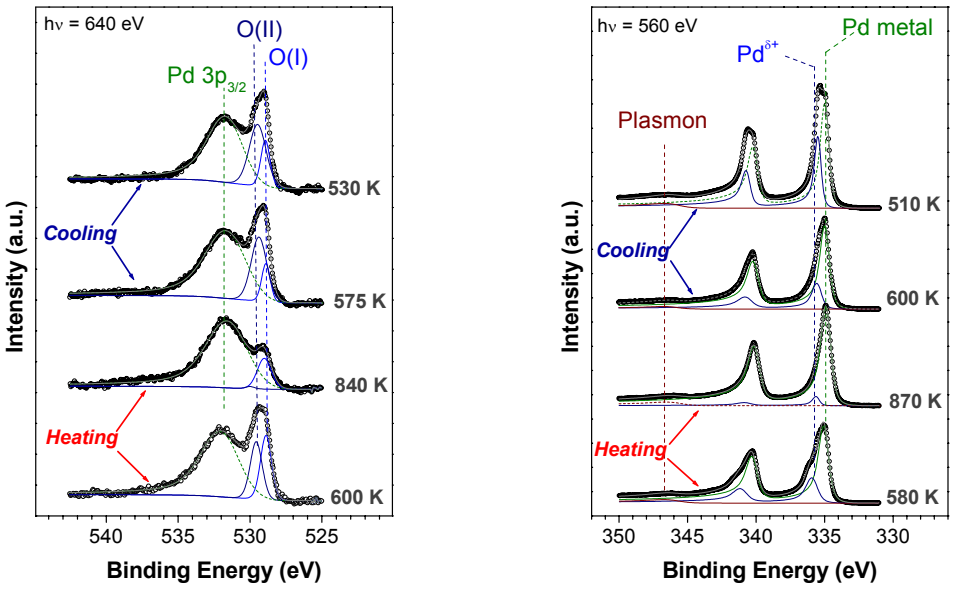

Figure 1 O 1s and Pd 3d spectra obtained *in-situ* during heating and then cooling Pd(111) in 10^{-4} Torr O_2.

represent the dynamic surface chemistry at realistic pressure? In order to address this

* E-mail: dima.zemlianov@ul.ie

question, the present project aims to investigate the interaction between oxygen and palladium in the mbar pressure range by *in-situ* X-ray photoelectron spectroscopy. The key feature is to correlate adsorbed species formed in the close-to-real-pressure conditions and in UHV.

2. Results

Figure 1 shows O 1s and Pd 3d spectra obtained *in-situ* during heating and cooling cycle of Pd(111) in 10^{-4} Torr O_2. The O 1s spectra were fitted with three components: Pd $3d_{3/2}$ peak (531.9 eV) and two, O(I) and O(II), peaks (528.9 and 529.5 eV) assuming Doniach Sunjic profiles. The O(I) and O(II) peaks, which were observed at 600 K, can be assigned to a 2D surface oxide [4]. The formation of the 2D oxide was supported by high binding energy component in Pd 3d spectra. The $Pd^{\sigma+}$ component disappeared and the O(I) and O(II) peaks lost the intensity after 720 K that evidenced the surface oxide decomposition. Noteworthy, the O(I) component did not disappeared even at 870 K. The nature of the oxygen species was investigated at 600 K and 840 K using depth profiling by varying the energy of incident photon (spectra not shown here). The O(II) component demonstrated the surface nature as was expected for the surface oxide oxygen, whereas the O(I) peak has a surface and bulk contributions. Likely, the O(I) peak represented two oxygen species: oxygen belonged to the surface oxide and oxygen species dissolved in the palladium bulk. Indeed the binding energy of 529.2 V reported for the dissolved oxygen [3] is close to the value of the O(I) peak. The oxygen species and palladium oxidation state observed during cooling in 10^{-4} Torr O_2 were little different those formed during heating. The O(II) component was dominating in the O 1s spectra and the $Pd^{\sigma+}$ peak became more intensive than during the heating stage.

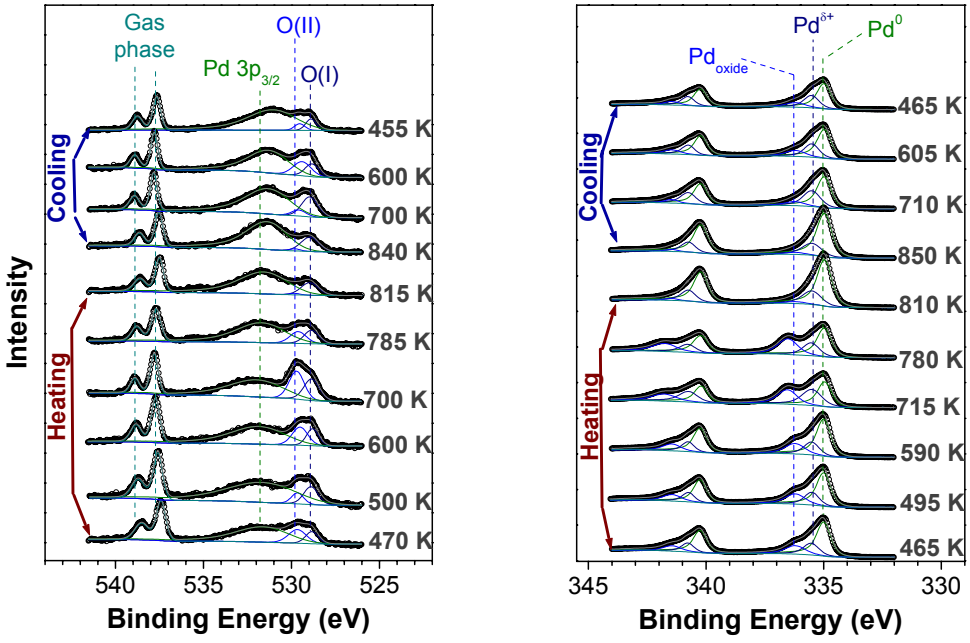

Figure 2 O 1s and Pd 3d spectra obtained *in-situ* during heating and then cooling Pd(111) in 0.5 Torr O_2.

In order to investigate palladium oxidation, the O 1s and Pd 3d spectra were collected when Pd(111) was heating and cooled in 0.5 Torr O_2 (Figure 2). The O 1s spectra contain gas phase contribution as shown in the left panel. As before the O 1s spectra were fitted with three components: Pd $3d_{3/2}$ peak (531.9 eV) and two, O(I) and O(II), peaks (528.9 and 529.5 eV) assuming Doniach Sunjic profiles. The position of the O(I) and O(II) components were not fixed. Pd 3d peaks were fitted with three components, Pd^0, $Pd^{\sigma+}$ and Pd_{oxide}, which were assigned to palladium metal, 2D oxide and bulk oxide. As expected the interaction of oxygen

and palladium proceeded differently in 10^{-4} Torr and 0.5 Torr. The main difference is that the bulk palladium oxide formed in 0.5 Torr O_2 above 600 K: the Pd_{oxide} component (336.6 eV) become well-resolved above 650 K, whereas the O(II) peak shifted towards higher binding energies. This reflected the transformation of the surface oxide to the bulk oxide. The oxidation states of palladium disappeared above 810 K. However, the O(I) peak was observed event at 870 K. This is consistent with the hypothesis about O dissolution. At high temperature, it is easier for oxygen species to overcome the activation barrier and diffuse to the bulk. Thus during cooling, the intensity of O(I) peak increased but oxidation state of palladium did not change noticeably. This mean the oxygen species diffused to the bulk without palladium oxidation. The $Pd^{\sigma+}$ peak started to grow together with the O(II) peak evidencing the 2D oxide formation. However, the O(I) peak was dominated in the spectra. It is very remarkable that no bulk oxide form during the cooling cycle.

3. Summary and Conclusions

The first conclusion is that the 2D surface oxide serves as a precursor of bulk PdO. Indeed the surface oxide can transform to PdO, whereas the bulk oxide did not appear when the Pd(111) surface was cooled in oxygen and the 2D oxide could not form thermodynamically. This is despite the fact that the near surface region was saturated with the dissolved oxygen. This can be explained by high diffusion rate of oxygen to the bulk at high temperature. The adsorption rate is not very high at these conditions and could not provide enough oxygen for oxidation. The surface oxide started to reappear below 600 K but this is to low for oxidation.

The other conclusion is oxygen dissolved in the palladium bulk above 600K. Oxygen dissolution was observed for 10^{-4} Torr and 0.5 Torr treatments. Diffusion of oxygen in the bulk is dominating process at high temperature. Oxygen diffusion occurred oxide precursor. Moreover during cooling it competes with oxidation. The dissolved oxygen led to the surface reconstruction. As shown in Figure 3, the surface structure after 1 Torr oxygen treatment did correspond to a (111) surface. The corrugation was remarkably high that might be due to opening the channel for oxygen diffusion.

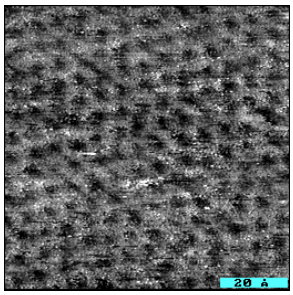

Figure 3 *Ex-situ* STM image of the Pd(111) surface exposed to 1 Torr at 820 K for 10 min.

The presented *in-situ* XPS results provided deeper inside of the palladium oxidation. The process started from the surface oxide formation. Likely some imperfections in the 2D oxide acted as a precursor of the bulk PdO. The formation of the surface oxide is not favourable at high temperatures, therefore no the bulk PdO formed during cooling.

4. Acknowledgement

"This work was supported by the European Community - Research Infrastructure Action under the FP6 "Structuring the European Research Area" Programme (through the Integrated Infrastructure Initiative" Integrating Activity on Synchrotron and Free Electron Laser Science - Contract R II 3-CT-2004-506008)".

5. Reference

1 K. W. Beebe, K. D. Cairns, V. K. Pareek, et al., Catal. Today **59**, 95 (2000).
2 P. Salomonsson, S. Johansson, and B. Kasemo, Catal. Lett. **33**, 1 (1995).
3 F. P. Leisenberger, G. Koller, M. Sock, et al., Surf. Sci. **445**, 380 (2000).
4 E. Lundgren, G. Kresse, C. Klein, et al., Phys. Rev. Lett. **88**, 246103/1 (2002).
5 E. H. Voogt, A. J. M. Mens, O. L. J. Gijzeman, et al., Surf. Sci. **373**, 210 (1997).
6 G. Zheng and E. I. Altman, Surf. Sci. **462**, 151 (2000).
7 G. Zheng and E. I. Altman, Surf. Sci. **504**, 253 (2002).
8 G. Zheng and E. I. Altman, J Phys. Chem. **106**, 1048 (2002).

Combined high pressure XPS and PTRMS study of ethylene epoxidation over silver

V. I. Bukhtiyarov[1], A.I. Nizovskii[1],

H. Bluhm[2*], M. Hävecker[2], E. Kleimenov[2], A. Knop-Gericke[2] and R. Schlögl[2]

1 - Boreskov Institute of Catalysis, Lavrentieva ave. 5, Novosibirsk, 630090, Russia

2 - Fritz-Haber-Institut der MPG, Faradayweg 4-6, Berlin-Dahlem, Germany

Silver catalysts for ethylene epoxidation have in the past mostly been studied under ex situ conditions with high-vacuum based surface science techniques. The evacuation of the reaction gas mixtures, which is usual step of the post-reaction analysis, could lead to the destruction of the active centers on the catalyst surface. As a consequence, silver surfaces under operating catalytic conditions (P > 1 mbar) could be quite different from the same surfaces when investigated using physical methods under high vacuum conditions (P < 10^{-6} mbar). Due to the absence of real *in situ* investigations, the exact mechanism of this reaction is still under debate.

To avoid this drawback, we have performed simultaneous *in situ* X-ray photoelectron spectroscopy (XPS) and proton-transfer reaction mass spectrometry (PTRMS) study of the ethylene epoxidation over silver. Being one of the most powerful methods for studying the surface of heterogeneous catalysts, XPS can be applied in millibar pressure range, where according to literature data ethylene oxide appears among the reaction products. The main advantage of PTRMS, which has been used to measure the yield of ethylene oxide, is its high sensitivity to organic molecules, such as ethylene and ethylene oxide. We have studied the ethylene epoxidation over silver in the temperature range from 300-520 K and under varying total pressures (from 0.07 to 1 mbar) and ethylene-to-oxygen mixing ratios (from 1:1 to 1:10).

Fig.1 shows the PTRMS signals of ethylene and ethylene oxide as a function of temperature and time measured for two sets of conditions: (a) $P(C_2H_4)$ = 0.1 mbar, $P(O_2)$ = 0.25 mbar; and (b) $P(C_2H_4)$ = 0.24 mbar, $P(O_2)$ = 0.25 mbar. Ethylene oxide formation is negligible at ambient temperatures, but is increased with temperature. After stopping the O_2 flow the PTRMS signal of ethylene oxide decreases rapidly to the background level. These data indicates that in the millibar pressure range and at T ≥ 420 K ethylene oxide is formed as a result of ethylene epoxidation over silver. The O1s and C1s spectra measured *in situ* simultaneously with the PTRMS data in Fig. 1a and normalized with respect to Ag3d intensity are shown in Fig. 2. One can see that the spectra change strongly with temperature.

* Present address: Lawrence Berkeley National Laboratory, Chemical Sciences Division, Berkeley, CA 94720

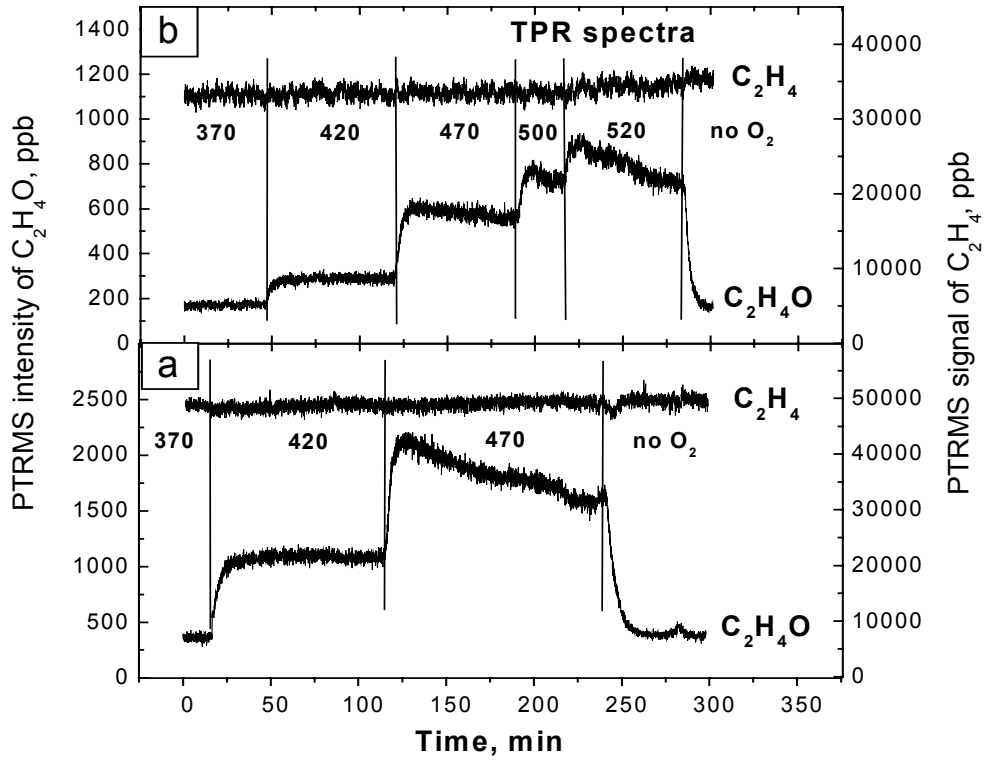

Fig.1. Variation of the PTRMS signal from ethylene and ethylene oxide with temperature, measured in various reaction mixtures (see the text).

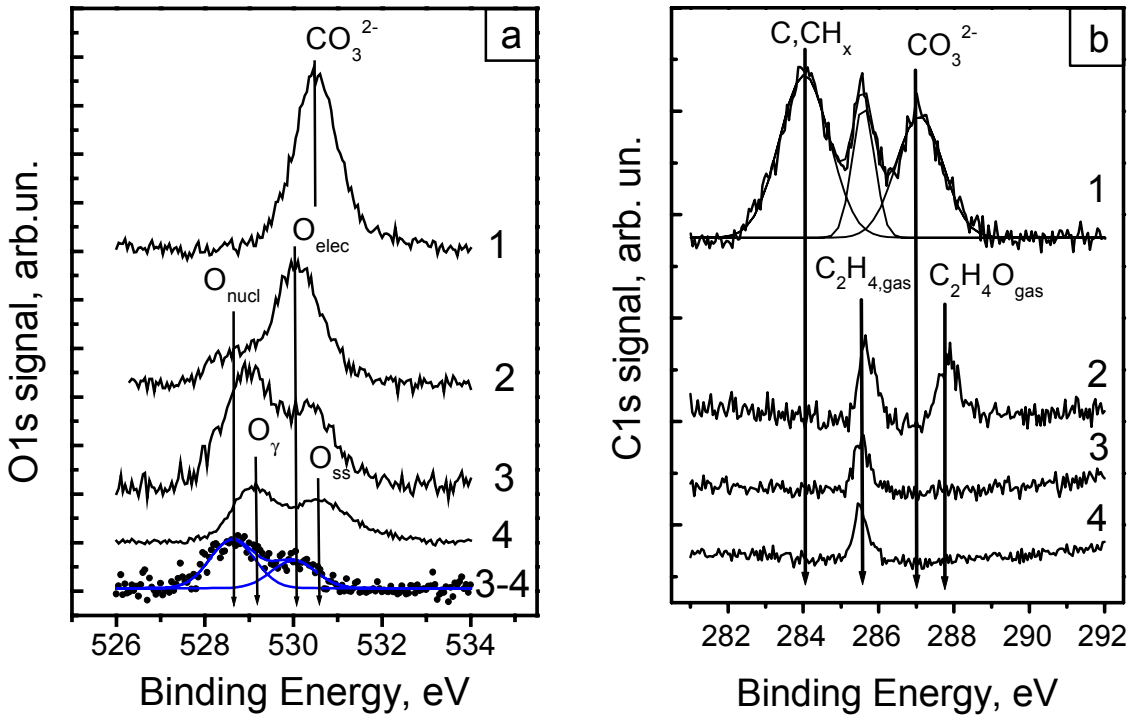

Fig.2. O1s (a) and C1s (b) spectra measured *in situ* under the reaction mixture flow at various temperatures: 1 – 370 K, 2 – 420 K, 3 – 470 K. Spectrum (4) was measured at 470 K after the oxygen flow was stopped; 3-4 is the difference spectrum.

A simple comparison of the catalytic (Fig. 1a) and spectroscopic (Fig. 2) data, which were identified on the basis of literature data and own experience (see comments in Fig.2a), allows us to propose a preliminary explanation for the temperature-dependence of the catalytic properties of silver. The low activity of silver at T < 420 K is caused mainly by the presence of carbonates and carbonaceous residues at the silver surface that block the available silver surface. The silver surface becomes catalytically active for ethylene oxide formation, when those contaminations are removed at T = 420 K. The active surface is characterized by the presence of nucleophilic (O1s feature at 528.5 eV) and electrophilic (530.0 eV) oxygen. The enhancement of the ethylene oxide yield at T > 420 K is most likely determined by the Arrhenius dependence of the reaction rate on temperature. The decrease of the rate of ethylene oxide formation with time observed for T ≥ 470 K can be explained by the accumulation of embedded oxygen species, O_γ (529.0 eV) and $O_{subsurface}$ (530.6 eV) at the silver surface which decrease the surface area that is available for the formation of the active species. Nucleophilic and electrophilic oxygen, which were the main species at 420 K, are still present on the silver surface at 470 K; however, they are rapidly removed in the absence of oxygen in the gas phase (see the difference spectrum in Fig. 2). These observations confirm the reactivity of nucleophilic and electrophilic oxygen species towards ethylene.

In order to elucidate the role of these species in the mechanisms of ethylene epoxidation, a quantitative comparison of the XPS and MS data for the experiments at 420 K was made. This comparison revealed a clear correlation between the abundance of oxygen species on the silver surface and the yield of ethylene oxide. Experimental data were successfully modeled under the assumption that the epoxidation of ethylene proceeds via a Langmuir-Hinshelwood mechanism between oxygen species adsorbed in the electrophilic state and ethylene, which is chemisorbed on silver ions produced by nucleophilic oxygen:

$$O_{elec} + C_2H_{4,ads} \rightarrow C_2H_4O.$$

The key role of electrophilic oxygen is confirmed by the data of low-pressure experiment which shows that very small yield of the ethylene oxide (~ 0.001) is correlated with low concentration of electrophilic oxygen, but not with the amount of nucleophilic oxygen, which was ten times more. In agreement with this mechanism, the highest yields of ethylene oxide are observed for Ag surfaces that are characterized by similar concentrations of nucleophilic and electrophilic oxygen.

Our experiments also show that the chemical composition of the active silver surface under reaction conditions is different from the chemical composition that is measured when the surface is measured under vacuum conditions. This underlines the importance for using *in situ* methods to investigate the properties of active catalyst surfaces.

The Local Adsorption Geometry of Alanine on Cu{110} studied by NEXAFS

L.B. Jones[1,2], E.A. Seddon[1], R. Raval[2], F. Thibault-Starzyk[3] and G. Held[3]

[1]*CCLRC Daresbury Laboratory, Warrington, UK*

[2]*Surface Science Research Centre and Department of Chemistry, University of Liverpool, UK*

[3]*University of Cambridge, Department of Chemistry, Lensfield Rd, Cambridge CB2 1EW, UK*

Metal-organic interfaces show a great variety of unusual surface phenomena which depend on the coverage and thermodynamic conditions, but also on the chemical states, molecular orientations and intermolecular bonding interactions at the surface [Barl03,Rose03,Humb04]. In many of these systems, supramolecular interactions govern the formation of superstructures, which depend on the balance of molecule-substrate and molecule-molecule interactions. Among the best studied metal organic surface systems are thin layers of the smallest chiral amino acid, alanine ($OOC–CHNH_2–CH_3$), on Cu{110}. Of particular technological interest is the fact that it forms chiral superstructures, which can exist in two distinguishable and non-superimposable mirror forms (see [Humb04,Barl04] and references therein). In addition, this system provides a model for the behaviour of protein-based biomaterials and for heterogeneous asymmetric catalytic systems, where the molecule acts as chiral modifier stereo-directing reaction pathways. It has been shown that in the temperature range 300-470K alanine bonds strongly to the Cu{110} surface in its deprotonated alaninate form, with the integrity of the chiral centre preserved. The alaninate/Cu{110} system displays a variety of chiral and achiral surface superstructures; in this report we concentrate on the local adsorption structure within the (3x2) adsorbate layer.

The experiments were performed at the beamline UE52-PGM (CRG) at BESSY II with a spot size of about 100µ x 200µ at the sample. XPS data were recorded using a Scienta 200 mm electron energy analyser with pass energies of 20 and 40 eV at a photon energy of 630 eV. The binding energies (BE) were calibrated with corresponding measurements at the Fermi energy for the same photon energy and pass energy. For the NEXAFS data shown here, the synchrotron beam hit the surface either at normal incidence or at 70˚ off normal incidence, the orientation of the electrical field vector, **E**, within the surface plane was controlled by the undulator settings to be either parallel or perpendicular to the close packed rows of Cu atoms in the surface (the [1-10] direction). A partial yield detector (PYD) was used with the retarding voltage set to accept electrons in the kinetic energy range up to 50 eV below the lowest photon energy in order to avoid detection of Cu d-band photoelectrons. The raw NEXAFS data were normalised with respect to the ring current and spectra of the clean sample.
The Cu sample was prepared using standard procedures including electro-polishing, Ar-ion sputtering and oxygen treatment in UHV followed by a final annealing step to 900 K. R or S-alanine was adsorbed by evaporating a coverage in excess of the amount actually needed at a sample temperature of 370 K. After the adsorption was complete the sample was annealed to about 400 K in order to create the chiral (2 –2 / 5 3) structure or to 440 K to create the achiral p(3x2) overlayer. The latter structure is the subject of this report; the long-range order of the adsorbate layer was checked by LEED, which showed the expected p(3x2) diffraction pattern with somewhat broadened spots. All data were recorded at room temperature. The base pressure of the UHV system was $3x10^{-10}$ mbar.

Both XPS (not shown) and NEXAFS spectra with linear polarisation were identical for R and S-alanine layers prepared under the same conditions. For the p(3x2) layer narrow O 1s and N 1s XPS peaks were found at BE 531.3 and 399.5 eV, respectively. The absence of a second O 1s peak indicates that both oxygen atoms in the molecule are involved in the bond formation with the substrate. The C 1s spectra show two peaks at BE 288.0 and 285.5 eV. According to [Barl04] we assign the first peak to the OO**C**– carbon atom of the carboxylic acid group and the second, more intense, peak to the two –**C**HNH_2–**C**H_3 carbon atoms, which only take part in C-C single bonds. The XP spectra are very similar to data for glycine ($OOC–CH_2NH_2$) on Cu{110} [Hass98]. The fact that alanine contains one more singly bonded carbon atom than glycine leads to a higher relative intensity and some broadening of the 285.4 eV peak.
C, N, and O K-edge NEXAFS spectra are shown in Figures 1, 2, and 3, respectively, for **E** orientations within the surface, parallel to the [001] and [1-10] directions, and 70˚ off the surface

plane (only for O). The O and N spectra are, again, remarkably similar to the corresponding spectra for glycine [Hass98], which indicates that the adsorption geometries are very similar in both cases. The polarisation dependence of the π^* resonance clearly shows that the O-C-O triangle is tilted with respect to the surface normal and essentially parallel to the [1-10] direction along the rows of close packed Cu atoms [Stoe92]. The shape of the N K-edge spectrum with high intensity all the way down to the Fermi level is in agreement with the formation of a N-Cu bond. The sharp feature at 398.5 eV is an indication for some beam-induced dissociation in the adsorbate layer, as similarly observed for glycine [Hass98]. The finding that the molecules form bonds with the Cu substrate through three atoms, two O and one N, explains the tilt of the O-C-O group and is in good agreement with results from RAIRS [Barl04] and recent DFT calculations.

The C K-edge spectra are different from the ones for glycine in that they show an additional sharp peak at 285 eV in the [1-10] spectrum. The origin of this peak is not entirely clear; it might be due to impurities of atomic carbon, which does, however, not explain its strong polarisation dependence. Following the arguments given by Hasselström et al. [Hass98], we assign the feature near 292 eV to $\sigma_{C\text{-}N}$ /$\sigma_{C\text{-}C}$ resonances. This feature is more intense with **E** ‖ [100] but does not disappear in the [1-10] spectrum, which indicates that the C-C and C-N bonds are tilted with respect to both directions, in contrast to glycine. This is expected, however, because of the tetrahedral arrangement of C-C, C-N and C-H bonds around the central carbon atom in alanine. The peaks at 298 and 302 eV are assigned to $\sigma_{C\text{-}O}$ resonances.

We note here that the NEXAFS spectra for the chiral (2 –2 / 5 3) phases of both enantiomers are almost identical to the ones shown here [JoneXX]. This indicates that the local adsorption geometries are very similar in these two phases of alanine on Cu{110}.

This study was supported by the European Commission under the Contract No R II 3-CT-2004-506008 / project BESSY-ID.04.1.052 and by EPSRC. We would like to thank the BESSY staff for their help during the beamtime, in particular Drs T. Schmidt and D. Batchelor.

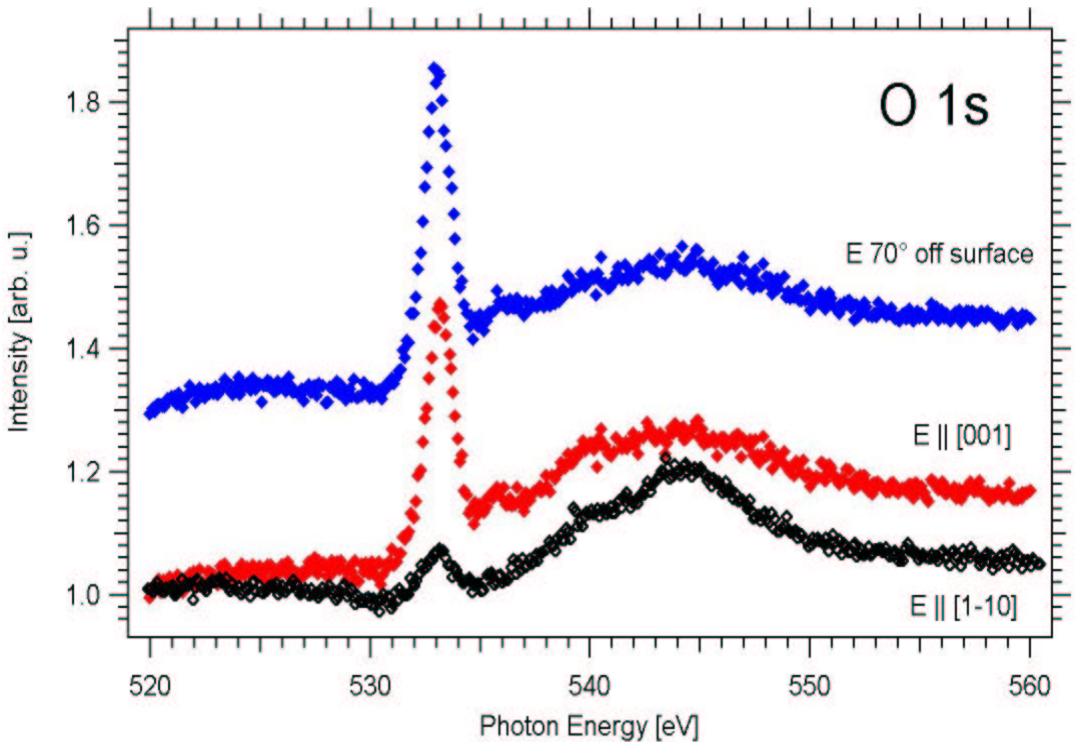

Figure 1: *O K-shell NEXAFS spectra from a (3x2) layer of alanine on Cu{110} for **E** parallel to the [001] and [1-10] directions within the surface and tilted by 70° away from the surface plane.*

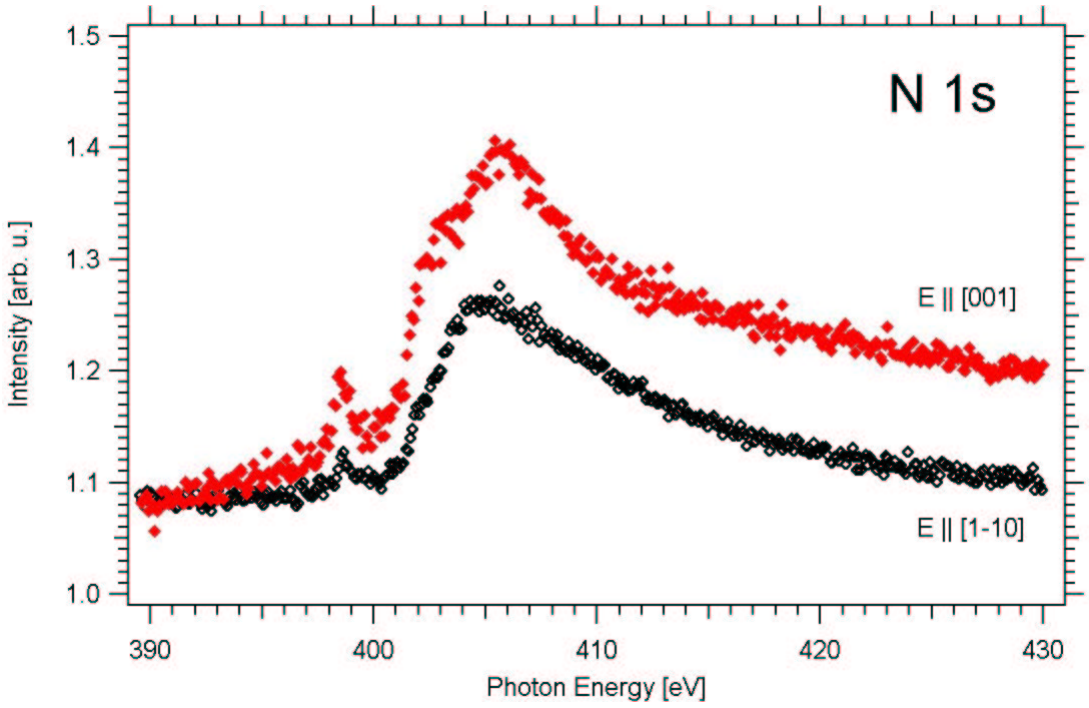

Figure 2: *N K-shell NEXAFS spectra.*

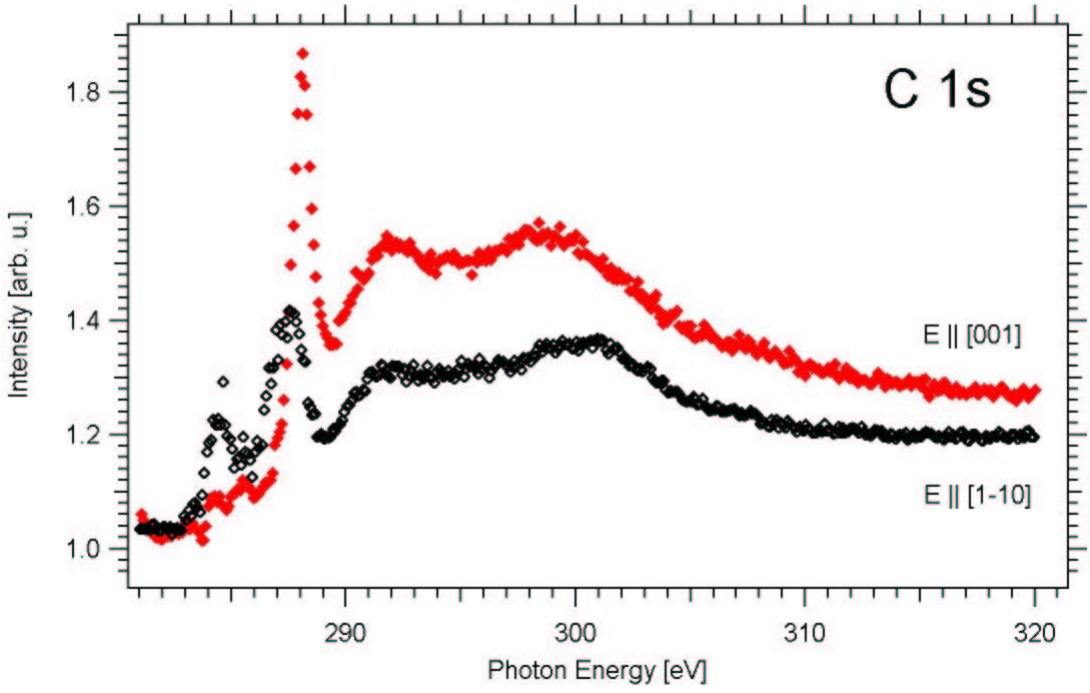

Figure 3: *C K-shell NEXAFS spectra.*

References:

[Barl03] S.M. Barlow and R. Raval. Surface Science Reports 50, (2003) 201
[Barl04] S. M. Barlow et al. Langmuir 20 (2004) 7171.
[Hass98] J. Hasselström et al. Surf. Sci. 407 (1998) 221.
[Humb04] V. Humblot, S.M. Barlow and R. Raval. Prog. Surf. Sci. 76 (2004) 1.
[JoneXX] L.B. Jones, E.A. Seddon, R. Raval, G. Held, in preparation.
[Rava01] R. Raval, CATTECH (2001) 5 12.
[Rose03] F. Rosei et al., Prog. Surf. Sci. 71, (2003) 95.
[Stoe92] J. Stöhr 'NEXAFS spectroscopy', Springer, 1992.

Catalytic Centres in Noble Metal Free Catalysts for PEM Fuel Cells investigated by X-ray Absorption Near Edge Spectroscopy

G. Schmithals, S. Fiechter, P. Imperia

Hahn-Meitner-Institut Berlin, Glienicker Str. 100, D-14109 Berlin

1. Introduction

The polymer electrolyte membrane fuel cell (PEM-FC) system is considered as a promising future technology for converting chemical into electrical energy under clean environmental conditions. At present, platinum and its alloys are the favoured electrocatalysts in these systems, but alternative catalysts are under development to replace the cost effective platinum. The material system of the present investigation shows an electrochemical activity for oxygen reduction of the same order of magnitude as platinum [1]. The catalysts were prepared by pyrolysis of a mixture of metal porphyrins (Co- or Fe- tetramethoxyphenyl-porphyrin (TMPP)) and oxalates in an inert gas atmosphere. Catalytic activity is further enhanced by the addition of sulfur precursors during the heating process. The obtained catalysts exhibit a highly porous structure (Fig. 1). For a similar type of catalysts different models have been discussed to explain the nature of the catalytic centres [2, 3]. Structural analysis performed at BESSY is suited to compare these considerations with our material. Although neutron activation analysis showed Fe- and Co-concentrations of about 2 wt%, no metal particles of nanometer size could be detected neither by scanning nor by transmission electron microscopy. Therefore, it is assumed that the catalytic centres consist of metal clusters smaller than 1 nm or atoms integrated in the surfaces of the in-situ formed carbon support via pyridinic-type nitrogen.

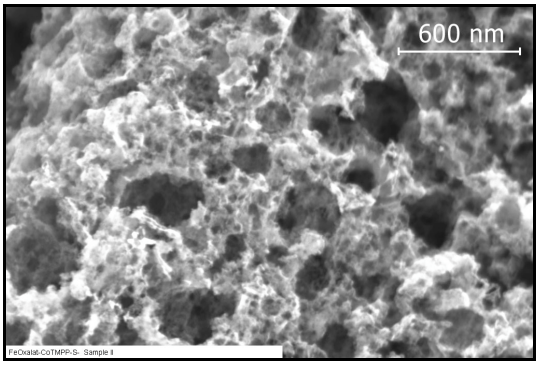

Fig. 1: SEM image of a Co-Fe-catalyst prepared by pyrolysis of CoTMPP and iron oxalate

2. Experimental

XANES measurements were performed at beamline UE46 PGM. The spectroscopy chamber pressure during the measurements was better than 4×10^{-10} mbar. The spectra were measured in total electron yield detecting the drain current. The samples were examined at the Co L_3/L_2, Fe L_3/L_2, S L_3/L_2 and N K edges. In a first series of measurement a focussed beam with linear polarisation was used (60µm x 16µm, ϑ=20° sample surface with respect to the incident light beam). The samples investigated were pressed to pellets. Mixing with an equal amount of graphite was necessary due to the low cohesion forces of the catalyst powder. Only a limited series of satisfying experiments could be taken with this setup. Most of the spectra were superimposed by strong oscillations of the signal intensity. This effect could not be compensated for by averaging over multiple measurements due to their unchanged periodicity between the spectra. The source of the oscillations has not

been clarified. It could have been related to charging effects due to an insufficient conductivity of the pellets. As the incident beam and the sample particles were of same size also small variations in beam position could have led to the observed effect.

To improve the measurements output, beam conditions and sample preparations were successfully changed in a second measurement period resulting in a drastically improved signal to noise ratio. A wide beam (1x1 mm) with linear polarisation under an angle of ϑ=20° was used, for Fe- and Co-edge the beam was 90% circular polarised. This time the catalyst particles were pressed on indium foil. The increased beam dimensions allowed to average over a larger sample surface, while the preparation on indium foil improves sample conductivity.

3. Results

The measurements at the S $L_{3,2}$ edge reveal that in samples prepared with CoTMPP the majority of sulfur is bonded to cobalt in a structure similar to that of CoS_2 (Fig. 2).

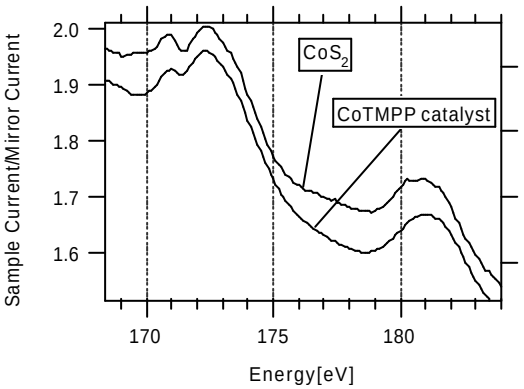

Fig. 2: S $L_{2,3}$ edge of CoTMPP catalyst and CoS_2

While the presence of high amounts of sulfur has been verified by Mass Spectroscopy, by X-ray Diffractometry (XRD) no sulfur compounds has been detected. It can be easily assumed that the particles of the sulfur containing species are too small with respect to the sensitivity of XRD that can not detect particles smaller than 2 nm.

Measurements at the Co $L_{3,2}$ edge yield different resonance structures for samples prepared with and without sulfur precursors (Fig. 3). Unexpectedly, probes prepared with sulfur exhibit a significantly stronger Co-edge resonance signal. It has been shown chemically that the metallic by-products of pyrolysis can more easily be removed during preparation in form of sulfides. The observed effect could therefore either be related to a higher cobalt volume fraction or a shielding effect due to the iron by-products.

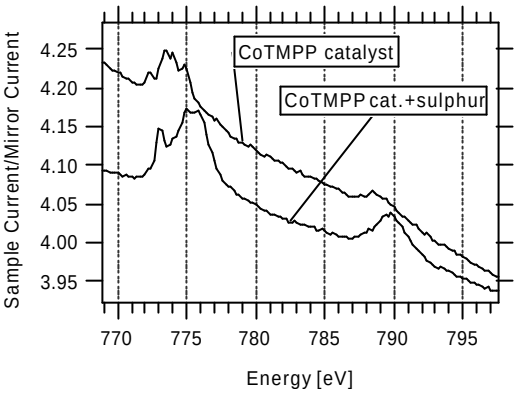

Fig. 3: Co $L_{2,3}$ edge of CoTMPP catalysts

Thus, the spectra of these catalysts are presumably dominated by inactive compounds. From the spectra L_3 edge splitting the presence of cobalt oxides is evident. This result is also supported by EXAFS measurements. In XRD measurements no oxides are detectable in these samples which analogously indicates their small particle size. In contrast to the visibility of a cobalt/sulfur compound at the sulfur edge no analogous structures emerge at the cobalt edge. This can be explained by cobalt, preferably bonded in the active N_4-chelate ring.

Measurements at the $L_{3,2}$ N-edges show a similar electronic structure of the environment of the nitrogen species in the iron- and cobalt porphyrins (Fig. 4). In contrast, the spectrum of

the porphin that lacks the metal centre shows a shift towards lower energies. Analogously, iron- and cobalt catalysts exhibit similar N-edge spectra suggesting that the centres are bonded in an identical ligand field to the carbon matrix in both systems. However, the line shape of the spectra of catalysts and porphyrin precursors differ significantly. This effect is in agreement with EXAFS measurements which indicate that the carbon ring structure is not present anymore after heat treatment.

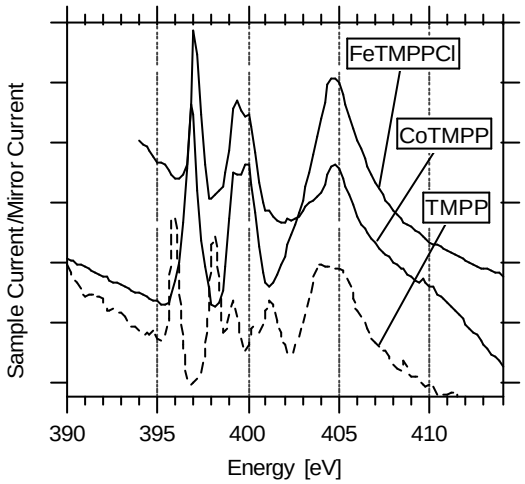

Fig. 4: N K edge of porphyrin precursors

Studying the Fe $L_{3,2}$ spectra, in catalysts prepared without sulfur species the presence of by-products (metallic iron) are dominating as similarly observed at the cobalt edge. FeTMPP-catalysts prepared adding iron oxalate and sulfur species show a spectrum that closely resembles that of the porphyrin precursor. However, when cobalt was present during pyrolysis in the form of cobalt oxalate the spectra exhibit a completely different shape. The underlying effects have not been identified so far. From the study of EXAFS measurements it has been inferred that a replacement of iron by cobalt as a catalytic centre during pyrolysis is feasible. Such an effect would be in agreement with the XANES measurements under the assumption that the majority of iron were replaced.

4. Conclusions

Catalysts prepared from metal porphyrin precursors have been measured by XANES. The samples prepared by pressing the catalyst on an indium foil and measured with a wide incident beam exhibited spectra of excellent quality. Analysis of the spectra reveals information about the structure of the catalysts and the preparation process that supplements EXAFS measurements.

5. References

[1] Bogdanoff, P., I. Herrmann, et al. (2004). J. New Mat. Electrochem. Systems (7): 85-92.

[2] A.L. Bouwkamp-Wijnoltz, W. Visscher, J.A.R. van Veen, J. Phys. Chem. B, 106, 12993 (2002)

[3] B. van Wingerden, J. A. R. van Veen, et al. (1988). J. Chem. Soc. F. Transact. 84(1): 65-74

In situ X-ray photoelectron spectroscopy of the methanol oxidation over Cu(110)

S. Günther[1], L. Zhou[2], R. Imbihl[2], M. Hävecker[3], A. Knop-Gericke[3], E. Kleimenov[3], R. Schlögl[3]

[1]*Department Chemie, LMU München, Butenandtstr. 11 E, 80377 München, Germany*

[2]*Institut für Physikalische Chemie und Elektrochemie, Callinstr. 3-3a, 30167 Hannover, Germany*

[3]*Fritz-Haber-Institut der Max-Planck-Gesellschaft, Faradayweg 4-6, D-14195 Berlin, Germany*

Introduction

We have used *in situ* X-ray photoelectron spectroscopy (XPS) to investigate the partial oxidation of methanol over Cu(110) in the pressure range between 10^{-7} and 10^{-3} mbar. The aim of the present study was to investigate the adsorbate structures present on the Cu(110) surface and relate them to the observed catalytic reactivity. The identification of distinct adsorbate phases was achieved by resolving different components in the C 1s and O 1s core level peaks. Especially, the everlasting question, whether formate is present on the surface during the reaction and if yes, how it influences the reactivity of the Cu(110) surface was to be addressed [e.g. 1, 2, 3]. The systematic study mainly in the 10^{-5} mbar pressure range provided insight, why UHV experiments of the partial methanol oxidation and measurements under more technical conditions at higher total pressure monitor two separate reaction regimes. In the future it is planed to extend the study into the higher pressure range in order to resolve the still existing contradictive assignments of adsorbate species during the catalytic reactions.

Experimental

A Cu(110) single crystal was mounted onto a temperature-controlled sample stage in the experimental cell. The partial pressures were adjusted using leak valves. X-rays are admitted to the experimental cell through a 100 nm thick SiN_x window, where they illuminate the sample surface. The emitted photoelectrons enter a differentially pumped electrostatic lens system and are focused on the entrance slit of a standard electron energy analyser, where high vacuum conditions are maintained by another pumping stage. The setup allows tuning the total pressure in the reaction cell between 10^{-7} mbar and 1 mbar. The reaction products were monitored with the help of a differentially pumped mass spectrometer. The sample temperature was varied with the help of a infrared laser heating system in the range from 300 K ... 800 K. The experiments were performed at the undulator beam line U49/2-PGM1.

Results:

Fig. 1 A) shows a set of TPR spectra at varying total pressure. The occurrence of a low temperature peak at a total pressure < 10^{-3} mbar is pronounced in the 10^{-5} mbar range at a $CH_3OH:O_2$ mixing ratio between 1:0.6 and 1:0.8 [4]. The question arising was, why it forms and what causes its decay. Fig. 1 B) shows the O 1s and C 1s spectra where separate peaks can be resolved that are related to O_{ad}, formate and methoxy species.

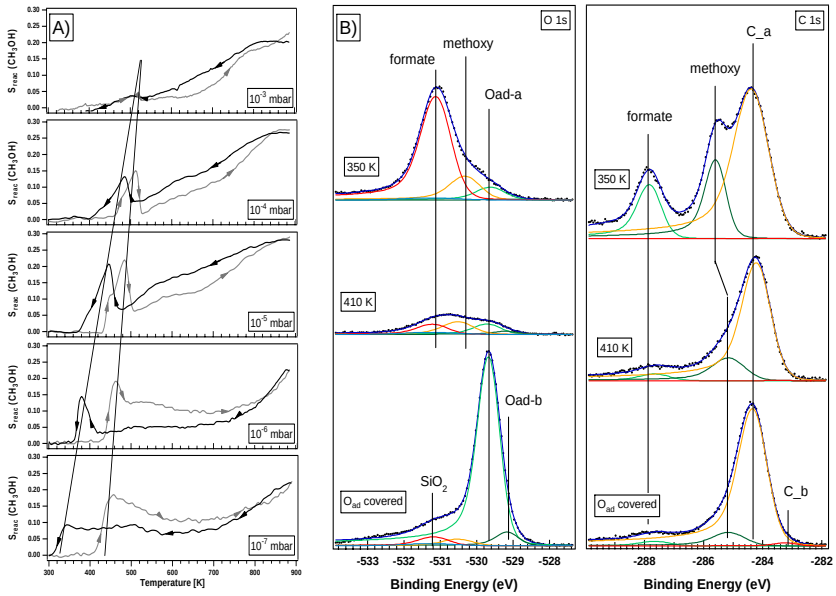

Fig. 1:

A) Reactive sticking S_{react} of Methanol over Cu(110) applying a CH_3OH: O_2 mixing ratio of 1:0.8 at different total pressures.

B)O 1s and C 1s components for different adsorbate species on Cu(110) formed applying unstationary reaction conditions: Oad-a (ordered O-(2×1)), Oad-b (disordered), formate, methoxy, C_a and C_b contamination and a small SiO_2 impurity.

In order to obtain well resolved methoxy related C 1s and O 1s peaks an oxygen covered Cu(110) sample was annealed in a methanol rich atmosphere of $P(CH_3OH)=1.4\times10^{-6}$ mbar and $P(O_2) = 0.2\times10^{-6}$ mbar. Upon cooling down the sample a significant amount of methoxy was temporarily formed on the surface. The adsorption species indicated in Fig. 1 B) could be resolved in accordance with values found in the literature. Within a day a SiO_2 contamination below 0.06 ML was slowly accumulated, which could be readily removed by Ar^+ sputtering. A carbon contamination accumulated when a high methanol and a low oxygen partial pressure were chosen, as visible in Fig. 1 B). The C_a contamination (and a very small amount of C_b) occurred probably due to a C_xH_y species possibly generated at the chamber walls (note the negligible O 1s signal in the 2nd spectrum). Applying constant pressures and waiting for stationary conditions at 300 K (e.g. at $P(CH_3OH)=0.5\times10^{-5}$ mbar and $P(O_2) = 0.3\times10^{-5}$ mbar) apart from the C-contamination exclusively formate is formed on the surface. Since under similar reaction conditions a c(2×2) ordered structure was seen in LEED [4], we can state that the c(2×2) described in [4] and possibly the one in [1] should correspond to formate and not to methoxy as controversially discussed in [2]. The adsorbate coverages were calibrated using the O 1s intensity of the well

known 0.5 ML of an O-(2×1) phase. Using the fact that the methoxy molecule consists of C:O=1:1, while for formate this is 1:2, the relative sensitivity factor for C 1s and O 1s can be obtained. Within the errors of the experiment the coverage of all adsorbates can be calculated, where coverage is defined as covered adsites (note that one formate molecule is bound to 2 adsorption sites via its two O atoms). Fig. 2 displays the different adsorbates present on Cu(110) during the partial methanol oxidation together with the corresponding formaldehyde production, determined by differentially pumped mass spectrometry.

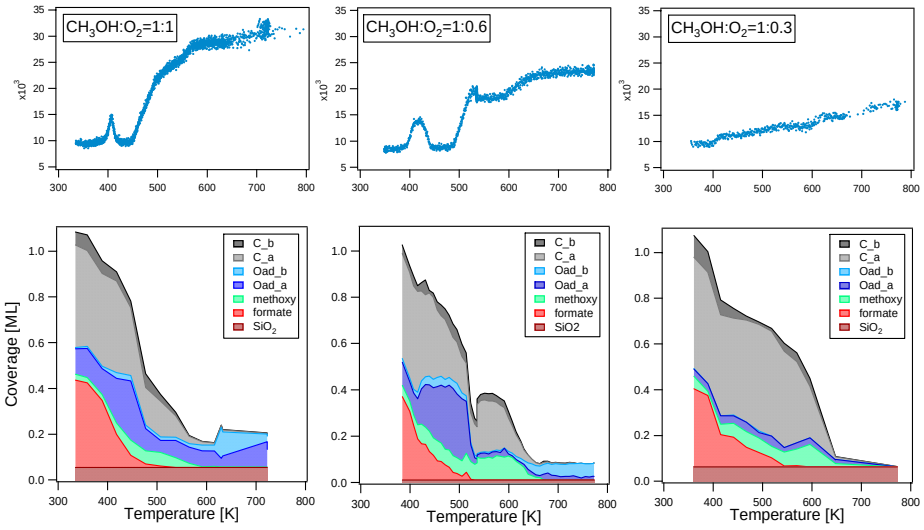

Fig. 2:
Adsorbates present on Cu(110) during the partial methanol oxidation at $P(CH_3OH)=0.5\times10^{-5}$ mbar and different mixing ratios. The upper panel displays the formaldehyde production.

Note, that a maximum of 1 ML coverage is reached, which means that at least the C-contamination can fill empty ad-sites in ordered adphases, e.g. in the O-(2×1) phase with a total O-coverage of 0.5 ML. The following facts can be extracted directly from the graph of Fig. 2, which will be used to identify the different reaction steps involved:

1) The surface at 300 K is completely adsorbate covered, while no reaction takes place.
2) Formate and C-contamination are the most prominent adsorbates at 300 K.
3) The decomposition of formate initiates the low temperature production of formaldehyde.
4) Parallel to the decrease of adsorbed formate, the O_{ad} coverage increases until the surface is O-poisoned and the reaction is blocked.
5) Above the second onset of the reactivity the oxygen coverage significantly drops and free surface area exists. To a small extend methoxy is present on the surface.
6) At T > 700 K oxygen and eventually C-contaminations are the only adsorption species.

Acknowledgements

The BESSY staff is acknowledged for its continuing support of our experiments.

References

[1] M. Bowker, R. A. Bennet, S. Poulston, P. Stone, Catal. Lett. 56 (1998) 77.
[2] S. L. Silva, R. M. Lemor, F. M. Leibsle, Surf. Sci. 421 (1999) 135.
[3] A. F. Carley, P. R. Davies, G. G. Mariotti, S. Read, Surf. Sci. 364 (1996) L525.
[4] L. Zhou, S. Günther, R. Imbihl, J. Catal. (in press).

Catalytic activity of oxide supported metal nanoparticles: surface oxygen - surface oxides - subsurface oxygen

T. Schalow, M. Laurin, B. Brandt, S. Schauermann, J. Libuda,
S. Guimond, H. Kuhlenbeck and H.-J. Freund
Fritz-Haber-Institut der Max-Planck-Gesellschaft, Faradayweg 4-6, 14195 Berlin, Germany

Oxide supported palladium particles are widely used catalysts for oxidation reactions. In Pd single crystal studies the interactions between oxygen and Pd have been shown to be rather complex under reaction conditions since various oxide species, i.e. surface oxygen, surface oxides and subsurface oxygen, can be formed [1]. For oxide supported Pd nanoparticles, the situation becomes even more complex because of the simultaneous presence of different facets and a higher defect density. Additionally, interface related effects, e.g. oxygen exchange between PdO_x species and the oxide support, have to be taken into account. In general, the formation of such oxide species and their influence on the activity of the catalyst in oxidation reactions are not well understood.

In this study, thin well-ordered Fe_3O_4 films (100 Å thickness) grown on Pt(111) have been used as an oxide support [2]. Pd particles in the size range of a few nm in diameter (4 Å nominal Pd thickness) were grown on the oxide film by metal evaporation at a surface temperature of 115 K and subsequently annealed at 600 K . In order to characterize the nature and formation of oxide species under reactions conditions, various standard surface science techniques, IRAS, STM and X-ray photoelectron spectroscopy (XPS) using synchrotron radiation (Bessy II, Beamline UE52-PGM1), as well as molecular beam methods have been employed in this study.

Fig. 1 shows the XPS spectra of the Pd3d region for the pristine Pd particles (a) and after oxygen exposure (~1500 L) at different temperatures (b-d). For clean Pd particles, the $Pd3d_{5/2}$ region is clearly centered at 335.2 eV, close to the binding energy expected for metallic bulk Pd [3]. After oxygen exposure at 300 K (b) a second feature at about 335.7 eV appears while the metallic Pd component loses some intensity. The feature at 335.7 eV can be assigned to the presence of a chemisorbed oxygen overlayer on the Pd surface. Oxygen exposure at 500 K results in a $Pd3d_{5/2}$ spectrum consisting of at least three features (c). The metallic Pd component at 335.2 eV is still present but significantly less intense than in the two previous cases. Additionally, a shoulder at approx. 336.5 eV appears which can be attributed to the formation of an oxide, likely being surface PdO according to the literature [3]. Since the binding energy for metallic Pd remains unaffected, it is unlikely that significant amounts of

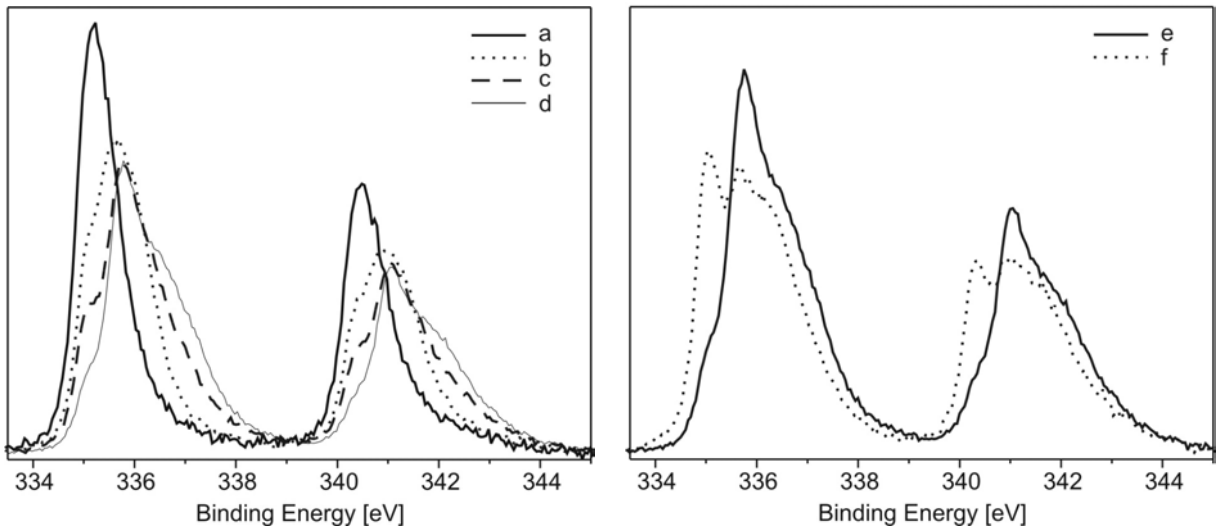

Figure 1: XPS spectra of Pd3d region. Left: Pd after deposition (a) and after oxygen exposure at 300 K (b), 500 K (c) and 600 K (d), hν=840 eV. Right: Pd after oxygen exposure at 600K, Photon energy 465eV (e) and 840eV (f)

oxygen are stored in interstitial sites of the Pd lattice. Theoretical calculations have also concluded that dissolution of oxygen in Pd is less favorable than formation of oxide structures [4]. For oxygen exposure at 600 K (d), the spectrum is similar to 500 K but the lower binding energy feature is further attenuated and the shoulder at higher binding energies gains additional intensity. In general, it can be seen that with increasing oxidation temperature the metallic Pd peak at lower binding energy becomes less intense while the shoulders at higher binding energy gain intensity. From the present data we conclude that more oxide is formed at higher oxidation temperatures. The oxide species formed during oxidation at 500 K can be reduced completely by subsequent CO exposure at 500 K via formation of CO_2, as shown in Fig. 2.

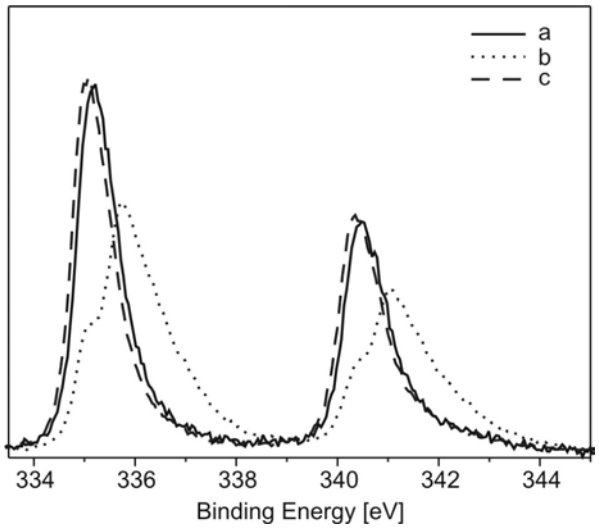

Figure 2: XPS spectra of Pd3d region. Pd after deposition (a), after oxygen exposure at 500 K (b) and after subsequent CO exposure at 500 K (c), hν=840 eV

These results are in good agreement with molecular beam experiments in which an onset temperature of 500 K for the formation of surface PdO_x species and more oxide formation at higher oxidation temperatures were observed. In these experiments it was found that after oxidation at 500 K, four times more oxygen is incorporated into Pd than at 400 K. Additionally molecular beam experiments have shown that the oxide species alter the adsorption properties of Pd particles and contribute oxygen to reactions, i.e. CO oxidation.

To gain information on the mechanism of oxide formation for our supported Pd model catalysts, XPS spectra with different photon energies (hν=465 eV and 840 eV) were taken after oxygen exposure at 600 K (Fig. 1, right), corresponding to higher and lower surface sensitivity, respectively. Interestingly, the metallic Pd feature is more intense in case of the lower photon energy (e) and the shoulder at higher binding energies, which we previously assigned to PdO, is more intense for higher photon energy (f). This indicates that most of the oxide is not formed on the surface of the particles but on the interface between Pd and oxide support. IRAS spectra using CO as a surface sensitive probe molecule show that the major fraction of the Pd surface is still metallic after oxidation at 500 K even tough a significant amount of oxygen is incorporated into Pd. These findings are in agreement with the XPS data and give additional evidence for oxide growth at the particle/support interface.

XPS spectra of the Fe2p region show no major shifts after oxygen exposure at elevated temperatures indicating that most of the oxygen is incorporated into the Pd particles and not into the iron-oxide lattice. However, isotope exchange experiments on a $Fe_3{}^{18}O_4$ film have shown that oxygen exchange between Pd and the iron-oxide support cannot be excluded completely.

References

[1] F.P. Leisenberger, G. Koller, M. Sock, S. Surnev, M.G. Ramsey, F.P. Netzer, B. Klötzer, K. Hayek, Surf. Sci. 445, 380 (2000)

[2] W. Weiss, M. Ritter, Phys. Rev. B 59, 5201 (1999)

[3] J.F Moulder, W.F. Stickle, P.E. Sobol, K.D. Bomben, Handbook of X-ray Photoelectron Spectroscopy, Perkin-Elmer-Corporation, Eden Prairie, Minnesota, USA, 1992

[4] M. Todorova, K. Reuter, M. Scheffler, Phys. Rev. B, submitted

Hydrogen diffusion in orthopyroxene

Roland Stalder
Geowissenschaftliches Zentrum, Göttingen University

Orthopyroxene is the second most abundant mineral in the Earth's upper mantle and incorporates by weight several 100 ppm water, and may therefore be a major host for water in the Earth's upper mantle. However, orthopyroxene crystals from the Earth's mantle transported by basaltic or kimberlitic magmas to the Earth's surface may have undergone hydrogen loss during ascent and may therefore not reflect their original water content. In order to quantify the dehydration kinetics of mantle minerals, hydrogen diffusion coefficients in orthopyroxenes are currently investigated. One important feature is the anisotropic behaviour of hydrogen diffusion, i.e., in natural Fe-bearing samples hydrogen diffusion along the [001]-direction is faster by one order of magnitude than along [010], which may contribute to the observed electrical anisotropy of the asthenosphere inferred from magnetotelluric data.

In this study synchroton IR-spectroscopy has been used for the first time to map OH- and OD-concentrations in orthopyroxene crystals exhibiting a diffusion profile due to thermal treatment in atmospheres with different H_2-, H_2O- and D_2O-pressures. During IR-analysis an automatic X-Y-stage moved the sample to the next analysis point. The higher beam brilliance and intensity of synchroton IR-spectroscopy in comparison to usual IR-spectroscopy was insofar advantageous as smaller beam diameters (10-20 µm) and shorter counting times (8-32 scans) generated sufficiently strong absorption signals in the OH- and OD-vibration regions, and hence enabled mapping with high spatial resolution. All spectra were automatically processed by peak height, peak area, peak height ratio or peak area ratio of two chosen peaks, and encoded as colours (Fig. 1 and 2).

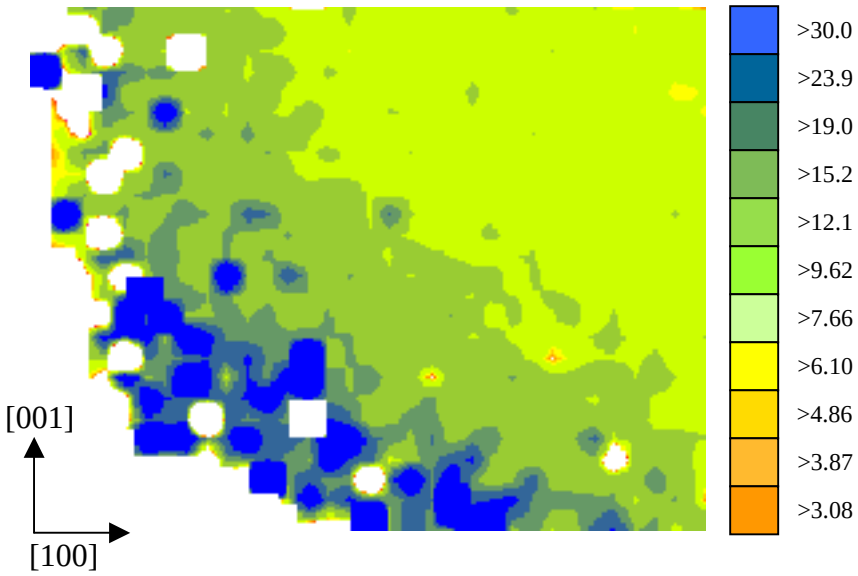

Abb.2: OH/OD-distribution map (discriminated by peak area ratio). The orthopyroxene crystals contained originally OD and was cooked in H_2O at 2 kbar and 800°C for 3 hours. The different diffusivities along [100] and [001] are clearly visible. At the outermost edge of the crystal (left) outliers (white dots, where processing of the spectra was not possible) occur frequently due to refraction at the crystal surface. Image size 400 x 350µm.

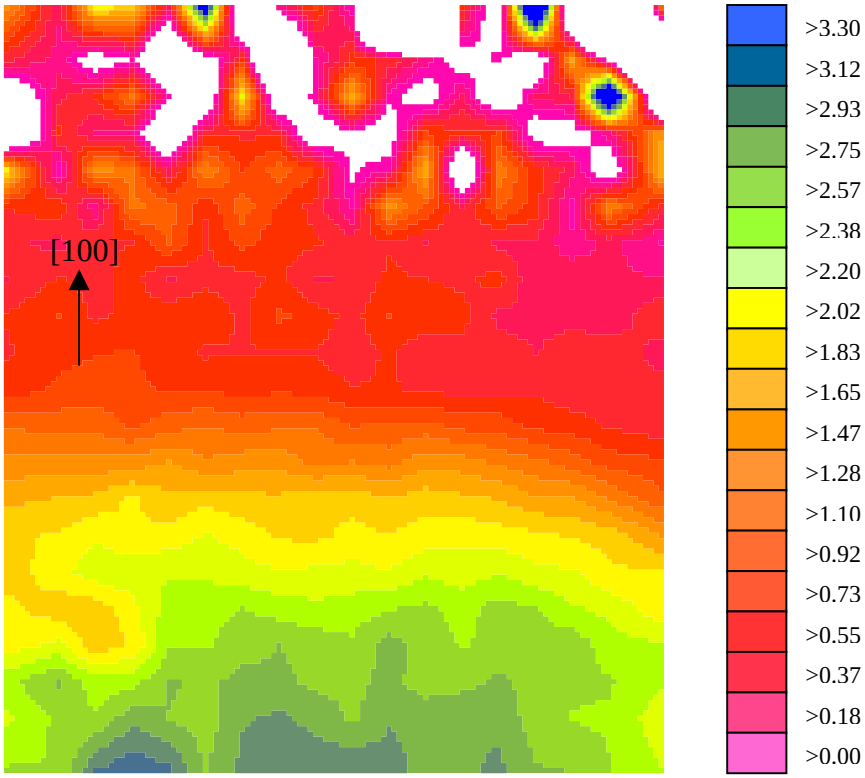

Abb.1: OH-distribution map of a partly dehydrated orthopyroxene crystal. A diffusion profile along the [100]-direction developed, the hydrogen loss towards the crystal rim is much more pronounced. Image size 250 x 300µm.

This new method has a high potential to visualize the homogeneity of a sample, detect unvisible cracks (i.e., additional undesired sinks during diffusion experiments) as well as extracting diffusion profiles to determine diffusion coefficients.

Acknowledgements: the author kindly acknowledges a travel grant of the BMBF (05 ES3XBA5)

Anomalous reorientation of self-assembled monolayers upon metal evaporation

Y. Tai, A. Shaporenko, W. Eck, M. Grunze, and M. Zharnikov

Angewandte Physikalische Chemie, Universität Heidelberg, Im Neuenheimer Feld 253, 69120 Heidelberg, Germany

Metallization of organic materials and fabrication of metal films on organic substrates are important issues, which are relevant for many areas of science and technology. Since organic surfaces are usually ill-defined on the macroscopic scale, both chemically and structurally, many model studies have been done on a specific organic support – self-assembled monolayers (SAMs). So far, different combinations of metal adsorbates and SAM substrates have been studied. It was found that the basic idea of a well-defined organic substrate works only to a limited extent, since metal atoms penetrate into the SAM forming metal-C bonds and diffuse to the SAM-substrate interface. While metal penetrates into the SAMs they usually lose their orientational order and heterogeneous metal-organic complexes are formed.

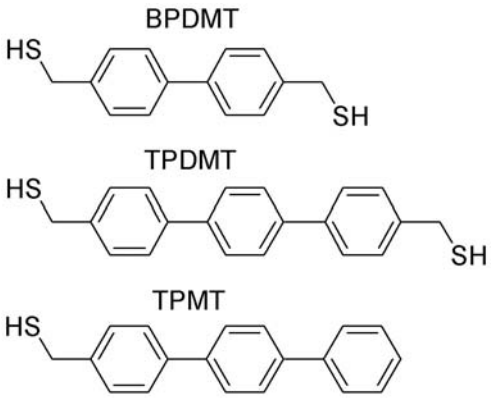

Fig. 1. Systems of this study

Here we describe a so far not observed effect in the metallization of SAMs, the metal-adsorbate-induced reorientation of SAM, which is distinctly different from the usual disordering scenario. We used SAMs formed from conjugated molecules [1,1'-biphenyl]-4,4'-dimethanethiol (BPDMT), [1,1';4',1"-terphenyl]-4,4"-dimethanethiol (TPDMT) and [1,1';4',1"-terphenyl]-4,4"-methane-thiol (TPMT) on Au (Fig. 1). These SAMs can be considered as prototypes of molecular-based devices. As a metal adsorbate, we used Ni, which is interesting in view of magneto-electronic devices.

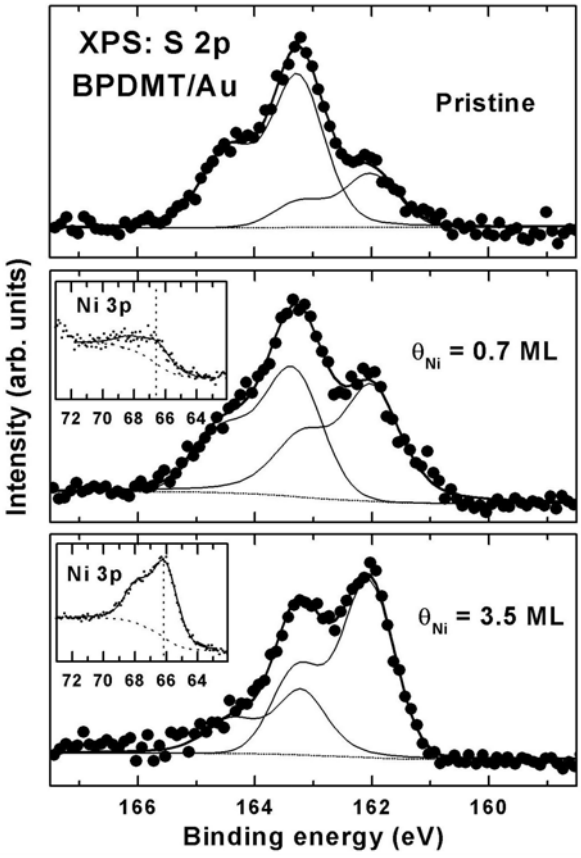

Fig. 2. S 2p and Ni 3p (inserts) XPS spectra of pristine and Ni-covered BPDMT/Au. The S 2p spectra are decomposed into the components associated with the thiolate and thiol sulfur (dashed lines).

S 2p and Ni 3p XPS spectra of pristine and Ni-covered [the coverage θ_{Ni} is given with respect to the Au(111) surface] BPDMT/Au are presented in Fig. 2. The S 2p spectra are decomposed into the components assigned to the thiolate (≈162.0 eV for S $2p_{3/2}$) and thiol (≈163.2 eV for S $2p_{3/2}$) sulfur. Changes in the relative intensity of both components during Ni evaporation suggest a continuous formation of Ni thiolate species at the SAM-ambient interface. The respective growth of the metal film is, however, accompanied by the penetration of Ni into the SAM, which starts at θ_{Ni} > 0.7-1 ML, as evidenced by the downward shift of the

Ni 3p doublet at higher θ_{Ni} and ion scattering spectroscopy data (not shown). The later data show that most of Ni is located at the SAM-substrate interface at high θ_{Ni}.

The start of the Ni penetration is associated with structural changes in the SAMs, as calculated from the NEXAFS data. Carbon K-edge NEXAFS spectra of pristine and Ni-covered (0.7 and 3.5 ML) BPDMT/Au acquired at X-ray incidence angles of 90° and 20° are shown in Fig. 3. The spectra exhibit characteristic adsorption features of oligophenyl chains and are dominated by a pronounced π_1^* resonance at ≈285.0 eV. The difference in the intensity of this resonance for the 90° and 20° spectra is a direct fingerprint of the orientational order and molecular tilt in the film. Comparing the spectra of the pristine film with those for θ_{Ni} = 0.7 and 3.5 ML, it is obvious that the 0.7 ML film exhibits a smaller tilt than even the pristine one. The quantitative evaluation of the NEXAFS data shows that the molecular tilt angle decreased by 11° at small θ_{Ni} (from 21.6° for the pristine film to 10.5° for θ_{Ni} = 0.7 ML), before the expected disordering was observed at higher Ni coverage.

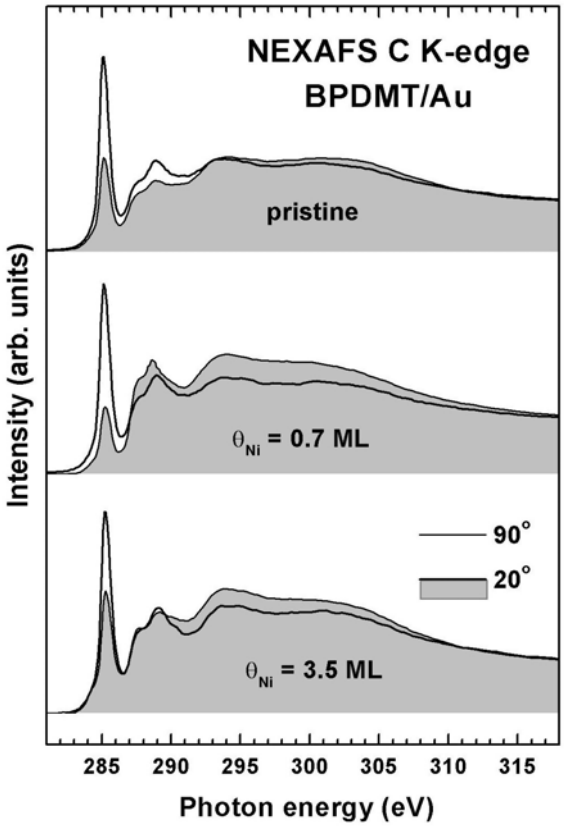

Fig. 3. Carbon K-edge NEXAFS spectra of pristine and Ni-covered BPDMT/Au acquired at X-ray incidence angles of 90° and 20°.

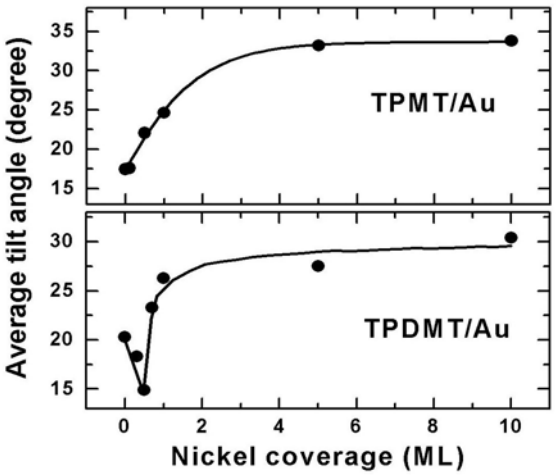

Fig. 4. Dependence of the average tilt angle of the terphenyl chains in TPMT/Au (top panel) and TPDMT/Au and (bottom panel) on the Ni coverage.

The reason of the reorientation effect could be either a change in the bonding geometry of the thiolate headgroups, or a rearrangement of the thiol tailgroups. To distinguish between these two possibilities, we performed Ni evaporation on TPMT/Au and TPDMT/Au and monitored the tilt of the terphenyl chains in the same manner as for BPDMT/Au. The results are given in Fig. 4: The thiol-terminated TPDMT/Au exhibited a similar decrease in the molecular tilt at small θ_{Ni} as BPDMT/Au, whereas H-terminated TPMT/Au revealed a usually observed continuous increase in molecular tilt with increasing θ_{Ni}.

Thus, the abrupt decrease of the molecular tilt by Ni absorption is obviously related to the effect of the thiol tailgroups. Presumably, Ni-sulfur complexes (NiS_2 and Ni_2S_3) form at the SAM/ambient interface, which affect the balance of the structural forces in the SAM and results in a molecular rearrangement. Formation of the Ni thiolate is directly exhibited by the S 2p spectra, as e.g. for BPDMT/Au in Fig. 2.

This work has been supported by DFG (JA 883/4-2) and BMBF (05KS4VHA/4 and 05 ES3XBA/5).

Inhomogeneous irradiation-induced cross-linking in aromatic self-assembled monolayers

A. Shaporenko, Y. Tai, W. Eck, M. Grunze, and M. Zharnikov

Angewandte Physikalische Chemie, Universität Heidelberg, Im Neuenheimer Feld 253, 69120 Heidelberg, Germany

Self-assembled monolayers (SAMs) attract considerable interest in physics, chemistry and biology. In particular, aromatic SAMs became very popular in view of their potential applications in molecular electronics and conventional or chemical lithography. The lithographic applications of aromatic SAMs are based on their resistance toward ionizing radiation such as X-rays or electrons. Contrary to aliphatic SAMs, which are damaged by such irradiation, aromatic SAMs undergo extended cross-linking, which transforms the film into a quasi two-dimensional polymer and prevents complete loss of the orientational order and an extended damage of the headgroup-substrate interface.

So far, it was assumed that irradiation-induced cross-linking develops homogeneously over the entire depth of aromatic SAMs. Here we present evidence that cross-linking occurs more likely close the SAM-ambient interface. As a test system, we used SAMs of [1,1';4',1"-ter-phenyl]-4,4"-dimethanethiol (HS-CH_2-$(C_6H_4)_3$-CH_2-SH: TPDMT) on polycrystalline Au(111) substrates.

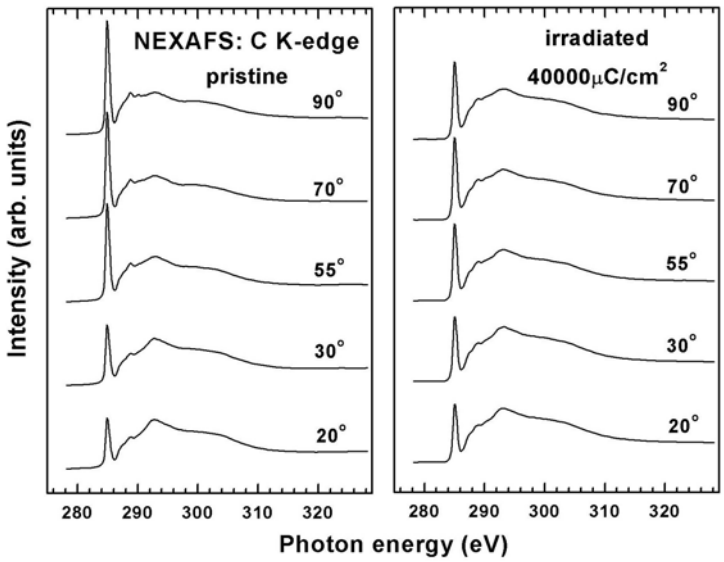

Fig. 1. Carbon K-edge NEXAFS spectra of pristine and irradiated (40000 μC/cm^2) TPDMT SAMs acquired at different angles of X-ray incidence.

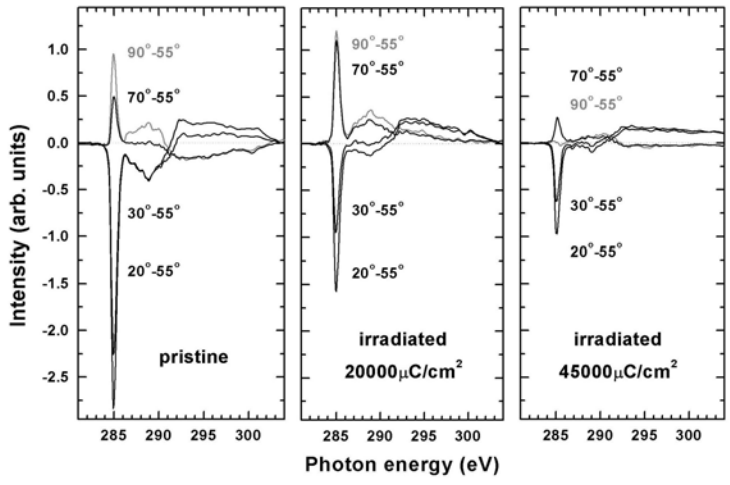

Fig. 2. Differences between the C K-edge NEXAFS spectra of pristine and irradiated (20000 and 40000 μC/cm^2) TPDMT SAMs acquired at different X-ray incidence angles.

Carbon K-edge NEXAFS spectra of pristine and strongly irradiated TPDMT SAMs acquired at different angles of X-ray incidence (Fig. 1) are dominated by the intense π_1^* resonance of the phenyl rings at ≈285.0 eV. The spectra of the pristine film exhibit a pronounced linear dichroism, which suggests high orientational order in these SAMs. The dichroism can be highlighted by difference spectra, which are shown in the left panel of Fig. 2, with the spectrum acquired at the magic angle of X-ray incidence (≈55°), taken as a reference. The most intense feature in these spectra is the π_1^* difference peak, which vary its amplitude gradually from negative values for the 20°-55° and 30°-55° spectra to positive values for the 70°-55° and 90°-55° spectra.

The intensity and, especially, linear dichroism of the absorption

resonances decreased significantly after prolonged (20000 and 40000 μC/cm^2) electron irradiation of the TPDMT films, as shown in Figs. 1 and 2, where the original and difference spectra of the irradiated films are presented. But even though there is a partial loss of the orientational order, there should be a gradual change (either an increase or a decrease) in the amplitude of the π_1^* peak with increasing X-ray incidence angle. However, this is not the case, at least for the 90° spectrum. This deviation from the normal behavior is especially pronounced in the respective difference spectra in the right panel of Fig. 2 - the intensity of the π_1^* difference peak in the 90°-55° spectrum is even lower than that for the 70°-55° spectrum. Interestingly, this effect develops gradually during the irradiation. As seen in the middle panel of Fig. 2, the π_1^* difference peak in the 90°-55° spectrum of the TPDMT film exposed to a dose of 20000 μC/Cm^2 has an intensity close to that in the respective 70°-55° spectrum.

Since a gradual change in the intensity of an absorption resonance with varying X-ray incidence angle is a common property of NEXAFS spectroscopy, the observed abnormal behaviour can only be related to some specific parameters of our samples and/or the experimental setup. The analysis of the experimental geometry suggests that this anomaly can only be explained by an inhomogeneous distribution of the irradiation-induced scission of the C-H bonds and the subsequent cross-linking within the TPDMT film - the topmost part of the film should be affected to a much higher extent by these processes as compared to the regions close to the headgroup-substrate interface (see Fig. 3). Since the excitation of the individual bonds should occurs uniformly over the film, such an uniform distribution can only be related to a preferable quenching of the electronically excited C-H* states close to the film-substrate interface. In fact, there is a mechanism for such a process, namely a dipole-dipole coupling of the electronically excited state with its image at the metal surface.

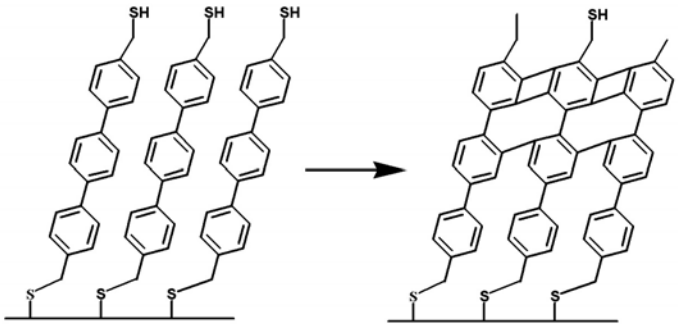

Fig. 3. Schematic drawing of irradiation-induced inhomogeneous cross-linking in the TPDMT SAMs.

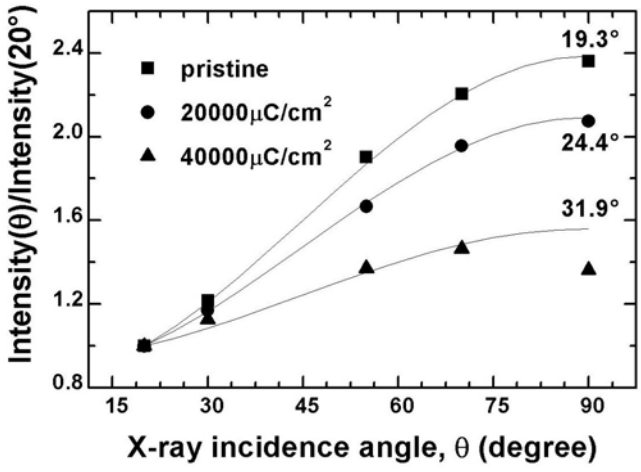

Fig. 4. Angular dependencies of the π_1^* resonance intensity ratio *I(θ)/I(20°)* for pristine (squares) and irradiated (circles for 20000 μC/cm^2 and triangles for 40000 μC/cm^2) TPDMT SAMs along with the best theoretical fits (solid lines). The values of the derived average tilt angle of the terphenyl moieties in the TPDMT films are given at the respective fit curves.

Along with the inhomogeneous distribution of the C-H bond scissions, an extremely high resistance of the TPDMT film to ionizing radiation has to be mentioned. Even after irradiation with a dose of 40000 μC/cm^2, there is still orientational order within the TPDMT film. The analysis of the NEXAFS data (see Fig. 4) suggests there is an increase in the average tilt angle of the terphenyl backbones by only ≈5° and ≈12° for the irradiation with doses of 20000 μC/cm^2 and 40000 μC/cm^2, respectively.

This work has been supported by DFG (JA 883/4-2) and BMBF (05KS4VHA/4 and 05 ES3XBA/5).

Study of thermal phase transitions in statistical block copolymers with X-ray diffraction methods and DSC

J. Reiche*, A. Kulkarni, H. Kosmella[$], H. Kamusewitz[$], K. Kratz[$], A. Lendlein[$],
Y. Bodenthin[%], W. Leitenberger[%], U. Pietsch[%]

University of Potsdam, Institute of Physics, Experimental Physics, Am Neuen Palais 10, D-14469 Potsdam, Germany

** Corresponding author: Tel.: +49-(0)331-977-1504, e-mail: jreiche@rz.uni-potsdam.de*

[$)] *GKSS Forschungszentrum Geesthacht GmbH, Institute of Chemistry, Kantstrasse 55, D-14513 Teltow, Germany*

[%)] *University of Potsdam, Institute of Physics, STAN, Am Neuen Palais 10, D-14469 Potsdam, Germany*

Energy dispersive X-ray diffraction studies of the thermal phase transitions in statistical block copolymers consisting of poly - ε - caprolactone- (PCL-) blocks and poly– p - dioxanone- (PPDO-) blocks with variable block number ratios of 67:33 (sample L20), 50:50 (sample L21) and 33:67 (sample L22) were carried out. The foils of these copolymers were investigated at the EDR-beamline of the BESSY synchrotron radiation source in the temperature range from 223 K to 403 K. The application of the materials as shape memory polymers with thermally stimulated shape recovery requires a detailed understanding of their phase behaviour [1]. The variation of block length and block number ratio gives rise for shifts in the glass transition temperature and the melting points of the segregated blocks. The data indicate the possibility of a mixed crystalline phase consisting of PCL- and PPDO-chains. The blocks of the PCL crystalline phase melt on heating above 50°C, while the PPDO crystals have a melting point in the temperature range above 85°C [2,3]. The melting of PCL-crystals is easily observed via the (110) peak corresponding to the lowest energy in the spectrum (Figure 1). The

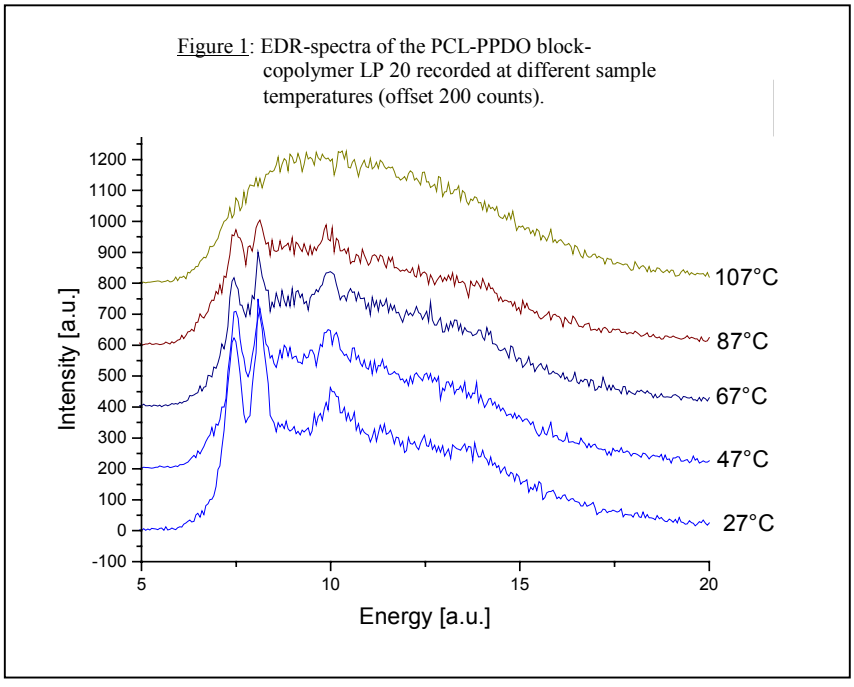

Figure 1: EDR-spectra of the PCL-PPDO block-copolymer LP 20 recorded at different sample temperatures (offset 200 counts).

neighbouring peak results from the overlap of (111) peaks of PCL and PPDO [4]. In the first heating cycle from room temperature up to 107°C we observe only one phase transition in the temperature range corresponding to the melting transition of PPDO crystals. This can be explained in two different ways:

- The melt-pressed films formed from the precipitate do not contain crystalline PCL, but only amorphous PCL, or
- a new mixed crystalline phase with a characteristic phase transition temperature of about 90°C is formed.

The DSC-data show two melting peaks in the corresponding temperature range, supporting the hypotesis of a "mixed" crystalline phase.

Fig. 2: X-ray data of PPDO-PCL copolymers / homopolymers

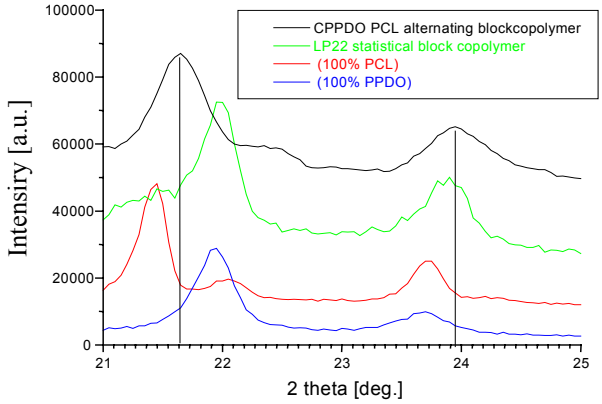

Conventional X-ray diffraction data of an alternating block copolymer, a statistical block copolymer and of the homopolymers yield further evidence for the existence of a mixed crystalline phase (Fig. 2). The alternating blockcopolymer shows a net plane distance (left peak) exactly beetween the values of the corresponding homopolymer lattices. Further, both copolymers show a peak (right peak) at a position, where neither of the homopolymers shows a peak. The peaks might be explained by a new phase consisting of blocks of both PCL and PPDO. The existence of such phase would be of great impact for the theoretical understanding of the shape memory effect in statistical PCL - PPDO block copolymers. Further experiments including the detaild study of the second heating / cooling cycle should be suitable to decide, wether the mixed crystal phase exists or not. Unfortunately, a second heating-cooling cycle was not yet investigated with the energy dispersive X-ray setup at BESSY.

References:

[1] A. Lendlein and R. Langer: *Science,* **296** (2002) 1673.

[2] J.S.Chawla and M. M. Amiji: *Int. J. Pharm*. **249** (2002) 127.

[3] M. A. Sabino, J. Albuerne, A.J. Müller, J. Brisson, R. E. Prud`homme: *Biomacromolecules* **5** (2004) 358.

[4] L.L. Arnal, F. Lopez-Carrasquero, E. Laredo and A. J. Müller: *Europ. Polym. J.* **40** (2004) 1461.

SYNCHROTRON-BASED INFRARED MICROSPECTROSCOPY AS A USEFUL TOOL TO STUDY HYDRATION STATES OF METEORITE CONSTITUENTS

L. V. Moroz[1] , M. Schmidt[2], U. Schade[2], T. Hiroi[3] and M. A. Ivanova[4]

[1]*German Aerospace Center (DLR), Institute of Planetary Research, Rutherford Str. 2, D-12489, Berlin, Germany,*
[2]*BESSY GmbH, Albert-Einstein-Str.15, Berlin, D-12489, Berlin, Germany,*
[3]*Department of Geosciences, Brown University, Providence, RI 02912, USA,*
[4]*Vernadsky Institute of Geochemistry and Analytical Chemistry RAS, Kosygin St. 19, Moscow 119991, Russia.*

Introduction

The meteorites Dho 225 and Dho 735 were recently found in Oman. Studies of their mineralogical and chemical composition suggest that these unusual meteorites are thermally metamorphosed CM2 chondrites [1,2,3]. Similar to Antarctic metamorphosed carbonaceous chondrites, the Dho 225 and Dho 735 are enriched in heavy oxygen compared to normal CMs [1,2]. However, IR studies indicating dehydration of matrix phyllosilicates are needed to confirm that the two new meteorites from Oman are thermally metamorphosed [4]. Synchrotron-based IR microspectroscopy is a new promising technique which allows the acquisition of IR spectra from extremely small samples. Here we demonstrate that this non-destructive techinique is a useful tool to study hydration states of carbonaceous chondrites *in situ*. In addition, we acquired reflectance spectra of bulk powders of the Dho 225 and Dho 735 in the range of 0.3-50 μm.

Experimental Procedures

We used synchrotron-based IR microspectroscopy to study hydration states of matrices in two polished sections of metamorphosed CM meteorites Dho 225 and Dho 735. We also studied polished sections of normal CM2 chondrites Mighei, Murrey, and Cold Bokkeveld for comparison. The IRIS IR Beamline at the BESSY II synchrotron facility in Berlin [5] is equipped with a Nicolet Continuμm IR microscope coupled to a FTIR spectrometer operating between 1 and 14 μm. An LN_2-cooled MCT detector was used for the spectral reflectance measurements. We deposited 1 mm–wide and 100 μm-thick gold layers directly onto the meteorite polished sections to provide gold surfaces for standard measurements. The use of a synchrotron source allowed us to probe meteorite matrices with a spot size as small as 20 x 20 μm, hence we avoided numerous sulfide, taenite, and tetrataenite grains in our measurements. We used smaller spot sizes of 10 x 10 μm and 5 x 5 μm to acquire IR spectra of the new Ca, Fe-oxysulfide phase recently found in the Dho 225 meteorite [1].

We acquired Vis-NIR reflectance spectra of bulk powders of Dho 225 and Dho 735 using the NASA-supported RELAB bidirectional spectrometer in the range of 0.3-2.6 μm at i=30° and e=0°. FTIR reflectance spectra were measured in the range of 2-50 μm at biconical geometry using a Nicolet 740 spectrometer. The FTIR spectra were merged with RELABbds spectra at ~2.4 μm to obtain the composite spectra.

Results and Discussion

We detected no signatures due to O-H stretching vibrations (in structural OH and/or bound H_2O) in the 2.7-3 μm spectral region in the Dho 225 and Dho 735 matrices by synchrotron-based IR microspectroscopy. We carefully scanned all the surfaces of our polished sections using a mapping stage but detected no O-H signatures in the spectra of any constituents of these two meteorites. We are aware that the absence of O-H features in reflectance spectra of polished surfaces does not prove the *absence* of hydrated phases in the samples. A significant contribution from specular reflection may mask the O-H stretching features in the 3-μm region. However, we detected the O-H absorption bands in the matrix spectra of normal CM2 meteorites Cold Bokkeveld, Murray and Mighei (Fig.1), and in tochilinite inclusions of Murray (Fig. 2), studied for comparison. This suggests lower contents of hydrated phases in the Dho 225 and Dho 735 matrices, compared to those in CMs.

Further evidence for the dehydrated state of the Dho 225 and Dho 735 matrices is the position and shape of strong Reststrahlen bands around 10-12 μm due to Si-O stretching vibrations (Fig. 3), consistent with fine-grained Fe-rich olivine. The positions and shapes of the Si-O bands in the IR spectra of the typical CM2 matrices are different, being consistent with mixtures of Fe-rich and Mg-rich phyllosilicates. Such a dramatic difference between non-metamorphosed and

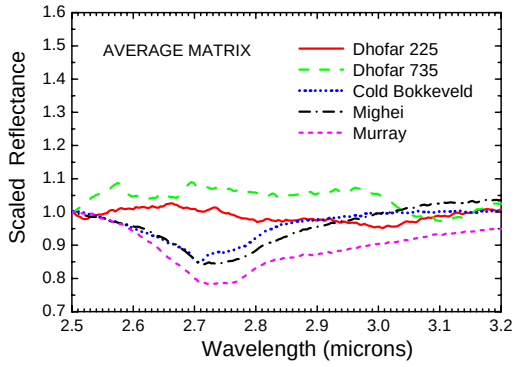

Fig. 1. Average matrix spectra of Dho 225, Dho 735 and normal CM2 chondrites in the region of O-H stretching vibrations.

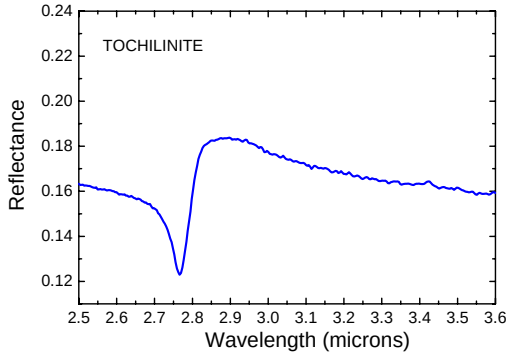

Fig. 2. O-H stretching feature in reflectance spectrum of tochilinite inclusion from CM2 chondrite Murrey.

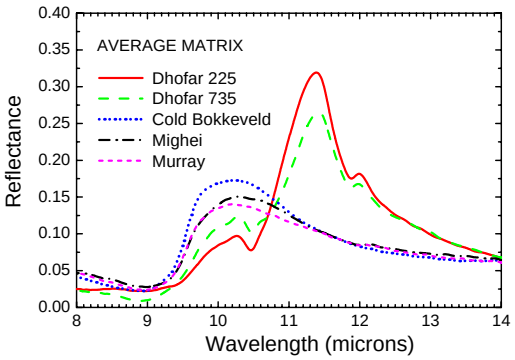

Fig. 3. Average matrix spectra of Dho 225, Dho 735 and normal CM2 chondrtites in the spectral region dominated by Si-O stretching features.

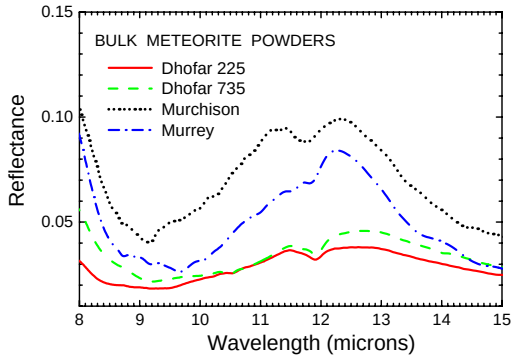

Fig. 4. RELAB spectra of Dho 225 and Dho 735 bulk powders compared to the spectra of normal CM2 chondrites Murchison and Murrey (from ASTER library, particle size <75 μm).

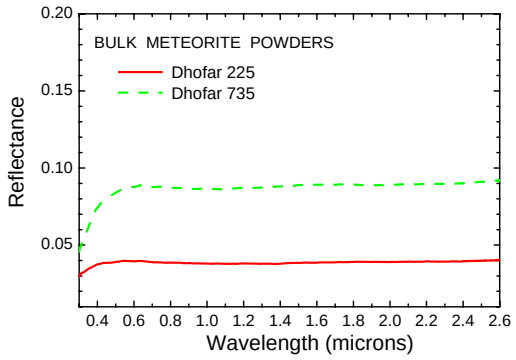

Fig. 5. Bidirectional Vis-NIR spectra of Dho 225 and Dho 735 bulk powders. Particle sizes are <125 μm and <150 μm, respectively.

metamorphosed CMs in this spectral region is not observed in the reflectance spectra of their bulk powders (Fig. 4). Signatures of olivine dominate the spectra of all CMs in this spectral region. Due to fine grain sizes, transparency features are evident between 12 and 14 μm. In CM2 chondrites olivine is present in chondrules, inclusions, and as single grains in the matrix.

Dho 225 contains the first Ca, Fe-oxysulfide phase found in nature [1]. Its best-fit stoichiometry and low analytical total indicate a formula of $(Ca_{4.66}\ Fe^{2+}_{0.34})5Fe^{3+}_{6}S_5O_9$ [1]. Another possible formula is $Ca_4Fe^{2+}_{5}S_4(OH)_4O_3$ [1], but the Ca, Fe-oxysulfide inclusions appear to lack OH, since they are stable under an electron beam. We have not detected absorption bands of structural OH at 2.7 μm in these grains. Taking into account the presence of strong structural OH signatures in our spectra of an OH-bearing sulfide mineral tochilinite (Fig. 2), this result strongly suggests the lack of OH in the structure of the Ca, Fe-oxysulfide.

Fig. 5 shows the Vis-NIR reflectance spectra of powdered Dho 225 and Dho 735 samples. The spectra have flat NIR slopes and are featureless, except for the UV-falloff typical of carbonaceous chondrites.

Conclusions

Our results confirm that the matrices of Dho 225 and Dho 735 are dehydrated compared to normal CM2 chondrites. Along with chemical, mineralogical, and isotopic studies, this indicates that the two new meteorites from Oman are the first non-Antarctic metamorphosed carbonaceous chondrites. Synchrotron-based IR microspectroscopy is a useful non-destructive method to study the hydration state of meteorite phases. For silicates, the spectral region where Si-O stretching vibrations occur is particularly promising.

Acknowledgments: The samples were provided by the Meteorite Committee RAS. Reflectance spectra of the meteorite powders were acquired at RELAB, a multiuser facility operated under NASA grant NAG5-13609.

References:

[1] Ivanova M. A. et al. (2002) *LPS XXXIII*, Abstract #1437.
[2] Ivanova M. A. et al. (2003) *MAPS* 38, A28.
[3] Ivanova M. A. et al. (2005) *LPS XXXVI*, Abstract #1054.
[4] Clayton R. N. and Mayeda T. K. (1999) *GCA*, 63, 2089-2104.
[5] Schade U. et al. (2002) *Rev. Sci. Instr., 73*, 1568-1570.

NEXAFS - spectroscopy on plasma-polymerised films prepared from organic molecules (Acrylic acid, allylamine, ethylene)

Sufal Swaraj, Umut Oran, Andreas Lippitz, Wolfgang Unger
Bundesanstalt für Materialforschung und –prüfung (BAM), D-12203 Berlin, Germany

Deposition of Plasma-polymerised thin films made from organic molecules is a technologically attractive way to obtain films with unique properties, e.g. adhesion, wettability, conductivity or selected chemical functionalisation. Characterisation of these films has been a great challenge to the analysts due to the co-existence of a great number of chemical species. To investigate such films in detail we employed a multi-method approach using photoelectron spectroscopy (XPS), absorption spectroscopy (NEXAFS) and time-of-flight secondary ion mass spectroscopy (ToF SIMS). In order to do this a dedicated plasma preparation chamber was designed which could be attached to the main analysis chamber of the NEXAFS apparatus at the HE-SGM beamline at BESSY II and at the ESCA and ToF-SIMS facilities at BAM. This facilitates "in-situ" analysis of the plasma-polymerised samples as well as analysis of samples after exposure to air.

The investigations were dedicated to find the correlation between basic chemical properties of the deposited films and a variation of plasma deposition parameters, e.g. pulsed or cw plasma condition, duty cycle in pulsed plasma, power of discharge, pressure of organic monomers and ratio of monomer partial pressures in co-polymerisation. Co-polymerised products are of special interest because it is assumed that technologically requested film properties may be "tailored". Monomers to be used are simple organic molecules with a polymerisable C=C bond, e.g. ethylene, allyl amine, acrylic acid, allyl alcohol and styrene.
Chemical properties of interest are:

- Concentration of unsaturated species like C=C, C=N, C≡N and C=O.
- Oxygen uptake and formation of oxygen species due to "ageing" in atmosphere.
- Retention of the principal structure unit of the used monomers in the film, (e.g. the phenylene ring from styrene) or the concentration of the number of well-defined functional groups (e.g. OH or COOH).
- Branching or/and cross linking in the film.

NEXAFS spectroscopy is well suited to give answers to some of the questions raised above because of its high sensitivity to unsaturated carbon species. An intense C1s, O1s or N 1s $\rightarrow\pi^*$ resonance features in the C K-edge, O K-edge or N K-edge spectra, respectively, is observed when these species exist in the plasma deposited films.

In the following we describe some results obtained from plasma polymerised films from allyl amine, acrylic acid and ethylene-acrylic acid monomer mixture. Films of around 100 nm thickness were deposited on clean silicon wafers. The spectra were obtained with grating 1 and 150 μm slit width at the HESGM beamline. All samples were analysed without exposure to air.

Plasma polymerised allyl amine films-Effect of discharge power variation: Fig. 1 presents the N K-edge spectra of the plasma polymerised allyl amine films. Four different plasma polymerised Allyl amine samples were prepared at continuous wave mode and constant monomer pressure (5.1 Pa) but different discharge powers (10W, 20W, 40 W, 50W). Feature A (398.2 eV) indicating a π^*(C=N) resonance, feature B (399.2 eV) indicating a π^*(C≡N) resonance, feature C (401 eV) indicating a π^*(N-ph) resonance and feature D indicating a σ^*(C-N) resonance are observed. The retention of the monomer structure is found to be more in films with lower C=N and C≡N bonds. Fig. 1 clearly indicates that at higher plasma powers

the formation of these bonds is the preferred process. A clear trend is observed from 10 W to 50 W. The presence of these bonds is technologically undesirable and the results indicate the use of milder deposition conditions for minimising their concentration.

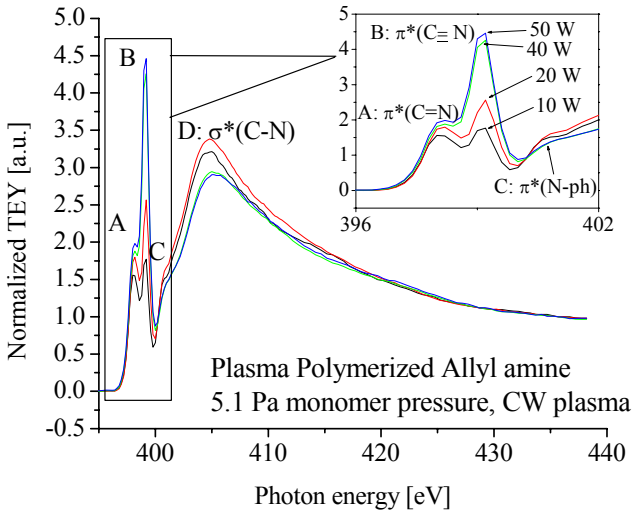

Figure 1: N K-edge NEXAFS spectra of Plasma polymerised allyl amine films.

Plasma polymerised acrylic acid films-Effect of duty cycle: Fig. 2 gives the C K-edge spectra of plasma polymerised acrylic acid films. A set of samples were prepared with a constant discharge power (20 W) and monomer pressure (5.1 Pa) but with varying r.f. duty cycles (0.05, 0.25, 1). Feature A (284.8 eV) indicating a π*(C=C) resonance, feature B (286.4 eV) indicating a π*(C=O) resonance, feature C (288.3 eV) indicating a π*(ROC=O) resonance and feature D indicating a σ*(C-O) resonance are observed in the spectra. Significant decrease in the intensity of π*(ROC=O) feature is observed with the increase in duty cycle. This might be because of the increased fragmentation of the monomer molecules with increase in effective power at higher duty cycle. Feature B is absent in the case of 0.05 duty cycle. Since the effective power is less in this case the monomer molecules might not dissociate to a greater extent. Hence, the chances of monomer fragments recombining to form other chemical species are less. The decrease in the ROC=O species in the film at higher duty cycles was also been cross-checked by XPS measurements (taken after the films were exposed to air).

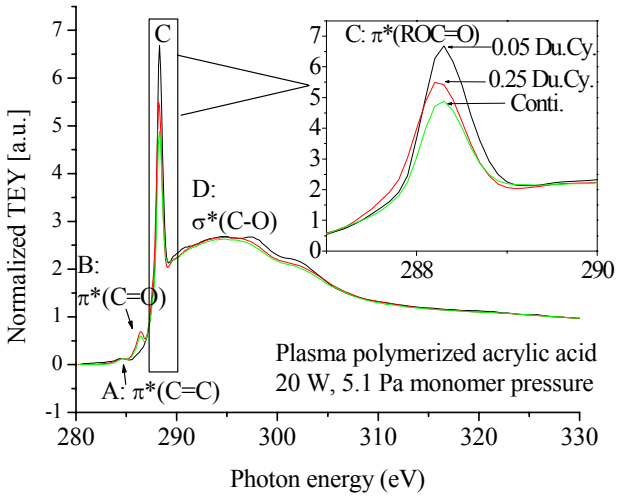

Figure 2: C K-edge NEXAFS spectra of Plasma polymerised acrylic acid films.

Plasma-polymerised acrylic acid-ethylene copolymer films-Effect of partial pressure: A set of copolymer films were prepared between ethylene and acrylic acid at varying partial pressures and the C K-edge spectra of the samples were analysed (fig. 3). The samples were prepared at a total discharge power of 20W, a total pressure of 5 Pa and duty cycle of 0.5. The intensity of the feature C representing the COOR group was found to increase with increase in partial pressure of acrylic acid. This indicates an increase in concentration of carboxylic acid groups on the surface of the films with an increase in the partial pressure of the acrylic acid co-monomer. These results were cross-checked by XPS after exposure of the films to air.

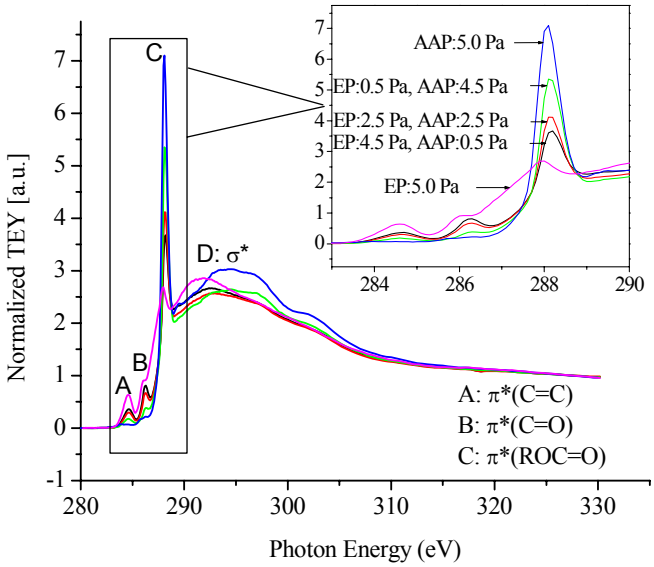

Figure 3: C K-edge NEXAFS spectra of Plasma polymerised ethylene-acrylic acid copolymer films.

Acknowledgements: Thanks are due to BESSY staff and other CRG members for the excellent collaboration during commissioning of the HESGM beamline. Special thanks to Matthias Mast (BESSY) and Olaf Schwarzkopf (BESSY) for support during experiments.

Probing the antiferromagnetic spin structure of ultrathin FeMn films by photoelectron emission microscopy

W. Kuch, L. I. Chelaru, F. Offi, J. Wang, M. Kotsugi, J. Kirschner
Max-Planck-Institut für Mikrostrukturphysik, Weinberg 2, D-06120 Halle, Germany
(BMBF No. 05 KS1EFA6)

In ferromagnetic materials the spins of the individual atoms are subject to long range parallel order, giving rise to a macroscopically observable magnetization. In antiferromagnetic materials, in contrast, the atomic moments—although also long range ordered—average to zero within a few atomic distances, and are thus much more difficult to detect. The spin structure of many antiferromagnetic materials has been investigated in bulk samples already decades ago by methods like neutron scattering or Mössbauer spectroscopy. The spin structure of ultrathin antiferromagnetic films with thicknesses of only a few nanometers, however, has mainly remained concealed, because these methods require thick samples to obtain sufficient signal. In atomically thin films the spin structure may be altered significantly compared to bulk materials by the enhanced influence of the interfaces and the reduced dimensionality. Ultrathin antiferromagnetic films are frequently employed in magnetic thin film devices like magnetoresistive sensors in magnetic hard disk read heads to manipulate the magnetic properties of adjacent ferromagnetic layers. The knowledge of the spin structure of the antiferromagnetic layer is crucial for both the design and operation of these devices as well as the fundamental understanding of the magnetic interaction between ferromagnetic and antiferromagnetic layers, often referred to as the exchange bias effect.

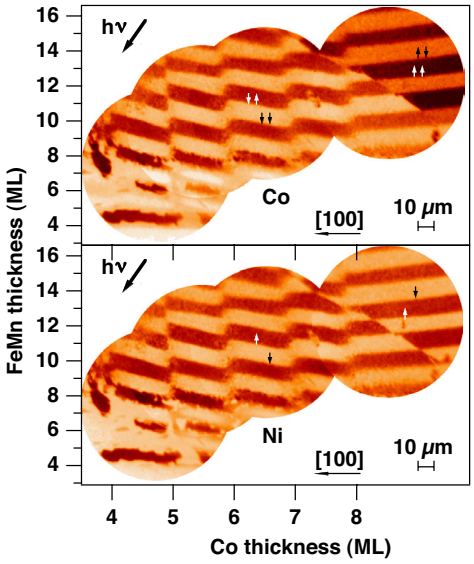

Fig. 1: Element-resolved magnetic domain images of 3 ML Co/15 ML Ni/FeMn (wedge)/Co (wedge)/Cu(001). Top: domain image at the Co L_3 edge, bottom: domain image at the Ni L_3 edge.

We have used photoelectron emission microscopy (PEEM) with X-ray magnetic circular dichroism (XMCD) as magnetic contrast mechanism to study the magnetic interface coupling in single-crystalline stacks containing ultrathin antiferromagnetic FeMn layers that are sandwiched between two ferromagnetic layers. XMCD-PEEM detects the difference in absorption of circularly polarized x-rays that are resonantly tuned to elemental absorption edges between parallel and antiparallel alignment of sample magnetization and helicity of the exciting x-rays.

By assembling trilayer stacks that have non-collinear axes of magnetization of the ferromagnetic layers we can probe the collinearity of the antiferromagnetic spin structure.

Single-crystalline, virtually unstrained fcc FeMn films with no indications for chemical order were obtained by deposition on a Cu(001) single crystal substrate [1]. Scanning tunneling microscopy measurements had revealed that the FeMn films grow on Cu(001) in a near-perfect layer by layer-mode [2], in which the surface roughness is confined to monatomic islands or vacancy islands [2] due to the low lattice mismatch between FeMn and Cu ($\approx 0.4\%$). Some of the layers were prepared as wedges suitable for microscopic imaging in order to explore the thickness dependence of the magnetic domain patterns. The XMCD-PEEM measurements were performed at the UE56/2–PGM2 beamline of the Max-Planck-Society.

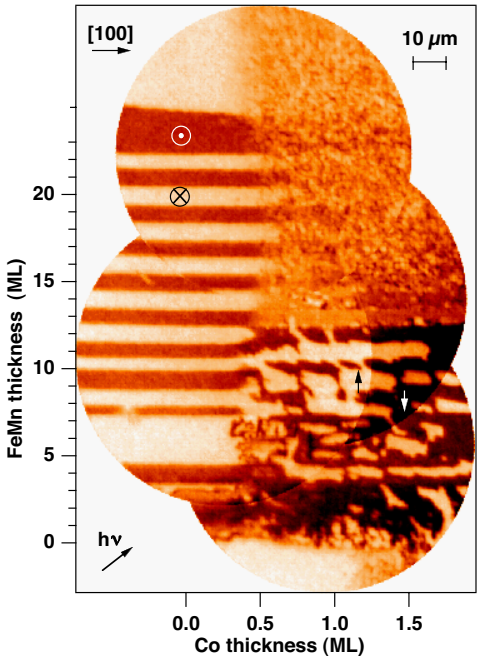

Fig. 2: Magnetic domain image at the Ni L_3 edge of Co (wedge)/15 ML Ni/FeMn (wedge)/15 ML Ni/Cu(001). In the left part of the image the magnetization of the top layer is perpendicular to the film plane, while it is in-plane for Co thicknesses above 0.5 ML.

Fig. 1 shows element-resolved magnetic domain images of a sample in which an FeMn wedge (thickness increasing from bottom to top, left axis) was sandwiched between a Co wedge as the bottom ferromagnetic layer (thickness increasing from left to right, bottom axis), and a top ferromagnetic layer consisting of 15 atomic monolayers (ML) of Ni and 3 ML Co. The top panel shows the magnetic domain image obtained at the Co L_3 absorption edge; its signal is therefore composed by contributions of both the bottom and top ferromagnetic layers, since both of them contain Co. The bottom panel shows the magnetic domain pattern obtained at the Ni L_3 edge, which represents the domain pattern of the top ferromagnetic layer only. Regular stripes with alternating parallel and antiparallel coupling between the two ferromagnetic layers across the antiferromagnetic FeMn spacer layer are recognized as the FeMn thickness is increased. The period of 2 ML in FeMn thickness indicates direct exchange coupling through the antiferromagnetic spacer layer. In addition to these stripes, a sawtooth-like wiggling of the phase of this periodic interlayer coupling is observed as the Co bottom layer thickness is increased. It is attributed to the periodic modulation of the bottom interface roughness due to the layer-by-layer growth of the films.

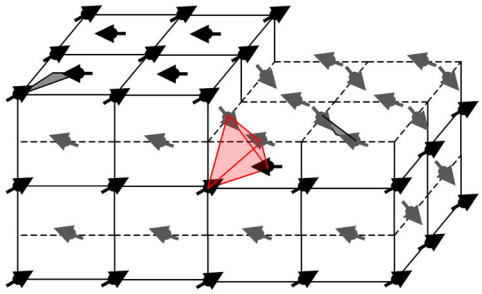

Fig. 3: Sketch of the $3Q$ non-collinear antiferromagnetic spin structure. Monatomic steps at the (001) surface exhibit 90° different axes of the spin component in the film plane, and opposite sign of the spin component perpendicular to the film plane.

Fig. 2 shows the magnetic domain pattern at the Ni L_3 edge of a trilayer in which an FeMn wedge (left axis) is sandwiched between 15 ML Ni on the bottom and Co (wedge, bottom axis)/15 ML Ni on the top. The bottom layer had been magnetized into a single domain state by an external magnetic field after deposition. The image thus represents the domain pattern of the top Co/Ni layer. In the left part of the image, for zero or low Co thickness, a stripe-like domain pattern with a stripe period of 2 ML FeMn thickness as before is observed at FeMn thicknesses above 9 ML. Here the magnetization directions of the bottom and top ferromagnetic layers are perpendicular to the film plane, with alternating parallel and antiparallel alignment. At Co thicknesses above 0.5 ML the magnetization of the top ferromagnetic layer turns into the film plane. The small domains observed in this region for FeMn thicknesses above 12 ML show that in addition to an oscillatory coupling of the spin component perpendicular to the film plane, the spin component in the plane experiences a laterally fluctuating pinning [3]. The simultaneous presence of both, oscillatory coupling of the spin component parallel to the bottom FM layer magnetization, and laterally fluctuating pinning of the spin component perpendicular to it, provides direct experimental evidence that a three-dimensional non-collinear antiferromagnetic spin structure, reminiscent of that of bulk FeMn, must be also present in its near-two dimensional realization. Such a spin structure, the so-called $3Q$ structure, is schematically depicted in Fig. 3. It is characterized by four different sublattices in which the spins point along four different $\langle 111 \rangle$ directions. This interesting result has also major implications on theoretical models of the interaction between antiferromagnets and ferromagnets that try to describe the exchange bias effect.

References

[1] F. Offi, W. Kuch and J. Kirschner, Phys. Rev. B **66**, 064419 (2002)

[2] W. Kuch, L. I. Chelaru and J. Kirschner, Surf. Sci. **566–568**, 221 (2004)

[3] W. Kuch, L. I. Chelaru, F. Offi, J. Wang, M. Kotsugi and J. Kirschner, Phys. Rev. Lett. **92**, 017201 (2004)

Exploring magnetization reversal dynamics in magnetic multilayers with temporal, spatial and layer resolution

W. Kuch[1], J. Vogel[2], J. Camarero[3], K. Fukumoto[1], Y. Pennec[2], S. Pizzini[2], M. Bonfim[2], J. Kirschner[1]

1 Max-Planck-Institut für Mikrostrukturphysik, Weinberg 2, D-06120 Halle, Germany

2 Laboratoire Louis Néel, CNRS, 25 avenue des Martyrs, F-38042 Grenoble, France

3 Universidad Autónoma de Madrid, E-28049 Madrid, Spain

(BMBF No. 05 KS1EFA6,

EU BESSY-EC-HPRI 1999-CT-00028)

How long does it take to load this text from the hard disk of your computer? With the current technology this depends on the time needed to turn the magnetization of a soft magnetic layer in the read head of the hard disk drive. A magnetoresistive spin valve sensor, as it is nowadays commonly used in magnetic hard disk read heads, consists of two ultrathin ferromagnetic layers that are separated by a non-magnetic spacer layer. The magnetization direction of one of the magnetic layers is switched by the magnetic bits on the disk over which the head passes, leading to a change in electrical resistance. Presently, read and write times approach one nanosecond, corresponding to 1 GHz frequency. Controlling and understanding the magnetization reversal dynamics in magnetic thin films is thus a major issue for accelerating the speed at which data can be stored and read back.

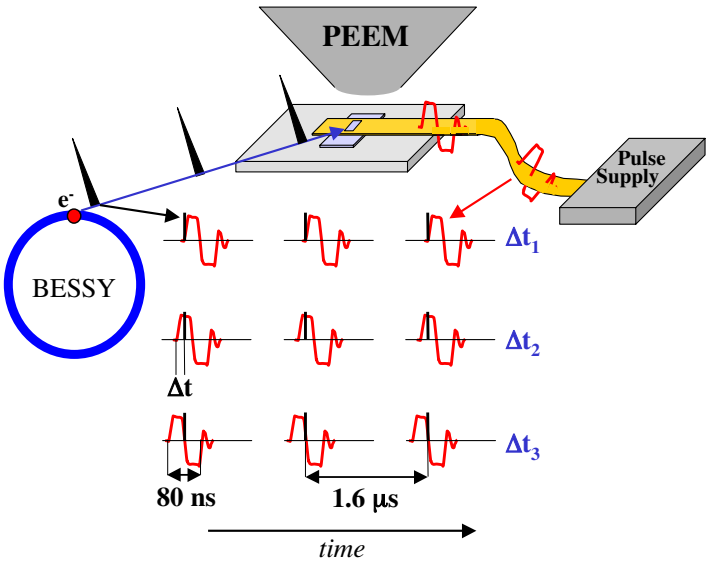

Fig. 1: Sketch of the stroboscopic time-resolved magnetic imaging technique. Current pulses from a fast pulse power supply induce magnetic field pulses of several nanoseconds (red curves) in a microcoil close to the sample position. Synchronized X-ray pulses in single-bunch mode of about 60 ps length hit the sample at a variable time delay Δt relative to the magnetic pulses [2]. Electrons excited by these x-ray pulses are used to obtain dynamic stroboscopic and layer-resolved domain images in a photoelectron emission microscope (PEEM).

Only very few experimental techniques can address the microscopic magnetization reversal behavior of the different magnetic layers in a spin valve separately. One of them is photoelectron emission microscopy (PEEM) with synchrotron radiation, which employs x-ray magnetic circular dichroism (XMCD) as magnetic contrast mechanism [1]. Because of the element selectivity of XMCD, different magnetic layers in a multilayered stack can be imaged separately.

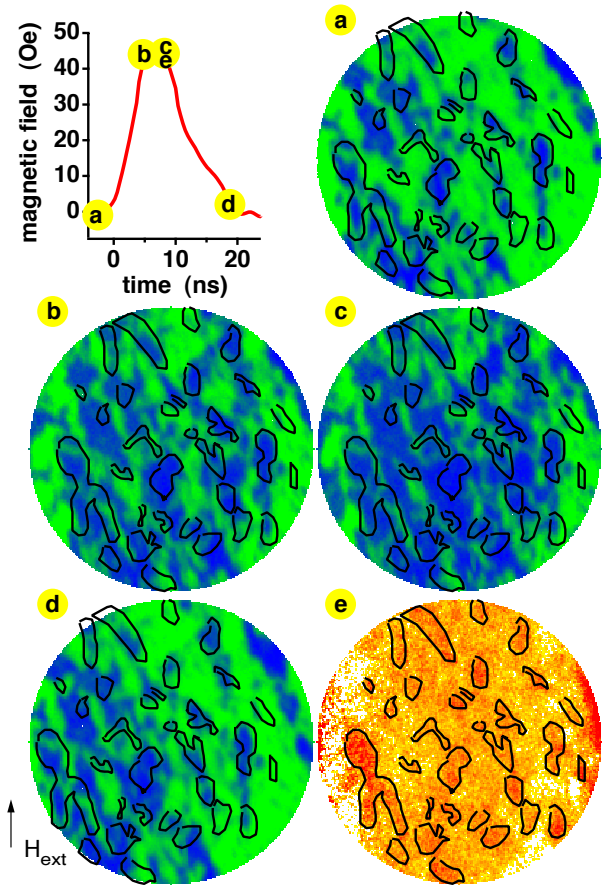

Fig. 2: Layer-resolved stroboscopic magnetic domain images of an $Fe_{20}Ni_{80}$/Cu/Co spin valve at different times during the periodic application of 18 ns-long magnetic field pulses (red curve). Panels a–d represent the magnetic domain pattern of the magnetically softer $Fe_{20}Ni_{80}$ layer at the time delays indicated in the graph, panel e represents the magnetic domain pattern of the magnetically harder Co layer. Black lines in the images indicate the position of domains in the Co layer.

Time resolution is obtained using a pump–probe approach (Fig. 1). Magnetic field pulses provided by a microcoil and a fast power supply (the pump) are synchronized with the synchrotron X-ray photon pulses (the probe) [2]. Images are acquired for different constant delays between pump and probe, i.e., at different times before, during, or after the application of the magnetic field pulses. In this way the magnetization dynamics of each magnetic layer can be visualized separately with a time resolution limited by the X-ray pulse width (about 60 ps).

We have used the combined temporal, spatial, and layer resolution of time-resolved XMCD-PEEM to study the magnetization reversal dynamics of a 5 nm $Fe_{20}Ni_{80}$/4 nm Cu/5 nm Co spin valve on the nanosecond time scale. The measurements have been performed at the UE52–SGM beamline. Fig. 2 shows stroboscopic domain images of the $Fe_{20}Ni_{80}$ layer (domain contrast green/blue) and of the Co layer (domain contrast yellow/red). The two magnetic layers are separated by a 4 nm non-magnetic metallic Cu spacer layer. The images were acquired at different times during the application of short field pulses as indicated in the upper left panel. The magnetization of the magnetically harder Co layer is not affected by these pulses, i.e., the Co layer shows the same pattern as in panel e for all times. In the $Fe_{20}Ni_{80}$ layer, the magnetic field pulses favor the growth of the blue domains through propagation of domain walls (panels

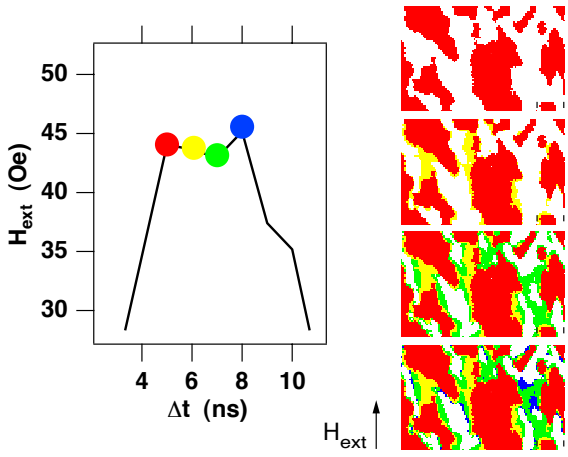

Fig. 3: Analysis of magnetic switching of the $Fe_{20}Ni_{80}$ layer by expansion of domains during the plateau of the field pulse, shown in a magnified view on the left. The images at the right represent the expansion of the switched areas in one nanosecond time steps. Differently colored areas indicate the increase of switched domains at the times indicated by symbols of the corresponding color in the graph on the left.

a–c). Upon reduction of the field, magnetic coupling to the Co layer leads to a shrinking of the blue domains (panel d), until after 1.6 μs eventually the starting configuration is restored (panel a), and the same cycle starts over again.

Closer analysis of the domain wall motion of the $Fe_{20}Ni_{80}$ layer during the plateau of the field pulse (between panels b and c of Fig. 2) is shown in Fig. 3. The right hand side shows the evolution of the $Fe_{20}Ni_{80}$ domain pattern in time steps of 1 ns. Different colors represent the incremental expansion of regions of switched magnetization at the times indicated in the graph at the left hand side, which represents a blow-up of the peak of the field pulses. The biggest changes, i.e., the highest domain wall velocities, are seen in regions where two existing domains are getting connected. In these areas, the evolution of reversed domains is somehow reminiscent of merging water droplets. This is due to the domain wall energy, which opposes the expansion of small domains. The domain wall velocity is thus greatest in areas where the total domain wall length is preserved or reduced [3]. Measurements on similar samples have shown that the magnetization reversal dynamics depends also on the competition between local magnetic interlayer coupling and intrinsic properties of the sample [4]. The combination of temporal, spatial and layer resolution makes this technique so extremely powerful for studying magnetization dynamics in layered magnetic systems.

References

[1] W. Kuch, Appl. Phys. A **76**, 665 (2003)

[2] J. Vogel, W. Kuch, M. Bonfim, J. Camarero, Y. Pennec, F. Offi, K. Fukumoto, J. Kirschner, A. Fontaine and S. Pizzini, Appl. Phys. Lett. **82**, 2299 (2003)

[3] W. Kuch, J. Vogel, J. Camarero, K. Fukumoto, Y. Pennec, S. Pizzini, M. Bonfim and J. Kirschner, Appl. Phys. Lett. **85**, 440 (2004)

[4] J. Vogel, W. Kuch, J. Camarero, K. Fukumoto, Y. Pennec, M. Bonfim, S. Pizzini, F. Petroff, A. Fontaine and J. Kirschner, J. Appl. Phys. **95**, 6533 (2004)

ITO SURFACE AND INTERFACE POTENTIALS

Y. Gassenbauer, A. Klein
Darmstadt University of Technology, Institute of Materials Science, D-64287 Darmstadt

Keywords: TCO, ITO, photoelectron spectroscopy, surface potentials

Introduction

Transparent conducting oxides (TCOs) such as ZnO, TiO_2, SnO_2, In_2O_3 and ITO (In_2O_3:Sn) are widely used as electrode materials in optoelectronic devices for example in organic light emitting diodes (OLEDs), flat panel displays or thin film solar cells. Here the electronic surface and interface properties are decisive for device functionality where the electronic potentials are of particular importance. As ITO is used as a hole injection material in OLEDs the barrier height for hole injection is given by the distance between the Fermi level position with respect to the highest occupied molecular orbital (HOMO) in the organic material. The surface and interface electronic potentials strongly depend on preparation conditions of the different layers and the material combination. ITO as a degenerate semiconductor is often treated as a metal. However the bulk and surface electronic properties differ [1]. Under reducing preparation conditions the bulk Fermi level position lies well above the conduction band minimum whereas the surface Fermi level is inside the forbidden bandgap. The origin of the surface band bending is not understood in detail so far. Under less reducing conditions the surface fermi level moves downwards in the bandgap which causes an increase in work function that may lead to smaller barrier heights for hole injection in OLEDs. One has to consider that by interface formation and reaction or surface treatments the initial Fermi level position and carrier concentration can be changed again.

Experimental

The preparation of thin films was done in UHV chambers that were attached to a photoelectron spectrometer system (SOLIAS), which was connected to the beamline U49-2/PGM2. The ITO films were prepared by radio frequency magnetron sputtering using ceramic targets (90 % In_2O_3, 10 % SnO_2) changing the sputter gas mixture (argon, oxygen) and substrate temperature. The pressure during ITO deposition was kept constant at $5x10^{-5}$ Pa. Then organic films were grown by sequential thermal evaporation onto the freshly prepared ITO substrates using homemade effusion cells. The samples were characterized using photoelectron spectroscopy after each deposition step.

Results and Discussion

Interfaces between Zn-phtalocyanine (ZnPc) and ITO prepared with pure Ar and with 10 % O_2 and 90 % Ar and in the sputter gas were examined. In the first case the ITO shows a metallic surface indicated by a Fermi edge emission. With increasing ZnPc coverage no chemical reactions can be observed. The final barrier height can be determined to 1.05 eV. In the latter case the ITO exhibits a low initial Fermi level and no metallic surface. However with ZnPc film deposition a strong upward shift of the surface Fermi level accompanied by reappearance of a Fermi edge can be observed (Figure 1). This indicates an interface reaction leading to a partial reduction of the ITO already with low ZnPc coverages. This is confirmed

by the C 1s spectra that show an emission at 289.4 eV and can be attributed to formation of C-O bonds (Figure 2). Additionally the C 1s line shape characteristic for ZnPc is not achieved until a thick layer is deposited. The final barrier height is also 1.05 eV but an interface compound has to be taken into account.

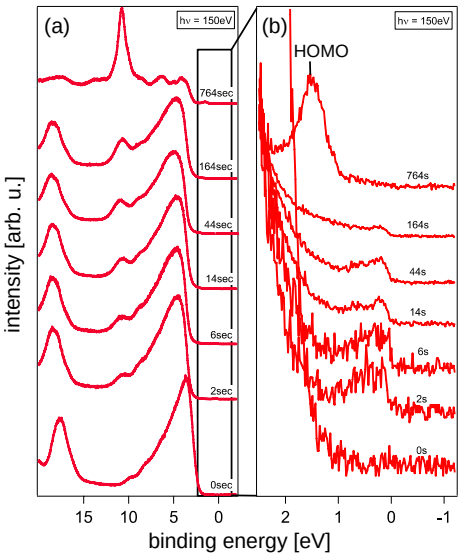

Figure 1. Valence band spectra of ITO films and sequentially deposited ZnPc. The ITO was sputtered with 90 % Ar and 10 % O_2 at a substrate temperature of 400 °C. The valence band maximum region of (a) is magnified in (b).

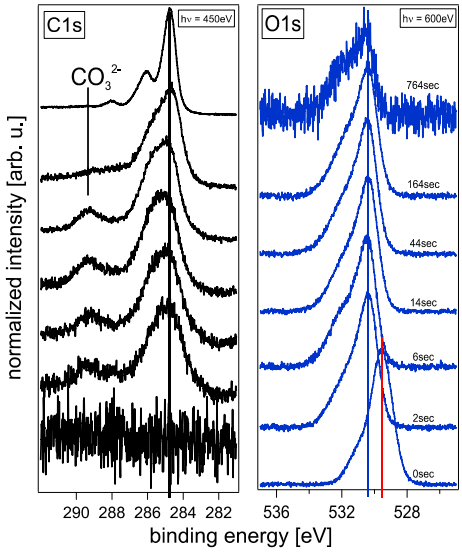

Figure 2. Normalized core level spectra of the C 1s and O 1s emission lines measured after each deposition step. An emission line at 289.4 eV in the C1s spectra for low ZnPc coverages can be attributed to formation of C-O bonds indicating an interface reaction.With the first ZnPc film deposition a strong shift of the O 1s emission line occurs reducing the initial band bending at the surface.

Conclusion

Though ITO is a degenerate semiconductor the surface Fermi level position of ITO is strongly affected by preparation conditions or interface formation. This has to be taken into account choosing better material combinations and determining the barrier heights.

References

[1] Y. Gassenbauer et al., Solid State Ionics 173 (2004) 141.

Scattering from Magnetic Nanostructures in Transmission Geometry

Olav Hellwig[1,2], Stefan Eisebitt[1], Johannes Grabis[3], Alexei Nefedov[3] and Hartmut Zabel[3]

[1]*BESSY GmbH, Albert Einstein Str. 15, 12489 Berlin, Germany*
[2]*San Jose Research Center, Hitachi Global Storage Technology, 650 Harry Road, San Jose, CA 95120, USA*
[3]*Institut für Experimentalphysik/Festkörperphysik, Ruhr-Universität Bochum, Universitässtr. 150, 44780 Bochum, Germany*

In a recent effort we have upgraded the ALICE reflectometer [1] at BESSY for Small Angle Scattering (SAS) experiments in transmission geometry. In such a transmission setup it is possible to obtain detailed information about the lateral heterogeneity of thin film systems, such as for example chemical and magnetic grain sizes and grain size distributions [2,3], chemical segregation processes [4], nanoparticle arrays [5], magnetic domain structures [6-8] and otherwise laterally nanostructured systems. The different scattering terms allow probing both, electron density variations as well as variations in the magnetic moment density. The resolution of the scattering studies is only limited by the wavelength, such that in the soft X-ray range heterogeneity on the length scale of a few nanometers up to one micrometer can be investigated. However, this approach usually requires sample deposition onto Si_3N_{4-x} membrane substrates that are commercially available today, but do not allow easily the deposition of single crystalline thin films.
The general geometry for SAS in transmission is shown in Fig.1 together with a demonstration scattering experiment that was performed on stripe domains in Co/Pt multilayers with perpendicular anisotropy.

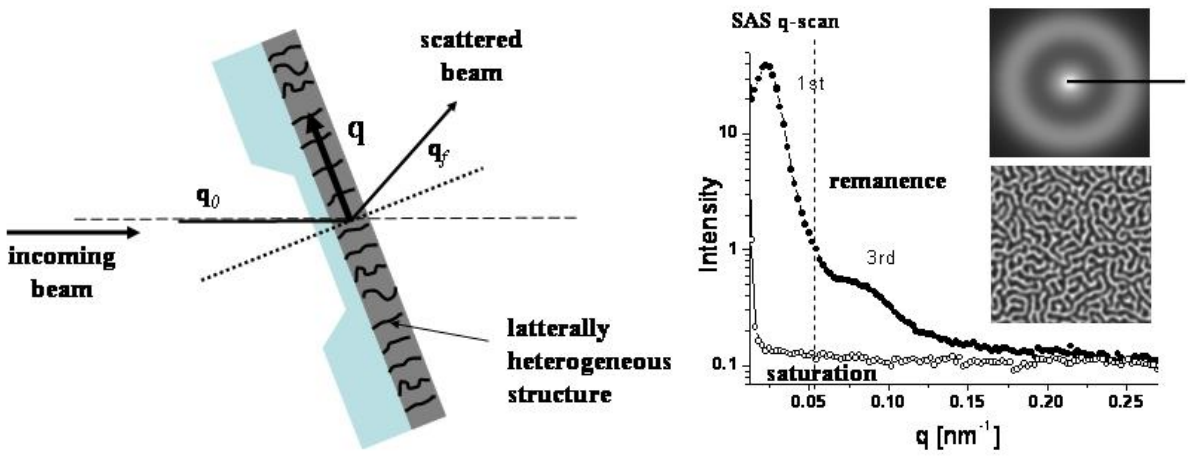

Fig. 1: Left: SAS in transmission geometry. The thin film sample (dark grey) has been deposited onto a Si_3N_{4-x} membrane substrate (light blue). The soft X-ray beam is coming in from the left and is scattered by the lateral heterogeneous nanostructures of the thin film. Notice that the scattering vector **q** lies within the film plane rather than perpendicular to it as common in reflection geometry. Right: SAS data at the Co-L_3 absorption edge from perpendicular magnetic stripe domains. The lower inset shows a (5 μm)^2 MFM image of the domain structure that was investigated by scattering. The upper inset exhibits the corresponding 2-D SAS intensity as detected with a CCD camera that was positioned behind the membrane sample. In the center the transmitted direct beam is visible, while the diffraction ring originates from the regular domain spacing. Here the radius of the ring is inversely proportional to the domain periodicity and the width of the ring is a measure for deviations from this periodicity (the sharper the ring the more well defined is the periodicity). The solid symbols in the intensity versus scattering vector **q** plot are a one dimensional radial scan through the diffraction ring at remanence as indicated by the black line in the CCD image. The q-range limit as probed by the CCD is marked by a dashed line in the plot. However, the photo diode detector on a rotation arm provides access to radial profiles up to much higher q values and reveals 1st and 3rd order reflections from the domains. In saturation the diffraction ring vanishes (open symbols), since all domains are annihilated and the sample becomes magnetically uniform with no SAS.

The usual transmission geometry is especially sensitive to perpendicular anisotropy systems. However also in-plane magnetic systems have been investigated as shown in previous longitudinal media studies [2,3]. Due to the implementation of the transmission geometry it was also possible to increase the externally available field up to 6.5 kOe perpendicular to the membrane by reducing the pole gap down to 4 mm. Combined with a standard cryostat setup that can provide temperatures down to about 30 Kelvin the system allows to cover a wide parameter range for studies in transmission geometry down to the nanometer length scale.
We use the X-ray dichroism effect of the incident circularly polarized beam in absorption through the membrane to obtain element specific information about the hysteresis loop of the average macroscopic magnetization M. On the other hand one can probe the SAS intensity during external field reversal at any scattering vector **q**, i.e. at any desired nanoscopic length scale (from half the wave length to about a micrometer). Fig.2 shows the resonantly enhanced contrast of the dichroism in the direct beam absorption through the membrane (Fig.2a and b) and in the SAS (Fig.2c) diffraction ring across the Co-L_3 absorption edge.

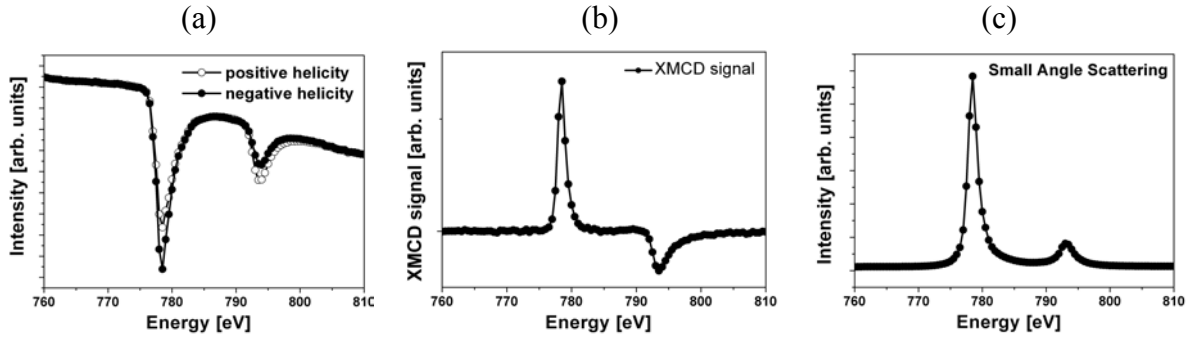

Fig.2. (a): Energy scan of the direct beam across the Co-L_3 absorption edge after transmission through the Co/Pt multilayer membrane sample with positive (solid symbols) and negative (open symbols) helicity. (b): Relative X-ray Magnetic Circular Dichroism (XMCD) signal of the two energy profiles in (a). (c): Energy dependence of the SAS diffraction ring intensity at q=0.025 nm^{-1} (~ 250 nm) across the Co-L_3 absorption edge. The dichroism in (a) and (b) can only be exploited using circular polarized light, while the small angle scattering in (c) is an interference effect that can be observed also for linearly polarized light since negative and positive helicity photons are scattered into the same reciprocal space element.

This contrast can be used to record hysteresis loops in an externally applied field. This is shown in Fig.3. In absorption we tune the energy to the peak XMCD signal in Fig. 2b and in SAS to the peak intensity in Fig. 2c. Depending on the strength of the absorption versus the scattering there can be slight difference in the optimum energy position for both cases.
The SAS hysteresis loop (Fig.3, bottom) is extremely sensitive to initial domain nucleation and final domain annihilation processes as demonstrated in a recent study [9]. Thus it becomes possible to determine the real microscopic nucleation and saturation fields in magnetic thin film systems that reverse via magnetic domain formation. Furthermore element specificity allows separating contributions from different layers (elements) in more complex magnetic heterostructures. Element specificity has also been used to put marker layers into an exchange spring magnet structure to obtain depth resolved information about the detailed reversal behavior and twist [10]. Such techniques promise detailed information about the reversal behavior and domain formation at a certain position within a system or a device.
In addition one can combine reflection and transmission geometry to fully characterize the magnetic structure of sophisticated thin film systems laterally as well as perpendicular to the surface. However, in general in-plane systems are better suited for reflection geometry, while out-of-plane systems provide larger signal in transmission geometry due to the structure of the magnetic polarization pre-factor of the first order magnetic scattering term $p_m = i(\mathbf{e}_f^* \times \mathbf{e}_o) \cdot \mathbf{m}$. Since the polarization vectors $\mathbf{e}_f$ and $\mathbf{e}_0$ are always perpendicular with respect to the incoming and scattered wave vectors $\mathbf{q}_0$ and $\mathbf{q}_f$ (see Fig. 1), the reflection

geometry provides more signal for in-plane systems especially at grazing incidence. On the other hand perpendicular systems are better suited for transmission geometry, especially for larger domain structures that result in SAS diffraction rings at small angles around the direct beam. Additional tilting of the sample with respect to the incoming beam allows improving this situation for in-plane systems. In that case one can still scatter from the corresponding projection of the lateral heterogeneity or nanostructure in the sample.

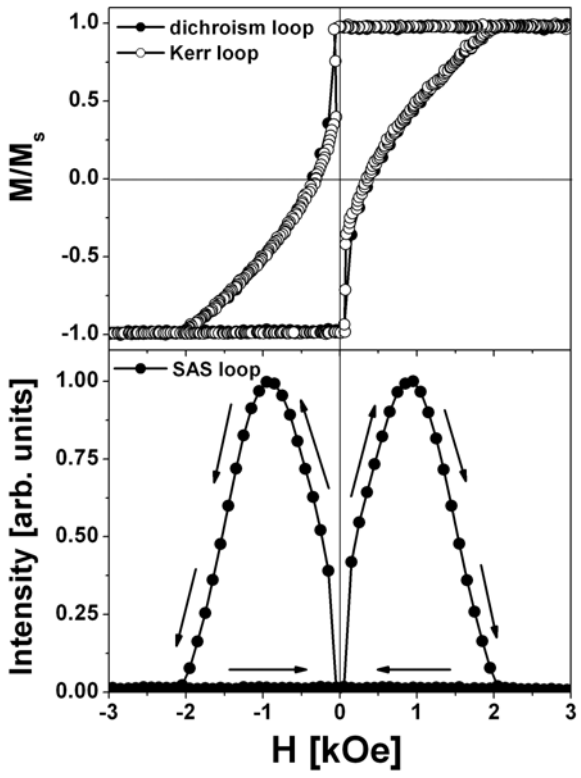

Fig. 2. Top: Kerr hysteresis loop (open symbols) compared to a dichroism hysteresis loop (solid symbols) of a Co/Pt multilayer obtained at the Co-L_3 absorption edge in transmission geometry. For the dichroism loop the photo diode detector was positioned at 0 degrees in the direct circularly polarized beam transmitting through the membrane sample. The hysteresis loop provides macroscopic information about the evolution of the average magnetic moment M of the sample during an external field sweep. Here Kerr and dichroism loops are the same. However for more complex structures the dichroism technique allows separating contributions from different chemical elements.
Bottom: Small Angle Scattering (SAS) hystesis loop of the same sample obtained at the Co-L_3 absorption edge from domain scattering at 0.5 degrees off the direct linearly polarized beam (corresponding to the diffraction ring in Fig.1 at a **q** vector of 0.025 nm^{-1}). The SAS loop measures the magnetic heterogeneity or the deviations from the average magnetic moment M of the sample during an external field sweep at a certain length scale (here ~250 nm) and thus provides nanoscopic information about the lateral magnetic structure of the sample. Element specificity is certainly also valid for SAS.

Such detailed lateral structure characterization with SAS during external field sweeps will become increasingly important in the future for nanostructured magnetic devices such as magnetic recording media as grain or pattern sizes decrease below the resolution limit of currently used magnetic imaging techniques [11-13].

References

[1] J.Grabis, A.Nefedov, H.Zabel, Rev. Sci. Instr. **74** (2003) 4048.
[2] O. Hellwig et al., Appl. Phys. Lett. **80** (2002) 1234.
[3] J. B. Kortright, O. Hellwig, D. T. Margulies, and E. E. Fullerton, JMMM **240** (2002) 325.
[4] J. B. Kortright et al., NIM B **199**, 301 (2003).
[5] J. B. Kortright, O. Hellwig, S. Sun and E. E. Fullerton, Phys. Rev. B **71** (2005) 012402.
[6] O. Hellwig et al., Physica B: Condensed Matter **336** (2003) 136.
[7] H. A. Dürr et al., Science **284**, 2166 (1999).
[8] S. Eisebitt et al., Nature, **432** (2004) 885.
[9] J. E. Davies et al., Phys. Rev. B **70** (2004) 224434.
[10] O. Hellwig, J. B. Kortright, K. Takano, E. E. Fullerton, Phys. Rev. B **62** (2000) 11694.
[11] X. Qi et al., IEEE Transactions on Magnetics, Vol., **40**, NO.4 (2004) 2476.
[12] E. E. Fullerton , O. Hellwig, K. Takano and J. B. Kortright, NIM B **200** (2003) 202.
[13] E. E. Fullerton et al., IEEE Trans. Mag. **38** (2002) 1693.

Interfacial structure of MnAs grown on GaAs(001) and GaAs(113)A studied by grazing-incidence x-ray diffraction

D. K. Satapathy, W. Braun, B. Jenichen, V. M. Kaganer, L. Däweritz, K. H. Ploog

Paul-Drude-Institut für Festkörperelektronik Hausvogteiplatz 5–7, D–10117 Berlin, Germany

Epitaxial interfacing of two materials with very different structural properties is not only interesting for technological applications, but also for basic research. The growth of hexagonal ferromagnetic MnAs on the cubic semiconductor GaAs is a typical example of such a system. The lattice mismatch between MnAs and GaAs is about 7.5% along the $[11\bar{2}0]$ direction (*a*-axis) and 30% along the [0001] direction (*c*-axis). In heterostructures grown by molecular-beam epitaxy, the misfit is released either by the formation of misfit dislocations (MD) at the interface or by the formation of a coincidence site lattice (CSL). Both mechanisms are realized at the MnAs/GaAs interface in different directions, which make it a model system for investigations of the interfacial configuration. MnAs films of about 35 nm thickness are used in the study.

Depth-resolved grazing-incidence x-ray diffraction allows us to separate the signal of the interface structure from the signal of the epitaxial film. We tune the probing depth by varying the grazing incidence angle α_i in the range from 0.2° to 0.8°. Figure 1 shows the radial scan recorded in a grazing incidence-grazing exit geometry with a grazing incidence angle of about $3\alpha_c$, where α_c is the critical angle for total external reflection in MnAs. The dependence of the satellite reflections on the x-ray penetration depth proves that they originate from the interface. The 30% mismatch along the *c*-axis of MnAs is released by the formation of a CSL with both 4th to 6th and 6th to 8th plane matches [A. Trampert *et al.*, Appl. Phys. Lett. **78**, 2461 (2001)]. These plane matches coincide well and are very regular as demonstrated by the narrow satellites in Fig. 1. The periodicity calculated from the spacing of these satellites is (8 ± 0.05) nm, which requires a unit cell to contain four 4th to 6th and two 6th to 8th matches. This allows us to conclude that a super-periodicity of coincidence lattice unit cells exists along the *c*-axis.

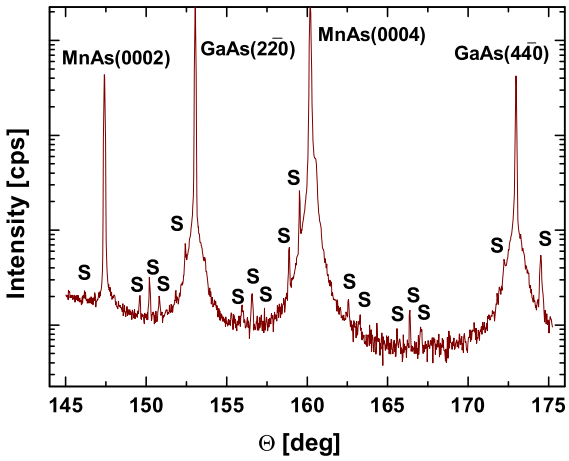

Fig. 1. Radial (θ-2θ) scan along the MnAs [0001] direction during deposition of MnAs. The scan is recorded at a grazing-incidence angle of 0.65°. S denotes the satellites due to the super-periodicity of the coincidence lattice. The satellites are equally spaced.

Figure 2(a) shows the corresponding radial scan along the MnAs *a*-axis recorded for different α_i. Equally spaced satellite reflections S_i appear, when α_i exceeds α_c, and grow further in intensity with α_i. The corresponding periodic structure therefore does not originate from the surface, but from within the layer structure. Since the interface between MnAs and GaAs is

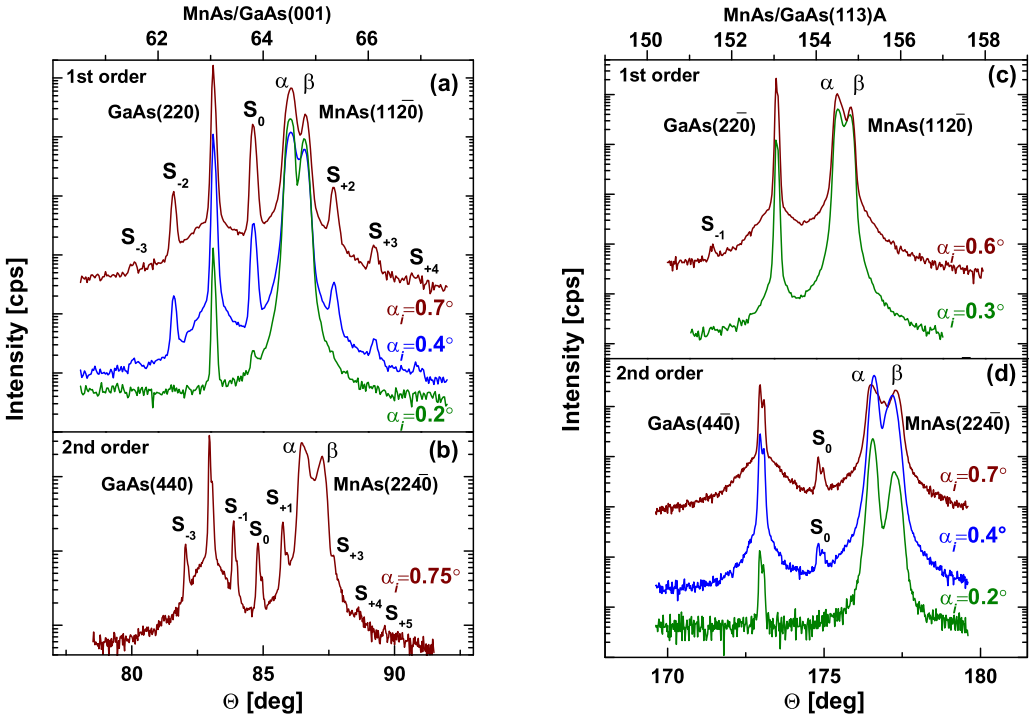

Fig. 2. Radial (θ-2θ) scans recorded along the *a*-axis of MnAs for different grazing incidence angles α_i as indicated in (a) 1st and (b) 2nd order reflection of MnAs grown on a (001) template of GaAs as well as (c) 1st and (d) 2nd order reflection of MnAs grown on (113)A template of GaAs. S_i indicates the satellites originating from the periodic array of misfit dislocations. The scans are recorded at room temperature. Peaks labelled α and β refer to the different phases of MnAs.

sharp and abrupt, this confirms that the peaks are due to periodic strain variations around MDs at the film-substrate interface. The substrate reflection is not significantly broadened, and we observe several orders of narrow satellite peaks. We can therefore conclude that the array of MDs is periodic. This indicates that the MDs can glide along the interface at the growth temperature and that a strong repulsive interaction exists between them. In the next higher order of the same reflection, three satellite peaks instead of one appear between the substrate peak and the layer peak Fig. 2(b). From the number of satellite peaks, we find the Burgers vector to be 1/3 [11$\bar{2}$0]. The Burgers vector lies in the plane, which further facilitates the glide of MDs to become periodic and to minimize their energy. Theses edge dislocations have a spacing of (4.9 ± 0.05) nm. A splitting of the substrate peak and the satellites from the MD array is resolved in Figs. 2(b) and 2(d). This results from the coexisting elastic domains of α and β MnAs that modulate the substrate lattice constant near the interface underneath each domain.

During the growth of MnAs on a GaAs(113)A template, the misfit is released by the formation of a periodic array of MDs as on GaAs(001), but with a different periodicity. Figures 2(c) and 2(d) show the presence of satellite reflections from the periodic MDs. The spacing of the satellites coincide with the one between the layer and the substrate reflection in first order. The second diffraction order shows a satellite between the layer and the substrate reflection [cf. Fig. 2(d)]. The period of the MD array is (2.5 ± 0.05) nm. The density of dislocations is about two times larger at the MnAs/GaAs(113) than at the MnAs/GaAs(001) interface.

Optical conductivity of $La_{1.875}Ba_{0.125-y}Sr_yCuO_4$ in the THz gap

M. Ortolani[1]*, U. Schade[2], A. Perla[1], P. Calvani[1]*, S. Lupi,[1] M. Fujita[3], and K. Yamada[3]

[1] *Coherentia*-INFM and Dipartimento di Fisica, Università La Sapienza, Roma, Italy
[2] Berliner Elektronenspeicherring-Gesellshaft für Synchrotronstrahlung mbH, Albert-Einstein Strasse 15, D-12489 Berlin, Germany
[3] Institute for Chemical Research, Kyoto University, Gokasho, Uji 610-0011, Japan
*Authors supported at BESSY by the UE contract BI3A-27/011104

The ab-plane optical conductivity of a high-T_c cuprate ($La_{1.875}Ba_{0.125-y}Sr_yCuO_4$) has been measured for the first time from 5 through 30 cm^{-1} (and from 295 K to 5 K). To do that we used the bright, coherent radiation at the IR-Spectroscopy beamline of BESSY-II, working in the low-α mode. The existence of extra-Drude, far-infrared peaks related to charge ordering has been definitely proven. A Josephson plasma resonance along the crystal c axis has been also observed below T_c with unprecedented clarity.

The competition between a charge-ordered (CO) and a superconducting (SC) quantum ground state has become a key issue in the physics of high Tc cuprates since the discovery of static CO in the Cu-O planes of non-superconducting $(La,Nd)_{2-x}Sr_xCuO_4$ [1]. The CO state of the 2D Cu-O plane is in form of one-dimensional stripes and appears only in the Low Temperature Tetragonal (LTT) phase. However, fluctuating CO was proposed to produce anomalous far-infrared peaks (FIP) in the Nd-free superconductor $La_{2-x}Sr_xCuO_4$, thus indicating a possible coexistence of CO and SC. [2] This important finding would be confirmed by the observation of similar peaks in a superconducting system with static charge order.

Such a compound is $La_{1.875}Ba_{0.125-y}Sr_yCuO_4$ (LBSCO), where CO super-lattice peaks appear together with a corrugated LTT symmetry [3] for y = 0.085 (T_C = 31 K) and 0.075 (T_C = 10 K) below a temperature called T_{d2}. We performed preliminary measurements of the reflectivity $R(\omega)$ at both those y values on LBSCO single crystals grown by the travelling-solvent floating-zone method. Those data were taken with conventional infrared sources from 30 cm^{-1} to 20000 cm^{-1} and did not provide clear imprints of a FIP in the resulting conductivity $\sigma(\omega)$. However, there were indications that the FIP could be hidden in the THz gap (1 THz = 30 cm^{-1}). BESSY-II, when working in the low-α mode, [4] provides exceptionally brilliant, coherent and wide-band radiation in the THz gap. During a dedicated week at the end of November 2004 we measured (for the first time in a high-T_c cuprate) the reflectivity of the *ab* superconducting plane of LBSCO well below 1 THz. The minimum frequency was fixed to 5 cm^{-1} by diffraction, due to the finite size of the crystals, but the apparatus could provide excellent data down to 1 cm^{-1}. We also measured, with unprecedented signal quality, the *c*-axis reflectivity of the LBSCO sample with y = 0.085 and T_c = 31 K, detecting the Josephson plasma resonance below T_c.

$R(\omega)$ is shown for the *ab* plane in Fig. 1. BESSY-II data below 1 THz match with those taken at higher ω with a black body. At high T, they follow the Hagen-Rubens extrapolations (dashed lines) which hold for conventional metals. However, below 50 K and still in the normal phase, they clearly deviate from this behavior. Once the whole data sets are processed by Kramers-Kronig transformations to obtain $\sigma(\omega)$, those deviations produce clear peaks below the charge-ordering temperature T_{d2} in the optical conductivity (Fig. 2).

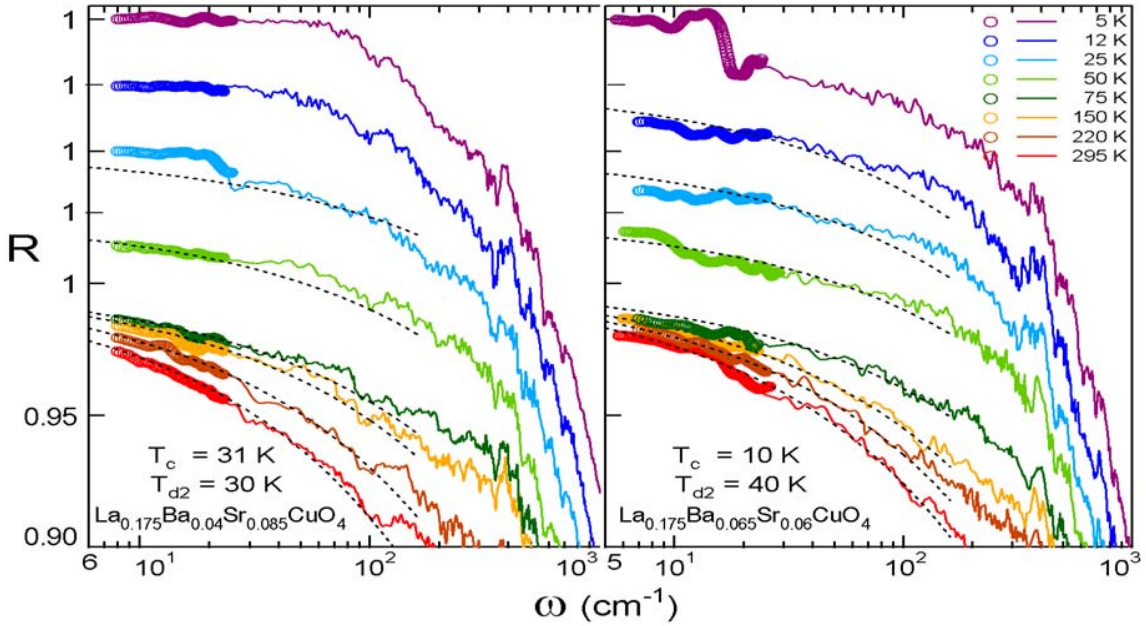

Fig. 1 Far-infrared reflectivity of the *a-b* (Cu-O) plane for two LBSCO single crystals, at different temperatures. Thin lines: data collected at University La Sapienza with conventional sources. Thick lines: data taken at the IR-Spectroscopy beamline of BESSY II working in the low-α mode. Dashed lines: Hagen-Rubens extrapolations.

In the superconducting phase of the sample with T_c = 31 K, $\sigma(\omega)$ is increasingly suppressed for $\omega < 2\ \Delta \approx 100$ cm^{-1}, where Δ is the superconducting gap. For *d*-symmetry Cooper pairs as in LBSCO, Δ depends on the wavevector **k**, and may also vanish for certain **k**. For this reason the Drude conductivity, which is an average response over the **k** space, is not entirely suppressed below $2\ \Delta$. The spectral weight lost below T_c condenses mostly into a zero-frequency delta function, but partly also in states at midinfrared energies (not shown in the Figure). This behavior is characteristic of high-T$_c$ superconductors and is related to their nature of correlated systems.[5]

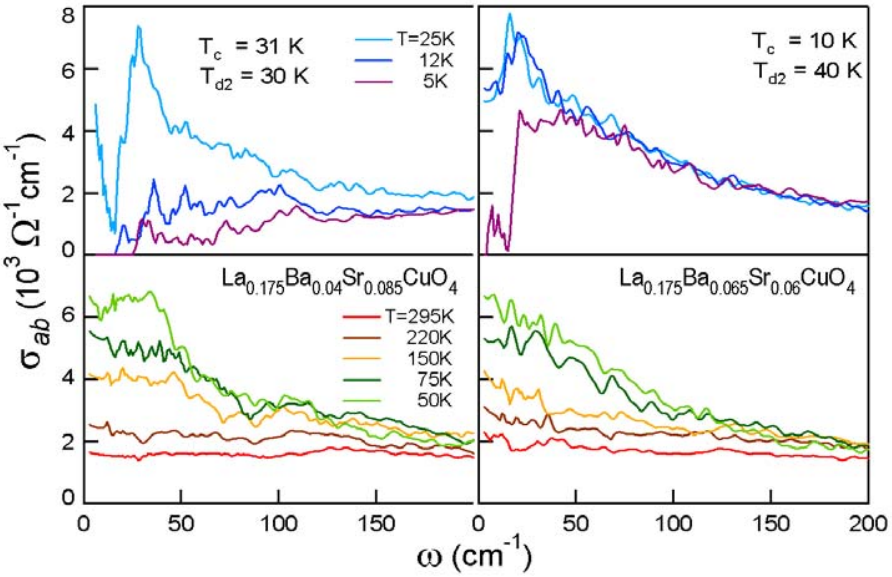

Fig. 2 Optical conductivity of the *a-b* (Cu-O) plane for two LBSCO single crystals, obtained by Kramers-Kronig transformation from the reflectivity data of Fig. 1. Top panels refer to $T < T_{d2}$.

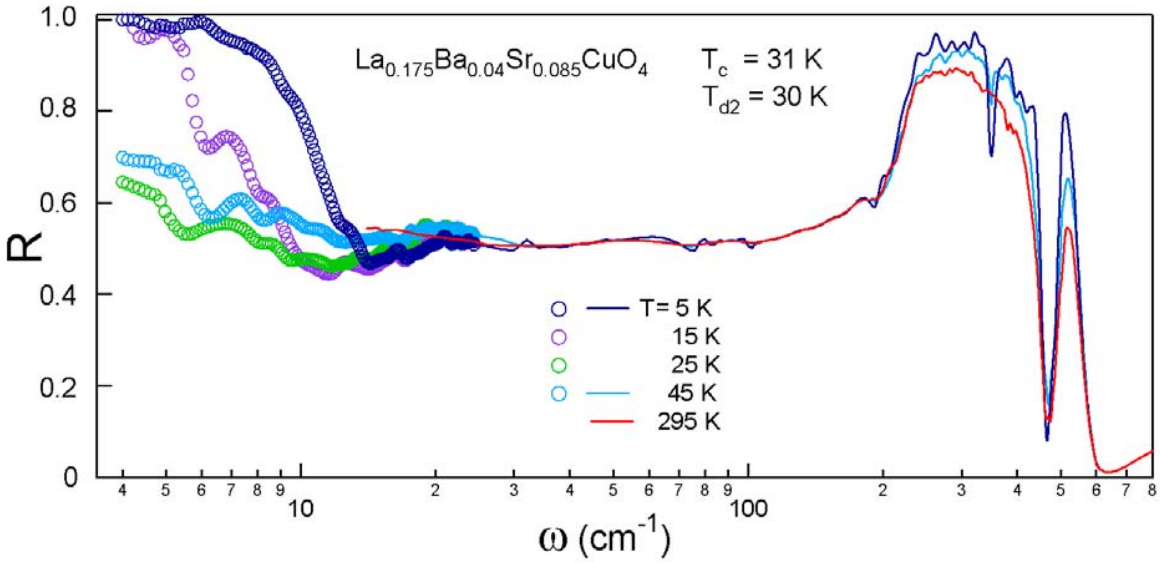

Fig. 3 Far-infrared reflectivity of the *c* axis for two LBSCO single crystals, at different temperatures. Thin lines: data collected at University La Sapienza with conventional sources. Thick lines: data taken at the IR-Spectroscopy beamline of BESSY II working in the low-α mode.

Data of Fig. 2 then confirm that FIP's in $\sigma(\omega)$ are associated with charge order also in superconducting samples. Therefore, in superconductors like ordinary LSCO free of Nd or Ba pinning centres, where diffraction techniques do not detect it but the FIP is still observed, charge order should exist on the fast time scale of infrared spectroscopy.[6]

Finally, Fig. 3 shows the far-infrared reflectivity of the LBSCO crystal with T_c = 31 K, as measured with radiation polarized along the *c* axis. The insulating character of this axis shows up by phonon modes above 200 $cm^{-1}$and, at lower frequencies, by a flat $R(\omega)$ at high temperature. However, below T_c the *c* axis also becomes superconducting, through a series of Josephson junctions connecting the superconducting *ab* planes with each other. This is shown in the Figure by $R(\omega)$ jumping to 1 below *Tc*. The superconducting gap starts opening at ?? K, where the no-loss range $R(\omega)$ = 1 is confined below 10 cm^{-1}, to increase to 15 cm^{-1} at 5 K.

[1]. J. M. Tranquada, B. J. Sternlieb, J. D. Axe, Y. Nakamura, and S. Uchida, Nature **375**, 561 (1995).
[2]. A. Lucarelli, S. Lupi, M. Ortolani, P. Calvani, *et al.*, Phys. Rev. Lett. **90**, 037002 (2003).
[3]. M. Fujita, H. Goka, K. Yamada and M. Matsuda, Phys. Rev. Lett. **88**, 167008 (2002).
[4]. M. Abo-Bakr, J. Feikes, K. Holldack, P. Kuske, W. B. Peatman, U. Schade, G. Wüstefeld, and H.-W. Hübers, Phys. Rev. Lett. **90**, 094801 (2003)
[5]. M. Ortolani, P. Calvani, and S. Lupi, Phys. Rev. Lett. in press (2005).
[6]. S. Caprara, C. Di Castro, S. Fratini and M. Grilli, Phys. Rev. Lett. **88**, 147001 (2002).

XMCD fine structure measurements at Fe L-edges

H. Rossner, D. Schmitz, P. Imperia and H. Maletta
Hahn-Meitner-Institut Berlin, Glienicker Str. 100, 14109 Berlin

The X-ray magnetic circular dichroism (XMCD) signal is usually measured in the near-edge energy range and is analyzed to study magnetic characteristics of the absorbing atom. For instance, measuring the absorption coefficient at the $L_{2,3}$ edges of 3d transition metals, the spin-dependent density of states of the final 3d states are probed by electric dipole transitions. The difference in the absorption coefficients using right and left circularly polarized X-rays is caused by the difference of the spin-dependent densities of empty states. Applying the so-called sum rules to the energy integrated difference spectra, magnitude and alignment of the spin moment μ_S and the orbital moment μ_L of the absorbing atom can be determined.

Up to now, measurements of the XMCD fine structure in the extended energy region are scarce. This structure is related to the propagation and scattering of spin-polarized photoelectrons by other atoms in the material. The amplitude of its oscillation is roughly two orders of magnitude smaller than the XMCD signal in the near-edge region. Measurement and interpretation of these tiny signals represent a challenge for experiment and theory as well, and will contribute to understand the magnetic coupling between atoms and to develop detailed models for the scattering of spin-polarized electrons. In combination with extended X-ray absorption fine structure (EXAFS) data the magnetic EXAFS data facilitate to distinguish between magnetic and non-magnetic atoms in the near neighbor shells of the absorbing atom.

To measure the XMCD fine structure at the beamline UE46-PGM we applied the gap-scanning technique, where plane mirror and grating of the monochromator are adjusted together with the gap size of the undulator for each energy setting. This technique ensures a constancy of the degree of circular polarization in combination with a high photon flux. Using the 1200 l/mm blazed grating and circularly polarized light of the elliptical undulator UE46 the maximum position of the fifth harmonic light intensity was measured in the energy range of 700-1600 eV in steps of 50 eV. With these values an improved table for the parameters of shift and gap size has been generated.

The sample material was prepared under UHV conditions growing ~60 Å thick Fe films *in situ* by e-beam evaporation onto V(110) substrate. The crystal structure of the film is known as crystalline bcc type [1]. The sample was measured at room temperature in remanence and an external field of ~350 Oerstedt has been applied to magnetize the Fe film along its easy axis parallel to the surface plane. Energy scans in the range of 690 eV ≤ E ≤ 1160 eV were taken storing the drain currents of the sample and the last mirror of the beamline in addition to the ring current. At each energy step four absorption measurements were performed with magnetization vector roughly parallel (μ^+), anti-parallel (μ^-), anti-parallel (μ^-), and parallel (μ^+) to the photon momentum vector.

The spin independent absorption coefficient μ and the XMCD signal μ_M were defined by

$$\mu = \frac{\mu^+ + \mu^-}{2} \quad , \quad \mu_M = \frac{\mu^+ - \mu^-}{\mu} .$$

The EXAFS data displayed in Figs. 1 were normalized to the FEFF code results using the procedure described in [2], and the XMCD data presented in Figs. 2 were normalized to full polarization with magnetization vector parallel to the photon wave vector.

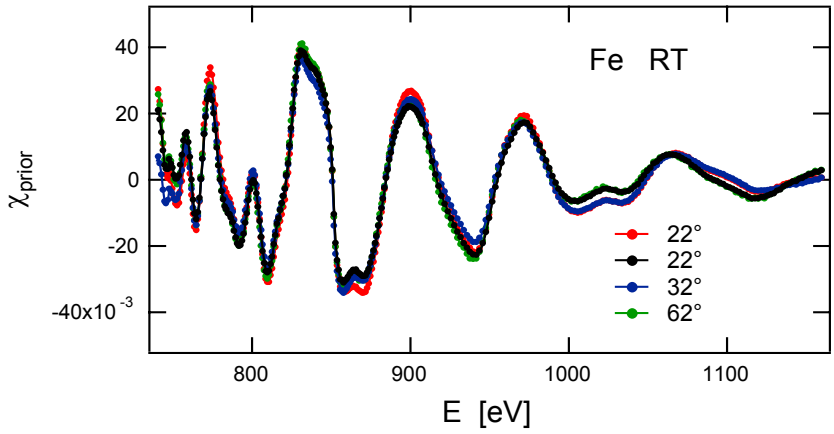

Fig. 1:

EXAFS signal measured at angles of 22°, 32° and 62° between beam direction and sample surface plane. The data were normalized to FEFF results

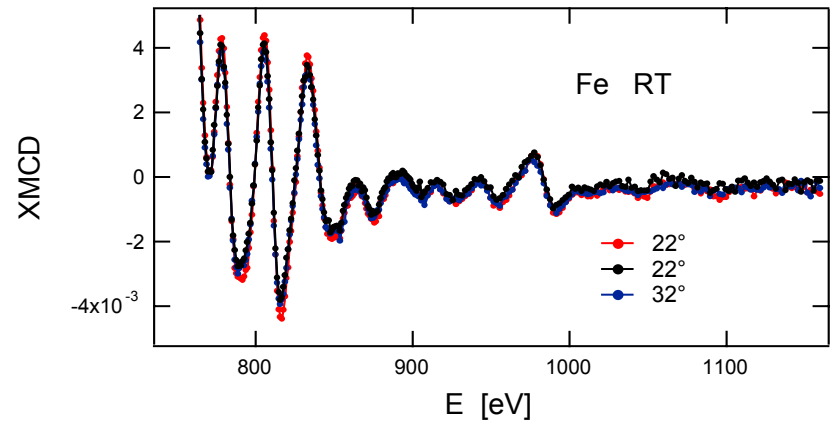

Fig. 2:

XMCD signal in the extended energy region measured at angles of 22° and 32° between beam direction and magnetic field vector.

Using a constant pressure of ~5*10^{-10} mbar in our experimental chamber we did not observe any changes in the shape of the spectra during one week. This is shown by the two runs taken at an angle of 22° with a time difference of one week (Figs. 1 and 2). These spectra not only demonstrate the stability of the sample configuration but also the stability of the undulator beam.

Whereas at K-edges the oscillations of the absorption coefficient μ (EXAFS) are in phase with the oscillations of the XMCD signal μ_M (MEXAFS), and for separated L-edges the corresponding phase difference often is π/2 [3], this relation is not very well established for overlapping L-edges that are caused by a small spin-orbit splitting (13.1 eV for Fe). In that case the phase difference between EXAFS and MEXAFS may even be energy dependent.

The high quality of the data and the simultaneous measurement of EXAFS and MEXAFS not only facilitate the identification of local crystallographic and magnetic structure but also enable an accurate determination of the relative phase between these signals and thus provide a severe test of existing absorption models. Computations are in progress using the well known computer code FEFF to study the interplay of spin-polarization and spin-orbit coupling that is revealed in the phase relation between EXAFS and MEXAFS.

References

[1] D. Schmitz, J. Hauschild, P. Imperia, Y.T. Liu and H. Maletta, J. Magn. Magn. Mater. **269**, 89 (2004)

[2] H.J. Krappe and H.H. Rossner, Phys. Rev. B **70**, 104102 (2004)

[3] H. Wende, Rep. Prog. Phys. **67**, 2105 (2004)

Growth kinetics of GaSb(001) studied by in situ synchrotron surface x-ray diffraction

W. Braun, B. P. Tinkham, V. M. Kaganer, B. Jenichen, D. K. Satapathy, K. H. Ploog

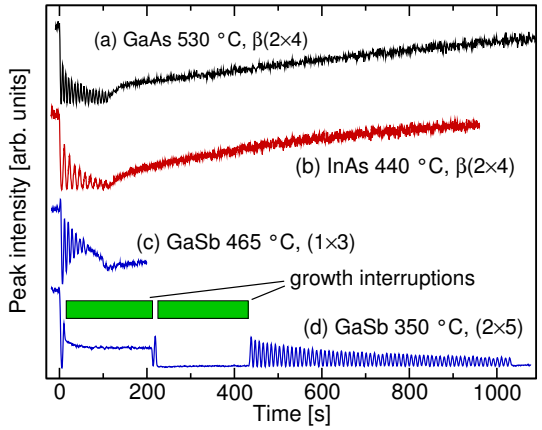

Figure 1: X-ray diffraction intensity oscillations during the growth of (a) GaAs(001), (b) InAs(001), and GaSb(001) at (c) 465 °C and (d) 350 °C. The growth interruptions for the low-temperature GaSb growth in (d) demonstrate the extremely slow recovery in this case.

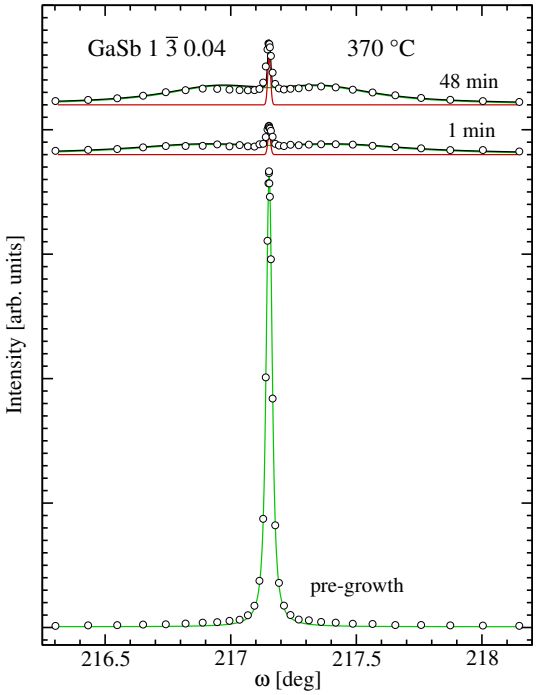

Figure 2: Fits to the GaSb 1 $\bar{3}$ 0.04 azimuthal profiles before and after the deposition of 0.38 ML. The low-temperature deposition creates a peaked island size distribution with a mean size of 9.5 nm, evolving to 12.2 nm at 48 min. The integrated intensities of all three curves are equal.

To compare the surface kinetics of GaAs studied previously, we have investigated the closely related materials InAs and GaSb using the same analysis techniques. We find that the surface kinetics of GaSb strongly differs from GaAs and InAs. In analogy to the two other systems, we have investigated the behavior of the GaSb surface under molecular-beam-epitaxial (MBE) conditions in real time using our setup at BESSY. For the in-situ surface x-ray diffraction experiments described here, homoepitaxy was performed on GaSb(001) at substrate temperatures of 350 and 465 °C. The surface reconstruction prior to growth was (1×5) at 350 °C and (1×3) at 465 °C. The surface was annealed at 515 °C for one minute prior to the experiments to prepare large flat terraces.

At 350 °C, GaSb exhibits very good layer-by-layer growth, characterized by large amplitude x-ray intensity oscillations with low damping as shown in Fig. 1. The growth is even better than for the GaAs and InAs reference samples grown in the same MBE chamber that were also optimized for best layer-by-layer growth. The surface recovery, however, is extremely slow, which is obvious from the two 200 s growth interruptions shown in Fig. 1. After the growth interruptions, the growth resumes almost without any change in the oscillations, which leads us to conclude that the non-growing surface is practically immobilized at this temperature. Peak profiles taken before and during the recovery at this temperature are shown in Fig. 2. The intensity distribution after deposition reveals a broad diffuse profile with a local maximum on each side of the peak, indicating an island sized distribution with a preferred mean size. Since the deposition is not exactly 0.5 in this experiment, a sharp coherent central peak with an instrument-

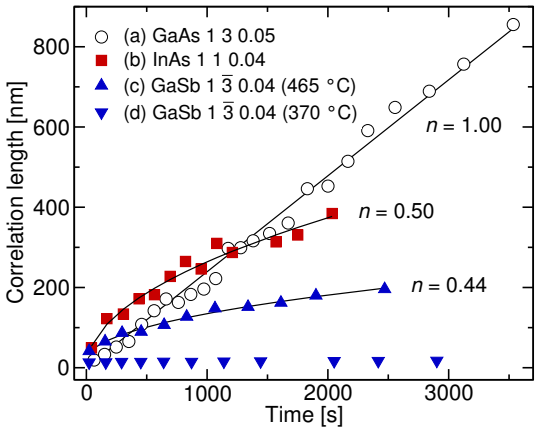

Figure 3: Comparison of the mean correlation length during recovery after fractional layer depositions for GaAs(001), InAs(001), and GaSb(001). The exponents obtained from the fits of the experimental data to $L(t) = (L_0^{1/n} + at)^n$ are indicated for each curve.

limited width is present. The mean correlation length increases from 9.5 nm 1 min after deposition to only 12.5 nm almost one hour later, compared to a value of 325 nm before growth.

Only at much higher temperatures, where continuous GaSb deposition is already unstable (Fig. 1c), GaSb starts to show significant coarsening as shown in Fig. 3. At 465 °C, the static surface is still sufficiently stable against decomposition, and fractional-layer depositions do not deteriorate this state. Since the {110} reflections on GaSb along the main surface symmetry directions are too weak for a detailed analysis of the profiles, we chose two nearby orthogonal {130} reflections to measure the profiles during the recovery. An azimuthal profile of a given reflection represents the surface correlations in the direction perpendicular to the diffraction vector. The results are shown in Fig. 4. We deposited 0.5 monolayers (ML) of GaSb for the $\bar{3}10$ measurement so that the coherent intensity is zero. For the $1\bar{3}0$ measurement, the coverage was 0.4 ML, and a corresponding coherent contribution (central narrow peak) is included in the fits.

The profiles in the $1\bar{3}0$ reflection shown in Fig. 4(b) are well fitted by Lorentzians, approximating the correlations along [110] in real space. The resulting mean correlation lengths can be fitted by $L(t) = (L_0^{1/n} + at)^n$, with an exponent $n = 0.44$ and an initial island size $L_0 = 35$ nm. This value of the finite island size at $t = 0$ is necessary to obtain a good fit. It can be understood from Fig. 2 through the morphology cre-

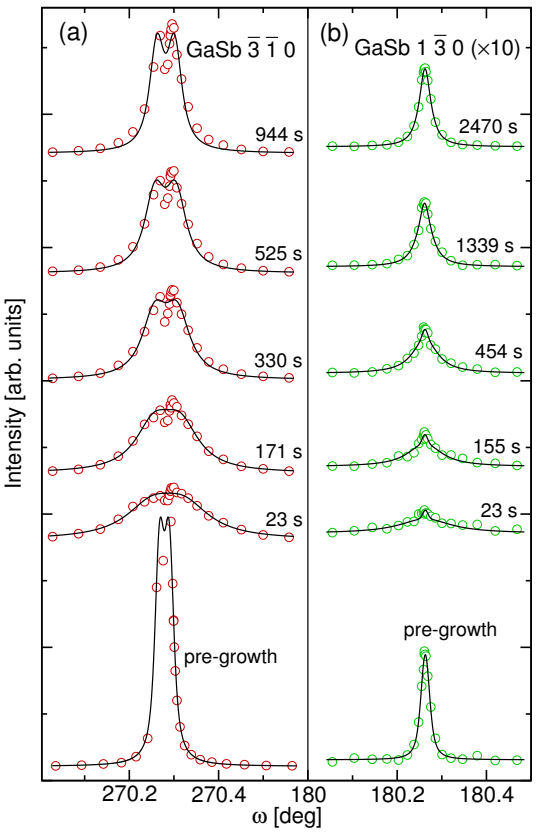

Figure 4: GaSb profiles recorded in two orthogonal azimuths at 465 °C. The profiles in (a) approximate the surface correlations along the $[1\bar{1}0]$ and in (b) along the [110] direction. The split peaks in (a) are related to the coarsening kinetics. The fit to the pre-growth profile yields a correlation distance of 385 nm.

ated by the nucleation mechanism during deposition. The subsequent coarsening starts from this morphology. The required L_0 values are large, but seem reasonable considering the good mobility during deposition deduced from Fig. 1.

The $\bar{3}10$ reflections, which are a measure of the correlations along $[1\bar{1}0]$ in real space, are split in Fig. 4(a). The correlation length (island size) obtained from these profiles can be fitted with $n = 0.68$ and $L_0 = 50$ nm. The mean correlation length therefore is almost isotropic, despite the strong difference in profile shape and hence in the length distributions. A miscut measurement on the sample yields a tilt of 0.04° towards 310, corresponding to a maximum terrace size of 430 nm in the orthogonal direction. The observed split in $\bar{3}10$ can therefore not be attributed to the miscut. It is rather a consequence of the coarsening mechanism. Such peaked island-size distributions are characteristic for Ostwald ripening, but it is astonishing that

among GaAs(001), InAs(001), and GaSb(001) only this one azimuth of GaSb shows this classical behavior.

Comparing the low-and high-temperature deposition and coarsening results, the extreme difference in surface kinetics between growth and recovery on GaSb is obviously due to the different origin of adatoms during growth and recovery. Whereas during growth, the adatoms are directly created from the deposition flux, they need to be detached from existing step edges during recovery. Obviously, this step is strongly inhibited on GaSb(001) compared to GaAs and InAs.

Application of μ-EXAFS for the determination of the crystallization ratio of vitro-ceramic materials.

F. Pinakidou, M. Katsikini, E. C. Paloura*, P. Kavouras, Ph. Komninou, Th. Karakostas
Aristotle Univ. of Thessaloniki, Dept. of Physics, GR54124 Thessaloniki, Greece
A. Erko
BESSY GmbH, Albert Einstein Str. 15, 12489 Berlin, Germany.

The vitrification of Pb and Fe-rich hazardous industrial waste is a stabilization process that allows for its safe disposal[1]. The highest content of solid waste for the synthesis of vitreous products was found to be 60% w.t., with SiO_2 and Na_2O additional batch materials, while compositions with higher waste content lead to spontaneous crystallization and formation of vitroceramic materials[2]. Vitroceramic materials are also produced after annealing-induced devitrification of glasses. Devitrification alters the composition of the residual amorphous matrix, resulting to the potential alteration of its chemical resistance. The effectiveness of the stabilization technique depends also on the composition and structure of the crystalline inclusions. In this report, we propose a method for the determination of the crystallization ratio of vitroceramic materials by combining conventional and micro-EXAFS (μ-EXAFS).

The under study sample is the vitrified product of Pb-rich ash co-melted with SiO_2 and Na_2O at 1400°C and followed by quenching[2]. It consists of 60% ash, 25% SiO_2 and 15% Na_2O. The sample was subjected to residual stress relaxation by heating at temperature slightly above the glass transition temperature (440°C). Furthermore, in order to investigate the growth of crystalline phases as a function of annealing, the sample was subjected to further thermal annealing at 600°C and 800°C.

The EXAFS measurements were conducted at the KMC2 beamline which is equipped with a double-crystal monochromator. The use of capillary optics results in reduction of the beam diameter to 5μm and allows the application of X-ray fluorescence (XRF) mapping and micro (μ)-XAFS. The μ-EXAFS spectra were recorded at the Fe-*K* edge, in the fluorescence yield mode using an energy dispersive fluorescence detector and they were collected from different positions of the sample. Conventional EXAFS spectra (i.e. without the use of capillary optics) were recorded using a photodiode at an angle of incidence of 85° in order to avoid self-absorption effects. A spectrum from the hematite (Fe_2O_3) reference sample was recorded in the transmission mode using ionization chambers.

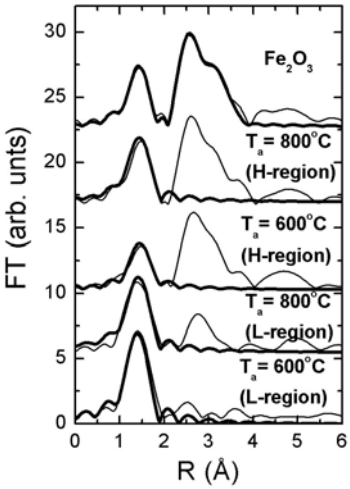

Figure 1: Fourier transforms (FT) of the $k^3 \times \chi(k)$ Fe-*K* μ-EXAFS spectra recorded at the H and L-regions of the sample annealed at 600°C , 800°C and the reference Fe_2O_3 sample. The experimental curve and the fitting are shown in thin and thick solid lines, respectively.

XRF mapping revealed that Fe is homogeneously incorporated in both the as-casted sample and the sample after annealing at 440°C, while annealing at higher temperatures results in the inhomogeneous distribution of Fe. In order to investigate the effect of the different Fe concentration in the phase where Fe belongs, μ-EXAFS spectra were recorded at the regions with high and low Fe concentration (denoted as H and L, respectively). Figure 1 shows the Fourier transforms (FT) of the k^3-weighted Fe-*K*-edge μ-EXAFS spectra (k-range 2.8-9.8 $Å^{-1}$) recorded at the L and H-regions, while FT's of the k^3-weighted Fe-*K* edge EXAFS spectra (k-range 3-10$Å^{-1}$) are shown in Fig 2. The EXAFS analysis of the spectra from the hematite reference sample

* *e-mail: paloura@auth.gr*

reveals the expected trigonal distortion of the FeO_6 octahedron, which causes a splitting of the first nearest neighboring shell (three oxygen atoms at 1.93Å and three oxygen atoms at 2.09Å, respectively).[3] In contrast, in the as-casted material (Fig. 2), Fe is tetrahedrally coordinated and therefore it can participate in the formation of the glass network.[4] The FT's of the under-study samples, shown in Fig. 1, reveal the existence of mid-range order in the H-region, in contrast to the short range order that exists in the L-regions where contribution only from the 1st nearest neighbor shell can be distinguished. It can thus be concluded that annealing promotes the formation of crystalline inclusions with high Fe concentration. Furthermore, the Fe-O distance is different in the Fe-rich crystalline and the amorphous regions of the sample. More specifically, the Fe-O distance is 1.92-1.93Å in the H-region and 1.87Å in the L-regions, independent on the annealing temperature. These two distances present direct evidence that the Fe atoms preferentially occupy tetrahedral sites into the vitreous matrix and octahedral sites in the crystalline regions.

The change in the environment around the Fe atom, as determined by the μ-EXAFS analysis, lies in agreement with the EXAFS results. The EXAFS spectra of the as-casted sample and the sample annealed at 440°C where fitted assuming one shell consisting of O atoms. In the case of the inhomogeneous samples, the spectra were fitted using a mixed model that assumes both a crystalline and an amorphous environment around the Fe atom. More specifically, for the sample annealed at 600°C the spectra were fitted using a mixed model comprised of X% of the magnetoplumbite and (100-X)% of the amorphous model. In addition, the spectra from the sample annealed at 800°C were fitted assuming that Y% of the sample has the hematite structure while and (100-Y)% is amorphous. In both cases, the spectra were fitted in the nearest four neighbor shells. The Fe-O 1st nearest neighbor (nn) distances in both the amorphous and the crystalline phases are kept fixed to the values found from the μ-EXAFS analysis. It is found that in the as-casted and the sample annealed at 440°C, the Fe atom is tetrahedrally coordinated with 4 oxygen atoms, at a distance of 1.87Å. This distance designates that the Fe atom participates in the formation of the glass matrix. On the other hand, in the samples annealed at 600°C and 800°C, a percentage of the Fe atoms belong to the crystalline (magnetoplumbite or hematite, respectively) phase. More specifically, in the samples annealed at 600°C and 800°C, 44% and 61%, respectively, of the Fe atoms belong to a crystalline phase where they form FeO_6 polyhedra (R_{Fe-O}=1.93Å). The rest of Fe atoms participate in the formation of the vitreous network by constituting FeO_4 tetrahedra with a Fe-O distance equal to 1.88Å. It can thus be concluded that annealing induces the loss of homogeneity and increases the crystallization ratio of the sample, which can be determined from the non-destructive EXAFS measurements.

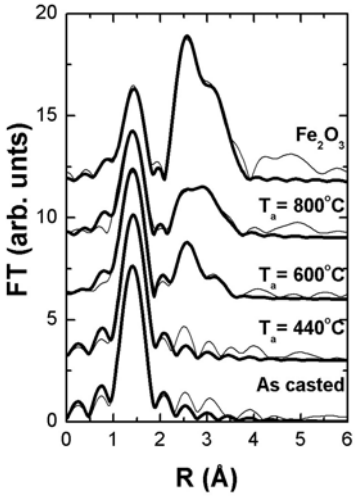

Figure 2: Fourier transforms (FT) of the $k^3 \times \chi(k)$ Fe-*K* EXAFS spectra of the as-casted, annealed at 440°C, 600°C, 800°C and the Fe_2O_3 reference sample. The experimental curve and the fitting are shown in thin and thick solid lines, respectively.

Acknowledgements: *The measurements were conducted with financial support from the BI3A-16/280604 program. F. Pinakidou also acknowledges support from the HERAKLEITOS program.*

References

[1] G. Scarinci et al., J. Eur. Ceram. Soc. 20, 2485 (2000).
[2] P. Kavouras et al., J. Eur. Ceram. Soc. 23, 1305 (2003).
[3] R. W. G. Wyckoff, Crystal Structures, vol. 2, (John Wiley & Sons 1964), p. 8.
[4] F. Pinakidou et al., Physica Scripta (in press).

μ-XRF and μ-NEXAFS study of annealing induced devitrification of stabilized industrial waste glasses

F. Pinakidou, M. Katsikini, E. C. Paloura*, P. Kavouras, Ph. Komninou, Th. Karakostas
Aristotle Univ. of Thessaloniki, Dept. of Physics, GR54124 Thessaloniki, Greece
A. Erko
BESSY GmbH, Albert Einstein Str. 15, 12489 Berlin, Germany.

The method of vitrification is a promising waste management technique, with its main advantage being the production of vitreous-ceramic material possessing a satisfactory chemical stability. The solidification and stabilization of lead oxide-contaminated ash (which is a toxic industrial waste) via vitrification, leads to the production of vitreous materials that can homogenously incorporate into their matrix numerous toxic elements (such as heavy metals) and can be freely disposed, with evident benefits in terms of storage.[1] The highest content of solid waste for the synthesis of such non-toxic vitreous products was found to be 60% w.t. with SiO_2 and Na_2O additional batch materials, while compositions with higher waste content lead to spontaneous crystallization.[2] Therefore, the presence of a high waste content in a stabilized homogenous vitreous product can give rise to crystal phase separation, i.e. devitrification. Devitrification alters the composition of the residual amorphous matrix, resulting to the potential alteration of its chemical resistance.

The under study sample is the vitrified product of lead-rich ashes, produced by incineration of sludges that contain large quantities of toxic organic compounds. The incineration process involves co-melting of lead contaminated ash with the appropriate quantities of vitrifying and flux agents (SiO_2 and Na_2O, respectively) at high temperatures (1400°C), followed by quenching in order to form vitrified materials[2]. The under study sample consists of 60% ash, 25% SiO_2 and 15% Na_2O and was subjected to thermal annealing by heating at temperature slightly above the glass transition temperature (440°C). A powder hematite (α-Fe_2O_3) sample is studied as reference material. The μ-XRF and μ-NEXAFS measurements were conducted at the KMC2 beamline at the electron storage ring BESSY-II in Berlin. The beamline is equipped with a double-crystal monochromator and capillary optics reduce the beam diameter to 5μm. The XRF maps were recorded using excitation photons of 7200eV, i.e. higher than the Fe-*K* absorption edge. The angle of incidence of the SR beam was 45° and the energy dispersive (Röntec) fluorescence detector was positioned normal to the beam. The μ-NEXAFS spectra were recorded at the Fe-*K* edge at different positions of the sample in the fluorescence yield mode, while the spectrum of the Fe_2O_3 reference sample was recorded in the transmission mode using ionization chambers.

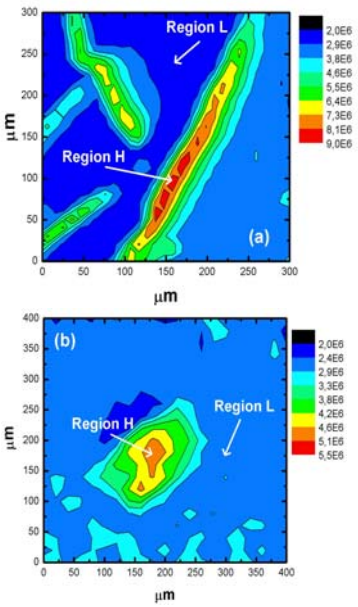

Figure 1: (a) 300x300μm XRF map of the sample annealed at 600°C and b) 400x400μm XRF map of the sample annealed at 800°C. The regions depicted as L and H, contain low and high iron concentration, respectively.

The XRF maps of the as-casted sample and the sample annealed at 440°C demonstrate that the distribution of Fe is homogeneous thus iron has been successfully incorporated into the vitreous matrix. Contrary to that, annealing at $T_a \geq 600$°C causes loss of homogeneity and the formation of islands where the Fe concentration is about 3 times higher than the background Fe concentration in the glass matrix. The XRF maps from the samples annealed at 600°C and 800°C are shown in Fig. 1(a) and (b), respectively. The change in

* *e-mail: paloura@auth.gr*

the environment around Fe is consistent with previous work implemented on the under study samples and revealed the formation of crystalline magnetoplumbite ($PbFe_{12}O_{19}$) and hematite (Fe_2O_3) crystallites in the samples annealed at 600° and 800°C.[2] These two phases are characterized by the octahedral coordination of the Fe atom.

In order to investigate the alteration in the bonding environment around the Fe atoms at different positions of the sample as a function of the annealing temperature, μ-NEXAFS spectra at the Fe-*K* edge were recorded at the regions with high and low Fe concentration (denoted as H and L, respectively). The NEXAFS spectra of Fe-containing compounds are characterized by a pre-edge feature that is attributed to 1s → 3d transitions.[3] In a centrosymmetric environment (e.g. octahedral) the intensity of the pre-edge feature is weak due to the quadrupole character of the transition. Contrary to that, in a non-centrosymmetric environment (e.g. tetrahedral) the pre-edge peak gains intensity due to the d-p mixing of the final state, that gives dipole character to the transition. Thus, the intensity of the pre-edge peak is inversely proportional to the coordination number of the absorbing atom due to the loss of inversion symmetry of the iron site. As shown in Fig. 2, the Fe-*K* NEXAFS spectra exhibit differences in the intensity of the pre-edge peak, in the two distinct regions (H and L) of the under study samples. The increased intensity in the L-regions is therefore indicative of the alteration of the local environment around the Fe ion, i.e. the Fe atom tends to occupy tetrahedral sites into the glass matrix. Not only the intensity but also the shape of the pre-edge feature depends on the local coordination around Fe. According to Westre et al,[3] fitting of the pre-edge feature with one Lorentzian is a fingerprint of the tetrahedral coordination of the Fe atoms. Contrary to that, two Lorentzians are necessary to fit the pre-edge peak when Fe occupies octahedral sites. The fitting of the pre-edge feature in the spectrum of the sample annealed at 600°C is shown in the inset of Fig. 2. In the hematite sample, where Fe is octahedrally coordinated, two Lorentzians were necessary to fit the pre-edge region. The same is valid for the spectra recorded at the H-region of the vitrified sample. The pre-edge peaks of the spectra recorded at the L-region, as well as from the as-casted sample, were fitted using one Lorentzian, which suggests a tetrahedral coordination around the Fe atom. Furthermore, the position of the pre-edge peak, which is a measure of the portion of various oxidation states of Fe in a mixed valence sample,[4] is found to be invariant and independent on both the Fe concentration and the annealing temperature i.e., no alteration occurs in the $Fe^{+3}/\Sigma Fe$ ratio in both the H and L-regions. It should be pointed out that, Mössbauer measurements conducted in the under study samples revealed the absence of the Fe^{+2} ions in all under study samples. Therefore, the observed invariability of the position of the pre-edge peak suggests that the alteration in the microstructure around the Fe atom can be exclusively attributed to the change in the local environment around the Fe^{+3} ion.

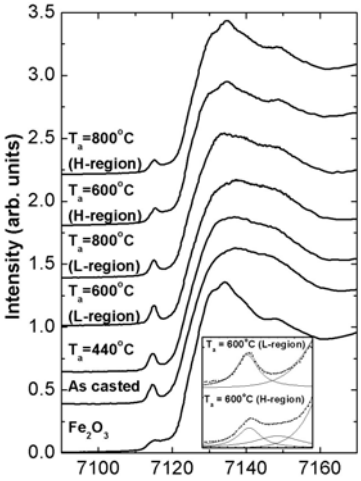

Figure 2: Fe-*K* edge NEXAFS spectra recorded at the H and L-regions of the sample annealed at 600 and 800°C and reference Fe_2O_3 sample. The fitting of the pre-edge feature of the sample annealed at 600°C is shown in the inset.

Acknowledgements: ***Acknowledgements:*** *The measurements were conducted with financial support from the BI3A-16/280604 program. F. Pinakidou also acknowledges support from the HERAKLEITOS program.*

References

[1] G. Scarinci et al., J. Eur. Ceram. Soc. 20, 2485 (2000).
[2] P. Kavouras et al., Waste Manag. 23, 361 (2003).
[3] T. Westre et al., J. Am. Chem. Soc. 119, 6297 (1997).
[4] S. Bajt, S. R. Ruton and J. S. Delabey, Geochim. Cosmochim. Acta, 58 (23), 5209 (1994).

Temperature dependence of FWHM of γ' Phase in Creep-deformed Superalloy SC16

G. Schumacher, N. Darowski, I. Zizak
Structure Research, Hahn-Meitner-Institut Berlin GmbH

H. Klingelhöffer
Federal Institute of Materials Research and Testing

W. Chen and W. Neumann
Institute of Physics, Humboldt University to Berlin

The single crystal superalloys are strengthened by cuboidal γ' precipitates, which have a $L1_2$ super lattice structure and are embedded coherently in a solid solution γ matrix with an fcc crystal structure. The lattice mismatch between both of the phases influences strongly the mechanical behaviour of the superalloys as well as the microstructure stability under service conditions. From the viewpoint of alloy development as well as of applications, It is essential to know the *lattice distortion* of γ' precipitates and γ matrix in superalloys and *its evolution* during inelastic deformation.

In a recent study Royer and co-workers have reported a reduction of full width at half maximum (FWHM) of 100 γ' intensity profiles with increasing temperature in the single crystal superalloy AM1 after creep deformation [1]. The phenomenon was, however, not discussed in detail. An increase in temperature is related to an increase in Debye-Waller factor which is expected to decrease the peak intensity at constant FWHM.

In the present alloy system the FWHM reflects both the particle size and the strain state. A number of factors, such as the relaxation of deformation substructure at the γ'/γ interface, the different thermal expansion coefficients, the different temperature dependence of elastic constants of γ and γ' phases can affect the distribution of internal strain and therefore the FWHM of the measured intensity profiles. At sufficiently high temperatures the γ' precipitates can in principle change their size and shape. In the present study the temperature dependence of FWHM of {100} γ' superlattice reflections in creep-deformed specimens of single crystal superalloy SC16 was measured.

The investigation was carried out on a model single crystal superalloy SC16 (chemical composition in at %: 7.35Al-17.5Cr-1.8Mo-1.1Ta-4.15Ti-68.1Ni). The initial microstructure consists of cuboidal γ' precipitates with an average edge length of 450 nm and a volume fraction of 40 %. Prior to the X-ray measurements the specimens were deformed at 1223 K up to ±0.5 % strain under external load of ±150 MPa.

The X-ray measurements have been performed at the 6-circle diffractometer at KMC-2. The specimens were cut in way that their surfaces were parallel to the (001) lattice plane (perpendicular to the load axis) or to the (100) plane (specimen surface parallel to the load axis). For the diffraction measurements X-ray energy of 8 keV was used. The measurements were performed in vacuum (10^{-6} – 10^{-7} mbar) in the temperature range between room temperature and 1173 K.

Fig. 1a shows the intensity profiles of the 001 super lattice reflections after tensile creep deformation. With increasing temperature the intensity profile peaks become narrower. The same tendency of temperature dependence was observed for the 100 peak of the specimen creep-deformed under tensile stress (Fig. 1b) and for the 001 peak of the specimen creep deformed under compressive stress (Fig. 1 c). The FWHM values of 001 and 100 super lattice reflections as a function of temperature is shown in Fig. 2 for the tensile creep-deformed specimen.

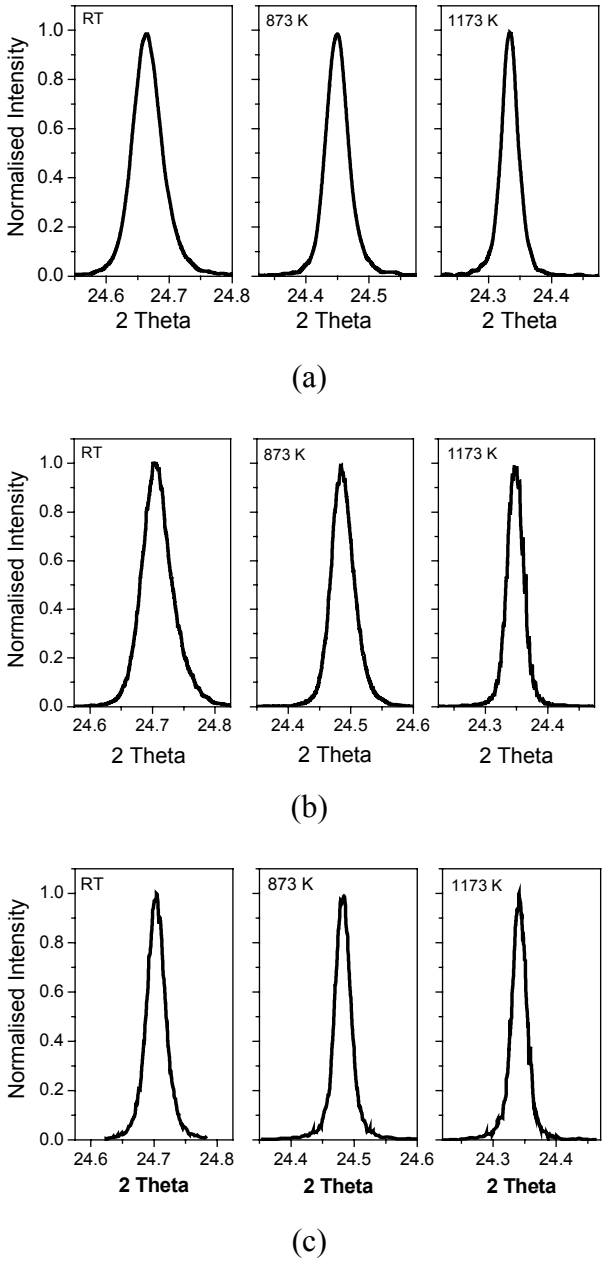

Fig. 1 Intensity profiles of a) 001 and b) 100 γ' super lattice reflections taken on the tensile creep deformed specimens and of c) 001 reflection obtained from the specimen after compressive creep deformation

The reasons for the narrowing of the peaks with increasing temperature are not quite clear. Rapid cooling of a specimen from high temperature back to room temperature restored the initially at room measured value. This experiment excludes change in particle size and/or shape as a possible reason for the observed temperature dependent changes in FWHM. The stability in microstructure is in agreement with expectations from standard heat treatment of this alloy (SHT = 1373 K/4H/air cooling + 1123 K/24 H/air cooling). The microstructure is stabilized at this temperature. Appreciable changes of precipitate size and shape at temperatures below 1123 K are not expected.

The lattice misfit as well as the elastic constants of the two phases affect however the {100} peak widths. The changes in lattice misfit in *non-deformed* material are determined by the different thermal expansion coefficients of the two phases [2]. The lattice misfit is positive at room temperature and decreases with increasing temperature. At about 850 K the lattice misfit is zero and becomes negative at higher temperatures. In the non-deformed material, the misfit stresses in both phases are zero when the misfit is zero. The decrease in internal stresses are related to a decrease in the widths of {100} reflections. As the misfit becomes negative above this temperature the internal stresses increase again and may cause an increase in peak width. As the elastic constant of the γ' phase is larger than that of the γ phase, the stresses are concentrated in the γ phase. The misfit stresses in the γ' phase and the expected increase in FWHM at high temperatures should therefore be relatively small. The changes in FWHM of *non-deformed* material will be studied in 2005.

In *creep-deformed* material (studied in this work) the situation is more complex. During creep deformation an anisotropic dislocation network is built-up at the γ/γ‘ interfaces [3]. Dislocation pairs formed during deformation will glide on the same plane and will be fixed at the γ/γ' interfaces but depending on the orientation of the interfaces the dislocations will be located in the matrix or in the γ'-phase [4]. This causes the misfit to increase when measured in 001 direction and to decrease

when measured in [100] and [010] direction [4]. During the creep-deformation another phenomenon has however to be taken into account which is called γ' rafting. It describes the anisotropic growth and agglomeration of γ' precipitates during the creep process. In the material studied here the γ' precipitates form disc shaped plates which are aligned perpendicular to the stress axis when tensile stress is applied. Needle shaped rafts are formed when a compressive stress is applied. Due to this rafting process the influences of the differently oriented γ/γ' interfaces on the FWHM are not equal. If the externally applied stress is a tensile stress, the (001) plane dominate the stress while the (010) and (100) planes dominate the stress in case of compressive load. This might explain the continuous decrease in FWHM measured after tensile-creep deformation and the continuous decrease in FWHM after compressive creep deformation.

This work was supported by the German Research Foundation (DFG) through the grants of NE 646/5-3 and Schu 1254/3-4. The authors would like to thank C. Förster, H. Kropf and W. Becker for their technical assistance in specimen preparation.

[1] A. Royer, P. Bastie and M. Veron, Mat. Sci. Eng., A234-236 (1997) 1110
[2] G. Bruno, H. C. Pinto, C. Schulze, G. Schumacher, Metallurgical and Materials Transactions A 34 (2003) 193.
[3] H. Gabrisch, D. Mukherji and R.P. Wahi, Phil. Mag., A74 (1996) 229
[4] W. Chen, N. Darowski, I. Zizak, G. Schumacher, H. Klingelhöffer, N. Wanderka and W. Neumann, Mat. Sci. Forum, 426 (2003) 4555

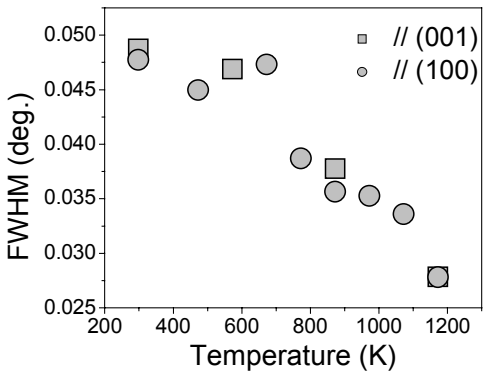

Fig. 2 FWHM values of 001 and 100 super lattice reflections of γ' phase in single crystal superalloy SC16

The Influence of the Blowing Agent on the Metal Foam Structure Investigated by Synchrotron Tomography

A. Haibel[1], A. Bütow[1], A. Rack[1], G. Weidemann[2], H. Riesemeier[2], J. Goebbels[2], J. Banhart[1]

[1]Hahn-Meitner-Institute Berlin, 14109 Berlin, Germany
[2]Federal Institute for Materials Research and Testing, 12200 Berlin, Germany

Metallic foam characterization and development are of high interest in the material science [1, 2]. The precursor material consists of pressed aluminium alloy powder AlSiCu mixed with titanium hydride powder acting as blowing agent TiH_2. After heating the precursor above both the decomposition temperature of the blowing agent and the melting temperature of the metal, hydrogen is released in the melt and a porous structure is generated [3]. In this report the influence of the blowing agent particle sizes and its pre-heat treatment on the pore structure are investigated.
Two sample series were prepared, one using pre-heat treated blowing agent powder with particle sizes (>20 μm, 40-20 μm, 40-80 μm), the other using untreated powder (40-20 μm, 40-80 μm and 80-160 μm). The treated TiH_2 powder causes a hydrogen release at higher temperatures (decomposition temperature T=520°C) than the untreated powder (T=400°C) [4]. For all samples the foaming process was interrupted at the same foaming state 20 seconds after reaching the melting temperature. For the tomographic measurements rectangular samples with a profile of 4×4 mm were cut [5].
The tomographic images of the aluminium alloy foams AlSiCu with different blowing agent particle sizes are displayed in Fig. 1. The first four pictures show the pore size distribution of the me-

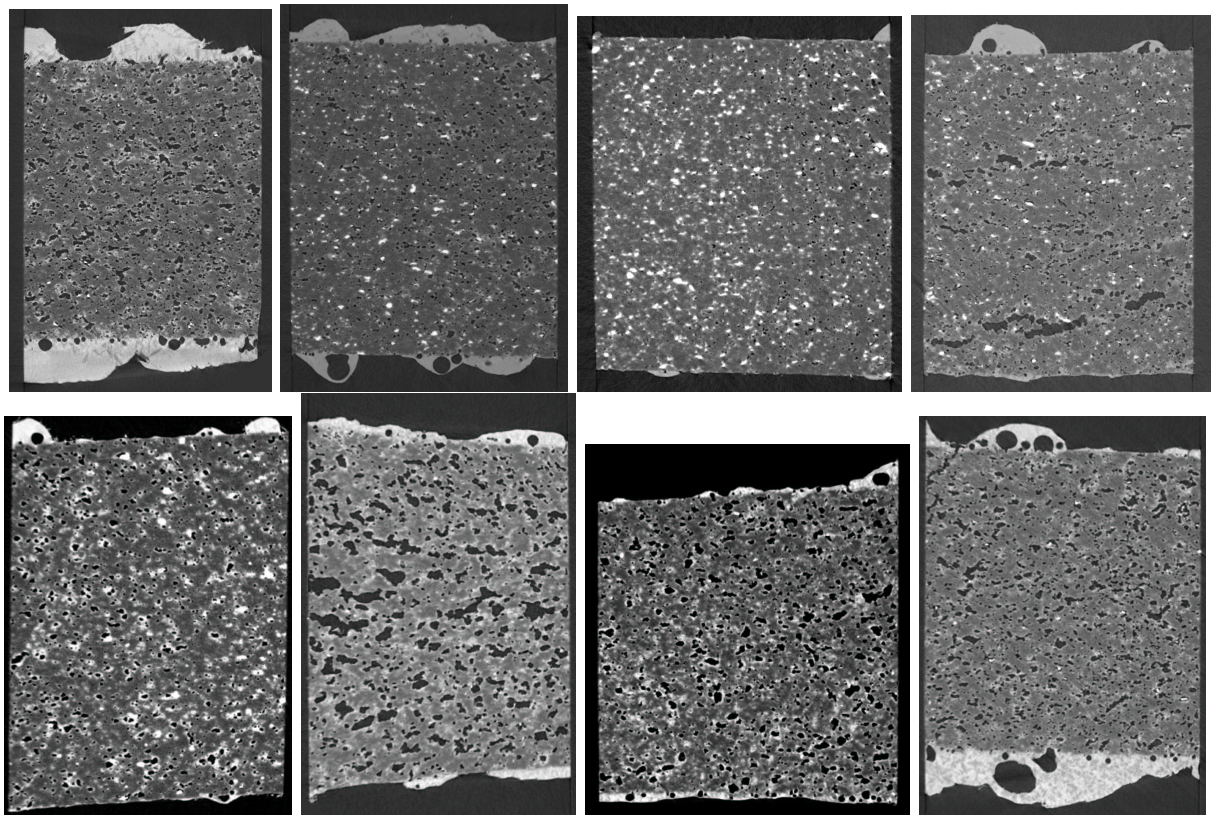

Figure 1: Tomographic slices of the foamed aluminium alloy AlSiCu. The first four samples were foamed with untreated blowing agent particles (size from left to right: 20-40 μm, 40-80 μm, 80-160 μm, and unsieved), the second four with pre-heat treated particles (size from left to right: <20 μm, 20-40 μm, 40-80 μm, and unsieved).

tallic foam produced with untreated TiH_2 whereas the second four pictures show the tomographic measurements of the material foamed with treated TiH_2.
As a first result we see the pores of the samples with treated TiH_2 are always larger than the pores foamed with untreated TiH_2. Furthermore the pore size distribution of the material with untreated blowing agent is mostly independent of the used TiH_2 particle size (except the sample with the unsieved blowing agent powder, where cracks vertical to the pressure direction occur). For the sample series with pre-heat treated blowing agent the pore size maximum was observed for at titanium hydride particles of 20-40 μm. In all pictures a copper enriched phase appears at the sample surfaces.
The quantitative correlation between pores and blowing agent particles for the aluminium foam AlSiCu was calculated by counting the pores with a labeling algorithm using Boolean records of these data and by specifying their volume [6]. In Fig. 2 the results are listed. Generally the porosity of samples foamed with untreated blowing agent is lower for all TiH_2 particle sizes as well as for unsieved particles (see Fig. 2 right, red boxes). The higher porosity of the samples prepared with treated blowing agents is due to the shift in the hydrogen release at higher temperatures (520°C) of this powder, which coincides much better with the melting temperature of the alloy (525°C). Therefore the hydrogen does not leak and produces much more pores. The untreated powder,

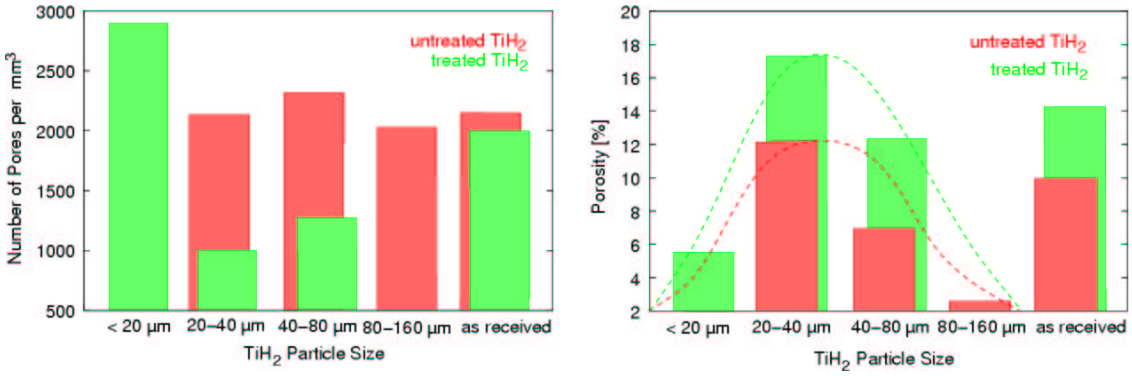

Figure 2: Results of the correlation between pores and the blowing agent particle size and treatment. The green boxes represent the results for the treated blowing agent powder, the red boxes for the untreated powder. The left figure shows the number of pores versus the blowing agent particle size and in the right figure the porosity versus the blowing agent particle size is displayed. (The dashed lines are guides for the eyes.)

where the decomposition starts at T=400°C, looses a part of the hydrogen before the alloy melts. Furthermore it seems that the blowing agent particle size for untreated powder has no influence on the pore size distribution (see Fig. 2 left, red boxes). However, for the samples foamed with treated blowing agent the pore size distribution seems to depend on the TiH_2 particle size (see Fig. 2, green boxes). All samples contain 1vol.% TiH_2. Therefore the sample with the smallest particle sizes has the highest number of particles and after the foaming also the highest number of small pores. The particles with larger particle sizes (20-40 μm and 40-80 μm diameter), i.e. with a smaller number of particles produce a much lower number of pores but a higher porosity. The samples foamed with unsieved blowing agent powder show an average of the results produced with sieved blowing agents with respect to the number of pores as well as to the porosity. The highest porosity seems to occur with the particle size of 20-40 μm for the treated as well as for the untreated powder.

References

[1] M. Ashby et al., Metal foams: A Design Guide, Butterworth-Heinemann (2000)

[2] J. Banhart, N. Fleck, and A. Mortensen, eds., Cellular Metals: Manufacture, Properties, Applications, MetFoam 2003, Berlin, 3-5 September 2003, MIT-2003

[3] J. Banhart, Manufacture, characterisation and application of cellular metal foams, progress in material science 46 (2001), 559-632

[4] B. Matijasevic, S. Fiechter, J. Banhart, Decomposition behaviour of as-received and oxidized TiH2 powder, Powder Metallurgy World Congress, conference book (2004)

[5] A. Bütow, diploma thesis, Strukturuntersuchungen verschiedener Metallschäume in verschiedenen Entwicklungs-stadien, Hahn-Meitner-Institut Berlin, SF3 (2004)

[6] J. Ohser and K. Schladitz, Statistical Analysis of Microstructures in Material Science, Wiley & Sons (2000)

Tomographic studies on boron and gadolinium disc chopper coatings

A. Haibel[1], J. Peters[1], A. Rack[1], G. Weidemann[2], H. Riesemeier[2], J. Goebbels[2], J. Banhart[1]

[1]Hahn-Meitner-Institute Berlin, 14109 Berlin, Germany
[2]Federal Institute for Materials Research and Testing, 12200 Berlin, Germany

Disc choppers (see Fig. 1) permit to produce well defined neutron pulses and to apply the time–of–flight technique at a continuous source. To guarantee the proper cut–out of the pulse by the windows, the impermeable surface of the disc has to compose of a neutron absorbing coating, for instance gadolinium or boron ^{10}B, on a carrier substance, which is for the modern discs by now often composed of CFRP (carbon fiber reinforced plastic) epoxy. The absorption of the coating depends on the selected material, its thickness and the homogeneity of the coating layer. A typical requirement is absorption $> 99.99\%$ of wavelengths ≥ 0.7, as asked for the choppers of the instrument EXED at the HMI. To check the homogeneity of the coating layer, a tomographic studies have been done at

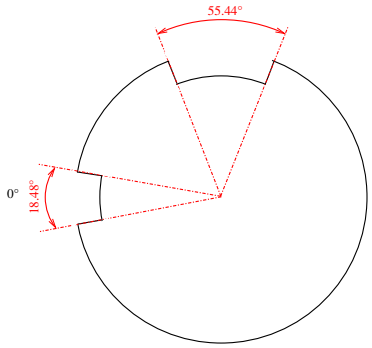

Figure 1: Sketch of a disc chopper with two windows.

the BAMline at BESSY on three samples with both absorbing coatings, boron and gadolinium. The spatial resolution of 3.6 μm has been chosen. The incident energy of 15 keV was chosen for boron and due to the higher X–ray energy absorption coefficient the energy for gadolinium was 30 keV. For each measurement 900 radiographic images have been taken. The angular increment was of 0.2° (total sample rotation 180°).

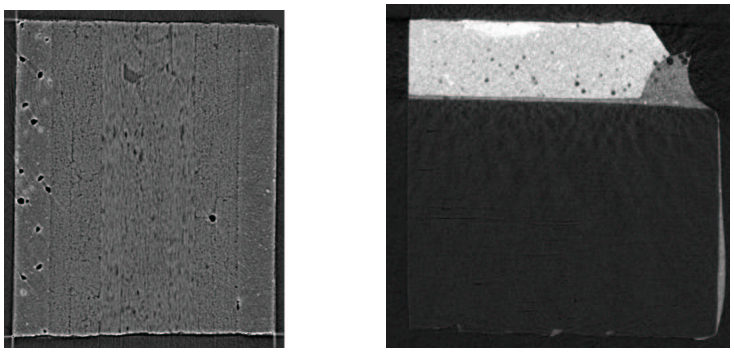

Figure 2: a) Tomographic 2D slice of the boron coated chopper material. At the right side the homogeneous boron layer can be recognized whereas the left coating shows various pores. Pores diameter was about 0.05 mm. (sample size: 2×2.5 mm); b) Tomographic 2D slice of the gadolinium coated chopper material (light grey layer). Various pores are detected, too. (sample size: 4×4 mm)

The first measurement, presented in Fig. 2 a), shows an epoxy supported layer (thickness 1.5 mm) coated with ^{10}B layers of a thickness of 0.3 mm on both sides. On the left side, a standard coating with various pores is to seen whereas the right side, very precisely produced layer looks very homogeneous.
The second investigated sample has an absorbing layer of 1.064 mm gadolinium only on one side (see Fig.2 b)). Various pores are detected, too. In Fig.3 the tomographic image of the original chopper coating material, used for the new experiment in the new neutron hall, is plotted. We chose the gadolinium coated chopper material.
In Fig. 3 the tomographic image of a cut out of the real chopper, used for the new instrument EXED in the new neutron hall, is plotted. We chose the gadolinium coated chopper material. In

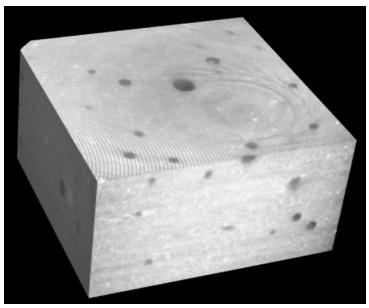

Figure 3: Tomographic picture of the chopper coating material, used in the new neutron hall. (sample size: 1.5×1.5×1mm)

all samples pores with size between 20 and 120 μm have been found (see Fig. 4). Whereas in the chopper material made of ^{10}B (red) more small pores and a small pore size distribution were located, the chopper material made of gadolinium (green) shows a broad pore size distribution and larger pores. For the chopper material, used in the new neutron hall (blue), the lowest porosity was found. In this material the pore size distribution is homogeneous enough to guarantee that the absorbing layer is everywhere sufficient for the absorption requirements.

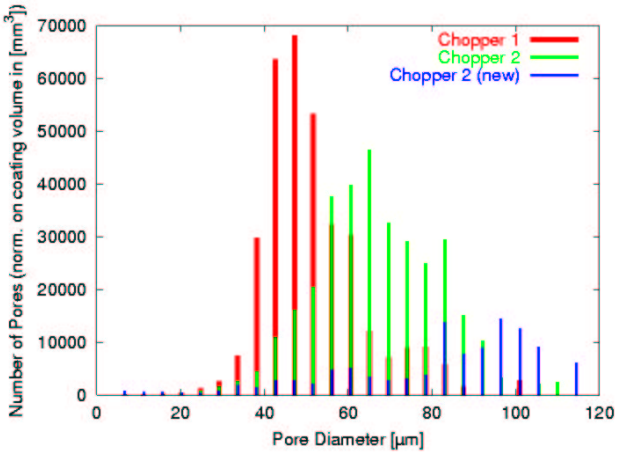

Figure 4: Pore size distribution of the three investigated coatings.

Nano-XAS and Spectral Microscopy of $LiCu_2O_2$

R. Mitdank[1], C. Janowitz[1], A. Sokolov[2], A. Krapf[1], M. Koleśnik[3], A. Vasiliev[2], R. Manzke[1]

[1] Humboldt University Berlin
[2] Lomonossov University Moskow
[3] Jagiellonian University Krakow

The investigations on $LiCu_2O_2$ are motivated by the unusual magnetic properties of this material. $LiCu_2O_2$ contains an equal number of Cu^+ and Cu^{2+} ions in distinct nonequivalent crystallographic positions. The magnetic Cu^{2+} ions carry S=1/2 and form "triangular" two-leg ladders, which can also be viewed as zigzag chains. These chains run along the b axis, and are well separated from each other by double chains of nonmagnetic Li^+ ions and layers of nonmagnetic Cu^+ sites. Since the growth of good quality crystals is crucial for a precise determination of the electronic and magnetic structure, we performed an intensive study of the sample morphology.

The new X-PEEM equipment of our group was installed and tested at the BUS-beamline at the undulator U125/2. The energy resolution of the SGM-monochromator was adjusted to a value below 100meV. The measurements discussed here were carried out in the energy range 40 eV≤hv < 130eV. In Fig._1 the setup of the equipment is presented.

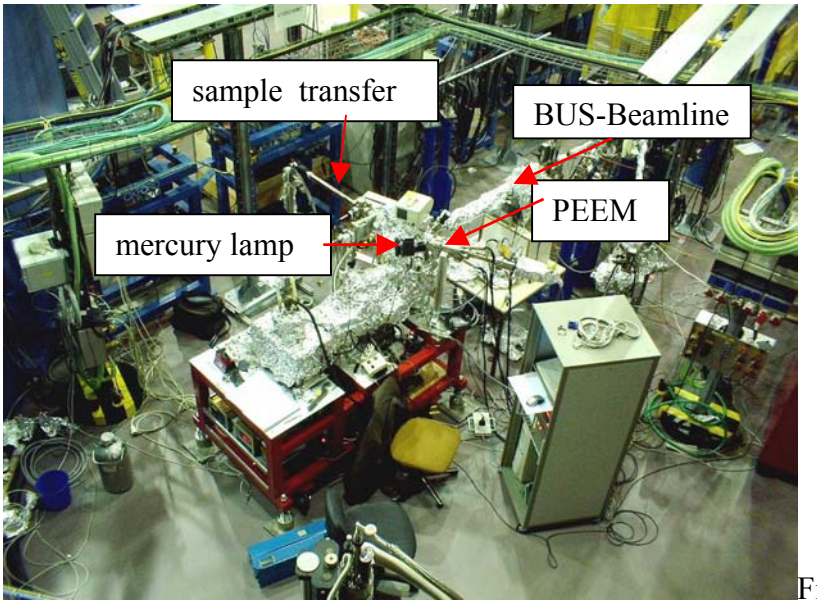

Fig._1: X-PEEM setup at BUS.

The photoemission electron microscope (IS-PEEM of OMICRON) consists of 3 electrostatic lenses (one objective and three projective lenses) and is equipped with an energy filter. The synchrotron beam impinges at an angle of 65° to the optical axis of the microscope on the sample. A mercury lamp (hv = 4,9 eV) is available as additional source of monochromatic radiation for threshold studies. The samples are transfered into an internal sample stage, which is connected with the PEEM. During the experiment, the vacuum pressure near the sample was $7 \cdot 10^{-10}$. To get clean surfaces the samples were cleaved in the vacuum chamber.

The investigated orthorhombic single crystals of $LiCu_2O_2$ were grown using the self-flux method and showed a black shining surface. The initial chemicals of Li_2CO_3 and CuO were

mixed in molar proportion 1:4 and put into a corundum crucible. The mixture was heated to 1200 C and slowly cooled to 930 C with the rate of 4-5 C/h. At 930 C the flux was quenched.

Two absorption spectra are plotted in Fig._2. The blue curve integrates the electron yield over a region with a diameter of nearly 130µm (cf. Fig._3). The green curve is from a region with a diameter of about 5µm with higher Li-content. The iris aperture of the PEEM was set over an area with a maximum of the electron signal at 59eV. The spectra are dominated by two groups of emissions "A" and "B". The locally resolved spectrum exhibits four peaks for A_i and B_i each. We found an energy shift $A_i - B_i$ = 14,8eV. The energies of the peaks are plotted in table 1.

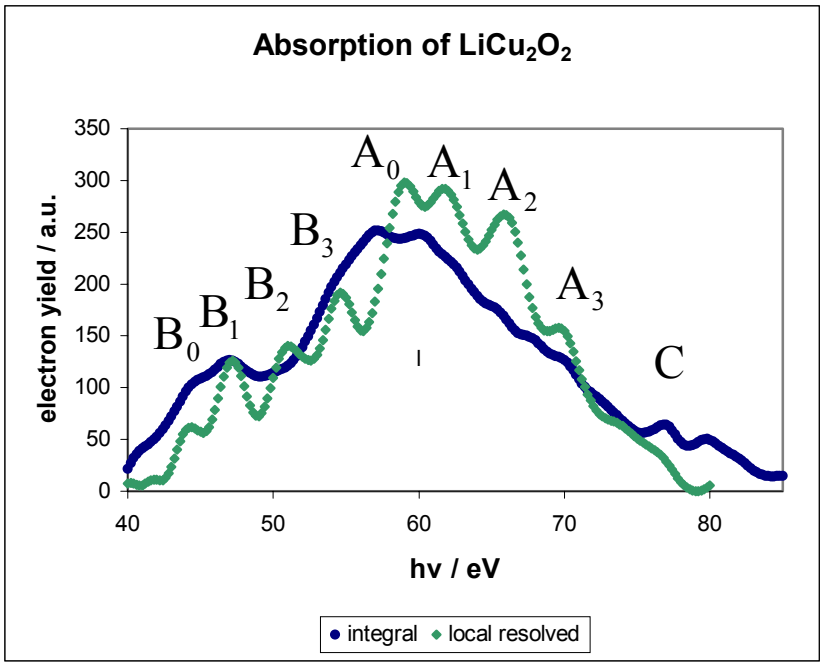

table 1

Peak	hv / eV
A_0	59,0
A_1	61,7
A_2	65,9
A_3	69,6
B_0	44,3
B_1	47,2
B_2	51,1
B_3	54,7
C_0	76,8
C_1	79,8

Fig._2
Integral (diameter 130µm) and locally resolved (diameter 5µm) X-ray absorption of a Li rich region ; peak energies from the locally resolved spectrum in table 1

The peak A_0 is assigned to the transition from an occupied Li-1s state into an empty Li-2p state. This interpretation is derived from the energy level scheme for neutral Li-atoms given in /1/. The peak A_1 near the continuum edge of Li is then due to an excitation of 1s electrons into higher empty p-states.

The energy of the peaks A_2 and A_3 exceeds the ionisation energy of Li-1s state from what follows that an additional emission of an excitation whereas the absorption occurs. In the case of sufficient strong electron-electron interaction the emission of electron pairs with opposite momentum and angular momentum fulfils the conservation laws. Here, besides the excitation of an electron from the 1s into a 2p state, this transition is accompanied by an excitation of electrons from the highest occupied states into either the continuum or an higher empty state. The energy difference $E(A_3) - E(A_0)$ = 2 x 5,3 eV corresponds very well with the first ionisation energy for lithium. The energy difference $E(A_2) - E(A_1)$ = 2 x 2,1 eV corresponds to the transition of Li-electron pairs from the Fermi level into a 2p state. We therefore have an additional indication for the existence of correlated electron pairs in this material .

The constant energy shift of the B_i-peaks with respect to the A_i-peaks indicates, that the A_i and B_i peaks have the same final states. An energetic higher initial 1s state (B_i-peaks) is known for ionized Li^+- ions /1/ where the difference was about 6eV. Our difference could be due to the changed environment in the solid $LiCu_2O_2$. Other possible transitions from deeper states of the other constituents of $LiCu_2O_2$ into unoccupied energy levels do not exist.
The peaks C_i are due to transitions from Cu-3p into Cu-3d-states. This peaks dominate the integral spectrum. There from follows, that Li-rich regions (locally resolved spectrum) and Cu-rich regions (integral spectrum) exist.

Besides the microspectroscopy, spectromicroscopic images were taken. From the raw images an image taken with the mercury lamp was subtracted. This was found necessary to remove topographic effects and inhomogenities of the imaging unit, especially the multichannelplate.

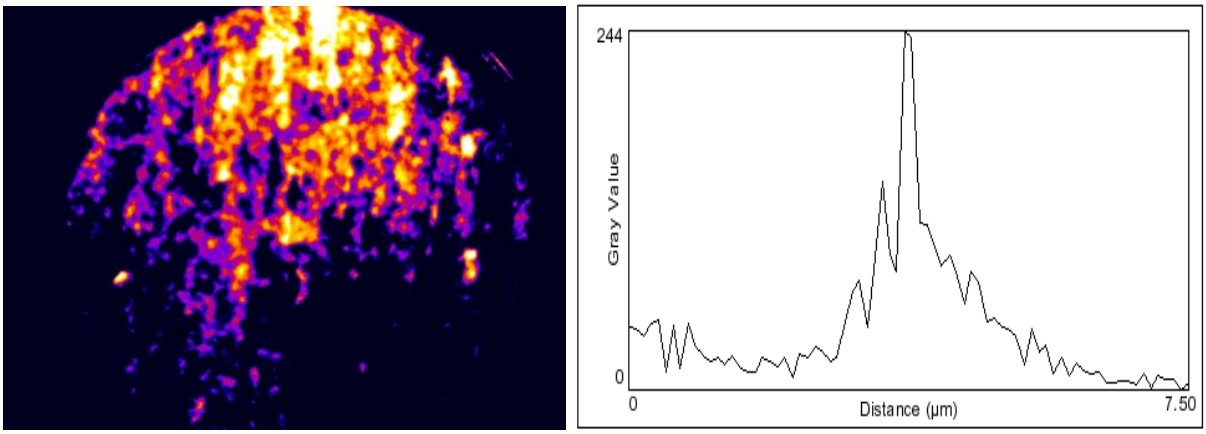

Fig._3: Intensity (Li) distribution at A_0 (hv = 59 eV), diameter of sector: 130µm

Fig._4: A typical profile through a bright spot (high Li-concentration) demonstrates the sub-micrometer local resolution of the instrument

In Fig._3 the Li-distribution in an area of about 130µm diameter is shown. The image confirms the expectation that the Li-distribution in this sample is very inhomogeneous. We have regions with Li-reduction and Li-accumulation. The accumulated Li formes stripes in the ab-plane. Along the stripes the intensity (Li-concentration) has a dotted structure. The islands, as shown in Fig._4, have diameters of 1µm. The resolution amounted to 0,1µm.
A possible explanation for the A- and B-bands could be due to different phases in the material, evt. Li_2CuO_2 islands in $LiCu_2O_2$.

References:
/1/ N. Berrah et. al. , Phys. Rev. Lett. 87, 253002 (2001)

XANES of Binary CN and Ternary BCN Compounds with Fullerene-like and Diamond-like Structures.

I. Jiménez,[a,b] I. Caretti,[b] M. Camero,[b] R. Gago,[c,d] G. Abrasonis[d].

(a) Instituto de Ciencia y Tecnología de Polímeros (ICTP-CSIC), Juan de la Cierva 3, 28006 Madrid (Spain).
(b) Instituto de Ciencia de Materiales de Madrid (ICMM-CSIC), Campus Cantoblanco, 28049 Madrid (Spain).
(c) Centro de Microanálisis de Materiales, Universidad Autónoma de Madrid, 28049 Madrid (Spain).
(d) Institut für Ionenstrahlphysik und Materialforschung, Forschungszentrum Rossendorf. Postfach 510119 - 01314 Dresden (Germany)

Carbon Nitride with fullerene-like structure.

Carbon nitride films are based on a graphitic network, with the nitrogen atoms appearing in different coordination environments, mainly graphite-like , pyridine and cyanide sites. Due to the presence of nitrogen, the basal planes are no longer flat and exhibit a curvature that under certain conditions yields a fullerene-like (FL) structure [1]. The curvature and FL structure affects the density of π^* states that can be monitored through XANES spectroscopy [2].

The formation of the FL structure, monitored through High Resolution Transmission Electron Microscopy (HR-TEM) depends on fine details of the growth parameters (temperature, ion energy, …) of the carbon nitride films [3]. Samples with a well characterised FL structure have been studied by XANES spectroscopy at BESSY II (beamline PM3) revealing a relationship between the FL structure and the XANES spectral shape [4]. As an example, Figure 1 shows the N(1s) XANES spectra from three diferent carbon nitride films, obtained by low energy (<100 eV) ion beam assisted deposition (LE-IBAD), ion beam sputtering (IBS) and magnetron sputtering (MS), evidencing the different relative intensities of the peaks in the 397-401 eV region. Four different peaks have been identified as corresponding to pyridine, cyanide, graphite-like, and embedded molecular nitrogen, at increasing photon energies. The FL structure is found for a certain relative intensity ratio of these peaks. Our current studies try to correlate this observation with the relative number of nitrogen atoms in graphite-like , pyridine and cyanide sites, and discern the nature of the cross-linking sites.

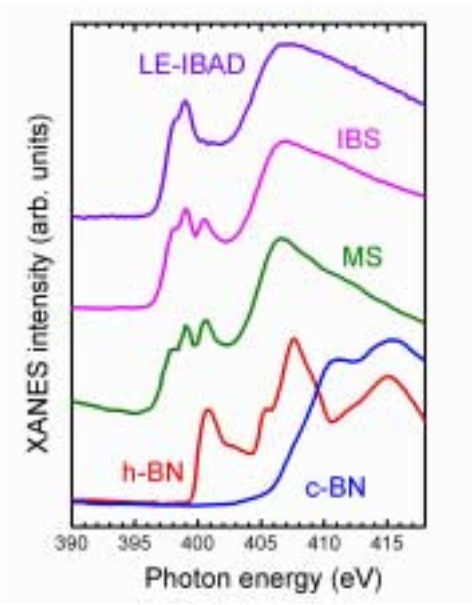

Figure 1. N(1s) XANES spectra from carbon nitride films grown by different methods: low energy (<100 eV) ion beam assisted deposition (LE-IBAD), ion beam sputtering (IBS) and magnetron sputtering (MS). The bottom spectra correspond to reference hexagonal BN and cubic BN crystalline materials.

Ternary Boron-Carbon-Nitrogen (BCN) compounds with diamond-like structure.

The possibility of obtaining ternary BCN compounds stems from the similarity between the carbon and boron nitride allotropes. Ternary BCN compounds with hexagonal structure have been obtained with a variety of techniques, based on physical and chemical processes. The cubic structure, however, remains elusive both by bulk techniques like High Pressure High Temperature methods and by thin film growth techniques. Although the synthesis of tetrahedral (cubic-like) BCN films with C contents below 5% is possible [5], the growth of tetrahedral BCN with large carbon contents remains a challenge. In particular, the stoichiometries BC_2N and BC_4N are of special interest due to the predicted mechanical properties [6].

Our research group is producing BCN films by using independent B, C and N atomic sources that permit a full composition control [7]. We want to study by XANES the bonding structure of these carbon rich BC_xN compounds, since more conventional techniques provide ambiguous results. Figure 2 shows a series of B(1s) and N(1s) spectra from BCN films with different carbon contents obtained at BESSY II in beamline PM3. The carbon content in the films increases from the bottom to top spectra, from 5% to 75%. Two direct observations from the set of spectra are: (i) there is an increasing number of π^* peaks, corresponding to new bonding environments, with the carbon intake, and (ii) the intensity of the π^* region decreases with the carbon intake. The last result indicates the formation of an amorphous diamond-like BCN material for large C contents.

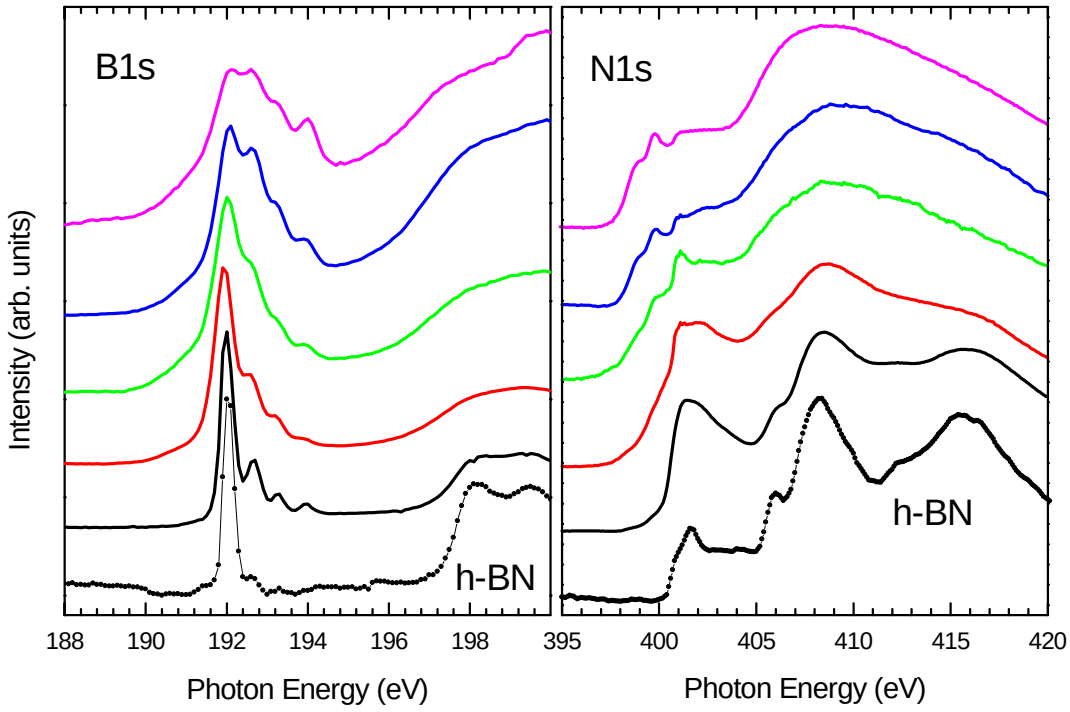

Figure 2 . B(1s) and N(1s) XANES spectra from BCN films with different carbon contents, together with h-BN references. The carbon content increases from bottom to top, from 5% (bottom curve) to 75% (top curve).

We are indebted to R. Mitdank, T. Kachel and the BESSY staff for their help with the experiments. The study of fullerene-like Carbon Nitride is part of the european network "Synthesis, structure and properties of new-carbon based fullerene-like materials" from the Improving Human Potential (IHP) program. The study of diamond-like BCN is part of the 5th. Framework European Program "New Coating Materials for High Performance Cutting Tools, HIPERCUT).

REFERENCES.

[1] H. Sjöström, S. Stafström, M. Boman, J. E. Sundgren, Phys. Rev. Lett. 75 (1995) 1336.

[2] I. Jiménez, R. Gago, J. M. Albella, D. Cáceres and I. Vergara, *Spectroscopy of π-bonding in hard graphitic carbon nitride films: superstructure of basal planes and hardening mechanisms.* Phys. Rev. B 62 (2000) 4261.

[3] J. Neidhart, Zs. Czigány, I.F. Brunell, L. Hultman, J. Appl. Phys. 93 (2003) 3002.

[4] R. Gago, I. Jiménez, J. Neidhart, B. Abendroth, I. Caretti, L. Hultman, and W. Möller. *X-ray absorption study of fullerene-like carbon nitride thin films: curvature of basal planes and electron localisation,* Phys. Rev. B. (2005) in press.

[5] R. Gago, I. Jiménez, T. Sajavara, E. Raühala and J.M. Albella. *X-ray absorption studies of cubic Boron-Carbon-Nitrogen films grown by ion beam assisted evaporation*, Diamond and Related Materials 10 (2001) 1161.

[6] Y. Zhang, H. Sun and C. Chen, Phys. Rev. Lett. 93 (2004) 195504.

[7] I. Caretti, I. Jiménez and J. M. Albella, *BCN films with controlled composition obtained by the interaction between molecular beams of B and C with nitrogen ion beam.* Diamond and Relat. Mater. 12, (2003) 1079 .

Analysis of binding media in cross sections using synchrotron infrared radiation

Oliver Hahn[1], Jens Bartoll[2], Timo Wolff[1,3], Ulrich Schade[4]

[1]*Bundesanstalt für Materialforschung und –prüfung (BAM),12200 Berlin*
[2]*Stiftung Preußische Schlösser und Gärten Berlin-Brandenburg (SPSG), 14414 Potsdam*
[3]*Institut für atomare Physik und Fachdidaktik, Technische Universität Berlin (TUB), Berlin*
[4]*BESSY GmbH, Albert-Einstein-Straße 15, 12489 Berlin*

The characterisation of different organic compounds in paint layers of art objects is of special interest in conservation science and art history. Usually binding media of art objects are identified by infrared spectroscopy in transition mode. Therefore it is necessary to separate each layer from the other mechanically which is very difficult or often impossible because of the smallness and complexity of the samples.

It was the aim of the present study to analyse binding media in cross sections. In order to prepare cross sections, small samples of about 1 mm^3 are taken from the art objekt. They are embedded in resin, ground and polished (Fig. 1). Usually only microscopic methods are applied to study the inorganic pigment grains within the cross section. Until now there are no satisfying methods for the analysis of organic compounds. The method described here presents a direct investigation without any mechanical separation in high local resolution by using infrared spectroscopy. Due to the fact that synchrotron infrared light is 1000 times brighter than a conventional infrared source (e.g. globar) it is possible to carry out non-destructive FTIR measurements in reflectance with high lateral resolution (10 µm × 10 µm).

The measurements were performed at the synchrotron infrared beamline IRIS. A FTIR spectrometer (Bruker 66/v) and an IR microscope (Thermo Nicolet Continuum and Nexus) were used. In order to collect reference data selected samples of typical binding media such as dry oil, resins, waxes, and glues were measured (Fig. 2). A silicon wafer and gold sputtered surfaces (Fig. 3) of different texture were measured for background substraction.

The results indicate, that the smoothness of the sample surface has a strong influence on the quality of the detected reflection spectra. But it is possible to distinguish between different classes of binding media using this method. This works not only for standard samples but also for original samples extracted from old furniture coatings. Spectra of glue, shellac and oil coatings could be detected (Fig. 4). The reflection spectra resemble the transmission spectra of the binding media. Only the relative intensity of some signals is different (Fig 5). All in all these first results indicate that this technique provides a suitable method for organic analyses in the field of archaeometry.

References

M.R. Derrick, D. Stulik und J.M. Landry, Infrared Spectroscopy in Conservation Science, The Getty Conservation Institute Los Angeles (ed.) 1999.

S. Wülfert, Der Blick ins Bild, Lichtmikroskopische Methoden zur Untersuchung von Bildaufbau, Fasern und Pigmenten, Bücherei des Restaurators Bd. 4, U. Schießl (Hrsg.) Ravensburger Buchverlag 1999.

Fig. 1: Cross section, panel painting 18th century

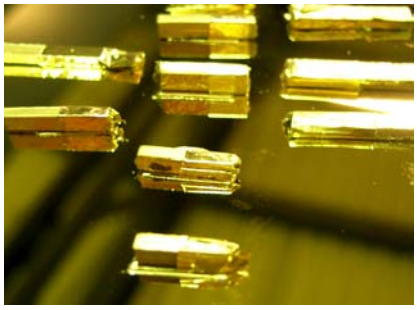

Fig. 3: Gold sputtered samples

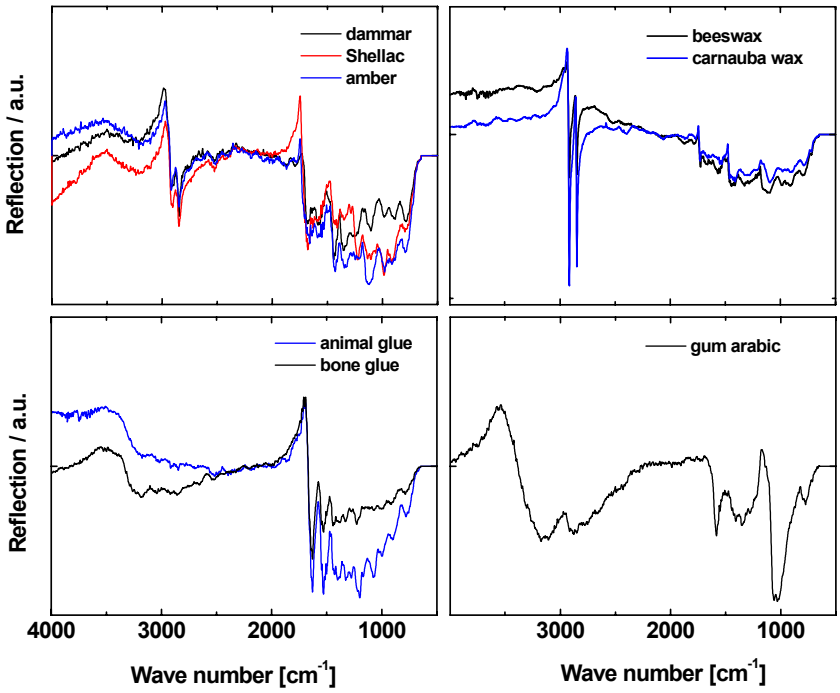

Fig. 2: FTIR-spectra of different reference materials

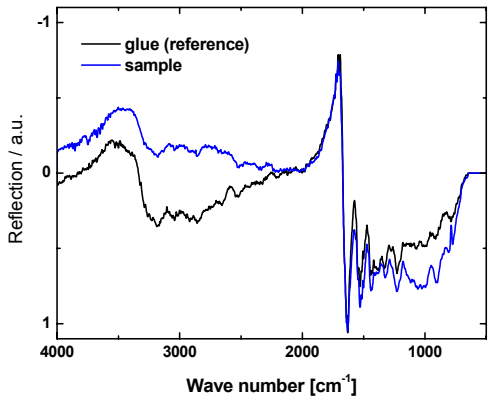

Fig. 4: Identification of glue in a furniture coating

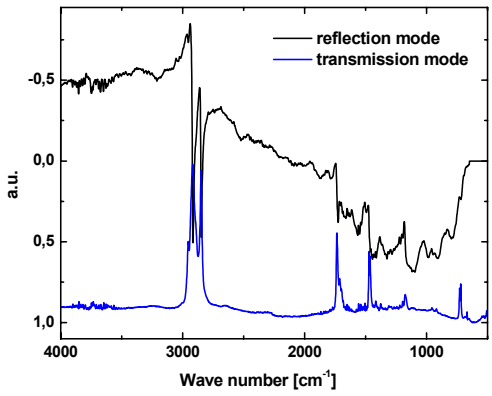

Fig. 5: Comparison between reflection and transmission spectra; sample: beeswax

Structure of crystalline Pr_2O_3 on Si(001) studied by synchrotron surface x-ray diffraction

X.X. Guo, W. Braun, B. Jenichen, V. M. Kaganer, K. H. Ploog

We have investigated the structure of crystalline Pr_2O_3 on Si(001) grown in a molecular-beam epitaxy (MBE) system, which has been recently set up at the PHARAO beamline. The system is designed for optimizing the interfacial properties through the analysis of the MBE growth by in-situ surface x-ray diffraction. We find that the Pr_2O_3 layer consists of two types of orthogonal domains, both of which have a good crystallinity. Up to now, there is no evidence of any interfacial layer, indicating an abrupt interface in the investigated Pr_2O_3/Si(001) system.

The sample discussed here was grown by an e-beam evaporator in the MBE system on the (2×1)-reconstructed Si(001) surface at 600 °C. The source material is a sintered Pr_2O_3 ceramic rod, which was thoroughly degassed before deposition. The pressure was in the lower 10^{-9} mbar range during the deposition at a typical growth rate of 3 Å/min. After growth, the film was transferred into the measurement chamber mounted on the x-ray diffractometer without leaving ultra-high vacuum.

Fig. 1 presents in-plane grazing-incidence x-ray diffraction measurements (θ-2θ scans). Assuming the cubic Mn_2O_3 structure for the epitaxial Pr_2O_3 layer, we can assign the dominant peaks to two kinds of orthogonal [101]-oriented domains, with the $[10\bar{1}]$ direction of one and the [010] direction of the other being parallel to the Si [110] direction. The higher order reflections obtained in this measurement allow us to calculate the domain sizes by drawing Williamson-Hall plots in the reciprocal-lattice representation for Gaussian peak profiles. The fit yields an average in-plane size for one type of domains of about 22 nm, and for the other about 19 nm, both of which are larger than the layer thickness (∼ 18 nm). This result indicates a good crystallinity of the domains.

Rod scans have been carried out for the reflections of the layer. Fig. 2 and Fig. 3 show the results of the scans perpendicular to the surface

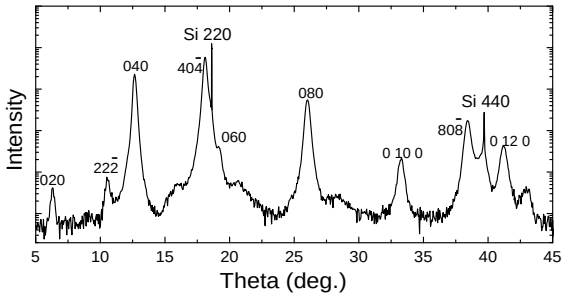

Figure 1: In-plane grazing-incidence x-ray diffraction measured along the Si[110] direction in UHV. (020), (040), (060), (080), (0 10 0), and (0 12 0) are attributed to one type of Pr_2O_3 domains. $(40\bar{4})$ and $(80\bar{8})$ are attributed to the orthogonal ones. Some minor peaks arise from a small amount of other domain orientations.

along the Pr_2O_3 $\ell 4\ell$ and $\ell 8\ell$ rods, which correspond to one kind of domains. Four Bragg reflections with ℓ from 1 to 4 can be observed in the measured range. This is also the feature of the rod scans for other reflections of this kind domains, such as $\ell 2\ell$, $\ell 10\ell$, and $\ell 12\ell$. There are only two Bragg reflections with ℓ values of 2 and 4 in the rod scans of reflections from the other kind domains, as shown in Fig. 4. Therefore, these high order Bragg reflections along the rods clearly indicate the high-quality crystal structures of the domains, because forbidden reflections are indeed absent.

The in-plane and out-of-plane lattice constants are calculated from the above scans. Combining the different order reflections obtained from the in-plane measurement, we determine the lattice constants of 10.88 Å and 7.75 Å in the [010] and $[10\bar{1}]$ directions, respectively. When comparing with the corresponding bulk values (11.15 Å and 7.88 Å), the domains are compressed by 2.4 % and 1.6 % in the [010] and

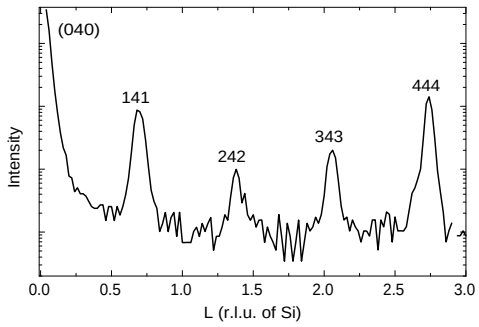

Figure 2: X-ray scan perpendicular to the surface along the Pr_2O_3 $\ell 4\ell$ rod. L and ℓ is the perpendicular moment transfer in the reciprocal lattice units of Si and Pr_2O_3, respectively.

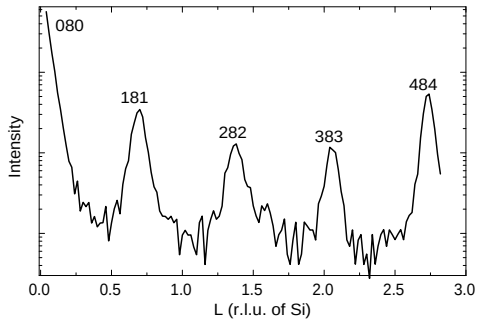

Figure 3: X-ray scan perpendicular to the surface along the Pr_2O_3 $\ell 8\ell$ rod. L and ℓ is the perpendicular moment transfer in the reciprocal lattice units of Si and Pr_2O_3, respectively.

$[10\bar{1}]$ directions. In the same way, from the lattice spacing between the different order reflections in the rod scans, the lattice constant in the $[10\bar{1}]$ direction is determined to be 8.01 $\AA$ for one kind domains and 8.05 $\AA$ for the other. The difference between the two values is within 0.5 %. Taking into account the lattice constant of 7.88 $\AA$ in the bulk, the crystalline domains are expanded by about 2.0 % in the direction perpendicular to the surface. Thus, the domains are expanded out-of-plane due to the compressive in-plane strain.

The presence of possible interfacial layers has been investigated by in-plane scans with varying grazing incidence angle. So far, there is no evidence of any interfacial layer, indicating that the Pr_2O_3 structure extends directly to the substrate. This finding is confirmed by high-resolution transmission electron microscopy.

In summary, using our MBE system combined with synchrotron surface x-ray diffraction, we have investigated the structure of crystalline

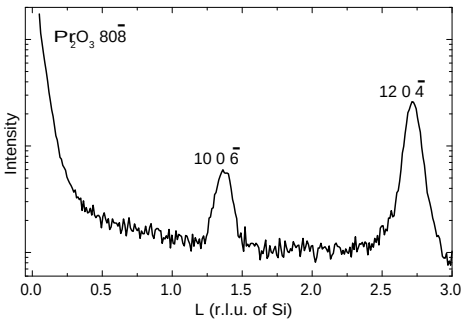

Figure 4: X-ray scan perpendicular to the surface along the Pr_2O_3 $8{+}\ell\ 0\ \bar{8}{+}\ell$ rod. L and ℓ is the perpendicular moment transfer in the reciprocal lattice units of Si and Pr_2O_3, respectively.

epitaxial Pr_2O_3 grown on Si(001). Structural features including the epitaxial relationship, the domain quality, and the lattice distortion have been obtained. We achieve an abrupt interface in the Pr_2O_3/Si(001) system, most probably attributed to the optimized growth parameters.

Influence of Restoration Treatments on Ink Corroded Manuscripts

Oliver Hahn[1], Birgit Kanngießer[2], Max Wilke[3], Wolfgang Malzer[2],
Bettina Nekat[3], Timo Wolff[1,2], Alexei Erko[4]

[1] *Bundesanstalt für Materialforschung und –prüfung (BAM), IV.2, 12200 Berlin*
[2] *Institut für Atomare Physik und Fachdidaktik, Technische Universität Berlin, 10623 Berlin*
[3] *Institut für Geowissenschaften, Universität Potsdam, Postfach 601553, 14415 Potsdam*
[4] *BESSY GmbH, Albert-Einstein-Straße 15, 12489 Berlin*

Introduction: In order to determine the success of different restoration processes on ink corroded manuscripts we studied historical samples and artificial dummies before and after restoration treatments. Due to the fact that there are two main reasons for the ink corrosion, first of all the acidity of the inks which leads to hydrolytic splitting of the cellulose, and secondary the capacity of soluble iron and other compounds that act as catalyst for the oxidative decomposition of the cellulose, all restoration treatments try to decrease the concentration of acids and/or the concentration of soluble 3d-elements.

Former investigations show that a combination of micro X-ray fluorescence analysis (micro-XRF) and micro X-ray absorption near edge structure spectroscopy (micro-XANES) is a step forward in the understanding of the complicate and complex paper degradation process in the context of iron gall ink corrosion [1]. With elemental mapping by micro-XRF the correlation of the minor elements zinc, manganese and copper in the ink to the major element iron was investigated. Along concentration profiles of iron micro-XANES measurements were carried out in order to determine the oxidation state of iron and its local environment. The first results indicate that non-aqueous as well as aqueous treatments both influence the chemical composition of the inks and therefore change the archaeometrical fingerprint [2] of the historical sample.

Experimental: The experiments were carried out at the bending magnet beamline KMC-2 at BESSY. Final focussing to a spotsize of about 20 µm at the experiment was done by use of a polycapillary half-lens. In order to obtain higher fluorescence intensities and to decrease effects by sample inhomogeneities, the data were collected with a bigger spot size of 30 µm. The elemental mapping was performed with a step width of 50 µm. Micro-XANES spectra at the Fe K-edge were collected in fluorescence mode using an energy step width around the absorption edge of 0.5 eV. Total acquisition time for one absorption spectrum is about 15 minutes. The XANES spectra were corrected for background absorption by subtracting a polynomial function that was fitted to the spectral region before the pre-edge. The spectra were then normalized for atomic absorption by fitting an arc tangent function and a gaussian function to the spectra and setting the arc tangent function to equal step height for all spectra. According to former investigations, we used the inflection point of the absorption edge as a figure of merit for determination of the valence state. The inflection point indicates the energetic shift of the edge position if the bulk chemical composition is not changing.

Results: Based on one example (Fig. 1) the influence of a non-aqueous treatment is demonstrated in detail. The historical ink of interest contains iron, copper, zinc, and manganese (the relative concentrations $<W_i>$ of the elements Cu, Mn, and Zn before the restoration treatment are given in

Table 1). Based on the fingerprint value W_{Zn} in comparison to the distribution of Fe in the ink material it can be seen that there is a quite homogeneous distribution of the element Zn in relation to the main consistent iron (Fig. 2a). For more details see Kanngießer *et al*. 2004 [3] and [1]. During the restoration process a significant change took place: the distribution of the element Zn – in relation to Fe – becomes more inhomogeneous (Fig. 2b). The same is true for the other 3d-elements Cu and Mn. This change can also be seen while comparing the mean fingerprint value of Zn before and after treatment. It is obvious that this value shifts to higher values; that means that the restoration process enlarges the concentration of Zn in the ink in relation to the iron (Fig. 3). The following Table 1 summarizes different influences of one certain restoration process on several fingerprints. Due to the fact that the relative concentrations of Mn and Zn apparently enlarge whereas the relative concentration of Cu remains constant we have to draw the conclusion that the element Cu is "washed out" in the same way like the main inorganic compound Fe.

Table 1: Different fingerprint values $<W_i>$ and the area density, $<a_{Fe}>$ before and after the restoration treatment.

	$<W_{Mn}>$	$<W_{Cu}>$	$<W_{Zn}>$	$<a_{Fe}>$ / g cm^{-2}
Before treatment	0.006 ± 0.003	0.027 ± 0.005	0.007 ± 0.004	0.09
After treatment	0.018 ± 0.003	0.025 ± 0.003	0.012 ± 0.004	0.06

Concerning the micro-XANES measurements Fig. 4 shows the results of the first measuring series before treatment (black lines). In contrast to former investigations, no significant increase of the Fe^{2+}/Fe^{3+} ratio with increasing the iron account in the ink spot could be observed (with respect to measurement uncertainties). The red curves show the measurements after restoration. Based on the present results we can say that no significant changes take place. We might perhaps assume a little trend to a more reduced state. These findings were approved by means of more investigations – based on artificial dummies as well as on original documents. However, in some cases the results were slightly different. In order to test the mode of action of further conservation treatments, simulation experiments for ink corrosion have to be developed.

Conclusion: Our present results show that micro-XRF measurements in combination with micro-XANES experiments are necessary to prove the success of treatments of ink corroded manuscripts in the future. First analyses on artificial dummies treated with aqueous restoration methods indicate that the chemical compositions of the inks change remarkably. However, due to the fact that the significant differences of the varying inks remain stable it seems to be possible to carry out further archaeometrical investigations on the historical documents after restoration treatments [4].

References

[1] Hahn O, Malzer W, Kanngießer B, Investigation of oxidation and migration processes of inorganic compounds in ink corroded manuscripts, BESSY, Annual Report 2003, 371-373.

[2] Malzer W, Hahn O, Kanngießer B, A fingerprint model for inhomogeneous ink paper layer systems, X-Ray Spectrometry 33, 229-233 (2004).

[3] Kanngießer B, Hahn O, Wilke M, Nekat B, Malzer W, Erko A, Investigation of Oxidation and Migration Processes of Inorganic Compounds in Ink Corroded Manuscripts, Spectrochimica Acta B, Vol 59/10-11, 1511-1516 (2004).

[4] Hahn O, Kanngießer B, Malzer W, Nekat B, Stiebel N, Wilke M, Wolff T, Influence of restoration processes on archaeometrical investigations, Studies in Conservation, in preparation.

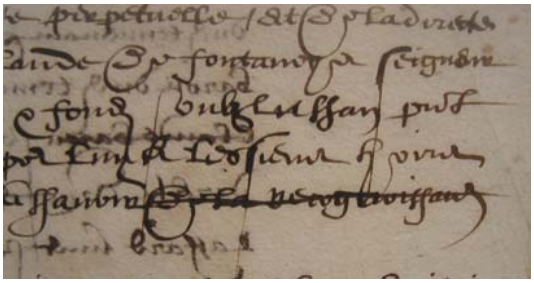

Fig.1: Iron gall ink on rag paper, showing ink corrosion

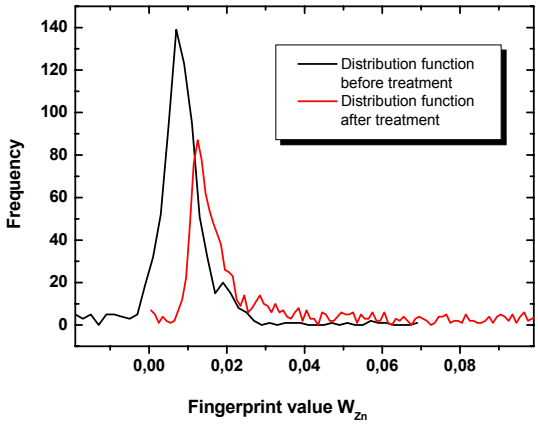

Fig.3: (on the right) Shift of the fingerprint value W_{Zn} due to restoration

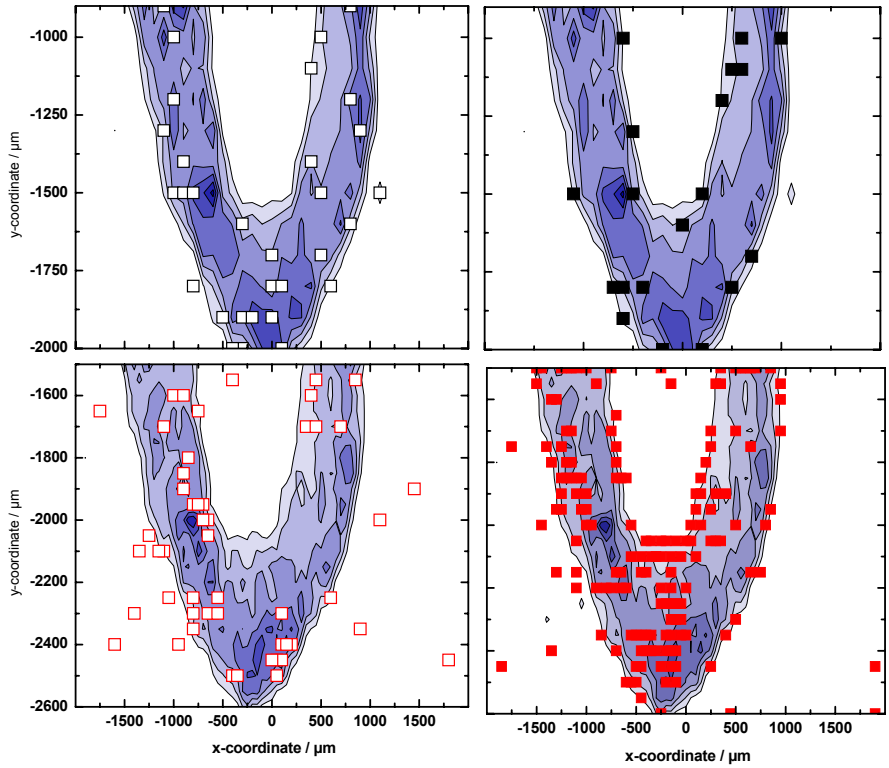

Fig.2: Comparison of the Zn distribution in relation to Fe before and after restoration. The fingerprint values of Zn are mapped in the Fe concentration profile [3]. White squares symbolise below average values, coloured squares above average values. The black colour indicates measurements before, the red colour indicates measurements after restoration.

Fig. 4: X-ray absorption profiles around K-edge of iron. The position of the absorption edge as well as the pre-peak is an indication of the oxidation state and coordination state of iron. For the determination of the valence state we used the inflection point of the absorption edge as a figure of merit. The inflection point indicates the energetic shift of the edge position if the bulk chemical composition is not changing. The comparison of the measurements before (black lines) and after (red lines) restoration indicates that no change takes place.

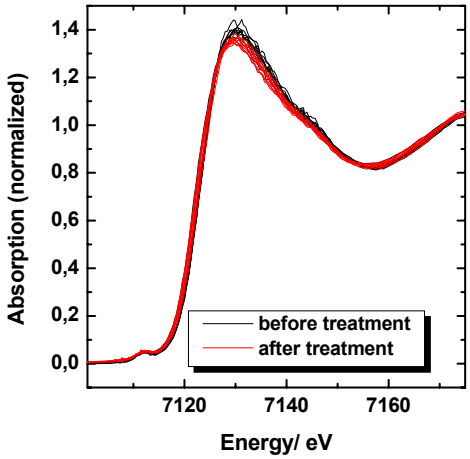

"Implementation of Co_2MnSi electrodes in magnetic tunnel junctions: magnetic and chemical bulk properties compared to the interface"

J. Schmalhorst, M. Sacher, S. Kämmerer, V. Höink, A. Hütten, G. Reiss
Nano Device Group, Department of Physics, University of Bielefeld, D-33615 Bielefeld, Germany

D. Engel, A. Ehresmann
Department of Physics, Kaiserslautern University of Technology, D-67663 Kaiserslautern, Germany

Half-metallic materials will improve spintronic devices considerably. We produced magnetic tunnel junctions showing impressive 95% tunneling magnetoresistance and compared their magnetic and chemical properties at the Co_2MnSi / AlO_x interface with the Co_2MnSi bulk material by using X-ray absorption spectroscopy (XAS) and magnetic circular dichroism (XMCD) techniques.

The 100% spin polarization predicted theoretically for some Heusler alloys like Co_2MnSi [1] make them attractive for spintronics applications [2], e.g., as electrode material in magnetic tunnel junctions (MTJs) with highest tunneling magnetoresistance (TMR). The formation of a high quality tunneling barrier without generating defects in the adjacent half-metallic electrode is the crucial preparation step. We fabricate Co_2MnSi / AlO_x / Co-Fe MTJs with 95% TMR at low temperature and low bias voltage [3-7]. However, the TMR bias voltage and temperature dependence is considerably stronger than usually found for optimized MTJs with 3d-alloy electrodes. In this work, we used soft X-ray absorption and magnetic circular dichroism in total fluorescence yield detection (TFY), total electron yield detection (TEY) and reflection to compare the magnetic and chemical properties at the Co_2MnSi / AlO_x interface, which has considerable impact on the transport properties of the MTJs, with the Co_2MnSi bulk material.

We used the "BESSY polarimeter" at beamline UE56/1-PGM-b utilizing 90% right / left elliptically polarized X-rays at the V, Co and Mn $L_{2,3}$-edges. Recently, the polarimeter has been upgraded to enable X-ray absorption spectroscopy in TEY and TFY detection in addition to the X-ray reflectivity measurements. All data were normalized with respect to the incoming photon flux. Because of the different information depth of the two XAS detection modes (a few nm for TEY, some 10nm for TFY), a comparison of surface and bulk properties of the investigated samples is possible. The TEY measurements were done in the remanent state of V^{42nm} / Co_2MnSi^{100nm} / $AlO_x{}^{1.8nm}$ stacks. This ensured equal detection efficiencies of the secondary electrons for parallel (+) and antiparallel (-) alignment of the remanent sample magnetization and the photon spin. To eliminate an unwanted influence of the secondary electrons on the TFY signal which was measured by a photo diode mounted about 10mm above the sample surface, we performed the investigations of the bulk material in the saturated state of V^{42nm} / Co_2MnSi^{100nm} / $AlO_x{}^{1.8nm}$ / Ta^{5nm} samples. The Ta capping layer resulted in a nearly constant electron yield in the energy ranges of the V, Co and Mn $L_{2,3}$-edges. The shape of the TFY spectra was, therefore, not altered by parasitic secondary electrons. The angle of incidence of the X-rays was $\theta = 30°$ with respect to the surface for XAS and varied from $\theta = 0°$ to $\theta = 40°$ for reflectivity measurements.

Figures 1 and 2 show the TFY and TEY spectra of the Co_2MnSi bulk material and the Co_2MnSi / AlO_x interface for as prepared samples and after annealing at 500°C. Annealing of the samples after magnetron sputter deposition is necessary to induce the atomic ordering of the Co_2MnSi thin films. An important signature of the ordering process is an increased bulk magnetic moment of nearly $5\mu_B$ per formula unit and the development of superlattice peaks in the large angle Cu-K_α diffraction patterns [3]. The ordering process of the material is reflected by two features in the TFY spectra: (1) After annealing we found additional shoulders (see black arrows in Fig. 1) about 4eV above the maximum intensities of the Mn and Co $L_{2,3}$-resonances not present in the as prepared state. (2) Mn and Co exhibit clear EXAFS oscillations indicating a well ordered state of the bulk material (see red arrows in Fig. 1).

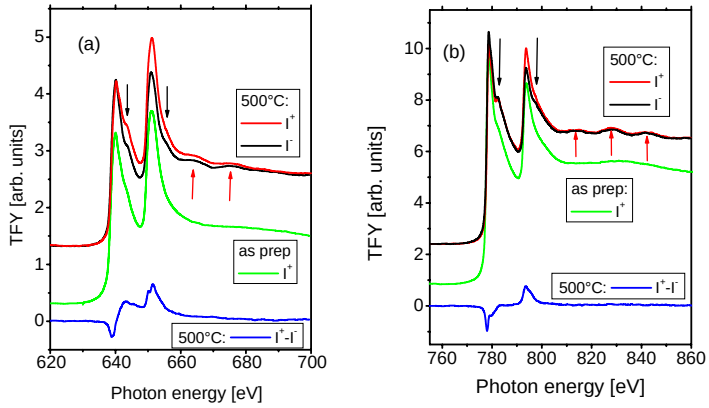

Figure 1: Total fluorescence yield spectra at the (a) Mn $L_{2,3}$-edges and the (b) Co $L_{2,3}$-edges measured on V^{42nm} / Co_2MnSi^{100nm} / $AlO_x^{1.8nm}$ / Ta^{5nm} samples in the as prepared state and after annealing at 500°C.

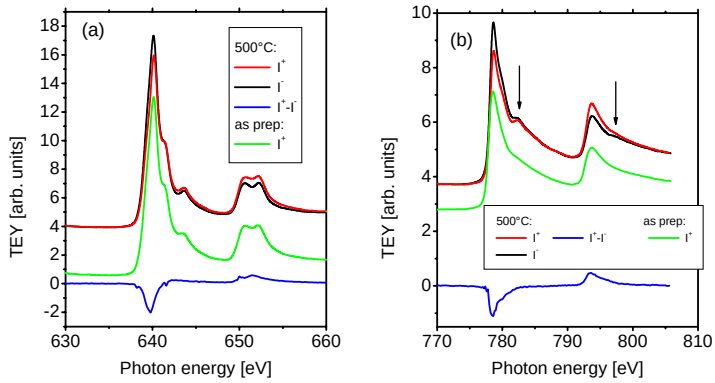

Figure 2: Total electron yield spectra at the (a) Mn $L_{2,3}$-edges and the (b) Co $L_{2,3}$-edges measured on V^{42nm} / Co_2MnSi^{100nm} / $AlO_x^{1.8nm}$ samples in the as prepared state and after annealing at 500°C.

Because of the large Co_2MnSi layer thickness of our samples the quantitative analysis of the XMCD asymmetry (I^+-I^-) by means of "sum-rules" [8] is inhibited by self-absorption and saturation effects. But the comparison of the TFY spectra with the TEY measurements (Fig. 2) probing the Co_2MnSi / AlO_x interface shows an important difference between Co and Mn. Whereas the Co TFY and TEY spectra are comparable (the reduced maximum intensities at the $L_{2,3}$-resonances are due to the saturation effects mentioned above), the TEY signal of Mn exhibit a multiplet structure not present in TFY. Recently, we have attributed this multiplet structure in the TEY spectra to the formation of interfacial MnO_x [7], now the TFY spectra show clearly the difference between the (metallic) bulk and the (oxidized) interfacial Mn. The comparison of the TFY data as a fingerprint of the Co_2MnSi bulk material with fully relativistic band structure calculations [9] is being in progress. To overcome the problem of saturation effects we will extend our measurements to stacks with thinner Co_2MnSi films. We like to emphasize that the knowledge of the shape of the absorption spectra of the bulk material is important for analyzing the resonant reflectivity data (see below) of layer stacks containing Co_2MnSi quantitatively, because the real part of the optical constant is connected to its imaginary (absorptive) part via the Kramers-Kroning relations.

In addition to the TFY / TEY studies we performed first X-ray reflectivity measurements (resonant at the V, Co and Mn $L_{2,3}$-edges and non-resonant in the pre edge regions) of V^{42nm} / Co_2MnSi^{100nm} / Co^{0-3nm} / $AlO_x^{1.8nm}$ samples in the as prepared as well as the annealed state (500°C) to investigate the influence of thin Co interlayers (0-3nm thickness) between the Co_2MnSi electrode and the AlO_x on the interfacial magnetic properties. Figure 3 shows typical θ-2θ scans of the intensity reflected by magnetically saturated samples with d_{Co}=3nm for the as prepared and the annealed state. Although the quantitative analysis of the data hasn't been finished yet, some preliminary results shall be presented here:

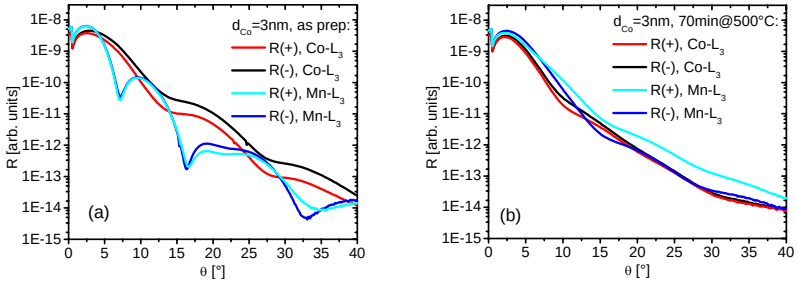

Figure 3: Soft X-ray reflectivity (θ-2θ scans) at Co and Mn L_3-edge photon energies with right (+) and left (-) elliptical polarization of V^{42nm} / Co_2MnSi^{100nm} / Co^{3nm} / $AlO_x^{1.8nm}$ samples in (a) the as prepared state and (b) after annealing at 500°C.

Whereas we didn't find a magnetic moment neither for Co nor for Mn in the as prepared samples (disordered Co_2MnSi) with d_{Co} = 0nm, significant moments were found for $d_{Co} \geq$ 1nm indicated by clear XMCD asymmetries in the θ-2θ scans. Probably, the main part of the Co magnetic moment is localized in the Co interlayer, whereas the Mn moment is induced at the Co_2MnSi / Co interface. Furthermore, the thin Co interlayer results in pronounced minima in the resonant Mn L_3-edge reflectivity (Fig. 3a). After annealing these minima disappear and the XMCD asymmetry at the Co and Mn resonances become very similar for all interlayer thicknesses d_{Co}. Especially the θ-dependent XMCD asymmetry of Co is reduced with respect to the as prepared state, whereas for Mn the asymmetry becomes considerably larger. These results show, that the annealing procedure results in an interdiffusion at the Co_2MnSi / Co interface. The quantitative evaluation of the reflectivity data by fitting the reflected intensities and the asymmetries and the according TEY data will be performed in the future.

The authors gratefully acknowledge the valuable help of Dr. A. Gaupp and D. Abramsohn during beamtime at BESSY.

[1] S. Ishida, T. Masaki, S. Fujii and S. Asano, Physica B **245** (1998) 1
[2] S.A. Wolf et al., Science 294, 1488 (2001)
[3] A. Hütten, S. Kämmerer, J. Schmalhorst, G. Reiss: *„Heusler alloyed electrodes integrated in magnetic tunnel junctions"*, in *„Halfmetallic Alloys: Fundamentals and Applications"*, editors: I. Galanakis and H. Dederichs, Lecture Notes on Physics, Springer Verlag (2004), in press[4] S. Kämmerer et al. Appl. Phys. Lett. **85** (2004) 79
[5] J. Schmalhorst et al.: *"Inelastic electron tunneling spectroscopy and bias voltage dependence of magnetic tunnel junctions with polycrystalline Co_2MnSi electrode"* , Appl. Phys. Lett., in press
[6] A. Hütten et al., phys. stat. sol. (a) **201** (2004) 3271 [7] J. Schmalhorst et al., Phys. Rev. B **70** (2004) 024426
[8] C. T. Chen et al., Phys. Rev. Lett. **75** (1995) 152
[9] *The Munich SPR-KKR package, version 2.1*, H. Ebert et al., http:/olymp.cup.uni-münchen.de/ak/ebert/SPRKKR; H. Ebert, *Fully relativistic band structure calculations for magnetic solids-Formalism and Application*, in *Electronic Structure and Properties of Solids*, editor: H. Dreyssé, Lecture Notes in Physics, vol. 535, p.191, Springer Berlin

Sexiphenyl and sexithiophene (hetero-)structures

G. Koller, S. Berkbile, F. Pfuner and M.G. Ramsey

Institut für Physik, Karl-Franzens-Universität Graz, A-8010 Graz, Austria

Organic devices often consist of a multiplicity of organic layers making the understanding of the organic/organic interface and organic-on-organic growth a technologically important issue. On the one hand details of the interfaces are important for charge injection, while the molecular/crystallite orientation and film morphology determine charge transport, light emission/absorption – for optimum performance these key factors need to be tailored for the specific device applications as OLEDs, OFETs and photovoltaic devices have different requirements [1]. For instance, in an OFET the molecular orientation should be such that the direction of maximum charge carrier mobility lies between the source and the drain contact, while in an OLED or photovoltaic device the orientation of the axis of maximum light absorption/emission is the determining factor. The molecules used in this study are device relevant, e.g. para-sexiphenyl (p-6P) is a promising material for blue light emitting diodes and solar cells, while alpha-sexithiophene (α-6T) can be used in field effect transistors. Here we report investigations into the orientation of α-6T molecules from monolayer coverages to thin films (up to 50 nm) grown on highly crystalline (20$\underline{3}$) and (001) oriented p-6P films, which corresponds to p-6P films where the molecular axes is parallel and near (17° off normal) normal with respect to the anorganic substrate.. The surfaces were prepared and investigated in the MUSTANG end station attached to the Russian-German beamline. SXPS, UPS and C_K- and S_L- edge Auger yield NEXAFS spectra were obtained with a Phoibus 150 analyser from SPECS.

The inset of Fig. 1 a shows C_K-edge NEXAFS spectra of a 400 Å thick p-6P film grown on a TiO_2(110) single crystal at RT . The spectra were recorded with the polarisation parallel to the [001] and [1$\underline{1}$0] substrate azimuth and for incidence angles α between normal N.I. (θ=0°) and gracing incidence G.I. (θ =80°). The π^* features for N.I. and polarisation along [001] are very weak, whereas they are strong in [1$\underline{1}$0] polarisation. For both polarisation directions they have there maximum at G.I., indicating that the molecular axis is parallel to the [001] azimuth and that the molecular plane is tilted with respect to the substrate surface. A molecular orbital tilt angle analysis, shown in fig. 1 a, yielded a tilt of 33° ± 5° of the molecular plane relative to the substrate surface in excellent agreement with the expected molecular orientation in the p-6P (20$\underline{3}$) organic crystal orientation determined from ex-situ XRD measurements [3].

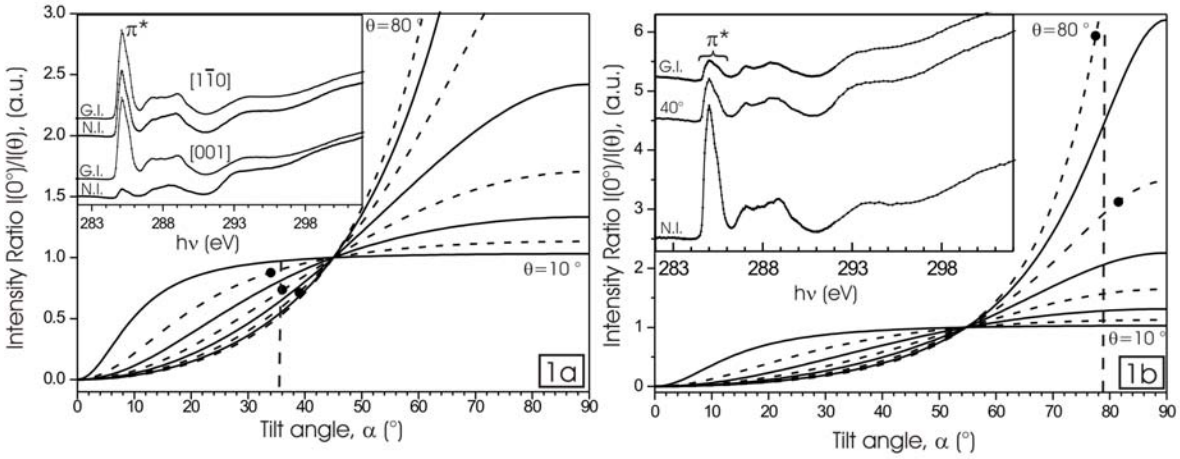

Fig. 1: C_K – edge NEXAFS spectra for a (a) 400 Å thick p-6P film grown on TiO_2 (110) and a (b) 80 Å thick p-6P film grown on AlO_x together with the molecular tilt angle analysis. The dashed line indicates the measured tilt angle of the molecular plane with respect to the substrate.

The angular dependence of resonant intensities observed in NEXAFS of an 80 Å thick p-6P film on Al-O_x is completely reversed, as shown in fig 1 b. Here the C_K to π* transition is strongest in N.I. and weaker in G.I.. The molecular plane is tilted 77°± 5° with respect to the substrate as determined in fig. 1 b, which corresponds to a (001) oriented p-6P film. The good crystalline quality of these molecular films together with the flat and homogeneous morphology observed in ex-situ AFM are the necessary prerequisites for a controlled investigation of the formation of organic heterostructures.

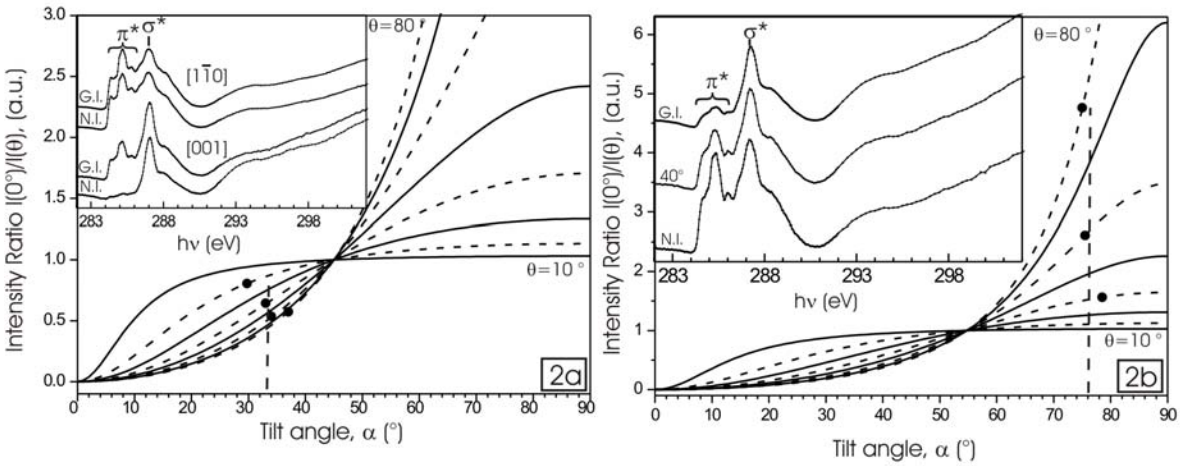

Fig. 2: C_K – edge NEXAFS spectra for a (a) 400 Å thick α-6T film grown on the 400 Å thick (20$\underline{3}$) oriented p-6P structure of fig. 1 a) and a (b) 165 Å thick α-6T film grown on the 80 Å thick (001) oriented p-6P film of fig. 1 b) together with the molecular tilt angle analysis. The dashed line indicates the measured tilt angle of the molecular plane with respect to the inorganic substrate.

In the inset of fig. 2 a the NEXAFS spectra of a 400 Å thick α-6T film grown on the (20$\underline{3}$) oriented p-6P layer at RT are shown. Comparable to the underlying p-6P spectra little or no

π* features can be observed at N.I. in [001] and the spectrum is dominated by the C_K to σ*(C-S) resonance at 287.2 eV, while for x-ray polarisation along [1$\underline{1}$0] in N.I. both π* and σ* transition are strong. On increasing the incidence angle to G.I. the π* transitions increase for both polarisations. This shows that the α-6T molecules are aligned parallel to the TiO_2 (001) direction and the underlying p-6P molecules and is supported by the S_L-edge NEXAFS (not shown). The tilt angle of the molecular plane was determined to 33 ± 5° with respect to the TiO_2 surface plane (fig 2 a) in good agreement with the ex-situ XRD, where an α-6T(020) orientation was observed. If however, the α-6T molecules are grown on a film of standing p-6P molecules their orientation is quite different. The NEXAFS spectra (fig 2 b) of an 165 Å thick α-6T film on the 80 Å p-6P (001) film show that the π* resonances are strongest in N.I. and weak in G.I. The quantitative analysis shows that the molecular plane is tilted 75 ± 5° with respect to the substrate plane thus reproducing the orientation of the organic substrate.

An interesting corollary is that the NEXAFS of p-6P appears very similar to that of the monomer benzene and no differences have been observed between a planar and twisted molecular conformation [4]. In contrast the C_K - NEXAFS of the planar molecule sexithiophene is distinctly different from the monomer thiophene or the dimer bithiophene, with both initial and final state effects being present [5]. However, the S_L-edge NEXAFS spectra of thiophene, bithiophene and sexithiophene are similar suggesting a higher localisation at the sulphur site.

This work has been supported by the Austrian Science Foundation and the EU via HPRI-CT-1999-00028

References:

1. J. Ivanco, B. Winter, F.P. Netzer, and M.G. Ramsey, Adv. Mater.**15**,1812(2003).
2. B. Winter, J. Ivanco, I. Salzmann, R. Resel, F.P. Netzer, M.G. Ramsey, Langmuir **20**, 7512(2004)
3. G. Koller, S. Berkebile, J. Krenn, G. Tzvetkov, G. Hlawacek, O. Lengyel, F.P. Netzer, M.G. Ramsey, C. Teichert, R. Resel, Adv. Mater.**16**, 2159(2004).
4. G. Koller, S. Berkbile, G. Tvetkov and M.G. Ramsey, BESSY Report 2003
5. G. Koller, R.I.R. Blyth, S. Sardar, F.P. Netzer, M.G. Ramsey, Surf. Sci. **536**, 155 (2003)

Coarsening kinetics of the InAs(001) surface

V. M. Kaganer, W. Braun, B. Jenichen, and K. H. Ploog
Paul-Drude-Institut für Festkörperelektronik
Hausvogteiplatz 5–7, D–10117 Berlin, Germany

The deposition process of the layer-by-layer growth in molecular beam epitaxy brings the surface into a non-equilibrium state with a large density of two-dimensional islands. After the deposition is terminated, the surface recovers to minimize the total length of the steps (island edges). The most prominent process of coarsening is Ostwald ripening, with the larger islands growing at the expense of smaller ones, which dissolve because of their larger specific line energy. The Ostwald ripening laws are remarkably universal and do not depend on the details of the system under consideration. The mean domain (or island) size $l(t)$ is the only scale of the problem so that the size distribution remains time independent when all the sizes are scaled by $l(t)$. The mean domain size follows a power law $l(t) \propto t^n$ with an exponent $n = 1/3$ for diffusion-limited kinetics and $n = 1/2$ for attachment-limited kinetics.

Recently, we have studied the coarsening kinetics of the GaAs(001)$\beta(2\times4)$ surface by depositing a fractional number of layers and monitoring the recovery by in-situ, grazing-incidence x-ray diffraction (XRD). We obtained the unexpected result that the coarsening exponent n is exceptionally large ($n \approx 1$). The aim of the present work was to study the coarsening of the InAs(001)$\beta(2\times4)$ surface in the same growth environment. The results presented below show that we arrive at a coarsening exponent $n \approx 1/2$, remarkably different from the GaAs(001) results and close to a value expected for attachment-limited Ostwald ripening.

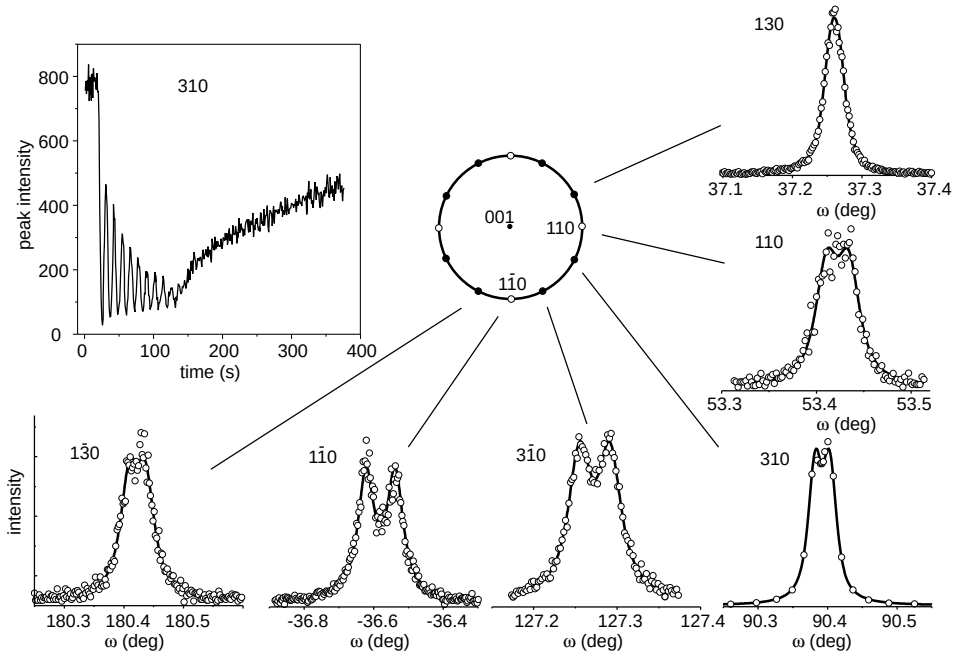

Fig. 1. XRD-peak profiles for different in-plane orientations on the InAs(001) surface. The split peaks are due to a 0.08° miscut of the surface. The inset shows x-ray intensity oscillations during layer-by-layer growth.

The experiment was performed at the molecular-beam-epitaxy facility integrated into a six-circle diffractometer at the PHARAO beamline at U125/2-KMC. Figure 1 presents the XRD-peak profiles of different in-plane reflections. The splitting of the peaks, most pronounced in the $[1\bar{1}0]$ direction, is due to an unintentional surface miscut. The presence of sharp peaks is an indication of a highly periodic step array. From the peak separation, we obtain the mean terrace width of 240 nm, corresponding to the miscut of 0.08°. Subsequent ex-situ XRD measurements confirmed the direction of the miscut and terrace width. The steps run along the $[1\bar{1}0]$ direction. The measurement along the terraces in the 130 reflection gives a Lorentzian peak profile (after the convolution with the Gaussian resolution function, it is described by a Voigt function, which is shown in the Fig. 1). Hence, the height-height correlation function in this direction is exponential, similar to the ones that we obtained for the GaAs(001) surface. This reflection is less influenced by the miscut and has been chosen for further studies of the coarsening kinetics.

The inset in Fig. 1 shows the oscillations of the peak intensity during the InAs deposition. They are characteristic for layer-by-layer growth. We conclude that the two-dimensional islands nucleate on the surface, then grow and merge during deposition of each single layer. When the deposition is interrupted at a non-integer number of layers, the surface contains islands that coarsen during the surface recovery process.

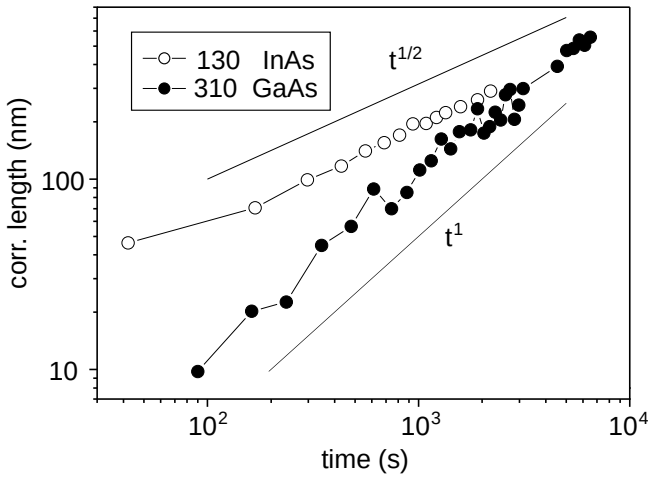

Fig. 2. Evolution of the mean island sizes determined from the fits of the peak profiles measured during recovery. The recovery behavior is distinctly different on InAs(001) and GaAs(001) surfaces.

Figure 2 presents the correlation lengths obtained from the (resolution corrected) widths of the XRD peaks measured during the recovery of the InAs(001) and GaAs(001) surfaces after homoepitaxial deposition of 0.5 monolayers. The coarsening exponent $n = 1/2$ of the InAs(001) surface points to the classical Ostwald ripening process with the attachment-detachment limited kinetics. This is in remarkable contrast to the GaAs(001) coarsening kinetics. We note that both GaAs and InAs measurements were performed in the same experimental setup and analyzed in the same way.

The comparison of the recovery kinetics of the closely related cubic III-V compounds GaAs and InAs demonstrates that detailed processes on the atomic scale determine the behavior of the system on the mesoscopic and even macroscopic scale. Therefore, only a detailed study of the surface kinetics on the atomic scale can provide an explanation of the observed phenomena. The strong variation in the surface kinetics of the different materials should provide sufficient information to compare and distinguish results from different atomistic models.

Compositional and electronic characterisation of Zn(O,OH) by PES for a better understanding of interfaces in chalcopyrite solar cells

M. Bär, J. Reichardt[a)], A. Grimm, I. Kötschau, I. Lauermann, K. Rahne, S. Sokoll, M.C. Lux-Steiner, and Ch.-H. Fischer, *Hahn-Meitner-Institut Berlin, Dept. SE 2, Berlin, Germany*
L. Weinhardt and E. Umbach, Exp. Physik II, Universität Würzburg, Germany
C. Heske*, Dept. of Chemistry, University of Nevada, Las Vegas, USA*
C. Jung and W. Gudat *BESSY Berlin, Germany*
T. P. Niesen and S. Visbeck *Shell Solar GmbH, Munich, Germany*

Nowadays, the necessity of alternative energy use is widely accepted. In photovoltaic solar energy technology, crystalline silicon cells are currently dominating in the market, though their cost reduction potential is seen to be limited. Thin film solar technology based on the chalcopyrites $Cu(In_{(1-X)}Ga_X)(S_YSe_{(1-Y)})_2$ ("CIGSSe") with $0 \leq X \leq 1$ and $0 \leq Y \leq 1$ is very promising due to expected lower production costs and shorter energy pay back times. Meanwhile, the efficiency of CIGSSe based laboratory cells (0.408 cm^2) has reached almost 20 % [1], while industrially produced CIGSSe module prototypes (60x90 cm^2) have demonstrated efficiencies above 13% [2]. A chalcopyrite-based solar cell is a multilayer system and the quality of the interfaces crucially determines the photovoltaic performance of the cell. Successful interface engineering requires compositional and electronic material characterisation as a prerequisite for understanding and intentionally generating interfaces. In the following, we present an example for such an approach. Photoelectron spectroscopy with synchrotron radiation is used for both, chemical analysis and determination of the valence band maximum. These data are successfully correlated with the process temperature of the layer deposition as well as with the resulting solar cell efficiencies.

In conventional chalcopyrite solar cells the buffer layer between absorber and window consists of CdS. Despite the small quantity, this is an ecological drawback. Consequently, there is a demand for a non-toxic, more transparent buffer material. One promising approach is the replacement of CdS by a ZnO buffer layer, deposited by the ion layer gas reaction (ILGAR) method. This method has already led to superior cell efficiencies compared to CdS-containing references [3]. Since the chemical, cyclic, and sequential ILGAR deposition of oxide layers occurs via the corresponding hydroxide [4], which is subsequently dehydrated in the heated reaction chamber, the process temperature directly determines the O/OH-ratio of the samples. Therefore, it is possible to prepare ILGAR layers ranging from almost pure $Zn(OH)_2$ (deposition at room temperature) to nearly hydroxide-free ZnO (process temperature > 200°C) [5]. Hence, these ILGAR buffers consist of a Zn(O,OH) compound when processed at slightly elevated process temperatures (55 °C – 125 °C), as in our case are used. For simplicity, we will still refer to this material as "ILGAR-ZnO".

---

a) present address: Institute of Theoretical Physics, Otto-Hahn-Allee, 28359 Bremen, Germany

Experiments have shown a pronounced drop in solar cell performance when ILGAR-ZnO buffers are prepared above 100°C [3]. One suggested explanation was a deteriorating impact of an increasing O/OH-ratio, influencing the band alignment at the ILGAR-ZnO/CIGSSe hetero-interface.

In order to study this subject, the O/OH-ratio of ILGAR-ZnO layers was investigated in the CISSY apparatus by means of photoelectron spectroscopy (PES) and correlated with the determined position of the valence band maximum (VBM). An approx. 20 nm thick ILGAR Zn(O,OH) layer, consisting mainly of hydroxide, was irradiated with synchrotron radiation of 654 eV (at the undulator beamline U41-PGM) and the O 1s PES signal was measured in intervals of a few minutes (using a VG CLAM 4 electron analyser). One clearly sees that the oxide peak (530.9 eV) grows at the cost of the hydroxide peak (533.0 eV, peak assignments according to [6]) due to dehydration by the energy input of the synchrotron beam, which also heats the sample. Directly after each O 1s measurement, the excitation energy was tuned to 170 eV and the Zn 3d and valence band signals were recorded (Fig. 1, right). One can observe that the continuous dehydration of the ILGAR-ZnO layer goes along with a shift of the Zn 3d signal from 11.2 eV to 10.4 eV (typical for ZnO [7]) and a shift of the VBM at the surface from 3.8 eV to 2.4 eV. By fitting and integrating the hydroxide and oxide contributions to the O 1s emission, respectively, the ZnO/(ZnO+Zn(OH)$_2$) ratio at the surface could be determined.

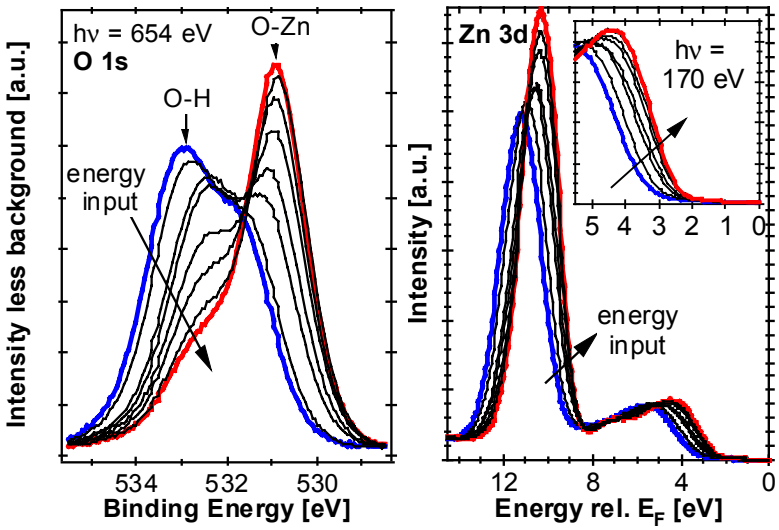

Fig.1 Changes in PES detail spectra of an ILGAR-Zn(O,OH) layer on a CIGSSe absorber due to the energy input of the synchrotron beam (at hν = 654 eV).
Left: O 1s emission at an excitation energy of hν = 654 eV.
Right: Zn 3d emission and the valence band edge (insert) at an excitation energy of hν = 170 eV.

The corresponding positions of the conduction band minimum (CBM) are estimated using the band gap energies E_g revealed by optical measurements of respective ILGAR-ZnO layers on glass. CBM and VBM data of the Zn(O,OH) are plotted against oxide content at the surface (Fig.2, bottom). Previous results from x-ray- (XPS) and UV-light-excited photoelectron (UPS) as well as inverse photoemission spectroscopy (IPES) [6] (full triangles) are in good agreement with CBM and VBM values determined in this way. The dotted lines represent the data for the Cd^{2+}/NH_3-treated CIGSSe substrate [6]. In Fig. 2 (top) the resulting power

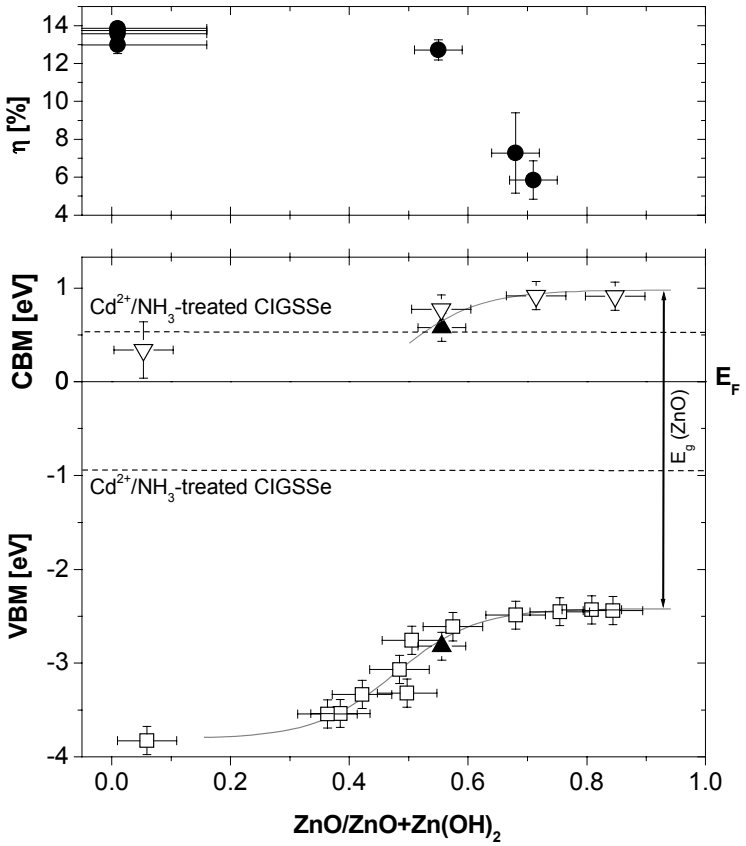

FIG. 2 ,bottom: The determined VBM values (squares) and estimated CBM (≈ VBM + E_g) values (open triangles) of ILGAR-ZnO layers with different ZnO/(ZnO+Zn(OH)$_2$) composition compared to previous values [6] for VBM and CBM (directly determined by UPS and IPES, full triangles). The CBM trend line is separated from the VBM trend line by E_g(ZnO) = 3.35 eV [8]. The dashed lines represent the VBM and the CBM, respectively, of a Cd^{2+}/NH_3-treated CIGSSe absorber [6].
top: Power conversion efficiency η of CIGSSe based solar cells with ILGAR-ZnO buffers deposited at different process temperatures [3], shown as function of the Zn(O,OH) composition of the buffer.

conversion efficiencies (η) of ILGAR-ZnO/ CIGSSe cells versus the respective buffer compositions are shown. The η-drop may now be directly linked to the ZnO/(ZnO+Zn(OH)$_2$) ratio of the buffer. A detailed discussion will be published elsewhere [9]. However, while a predominantly flat conduction band offset (CBO) can be achieved for ZnO/ (ZnO + Zn(OH)$_2$) ~ 0.56 with a decreasing hydroxide content (assuming that interface-induced band bending effects are negligible), an increasing spike-like CBO above 0.4 eV for oxide-rich ILGAR layers is predicted. The latter may partially (but not exclusively) explain the drop of the power conversion efficiency of resulting solar cells if the ILGAR-ZnO layer is prepared above a process temperature of 100°C, resulting in a hydroxide-poor buffer composition.

ACKNOWLEDGEMENT
Financial support by the German BMBF (# 01SF0007) and BMWA (# 0329889) is gratefully acknowledged.

REFERENCES

[1] K. Ramanathan, M.A. Contreras, C.L. Perkins, S. Asher, F.S. Hasoon, J. Keane, D. Young, M. Romero, W. Metzger, R. Noufi, J. Ward, and A. Duda, Prog. Photovolt.: Res. Appl. 11, 225 (2003).
[2] V. Probst, Technical Digest of the 14th International Photovoltaic Science and Engineering Conference, 2004, p. 663.
[3] M. Bär, Ch.-H. Fischer, H.-J. Muffler, B. Leupolt, T.P. Niesen, F. Karg, and M.C. Lux-Steiner, Proc. 29th IEEE Photovoltaic Specialists Conference, New Orleans, USA, 636 (2002).
[4] M. Bär, H.-J. Muffler, Ch.-H. Fischer, and M.C. Lux-Steiner, Sol. Energy Mater. Sol. Cells 67, 113 (2001).
[5] Ch.-H. Fischer, H.-J. Muffler; M. Bär, S. Fiechter; B. Leupolt, M. Ch.Lux-Steiner, J. Crystal Growth, 241, 151 (2002)
[6] L. Weinhardt, M. Bär, H.-J. Muffler, Ch.-H. Fischer, M.Ch. Lux-Steiner, T.P. Niesen, F. Karg, Th. Gleim, C. Heske, E. Umbach, Thin Solid Films 431-432, 272 (2003).
[7] S.W. Gaarenstroom, N. Winograd, J. Chem. Phys. 67, 3500 (1977).
[8] Landolt-Börnstein, *Halbleiter. II-VI Compounds*, III 22a, Springer Verlag, Berlin (1985).
[9] M. Bär et al., in preparation.

Corrosion of Cu on the surface of historic objects

M. Wilke [1], O. Hahn [2], G. Eggert [3]

[1]*Institut für Geowissenschaften, Universtät Potsdam, Postfach 601553 , 14415 Potsdam*
[2]*Bundesanstalt für Materialforschung und –prüfung (BAM), IV.2, 12200 Berlin*
[3]*Staatliche Akademie der bildenden Künste, 70191 Stuttgart*

Many copper-bearing materials kept in museums show considerable corrosion features, mainly in appearance of mould-like black spots on the surface. These spots contain mostly copper, sulphur and oxygen. Sometimes also Cu-chlorides are found [1]. This type of corrosion is found both on historic as well as modern metallic copper or bronze objects. Analysis by X-ray diffraction yields that these products are mostly amorphous, thus hampering the identification of the phases formed in most cases. In some cases stoichiometric phases like Covellin (CuS), Digenit ($Cu_{31}S_{16}$) or Chalkosin (Cu_2S) could be identified [2].

In order to identify or at least better characterize also the amorphous corrosion products, we performed XANES measurements at the Cu K-edge. Measurements were performed in transmission mode on powdered material that was scraped off from the objects. The XANES provides insight to the Cu oxidation-state. From the spectral fine structure found near the edge a finger print of the local structure around Cu in the material is derived. By comparison to model compounds of known oxidation state and crystal structure an idea on the compounds involved in the corrosion process can be developed.

In Fig. 1 corrosion products found on Cu-sulfide minerals (Algodonit, Covellin) and metallic objects such as coins, bracelets, and clasps are shown. The fine structure at the edge indicates that the corrosion products are probably quite similar. However, in detail some slight differences are observed, especially between the sulfide minerals and the other metallic objects.

Spectra of model compounds were collected on substances containing Cu in a variety of oxidation states and structural environments. Cu^{2+}: Cu-sulfate, Malachit, Cu-acetat, CuO, Kupferkies ($CuFeS_2$) Cu^{+}: CuCl, Cu_2O.

The spectra of the corrosion products indicate that none of the model compounds studied is directly transferable to these unknowns. Shown in comparison to the spectra of the corrosion products are calculated ternary mixtures of model compounds as indicated (Fig. 1). Both mixtures show quite some similarity to the spectra of the unknowns, which indicates that corrosion products are certainly a mixture of more than two compounds. Potential candidates are Cu-sulfate, Cu-(I)-oxide, Cu-(II)-oxide and Cu-sulfides. Due to the similarity of spectra of some of model compounds (e.g. Cu_2O and Kupferkies) it is difficult to rule out completely each component. In addition, the existence of hydroxyl-bearing compounds has to be taken into account. Further constraints could provide by performing a XANES analysis at the S K-edge.

Acknowledgements
We thank A. Erko (BESSY), B. Nekat (Uni Potsdam), and T. Wolff (BAM/ TUB) for their support during beamtime.

References

[1] G. Eggert und U. Sobottka-Braun, Black spots on bronzes and elemental sulphur, in: ICOM-CC (Ed.), 12th Triennial Meeting Lyon, Preprints Vol. 2 James & James (London) 1999, S.823-827.

[2] N. Hjelm-Hansen, *Cleaning and Stabilization of sulphide-corroded bronzes*, Studies in Conservation 29(1), 1984, S. 17-20.

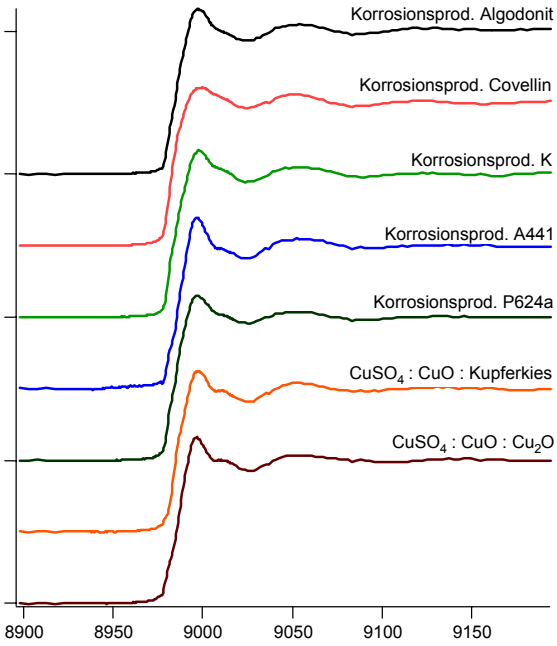

Fig.1: Normalized XANES of corrosion products as indicated (top five spectra). Calculated mixed spectra for the mixtures indicated (bottom two spectra). Mixtures are based on spectra shown in Fig. 2.

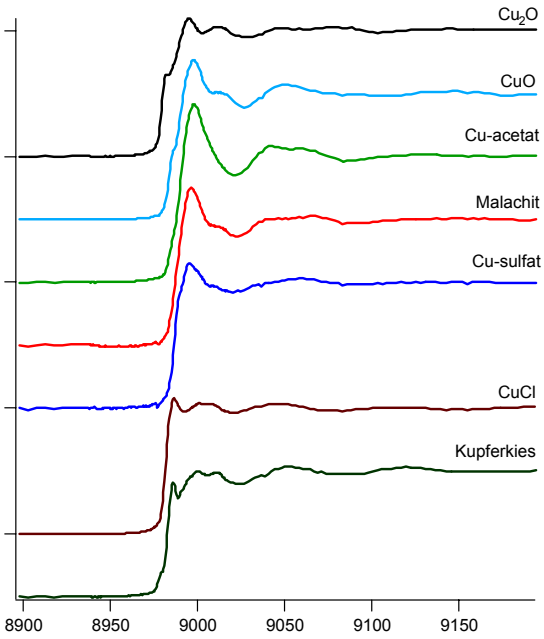

Fig. 2: Normalized XANES of Cu model compounds as indicated

Tomographic investigation of morphological changes in the microstructure of semi-solid Aluminium and Magnesium alloys

S. Zabler[1], A. Haibel[1], A. Rack[1], G. Weidemann[2], H. Riesemeier[2], J. Goebbels[2], J. Banhart[1]

[1]Hahn-Meitner-Institute Berlin, 14109 Berlin, Germany
[2]Federal Institute for Materials Research and Testing, 12200 Berlin, Germany

The thixotropic effect designs the property of certain non-newtonian fluids to show a decreasing viscosity when increasing shear forces apply. The viscosity is shear-rate dependant and goes back to normal once the shear forces disappear. We can model such a behaviour by considering small solid round particles in a liquid suspension. In analogy metallic alloys are heated up to semi-solid temperature where both solid and liquid phase coexist. At this state the thixotropic effect can be observed given the solid phase present in a globular-like form. Forging and Casting by means of this effect beholds great advantages to the light metal industry, i.e. lower working temperatures, homogeneous filling of thin-walled machine-housings and an overall better quality of the as-cast dies. The fields we explore using synchrotron tomography at BESSY are: new methods of preparation of globular formed microstructures, the complete understanding of the semi-solids rheological behaviour under varying shear stress and the optimization of Rheocasting of Magnesium alloys. In order to achieve these goals we deploy high resolution tomography and computerized image analysis.

Three different alloys were investigated in series of big numbers of samples, each sample representing a different set of parameters in the forming or casting process of the globular microstructure. Al-Ge32 and Al-Cu21 are both binary Aluminium alloys that are quite exotic in their applications but ideal for producing well-contrasted 3D images in absorption tomography. The third system, AZ91D is a Magnesium alloy prepared at the university of Erlangen and used in the production of thin-walled structures both in the automotive and in the consumer-electronics industry [1].
Figure 1 shows a slice from a 3D tomographic image taken from an AZ91D sample, representing 90wt.% Mg, 9wt.% Al and 1wt.% Zn. In order to separate numerically the primary solid Magnesium particles (appearing dark on the greyscale) that connect to each other when the alloy is quenched we had to construct a specific separation algorithm. It is based on the watershed–transformation and the Euclidean distance transformation (EDT) of the primarily binarized boolean image. Isolating the solid Magnesium particles is compulsery for any statistical analysis (e.g. three-dimensional distributions of particle size, particle orientation and sphericity).

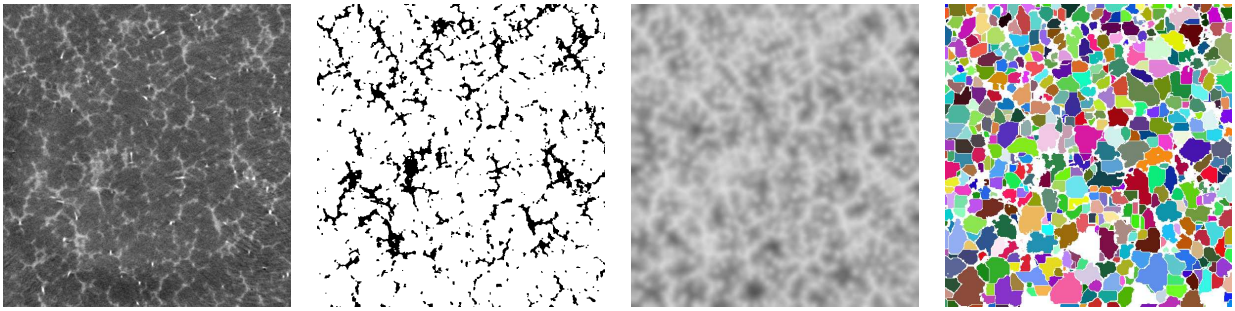

Figure 1: 2D slice from the tomography of AZ91D. From left to right: original tomographic slice, Boolean slice, Euclidean distance map (EDT), and the watershed–transformed EDT slice.

The 3D tomographic visualization of an Al-Ge32 alloy is shown in figure 2. The Al-Ge32 composition had been mixed with 4wt.% of Al-Ti5-B1 master alloy that acted as a grain refiner. The alloy is produced in an electromagnetic levitation furnace and the numerous Ti-B nanoparticles

are acting as nucleation sites when the alloy is quenched thus preventing the condesation of the primary solid phase as didrites. Without grain refining large oriented hooked dendrites would form by constitutional under-cooling making the alloy useless for any semi-solid casting process. Figure 2 diplays the population of primary Al-particles as well as the highly absorbing Ti-B particles after one hour of sintering at 460 °C. Apart from the analysis of the primary Al-particles and their spatial

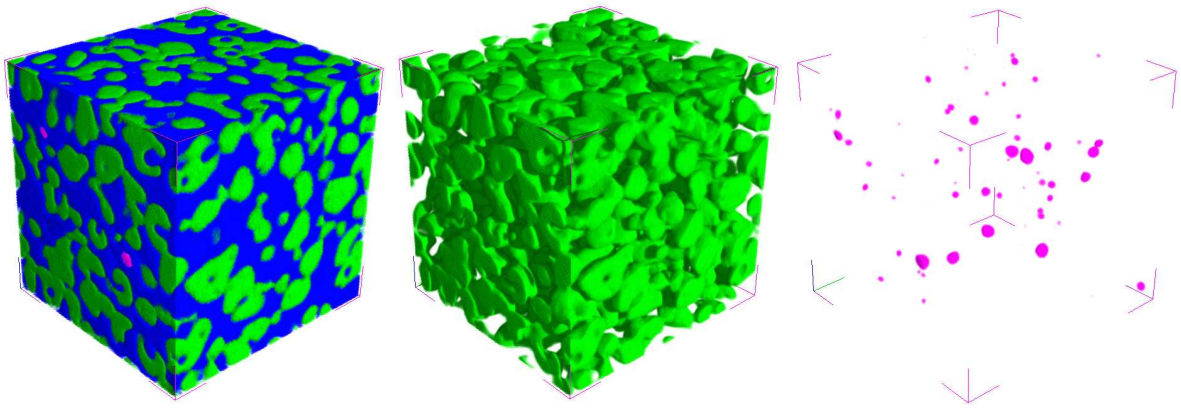

Figure 2: 3D tomographic representations of Al-Ge32 grain refined alloy after one hour sintering at 460 °C: Al-particles are pictured in green, the Al-Ge-matrix in blue and Ti-B particles in magenta.

correlation with the small grain-refiner particles we are interested in the coagulation of the round particles due to Ostwald ripening and the amount of entrapped liquid phase in the Al-clusters core.
In the case of Al-Cu21 alloy Aluminium and Copper powders are mixed and mechanically compressed before sintering small samples at 545 °C, i.e. at semi-solid state. Synchrotron Tomography allowed the three-dimensional ex-situ analysis of the sintering process and the influence the initial grain size has on the process. Just like grain refined Al-Ge after one hour of sintering, the Al-Cu samples yield a globular-like microstructure that is ideally suited for the Thixocasting process. Figure 3 shows three 3D images of an Al-Cu21 alloy (initial grain size $\leq 40\mu m$) representing 5 min, 20 min and one hour of sintering time. Due to entrapped oxygen large cavities can form. All the six volumes displayed in the figures 2 and 3 represent cubes of $0.64mm$ side length.

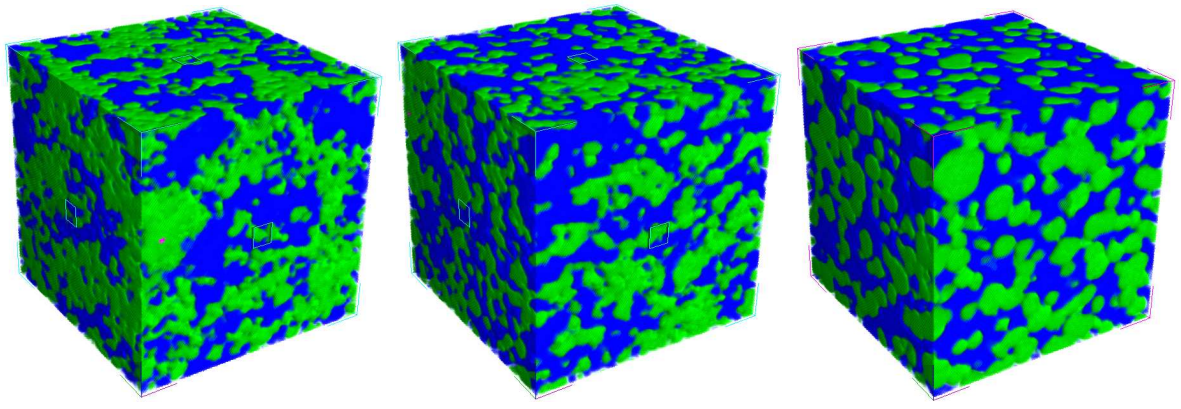

Figure 3: Series of compressed Al-Cu21 powder after (from left to right) 5 min, 20 min and one hour sintering at 545 °C. Al-particles are depicted in green, the former liquid Al-Cu-matrix in blue.

References

[1] D. Kirkwood, *Semisolid metal processing*, International Materials Reviews, Vol. 39, No. 5, pp. 173-189, 1994

Orientation of alkyl-substituted phthalocyanines on gold: distinguishing between the first layers and thin films

H. Peisert[1], I. Biswas[1], L. Zhang[1], M. Knupfer[2], M. Hanack[3], D. Dini[3], T. Chassé[1]

[1]*University of Tübingen, IPC, Auf der Morgenstelle 8, 72076 Tübingen, Germany*

[2]*Leibniz Institute for Solid State Research Dresden, P.O. Box 270116, D-01171 Dresden*

[3]*University of Tübingen, Inst. Organ. Chem., Auf der Morgenstelle 18, D-72076 Tübingen*

Recently it has been shown that improved crystal perfection enhances electronic and transport properties of organic thin films, the ordering and orientation of organic molecules is crucial for device efficiency. In addition, for highly ordered organic molecules, the anisotropy of the transport properties has to be taken into account and its influence on the device characteristics. But not only is the orientation of the film as a whole important, the interface is crucial to determining the device properties and thus the orientation of the first layer cannot be overestimated. The orientation of the molecules directly at the interface may not only affect the probability of a charge carrier injection (e.g. due to the overlap of wavefunctions of the metal and the organic molecule), but also electronic properties such as the interface dipole for organic polar molecules.

The family of Phthalocyanines (Pc's) is a model system for the entire class of low molecular weight organic molecules and one of the most promising candidates for a variety of applications. Evaporated films of Pc's show often a very high degree of ordering. On the other hand, the preparation of oriented organic films by self assembly, Langmuir-Blodgett techniques, or even by spin coating became more important. Since a preparation for Pc molecules from the solution requires at least a partial solubility, only substituted Pc's are applicable. In recent years, efforts have been made to synthesize Pc derivatives with alkoxy, alkyl and other lipophilic substituents (see, e.g. [1]).

We have studied the orientation of several substituted Pc's (Fig. 1), we focus on the orientation of the *first layers* of the organic material on a polycrystalline gold substrate. In this context, polarization dependent X-ray absorption spectroscopy represents an ideal tool to investigate the geometry of molecular adsorbates and thin films especially on disordered substrates. We have measured the relative intensity of core level excitations from the N1s level into either the π^* or σ^* molecular orbitals of the Pc as a function of the angle of incidence or of the polarization of the synchrotron radiation. The measurements were

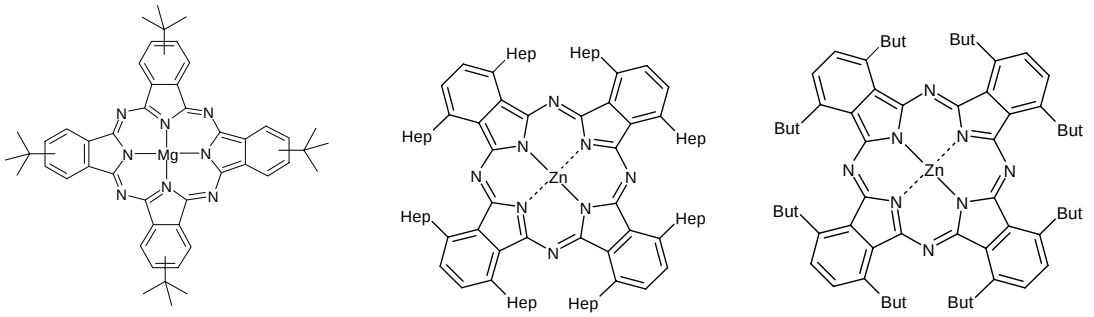

Fig.1 Chemical structures of 1,2- tetrasubstituted (*t*-But)$_4$PcMg **(left)** (*t*-But = *n*-C_4H_9) and of 1,4- octa-alkyl-substituted zinc phthalocyanines (But)$_8$PcZn **(middle)** (But = *n*-C_4H_9) and (Hep)$_8$PcZn **(right)** (Hep = *n*-C_7H_{15}).

performed using the UE 52-PGM beamline. The absorption was monitored indirectly by measuring the partial electron yield.

In Fig. 2 N1s excitation spectra of (*t*-But)$_4$PcMg on a polycrystalline gold foil as a function of the incidence angle θ of the linearly polarized synchrotron radiation are compared for a coverage of 1-2 nm and of 10 nm. In order to increase the degree of ordering, the sample was annealed during evaporation, the temperature was kept at about 150 °C. The geometry of the measurement is depicted in the inset of Fig. 2, normal incidence corresponds to θ = 90° and for grazing incidence θ = 10°. The two lowest lying features below about 402 eV (see dotted line in Fig. 2) have out-of-plane character, thus these features were used in the following to evaluate the intensity of the π* resonances. In Fig. 2a (film thickness 10 nm) we observe a very clear angular dependence of the π* resonances (E < 402 eV), their maximum intensity is found at normal incidence. This means that even on the ill defined polycrystalline gold substrate (*t*-But)$_4$PcMg forms well- ordered films in which the molecular plane is perpendicular to the substrate surface - in good agreement to the recently observed 'standing' orientation of unsubstituted Pc's at room temperature on rough substrates [2]. However, in contrast to the 10 nm film, the maximum of the N 1s → π* intensities is found in Fig. 2b at small angles (θ = 10°, 30°). This demonstrates that the organic molecules are well ordered, but that the adsorbate geometry is different for the first layer(s) (lying orientation) and for the 10 nm thick film (standing molecules).

From the results above the question arises, whether other substituted Pc's show a similar behavior. For the growth process, the strength of molecule-molecule interactions is a crucial parameter which can be altered by chemical substitutions. For these investigations, we have chosen 1,4-octasubstituted phthalocyanine compounds (Fig.1). They show a strong dependence of the intermolecular distance (and thus of the intermolecular interaction) on the length of the alkyl chain. Crystal structure data of analogous octa-hexyl zinc phthalocyanine

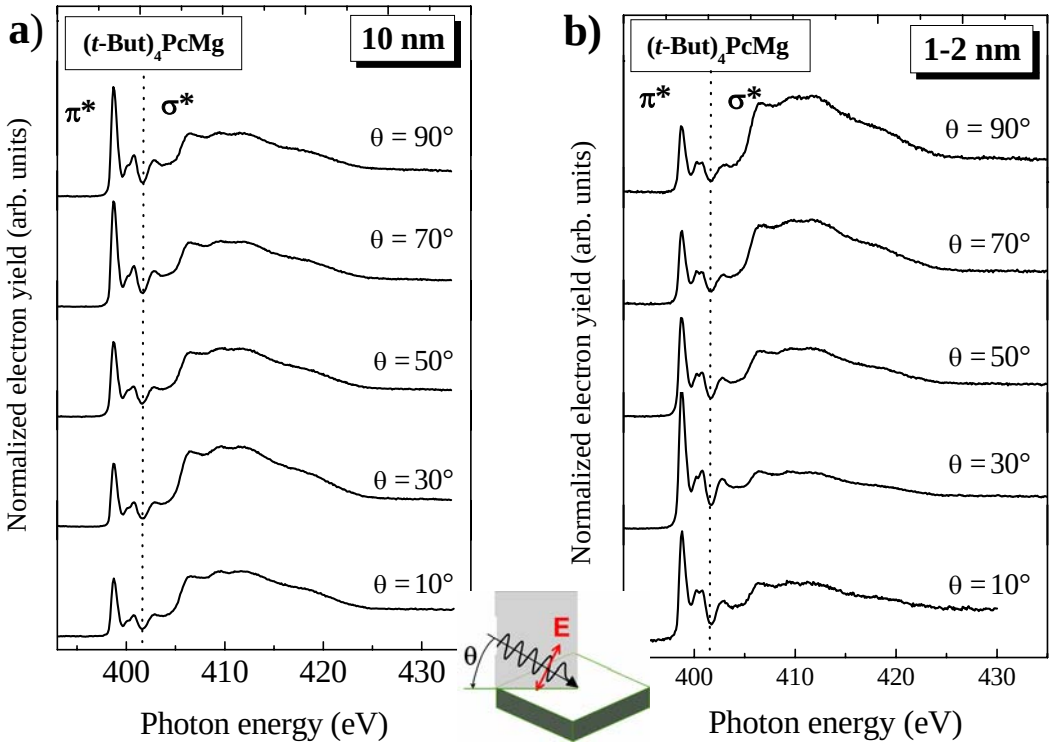

Fig. 2 N1s excitation spectra of (*t*-But)$_4$PcMg grown on polycrystalline Au: Different angular dependences are observed for a 10 nm thick film (a) and for a film thickness of 1-2 nm (b). The lower energy features (E < 402 eV) represent the π* resonances, whereas those features above 402 eV are related to the σ* resonances. The sketch illustrates the experimental geometry for p-polarized light.

and octa-iso-pentyloxy nickel phthalocyanine show, that two of the eight substituents act as a spacer between the aromatic cores [3]. A clear angular dependence of the π* and σ* resonances can be observed in angle dependent N 1s excitation spectra of $(But)_8PcZn$ (not shown). However, the molecular orientation for thickness of 1-2 nm and of 20 nm is radically different, the Pc molecules lie within the first layers and for higher coverages a standing orientation on the gold substrate is preferred. Importantly, the basic orientation of the thicker film does not depend on the substrate temperature (room temperature or 150 °C). In particular the 1-2 nm thick film prepared by annealing indicates a surprisingly high degree of ordering from the angle-dependence of the first pair of π*-resonances. Even an subsequent evaporation of $(But)_8PcZn$ on this annealed layer (with lying molecules) at a substrate temperature of 150 °C gives thicker films with standing molecules.

A quantitative analysis of the angle-dependence of the N1s-π* resonance intensity for both $(t\text{-But})_4PcMg$ and $(But)_8PcZn$ is shown in Fig. 3. Whereas the data points for thicker films (>10 nm) film follow the expected curve for standing molecules, a preferential

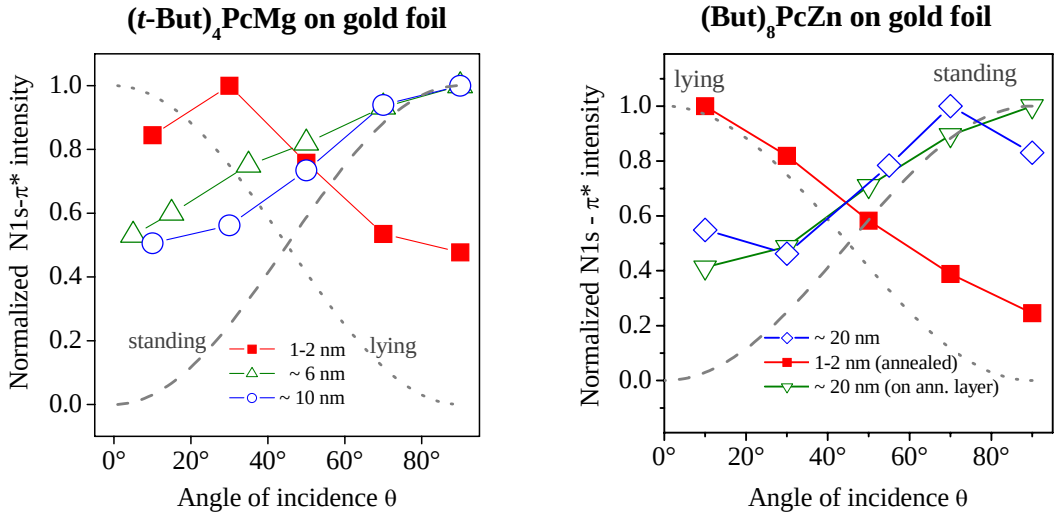

Fig. 3 Angle-dependence of the intensity of the N1s → π* resonances for $(t\text{-But})_4PcMg$ and $(But)_8PcZn$. The expected intensity profiles for standing and lying molecules are indicated by dotted and dashed lines, respectively. For both molecules an opposite molecular orientation was found within the first organic layers and for higher coverages.

orientation parallel to the surface is clearly visible for the 1-2 nm thick overlayers. The different growth modes observed on various substrates can be understood in terms of different molecule-substrate and molecule-molecule interactions. The metal-substrate interaction is in particular crucial for the first few layers of the molecules on the metal substrate, for higher coverages the molecule-substrate interaction becomes negligible. Especially on ill defined substrates, the initial growth mode is not "locked-in" and a different orientation is observed in thicker films. For details see refs. [4,5].

For valuable discussions and technical assistance we thank D. Batchelor, H. Kuhlenbeck, M. J. Cook, I. Chambrier, S. Pohl, Ch. Jung, W. Neu and R. Hübel. Financial support by BESSY is gratefully acknowledged.

[1] S. Vagin, M. Hanack, Eur. J. Org. Chem. (2004) 600.
[2] H. Peisert, T. Schwieger, M. Knupfer, M. S. Golden, J. Fink, J. Appl. Phys. **88** (2000) 1535.
[3] I. Chambrier, M. J. Cook, M. Helliwell, A. K. Powell, J. Chem. Soc.; Chem. Commun. (1992) 444.
[4] H. Peisert, I. Biswas, L. Zhang, M. Knupfer, M. Hanack, D. Dini, M.J. Cook, I. Chambrier, T. Schmid, D. Batchelor, T. Chassé, Chem. Phys. Lett. **403** (2005) 1.
[5] I. Biswas, H. Peisert, T. Schwieger, D. Dini, M. Hanack, M. Knupfer, T. Schmidt, T. Chassé, J. Chem. Phys. **122** (2005) (in press).

FT-IR synchrotron ellipsometry of ultra-thin nitrobenzene films

M. Gensch[1], R. Hunger[2], K. Roodenko[1], U. Schade[3], A. Röseler[4], E.H. Korte[1], N. Esser[1], J. Rappich[5] and K. Hinrichs[1]

[1]ISAS - Institute for Analytical Sciences, Department Berlin, Albert-Einstein-Straße 9, 12489 Berlin
[2]Institute of Material Science, TU Darmstadt, Petersenstr. 63, 64287 Darmstadt
[3]Berliner Elektronenspeicherring Gesellschaft für Synchrotronstrahlung mbH, Albert-Einstein-Straße 15, 12489 Berlin
[4]Gesellschaft zur Förderung angewandter Optik, Optoelektronik, Quantenelektronik und Spektroskopie e.V., Rudower Chaussee29 , 12489 Berlin
[5]Hahn-Meitner-Institut Berlin GmbH, Abteilung Silizium-Photovoltaik, Kekuléstr. 5, 12489 Berlin

Recently a novel electrochemical grafting process [1] has been proposed that allows deposition of ultra-thin films of benzene derivatives onto hydrogen terminated silicon substrates in the monolayer regime. Up to now this process was studied only by the changes in the surface electronic properties of the samples during preparation (namely by pulsed photovoltage and photoluminescence techniques or monitoring of the current [1]). The structural properties of the prepared films such as composition, molecular orientation or density, and their dependence on preparation parameters have not been investigated previously.

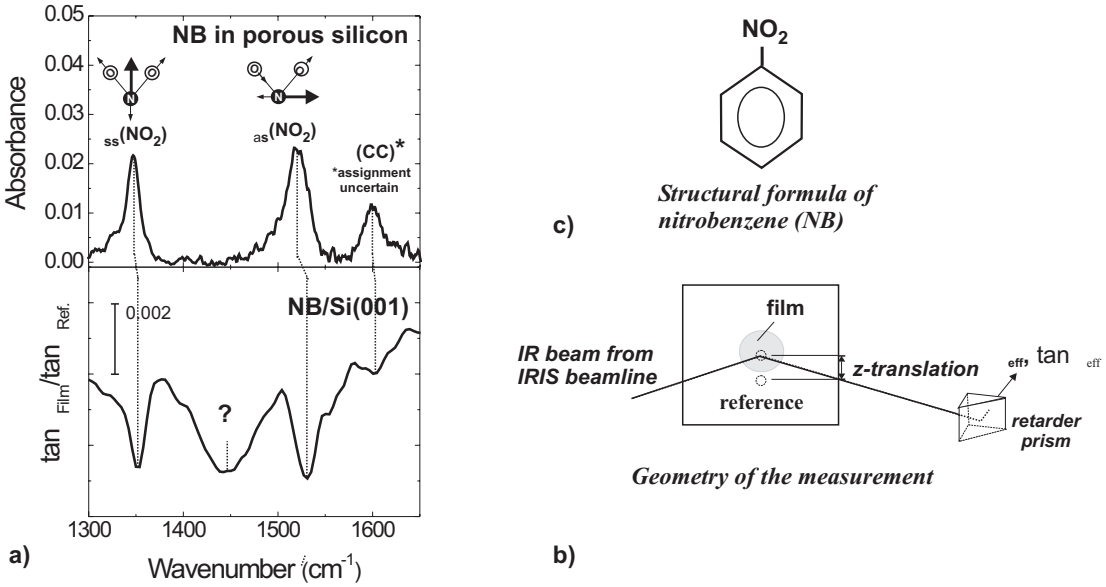

Figure 1: a) (*bottom*) Ellipsometric parameter tan as determined for an ultra-thin film of nitrobenzene (NB) grafted onto Si(001) referenced to a measurement of a virgin area of the wafer for clarity . (*top*) Absorbance of NB grafted into a ~300 nm layer of porous silicon. Additional bands are observed in the films on Si(001) that indicate presence of contaminations in the films. b) The geometry of the measurement at the IRIS beamline. c) Structural formula of NB.

In the following, first results for nitrobenzene (NB) films grafted on Si(001) derived from measurements with the FT-IR ellipsometer [2] at the infrared synchrotron beamline IRIS at BESSY II are presented. Evaluation of the contributions of vibrational modes to the infrared ellipsometric parameters can reveal insights into the chemical composition of the films, as is shown exemplarily in figure 1a. Bands at around 1600 cm^{-1}, 1520 cm^{-1} and 1350 cm^{-1} are observed in the investigated NB film and a preparation of NB in porous silicon [3]. The bands at 1520 cm^{-1} and 1350 cm^{-1} can safely be assigned to the symmetric and asymmetric stretching vibrations of the NO_2 group of the NB molecules. However the contributions at around 1450 cm^{-1} are only observed on the flat substrate, indicating that the preparation on the Si(001) surface and in porous silicon does not yield equivalent films. These additional contributions cannot be assigned to fundamental vibrational modes of NB molecules in gaseous or liquid phase [4], but interestingly have been found earlier in other electrochemically prepared solid phase NB films [5]. Evidence for impurities and/or modified molecules is also found in complementary carried out XPS measurements (see figure 2). A

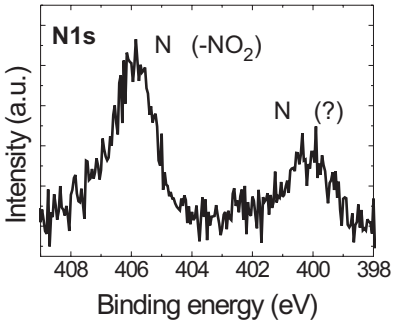

Figure 2: Emission from the N1s core level.

chemically shifted component is observed in the photoemission from the N1s core level, evidence for presence of nitrogen atoms in a chemical environment different to the NO_2 group.

The orientation of the molecules within these films is another important but previously unknown quantity. It has been shown recently that infrared ellipsometric parameters can be used to deduce a preferred molecular orientation in organic layers from specific line shapes [6]. With the improved sensitivity of the FT-IR synchrotron ellipsometer such an analysis is now possible also for films on the scale of a monolayer [3]. For the case of the investigated preparations of NB on Si(001) molecular orientations parallel to the surface normal or perpendicular to it can be ruled out. These orientations were reported previously for NB grafted on silicon [7] or deposited on Gold substrates [8], respectively, but would give rise to line shapes that are distinctly different to those observed in the experiment [9].

It was earlier proposed that electrochemically grafted layers of benzene derivatives may passivate silicon substrates against oxidation. Infrared ellipsometry is well suited to study oxidation of adsorbate-to-silicon interfaces [10], in particular also through an organic adlayer [11]. From analysis of the infrared ellipsometric parameters in the spectral region of the ν(Si-O-Si) stretching vibrations (see e.g. figure 3) it was observed, that none of the investigated NB films inhibited oxidation of the underlying silicon substrate completely. However, it was found that the initial stages of oxidation and the timescale depend critically on preparation parameters [11].

The recent improvements of the FT-IR synchrotron ellipsometer and of the performance of the IRIS beamline allow now to study organic films and interfacial layers in the monolayer regime with high spatial resolution [3]. The development of a purpose-built micro-aperture for the ellipsometer is scheduled for 2005 and funded by the European Union through the EFRE program (ProFIT No. 10125494).

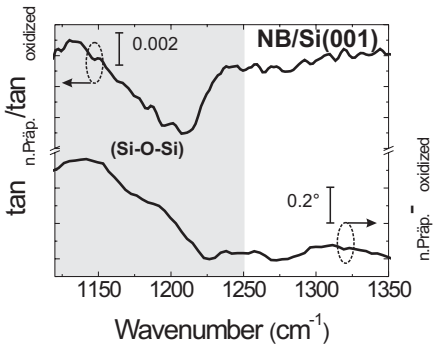

Figure 3: Relative changes of the infrared ellipsometric parameters upon oxidation in air. The region of contributions from silicon oxide is shadowed in grey.

Acknowledgment

The financial support by the Senatsverwaltung für Wissenschaft, Forschung und Kultur des Landes Berlin and of the Bundesministerium für Forschung und Wissenschaft as well as through BMBF grant 05 SR8KK19 is gratefully acknowledged. K. Roodenko is thankful for support from the Minerva foundation.

References

[1] P. Hartig, J. Rappich, Th. Dittrich, Appl. Phys. Lett. 80, 67 (2002).
[2] M. Gensch, K. Hinrichs, A. Röseler, E.H. Korte and U. Schade, Anal. Bioanal. Chem. 376, 626 (2003).
[3] M. Gensch, K. Roodenko, K. Hinrichs, R. Hunger, A.G. Güell, A. Merson, U. Schade, Y. Shapira, Th. Dittrich, J. Rappich, N. Esser, J. Vac. Sci. Technol., *submitted* (2005).
[4] J. Clarkson, W.E. Smith, J. Mol. Struct. 655, 413 (2003).
[5] P. Allongue, C.H. Villeneuve, J. Pinson, F. Ozanam, J.N. Chazaviel, X. Wallart, Electrochimica Acta 43, 2791 (1998).
[6] K. Hinrichs, A. Röseler, M. Gensch, E.H. Korte, Thin Solid Films 455-456, 266 (2004).
[7] C.H. Villeneuve, J. Pinson, M.C. Bernard, P. Allongue, J. Phys. Chem. B 101, 2415 (1997).
[8] D. Syomin, J. Wang, B.E. Koel, Surf. Sci. Lett. 495, L827 (2001).
[9] M. Gensch, R. Hunger, K. Hinrichs, E.H. Korte, A. Röseler, J. Rappich, N. Esser, *in preparation*.
[10] K. Hinrichs, M. Gensch, N. Esser, A. Röseler, J. Phys.: Cond. Matt. 16, S4335 (2004).
[11] K. Roodenko, M. Gensch, K. Hinrichs, N. Esser, J. Rappich, *in preparation.*

Spectral and Photophysical Characteristics of Donor-Acceptor-Polyenes

Hani El-Gezawy [a], **Wolfgang Rettig** [a], **René Lapouyade** [b]
[a] *Institut für Chemie, Humboldt-Universtät zu Berlin, Brook-Taylor-str. 2, D-12489 Berlin, Germany*
[b] *CNRS, 10 rue des Vergers, 33170 Gradignan, France*

Abstract:

4-dimethylamino-4´-cyano-1,4-diphenylbutadiene (DCB) and 4-dimethylamino-2,6-dimethyl-4´-cyano-1,4-diphenylbutadiene (DMDCB) have been characterized spectroscopically. Quantum chemical calculations were performed for comparison. Solvatochromic shifts of the fluorescence were in accordance with Onsager's continuum model, whereas shifts in the absorption spectra only correlated with the polarizability of the solvents. Excited state dipole moments were similar for both compounds.. The two methyl groups in DMDCB do not induce enhanced nonradiative decay. This suggests that neither a fluorescent nor a nonfluorescent TICT state is involved in DCB and DMDCB.

Introduction:

The photophysical properties of stilbenes and so-called push-pull stilbenes, i.e. stilbenes substituted with a donor and an acceptor group in conjugated positions, have attracted interest. The excited state behavior of trans-stilbene is one of the best-known examples of an adiabatic photoreaction: it reacts to a twisted conformation, which is often referred to as the "phantom-singlet". This conformation corresponds to a maximum on the ground state surface to which it is strongly coupled, and this pathway thus provides an effective deactivation funnel [1, 2]. One interesting phenomenon about these molecules is the twisted intramolecular charge transfer (TICT) [3], which is characterized by enhanced charge transfer in the excited state associated with rotation around one of the chemical bonds. The main focus of this project is to study the photophysics of donor-acceptor-polyenes and bring new evidence regarding a possible connection to the TICT phenomena. For this purpose DCB and DMDCB have been synthesized and characterized spectroscopically and photophysically here, including a variation of polarity and temperature.

The Investigated Compounds:

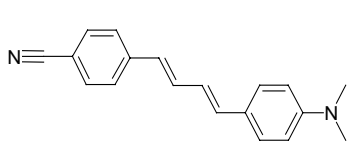

DCB

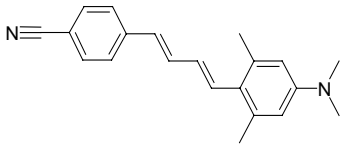

DMDCB

Temperature Dependence of the Fluorescence Spectra:

Fig.1 shows the temperature dependent emission spectra and the room temperature absorption spectrum of DCB and DMDCB, respectively in diethyl ether. The two compounds under investigation show a similar behaviour. At room temperature the fluorescence intensities are relatively low and the spectra show large Stokes shifts between absorption and fluorescence spectra. The fluorescence decay at 153 K (-120 ^{o}C) was measured using Synchrotron radiation at different emission wavelengths in the rather broad emission spectrum of DMDCB in diethyl ether resulting in a single exponential decay with the same time constant everywhere (1.15 ± 0.05 ns). The single exponential decay may be explained by the presence of only one single excited species and rules out

the population of an emitting TICT state.

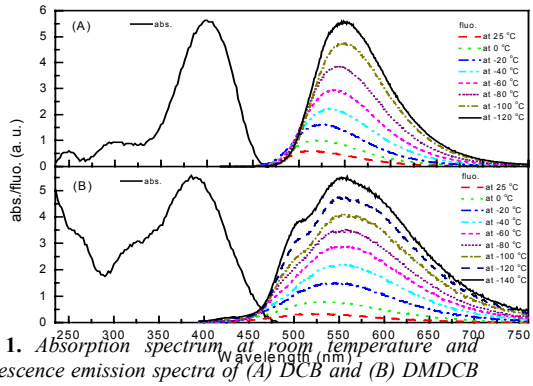

Fig. 1. *Absorption spectrum at room temperature and fluorescence emission spectra of (A) DCB and (B) DMDCB at different temperatures in diethyl ether.*

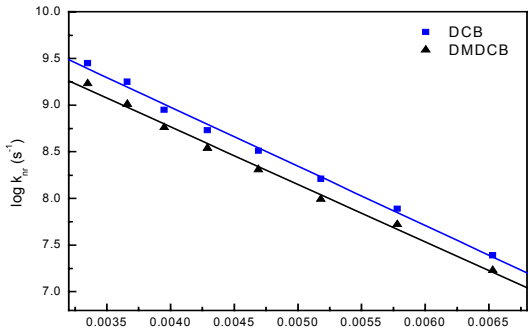

Fig. 2. *Arrhenius plots of the nonradiative decay rate constants derived from the fluorescence quantum yields and radiative rate constants k_f for DCB and DMDCB in diethyl ether.*

The Arrhenius plots, Fig. 2, are linear for both compounds within the investigated temperature range. The E_A values are quite similar for DCB (18.2 kJ/mol) and DMDCB (17.7 kJ/mol).

Table 1. Photophysical parameters of DCB and DMDCB in diethyl ether at low temperatures.

Compound	T (K)	λ_f (nm)	Φ_f	τ_f (ns)	k_f (s^{-1})	k_{nr} (s^{-1})
DCB	298	509	0.085	0.324	2.62×10^8	2.82×10^9
	273	520	0.127			1.81×10^9
	253	525	0.262			7.38×10^8
	233	533	0.393			4.05×10^8
	213	538	0.506			2.56×10^8
	193	541	0.673			1.27×10^8
	173	548	0.792			6.88×10^7
	153	550	0.923			2.19×10^7
	77			1.651		
DMDCB	298	527	0.082	0.493	1.66×10^8	1.86×10^9
	273	529	0.098			1.36×10^9
	253	547	0.213			5.46×10^8
	233	551	0.327			3.12×10^8
	213	555	0.462			1.78×10^8
	193	557	0.583			9.79×10^7
	173	552	0.714			5.86×10^7
	153	553	0.893			1.68×10^7
	77			1.793		

Conclusion:

The two methyl groups in DMDCB do not induce enhanced nonradiative decay or forbidden emissive character as would be expected from an active participation of the TICT state. This suggests that a luminescent or nonluminescent TICT state is not the lowest excited state in DCB and DMDCB.

References:

[1] D.H. Waldeck, Chem. Rev. 91(1991) 415; J. Saltiel and Y.-P. Sun, in: Photochromism - molecules and systems, eds. H. Dürr and H. Bouas-Laurent, Elsevier, Amsterdam, 1990, p. 64.

[2] J. Michl and V. Bonačić-Koutecký, Electronic aspects of organic photochemistry, Wiley, New York, 1990, and references therein.

[3] Z.R. Grabowski, K. Rotkiewicz, W. Rettig, Chem. Rev. 103 (2003) 3899.

Magnetization depth profile of Co in a Cu/Co/Pt sandwich

[(1)]U. Grüner, [(1)]M. Harlander, [(1)]E. Goering, [(2)]D. Schmitz, and [(2)]H. Maletta and [(1)]G. Schütz

[(1)]Max-Planck-Institut für Metallforschung, Heisenbergstr. 3, Stuttgart, Germany

[(2)]Hahn-Meitner-Institut, Glienicker Strasse 100 , Berlin, Germany

X-rays resonant magnetic scattering (XRMS) has used as a technique to extract element selective structural magnetic information of a buried system, which basically consists two layers of Co. In the soft X-ray region large scattering angles are present and the "hard X-ray" small angle dipole approximation breaks down. Therefore, we have developed an improved algorithm for magnetic reflectivity simulations, which takes into account the full angular and polarization dependencies of the magnetic scattering amplitudes for π and σ scattering channels for polarized light.

Layered systems, consisting of few magnetic and non magnetic components, are of substantial interest from a fundamental physical point of view as well as because of their technical applications. Prominent examples are magnetic sensors, magneto- and spin-electronic devices, magnetic random access memories (MRAMs) and giant magneto resistive (GMR) read heads in hard disc applications [1]. One important observation is that magneto transport and other magnetic properties of multilayer systems exhibit a strong dependency on the growth and preparation conditions and the interface morphology [2]. The reliable and element specific determination of magnetic and chemical interface properties and their influence on magneto transport properties is crucial for further improvements and optimization of those devices. All mentioned so called "spintronic" devices have buried interfaces, which are hidden for surface sensitive methods.

X-ray magnetic circular dichroism (XMCD) absorption spectroscopy is now a well established method to determine average magnetic moments in a element- and symmetry-selective way. The dependency of the soft X-ray optical properties at the $L_{2,3}$-edges on the magnetization results in corresponding changes in the soft X-ray reflectivity. In the past, resonant magnetic scattering with polarized X-rays (XRMS) has been used as a powerful technique to extract element selective structural and magnetic information. In addition, multilayer systems have been used to simplify the theoretical procedure of the magnetic profile determination, but interface variations as a function of substrate distance can not be addressed [3,4].

Recent magnetic resonant reflectivity measurements in the hard and soft X-ray range have given detailed element-specific and quantitative insight into the induced Pt and Co magnetization profile of a single Pt/Co interface [3]. In the soft X-ray region large scattering angles are present and the hard X-ray small angle approximation in dipole approximation breaks down [4,5]. We demonstrate here the quantitative determination of a Co bilayer systems magnetization profile, by a single reflectivity measurement, and taking into account all the different angular dependencies of the magnetic scattering amplitudes for σ and π scattering channels.

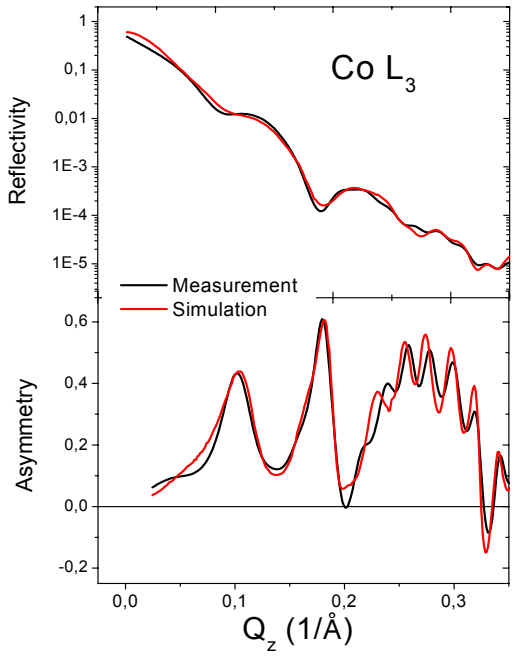

Figure 1: Upper part shows resonant magnetic reflection measured at the Co L3 resonance, while the lower part shows the corresponding magnetic asymmetry ratio. The red curves are the corresponding full angle simulations.

The sample has been prepared at Robert BOSCH science and development (Schillerhöhe, Stuttgart) by DC-sputter deposition at room temperature on a Si wafer. Thicknesses and corresponding interface roughness of the stack were determined separately by non-resonant Cu K_a reflectometry,

utilizing a dynamical optical approach, which leads to a recursive equation formalism first carried out by Parratt [6] and extended for roughness corrections by Névot and Croce [7]. The extracted stack parameters are shown in Fig.2.

Resonant soft X-ray reflectivity measurements have been performed at the Co L_3 edge at the maximum magnetic absorptive scattering factor, corresponding to the maximum in the XMCD effect. The q-2q measurements were performed at the HMI beamline UE46-PGM located at BESSY II using elliptically polarized radiation. The inplane sample magnetization was flipped at each scattering angle by an *in situ* water cooled electromagnet along the projection of the incoming light. All experiments have been performed under UHV conditions. The upper part of Figure 1 shows the nonmagnetic resonant reflectivity, while in the lower part the measured asymmetry ratio is plotted. The red curves show the corresponding magnetic simulations. These simulations are based on the dipole approximation of the resonant X-ray atomic form factor of a magnetic atom, which is described by the well known formula of Hannon *et al.* [8]

$$f_{res}^{E1} = -r_0 \left\{ \left(\varepsilon'^{*} \cdot \varepsilon \right) \left[f_0 + f' + if'' \right] + i \left(\varepsilon'^{*} \times \varepsilon \right) \cdot z \cdot \left[m' + im'' \right] \right\}$$

We have derived the charge β and magnetic $\Delta\beta$ imaginary parts of the optical constants for resonantly exited Co from an adaptation to a Co $L_{2,3}$ XMCD transmission experiment (see. ref.[9]) to anomalous scattering amplitudes (f'', m'') of Henke's tables. The dispersive parts are deduced by Kramers-Kronig relations. In contrast to the previously published results, we have now included the full angular dependency for σ and π scattering. For the calculation of the asymmetry ratio the intensities of the σ and π components have been added in a kinematic approximation. It should be mentioned here that the kinematic approach breaks down at very small scattering angles, due to the enhanced influence of multi-scattering processes. Nevertheless, for systems with a nonmagnetic protective top layer the asymmetries are usually small at small angles. This is related to the fact, that at very small angles the first interface between the topmost layer and the vacuum dominates the reflection, due the presence of a large effective absorption length and a small penetration depth, which usually prevents large reflected intensities from below. This explains the extraordinary good agreement, even for very small angles of incidence, between the simulated and measured asymmetry ratios in the lower part of figure Fig.1.

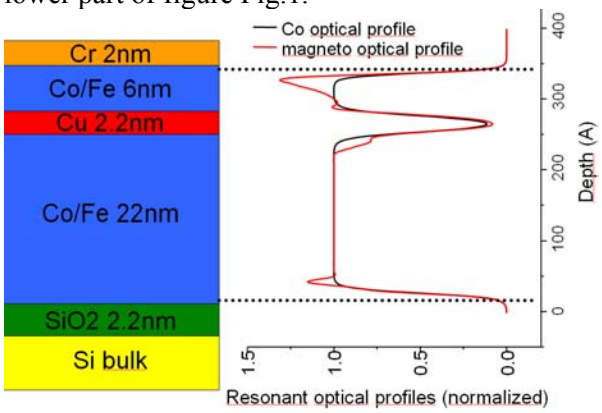

Figure 2: Left site shows the layer stack, and the right site the fitted optical (black line) and magneto optical profiles (red line) for Co.

For the simulation of the Co asymmetry ratio in Fig. 1 the magnetic profile has been modified to give the best match to the experimental asymmetry results. The resulting chemical and magnetic resonant optical profiles are shown in the right part of Fig.2. The magnetic contribution plays a large and important role to the optical properties. The differences between the red and the black curve are related to deviations of Co magnetization from the bulk value, with significant reduction at the Cu site and enhancements at the other interfaces.

Despite the fact that the new magnetic Parratt implementation is roughly 300 times faster and without the mentioned simplifications for the angular dependency, the magnetic simulations are very time consuming and complicated. Therefore, we would like to mention, that these fitting results could be further improved and especially the magnetic profile is still preliminary.

We would like to thank P. Imperia for additional support during the beamtime, and the Max-Planck-Society and the Hahn-Meitner-Institute for financial support of this project.

References

1. G. Binasch *et al.*, Phys.Rev.B **39**, 4828 (1989).
2. L. Krusin-Elbbaum *et al.*, Nature **410**, 444 (2001).
3. J. Geissler *et al.*, Phys.Rev.B **65**, 020405(R)-1 (2001).
4. J. Geissler *et al.*, Z.Metallkd. **93**, 946 (2002).
5. L. Seve *et al.*, Phys.Rev.B **60**, 9662 (1999).
6. L. G. Parratt, Phys.Rev. **95**, 359 (1954).
7. L. Névot and P. Croce, Revue.Phys.Appl. **15**, 761 (1980).
8. J. P. Hannon *et al.*, Phys.Rev.Lett. **61**, 1245 (1988).
9. E. Goering *et al.*, Phys.Rev.Lett. submitted (2005).

Mechanisms of Cement Hydration studied by X-ray microscopy

J. Thieme[1], R. Trettin[2], C. Schmidt[1], K.Böttger[2], P. Guttmann[1], F. Winnefeld[3], J. Rieger[4], S. Becker[4]
[1]Institut für Röntgenphysik, Georg-August-Universität Göttingen, Geiststraße 11, 37073 Göttingen
[2]Institut für Bau- und Werkstoffchemie, Universität Siegen, Paul-Bonatz-Straße 9-11, 57078 Siegen
[3]EMPA, Abt. 135, Gruppe Bauchemie, Überlandstrasse 129, CH-8600 Dübendorf
[4]BASF AG, Polymer Physics, 67056 Ludwigshafen

Motivation

The mechanism of the hydation of cement is a rather complex process, passing through five stages. Although cement is the most abundant building material, this mechanism is still not fully understood. To learn more about it, the nanometer scale is important to visualize early reaction products.

What is cement?

Cement can be defined as a complex mixture of calcium silicates and aluminates that is made by heating a mixture of clay and limestone to about 1500° C in a kiln. The mixture is then cooled, pulverized, and finally gypsum ($CaSO_4 2H_2O$) and anhydrite $CaSO_4$ is added 1:1. When the powder is mixed with water, complex reactions take place and the cement sets to a solid mass. Chemical compositions vary from cement to cement according to the kiln conditions and the detailed composition of the local ingredients with which the kiln is fed. The physical state of the powder, such as the size distribution of all the particles, also affects reactivity. The main reaction in setting is hydration by water, and this is largely surface controlled. Even a small variation in the chemical composition or physical state of cement can cause substantial variations in performance, usually in ways that cannot be foreseen at all.

Principal compounds in Portland cement, the most abundant type of cement:

Name	Shorthand formula	% in cement
Tricalcium silicate	C3S	45-65
Dicalcium silicate	C2S	10-25
Tricalcium aluminate	C3A	7-12
Tetracalcium aluminoferrite	C4AF	5-11

Gypsum: Calcium sulphate

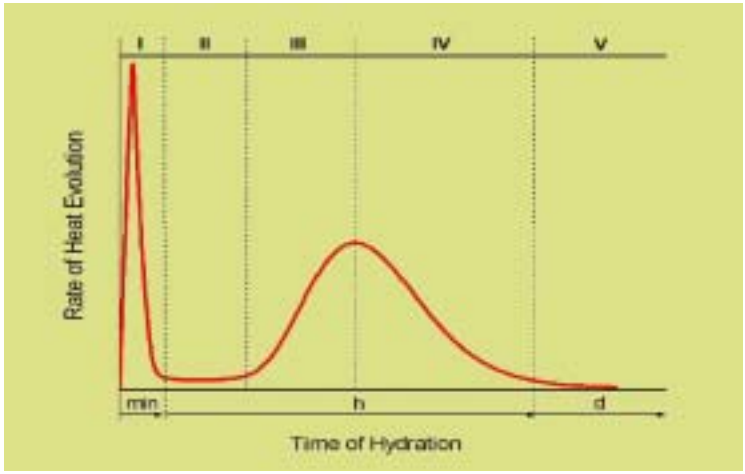

Fig. 1: Stages of Hydration:
I Pre-induktion period
II Induktion period
III Acceleration period
IV Post-acceleration period
V Final period

X-Ray Microscopy
All three pictures have been taken at E = 523 eV, using the transmission X-ray microcsope TXM at BESSY II. The picture size is 12 x 12 μm^2, resolution is ≈ 25 nm.

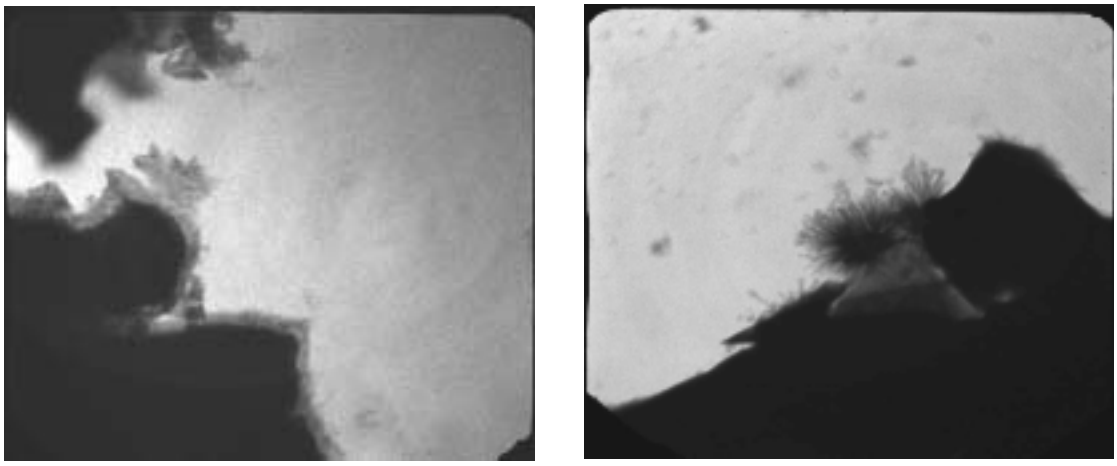

Fig. 2: Hydration of Ca_3SiO_5 = C3S, which is the main constituent of Portland Cement. Left image taken at the end of stage I, right at the end of stage II (see fig.1).

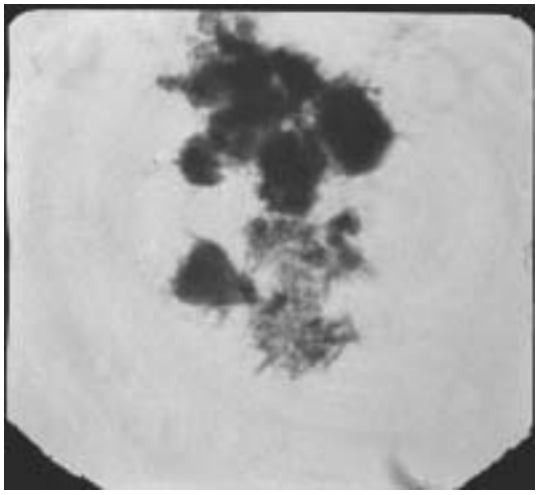

Fig. 3: Hydration of C3S in presence of $Ca(OH)_2$

Results and Conclusions
X-ray microscopy shows at the beginning of the hydration reaction the formation of a gel-like cover layer responsible for a retardation of the hydration. The very reason for the induction period itself is this impermeable protective layer (left image). At the end of this period (1-2 hours) structured CSH (= calcium silicate hydrates) phases become visible (center image). The acceleration period is then controlled by CSH-nucleation on the gel-like cover layer. The addition of $Ca(OH)_2$ crystallites to accelerate nucleation and shorten the induction period is not effective due to the formation of CSH phases on the crystallites.

Acknowledgements
This work has been supported by the Federal Minister of Education and Research (BMBF) under contract number 05ES3XBA/5. We would like to thank the staff of BESSY for providing excellent working conditions.

X-ray absorption spectroscopy study at the Si K-edge of tungsten carbide-silicon carbide thin films

S. Palacín [a], A. Gutiérrez [a], J. E. Krzanowski [b], F. Schäfers [c], M. Mertin [c], J. L. Endrino [d], L. Soriano [a]

[a] Dep. Física Aplicada, Universidad Autónoma de Madrid, 28049 Madrid, Spain
[b] Mechanical Engineering Department, University of New Hampshire, Durham, NH03824, USA
[c] BESSY GmbH, Albert-Einstein-Straβe 15, 12489 Berlin, Germany
[d] Balzers AG, Iramali 18, FL-9496 Balzers, Liechtenstein

The influence of microstructure on the mechanical properties of nanocomposite ceramic films is currently a subject of active research and investigation[1-3]. Microstructural features in thin films that can influence mechanical properties include grain size and morphology, defect content, film porosity and phase content. The presence of multiple phases within the film can enhance film strength and toughness, as well as provide multifunctional capabilities. Therefore, a detailed understanding of microstructural evolution in thin films is essential to understanding and controlling their mechanical and physical properties.

In our present work, we are investigating the effects of Si additions on microstructure and phase formation in WC thin films[4-6]. The films are deposited by co-deposition from WC and SiC targets in a magnetron sputter deposition system, a method that easily allows us to maintain the WC-SiC stoichiometry. By using the co-deposition method, we also can explore the complete compositional range between WC and SiC, or more closely examine a specific compositional range of interest. Previous X-ray diffraction and TEM studies revealed that an increase of SiC content in WC produced a grain refining and amorphizing effect. In the range of 11 to 26% SiC, a hierarchical dense structure composed of sharp boundaries and refined grains was observed. At this point, a chemical analysis of the observed phases to determine their composition seems crucial to carry out our investigations.

The driving force for microstructure development in these films is the bonding differences between SiC and WC. SiC is covalently bonded and exhibits tetrahedral bonding arrangements between Si and C atoms. For the metallic carbide, the most common structure in the deposited films (the B1 structure) results in C atoms occupying octahedral sites with six nearest neighbors. This difference in bonding drives phase segregation, and in equilibrium complete phase separation between the metallic carbide and SiC is expected. However, the deposition conditions typical of our experiments represent significant kinetic constraints that result in highly disordered phases and incomplete phase separation.

The small size of the phases, in the nanometer scale, makes it difficult to obtain their chemical composition by conventional spectroscopic techniques. On the other hand, X-ray absorption spectroscopy is very sensitive to the local chemical environment around a specific atomic element. Consequently, we have performed X-ray absorption spectroscopy experiments at the Si-K edge of WC-Si thin films grown under different conditions. Samples were grown by magnetron sputtering codeposition using a power of 200 W on the WC target and 150 W on the SiC target. at a magnetron power. Substrate temperature was varied between RT and 600'C. An additional sample was grown with a different power ratio (150 W on the WC target an 200 W on the SiC target) with the substrate at 350ºC for comparison. A Si wafer, a SiC wafer, and a SiC sample grown by sputtering, were also measured as references. XAS measurements were carried out at the BESSY KMC1 line, using a standard chamber equiped with fluorescence and total electron yield detection.

Figure 1 shows X-ray absorption spectra, recorded in Fluorescence Yield (FY) mode of samples grown by magnetron sputtering at 200 W power on the WC target and 150 W on the SiC target, and with different substrate temperature. The top spectra correspond to crystalline Si, crystalline SiC, and sputtered SiC, and are included as reference samples. The sputtered

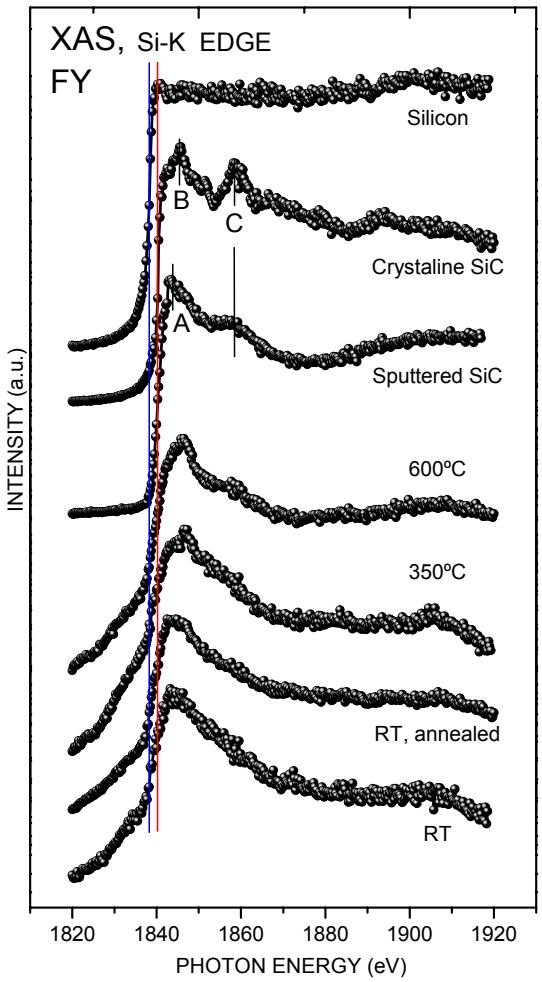

Figure 1: Si-K edge X-ray absorption spectra of WC-Si samples grown with different substrate temperature. Crystalline Si and SiC, and amorphous SiC are also shown for comparison

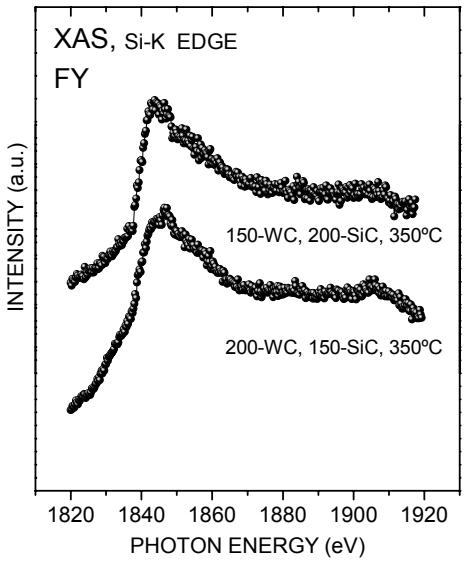

Figure 2: Si-K edge X-ray absorption spectra of two WC-Si samples grown with a substrate temperature of 350ºC but with different composition

SiC sample was obtained by magnetron sputtering with 200 W on the SiC gun. XAS spectrum of Si is almost featureless, with an absorption threshold at 1838.3 eV (marked with a solid line), and a small peak just above the threshold, at 1840.8 eV. The height of this peak is very sensitive to the incidence angle of the synchrotron linear polarized light on the sample.[7] The lineshape of this spectrum agrees well with previous results from other works.[8]

The absorption threshold of both SiC samples is shifted 2 eV with respect to pure Si, being located at 1840.3 eV. Nevertheless, there are clear differences in the lineshape of both spectra. The first peak after threshold is located at lower energy for the sputtered sample (feature A, at 1844 eV), as compared with the SiC wafer (feature B, at 1845.7 eV). On the other hand, feature C is present in both spectra and at the same energy position, 1858 eV, although with a higher intensity in the case of the crystalline sample. An additional feature, at an energy of 1894 eV, is only present in the spectrum of crystalline SiC. These observations allow us to assign feature C to SiC, independently whether it is crystalline or not. Feature A could be assign to non-crystalline SiC, whereas features B and that at 1894 eV are typical of crystalline SiC.

For the WC-Si samples it is not easy to determine the absorption threshold, because, due to the poor signal to background intensity, the pre-edge region is not well defined, as it is not the threshold itself. However, for all samples the threshold seems to be at an intermediate value between those of Si and SiC, which could be a proof that both species are present. Feature C is absent in sample grown at RT, but it starts to be visible for the annealed sample and that

grown at 350ºC. In the latter case, feature B, typical of crystalline SiC, starts to develop, suggesting that, at this temperature, SiC grows in crystalline form. Finally, the sample grown at 600ºC shows a clear feature C and, again, a peak at the position of feature B, which suggests that, in this case, the amount of SiC is the highest, and it is in crystalline form.

Figure 2 shows XAS spectra of two samples grown at 350ºC with different power ratios. The intensity of feature A, assigned to non-crystalline SiC, seems more intense for the sample grown at higher SiC power, suggesting the higher the Si content, the lower the degree of crystallization.

Acknowledgements:

This work was supported by the EU Research Infrastructure Action under the FP6 *Structuring the European Research Area* Programme, through the contract R II 3-CT-2004-506008; and by the Spanish CICYT through the contract BFM2003-03277. A.G. thanks the Spanish *Ministerio de Educación y Ciencia* for financial support through the *"Ramón y Cajal"* Program. J. E. K, and J. L. E. would like to acknowledge the financial support of the Air Force Office of Scientific Research under grant# F49620-98-1-0499.

References:

1. W.J. Meng, X.D.Zhang, B. Shi, R.C. Tittsworth, L.E. Rehn, and P.M. Baldo, J. Mater. Res. **17** (2002) 2628.
2. S. Veprek, S. Reiprich, and Li Shizhi, Appl. Phys. Lett., **66** (1995) 2640.
3. S. Veprek, A. Niederhofer, K. Moto, T. Bolom, H.D. Mannling, P. Nesladek, G. Dollinger, and A. Bergmaier, Surf. Coat. Tech.**133-134** (2000) 152.
4. Jose L. Endrino and J.E. Krzanowski, J. Mater. Res. **7** (2002) 3163.
5. Jose L. Endrino, PhD dissertation "The influence of coating architecture on the hardness, friction, and wear resistance of hard and tribological nanocomposite coatings", University of New Hampshire (2003).
6. S.H. Koutzaki, J.E. Krzanowski, and J.J. Nainaparampril, J. Vac. Sci. Tech. **19A** (2001) 912.
7. R. Sammynaiken *et al.*, J. Appl. Phys. **92** (2002) 3000
8. Y.F.Hu *et al.*, J. Eletron Spectr. **135** (2004)143; Y.F.Zhang *et al.*, Phys. Rev.B **61** (2000) 8298; J. Dürr *et al.*, BESSY Annual Reports 96, p.242

Pr-Silicate formation on SiO_2 covered SiC surfaces

R.Sohal, K.Henkel, D.Schmeißer, and H.-J. Muessig*

Angewandte Physik - Sensorik, BTU Cottbus, Postfach 10 13 44, 03044 Cottbus, Germany
**ihp, Im Technologiepark 25, 15236 Frankfurt/Oder, Germany.*

Photoelectron spectroscopy (PES) with synchrotron radiation is used to study the solid state interaction of Pr with SiO_2 covered SiC substrates. We report on the formation of a stable Pr-silicate phase to yield a high-K dielectric layer. Here is no noticeable destructive interaction to the SiC substrate. We also find a silicate intermediate as on the Si(001) surface. Our data are a step towards a full description of the interface properties of that high K material, a prerequisite for its possible application in storage, logic, and power electronic devices.

The application of SiC substrates for electronic devices is of current interest in materials science and interface engineering is of crucial importance to reach a low interface density, a prerequisite for electrical performance. Pr_2O_3 and Pr-silicates are promising candidates for high-K hetero oxides and are currently investigated. The current roadblock in the semiconductor technology road map (and in Moore's law) is the shrinking width of the SiO_2 layer that insulates the gate from the channel of a transistor. This has triggered an intensive search for gate insulators with a high DK where the layer can be made thicker without compromising the capacitance[1, 2].

We studied the fundamental interface properties of such a material (praseodymium oxide) at the Si(100) interface[2-5] and we compare these results to Pr_2O_3 films grown on SiC surfaces. Previous studies used direct deposition of Pr_2O_3 on SiC(0001) surfaces[6]. At SiC surfaces we have deposited Pr_2O_3 films by several methods. A wet chemical treatment[6] result as well as thermal deposition of Pr_2O_3 results in a destructive interaction with the 4H-SiC(0001) surfaces[6] .Here, we use photoelectron spectroscopy to characterize the reactivity of elemental Pr evaporated onto SiO_2 covered 3C-SiC(111) substrates epitaxial grown by a CVD process on Si(111) substrates[7]. We analyze the Si2p, C1s, and O1s core levels and find that Pr reacts at RT with the SiO_2 layer. In earlier contribution we focused on the Pr4f occupancy in the occupied VB states and in the empty CB states[4, 5]. At the Si(001) interface in-situ prepared epitaxial layers (d<5nm) enable us to study the contribution of the Pr4f electronic states in the valence band population as a function of layer thickness. We find a silicate intermediate which is deduced from the core level shift of the Si2p and the O1s levels[2, 4]. We obtain such kind of chemical information by comparing the resonant PES around the O1s threshold for CeO_2, Ce_2O_3, and Pr_2O_3 in the bulk oxidic phase which represents a series with increasing the number of available f-electron in the particular system. We realize, that upon increasing the number of 4f electrons also the covalent contribution increases. This is the main reason why in the Pr-O-Si system we deduce that the localized nature of the 4f electrons is fully vanished and we find covalent broadened 4f states as gap states with a continuous density of states (DOS). At the Si(001) interface we use in-situ prepared epitaxial layers (d<5nm) to study the contribution of the Pr4f electronic states in the valence band population as a function of layer thickness.

Here we report on experiments that are performed at the U49/2 beam line at BESSY equipped with a PEEM used to record the XAS data and a hemispherical electron energy analyzer for the photoelectron spectra[8]. Pr is evaporated from a thermal evaporator. The 3C-SiC(111) surfaces are grown in a CVD process on Si(111) substrates and will be characterized elsewhere[9]. The 3C-SiC(111) samples are oxidized in air at 600°C to enhance the thickness of the native SiO_2 layers. After 2min the thickness of the SiO_2 layer reaches about 3nm.

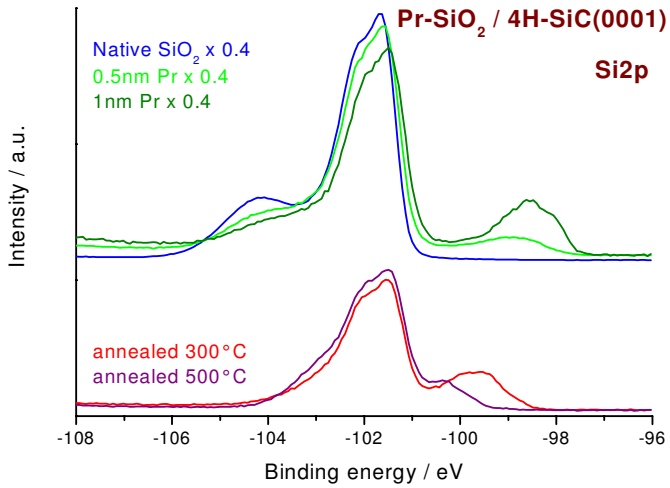

Fig.1: The Si2p core level spectra (440eV) for the bare SiO_2 / 4H-SiC(0001) surface (blue), after the evaporation of Pr 0.5nm (light green), 1nm (dark green), and after the annealing steps 300°C (red), 500°C (purple).

In fig.1 we report on our experiment by following the development of the Si2p core levels as studied by excitation of 400eV photons. Here, Pr is exposed to a native oxide covered 4H-SiC(0001) surface. Pr causes a decomposition of the SiC substrate and results in the formation of Pr-silicides and Pr-carbides as monitored by the respective core level shifts. In former experiments with Pr and Pr_2O_3 being exposed to clean SiC surfaces we learned that there is also a destructive interaction[6, 7]. In the corresponding Pr / SiO_2 / Si(001) system we find that the Pr silicides convert to the Pr-silicates which are more stable and form upon slight annealing[4, 5]. However, on the SiC surfaces with the native SiO_2 layer the silicides are not completely transformed after the annealing to 500°C indicating the destructive interaction to the substrate. We deduce from the broad C1s emission and the remaining shoulder at the Si2p that Pr has attacked the SiC substrate irreversibly[7].

On the other hand, if we increase the thickness of the native oxide by annealing that surface in air for 2 minutes, we find formation of a stable Pr-silicate. The spectrum of the 3nm SiO_2 covered 3C-SiC(111) surface where the SiO_2 component peaks at –104eV is shown in fig.2. Evaporation of 1nm of elemental Pr causes a general reduction of the intensity as well as a shift of the SiO_2 component. Upon slight annealing to 300°C we find the characteristic emission of Pr-silicate at around –103.5eV with no noticeable emission from Pr-silicides.

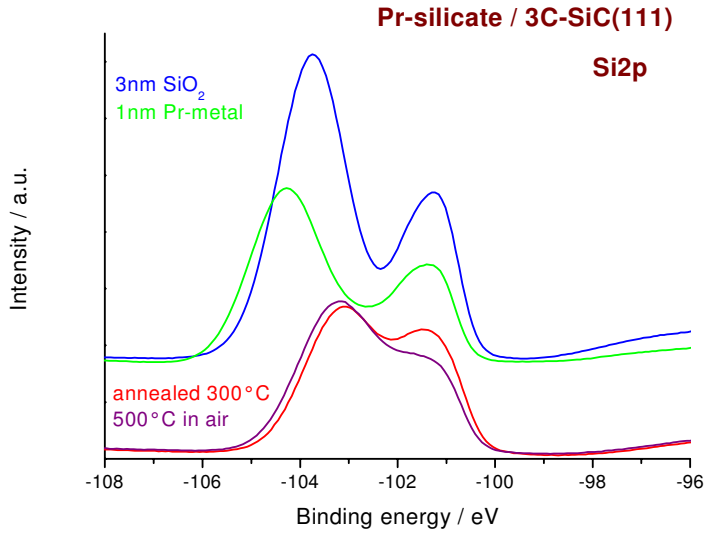

Fig.2: The Si2p core levels (400eV) for bare SiO_2 / 3C-SiC (blue), after evaporation of Pr (green), annealing at 300°C (red) and 500°C in air (purple).

In this experiment we succeeded to form a stable Pr-silicate by increasing the thickness of the SiO_2 layer. As shown in fig.2 the evaporation of 1nm of Pr on the 3nm SiO_2 layer does not cause a destructive formation of SiC by the formation of Pr-silicide as we found to occur on a much thinner native oxide layer. Instead we find the formation of a Pr-silicate emission as characterized by the Si2p emission at around 103eV. We also studied the corresponding Pr and C core levels and find no evidence for a destructive interaction any more[9]. In our experiments we learn that SiO_2 is completely decomposed after annealing the Pr exposed films to form Pr-silicates. Here the Pr-silicate forms an amorphous layer with a thickness of about 3nm coexisting with about 50% of Pr_2O_3. The mixed Pr_2O_3 / Pr-silicate layer is amorphous and is stable even after annealing to 500°C in air as shown in fig.2. As Pr-silicates are known to have a dielectric constant higher than 12[4, 5] we believe this reaction to cause a stable interface for further deposition of Pr_2O_3 for dielectric gate stacks on SiC surfaces.

This work is supported by DFG (SCHM 745/9-1).

1. G.D.Wilk. R.M.Wallace, J.M.Anthony, J.Appl.Phys. 89 (2001) 5243.
2. D.Schmeißer, Materials Science in Semiconductor Processing 6 (2003)59.
3. D.Schmeißer, H.-J.Müssig, J. Physics: Condensed Matter 16 (2004) S153.
4. D.Schmeißer, H.-J.Müssig, MRS Spring Meeting 2004 (Symposium D) Proceedings Volume 811, in press.
5. D.Schmeißer, G.Lupina, H.-J.Müssig, Materials Science in Semiconductor Processing, submitted.
6. A.Goryachko, I.Paloumpa, G.Beuckert, Y.Burkov, D.Schmeißer,Physica Status Solidi C 1 (2004) 265.
7. A. Goryachko, Y. Yeromenko, K. Henkel, J. Wollweber, D. Schmeißer, Physica Status Solidi A 201 (2004) 245.
8. D.R.Batchelor, R.Follath, D.Schmeißer, Nucl. Inst. Methods in Physics Research A 467 (2001) 470.
9. R.Sohal, K.Henkel, D.Schmeißer, to be published.

The interaction of Titanium to Pr_2O_3 thin film dielectrics

M. Torche and D. Schmeißer
Angewandte Physik-Sensorik, BTU Cottbus, Postfach 10 13 44, D-03013 Cottbus, Germany

We focus on the metal interaction towards insulating dielectric layers in metal-insulator-semiconductor gate stacks. Here we report on a study of the metal interaction, the thermal stability, and the diffusivity of Al, Ag, Au, Ti evaporated on Pr_2O_3/Si substrate. Pr_2O_3 is one of the promising high-k oxides to use in the microelectronic devices as an alternative dielectric gate of SiO_2 for the next generations of compounds like MOS and MIM based transistors. Its high dielectric constant qualifies it to play this important role in the future [2]. However the dielectric behavior of Pr_2O_3 with a film thickness of a few nm only can be strongly affected by the metal contact atoms. The metals may form an additional oxidic interface which may have worse dielectric properties or cause instabilities, or may form metallic channels through the thin layers or diffuse along cracks or grain boundaries. Looking for the best metal contact is a key issue to ensure the intrinsic dielectric properties of the Pr_2O_3 insulating layer. Titanium is known by its rapid and easy oxidation, its contact with the Pr_2O_3 will certainly provoke a partial oxidation of the Ti layer, the questions then are: what is the amount of the oxidized layer and is this Titanium oxide stable or not?. In order to answer to these questions, we have done SRPS measurements in Bessy which give us the possibility to study the depth profiling of the Ti layer by changing the excitation energy.

A Pr_2O_3 film (2 nm) was deposited at room temperature on Si(100) substrate by electron beam evaporation. Ti layer (1.4 nm) was deposited by sublimation from a Ti wire. Two excitation energies were used (1213.4eV and 653.4eV) in order to study the depth profiling of the Ti deposited layer (bulk and surface, respectively) after different annealing steps (room temperature, 300 °C, 500 °C, and 700 °C). For further details about our PES system at Bessy, see reference [3].

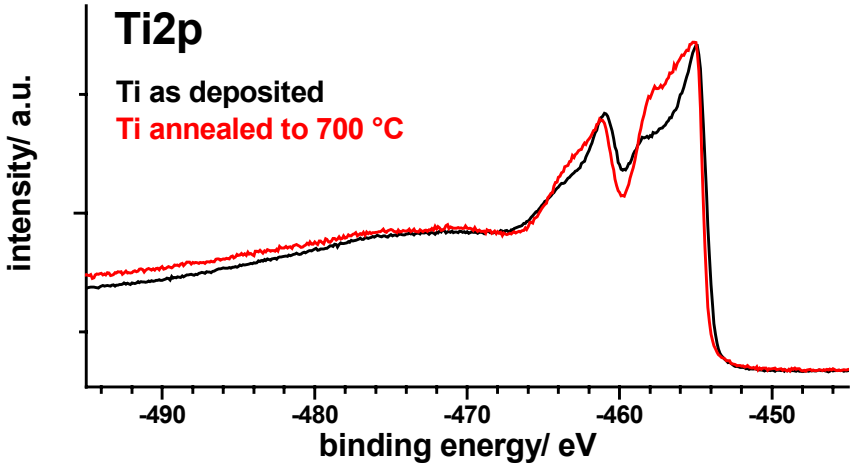

Figure1. Comparison between Ti2p emissions of Ti as deposited and after annealing to 700 °C measured with the surface sensitive excitation energy of 653.4eV.

The Ti2p emissions measured are shown in the figure 1. Two contributions with variable intensities depending on the annealing temperature are observed, one from the metallic Ti which appears at –455eV and –461eV for the $Ti2p_{3/2}$ and $Ti2p_{1/2}$ respectively, and the other one from TiO_2 appearing at –458eV and –464eV. We have found in all the spectra a plasmon excitation peak at –472.5eV. To more quantitatively evaluate the Ti and the TiO_2 contributions, the spectra were analyzed by a curve-fitting procedure [4].

The Ti2p emissions measured with the more surface sensitive excitation energy of 653.4eV have a stronger emission from Ti and a weaker one from TiO_2, this is an indication that the oxidized part of the Ti layer is in the interface between the metallic part and Pr_2O_3. The fit results of the Ti2p emissions measured with the more bulk sensitive excitation energy of 1213.4eV have shown a weak dependence of the TiO_2 percentage with the annealing temperature which is considered to be a proof of the double layer thermal stability. After Ti deposition and without any annealing 30% of Ti layer was oxidized, a part of the oxide could be from the Ti wire and not only provoked by the Ti-Pr_2O_3 contact. The Ti oxidized layer reach 40% of the total deposited layer after annealing to 700°C.

In contrast to Ti, we have found [1] that evaporated films of Al, Ag, and Au thin layers (all about 3nm thick) disappeared after a short annealing to 300°C because of diffusion process (figure 2). The thickness were calculated by measuring the attenuation of the XPS Si2p emission, from the Si substrate, before and after the metal deposition.

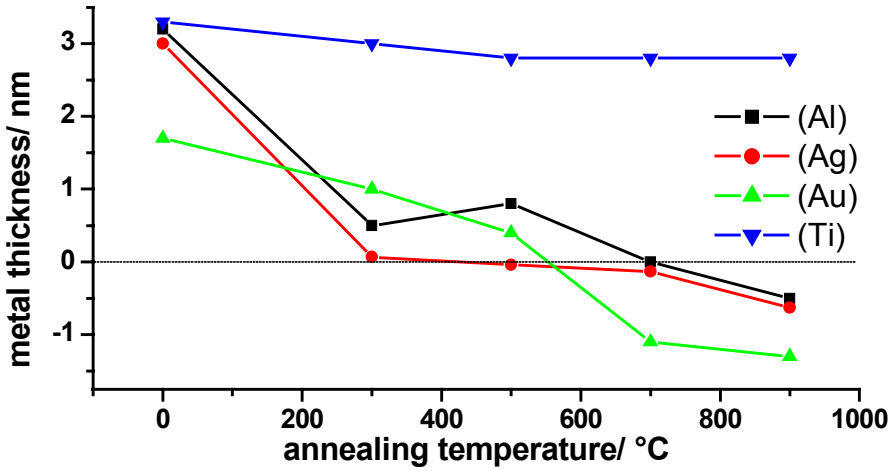

Figure 2. Thickness evolution of Al, Ag, Au, and Ti metals versus annealing temperature

In summary, for the metal gate electrodes in thin dielectric layers of Pr_2O_3 we report on the initial interaction of Ti to Pr_2O_3 thin film dielectrics. We find that already at RT there is formation of a ultra thin (<2nm) TiO_2 layer on top of which metallic Ti exists. This bilayer also determines the thermal stability of such Ti metallic contacts in the MOS and MIM based transistors. The Ti2p analysis has shown that the relative amount of these two films remains stable up to 700°C. We have found that a single TiO_2 layer is located in the interface between the metallic Ti and Pr_2O_3. Ti makes a stable and durable interface with Pr_2O_3 as the percentage of the oxidized amount of Ti depends only weakly on the annealing temperature up to 700°C and is an excellent gate electrode material or a good diffusion barrier between other electrode metal and Pr_2O_3. We find that this double layer is stable and there is no diffusion of Ti atoms in the Pr_2O_3 layer, in contrast to other metals (Al, Ag, and Au).

We would like to thank the technical assistance of G.Beuckert, P.Hoffmann, and of the BESSY staff.

[1] M.Torche, D.Schmeißer, to be published
[2] D.Schmeißer, Material Science in Semiconductor Processing 6 (2003) 59.
[3] D. Schmeißer, P. Hoffmann, G. Beuckert, Materials for Information Technology, Springer Verlag, submitted.
[4] J.J. Paggel, W. Theis, K. Horn, Physical Review, B50 (1994) 18686.

Oxynitride Growth on 4H-SiC(0001) by N_2O

P.Hoffmann, A.Goryachko, D.Schmeißer
BTU Cottbus / LS Angewandte Physik II / Konrad-Wachsmann-Allee 17 / 03046 Cottbus

Introduction

SiC is a semiconductor material which has the ability to replace Si in high-temperature or high-power applications because the higher band gap (3.28eV in the case of the polytype 4H-SiC investigated here) allows doping-controlled conductivity at higher temperature compared to Si. The good heat conductivity of SiC (>20W/(m·K) for 4H-SiC) additionally improves the heat drain in high-power applications.

A major problem in the use of SiC for semiconductor applications is the poor quality of the native growing dielectric SiO_2: Despite of several pre-/postoxidation treatments [1] the density of the interface states (DIS) is still 1 .. 2 orders of magnitude higher than on SiO2/Si interfaces. This is mainly due to excess carbon or silicon at the SiC/SiO_2 interface. Later it was shown that the DIS can be reduced by the passivation of this excess interfacial carbon or silicon by nitrogen incorporation [2]. In this paper we report on the investigation of the growth of ultrathin oxynitride layers on 4H-SiC(0001) surfaces by direct oxidation in N_2O.

Experimental

As substrate material 4H polytype SiC single crystals (Ø 35mm | n-doped by nitrogen incorporation) were used. The crystals were grown at the Institute for Crystal Growth (IKZ) in Berlin/Adlershof using vapour growth. Additionally an epi-layer of 9µm thickness was grown on the cut wafers.

For preparation in vacuum the samples cut from the wafer (10×10mm) were mounted between Ta clips to allow direct heating by passing a current through the SiC. To show the crystallinity of this surface the wafers were investigated in-situ by STM using an Omicron UHV STM/AFM. The growth of the oxynitride layer was realised in a special UHV chamber allowing N_2O pressures of 10^{-2}Pa up to 1000Pa (10^{-4}mBar .. 10mBar). Afterwards the prepared layers were investigated by photoelectron spectroscopy at the ASAM end-station operating on the beamline U49/2-PGM2.

Preparation of the SiC surface

After introducing into vacuum the SiC samples were heated first slowly to 400°C and then shortly (20 Seconds) to 1250°C to remove carbon-hydroxide contamination and oxide. Afterwards the surface of the sample was investigated by STM. On the STM image (shown in Figure 1 on the top left) the surface was found to be crystalline although it was rich of terraces.

The photoelectron spectra show low contamination with residual oxygen (overview spectrum on the bottom of Figure 1) and now SiO_2 but remarkable contamination with excess carbon (graphite). This is shown in the surface sensitive spectra of C1s and Si2p on the top right of Figure 1. These graphitic contamination are due to decomposition of SiC at 1250°C and depletion of Si due to Si evaporation. Long heating to 1250°C leads to further graphite formation.

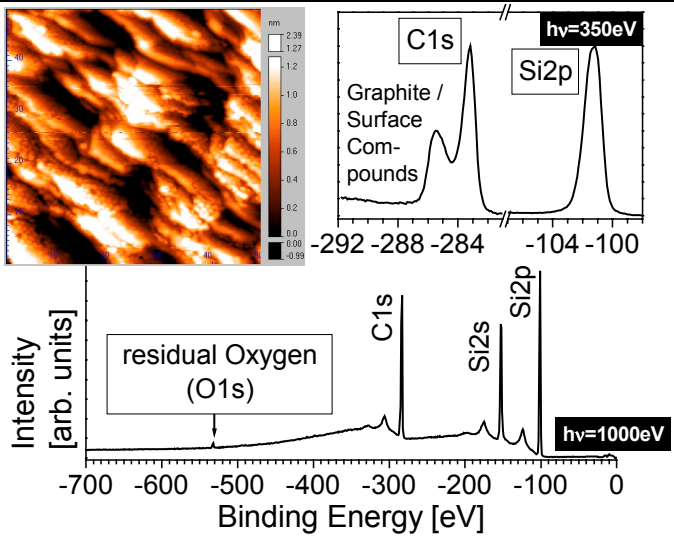

Figure 1: STM image(50×50nm) and surface-sensitive C1s- and Si2p spectra of the 4H-SiC(0001) surface heated to 1250°C in vacuum.

Direct N_2O oxidation of the bare SiC surface

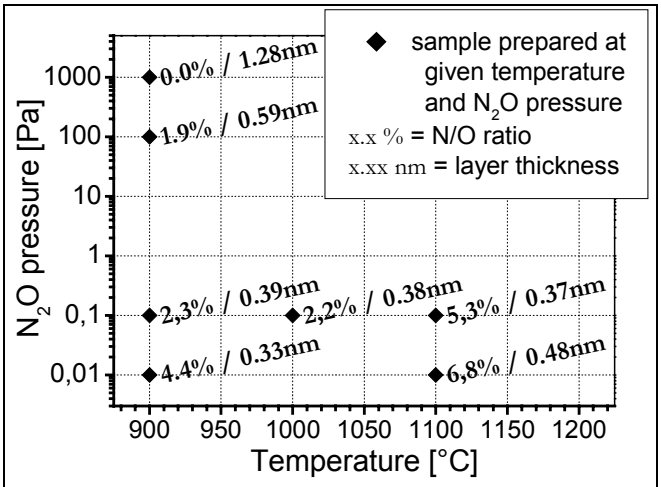

Figure 2: Summary of the investigation of nitrogen incorporation and layer thickness for different preparations by direct growth in N_2O.

After the preparation of the clean SiC surface the sample was heated to temperatures between 900°C and 1100°C in N_2O ambient. This was done in a special high-pressure vacuum vessel to allow N_2O pressures from UHV conditions to air pressure. In this experiment pressures of 10^{-2} .. 1000 Pa (10^{-4} ..10mBar) were used. The preparation time always was 10 minutes. The grown oxynitride layers were investigated by photoelectron spectroscopy mainly regarding the thickness of the grown layers and the amount of incorporated nitrogen. A summary of that investigation is shown in Figure 2. From this it is evident that for high nitrogen incorporation the layers have to be grown at high temperature and low N_2O pressure. This results in the highest found nitrogen incorporation (Nitrogen-to-oxygen ratio then is nearly 7%). But at these growth conditions (low N_2O pressure) the thickness of the layers is very low - only ~0.5nm can be reached within 10Min. The second problem at these growth conditions is the formation of graphite. Like shown in Figure 1 already short heating (20 Seconds) leads to enrichment of carbon. Although the temperature here is lower (1100°C) the long preparation time needed for thicker layers (only 0.5nm were grown in 10 Minutes) would lead to an unacceptable amount of graphite. Therefore the two problems - low nitrogen incorporation and graphite formation due to SiC decomposition - had to be solved.

Evaporation of silicon

Investigations of the oxynitride growth on Si by N_2O had shown that nitrogen incorporation is also increased at high temperatures and low N_2O pressures [3]. But in general the nitrogen incorporation is much higher (N/O ratios of 80% are reachable) and growth rates are superior to those on SiC. From this it can be concluded that the availability of silicon while the N_2O oxidation process leads to higher incorporation of nitrogen. On the other hand it is known [4] that additional Si (evaporated onto the SiC surface) prevents the formation of graphite while heating the SiC and even leads to reduction of graphite. This is shown in Figure 3 in the C1s spectrum recorded at hν=350eV. The contribution attributed to graphitic or amorphous carbon (at binding energies between -284eV and -286eV) is reduced by more then a factor of 4 compared to the best SiC surface prepared without Si-evaporation (see Figure 1). It should be noted that still elemental Si is observable at binding energies around -98.9eV. This indicates the formation of Si cluster on the surface. This is in agreement with former STM investigations which showed Si cluster also.

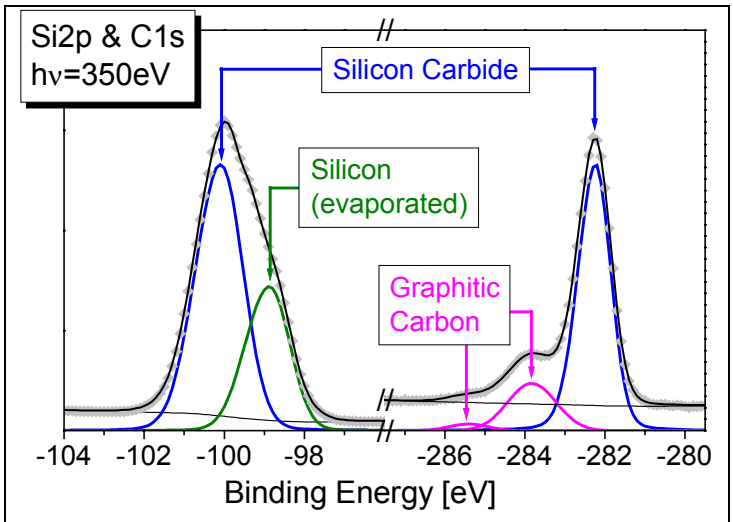

Figure 3: Si2p and C1s spectra recorded after evaporation of Si and heating to 1000°C

Following the above mentioned idea, that the presence of Si leads to higher nitrogen incorporation, this Si rich SiC surface was oxidised in N_2O {0.1Pa (10^{-3}mBar) N_2O at 900°C}. Although the amount of available Si was very low, this preparation showed a N/O ration of nearly 16%, 3 times higher then under the same preparation conditions on a surface what is depleted of Si (see Figure 2). Nevertheless the layer thickness is still insufficient (0.35nm were calculated from the Si2p spectra). But the formation of graphite is very low (see surface sensitive C1s spectrum recorded at hν=350eV in Figure 4) and was even decreased in comparison to the clean surface before (refer to Figure 3). The N1s photoelectron spectra (In Figure 4 the spectrum recorded at hν=650eV is given exemplary.) show that most of the nitrogen is incorporated as silicon nitride. This is evident by the low binding energy of the main N1s peak, what arises around -396.2eV.

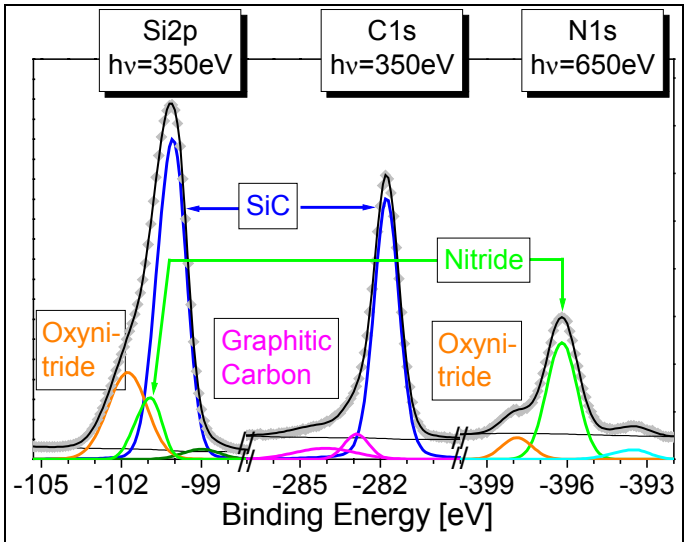

Figure 4: Si2p, C1s, and N1s spectra of the 0.1Pa N_2O-preparation at 800°C on the Si rich surface.

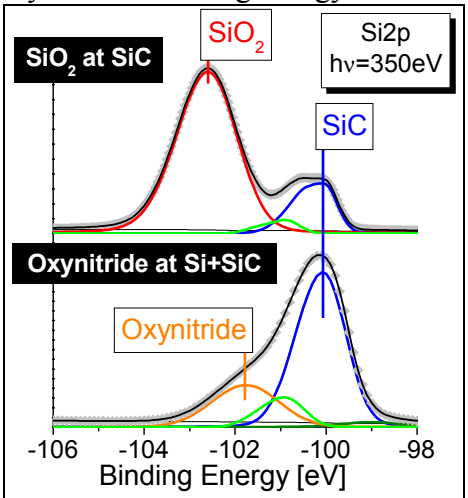

Figure 5: Si2p spectra of SiO_2 on SiC (top) prepared at 1000Pa N_2O and nitrogen-rich oxynitride (bottom) prepared at 0.1Pa N_2O on Si-rich SiC surface.

In Figure 5 the Si2p spectra of the preparation at 1000Pa N_2O (no nitrogen incorporation) is compared to the nitrogen-rich preparation of Figure 4. The emission around -103eV at the 1000Pa preparation shows that there only SiO_2 was grown. The emission around -102eV (binding energy typical for oxynitrides on Si) at the 0.1Pa preparation indicates that here already oxygen was replaced by nitrogen. Suboxides are also visible in the Si2p spectra. On the one hand this can be attributed to a silicate layer between the SiC and the SiO_2 in the case of silicon dioxide (top of Figure 5). On the other hand also contribution of silicon nitride could not be ruled out at the nitrogen-rich preparation (bottom of Figure 5).

With this method of Si evaporation and using it as a sacrificial layer it should be possible in future to grow oxynitrides on SiC with a higher layer thickness and a larger amount of incorporated nitrogen.

Acknowledgement

The authors like to thank Dr.Siche and the IKZ staff for supplying the 4H-SiC single crystals as well as the BESSY staff for instrumental assistance. The financial support by the DFG (Grant-No. SCHM 745/9-1) is gratefully acknowledged.

[1] V.V.Afanasev, M.Bassler, G.Pensl, M.J.Schulz, E.v.Kamienski: J.Appl.Phys. **79** (1996) 3108.

[2] K.McDonald, R.A.Weller, S.T.Pantelides, L.C.Feldman, G.Y.Chung, C.C.Tin, J.R.Williams: J.Appl.Phys. **93** (2003) 2719-2722.

[3] P.Hoffmann, R.P.Mikalo, D.Schmeißer: J.Non-Cryst.Solids **303** (2002) 6-11.

[4] F.Amy, P.Soukiassiana, Y.-K.Hwu, C.Brylinski: Appl.Phy.Lett. **75** (1999) 3360-3362.

Shining light on magnetic microstructures

A. Remhof, C. Bircan, A. Westphalen, J. Grabis, A. Nefedov and H. Zabel
Institut für Experimentalphysik/Festkörperphysik, Ruhr-Universität Bochum, 44780 Bochum, Germany

We demonstrate the possibility to extend the established Bragg-MOKE technique, which measures the Kerr effect on off-specular diffracted polarized laser light to soft x-rays. The shorter wavelength, which allows to investigate smaller structures, and the element selectivity of the resonant scattering make soft x-rays an attractive tool to study patterned ferromagnetic heterostructures. We illustrate this technique on permalloy islands and on exchange biased iron islands on CoO as two model systems. The results so far are in agreement with other experimental techniques and show the feasibility of off-specular resonant magnetic soft x-ray scattering. (XRMS). In this contribution, two different micro structured ferromagnetic samples are discussed in order to illuminate the technique. The first sample is a regular array of single domain permalloy (Ni_{80}/Fe_{20}) islands on a silicon wafer, the second is a patterned Fe on CoO exchange bias system.

The soft x-ray measurements were carried out using the ALICE diffractometer [1] at the dipole beamline PM3 (Py sample) and at the undulator beamline UE56/2 (Fe/CoO sample) at the BESSY II synchrotron in Berlin. The sample is fixed to the cold finger of a closed cycle cryostat, placed between two magnetic poles. This set-up covers temperatures between 10 K and 350 K and magnetic fields up to 2.5 kOe. The magnetic field is applied parallel to the scattering plane. Thus using circularly polarized light longitudinal Kerr effect (L-MOKE) geometry can be realized, in which the magnetic moments are both parallel to the scattering plane and to the sample surface. The reflected beam yields magnetic information as it uses the resonant absorption of polarized synchrotron radiation in the vicinity of the L edges in the transition metals. The structural diffraction pattern exhibits satellite peaks around the central specular reflection. The application of an in-situ magnetic field at photon energies near the absorption edges allows to monitor the magnetic contribution of each individual satellite peak through the whole hysteresis loop from one saturated state to the other one. While the HL recorded at the central specular reflection yields the average magnetization of the sample, the ones recorded at higher orders yield the Fourier components of the magnetic form factor, i.e. information about the magnetization profile of the ferromagnetic ellipses during the remagnetization process.

For the Py sample an incident angle of 4° and a photon energy of 863.5 eV (close to the Ni edge) was chosen. The figure (left panel) depicts the two respective off-spectular q_x scans, recorded in-situ in an applied magnetic field of ±1500 Oe along the short axis of the rectangular islands, respectively. The specular reflection at q_x=0 is accompanied by two Yoneda wings at q_x=±0.03 nm^{-1} and by numerous equally spaced diffraction peaks originating from the regular Py pattern. The magnetic contrast at those satellite reflection can clearly be seen. Off-specular hysteresis loops could be measured up to the 35^{th} order of diffraction. A selection of those are displayed in the figure (right panel). All hysteresis exhibit a S-like shape with the same coercive field of 35 Oe, the same remanence of $0.3M_{sat}$ and a saturation of 400 Oe. Unlike the hysteresis loops recorded with visible light, there is no change in sign of the hysteresis loops is observed for negative orders of diffraction. Also the patterned Fe/CoO sample shows order independent hysteresis loops. As for the Py sample one could infer from this a single domain behavior or a coherent rotation. Another scenario is

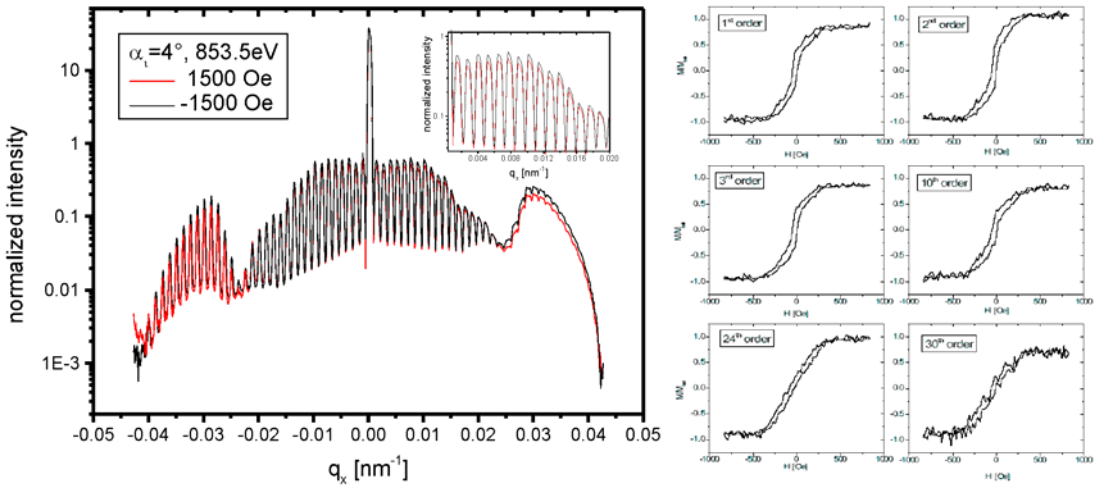

Figure 1: Left: Q_x scans recorded in both magnetic saturations. An incident angle of 4° and at a photon energy of E=863.5eV (Ni-edge) was chosen. The specular reflection at q_x=0 is accompanied by more than 30 equally spaced satellite reflections. The magnetic asymmetry reaches up to 25%. The inset shows a detail Right: Selected off-specular hysteresis loops recorded at the corresponding diffraction peaks.

also feasible, and may in fact explain the data better. Radu et al. [2] observed the formation of antiferromagnetic domains at the FM/AF interface induced by the first magnetization reversal. These domains are preserved in saturation and they serve as seeds for the following magnetization reversal. In this picture the individual Fe islands break up into numerous ferromagnetic domains, that switch independently their magnetization upon field reversal. There is also no interaction between the individual Fe islands, so each island, consisting itself of many magnetic domains, undergoes the magnetization reversal independent from the magnetic state of the other islands. Consequently, the magnetic form factors of the individual islands differ from each other. The averaged magnetization component in the scattering plane appears again homogeneous. The numerous domains cause a uniform magnetization distribution [3].

The authors are grateful for technical support by P. Stauche (Bochum), B. Zada (UE56/2), W. Mahler (UE56/2), and T. Kachel (PM3). We would like to thank the DFG for financial support of this work within the SFB 491 “Magnetic Heterostructures: Structure and Transport”. The soft x-ray work was supported by the BMBF under contract O3ZAE8BO.

References

[1] J. Grabis, A. Nefedov, H. Zabel, *Rev. Sci. Instr.* **75**, 4048 (2003).

[2] F. Radu, M. Etzkorn, R. Siebrecht, T. Schmitte, K. Westerholt, H. Zabel, *Phys. Rev. B* **67** 134409 (2003).

[3] A. Remhof, C. Bircan, A. Westphalen, J. Grabis, A. Nefedov, H. Zabel, *Superlattices and Microstructurs*, submitted.

Effect of Tensile and Compressive Creep Deformation on γ/γ' Lattice Misfit in Single Crystal Superalloys

I. Zizak, N. Darowski, G. Schumacher
Structural Research, Hahn-Meitner-Institute Berlin GmbH

H. Klingelhöffer
Federal Institute of Materials Research and Testing, Berlin, Germany

W. Chen and W. Neumann
Institute of Physics, Humboldt University Berlin, Germany

Due to their excellent properties at elevated temperatures single crystal nickel base superalloys are widely used for critical structural components for applications at high temperature, such as first stage blades in modern gas turbines in aircraft and for power generation. The superalloys are strengthened by ordered intermetallic γ' precipitates with a super lattice of type $L1_2$ and a cuboidal morphology. They are embedded coherently in a fcc solid solution γ matrix. The lattice distortion induced by coherency between the γ matrix and γ' precipitates leads to a high resistance against creep deformation and at same time, however, also to the instability of microstructure – formation of γ' rafts [1]. Typically the parameter, *lattice mismatch*, is used to describe the lattice distortion in alloys strenthened by coherent precipitates. Because of its technological importance the γ/γ' lattice mismatch was investigated extensively on the superalloys both in the non-deformed state and after creep deformation [2 - 6]. It is the purpose of the present study to investigate the influence of the sign of creep loading on the evolution of γ/γ' lattice mismatch between the γ' precipitates and γ matrix in the creep-deformed superalloys. The following definition of lattice mismatch is used in this investigation

$$\delta = 2 \cdot \frac{a_{\gamma'} - a_{\gamma}}{\left(a_{\gamma'} + a_{\gamma}\right)},$$

where a_{γ} and $a_{\gamma'}$ are the lattice parameters of the γ matrix and the γ' precipitates, respectively.

A model single crystal superalloy SC16 with chemical composition of $Ni_{68.1}Cr_{17.5}Al_{7.35}Ti_{4.15}Ta_{1.1}Mo_{1.8}$ (at %) was used for the study. The initial microstructure consisted of cuboidal γ' precipitates which had monomodal size distribution with an average edge length of about 450 nm and a volume fraction of about 40 %. The creep tests were conducted at 1223 K and 150 MPa both under tensile and compressive load along [001] direction, respectively. The creep strain in both of the tests was 0.5 %. The X-ray measurements were carried out in two orientations parallel and perpendicular to the load axis, respectively. High resolution X-ray diffraction using an X-ray energy of 8 keV at the KMC-2 beam line at

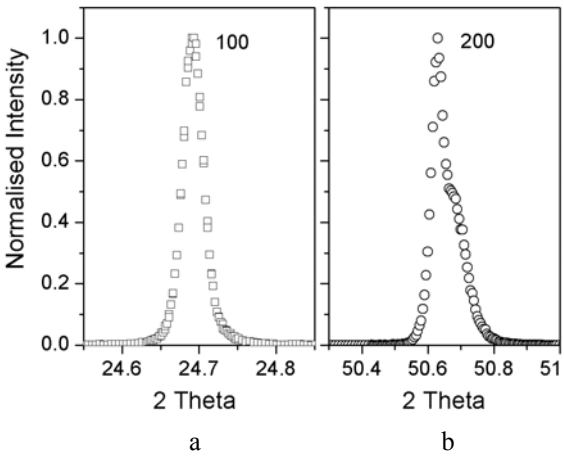

Fig. 1 Intensity profiles of a) 100 super lattice reflection and of b) 200 reflection measured on the non-deformed specimen, respectively

BESSY II in Berlin was used to measure the lattice parameters. The non-deformed material and the creep-deformed material were investigated at ambient temperature.

Figs. 1a and 1b show the intensity profiles of the 100 super lattice reflection and of the 200 reflection measured on the non-deformed specimen, respectively. Due to the similar crystal structure ($L1_2$ and fcc) and the small difference in lattice parameters the γ and γ' peaks at 200 reflection overlap, see Fig. 1b. The alloy has a positive lattice misfit at room temperature.

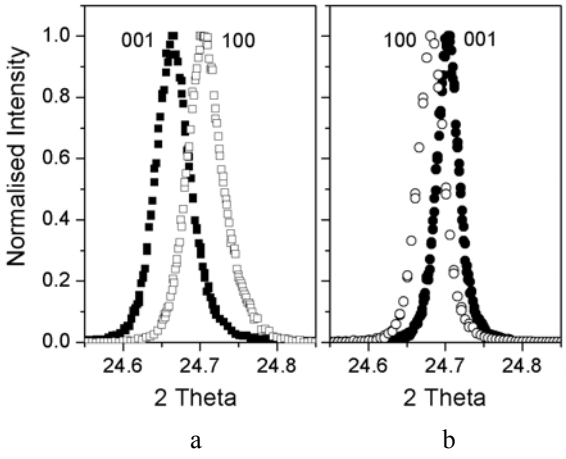

Fig. 2 Intensity profiles of 100 and 001 super lattice reflections taken on the specimens after a) tensile and b) compressive creep deformation, respectively

Fig. 2a shows the intensity profiles of the 100 and 001 super lattice reflections of γ' precipitates, respectively, measured on the tensile creep-deformed material. The peak position of the 001 intensity profile has clearly a smaller 2θ value than that of the 100 intensity profile. The above results indicate that the lattice parameter of γ' phase in 001 orientation is larger than that in 100 orientation. The γ' precipitates in the specimens after tensile creep deformation has a tetragonal lattice distortion [7]: $a_{\gamma'}(001)/a_{\gamma'}(100) > 1$. After compressive creep deformation, however, an inverse effect was observed: $a_{\gamma'}(001)/a_{\gamma'}(100) < 1$ (Fig. 2b) [7]. Obviously, the tensile and compressive creep deformation result in different inelastic deformation in 100 and 001 orientations. The relative shift of the 100 and 001 peaks in the tensile creep-deformed material is more pronounced compared to that after compressive creep deformation. Also the full width at half maximum (FWHM) of both the intensity profiles recorded on the tensile creep-deformed specimens is larger than that of the compressively creep-deformed specimens. These observations lead to the conclusion that the same macroscopic creep strain (± 0.5 % in the present study) result in different lattice distortions, depending on the sign of creep load.

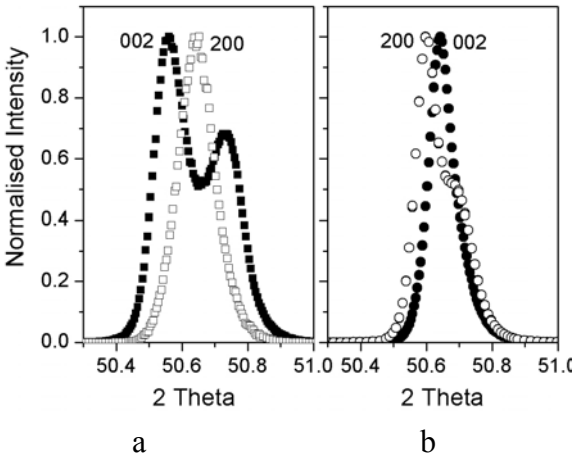

Fig. 3 Intensity profiles of 200 and 002 reflections measured after a) tensile and b) compressive creep deformation, respectively

Figs. 3a and 3b show the intensity profiles of 200 and 002 reflections after a) tensile and b) compressive creep deformation. A similar trend in the shift of intensity profiles can be observed as for the 100 and 001 super lattice reflections. Compared to the non-deformed state a relative shift of γ and γ' peaks took place due to creep deformation. In the tensile creep-deformed specimens the γ' and γ peaks of the 200 reflection move to each other. For the 002 reflection they move away from each other in comparison with that of the non-deformed specimen (Fig. 1b). In the compressively creep deformed specimens again an inverse effect was observed. The effect induced by creep deformation under compressive load is also found to be clearly smaller than that found after tensile creep deformation.

The lattice parameters of γ' precipitates were determined using the super lattice reflections. To obtain that of γ matrix a deconvolution method was employed [6]. Using the above lattice parameter data the lattice mismatches were calculated according to the definition mentioned above. All data are summarised in Table 1. In the non-deformed state the γ/γ' lattice mismatch shows a positive value of about 1.0 x 10^{-3} at ambient temperature. This agrees with experimental results of previous investigations on the same superalloy [8].

Table 1 Lattice parameters of γ' and γ phases and γ/γ' lattice mismatch

Creep	Reflection	Lattice Parameter (nm)		Lattice Mismatch
		γ	γ'	x10^{-3}
As-treated	100/200	0.35806	0.358375	0.8793
Tensile	001/002	0.35770	0.358690	2.7639
	100/200	0.35833	0.358095	-0.6560
Compres-sive	001/002	0.35811	0.358140	0.0838
	100/200	0.35789	0.358450	1.5635

The observed effect of the sign of creep load on the development of γ/γ' lattice mismatch can be understood qualitatively by consideration of the respective preferential sites of inelastic deformation under both kinds of creep load and of the differences in the mobile dislocations at the horizontal and vertical γ/γ' interfaces [6]. Dislocation pairs formed during deformation at high temperature will glide on the same plane and will be fixed at the γ/γ' interfaces, but depending on the orientation of the interfaces the dislocations will be located in the matrix or in the γ'-phase [6]. Cooling to room leads to the orientation dependent misfit reported above.

The authors would like to thank C. Förster, H. Kropf and W. Becker for the preparation of the specimens. Financial support of the German Research Foundation (DFG) through grants Ne 646/5-3 and Schu 1254/3-4 is gratefully acknowledged.

References

[1] D. Mukherji, H. Gabrisch, W. Chen, H.-J. Fecht and R.P. Wahi, Acta mater., 45 (1997) 3143
[2] M. Fahrmann, J.G. Wolf and T.M. Pollock, Mat. Sci. Eng., A211 (1996) 8
[3] R. Völkl, U. Glatzel and M. Feller-Kniepmeier, Scripta. mater., 38 (1998) 893
[4] A. Müller and W. Reimers, Phys. Stat. Sol., (a) 156 (1996) 47
[5] A. Royer, P. Bastie and M. Veron, Mat. Sci. Eng., A234-236 (1997) 1110
[6] W. Chen, N. Darowski, I. Zizak, G. Schumacher, H. Klingelhöffer, N. Wanderka and W. Neumann, Mat. Sci. Forum, 426-432 (2003) 4555
[7] W. Chen, N. Darowski, I. Zizak, G. Schumacher, H. Klingelhöffer and W. Neumann, Z. Kristall., Suppl. 21, (2004) 136
[8] G. Bruno, G. Schumacher, H.C. Pinto and C. Schultze, Metall. Mater. Trans. 34A (2003) 1

Superexchange coupling in metallo-organic assemblies

Y. Bodenthin[1], U. Pietsch[1], G.Schwarz[2], O. Henneberg[1], D. Kurth[2] and H. Möhwald[2]
[1]Institute of Physics, University of Potsdam, P.O. Box 601553, D-14415 Potsdam
[2]Max-Planck-Institute of Colloids and Interfaces, D-14424 Golm

3D assemblies of metallo-supramolecular polyelectrolyte units (Fe^{2+}bis-terpy) show molecular ferromagnetism above room temperature induced by the attachment of amphiphilic molecules at $Fe^{2+}N_6$ octahedra. The spacing between two neighbored Fe^{2+} ions (d = 15 Å) is too large in order to stabilize a ferromagnetic coupling by spin-exchange. Measurement of the element-selective X-ray magnetic circular dichroism (XMCD) reveal opposite magnetization of the neighbored nitrogen atoms with respect to that of Fe^{2+} ions which suggests that the ferromagnetic coupling is realized by a super-exchange coupling mechanism via the bis-terpyridine ligands. Ab initio Hartree-Fock calculations confirms this hypothesis qualitatively.

The system of interest consists in the self-assembly of bis-terpyridin bridging ligand and Fe^{2+} results forming a metallo-supramolecular polyelectrolyte (Fe^{2+}bis-terpy). Self-assembly of Fe^{2+}bis-terpy and dihexadecyl phosphate amphiphiles (DHP) results in a polyelectrolyte-amphiphile-complex (PAC). The molecular geometry of the complex with a rod-like backbone and mobile amphiphiles enables the formation of Liquid Crystals (LC) as well as the preparation of Langmuir Blodgett (LB) films.

The length of the bis-terpyridine spacer is too large in order make a process of spin-exchange coupling very favorable. Therefore other processes may be responsible for the ferromagnetic coupling. In order to clarify this question we measured X-ray circular dichroism (XMCD) at the iron L-edge as well as at the nitrogen K-edge at room temperature. The measurements were performed at the UE56/2 PGM1 beamline at BESSY II. Here, the X-ray reflectivity of the multilayer is measured at fixed angle of incidence (α_i=2°) using alternate left- and right-hand circularly polarized synchrotron radiation. This method offers high accuracy and is an element selective probe of the magnetism. Figure 1 and 2 show typical XMCD measurements of PAC at the iron L-edge (a) and nitrogen K-edge (b). Figure 1 shows two distinct minima at 706 eV and 718 eV corresponding to the L_3 and L_2 absorption edges of iron. Applying a longitudinal external magnetic field of H = 2,7 kOe the intensities of the minima differ for using right (+) or left (-) circularly polarized incident light. The difference in reflectance is displayed by the asymmetry ratio $A(E) = (I_+ - I_-)/(I_+ + I_-)$. We found an asymmetry of about (1 ± 0,2)% at the iron L_3 edge at 706 eV which is clear evidence that the ferromagnetism is originated by the iron ions in the PAC.

To interpret the data, we used the results of ab-initio calculations from literature to determine the energy dependent contributions of Δδ(E) and Δß(E) to the reflectance. These values are used to determine the complex refractive index, which, in turn, serves to compute the energy dependent reflectance with the Fresnel equations. Applying sum rules to the absorption part β□±□Δβ of n, we obtain a magnetic moment of (0.3±0.1) μ_B/Fe^{2+} for the spin-momentum.

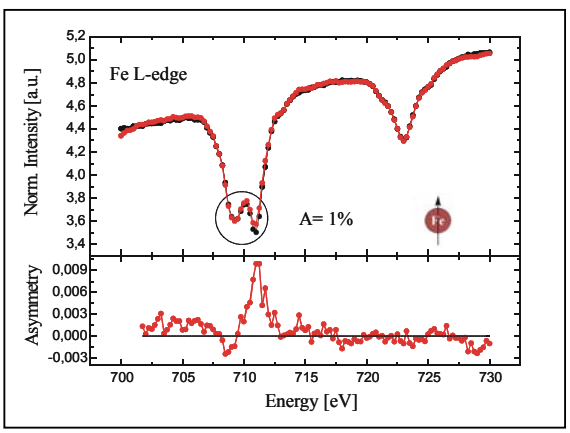

Figure 1: XMCD measurement of PAC. The two minima at 706 eV and 718 eV corresponding to the L_3 and L_2 absorption edges of iron. An external field of H = 2,7 kOe in a longitudinal geometry. The intensities of the minima differ for using right (+) or left (-) circularly polarized incident light. The Asymmetry ratio $A(E) = (I_+ - I_-)/(I_+ + I_-)$ of (1 ± 0,2)% at the iron L_3 is a clear evidence for magnetism caused by the iron ions in the PAC and correspond to a magnetic moment of (0.3±0.1) μ_B/Fe^{2+}.

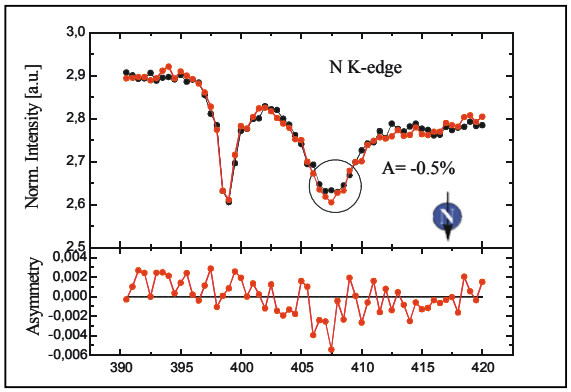

Figure 2: XMCD measurements at the nitrogen K- edge. The two minima at 399 eV and 407 eV corresponding to π* and σ* transitions of the nitrogen atoms which surround the iron. Considering the experimental error of 0.2% we found a negative asymmetry ratio $A(E) = (I_+ - I_-)/(I_+ + I_-)$ of -0.5% at the σ* transition corresponding to a negative spin polarization of nitrogen electrons.

In order to proof the concept of super-exchange coupling behind the ferromagnetic behavior we performed XMCD measurements at the nitrogen K- edge shown in Figure 2. There are two absorption edges at 399 eV and 407 eV corresponding to π* and σ* transitions of the nitrogen atoms which surround the iron. Considering the experimental error of 0.2% we found a negative asymmetry of -0.5% at the σ* transition corresponding to a negative spin polarisation of nitrogen electrons. According to crystal field theory of octahedral $Fe^{2+}N_6$ configuration the σ* absorption correspond to transitions of s electrons into the weak antibonding $2e_g$ molecular orbitals. Consequently the negative asymmetry at the σ* transition represents a direct proof of the high spin state of the iron and the anti-ferromagnetic arrangement of spins in nitrogen and iron respectively.

To confirm this finding we performed ab-initio studies of spatial distribution of the spin density of a single Fe^{2+}-bis-terpyridine coordination center. The calculations were performed in terms of an unrestricted Hartree-Fock (UHF) approach using the GAMESS package. The structure of the complex was optimized by minimizing the total energy. Slater-type orbitals (STO-3G basis), a charge of +2e for iron and a spin-multiplicity of 5 were used for calculations. Figure 3 shows the resulting spin-density distribution of one terpyridine iron coordination center. In fact, we obtained anti-ferromagnetic arrangement of spins; the sign of the spins alters between iron and nitrogen and between carbon and nitrogen within the pyridine rings again. The two carbon atoms bridging two pyridine rings show ferromagnetic correlation. Unfortunately the numerical accuracy is not sufficient to quantify the results. Further calculations are in progress.

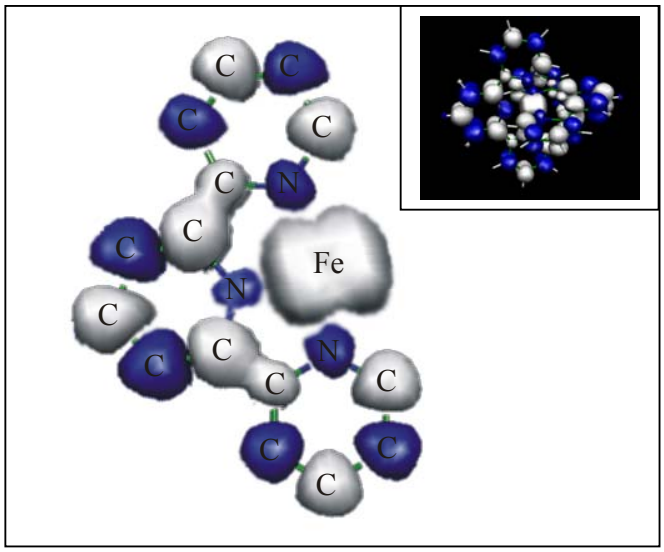

Figure 3: Calculated spin-density of a Fe^{2+}-bis-terpyridine coordination center using spin-unrestricted Hartree-Fock method. For a better view a single terpyridine molecule and iron shown as a part of the whole coordination center (Inset). We obtained anti-ferromagnetic arrangement of spins; the sign of the spins alters between iron and nitrogen and again between carbon and nitrogen within the pyridine rings. The two carbon atoms bridging between two pyridine rings show a ferromagnetic correlation.

This Project is supported by the DFG Schwerpunktprogramm 1137 “Molekularer Magnetismus” and by the BMBF (ALICE diffractometer).

EXAFS measurements on metallo-supramolecular assemblies

Y. Bodenthin[1], U. Pietsch[1], D. Kurth[2] and H. Möhwald[2]
[1]Institute of Physics, University of Potsdam, P.O. Box 601553, D-14415 Potsdam
[2]Max-Planck-Institute of Colloids and Interfaces, D-14424 Golm

The investigated system consists of metallo-polyelectrolytes (MEPE **1**), prepared by self-assembly of ditopic 1,4-bis(2,2':6',2''-terpyridin-4'-yl)benzene and Fe^{2+} ions. The subsequent self-assembly of MEPE and dihexadecyl phosphate amphiphiles (DHP) lead to a polyelectrolyte-amphiphile-complex (PAC **2**)[i]. Thin films of PAC were prepared by means of Langmuir Blodgett technique (Fig.1).
The experiments were performed at the KMC 2 beamline exploiting the fluorescence yield $I_{fluo}(E) \sim \mu(E)$ of the Fe^{2+} ions[ii]. The incoming light was striking the sample under grazing incidence conditions (α_i = 0.15° – 0.2°). We used an energy-dispersive Röntec detector attached perpendicular to the sample surface. The background-noise could be suppressed by setting a region of interest giving rise to higher accuracy of the measurements.
Fig 2. shows a typical EXAFS-function $\chi(k) = (\mu(k) - \mu_0(k))/\mu_0(k)$ of Fe-PAC films and its theoretical fit at room temperature (RT). It is obvious that the EXAFS data cannot be fitted by a single shell model. The fit was done in terms of a two core approximation with two different iron-nitrogen distances r_1 = 1.76 ± 0.01 Å and r_2 = 2.18 ± 0.02 Å and occupation numbers 4 and 2, respectively. These numbers define a deformed octahedron with the long axis perpendicular to the film normal.

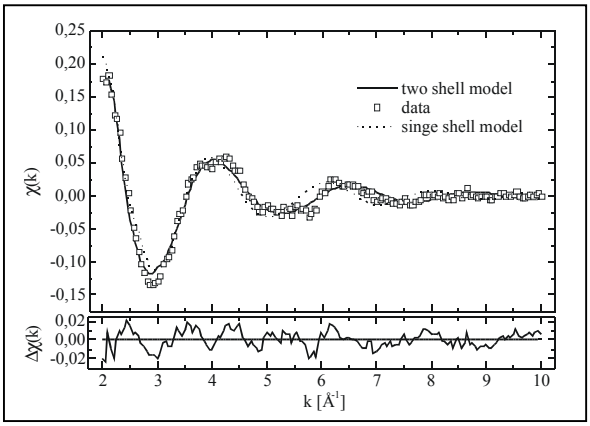

Fig.2: EXAFS function of a 11 Monolayer film and theoretical calculation

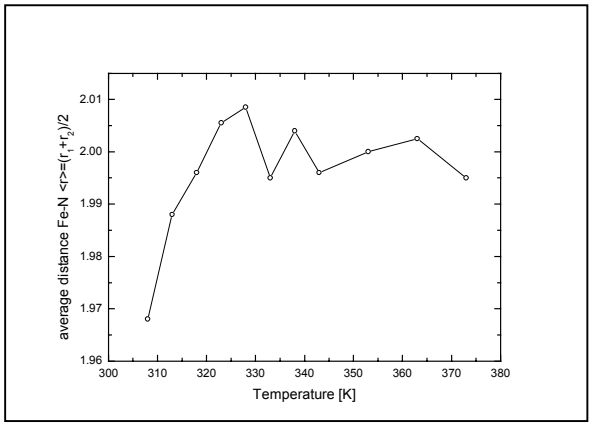

Fig.3: Increasing deformation of coordination sphere of metallo-centres

Temperature dependent EXAFS measurements indicate a structural change in the coordination geometry. Increasing the temperature the average distance $\langle r \rangle = (r_1+r_2)/2$ of the Fe-N bonds increase from 1.97 Å at RT to 2.01 Å at 328 K. The ratio r_2/r_1 remains unchanged at 1.24 on the entire temperature scale. The increasing deformation of the Fe-N octahedron is in accordance with the strong rearrangement of the film structure found in temperature dependent simultaneous measurements of grazing incidence diffraction (GID) and specular reflection (XRR) [iii]. This amphiphilic phase transition induce a mechanical strain to the MEPE and deforms the Fe-N octahedron opening the way for spin cross-over in the material.

The authors would thank BESSY and A. Erko for supporting the experiments.

[i] D. G. Kurth, P. Lehmann, M. Schütte, *Proc. Natl. Acad. Sci*. 97 , 5704- 5707 2000
[ii] A. Erko, I. Packe, C. Hellwig, M. Fiber-Erdmann, O. Pawlitzki, M. Veltkamp, W. Gudat, *AIP Conference Proc*. 521, p.p. 415-418, 2000, A. Erko, I. Packe, W. Gudat, N. Abrosimov, A. Firsov, *SPIE* 4145, p.p. 122-128, 2000
[iii] Y. Bodenthin, J. Grenzer, R. Lauter, U.Pietsch, P.Lehmann, D.G. Kurth and H. Möhwald, J. Synchr. Rad. 9, 206-209, (2002)

High-temperature ferromagnetism of metallo-supramolecular assemblies

Y. Bodenthin[1], U. Pietsch[1], P. Esquinazi[3], A. Nefedov[4], G. Schwarz[2], D. G. Kurth[2], H. Möhwald[2]

[1]University Potsdam, Department of Physics, D-14469 Potsdam (Germany)
[2]Max Planck Institute of Colloids and Interfaces, D-14424 Potsdam (Germany),
[3]University of Leipzig, Department Superconductivity and Magnetism, D - 04103 Leipzig (Germany)
[4]Ruhr-Universität Bochum, Institute for experimental physics 4, 44780 Bochum (Germany)

Metallo-supramolecular assemblies can show permanent magnetization at room temperature. This behaviour is induced by the attachment of amphiphilic molecules to a rigid like backbone (Fe^{2+}bis-terpy) containing a octahedral surrounded Fe^{2+} ion. An enhanced requirement of space of the amphiphiles induces a static distortion of $Fe^{2+}N_6$ octahedra and subsequent reduction of ligand field splitting results in a rearrangement from t_{2g}^6 (low-spin) to $t_{2g}^4e_g^2$ (high-spin) electronic configuration. The ferromagnetism exists in the supra-molecular arrangement only, while isolated Fe^{2+}bis-terpy behaves diamagnetic. The system is build by self-assembly of ditopic bis-terpyridine ligand and Fe^{2+} results in formation of a chain-like metallo-supramolecular polyelectrolyte (Fe^{2+}bis-terpy). Subsequent self-assembly of Fe^{2+}bis-terpy and dihexadecyl phosphate amphiphiles (DHP) results in a completely non-covalent polyelectrolyte-amphiphile-complex, PAC, shown in Figure 1. Under these conditions different Fe^{2+}bis-terpy to DHP ratios of 1:2, 1:4, 1:6 can be realized. The investigated ferromagnetic systems is realized with a Fe^{2+}bis-terpy to DHP ratio of 1:2.

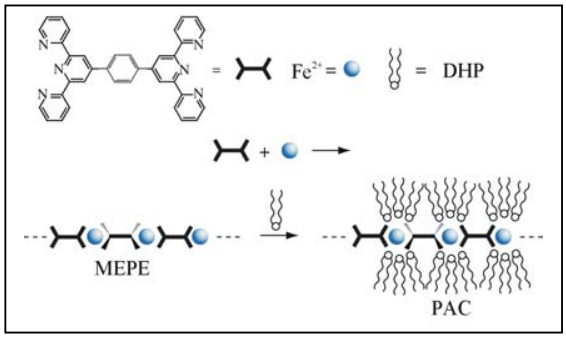

Figure 1 Self-assembly of ditopic ligand 1 and $Fe(OAc)_2$ results in formation of the linear, rigid-rod type metallo-supramolecular polyelectrolyte (MEPE). In a consecutive step, MEPE is assembled with dihexadecyl phosphate resulting in formation of the corresponding polyelectrolyte-amphiphile complex (PAC).

The magnetic properties of the system was probed by measurements using a superconducting quantum interference device (SQUID) from Quantum Design providing a sensitivity of $\leq 10^{-7}$ emu. Figure 2a shows the measured magnetic moment M_{Fe} in terms of Bohr magnetons (μ_B) per iron ion as a function of magnetic field of a LB film at different temperatures of 300K and 500K, respectively. The external field H was applied parallel to the sample surface. After correcting the diamagnetic background we measured a coercitive field of H_C=130 Oe, a remanescence of M_R=0.05 μ_B/Fe^{2+} and observed saturation M_S of about ~0.2 μ_B per iron ion at 300 K. In saturation only 4% of the overall iron concentration is situated in high spin state and contribute to the magnetic signal. The rest occupies low spin S=0 states and does not contribute to M_S.
Also at 500 K we found small hysteresis with coercitive field of H_C=65 Oe and remanescence of M_R=0.015 μ_B/Fe^{2+} and no saturation. At higher temperatures we have to distinguish between two different processes contributing to magnetic signal. The number of permanently situated high spin iron decreases with increasing k_BT and subsequently the ferromagnetic signal. Simultaneously the

phase transition of the amphiphilic mesophase induces spin transition of iron ions into the high-spin states changing the paramagnetic background. The spin transition temperature T_C is estimated to be 315 K and below the paramagnetic signal is neglectable.

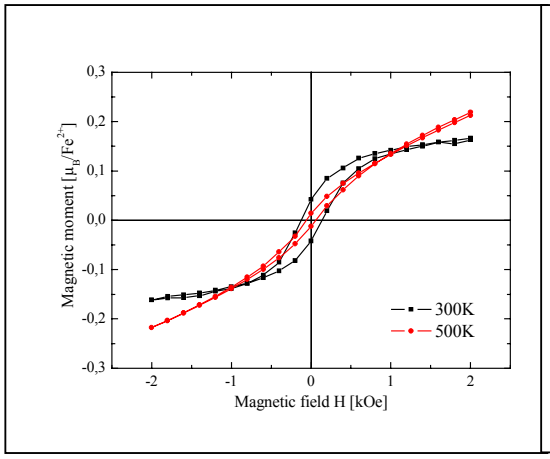

Figure 2a: Measured magnetic moment per iron ion as a function of magnetic field of a 11 monolayer LB film at 300K and 500K. The field was applied parallel to the sample surface.

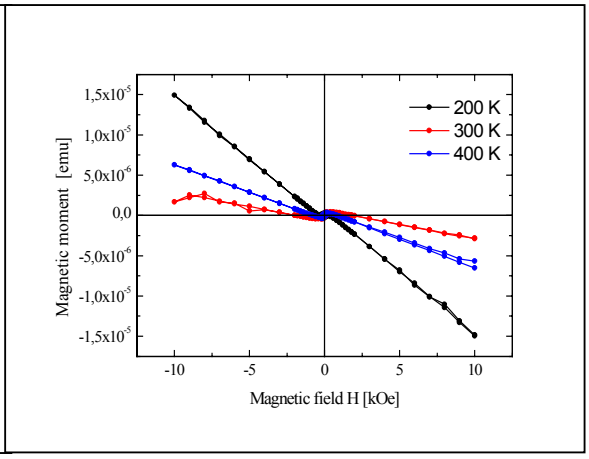

Figure 2b: Magnetic measurements of (Fe^{2+}bis-terpy)-powder containing $Fe^{2+}N_6$ octahedra connected via ligands without amphiphilic molecules.

Figure 2b shows the results of SQUID measurements at Fe^{2+}bis-terpy powder, which is the molecule containing the same $Fe^{2+}N_6$ octahedra connected via the same ligand but without amphiphilic molecules. This material behaves diamagnetic with magnetization close to the resolution limit of the instrument. This result is a clear hint for the fact that the ferromagnetism of the material is originated by the 3D arrangement of Fe^{2+}bis-terpy to the amphiphilic dihexadecyl phosphate molecules.

To support this conclusion element specific X-ray Magnetic Circular Dichroism (XMCD) measurements were performed at the UE56/2 PGM1 beamline at BessyII recently. We measured hysteresis loops in specular and off-specular scattering geometries at the iron L-absorption edge. We measured a cooercitive field strength of ~70 Oe (Figure 3) . This value fairly good corresponds to that value found by the SQUID measurements for magnetizations parallel to the sample surface.

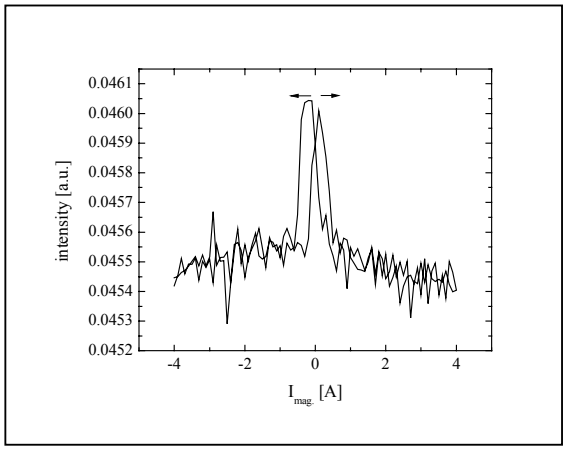

Figure 3: Off-specular measured hysteresis loops at the iron L-edge. Here the reflected intensity at 711eV is measured as function of applied externalfield. The peaks corresponds to cooercitive field strength of ~70 Oe.

This Project is supported by the DFG Schwerpunktprogramm 1137 “Molekularer Magnetismus”.

Is there an ultrafast magnetization response upon optical spin injection in (GaMn)As?

F. Kronast,* R. Osyannikov, A. Vollmer, H.A. Dürr, and W. Eberhardt
BESSY, Albert-Einstein-Strasse 15, 12489 Berlin

P. Imperia and D. Schmitz
Hahn-Meitner-Institiut, Albert-Einstein-Strasse 15, 12489 Berlin

W. Widdra
Max Born Institute, Max-Born-Strasse 2A, 12489 Berlin

G.M. Schott, C. Ruester, C. Gould, G. Schmidt, K. Brunner, and L.W. Molenkamp
Universität Würzburg, am Hubland, 97074 Würzburg

$III-V$ ferromagnetic semiconductors like (GaMn)As have recently received a large interest in connection with new concepts for spin manipulation [1]. In (GaMn)As the Mn atoms replacing Ga provide local magnetic moments and holes due to their acceptor nature. Ferromagnetism is considered to originate from the coupling of valence holes to local magnetic moments [2]. The possibility to manipulate Mn spins in (GaMn)As by the injection of photo induced spinpolarized carriers (conduction electrons / valence holes) has been recently investigated by two experiments [3, 4]. (GaMn)As has a zink-blende structure and bandgap energy of about $1.5eV$ similar to bulk GaAs. Spin polarized electron hole pairs can be excited by band gap photoexcitation with circular polarized laser light. The polarization of the electron hole pairs can be easily changed by reversing the helicity of the laser. A large photoinduced magnetization (up to 15% of the saturation magnetization) was found in ref. [3] using a continuous laser for photoexcitation. Whereas in a time resolved experiment studying the magnetization change on a ps timescale after the photoexcitation by a fs laser pulse almost no effect could be found [4]. However both experiments did not probe the magnetization of Mn atoms directly.

We used the combination of laser and x-ray techniques at BESSY to study the influence of optical pumping on the ferromagnetism in (GaMn)As element specifically with ps time resolution. In contrast to previous experiments we used x-ray magnetic circular dichroism (XMCD) at the Mn $2p-3d$ resonance to probe the ferromagnetic coupling of the Mn atoms directly. For photoexcitation a modified MIRA Titanium-Sapphire fs laser with the repetition rate reduced to 1.25MHz and synchronized to the BESSY single bunch mode was used. Thus the temporal evolution of Mn magnetic moments could be measured as a function time-delay between laser and synchrotron pulses. The experiments were done at the UE-46 PGM beamline using the HMI spectroscopy chamber. We studied a ferromagnetic, low temperature grown (GaMn)As sample with a Mn concentration of 6% and Curie temperature of $80K$. The laser photon energy was matched to the bandgap of $1.52eV$. XAS measurements were performed by monitoring the sample drain current. The sample was kept at $15K$ in an applied magnetic field of $200Oe$ to align the magnetization along the in-plane easy axis.

Before turning to the time resolved measurements we will describe the effect of continuous laser illumination. We measured the dependence of the Mn magnetization on the flux and polarization of the laser. This was done at gracing incidence of x-ray and laser beam with the magnetization axis parallel to the incoming light and at normal incidence with the magnetization axis orthogonal to x-ray and laser beam. A strong laser induced reduction of the Mn XMCD signal occurred at gracing incidence when the x-ray probing is sensitive to the in-plane magnetization axis of the sample. The decrease of the Mn magnetization scales almost linearly with the flux of the laser as shown in Fig. 1. Within the experimental error this effect is identical for both helicities of the laser polarization. At normal incidence of x-ray and laser beam when the experiment is sensitive to the out-of-plane magnetization axis no XMCD signal and no laser induced magnetization effect could be observed. This demonstrates that the sample is always magnetized along the in-plane easy axis and the laser illumination causes a real demagnetization and does not induce a rotation of the magnetization axis.

For a rough estimation of the number of photoexcited carriers we assume that the penetration depth of the laser is equivalent to its wavelength and all laser photons get absorbed in our sample. At a laser power of $5W/cm^2$ this would lead a number of $10^{11}/cm^3$ to $10^{12}/cm^3$ laser induced holes if their lifetime is about $2ps$ as recently reported by [5]. Comparing these numbers to the intrinsic hole concentrations of (GaMn)As in the range of $10^{20}/cm^3$ to $10^{21}/cm^3$ indicates that the continuous laser illumination is unlikely to induce a significant change in carrier density

*Electronic address: kronast@bessy.de

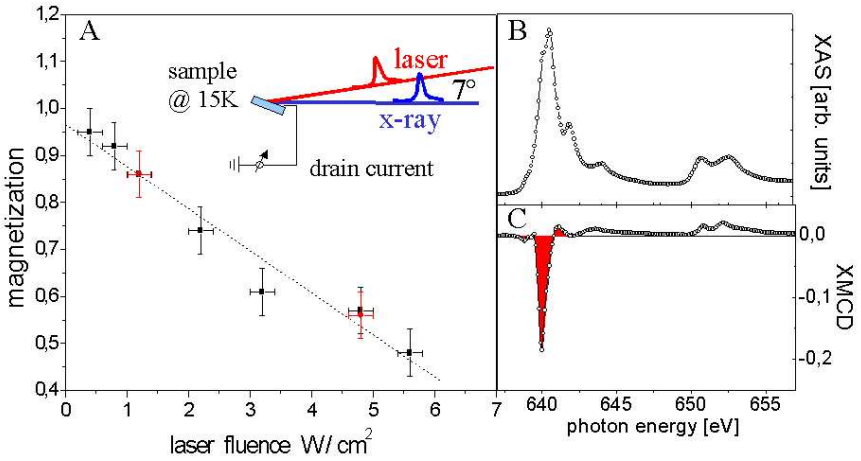

FIG. 1: A) shows the effect of continuous laser irradiation on the sample magnetization at different laser intensities. Excitation by negative laser helicity correspond to black squares and positive laser helicity to red circles, respectively. The dashed black line is a linear fit to the data recorded at negative laser helicity. The sample magnetization was determined by the integral of the XMCD signal at the Mn L_3 edge as shown in C). The corresponding x-ray absorption spectrum is displayed in B). The inset of A) displays a schematic view of the experimental setup. The data were recorded by the total electron yield signal at an incidence angle of 20^o for the x-rays and 27^o for the laser. The photon energy of the laser was $1.52eV$.

or polarization. The fact that we observe no difference for the two laser helicities indicates that the laser induced changes in magnetization are caused by heating up the sample. This may be different in heterostructures such as (In,Mn)As/GaSb where the bandbending at the interfaces can cause an effective mechanism for the separation of electrons and holes preventing their fast recombination [6].

The time resolved data were obtained during the BESSY single bunch low alpha mode with a repetition rate of $1.25MHz$. This reduced the integrated heat load by more than a factor of 50 compared to the continuous laser excitation. Due to the short x-ray pulse length in the low alpha mode the time resolution of our experiment was only restricted by the jitter of the synchronization signal ($\leq 30ps$). To improve the statistics of our data we measured at fixed photon energy and varied only the time delay between laser and x-ray pulses. In addition we choose a negative time delay (x-ray pulse arrives before laser pulse) as a reference and repeated this reference measurement after each point to eliminate experimental drifts.

After normalization of the raw data we evaluated only the relative change of the signal between each delay and the reference. The data displayed in Fig. 2 were recorded at a photon energy of $639.9eV$ corresponding to the maximum dichroic signal at the Mn L_3 peak. At a sample temperature of $15K$ the laser pulse induces a transient decrease of the electron yield signal. Fitting the electron yield signal by the sum of two exponential functions i.e.

$$I = I_o + I_1 \times exp(-t/\tau_1) + I_2 \times exp(-t/\tau_2) \quad (1)$$

results in a time constant of $\tau_1 = 0.44ns$ for the laser excited decrease of the electron yield signal (see inset of Fig. 2) and a time constant $\tau_2 = 74ns$ for the system relaxing into the equilibrium state. $250ns$ after the laser pulse the electron yield signal reaches a level which is constant within the experimental error until the next laser pulse arrives after $800ns$. Within the experimental error this effect does not depended on the laser polarization and also not on the x-ray helicity. Even with the x-ray photon energy tuned away from the Mn 2p resonance we still measure a laser induced change in the drain current signal. Interestingly the effect changes sign when the temperature is raised above the critical temperature of the sample.

The timescale observed for the decrease in the electron yield signal excludes that this effect is due to a direct interaction of laser induced valence holes and Mn spins. The green curve in the inset of Fig. 2 indicates the delay at which a direct interaction would be expected. It represents a convolution of the lifetime of laser exited holes (2ps [5]) with the $10ps$ pulse width of the x-ray probe pulse taking into account the $30ps$ jitter of the synchronization signal. Within the experimental error of about 3% we can exclude the presence of such an ultrafast magnetization response. This is in agreement with recent pump-probe experiments that also observed no changes of the magnetization due to direct interactions of Mn spins with valence holes excited by a optical fs laserpulse [4, 5]. The appearance of the effect

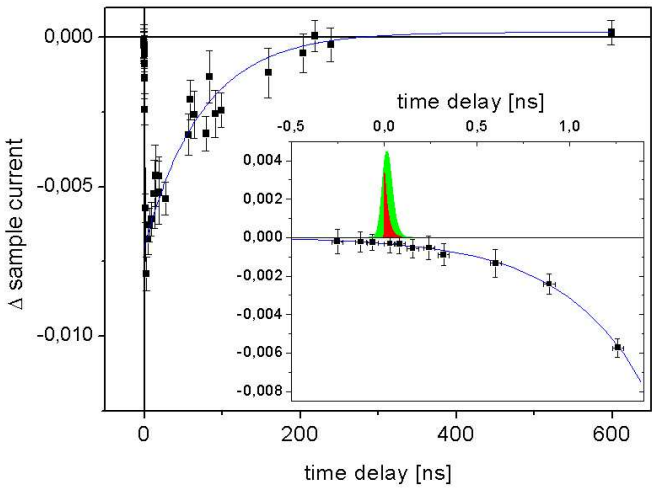

FIG. 2: Changes of the sample drain current for different time delays between x-ray and laser pulse relative to the delay $-500ps$ (x-ray pulse arrives before laser pulse). The photon energy of the laser was $1.52eV$ and the pulse energy $1.6\mu J/cm^2$. The time delays around zero are enlarged in the inset. The red curve demonstrates the carriers excited by the $140fs$ laser pulse assuming a lifetime of $2ps$. The green curve is the calculated convolution of a $10ps$ x-ray pulse with the exited carriers taking into account a synchronization jitter of $30ps$. It indicates the timescale on which a direct interaction of laser induced carriers and Mn spins would be expected. The lines are exponential fits to the data.

even off the Mn $2p-3d$ resonance makes it clear that no change of the magnetic or electronic configuration of the Mn impurities occures. We also can exclude an effect of laser induced carriers. In that case it should appear faster and with opposite sign below T_c.

In magnetic metals and semiconductors a critical behaviour of the resistance is observed [7]. The resistance has a local maximum close to the critical temperature due to the scattering of carriers by magnetic spin fluctuations. Since we measure the drain current a laser induced change in resistance could explain the transient decrease of the signal below and the transient increase above T_c, respectively. This would also explain the slow appearance wit $\tau = 0.44ns$. In GaAs the thermalization between the hot carriers excited by an optical laser pulse and the lattice takes a few tens of ps [8]. The thermalization between phonon and spin system should take even longer since it involves phonon-magnon coupling.

In conclusion, we studied the manipulation of Mn spins in (GaMn)As by optical photoexcitation. I contradiction to earlier results [3] we find a laser induced demagnetization in (GaMn)As using continuous laser illumination. In the time resolved measurement using a fs laser pulse to excite carrier densities up to $10^{18}/cm^3$ we detect no influence on the Mn spins within the lifetime of the valence holes. Only at longer time delays we observe an effect that is likely due to spin fluctuations caused by the thermalization of optically excited carriers. We thank Rainer Schumann for his technical support and the BESSY staff for providing excellent operation conditions.

[1] H. Ohno, Science **281**, 951 (1998).
[2] T. Dietl, H. Ohno, F. Matsukura, J. Cibert, and D. Ferrand, Science **287**, 1019 (2000).
[3] A. Oiwa, Y. Mitsumori, R. Moriya, T. Slupinski, and H. Munekata, Phys. Rev. Lett. **88**, 137202 (2002).
[4] A. Kimel, G. Schott, A. Kirilyuk, D. Yakovlev, G. Kraczewski, W. Ossau, G. Schmidt, L. Molenkamp, and T. Rasing, Phys. Rev. Lett. **92**, 237203 (2004).
[5] G. Khodaparast, J. Wang, J. Kono, A. Oiwa, and H. Munekata, cond-mat/0305017 v2 (2004).
[6] S. Koshihara, A. Oiwa, M. Hirasawa, S. Katsumoto, Y. Iye, C. Urano, H. Takagi, and H. Munekata, Phys. Rev. Lett. **58**, 812 (1987).
[7] F. Matsukura, H. Ohno, A. Shen, and Y. Sugawara, Phys. Rev. B **57**, R2037 (1998).
[8] A. Cavaleri, C. Siders, C. Rose-Petruck, R. Jimenez, C. Toth, J. Squier, C. Barty, K. Wilson, K. Sokolowski-Tinten, M. H. van Heogen, et al., Phys. Rev. B **63**, 193306 (2001).

VUV-XUV Dielectric Function of InN

M. Rakel[1,3], C. Cobet[1,3], R. Goldhahn[2], W. Richter[1] and N. Esser[3]

[1]Institut für Festkörperphysik, TU Berlin, Hardenbergstr. 36, D-10623 Berlin
[2]Inst. f. Physik, Zentrum f. Mikro- und Nanotechnologien, TU Ilmenau, D-98684 Ilmenau
[3]ISAS- Institute for Analytical Sciences, Albert-Einstein-Str. 9, D-12489 Berlin
BMBF (DESY): 05 KS4KTB/3

An ellipsometric study on InN and GaN in a spectral region from 2.5 till 30eV is presented. These nitrides crystallize in the thermodynamically stable wurtzite (hexagonal) structure and in the metastable zinc blende (cubic) structure. Especially for InN relatively few experimental studies of the optical properties have been carried out although the recently found small band gap value of 0.7 eV increases the possible emission range of III-nitride optoelectronic devices from the deep UV down to the near IR region. A further advantage of InN is the small electron effective mass what leads to a large saturation velocity. That makes InN to a promising material for high speed or high frequency electronic devices.

By taking advantage of using linear polarized light in an ellipsometric measurement, the dielectric tensor components corresponding to the electric field vectors along the crystallographic axes, can be separately examined. This allows a separation of direction dependent electronic contributions and thus a study of the anisotropy of the chemical bondings. In particular for the wurtzite structure (coordination number 4) the anisotropy in the chemical bonds along the c axis and in the plane (slightly tilted with respect to the c plane) defines the amount of optical transitions in different directions. For the ellipsometric investigation of this anisotropic electronic properties hexagonal samples are required for which the c-axis lies in the surface plane, like in m-plane GaN (1-100) and a-plane InN (11-20). As recently reported in Ref. [6] one succeeded in depositing high quality a-plane InN on r-plane sapphire with an AlN nucleation and GaN buffer layer using plasma assisted MBE. By use of these samples measurements of the different components were realized by rotating the sample in the two high symmetry orientations were the optical axis is either parallel or perpendicular to the plane of incidence.

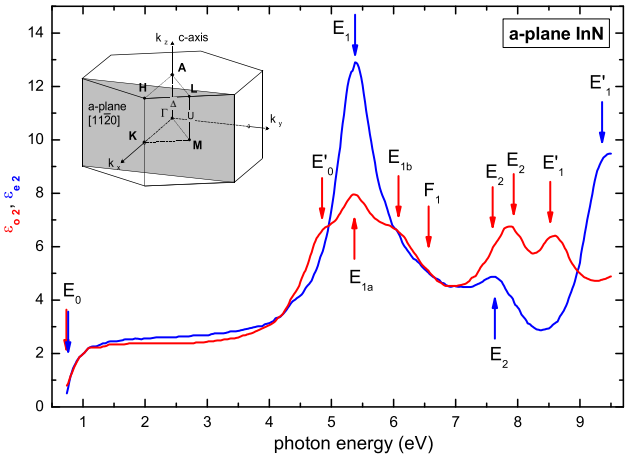

Figure 1: The imaginary parts of the ordinary ε_{o2} and extraordinary ε_{e2} DF of a-plane InN in the spectral range of interband transitions.

The ordinary and extraordinary dielectric function (DF) where determined the first time with the BESSY ellipsometer at the 3m-NIM-monochromator in the spectral range above the common band gap of about 0.7 eV [4, 5]. The imaginary parts of both components (Fig. 1) show remarkable differences. While for the ordinary component at least seven absorption structures at 4.82, 5.38, 6.18, 6.54, 7.66, 7.94 and 8.54 eV contribute to the DF, we can identify only three at 5.40, 7.61 and 9.16 eV in the extraordinary component up to 10 eV . Furthermore, correlated absorption peaks differ in the magnitude and are shifted in their energy against each other. A heuristic assignment of the different structures can be found in comparison with earlier results on wurtzite-type GaN [3] and *CdS* or *CdSe* [1]. Within this assignment the cubic E_1 transitions are understood in terms of critical points (CP) or lines along the $\pm[111]$ directions of the corresponding zinc-blende Brillouin

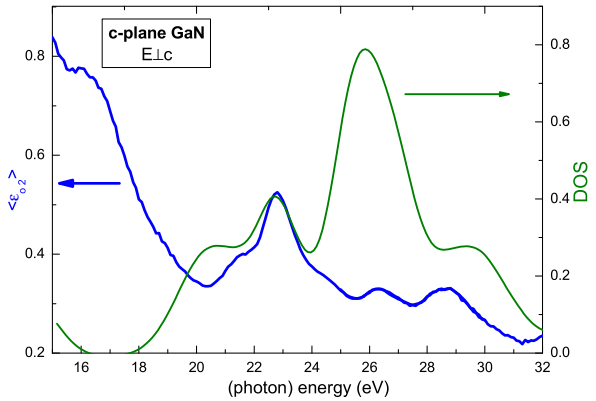

Figure 2: Imaginary part of the hex. GaN ordinary DF in comparison with the DOS of p-like conduction bands (DFT-LDA [7]). The energy position of the DOS was calculated in relationship to the Ga3d-core states and shifted by 1.5 eV.

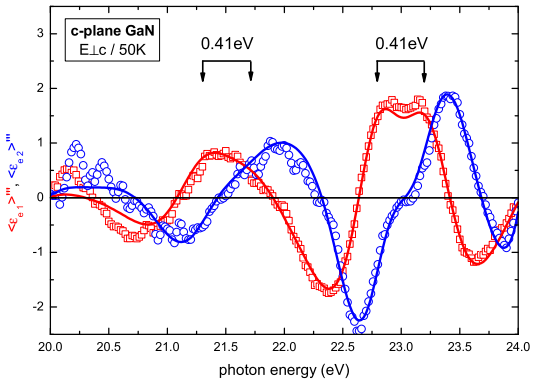

Figure 3: Third derivative of the ordinary DF of the hex. GaN. Both Ga3d valance band transitions structures show distinct a spin-orbit splitting of 0.41 eV.

zone. In the cubic crystals, these states are degenerated with the corresponding stats in the $\pm[1\bar{1}\bar{1}]$, $\pm[\bar{1}1\bar{1}]$, and $\pm[\bar{1}\bar{1}1]$ directions. The symmetry of the $\pm[111]$ directions are very similar to that of the corresponding $\pm[0001]$ c axis of wurtzite crystals, while the other three split in wurtzite structures from $\pm[111]$ but remain degenerate with each other due to the sixfold symmetry around the c axis. Together with the corresponding cubic E'$_0$ CP this two CP's can be attributed to the three absorption structures at 4.82, 5.38, 6.18 eV in the ordinary component. A symmetry consideration indicates that the [111]-like singlet appears only for $\varepsilon_{\|}$ while the $\pm[1\bar{1}\bar{1}]$ triplet should appear for both polarizations. According to this interpretation, the measured extraordinary component shows only one strong absorption structure at 5.40 eV where the $\pm[1\bar{1}\bar{1}]$ triplet is found degenerated with the E'$_0$ transitions. Within this argumentation the following two major absorption structures in the ordinary component of the DF can be attributed to the cubic E$_2$ (located along the $\pm[111]$ direction) and E'$_1$ CP's. But in the hexagonal crystal structure no associate high symmetry axis could be related to the cubic $\pm[111]$ direction. Consequently, the correlated hexagonal InN E$_2$ CP's are found in both components of the DF while the E'$_1$ CP is showing again a strong anisotropic behaviour. But, in the limitation of the presented spectral range no comparable splitting in the ordinary component is found like for the E$_1$ transition. Anyhow, discrepancies beyond the pure symmetry argumentation can be attributed to anisotropic chemical bonds parallel and perpendicular to the c axis.

In a spectral region above 15eV the DF of GaN and InN is dominated by optical transitions between the Ga3d/In4d semicore and the p-like unoccupied (conduction) electron states. Because of the nondispersive behaviour of the d-band one gets a characteristic view of the p-like conduction bands. The electron transition is governed by the dipole selection rules what results in the fact, that a d electron can only be excited to p- or f-orbital. In the case of c-plane GaN the DFT-LDA calculations for the p-like DOS are fitting into the experimental spectra what is shown in Fig. 2. With a resolution better than 0.02eV we find also evidences for the predicted spin-orbit splitting of the d-bands. Similar to the theoretical predictions or photo emission measurements we determine a spin-orbit splitting of 0.41 eV for GaN (Fig. 3). In Fig. 4 the DF of a-plane InN is shown for both components. From the pure symmetry argumentation no principle differences are expected between the hexagonal ordinary and extraordinary or the cubic DF. But the two measured components differ considerable in the principal line shape and emphasis the assumption of a large anisotropy in the chemical bonding. For the In4d levels a somewhat higher spin-orbit splitting is predicted than for GaN. Possibly, this is not resolved due to the low crystal quality of the available samples.

For the XUV-measurements (12-30eV) the TGM-4 beamline was used as light source.

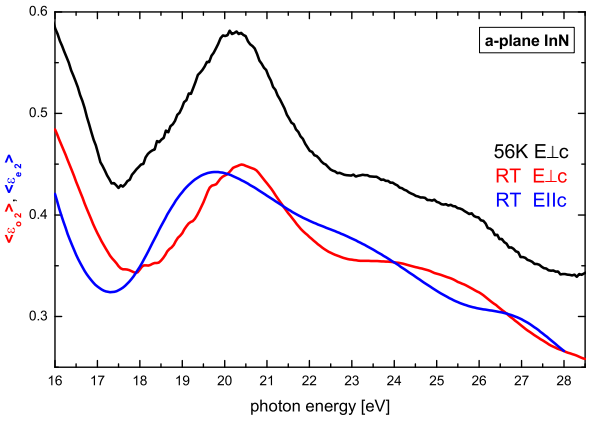

Figure 4: Imaginary parts of the ordinary ε_{o2} and extraordinary ε_{e2} effective DF of a-plane InN in the spectral range of the In4d excitations.

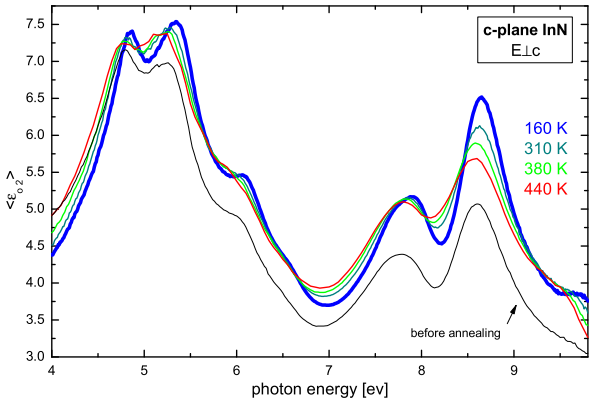

Figure 5: Imaginary part of the ordinary ε_{o2} DF function of c-plane InN at different temperatures.

Finally VUV ellipsometric measurements were also taken on c-plane MBE grown InN (1070 nm layer thickness) at the 3m-NIM1 beamline. It is assumed that InN forms a native oxide on the surface and is highly water contaminated while leaving it in air atmosphere. In order to get rid of these contaminations, the sample was annealed at 480°C for 10 min in UHV. This kind of "deoxidation" yields to a considerable change in amplitudes like shown. For temperature dependent investigations, spectra were taken between 440 K and 160 K. Fig. 5 shows a comparison with the room temperature spectra. Like expected there is a blue shift for the low and a red energy shift for the high temperature structures, whereas the low temperature spectra has a much sharper quality. After first and second derivation analysis under consideration of the Kramers-Kronig consistency we can clearly verify seven interband transition peaks for energies till 10eV as discussed above. But surprisingly, we observed remarkable variations in the amplitude behaviour for the different interband transitions, especially for the structure at 8.6 eV. The latter shows a much stronger increase of peak height with decreasing temperature than the other structures. A closed cycle cryostate will be mounted in the future in order to enhance interband transition structures and to resolve the predicted anomalous spin-orbit splittings of the top valence bands [2].

[1] M. Cardona. *Solid State Communications*, 1:109, 1963.

[2] M. Cardona and N. E. Christensen. *Solid State Communications*, 116(8):421, 2000.

[3] C. Cobet, N. Esser, J. T. Zettler, W. Richter, P.Waltereit, O. Brandt, K. H. Ploog, S. Peters, N. V. Edwards, O. P. A. Lindquist, and M. Cardona. *Phys. Rev. B*, 64:165203, 2001.

[4] R. Goldhahn, V. Cimalla, O. Ambacher, C. Cobet, W. Richter, N. Esser, H. Lu, and W.J. Schaff. *BESSY Jahresbericht*, pages 377–379, 2003.

[5] R. Goldhahn, A. T. Winzer, V. Cimalla, O. Ambacher, C. Cobet, W. Richter, N. Esser, J. Furthmüller, F. Bechstedt, H. Luf, and W. J. Schaff. *Superlattices and Microstructures*, 36:591–597, 2004.

[6] H. Lu, W. J. Schaff, L. F. Eastman, J. Wu, W. Walukiewicz, V. Cimalla, and O. Ambacher. *Appl. Phys. Lett.*, 83(6):1136–1138, 2003.

[7] W. G. Schmidt, 2004. Institut für Festkörpertheorie und -optik, Friedrich-Schiller-Universität Jena, Germany, priv. com.

Stroboscopic XMCD-PEEM imaging of nonlinear spin-wave excitation

A. Krasyuk, F. Wegelin, S. A. Nepijko, C. M. Schneider*, H. J. Elmers and G. Schönhense

Institut für Physik, Johannes Gutenberg Universität Mainz
* Institut für Festkörper- und Grenzflächenforschung, Forschungszentrum Jülich GmbH

We have used time resolved X-ray photoemission electron microscopy (TR-XPEEM) to explore the spatial and temporal character of ultrafast magnetic processes. The preparation of patterned ultrathin films on coplanar waveguides allows the investigation of fast remagnetization processes and spin wave excitations within confined geometries which makes the method interesting for numerous applications in magnetic data storage.

A detailed description of our technique and TR-XPEEM has been reported elsewhere [1,2]. For the presented results the low-α multi-bunch mode was used providing a typical X-ray pulse length below 2 ps. The experiment is realized in a pump-probe like set up, in which the X-ray pulses are used as a probe to acquire XMCD images (Fig. 1). The excitation is realized by an amplified electrical pulse generator which feeds pulses ≤ 7V amplitude at a frequency phased with the synchrotron cavity frequency (500 MHz) into a coplanar waveguide (microstrip line). The magnetic structures are deposited onto the Cu microstrip line by photolithography and ion etching. Short current pulses generate fast magnetic field pulses (Oerstedt field) as illustrated in Fig. 2a. An internal electronics unit controls the delay of the pulse generator with respect to the photon pulse with an accuracy of 10 ps.

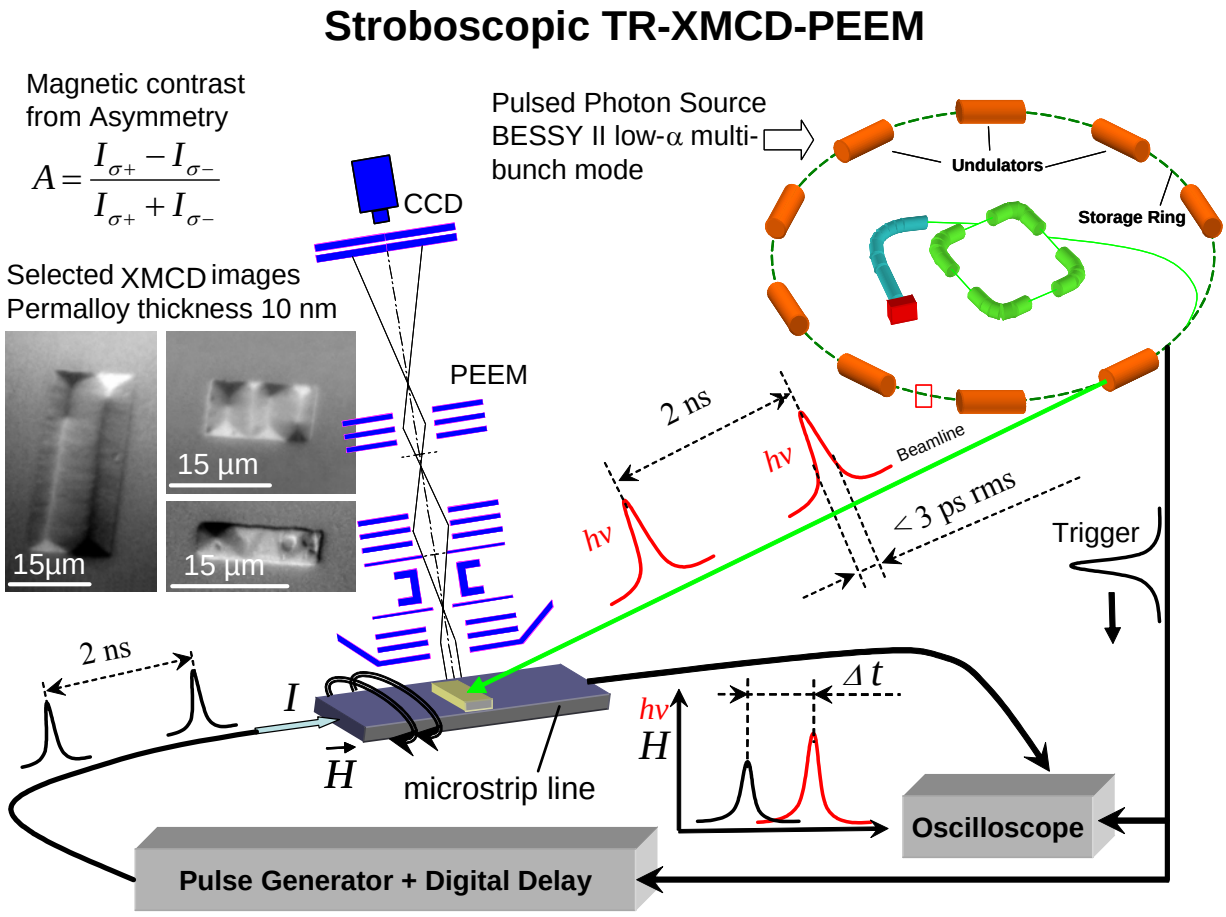

Fig. 1: *Experimental setup of time- resolved observation of remagnetisation dynamics*

Upon stepwise variation of the delay times (minimum increment 10 ps), the XMCD images can be acquired stroboscopically and sequences of remagnetization processes can be recorded. Typically, a jitter between 8 ps and 14 ps has been measured comparing synchrotron bunch marker and pulse generator output. The width of the leading edge (< 200 ps) is smaller compared to the trailing edge (cf. Fig. 2 b). The fast leading edge is associated with Fourier components in the pulse profile that can excite oscillatory eigenmodes with characteristic frequencies up to several GHz [3]. Previously, such modes have been observed in microfocus Brillouin light scattering [4]. Rectangular permalloy microstructures with a thickness of 10 nm were investigated. The XMCD-PEEM imaging of their domain structure utilized the magnetic contrast at the Fe L_3 absorption edge (beamline UE46 PGM). Static domain patterns of structures of 16 × 32, 16 × 8 and 16 × 4 μm^2 are shown in the upper left part of Fig. 1. The magnetic elements show higher-order Landau structures with Neél walls and a cross-tie wall like magnetic ripple inside of the domains (in particular of the largest element on the left).

The microstrip line is oriented so that the external magnetic field is applied parallel to the projected photon impact direction (Fig. 2a). XMCD-PEEM sequences were recorded along the electrical pulse shown in Fig. 2b. The profile of the voltage pulse running along the stripline has been determined utilizing a slight change in magnification originating from the chromatic aberration of the objective lens, see [5]. The peak magnetic field was estimated to be about 0.25 mT. The rectangular magnetic particle exhibits a Néel wall which divides it magnetically into a flux-closed fourfold Landau configuration (depicted in Fig. 2a). Selected images from these series reveal oscillatory behaviour of the magnetization in the areas magnetized perpendicular to the direction of the field pulse **H**. The angle of the magnetization direction with respect to the incident photon beam (projected onto the surface) can be extracted from the quantitative asymmetry values in the observed domain pattern. For the areas of interest marked in Fig. 2a as *1* and *2* we analyzed the gray scale values in the corresponding regions of the sequence in Fig. 3. The result of this gray value analysis is plotted directly as rotation angle in Fig. 2c, curves 1 and 2. The oscillatory behavior of the magnetization direction is obvious. It is related to the excitation of a spin wave in a confined element.

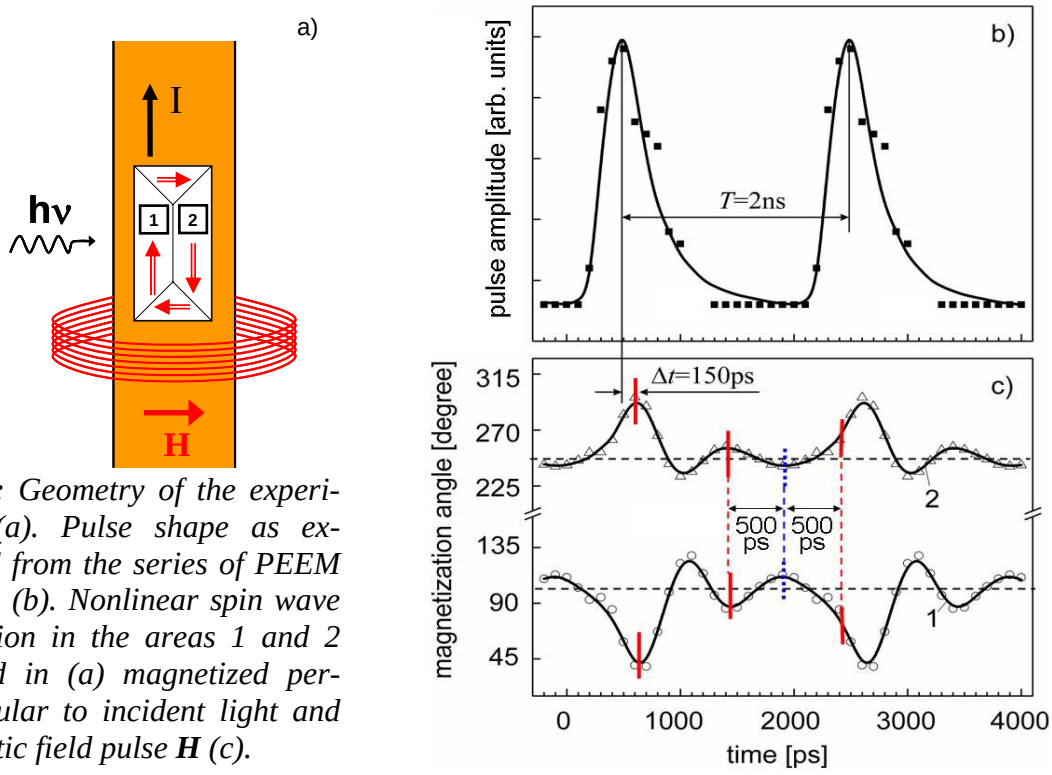

Fig. 2: *Geometry of the experiment (a). Pulse shape as extracted from the series of PEEM images (b). Nonlinear spin wave excitation in the areas 1 and 2 marked in (a) magnetized perpendicular to incident light and magnetic field pulse* ***H*** *(c).*

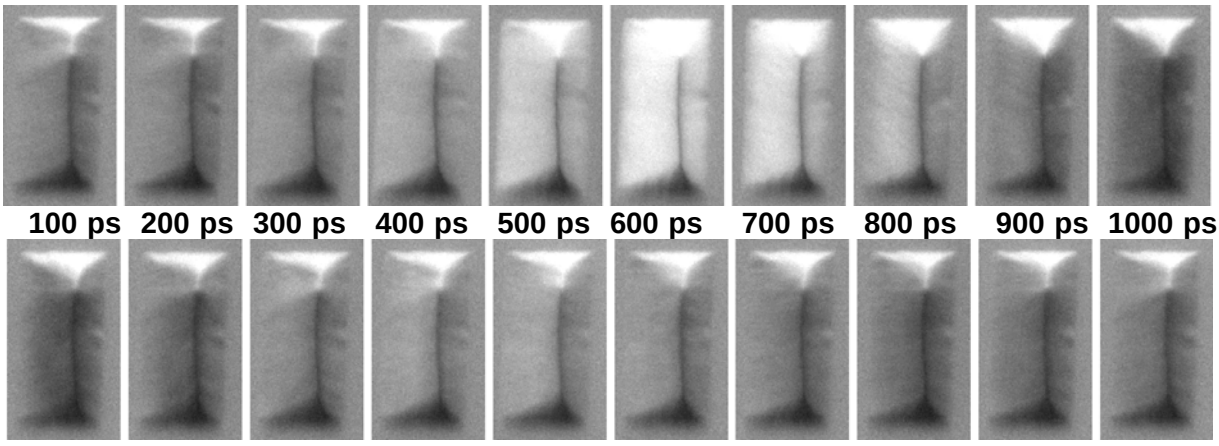

Fig. 3: *Time variation of XMCD-PEEM images. The numbers denote the delay time as defined in Fig. 2.*

The strong contrast variation visible in Fig. 3 reflects high precession angles with the extremum (curve 1 in Fig.2c) reaching 43°, i.e. 60° off the equilibrium angle of 103°. Note that the equilibrium angles (dashed horizontal lines) are rotated away from the symmetric arrangement of 90° and 270° due to the presence of the Neèl wall. Such large precession angles are in the nonlinear regime of spinwaves. The period of T = 2 ns is forced by the sequence of magnetic field pulses, the system responds like a parametric oscillator. In order to guide the eye we have shown two periods in Fig. 2 b and c. The precessional motion of the magnetization vector in the two domains continues during the time when the field amplitude is zero. From the distance of 500 ps between the last two extrema of the precession angle in curves 1 and 2 (indicated by bars) we derive a characteristic eigenfrequency of this precessional mode of about 1 GHz (in the field-free state). The third extremum at 2400 ps is not resolved (though visible in the profile) because it falls already into the left wing of the next forced extremum. In addition, we recognize a phase lag of Δt = 150 ps (corresponding to 0.3 π) between the maximum of the field pulse and the first extremum of the precession angle. This indicates that the system is close to resonant excitation, i.e. the first overtone (1 GHz) of the excitation frequency (being contained in the Fourier spectrum of the pulse) lies in the low-frequency wing of the resonance curve of the oscillator.

Due to the very short light pulses (< 3 ps rms) the low-α mode at BESSY has proven to be most suitable for the investigation of magnetization dynamics. The increment of the time delay can be reduced to the electronic jitter limit of 15 ps and thus ultra-fast magnetization processes in the range of several GHz can be studied (see also [3]). Of particular interest for the future is the possibility of non-stroboscopic illumination and exploitation of the (x,y,t)-resolving delayline image detector for time-resolved acquisition as demonstrated recently [6].

We thank the BESSY staff for excellent support during the low-α mode beamtime and gratefully acknowledge the support by D. Schmitz from HMI. The instrument development was partly funded by BMBF, DFG (Schwerpunktprogramm SPP 1133) und Stiftung Rheinland Pfalz für Innovation.

[1] A. Krasyuk et al., *Appl. Phys.* A **76** (2003) 863
[2] C. M. Schneider et al., *Appl. Phys. Lett*., **85** (2004) 2562
[3] A. Krasyuk et al.; BESSY *Annual Report* 2003 p. 329 and to be published
[4] V.E. Demidov et al., *Appl. Phys. Lett*. **85** (2004) 2866
[5] D. Neeb et al., *J. Phys.: Condens. Matte*r **17** (2005) in print
[6] A. Oelsner et al., *J. Electron. Spectr. Relat. Phenom,* (2005) in print

Imaging of doped semiconductor surfaces using X-PEEM and Nano–ESCA

K. Kroth, G. H. Fecher, J. Morais*, C. Felser, and G. Schönhense
Johannes Gutenberg - Universität, 55099 Mainz
* Universidade Federal do Rio Grande do Sul, Porto Alegre, 91501-970 RS, Brazil

CoTiSb is a semiconducting and paramagnetic compound crystallising in the $C1_b$ Half-Heusler structure [1]. Its paramagnetic state accords to the 18 valence electron rule predicting that the total magnetic moment of 3d-metal based Half Heusler compounds is equal to the difference between 18 and the overall number of valence electrons in one unit cell [2]. Our experiments showed that titanium can be replaced up to 5% by iron without changing the $C1_b$ structure. At the same time, the magnetic moment of the compound raises up to $0.2\mu_B$ per unit cell for the 5% iron doped compound.

Preparation of the samples is done according to the following procedure: Stoichiometric amounts of pure metal granules are arcmelted under argon atmosphere. The ingots obtained by arcmelting are cut into pieces, while one piece (polycrystalline bulk material) is polished and kept for synchrotron measurements and the remaining pieces being crushed for SQUID magnetometry and X-ray powder diffraction measurements as shown in Fig. 1. The diffractogram proves the correct order of the sample. The magnetization curve reveals a vanishing remanence but still a high paramagnetic slope at large fields.

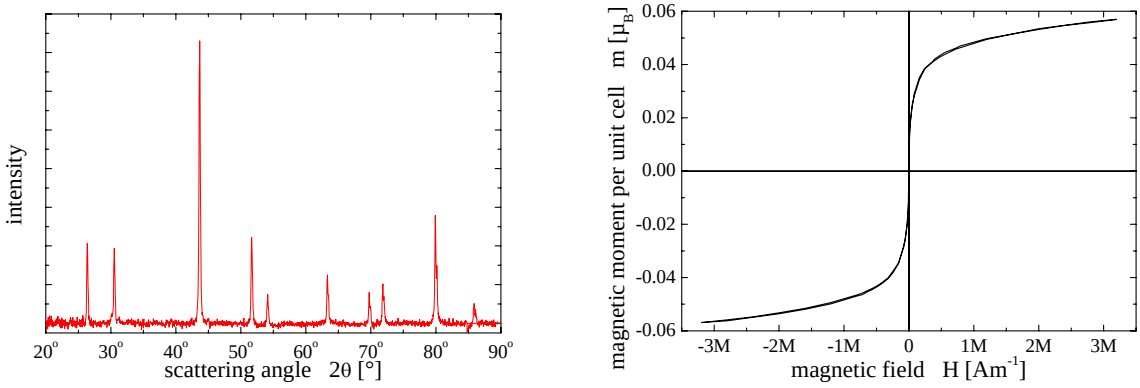

Fig. 1: *$CoTi_{0,99}Fe_{0,01}Sb$ X-ray powder diffractogram (left) and magnetization at 5K (right).*

Synchrotron radiation was applied to investigate the surface of the samples by means of X-PEEM and Nano-ESCA. While taking PEEM images, the sample surface is exposed to soft X-rays with wavelengths corresponding to the L-edge energies of cobalt, iron or titanium. The brightness of the obtained images corresponds to the absorption signal and is used to determine whether the synthesis of ferromagnetic samples was successful, i.e. the intensity of each metal is checked to be uniformly distributed. Observation of magnetic domain structures is also possible by making use of XMCD. For that purpose images are taken with circularly polarized photons with opposite helicities σ+ and σ-. The sum image represents the chemical contrast of Fe (Fig. 2, left). The contrast of the asymmetry image (ratio of difference image and sum image) is then proportional to the dichroic signal at the L_2 or L_3 edge, and domains of opposite magnetisation appear red or blue (Fig. 2, right).

The XMCD image clearly shows a magnetic contrast, i.e. irregularly shaped ferromagnetic domains are present on the sample.

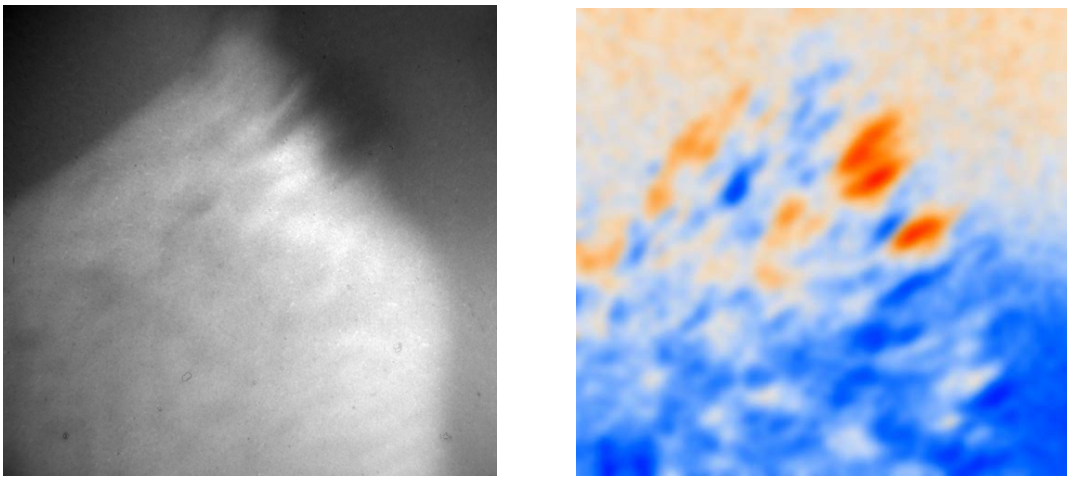

Fig. 2: *Fe L_3-intensity (left) and XMCD-PEEM asymmetry image (right) of a $CoTi_{1-x}Fe_xSb$ (x=0.05) sample. The asymmetry image reveals oppositely magnetized ferromagnetic domains (red and blue). The field of view is about 50 x 50 μm^2.*

A second attempt to produce iron doped CoTiSb has been made by preparing a sample of CoTiSb (polycrystalline) as described above and treating it with Fe ion implantation. During implantation, the surface had been partially covered with a microscopic grid in order to achieve regions on the sample which correspond to the doped compound and others that remain undoped. These structures are seen very well by means of X-ray absorption at the Fe L_3 edge in PEEM (Fig. 3, left) as well as at the Fe 2p emission images taken using the Nano-ESCA (Fig. 3, right). In particular the latter image shows a high contrast ensuring strongly patterned lateral doping profiles.

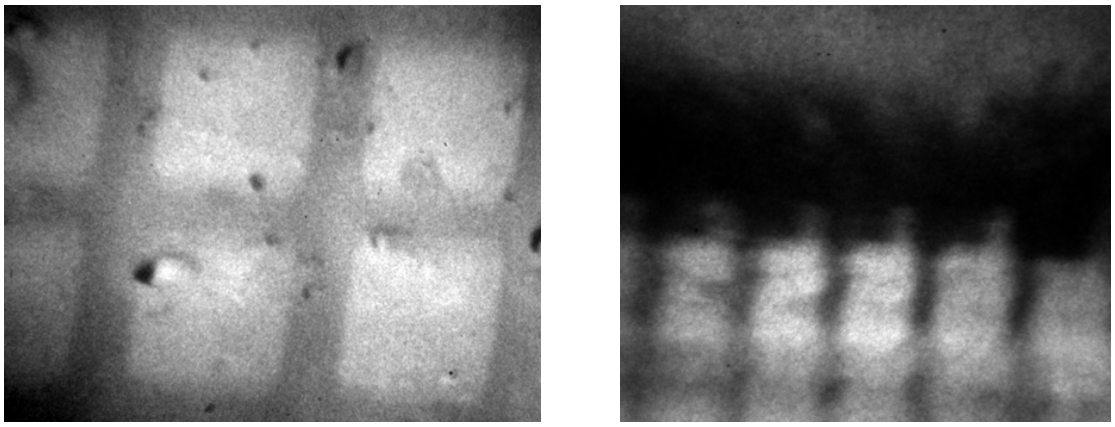

Fig. 3: *X-PEEM image at the Fe L_3 edge (left) and Nano-ESCA image (right) of different regions of a Fe-ion implanted CoTiSb sample. The square structure has a width of 25μm*

We thank the BESSY staff, D. Schmitz (HMI, Berlin), A. Krasyuk, A. Oelsner (Mainz), and N. Weber (FOCUS GmbH) for fruitful cooperation. Financial support by Deutsche Forschungsgemeinschaft (Scho 341/6-1) and DAAD, CAPES-PROBRAL (167/04) is gratefully acknowledged.

[1] P. Villars, L.D. Calvert, *Pearson's Handbook of Crystallographic Data 2nd edition, Band* 2 (1991).
[2] J. Kübler, *Physica* **127B** (2002) 257

Texture modification in nanocrystalline materials using swift heavy ions

Zizak[1], N. Darowski[1], G. Schumacher[1], S. Klaumünzer[1], W. Assmann[2], J. Gerlach[3]

[1]*Hahn-Meitner-Institut, Glienicker Straße 100, D-14109 Berlin,*
[2]*Sektion Physik der Universität München, Am Coulombwall 1, D-85748 Garching*
[3]*Leibniz-Institut für Oberflächenmodifizierung, Permoserstr. 15, D-04318 Leipzig*

Introduction

Physical vapour deposition (PVD) is a standard method used to produce thin polycrystalline layers on industrial scale. Since different lattice planes have different surface energies, during growth the energetically favoured lattice plane is selected to be parallel to the surface. Application relevant material properties depend strongly on the characteristics of the plane parallel to the surface. Mechanical properties, like wearing, are affected by the packing density. As the work needed to emit an electron depends on the surface properties, also electrical and, specially, electro-optical characteristics are influenced. The lattice plane, which is preferred during the deposition, may not be the best choice for application. Large effort in last few years was made to influence the orientation of the grains in deposited layers.
We systematically studied the change in orientation distribution of grains in nanocrystalline vapour-deposited Ti layers after irradiation with high-energy heavy ions.

Experiment

Polycrystalline layers were irradiated with 350 MeV Au ions with different fluences up to 10^{15} ions/cm^2. We studied systematically α-Ti [1], ω-Ti and TiN, varying the layer thickness, grain size, and the direction of the impinging ion beam.
Textures were measured at HMI diffractometer at the KMC2 bending magnet beamline at BESSY using an energy of 8 keV. A combination of an area-sensitive wire detector and intense synchrotron beam allowed very fast acquisition of complete orientation distribution of the sample.

Results

In different nanocrystalline materials the orientation distribution changed in different ways. In case of α-Ti the rotational symmetry around the surface normal disappeared, and the grains aligned with one preferred axis towards the ion beam direction [1]. During irradiation α-Ti undergoes a phase transformation to the high-pressure ω-phase and back, a process which makes the understanding of the already complicated mechanisms in the layer even more difficult. Therefore it was necessary to change the studied system. If the sample is cooled during the irradiation, the ω-phase remains stable even at room temperature and pressure. In case of low-temperature exposure at the beginning the sample transformed completely into ω-phase without further phase during the irradiation. In ω-Ti the texture continuously rotated away from the ion beam direction, shown in figure 1 for increasing fluence, i.e. exposure time. Additionally the cylindrical symmetry was disturbed.
To proof that this effect does occur not only in hexagonal systems, cubic TiN was studied. In nanocrystalline TiN layers both effects, i.e., the disappearing of the cylindrical symmetry and the rotation of the texture, were observed.

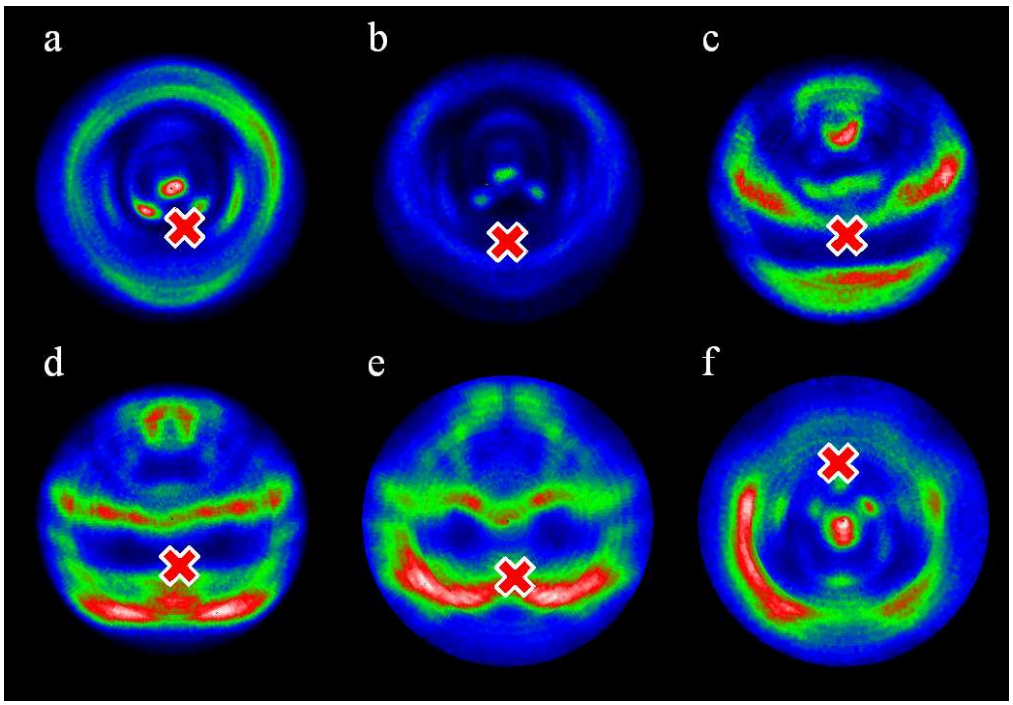

Fig. 1. Orientation distribution (texture) of the (101) planes in ω-Ti layer after irradiation with 350 MeV Au ions with different fluences; The applied fluences are a) 1x10^{14}, b) 3x10^{14}, c) 7x10^{14}, d) 12x10^{14}, and e) 18x10^{14} ions/cm^2. We observe two changes compared to the pattern of an as-deposited sample which is symmetrical around the surface normal: (i) the pattern moves upwards, (ii) the ring structure disappears.
f) The sample irradiated with 7x10^{14} ions/cm^2 (d) was irradiated with the same fluence but with an ion beam in opposite direction. The ring structure moved back, i.e. the original texture was restored. The direction of the ion beam is marked with the red 'X'.

The most astonishing result was the continuous rotation of the orientation distribution observed in ω-Ti and TiN. During the irradiation of ω-Ti with 18x10^{14} ions/cm^2 the texture rotated about 75°. TiN was not irradiated with such a time consuming high fluence, but it showed a similar dependence.

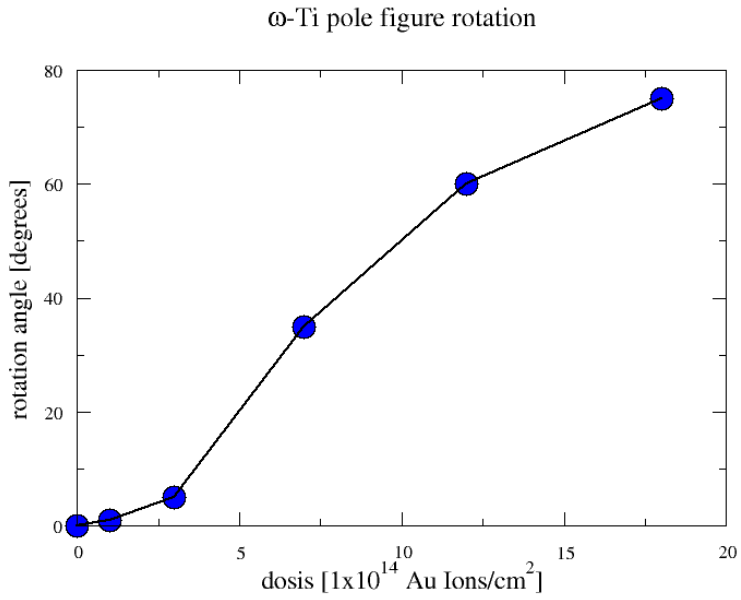

Fig. 2. Dependence of the angle of the grain rotation on the fluence.

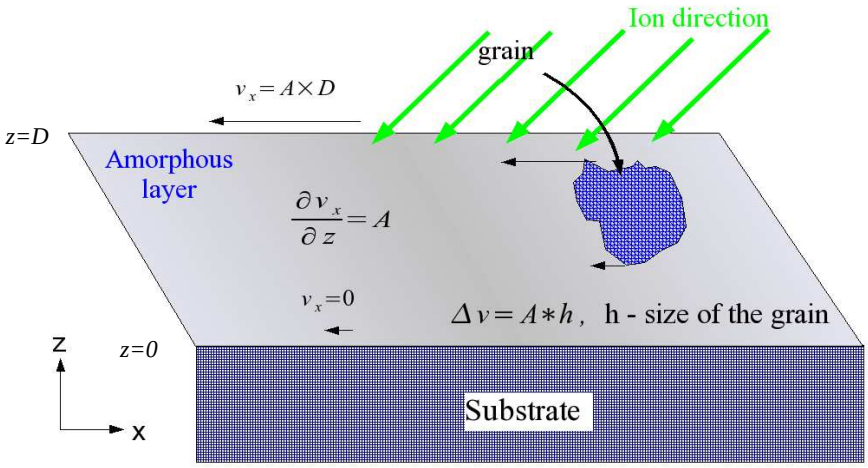

Fig. 3. Simple model for the grain rotation in amorphous matrix.
Due to the geometry of the ion track, the amorphous layer is plastically sheared. A crystalline grain embedded into this matrix would have to rotate.

Discussion

Since the understanding of processes in α-Ti is more complicated than in other cases, we concentrate on the effects observed in ω-Ti and TiN.

Since the texture in ω-Ti rotated almost 75°, we can not explain the rotation through the interaction of the ion beam with the crystalline grains in the sample. A possible explanation could be the interaction between ion beam and isotropic material in the sample. The grain boundary, which is supposed to be amorphous, is in polycrystalline materials few nanometers thick. If the grains are of the size of 10-100 nm, large part of material is located in the grain boundaries, i.e. amorphous.

Indeed, there is a well-known effect, referred as 'ion hammering', which describes anisotropic elongation of amorphous materials during ion irradiation [2]. Swift heavy ions deposit their energy in solids mainly through electronic interaction. Since the collisions with solid nuclei are unlikely at high energies, ions travel through the solid on a straight path. The energy deposition is concentrated in the volume few nanometers around the ion path. Due to the cylindrical shape of this volume, the material is plastically lengthened in the direction normal to the ion path and shortened in the direction parallel to it. If the amorphous layer fixed on the substrate is bombarded with swift heavy ions from a direction other than normal, elongation is transformed into shearing of the layer away from the direction of incoming ion beam.

Further experiments are planed to test this model. If the effect could be proved for other materials, it would be not only an interesting fundamental property of the ion-solid interaction, but also a nice tool for the modification of surface properties of thin layers.

[1] I. Zizak, N. Darowski, G. Schumacher, S. Klaumünzer, W. Asmann, J. Gerlach, I. Großhans, Ti Texture Modification Using Swift Heavy Ions, BESSY Annual Report 2003
[2] S. Klaumünzer, Plastic flow of amorphous materials induced by swift heavy ions, *Mater. Sci. For.* **97-99**, 623-630 (1992)

A study of the (4x2) surface reconstruction of $CuInSe_2$(001) by LEED and synchrotron X-ray photoelectron spectroscopy

Thalia Deniozou, Norbert Esser

Institute for Analytical Sciences, Department Berlin, Albert-Einstein-Str. 9, 12489 Berlin

Keiichiro Sakurai, Shigeru Niki

Research Center for Photovoltaics, Advanced Institutes of Industrial Science and Technology, Tsukuba Central #2,Umezono 1-1-1, Tsukuba, Ibaraki, Japan

Thomas Schulmeyer, Ralf Hunger[1]

Fachgebiet Oberflächenforschung, Institut für Materialwissenschaft, TU Darmstadt, Petersenstr. 23, 64287 Darmstadt

(funding by BMBF contracts 05 SE8KTA3 and 05 KS4RDA/0)

The copper chalcopyrite semiconductors $CuInSe_2$, $CuGaSe_2$ and $CuInS_2$, and their solid solutions are successfully applied as polycrystalline absorber films in thin film solar cells [1, 2]. For a further optimisation of these devices, the understanding of the function of grain boundaries becomes ever more important. A model system for grain boundaries, i.e. internal surfaces, are the surfaces of single crystals or epilayers.

We have developed two surface preparation routes, by which clean and ordered copper chalcopyrite (001) surfaces can be prepared: (i) a selenium capping and decapping process in conjunction with the MBE of $CuInSe_2$ [3] (ii) a combined sputter/annealing process demonstrated for MOVPE-grown $CuGaSe_2$ [4]. Before these developments, surface reconstructions of cleaved single crystals or epilayer surfaces had not been reported, yet [5, 6]. In laboratory experiments we had found that by decapping and/or sputter+annealing of $CuInSe_2$(001) epilayers a (4x2) surface reconstruction can be prepared. In order to understand the chemistry and structure of this reconstruction, we have analysed such surfaces by high-resolution synchrotron photoelectron spectroscopy.

Near-stoichiometric $CuInSe_2$(001)/GaAs epilayers were grown by molecular beam epitaxy and subsequently selenium capped at the AIST [3, 7]. They were brought to BESSY and introduced into the SoLiAS experimental station [8]. After thermal desorption of the covering selenium cap layer by a vacuum anneal to ~350°C, the $CuInSe_2$(001) surfaces showed a low-energy-electron-diffraction pattern with a faint (4x2) superstructure, shown in Figure 2a). Subsequently, the surface was exposed to several sputtering cycles with 0.4 keV Ar ions, during which the sample was kept at an elevated

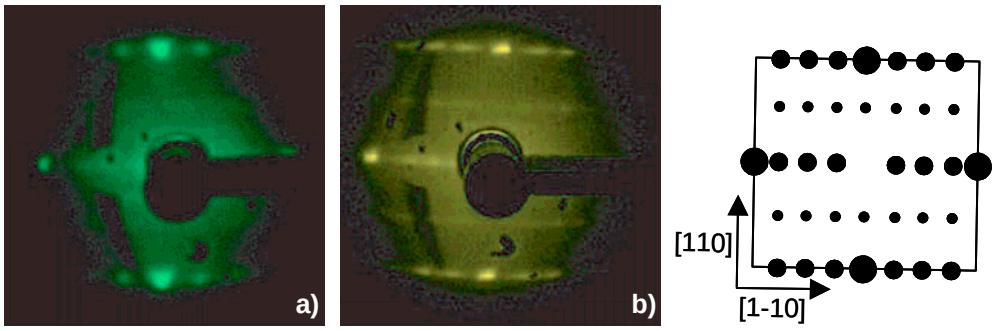

Figure 1: LEED patterns of $CuInSe_2$(001) after decapping (a) and after 2.5 hours Ar sputtering and simultaneous annealing (E_p = 61 eV). The initially faint 4x2 superstructure becomes brighter and sharper with the sputter/ anneal treatment. The spots become elongated along [1-10] which indicates a pronounced step formation.

[1] hunger@surface.tu-darmstadt.de

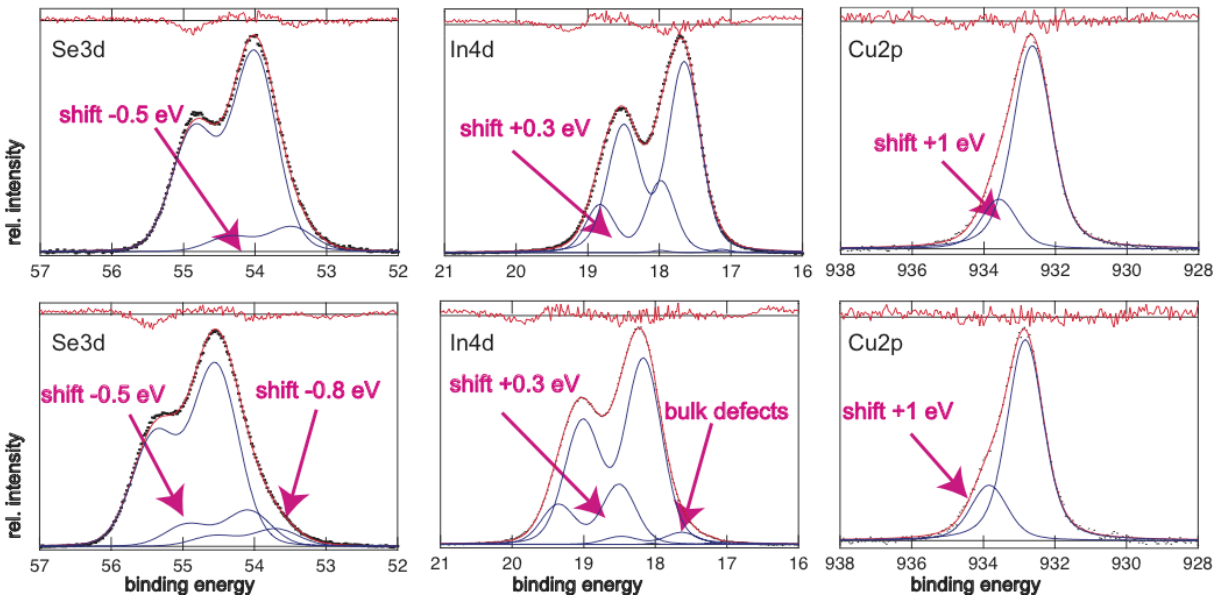

Figure 2: Core level photoelectron spectra of $CuInSe_2$(001) after decapping (top row, faint 4x2) and after several sputter/annealing cycles (bottom, clear 4x2, stepped). The Se3d and In4d photoelectron spectra were excited with hν = 95 eV, the $Cu2p_{3/2}$ emission line with hν = 1138 eV. Surface-related components were observed in these core levels and fitted by Voigt profiles.

temperature around ~350°C. After an initial blurring of the LEED pattern, a clear (4x2) superstructure reappeared (Figure 1b) after 2 hours of simultaneous sputtering and annealing. The elongation of the spots along [1-10] is indicative of surface steps.

The preparation steps were analysed by photoelectron spectroscopy in normal emission, using a Phoibos 150 analyser on the U49/2-PGM2 undulator beamline of BTU Cottbus. Yet the decapped surface appeared clean and free of carbon or oxygen contamination. The core level spectra of Se3d, In4d, and $Cu2p_{3/2}$ are displayed in Figure 2. Surface core level components were identified by their excitation energy dependence and analysed by curve fitting. The analysis suggests that the (4x2) surface comprises copper and indium as well as selenium surface atoms. We propose for the structure of the CuInSe2-(4x2) surface a Se-terminated surface with ¼ monolayer of indium and copper adatoms, where the non-covered Se atoms dimerize [9]. Such a (4x2)-structure is compliant with the electron counting rule [10] and was discussed for the binary analogue ZnSe(001) [11].

Acknowledgements

We thank Patrick Hoffmann of BTU Cottbus for the ever careful commissioning and maintenance of the U49/2-PGM2 beamline. The BMBF travel grant No. 05 ES3XBA/5 (T.S.) is gratefully acknowleged.

References

[1] U. Rau and W. Schock, Appl. Phys. A **69** (1999) 131.
[2] R. Hunger, K. Sakurai, A. Yamada, P. Fons, K. Iwata, K. Matsubara and S. Niki, Thin Solid Films **431-432** (2003) 16.
[3] R. Hunger, T. Schulmeyer, A. Klein, W. Jaegermann, K. Sakurai, A. Yamada, P. Fons, K. Matsubara and S. Niki, Surf. Sci. **557** (2004) 263.
[4] T. Deniozou, N. Esser, S. Siebentritt, P. Vogt and R. Hunger, Thin Solid Films (2005) In Press.
[5] R. Scheer, Research Trends in Vacuum Science and Technology **1** (1997) 77.
[6] R. Hunger, C. Pettenkofer and R. Scheer, Surf. Sci. **477** (2001) 76.
[7] S. Niki, Y. Makita, A. Yamada, O. Hellman, P.J. Fons, A. Obara, Y. Okada, R. Shioda, H. Oyanagi, T. Kurafuji, S. Chichibu, H. Nakanishi, J. Cryst. Growth **150** (1995) 1201.
[8] T. Mayer, M.V. Lebedev, R. Hunger and W. Jaegermann, Appl. Surf. Sci. (2004) in press.
[9] T. Deniozou, N. Esser, S. Niki and R. Hunger, in preparation.
[10] M.D. Pashley, Phys. Rev. B **40** (1989) 10481.
[11] C.H. Park and D.J. Chadi, Phys. Rev. B **49** (1994) 16467.

X-ray natural birefringence in graphite

S. Valencia, W. Gudat, F. Senf and P. R. Bressler
BESSY GmbH, Albert-Einstein-Straße 15, D-12489 Berlin, Germany
H.- Ch. Mertins
University of Applied Sciences Münster, Stegerwaldstr. 39, D-48565 Steinfurt, Germany
P. M. Oppenneer
Dept. of Physics, Uppsala University,Box 530, S75121 Uppsala, Sweden

Graphite or related graphene layer materials are considered to be promising candidates for applications in future spin electronic devices because of the possible existence of ferromagnetism. This has been studied theoretically [1-3] and experimentally [4-6], as well as the possibility to become super-conducting after electron doping [7]. Moreover, in 1998 Machavariani [8], inspired by measurements of anisotropies in the x-ray reflection from hexagonal BN crystals, predicted the existence of a large x-ray natural birefringence in reflection from graphite. This optical effect could have technical and scientific impact since, it would allow the development of new soft x-ray components such as quarter-wave or half-wave plates.

In this report we demonstrate experimentally the existence of the x-ray natural birefringence in reflection from graphite. The effect, which appears due to different optical constants in two non-equivalent crystallographic axes, manifests itself as a rotation of the polarization plane and ellipticity appearing upon reflection of linearly polarized synchrotron radiation. By means of a complete polarization analysis of the reflected light across the C 1s edge of a highly-oriented pyrolytic graphite (HOPG) sample, extraordinarily large birefringence rotation and ellipticity values up to ±90 and 30 degrees have been found, respectively.

Our proposition, the observation of the x-ray natural birefringence, is compellingly underpinned by supplementary measurements of the Stokes parameters and the x-ray natural dichroism, for which analytical expressions can be derived relating these spectra to the birefringent polarization spectra . Moreover our finding is supported experimentally by corresponding measurements of the effect in an amorphous carbon sample exhibiting negligible birefringence as expected.

The room temperature experiments where done at the UE52-SGM beam line at BESSY using the UHV polarimeter [9]. The degree of linear polarization was P_L>0.99 and the spectral resolution near 280 eV was $\Delta E/E$=2000. The experimental set-up is shown in Fig. 1a. The incident light is at gracing angle to the surface (θ_i= 87.5 degrees with respect to the normal) of the sample while the polarization plane is tilted 45 degrees with respect to the refraction plane. The polarization of the reflected beam was analyzed by rotating a W/C reflection multilayer (25 periods, of 3.09 nm each, angle of incidence close to the Brewster angle) around the azimuthal angle γ (see **Fig. 1**) while the reflected intensity was monitored by a GaAs:P diode.

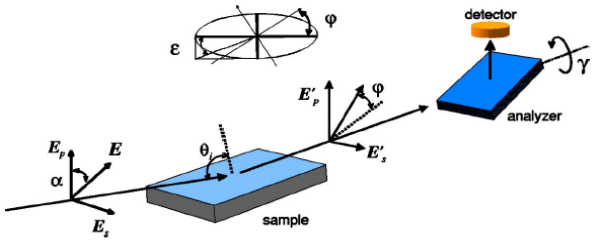

Fig. 1Experimental setup.

In such geometry the incident light presents components of both *s*- and *p*-polarized light. The optical axis of graphite is normal to the surface. As is well known the dielectric tensor of graphite presents -accounting for the hexagonal crystal symmetry- two non equal diagonal elements, denoted $\varepsilon_\perp$ and $\varepsilon_\parallel$, which refer to the directions perpendicular and parallel, respectively, to the optical axis of the film..

The rotation of the polarization plane (φ) as well as the ellipticity (ε) after reflection can be expressed directly in terms of the reflections coefficients for *s* (r_s) and *p* (r_p) [10, 11] polarized light. A simplification of the final expression can be obtained by taking into account the selected gracing incidence geometry and keeping terms to first order in the small quantity $\Delta=\varepsilon_\perp-\varepsilon_\parallel$:

$$\tan 2\varphi + i \sin 2\varepsilon \approx 2(n_\perp^2 - n_o^2)^{1/2} \frac{\sin\beta}{n_o} + \frac{n_o \Delta \sin\beta}{(n_o^2 - n_\perp^2)^{3/2}} \qquad (1)$$

where $\beta=\pi/2-\theta_i$ and n_o is the optical constant of the initial dielectric medium.

The first term of eq. 1 is not related to the natural birefringence since it is present even for isotropic materials, while the second one appears only for anisotropic materials ($\Delta=\varepsilon_\perp-\varepsilon_\parallel\neq 0$). This expression shows also why this effect has not yet been detected in the visible regime, since the second term is much smaller than the first one. On the other hand, in the soft x-ray regime, where n_o and $n_\perp$ are both very close to one, the first term nearly vanishes and can be neglected in front of the second one, which is strongly enhanced due to its $(n_o^2 - n_\perp^2)^{-3/2}$ dependence.

The rotation and ellipticity, φ and ε, can also be related to the conventional Stokes parameters by $tan2\varphi=S_1/S_2$ and $sin2\varepsilon=S_3$, where S_1, S_2 and S_3 are determined by polarization analysis of the reflected light. The former quantities refer to degree of linear polarization in the x-k plane and in the plane diagonal to the x-k and y-k planes, respectively, with k the wave vector of the light. The later reflects the degree of circular polarization.

This notation is useful for demonstrating that the x-ray birefringence rotation can also be measured by means of an intensity measurement of the s ($R_s=\left|r_s\right|^2$) and p ($R_p=\left|r_p\right|^2$) reflectivities. By the definition of the asymmetry parameter $A=(R_s-R_p)/(R_s+R_p)$ we found that

$$A = S_1 \quad and \quad at \quad gracingincidence \quad A \approx 2\varphi, \tag{2}$$

which means that at grazing incidence A is proportional to the difference between $\varepsilon_\perp$ and $\varepsilon_\parallel$. The asymmetry represents then the x-ray natural dichroism in reflection, a pure intensity effect.

Similar results where recently found for the longitudinal magneto-optical Kerr effect (*L-MOKE*) which also needs polarization analysis for its direct determination. It was however shown that the measurement of the x-ray circular dichroism as well as the transversal-MOKE, both pure intensity measurements, give access to the Kerr-rotation and ellipticity respectively [12].

Fig.2 shows the measured spectra for the reflected light together with the change of the Stokes parameters across the C 1s edge due to the natural birefringence of graphite. Those values have been obtained by fitting the reflected intensity dependence at the analyzer, $I=I_0(1+P(S_1\ cos2\gamma+S_2\ sin2\gamma))$, supposing fully polarized light $S_3=(1-S_1^2-S_2^2)^{1/2}$. The polarizing power of the analyzer was measured to P=0.985.

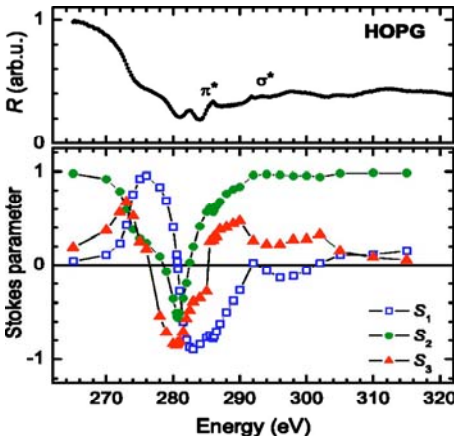

Fig. 2 Reflectivity of the HOPC sample (to) and Stockes parametrs across the C 1s edge

As clearly seen from this figure, the initial linearly polarized light with diagonal orientation (S_2=1) is rotated at about 276 eV by 45 degrees yielding a vertical orientation of the linear polarization, S_1= +1, At about 280 eV the reflected light becomes almost completely circularly polarized (S_3= 0.9) and at 283 eV, the light is again fully linearly polarized, but in the horizontal direction, S_1= -1. Finally at 292 eV the reflected light resembles the incident one with S_2=1. The energy range where those effects take place are thus between 270 and 290eV. This region as shown in Fig 2a is related to the weak van der Waals type π* bonding properties between adjacent planes of graphite, while in the region of the covalent interplanar σ* bonds almost nothing is observed.

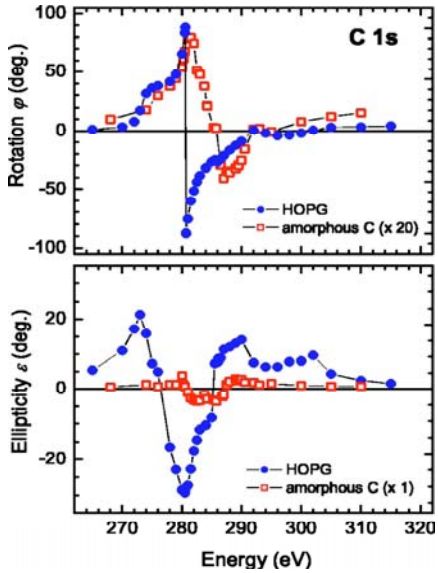

Fig. 3 rotation and ellipticity spectra for the HOPC (fill dots) and amorphous C (open squares) sample.

Fig. 3 shows for the graphite sample the values for the rotation and ellipticity of the reflected light obtained using $I=I_0(1+PP_L\ \cos(2\gamma-2\varphi))$ for fitting the analyzer intensity dependence and $P_L=\left|cos2\varepsilon\right|$. Extremely large values of up to 90 degrees are observed near 280 eV, within the π* related transitions as well as ellipticities of up to -30 degrees (the sign has been determined through Kramers-Kronig relations).

In order to test our conclusion on the origin of the observed birefringence effect, an amorphous carbon sample has been measured for comparision (see also **Fig. 3**). This material is optically isotropic due to its unoriented local sp^2 coordination and no birefringence is expected. Indeed, observed effects are twenty times smaller. The non-zero rotation and ellipticites could be explained by the presence of some sp^2 coordinated carbon at the surface and even by the non-zero contribution of the first term of eq. 1.

Our results thus confirm the predictions of Machavariani [8] where large rotations were expected. However, the agreement with regard to the magnitude of the effect and the shape of the spectra is not convincing. This could be due to the fact that the calculations where done for an angle of incidence θ_i=83º while our experiment was performed at 87º.
Finally in **Fig. 4** we show the direct correspondence between the X-ray natural birefringence effect and the X-ray natural dichroism (eq. 2). The asymmetry *A* obtained after the measurements of the *s* and *p* reflectivities agrees almost perfectly to the change observed in S_1 obtained by polarization analysis. Some discrepancies are present for the range near 280 eV, where the measured reflected signal is perturbed by fluorescence decay, being stronger at the edge of the absorption.

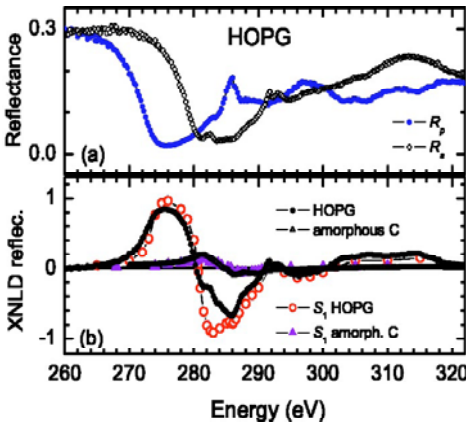

Fig. 4. *Rp* and *Rs* refelctance (top panel) and comparison between the XNLD and the change in S_1 due to the birefringence.

We have demonstrated the existence of x-ray natural birefringence in graphite by means of a complete polarization analysis of the reflected light. The direct relation between such an effect and the X-ray natural longitudinal dichroism has been probed theoretically as well as experimentally, giving access to the possibility of measuring the natural birefringence effect by just an intensity measurement. The large birefringence rotations and ellipticities observed in our experiments open up the possibility of designing novel optical elements like x-ray polarization modulators, quarter-wave or even half-wave plates at the C 1*s* edge allowing for a tunable conversion of linearly to fully circularly polarized X- rays as well as for the rotation of the polarization plane across the carbon 1*s* edge. The latter can be of great interest as e.g., for biological investigations using polarization sensitive x-ray microscopy.

References

[1] K. Harigaya, J. Phys.: Condens. Matter **13**, 1295 (2001).
[2] D. V. Khveshchenko, Phys. Rev. Lett. **87**, 246802 (2001).
[3] G. Baskaran and S. A. Jafari, Phys. Rev. Lett. **89**, 016402 (2002).
[4] T. L. Makarova et al, Nature (London) **413**, 716 (2001).
[5] P. Esquinazi et al., Phys. Rev. B **66**, 024429 (2002).
[6] P. Esquinazi et al., Phys. Rev. Lett. **91**, 227201 (2003).
[7] A.F.Hebard et al., Nature, London **350**,6001991.
[8] V. Sh. Machavariani, Phys. Rev. Lett. **80**, 1541 (1998).
[9] F.Schäfers et al.,Appl.Opt.**38**,4074 (1999)
[10] R.M.A.Azzamand, N.M.Bashara, Ellipsometry and Polarized Light North-Holland,Amsterdam,(1987).
[11] D.S.Kliger, J.W.Lewis and C.E.Randall,Polarized Light in Optics and Spectroscopy, Academic Press, Boston, (1990).
[12] H.-Ch.Mertins et al., Phys.Rev.B **69**,064407 (2004).

Energy dispersion of 4*f* electron states of the heavy-fermion compound $YbIr_2Si_2$

S. Danzenbächer,[1] D.V. Vyalikh,[1] Yu. Kucherenko,[2] Yu.S. Dedkov,[1] C. Laubschat,[1]
Z. Hossain,[3] Ch. Geibel,[3] and S.L. Molodtsov [1]

[1] *Institut für Festkörperphysik, Technische Universität Dresden, D-01062 Dresden, Germany*
[2] *Institute of Metal Physics, National Academy of Sciences of Ukraine, UA-03142 Kiev, Ukraine*
[3] *Max-Planck-Institut für Chemische Physik fester Stoffe, Nöthnitzer Strasse 40, D-01187 Dresden, Germany*

Heavy fermion systems are characterized by large effective masses of the conduction electrons that exceed the ones of free electrons by a factor of more than thousand [1]. For rare-earth based solids this effect is due to interactions of the conduction electrons with the partly filled 4*f* shell. The 4*f* orbitals are strongly localized and do almost not overlap each other in the solid. In the framework of the local-density approximation this leads to the formation of narrow bands with a width of less than 1 eV that are intersected by the Fermi energy (E_F). In spite of this energy position close to E_F, however, the 4*f* states usually do not contribute directly to the conductive properties of the systems since due to large Coulomb correlation energies arising from their localized character changes of *f* occupation are accompanied by energy shifts of several eV leading to a break-down of the simple one-particle energy-band picture. Only in cases where two 4*f* configurations are energetically degenerated in the ground-state 4*f* emissions appear at E_F. Respective mixed-valent properties have been observed for many compounds of Ce, Sm, Eu, Tm, and Yb but among them only a few Ce and Yb systems reveal heavy-fermion behavior. Thus, for a deeper understanding of the phenomenon more insight into the interaction of the 4*f* states with the valence band (VB) is required.

In this contribution we report on an angle-resolved photoemission (PE) study of heavy-fermion single-crystalline system $YbIr_2Si_2$(100) using photon energy 110 eV that allows to emphasize 4*f*-derived signals. The experiments were performed at the U125/2-SGM (BUS) beamline applying a display type SIENTA SES-100 analyser.

For the binding-energy (BE) region of the $4f^{13}$ emissions, Fig. 1 shows a series of angle-resolved PE spectra measured along (100) direction in the surface Brillouin zone. The data were taken at different detection angles, Θ allowing systematic variation of the wave vector, ***k*** and a temperature of 49 K. At photon energy 110 eV the cross-section of the Ir 5*d*-derived states are in a Cooper minimum, and since Si 2*p* and Yb 5*d* states are also known to have low cross-section at this energies the spectrum is dominated by Yb 4*f*-derived emissions. Two $4f^{13}$ final-state doublets appear in the spectra: A relatively weak bulk component [Yb 4*f* (b)] is found close to E_F and 1.2 eV BE, respectively, while an additional surface component at 0.8 and 2.0 eV BE,

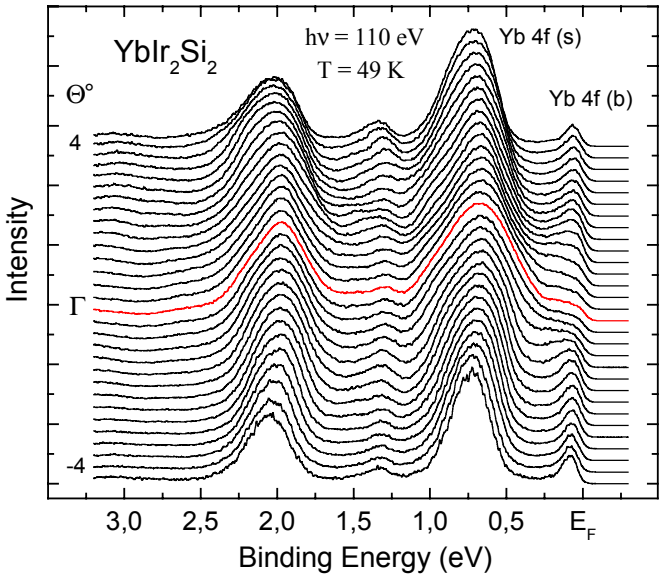

Fig. 1 Angle-resolved PE spectra of $YbIr_2Si_2$ taken close to the normal emission.

respectively, reveals larger intensity. It should be noted that BE position and intensity of the surface emission change as a function of the preparation conditions pointing to varying concentrations and lattice positions of the Yb atoms in the outermost surface layer. In all cases, however, the width of the surface emission was small indicating that the Yb atoms occupy predominantly equivalent surface sites.

Most important features of the measured spectra are ***k***-dependent intensity variations of the 4*f* emissions, which are particularly pronounced for the low intensity bulk component [Yb 4*f* (b)]. In the region of the normal emission the E_F 4*f* signal is significantly suppressed revealing also splitting into two structures, which value changes upon Θ variation. This behavior can also be described as seeming dispersion of the 4*f* states close to the Fermi level. Other bulk 4*f* contribution at 1.2 eV BE shows ***k***-dependent splitting as well although a few degrees away from the normal emission. In order to emphasize the observed changes the following procedure for data evaluation was applied. The intensities of all angle-resolved spectra were summed up and divided by a number of the spectra considered. Then, the averaged signal was subtracted from each individual experimental spectrum. The results are shown in Fig. 2 in form of a grey-scale plot. The presented data can be interpreted as dispersive parts of electron states having 4*f* angular momentum character.

The experimental data were compared with our results of LMTO band-structure calculations for a 5 layer slab of $YbIr_2Si_2$; in the outermost atomic layers of the slab Yb was replaced by divalent Sr to simulate the surface valence transition. Like the $4f^{13}$ component of the bulk emission in the PE spectra, the 4*f* states appear as narrow bands close to E_F and in form of a spin-split side band at 1.2 eV BE. Around the normal emission a group of parabolic VBs with hole-like dispersions is observed between 0.5 and 2.5 eV BE, and another group of VBs with electron-like dispersions is found close to E_F. Since individual bands correspond to different symmetries and momentum characters, only some of them may be observed by PE. Around the intersection points of VB and 4*f*-derived bands of the same symmetry hybridization occurs reflected by the formation of small gaps and *f* admixtures to the VB states. Thus, the scenario described is rather similar to the one observed for $4f^{13}$ bulk experimental emission. For the surface layer, band-structure calculations reveal a pinning of the 4*f* bands at E_F in contrast to the experimental observation. This is due to the hybridization of the *f* states and illustrates that LDA does not describe correctly the many-body properties of the *f* states.

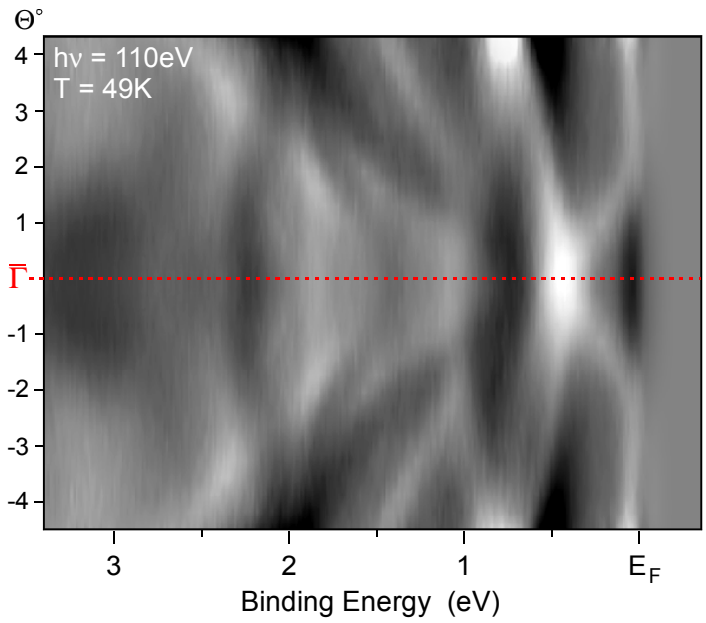

Fig. 2 Dispersive contributions into PE signal of Yb 4*f* states close to the normal emission (see text).

The behavior of the 4*f* emission was described in the framework of a simplified periodic Anderson model [3], where instead of electrons electron holes are considered taking advantage from the fact that for Yb the 4*f* shell is nearly filled. For the divalent surface layer contributions of the trivalent $4f^{12}$ configuration may be neglected in order to achieve ***k*** conservation. In this case, the problem reduces to diagonalization of an effective one-particle Hamiltonian, and the splitting of the 4*f* emission at the intersections with VB states is

assigned to formation of symmetric and antisymmetric linear-combinations of 4*f* and VB states. Additionally, the model predicts the appearance of a weak 4*f* signal with predominant $4f^{14}$ character at E_F in analogy to the "Kondo-peak" in trivalent Ce systems. In fact, a shoulder observed for the 4*f* bulk emission at E_F may be interpreted in this way. For the bulk emissions the situation is complicated due to the involvement of the $4f^{12}$ configuration that leads to a partial integration over ***k***-space and violation of ***k*** conversation. However, since the energy separation between the $4f^{12}$ and the energetically degenerated $4f^{13}$ and $4f^{14}$ configurations is large, $4f^{12}$ admixtures to the ground state and, consequently, to the 4*f* configurations observed close to E_F are expected to be weak and may be neglected. In this case, ***k*** conservation is fulfilled for the respective final states, and the 4*f* bulk emissions close to E_F may be discussed like the surface emissions. Since these emissions appear at energies where the 4*f* bands are expected in the framework of LDA similar hybridization phenomena are expected as predicted in band-structure calculations. In fact, strong interactions of 4*f* and VB states are found at the Γ-point leading to formation of a hybridization gap and strong 4*f* admixtures to the bands below and above the gap in analogy to the PE results.

Acknowledgment: This study was supported by the Sonderforschungsbereich 463, TPs B4 and B16.

References:

[1]. G.R. Steward, Rev. Mod. Phys. **73**, 797 (2001).
[2]. F. Steglich, J. Magn. Magn. Mater **226-230**, 1 (2001).
[3]. A.N. Tahvildar-Zadeh, M. Jarrell, and J.K. Freericks, Phys. Rev. Lett. **80**, 5168 (1998); M.-W. Xiao, Z.-Z. Li, and Wang Xu, Phys. Rev. B **65**, 235122 (2002).

Resonant magnetic soft x-ray scattering at 6 K: The antiferromagnetic phase transition in monocrystalline EuTe films

E. Schierle,[1] E. Weschke,[1] G. Springholz,[2] G. Kaindl[1]
[1]*Institut für Experimentalphysik, Freie Universität Berlin, D-14195 Berlin, Germany*
[2]*Institut für Halbleiter- und Festkörperphysik, Johannes Kepler Universität, A-4040 Linz, Austria*

Magnetic soft x-ray scattering at the lanthanide $M_{4,5}$ resonances provides a very sensitive tool for the study of magnetic structures and allows to study phase transitions of complex magnetic structures in thin films [1]. In a recent study, the technique was applied to chracterize the thickness-dependent magnetic properties of thin Ho metal films [2], where magnetic ordering is induced by indirect coupling of the *4f* moments via long-range RKKY interaction. In comparison to these systems, it is interesting to study the behavior of thin films of EuTe, where the Eu *4f* moments are antiferromagnetically coupled by indirect superexchange via the Te valence orbitals. With a NaCl structure, EuTe closely resembles the classical oxide antiferromagnet NiO, with analogous antiferromagnetic order of adjacent (111) planes. While thin films of NiO are intensively studied by spectroscopic techniques, a characterization of the magnetic structure by resonant scattering has not been carried out up to now. In particular, the strong dipole resonance at the Ni L_3 cannot be exploited, since the lattice parameter is too small for the magnetic superstructure peak to be accessible at this wavelength. The larger lattice parameter of EuTe and the higher photon energy of the Eu M_5 resonance, on the other hand, perfectly match to permit magnetic scattering experiments with very high sensitivity, rendering the system ideal for the study of thin magnetic films with superexchange coupling using this powerful technique.

Due to the strong absorption of soft x rays in air, the experiments require vacuum-compatible diffractometers. Such diffractometers are now available, albeit technical solutions often compromise with respect to sample environment like ultrahigh vacuum (UHV) or low temperatures for the sake of sample manipulation. Magnetic ordering of EuTe occurs around 10 K, which puts serious demands on sample cooling. The experiments reported here were carried out with a UHV-compatible Θ-2Θ diffractometer designed and set up at the Insitut für Experimentalphysik of the Freie Universität Berlin. The instrument allows to use a liquid-He cryostat with rigid sample mounting, providing a minimum sample temperature of less than 6 K.

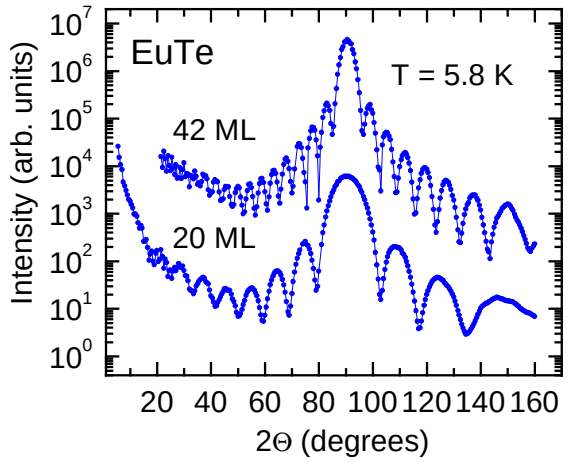

Fig. 1. Magnetic x-ray scattering from monocrystalline EuTe films at the M_5 resonance of Eu. For better comparison, the curves are arbitrarily offset.

In a first experiment, monocrystalline EuTe(111) films with thicknesses of 42 and 20 monolayers (ML) were studied. Samples were prepared by molecular-beam epitaxy on BaF_2 with a PbTe buffer layer and were subsequently covered by a thick PbTe layer [3]. Fig. 1 displays reflectivity curves of the two samples, recorded with a photon energy corresponding to the M_5 resonance maximum. At 5.8 K, i.e., well below the magnetic ordering temperature, pronounced magnetic Bragg peaks are observed, which correspond to the antiferromagnetic superstructure of EuTe. With the high magnetic sensitivity of the method, the magnetic signal can be monitored over several orders of magnitude.

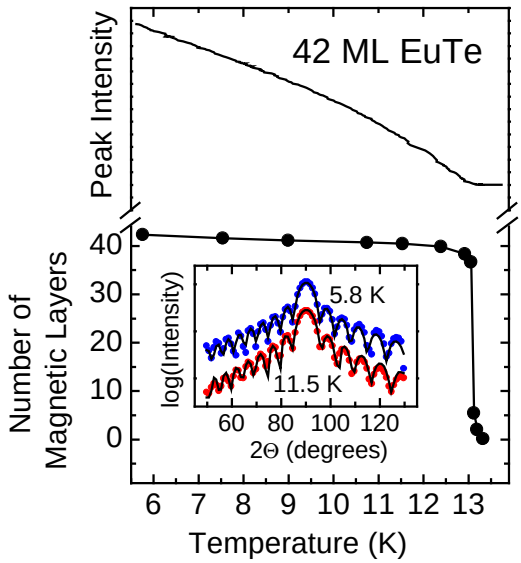

Fig. 2: Peak intensity of the magnetic superstructure as a function of temperature, reflecting the magnetic phase transition around 13 K (top). Bottom: Number of magnetic layers as a function of temperature. The inset displays two representative reflectivity curves.

The magnetic Bragg peaks exhibit pronounced Laue oscillations due to the finite number of layers contributing to the magnetic signal. The present samples are characterized by a high perfection of crystal and magnetic structure, hence, these intensity oscillations are readily resolved. EuTe further represents an ideal case, since the magnetic peak, recorded at the M_5 resonance, occurs almost exactly at the Brewster angle, leading to substantially suppressed charge scattering: The magnetic peak can be monitored virtually free of background, at least at the position of the main maximum.

The Laue oscillations provide detailed information on the number of magnetically ordered planes. At low temperatures (5.8 K), the films are fully magnetized and the number of magnetic layers equals the total number of film layers. With increasing temperature, the side maxima move away from the main maximum as shown in the inset of Fig. 2 for the 42-ML film, demonstrating that the number of magnetically ordered planes decreases. An analysis of data as shown in the inset provides the number of magnetic layers as a function of temperature displayed in the lower panel of Fig. 2. While decaying substantially at the Néel temperature, the number of magnetic layers already decreases well below T_N, from 42 ML at 6 K to 39 ML at 13 K.

The high magnetic sensitivity further permits to extend the characterization of the phase transition to well above the ordering temperature into the regime of critical scattering. The width of the magnetic peaks corresponding to magnetic correlations within the film plane (transverse width) and in the direction perpendicular to the film plane (longitudinal width) is shown in Fig. 3. Obviously, the temperature dependence of transverse and longitudinal width are different, providing information on the anisotropic decay of the magnetic order in the regime of short-range magnetic correlations.

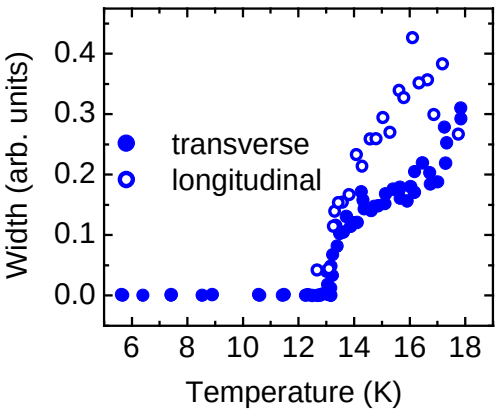

Fig. 3: Temperature dependent widths of the magnetic superstructure peak of the 42-ML-thick EuTe film.

The present results show that the interesting properties of antiferromagnetic phase transitions in thin superexchange films can be readily studied as a function of thickness down to only a few monolayers, which will be the subject of further investigations.

The work was financially supported by the BMBF, project 05KS1KEE/8.

References:

[1] E. Weschke *et al.*, Synchrotron Radiation News **17**, **No. 6**, 11 (2004).
[2] E. Weschke *et al.*, Phys. Rev. Lett. **93**, 157204 (2004).
[3] G. Springholz and G. Bauer, Appl. Phys. Lett. **19**, 2399 (1993) .

Oxygen K-edge X-ray absorption and emission spectra of silicon sub-oxides

A. Hohl[1], T. Wieder[1], H. Fuess[1], A. Njeh[2], and D. Schulze[3]

[1]*Institute for Materials Science, Darmstadt University of Technology, D-64287 Darmstadt, Germany*
[2]*Science Faculty, Materials Physics Laboratory, Sfax University, TN-3018 Sfax, Tunisia*
[3]*Wilhelm Ostwald Institute of Physical and Theoretical Chemistry, University of Leipzig, D-04103 Leipzig, Germany*

The atomic structure of amorphous silicon monoxide (SiO) is a still controversial issue. SiO is a frozen non-equilibrium system of a disproportionation in the initial state. The structure depends strongly on the production conditions. SiO films can have a structure with a broad distribution of silicon (Si) oxidation states. For bulk SiO we recently developed a new structural model, the interface clusters mixture model [1]. This SiO modification consists of amorphous silicon dioxide (SiO_2) clusters, nano-sized clusters of amorphous Si, and a significant amount of sub-oxide (approximately 10 at.%) between the clusters. An increased degree of disproportionation into Si und SiO_2 (increased cluster sizes) and a decreased volume amount of the interface can be observed for increased annealing temperature. On the other hand, amorphous silicon sesquioxide (Si_2O_3) is a single-phase material, which consists only of Si_2O_6 building units (containing Si-Si dumb bells).

The present investigations of the electronic structure of silicon sub-oxides (SiO_x) using oxygen (O) K-edge X-ray absorption and emission spectroscopy (XAS and XES) are of particular interest, as one can get additional information about atomic structural parameters.

The spectra at the O K-edge (about 532 eV) were recorded at room temperature at the U41-PGM beamline. Here, we present XAS data detected in the total electron yield mode. The data were corrected for the energy dependence of the incident beam intensity I_0 by division through monitored I_0. For resonant XES the ROSA spectrometer (Rowland geometry) was used, which had a fixed 90° angle between incident beam and detector. The XES energy resolution was about 1 eV.

We measured and compared spectra for four different modifications of SiO_x as follows. We had a sample of native (unannealed, amorphous), bulk SiO, that is commercially available as Patinal® from Merck KGaA (Darmstadt, Germany). This sample had been produced at approximately 600 °C with a deposition rate of about 200 nm/s in an induction vacuum sintering system. The next sample was a similar piece of bulk SiO, which additionally had been annealed in vacuum for one hour at 1150 °C (thus containing a partly crystallized Si fraction). Then a native film sample of SiO with 1000 nm thickness was measured, which had been deposited at approximately 230 °C with a deposition rate of about 2 nm/s on a 100 nm thick chromium layer on a glass substrate. Furthermore, we measured a dense powder sample of Si_2O_3. In addition, an SiO_2 sample was measured for comparison.

Except a non-significant amount of defect states all O atoms are in the state of bridging O bonded to two Si atoms. Thus, there exist the same unique XAS feature and the same unique XES peak for all samples, and slight differences cannot be related to the bond type.

XAS (Fig. 1) shows slight shifts in energy due to different distributions of local stoichiometry (related to a different electronic band gap) in the structure of different samples.

Fig. 2 shows a comparison of XES for the four samples and the SiO_2 sample. XES peak shapes showed no significant dependence on excitation energy. The SiO film has a narrower band gap (estimated from the difference of XAS and XES energy position). Obviously, the different shifts and shapes of the XES peak cannot be explained by the stoichiometric regions alone (pure SiO_2 is not the limit), but by differences in the Si-O-Si bond angle, in the Si-O

bond length, and at last in stress (strain). Compressive stress and smaller Si-O-Si bond angles could result in intensity at higher emission energy (smaller band gap) and vice versa.
The following interpretation of our XES data is given here as a tentative hypothesis. Bulk SiO contains tensile stress, and annealing causes rearrangement processes including cluster growth. The increasing structural homogeneity [1,2] is reflected in the sharper peak. The SiO film shows compressive stress and a smaller mean Si-O-Si bond angle, as the oxide is influenced by the Si regions [1,2]. Si_2O_3 is expected with low stress resulting from its different production process (polymerization by a sol-gel process [3]).
It seems possible to distinguish not only between the local stoichiometry and the different structural homogeneity, but also between differences in mean bond angles, bond lengths and stress, which can be estimated from the XES peak for bridging O atoms. We will check our results by continuative measurements.

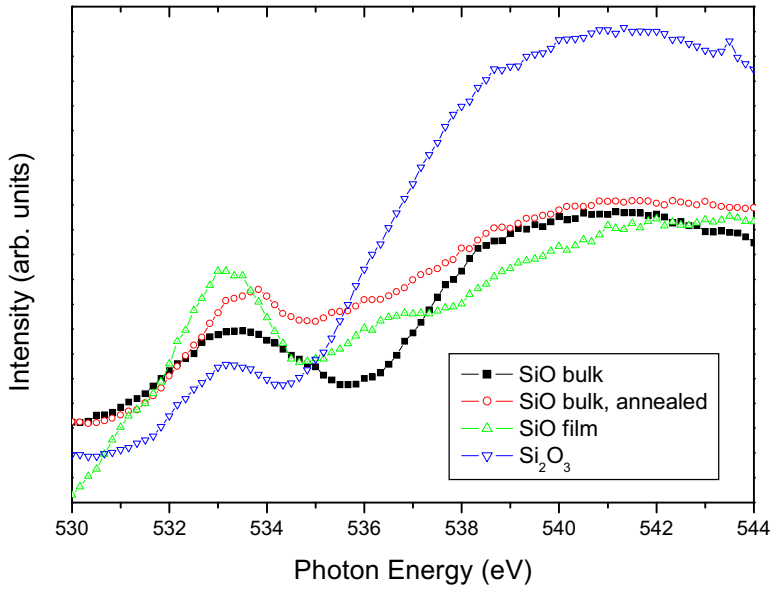

Fig. 1. Oxygen K-edge X-ray absorption spectra for different samples as described in the text. The spectra have been scaled to comparable intensity for clarity.

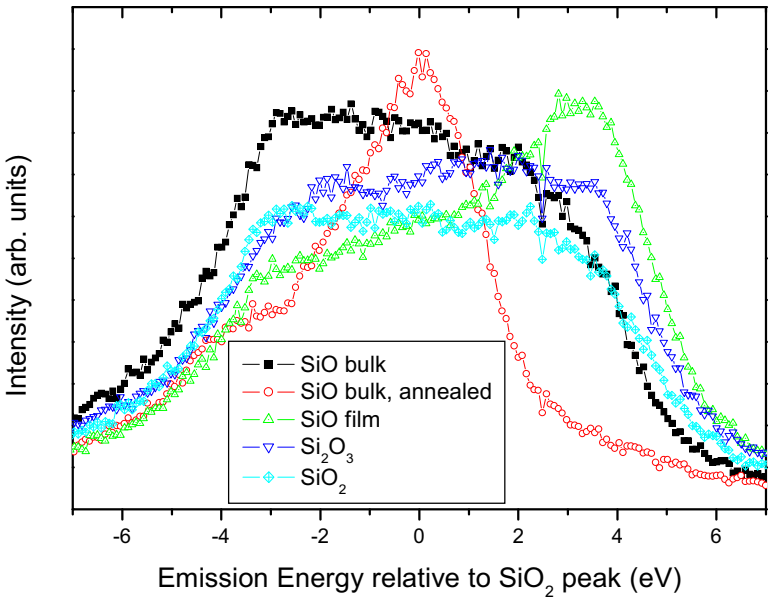

Fig. 2. Oxygen K-edge X-ray emission spectra recorded with 575 eV excitation energy for different samples as described in the text. The spectra have been scaled to comparable intensity.

References

[1] A. Hohl, T. Wieder, P.A. van Aken, T.E. Weirich, G. Denninger, M. Vidal, S. Oswald, C. Deneke, J. Mayer, and H. Fuess, J. Non-Cryst. Solids **320** (2003) 255.
[2] A. Hohl, doctoral thesis, Technische Universität, Darmstadt, 2002.
[3] R.M. Hagenmayer, B. Friede, and M. Jansen, J. Non-Cryst. Solids **226** (1998) 225.

X-ray Crystallography at the Protein Structure Factory

Uwe Müller[1,2], Andrew Turnbull[1,3], Babu A Manjasetty[1,3,4], Martin Fieber-Erdman[1,2], Ronald Förster[1,2], Martin Fuchs[1,2] and Udo Heinemann[2,3,#]

[1]Protein Structure Factory, c/o BESSY GmbH, Albert-Einstein-Str. 15, 12489 Berlin, Germany.

[2]Institut für Chemie/Kristallographie, Freie Universität, Takustr. 6, 14195 Berlin, Germany.

[3]Forschungsgruppe Kristallographie, Max-Delbrück-Centrum für Molekulare Medizin, Robert-Rössle-Str. 10, 13092 Berlin, Germany.

[4]Present address: National Synchrotron Light Source, Building 725, Brookhaven National Laboratory, Upton, New York 11973, USA.

[#]Corresponding author:

Udo Heinemann
Max Delbrück Center for Molecular Medicine
Robert-Rössle-Str. 10
D-13092, Berlin, Germany
Phone: +49 (30) 9406 3420
Fax: +49 (30) 9406 2548
E-mail: heinemann@mdc-berlin.de

HYPERLINK

Abstract

The Protein Structure Factory at BESSY comprises three macromolecular crystallography beamlines: Two beamlines, BL1 and BL2, are almost identical in design and are optimised for rapidly measuring anomalous diffraction data sets (MAD/SAD) whereas the third beamline, BL3, has been designed to operate at a constant wavelength near the critical energy. The PSF beamlines have a proven track record as a powerful facility for macromolecular structure analysis with several novel protein structures being determined in 2004. Furthermore, during the year, beamtime used by the Protein Structure Factory project has resulted in the determination of 6 new protein structures.

1. Introduction

The Protein Structure Factory (PSF) represents a collaborative structural genomics initiative aimed at the high-throughput structure analysis of human proteins (*1*)ADDIN. The PSF X-ray diffraction data collection facility and structure determination unit are located at the third generation synchrotron source, BESSY. During 2004, the Protein Structure Factory has carried out X-ray diffraction experiments on 11 different human proteins and have determined 6 protein structures. Additionally, the group has provided scientific support for both industrial and academic users which has lead to 20 publications in reputable journals.

2. Results

Details of the X-ray diffraction experiments carried out at the PSF beamlines during 2004 are summarized in Table 1. Five structures were determined by the single-wavelength anomalous diffraction (SAD) method and a sixth using molecular replacement methods. The biological

insight gained from the work carried out by the PSF is briefly described below for two sample proteins.

Table 1. Protein Structure Factory data collection status 2004

No.	Protein	Variant	Data Limit	Experiments	Status/PDB ID
1	BET3	Native	1.55	-	Solved/1SZ7
2	FLJ36880	Native	2.2	-	Solved/1SAW
3	APEG-1	Native	0.98	3	Solved/1U2H
4	PTD012	Native	1.7	2	Solved/1XCR
5	Peptidase D	Mn soak	2.4	1	Variant/Solved
6	CGI-32	SeMet	2.5	12	Solved
7	Tumor protein	Native	3.5	6	Tested
8	AAAS	Native	2.7	17	Tested
9	CW-1p	Native	3.3	9	Tested
10	DKFZ_phamy2_1515: frame3	Native	3.25	5	Tested
11a	DKFZphamy2_1n1-frame2	Native	2.3	5	Tested
11b	DKFZphamy2_1n1-frame2	Zn/Kr Peak	3.2	3	Variant search

2.1. BET3

BET3 is a component of TRAPP, a large complex (~800 kDa) involved in the tethering of endoplasmic reticulum-to-Golgi transport vesicles with their acceptor compartment (*2-4*). The three-dimensional structure of recombinant human BET3 was determined to 1.55-Å resolution by X-ray crystallography using the technique of single-wavelength anomalous diffraction (SAD) phasing and data collected on PSF-BL2 (*5*). The structure of BET3 comprises an α/β-plait fold (Figure 1) and adopts a dimeric quaternary organization *in vivo*. The dimeric BET3 structure has important implications for the architecture of TRAPP where subunits are thought to be present in equimolar stoichiometry. An extensive pocket within the core of the α-helical face of the BET3 subunit is predominantly lined by highly conserved, hydrophobic residues. A palmitate molecule, covalently attached to the protein through a thioester linkage to cysteine 68, is embedded within this pocket. BET3 and yeast Bet3p are palmitoylated in recombinant yeast cells, the mutant proteins BET3 C68S and Bet3p C80S remain unmodified. A BET3 mutant in which Cys68 was replaced by a serine residue has revealed that palmitoylation is neither required for viability or sufficient for membrane association of BET3 which may depend on protein-protein contacts within TRAPP or additional, yet unidentified modifications of BET3. A conformational change may facilitate palmitoyl extrusion from BET3 and allow the fatty acid chain to engage in intermolecular hydrophobic interactions (Figure 2).

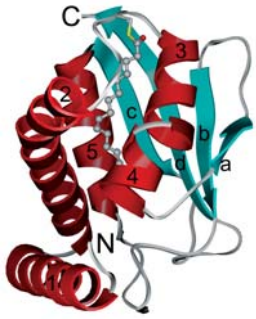

Figure 1. Secondary structure of Bet3**.**

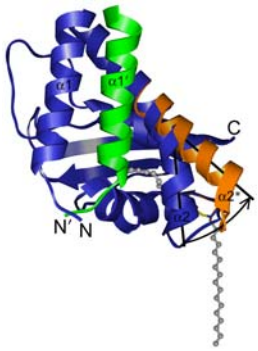

Figure 2. Proposed hinge motion in BET3 to facilitate the extraction of the palmitoyl group from the hydrophobic pocket.

2.2 Peptidase D

Peptidase D (PEPD) is a ubiquitous metallo-aminopeptidase which cleaves dipeptides carrying a C-terminal *trans*-Pro residue with a narrow substrate specificity. The biological function involves the processing of specific substrates including bioactive peptides involved in cardiovascular and pulmonary systems and degradation products of collagen. Several mutations in the PEPD encoding gene lead to PEPD deficiency, a lethal autosomal recessive disorder in man (*6*). In order to analyze the three-dimensional structure of this 54 kDa, homodimeric protein (Figure 3), X-ray diffraction experiments were carried out at PSF-BL1 and PSF-BL2. The three-dimensional structure has been refined to a final R/R_{free} of 16.3/19.1 % to a maximum resolution of 1.82 Å. The structure was determined by the single wavelength anomalous scattering (SAS) technique, using data collected on Se-Met incorporated PEPD. Recently, data have been collected on a Mn-soaked crystal which has led to the identification of the metal binding site, providing further insights into the catalytic mechanism of this enzyme. Analysis of the structure is currently underway.

Figure 3. Quaternary structure of Peptidase D.

3. Summary

Our efforts have yielded several protein structures for the year 2004, some of which have been described here. All these proteins have interesting biological functions: some are clearly related to human disease and others provide the basis for further work aimed at structurally elucidating the functional networks in which these proteins are active. Worldwide efforts aimed at streamlining X-ray crystallographic protocols and methodological platforms and the implementation of new technologies will hopefully increase the rate of protein structure determination in the future.

Acknowledgements

Funded by the German Federal Ministry for Education and Research (BMBF) through the "Leitprojektverbund Proteinstrukturfabrik" and with support by the Fonds der Chemischen Industrie to U.H. We wish to thank all Protein Structure Factory members.

References

1. Heinemann, U., Bussow, K., Mueller, U., and Umbach, P. (2003) *Acc Chem Res* **36**, 157-63.
2. Sacher, M., Jiang, Y., Barrowman, J., Scarpa, A., Burston, J., Zhang, L., Schieltz, D., Yates, J. R., 3rd, Abeliovich, H., and Ferro-Novick, S. (1998) *EMBO J* **17**, 2494-503.
3. Sacher, M., Barrowman, J., Schieltz, D., Yates, J. R., 3rd, and Ferro-Novick, S. (2000) *Eur J Cell Biol* **79**, 71-80.
4. Sacher, M., Barrowman, J., Wang, W., Horecka, J., Zhang, Y., Pypaert, M., and Ferro-Novick, S. (2001) *Mol Cell* **7**, 433-42.
5. Turnbull, A.P., Kümmel, D., Prinz, B., Holz, C., Schultchen, J., Lang, C., Niesen, F.H., Hofmann, K.-P.,Delbrück, H., Behlke, J., Müller, E.-C., Jarosch, E., Sommer, T. and Heinemann, U. *EMBO J* (in press).
6. Kikuchi, S., Tanoue, A., Endo, F., Wakasugi, S., Matsuo, N., and Tsujimoto, G. (2000) *J Hum Genet* **45**, 102-4.
7. Timm, D. E., Mueller, H. A., Bhanumoorthy, P., Harp, J. M., and Bunick, G. J. (1999) *Structure Fold Des* **7**, 1023-33.
8. Tame, J. R., Namba, K., Dodson, E. J., and Roper, D. I. (2002) *Biochemistry* **41**, 2982-9.
9. McIninch, J. K., McIninch, J. D., and May, S. W. (2003) *J Biol Chem* **278**, 50091-100.
10. Manjasetty, B. A., Niesen, F. H., Delbrück, H., Goetz,F., Sievert,V., Büssow, K., Behlke, J. and Heinemann, U. (2004) *Biol. Chem.*, **s385 (10)**, 935-942.

Structure determination of β-Xylosidase from *Geobacillus stearothermophilus*

C. Bruex, K. Niefind, D. Schomburg

Institute of Biochemistry, University of Cologne. Zülpicher Str. 47, 50674 Cologne/Köln, Germany

Poly xylose (also called xylan) is one of the most important parts of hemicellulose in plants. The enzyme β-xylosidase hydrolyses the β-1-4 bound between two xylose saccharides in xylan and therefore plays an important role in the natural degradation of xylan. The enzyme is part of the glycoside hydrolase family 43 [1]. It has a molecular mass of 61 kDa and is a tetramer in solution. β-xylosidase might be biotechnologically relevant in industrial paper and pulp production.

β-xylosidase was purified using standard liquid chromatographic techniques. It was concentrated and could be reproducibly crystallised (Fig. 1). The crystals were transferred into cryo protectant buffer and characterized by X-ray diffraction using an in-house rotating copper anode (Tab. 1).

Figure 1: Crystals of β-xylosidase

A selenomethione-derivative of β-xylosidase was prepared and crystallized. Unfortunately the crystals of SeMet-β-xylosidase possess much worse diffraction properties than the native ones. Typically lots of crystals have to screened to identify very few ones suitable for diffraction experiments. With one of such crystals we collected an MAD data set at BESSY, Berlin (Tab.1).

Table 1: statistics of ß-xylosidase data sets. The MAD data were collected at BESSY, Berlin

Data set	MAD Se peak	MAD inflection	MAD remote	native ß-xylosidase
Wavelength (Å)	0.9798	0.9799	0.9215	0.8221
Space group	$P2_12_12_1$	$P2_12_12_1$	$P2_12_12_1$	I422
a (Å)	106.13	106,7	105,9	196.26
b (Å)	196.6	197.2	196.8	196.26
c (Å)	258.8	258.2	257.4	215.0
Unique reflections	186 950	132 465	77 422	153 388
Resolution range (Å)	20.0-2.5	20.0-3.08	20.0-2.8	20-1.96
Completeness (final shell)(%)	100.0 (98.6)	99.1 (98.4)	58.2 (61.1)	99.7 (94.7)
$\langle I \rangle / \langle \sigma \rangle$ (final shell)	10.9 (3.1)	5.2 (1,3)	12.2 (4.1)	31.1 (5.2)
R_{sym} (%) (final shell)	20.0 (93.0)	22.1 (61.5)	22.8 (9.7)	6.8 (32.6)

Currently the structure determination and phasing procedures are in progress.

References

[1] Bourne, Y. & Henrissat, B. (2001). Glycoside hydrolases and glycosyltransferases : families and functional modules. *Curr. Opin. Struct. Biol.* **11**, 593-600.

Structure determination of ternary complexes of L-amino acid oxidase from ***Rhodococcus opacus***

A. Faust, K. Niefind, D. Schomburg

Institute of Biochemistry, University of Cologne, Zülpicher Str. 47, D-50674 Cologne, Germany

The L-Amino acid oxidase catalyzes the stereospecific oxidative deamination of an L-amino acid substrate to an α-keto acid along with the production of ammonia and hydrogen peroxide [1]. The enzyme is often found in snake and insect venom, but also in fungi, algae and some cyano- and soil bacteria. The role of this enzyme in the bacterial metabolism is unknown so far.

The L-Amino acid oxidase from *Rhodococcus opacus* (LAO, EC 1.4.3.2) is a dimeric flavoprotein which contains non-covalently bound FAD as cofactor. One subunit consists of 489 amino acids and one FAD molecule with a molecular weight of 54.2KDa. The enzyme was overexpressed in *Rh. opacus* and *Streptomyces*, purified to homogeneity [1] and crystallized. Two different orthorhombic crystal forms are obtained with very good diffraction properties (Fig. 1).

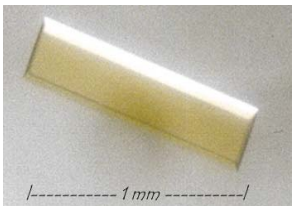

(a) in space group $P2_12_12_1$

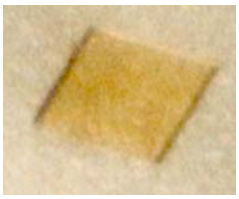

(b) in space group $C222_1$

Figure 1: different crystalforms of LAO

The structure of LAO (Fig. 2) was solved from the anomalous signal of mercury by the SAD method [2] using LAO crystals with $P2_12_12_1$ symmetry (Fig. 1a) [3]. To get deeper insight into the reaction mechanism of the enzyme we collected diffraction data sets of crystalline LAO in complex with FAD and either substrate or inhibitor molecules at the Protein Structure Factors beamline BL14.2 of BESSY (Tab. 1).

Table 1: statistics of LAO data sets collected at BESSY, Berlin

substrate/inhibitor	**L-alanine**	**L-phenylalanine**	**o-amino benzoate**
wavelength [Å]	0.9195	0.9195	0.9195
Space group	$P2_12_12_1$	$P2_12_12_1$	$P2_12_12_1$
a [Å]	65.9	66.05	65.65
b [Å]	109.93	110.06	109.68
c [Å]	134.49	134.53	134.37
Unique reflections	142028	157853	83174
Resolution [Å]	15 – 1.55	30 – 1.45	30 – 1.85
Completeness (final shell) [%]	99.8 (99.6)	91.3 (86.1)	99.2 (98.7)
R_{sym} (final shell) [%]	8.3 (23.3)	10.4 (47.7)	14.9 (50.3)
I/σ (final shell)	25.3 (10.0)	11.9 (2.1)	9.5 (2.0)

The ternary complexes were refined with REFMAC5 [4] to reasonable R-factors and stereochemical characteristics (Tab. 2).

Table 2: refinement statistics of LAO complex structures

substrate/inhibitor	L-alanine	L-phenylalanine	o-amino benzoate
Resolution range [Å]	15 – 1.55	15 – 1.45	20 – 1.85
R_{work} [%]	14.7	18.1	15.0
R_{free} [%]	17.3	20.6	20.4
RMS deviations			
Bonds [Å]	0.009	0.009	0.013
Angles [°]	1.248	1.259	1.446
Number of amino acids (chain A/B)	478/477	478/477	478/477
Number of FAD atoms	212	212	212
Number of substrate/inhibitor atoms	14	24	20

The ternary complexes had been obtained by soaking of the previously yellow-coloured LAO/FAD crystals in substrate containing solutions. In the case of the substrates L-alanine and L-phenylalanine we observed chemical reactions since the crystals lost their colour gradually indicating the formation of FADH. In fact we could identify FADH rather than FAD in the structure due to the strong curvature of the isoalloxazine ring (Fig. 3).

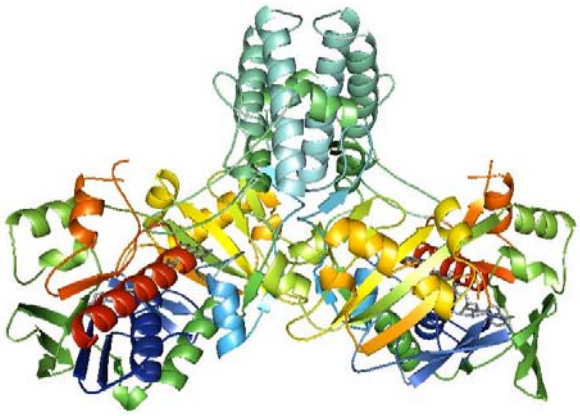

Figure 2: overall structure of an LAO dimer from *Rhodococcus opacus*

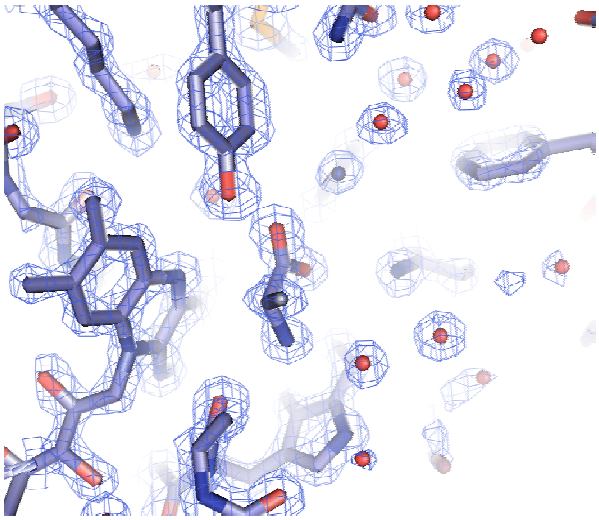

Figure 3: $2DF_o$-mF_c electron density map at the active side of LAO containing the FAD cofactor and L-alanine contoured at 2σ

In summary we could derive a plausible model of reaction mechanism which will be described elsewhere in detail (manuscript in preparation).

References:

1. Geueke, B., Hummel, W., *A new bacterial L-amino acid oxidase with a broad substrate specificity:purification and characterization.* Enzyme and Microbiol. Technology, 2002. **31**: p. 77-87.
2. Wang, B.C., Methods in Enzymology, 1985. **115**: p. 90-112.
3. Faust, A., *Die Struktur der L-Aminosäure-Oxidase aus Rhodococcus opacus in verschiedenen funktionellen Zuständen*. PhD-thesis, University of Cologne, 2004.
4. Collaborative Computational Project, N., *The CCP4 Suite: Programs for Protein Crystallography.* Acta Cryst. D, 1994. **50**: p. 760-763.

Successful Setup and Test of a BioXAS Experiment at Beamline KMC-1

Paola Loja[1], Marcos Barra[1], Simone Löscher[1], Peter Liebisch[1], Marcel Mertin[2], Franz Schäfers[2], Michael Haumann[1], Holger Dau[1*]

[1]*Freie Universität Berlin, FB Physik, Arnimallee 14, D-14195 Berlin, Germany;*
[2]*BESSY-II, Albert-Einstein-Str. 15, D-12489 Berlin, Germany;*
[*]*E-mail: holger.dau@physik.fu-berlin.de*

X-ray absorption spectroscopy (XAS) has become one of the most important techniques to analyze the nuclear geometry at the atomic level (by EXAFS) and oxidation state (by XANES) of metal centers in biological metalloenzymes during catalysis. At the bending-magnet crystal-monochromator beamline KMC-1 at BESSY-II in December 2004/January 2005, we installed and tested a new setup for XAS on biological samples (BioXAS [1,2]). XAS measurements at the Mn K-edge were performed on reference samples and on the metal complex of a metalloenzyme, the manganese complex of photosynthesis in plants [3]. The properties of the beamline KMC-1 and of the newly purchased equipment (Figs. 1,2) are well suited for BioXAS on ultra-dilute samples.

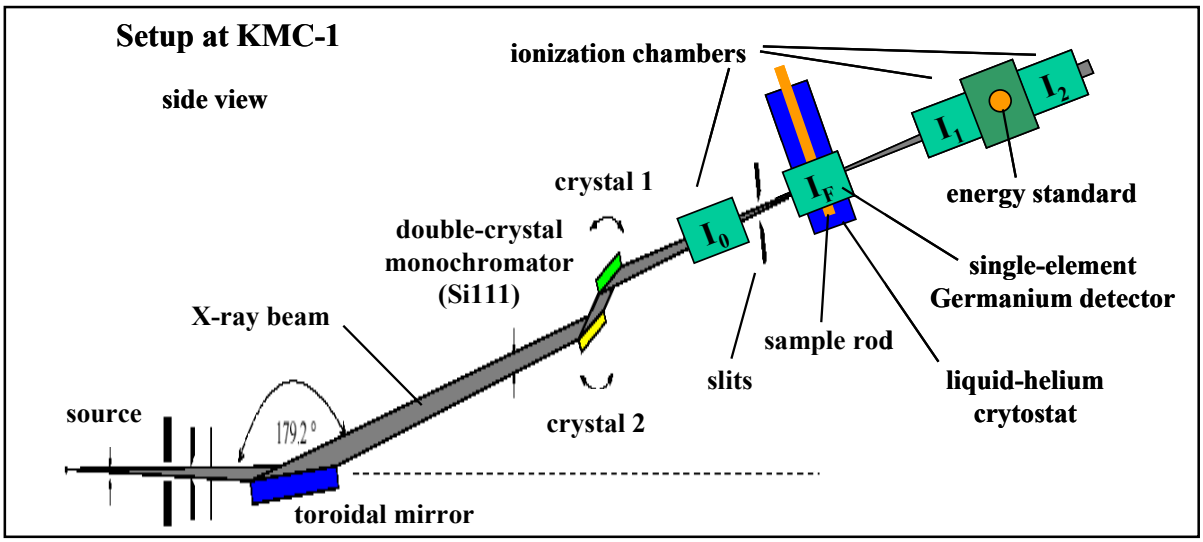

Fig. 1: Scheme of the experimental setup at beamline KMC-1 (not drawn to scale). The cryostat (Optistat, Oxford) with the sample was placed about in the beam focus (spot size ~0.5 mm^2; ~10^{11} photons s^{-1} mm^{-2} at ~6 KeV; energy resolution (FWHM) with Si111 crystal ~3 eV). For X-ray fluorescence detection at right angle to the incident beam, a single-element Germanium detector (Canberra, active area 100 mm^2) was used. To obtain an absolute energy calibration, a $KMnO_4$ powder sample plus a 5 µm Fe foil were used as standards placed behind the sample.

An energy-resolving Ge detector (reset type, Canberra, maximal countrate ~300 Kcps), a digital signal processor (DXP multichannel analyzer from XIA), and a helium cryostat plus electronics (Oxford) had been purchased and appropriately modified (by the workshop of the FB Physik, FU-Berlin). The cryostat was flanged to the detector so that the retractable Ge element was at a distance of only ~2 cm from the sample, for maximal X-ray fluorescence count rates (Fig. 2). Cryostat and detector were mounted on a home-built stage permitting for vertical and horizontal movement of the setup to measure separate spots on the same sample. By the DXP, pulses were shaped, selected, and converted to TTL pulses for counting by the beamline electronics. The energy resolution of the detector system was about 300 eV at a total count rate of 50 Kcps allowing for highly efficient suppression of scattered X-rays and for the collection of EXAFS spectra with negligible background (Fig. 3). EXAFS scans were performed using the beamline software by scanning of the Si111 monochromator at the Mn

K-edge (scan range 6400-7200 eV, the monochromator driving and ion-chamber electrometer readout times were optimized so that the deadtime was smaller than 0.5 s at 1.5 s acquisition time per data point). An energy calibration of XAS spectra was obtained by simultaneous measurement of the absorption spectra of standards with known features placed behind the sample (Figs. 1,3). Measurements on ultra-dilute biological test samples (manganese complex of a photosystem II protein preparation, Mn concentration ~1 mM) revealed the following:

1) At ~150 mA ring current, the total count rate was >100 Kcps at ~7 KeV.
2) Mn K_α fluorescence yielded ~20 Kcps (300 eV window around 5.9 KeV).
3) The sample temperature of 10 K was highly stable; cryostat operation was reliable.
4) The high fluorescence count rates allowed for the collection of Mn EXAFS spectra exhibiting a reasonable signal-to-noise ratio in a single scan of ~1 h duration (Fig. 3).

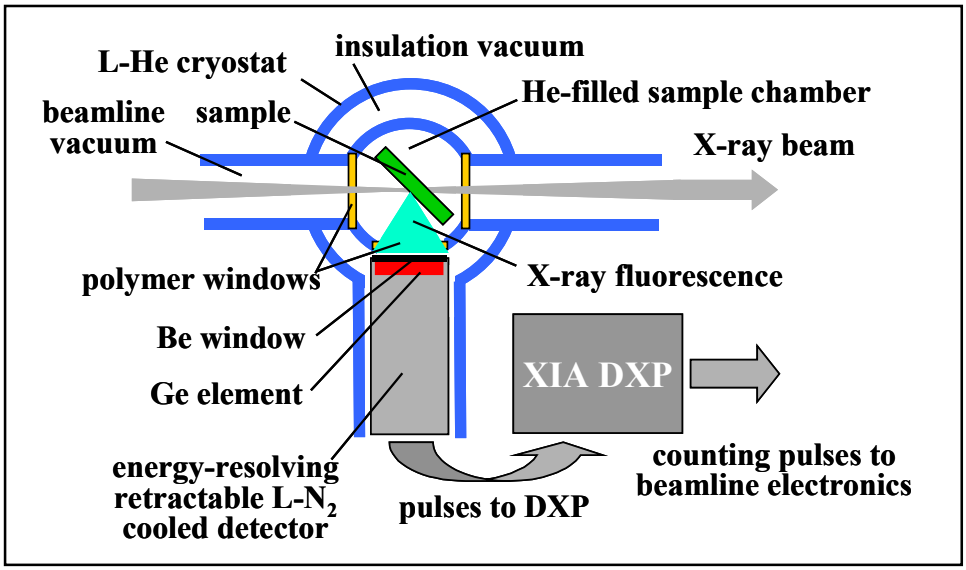

Fig. 2: Details of the cryostat and detector setup.

EXAFS spectra at the Mn K-edge were measured (1) at 20 K on the Mn complex of photosystem II protein (Mn concentration <1 mM) and (2) in a temperature range between 10 K and 300 K on an aqueous 10 mM $MnCl_2$ sample (for representative spectra see Fig. 3).

Current Achievements / Conclusions:

1) The technique/setup for EXAFS measurements in fluorescence mode on dilute samples has been established at KMC-1.
2) The energy axis was stable during successive EXAFS scans within ~0.5 eV (as estimated from the energy position of the narrow pre-edge peak of the $KMnO_4$ standard, Fig. 3B) proving that the stability of the monochromator was sufficient.
3) Mn EXAFS spectra were free of artefacts (glitches) permitting for the collection of spectra up to (at least) 600 eV above the Mn K-edge.
4) It was estimated that for a single high quality EXAFS spectrum on an enzyme sample (~1 mM Mn) averaging of about 10 scans each of ~1 h duration will suffice.
5) The performance of the XAS setup at KMC-1 was at least comparable to, e.g., the BioXAS station of the EMBL at HASYLAB, DESY, Hamburg.

Future Improvements:

i) The experimental stage will be mounted at ~3 m behind the beam focus for a larger spot (about 5x2 mm^2) on the sample to minimize radiation damage to the biological samples. ii) Slits in front of the I_0 detector for accurate beam shaping will be used. iii) The I_0 detector will be directly flanged to the cryostat for maximal signal quality. iv) Customized software for the

DXP may allow for optimized correction of spectra for detector deadtime and for the use of the maximal available countrate. v) Adapted beamline software could allow for properly weighted EXAFS scans for improved signal-to-noise ratio at high k-values.

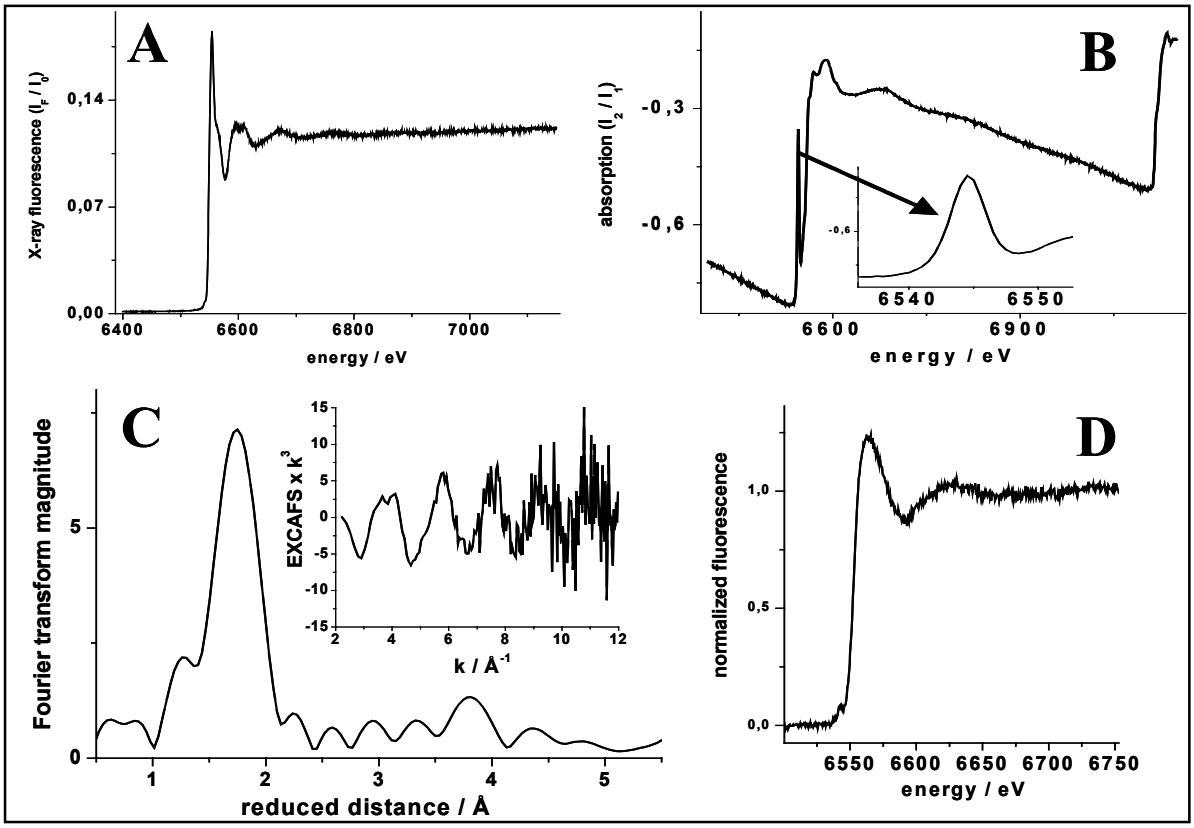

Fig. 3: Mn EXAFS spectra at 20 K. (A) Single scan fluorescence data from 10 mM $MnCl_2$; (B) Absorption spectra of Mn and Fe standards (note the narrow pre-edge peak of $KMnO_4$ (arrow) demonstrating the energy resolution); (C) Fourier transform of data in (A) (inset: k^3-weighted EXAFS oscillations); (D) Normalized single-scan fluorescence-mode XANES spectrum of a photosystem II protein sample (~1 mM Mn).

Summary: Successful setup and testing of a fluorescence-mode BioXAS experiment with a new cryostat and detector system at beamline KMC-1 was performed. First EXAFS measurements revealed that good quality spectra can be obtained at 10 K in reasonably short measuring periods. Spectra of ultra dilute biological and reference samples were obtained. In the future, it is intended to improve the setup so that routine collection of BioXAS data becomes possible, for X-ray energies ranging from 2.5 to 10 KeV.

We are indebted to the beamline staff of KMC-1 and to the IT-group of BESSY for outstanding engagement and excellent support. Financial support from the DFG (SFB 498, projects C6 and C8) is gratefully acknowledged.

[1] H. Dau, P. Liebisch, M. Haumann **(2003)** X-ray absorption spectroscopy to analyze nuclear geometry and electronic structure of biological metal centers. *Anal. Bioanal. Chem.* 376, 562-583.

[2] H. Dau, M. Haumann **(2003)** X-ray absorption spectroscopy to watch catalysis by metalloenzymes - Status and perspectives discussed for the water-splitting manganese complex of photosynthesis. *J. Synchrotron. Rad.* 10, 76-85.

[3] M. Haumann, C. Müller, P. Liebisch, L. Iuzzolino, J. Dittmer, M. Grabolle, T. Neisius, W. Meyer-Klaucke, H. Dau **(2005)** Structural and oxidation state changes of the photosystem II manganese complex in four transitions of the water oxidation cycle ($S_0 \rightarrow S_1$, $S_1 \rightarrow S_2$, $S_2 \rightarrow S_3$, $S_{3,4} \Rightarrow S_0$) characterized by X-ray absorption spectroscopy at 20 K as well as at room temperature. *Biochemistry*, Epub. ahead of print.

Extended Ultra-Violet Circular Dichroism Spectroscopy on Proteins and First Measurements at an Undulator Beamline

Peter Baumgärtel[1], Jan Lengefeld[1], Benjamin Schuler[1], Gerd Reichardt[2], Markus Sauerborn[2], Robert Seckler[1]

[1] Universität Potsdam, Physikalische Biochemie; [2] BESSY GmbH

Circular dichroism spectroscopy on proteins

Circular dichroism spectroscopy (CD) is a form of light absorption spectroscopy that measures the difference in absorbance of right- and left-circularly polarized light by a substance. It has been shown that CD spectra can be analysed for the different secondary structural types of proteins: alpha helix, parallel and anti parallel beta sheet, turn, and other (see box below). CD spectra of proteins arise from electronic transitions between ground and excited states of molecular orbitals. The most significant chromophore is the amide group of the polypeptide backbone. Secondary structures impose positional and intensity constraints on these transitions, and give rise to characteristic far-UV spectra (Wallace 2001).

Extended ultra-violet circular dichroism spectroscopy on proteins

A very important requirement for successful secondary structure analysis is that the CD spectra need to be recorded from about 260 nm to at least 178 nm and preferable below (Johnson, 1990). However no commercial-type CD spectrophotometer is capable of measuring the CD in the vacuum ultraviolet (VUV) region below 175 nm because of technical difficulties involved in the light source, optical devices and sample cell. By using synchrotron light as the ideal light source for CD measurements (Sutherland 1996, see also next chapter) we could concentrate on developing a preparation technic for thin aqueous protein films. The preparation of the sample cell consists mainly in pressing a drop of high concentrated protein solution (100 - 300 mg/ml) between two CaF_2 windows. The short path length of such a "squish cell" guarantees the overcoming of the high absorbance of water (Segelstein 1981) in the extended VUV range. Figure 1 shows the extended CD spectrum of Lysozym recorded at Dipol D12-1B (3m NIM C) as an example. The spectrum seems to look very promising. However stress-strain birefringence in the CaF_2 windows caused by capillary forces makes the reproducibility of such scans difficult. Therefore we plan further investigations regarding window material and design.

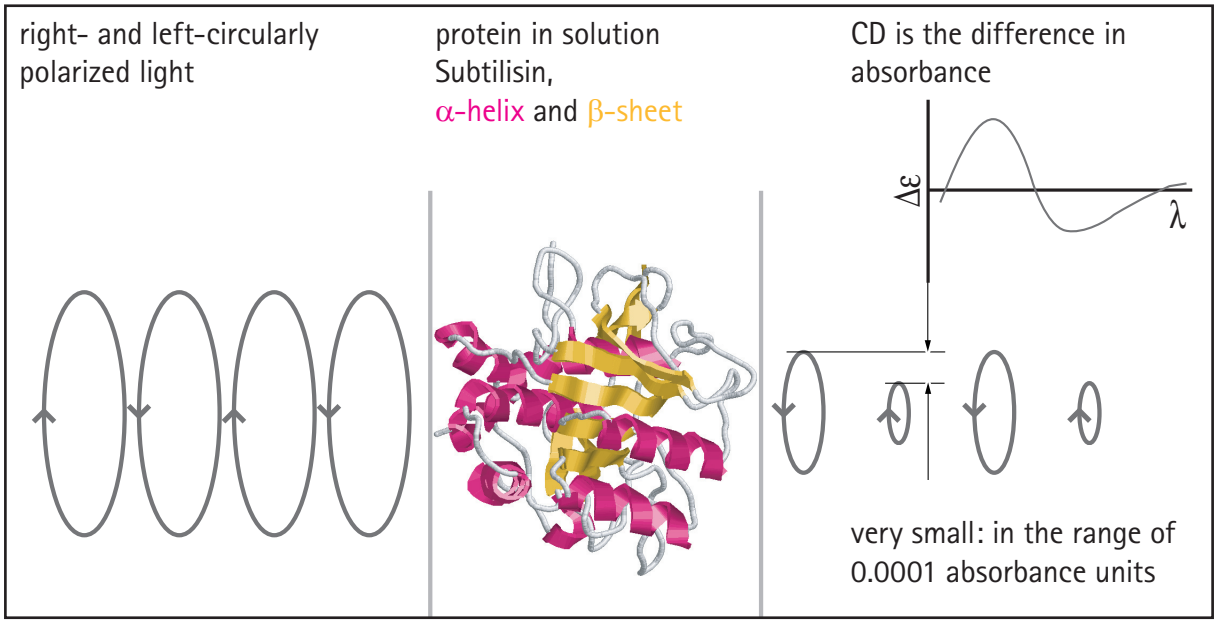

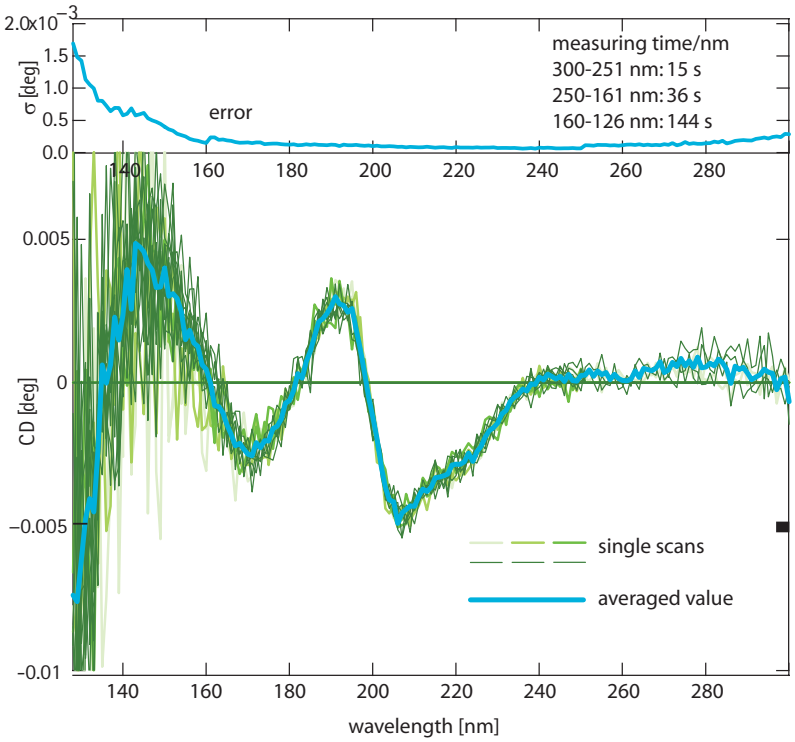

Fig. 1: Extended CD spectrum of a high concentrated aqueous Lysozym solution recorded at Dipol D12-1B. The blue line in the bottom diagram shows the averaged values of 6 single CD spectra. The upper diagram gives the error of the averaged CD signal. The measuring time per 1 nm was increased in the range of the big water absorption peak at about 150 nm. Via the amplitude of this absorption peak (absorption spectrum is not shown here) we estimated the pathlength to about 300 nm. The recording time of allto-gether was about 2.5 h.

First CD Measurements at an Undulator Beamline

One of the project aims was to build up an experimental station for CD measurements at the dipol beamline D12-1B with its monochromator 3m NIM. This beamline was designed for high resolution experiments (Reichardt 2001), which is not ideal for CD measurements. The small maximal bandwidth (0.1%) takes away a lot photon flux, which is needed for getting a good signal to noise ratio. Also focus and divergence are not small enough for future planned time resolved experiments. Ideal dimensions for latter one we could now find at undulator U125 in connection with the 10m NIM monochromator. As far we know, the first time an undulator beamline was used for CD experiments on proteins. The analysis of the experimental data are still going on. It seems that the optical devices (for example the photoelastic modulator) perform better because of the small divergence. Beam damage because of the high intensity could be seen after exposing a aqueous lysozym solution several minutes. Further investigations with time resolved technics (stopped flow and continuous flow) are planned at both beamlines.

References

Johnson WC jr., Proteins 7, 205 (1990); **Johnson** WC jr., in Circular Dichroism and the Conformational Analysis of Biomolecules, edited by Fasman GD, Plenum Press, 648 (1996); **Sutherland** JC, in Circular Dichroism and the Conformational Analysis of Biomolecules, edited by Fasman GD, Plenum Press, 599 (1996); **Reichardt** G et al., NIM A 467-468, 458 (2001); **Wallace** BA, Janes RW, Current Opinion in Chemical Biology 5, 567 (2001);

The project was initiated by the „UV/Vis Initiative Synchrotronstrahlung" (UVIS).
The authors are pleased to acknowledge the financial support of the project by the German Federal Ministry of Education and Research (BMBF) under Contract 05 KS1IP1/1 and /2.

Comparative XAS study of synthetic manganese oxides and biogenic deposits on the cell-wall of the green alga *Chara corallina*

Andreas Schoeler[1], Peter Liebisch[1], Claudia Müller[1], Christoph Plieth[2], Alexej Erko[3], Holger Dau[1]

[1]*Institut für Experimentalphysik, Freie Universität Berlin, Arnimallee 14, 14195 Berlin*
[2]*Christian-Albrechts-Universitaet, Zentrum für Biochemie und Molekularbiologie, Am Botanischen Garten 5-9, 24118 Kiel*
[3]*BESSY GmbH, Albert-Einstein-Strasse 15, 12489 Berlin*

While it is well known that manganese is an essential trace element in plants and crucial for photosynthetic oxygen evolution [1] as well as for other enzymatic reactions, manganese toxicity has long been recognized as a factor limiting growth when organisms are exposed to high concentrations of Mn. Presumably related to a detoxification mechanism cells of the green alga *Chara corallina* develop brown deposits on the outer cell wall when cultured in an alkaline, Mn-containing medium.

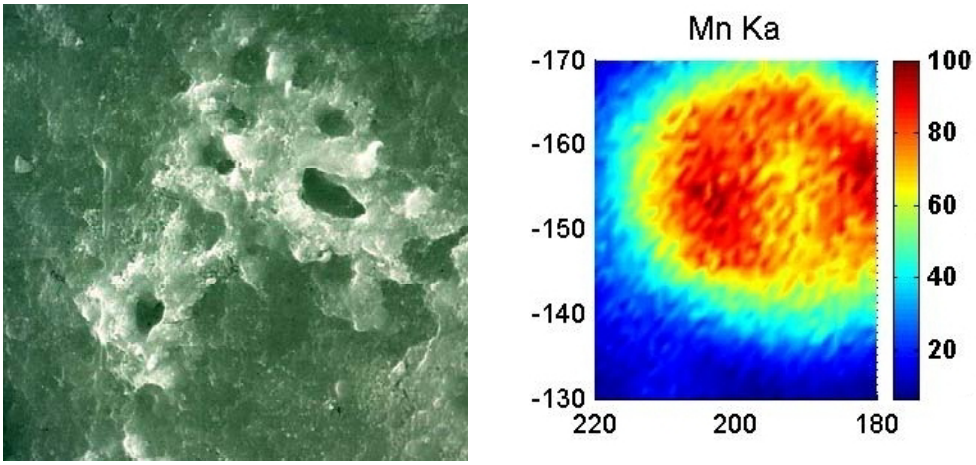

Figure 1: Electron microscopic images (*left*: magnification 2000, vulcano shaped deposits of about 10 μm diameter) and Mn-K_α microfocus data (*right*: manganese distribution of deposit on alga cell wall).

To address the questions of spatial distribution and chemical speciation of relevant elements microfocus XAS measurements have been performed in a previous experiment at KMC1. Elemental 2D-mapping by means of characteristic X-ray fluorescence as well as X-ray absorption measurements on selected spots on the cell wall had been carried out successfully. In the present investigation, to get reference data from synthetically produced manganese oxides in different structures (layers, tunnels, bulk), a set of Mn(IV)-oxides was synthesized and X-ray absorption spectra were recorded at room temperature.

MnO_2 synthesis

It is widely assumed that the majority of naturally occurring MnO_2 is of biogenic origin [2-4]. The early amorphous primary products are usually transformed into secondary products over geologically long periods of time [5]. Since the manganese deposits in *Chara corallina* develop over relatively short time intervals, only the group of primary products need to be analysed for comparison. This group consists of layer structures such as birnessite, buserite and vernadite as well as the tunnel structure todorokite. The birnessite and buserite structures were synthesised by double aging as described in [6]. The buserite was then transfomed into

the todorokite tunnel structure [7]. In another approach *Acid buserite* and δ-MnO_2 were synthesized following [4].

X-ray absorption spectroscopy

For all synthesized substances (as well as for commercially available manganese oxides) X-ray absorption spectra were recorded in transmission at room temperature at KMC-2. Two to five single scans were averaged.

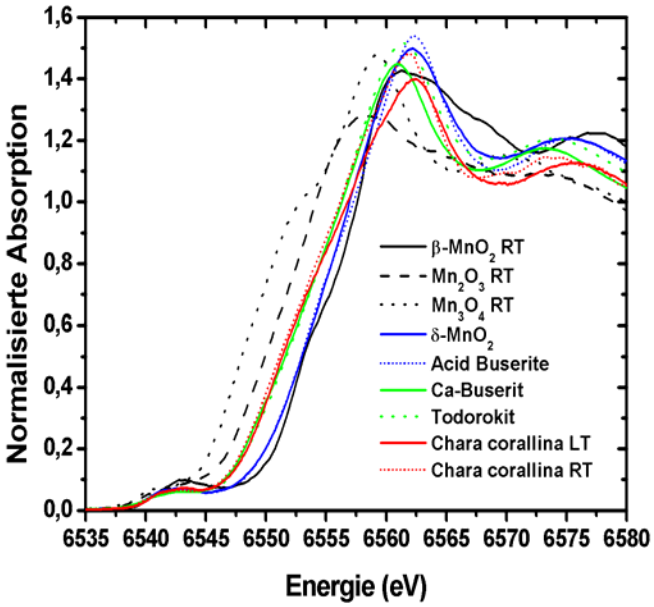

Figure 2: XANES spectra of commercially available manganese oxides (black lines), synthesised MnO_2 structures (blue and green lines) and data from the alga recorded at 20 K (red solid line) and at 298 K in a microfocus setup (red dotted line).

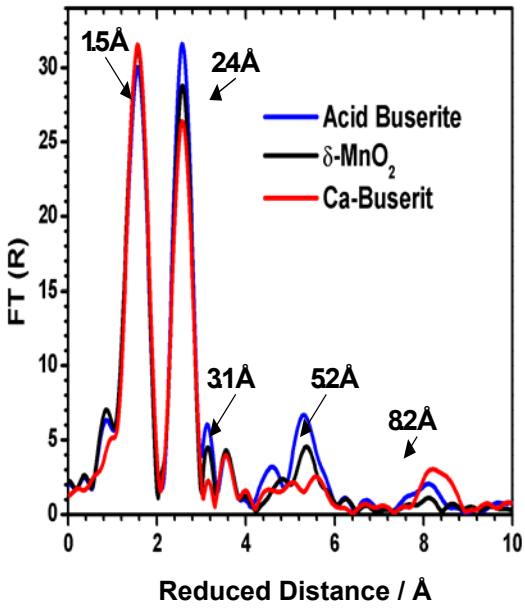

Figure 3: Fourier transform of EXAFS data from three selected MnO_2 structures. The main peaks are labeled and there are characteristic differences in all features above 2.0 Å reduced distance.

On the first glance the XANES spectra in Fig. 2 show good agreement between the alga data and Ca-buserite as well as todorokite in the lower edge region, but the position of the maximum of absorption of the alga data is shifted. The shoulder in the edge at 6550 eV indicates the presence of free Mn(II) and indeed, if the alga spectra are corrected by about 12 % Mn(II) contribution very good agreement of the alga data with *Acid buserite* and δ-MnO_2 is found.

Probe	N		R [Å]		$2\sigma^2$ [$Å^2$]		Rf [%]		ΔRf ($\Delta Rf/Rf_{yellow}$)
δ-MnO_2	6	5.71	1.883	1.883	0.008	0.007	**13.9**	**12.8**	**1.1**
		0.28		**2.319**		0.001			**(7.9 %)**
	6	6	2.866	2.866	0.011	0.011			
***Chara corallina* RT**	6	5.56	1.886	1.886	0.005	0.004	**14.8**	**12.2**	**2.6**
		0.43		**2.214**		0.001*			**(17.6 %)**
	6	6	2.873	2.873	0.015	0.015			
Ca-Buserit	6	5.24	1.901	1.900	0.006	0.004	**13.4**	**8.68**	**4.72**
		0.75		**2.298**		0.001			**(35.2 %)**
	6	6	2.896	2.895	0.012	0.012			

Table 1: Fit results for δ-MnO_2, *Chara corallina* (RT) und Ca-Buserit. A two-shell fit approach (*yellow*) is compared to a three shell fit approach (*blue*). Fit range: 20 eV to 540 eV; R_f-range: 1 Å-2,9

Å; *parameter fixed. Addition of a fraction of longer distances in the three-shell fit-approach significantly improves the fit quality and allows the separation of Mn(II) (~2.2 Å) from Mn(III) (~2.3 Å) contributions (bold).

This finding is confirmed by EXAFS analysis. In Fig. 3 the Fourier transforms for EXAFS spectra from three different MnO_2 structures are shown. The characteristic differences indicate the possibility to distinguish between those structures and therefore to identify the structure present in the alga deposits. The first peak (1.5 Å reduced distance) corresponds to Mn-O interaction in the first coordination shell (octahedron). This peak is very similar for all spectra. The second peak results from Mn-Mn scattering between neighbouring octahedrons that share one edge. The third peak contains contributions from Mn-Mn scattering between octahedrons that share one edge and from multiple Mn-O-Mn scattering. Both peaks show increasing height from Ca-buserite over δ-MnO_2 to Acid buserite. The peaks at 5.2 Å and 8.2 Å are due to higher order multiples scattering (collinear three or four octahedrons).
Furthermore, detailed analysis of the EXAFS data reveals the possibility to distinguish between Mn(II) contamination and longer distances expected for Mn(III) contributions. While Mn(III) ions give rise to distances of about 2.3 Å, which are observed for Ca-busertite and δ-MnO_2 with the stoichiometry reported in the literature, free Mn(II) ions yield distances of about 2.21 Å. Representative fit results are given in Tab. 1.

Conclusion

The XAS results of the microfocus experiment on manganese deposits were compared to synthetic MnO_2 structures. It appears that the biogenic deposits consist of relatively amorphous layered Mn(IV) oxide which shows high similarity with the synthetic δ-MnO_2 and acid buserite compounds. This is in agreement with the stoichiometric element ratio of manganese and calcium found from x-ray fluorescence elemental mapping [8].

References

1. Dau H., Liebisch P., Haumann M. (2003) *Anal. Bioanal. Chem.* 376: 562-583
2. DePalma S.R. (1993) PhD Thesis Thesis, Harvard University, Cambridge
3. Tebo B.M., Barger J.R., Clement B.G., Dick G.J., Murray K.J., Parker D., Verity R., Webb S.M. (2004) *Ann. Rev. Earth. Planet. Sci.* 2004 32: 287-328
4. Villalobos M., Toner B., Bargar J., Sposito G. (2003) Geochimica et Cosmochimica Acta 67: 2649-2662
5. Post J.E. (1999) *Proc. Nat. Acad. Sci.* 96: 3447-3454
6. Luo J., Zhang Q., Suib SL (2000) *Inorg. Chem.* 39: 741-747
7. Luo J., Zhang Q., Huang A., Giraldo O., Suib S.L. (1999) *Inorg. Chem.* 38: 6106-6113
8. Schoeler, A. (2005) Diploma thesis, Fachbereich Physik, Freie Universität Berlin

Investigations of mamma biopsies by means of μ-tomography

W. Treimer[1),2)], U. Feye–Treimer[1)], C. Radke[3)], A. Hilger[1),2)], O. Neumann[1)], I. Manke[2)], A. Haibel[2)], A. Rack[2)], H. Riesemeier[4)]

[1)] University of Applied Sciences (TFH) Berlin, FB II, 13353 Berlin
[2)] Hahn-Meitner-Institut Berlin, SF3, 14109 Berlin
[3)] DRK Kliniken Berlin, Institut für Pathologie
[4)] Bundesanstalt für Materialprüfung Berlin und BESSY II Berlin Adlershof

This work was supported by the BMBF project 03TRE6B9 "Tomographie mit kalten Neutronen und Synchrotronstrahlung"

Biopsies with the diagnosis of partial mamma carcinomas were investigated by means of x-ray μ-tomography (μCT). By means of μ-CT, using different photon energies, one should be able to extract malign from benign tissues due to the (small) different and (small) energy dependent mass absorption coefficients. The proliferation of the structure of cancerous breast tissues shall be revealed three dimensionally on a scale from mm until μm. To get a complete 3D structural information one has to study cancerous and healthy regions on a scale ranging from μm until nm, what can be done by position resolved small angle x-ray scattering. The first step, however, to separate cancerous from healthy strands is energy dependent μ-CT, that shall enhance the information got by μ-tomography.

We investigated four samples, each of them with the suggestion to contain cancerous parts embedded in healthy tissues. Each sample was kept in a paraffin block, having a size of app. 6x6x6 mm^3. First the sample was adjusted in the x-ray beam in such a way, that it was fully illuminated for all energies of 9keV until 13 keV. The proposed range of 6 keV to 30 keV could not be realized. From 15keV and higher the transmission of radiation was to strong. Therefore the energy range was reduced to 9, 10, 11, 12 and 13 keV. The sample was supposed to have for all energies the same x-y-z-coordinates for all voxels of the sample volume i.e. no individual alteration of the sample and stage. The geometrical adjustment for one sample could be used for all other ones, because oft their similar shape and volume. So one can compare the results from a given energy to all other energies. After adjusting the rotation center of the sample and optimizing the region of interest the mean exposure time was determined, keeping in mind, that the incident photo flux decreases with time. After registering the black field measurement, the sample was rotated from 0° to 180° in 900 steps (angles), interrupted by several series of flat field measurements which ensured and registered the actual photon flux for the running measurement. The data acquisition had to be parted into three sections to reduce the size of one data file for one energy. A severe problem – not solved up to now for this experimental set up - was to monitor the incident photon intensity. Due to the continuous decrease of the incident photon flux during one measurement – balanced by the flat field measurements - and the different photon flux at different energies one must compare only ratios of reconstructed absorption values of different parts of one slice with another energy. This can roughly estimated by the particular histograms of one slice at different energies. Fig. 1 shows the energy dependence of the gray level statistics for two different samples.

The data evaluation had to be done in several steps, to transfer and convert the data into formats that can be read by programs used in our institutes. Moreover for the first – rough and selecting – evaluation the data volume had to be reduced dramatically to use signal and

imaging tools that had to handle these huge data sets of app. 12 Gigabytes. The reduction was the decrease of gray levels from 32bit down to 16bit and a 2x2x2 pixel binning. As first results of reconstructed slices are shown. The spatial resolution of the measurement was 3.5µm, the one of the reconstruction 7µm.

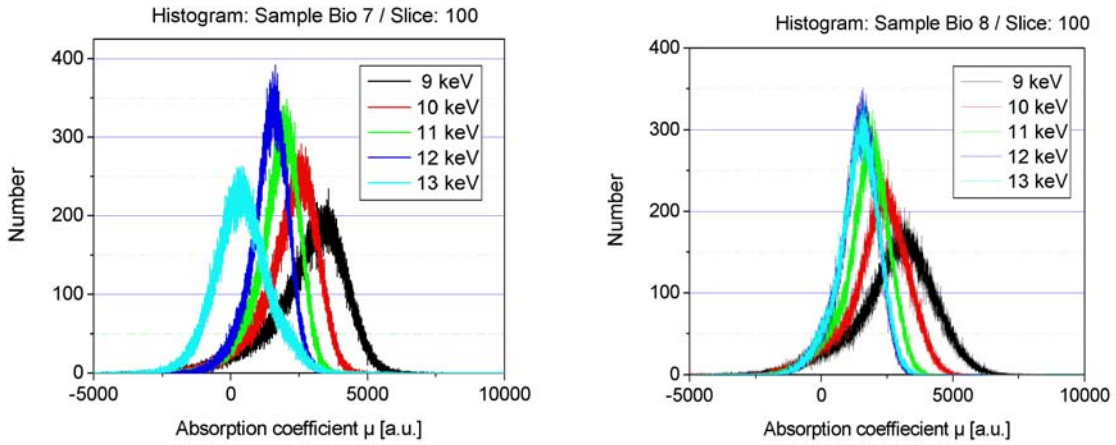

Fig.1 Energy dependent gray-level statistic for two different samples. There is a unique tendency of from high to low intensity behavior; 13keV histogram of sample Bio 7 fails due to experimental interruption.

The 3D reconstruction of the first two samples showed typically structures of mamma biopsies containing lipoma tissue, part of adipose tissue, glandular tissue and/or tissue containing cancerous regions. The indication of cancerous tissue in sample 8 is – up to now - not assured. Fig. 2 shows slices of the reconstruction

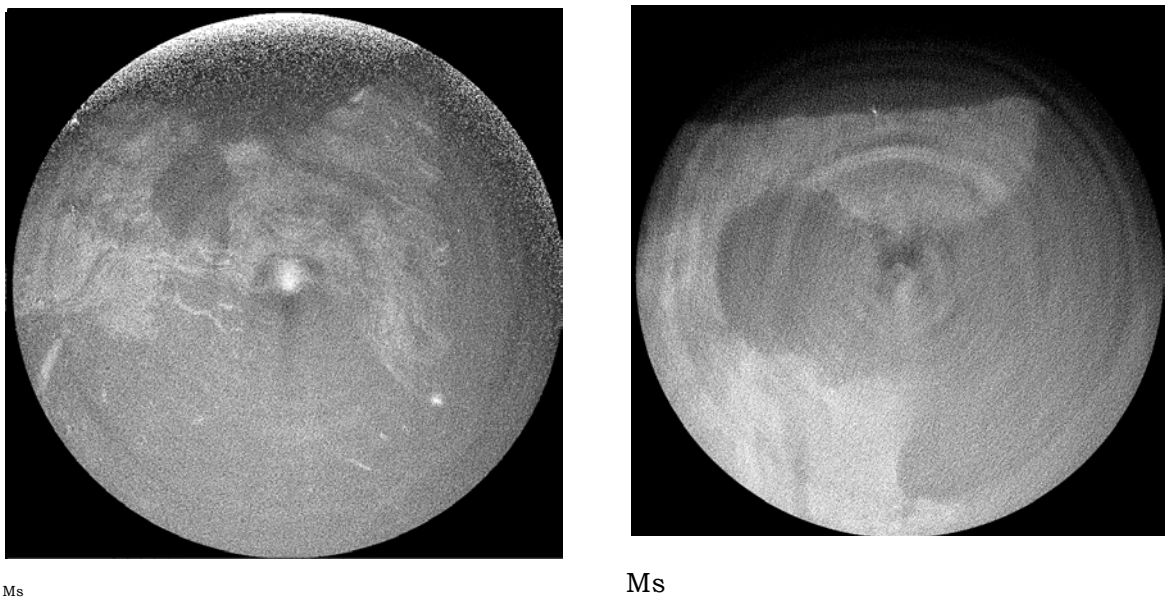

Ms

Ms

Fig.2 Left sample Bio 7, slice 100, right sample Bio 8 with the presumption of a large cancerous region, both measured at an energy of 9 keV.

Light-induced changes of secondary structure in Photoactive Yellow Protein

Berthold Borucki, Harald Otto, Maarten P. Heyn
Freie Universität Berlin, Physics Department, Arnimallee 14, 14195 Berlin

Photoactive Yellow Protein (PYP) is a bacterial blue-light photoreceptor from *Halorhodospira halophila* that is the prototype of the large class of PAS-domain signal proteins (1). Photoexcitation of the p-hydroxycinnamoyl chromophore initiates a photocycle consisting of a number of spectrally distinguishable intermediates. The formation of long-lived signaling state I2 is associated with a major global structural change that has been described as a partial unfolding (2). These light-induced changes of secondary structure could also be observed with Far-UV CD spectroscopy for wavelengths above 200 nm (3,4). Here we show that the experimental station at the 3m-NIM monochromator allows to detect secondary structural changes in PYP over an extended wavelength range. With respect to the dark state, the photostationary state at pH4.1 of about 50% I2 accumulation displays a moderate decrease of the CD signal around 220 nm, in agreement with previous measurements (3,4). In contrast, the CD signal at 190 nm is strongly decreased suggesting large scale structural changes in the formation of the signaling state.

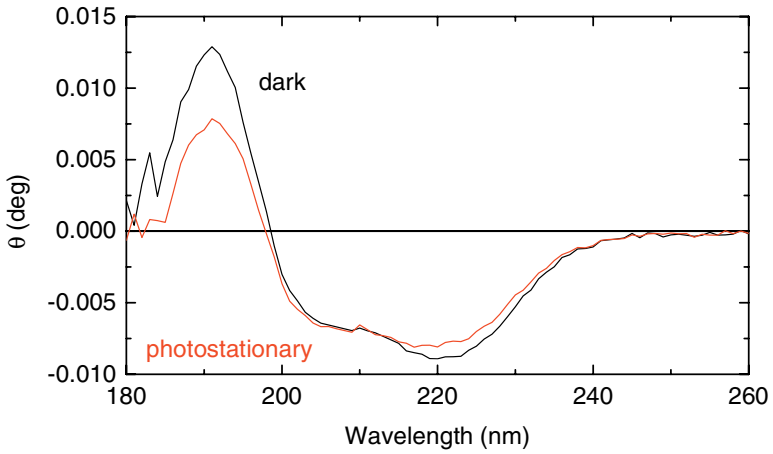

Fig. 1: CD spectra of ~ 60 µM WT PYP at pH 4.1, 0.1 mm path length, in the dark and under continuous illumination (photostationary state), respectively. The fraction of I2 in the photostationary state of about 50% was estimated from the bleach of the chromophore absorption band in the visible.

References

(1) Cusanovich, M.A., Meyer, T.E. (2003) Biochemistry, 42, 4759. (2) Rubinstenn, G., Vuister, G. W., Mulder, F. A. A., Düx, P. E., Boelens, R., Hellingwerf, K. J., and Kaptein, R. (1998) Nat. Struct. Biol. 5, 568. (3) Lee, B.-C., Croonquist, P. A., Sosnick, T. R., and Hoff, W. D. (2001) J. Biol. Chem. 276, 20821. (4) Harigai, M., Imamoto, Y., Kamikubo, H., Yamazaki, Y., Kataoka, M. (2003) Biochemistry 42, 13893.

X-ray absorption spectromicroscopy of hemocyanine in buffer solution utilizing XANES-PEEM

U. Kleineberg, M. Pohl, A. Brechling, U. Heinzmann, M. Möller#, H. Decker#, A. Oelsner*, A. Krasyuk*, G. Schoenhense*
Molekül- und Oberflächenphysik, Fakultät für Physik, Universität Bielefeld, Universitätsstr.25, 33615 Bielefeld;
*Institut für Physik, Staudinger Weg 7, 55128 Mainz;
#Institut für Molekulare Biophysik, Welderweg 26, 55128 Mainz

Photoelectron Microscopy utilizing photoemission by energy-tunable soft x-ray radiation (X-PEEM) has been proven to be a valuable tool for spectromicroscopic imaging of surface structures (chemical, topographic or magnetic contrast) on a mesoscopic size scale (spatial resolution < 100 nm, energy resolution < 1 eV). While almost all experiments performed so far have been carried out by *directly illuminating the sample surface* only very few experiments have been reported about photoelectron microscopy *in transmission geometry*. The transmission setup requires the use of thin samples attached to ultrathin (silicon) membranes (thickness 100-200 nm), both being (semi-) transparent for the incident soft x-ray radiation. Although Transmission Photoelectron Microscopy (T-PEEM) is similar in construction to the X-PEEM technique it is functionally different in the sense that it images the secondary electron distribution produced by the *x-ray shadowgraph* of the sample on the backside of the transparent photocathode and not the photoelectron yield of the sample surface itself. Transmission spectromicroscopy has considerable applications beyond material sciences e.g. in life sciences where a major advantage is the compatibility to sealed environmental sample cells where the sample can be held under controlled (e.g. hydrated) conditions.

We have performed first XANES microspectroscopy measurements on hemocyanine aggregates enclosed in a sealed wet cell in an experimental setup consisting of a transmission photoelectron microscope operated at the UE56/1-SGM beamline at BESSY II.

Hemocyanine (Hc) is a functional respiratory protein in molluscs and anthropodes, which incorporates a molecular oxygen clamp between two copper atoms. The molecule undergoes conformational changes when switching from the oxy to the deoxy state resulting in chemical shifts of the binding energies at the oxygen-K and copper L-edge.

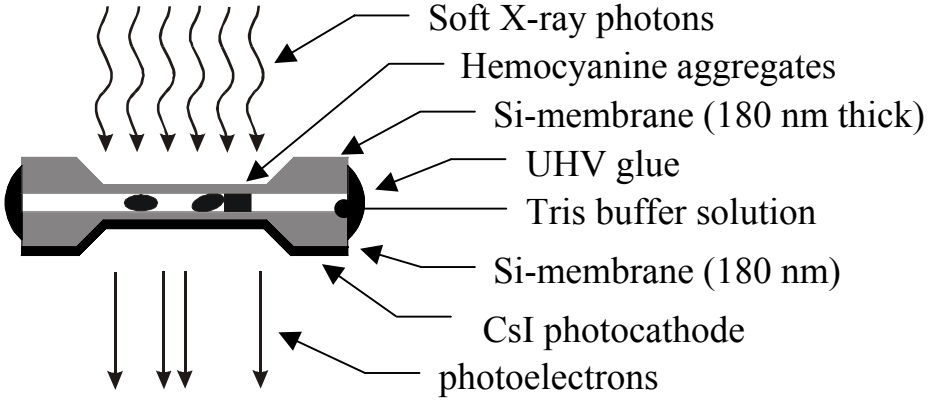

Fig. 1 : *Experimental scheme of the XANES-PEEM wetcell incorporating hemocyanine aggregates in aqueous solution*

The wet cell (Fig. 1) consists of two silicon membranes (thickness of the transparent window 180 nm each) which are glued together at the side edge by a UHV compatible epoxy glue. A droplet of a Tris buffer solution containing hemocyanine molecules (0.5 mg/ml) has been applied on the surface of one membrane before sealing the stack.
Figure 2 display a set of PEEM images (field of view approx. 50 micron) of a (dehydrated) Hc sample recorded in the transmission mode by irradiating the sample at photon energies at the oxygen K-edge. The image clearly displays bright (transparent) and darker (opaque) areas within the Hc aggregates. XANES spectra of defined different regions of interest (ROI) have been measured by recording a set of PEEM images of the same sample area for different photon energies varying from 525 to 565 eV. The image intensity integrated over the marked ROI has been plotted versus the photon energy.
The XANES spectra of different sample areas show distinct differences : While the three peaks (B at 530 eV, C, D) in the red spectrum (corresponding to red area) can be attributed to the oxygen edge of CuO, the magenta spectrum (corresponding to magenta area) represents the spectrum of Cu_2O (peak A at 526 eV). The identification of these different oxidation states has been performed by comparing our measured spectra with spectra of thin Cu, CuO and Cu_2O foils published in the literature [PhD thesis M. Hävecker, TU Berlin 2000]. Background corrected images (by dividing an image recorded at the high energy side of the O-K edge) display the distribution of CuO (top left image) and Cu_2O (center left image) within the sample area. The differences in the distribution between CuO and Cu_2O are highlighted in the bottom left image (CuO appearing bright).

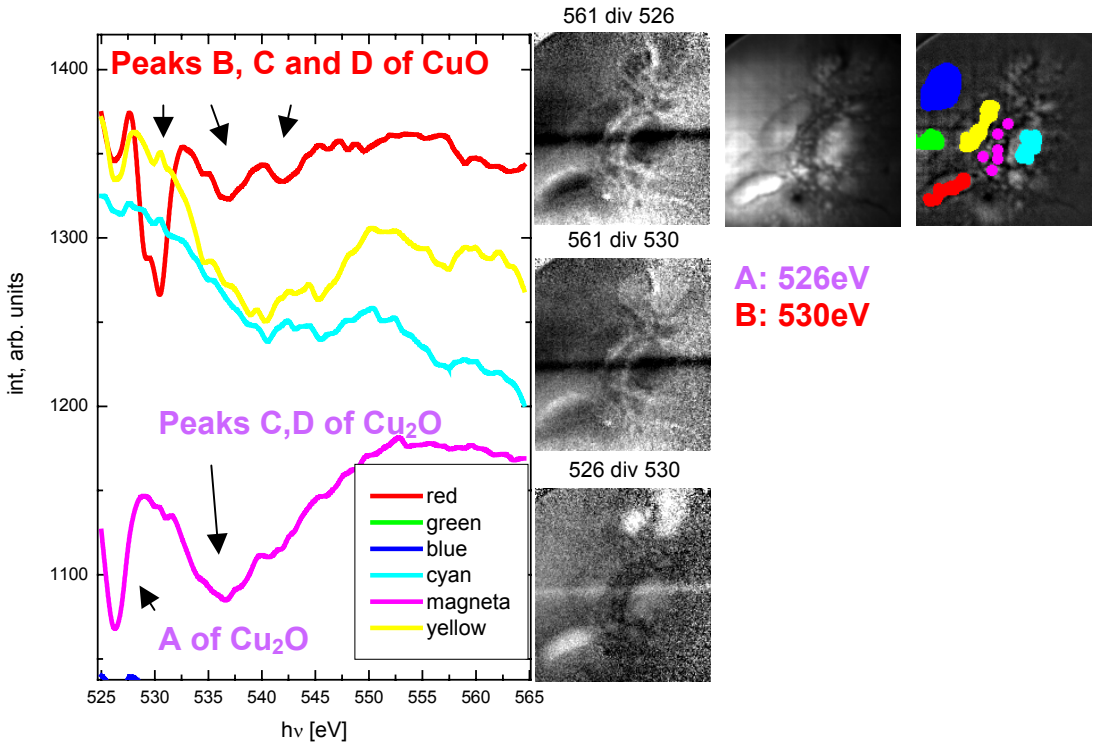

Fig. 2 : *PEEM raw image recorded at 526 eV photon energy (center top image) and attributed Regions of interest (ROI) marked by color blobs (center right). The corresponding XANES spectra have been recorded by extracting the image intensity within the marked areas at different photo energies in the 525 to 565 eV photo energy range (left).*

The authors are thankful to Prof. Salditt and Th. Gronemeier for their support in preparing Si membranes. Furthermore the support by the BESSY staff is gratefully acknowledged.
The work has been financially supported by the BMBF (FKZ 05KS1PBA-8 and 05KS1UMC-0) and the DFG (SFB 625, project B5).

Polarization Modulation Setup for Synchrotron Infrared Microspectroscopic Studies of Vibrational Linear Dichroism at the IRIS Beamline

M. Schmidt[a], U. Schade[b] and M. Grunze[a]

[a] *Angewandte Physikalische Chemie, Universität Heidelberg, Im Neuenheimer Feld 253, 69120 Heidelberg, Germany*

[b] *Berliner Elektronenspeicherring-Gesellschaft für Synchrotronstrahlung mbH, Albert-Einstein-Straße 15, 12489 Berlin, Germany*

Abstract. We realized a polarization modulation (PM) setup at the infrared (IR) microscope of the IRIS beamline in order to perform dichroitic measurements with high spatial and temporal resolution. The setup is comprised of a beam compressor in the FT-IR spectrometer accounting for the altered optics and a unit containing a linear polarizer and a photoelastic modulator (PEM) between the spectrometer and the microscope. We showed on thin films of polypropylene (PP) and polyethylene terephthalate (PET) that an almost diffraction-limited spatial resolution of 15 x 15 μm^2 can be achieved with this polarization setup using synchrotron IR radiation. This new instrumentation will enable polarization-dependent measurements for microspectroscopic investigations of vibrational linear dichroism (VLD) and hence to determine the preferred molecular orientation and anisotropy in a variety of samples, ranging from e.g. synthetic polymers to biologically relevant samples. The high spatial resolution allows mapping of small and heterogeneous sample areas while the good time resolution can be exploited to probe dynamic processes such as a sample's response to mechanical stress.

Introduction. The infrared beamline IRIS at BESSY II provides brilliant synchrotron IR radiation and is equipped with a microscope which allows diffraction-limited IR vibrational microspectroscopy.[1] It facilitates IR microanalysis of a wide variety of samples, ranging from e.g. synthetic polymers to biologically relevant samples, and can thus provide information on composition, structure, environment and interaction of matter in localized sample areas. The properties of many materials depend strongly on the degree of alignment or orientation of their constituent molecules. Oriented samples absorbing in the IR exhibit VLD, i.e. differential absorption between orthogonal states of linearly polarized IR light. Therefore, polarized IR spectroscopy and studies of VLD offer a means of characterizing molecular orientation and of quantifying anisotropy, order and disorder. The use of polarized IR microspectroscopy extends this useful technique to the investigation of small or heterogeneous samples. Furthermore, it can provide valuable information, e.g. for defect analysis and domain and boundary identification, being limited by the available spatial resolution. It was shown that combining FT-IR spectroscopy with the PM technique gives a powerful tool for fast and highly sensitive VLD measurements.[2,3] This method was also applied to the investigation of microscopic IR dichroism.[4]
Therefore, a PM setup for synchrotron IR microspectroscopic studies of VLD was established at the IRIS beamline. This setup described in detail below benefits from the brilliant synchrotron IR source and offers a unique spatial resolution which is almost diffraction-limited.

Experimental Setup. The key component in the PM setup is the PEM (HINDS Instruments, ZnSe PEM-90, II-ZS50) which has a limiting useful aperture of 14 mm. Therefore, the optical design had to be adapted so that the collimated IR beam passing from the interferometer into the microscope could be fully accommodated in the new setup. This was achieved by the insertion of a compact custom-built, adjustable beam compressor which was fitted into the restricted available space in the spectrometer (Nicolet Nexus 870). The beam compressor

consists of two 90°-off-axis parabolic mirrors with short focal lengths and two plane mirrors. It compressed the IR beam from 40 mm to 13mm by choosing the appropriate focal lengths' ratio of the two parabolic mirrors. The performance of the beam compressor was greatly improved by the superior collimation quality of the synchrotron IR beam compared to light from the conventional globar source.

The PM unit is situated between the spectrometer and the IR microscope (SpectraTech Continuμm). It consists of a linear polarizer (LOT-Oriel, wire grid polarizer, KRS-5) and a PEM which are both mounted on an adjustable bench and housed in a purgeable polycarbonate box. The polarizer generates linearly polarized IR light with a desired orientation of the electric field. It should be noted that the inherent polarization of the synchrotron IR needs to be taken into account and may be advantageously exploited. The PEM serves as the PM device and is placed in the beam path directly after the polarizer with the PEM ZnSe crystal's optical axis being tilted at 45° with respect to the plane of polarization of the incident IR radiation. The operation of the PEM is based on the phenomenon of photoelasticity. By means of a piezoelectric transducer the crystal is stressed by compression or stretching generating an oscillating birefringence at a frequency of 50 kHz. When operated with a peak retardation of λ/2 and incident linearly polarized light the PEM modulates the light beam between two perpendicular, linearly polarized states at the PEM's 2nd harmonic, i.e. 100 kHz. The PEM optical head is linked to the PEM controller which governs the retardation and which also sends the required reference frequency to the demodulator unit. In the whole setup the IR beam experiences a double modulation due to the interferometer (Fourier frequencies) and the PM device. The detector electronics were modified so that the IR signal from the MCT detector can be extracted after the preamplifier and fed into a demodulator unit. The demodulator (GWC Instruments, Synchronous Sampling Demodulator 100) demodulates the differential polarization signal for the two perpendicular, linearly polarized states from the modulated interferogram and generates the average and differential FT-IR interferograms.[5,6] The demodulated output signals are returned to the detector electronics and converted by the ADC. The IR vibrational spectra are calculated from the obtained interferograms via FFT by a computer. A scheme of the experimental setup is given in Figure 1.

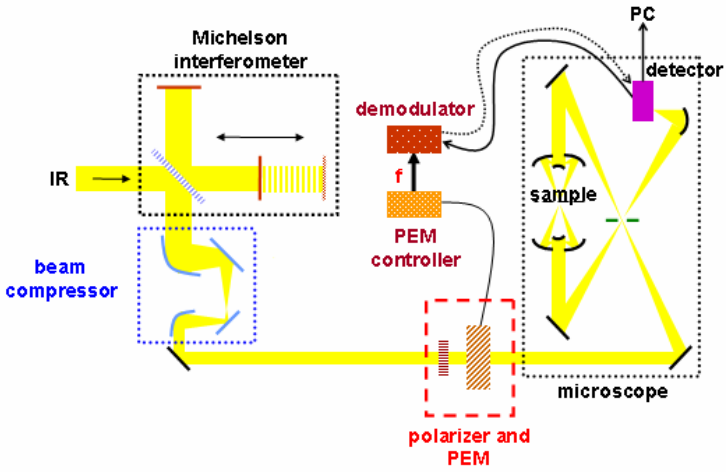

Figure 1. Schematic representation of the experimental setup

Preliminary Results. Initial tests to evaluate the capability of the PM setup were performed on thin films of PP and PET. The samples were measured with the confocal microscope in transmission and it was found that spectra could be recorded at a spatial resolution of 15 x 15 μm^2 using synchrotron IR. In general, the raw experimental results obtainable from the PM measurement are the difference spectrum ($I_{diff} = I_{\parallel} - I_{\perp}$) and the sum spectrum ($I_{sum} = I_{\parallel} + I_{\perp}$), the ratio I_{diff} / I_{sum} yields the uncorrected raw differential absorption spectrum. The results for the PP and PET samples are shown in Figure 2. It should be pointed out that after rotation of the samples by 90° the dichroitic band features in the differential absorption spectra were observed to invert as is expected.

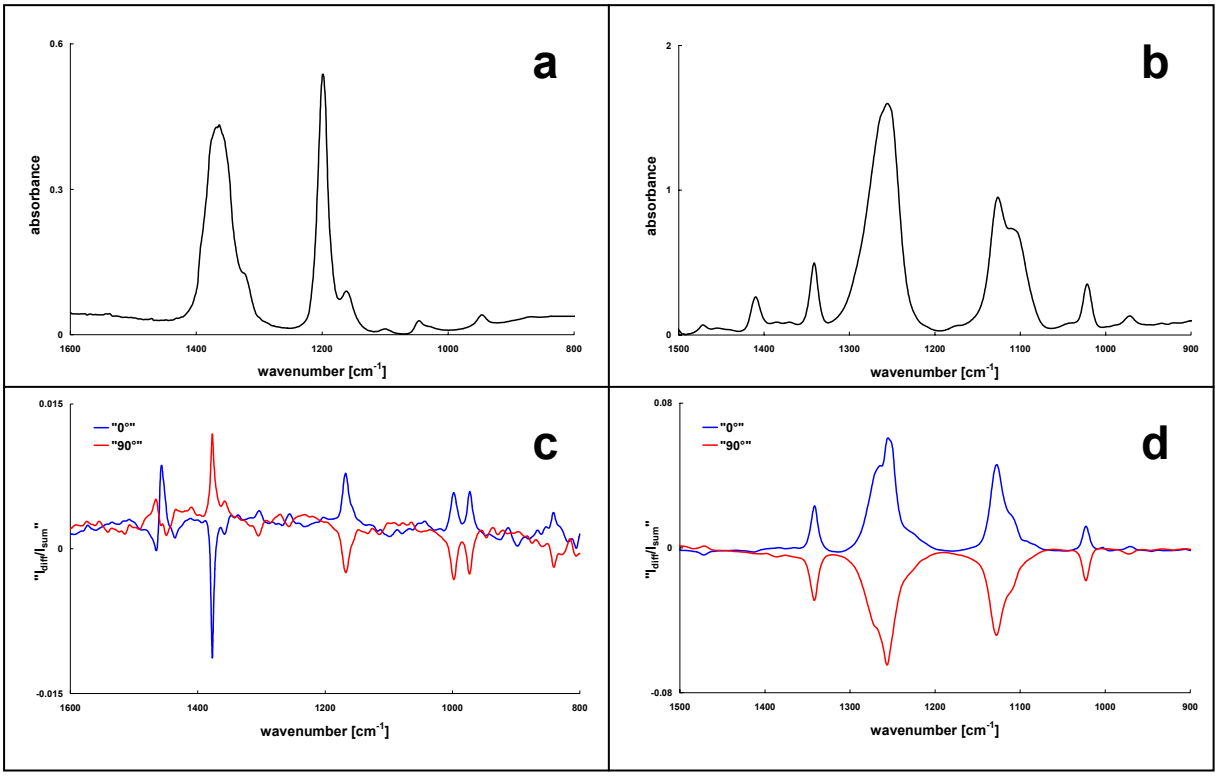

Figure 2. Absorbance spectra of a) a 20 µm thin film of PP and b) a 3 µm thin PET film, and raw differential absorption spectra of c) the PP sample and d) the PET sample. 128 scans each with a spectral resolution of 8 cm^{-1} and a spatial resolution of 15 x 15 μm^2 were recorded.

Outlook. A treatment of the experimental results with respect to calibration and correction for experimental artifacts is indispensable. This may be achieved using thin film IR polarizers as reference standards in place of the sample. The preliminary results indicate that the PM setup can afford fast and sensitive VLD measurements at a high spatial resolution. Thus, dichroitic investigations and mapping of small and heterogeneous sample areas as well as probing of dynamic processes of oriented materials should be feasible.

Acknowledgements. We would like to thank R. Dahint (Universität Heidelberg) for providing the PM equipment for the test measurements and K. Hinrichs and M. Gensch (ISAS, Berlin) for helpful discussions. We also gratefully acknowledge G. Hinte (ISAS, Berlin) and the BESSY workshop team for help with the construction of the setup.

References.

[1] U. Schade, A. Röseler, E.H. Korte, F. Bartl, K.P. Hofmann, T. Noll and W.B. Peatman, Rev. Sci. Instrum. **73**, 1568 (2002).

[2] L.A. Nafie and M. Diem, Appl. Spectrosc. **33**, 130 (1979).

[3] T. Buffeteau, B. Desbat, M. Pézolet and J.M. Turlet, J. Chim. Phys. **90**, 1467 (1993).

[4] Y. Shigematsu, A. Takada, N. Nemoto and K.H. Nitta, Rev. Sci. Instrum. **72**, 3927 (2001).

[5] M.J. Green, B.J. Barner and R.M. Corn, Rev. Sci. Instrum. **62**, 1426 (1991).

[6] B.J. Barner, M.J. Green, E.I. Sáez and R.M. Corn, Anal. Chem. **63**, 55 (1991).

U41-PGM: beamline performance improved

Ch. Jung and M. Mast, Th. Zeschke

BESSY mbH, Albert Einstein Straße 15,
D 12489 Berlin, Germany

When the U41-PGM was put into operation in spring 2000, it immediately achieved the predicted photon flux, which is on the order of 10^{13} photons per second (exit slit width 100 µm, c_{ff} = 0.65) [1]. Since this monochromator is designed to conserve the high brilliance of the low-β-source, the energy resolution for normal operation is at about 2000 over the entire energy range. Although these results are remarkable, it turned out pretty soon, that the beamline performance suffered to some extent from two limitations: *i)* the focus size in the horizontal direction was larger than expected, and *ii)* the photon flux available at the sample showed an unexpected instability.

From the inspection of the measured parameters of all optical elements it turned out that the slope error of the first mirror (M_1), which collimates the synchrotron beam in the dispersion plane and focuses it in the horizontal direction onto the sample, was out of specification. The slope error along the meridioinal axis was 0.7 arcsec, instead 0.2 arcsec as specified. The deviation from the specified curvature in general influences the size of the focus. Its contribution depends strongly on the distance between mirror and focus: the longer the path, the broader the spot.

Calculations with the optical engineering tool RAY [2] for both values for the slope error showed, that the increased slope error should not affect the vertical beam size at the focus, but that the horizontal width should be broadened by about 25%. The result is shown in figure 1.

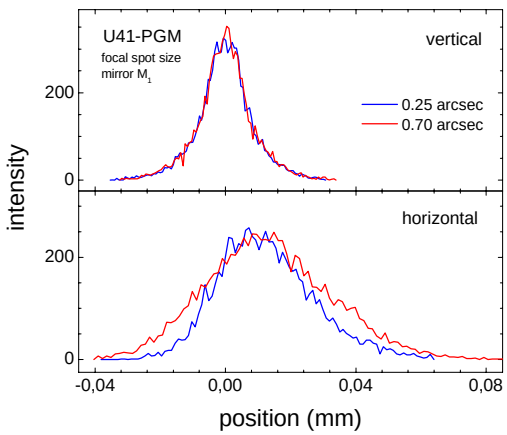

Fig. 1: Horizontal and vertical focus size for different slope errors of M_1.

We thus decided to replace the first mirror by a new one, this time with the slope error as specified. After delivery and the routine check of its performance M_1 was replaced during the shut down in march 2004. The subsequent beamline commissioning showed interesting results: the horizontal beam size could be reduced from 54 µm down to 44 µm. A nice confirmation of the calculated performance.

For those users, who need an even smaller horizontal focal spot, we implemented an additional slit close to the position of the exit slit. The width of this slit is 50 µm, the resulting beam size is 27 µm (the vertical beam size is not affected by this slit). The focii achieved with and without this additional slit are shown in figure 2.

Nevertheless, there is still some work to do, since the spot dimensions presented here are larger than expected. In their study for a microfocus beamline Weiss *et al.* [3] predict a focal size of 23 µm x 12 µm (hor. x ver.). This value holds for an optimal alignment of the beamline. From our recent measurements on the performance of the focus we know that we can optimise the focus in either the horizontal or the vertical direction to meet the specified value. But in this case the two focii do not coincide. Since coincidence of both focii is a

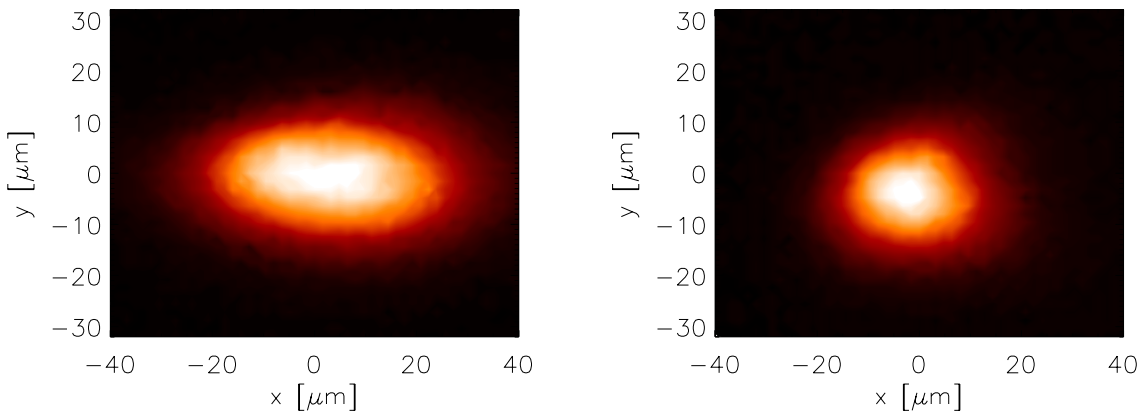

Fig. 2: Focal spot at the U41-PGM. Vertical size: 20 μm (exit slit width 40 μm); horizontal size: 44 μm (full acceptance, left), 27 μm (limited horizontal acceptance).

fundamental criterion for the alignment of the beamline, the broadening of the spot size has to be accepted.

The instability of the photon flux could not be solved in such a stringent way. From a carefull observation we concluded that the problem typically occured when the beam shutter was opened after a longer break or if the ID-gap was set close to its smallest value – delivering the highest heat load on the first optical elements. Although the intensity could be optimised again by tuning the angel of incidence of the first mirror, the situation was not satisfying.

In a time consuming procedure we analysed all possible reasons. We recorded the temperatures at the front and back end of M_1 under different conditions of illumination and heat load. We carried out FEM calculations (Th.Z.) to model the influence of heat load on the mirror and finally concluded, that the first mirror suffered from insufficient cooling. During the replacement of M_1 we decided to modify the cooling brackets of this mirror, since the length of the brackets was determined by the calculated length of the area illuminated on the mirror. This turned out to be not sufficient, the mirror now is cooled over its full length

The result is convincing: the stability of the beam position could be significantly improved, and we can offer now a stable photon flux for experimental use.

Nevertheless, maintenance and commissioning of a beamline is a never ending story. Recently we got the information, that the vertical spot size was by broadened by a factor of five. When we checked the parameters we found out, that the refocusing mirror was misaligned. Using the focus test chamber, we could determine the status, and we realigned the mirror. The conclusion for future work is to keep an eye on the beamline adjustment, especially for the last mirror, and to control the performance routinely. This, in fact, means, that we have to apply for one week of beamtime every year. Less time for user experiements, but still a good investment.

References:

[1] Ch. Jung et al., Nucl. Instr. Meth. **A 467-468** (2001) 485 – 487;
see also www.bessy.de/users_info/

[2] F. Schäfers, M. Krumrey, Technischer Bericht, BESSY TB 201, 1-17 (1996)

[3] M.R. Weiss, R. Follath, F. Senf, W. Gudat, J. Elect. Spec. **101-103** (1996) 1003 - 1012

A New In House Photoemission Chamber at BESSY

A. Vollmer, O. Rader, H. Dürr, W. Gudat, and W. Eberhardt
BESSY G.m.b.H., Albert-Einstein-Str. 15, D-12489 Berlin, Germany

SurICat (**Sur**face **I**nvestigation and **Cat**alysis) is a new photoemission chamber[1] equipped with the high resolution electron energy analyser Scienta SES100 that allows angular resolved as well as integrated measurements. Mu-metal shielding and a liquid He cryostat permit magnetism studies; preparation chambers, transfer (including a vacuum case, not shown here) and the use of Omicron standard sample plates facilitate fast access. In order to provide excellent experimental conditions, the set up was designed as a three chamber system keeping the analyser chamber free of contaminating materials such as dosed or evaporated adsorbates.

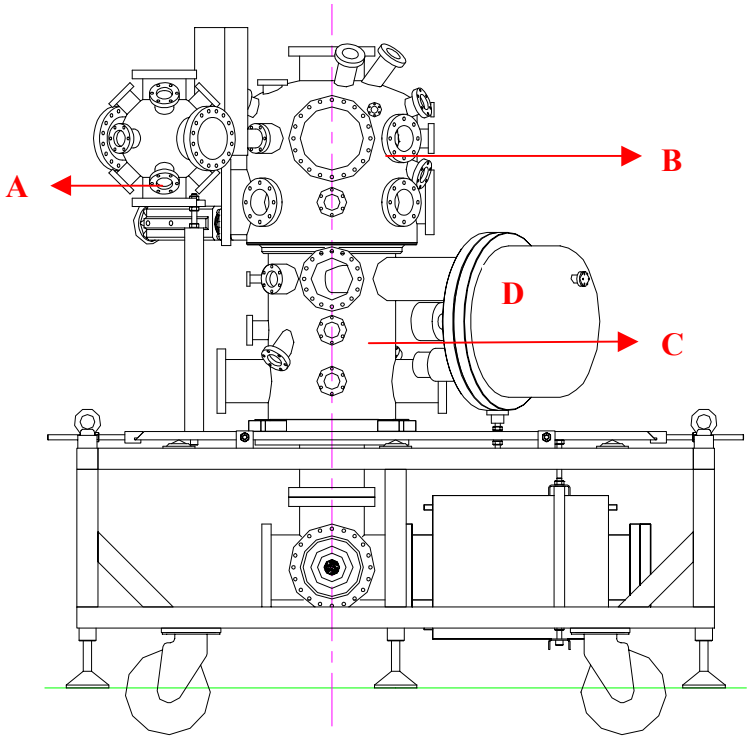

Figure 1: design of the SurICat chamber, A: Load lock and preparation chamber for possibly reactive or contaminating materials; B: "clean preparation" chamber with several analytical tools separated from B and C by valves, and C: analyser chamber with a Scienta SES100 electron energy analyser D.

The chamber part referred to as B in figure 1 houses several analytical tools such as a LEED optics and a microbalance and allows non contaminating preparation like metal evaporation or sputtering. An internal valve separates B from part C which is the mu-metal shielded analyser chamber. Specimens that hold the risk of polluting the UHV recipient can be prepared in chamber A that is also separated from B by a valve and serves as a load lock, too.

The system was set up and tested in 2004 and is now fully operational as shown in several experiments, i.e. studies on pentacene thin films and single crystals (Vollmer at al., in this annual report), lateral electron confinement on stepped surfaces (Varykhalov et al.), plasma cleaning and coating studies (Vollmer at al., in this annual report) and semi conductor investigations (Vogt at al.).

Future developments include the implementation of a total yield detector and a mass spectrometer into the system.

This new end-station is located at the optics beamline PM4, a dipole beamline delivering photon energies between 25 and 1800eV

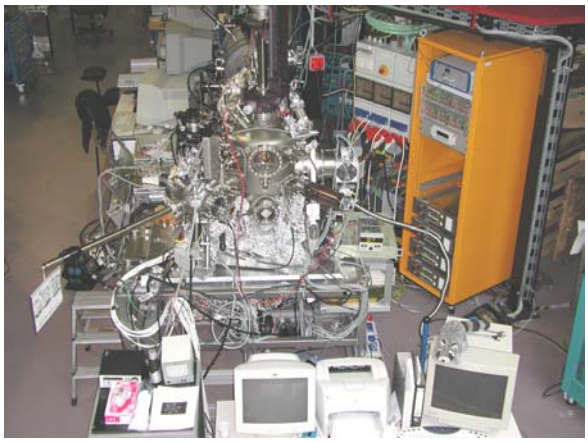

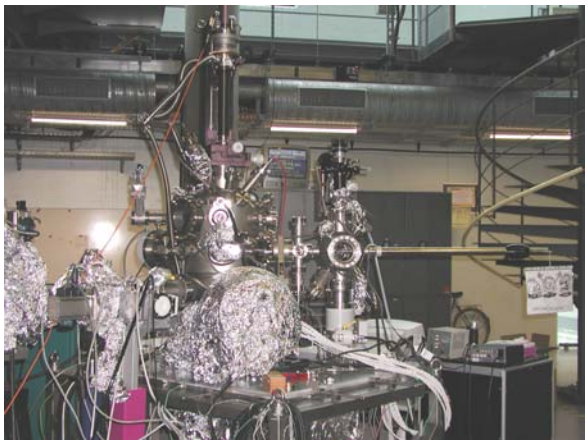

The authors wish to thank P. Rotter, B. Lanz, C. Kalus, O. Pawlizki, W. v. Scheibner and the team of the BESSY workshops for great support during design, construction and set up of SurICat.

---

[1] manufactured by Thermo Vacuum Generators, Hastings, UK

Plasma cleaning and coating procedures depending upon antenna materials and plasma gases

A. Vollmer and F. Eggenstein
BESSY G.m.b.H., Albert-Einstein-Str. 15, D-12489 Berlin, Germany
I. Salzmann
Humboldt-Universität zu Berlin, Institut f. Physik, Newtonstr. 15, D-12489 Berlin

Plasma cleaning of surfaces seems to be a powerful tool in UHV systems and is widely used to remove contaminants on optical elements. Under certain conditions this method can also be used to coat surfaces. However systematic studies by XPS and UPS were still missing. Using the BESSY end station SurICat on the optics beamline ex situ and in situ investigations of cleaned/coated surfaces were carried out by means of XPS and UPS to enlighten both the influence of the gas and the role of the antenna. Standard conditions were $2 \cdot 10^{-3}$mbar partial pressure of the plasma gas and 14W RF power intake for 3 hours.

1. Role of the plasma gas

Au films on polycrystalline Molybdenum surfaces have been prepared with an Au coated antenna using Ar, N_2 and O_2 as gases in a plasma discharge process. The carriers, used in these investigations, were unpolished polycrystalline Mo plates (10mm x 15mm) of scratchy appearance. After preparation and exposure to air for several hours, the samples have been mounted into a UHV system investigated thoroughly with XPS. With an Ar as well as with a N_2 plasma one can clearly see a gold film as identified by the Au 4f signals (Fig1); however C and O contaminations are detectable, which might origin from exposure to air prior to the measurements. O_2 as plasma gas leads to a completely different surface composition; the O_2 signal is significantly enlarged and one finds also more carbon on these samples than on those from the N_2 and Ar plasma. Additionally oxidic signals originating form Au_2O_3 can be found. Depth profiling investigations using excitation energies from 190 to 630 eV reveal a dependency due to the instability of Au_2O_3 under UHV conditions: the ratio of the Au to Au_2O_3 changes from about 1:2 at 630eV photon energy to 1:0.7at 190eV indicating more oxidic species in the bulk than in the surface near region. Since the high impurity signals (O1s, C1s) are rather disconcerting and since their origin can not be fully elucidated, accordant in situ experiments were carried out subsequently.

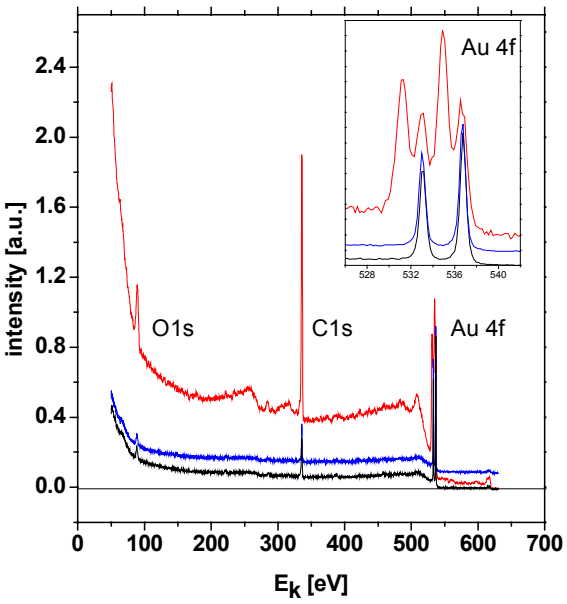

Fig.1: XPS data of ex situ prepared Au films from different plasma gases: red O_2, blue Ar, black N_2; normalised to the Au4f signal, photon energy 630eV

2. Role of the antenna

An antenna was implemented into the preparation chamber of the UHV system SurICat. The samples used were standard Omicron sample holders made of Molybdenum, which have not undergone any UHV cleaning procedure previously. XPS measurements of the raw sample clearly show a rather large amount of carbon and oxygen with only very small signals of Mo 3d. These data are shown in Figure 2 and serve as a reference for further investigations into the cleaning abilities of our method and the chemical composition of the plasma treated surface. Figure 3 delivers a comparison of the plasma cleaning process depending upon the plasma gas and the antenna material at an excitation energy of 365eV. This is only one representative set of data. Further investigations at several photon energies varying from UPS to 630eV fully corroborate the following statements and conclusions.

2.1 Aluminium antenna

2.1.1. With N_2 as plasma gas

XPS data clearly indicate that the cleaning is very efficient to remove carbon contamination; however the oxygen signal is even increased with respect to the raw and uncleaned sample. Additionally Al can be found and identified by the Al2p and Al2s peaks. Furthermore a small Au signal, the Au4f, must be ignored due to its origin from Au on the wall of the chamber, which is most likely is sputtered onto the sample. This result unfortunately shows quite plainly that various materials inside a UHV system can contaminate the sample and spoil the cleaning procedure by sputtering processes. Subsequently the next step was to use a plasma gas that has a much lower sputter cross section than nitrogen and possibly good cleaning properties:

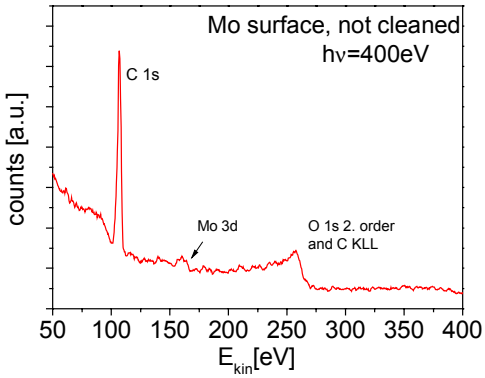

Fig.2: XPS spectrum of a bare sample of Mo, not cleaned previously. Clearly visible are the main contaminants carbon and oxygen

2.1.2. With H_2 as plasma gas

No or only minor Al or Au signals are visible, which confirms the poor sputtering capacity of hydrogen. However, the cleaning capabilities of a hydrogen plasma are poor as can be seen by C1s and O1s peaks in the spectra.

2.2. Gold antenna

2.2.1. With H_2 as plasma gas

again an insufficient cleaning of the surface but no sputtered products were observed.

2.2.2. With N_2 as plasma gas

A very clean Au spectrum has been obtained not giving any indication of impurities. In addition no Mo signal could be observed, which hints to a thickness of the Au film of more than 5 monolayers or 20Å. This is rather significant since it provides a nice possibility to gild

large areas evenly. Investigations into the nature of these gold films on a Si wafer by AFM show that the roughness of the gold film is comparable to the roughness of the bare silicon wafer.

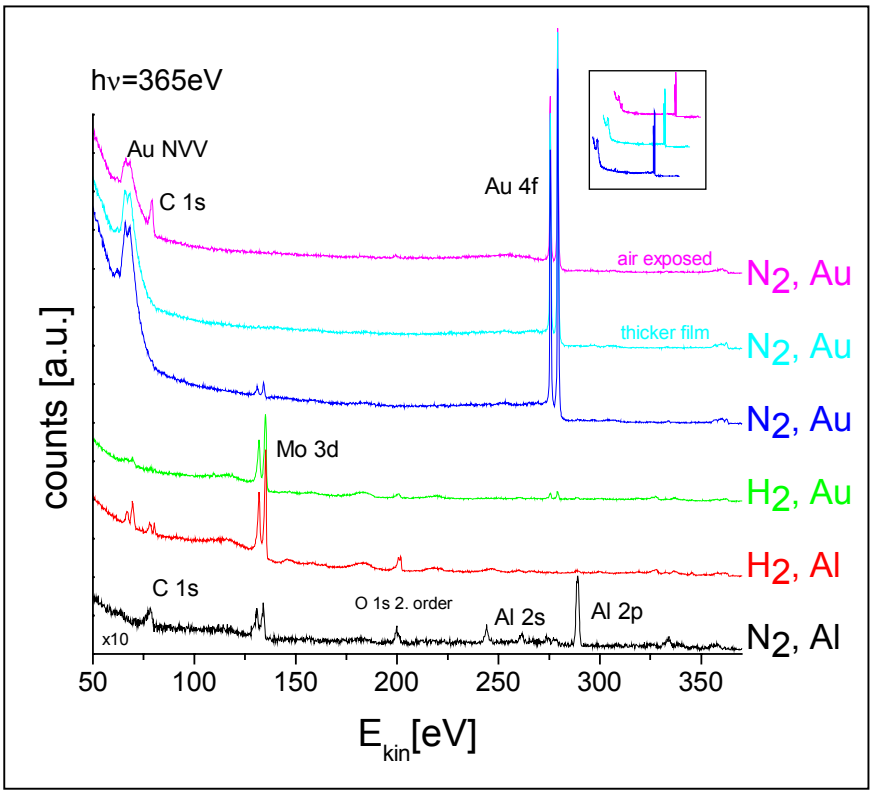

Fig.3: XPS data of the Mo specimen after cleaning procedures with different gases and antennas. The photon energy in this experiment was 365eV. N_2 always sputters the antenna material onto the surface as can be clearly seen by the Al 2p and Au 4f signals, H_2 does not fully remove C and O. The combination H_2/Au shows a minute Au signal, however no Al peak can be found for H_2/Al.

Since material originating from the chamber walls could be detected on the treated surfaces, we have repeated the experiments with the sample shaded from direct exposure to the antenna. Both materials from the chamber (Au) as well as from an Al antenna (we could not see any aluminium in the chamber nor on the sample in the last experiments) could be found on the sample, which means that shading a surface is not fully possible.

3. Conclusions and future investigations

No matter what condition, antenna material or plasma gas is being used, significant amounts of antenna material and/or sputtered material from the chamber wall can be detected. An exception hereof is the combination of hydrogen and an Al antenna, which however leaves an otherwise crowded spectrum. Even shading the sample from the antenna does not solve the problem.
The solution might be to always use the appropriate antenna material, i.e., the material of the devices that should be cleaned.
Plasma sputtering however leads to chemically very clean films. Due to the underlying material however the morphology could not be determined.

Realisation of a Fresnel Bi-mirror for X-rays

Wolfram Leitenberger
Universität Potsdam, Institut für Physik, Am Neuen Palais 10, D-14469 Potsdam, Germany,

In the last years numerous methods have been reported to determine the degree of coherence of hard X-rays. Among others there are two observation of beam interferences [1-3], diffraction gratings [4] Fresnel diffraction at a fibre [5] or intensity interferometry [6]. The quantitative characterisation of the X-ray beam is of interest for the application of coherent X-rays for imaging, speckle correlation spectroscopy characterisation of optical elements and others. From the contrast of the interference fringes experimentally measured one can determine the degree of coherence. In the case of a Young's experiment the fringe contrast is a direct measure of the degree of coherence.
The experiments were done using white synchrotron radiation of a BESSY bending magnet at the EDR-beamline and as a second test experiment we used Wiggler radiation at the material science beamline at the SLS (Villigen, Switzerland). (see next abstract)
A new version of a two beam interferometer was tested using a modified Fresnel bi-mirror arrangement. Small mirrors observed at a very low incident angle (typically α=0.1 deg) act as narrow slits of width b sin α. In contrary to previous reports of Fezzaa et al. [1, 7] using two independent mirrors we used a *monolithic* bi-mirror (Fig. 1). Two equal mirror planes of length *b* are separated by a distance *B* using a grove in the mirror. This set-up has the big advantage, that both mirrors are already aligned and only a single goniometer is needed for alignment. For example a one mm wide mirror observed at 0.1deg is seen as a slit of 1.7 µm width. A second mirror in a distance B = 1 cm this is seen in 17 µm distance of the first one. Hence diffraction phenomena even of hard X-rays can be observed in a distance of some meters behind the mirror. The evaluation of the interference fringes can be performed in good approximation with the standard formalism for Young's experiment[1, 8].

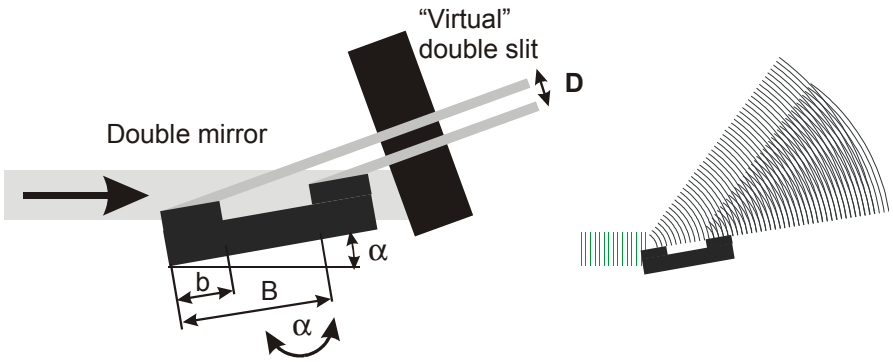

Fig. 1 Experimental set-up of a modified Fresnel bi-mirror.

For energy discrimination an energy dispersive detector with an energy resolution of about 200 eV was used. The detector was placed at 1.3 m behind the double mirror. The spatial resolution was 5 µm and was determined by the diameter of the pinhole directly in front of the detector. The result of a vertical line scan of the detector is a Young's fringe pattern with 5 µm resolution within an energy interval of 5...15 keV (Fig. 2). The mirror parameter are as follow: a_i = 0.05 deg, b = 0.5 mm, B = 7 mm. The parameter of the equivalent Young's slit are two slits of 0.4 µm width separated by 6 µm which would be difficult to manufacture as a pure absorption pattern in a mask. The 'macroscopic' structures of mm size makes the preparation of the such a device comparably simple.

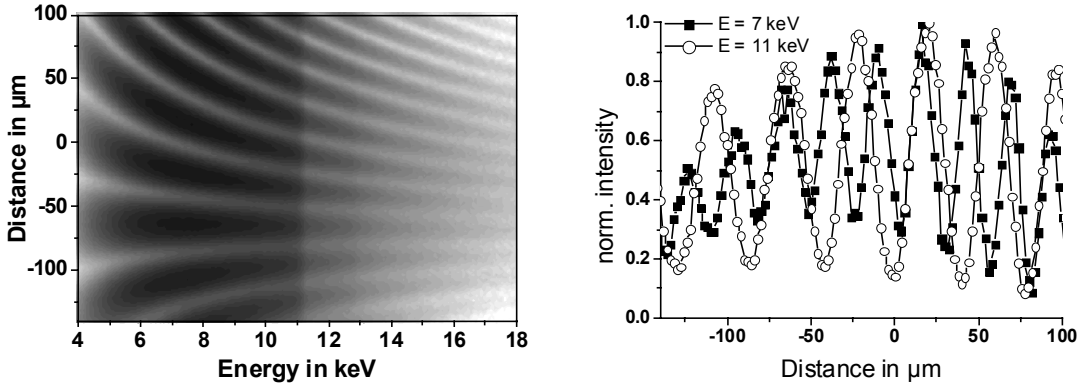

Fig. 2: a) Diffraction pattern of a Bi-mirror (parameter see text). In the range of ±100 µm from the optical axis, 120 energy spectra (5...15 keV) were recorded. In this plot, each horizontal line is an energy spectrum and black represents high intensity. b) Diffraction profiles for 7 keV and 11 keV extracted from part a)

This particular bi-mirror layout gives the possibility to additionally change the effective "slit" width and slit separation within some limits by changing the angle of incidence. This bi-mirror is only usable below the angle of total external reflection of the mirror. The reflection geometry does not cause problems with unwanted transmission of thin metal foils containing microstructures as it was used previously [9].
The first preliminary experiments were performed using float glass mirrors having a small but disturbing surface curvature of several arcsec. Experiments with an extremely flat mirror are in preparation. From this experiments we expect to extract first quantitative results for the degree of coherence fitting the fringe contrast to the model function.

References:

[1] K. Fezzaa, F. Comin, S. Marchesini, R. Coisson, M. Belakhovsky, X-Ray Interferometry at ESRF Using Two Coherent Beams from Fresnel Mirrors, X-Ray Sci. Technol. **7** (1997) 12-23.
[2] A.R. Lang, A.P.W. Makepeace, Production of syncrotron X-ray biprism interference pattern with control of fringe spacing, J. Synchrotron Rad. **6** (1999) 59-61.
[3] W. Leitenberger, S.M. Kuznetsov, A. Snigirev, Interferometric measurements with hard X-rays using a double slit, Opt. Commun. **191** (2001) 91-96.
[4] J.-P. Guigay, S. Zabler, P. Cloetens, C. David, R. Moksoa, M. Schlenker, The partial Talbot effect and its use in measuring the coherence of synchrotron X-rays, J. Synchrotron Rad. **11** (2004) 476-482.
[5] V. Kohn, I. Snigireva, A. Snigirev, Interferometric characterization of spatial coherence of high energy synchrotron X-rays, Opt. Commun. **198** (2001) 293-309.
[6] M. Yabashi, K. Tamasaku, T. Ishikawa, Characterization of the Transverse Coherence of Hard Synchrotron Radiation by Intensity Interferometry, Phys. Rev. Lett. **87** (2001) 140801-140801.
[7] K. Fezzaa, W.K. Lee, An X-ray interferometer with a large and variable path length difference, J. Appl. Cryst. **34** (2001) 166-171.
[8] M. Born, E. Wolf, *Principles of Optics*, Cambridge Univ. Press, 1999.
[9] W. Leitenberger, H. Wendrock, L. Bischoff, T. Weitkamp, Pinhole Interferometry with Coherent Hard X-rays, J. Synchrotron Rad. **11** (2004) 190-197.

Investigation of the properties of Bragg-Fresnel gratings

Alexei Erko, Alexandre Firsov
BESSY GmbH, Albert-Einstein-Str.15, 12489 Berlin, Germany

Systematic experimental investigations of Bragg-Fresnel gratings are discussed. Gold and nickel masks with periods of 0.4 μm – 5 μm were evaporated on the surfaces of Si [111] symmetric and asymmetric crystals. These have been used to obtain x-ray diffraction in the energy range of 8000 eV – 8500 eV. A theoretically calculated maximum of diffraction efficiency of the order of 30 % was measured experimentally for gratings with grooves parallel to the beam direction (sagittal gratings). Diffraction effects in the crystalline substrate for the gratings with grooves perpendicular to the beam direction (meridional gratings) limit the diffraction efficiency on the order of a few percent. Experimental data are compared with the theoretical calculations dispersion and efficiency of Bragg-Fresnel gratings.

In this paper we report on systematic experimental investigations of Bragg-Fresnel gratings made with a metallic structure on the surface of symmetric and asymmetric Si [111] crystals. A Bragg-Fresnel grating is a basic optical element for the construction of a variety of x-ray optical devices. Understanding its properties is an essential step toward effective designs and high resolution focusing dispersive x-ray optics.

The angular spectra measurements were done using the experimental arrangement shown in figure 1. The monochromatic synchrotron beam with an energy bandwidth of $\lambda/\Delta\lambda \sim 5000$ was collimated by a toroidal mirror and filtered by a pinhole of 100 μm in diameter. An angular spectrum of reflection gratings was measured at the distance of ~ 1000 mm with a one-crystal Si [111] Bragg spectrometer in non-dispersive geometry. An input beam divergence after pinhole, measured with a crystal spectrometer, was of the order of 4.5 arcsec. The sample was moved along the beam direction with a translation stage. The spectra from the different parts of the substrate were measured and compiled on the same graph to build a complete angular spectrum of a Bragg-Fresnel grating. The reflection on the grating - free surface of the crystal was also measured to obtain a reference spectrum of the direct beam.

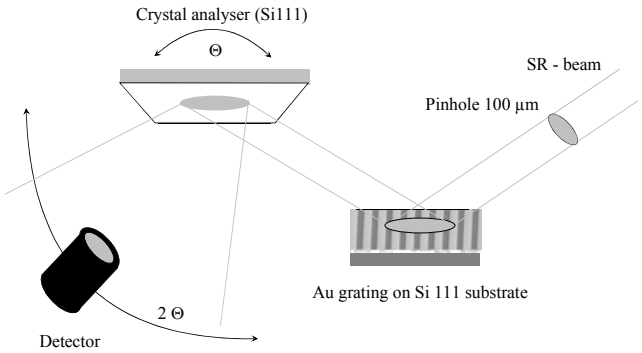

Figure 1. Experimental setup for the angular diffraction spectra measurements.

The definition of a meridional grating is given in figure 1. The complex refractive index of a grating material is

$$\tilde{n} = 1 - \delta - i\beta\,, \quad \chi = \frac{\beta}{\delta} \tag{1}$$

with β the absorption index and χ the optical characteristic of the material.

The diffraction properties of a meridional grating on a mirror surface can be described in first approximation using the conventional grating equation. The basic grating equation may be written as:

$$\lambda m = d\left[\cos\,\alpha - \cos(\,\alpha + \Delta\theta_m)\right] \tag{2}$$

with the grazing incidence angle α and $\Delta\theta_m$ the angular dispersion.

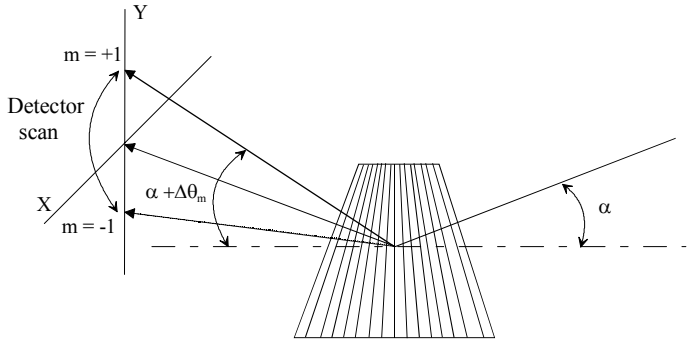

Figure 2. Experimental geometry for meridional grating measurements.

The experimental geometry and angular definitions are shown in figure 2. A detector scan was done in the optical plane, which corresponds to the meridional diffraction plane.

In the case of a meridional grating the angular dispersion in the m^{th} order can be defined using the formula:

$$\Delta\theta_m = \arcsin\left(\cos\,\alpha + \frac{\lambda m}{d}\right) - 90\,° + \alpha \tag{3}$$

where α is the grazing angle of incidence. The positions of the positive and negative orders are defined in figure 2.

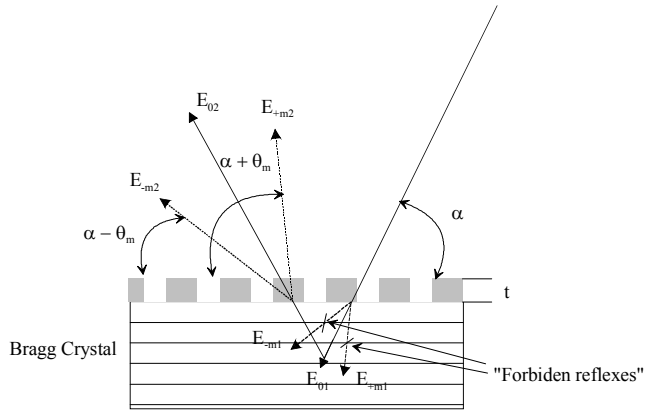

Figure 3. X-ray diffraction on a meridional Bragg-Fresnel grating with the thickness t. Bragg diffraction inside of the crystal rejects all diffraction orders which do not fulfill the Bragg conditions.

A crystalline or multilayer substrate has an angular selectivity according to Bragg law. Such a mirror can reflect a monochromatic beam only in the limited angular interval inside the so-called *rocking curve*. The diffraction on a meridional Bragg-Fresnel grating can be divided into three steps (figure 3). First, the incoming beam is diffracted on a surface transmission grating and penetrates into the crystal. If an angular dispersion of a grating $\Delta\theta_m$ is larger than the intrinsic rocking curve of the crystal, only the zero order, corresponding to the Bragg condition, is reflected by the crystal. The intensities of the diffraction orders outside of the Bragg peak will be rejected and absorbed in the substrate. The reflected zero order beam is diffracted the second time on a surface diffraction grating. Finally, the crystal substrate does not limit the angular spectrum of the outgoing beam but limits the angular acceptance of the Bragg-Fresnel grating.

The first diffraction process on a surface grating leads to a loss of output intensity. The accepted angular spectrum of the input beam is limited by a crystal rocking curve. After the he second diffraction on the surface grating produces higher diffraction orders, measured in the experiment.

If the grazing incidence angle corresponds to the Bragg conditions of the crystal, then only zero order of the primary diffracted beam will be diffracted a second time on a surface grating after reflection on a crystal. The total efficiency of the diffraction orders on a Bragg-Fresnel grating can be written as:

$$E_m = \frac{1}{4m^2\pi^2}\left\{\left(1 + \exp(-2\chi\Phi_{opt})\right)^2 - 4\cos^2(\Phi_{opt})\exp(-2\chi\Phi_{opt})\right\} \quad (4)$$

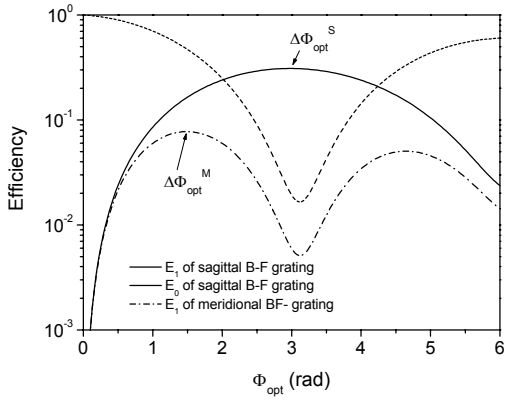

The maximum diffraction efficiency of a meridional grating is limited according to Eq.4 to the value of 0.1 in comparison with 0.4 for a sagittal Bragg-Fresnel grating.

Figure 4. Diffraction efficiency of sagittal and meridional Bragg-Fresnel gratings with a gold structure (χ = 0.095) on a Si [111] crystal substrate at 8500 eV

Consequently the diffraction efficiency of an amplitude (absorbing) meridional grating is limited by the value of 0.025 in comparison with 0.1 for a sagittal Bragg-Fresnel grating. The value of the optimal phase-shift which related to a meridional grating is less than in the case of a sagittal grating (e.g. figure 4). The optimal phase-shift for a gold mask at 8500 eV is equal to 2.89 rad for a sagittal grating and 1.48 rad for a meridional one. The optimal mask thickness has in both cases almost the same value because of the factor of 2 in the equation for the optimal thickness of meridional grating:

$$t_{opt} = \frac{\Phi_{opt}\lambda\sin\theta_B}{2\pi\delta} \quad (5),$$

Figure 4 show the relative efficiency of sagittal and meridional gratings with a gold mask of a surface of Si [111] crystal.

The optimal value of a phase-shift in a gold mask of 1.48 rad yields the theoretical maximum grating efficiency of 7.7%. Taking into account corresponding Bragg angle of 13.43 deg for Si [111] reflection and the optical parameters of gold one obtains the value of optimal thickness: 190 nm.

A gold mask for the meridional grating on a surface of Si [111] crystal was fabricated by electron-beam lithography and lift-off technology. Three gratings were investigated. The grating periods were equal to 5 μm

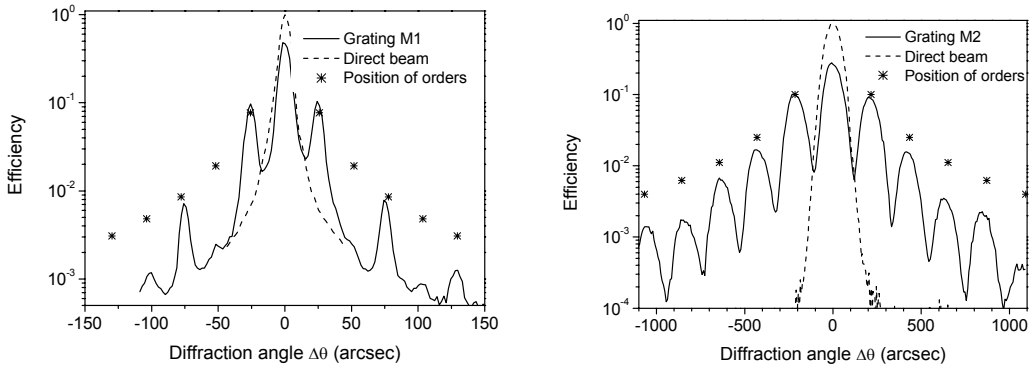

Figure 5. The diffraction spectra of the meridional gratings M1 and M2. Theoretical positions and efficiencies of the m^{th} diffraction orders (*).

(2.5 μm x 2.5 μm) for the grating M1, 0.6 μm (0.24 μm x 0.36) μm for the grating M2 and 2 μm (1 μm x 1 μm) for the grating M3. A symmetric Si [111] crystal has been used as a grating substrate. According to the experimental scheme shown in figures 1 and 3 a detector scan by the crystal analyzer was done in the vertical (optical) plane, which corresponds to the meridional diffraction plane.

The meridional gratings have a gold thickness of 190 nm. In spite of the same value of the thickness of a phase-shifting material (gold) for the gratings M1,M2 and M3, the gratings M2 and M3 have lower integral efficiency because of the shadow effect at a grazing incidence angle. As in the case of a sagittal grating, for the meridional grating with groove-to-space ratio not equal to one, odd and even orders of diffraction exist (figure 5, right).

The results of M1 and M2 measurements approved the validity of our theoretical estimate of the optimal thickness of phase-shifting material of the Bragg-Fresnel grating in the meridional direction (Eq.5). Using inclined grazing incident beam it is possible to achieve dispersion angle much large, than for a transmission angle.

In the case of sample M2 an effective period of the grating at a normal incidence is equivalent to 139 nm. The validity of the concept *the three step diffraction process* on a meridional Bragg-Fresnel grating was verified by the experimental measurements of a meridional grating M3 with period of 2 μm. A two-dimensional θ –2θ mapping has been done to record the diffraction spectra in reciprocal space. The result is represented in figure 6.

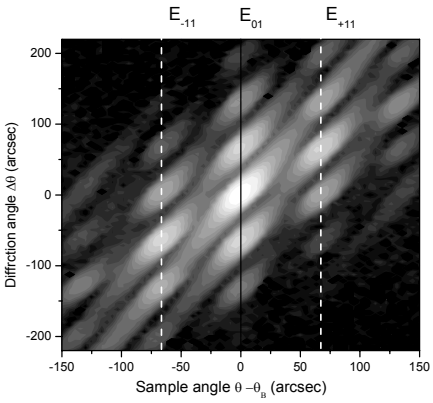

Figure 6. Intensity distribution in a reciprocal space for the meridional Bragg-Fresnel grating M3. Grating

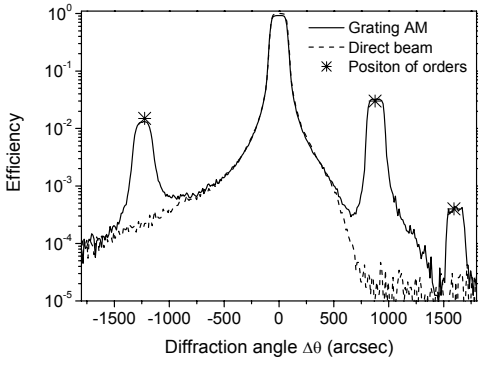

Figure 7. The diffraction spectra of the meridional gratings (AM) and sagittal grating (SM) on a surface of an asymmetrical crystal.

The diffraction angles were measured by a detector scan (2θ scan) for each value of grazing incidence angle around the Bragg maxima of the crystal. In accordance with figure 3 crystals do not reflect the x-ray beam at the angles which do not correspond to Bragg conditions. The secondary resonances appearing when $+1^{st}$ and -1^{st} diffraction orders fulfill Bragg conditions are shown in figure 6 as E_{-11} and E_{+11}. At these angles in the detector plane one can measure the same angular spectrum as at exact Bragg conditions for the primary beam analogous to one in figure 5.

According to Eqs. 2 and 3 to increase an angular dispersion of a diffraction grating and decrease an optimal grating thickness one has to use a small grazing angle for the primary beam. Conventional crystals such

as Si or Ge provide Bragg angles on the order of 10-15 deg in the energy range around 10 keV. Smaller reflection grazing angles can be realized using asymmetrical crystals with a high asymmetry parameter or multilayer mirrors with nanometer-scale periods. In our investigation we have measured samples of the grating placed on an asymmetrically cut Si [111] crystal with 13.06 deg asymmetry angle. Both sagittal and meridional gratings were investigated. The meridional grating, AM, and sagittal grating, AS, on an asymmetrical crystal Si [111] were irradiated at the grazing angle of 27 deg and 26.5 deg at the energy of 8200 eV and 8500 eV respectively. In both cases the mask thickness was of 20 nm of evaporated nickel.

The spectra, shown in figure 7, support the results of theoretical calculations of the optimal mask thickness. A small grazing angle on a meridional grating provides a dispersion angle as high as 1224 arcsec (figure 7). This value corresponds to the grating period of 25.5 nm at normal incidence. The spectra shown for the gratings M2, M3 and AM were measured using 50 μm slit placed at a distance of 1000 mm from the sample. For this the crystal analyzer was removed.

The investigation of a meridional Bragg-Fresnel grating shows completely different diffraction properties in a comparison with conventional reflection grating. First, for a monochromatic beam, an angular spectrum of the input beam is limited by the value of crystal angular acceptance (rocking curve). All the other angular spectral components are rejected. The output angular spectrum is not limited and all higher diffraction orders are present. The inclined geometry at small grazing incidence angles makes it possible to enlarge the angle of dispersion of a meridional grating. To check the value of the angular dispersion in the meridional direction the performance of a meridional Bragg-Fresnel grating has been measured. A 2 μm period, 20 nm thick nickel grating was evaporated on the surface of an asymmetrically cut Si [111] crystal with an asymmetry angle of 13 deg. A diffraction efficiency of 1% was obtained at the energy of 8.2 keV and grazing angle of 0.9 deg. This value corresponds to an effective period for a transmission grating at normal incidence of 25.5 nm. This property of a meridional Bragg-Fresnel grating opens up the possibility of producing a Bragg-Fresnel zone plate with nanometer spatial resolution.

REFERENCES

1. A.I. Erko V.V. Aristov B. Vidal, Diffraction x-ray optics, IOP Publishing, Bristol, (1996)
2. A. Firsov, A. Svintsov, A. Erko, W. Gudat, S. Kuznetsov, M. Grigoriev, A. Asryan, M. Ferstl, S. Shapoval, V. Aristov Nuclear Instruments and Methods in Physics Research, **A467**-**A468**, 366-369 (2001)
3. A. Firsov, A. Svintsov, S.I. Zaitsev, A. Erko, V. Aristov "The first synthetic X-ray hologram: results", Optics Communications, **202**, 55-59, (2002)

A raytracing code for zone plates

Alexei Erko, Franz Schaefers, Nikolay Artemiev[a]

BESSY GmbH, Albert-Einstein-Str.15, 12489 Berlin, Germany
[a] Laboratoire d'Optique Appliquee ENSTA Ecole Polytechnique Chemin de la Huniere F-91761 Palaiseau cedex, France.

A raytracing code for zone plates incorporated in the BESSY raytracing program RAY is described. This option allows one to calculate intensity distributions in a focal plane of circular or linear zone plates considering diffraction limited resolution. Zone plate material properties are also taking into account using optical constants data tables. The complete code is available as PC-Windows version.

Raytracing is an indispensable tool for the design of optical systems for synchrotron radiation sources, and various programs have been developed during the last decades [1-2]. By using a general purpose raytrace program, it is possible to obtain detailed information about the overall performance of the beamline optical system. Usually, the optical elements that are treated by a raytrace program are slits and screens, mirrors and gratings, Bragg crystals and multilayers. Modifications of the wave front of light produced by these optical elements are described in the frame of geometrical optics and analytical equations rather well. However, the weak point of the ray-optics is micro-focusing with diffraction limited imaging. In this paper a raytracing code for zone plates incorporated into the program RAY [3] which is extensively used for beamline performance calculations at BESSY is described. The mathematical model allows one to follow a chromatic blurring of the focal spot as well as the smearing of the focus due to an unevenness of the incident wave front (described by rays). Another advantage of the model is that it gives an intensity distribution, including auxiliary maxima and background radiation in the focal position.

Using the Fresnel – Kirchhoff diffraction integral one may obtain the form of the diffraction pattern [4]. Referring to figure 1, this gives the complex amplitude A(x',y',z') as

$$A(x',y',z') = -(i/2\lambda)\cdot\iint A(x,y,z)\frac{\exp[ik(\bar{r}+\bar{s})]}{(\bar{r}+\bar{s})}dxdydz \qquad (1)$$

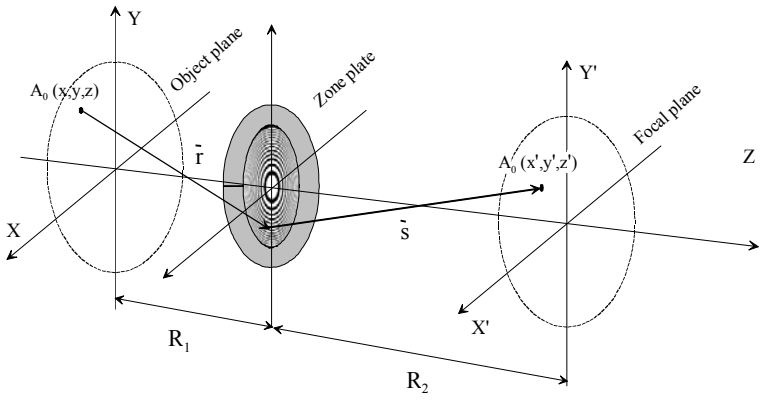

Figure 1. The coordinate system used in the calculation of the diffraction pattern of a circular aperture

where *A(x,y,z)* and A(x',y',z') are the amplitudes in the object and image planes, *k* is the wave number ($k = 2\pi / \lambda$), $\bar{r}$ and $\bar{s}$ are the propagation vectors, *dx* x *dy* x *dz* is an area element of the aperture, and the integral is carried out over the whole object aperture.

In practice in order to get the intensity distribution behind a zone plate one must take the double integral Eq. 1 for each point A(x',y',z') on the screen and that would be just the distribution for a point source at $A_0(x,y,z)$. In turn, if the source is not just a point, this procedure must be repeated for each point of the source. This method can give a good result but the time needed for such calculations is awfully long.

On the other side the intensity distribution in the focal plane of a zone plate for the point source can be calculated analytically [4]. Supposing a non-coherent irradiation, that is valid for all existing x-ray sources, one can reconstruct the image as a superposition of the images of the point sources, distributed in the object plane. Each point source will be transferred through a zone plate with a resolution defined by the zone plate aperture, the so-called diffraction limited resolution. One can use an approximated analytical solution of the Eq. 1 for the point source to define the position of the image for each object point. At this step one can replace a wave front presentation with a ray-presentation. In the case of ray transmittance each point of the source (or preceding element on an optical arrangement) produces a ray with defined parameters: spatial coordinates and energy. After interaction with a zone plate the ray angular coordinates are changed according to the defined probability. The probability distribution can be calculated using analytical formulas, represented in the following parts of the paper.

Consider a zone plate in which odd zones are transparent and even zones are covered by a material with a rectangular form of grooves (phase-amplitude zone plate) [5]. The phase shift and attenuation of the amplitude produced by the even zones are given by

$$\Delta\phi = 2\pi\delta t /\lambda; \tag{2a}$$

$$\Delta\beta = 2\pi\beta t /\lambda - \chi\Delta\phi; \tag{2b}$$

where $\chi = \beta/\delta$; β and δ are the absorption and refraction indexes respectively.

Combining the amplitudes of the waves, transmitted through the transparent and covered zone, one can calculate the diffraction efficiency in the m^{th} order [6]:

$$E_m = I_m / I_{in} = [1/(\pi^2 m^2)][1 + \exp(-2\chi\Delta\phi) - 2\cos(\Delta\phi)\exp(-\chi\Delta\phi)]; \tag{3}$$

for the odd orders $m = \pm1; \pm3; \pm5;...$ Even orders do not exist. The I_{in} is the incoming wave integral intensity and I_m the integral intensity in the m-th order of diffraction.

The maximum of the function I_m/I_{in} can be found taking the derivative of the Eq. 3:

$$\sin(\Delta\phi_{opt}) + \chi[(\cos(\Delta\phi_{opt})\exp(-\chi\Delta\phi_{opt})] = 0; \tag{4}$$

where the value of $\Delta\phi_{opt}$ is the optimum phase shift in the zone plate material.

The optimum thickness of the zone plate can be calculated using Eq.(4) as:

$$t_{opt} = \Delta\phi_{opt}\,\lambda / (2\pi\delta); \tag{5}$$

Analogous to Eq.(3), the efficiencies of the zero order diffraction E_0 and the part absorbed in the material of a zone plate E_{abs} can be calculated using expressions:

$$E_0 = 0.25[1 + \exp(-2\chi\Delta\phi) + 2\cos(\Delta\phi)\exp(-\chi\Delta\phi)]; \tag{6}$$

and

$$E_{abs} = 0.5[1 - \exp(-2\chi\Delta\phi)]. \tag{7}$$

Depending of the value of parameter χ all materials can be called as a "phase" material or an "amplitude" one. Usually effective phase-shifting materials could be characterized by the value of $\chi < 0.1$.

Although the above analysis indicates the positions of the foci and the diffraction efficiency of a zone plate, it does not give the form of the diffraction maxima, which can be obtained using the Fresnel - Kirchhoff diffraction integral.

The solution of the two-dimensional Fresnel - Kirchhoff diffraction integral can be found in a form of the Bessel or sin(x)/(x) function of first order with an argument [4]:

$$\nu_m = r_N\, k\, (r'/F_m); \tag{8}$$

where r' the radial distance between the optical axis and an arbitrary point in the image plane.

The radial intensity distribution at the focus of a circular zone plate is well described by an Airy pattern analogous to a perfect thin lens:

$$I_m'(\nu_m) \sim [2J_1(\nu_m)/\nu_m]^2 \tag{9}$$

Tracing the zone plate the program first solves the standard raytracing task of the ray surviving probability. The ray, which falls into the aperture of the zone plate, is considered to be partially absorbed by the zone plate material. Together with the rays diffracted to negative ($m < 0$) and high ($m > 5$) orders this ray is considered as "lost" because its intensity at the first order focus is infinitesimally weak. So, the ray must be thrown away with the probability:

$$E_{lost} = E_{abs} + \sum_{m=-\infty}^{m=-1} E_m + \sum_{m=5}^{m=\infty} E_m \tag{10}$$

for all $m < 0$ and $m > 5$.

If the ray is still considered as a survived one, then its destiny has also two ways:

1). A ray is not diffracted (zero order) and its angle ξ to the optical axis remains unchanged with probability E_0.

2). The remaining probabilities for the ray to be diffracted into first, third and fifth positive orders according to Eq.(3) are: E_1, E_3, E_5.

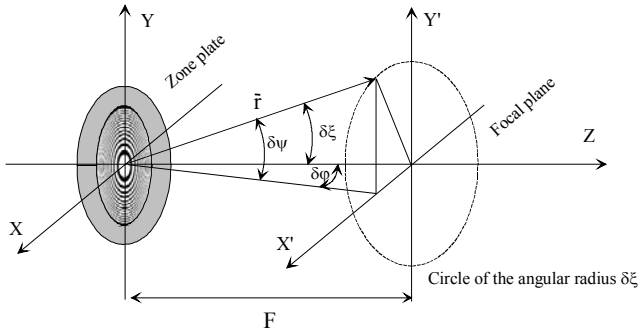

Figure 2. The reference frame of the program, the angles of diffraction of a ray and the circle of the angular radius δξ at the position of the first order maximum of a zone plate

For the diffracted ray the probability to be deflected by the diffraction angles δφ, δψ and δξ to the X, Y and Z axis respectively, is defined by I_m' (ν_m) and calculated by Eq.(10). The definition of the RAY-coordinate system is shown in figure 2.

The ray is deflected randomly by the angle of $0 <= \delta\xi <= \delta\xi_{max}$. According to figure 2 the values of the diffraction angle δφ and δψ are defined in small angle approximation by the expression:

$$(\delta\xi)^2 = (\delta\psi)^2 + (\delta\varphi)^2 \qquad (11)$$

For each ray the values δψ and δφ are randomly selected within the angular range of $0 <= \delta\psi, \delta\varphi <= 0.707\ \delta\xi_{max}$. Then the value of δξ calculated according to Eq.11 passes through the probability generator in accordance to Eq. 10. Only those angles which pass this filter and have a Bessel-function-like probability distribution are used in the further procedure. Respecting the real intersection point of the ray with the zone plate, the real angles of its deflection are calculated as follows:

$$\Delta\varphi = \delta\varphi - y_{zp} / F_m; \quad \text{and} \quad \Delta\psi = \delta\psi - x_{zp} / F_m; \qquad (12)$$

where y_{zp} and x_{zp} are the coordinates, where the ray hits the zone plate.

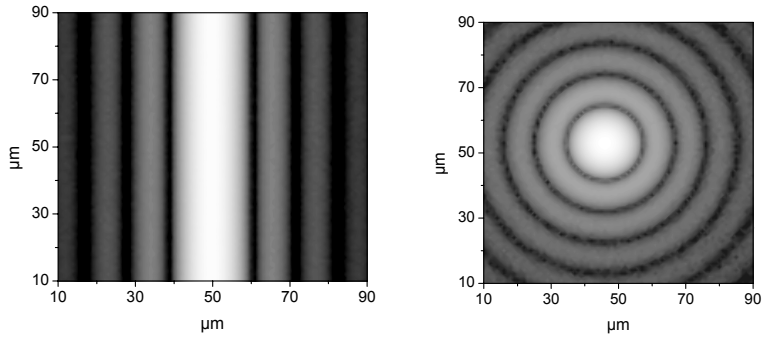

Figure 3. Diffraction limited resolution for a linear (left) and a circular (right) zone plate

Diffraction limited resolution has been checked using a point source and a divergent beam. An image aperture was placed in a distance calculated by the thin-lens formula. The results, obtained with the RAY program are shown in figure 3 for a linear (left) and circular (right) zone plate, respectively. The zone plate parameters are listed in the table. The same zone plate was calculated using a diffraction program used for x-ray holograms [6]. The results were found to be identical.

The calculations are performed for a monochromatic point source at the energy of 100 eV, located on the optical axes of the zone plate. The zone plate material is a carbon with an optimum thickness of 171 nm. The two-dimensional intensity profile in the focal plane for the zone plates, shown in figure 3, was obtained by raytracing of 10^8 rays.

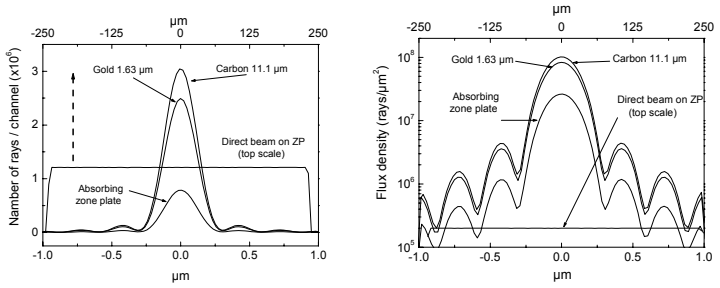

Figure 4. Number of rays per channel (a) and flux density (b) in the focal plane of a zone plate made with different materials (bottom scale). Shown also is the direct beam flux (a) and flux density (b) on a zone plate (top scale). The total number of rays is 10^8.

The integral efficiency of zone plates made with different materials is shown in figure 4. In this case, to demonstrate the RAY performance in different energy ranges, a parallel beam with photon energy of 8500 eV have been chosen. The linear zone plate focuses in horizontal (X) direction. The outer zone width is equal to 0.3μm. At the focal distance of 1000 mm the corresponding lens aperture is 500 μm. Three materials were chosen: gold with an optimum thickness of 1629.5 nm, carbon with optimum thickness of 11.1 μm and finally a non-transparent material for the simulation of an amplitude zone plate.

RAY presents the results in form of a 100 x 100 pixel array of a multi-channel analyzer. The size of each channel depends on the aperture, covered with scattered rays. This aperture can be defined by a slit placed in the image plane, as was done for calculations shown in figure 4. Figure 4a represents the number of rays, collected

in channels in X direction, integrated vertically, for three zone plate materials (bottom scale). The slit is placed in the focal plane, the corresponding width of the channel is 0.03 μm. Shown also is the direct beam, measured in the plane of the optical element (upper scale). Zone plate aperture is 500 μm and the corresponding width of each channel in horizontal (X) direction is 6.05 μm. The area covered by each curve in figure 4a corresponds to the integral diffraction efficiency. In the table 1 these areas are normalized to the incident number of rays of 10^8. In figure 4b the corresponding flux density in rays / μm^2. is shown. A flux density gain in rays /μm^2 can be obtained using the data in figure 4b.

For the development of a raytracing procedure for such an optical element like a Fresnel zone plate one has to combine two opposite descriptions of the nature of light, which usually exclude each other: wave theory and geometrical optics. As a result, a correct intensity distribution is calculated in a close vicinity of the positive order foci. Material properties of a zone plate are taken into account using a transformation of integral diffraction efficiencies to a probability of ray deflection or absorption. The same principle is used for the calculation of a diffraction limited resolution. Using the RAY cod a zone plate can be calculate also as an imaging device. The main advantage of this model is that we avoid double integration over the area of a zone plate as well as over the area of its focal plane.

1 C. Welnak, G.J.Chen, F. Cerrina Nucl. Inst. and Meth. A347, (1994), 344-347

2 T. Yamada, N. Kawada, M. Doi, T. Shoji, N. Tsuruoka, H. Iwasaki, J. Synchrotron Rad. 8, (2001), 1047-1050

3 F. Schaefers *RAY - the BESSY raytrace program to calculate synchrotron radiation beamlines*, Technischer Bericht, BESSY TB 202, (1996), 1-37

4 M. Born and E Wolf, *Principles of Optics*, 5th ed., Pergamon Press, Elmsford, N.Y. (1975) 378 - 386

5 Erko, V.V.Aristov, B.Vidal, *Diffraction X-Ray Optics* IOP Publishing, Bristol, (1996) 26-36

6 J. Kirz, J. Opt Soc Am., **64**, (1974), 301-309

7 Firsov, A. Svintsov, S.I. Zaitsev, A. Erko, V. Aristov *The first synthetic X-ray hologram: results*, Optics Communications, 202, (2002), 55-59,

Angular spectral analysis of reflection zone plates

Alexei Erko, Franz Schaefers, Alexandre Firsov
BESSY GmbH, Albert-Einstein-Str.15, 12489 Berlin, Germany

Conventional zone plates as well as reflection or Bragg-Fresnel zone plates can be described as a superposition of diffraction gratings with different periods (spatial frequencies). This model is very common in the mathematical analysis of holograms and diffraction images [1]. An illustration of this model is shown in figure 1. A zone plate irradiated with a parallel beam produces diffraction limited images of different orders F_1 F_3 F_5 etc. at distances of F_1, F_2, F_3 from the optical element. Each grating, located on the radius r_i from the optical axis has a local period of d and directs the diffraction orders to point F_n. In figure 1 three periods, d_1 d_2 and d_3 are shown, but in reality we have a continuous change of the period within the zone plate radius. Using a raytracing presentation, one can define each direction of diffraction as a ray, deflected by the optical element toward to the focal points of the diffraction orders. Therefore the angular spectra of these rays will correspond to the angular spectra of diffracted beams in diffraction theory. According to general principles of diffraction optics this spectra can be used for the calculation of the focal spot size by Fourier transform of the angular distribution. In figure 2 an angular spectrum calculated with RAY for a zone plate is shown.

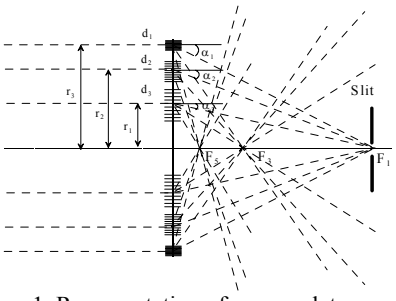

Figure 1. Representation of a zone plate as a superposition of diffraction gratings with variable period

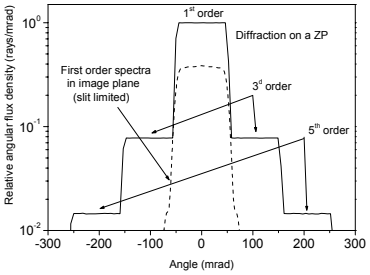

Figure 2 Angular spectra calculated just behind a ZP (solid line) and in the focal plane limited by a slit of 10 μm (dashed line)

The raytrace program RAY was used for the development of a practical method for measurements of zone plate parameters: efficiency and resolution [2]. In figure 2 an angular spectra of the rays is shown, diffracted on a zone plate and calculated just behind an optical element. One can evidently see different angular regions, responsible for focusing in different diffraction orders: +1; +3; +5. These spectra can be used for a direct measurement of zone plate resolution and efficiency. With the help of a Fast Fourier Transform program the spatial frequency spectrum can be converted into an intensity distribution in the focal plane. Our calculations show identical results obtained by Fourier transformation of the spectra and by raytracing. The parameters measured by this method are free from experimental errors, caused by a source size. A parallel beam spatially filtered through a pinhole is used in this experiment.

Measurements of zone plate spatial frequency spectra where done at the BESSY beamline KMC-2 using highly a collimated x-ray beam at an energy of 8500 eV. A linear meridional (lines perpendicular to beam direction) Bragg-Fresnel reflection zone plate made on the surface of a Si(111) crystal has been used. The zone plane parameters are listed in table 3. The optimum thickness of the phase-shifting material was calculated taking into account the Bragg angle for Si 111 reflection at 8500 eV [9].

$$t = 0.5\, t_{opt} \sin \theta_B \qquad (1)$$

In the case of gold at 8500 eV the optimum thickness was found to be 190 nm.

Table 3. Parameters of the Bragg-Fresnel zone plate used for the measurements

Energy range	8500 eV
Bragg angle for Si 111	13.45 deg
Minimum zone width	1.47 μm
Optimal gold thickness	190 nm (1630 nm at normal incidence)
Lens aperture along the crystal surface perpendicular beam direction	740 μm (170 μm projection on the beam direction) 600 μm

The angular spectra measurements were done using the experimental arrangement shown in figure 3. The monochromatic beam with $\Delta\lambda/\lambda \sim 5000$ was collimated by a toroidal mirror and filtered by a pinhole of 100 μm in diameter. An angular spectrum of the zone plate was measured at a distance of ~ 1000 mm with one-crystal Si 111 Bragg spectrometer in non-dispersive geometry. The incident beam divergence after the pinhole, measured with a crystal spectrometer, was of the order of 4.5 arcsec. Due to the small beam size the sample was scanned along the beam by a translation stage. The spectra from the different parts of the zone plate have been measured and composed on the same graph to build a complete angular spectrum of the Bragg-Fresnel lens. The reflection on the free crystal surface also has been measured to produce a reference spectrum of the direct beam.

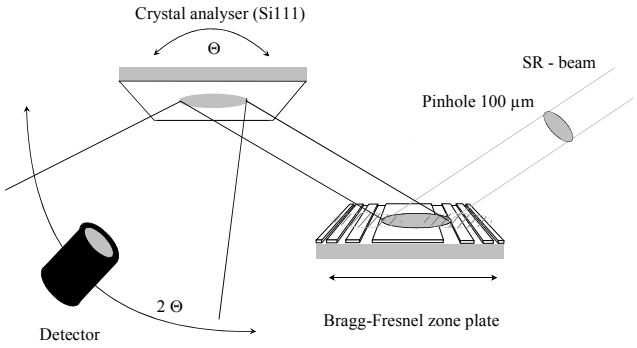

Figure 3. Experimental setup for the measurements of the angular diffraction spectra

The diffraction spectrum of the lens is shown in figure 4. All the measured spectra overlap on one graph and are normalized to the reflection from the free crystal surface. On the same figure 9 the calculated spectrum obtained by raytracing the zone plate with an input beam divergence of 4.5 arcsec is also shown. A minimum zone width for the best fit was found to be 0.34 μm and a gold thickness of 1350 nm. These values are in good correspondence to the projections on the beam direction of the outer zone with and gold layer thickness of the BFL.

In figure 9 (right) is shown a reconstructed flux distribution in the focal plane obtained by Fourier transformation of the calculated raytracing spectra and the shape of the experimental spectra. Both curves are in very good agreement and have the same Full Width Half Maximum (FWHM) of 0.3 μm.

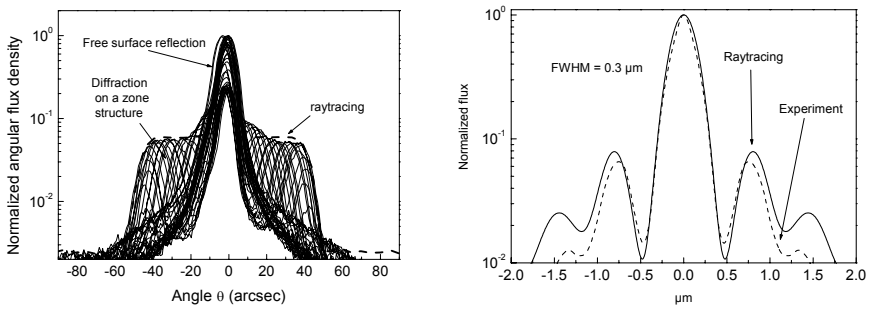

Figure 4. The measured angular diffraction spectra in comparison with raytracing calculations (left) and a reconstructed flux distribution in the focal plane (right)

To prove the resolution in the meridional direction the performance of a meridional Bragg-Fresnel grating has been measured. A 2 μm period, 20 nm thick nickel grating was evaporated on the surface of an asymmetrically cut Si (111) crystal with asymmetry angle of 13 deg. A diffraction efficiency of 1% was obtained at 8.45 keV at a grazing angle of 0.48 deg, corresponding to an effective period for a transmission grating at normal incidence of 16.8 nm or, for a zone plate, an outer zone width of 8.4 nm.

Analysis of the angular distribution of diffracted rays leads to the possibility to fit experimental spectra and find zone plate characteristics, such as the outer zone width and the thickness of a phase-shift layer. These characteristics can be obtained almost independently from the experimental conditions, taking into account only beam divergence. Using this method a considerable resolution improvement for the meridional Bragg-Fresnel lens in comparison with a normal-incidence zone plate with the same outer zone width could be shown. The resolution enhancement of 4.3 times was measured experimentally. The measured efficiency of the Bragg Fresnel zone plate with a thickness of 190 nm corresponds to the efficiency of a transmission zone plate with a thickness of 1350 nm.

1. Collier R. J., Burckrardt Ch. B., Lin L. H., *Optical Holography*, Academic Press, New York, London, (1971)
2. Erko, F. Schäfers, A. Firsov, W.B. Peatman, W. Eberhardt, R. Signorato, "The BESSY X-Ray Microfocus Beamline project", Spectrochimica Acta A, 2004, **Part B 59**, 1543-1548

μ-CT with asymmetric Bragg reflection as magnifying optics

P. Modregger†, P. Schäfer†, D. Lübbert†, J. Goebbels‡, H. Riesemeier‡, R. Köhler†

†*Institut für Physik, Humboldt-Universität zu Berlin, Newtonstraße 15, D-12489 Berlin*
‡*Bundesanstalt für Materialforschung und -prüfung, Unter den Eichen 87, D-12205 Berlin*

Generally, the resolution limit for images in the hard x-ray regime is determined by available detectors (i.e. a few $10\mu m$ for commercial CCD-cameras and $\approx 1\mu m$ for x-ray sensitive photo plates). The x-ray image magnification with asymmetric Bragg reflection (the so-called Braggmagnifier) is a promising way to overcome this resolution limit, simultaneously providing a high detector efficiency and a strong phase contrast. Although this technique was first presented by Förster *et al.* in 1980 [1], the imaging process is currently not understood in detail.

The phase contrast is introduced by an analyzer crystal (which also acts as a magnifier crystal) placed between sample and detector. After transmission of the incident x-ray wave through the sample the local propagation directions of the wave are changed according to its phase [2]. The analyzer set to fulfill the Bragg condition for the undeviated propagation direction acts as an angular filter and rejects the deviated propagation directions.

For two dimensional magnification a second magnifier crystal set perpendicular to the first is needed and we have chosen the Si-(422) for the first and the Si-(004) for the second reflection (figure 1). The nearly perpendicular exit angle of the first reflection allows a rather compact design. This approach is justified by numerical simulations recently done by our group indicating the importance of reducing the sample to analyzer distance to avoid the strong influence of Fresnel diffraction. The miscut of both magnifier crystals was chosen to provide a 40fold magnification at an energy of $8.047\,keV$.

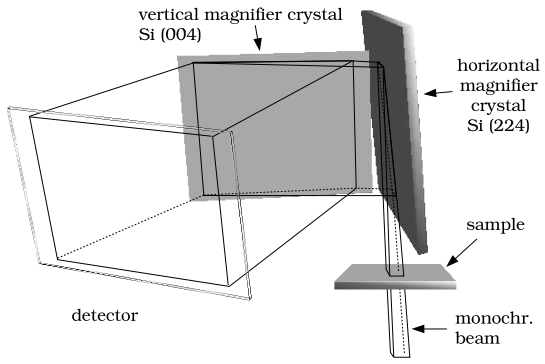

Figure 1: Setup for two dimensional magnification.

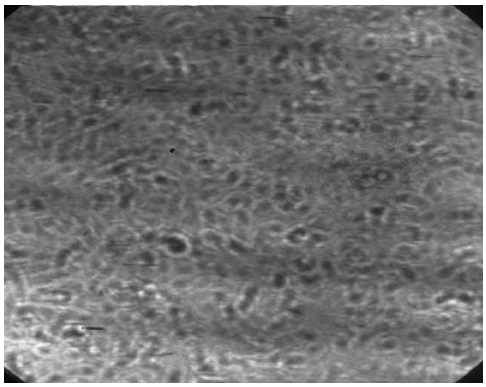

Figure 2: Background image in absent of a sample in the beam.

The first investigations of the imaging with the Braggmagnifier by our group were made in 2000 [3]. The images showed an unexpected strong distortion due to misalignment of the second magnifier crystal [4]. Introducing the possibility to align the second magnifier we successfully reduced the distortion. This encouraged us to investigate the possibility to apply tomographic reconstruction on images taken on different rotation angles with respect to an axis perpendicular to the incident beam. In this first approach we were aware of the fact that the algorithms for tomographic reconstruction are based on absorption contrast while the acquired images mainly show phase contrast. Therefore, we expected artifacts and obtained only geometric information about the sample.

The experiment was carried out at the beamline ID-02-01 (BAMline) in March 2004. Due to a phase object present in the beam (probably an unpolished Be-window) we encountered heterogenous artifacts in the images (figure 2). A CCD-camera (Proscan, Legerlechfeld) with an image amplifier was used as an area detector. Although, the beam intensity was comparatively small, we surprisingly had exposure times of just $100\,ms$, which strongly emphasizes the high detector efficiency of the presented imaging technique. The camera had 1024x1024 pixels each sized $19\times19\,\mu m^2$ resulting in a voxel size of about $0.5\times0.5\,\mu m^2$. However the CCD-camera provided a comparable small dynamic range of just about 8 bit, rejecting the larger contrast variations the Braggmagnifier delivers.

Because thin, cylindric objects are most suitable for tomographic reconstruction and because the Bragg magnifier is designed to be used in biological and material science imaging, we have chosen a spider leg as a sample. The sample was mounted on a rotation stage with a wobble in the range of a few micrometer. On each rotation angle 10 images were acquired and summed up to reduce background noise. Figure (3) shows an example of an image taken on a certain rotation angle.

M. Riesemeier of the Bundesanstalt für Materialforschung und -prüfung kindly made calculation for the cross section. Figure (4) shows the result. An estimation from the smallest detail visible leads to an achieved resolution of about $3\,\mu m$.

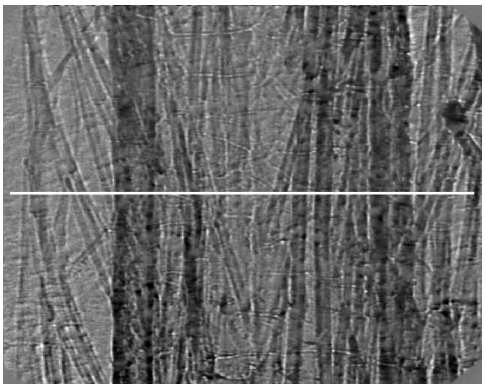

Figure 3: Background corrected 2d image of the spider leg. The line indicates the position of the cross section shown in figure 4.

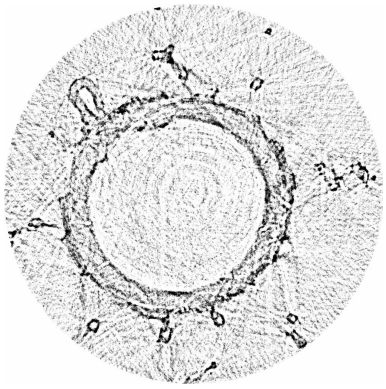

Figure 4: Cross section of the spider leg. The image diameter is $450\,\mu m$.

Taking into account the difficulties we encountered (strong beam artifacts, the limited dynamic range and field of view of the CCD-camera - some hairs of the spider leg moved out of the field of view during rotation - and the too low accuracy of the rotation stage) the results are already surprisingly good. In further experiments an improved resolution below 1 m is expected and this yields the possibility for three dimensional phase contrast imaging with a spatial resolution in the sub-mircometer regime.

[1] E. Förster, K. Goetz and P. Zaumseil, Kristall und Technik **15** (1980) 937

[2] M. Born and E. Wolf: *Principles of Optics* (7th edition; 1999), Cambridge University Press

[3] R. Köhler, P. Schäfer, J. Richter, R. Schubert, ESRF-report HS-1043 (2000)

[4] R. Köhler, P. Schäfer, Cryst. Res. Technol. **37** (2002) 734-746

Computed tomography experiments at BAM*line*

G. Weidemann, J. Goebbels, H. Riesemeier, Th. Wolk
Federal Institute for Materials Research and Testing (BAM)
Unter den Eichen 87, 12205 Berlin, Germany

In cooperation with HMI the spatial resolution of the computed tomography experimental set-up was improved (1.5 µm voxel size) using a microscope objective together with a YAG szintillator screen of 7.5 µm thickness. The major field of investigations were further studies on bone remodelling and implants together with the Technical University Dresden as well as the characterization of polyethylene aggregates together with the TU Berlin (M. Patzlaff, Institute for Technical Chemistry).
Polypropylene particles of different size classes were polymerized with $TiCl_4/MgCl_2$-catalyst in gas phase or liquid pool. The particle morphology was studied at an energy of 10 keV with CT. The inner particle porosity (cracks and voids) is visible.
The knowledge of morphology is necessary for evaluation of diffusion coefficient of penetrant into polymer particle estimated from sorption experiments.
Fig. 1 and 2 show two samples from the polymerization performed in liquid pool with a mean particle size of 750 µm and 400 µm.

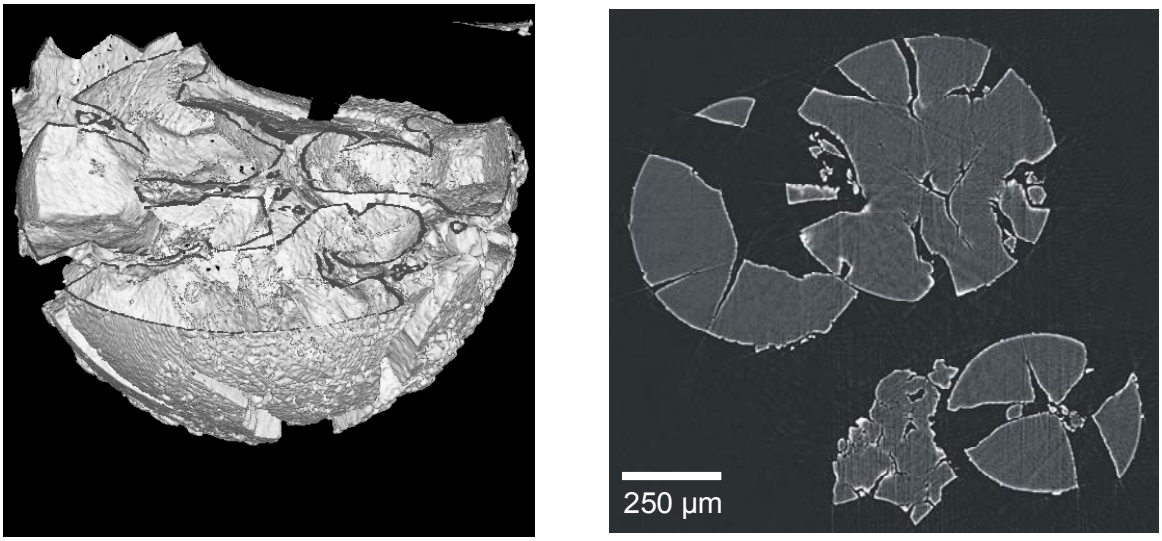

Fig. 1: Cross section (right) and isosurface representation (left) of polypropylene particles with mean particle size of 750 µm.

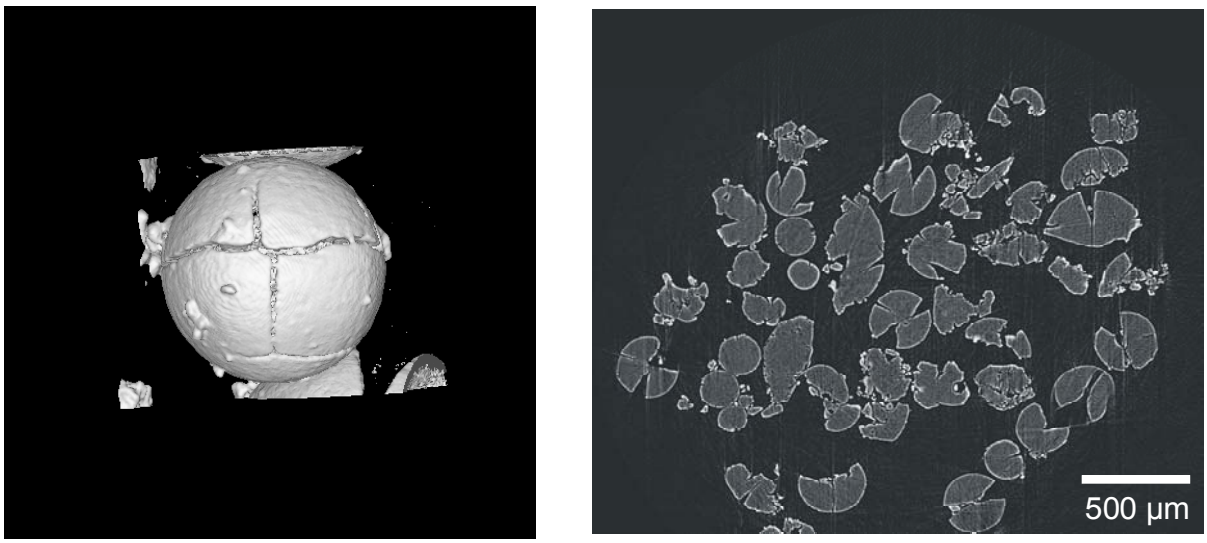

Fig. 2: Cross section (right) and isosurface representation (left) of polypropylene particles with mean particle size of 400 µm.

First experiments are performed at BAM*line* to visualize the dendrite structure of high-temperature single crystal material CMSX-4 (cooperation with TU Berlin, Institute for Materials Science and Technology). The shape of dendrites becomes visible due to the increased occurrence of pores in the interstices. Fig. 3 shows at left a cross section parallel to the [001] axis of the single crystal (dimension 0,42 x 0,6 x 10 mm^3). The right image shows an isosurface representation of pores along the [001] axis. The experiments were done at energy of 42 keV. The voxel size was $(3.5\ \mu m)^3$.

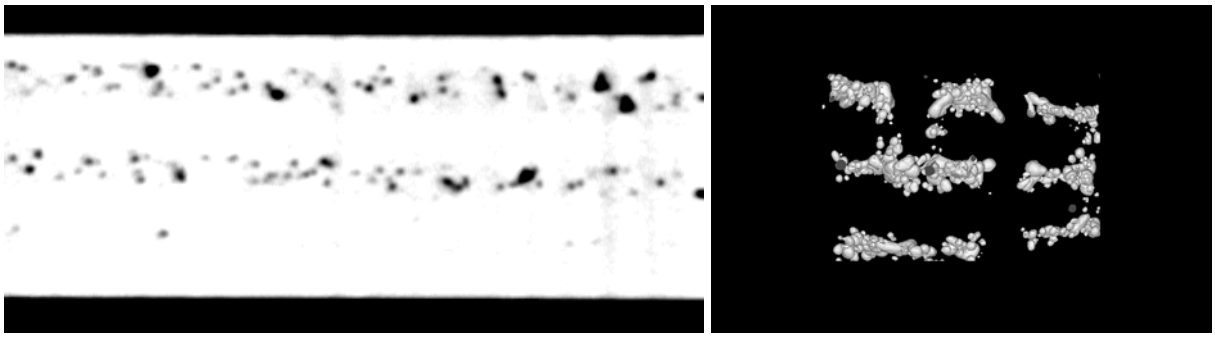

Fig. 3: left: cross section parallel to the long axis; right: isosurface representation of pores, view along long axis

Characterization of Metal Composites by Synchrotron-Refraction-CT

Bernd R. Müller, Manfred P. Hentschel, Axel Lange, Michael Harwardt
Bundesanstalt für Materialforschung und -prüfung (BAM), D-12200 Berlin, Germany

Introduction

X-ray refraction reveals the inner surface and interface concentrations of nanometer dimensions due to the short X-ray wavelength near 0.1 nm. Sub-micron particle, crack and pore sizes are easily determined by "X-ray refractometry" without destroying the structure by cutting or polishing for microscopic techniques. The physics of X-ray refraction is quite similar to the well known refraction of the visible light by optical lenses and prisms, which is governed by Snell's law. However a major difference to the visible optics is, that the refractive index n of X-rays in matter is nearly one ($n < 1$) [1]. This causes deflections at very small angles in the order of a few minutes of arc.

The specimens for the test programme have been provided by MTU Aero Engines. They consist of a titanium matrix (Ti6242) reinforced by SiC fibres (SCS6). The investigations have been performed at the materials research station of BAM (BAM*line*).

Physics and Instrumentation

The refracted intensity distribution of a cylinder without absorption effects can be expressed as $I^*_R(2\theta) = I_R(2\theta) - I_{R0}(2\theta) \cdot I/I_0 = I \cdot k \cdot d \cdot N \cdot R$ [2] where I^*_R depends on the transmitted intensity I, the thickness d and the inner surface density $\Sigma = N \cdot R$ (N is the amount of fibres) of the sample, respectively. R is the radius of the fibre, θ is the scattering angle and I_0 the intensity of the incident beam. The proportional factor k is a specific constant of the used apparatus and can be determined by measuring a probe with a known inner surface density. The proportional factor k and the inner surface density Σ define the refraction value $C = k \cdot \Sigma$, which is a relative measure of the surface density of the sample. For practical measurements the surface density of the sample can be measured according to $C = 1/d \cdot (I_R/I - I_{R0}/I_0)$. A detailed description of the method and measurement can be found elsewhere [3].

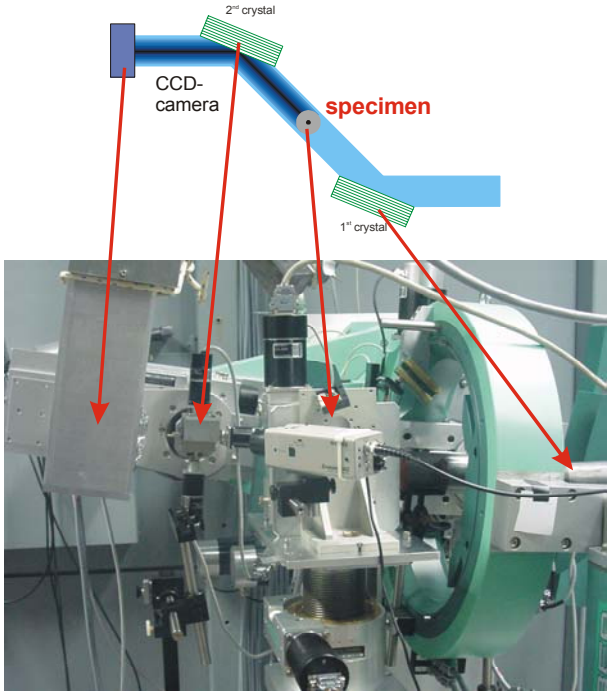

Figure 1: Sketch and photograph of the experimental set up at the BAMline

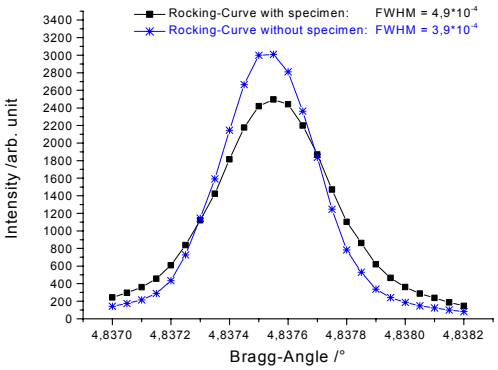

Figure 2: Rocking curve of the Si(111) single crystal pair in symmetric configuration from Fig. 1; with specimen (filled square) and without specimen (star) between the two crystals. The area under the curves is set to equal.

The experimental set up is sketched in Fig. 1. A parallel and monochromatic beam (up to 60 keV) with a band width of about 2% is delivered by the Double-Multilayer-

Monochromator (DMM) of the beamline. For a good transparency of the specimen we used a 50 keV photon beam. The beam has a horizontal width of up to 30mm and a vertical width of a few millimetres, respectively. The beam from the DMM is than reflected by two Si(111) single crystals in a symmetric configuration. They are set to there Bragg condition for the chosen energy. An X-ray sensitive CCD-camera is placed behind the second crystal. It detects the photons reflected by the second crystal with a lateral resolution of about 5,3 x 5,3 μm^2. The Rocking curve width of the second crystal against the first crystal is FWHM=$3{,}9 \cdot 10^{-4}$ Degree (see Fig. 2, stars). Different from the set up for phase contrast CT, the sample is situated in the X-ray beam between the two crystals. The highly collimated and monochromatised beam from the first crystal transmits the specimen and will be attenuated according to the absorption properties of the specimen. Additionally, the beam is deflected due to the refraction effect at all interfaces in the composite as explained above. This leads to a broadening of the Rocking curve as shown in Fig. 2 to FWHM=$4{,}9 \cdot 10^{-4}$ Degree (curve with filled squares).

Measurements and Results

The cylindrical specimens for the test programme have been provided by MTU Aero Engines. As reinforcing fibre the SCS6-fibre from Textron was taken. It has a 33 µm diameter carbon fibre as a core with a 1 µm pyro-C-protective coating, followed by SiC an again by a pyro-C-protective coating of 3 µm. The overall diameter of the fibre measures 140 µm. The fibres are coated (30 µm) with the titanium base alloy Ti6242 by magnetron sputtering and than bundled and formed by Hot Isostatic Pressing (HIP). Static and cyclic forces were applied parallel to the fibres which leads to the evaluation of the mechanical parameters. After the tests the specimens were examined by metallographic methods and the fractured surfaces were analysed. As a new approach for non-destructive testing the specimens were investigated by 3D X-ray Refraction Computed Tomography at the BAM*line*. The measurements were performed by rotating the specimens around there cylindrical symmetry axis for 360 degrees in steps of 1 degree. After each step an exposure was taken. The data sets were analyzed by filtered back projection as known from the data treatments for conventional absorption CT.

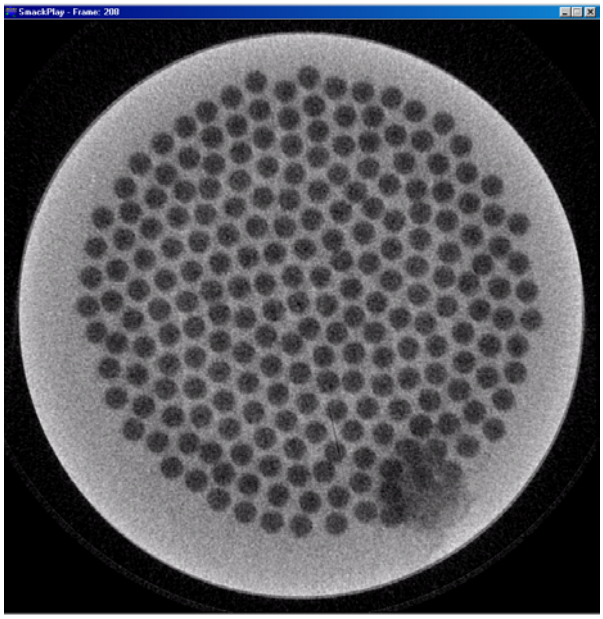

Figure 3: Reconstruction of the absorption measurement. 100 kV, 4,7 x 4,7 x 4,7 μm^3 Voxel.

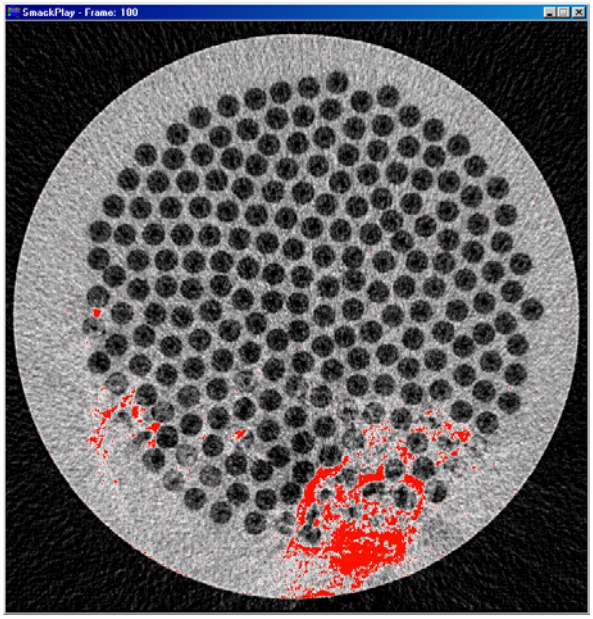

Figure 4: Reconstruction of the refraction measurement. 50 keV, 5,3 x 5,3 x 5,3 μm^3 Voxel. Specimen between two crystals.

Fig. 3 shows the reconstruction of one plane out of 300 planes of the absorption data set, which was taken in our CT-laboratory (100 kV, 4,7 x 4,7 x 4,7 μm^3 Voxel). It shows the cross section of a LCP specimen. The reinforcing SiC-fibres are shown up as dark discs with a slightly darker core. They are not symmetrically arranged to the rotational axis of the specimen. A crack (dark area) can be realised in the lower right part of Fig 3, which

corresponds very well with the visible crack at the cladding of the specimen. No further indications can be seen for cracks or fibre failure in the remaining area. Fig. 4 demonstrates the feasibility of X-ray refraction computed tomography performed at the BAM*line* (50 keV, 5,3 x 5,3 x 5,3 μm^3 Voxel). It shows the same part of the specimen as Fig. 3 does, but even if the filtered back projection and the reconstruction is not jet adapted to the refraction effect, the information content is much higher. The absorption information is the same as in Fig. 3. But in addition the refraction effect reveal, that the crack distribution in the matrix (red coloured areas) is much broader than expected from the absorption information. Furthermore the grey discs in the lower and left part of the picture evince single fibre failure.

CONCLUSIONS

X-ray refraction techniques combine analytical capabilities of sub-micrometer structure detection with the requirements of non-destructive full volume characterization. Its potential of contrasting cracks and pores will be an alternative to other attempts on raising the spatial resolution of CT machines. X-ray refraction therefore might help faster materials development, better understanding of meso-structures and partly replace micro analysis and mechanical testing in advanced materials science.

References

[1] A. H. Compton, S.K. Allison: “X-ray in Theory and Experiment”, Macmillan and Co. Ltd., London (1935).

[2] M.P. Hentschel, R. Hosemann, A. Lange, B. Uther, R. Brückner: “Röntgenkleinwinkelbrechung an Metalldrähten, Glasfäden und hartelastischem Polypropylen”, Acta Cryst. A 43 (1987) 506.

[3] B.R. Müller, A. Lange, M. Harwardt, M.P. Hentschel, B. Illerhaus, J. Goebbels, J. Bamberg, F. Heutling: „Refraction computed tomography“, Materialprüfung Jahrg. 46 (2004) 6, 313-319.

Location and quantification of OH in nominally anhydrous minerals

M. Koch-Müller, GeoForschungsZentrum Potsdam, Telegrafenberg 14473 Potsdam

We report here the results of our studies on the location of OH in **Superhydrous Phase B** (shy B), $Mg_{10}Si_3O_{14}(OH)_4$. Although shy B is definitely not an anhydrous mineral but contains about 5 wt % H_2O, we investigated this phase in the context of our project "Location and quantification of OH in nominally anhydrous minerals", since the background and methods of this study are the same as for the above mentioned project.

The presence of water in the earth's crust and mantle has enormous effects on the dynamic of processes of the earth, because the incorporated hydrogen changes the physical properties of the minerals such as the melting point, rheological behavior (hydrolytical weakening) and the transformation kinetics. Beside in nominally anhydrous minerals (NAMs) such as pyroxene, garnet and olivine hydrogen may be stored in the Earth's mantle in hydrous minerals such as dense hydrous magnesium silicates (DHMS). Experimental studies have shown that DHMS could be important hosts for H_2O in the Earth's mantle. It is even discussed that dehydration of DHMS may be responsible for deep-focus earthquakes between 500 and 700 km (Pacalo and Parise, 1992). One of these DHMS phases is superhydrous phase B. Although the phase is known for more than 10 years now, its crystal structure especially with respect to hydrogen is still under debate. In this study we synthezised shy B at 22 GPa and 1200 (LT) and 1400 (HT) °C and investigated the samples by transmission electron microscopy (TEM), single crystal X-ray diffraction, Raman and infrared spectroscopy.

Our studies show that shy-B exist in two polymorphs. The LT polymorph crystallizes in a low symmetry form (Pnn2) and the HT polymorph in the higher symmetry space group Pnnm. TEM showed that both modifications consist of nearly perfect crystals. IR spectra taken on polycrystalline thin films exhibit just one symmetric OH band and 29 lattice modes (MIR-FIR) for the HT polymorph in contrast to two intense but asymmetric OH stretching bands and at least 48 lattice modes for the LT sample. The IR spectra differ not only in the number of bands, but also in the response of the bands to changes in pressure. The pressure derivatives for the IR bands are higher for the HT polymorph indicating that the high symmetry form is more compressible than the low symmetry form.

To locate the hydrogen in both structures polarised single crystal IR spectra were taken at Bessy's IR beamline with an spatial resolution of about 8 x 8 μm. The IR spectra indicate that in the LT-polymorph extensive ordering occurs at the hydrogen sites, whereas in the HT-polymorph just one H position is realised. The observed polarization behaviour of the OH band of shy B in structure Pnnm is in perfect agreement with the OH dipole orientation as proposed by Pacalo and Parise (1992). In the LT-polymorph 2 groups of OH bands can be distinguished according their polarisation behaviour (Fig. 1). By analogy with the high symmetry form we propose two groups of OH dipoles: OH1 and OH2 (Fig 1). The orientation of the dipoles are in accordance with the polarisation behaviour of the OH bands. These two groups are composed of several subsites with the some polarisation behaviour. Thus, in the low-temperature polymorph extensive ordering occurs not only at the Mg but also at the hydrogen sites. It seems that these order/disorder could stabilize superhydrous phase B in a wider P,T field than previously expected.

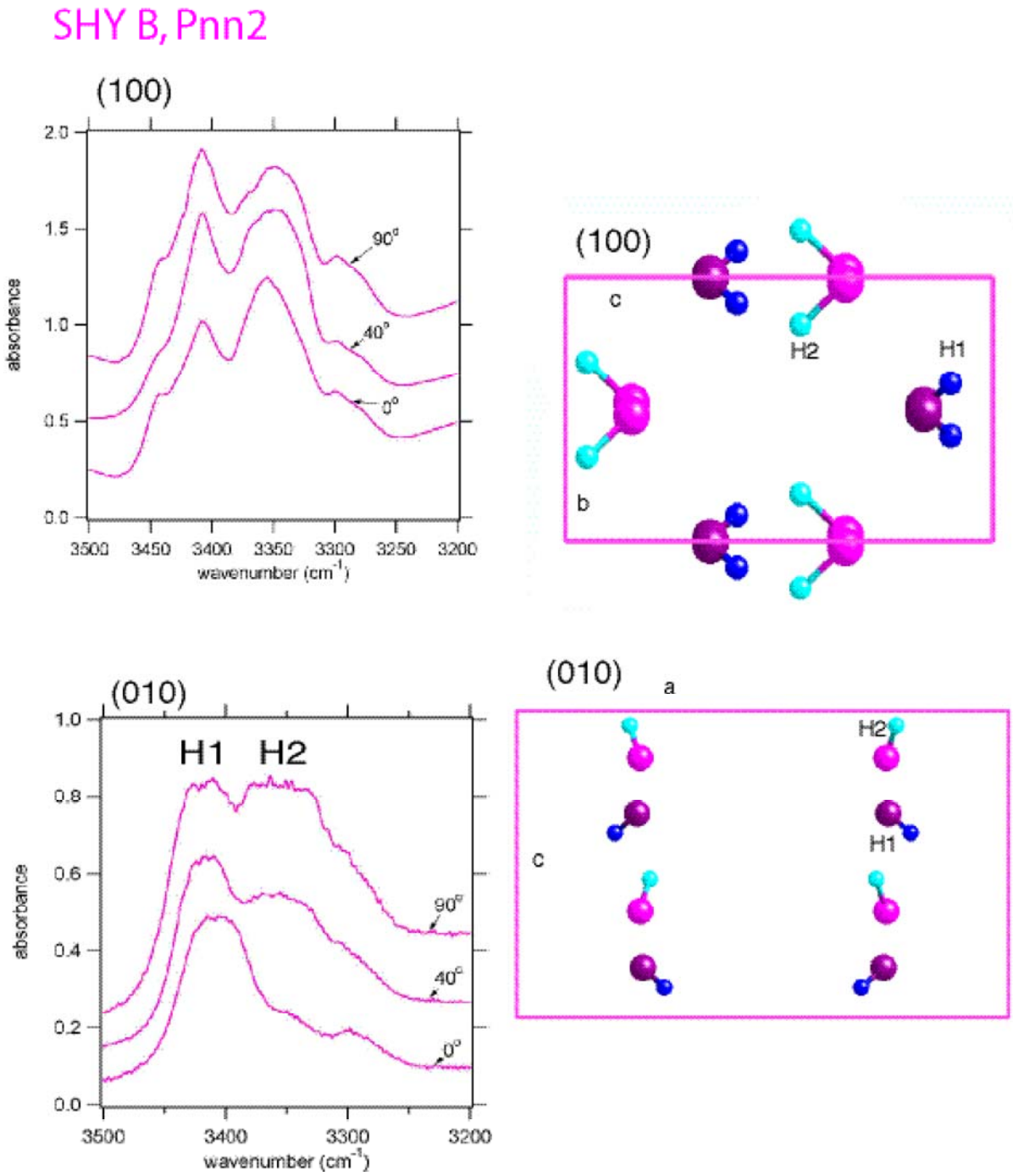

Fig 1: Polarised single crystal IR-spectra taken on (001) and (100) plates of the LT polymorph of shy B and the inferred orientation of the OH dipoles in the structure.

References

Koch-Müller M., Dera P., Fei Y., Hellwig H., Liu, Z.; van Orman J., Wirth R. (2004) Polymorphic Phase Transition in Superhydrous Phase B. 10th International Symposium on Experimental Mineralogy, Petrology and Geochemistry (Frankfurt/Main 2004) 2004. S59 p. Lithos, Suppl. to Vol. 73, Nos. 1-2

Pacalo R.E.G. and Parise J.B. (1992) Am. Mineral., 77, 681-684.

X-Ray Microscopy Investigation of the Aggregation of Swelling Clay Minerals, Synthetic and Natural Humic Acids and Natural River Colloids.

Laurent J. Michot[1], Isabelle Bihannic[1], Bruno S. Lartiges[1], Pierre Levitz[2], Fabien Thomas[1], Jürgen Thieme[3].

1. Laboratoire Environnement et Minéralurgie, CNRS-INPL-ENSG, BP40 54501 Vandoeuvre Cedex FRANCE.

2.Laboratoire Physique de la Matière Condensée. UMR 7643 CNRS-Polytechnique 91128 Palaiseau FRANCE

3. Institut für Röntgenphysik Universität Göttingen Geiststrasse 11 37073 Göttingen Germany.

The primary goal of the experiments carried out on the TXM at Bessy 2 in August 2004, was to test the applicability of this technique to various systems of environmental relevance. For this reason, three different subjects were chosen. The results presented in this report are then only preliminary.

Aggregation of swelling clay minerals.

These experiments aimed at studying the influence of ion valence, clay concentration and clay particle size on the coagulation behavior of swelling clay minerals [1]. The starting sample was a sodium montmorillonite from Wyoming which was first purified and rendered homoionic. Ultracentrifugation at chosen speeds yielded three different size fractions with average particle diameters of 400 nm, 200 nm and 75 nm, and a constant particle height of 1 nm [2]. Turbidity measurements were carried out for determining the critical coagulation fraction for three salts (sodium nitrate, calcium nitrate and lanthanum nitrate) at various clay concentrations and for the three different particle sizes. The critical coagulation concentration (Fig 1. left) depends on cation valence in a way that does not follow Schulze-Hardy rule, according to which the ccc should follow the sixth power of the valence. In addition there is a strong dependence of the ccc on clay concentration and a moderate dependence on particle size. In order to see if changes in aggregate structure could be observed, X-ray microscopy images yielding the internal structure of the flocs were obtained for various points of the phase diagram. X-ray images presented in Figure 1 (middle and right) correspond to flocs obtained with sodium and lanthanum (points 2 and 6 of the phase diagram) at high clay concentration and for the largest particles. In contrast with what could have been expected, the average thickness of the particles formed by coagulation does not appear to depend on cation valence. Complementary SAXS experiments were recently carried out and the patterns observed seem to confirm that the differences in particles thickness are only marginal for the various cases investigated.

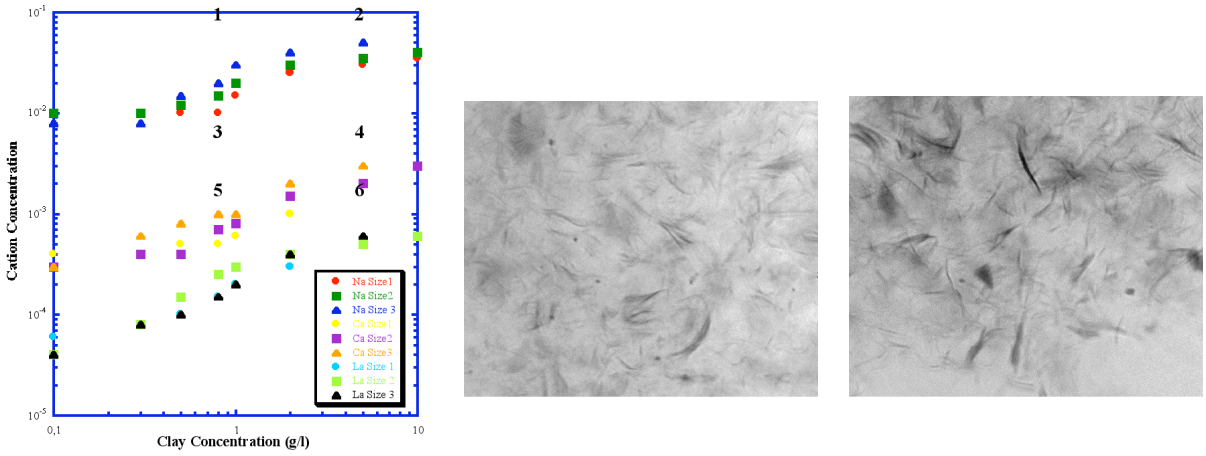

Figure 1 : Coagulation behavior of Na-Wyoming montmorillonite with different ions and TXM images obtained on montmorillonite coagulated with sodium (middle) and lanthanum (right) chloride. The total width of the X-ray image is 11 micrometers.

Aggregation of natural humic acids.

Natural Organic Matter (NOM) can cause serious problems in the coagulation process used for drinking water treatment [3]. In order to better understand the way in which coagulant species interact with NOM, we recently carried out various studies using natural humic acids, which are one of the most common classes of naturally occurring organics in river waters [4]. The humics used in this study were extracted from the Nyong river in Cameroon. They were aggregated at pH 8 using different iron chloride concentrations. TXM images of humic acid aggregates were then obtained for each concentration (Figure 2).

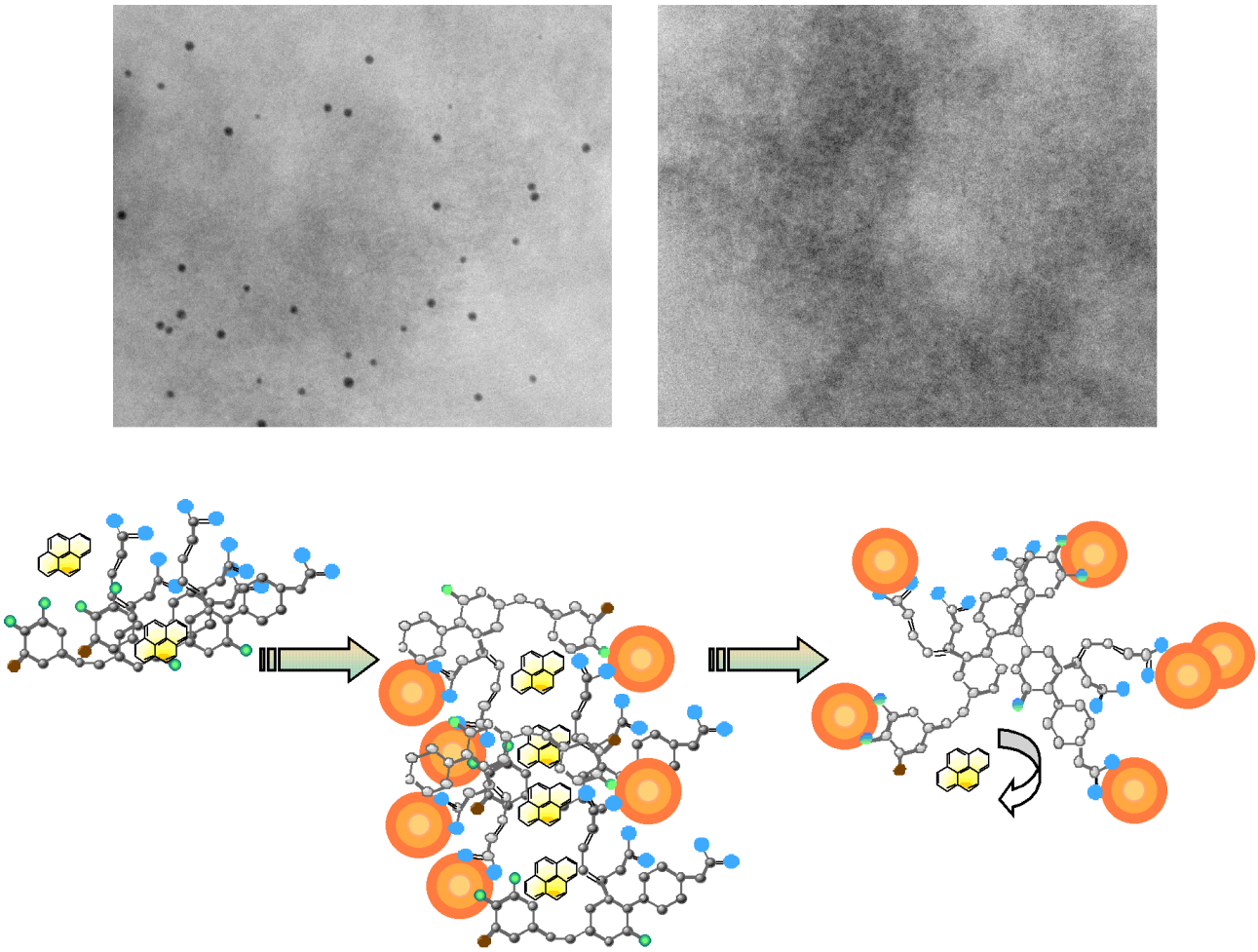

Figure 2 : TXM images obtained on humic acids coagulated by iron chloride (top) and schematic representation of the evolution of the organization of coagulated flocs with pyrene molecules.

At low coagulant concentration, one can observe the coexistence of relatively loose humic acid flocs together with dense spheroidal particles (Figure 2, top left). These latter particles disappear for higher coagulant concentration and only flocs are then observed (Figure 2, top right). Such observations, and particularly spheres formation can be correlated with pyrene fluorescence measurements. Indeed, for a particular range of coagulant concentration, the decrease of I1/I3 ratio calculated from pyrene fluorescence spectra, suggested the formation of hydrophobic microdomains trapping pyrene and enhancing its fluorescence. Further experiments are required for confirming those mechanisms but X-ray microscopy appears in that case as an extremely powerful tool for in situ examination of coagulated organics in water.

Natural river aggregates from Bangladesh rivers.

In order to understand erosion processes in the Himalaya and their influence on elements balance, it is important to study the nature and structure of sediments and suspended matters in various rivers transporting continental particles [5,6]. A sampling campaign was performed in Bangladesh at the beginning of August 2004 and both sediments and suspended particulate matter were collected. Two samples from the Ganges and from the Pussur river were examined by TXM, which allows to study natural samples without any pretreatment stage that may modify the state of aggregation of natural particles. As shown in Figure 3, significant differences are observed between the two rivers : In the Ganges (Figure 3 right) , aggregates are relatively dense and of relatively large size, whereas in the Pussur (Figure 3, left) much smaller aggregates are observed, with dominant clay particles. Many more experiments are required for a full understanding of these features and once again, X-ray microscopy appears as a very adapted tool for such studies.

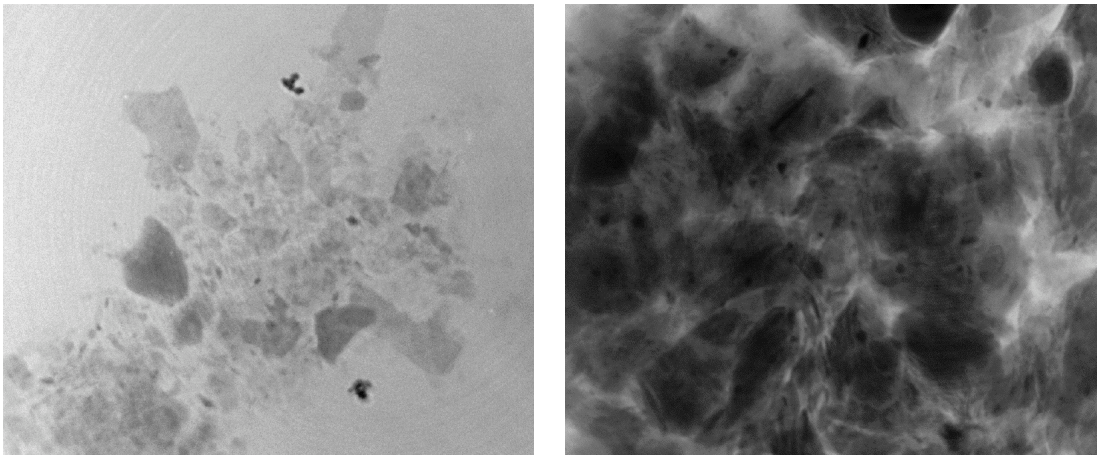

Figure 3 : TXM images of suspended particulate matter from the Pussur (left) and the Ganges (right).

References.

[1] Van Olphen, H. (1977) An introduction to clay colloid chemistry. 2nd edition. Wiley, New-York.
[2] Michot, L.J.; Bihannic, I.;. Porsch, K.; Maddi, S.; Baravian, C.; Mougel, J.; Levitz, P. Phase diagrams of Wyoming Na-montmorillonite. Influence of particle anisotropy. *Langmuir*, (2004), **20,** 10829-10837.
[3] Leenheer, J.A.; Croué, J.P. Characterizing dissolved aquatic organic matter. *Environmental Science and Technology*, (2003), **37,** 19A-26A.
[4] Jung A-V.; Chanudet, V.;. Ghanbaja, J.; Lartiges, B.S.; Bersillon, J-L. Coagulation of humic substances and dissolved organic matter with a ferric salt: an Electron Energy Loss Spectroscopy investigation. Submitted to *Water research*, (2005).
[5] Galy, A.; France-Lanord, C. Processes of the weathering in the Ganges-Brahmaputra basin and the riverine alkalinity budget. *Chemical Geology*, (1999), **159,** 31-60.
[6] Galy, A.; France-Lanord, C. Higher erosion rates in the Himalaya: geochemical constraints on riverine fluxes. *Geology*, (2001), **29,** 23-26.

Spatially resolved SR-XRF analyses of complex drawings by the Holbein family and silverpoint drawings by Rembrandt

I. Reiche[1], A. Berger[2], H. Bevers[3], G. Dupuis[1], A. Duval[1], W. Görner[2], H. Guicharnaud[1], S. Merchel[2], M. Radtke[2], J. Riederer[3], H. Riesemeier[2], M. Roth[3]

[1]Laboratoire du C2RMF – UMR 171 CNRS, 75001 Paris, France

[2]Bundesanstalt für Materialforschung und –prüfung (BAM), 12200 Berlin, Germany

[3]Kupferstichkabinett (KK), Staatliche Museen zu Berlin, 10785 Berlin, Germany

Introduction and investigated drawings and objects

Nowadays, artists have a large panoply of drawing materials at their disposal. But when you search for drawing materials used by Renaissance's artists in Europe only little information is available. To our knowledge, only two dated styli used as ancient drawing instruments are conserved, at least in Germany and France. Therefore, the possibility to get general insights into former drawing techniques is limited and based on the analysis of the drawings themselves.

Here, we report new analyses of two series of silverpoint drawings (table 1). The first was made by Rembrandt in the 17th century and the second by Hans Holbein the Elder and his workshop in the 1510/20. The latter drawings show the specificity that they were realised with metalpoints but also highlighted with red and white pigments and overdrawn with inks or gouaches. Various inscriptions and lead strokes are also present. The investigated drawings are kept today in the drawing cabinets of the State Museums of Berlin.

The interdisciplinary study of these drawing series permits to differentiate the drawing materials, to better understand the drawing technique and to give new insights into the genesis of some drawings. A large interdisciplinary project is planned and first results on the silverpoint marks using Synchrotron-induced X-ray fluorescence analysis (SR-XRF) are presented here.

In addition, it was possible to take samples of the two ancient silverpoints on paper, one from the Kestner museum in Hanover and another one from the “Karlsruher sketchbook” mounted in the 16th century containing the drawings of Hans Baldung Grien.

The investigated drawings and objects are listed in table 1.

Experimental set-up at BAM*line*

An ultra-sensitive element-analytical and non-destructive method is needed for analysis of metalpoint drawings, because only very thin scattered layers of metal particles are deposited on rag paper usually coated with a layer of bone white, a calcium phosphate obtained from burnt bone. Tests evidenced that SR-XRF provides the sensitivity required for the quantitative determination of the chemical composition of the metalpoint due to the linear polarisation that results in a lower scattering background, and the higher photon flux compared to conventional XRF with X-ray tubes [1]. Furthermore, a spatial resolution is necessary in order to obtain a high metal to paper background ratio for the analysis of the metal marks.

A spatially resolved SR-XRF set-up was mounted for analyses at the hard X-ray beam line (BAM*line*) [2] at BESSY. As an X-ray source a super conducting wavelength shifter with a maximum field of 7 Tesla was used. A W/Si Double-Multilayer-Monochromator (DMM) was used to produce a monochromatic X-ray beam with an energy of 33 keV. The beam was focused to a beam size of 100 × 200 µm^2. The drawings were fixed in air on a sample frame on a motorized xyz-stage at an angle of 45° to the X-ray beam. Fluorescence signals were detected for 300 s each with a Si(Li)-detector covered with a polyethylene filter at 90° with respect to the incident beam. This filter protects the detector against visible light. A video system and a long distance microscope permitted to observe and to select the analytical points on the drawings.

Data processing was performed by means of AXIL [3]. Relative concentrations of the silver points were determined by using a procedure based on different silver standards. When using high energy X-rays for chemical analysis, incident and fluorescence X-rays pass completely through the drawing. Thus, the silver mark cannot be analysed separately from the backing. Normalisation to an internal standard (Fe or Sr from the paper and coating), whose concentration is assumed to be homogeneous, is necessary prior to background subtraction to account for the contribution of X-ray fluorescence of elements from the paper and the coating. Normalisation to Ag counts is performed because the excitation spot size is significantly larger than the silver deposit on paper. Finally, we used a thin layer approximation without self-absorption correction to calculate concentrations. The spectra show a large and significant difference of the two intensities of the Ag K_α lines. In contrast the analogue differences of Cu K_α and Zn K_α are much smaller. Together with the microscopic heterogeneity of the paper backing and the paper itself, these are the reasons for the relatively high uncertainties of the concentration values. However, this procedure allows determining the characteristic chemical fingerprint of the metal stylus used for a drawing.

Results and discussion

About 20 points per drawing were analysed. All drawings by Rembrandt and Hans Holbein the Elder and his workshop were revealed to be realised with silverpoints. The detailed quantitative analysis of the silverpoint marks are shown in table 1. The results obtained on the silver marks from the ancient silverpoints are also reported in table 1.

The detailed analysis of the composition of the silver marks of the Holbein drawings shows that the drawings can be divided into two main groups: one group of drawings realized with a silverpoint of about (10 ± 5) wt.% copper and a second group with about (4 ± 2) wt.% copper.

Therefore, it is clear that Hans Holbein the Elder used at least two different silverpoints for the creation of this series of drawings. Concerning the chronology of the realization of the drawings, no classification can be made at the moment as the only dated reference is the drawing of Hans Holbein the Elder representing his two sons, Hans and Ambrosius, dated to 1511.

Interestingly, these portraits on the same sheet were not realized with the same point. This finding allows to conclude on a two step creation process of the drawing. First, the portrait of the older son, Ambrosius, was realized with a Cu-rich silverpoint and then the younger son, Hans was drawn with another silverpoint containing less Cu. In addition, the inscriptions indicating the names and the date of the drawings were also written with the second silverpoint. From an artistic point of view, the genesis of this drawing in two-steps seems convincing as both portraits are too close together on the same paper sheet to be made simultaneously. However, no information on the time scale between the production of both portraits can be obtained from the analyses.

The analysis of silver marks of the two ancient styli showed different compositions. The Hanover stylus has a homogeneous silver composition containing about 2 wt.% of copper whereas the Karlsruhe silver marks show an inhomogeneous copper content. This latter result can be explained by the used small silver layer on the point of the Karlsruhe brass stylus. Both styli do not contain any mercury. This confirms our previous conclusion that the mercury detected in the ancient silverpoint drawings originates from an uptake from the atmosphere over the centuries [1].

Table 1. SR-XRF results of silver marks of ancient drawings and of two ancient silverpoints. - = not present or under the limit of detection (LOD), x = present, empty space = quantification in progress.

Titel of the drawings	N° (KdZ)	Type of metal point	Cu (wt.%)	Presence of Hg	Presence of Zn
Sons of the artist, Ambrosius and Hans, by Hans Holbein the Elder	2507	Ag	Hans: 8±3 Ambrosius: 3±1	x	partially
Sigmund, the brother of the artist, by Hans Holbein the Elder	2508	Ag	20±15	x	x
Portrait of a young man by Hans Holbein the Elder	2523	Ag			
Leonard Wagner, profile half left, by Hans Holbein the Elder	2524	Ag			
Kungspergs Niclas, right profile, by Hans Holbein the Elder	2551	Ag	4±2	x	-
Portrait d'Agnes Dürer, by Hans Holbein the Elder	2561	Ag	4±2	x	-
Head of a beardless man, half right, by Hans Holbein the Elder	2566	Ag	13.5±4	x	partially
Elder beardless man, three-quarter right, by Hans Holbein the Elder	2574	Ag	2±0.8	x	-
Portrait of a young man by Ambrosius Holbein	298	Ag	13±4	x	-
Portrait of Saskia by Rembrandt	1152	Ag			
landscape	2117r/v	Ag			
Silverpoint of Kestern museum	Hanover	Ag	2.4±1.0	no	-
Silverpoint Karlsruher sketchbook	Karlsruhe	Ag	15.8±10.4 (variable)	no	1.1±1.0 wt.%

References

[1] I. Reiche *et al.*, Following the traces of Albrecht Dürer: Analysis of silverpoint drawings by spatially resolved synchrotron-induced X-ray fluorescence analysis, Nucl. Inst. and Meth. in Phys. Res. B 226, 83, (2004).

[2] H. Riesemeier, K. Ecker, W. Görner, B.R. Müller, M. Radtke, M. Krumrey, Layout and first XRF applications of the BAMline at BESSY II, X-Ray Spectrometry (in press), published online: 13 Sep 2004 DOI: 10.1002/xrs.750

[3] AXIL QXAS package, IAEA Vienna.

Acknowledgements

We gratefully acknowledge the support during beam time of E. Alex, C. Severit, R. Fricke, R. Wittich (KK Berlin). We also thank D. Schäfer (Kunsthalle Karlsruhe) and S. Schmidt (Kestner Museum Hannover) for providing the samples of the ancient silverpoints. This research project was partially financed by a French-German Procope project (contract n° D/0122896). We thank BESSY for allowing beam time.

Lifetime broadening of the C1s → π(C*≡N) resonance in self-assembled monolayers of CN-C_{16}-SH on Au substrates.

P. Feulner, K. Eberle, M. Glanz, R. Schneider, and D. Menzel
Physikdepartment E20, Technische Universität München, 85747 Garching
A. Shaporenko, and M. Zharnikov
Angewandte Physikalische Chemie, Universität Heidelberg, Im Neuenheimer Feld 253, 69120 Heidelberg

Self-assembled monolayers (SAMs) of alkane thiolates on noble metal substrates attract broad interest because of their wide range of possible applications in technology and biological science, e.g., as resists and templates for bio sensors etc. In a recent study we have shown that radiation damage of such layers which is a hazard in many applications can be dramatically reduced by cryogenic conditions [1]. To understand the microscopic processes of damage induced by electronic excitations in these systems in more detail, we focus in the present study on the lifetime of the electronically excited states, and on possible influences of the sample temperature. It is well known that bond breaking by electronic excitations is governed by the competition of the acceleration of the nuclei by excited electronic states with dissociative asymptotic behavior on the one hand, and the delocalization of those excitations on the other [2]. In other words, the excitation has to stay localized long enough on a certain bond to successfully break it; if it delocalizes too quickly, the bond will stay intact.

For our experiment at the U49-2-PGM-1 beamline we have selected SAMs formed from NC-C_{16}-SH on polycrystalline Au substrates with mainly (111) orientation [3]. The CN group has empty π* states which give rise to sharp C1s and N1s core to π resonances. X-ray absorption data for the C1s range are depicted in Fig.1.

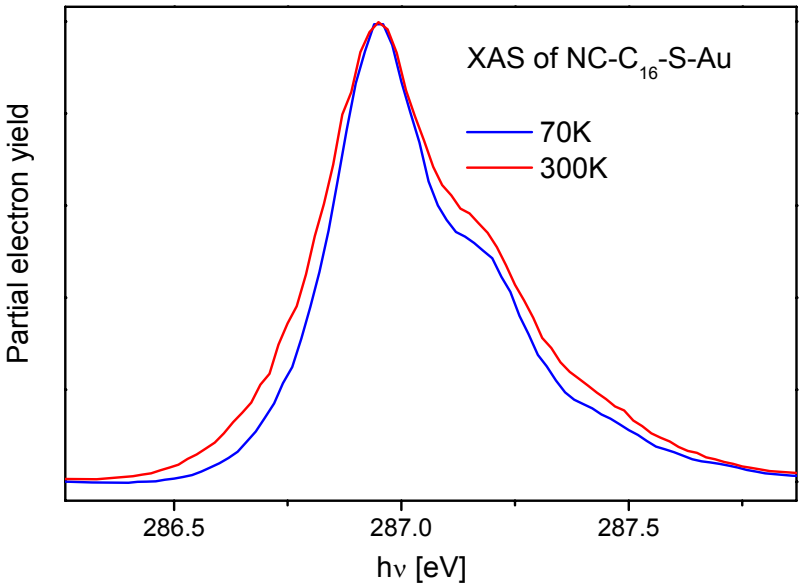

Fig.1: C1s to π(C*≡N) resonance for SAMs of NC-C_{16}-S/Au for 70K and 300K. A linear background has been subtracted.

The progression of the C-N stretch vibration is visible, however not well resolved [4]. Obviously broadening exists which goes beyond the broadening due to the limited lifetime of the C1s core hole which is in the 100 meV range and would be long enough to allow deep valleys between the vibrational peaks to be resolvable (the spectral width of the PGM-1 was set to 40 meV and can be neglected, therefore). Two different mechanisms are most likely

for this extra broadening: i) Inhomogeneous effects due to different environments for the individual CN groups, and ii) a limited lifetime of the resonantly excited electron. For diatomic chemisorbates on metal surfaces it is well known that excited electrons in the π-resonant state encounter extremely rapid inelastic processes by charge transfer with the substrate, giving rise to rather broad peaks, i.e., the lifetime of the resonance is much shorter than that of the core hole [5]. For isolated small molecules as CO or N_2, on the other hand, inelastic electron scattering is not possible and the lifetime of the resonance will be limited by that of the core hole. In our case charge transfer processes could occur either horizontally within the densely packed layer of CN head groups or vertically along the aliphatic chains of our molecules.

To discriminate between the two channels (i) and (ii), we monitored the spectra of the decay electrons. Without inelastic processes core excitation and de-excitation have to be interpreted in a one-step picture. The overall energy is preserved and the kinetic energy of the decay electrons will shift with the photon energy. If inelastic processes are rapid, this coherence will be destroyed and the system will "forget" the exact energy of its excitation. For intermediate cases, two different contributions with different energy behavior appear in the decay spectra, the ratio of which in combination with the lifetime of the core hole enables the extraction of the timescale of the inelastic processes. By utilizing short-lived core holes, processes in the attosecond regime can be analyzed [6].

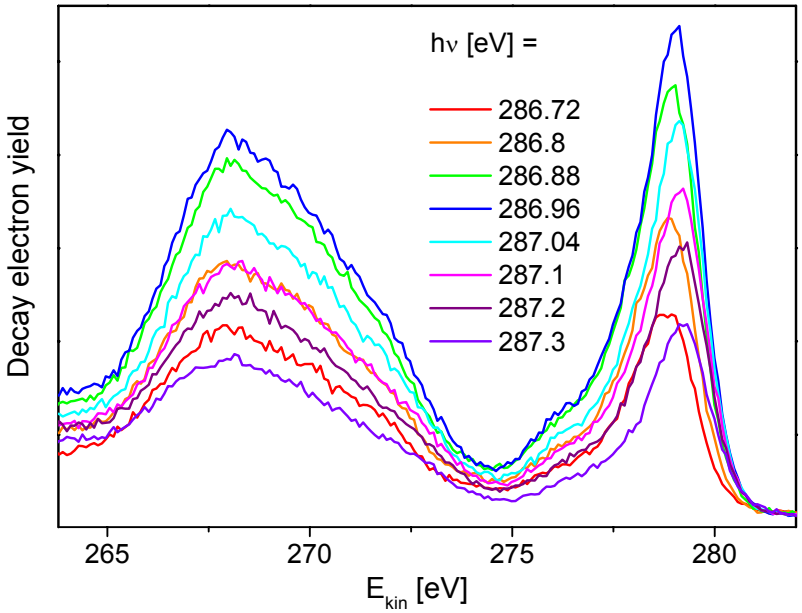

Fig.2: High kinetic energy part of decay electron spectra from CN-C_{16}-S/Au for the C1s to π*(C*≡N) excitation as a function of the photon energy

For our samples the two distributions can well be resolved. The position of the peak around 278 eV kinetic energy is a function of the photon energy. It is constant on a binding energy scale (not shown) and belongs to the scenario where the resonantly excited electron does not delocalize before core decay. The other contributions which dominate the broad lower peak appear at constant binding energy, indicating inelastic electron loss processes *before* core decay. From this result we can clearly conclude that the main broadening effect seen in XAS is due to the limited lifetime of the resonantly excited electron, a result that is not obvious from NEXAFS alone, and which has important implications for, e.g., bond tailoring by resonant core excitations. The nature of this electron delocalization process, either horizontal

or vertical, is not yet clear. We expect that future experiments with aliphatic chains of different lengths will supply unambiguous results on this question.

We finally focus on the temperature effect seen in Fig.1. Raw data from decay spectroscopy indicate a slight enhancement of the coherent part for 70K compared with 300K which would corroborate the findings of Fig.1. By a more careful inspection, however, we found that this effect was mainly due to a larger inelastic background at room temperature. After subtraction of this additional background the decay spectra traces are practically identical for 70K and 300K (Fig.3). The temperature induced broadening of the resonance which is clearly seen in Fig.1 is most likely not due to a temperature dependent electron localization but rather due to inhomogeneous local environments by thermal movement and disorder.

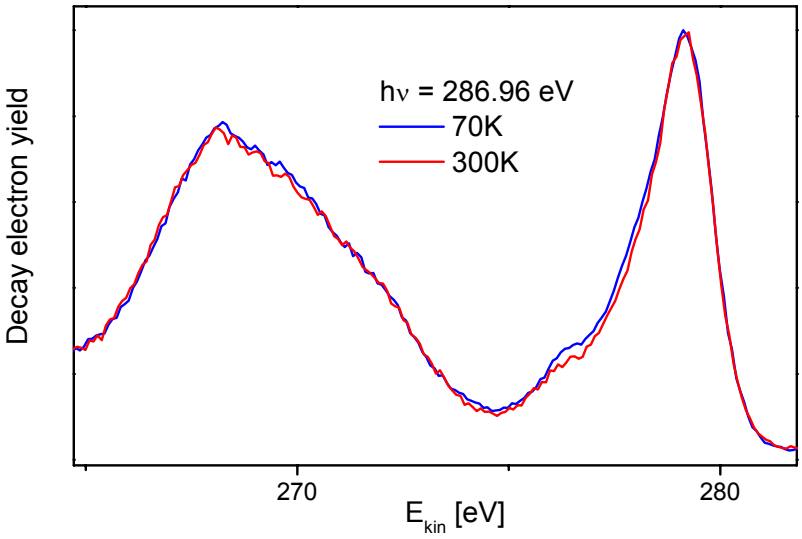

Fig.3: Comparison of decay spectra for the C1s to π(C*≡N) excitation in CN-C_{16}-S/Au taken at 70 K (blue) and 300K (red).

We thank D. Allara for providing us with the CN-C_{16}-SH substance, M. Grunze for the support, and the staff of BESSY, in particular O. Schwarzkopf, H. Pfau, C. Jung and W. Braun for help during the experiments. Financial support by the BMBF (05 KS4VHA/4 and 05 ES3XBA/5) is gratefully acknowledged.

References:

1. P. Feulner, M. Zharnikov et al., Phys. Rev. Lett. 93 (2004) 178302
2. D. Menzel and P. Feulner, J. Phys. Condens. Matter 13 (2001) 11249, and references therein.
3. S. Frey, M. Zharnikov et al., J. Phys. Chem. B 107 (2003) 7716
4. In the previous work [3] these vibrational states remained unresolved because of insufficient spectral resolution.
5. W. Wurth and D. Menzel, Chem. Phys. 251 (2000) 141.
6. A. Föhlisch et al., submitted to Nature

Vultures hit by beam

S. Schlosser[1], M. Radtke[2], E. Pernicka[3]

[1]TU Bergakademie Freiberg, [2]Bundesanstalt für Materialforschung und –prüfung, Berlin,
[3]Institut für Ur- und Frühgeschichte und Archäologie des Mittelalters, Universität Tübingen

In Precolumbian Costa Rica raptors, in most cases vultures, as well as crocodilians, frogs and anthropomorphic figurines were very often modeled in gold or - more typical for Central America - in tumbaga, an alloy of natural gold, often containing silver, and copper. Until today, very little is known about the development of metallurgy in the so-called Isthmo-Colombian Area, because almost all artifacts available for study do not derive from controlled excavations. Only for one of the largest collections of archaeological gold objects (ca. 300 specimens) from Costa Rica the place of origin, a cemetery in the Southwest of the country called Panteón de la Reina or El General, could be identified during the last years. Archaeologists uncovered a ceremonial center at the site connected by stairs to the cemetery on the hilltop, both dating 900 - 1300 AD [1, 2]. At the beginning of the 20 th century, when the tombs were heaviliy looted, the objects were spread over different collections in New York, Costa Rica and Berlin. Now the 44 objects of the Lehmann Collection in the Ethnological Museum Berlin became the first of the Panteón de la Reina materials to be analyzed archaeometrically [3].

The objects comprise pendants in different size made by lost wax casting, the biggest weighing 365 g, and four additional pectorals of sheet metal. Modeled are mainly raptors (possibly vultures) and anthropomorphic twin-figurines, furthermore animals like shark, spider, bat, crocodilian, pekari, cicade or monkey - all typical representations in Precolumbian Costa Rica (Fig. 1). Another typical trait is the gilding of the tumbaga pieces to make the objects appear golden, which was achieved by depleting the copper at the surface by oxidation and removal of the oxides with plant acids, a process called depletion gilding. The resulting porous surface that remained in unpolished areas and is visible in the SEM could be used as diagnostic sign to identify the use of this technique.

Fig. 1: One of the five vultures belonging to the find.

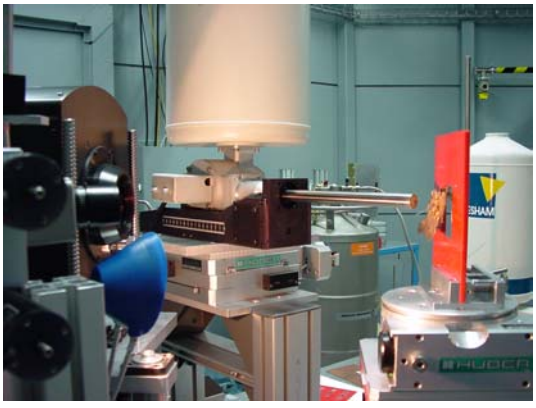

Fig. 2: Experimental set-up at the BAMline

As the Panteón de la Reina objects had originally been bought from different sources in Costa Rica [4] and as there obviously existed different states of preservation and certain differences in style and technology, the central question was to test their authenticity and if they originally belonged together. Apart from the detailed study of style and production by microscope and SEM, the non-destructive analysis of their composition including trace elements was the most important method employed. As special attention was devoted to the (preselected) gold rich objects and their relation to 24 additional Costa Rican gold objects from the Ethnological Museum in Berlin, the high sensitivity of synchrotron X-ray fluorescence (XRF) was crucial to obtain this information from the gold with high silver concentrations. As already shown in context with the Sky Disk of Nebra [5], the presence of silver makes it difficult to detect small concentrations of tin, a very important trace element for the identification of gold deposits. The BAMline also offers a high spatial resolution of the beam that was necessary to analyze the depletion gilded tumbaga. Because of the enriched gold layer with variable thickness, it would have been necessary to remove the surface layer at least partially. However, some decades ago all objects had been tested by a goldsmith by rubbing with a stone, resulting in the total removement of the gold rich surface - ideal for our analyses. Another important point is that the fragile objects - sometimes in bulky form - could be handeled very easily and savely in air, using the set-up at the BAMline with special supports and a moveable cartridge (Fig. 2).

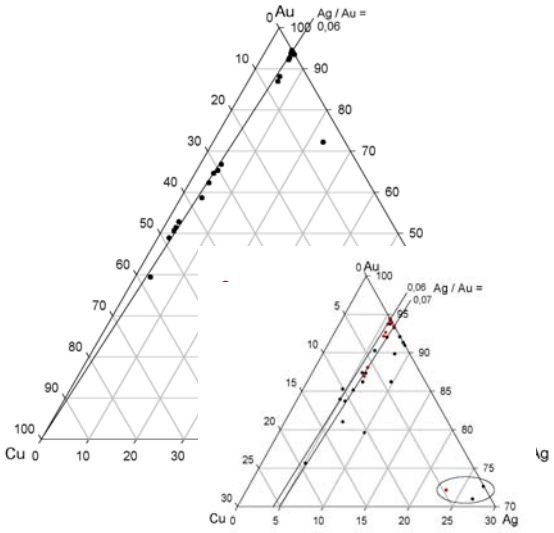

Fig. 3: a) Composition of the Panteón objects, wt%. Normalized to 100.

b) Enlarged part of the ternary plot comparing the Panteón and additional objects.

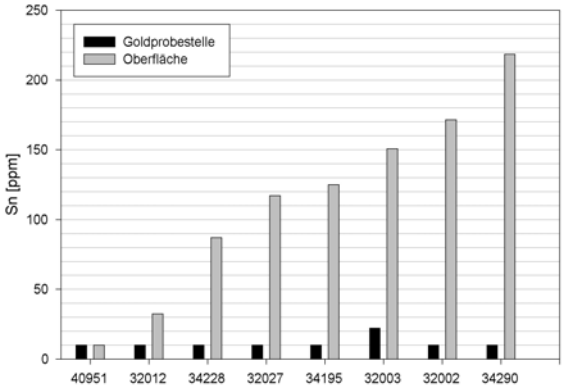

Fig. 4: Surface values of tin on the surface enriched in gold and in the original alloy.

The results of ten copper rich tumbaga pieces show a very uniform silver-gold-ratio scattering around 0,065 (Fig. 3 a) but quite variable copper contents which fit very well into the general picture of Central American metallurgy. It seems that the addition of copper to gold was more important than the actual quantitiy used, which is why the copper content cannot be used to check if the finds originally belonged together. Regarding the silver-gold-ratios it is obvious that the gold rich objects from Panteón de la Reina (except for one) fit quite well into the field between 0,06 and 0,07 definded by the tumbaga objects. This is not the case for most of the 24 additional objects (see above) analysed for comparison (Fig. 3 b). These are also finds without archaeological context, at best traceable to their place of purchase. Two of these

objects and the exceptional object from Panteón de la Reina show a very high silver content of about 25 wt%, a value that points to a non placer deposit origin of the gold. Mining for gold was only known in Colombia in Precolumbian times, and indeed these three objects show stylistic and technological features that point to a Colombian origin.

Concerning the trace element compositions it was surprising how pure even the copper rich objects were. This may be explained by the use of native copper for the production of the gold(silver)-copper alloys while smelting of copper ore was not practised. Apart from tin, antimony was the only trace element detected above the detection limit of about 70 ppm. Tin ranged up to 200 ppm in most of the objects, with a few higher values of up to 500 ppm. However, a comparison between surface measurements and at the spots where the surfcae was removed by the goldsmith indicated that most objects must have been contaminated with tin some time since their recovery (Fig. 4). The most likely explanation for this observationis the application of tin oxide for polishing for a better appearance, a practice still in use today by goldsmiths. As a result, only the two highest tin values (around 500 ppm) could be taken into further consideration, one of which is associated with a high silver and antimony content.

Archeological objects without context because of looting can nevertheless offer many possibilities for research, although there exist clear limitations in the interpretation. In combination with the results of the analyses of production technique and style, six of the Berlin objects from the Panteón de la Reina could be identified as different, while the bulk was probably produced at the same time, place and workshop. The origin of the objects with different composition is at present not identified but Colombia is a good candidate region.

[1] Quilter, Jeffrey (2000): The General and the Queen. Gold Objects from a Ceremonial and Mortuary Complex in Southern Costa Rica. In: McEwan, Colin (ed.): *Precolumbian Gold: Technology, Style and Iconography*. British Museum Press, London. 175-195.

[2] J. Quilter, Cobble Circles and Standing Stones: Archaeology at the Rivas Site, Costa Rica. University of Iowa Press (2004)

[3] Diplomarbeit TU Bergakademie Freiberg, S. Schlosser (2004)

[4] M. Künne, Baessler Archiv 50, 206 (2002)

[5] E. Pernicka et al., Highlights 2003. Annual Report BESSY, 8-9.

Study of Paleopathology and Paleodiet by Means of Micro X-ray Fluorescence and 3D Micro X-ray Fluorescence Spectroscopy

Francesca Bertoldi[1], Yvonne Höhn[2], Birgit Kanngießer[2], Stefano Lagomarsino[3], Wolfgang Malzer[2], Daniele Pelliccia[3]

[1] Dipartimento di Scienze dell'Antichità e del Vicino Oriente, Università di Venezia Ca' Foscari, Venezia
[2] Institut für Atomare Physik und Fachdidaktik, Technische Universität Berlin, Berlin
[3] Istituto Fotonica e nanotecnologie- CNR, Roma

Introduction

One of the most interesting issues of anthropology and archaeology is the reconstruction of the diet and nutrition and of the activity patterns of past human societies, together with knowledge of ancient pathologies. The archaeological and historical evidence relies on faunal and botanical remains, artefacts, written sources and artistical representations, while the anthropological data are obtained from human skeletal remains (teeth and bones).

Stature is a good indicator of the adequacy of the diet, while several pathologies show the lackness of certain elements in the human nutrition. Cribra orbitalia or orbital osteoporosis (orbital roofs showing "holes" on their surface) as cranial vault lesions named "porotic hyperostosis" (thinning of the outer table of the skull and thickening of the diploe) indicate iron deficiency anaemia, rickets or osteomalacia leave clear marks on the skeleton [1].

A direct evidence of the diet can be reconstructed by paleonutritional analyses by means of analytical methods such as Atomic Absorption Spectroscopy (AAS) or Neutron Activation Analysis (NNA) or microwear analysis of teeth. They both distinguish between a vegetable or meat-based diet, the former distinguishing between Sr and Zn contents of bones, the latter between horizontal and vertical striae on teeth. However, trace element analysis suffers of the ambiguity between biogenesis (uptake ante-mortem) and diagenesis (uptake post-mortem) due to ionic exchange with soil. Moreover, element uptake is different in cortical bone and trabecular bone. It is not easy to distinguish among these effects with standard analysis.

In this experiment we aim to study with Micro X-ray fluorescence (micro-XRF) and 3D Micro X-ray fluorescence (3D micro-XRF) bone remains coming from the Archaeological site of Tell Beydar in Syria, a village of the third millennium B.C., where human skeletal remains were already partly studied taking into consideration a "classical" anthropological approach. The human remains found at the site during several excavations campaigns since 1996 have been recently studied from an anthropological, palaeonutritional and paleopathological point of view. The sample is formed by 21 adults (7 males, 4 females and 10 undetermined of every class of age) and 25 juveniles ranging from birth to childhood.

Experimental Set-up

The 3D micro-XRF is realised by a confocal arrangement, which consists of X-ray optics in the excitation as well as in the detection channel. A micro-volume is defined by the overlap of the foci of both X-ray optics. If the sample is moved through this micro-volume, its chemical composition can be non-destructively investigated not only laterally along the surface but also within the sample at the depth of interest [2]. Furthermore, if synchrotron radiation is used as exciting radiation, the excitation energy is tunable, which facilitates micro XAFS investigation for chemical speciation at the same spot in the sample. Thus, not only depth information concerning the elemental distribution but also chemical speciation and phase information are obtainable at the same point of interest in the sample.

The information depth of the micro-volume depends on the energy of the exciting radiation, the energy of the fluorescence radiation, the incidence angle, the angle of reflection, and the sample composition. The spatial resolution of this 3D micro-XRF set-up depends on the FWHM values of the overlapping focal profiles. In addition, a better peak-to-background ratio can be achieved by restricting the detector field of view.

We realized the 3D micro-XRF set-up at the BAMline located at a 7T wavelength shifter at BESSY. To create the micro-volume we used a polycapillary halflens with a focus of about 30 μm at a working

distance of 16 mm in the excitation channel. In the detection channel a polycapillary halflens was adjusted directly on the snout of the Si(Li) detector. The focus of this polycapillary halflens has a FWHM of 20 μm at a working distance of 6.6 mm. The "standard" micro-XRF measurements were realized by removing the X-ray optic from the detection channel.
The characterization of the confocal arrangement was carried out with the help of a thin Cu-foil which was scanned through the micro-volume. The FWHM of the Cu intensity-curve excited at 18 keV is about 30 μm, which can be regarded as the spatial resolution of the set-up.

Measurements

12 different archaeological human bone samples and 1 animal bone sample have been investigated with micro-XRF and 3D micro-XRF. Additionally, two reference bone samples and one NIST reference glass standard were measured
As an example fig. 1 shows a depth scan on a human bone sample (beydar 32457 femur). The counts of the net peak areas of the respective elements is plotted in dependence of the relative position in the depth. The depth scan was carried out with a step width of 10 μm and a live time of 100 s at each point. The maximum of all element depth profiles can be found by the same relative position. The decrease of the depth profiles is due to the absorption which is becoming stronger with depth.
Fig. 2 shows the same element depth profiles but scaled to the same height for a better comparison. The different start positions of the element depth profiles reflects the dependence of the FWHM of the micro-volume on the fluorescence energy of the element detected: the lower the fluorescence energy the wider the FWHM of the micro-volume seen by the detector. The second increase of the Sr and Zn depth profile in the depth is probably due to density variation of the bone material.

Element	Fluorescence energy /keV	Maximum depth, /μm
P	2.0	150
Cl	2.62	160
K	3.31	260
Ca	3.69	> 260
Fe	6.4	240
Zn	8.6	230
Sr	14.1	> 260

Table 1 shows the elements measured, their fluorescence energy of the Kα line and the maximum depth measured with the experimental parameters given above:

Other elements, like S, V, Cr, Mn, As and Br, were measurable at some points only. For these elements the measurement time has to be increased.
Fig. 3 shows a spectrum obtained at the surface of the bone sample measured with 1000 s live time. The strong pile up peaks of the Ca Kα and Kβ line prevent the evaluation of Co, Ni and Cu. Hence, for the final evaluation of the whole sample set a pile up correction has to be included beside the absorption correction.

Element	Weight fraction /ppm	MDL /ppm
Fe	458 ± 9	6
Co	390	7
Ni	458.7 ± 4	4
Cu	444 ± 4	4
Zn	433	4
Rb	425.7 ± 0.8	4
Sr	515.5 ± 0.5	4

In order to get figures of merit for the detection sensitivities a NIST glass standard (SRM 611) has been measured (100 s live time) and evaluated.

Table 2 shows the elements evaluated, the certified weight fractions and the minimum detection limits (MDL) calculated thereof. These detection limits are 20 to 50 times lower than the usual concentrations of the trace elements in bones.

Conclusions

The first preliminary evaluation of a human bone sample excavated at Beydar, Syria demonstrates the usefulness of 3D micro X-Ray fluorescence analysis for the investigation of such kind of samples. Most of the elements of interest are detectable. Element depth profiles show different distributions of the elements in the depth and density fluctuation of the matrix material. A full evaluation of the whole sample set will elucidate trace element spatial distribution in bones remains and to discriminate between biogenesis and diagenesis elements uptake. These information will be applied to studies of ancient

populations of Syria, in order to clarify paleonutrition and paleopathologies. Furthermore, it can constitute a good starting point for further studies in archaeometry with synchrotron advanced methods.

References

[1] Roberts C. and Manchester K., 1995. The archaeology of disease. Sutton.
[2] B. Kanngießer, W. Malzer, I. Reiche, Nucl. Instr. Meth. B 211/2, 259-264 (2003).

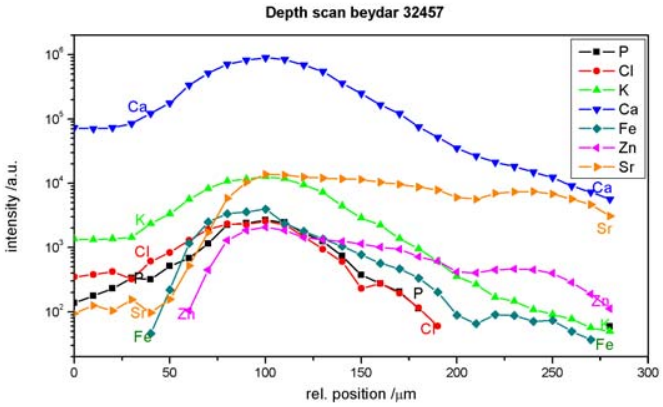

Figure 1 : Depth scan on a human bone sample with 100 s live time for each step.

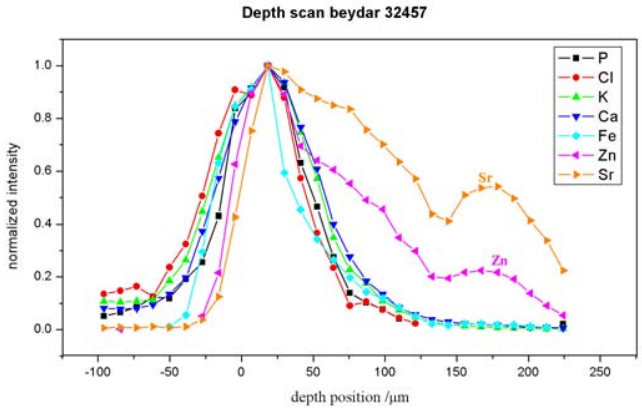

Figure 2 : Normalized depth scan on a human bone sample with 100 s live time for each step.

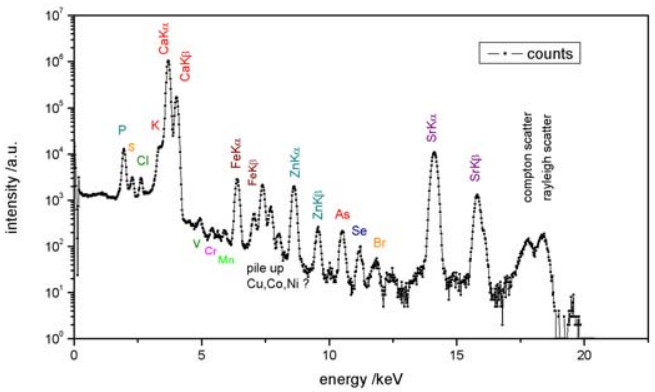

Figure 3 : Spectrum obtained at the surface of the bone sample measured with 1000 s live time.

ccuracy of Optical Components for Synchrotron Radiation.
Results of the Cooperative Research Project "Nanometer-Optikkomponenten" NOK

Heiner Lammert, Tino Noll, Thomas Schlegel, Frank Siewert, Thomas Zeschke
BESSY GmbH, Albert Einstein Strasse 15, D 12489 Berlin. http.//www.bessy.de/
E-mail: Lammert@Bessy.de
BESSY Annual Report 2004, (30.1.2005)

Introduction

The technological limit for the manufacturing of mirrors and gratings is determined by the metrology available to measure the figure quality. The first results of a cooperative research project "Nanometer-Optikkomponenten - NOK" of ten partners from German industries and scientific institutes, coordinated by BESSY has been reported last year in the BESSY Annual Report [1]. As a result of this in October 2004 finished project it was shown, that the technological limit of the figure errors of plane or slightly curved optical surfaces can be improved from the 0.1 arcsec rms limit to the new limit of 0.02 arcsec rms. This represents a breakthrough in the metrology and manufacture of optical elements. This report comprises the results of the project achieved on the field of surface measuring technique and surface finishing technology.

Success of the cooperative research project NOK

Three so-called NOK-demonstrators to be used as SR-components at two beamlines at BESSY exemplifies the progress achieved by the cooperation of all partners. A plane grating of 0.02 arcsec rms and a 310 mm plane mirror characterized by a slope error of 0.03 arcsec rms will be installed at one of BESSY`s Plane Grating Monochromators (PGM). The third demonstrator, an aspherical mirror, has already been described in detail [2]. The combination of the Nano-Optic-Measuring Machine - NOM- [3]; [4]; [5] and advanced surface finishing by ion beam etching [7] has led to the success of this research project. The low measurement uncertainty of the NOM required the development of a special small aperture autocollimator by Möller-Wedel Optical [6]. The three NOK-demonstrators and the measuring uncertainty achieved a five fold improvement of the technological limit for the manufacturing and a ten fold improvement in the measuring tools. The limit of 0.1 arcsec rms has been shifted to 0.02 arcsec rms for the manufacturing of optics and to 0.01 arcsec rms measuring uncertainty for surface measuring devices.

Results of the NOM development at BESSY

The final activity report for the NOK-project, dated December 2004 [8], of the activities at BESSY describes the achievements of the NOK project and of the NOM development in detail. They comprise 15 different results with respect to measurement and production technology for highly accurate optical components. Some of these results are:

- increase of the measuring accuracy compared to common deflectometry methods (LTP-II) tenfold,
- 3-d-topography with subnanometer accuracy (up to λ/3000 of light wave-length),
- the establishment of the NOM as an engineering model for a new generation of measuring machines for science and industry,
- reference surface free technology
- Furthermore the NOM is essential for the fivefold increase of the accuracy in the manufacture of optical SR-components,
- and the NOM well qualified for the determination of shape deviations of reference normal surfaces for interferometry.

Classical optical technology

The classical optical technology is based on the principle of a self-correcting polishing process by a large area contact between the polishing tool and the workpiece which is the key for the production of highly accurate optical components. Workpiece and polishing have complementary shapes. The shape

enerating and correcting process always leads to an ideal spherical shape and in a special case to a plane surface, plane means in praxis spherically, characterized by a very large radius. These surfaces of potentially very high accuracy were tested by wave front comparisons such as interferometric methods. The present limit of the common interferometric methods is about 5 nm (λ/100). Some special opticians, so called people with "golden hands", are able to make a wave front comparison with very sensible subjective observations of smallest shadows by eye. But such measurements can not be quantified or applied in routine work. By use of the NOM, shape deviations in the range < 0.5 nm (λ/1000) can be measured. To our surprise we determined a surface accuracy in the range of λ/100 for the shape deviations and slope errors of down to 0.02 arcsec rms of various plane and spherical surfaces, which were finished with the classical polishing methods.
Fig. 1 shows the result of a NOM measured shape deviation of the center line of a plane reference normal for an high precision interferometer. This fused silica plate of 100 mm diameter was manufactured about 40 years ago. The surface shows after fit of a 105 km radius in a center field of 75 mm a residual deviation of less than 0.5 nm rms (<λ/1000) and a slope error of less than 0.03 arcsec rms.

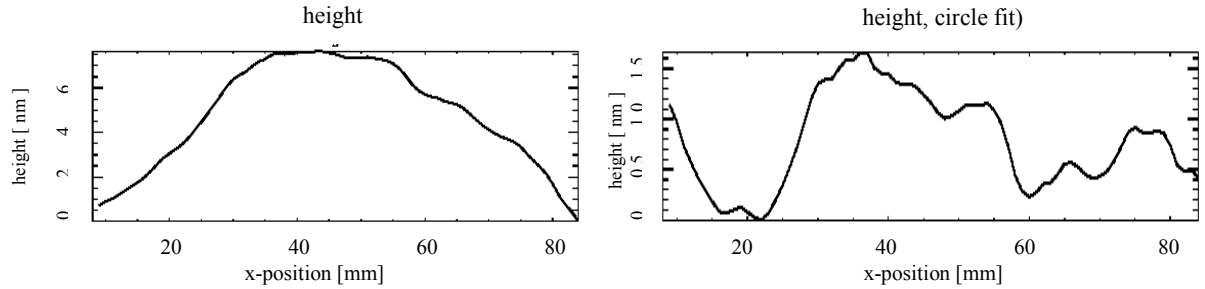

Fig. 1 Central section of 75 mm of a plan reference normal (material: fused silica), manufactured about 40 year ago by common classical optically polishing technology. **Left.:** The shape deviation is 7.6 nm p-v (λ/100) without fit. **Right:** After radius fit of 105 km: shape deviation: 1.7 nm p-v (λ/400) and 0.47 nm rms (<λ/1000). The slope error is without fit 0.05 arcsec rms and with fit 0.025 arcsec rms.

Five further objects, plane and spherical components finished by classical polishing technology from different partners of the NOK-project and other manufacturers, were measured with the NOM showing comparable results. Often the measured slope errors in the center region were less than 0.1 arcsec rms without previous knowledge of this high accuracy by the manufacturer. This formerly unknown high quality of optical elements explains in some cases the high functional efficiency and the success of synchrotron beamlines of the 80s and 90s of the last century. The advantage of the classic polishing method consists in a very good microstructure of down to 0.1 nm rms and in a relatively continuous gradient of the residual shape deviations. Based on surfaces as shown in Fig. 1 a last finishing process by ion beam etching could yield an excellent surface with slope errors less than 0.02 arcsec rms or shape errors of less than 0.2 nm rms (λ/3000). This has been done in the NOK-project by the Leibniz-Institut of Oberflächemodifizierung IOM [2]; [7] to generate the NOK-demonstration mirrors.

Conclusion and Perspectives

The improvement of the technological limit for the metrology of optical surfaces down to 0.01 arcsec rms together with improvements in the methods to finish these surfaces achieved in the course of the NOK project represent an essential breakthrough for synchrotron radiation facilities of the third generation and for the needs of VUV and soft x-ray free electron lasers of the future. With the development of the Nanometer-Optik-Messmaschine -NOM an essential step has been made. It has been demonstrated by NOM-measurements, that the shape and slope deviations of classically optical polished components are often much better than known up to now. On the other hand the advantages of classical polishing methods good microroughness and continuous gradient of residual deviations characterize the initial state required for ion beam finishing, leading to optical components of still higher quality in the future.

Acknowledgements

This work has been supported by the Bundesministerium für Bildung und Forschung and the Verein Deutscher Ingenieure VDI under Contract No.: 13 N 7929. We thank heartily the partners of the cooperative research project Nanometer-Optikkomponenten -NOK- for the very inspiring cooperation on the different fields of the nanometer-optical components for Synchrotronradiation in the last four years:

Axel Schindler, Thomas Hänsel, Andreas Nickel, Georg Böhm;
(Leibnizinstitut für Oberflächenmodifizierung IOM Leipzig)
Carsten Schlewitt, Bernd Grubert, David Kreitschik; (Möller Wedel Optical GmbH Wedel)
Olaf Schnabel (Schnabel Elektrische Messtechnik Wedel)
Ingolf Weingärtner, Michael Schulz, Ralf Geckeler, Jens Illemann;
(Physikalisch Technische Bundesanstalt Braunschweig)
Ingo Rieck; Chris Hellwig; (Berliner Glas KG Berlin)
Dieter Bergner, Uwe Jungstand; (Jenoptik Laser Optik Systeme GmbH Jena)
Klaus Becker, Gerhard Derst, Andreas Seifert
(Carl Zeiss Laser Optics GmbH Oberkochen)
Marion Berger, Fritz Hentschel; (Optikkomponenten und Kristalle O&K GmbH Berlin)
Stephan Rothe, Ulrich Glaubitz, Peter Hoffmann;
(Optik Elektronik & Gerätetechnnik OEG GmbH Frankfurt/O.)
Volker Herold (Friedrich Schiller Universität Jena, Technisches Institut)

References:

[1] Heiner Lammert, Tino Noll, Thomas Schlegel, Fred Senf, Frank Siewert, Thomas Zeschke, "Breakthrough in the Metrology and Manufacture of Optical Components for Synchrotron Radiation", BESSY Annual Report , Berlin 2003, p. 530-533. www.bessy.de

[2] Frank Siewert, Kai Godehusen, Heiner Lammert, Thomas Schlegel, Fred Senf, Thomas Zeschke, Thomas Hänsel, Andreas Nickel; Axel Schindler "NOM measurement supported ion beam finishing of a plan-elliptical refocusing mirror for the UE52-SGM1 beamline at BESSY", BESSY Annual Report , Berlin 2003, p. 534-537. www.bessy.de

[3] Heiner Lammert "Nanometer Optical Components for Synchrotron Radiation Beamlines", BESSY Annual Report , Berlin 2001, p. 301-304 www.bessy.de

[4] Heiner Lammert, Tino Noll, Thomas Schlegel, Fred Senf, Frank Siewert, Thomas Zeschke, "The Nanometer Optical Component Measuring Machine – NOM – at BESSY", BESSY Annual Report , Berlin 2002, p. 399-404. www.bessy.de

[5] Frank Siewert, Tino Noll, Thomas Schlegel, Thomas Zeschke and Heiner Lammert; "The Nanometer Optical Component Measuring Machine: a new Sub-nm Topography Measuring device for X-ray Optics at BESSY", 8. Int. Conf. SRI 2003, San Francisco, 2003 in AIP Conf. Proc. Vol. 705, Melville, New York, 2004, p. 847

[6] Bernd Grubert; Trends in autocollimator development; Proc. of 186th PTB-Seminar Braunschweig. 5th Nov. 2003 (PTB-F-49) 62-75
Möller-Wedel Optical GmbH, Wedel; www.moeller-wedel-optical.com/ .

[7] Axel Schindler, Thomas Haensel, Andreas Nickel, Hans-Jürgen Thomas, Heiner Lammert, Frank Siewert, "Finishing procedure for high performance synchrotron optics", SPIE`s 48th annual meeting, San Diego 2003

[8] Heiner Lammert, Nanometer-Optikkomponenten für die Synchrotronstrahlung – Messen und Endbearbeitung bis in den Subnanometer-Bereich unter λ/1000. Schlussbericht NOK-NOM des Teilvorhabens: Koordinierung des Verbundprojekts und Arbeiten zur hochgenauen Vermessung von Nanometer-Optikkomponenten". BESSY Berlin, 22.12.2004

Electromigration degradation mechanism in copper dual-inlaid interconnects studied by x-ray microscopy

S. Rudolph[1], M.A. Meyer[2], E. Zschech[2], P. Guttmann[3], S. Rehbein[1], S. Heim[1], G. Schneider[1]
[1]BESSY m.b.H., Berlin, [2]AMD Saxony LLC & Co. KG, Dresden, [3]Institut für Röntgenphysik, Göttingen

In state-of-the-art microprocessors more than 100 million transistors have to be integrated. As the number of devices increases, and both transistor and interconnect dimensions decrease, the overall performance of the microprocessor is more and more determined by interconnect design and materials. Electromigration (EM), stress-induced degradation and – in case of low-k materials – mechanical weakness are reliability concerns for inlaid copper interconnects. The current generation of highly integrated microprocessors, requiring dense interconnects and increased current densities, has highlighted the EM issue. Formation of voids in copper lines induced by EM during normal microprocessor operation will cause an interconnect to fail or high resistance resulting in malfunction or speed degradation. Although a lot of theoretical and experimental work has been done on EM, the understanding of the degradation process needs to be improved.

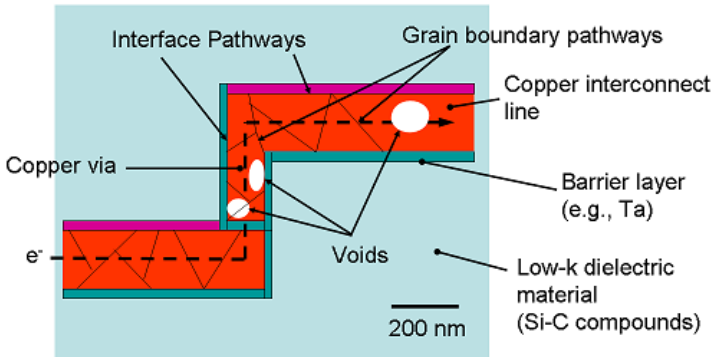

Figure 1. Scheme of the via/line copper test structure.

Particularly fast diffusion pathways have to be identified and failure mechanisms based on the directed transport of atoms have to be understood (see Figure 1). This knowledge is needed to improve interconnect reliability by process and material modifications. Cu is used instead of Al in currently manufactured microprocessors as interconnect material because of its higher electrical conductivity and better resistance against EM failure. Cu interconnects have to be encapsulated with special metallic or dielectric barriers to prevent Cu diffusion into the isolating material and eventually into the silicon. Therefore, the interfaces between Cu and the surrounding material could be easy EM pathways, and consequently, interface or surface diffusion may be very important for the EM behavior of a Cu multilevel metallization system. In passivated interconnects, the encapsulation leads to a high mechanical stress in the interconnect which influences the EM-induced material transport significantly. Stress in the device under test depends strongly on the layers surrounding the stressed interconnect. Thus, *in-situ* observation of EM should be done in an intact layer system including all barriers and passivation layers. For this purpose, an imaging technique is required which maintains high spatial resolution when penetrating through several microns of dielectrics.

Optical microscopy does not provide the necessary spatial resolution. Transmission electron microscopy can only image thin layers with significantly less than 1µm thickness. Surface sensitive techniques like atomic force microscopy or scanning electron microscopy either require destructive sample preparation or provide only a limited resolution due to electron scattering in thick passivation layers.

As X-rays can penetrate samples that are several micrometers thick, X-ray nanotomography is also a suited method to locate failures in interconnects without significant radiation damage to the sample. Although XRM provides not only the contrast needed for imaging voids in copper structures but also makes it possible to distinguish between different isolating materials in back-end-of-line stacks [1].

EM test structures in the wafer scribe line were used for the SEM and XRM *in-situ* experiments. These multilevel via/line interconnect structures, which consist of copper lines in two layers connected by one copper via at each end, were manufactured in dual inlaid technology at AMD Saxony in Dresden/Germany. The vias (diameter about 0.3 µm) and the upper line with a length of several hundred microns are the structures under test. The lower metal lines, which are several microns wide, are linked to bond pads to feed the current into the conductor line. The sample preparation was performed using focused ion beam (FIB) in such way that the structure of interest remains fully embedded in dielectric material. For the XRM experiment, the FIB technique was also applied to thin a lamella containing the structure of interest to a thickness of about 1.5 µm [2].
During the *in-situ* experiments, the test structures were stressed at a temperature of 230°C and a current density of about 10^7 A/cm^2. Temperature controlled indirect heating of the sample up to 300°C with an accuracy of 0.1 K was realized by heating the X-ray microscope's aperture in front of the sample area (see Figure 2). The distance between the heated aperture and the sample was adjusted to be about 100 µm. We measured that the temperature of the EM test sample was nearly identical to the heated aperture.

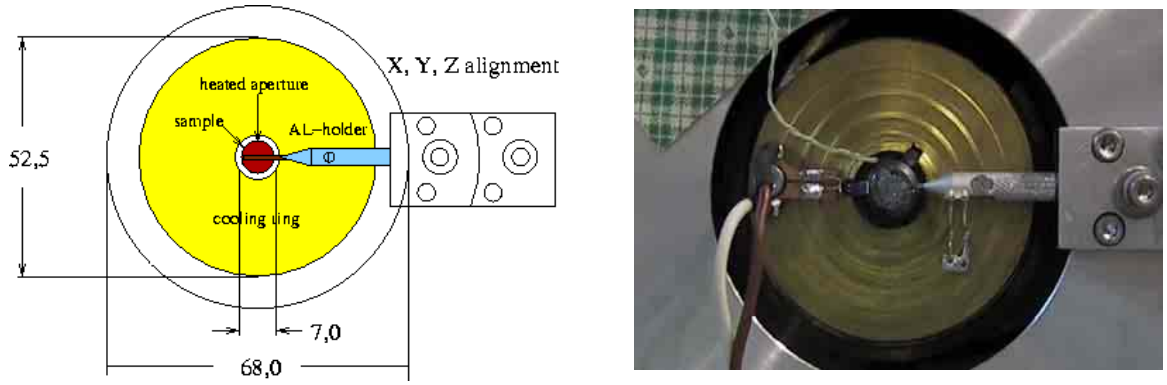

Figure 2. The aperture in front of the EM test structure was heated. To avoid heating of the microscope and drift of the object, we mounted a cooling device surrounding the heated aperture.

Figure 3 shows a sequence of X-ray micrographs of a copper/via/line interconnect structure, which were captured with 25 nm lateral resolution at 524.5 eV photon energy during an *in-situ* EM experiment. The electron flow was from left to right, and downwards through the via. The upper left micrograph shows the early state void formation. During the EM experiment, void formation, movement and agglomeration were seen in the via and in the interconnect line. The final state is shown in the lower right micrograph in Figure 3. The real-time X-ray microscopy images show that the voids are usually formed in the via and they migrate towards the top copper/dielectric (SiN_x) interface. In particular, the top copper/dielectric interface has been found to be the weakest interface due to the observed void movement along this pathway. The reason that copper/dielectric interfaces are rapid pathways for mass transport is the relatively weak bonding and the resulting poor adhesion between copper and the adjacent material from which the interface is composed (see Figure 3) [3]. For statistical analysis of EM behaviour, we plan to perform numerous EM experiments on different copper via/line structures. In addition, it is planned to measure quantitatively the mass transport and to identify the major copper diffusion pathways also in advanced Cu/low-k backend-of-line structures.

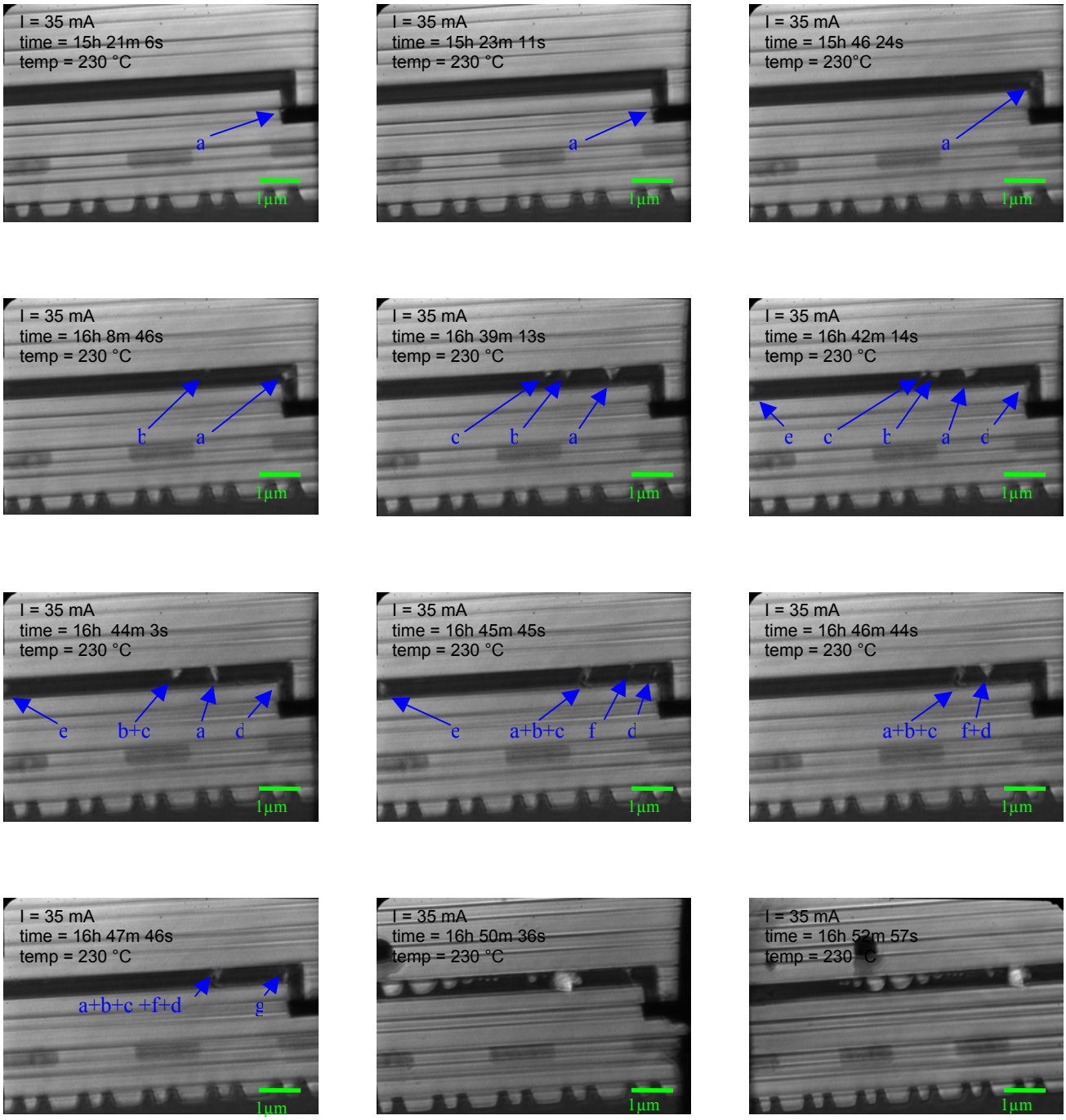

Figure 3. Selected X-ray micrographs taken at a photon energy of 524.5 eV visualizing the mass transport by EM in a passivated Cu interconnect with a thickness of 350 nm and a linewidth of 600 nm. The via was stressed at a temperature of about 230°C to accelerate the formation, growth and movement of voids. The current densities were increased up to 10^7 A/cm^2 during 16 hours and 52 min of observation. This current density was chosen to perform the *in-situ* experiment in a reasonable period of time. Note that the voids move along the top copper/dielectric interface which is found to be the main copper diffusion pathway.

References

[1] E. Zschech, M.A. Meyer, M. Grafe, G. Schneider, MP Materialprüfung, Carl Hanser Verlag, Jahrg. 46 (2004) 10, 513 – 516.

[2] G. Schneider, G. Denbeaux, E.H. Anderson, B. Bates, A. Pearson, M.A. Meyer, E. Zschech and E.A. Stach, *Appl. Phys. Lett.* 81, 14 (2002) 2535.

[3] E. Zschech et al., Proc. MRS Spring 2004

Commissioning of a Femtosecond X-Ray Source at BESSY

S. Khan, K. Holldack, T. Kachel, R. Mitzner, T. Quast

1. Introduction

Probing structural or magnetic changes in matter with X-rays on a sub-picosecond time scale offers exciting scientific opportunities. Contemporary synchrotron radiation sources, however, are limited in pulse duration to tens of picoseconds by the "natural" bunch length in electron storage rings. One way to surpass this limitation is to shorten the bunches by reducing the momentum compaction factor, where an rms bunch length of 0.7 ps (1.7 ps fwhm) was reached at BESSY [1]. Another possibility is to select radiation from a short fraction of the bunch (a "slice"), marked by a femtosecond laser pulse. This technique – now dubbed "femtoslicing" – was proposed [2] and experimentally demonstrated [3] at the Advanced Light Source in Berkeley, where radiation pulses from a bending magnet were produced with $\sim$ 300 fs (fwhm) duration. At the BESSY II storage ring, a first femtoslicing facility for ultrashort undulator radiation was completed and commissioned in 2004, producing soft X-ray pulses of $\leq$ 100 fs (fwhm) duration with linear or circular polarization at a photon energy of $\leq$ 1300 eV.

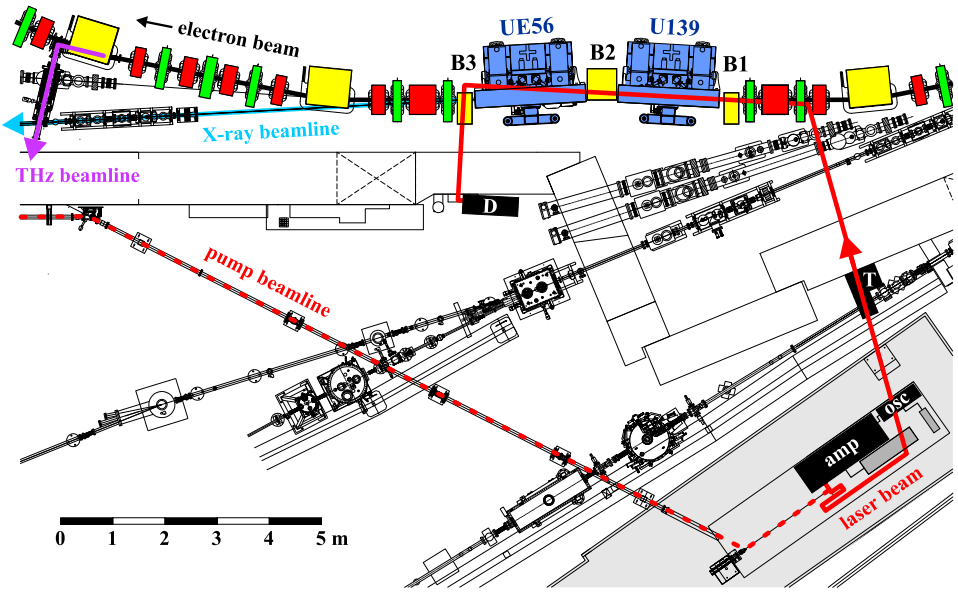

Figure 1: BESSY II floor plan showing the femtoslicing facility comprising the modulator (U139), the radiator (UE56) and three bending magnets (B1,B2,B3). The laser beam (red) is focussed by a telescope (T) and ends at a diagnostics station (D). The experiment is located at the end of the X-ray beamline (blue), THz radiation (magenta) monitors the laser-electron interaction.

2. Principle and Technical Implementation

A femtosecond laser pulse co-propagating with an electron bunch in an undulator (the "modulator") causes a modulation of the electron energy, if the laser wavelength equals the wavelength of spontaneous undulator radiation. In a subsequent bending magnet, the off-energy electrons are transversely displaced and their radiation emitted in the next undulator (the "radiator") has essentially the time structure of the initial laser pulse.

At BESSY, a dipole magnet between modulator and radiator with a bending angle of 112 mrad displaces the energy-modulated electrons by $\sim$ 1 mrad such that radiation from the bunch core does not overlap with the short-pulse component and can be blocked by an aperture. Since this angular separation scheme works without imaging elements, excessive background due to non-specular reflexion from mirror surfaces is avoided. The modulator (U139) is a planar undulator with 10 periods of 139 mm length. The radiator (UE56) is an APPLE-II-type undulator [4] with 30 periods of 56 mm length and produces any degree of elliptical polarization. As shown in Fig. 1, modulator and radiator are both placed in the same straight section of the storage ring to minimize lengthening of the electron distribution between them.

A 800 nm Ti:sapphire system in an air-conditioned hutch produces pulses of $\leq$ 2.8 mJ energy and $\geq$ 30 fs (fwhm) duration at a repetition rate of 1 kHz. For pump-probe applications, a fraction of each laser pulse is directed as pump pulse through an evacuated pipe to the experiment, thus providing natural synchronization with the respective X-ray probe pulse. Laser and synchrotron radiation from the U139 modulator are extracted by water-cooled mirrors to monitor their transverse and temporal overlap.

3. Commissioning Results

Path length differences of energy-modulated electrons cause a short dip ($\sim$ 0.1 mm) in the longitudinal electron distribution, giving rise to radiation in the THz regime. This radiation is routinely used to monitor and optimize the laser-electron interaction [5].

In dedicated shifts, the energy modulation was studied by blocking transversely displaced electrons with a scraper while monitoring the electron loss rate. Other signatures of the laser-electron interaction are changes of the beam lifetime due to the reduction of electron-electron scattering and a slight increase of the transverse beam size [6].

Electrons having lost energy in the laser field are aligned with the axis of the UE56 radiator using a closed orbit bump. This way, the short-pulse radiation component is within the beamline acceptance, while radiation from adjacent dipoles misses the beamline. After passing a plane-grating monochromator, photons are detected by an avalanche photodiode (APD) with sub-ns time resolution. A digital oscilloscope with 2 GHz bandwidth is synchronized with the laser system and the pulse height, averaged over 10^2-10^3 APD signals, is read out by a computer. Figure 2 shows the angular distribution of 3rd-harmonic radiation at 708 eV from the UE56 set to linear polarization in vertical direction, which was calculated using the code WAVE [7]. The dashed line predicts the characteristics of the short pulse from a numerical simulation of the laser-electron interaction [6]. Radiation measurements at four different observation angles indicate the presence of short-pulse radiation caused by laser-electron interaction, while the intensity is an order of magnitude lower when the laser is blocked. Under variation of the UE56 magnetic gap, radiation at 708 eV only shows the characteristics of the 3rd undulator harmonic, when the laser is present, proving that laser-electron interaction produces electrons close to the undulator axis. This is shown in Figure 3 for two examples at different observation angles. Similar results are obtained for radiation with circular polarization.

The expected rate of photons produced by femtoslicing is 10^6 per second and 0.1% bandwidth. Their time characteristics can be indirectly inferred from the spectrum of THz radiation which is consistent with the spectrum calculated from the simulated electron distribution.

While the commissioning program is continued to fully characterize the femtoslicing source, preparations for first pump-probe experiments are in good progress.

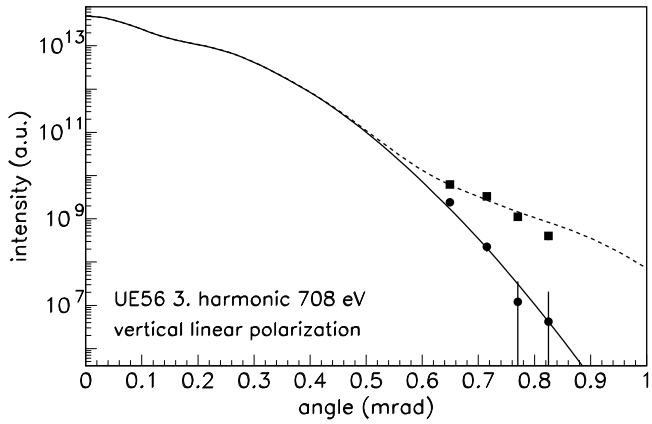

Figure 2: Angular distribution of synchrotron radiation from the UE56 radiator without (solid) and with (dashed) laser-induced energy modulation. The symbols indicate measured radiation with (square) and without (round) the presence of laser pulses.

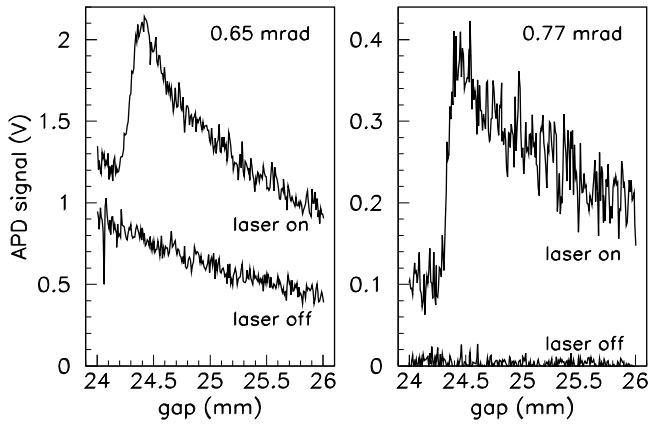

Figure 3: Radiation at 708 eV as function of the UE56 gap with and without laser. The 3rd undulator harmonic (peak) indicates the presence of on-axis electrons.

Acknowledgements

We would like to express our gratitude to all BESSY colleagues contributing to the femtoslicing project.

References

[1] J. Feikes, K. Holldack, P. Kuske, G. Wüstefeld, EPAC 2004, Lucerne, 1954.

[2] A. A. Zholents, M. S. Zoloterev, Phys. Rev. Lett. 76 (1996), 912.

[3] R. W. Schoenlein et al., Science 287 (2000), 2237.

[4] M. R. Weiss et al., Nucl. Inst. Meth. A 467 (2001), 449.

[5] K. Holldack, S. Khan, R. Mitzner, T. Quast, G. Wüstefeld, EPAC 2004, Lucerne, 2284.

[6] K. Holldack, T. Kachel, S. Khan, R. Mitzner, T. Quast, F. Senf, FEL 2004, Trieste.

[7] M. Scheer, BESSY, unpublished.

Projects in Basic Research
(January 2005)

Leader	Institution	Title	Funding	Contract Number
Andersen	Aarhus University	Structures of yeast translation factors		
Andersen / Nissen		Structures of the Ca2+ ATPase in various functional states		
Andersen / Thirup		Structure of bovine mitochondrial EFTu-EFTs complex		
Andersen / Thirup		Mitochondrial seryl-tRNA synthetase		
Andersen / Thirup		Elongation factor T (EF-Tu:EF:Ts) in complex with pulvomycin		
André	CNRS	X-ray Raman scattering with Bragg diffraction in a La-based superlattice	EU	3-CT-2004-506008
Arvanitis	Uppsala University, Department of Physics	Magnetic EXAFS of ultra-thin Fe films: Experiments and fully relativistic theory	EU	
Ast	MPI für Festkörperforschung	Electrons in surface superlattices		
Babanov/ Baberschke	Institute of Metal Physics RAS, Yekaterinburg/FU Berlin	EXAFS study of L-edges for FeCr systems		
Baczewski	Polish Academy of Sciences, Institute of Physics	Magnetic structure in RE/TM thin films studied by XMCD	EU	
Bansmann	Universität Rostock, Fachbereich Physik	Magnetismus von Inselschichten und Clustern auf Oberflächen	DFG	835/H-3
Bansmann	Universität Rostock	Magneto-optische Raster-Reflexions-Spektroskopie an in-situ deponierten Clustern		
Bansmann / Meiwes-Broer	Institut für Physik, Universität Rostock	Ferromagnetic clusters on surfaces: size-dependent magnetic properties	DFG	DFG BA 1612-3/1
Barth	MPI-FKF / IPN-EPFL / UBC Vancouver	Engineering Low-Dimensional Metallosupramolecular Systems at Metal Surfaces	other	
Bartl	Inst. f. Med Physik& Biophysik,	Infrarotspektroskopische Untersuchung an Rhodopsin		
Baumgärtel	Freie Universität Berlin, Institut für Chemie	Photoanregung und Photochemie von Molekülen im Bereich 5-25 eV (Photoabsorption, Photoionisation, Autoionistion)		
Baumgärtel	Universität Potsdam	Einbau einer Stopped Flow Zelle, Probemessungen, Kalibrierung Optimierung der Normierung für quantitative Absorptionsmessungen Undulator: Aufbau und Steuerung, Charakterisierung, Standardmesungen und Projekte		

Beaurepaire	IPCMS	Dilute MAGNETIC Semiconductors (Co, Zn)O studied by magnetic Circular Dichroism		
Becker	Fritz-Haber-Institut der Max-Planck-Gesellschaft	Coherence properties in atomic and molecular photoionization	BMBF DFG	05 KS1EB12 BE 860/18-2
Betti	Università di Roma La Sapienza	Growth of pentacene ordered layers on Cu(119) studied by NEXAFS	EU	BI3A-24/061204
Bodenthin	Uni-Potsdam	Determination of coordination spheres of metal centres in thin metallo-supramolecular films		
Bodenthin	Uni-Potsdam	Energy dispersive Grazing Incidence diffraction on monolayer films		
Boeglin	IPCMS-GSI	Thickness and temperature dependence of FM/AFM magnetic coupling in NiO/Fe/W(110)		
Bonanni	Johannes Keppler Universität	VUV-Ellipsometry: measurement of strain-induced optical anisotropies in hexagonal II-Nitrides and determination of the optical contrants for the GaN/AlGaN cubic system		
Borisenko	IFW Dresden	Ner-fermi-level electronic structure of the Zn- and Ni-doped BSCCO high-Tc superconductors		
Boronin	Inst. of Catalysis, RAS, Novosibirsk	Photoemission study of Ag and Au oxide films formed by microwave-excited oxygen		
Borucki	FU Berlin	Strukturänderungen in den Photorezeptoren Phytochrom und Photoactive Yellow Protein detektiert mittels CD-Spektroskopie		
Boyen	Universität Ulm	Electronic properties of mass-selected supported gold clusters (<60 atoms)		
Braun	Paul-Drude-Institut für Festkörperelektronik	Oberfläche, Grenzfläche und Schichtstruktur von MnAS, Fe und FexSi1-x auf GaAs während der Hteroepitaxie. Entstehung u. Analyse der Film - Substrat-Grenzflächenstruktur während der Epitaxie von Prasedym-Oxid auf Si(100)	BMBF	DI BM159
Bressler	BESSY	Determination of the 3d land widths of submonolayer Fe and Co on Cu(III)		
Bridge	University of Dublin, Dept. Of Chemistry	Organometallic chemistry on Silicon surfaces	EU	
Brückel	IFF, FZ Jülich GmbH	Investigation of orbital ordering in ferromagnetic insulating La1-xSrxMnO3(x=1/8) by soft X-ray resonant scattering		

Brückel	IFF-8, Forschungszentrum Juelich	Investigation of charge/orbital ordering in ferromagnetic insulating La1-xSrxMnO3 (x~1/8) by soft X-ray resonant scattering	other	
Bukhtiyarov	Boreskov Institut of Catalysis, Novosibirsk	Combined high pressure XPS and PTRMS study of ethylene epoxidation over silver	BMBF	
Bukhtiyarov	Inst. of Catalysis, RAS, Novosibirsk	XPS and XANES spectroscopy study of vanadium-based calalysts for selective oxidation of hydrocarbons		
Callmer	Humbold-Universität zu Berlin	Non-destructive XRF-analyses of the so-called "Hiddensee gold jewellery" (Viking Age archaeological objects, c. 1000AD)		
Calvani	Università di Roma La Sapienza	Far-infrared reflectivity of HCTS single crystals by use of synchrotron radiation	EU	BI3A-27/011104
Calvet	Hahn-Meitner-Institut Berlin GmH	Electronic band structure of epitaxial CuInxGa(1-x)S2 films (x=0..1)		
Calvet	Hahn-Meitner-Institut Berlin GmH, SE 6	Sodium (Na) and Lithium (Li) on differently orientated epitaxial CuInS2-films		
Calvet	Hahn-Meitner-Institut Berlin GmH, SE 6	Nucleation of Cu and In on wetchemical S-treated GaAs(100)		
Carbone	CNR Trieste	Magnetic surface impurities	EU	
Carbone	Consiglio Nazionale delle Ricerche	Photoemission spectroscopy of isolated Fe impurities on metal surfaces		
Cazorla-Amorós	Dpto. Química Inorgánica, Universidad de Alicante, Apartado 99, E-03080 Alicante, Spain.	Investigation of styrene production over carbon catalysts using high-pressure XPS.	EU	RII 3-CT-2004-506008
Chassé	Institute of Physical and Theoretical Chemistry, University of Tuebingen	Orbital mixing-originated fine features in x-ray emission spectroscopy and local partial density of states of sulfides and selenides studied by x-ray emission spectroscopy	BMBF	
Chassé	Universität Tübingen	Metal-sulfur bonding and chemical reaction at sulfide-involved heterojunctions detected by S L x-ray emission spectra		
Cobessi	ESBS	Structural studies of the pyoverdin receptor FpvA from Pseudomonas aeruginosa		
Comtet	Université de Paris Sud	Molecular Nanomachines		
Cramm	Forschungszentrum Jülich, IFF	Electronic structure and magnetism of Heusler alloys	CRG	
Cramm	Forschungszentrum Jülich, IFF	Magnetism in ferromagnetically filled carbon nanotubes	CRG	
Dähne	Technische Universität Berlin, Institut für Festkörperphysik Sekr. PN4-1	Photoelectron spectroscopy at MIS structures with external gate bias	BMBF	05 KSIKTA/4

Dähne	Technische Universität Berlin	Electronic structure of self-organized dysprosium silicide nanowires on Si(001)		
Dau	Freie Universität Berlin, FB Physik, Arnimallee 14, D-14195 Berlin	XAS on metalloenzymes and related model molecules - methodical progress by the use of a large-area energy-resolving detector	DFG	
Dau	Freie Univ. Berlin, FB Physik, Biophysik, Prof. Dr.	Comparative XAS study of synthetic manganese oxides and biogenic deposits on the cell-wall of the green alga Chara corallina	other	
De Groot	Utrecht University	The creation of active oxygen sites in Mn-ZSM5 using N2O and ozone: An in-situ soft A-ray absorption study		
Domashevskaya	Voronezh State University, Russia	Investigations of electron structure specificity and the nature of photoluminescence in porous materials and quantum points for indirect band-gap and direct-gap semiconductors (Si, GaP, InP, GaAs).	other	
Domashevskaya	Voronezh State University	XANES and XPS investigations of electron structure and phase composition in nanostructures with quantum dots and nanocomposites		
Drillon	IPCMS	New Co oxide showing quantum tunneling effect of the magnetisation: an XMCD study		
Dürr	BESSY	Optical sin injection in (GaMn)As	other	
Dürr	BESSY	Imaging current induced magnetization reversal in real time		
Dürr	BESSY	Valence electronic and magnetic structure of magnetoresistive Co2Cr1-xFexAl Heusler alloys probed by circular dichroism in 2p resonant photoemission		
Dürr	BESSY	Exploring the surface magnetisation deficit in (GaMn)As ferromagnetic semiconductors		
Ehresmann	TU-Kaiserslautern	Resonante magnetische Röntgenreflektometrie an FeMn/Co/Cu/Co-& Co/Cu/Co/IrMn-Spinvalves nach Modifikation durch He-Beschuss	DFG	Eh 187-2-2
Ehresmann	Universität Kaiserlautern, FB Physik	Rotationsaufgelöste Photodissoziation in neutrale Fragmente u. Ionenausbeuten aufgrund der Prädissoziation u. Autoionisation molekularer Rydbergzustände in CO und N2	DFG	Eh187/4

Ehresmann	Universität Kaiserlautern	Resonante magnetisce Röntgenreflektometrie an bis zur Tunnelbarriere aufgebrachten halben magnetischen Tunnelementen ….		
Einsle	Universität Göttingen	Cytochrome c Nitrite Reductase Complex NrfHA		
Einsle		Nitrous oxide reductase		
Eisebitt	BESSY	Soft X-ray spectroscopy in liquid environments: towards an understanding of the electronic structure in active centers of biomolecules		
Eisebitt	BESSY	Coherent resonant X-ray scattering from magnetic domain patterns		
Erdmann / Klussmann	Freie Universität Berlin	Crystallization and structure analysis of Spiegelmers		
Erko	BESSY GmbH, Berlin	Investigation of the properties of Bragg-Fresnel gratings	other	
Erko	BESSY GmbH, Berlin	A raytracing code for zone plates	other	
Erko	BESSY	Confocal capillary X-ray microscope		
Erko	BESSY	Investigation of Bragg-Fresnel Grating Properties		
Esser	ISAS- Institute for Analytical Sciences	Aufbau und Betrieb eines VUV-XUV-Ellipsometers mit Synchrotronstrahlung	BMBF	05 KS4KTB/3
Esser	ISAS - Institute for Analytical Sciences Department Berlin	Chemisch modifizierte Halbleiteroberflächen: Molekülterminierung und Oxidation am Beispiel Si(001) und InN(0001)	DFG	Es127-4/4
Esser	TU Berlin, Institut für Festkörperphysik Sekr. PN6-1	IR-Ellipsometrie: Spektroskopie an Oberflächen, epitaktischen Schichten und adsorbierten Molekülen	BMBF	
Esser	TU Berlin, Institut für Festkörperphysik Sekr. PN6-1	Oberflächen von MOVPE gewachsenem GaN(0001)	DFG	
Ettema	Technical University Delft	Electronic correlation effects in the electronic structure of metallic quantum wells	EU	
Fauth	Uni Würzburg	Size dependent magnetic properties of rara gas isolated transition metal (Fe, Co) clusters		
Fauth	Uni Würzburg	Magnetic anisotropy of small transition metal clusters on nonmagnetic metal surfaces		
Felsch	Universität Göttingen, I. Physikalisches Institut	Interfacial interactions in iron/vanadiumoxide bilayers studied by x-ray absorption spectroscopy	DFG	SFB 602, TP A1
Feulner / Menzel	Physikdepartment E20, TU-München	Photon induced dynamics	BMBF	05 ES3XBA/5
Fiechter	Hahn-Meitner-Institut Berlin, SE 5	Investigations of catalytic centers in noble metal free catalysts for direct methanol PEM fuel cell. EXAFS measurements		

Fiechter	Hahn-Meitner-Institut Berlin, SE 5	Investigations of catalytic centers in noble metal free catalysts for direct methanol PEM fuel cell. XANES measurements		
Fiechter	Hahn-Meitner-Institut Berlin	In-situ EXAFS measurements of Fe-, Co-catalysts for PEM fuel cells under oxygen reduction conditions		
Figueiredo	Cryst. & Miner. C., IICT, and CENIMAT, New Univ. Lisbon, 2829-516 Caparica, Portugal	Electronic state of oxygen vs. fluorine in rutile- and fluorite-type compounds: a comparative study of O and F 1s XAS spectra	EU	User Contract BI3A-01/100504
Fink	Universität Erlangen-Nürnberg	Elektronische Struktur von molekularen Nanomagneten		
Firsov	BESSY GmbH, Berlin	Design and fabrication of diffractive X-ray optics at BESSY.	other	
Follath	BESSY	Commissioning U125/1-PGM1 nach Umbau der Refokusieroptik		
Freund	Fritz-Haber-Institut der Max-Planck-Gesellschaft, Abt. Chemische Physik	Elektronische Struktur molekularer Schichten auf reinen und modifizierten Oxid-, Karbid- und Nitridsubstraten	MPG	
Galakhov	Institute of Metal Physics, Russian Academy of Sciences - Ural Division	Electronic structure and electronic holes in doped, defect, and nanocrystalline 3d oxides	other	RFBR No 04-03-96092-Ural
Galakhov	Institute of Metal Physics	Resonant X-ray emission study of layered oxides LixMO2		
Galakhov / Neumann	Inst. of Metal Physics RAS Yekaterinburg, University of Osnabrück	Electronic holes in doped and defect 3d oxides		
Gambardella	Ecole Polytechnique Federale de Lausanne, Institut de Physique des Nanostructures, EPFL	XPS investigation of localized 3d impurity states on free-electron hosts	EU	
Geue	Universität Potsdam, Institut für Physik Strukturanalyse	White X-ray scattering at colloidal crystals		
Gießel / Widdra / Weinelt	Max-Born-Institut	Pump-Probe Untersuchungen zur Dynamik von Oberflächenzuständen	other	
Glass-Maujean	Laboratoire de Dynamique des Ions, Atoms et Molécules ESA 7066	The hydrogen molecule: determination of the transition moments, dissociation and ionization of superexcited states		
Godehusen	Bessy	Bestimmung des b-Parameters an freien 3d-Übergangsmetall-Atomen		
Goering	Max-Planck-Institut für Metallforschung	Rauhigkeitsabhängigkeiten des Co Magnetisierungsprofils und der induzierten Kupfermagnetisierung	other	

Goering	MPI für Metallforschung	New fast ramping high field XMCD-system, High-performance permanent magnets and REBaCo2O5.5: Magnetocrystalline anisotropy, high orbital moments and Giant X-ray Natural Circular Dichroism		
Golden	Van der Waals-Zeeman Instituut	k-space microscopy of high Tc superconductors		
Goldhahn	TU Ilmenau, Inst. f. Physik, PF 100565, 98684 Ilmenau	Ellipsometrie an Nitridhalbleitern zur Bestimmung der dielektrischen Funktion und kritischer Punkte der Bandstruktur	other	B609-02004
Goldhahn	Technische Universität Ilmenau, Institut für Physik	Bestimmung der dielektrischen Funktion von InN im VUV	BMBF	
Gomoyunova	A.F. Ioffe Institute, Russian Academy of Sciences	Electronic structure of metastable iron silicide phases formed on Si(100)	BMBF	
Gordeev	Ioffe Physical-Technical Institute	Size Related Electron Structure Transformation of Isolated Silver Supported Clusters	BMBF	
Grunze	Universität Heidelberg, Angewandte Physikalische Chemie	Neutronenstreu- und Synchrotronstrahlungsexperiment e an biologisch relevanten organischen Monoschichten. Teilprojekt:Homogene und heterogene organische Schichten als Substrate für Anwendungen in der Biosensorik	BMBF	03 GRE1HD
Grunze	Universität Heidelberg, Angewandte Physikalische Chemie	Biomedical investigation of melanosomal defects using X-ray microscopy	BMBF	
Grunze	Universität Heidelberg, Angewandte Physikalische Chemie	Digital in-line holgraphy with synchrotron radiation: Characterization experiments for a 3D-imaging method	BMBF	
Gudat	BESSY	Magneto-optische Polarisationsspektroskopie mit Synchronstrahlung und magnetischen Schichtsystemen	BMBF	05KS1IPB/8
Güntherodt	RWTH Aachen, II. Physikalisches Institut	High-energy resolved spin-polarized photoemission of ferromagnet/insulator interfaces	BMBF	Fkz 05KS1PAA/7
Güntherodt	RWTH Aachen	All-oxide tunnel junctions and influence of the interface on the value of the tunnel magnetoresistance		
Gutiérrez	Universidad Autónoma de Madrid	X-ray Absorption Spectroscopy study of metal carbide-silicon carbide thin films	EU	BI3A-33/221104
Hague	Universität Pierre et Marie Curie, Laboratoire de Chimie Physique	Low energy electron excitations in complex oxides studied by X-ray Raman spectroscopy	EU	
Hahn	BAM	Analysis of binding media in cross sections using synchrotron infrared radiation	other	

Hahn	BAM	Investigation of oxidation and migration processes of inorganic compounds in ink corroded manuscripts	other	
Hahn	BAM, Labor IV.22	Untersuchung organischer Bestandteile von Malschichtsystemen in Kunstwerken-Bindemittelanalyse an Querschlissen mit hoher Ortsauflösung (5-10 µm) mittels Synchrotron Infrarotspektroskopie		
Hahn	BAM, Labor IV.22	Untersuchung von schwarzen Bronzeflecken auf historischen Kupferobjekten		
Haibel	Hahn-Meitner Institute	Microstructure Investigations on Thixotropic Alloys and Metal-Matrix-Composites by Synchrotron Computed Tomography	other	
Haibel	HMI	Investigation of pore formation in metallic foams by synchrotron computed tomography	DFG	2I7729 S8P1075
Haumann	FU Berlin, Physik	Setup and test of a heluim cryostat at beamline KMC-2 for XAS on metalloenzymes	DFG	SFB496/C6,C8
Hävecker	Fritz-Haber-Institut der MPG, Dept. Inorganic Chemistry, Faradayweg 4-6, 14195 Berlin	Spektroskopische Charakterisierung von Cu/ZnO Katalysatoren unter Reaktionsbedingungen der Methanoldampfreformierung mittels weicher Röntgenstrahlung	other	
Heinemann	Max Delbruck Centrum fur Molekular Medicin	Proteinstrukturfabrik	BMBF	
Heinemann / Fälber		IF2 in complex with initiator tRNA		
Heinemann / Halavaty		Studies of the electron transfer between components of the vertebrate mitochondrial hydroxylase system		
Heinemann / Khare		Crystal structure analysis of a transcriptional repressor, KorB, in complex with operator DNA and with its interacting partner IncC		
Heinemann / Kolbe		Structural studies on tight junction proteins		
Heinemann / Kolbe		Structural studies of the TTSS		
Heinemann / Kolbe / Kumar		Structure determination of SycD and SycD/YopB complex from Yersinia enterocolitica		
Heinemann / Max	MDC, FG Kristallographie	Structure determination of full-length Coenzyme A Synthase		
Heinemann / Max		Structure determination of full-length human p97		
Heinemann / Müller		Tail Spike protein HK620 from Bacteriophage E. Coli		

Heinemann / Roske		The second carbohydrate binding module of family 27 of Caldicellulosiruptor strain Rt8B.4		
Held	University of Cambridge, Dept. Of Chemistry	Probing chiral surfaces using circularly polarized light - the adsorption of chiral organic molecules	EU	BI3A-02/100504
Hellwig	BESSY GmbH	X-ray resonant magnetic scattering and X-ray magnetic circular dichroism from exchange coupled perpendicular films	other	-
Hellwig	BESSY	Magnetic SPECKLE studies of the domain evolution in perpendicular magntic films during external field reversal		
Hergenhahn	MPI for Plasma Physics	Photoelectron-Auger-Electron Coincidence Measurements with high Energy Resolution		
Hergenhahn	MPI for Plasma Physics	Photoionisation of a free cluster beam		
Heske	Universität Würzburg, Physikalisches Institut Lehrstuhl f. Exp. Physik II	Charakterisierung der elektronischen Struktur von organischen und biologischen Materialien mit resonanter inelastischer Röntgenstreuung	BMBF DFG	05KS1WW1/6 Um6/8-1
Heske	Universität Würzburg, Physikalisches Institut Lehrstuhl f. Exp. Physik II	Elektronische und chemische Eigenschaften von Halbleiter-Nanopartikeln	DFG	
Heske	Universität Würzburg, Physikalisches Institut Lehrstuhl f. Exp. Physik II	Röntgenspektroskopie an organischen Grenzflächen und Biomaterialien in Kontakt mit Lösungen	BMBF DFG	05KS1WW1/5 Um6/8-1
Heske	Universität Würzburg, Physikalisches Institut Lehrstuhl f. Exp. Physik II	NEXAFS investigations of organic materials for field effect transistors	BMBF DFG	05KS1WW1/5 Um6/8-1
Hillebrecht	FZ Jülich	Search for ferromagnetic order in CuMn/Cu/Co trilayers		
Hillebrecht	FZ Jülich	Exchange coupling at the NiO/magnetite interface		
Hillebrecht / Teterin	Research Center Karlsruhe, Kurchatov Institute RAS Moscow	Resonant photoemission on dilute U alloys		
Hinrichs	ISAS - Institute for Analytical Sciences	IR-Ellipsometrie zur Untersuchung der Struktur und der optischen Eigenschaften ultradünner Filme aus Benzolderivaten auf Silizium	BMBF	05 SR8kk19
Hjörvarsson	Uppsala University	XMCD and XRMS studies from AFM ordered FeNi/Al203 islands	EU	
HMI	HMI	HMI Literatur	other	01SF0007
Hodnett	University of Limerick	Defining high temperature and pressure Bayer digestion reactions: Dissolution and crystallisation mechanisms and kinetics		

Hohl	TU Darmstadt, Institut für Materialwissenschaft	Resonante inelastische Röntgenstreuung an amorphem Siliziummonoxid		
Horn	Fritz-Haber-Institut der Max-Planck-Gesellschaft	Electronic states in low-dimensional metal structures		
Horn	Fritz-Haber-Institut der Max-Planck-Gesellschaft	Magnetic order in quasicrystals		
Horn	Fritz-Haber-Institut der Max-Planck-Gesellschaft	Self-organized molecular structures on vicinal surfaces		
Hübers	DLR	Nonequilibrium population of impurity centers in silicon		
Hübers	DLR	THz spectroscopy of Impurity Centres in Semiconductors		
Hunger	Fachgebiet Oberflächenforschung, Institut für Materialwissenschaft, TU Darmstadt	Composition-dependent CuInSe2 and CuGaSe2 heterojunction properties	BMBF	05KS4RDA/0
Imbihl	Institut für Physikalische Chemie und Elektrochemie, Callinstr. 3-3a, 30167 Hannover	In situ X-ray photoelectron spectroscopy of the methanol oxidation over Cu(110)	DFG	
Ionov	Inst. of Solid State Physics RAS Chernogolovka	Investigation ofelectronic structure of 2D ordered array of epitaxial nanodots and metalattice conductors		
Ivanov	Free University of Brussels	Study of thin films of discotic and star-shaped molecules forming columnar mesophases		
Jaegermann	Fachgebiet Oberflächenforschung, Institut für Materialwissenschaften, TU Darmstadt	Photoelectron spectroscopy of interfaces for silicon/organic hybrid devices	BMBF	05KS4RDA/0
Jaegermann	Technische Universität Darmstadt, FB Materialwissenschaften Fachgebiet Oberflächenforschung	Potential inhomogenities at semiconductor and - interfaces	BMBF	329857
Jaegermann	Technische Universität Darmstadt, FB Materialwissenschaften Fachgebiet Oberflächenforschung	Electronic structure of ion conducting materials	DFG	SFB595
Jaegermann	Technische Universität Darmstadt, FB Materialwissenschaften Fachgebiet Oberflächenforschung	Characterisation of solid/electrolyte interfaces: Modification of CuInSe2 surfaces and interfaces by chemical-bath deposited II-VI compounds	BMBF	O KS1RD1/0
Jaegermann	Technische Universität Darmstadt	Electronic properties of van der Waals epitaxy interfaces		
Jaegermann	Technische Universität Darmstadt	Elementary Processes in Contact Formation at Semiconductor/Electrolyte Interfaces Exemplified by Dye Sensitive Solar Cells: TiO2-Dye-Solvent Interaction		

Jaskolski / Bujacz	Inst. Bioorg. Chem.	Plant hormone binding proteins		
Jaskolski / Kochman		Insect hormone binding proteins		
Jimenez	CSIC	XANES of Binary CN and Ternary BCN Compounds with Fullerene-like and Diamond-like Structures.	EU	RII3-CT-2004-506008
Kanngießer	Technische Universität Berlin, PN3-2	3D micro-X-ray spectroscopy on biological and geological samples (part I)	DFG	
Kanngießer	Technische Universität Berlin, PN3-2	Untersuchung von Farbursprüngen und Behandlung von Edelsteinen	DFG	
Kanunnikova	Phys-Technical Institute, Ural Branch RAS, Izhevsk	Composition and structure of spin-on-glass thin silica films		
Karlsson	Uppsala University, Department of Physics	Inner valence shell photoelectron spectroscopy of diatomic molecules	EU	
Keckes	Erisch Schmid Institute	Elevated-Temperature X-ray Diffraction Studies of Residual Stresses in Thin Films with a Thickness in the Nanometer Range		
Kersten	Gutenberg-Universität Mainz, Institut für Geowissenschaften	TXM-Tomographie von atmosphärischen Rußagglomeraten		
Kisker	Heinrich-Heine-Universität Düsseldorf, Institut für Angewandte Physik	Interface reactions in FM-AF-layered materials studied by micro-spectroscopy using magnetic dichroism	BMBF	05 KS1PFA/3
Kisker	Heinrich-Heine-Universität Düsseldorf, Institut für Angewandte Physik	Magnetic domain structure and interface coupling in ferromagnetic and antiferromagnetic metal/oxide heterostructures	BMBF	05 KSPFB/1
Klein	Technische Universität Darmstadt	Interfaces of polycrystalline conducting oxides	DFG	SFB 595
Klein / Jaegermann	FB Materialwissenschaften, TU Darmstadt	Properties of van der Waals-Epitaxy interfaces	DFG	JA 859/7
Kleineberg	Uni Bielefeld, Bereich Physik	In-vitro Transmissions-Photoemission-Elektronenemissionsmikroskopie im Wasserfenster am U125/1-ML bei BESSY II; Entwicklung von 3d ELEMENTAUFGLÖSTER Röntgen-Nanotomographie mit einem Transmissions-Photoelektronenmikroskop	BMBF	05 KS1PBA-8
Knop-Gericke	Fritz-Haber-Institut der Max-Planck-Gesellschaft	Selective gas-phase hydrogenation of C-5 multi-functional molecules using palladium and nickel based catalysts	DFG	SP 1091
Knop-Gericke	Fritz-Haber-Institut der Max-Planck-Gesellschaft	Spektroskopische Charakterisierung von Cu/ZnO Katalysatoren unter Reaktionsbedingungen der Methanoldampfreformierung mittels weicher Röntgenstrahlung	DFG	SP 1091

Knop-Gericke	Fritz-Haber-Institut der Max-Planck-Gesellschaft	Dehydrogenation of C4 hydrocarbons using vanadium and chromium based catalysts		
Knupfer	IFW Dresden, Dresden, Germany	X-ray absorption spectroscopy on layered cobaltates	other	
Knupfer	Leibniz-Institut für Festkörper- und Werkstoffforschung Dresden	Temperature dependence of the hole distribution in Sr14-xCaxCu24O41		
Knupfer	Leibniz-Institut für Festkörper- und Werkstoffforschung Dresden	Electronic Properties of electrochemically doped Li2-xCuO2		
Knupfer	Leibniz-Institut für Festkörper- und Werkstoffforschung Dresden	Electronic Structure of NaxCoO2 by means of x-ray absorption spectroscopy		
Knupfer / Aristov	IFW Dresden,/ Inst. of Solid State Physics RAS , Chernogolovka	Electronic properties of organic semiconductors and their interfaces		
Koch	Humboldt Universitaet zu Berlin	Photoemission experiments on pristine and oxygen-exposed pentacene	DFG	
Koch-Müller	Geoforschungszentrum Potsdam, Projektbereich 4.1	Location and quantification of OH in nominally anhydrous minerals	BMBF	
Köhler	Humboldt-Universität zu Berlin	Asymmetric Bragg reflection as magnifying optics	other	
Köhler	Humboldt Universität zu Berlin, Institut für Physik	X-ray image magnification by asymmetric Bragg reflection		
Konovalov	Uni Leipzig	Study of the band discontinuity and band bending at AgIn5S8 / CuI interface		
Kretlow	Robert-Koch-Institut	Infrared Microspectroscopy of CNS Tissue from Scrapie infected Syrian Hamsters		
Kuch	Max-Planck-Institut für Mikrostrukturphysik, Halle	Elementspezifische Abbildung magnetischer Domänen in gekoppelten magnetischen Dünnschichtsystemen	BMBF	05KS1EFA6
Kuch / Camarero	Freie Universität Berlin/Universidad Autónoma de Madrid	Element-resolved magnetic properties of epitaxial alloy films and multilayers	other	AI D/03/39337
Kuch / Vogel	Max-Planck-Institut für Mikrostrukturphysik, Halle/Laboratoire Louis Néel, CNRS Grenoble	Time and layer resolved magnetic imaging of spin-valve structures using PEEM	EU	R II 3 CT-2004-506008
Kuhnke	MPI für Festkörperforschung	Magnetism of FePt surface alloys on vicinal surfaces		
Lagomarsino	Istituto Fotonica e nanotecnologie, CNR, Roma, Italia	Study of paleopathology and paleodiet by means of microfluorescence and 3D micro XRS	EU	
Lammert	BESSY	Characterization of of focus and beam purity afte installation of an improved elliptical mirror and stray light shields		
Leach	Observatoire de Paris-Meudon	Photophysics of exobiological molecules		
Leitenberger	Universität potsdam	Simple X-ray interferometer	other	

Leitenberger	Uni-Potsdam	Application of X-Ray interferometry for beam characterisation and determination of mateial constants		
Lewerenz		Investigation of the surface chemistry of Si upon anodization in aqueous and alkaline solution by SRPES		
Ley	Friedrich-Alexander-Universität Erlangen-Nürnberg	Fermi Surface mapping by photoemission: The importance of indirect transitions	BMBF	# 05ES3XBA/5
Ley	Universität Erlangen-Nürnberg	Photelectron spectroscopy on SiC surfaces	other	
Ley	Universität Erlangen/Nürnburg	Photoelectron Diffraction using the Toroidal spectrometer	BMBF	05 ES3XBA/5
Ley	Uni Erlangen, Institut für Technische Physik	MCD stuies of Heusler alloys and chiral molecules		
Ley	Uni Erlangen, Institut für Technische Physik	Fermi surface of Ni2MnGa and CrV		
Ley	Uni Erlangen, Institut für Technische Physik	Elektronische und strukturelle Eigenschaften der Grenzflächen zwischen SiC und ALD-Dielektrika		
Lindsay	Institut de Ciència de Materials de Barcelona	Probing the structure of sulfur dioxide on TiO2 (110)		
Locht	Université de Liège	High resolution photoionization mass spectrometry of C2HXYZ and their isomers. Photoabsorption and Fluorescence spectroscopy of cyclic and heterocyclic organic compounds.	EU	RII -3CT-2004-506008
Locht	Université de Liège, Dtp. de Chimie	High resolution photoabsorption spectroscopy and photoionization of C2H2X (X=F, and/or Cl) and isomers) and the phtoionization of CH3X molecules (X=Br and I)	EU	
Luecke		Crystal structure determination of various eubacterial proteorhodopsins		
Luecke / Spudich	University of California	Crystal structure determination of Anabaena sp. sensory rhodopsin (ASR)		
Luecke / Spudich		Crystal structure determination of Anabaena sp. sensory rhodopsin associated transducer (ASRT)		
Luecke / Spudich		Crystal structure improvement of Sensory Rhodopsin II of Natronobacterium pharaonis (NpSRII)		
Lux-Steiner	Hahn-Meitner-Institut Berlin GmH	Synchrotron-Diagnostik zur Untersstützung der Material- und Technologie-Entwicklung von kostengünstigen Cu(In,Ga)(S,Se)2 Modulen	BMBF BMWi	01 SF0007 03 N8605/8

Lux-Steiner	Hahn-Meitner-Institut Berlin GmH	Röntgenemissions- und Photoelektronenspektroskopie an Dünnschichtslarzellen auf der Basis von Cu(In,Ga)(S,Se)2		
Lux-Steiner / Fischer	Hahn-Meitner-Institut Berlin	Synchrotron-Diagnostics to Support Material- and Technology-Development of Cost-Efficient Cu(In,Ga)(S,Se)2-Photovoltaic Modules	BMBF	01SF0007
Makhov / Kirm	Lebedev Physical Institute RAS, Moscow, /University of Hamburg	High-resolution, low-temperature pholoelectron spectroscopy of insulating crystals		
Maletta	Hahn-Meitner-Institut Berlin	Investigation of the MEXAFS method for thin films	BMBF	
Maletta	Hahn Meitner Institut Berlin	XMCD studies of magnetic nanoparticles prepared ex-situ by chemical synthesis	other	
Maletta	Hahn-Meitner-Institut Berlin GmH	In-situ investigation of the magnetization reversal of Fe on V(110)		
Maletta	Hahn-Meitner-Institut Berlin GmH	Test of the high-field reflectometer		
Maletta	Hahn-Meitner-Institut Berlin GmH	Exploration of the ((M)EXAFS method at the UE46-PGM		
Maletta	Hahn-Meitner-Institut Berlin GmH	XAS and XMCD studies on magnetic Co/CoO core/shell nanoparticles prepared in-situ		
Maletta / Schmitz	Hahn-Meitner-Institut Berlin	Determination of the magnetization depth profile of Fe on V(110) by combining X-Ray Magnetic Circular Dichroism with X-Ray Resonant Magnetic Scattering	other	
Manzke	Humboldt Universität ; Institut für Physik	Nano XAS at magnetic and superconducting Cuprates	other	
Manzke	Humboldt Universität Berlin ; Institut für Physik	XAS an Hochtemperatursupraleitern zur Bestimmung der Löcherdotierung in den CuO2-Ebenen von polykristallinen und einkristallinen Kupraten	other	
Manzke	Humboldt Universität zu Berlin, Institut für Physik / EES	Photoelektronenspektroskopie höchster Auflösung an kondensierter Materie mit Synchrotronstrahlung	BMBF	05 K51KH1/1
Manzke	Humboldt Universität zu Berlin, Institut für Physik / EES	Röntgen-Absorptionspektroskopie an Hochtemperatur-Supraleitern in Abhängigkeit von der Temperatur und der Löcherdotierung	BMBF	05 KS1KMA/0
Marmiroli	University of Parma	Characterisation of Arabodopsis thaliana tolerant towards high Cs concentrations: a schrotron light-based approach		
Martins	Universität Hamburg, II. Institut für Experimentalphysik	Correlation effects in atoms and schmall molecules		

Martins	Universität Hamburg	Charge transfer in free metal halides		
Maujean	Université P et M Curie	The hydrogen molecule: determination of the transition moments	EU	BI3A-05/170504
Meiwes-Broer / Bansmann	Universität Rostock	Magneto-optische Reflexions-Spektroskopie im EUV an in-situ präparierten ultradünnen Schichten und Clustern	BMBF	05KS4HRA2/4
Meyer	LURE, Centre Universitaire Paris-Sud	Symmetry and disscoiation dynamics of inner-shell excited molecules	EU	
Mikhlin	Institute of Chemistry and Chemical Technology, RAS, Krasnoyarsk	Synchrotron radiation photoemission spectroscopy of chemically modified surfaces of metal sulphides		
Molodtsov	TU Dresden	Electron correlation effects in YB and Eu compounds		
Molodtsov / Vyalikh / Pompe	Russian - German Laboratory at BESSY, TU Dresden	Magnetic oscillations in photoemission spectra of Cr/Fe(100) and Cr/W(100)		
Naumann	Robert-Koch-Institut Berlin, Projekt 13	Infrared microspectroscopy of CNS tissue from scrapie-infected Syrian hamsters		
Nazin	Kurchatov Institute, Moscow	UPS study of partly oxidated zirconium surface		
Neumann	Universität Osnabrück, Fachbereich Physik	Investigation of the orbital ordering of LaMnO3 by means of X-ray magnetic linear dichroism (XMLD)	BMBF	05 SR8OL1-2
Niehus	Humboldt Universität zu Berlin, Institut für Physik	High-pressure oxidation of the Ru (0001) surface at elevatd temperatures invetigated by in-situ XPS	EU	
Niehus	Humboldt Universität zu Berlin	Inter-atomic effects in resonant photoelectron spectra at the L23 edge in thin Vox films on Cu3Au(100)		
Nordlund	Stockholm University	Structural studies of the human mitochondrial deoxyribonucleotidase dNT-2		
Nordlund		Allosteric regulation and reaction mechanism in class II ribonucleotide reductase		
Nordlund		Structural studies of the human cytosolic deoxyribonucleotidase dNT-1		
Nordlund / Hallberg		Structural basis for eukaryotic and prokaryotic RNA-modification: pseudouridine synthases		
Ohm	Universitätsklinikum Charité, Med. Fakultät der HU Berlin, Inst. f. Anatomie	Lokalisation von Proteinablagerungen bei Morbus Alzheimer		
Okotrub / Mertins	Institute of Inorganic Chemistry Novosibirsk, /BESSY Berlin	Electronic state of carbons occurred in the carbonaceous chondrite meteorites		
Oubrie	University of East Anglia	Structure determination of ResA, a cytochrome c maturation factor of Bacillus subtilis		

Oubrie		Structural basis of substrate oxidation and specificity in a soluble glucose dehydrogenase		
Ovchinnikov	Inst. of Physics RAS , Krasnoyarsk	Crystal structure and photoinduced changes of magnetic properties of Fe/Si magnetic multilayers		
Ovchinnikov / Starke	Inst. of Physics RAS, Krasnoyarsk,/FU Berlin	The magnetic structure and magnetic properties of rare-earth ferroborates Gd1-xNdxFe3(BO3)4, GdFe3-xGax (BO3)4and ludwigites Cu2-xCoxGaBO5, Cu2-x Fe1-yVyGaxBO5 single crystals by magnetic X-ray scattering, XMLD and MEXAFS		
Paloura	Aristotle Univ. of Thessaloniki, Physics Dept., 54124 Thessaloniki, GREECE.	Study of glasses containing industrial wastes by μ-XRF and μ-XAFS	EU	BI3A - 16/280604
Paloura	Aristotle University of Thessaloniki, Dept of Physics	Micro-XAFS characterization of glasses containing industrial wastes	EU	
Panzner	Uni Potsdam , Strukturanalyse	Energy Dispersive Coherent X-Ray Reflectify	BMBF	
Panzner	Universität Potsdam, Institut für Physik	Static and dynamic speckles investigations with a polychromatic hard X-ray beam		
Pease	University of Conneticut	Employing doubly-curved focusing and monochromatizing HOPG optics for Non Resonant X-ray Raman Scattering in the hard x-ray range		
Peisert	IFW Dresden	Ladungsverteilung an Grenzflächen organischer Halbleitern	BMBF	01 BI163
Peisert / TChassé	Universität Tübingen, IPC, Auf der Morgenstelle 8, 72076 Tuebingen	Ladungsverteilung an Grenzflächen organischer Halbleiter	other	
Pernicka	Institut für Ur- und Frühgeschichte und Archäologie des Mittelalters, Universität Tübingen	Analysis of antique gold artifacts with synchrotron radiation	other	
Pernicka	TU Bergakademie Freiberg, Institut für Archäometrie	Analysis of archeological gold objects by SyXRF		
Pesin / Evsyukov / Milani / Heimann / Kavan	Pedagogical University Chelyabinsk,/ instrAction GmbH, Ludwigshafen, /Universita degli Studi di Milano, /Universität-Bergakademie Freiberg/Inst. of Physical Chemistry Prague	A comprehensive sludy of electron structure of carbynoids using synchrotron radiation		

Pettenkofer	Hahn-Meitner-Institut Berlin GmH, SE 6	Angle resolved photoemission spectroscopy (ARPES) on homoepitaxial prepared ZnO surfaces		
Pettenkofer	Hahn-Meitner-Institut Berlin GmH, SE 6	Angle resolved photoemission spectroscopy on chemically etched MBE rown CuInS2 films of different orientation		
Pettenkofer	Hahn-Meitner-Institut Berlin GmH	In-situ investigation of the aluminium induced layer exchange (ALILE) in amorphous silicon using photoelectron microscopy (PEEM)		
Pettenkofer	Hahn-Meitner-Institut Berlin GmH	Photoelectron emission microscopy (PEEM) on chemically etched epitaxial CuInS2 films of different orientation		
Piancastelli	Physics Dept, Uppsala University	Surface-induced circular dichroism in adsorbates	EU	BI3A-41/090804
Pietsch	Universität Potsdam, Institut für Physik	Inducing spin crossover in metallo-supramolecular polyelectrolytes through an amphiphilic phase transition		
Pietsch	Universität Potsdam	Spin coupling processes in thin metallo-supramolecular films		
Pietsch / Boenthin	Uni-Potsdam	Molecular magnetism on supramolecular assemblies	DFG	
Ploog	Paul-Drude-Institute, Berlin	Heteroepitaxie ferromagnetischer Materialien auf III-V Halbleiter für Spininjektion	BMBF	-20724
Ploog	Paul-Drude-Institute for solid state electronics	MBE von kristallinen Gate-Dielektrika und Grenzflächenengineering	BMBF	01 M 3142 B
Polcik	Fritz-Haber-Institut der Max-Planck-Gesellschaft	Photoelectron diffraction of adsorbed atoms, molecules and thin films		
Powis	University of Nottingham, School of Chemistry	Circular dichroism in the photoiionization of free chiral molecules	EU	
Pozdnyakov	Inst. Problems in Mechanical Engineering St. Petersburg	Studies of polyimide-fullerene [C60] films using X-ray photoelectron spectroscopy and near-edge X-ray-absorption fine structure		
Preobrajenski	MAX.LAB, Lund University	Nuclear motion and electron correlation in the core-excited NO3 and BO33 anions in the single-crystal nitrates and borates studied by resonant X-ray emission spectroscopy	EU	
Püttner	Freie Universität Berlin, Fachbereich Physik	Kanal- und winkelaufgelöste Messungen an den Doppelanregungszuständen in Helium	DFG	Pu 180/2-1
Rader	BESSY	Quantum stripes	DFG	RA1041/1-1
Rader	BESSY	Is the ferromagnetism of Ga1-xMnxN an artefact?	BMBF	05 KS1IPA/0
Rader	BESSY	Is the valence transition of Tm/Mo (110) an artefact?		

Rader	BESSY	Kondo effect for step decoration systems		
Rader	BESSY	Fermi surfaces of metal nanowires on stepped SiC		
Rader	BESSY	Spin resolved photoemission of Ga1-xMnxAs		
Ramsey	Institut für Physik, Karl-Franzens Universitaet Graz, Austria	Sexiphenyl and sexithiophene (hetero)structures on TiO2(110)	EU	BI3A-42/090804
Reiche	University of Potsdam	Phase transitions in shape-memory polymers	other	via Prof. U. Pietsch
Reiche	Laboratoire du C2RMF - UMR 171 CNRS	Spatially resolved SR-XRF analyses of drawings	other	D/0122896
Reiche	C2RMF-UMR 171 CNRS	Combined XRF and XANES measurements of drawings by Hans Holbein The Ancient	EU	
Reinert	Universität des Saarlandes	Abbildende Photoelektronenspektroskopie an hochkorrelierten Systemen		
Rettig	Humboldt Universität zu Berlin, Institut für Chemie	Time-resolved fluorescence of charge-transfer bichromophoric and of multichromophoric compounds		
Riesemeier	BAM	Synchrotron micro computed tomography, synchrotron refraction topography, X-ray fluoescence experiments at the 7T WLS		
Riley	La Trobe University	Mapping Disorder-Order Induced Changes To The Fermi Surface Of Cu3Au Using A New Toroidal Electron Energy Analyser	BMBF	05ES3XBA/5
Rüdiger	Universität Konstanz, Universitätsstr. 10, D-78457 Konstanz	Resonant Photoemission Study of Diluted Magnetic Semiconductor Ge1-xMnx	BMBF	
Rühl	Institut für Physikalische Chemie, Universität Würzburg	Experimentelle und theoretische Untersuchungen zur hochaufgelösten Anregung von Rumpfniveaus von Molekülen, Clustern und Adsorbaten	DFG	RU 420/5-1
Rühl	Universität Osnabrück, Fachbereich Physik	Projektverbund zum Aufbau und Test eines Messstandes zur Untersuchung gespeicherter Nanopartikel mit Synchrotronstrahlung: Untersuchung von flüssigen Partikeln mit weicher Röntgenstrahlung	BMBF	05 KSIMPA/8, 05 KSIOCI/2, 05 KSIBMA/0
Rühl	Universität Würzburg	Vibronische Kopplung in molekularen Clustern im Breich der Rumpfniveauanregung		
Rühl / Graf	Institut für Physikalische Chemie, Universität Würzburg	Struktur und Dynamik von strukturierten II-VI Halbleiter-Nanopartikeln in unterschiedlicher Umgebung	DFG	SFB 410-TP C8
Rühl / Meyer	Institut für Physikalische Chemie, Universität Würzburg	Rotations- und schwingungsaufgelöste Relaxation und Dynamik von element- und ortsselektiv angeregten Molekülen	other	DAAD-PROCOPE D/0333616
Saenger		MTH177		

Saenger / Alonso		Omega-DNA-complex		
Saenger / Athina		Crystallographic studies of Photosystem II and single subunits		
Saenger / Chames	FUB, Instit. für Kristallographie	HLA-A1:MAGE:Fab complex		
Saenger / Lanka		Structure studies on the inhibition of the hexameric DNA helicase RepA		
Saenger / Sandhoff		Human SA-proteins and their role in membrane lipid metabolism		
Saenger / Sandhoff		Structure and Mechanism of human beta-Hexosaminidase B		
Saenger / Uchanska-Ziegler		Peptide Presentation by Differentially Disease-Associated HLA-B27 Subtypes		
Saib	Schuit Institute of Catalysis, Eindhove University of Technology	In-situ NEXAFS und XPS measurements		
Sanyal	Saha Institute of Nuclear Physics, Surface physics division	Investigation of thermal properties of polymer films using dynamic energy dispersive X-ray reflectivity measurements		
Schade	BESSY	Synchrotron infrared microspectroscopic investigation on carbonaceouschondritic meteorites	other	
Scharnweber	Technische Universität Dresden, Max-Bergmann-Zentrum für Biomaterialien	Microtomography (µCT) for quantitative evaluation of the bone formation in the interface to an implantat and surrounding the implantat by stimulation of vascularization		
Schartner	1st Institute of Physics Giessen University	Radiative Decay of Doubly Excited Helium	DFG	scha 235/17-1
Schartner	Justus-Liebig-Universität, I. Physikalisches Institut	Cross sections and angular asymmetry parameter for radiation decay of doubly excited He	DFG	Scha 235/17-1
Schartner	Justus-Liebig-Universität, I. Physikalisches Institut	Partial wave analysis of interfering resonant (RA) transitions in the Raman regime with special emphasis of the contribution from direct processes	DFG	Scha 235/17-1
Schiller	Donostia International Physics Center	Wave-vector determination in thin Ag films, Low energy resonances in metallic quantum wells		
Schindler	Martin-Luther-Universität Halle-Wittenberg	Photoelectron Diffraction on Transition Metal Oxide Ultrathin Films	DFG	FG 404
Schmahl / Guttmann	Georg-August-Universität Göttingen, Institut für Röntgenphysik	Weiterentwicklung des röntgen-mikroskopischen Messplatzes am Undulator U41 am BESSY II und röntgenmikroskopische Experimente	BMBF	05 KS1MG1/9

Schmeißer	BTU Cottbus / LS Angewandte Physik II / Konrad-Wachsmann-Allee 17 / 03046 Cottbus	PEEM und Kelvin-AFM-Untersuchungen an dielektrischen Schichten für organische Feldeffekttransistoren	DFG	SCHM 745/8-1
Schmeißer	BTU Cottbus / LS Angewandte Physik II / Konrad-Wachsmann-Allee 17 / 03046 Cottbus	Pr – O – N - Schichten: Dielektrika für 4H-SiC Oberflächen	DFG	SCHM 745/9-1
Schmeißer	Brandenburgische Technische Universität Cottbus	Spektroskopische und mikroskopische Charakterisierung von Grenzflächen in O-FET-Schichtfolgen: Rauhigkeit, reaktivität und Potential-Verteilung		
Schmeißer	Brandenburgische Technische Universität Cottbus	Photoelektronen-spektroskopische Untersuchungen zur Pr2O3/Si(001)-Grenzfläche: Dielektrika für 4H-SiC Oberflächen		
Schmoranzer	TU Kaiserslautern	Nachweis von Dissoziationsprozessen molekularer N2-Rydberg-	DFG	Schm 379/11
Schneider	IFW Dresden, Institut f. Festkörper- u. Werkstoffforschung Dresdene.V.	Magnetooptical anisotropy at the 3d transition metal M edges	BMBF	05 KS1BD1/0
Schneider	IFW Dresden, Institut f. Festkörper- u. Werkstoffforschung Dresdene.V.	Magnetic domain structures and interdot coupling in submicron dot arrays	BMBF	05 KS1BDA/9
Schneider	IFW Dresden, Institut f. Festkörper- u. Werkstoffforschung Dresdene.V.	Soft X-ray magnetooptics with full polarization analysis	BMBF	05 KS1BD1/0
Schneider	IFW Dresden, Institut f. Festkörper- u. Werkstoffforschung Dresdene.V.	Spin-resolved photoemission studies of the valence band at the single crystalline interface MgO/Fe/GaAs(110)	BMBF	05 KS1BD1/0
Schneider / Guttmann	BESSY, IRP - Uni Göttingen	Hochauflösende Tomographie und Spektroskopie mit den Röntgenmikroskopen am Undulator U41 bei BESSY II	BMBF	05KS4BY1/7
Schoenes	Inst. f. Physik der Kondensierten Materie, TU Braunschweig	Photoemission investigation on Fe_(1-x)Co_(x)Si single crystals	BMBF	
Schoenes	IPKM TU Braunschweig	VUV-Ellipsometrie an Selten-Erd-Hydriden und magnetischen Materialien	BMBF	05 ES3XBA/5
Schoenes	TU Braunschweig, Institut für Halbleiterphysik und Optik	VUV-Ellipsometrie an -YHx(2.3<x<3)		
Schomburg	university of cologne	beta xylsosidase	BMBF	0221-4706452
Schomburg	Universität zu Köln, Institut für Biochemie, Zülpicher Str. 47, D-50674 Köln	Structure determination of ternary complexes of L-amino acid oxidase from Rhodococcus opacus	DFG	Scho245/12-1
Schomburg	Universität Köln	LAO MAD		

Schomburg		HNE		
Schomburg		Crystal Structure of Human Protein Kinase CK2 Catalytic Subunit		
Schondelmaier	BESSY	Determination of GBL content in SU-8 layers using FTIR microspectroscopy	other	
Schönhense	Johannes Gutenberg Univ., Institut für Physik, 55099 Mainz	Photoemissionsmikroskop für die zeitaufgelöste Beobachtung dynamischer Prozesse	BMBF	05 KS1 UM1/5
Schönhense / Felser	Johannes Gutenberg Universität´, Institut für Physik, 55099 Mainz	Materials with high spin polarization	DFG	Scho 341/6-1
Schönhense/ Schneider	Johannes-Gutenberg-Universität Mainz	Untersuchung neuer magnetischen Materialien mit hoher Orts-, Energie- und Zeitauflösung, Teilvorhaben:Spinanalytik und Delaylinedetektor		
Schuler	Universität Potsdam	Struckturelle Charakterisierung von Amyloiden Proteinkollaps und Sekundärstrukturbildung		
Schultz-Heienbrok	Freie Universität Berlin, AG Saenger	Domain rotation of E.coli 5'-nucleotidase		
Schulz	Paul-Drude-Institut	Molecular beam epitaxy growth studied by surface x-ray diffraction	other	
Schumacher	Hahn-Meitner-Institut Berlin	Lattice misfit in creep deformed superalloys	DFG	Schu 1254/3-4
Schumacher	Hahn-Meitner Institut	In-situ measurement of the evolution of lattice misfit in as-treated and highly creep deformed single crystal nickel base superalloy during exposure at high temperature	DFG	NE646/5-3
Schumacher	Hahn-Meitner Institut	The early stages of HE-bubble formation in titanium aluminium alloys: In-situ measurements by use of SAXS		
Schüßler-Langeheine	II. Physikalisches Institut, Universität zu Köln, Zülpicher Str. 77, 50937 Köln	Resonant soft x-ray diffraction from transition-metal oxides	DFG	SFB 608, TP C4
Schüßler-Langeheine	Universität Köln, II. Physikalisches Institut	Resonant soft X-ray scattering from transition-metal compounds	DFG	SFB 608TPC4
Schüßler-Langeheine	Universität Köln	Resonant soft X-ray scattering on epitaxial Fe3O4 thin films		
Schwentner	Freie Universität Berlin, Institut für Experimentalphysik	Hochaufgelöste Fluoreszenzspektroskopie an Molekülen in Matrizen		
Seckler	Universität Potsdam	Charakterisierung des Messplatzes für Circular-dichroismus Spektroskopie von Proteinen bei BESSY II, Erweiterung des Messbereichs bis 120 nm, und Ausbau der Messeinrichtungen für hohe Zeitauflösung	BMBF	KS1IP1/1 and /2

Seckler	Universität Potsdam, Physikalische Biochemie	Untersuchungen von Proteinen mittels Synchrotron Circular Dichroismus Spektroskopie (SRCD)	BMBF	05 KS1IP1/1
Senf	BESSY	Alignment characterisation and calibration of PGM2 after repair of plane mirror mechanism		
Senf	BESSY	Exchange of the grating vessel and commissioning of PGM2 at UE56/2		
Shabanova	Physical-Technical Inst. RAS, Izhevsk	The study of the electronic structure of compound copper oxides		
Shabanova	Physical-Technical Inst. RAS, Izhevsk	The study of electronic structure and magnetic properties of Invar alloys based on transitional metals		
Sheldrick	Universität Göttingen	Sulfatases and Sulfonatases		
Sheldrick		Proteins in sulfur metabolism		
Sheldrick		Crystal structure of Wind - a PDI related protein		
Sheldrick		Structure of complexes between Echinomycin and DNAs.		
Sheldrick		Structure of polyalanyl PNAs and chemical derivates.		
Sheldrick		Structures of d,l-alternating peptides		
Shikin / Gudat	State University St.-Petersburg,/BESSY Berlin	Electronic structure and catalytic activity of Au, Ag - low - dimensional nanoconstructions (nanoclusters) on stepped surface of oxygenated		
Sivkov	Syktyvkar state university	Absolute oscillator strength measurements for electron transitions in N1s absorption spectra of solid LiNO3 and NaNO3	other	
Skinner	University of South Australia, Ian Wark Research Institute	Surface and bulk electronic structure of base-metal sulphide minerals: structure-reactivity relationships		
Soriano	Universidad Autónoma Madrid	Electronic Structure of oxide nanostructures	EU	BI3A-10/140604
Soriano	Dep. Física Aöocada C-XII	Study of the electronic structure of shall particles and ultra-thin-films of metal oxides, nitrides and carbides: The NiO/HOPG system	EU	
Soriano	Universidad Autónoma de Madrid	Electronic structure of oxide nanostructures: The NiO/SiO2 interface		
Stalder	GZG Universität Göttingen	Hydrogen mobility in orthopyroxene	BMBF	05 ES3XBA/5
Stalder	Uni Göttingen	H-Diffusion in Orthopyroxen		
Stamm	Institut für Polymerforschung Dresden, Hohe Straße 6, 01069 Dresden, Germany	Optimization and characterization of polymeric nanotemplates	BMBF	05KS1BPA/4
Stamm	Institut für Polymerforschung DD	Nanotemplates from supramolecular block copolymer assemblies		

Starke	FU Berlin	Employing Soft X-Ray Magnetometry to Understand Temperature Driven Reversal of Exchange Coupling		
Starke	Freie Universität Berlin, Institut für Exp.-Physik	Looking quantitatively at magnetization reversal	BMBF	05-KS1 KEC/2
Starke	Freie Universität Berlin, Institut für Exp.-Physik	Spin structure of Gd- and Eu-oxide/metal interfaces	BMBF	05-KS1 KEC/2
Steinrück	Universität Erlangen-Nürnberg, Institut für Physikal. und Theoret. Chemie Physikalische Chemie II	Höchstaufgelöste Photoelektronenspektroskopie mit Synchrotronstrahlung zur in-situ Untersuchung von Oberflächenreaktionen	DFG	STE 620/4-1
Steinrück / Denecke	Lehrstuhl für Physikalische Chemie II, Universität Erlangen-Nürnberg	Höchstaufgelöste Photoelektronenspektroskopie mit Synchrotronstrahlung zur in-situ Untersuchung von Oberflächenreaktionen	DFG	Ste 620/4-2
Surkova / Neumann	Inst. of Metal Physics RAS Yekaterinburg, /University of Osnabrück	3d impurities in wide-gap II- VI semiconductors		
Szargan	Wilhelm-Ostwald-Institut, Universität Leipzig	Instrumentierung zur Röntgenemissionspektroskopie an modifizierten Festkörperoberflächen, Halbleitergrenzflächen und korrelierten Materialien	BMBF	05KS1OL1/3
Szargan	Universität Leipzig, Wilhelm-Oswald-Institut f. Physik. U. Theor. Chemie	Übergangschalkogenid-Dünnschichten und -Heterostrukturen	BMBF DFG	05 KS10L1/3 Sz 58/15-1
Szargan	Universität Leipzig, Wilhelm-Oswald-Institut f. Physik. U. Theor. Chemie	Orientierungsabhängige Röntgenfluoreszenzuntersuchungen an leitfähigen Polymeren	BMBF BMBF	03 WKI 10 05 KS10L1/3
Szargan	Universität Leipzig	Elektronenstruktur photochromer Verbindungen		
Teschner	Fritz-Haber-Institut der Max-Planck-Gesellschaft, Faradayweg 4-6, 14195 Berlin, Germany	Athena: Selective hydrogenation studied by in-situ XPS and XAS	other	
Thißen / Jaegermann	FB Materialwissenschaften, TU Darmstadt	Electronic structure of ion conducting oxides	DFG	SFB595
Tinkham	Naval Research Laboratory, Code 6876	Surface X-ray diffraction study of GaSb(001) epitaxial growth		
Titov	Inst. of Metal Physics RAS Yekaterinburg	ARPES – Study of electronic structure of titanium ditelluride intercalated with transition metals		
Trapeznikov	Physical-Technical Inst. RAS, Izhevsk	The peculiarities of the structure of zirconia-based nanoceramics		
Treimer	University of Applied Sciences (TFH) Berlin	Investigations of mamma biopsies by means of µ-tomography	BMBF	03TRE6B9
Treimer	FBII, Mathematics, Physics and Chemistry	Investigation of cancerous mamma biopsies by means of µ-tomography		
Troyanov / Slodorov	Humboldt Universität Berlin	Structural Chemistry of Fullerenes and their Derivatives		

Ulm	Physikalisch-Technische Bundesanstalt, Abbestr. 2-12, 10587 Berlin	Radiometrielabor der PTB	other	
Umbach	Experimentelle Physik II, Universität Würzburg	X-ray Spectroscopic Investigations of Materials for Organic Electronics	DFG	Um 6/8-1+-2, BMBF 05KS4WWC/2
Umbach	Universität Würzburg, Exp. Physik II	Höchstaufgelöste Elektronenspektroskopie mit dem fehlerkorrigierten SMART-Spektromikroskop		
Umbach	Universität Würzburg	NEXAFS Investigations of Organic Materials for Field Effect Transistors		
Umbach	Universität Würzburg	Höchstauflösende Gasphasen-NEXAFS-Messungen an großen organischen Molekülen		
Umbach	Universität Würzburg	Charakterisierung der elektronischen Struktur von organischen und biologischen Materialien mit resonanter inelastischer Röntgenstreuung		
Unger	Bundesanstalt für Materialforschung und -prüfung (BAM)	Untersuchung dünner, im Pulsplasma hergestellter Polymer· und Blockcopolymerfilme mit der Röntgenabsorptionsspektroskopie (NEXAFS)		
Unger	Bundesanstalt für Materialforschung und -prüfung (BAM)	Charakterisierung neuartiger Kohlenstoffschichten mit der Röntgenabsorptionsspektroskopie (NEXAFS) unter Berücksichtigung der Anforderungen industrieller QM Systeme	DFG	M1QN03114600
Varykhalov	BESSY	Electron structure and magnetism of Fe and Co nanowires on carbon-passivated (W110)		
Varykhalov	BESSY	Electron structureof self-assembled nonowires on carbon-passivated vicinal W surfaces		
Vinogradov	V.A. Fock Institute of Physics, St. Petersburg State University	High-resolution x-ray absorption and resonant photoemission in the transition metal acetylacetonates	other	
Vinogradov	V.A. Fock Institute of Physics, St. Petersburg State University	The comparative study of nickel acetylacetonate Ni(acac)2 and phthalocyanine NiPc with high-resolution x-ray absorption and resonant photoemission	other	
Vladimirov / Toennies	State University St. Petersburg/, MPI für Strömungsforschung Göttingen	Superlattice valence band umklapp at stepped W (110) and W (100)		
Walter	BESSY AZM	A Microfluidic System of a New Biosensor Chip for Measuring Antioxidative Capacity of Anti-Aging Products	BMBF	

Wanderka	HMI	In-situ Messung der Kristallisation metallischer Massivgläser		
Wende	Freie Universität Berlin	Neue Methoden zur Bestimmung magnetischer und elektronischer Grundzustandseigenschaften mit der Röntgenabsorptionsspektroskopie	BMBF	05 KS4KEB/5
Wende	Freie Universität Berlin, Fachbereich Physik	Spin-fluctuations in 2D ultrathin ferromagnets	BMBF	05 KS1 KEB4
Wende	Freie Universität Berlin	Oxygen polarisation and magnetic surface anisotropy of surfactant-grown ultrathin 3d ferromagnets		
Weschke	Freie Universität Berlin, Institut für Experimentalphysik	Resonant scattering in the ultrasoft X-ray region	BMBF	
Weschke	Freie Universität Berlin, Institut für Experimentalphysik	Resonant scattering in thesoft X-ray scattering from complex magnetic structures in thin films	BMBF	
Weschke	Freie Universität Berlin	Electronic structure of ultrathin NiO films		
Weschke	Freie Universität Berlin	Magnetic correlation in Co/Pt nanodot arrays		
Weschke	Freie Universität Berlin	Magnetic order in quasicrystals		
Widdra	Max-Born-Institut für Nichtlineare Optik und Kurzzeitspektroskopie	Pump-Probe Untersuchungen zur Dynamik an Halbleiteradsorbat- und Oberflächenzuständen		
Wilke	Institut für Geowissenschaften, Uni Potsdam	Corrosion of Cu on the surface of historic objects	other	
Winkler / Kirschner	Max-Planck-Institut f. Mikrostrukturphysik, Weinberg 2, D-06120 Halle	Two Electron Photoemission from Surfaces	BMBF	
Winter	Max-Born-Institut	Photoelectron Spectroscopy at Liquid Surfaces	other	
Winter	Max-Born-Institut für Nichtlineare Optik und Kurzzeitspektroskopie im Forschun gsverbund Berlin e.V.	Electronic structure of organic thin films		
Wöll	Ruhr-Universität Bochum, NL 5, Lehrstuhl für Phys. Chemie I	Investigation of the electronic structure of ZSM-5 type Zeolites by means of X-ray emission spectroscopy (XES)		
Wöll	Ruhr-Universität Bochum, NL 5, Lehrstuhl für Phys. Chemie I	Mikroskopische Mechanismen der Abscheidung von Palladiumschichten mittels CVD-Verfahren	DFG	WO(19-1)
Wollgarten	HMI	In-situ crystallisation measurement of Al-based metallic glasses (Al87Ni6La7 and Al87Ni5La7X1 (X=Ag or Zr))		
Woodruff	University of Warwick	Circular dichroism in core level photoemission from an adsorbed chiral molecule	EU	

Woodruff	University of Warwick	Structure determination of formic acid reaction products on TiO2(110)	EU	
Woodruff	University of Warwick, Physics Department Surface Science Group	Scanned-energy mode photoelectron diffraction at BESSY II	EU	
Wurth	Institut für Experimentalphysik Universität Hamburg	Interfaces of semiconductor systems studied by resonant inelastic X-ray scattering and NEXAFS: Molecular adsorption on Si-Surfaces, Interfaces of III-V semiconductor nanoclusters	DFG	SFB 508 Projekt C7 (Fo343/1-1)
Wurth	Universität Hamburg, 2. Institut für Experimentalphysik	Magnetic properties of small, size-selected, deposited transition metal clusters	BMBF	KS1-GUB/5
Wurth	Universität Hamburg	Spin polarized charge transfer processes and core-hole clock spectroscopy		
Wurth	Universität Hamburg	Magnetische Eigenschaften chemisch präparierter CoPT3-Nanokristalle		
Yashina / Püttner	State University Moscow, /FU Berlin	The behaviour of H2S molecules at PbS (100) fresh and oxidised surfaces		
Yubero	Instituto de Ciencia de Materiales	Resonant Ti LM23 V Auger emission and resonant photoemission of Ti4+ ions with tetrahedral coordination in Si-Ti oxide systems	EU	
Yulin	Fraunhofer IOF	High reflective Sc-based multilayer coatings for the EUV/sof X-ray range		
Yurii	Ioffe Institute of Russian Academy of Sciences	Magic Numbers in Electron Structure of Silver Supported Clusters	BMBF	
Yurii	Ioffe Institute of Russian Academy of Sciences	Fullerite Modification by Synchrotron Radiation	other	
Zabel / Nefedov	Ruhr-Universität Bochum	XMCD and XRMS studies from laterally ordered magnetic systems	BMBF	03ZAE8BO
Zahn	Technische Universität Chemnitz	VUV-Spectroscopic Ellipsometry on Organic Superlattices	BMBF	05 KS4KTB/3
Zahn	Technische Universität Chemnitz, Institut für Physik	Organisch modifizierte Metall/Halbleiterkontakte	BMBF	05 KS10CA/1
Zahn	Technische Universität Chemnitz, Institut für Physik	Vacuum ultraviolet spectroscopic ellipsometry investigations of DNA bases layers on seminconductor surfaces		
Zahn	Technische Universität Chemnitz	VUV-XUX Spectroscopy Ellipsometry Investigations of Organic Films on CaF2/Si(111) heterostructures		
Zahn	Technische Universität Chemnitz	Organisch modifizierte Metall/Halbleiterkontakte		
Zemlianov	University of Limerick	In situ XPS investigation of the palladium oxidation		

Zemlianov	Materials and Surface Science Institute and Physics Department, University of Limerick, Limerick, Ireland	Palladium oxidation	EU	BI3A-45/201204
Zharnikov / Grunze	Universität Heidelberg	Röntgenspektroskopie an organischen Grenzflächen und Biomaterialien in Kontakt mit Lösungen	BMBF	05KS4VHA/4
Zimina	BESSY	Electronic Structure of Si Nanoparticles in SiO2 Matrices studied by soft x-ray fluorescence spectroscopy	BMBF	
Zimina	BESSY	Chemical bonding effects in soft X-ray spectra of Sc compounds	other	
Zimina	BESSY	Electronic structure if Si nanoccrystals in SiO2 Matrices		
Zimmermann	TU-Berlin	Photoelectron and Photoion spectroscopy of two-and three-atomic molecules	DFG	Zi 183/16
Zimmermann	Technische Universität Berlin,	Hochauflösende Elektronenspektro-skopie an freien Atomen der 3d-Übergangsmetalle	DFG	Zi 183/16-3
Zizak	Hahn-Meitner-Institut Berlin GmH	Texture modifications in polycrystalline Ti layers on Si by irradition with swift heavy ions		

List of Publications 2004

M. Abo-Bakr, M. Hartrott, J. Knobloch, B. Kuske and A. Meseck
Start-To-End Injector and Linac Tolerance Studies for the BESSY FEL
FEL Conference, Trieste, Italy, (2004)

A. L. Ankudinov, J. J. Rehr, H. Wende, A. Scherz and K. Baberschke
Spin-dependent sum rules for x-ray absorption spectra
Europhysic Letters, **66**, 441, (2004)

K. Baberschke
The magnetism of ultrathin trilayers: A playground to study fundamentals
Journal of Magnetism and Magnetic Materials, **1130**, 272-276, (2004)

J. Bahrdt, W. Frentrup, A. Gaupp, B. Kuske, A. Meseck and M. Scheer
Undulators for the BESSY Soft X-Ray FEL
International FEL Conference, Trieste, Italy, (2004)

J. Bahrdt, W. Frentrupp, A. Gaupp, M. Scheer and U. Englisch
Magnetic Field Optimization of Permanent Magnet Undulators for Arbitrary Polarization
Nuclear Instruments and Methods A, **516**, 575-585, (2004)

K. Balewski, G. A. Blair, S. T. Boogert, G. Boorman, J. Carter, T. Kamps, T. Lefevre, H. Lewin, F. Poirier, S. Schreiber and K. Wittenburg
Beam profile measurements at PETRA with the laserwire compton scattering monitor
European Particle Accelerator Conference, Lucerne, Switzerland, (2004)

M. Bambynek, G. Hilgers and M. Krumrey
Bestimmung der räumlichen Varianten des Ansprechvermögens von Plastikszintillator-Detektoren
Medizinische Physik, **109**, (2004)

M. Bär, U. Bloeck, H.-J. Muffler, M. C. Lux-Steiner, C.-H. Fischer, M. Giersig, T. P. Niesen and F. Karg
Cd^{2+}/NH_3-treatment of $Cu(In,Ga)(S,Se)_2$: Impact on the properties of deposited ILGAR-ZnO layers and on the parameters of resulting solar cells
Journal of Applied Physics, **97**, 1490454, (2005)

M. Bär, H.-J. Muffler, M. C. Lux-Steiner, C.-H. Fischer, L. Weinhardt, C. Heske, E. Umbach, T. P. Niesen and F. Karg
Chemical Processes During Cd^{2+}/NH_3-Tretament of $Cu(In,Ga)(S,Se)_2$-Absorbers
Technical digest of the 14th International Photovoltaic Science and Engineering Conference, Chulalongkorn University, Bangkok, Thailand, 521-522, (2004)

M. Bär, M. Rusu, J. Reiß, T. Glatzel, S. Sadewasser, W. Bohne, E. Strub, H. J. Muffler, S. Lindner, J. Röhrich, T. P. Niesen, F. Karg, M. C. Lux-Steiner and C. H. Fischer
Insights into the Degradation Mechanisms of CIGSSe Devices based on different Heterojunctions
3rd World Conference on Photovoltaic Energy Conversion, Arisumi Printing Inc, Osaka, Japan, 335-9, (2003)

M. Bär, L. Weinhardt, C. Heske, H.-J. Muffler, M. C. Lux-Steiner, E. Umbach and C.-H. Fischer
Cd^{2+}/NH_3-treatment of $Cu(In,Ga)(S,Se)_2$ thin film solar cell absorbers - a model for the performance-enhancing processes in the partial electrolyte
Progress in Photovoltaics: Research and Applications, (to be published)

M. Bär, L. Weinhardt, C. Heske, H.-J. Muffler, E. Umbach, M. C. Lux-Steiner, T. P. Niesen, F. Karg and C.-H. Fischer
Chemical Insights into the Cd^{2+}/NH_3-Tretament - an Approach to Explain the Formation of Cd-Compounds on $Cu(In,Ga)(S,Se)_2$-Absorbers
Solar Energy and Materials and Solar Cells, (to be published)

J. Bartoll, S. Röhrs, A. Erko, A. Firsov, A. Bjeoumikhov and N. Langhoff
Micro-X-Ray absorption near edge structure spectroscopy investigations of baroque tin-amalgam mirrors at BESSY using a capillary focusing system
Spectrochimica Acta A, **Part B 59**, 1587-1592, (2004)

R. Bayon, R. Musembi, A. Belaidi, M. Bär, T. Guminskaya, M.-C. Lux-Steiner and T. Dittrich
Highly structured TiO_2 / $In(OH)_XS_Y$ / PbS / PEDOT:PSS for photovoltaic applications
Solar Energy Materials and Solar Cells, (to be published)

S. Bechstein, B. Beckhoff, R. Fliegauf, J. Weser and G. Ulm
Characterization of an Nb/Al/AlOx/Al/Nb superconducting tunnel junction detector
Spectrochimica Acta Part B: Atomic Spectroscopy, **221**, (2004)

G. Beernink, T. Strunskus, G. Witte and C. Wöll
The importance of dewetting in organic molecular beam deposition: pentacene on gold
Applies Physics Letters, **85** (3), 398-400, (2004)

S. Bengió, H. Ascolani, N. Franco, J. Avila, M. C. Asensio, A. M. Bradshaw and D. P. Woodruff
Local structure determination of NH_2 on Si(111)(7x7)
Physical Review B, **69**, 125340-1-9, (2004)

M. Bernien
Spinfluktuationen in gekoppelten magnetischen Schichten: eine temperaturabhängige Röntgenzirkulardichroismus-Studie, Diploma Thesis
Freie Universität Berlin, (2004)

R. Bienert, M. Zeeb, L. Dostál, A. Feske, C. Magg, K. Max, H. Welfle, J. Balbach and U. Heinemann
Single-stranded DNA bound to bacterial cold-shock proteins: Preliminary crystallographic and Raman analysis
Acta Crystallographica D, **60**, 755-757, (2004)

S. Biermann, A. Dallmeyer, C. Carbone, W. Eberhardt, C. Pampuch, O. Rader, M. I. Katsnelson and A. I. Lichtenstein
Observation of Hubbard bands in gamma-manganese
JETP Letters, **80**, 612, (2004)

I. Biswas
Charakterisierung von Phthalocyaninen mit temperaturprogrammierter Desorption und spektroskopischen Methoden, Doctoral Thesis
Universität Tübingen, (2004)

H. Bluhm, M. Hävecker, E. Kleimenov, A. Knop-Gericke, A. Liskowski, R. Schlögl and D. S. Su
In Situ Surface Analysis in Selective Oxidation Catalysis: n-Butane Conversion Over VPP
Topics in Catalysis, **23** (1-4), 99-107, (2003)

H. Bluhm, M. Hävecker, A. Knop-Gericke, D. Teschner, E. Kleimenov, V. I. Bukhtiyarov, D. F. Ogletree, M. Salmeron and R. Schlögl
Methanol Oxidation on a Copper Catalyst Investigated Using in Situ X-ray Photoelectron Spectroscopy
Journal of Physical Chemistry B, **108** (38), 14340-14347, (2004)

R. I. R. Blyth, J. Thomson, V. Arima, Y. Zou, R. Fink, E. Umbach, G. Gigli and R. Cingolani
Occupied and Unoccupied States of the Organic Infra-red Emitters Yb- and Er-tris(8-hydroxyquinoline) Studied by Photoemission and X-ray Absorption
Synthetic Metals, **142**, 293, (2004)

A. Borgna, B. G. Anderson, A. M. Saib, H. Bluhm, M. Hävecker, A. Knop-Gericke, E. T. Kuiper, Y. Tamminga and J. W. Niemantsverdriet
Pt-Co/SiO_2 Bimetallic Planar Model Catalysts for Selective Hydrogenation of Crotonaldehyde
Journal of Physical Chemistry B, **108** (46), 17905-17914, (2004)

W. Braun, V. M. Kaganer, B. Jenichen and K. H. Ploog
Non-Ostwald coarsening of the GaAs(001) surface
Physical Review B, **69**, 165405, (2004)

W. Chen, N. Darowski, I. Zizak, G. Schumacher, H. Klingelhöffer, N. Wanderka and W. Neumann
Measurement of Gamma/Gamma-Prime Lattice Mismatch in Creep Deformed Single Crystal Superalloy SC16 Using Synchrotron X-Radiation
Materials Science Forum, **426-432**, 4555-4560, (2003)

L. Chkoda, M. Schneider, V. Shklover, L. Kilian, C. Heske, E. Umbach and M. Sokolowski
Temperature-dependent morphology and structure of ordered 3,4,9,10-perylene-tetracarboxylic-dianhydride (PTCDA) thin films on Ag(111)
Chemical Physics Letters, **371**, 548, (2003)

N. Darowski, I. Zizak, G. Schumacher, H. Klingelhöffer, W. Chen and W. Neumann
Temperature Dependence of FWHM of Gamma Prime Phase in Creep-deformed Single Crystal Superalloy SC16
7 th Biennial Conference on High Resolution X-Ray Diffraction and Imaging, Pruhonice, Czechia, (2004)

J. E. Davies, O. Hellwig, E. E. Fullerton, G. Denbeaux, J. B. Kortright and K. Liu
Magnetization Reversal of Co/Pt Multilayers: Linking Macroscopic and Microscopic Level
Physical Review B, **70**, 224434, (2004)

T. Deniozou, N. Esser, S. Siebentritt, P. Vogt and R. Hunger
Surface structure of CuGaSe2 (001)
Thin Solid Films, (2004)

F. Diekmann, S. Diekmann, K. Richter, U. Bick, T. Fischer, R. Lawaczeck, W. R. Press and K. Schön
Near monochromatic X-rays for digital slot-scan mammography: initial findings
European Journal of Radiology, **14**, 1641-1646, (2004)

E. P. Domashevskaya, V. A. Terekhov, V. M. Kashkarov, E. Y. Manukovskii, S. Y. Turishchev, S. L. Molodtsov, D. V. Vyalikh, A. F. Khokhlov, A. I. Mashin, V. G. Shengurov, S. P. Svetlov and V. Y. Chalkov
Synchrotron investigations of the specific features in the electron energy spectrum of silicon nanostructures
Physics of the Solid State, **46** (2), 345-350, (2004)

A. Ehresmann, S. Klumpp, L. Werner, H. Schmoranzer, S. Kammer, S. Mickat, K.-H. Schartner, I. D. Petrov, P. V. Demekhin and S. V. L.
Observation and identification of doubly excited KrI $4s^2 4p^4 5s^n$ Rydberg series
Journal of Physics B: Atomic, Molecular and Optical Physics, **37**, L251-7, (2004)

A. Ehresmann, H. Liebel, H. Schmoranzer, O. Wilhelmi, B. Zimmermann and K.-H. Schartner
VUV-fluorescence spectroscopy of O_2 photodissociation into neutral excited fragments between 17 and 19 eV
Journal of Physics B: Atomic, Molecular and Optical Physics, **37**, 389-401, (2004)

A. Ehresmann, L. Werner, S. Klumpp, H. Schmoranzer, P. V. Demekhin, B. M. Lagutin, V. L. Sukhorukov, S. Mickat, S. Kammer, B. Zimmermann and K.-H. Schartner
De-excitation dynamics of Rydberg states in O2: II. Vibrational and rotational structure of $2\Pi_u^{-1}(c^4\Pi_u^-)(ns/nd)\Pi_g^3\Pi_u^-(v = 0, 1)$ states
Journal of Physics B: Atomic, Molecular and Optical Physics, **37**, 4406-22, (2004)

S. Eisebitt, M. Lörgen, W. Eberhardt, J. Lüning, S. Andrews and J. Stöhr
Scalable approach for lensless imaging at x-ray wavelengths
Applied Physics Letters, **84**, 3373, (2004)

S. Eisebitt, J. Lüning, W. F. Schlotter, M. Lörgen, O. Hellwig, W. Eberhardt and J. Stöhr
Lensless Imaging of Magnetic Nanostructures by X-ray Spectro-Holography
Nature, **432**, 885, (2004)

D. Engel, H. Schmoranzer, A. Ehresmann, H. C. Mertins, D. Abramsohn and W. Gudat
Soft X-ray resonant magnetic reflection investigations of FeMn/Co/Cu/Co spin valves modified by He ion bombardment
Physica B: Physics of Condensed Matter, **185**, 345, (2004)

z. Erdélyi, M. Sladecek, L.-M. Stadler, I. Zizak, G. A. Langer, M. Kis-Varga, D. L. Beke and B. Sepiol
Transient interface sharpening in miscible alloys
Science, **306**, 1913, (2004)

A. Erko, F. Schaefers and N. Artemiev
A ray-tracing code for zone plates Advances
Proc. SPIE, **5536**, 61-70, (2004)

A. Erko, F. Schäfers, A. Firsov, W. B. Peatman, W. Eberhardt and R. Signorado
The BESSY X-Ray Microfocus Beamline project
Spectrochimica Acta A, **Part B 59**, 1543-1548, (2004)

A. I. Erko and A. Firsov
Investigation of the properties of Bragg-Fresnel gratings
Proc. SPIE, **5539**, 148-159, (2004)

A. Faust
Die Struktur der L-Aminosäure-Oxidase aus Rhodococcus opacus in verschiedenen funktionellen Zuständen, Doctoral Thesis
University of Cologne, (2004)

P. Feulner, T. Niedermayer, K. Eberle, R. Schneider, D. Menzel, A. Baumer, E. Schmich, A. Shaporenko, Y. Tai and M. Zharnikov
Strong temperature dependence of irradiation effects in organic layers
Physical Review Letters, **93**, 178302, (2004)

M. O. Figueiredo and J. P. Mirão
Soft X-ray absorption at the O K-edge in rutile-type natural oxides
Synchrotron Radiation in Materials Science, Grenoble/France, 94, (2004)

A. Firsov, A. I. Erko and A. Svintsov
Design and fabrication of the diffractive x-ray optics at BESSY
Proc. SPIE, **5539**, 160-164, (2004)

C.-H. Fischer, M. Bär, T. Glatzel, I. Lauermann and M. C. Lux-Steiner
Interface Engineering in Chalcopyrite Thin Film Solar Devices
Solar Energy and Materials and Solar Cells, (2004)

R. Flesch, N. Kosugi, I. Bradeanu, J. J. Neville and E. Rühl
Cluster Size Effects in Core Excitations of N 1s-Excited Nitrogen
Journal of Chemical Physics, **70**, 8343, (2004)

R. Flesch and E. Rühl
Mechanism of Anion Formation in C 1s --> pi-Excited Carbon Dioxide*
Journal of Chemical Physics, **121**, 5322, (2004)

M. Freiwald, S. Cramm, W. Eberhardt and S. Eisebitt
Soft X-ray absorption spectroscopy in liquid environments
Journal of Electron Spectroscopy and Related Phenomena, **137-140**, 413, (2004)

J. Friedrich, G. Kühn, R. Mix, I. Retzko, V. Gerstung, S. Weidner, R. D. Schulze and W. Unger
Plasma Polymer Adhesion Promoters to be used for Metal-Polymer Composites
Polyimides and other High Temperature Polymers: Synthesis, Characterization and Applications, 359-388, (2003)

J. Friedrich, G. Kühn, R. Mix and W. Unger
Formation of plasmapolymer layers with functional groups of different type and density at polymer surfaces and their interaction to Al atoms
Polymer Processing and Plasmas, **1** (1), 28-50, (2004)

J. Friedrich, R. Mix, G. Kühn, I. Retzko, A. Schönhals and W. Unger
Plasma-based introduction of monosort functional groups of different type and density onto polymer surfaces. Part 1: Pulsed plasma polymerization
Composite Interfaces, **10** (2-3), 173-223, (2003)

J. Friedrich, W. Unger, A. Lippitz, I. Koprinarov, A. Ghode, G. Sh and G. Kühn
Plasma-based introduction of monosort functional groups of different type and density onto polymer surfaces. Part 1: Behaviour of polymers exposed to oxygen plasma
Composite Interfaces, **10** (2-3), 139-171, (2003)

T. Fuhrmann, M. Kinne, C. M. Whelan, J. F. Zhu, R. Denecke and H. P. Steinrück
Vibrationally resolved in situ XPS study of activated adsorption of methane on Pt(111)
Chemical Physics Letters, **390** (1-3), 208-213, (2004)

V. R. Galakhov, D. G. Kellerman, S. N. Shamin, N. A. Ovechkuna, V. S. Gaviko, V. E. Dolgikh, L. V. Elokhina, A. V. Korolyov, N. A. Skorikov and A. S. Shkvarin
X-ray spectrosopy determination of electronic-hole localization in deped and defect oxides of 3d transition elements
Regional Competition of the Russian Foundation of Basic Research "Ural", Sverdlovsk Region, (2005)

V. R. Galakhov, N. A. Ovechkina, A. S. Shkvarin, S. N. Shamin, E. Z. Kurmaev, K. Kuepper, A. F. Takacs, M. Raekers, S. Robin, M. Neumann, G.-N. Gavrila, A. S. Semenova, D. G. Kellerman, T. Kaambre and J. Nordgren
Electronic structure and x-ray spectra of defect oxides Li_xCoO_2
Physical Review B, (to be published)

M. Getzlaff, A. Kleibert, R. P. Methling, J. Bansmann and K. H. Meiwes-Broer
Mass-filtered ferromagnetic alloy clusters on surfaces
Surface Science, **566-568**, 332, (2004)

S. Girol, T. Strunskus and C. Wöll
The reactivity of ZnO-surface towards maleic anhydride
Journal of Physical Chemistry B, **108** (36), 13736-13745, (2004)

M. Glass-Maujean, S. Klumpp, L. Werner, A. Ehresmann and H. Schmoranzer
Photodissociation of doubly excited states of H_2 into H(2s) and H(2p) fragments
Journal of Physics B, **37**, 2677 - 2684, (2004)

E. Goering, S. Gold and A. Bayer
Ground-State-Moment-Analysis: A quantitative tool for X-ray magnetic circular dichroism analysis for 3d transition metals
Applied Physics A: Materials Science & Processing, **78** (6), 855-865, (2004)

R. Goldhahn, A. T. Winzer, V. Cimalla, O. Ambacher, C. Cobet, W. Richter, N. Esser, J. Furthmüller, F. Bechstedt, H. Lu and W. J. Schaff
Anisotropy of the dielectric function for wurtzite InN
Superlattices and Microstructures, **36** (4-6), 591-597, (2004)

M. V. Gomoyunova and I. I. Pronin
Photoelectron Spectroscopy of Atomic Core Levels on the Silicon Surface: A Review
Zhurnal Tekhnicheskoi Fiziki (Russian) 74 (2004) 10, 1 - translated in: Technical Physics Letters, **49** (10), 1249, (2004)

M. V. Gomoyunova, I. I. Pronin, N. R. Gall', S. L. Molodsov and D. V. Vyalikh
Silicon Surface Reconstruction Lost upon Cobalt adsorption
Pis'ma v Zhurnal Tekhnicheskoi Fiziki (Russian) 29 (2003) 25 - translated in: Technical Physics Letters, **29**, 496, (2003)

M. V. Gomoyunova, I. I. Pronin, N. R. Gall', S. L. Molodtsov and D. V. Vyalikh
Interaction of cobalt with the oxidized silicon surface
Pis'ma v Zhurnal Tekhnicheskoi Fiziki (Russian) 30 (2004) 20, 17 - translated in: Technical Physics Letters, **30**, 850, (2004)

M. V. Gomoyunova, I. I. Pronin, N. R. Gall', D. V. Vyalikh and S. L. Molodsov
Interaction of Co with the Si(100) surface, studied by photoelectron spectroscopy
Surface Science, (to be published)

M. V. Gomoyunova, I. I. Pronin, D. E. Malygin, N. R. Gall', D. V. Vyalikh and S. L. Molodsov
Interaction of cobalt atoms with the oxidized Si(100)2x1 surface
Physics of the Solid State (Russian), (2004)

M. V. Gomoyunova, I. I. Pronin, D. E. Malygin, S. M. Solovev, D. V. Vyalikh and S. L. Molodsov
Interaction of iron atoms with the Si(100)2x1 surface
Technical Physics (Russian), (to be published)

Y. S. Gordeev, V. M. Mikoushkin, V. V. Shnitov and S. L. Molodtsov
Modification of fullerite C60 by synchrotron radiation
6rd Biennial International Workshop "Fullerenes and Atomic Clusters", St.-Petersburg, Russia, 312, (2003)

Y. S. Gordeev, V. M. Mikoushkin, V. V. Shnitov and S. L. Molodtsov
Fragmentation of aggregated fullerenes C60 by synchrotron radiation
XXIII Internatonal Conference on the Physics of Electronic and Atomic Collisions, Stockholm, We 187, (2003)

A. Gottwald, S. V. Bobashev, U. Hahn, A. Hoehl, U. Jastrow, M. Richter, A. A. Sorokin and K. I. Tiedke
FEL beam metrology with a gas-monitor detector
Proc. SPIE, **164**, (2004)

A. Gottwald, R. Klein, R. Müller, M. Richter, A. A. Sorokin and G. Ulm
Absolute measurement of EUV radiation from an undulator
AIP Conference Proceedings, **556**, (2004)

A. Gottwald, U. Kroth, M. Letz, H. Schöppe and M. Richter
High-accuracy VUV reflectometry at selectable sample temperatures
Proc. SPIE, **164**, (2004)

A. Gottwald, R. Müller, M. Richter, A. Sorokin and G. Ulm
Pulse energy measurements of extreme ultraviolet undulator radiation
Measurement Science and Technology, **443**, (2004)

J. Grabis
Soft X-Ray Resonant Scattering on Magnetic Heterostructures, Doctoral Thesis
Ruhr-Universität Bochum, (2005)

M. Grimm, B. Langer, S. Schlemmer, T. Lischke, W. Widdra, D. Gerlich, U. Becker and E. Rühl
New Setup to Study Trapped Nanoparticles Using Synchrotron Radiation
AIP Conference Proceedings, **705**, 1062, (2004)

M. F. Guerra, T. Calligaro, M. Radtke, I. Reiche and H. Riesemeier
Fingerprinting ancient gold by measuring Pt with spatially resolved high energy Sy-XRF
Nuclear Instruments and Methods in Physics Research, (to be published)

O. Hahn, W. Malzer, B. Kanngießer and B. Beckhoff
Characterization of iron-gall inks in historical manuscripts and music compositions using x-ray
X-Ray Spectrometry, **33** (4), 234-239, (2004)

U. Hahn, T. Kamps, R. Lorenz, W. Riesch, H. J. Schreiber and F. Tonisch
Waveguide monitors: A new type of beam position monitors for the TTF FEL
Nuclear Instruments and Methods A, **527**, (2004)

A. Haibel, A. Bütow, A. Rack and J. Banhart
Quantitative Analysis of Pore-Particle-Correlations in Metallic Foams
Proceeding of the 16. World Conference on Nondestructive Testing, Montreal, Canada, (2004)

A. Haibel, A. Rack and J. Banhart
Metallschaumcharakterisierung mittels Synchrotron-Tomographie
Proceeding of the DACH-Jahrestagung, ZfP in Forschung, Entwicklung und Anwendung, Salzburg, (2004)

K. Hänel, S. Söhnchen, S. Lukas, G. Beernink, A. Birkner, T. Strunskus, G. Witte and C. Wöll
Organic molecular- beam deposition of perylene on Cu(110): Results from near-edge x-ray absorption spectroscopy, x-ray photoelectron spectroscopy, and atomic force microscopy
Journal of Materials Research, **19** (7), 2049-2056, (2004)

A. Härtl, E. Schmich, J. A. Garrido, J. Hernando, S. C. R. Catharino, S. Walter, P. Feulner, A. Kromka, D. Steinmüller and W. Stutzmann
Protein-modified nanocrystalline diamond thin films for biosensor applications
Nature Materials, **3**, 736-742, (2004)

M. Hävecker, A. Knop-Gericke, H. Bluhm, E. Kleimenov, R. W. Mayer, M. Fait and R. Schlögl
Dynamic surface behaviour of VPO catalysts under reactive and non-reactive gas compositions: an in situ XAS study
Applied Surface Science, **230** (1-4), 272-282, (2004)

J. D. Hecht, F. Frost, A. Sidorenko, D. Hirsch, H. Neumann, A. Schindler, S. Krasnikov, L. Zhang and T. Chasse
Influence of preparation parameters for low-energy ion beam nitridation of III-V semiconductor surfaces
Solid-State Electronics, **47**, 413-418, (2003)

M. Hecker, P. M. Oppeneer, H.-C. Mertins and C. M. Schneider
Layer selective Magnetization Reversal in GMR layer systems
Physica B, **173**, 185, (2004)

W. M. Heijboer, F. M. F. d. Groot, A. A. Battiston, A. Knop-Gericke, M. Hävecker, R. W. Mayer, H. Bluhm, R. Schlögl and D. Koningsberger
In-Situ Soft X-ray Absorption of Over-exchanged Fe/ZSM5
Journal of Physical Chemistry B, **107**, 13069-13075, (2003)

K. Heister, S. Frey, A. Ulman, M. Grunze and M. Zharnikov
Irradiation sensitivity of self-assembled monolayers with an introduced "weak link"
Langmuir, **20**, 1222-1227, (2004)

G. Held, L. B. Jones, E. Seddon and D. A. King
The Effect of Oxygen Adsorption on the chiral Pt{531} Surface
Journal of Physical Chemistry, (to be published)

O. Henneberg, T. Geue, U. Pietsch, M. Saphiannikova and B. Winter
Investigation of azobenzene side group orientation in polymer surface relief gratings by means of photoelectron spectroscopy
Applied Physics Letters, **84** (9), 1561-1563, (2004)

U. Hergenhahn
Vibrational structure in inner shell photoionization of molecules
Journal of Physics B: Atomic, Molecular and Optical Physics, **37**, R89-R135, (2004)

U. Hergenhahn, E. E. Rennie, O. Kugeler, S. Marburger, T. Lischke, I. Powis and G. Garcia
Photoelectron circular dichroism in core level ionization of randomly oriented pure enantiomers of the chiral molecule camphor
Journal of Chemical Physics, **120**, 4553-4556, (2004)

C. Heske
Spectroscopic investigation of buried interfaces and liquids with soft x-rays
Applied Physics A, **78**, 829, (2004)

K. Hinrichs, A. Roseler, M. Gensch and E. H. Korte
Structure analysis of organic films by mid-infrared ellipsometry
Thin Solid Films, **455-456**, 266, (2004)

F. Holch, Diploma
Universität Würzburg, (2004)

K. Holldack, T. Kamps and P. Kuske
Optical transition radiation based beam diagnostics at the BESSY synchrotron radiation source and FEL accelerators
European Particle Accelerator Conference, Lucerne, Switzerland, (2004)

M. Huber, S. Bechstein, B. Beckhoff, F. v. Feilitzsch, J. Jochum, M. Krumrey, A. Rüdig and G. Ulm
Characterization of an Al-STJ-based X-ray detector with monochromatized synchrotron radiation
Nuclear Instruments and Methods A, **236**, (2004)

M. Hülsmeyer, M. T. Fiorillo, F. Bettosini, R. Sorrentino, W. Saenger, A. Ziegler and B. Uchanska-Ziegler
Dual, HLA-B27 Subtypesubtype-dependent Conformation conformation of a Selfself-peptide
Journal of Experimental Medicine, **199** (2), 271-281, (2004)

R. Hunger, T. Schulmeyer, A. Klein, W. Jaegermann, M. V. Lebedev, K. Sakurai and S. Niki
SXPS investigation of the Cd partial electrolyte treatment of CuInSe2 absorbers
Thin Solid Films, **in press, corrected proof**, (2004)

R. Hunger, T. Schulmeyer, A. Klein, W. Jaegermann, K. Sakurai, A. Yamada, P. Fons, K. Matsubara and S. Niki
An option for the surface science on Cu chalcopyrites: the selenium capping and decapping process
Surface Science, **557** (1-3), 263-268, (2004)

W. Jaegermann and T. Mayer
Surface science studies of elementary processes in photoelectrochemistry: adsorption of electrolyte components on layered transition metal dichalogenides
Solar Energy Materials and Solar Cells, **83** (4), 371-394, (2004)

B. Jenichen, V. M. Kaganer, C. Herrmann, L. Wan, L. Däweritz and K. H. Ploog
Lateral periodicity of elastic domains in MnAs/GaAs(001) epitaxial layers studied by high resolution x-ray diffraction
Zeitschrift für Kristallographie, **219**, 201-204, (2004)

B. Jenichen, D. Satapathy, W. Braun, L. Däweritz and K. H. Ploog
Microstructure of epitaxial MnAs films on GaAs(001)- an in-situ x-ray study
Journal of Applied Physics, **96**, 6103-6108, (2004)

Y. H. Jiang, R. Püttner, R. Hentges, J. a. P. Viefhaus, M., U. Becker, J. M. Rost and G. Kaindl
Partial Cross Sections of Doubly Excited Helium Below the Ionization Threshold I7
Physical Review A, **69**, 042706, (2004)

S. Joshi
Synthese und Charakterisierung von II-VI-Nanopartikeln, Doctoral Thesis
Universität Würzburg, (2004)

V. M. Kaganer, W. Braun, B. Jenichen and K. H. Ploog
Two stages of post-growth recovery in molecular beam epitaxy: a surface X-ray diffraction study
Surface Science, **560**, 88-102, (2004)

V. V. Kaichev, V. I. Bukhtiyarov, M. Hävecker, A. Knop-Gericke, R. W. Mayer and R. Schlögl
The Nature of Electrophilic and Nucleophilic Oxygen Adsorbed on Silver
Kinetics & Catalysis, **44** (3), 432-440, (2003)

T. Kamps
Collimation system for the BESSY FEL
Free Electron Laser Conference 2004, Triste, Italy, (2004)

B. Kanngießer, O. Hahn, M. Wilke, B. Nekat, W. Malzer and A. Erko
Investigation of Oxidation and Migration Processes of Inorganic Compounds in Ink Corroded Manuscripts
Spectrochimica Acta A, **Part B 59**, 1511-1516, (2004)

D. Khare, G. Ziegelin, E. Lanka and U. Heinemann
Sequence-specific DNA binding determined by contacts outside the helix-turn-helix motif of the ParB homolog KorB
Nature Structural Molecular Biology, **11** (7), 656-663, (2004)

J. W. Kim, M. Carbone, J. H. Dil, K. Horn, R. Flammini, M. P. Casaletto and M. N. Piancastelli
Adsorption of 2,3-butanediol on Si(100)
Surface Science, **559**, 179, (2004)

M. Kinne, T. Fuhrmann, J. F. Zhu, B. Trankenschuh, R. Denecke and H. P. Steinrück
Coadsorption of D_2O and CO on Pt(111) studied by in situ high-resolution X-ray photoelectron spectroscopy
Langmuir, **20** (5), 1819-1826, (2004)

M. Kinne, T. Fuhrmann, J. F. Zhu, C. M. Whelan, R. Denecke and H. P. Steinrück
Kinetics of the CO oxidation reaction on Pt(111) studied by in situ high-resolution x-ray photoelectron spectroscopy
Journal of Chemical Physics, **120** (15), 7113-7122, (2004)

E. Kleimenov, H. Bluhm, M. Hävecker, A. Knop-Gericke, A. Pestryakov, D. Teschner, J. A. Lopez-Sanchez, J. K. Bartley, G. J. Hutchings and R. Schlögl
XPS investigations of VPO catalysts under reaction conditions
Surface Science, **575** (1-2), 181-188, (2005)

R. Klein, G.Ulm, M. Abo-Bakr, P. Budz, K. Bürkmann-Gehrlein, D. Krämer, J. Rahn and G. Wüstefeld
The Metrology Light Source of the Physikalisch-Technische Bundesanstalt in Berlin-Adlershof
Proceedings of EPAC, **2292**, (2004)

R. Klein, R. Thornagel and G.Ulm
BESSY II operated as a primary source standard
Proceedings of EPAC, **275**, (2004)

R. Klein, G. Ulm, M. Abo-Bakr, P. Budz, K. Bürkmann, D. Krämer, J. Rahn and G. Wüstefeld
The Metrology Light Source of the Physikalisch-Technische Bundesanstalt in Berlin-Adlershof
EPAC, Luzern, Schweiz, (2004)

A. Knop-Gericke, F. M. F. d. Groot, J. A. v. Bokhoven and T. Ressler
In situ Spectroscopy of Catalysts
American Scientific Publisher, (2004)

M. Knupfer and H. Peisert
Electronic properties of interfaces between model organic semiconductors and metals
Physics of the Solid State, **201**, 1055-1074, (2004)

M. Koch-Mueller, S. S. Matsyuk and R. Wirth
Hydroxyl in omphacites and omphacitic clinopyroxenes beneath the Siberian platform from upper mantle to lower crust origin
American Mineralogist, **89**, 921-931, (2004)

S. Korica, D. Rolles, A. Reinköster, B. Langer, J. Viefhaus, S. Cvejanovic and U. Becker
Partial Cross Sections and Angular Distributions of Resonant and Non-resonant Valence Photoemission of C_{60}
Physical Review A, **71**, 013203, (2004)

E. H. Korte, A. Roseler, K. Hinrichs and M. Gensch
Infrared spectroscopic studies of nanolayers
Revista de Chimie, **55**, 701, (2004)

I. M. Kötschau, M. Bär, C.-H. Fischer, A. Grimm, I. Lauermann, J. Reichardt, I. Sieber, S. Sokoll, M. C. Lux-Steiner, L. Weinhardt, O. Fuchs, C. Heske, C. Jung, W. Gudat, T. P. Niesen and F. Karg
X-Ray Emission Study of the ZnO/Cu(In,Ga)(S,Se)$_2$ Interface before and after Damp Heat Treatment
3rd World Conference on Photovoltaic Energy Conversion, Arisumi Printing Inc., Osaka, Japan, 523-6, (2003)

S. A. Krasnikov, A. B. Preobrajenski, T. Chasse and R. Szargan
Thickness dependence of photoemission and X-ray fluorescence spectra in epitaxial NiO layers on Ag(100)
Thin Solid Films, **428**, 201-205, (2003)

S. A. Krasnikov, A. S. Vinogradov, K.-H. Hallmeier, R. Höhne, M. Ziese, P. Esquinazi, T. Chasse and R. Szargan
Oxidation effects in epitaxial Fe_3O_4 layers on MgO and $MgAl_2O_4$ substrates studied by X-ray absorption, fluorescence and photoernission
Materials Science and Engineering B, **109**, 207-212, (2004)

A. Krasyuk, A.Oelsner, S. Nepijko, A. Kuksov, C. M. Schneider and G. Schönhense
Real-Time Observation of Magnetisation Processes in Magnetic Thin Films by Means of Time-Resolved Photoemission
Microscopy and Microanalysis, **9** (3), 254-255, (2003)

A. Krasyuk, A. Oelsner, S. Nepijko, A. Kuksov, C. M. Schneider and G. Schönhense
Time-Resolved Photoemission Electron Microscopy of Magnetic Field and Magnetization Changes
Applied Physics A, **76**, 863-868, (2003)

A. Krasyuk, A. Oelsner, S. A. Nepijko, A. Kuksov, Z. Celinski, C. M. Schneider and G. Schönhense
Dynamics of Magnetic Stray Fields During Magnetization Reversal of micrometer-sized Co Dots
Applied Physics A, **79**, 1925-30, (2004)

M. Krumrey, L. Büermann, M. Hoffmann, P. Müller, F. Scholze and G. Ulm
Absolute responsivity of silicon photodiodes in the X-ray range
AIP Conference Proceedings, **864**, (2004)

M. Krumrey, M. Hoffmann, G. Ulm, K. Hasche and P. Thomsen-Schmidt
Thickness determination of SiO_2 films on Si by X-ray reflectometry at the Si K edge
Thin Solid Films, **244**, (2004)

M. Krumrey, G. Ulm and E. Schmid
Dicentric chromosomes in monolayers of human lymphocytes produced by monochromatized synchrotron radiation with photon energies from 1.83 keV to 17.4 keV
Radiation and Environmental Biophysics, **43** (1), 1-6, (2004)

W. Kuch
X-ray magnetic circular dichroism for quantitative element-resolved magnetic microscopy
Physica Scripta, **T109**, 89-95, (2004)

W. Kuch, L. I. Chelaru, F. Offi, J. Wang, M. Kotsugi and J. Kirschner
Three-dimensional noncollinear antiferromagnetic order in single-crystalline FeMn ultrathin films
Physical Review Letters, **92** (1), 017201, (2004)

W. Kuch, J. Vogel, J. Camarero, K. Fukumoto, Y. Pennec, S. Pizzini, M. Bonfim and J. Kirschner
Exploring spin valve magnetization reversal dynamics with temporal, spatial and layer resolution: Influence of domain wall energy
Applied Physics Letters, **85** (3), 440-442, (2004)

O. Kugeler, G. Prümper, R. Hentges, J. Viefhaus, D. Rolles, U. Becker, S. Marburger and U. Hergenhahn
Intramolecular Electron Scattering and Electron Transfer Following Autoionization in Dissociating Molecules
Physical Review Letters, **93**, 033002, (2004)

O. Kugeler, E. E. Rennie, A. Rüdel, M. Meyer, A. Marquette and U. Hergenhahn
N2 valence photoionization below and above the 1s-1 core ionization threshold
Journal of Physics B: Atomic, Molecular and Optical Physics, **37**, 1353-1367, (2004)

A. Kuksov, C. M. Schneider, A. Oelsner, A. Krasyuk, D. Neeb, G. Schönhense, C. D. Nadal and N. B. Brookes
Investigating Magnetisation Dynamics in Permalloy Microstructures Using Time-Resolved X-PEEM
Journal of Applied Physics, **95**, 6530-6532, (2004)

J. Kunes, P. M. Oppeneer, S. Valencia, D. Abramsohn, H.-C. Mertins, W. Gudat, M. Hecker and C. M. Schneider
Understanding the XMLD and its magnetocrystalline anisotropy at the $L_{2,3}$-edges of 3d transition metals
Journal of Magnetism and Magnetic Materials, **272-276** (3), 2146-2147, (2004)

J. Kuper, A. Liamas, H.-J. Hecht, R. R. Mendel and G. Schwarz
Structure of the molybdopterinbound Cnx1G domain links molybdenum and copper metabolism
Nature, **430**, 803, (2004)

B. Kuske, M. Abo-Bakr and A. Meseck
Impact Studies of bunch parameter variations on the performance of the BESSY HGHG FEL
FEL Conference, Trieste, Italy, (2004)

B. Kuske, M. Abo-Bakr and A. Meseck
The Influence of the Seed Pulse Shape on the Output Performance of the BESSY Multi-stage HGHG-FEL
FEL Conference, Trieste, Italy, (2004)

B. M. Lagutin, P. V. Demekhin, V. L. Sukhorukov, A. Ehresmann, H. Schmoranzer and K.-H. Schartner
Alignment and orientation of the ionic states of rare gas atoms populated by resonant Auger effect
Proceedings of 12th international symposium on polarization and correlation in electronic and atomic collisions, AIP conference proceedings, **697**, 127-32, (2004)

H. Lammert
Nanometer-Optikkomponenten für die Synchrotronstrahlung – Messung und Endbearbeitung bis in den Subnanometer-Bereich unter Lambda/1000, (2004)

H. Lammert
Genauigkeitssteigerung um das Fünffache bei Nanometer-Optikkomponenten - NOK
Nano-Spotlight, **3**, (2004)

H. Lammert, T. Noll, T. Schlegel, F. Siewert and T. Zeschke
XUV-Optik - Messung mit der Nano-Optik-Messmaschine - NOM - bei BESSY.
DGaO-105. Jahrestagung 2004, Bad Kreuznach, (2004)

H. Lammert, T. Noll, T. Schlegel, F. Siewert and T. Zeschke
XUV-Optik – neue unkonventionelle Bestimmung ihrer Flächenformen bei BESSY
DGaO-105. Jahrestagung 2004, Bad Kreuznach, (2004)

H. Lammert and F. Siewert
Optical SR components below the 0.1 arcsec limit: The key for this accuracy in the measurement technique
Second International Workshop on Metrology for X-rax Oprics, Oliver Hignette, Grenoble, (2004)

M. Lebedev, R. Hunger, T. Mayer and W. Jaegermann
In situ Synchrotron Photoemission Analysis of Chemical Processes at Semiconductor/Frozen Electrolyte Interfaces:Interaction of HCl Solution with GaAs(100)
Journal of Physical Chemistry B, (to be published)

M. V. Lebedev, D. Ensling, R. Hunger, T. Mayer and W. Jaegermann
Synchrotron photoemission spectroscopy study of ammonium hydroxide etching to prepare well-ordered GaAs(100) surfaces
Applied Surface Science, **229** (1-4), 226-232, (2004)

M. V. Lebedev, T. Mayer and W. Jaegermann
Adsorption of solvated hydrosulfide ions at a GaAs(100) surface: The role of a solvent in surface structure modification
Semiconductors, **38** (2), 153-160, (2004)

R. Lebert, C. Wies, L. Juschkin, B. Jägle, M. Meisen, L. Aschke, F. Sobel and H. Seitz
High throughput EUV-reflectometer for EUV mask-blanks
Proc. SPIE, **817**, (2004)

W. Leitenberger, H. Wendrock, L. Bischoff and T. Weitkamp
Pinhole Interferometry with Coherent Hard X-rays
Journal of Synchrotron Radiation, **11**, 190-197, (2004)

F. Leunberger
Elemental resolved magnetism of Gadopliniumnitride layers and GdN/Fe multilayers, Doctoral Thesis
Universität Göttingen, (2004)

K. Lüdge, P. Vogt, W. Richter, B.-O. Fimland, W. Braun and N. Esser
Metallic nanostructures on Co/GaAs(001)(4x2) surfaces
Journal of Vacuum Science and Technology B, **22**, 2008, (2004)

B. A. Manjasetty, H. Delbruck, D. T. Pham, U. Mueller, M. Fieber-Erdmann, C. Scheich, V. Sievert, K. Bussow, F. H. Niesen, W. Weihofen, B. Loll, W. Saenger and U. Heinemann
Crystal structure of Homo sapiens protein hp14.5
Proteins, **54** (4), 797-800, (2004)

B. A. Manjasetty, H. Delbruck, D. T. Pham, U. Mueller, M. Fieber-Erdmann, C. Scheich, V. Sievert, K. Büssow, F. H. Niesen, W. Weihofen, B. Loll, W. Saenger and U. Heinemann
Crystal structure of Homo sapiens protein hp14.5
Proteins, **54** (4), 797-800, (2004)

B. A. Manjasetty, F. H. Niesen, H. Delbrück, F. Goetz, V. Sievert, B. K., J. Behlke and U. Heinemann
X-ray structure of Fumarylacetoacetate fumarylacetoacetate hydrolaseHydrolase(FAH) family Homo sapiens FLJ36880
Biological Chemistry, **385** (10), 935-942, (2004)

B. A. Manjasetty, F. H. Niesen, H. Delbruck, F. Gotz, V. Sievert, K. Bussow, J. Behlke and U. Heinemann
X-ray structure of fumarylacetoacetate hydrolase family member homo sapiens FLJ36880
Biological Chemistry, **385** (10), 935-42, (2004)

B. A. Manjasetty, C. Quedenau, V. Sievert, K. Bussow, F. Niesen, H. Delbruck and U. Heinemann
X-ray structure of human gankyrin, the product of a gene linked to hepatocellular carcinoma
Proteins, **55** (1), 214-7, (2004)

B. A. Manjasetty, C. Quedenau, V. Sievert, K. Büssow, F. Niesen, H. Delbruck and U. Heinemann
X-ray structure of human gankyrin, the product of a gene linked to hepatocellular carcinoma
Proteins, **55** (1), 214-217, (2004)

I. Manke, N. Kardjilov, R. Schneider, A. Haibel, A. Denker, A. Rack, A. Hilger, F. Garcia-Moreno and J. Banhart
Zerstörungsfreie Messmethoden am Hahn-Meitner-Institut, Neutronen, Ionen und Röntgenstrahlen für die Industrie
Carl Hanser Verlag, München, (2004)

S. Marburger
Experimentelle Untersuchungen zum Interatomaren Coulomb Zerfall an Neon Clustern: Nachweis eines ultraschnellen nichtlokalen Zerfallskanals, Doctoral Thesis
Technische Universität, (2004)

F. Marhauser
Photoinjector Studies for the BESSY Soft X-ray FEL
9th European Particle Accelerator Conference, European Physical Society Accelerator Group, Lucerne, Switzerland, (2004)

F. Marhauser and E. Weihreter
First Tests of a HOM-Damped High Power 500 MHz Cavity
9th European Particle Accelerator Conference, European Physical Society Accelerator Group, Lucerne, Switzerland, (2004)

M. Marutzky, U. Barkow, J. Schoenes and R. Troc
Optical and magneto-optical properties of single crystalline uranium nitride, (to be published)

B. Matijasevic-Lux, A. Rack, A. Haibel and J. Banhart
Influence of powder pre-treatments on metal foam pore structure, (to be published)

D. Mayer, K.-H. Hallmeier, D. Zerulla and R. Szargan
SXPS and XANES studies of interface reactions of organic molecules on sulphide semiconductors, in: K. Wandelt, St. Thurgate (Eds.) Solid-Liquid Interfaces - Macroscopic Phenomena - Microscopic Unterstanding
Topics of Applied Physics, **85**, 97-112, (2003)

R. W. Mayer, M. Melzer, M. Hävecker, A. Knop-Gericke, K. Weiss, J. Urban, H. J. Freund and R. Schlögl
Comparison of Oxidized Polycrystalline Copper Foil with Small Deposited Copper Clusters in Their Behavior in Ammonia Oxidation: An Investigation by Means of In Situ NEXAFS Spectroscopy in the Soft X-Ray Range
Catalysis Letters, **86** (4), 245-250, (2003)

T. Mayer, M. V. Lebedev, R. Hunger and W. Jaegermann
Elementary Processes at Semiconductor/Electrolyte Interfaces: Perspectives and limits of electron spectroscopy
Applied Surface Science, (2004)

B. Mertens, M. Weiss, H. Meiling, R. Klein, E. Louis, R. Kurt, M. Wedowski, H. Trenkler and B. Wolschrijn
Progress in EUV optics lifetime expectations
Microelectronic Engineering, **73-74**, 16-22, (2004)

H.-C. Mertins, P. M. Oppeneer, S. Valencia, W. Gudat, F. Senf and P. R. Bressler
X-ray natural birefringence in reflection from graphite
Physical Review B, **70**, 235106, (2004)

H.-C. Mertins, S. Valencia, D. Abramsohn, A. Gaupp, W. Gudat and P. M. Oppeneer
X-ray Kerr rotation and ellipticity spectra at the 2p edges of Fe, Co and Ni
Physical Review B, **69**, 064407, (2004)

H.-C. Mertins, S. Valencia, A. Gaupp, W. Gudat, P. M. Oppeneer and C. M. Schneider
Magneto-optical polarization spectroscopy with soft X-rays
Applied Physics A, **in print**, (2004)

H.-C. Mertins, S. Valencia, W. Gudat, P. M. Oppeneer, O. Zaharko and H. Grimmer
Direct Observation of local ferromagnetism on carbon
Europhysics Letters, **66**, 743, (2004)

A. Meseck, M. Abo-Bakr and B. C. Kuske
The Output Performance of the BESSY Multi-stage HGHG-FEL
EPAC, Luzern, Schweiz, (2004)

A. Meseck, M. Abo-Bakr and B. C. Kuske
Output Variability of the BESSY Soft X-ray FEL
EPAC, Luzern, Schweiz, (2004)

R. P. Methling
Mass-filtered ferromagnetic alloy clusters on surfaces, Doctoral Thesis
Universität Rostock, (2004)

J. A. Mirão
Mineralogy and geochemistry of niobotantalate minerals from pegmatites in Zambezia, Mozambique, Doctoral Thesis
University of Évora, (2004)

J. P. Mirão and M. O. Figueiredo
X-ray absorption spectroscopy at 3d-metal L2,3 and oxygen K-edges in columbites
5th European Conf. Mineralogy and Spectroscopy, Mitteilungen der Österreichischen Mineralogischen Gesellschaft, Vienna/Austria, 70, (2004)

T. Missalla, M. C. Schürmann, R. Lebert, C. Wies, L. Juschkin, R. M. Klein and F. Scholze
Metrology tools for EUV-source characterization and optimization
Proc. SPIE, **990**, (2004)

T. Mizokawa, A. Fujimori, J. Okabayashi and O. Rader
Photoemission of diluted Mn in and on solids
Journal of Electron Spectroscopy and Relative Phenomena, **136**, 21, (2004)

F. Morales, F. M. F. d. Groot, P. Glatzel, E. Kleimenov, H. Bluhm, M. Hävecker, A. Knop-Gericke and B. M. Weckhuysen
In Situ X-ray Absorption of Co/Mn/TiO2 Catalysts for Fischer-Tropsch Synthesis
Journal of Physical Chemistry B, **108** (46), 16201-16207, (2004)

H.-J. Muffler, M. Bär, I. Lauermann, K. Rahne, M. Schröder, M. C. Lux-Steiner, C.-H. Fischer, T. P. Niesen and F. Karg
Colloid attachment by ILGAR-layers: Creating fluorescing layers to increase quantum efficiency of solar cells
Solar Energy Materials and Solar Cells, (to be published)

H.-J. Muffler, M. Bär, M. C. Lux-Steiner, C.-H. Fischer, T. P. Niesen and F. Karg
Colloid Fixation by an ILGAR-Layer: the Use of Fluorescing Layers to Increase Quantum Efficiency of Solar Cells in the Blue Wavelength Region
Technical digest of the 14th International Photovoltaic Science and Engineering Conference, Chulalongkorn University, Bangkok, Thailand, 703-704, (2004)

B. R. Müller, A. Lange, M. Harwardt and M. P. Hentschel
Submikro-Computer-Tomographie an der BAMline
DACH Jahrestagung 2004, Berichtsband 89-CD DGZfP, Berlin, (2004)

B. R. Müller, A. Lange, M. Harwardt, M. P. Hentschel, B. Illerhaus, J. Goebbels, J. Bamberg and F. Heutling
Refraction computed tomography
Materialprüfung, **46** (6), 314-319, (2004)

B. R. Müller, A. Lange, M. Harwardt, M. P. Hentschel, B. Illerhaus, J. Goebbels, J. Bamberg and F. Heutling
Micro Crack Characterization of Metal Matrix Composites by 3D-Refraction- Computed-Tomography
Proceedings of 16th World Conference on Nondestructive Testing, Montreal, Canada, (2004)

A. Nefedov, J. Grabis, A. Bergmann, F. Radu and H. Zabel
X-ray resonant magnetic scattering of Fe/Cr superlattices
Superlattices and Microstructures, **37** (1), 99, (2005)

A. Nefedov, J. Grabis, A. Bergmann, K. Westerholt and H. Zabel
Soft X-ray resonant magnetic scattering studies on Co_2MnGe Heusler films
Physica B, **345**, 250, (2004)

S. A. Nepijko, M. Klais, G. Schönhense, N. Cramer, Z. Celinski, C. M. Schneider, S. Zennaro, N. Zema and N. N. Sedov
Micromagnetism of Two-Dimensional Permalloy Particles with Different Aspect Ratios
Applied Physics A, **76**, 809-815, (2003)

S. A. Nepijko, A. Oelsner, A. Krasyuk, A. Gloskovskii, N. N. Sedov, C. M. Schneider and G. Schönhense
Lateral Resolving Power of a Time-of-Flight Photoemission Electron Microscope
Applied Physics A, **78**, 47-51, (2004)

H. W. Nesbitt, A. G. Berlich, S. L. Harmer, I. Uhlig, G. M. Bancroft and R. Szargan
Identification of pyrite valence band contributions using synchrotron-excited X-ray photoelectron spectroscopy
American Mineralogist, **89**, 382-389, (2004)

H. W. Nesbitt, A. Schaufuss, M. Sciani, H. Hochst, G. M. Bancroft and R. Szargan
Monitoring fundamental reactions at NiAsS surfaces by synchrotron radiation X-ray photoelectron spectroscopy: As and S air oxidation by consecutive reaction schemes
Geochimica et Cosmochimica Acta, **67**, 845-858, (2003)

H. W. Nesbitt, I. Uhlig, G. M. Bancroft and R. Szargan
Resonant XPS study of the pyrite valence band with implications for molecular orbital contributions
American Mineralogist, **88**, 1279-1286, (2003)

T. Noll
Elastic Mechanisms - Design and Optimization of Parallel Kinematics with Flexure Joints
ProEngineer User Meeting - PTC World Event 2004, Friedrichshafen, Deutschland, (2004)

T. Noll
Elastische parallelkinematische Führungsgetriebe und Komponenten für ultrapräzise Bewegungen im Vakuum
3 Tutorials at FMB GmbH, Berlin, (2004)

T. Noll, F. Hoeft, K. Holldack, G. Reichardt, F. Senf and T. Zeschke
The new Switching Mirror Unit and its Mechanical Principals
3rd International Workshop on Mechanical Engineering Design of Synchrotron Radiation Equipment and Instrumentation - MEDSI2004, ESRF Grenoble, France, (2004)

T. Noll and H. Lammert
Rotationslager zur hochgenauen Winkelpositionierung eines Gegenstandes, (2004)

T. Noll and H. Lammert
Justiervorrichtung zur hochgenauen Positionierung eines Objekts, (2004)

A. Oelsner, A. Krasyuk, G. H. Fecher, C. M. Schneider and G. Schönhense
Image enhancement in photoemission electron microscopy by means of imaging time-of-flight analysis
Journal of Electron Spectroscopy and Related Phenomena, **137-140**, 757-761, (2004)

A. Oelsner, A. Krasyuk, D. Neeb, S. Nepijko, A. Kuksov, C. M. Schneider and G. Schönhense
Magnetisation Changes Visualised Using Photoemission Electron Microscopy
Journal of Electron Spectroscopy and Related Phenomena, **137-140**, 751-756, (2004)

C. Olesen, T. Sorensen, R. C. Nielsen, J. V. Moller and P. Nissen
Dephosphorylation of the calcium pumpcoupled to counterion occlusion
Science, **306**, 2251, (2004)

H. Ott
Magnetic Structures and Phase Transitions in Thin and Ultrathin Films of Heavy Lanthanide Metals Investigated by Resonant Magnetic X-Ray Scattering, Doctoral Thesis
FU Berlin, (2004)

A. A. Pavlychev, R. Flesch and E. Rühl
Line Shapes of 1s --> pi-Excited Molecular Clusters*
Physical Review A, **70**, 015201, (2004)

H. Peisert, I. Biswas, L. Zhang, M. Knupfer, M. Hanack, D. Dini, M. J. Cook, I. Chambrier, T. Schmidt, D. Batchelor and T. Chassé
Orientation of substituted phthalocyanines on polycrystalline gold: distinguishing between the first layers and thin films
Chemical Physics Letters, **403**, 1-6, (2005)

H. Peisert, X. Liu, D. Olligs, A. Petr, L. Dunsch, T. Schmidt, T. Chassé and M. Knupfer
Highly ordered phthalocyanine thin films on a technical relevant polymer substrate
Journal of Applied Physics, **96**, 4009-4011, (2004)

Y. Pennec, J. Camarero, J. C. Toussaint, S. Pizzini, M. Bonfim, F. Petroff, W. Kuch, F. Offi, K. Fukumoto, F. Nguyen Van Dau and J. Vogel
Switching-mode-dependent magnetic interlayer coupling strength in spin valves and magnetic tunnel junctions
Physical Review B, **69** (18), 180402(R), (2004)

M. Polcik, F. Allegretti, D. I. Sayago, G. Nisbet, C. L. A. Lamont and D. P. Woodruff
Circular dichroism in core level photoemission from an adsorbed chiral molecule
Physical Review Letters, **92**, 236103-1-4, (2004)

M. Polcik, M. Kittel, J. T. Hoeft, R. Terborg, R. L. Toomes and D.P.Woodruff
Adsorption geometry of CN on Cu(111) and Cu(111)/O
Surface Science, **563**, 159-168, (2004)

D. Pop, B. Winter, W. Freyer, R. Weber, W. Widdra and I. V. Hertel
Photoelectron spectroscopy on thin films of extended copper porphyrazines
Journal of Physical Chemistry B, **108** (26), 9158-9167, (2004)

A. B. Preobrajenski, A. S. Vinogradov, S. A. Krasnikov, R. Szargan and N. Martensson
Molecular nature of resonant x-ray scattering in solid LiNO3
Physical Review Letters, **69**, 115116, (2004)

A. B. Preobrajenski, A. S. Vinogradov, S. L. Molodtsov, S. A. Krasnikov, R. Szargan and C. Laubschat
Resonant Auger spectroscopy in solid alkali nitrates as a probe of nuclear motion in the core-excited NO3- anion
Chemical Physics Letters, **368**, 125-131, (2003)

M. Procop and F. Scholze
Synchrotron Radiation for the Characterization of Energy Dispersive X-ray Spectrometers
Microscopy and Microanalysis, **10** (2), 98-99, (2004)

J. Prokop, D. A. Valdaitsev, A. Kukunin, M. Pratzer, G. Schönhense and H. J. Elmers
Strain induced magnetic anisotropies in Co films on Mo(110)
Physical Review B, **70**, 184423, (2004)

G. Prümper, J. Viefhaus, S. Cvejanovic, D. Rolles, O. Geßner, T. Lischke, R. Hentges, C. Wienberg, W. Mahler, U. Becker, B. Langer, T. Prosperi, N. Zema, S. Turchini, B. Zada and F. Senf
Upper Limits for Stereoselective Photodissociation of Free Amino Acids in the Vacuum Ultraviolet Region and at the C 1s Edge
Physical Review A, **69**, 062717, (2004)

A. Rack, A. Haibel and J. Banhart
Characterization of Metal Foams with Synchrotron Tomography and 3D Image Analysis
Proceedings of the 16. World Conference on Nondestructive Testing, Montreal, Canada, (2004)

O. Rader, C. Pampuch, A. M. Shikin, W. Gudat, J. Okabayashi, T. Mizokawa, A. Fujimori, T. Hayashi, M. Tanaka, T. A. and A. Kimura
Resonant photoemission of Ga1-xMnxAs at the Mn L-edge
Physical Review B, **69**, 075202, (2004)

O. Rader and A. M. Shikin
An elastic "sieve" to probe momentum space: Gd chains on W(110)
Physical Review Letters, **93**, 256802, (2004)

J. Reichardt, M. Bär, A. Grimm, I. Kötschau, I. Lauermann, S. Sokoll, M. C. Lux-Steiner, C.-H. Fischer, C. Heske, L. Weinhardt, O. Fuchs, C. Jung, W. Gudat, T. P. Niesen and F. Karg
Inducing and Monitoring Photoelectrochemical Reactions at Surfaces and Buried Interfaces in $Cu(In,Ga)(S,Se)_2$ Thin Film Solar Cells
Applied Physics Letters, (to be published)

I. Reiche
Synchrotron-induzierte Roentgenfluoreszenzanalyse - Untersuchungen an Renaissance-Zeichnungen und indischen Miniaturen
Restauro, 378-384, (2004)

I. Reiche, A. Berger, A. Duval, W. Goerner, S. Merchel, M. Radtke, J. Riederer and H. Riesemeier
Metallstiftzeichnungen Albrecht Duerers - Zerstörungsfreie Spurenanalyse mit Synchrotron-induzierter Röntgenfluoreszenzanalyse
PapierRestaurierung - Mitteilungen der IADA (Internationale Arbeitsgemeinschaft der Archiv-,Bibliotheks- und Graphikrestauratoren), 30-38, (2004)

I. Reiche, A. Berger, W. Goerner, S. Merchel, M. Radtke, J. Riederer, H. Riesemeier and M. Roth
Following the traces of Albrecht Duerer: Analysis of silverpoint drawings by spatially resolved synchrotron-induced X-ray fluorescence analysis
Nuclear Instruments and Methods in Physics Research B, **226**, 83-91, (2004)

I. Reiche, M. Radtke, A. Berger, T. Ketelsen, S. Merchel, W. Goerner, H. Riesemeier, J. Riederer and M. Roth
Spatially resolved Synchrotron-induced X-ray fluorescence analyses of metal point drawings and their mysterious inscriptions
Spectrochimica Acta B, **59**, 1657-1662, (2004)

A. Reinköster, S. Korica, B. Langer, G. Prümper, D. Rolles, J. Viefhaus, S. Cvejanovic and U. Becker
Photoelectron and photoion study of the valence photoionization of C60
Journal of Electron Spectroscopy Relatated Phenomena, **in press**, (2004)

A. Reinköster, S. Korica, G. Prümper, J. Viefhaus, K. Godehusen, O. Schwarzkopf, M. Mast and U. Becker
The Photoionization and Fragmentation of C60 in the Energy Range 26-130 eV
Journal of Physics B, **37**, 2135, (2004)

I. Retzko and W. E. S. Unger
Analysis of carbon materials by x-ray photoelectron spectroscopy and x-ray absorption spectroscopy
Advanced Engineering Materials, **5** (7), 519-522, (2003)

M. Richter, U. Kroth, A. Gottwald, S. Bobashev, A. A. Sorokin, L. Shmaenok, J. Feldhaus, C. Gerth and K. Tiedtke
Verfahren und Monitordetektor zur Bestimmung der Intensität von gepulster VUV- oder EUV-Strahlung sowie Verwendung eines derartigen Monitordetektors
Patent Nummer, **102** (44), 3-52, (2004)

T. Richter, T. Wolf, K. Godehusen, M. Martins and P. Zimmermann
Interplay of intraatomic and interatomic effects: An investigation of the 2p core level spectra of atomic Fe and molecular FeCl2
Physical Review Letters, **93**, 0230021, (2004)

Y. Roske, A. Sunna, W. Pfeil and U. Heinemann
High-resolution Crystal crystal Structures structures of Caldicellulosiruptor Caldicellulosiruptor Strain strain Rt8B.4 Carbohydratecarbohydrate-binding Module module CBM27-1 and its Complex complex with Mannohexaosemannohexaose
Journal of Molecular Biology, **340** (3), 543-554, (2004)

S. B. J. Ruck, A. Koo, U. D. Lanke, F. Budde, H. J. Trodahl, G. V. M. Williams, A. Bittar, J. B. Metson, E. Nodwell, T. Tiedje, A. Zimina and S. Eisebitt
Filled and empty states of disordered GaN studied by x-ray absorption and emission
Journal of Applied Physics, **96**, 3571, (2004)

M. Sánchez-Agudo, L. Soriano, R. Fernández-Jiménez, A. Gutiérrez, M. Abbate, S. Wicklund and J. M. Sanz
3p --> 3d resonant photoemission spectroscopy of a TiO_2 monolayer grown on Al_2O_3
Surface Science, **566-588** (1), 515-519, (2004)

F. Sannibale, J. M. Byrd, Á. Loftsdóttir, M. Venturini, M. Abo-Bakr, J. Feikes, K. Holldack, P. Kuske, G. Wüstefeld, H.-W. Hübers and R. Warnock
A Model Describing Stable Coherent Synchrotron Radiation in Storage Rings
Physical Review B, **69**, (2004)

D. K. Satapathy, B. Jenichen, V. M. Kaganer, W. Braun, L. Däweritz and K. H. Ploog
In-situ investigation of MnAs/GaAs (001) growth and interface structure using synchrotron x-ray diffraction
Journal of Vacuum Science and Technology B, **22**, 2079-2083, (2004)

D. I. Sayago, M. Polcik, R. Lindsay, J. T. Hoeft, M. Kittel, R.L.Toomes and D.P.Woodruff
Structure determination of formic acid reaction products on TiO2(110)
Journal of Physical Chemistry B, **108**, 14316-14323, (2004)

U. Schade, K. Holldack, P. Kuske, G. Wüstefeld and H.-W. Hübers
THz near-field imaging employing synchrotron radiation
Applied Physics Letters, **84**, 1422-1424, (2004)

U. Schade, R. Wäsch and L. Moroz
Near-infrared reflectance spectroscopy of Ca-rich clinopyroxenes and prospects for remote spectral characterization of planetary surfaces
Icarus, **168**, 80-92, (2004)

A. Scherz
Spin-dependent X-ray Absorption Spectroscopy of 3d Transition Metals: Systematics and Applications, Doctoral Thesis
Freie Universität Berlin, (2004)

A. Scherz, H. Wende and K. Baberschke
Fine structure of X-ray Magnetic Circular Dichroism for early 3d transition metals
Applied Physics A, **78**, 843, (2004)

A. Schindler, T. Hänsel, A. Nickel, H. Thomas, H. Lammert and F. Siewert
Finishing procedure for high performance synchrotron optics
Proc. SPIE, **5180**, 64-72, (2003)

A. Schindler, T. Hänsel, A. Nickel, H. J. Thomas, H. Lammert, F. Siewert and T. Zeschke
Ionenstrahl-Polierfehlerkorrektur von Synchrotron-Beamline Optiken einer neuen Generation
Tätigkeitsbericht 2002/2003, Institut für Oberflächenmodifizierung e.V., Leipzig, (2004)

S. Schlosser, M. Radtke and E. Pernicka
Goldene Frösche und kupferne Vögel
Archäometrie und Denkmalpflege, Mannheim, (2004)

J. Schmalhorst, M. Sacher, V. Höink, G. Reiss, D. Engel and A. Ehresmann
X-ray absorption and magnetic circular dichroism studies of ion bombarded ferromagnet-antiferromagnet bilayers
Physical Review B, **70**, 184403, (2004)

C. M. Schneider, A. Kuksov, A. Krasyuk, A. Oelsner, D. Neeb, A. S. Nepijko, G. Schönhense, I. Mönch, R. Kaltofen, J. Morais, C. D. Nadai and N. B. Brookes
Incoherent Magnetisation Rotation Observed in Sub-Nanosecond Time-Resolving XPEEM Studies
Applied Physics Letters, **85**, 2562-2564, (2004)

A. Schöll, R. Fink, E. Umbach, G. E. Mitchell, S. Urquhart and H.Ade
Towards a detailed understanding of the NEXAFS spectra of bulk polyethylene copolymers and related alkanes
Chemical Physics Letters, **371**, 834, (2003)

A. Schöll, D. Hübner, T. Schmidt, R. Fink and E. Umbach
Vibronic Fine Structure in the High-Resolution O-K NEXAFS Spectra of a Large Organic Molecule
Chemical Physics Letters, **392**, 297, (2004)

A. Schöll, Y. Zou, M. Jung, T. Schmidt, R. Fink and E. Umbach
Line shapes and satellites in high-resolution x-ray photoelectron spectra of large pi-conjugated organic molecules
Journal of Chemical Physics, **121** (20), 10260-10267, (2004)

A. Schöll, Y. Zou, L. Kilian, D. Hübner, D. Gador, C. Jung, S. G. Urquhart, T. Schmidt, R. Fink and E. Umbach
Electron-vibron coupling in high-resolution X-ray absorption spectra of organic materials: NTCDA on Ag(111)
Physical Review Letters, **93** (14), 146406, (2004)

A. Schöll, Y. Zou, T. Schmidt, R. Fink and E. Umbach
High-resolution photoemission study of different NTCDA monolayers on Ag(111): bonding and screening influences on the line shapes
Journal of Physical Chemistry B, **108** (38), 14741-14748, (2004)

F. Scholze, R. Klein and R. Müller
Linearity of silicon photodiodes for EUV radiation
Proc. SPIE, **934**, (2004)

G. Schönhense
Surface magnetism studied by photoelectron spectromicroscopy with high spatial and time resolution
Journal of Electron Spectroscopy and Related Phenomena, **137-140**, 769-783, (2004)

G. Schönhense, A. Krasyuk, D. Neeb, A. Oelsner, S. Nepijko, H. J. Elmers, A. Kuksov and C. M. Schneider
Picosecond dynamics of magnetization processes observed using time-resolved X-PEEM
Recent Trends in Charged Particle Optics, Brno, 69-72, (2004)

G. Schönhense and H. Spiecker
Chromatic and Spherical Aberration Correction Using Time-Dependent Acceleration and Lens Fields
Microscopy and Microanalysis, **9** (3), 34-35, (2003)

U. Schühle, J. F. Hochedez, J. L. Pau, C. Rivera, E. Munoz, J. Alvarez, J. P. Kleider and P. Lemaire
Development of imaging arrays for solar UV observations based on wide band gap materials
Proc. SPIE, **238**, (2004)

T. Schulmeyer, R. Hunger, R. Fritsche, B. Jackel, W. Jaegermann, A. Klein, R. Kniese and M. Powalla
Interfaces of chalcogenide solar cells: a study of the composition at the Cu(In,Ga)Se_2/CdS contact
Thin Solid Films, **In Press, Corrected Proof**, (2004)

T. Schulmeyer, R. Hunger, A. Klein, W. Jaegermann and S. Niki
Photoemission study and band alignment of the CdS/$CuInSe_2$(001) heterojunction
Applied Physics Letters, **84** (16), 3067, (2004)

T. Schulmeyer, R. Kniese, R. Hunger, W. Jaegermann, M. Powalla and A. Klein
Influence of Cu(In,Ga)Se_2 band gap on the valence band offset with CdS
Thin Solid Films, **451-452**, 420-423, (2004)

M. P. Seah, S. J. Spencer, F. Bensebaa, I. Vickridge, H. Danzebrink, M. Krumrey, T. Gross and W. Oesterle
Critical review of the current status of thickness measurements for ultrathin SiO_2 on Si
Surface and Interface Analysis, **36**, 1269-1303, (2004)

T. Seyller
Passivation of Hexagonal SiC Surfaces by Hydrogen Termination
Journal of Physics: Condensed Matter, **16**, 1755, (2004)

T. Seyller, K. V. Emstev, R. Graupner and L. Ley
Initial stages of thermal oxidation of 4H-SiC(11-20) studied by photoelectron spectroscopy
Material Science Forum, **457-460**, 1317, (2004)

T. Seyller, K. Gao, L. Ley, F. Ciobanu, G. Pensl, A. Tadich, J. D. Riley and R. C. G. Leckey
Structural and electronic properties of the
6H-SiC(0001)/Al_2O_3 interface prepared by atomic layer deposition
Material Science Forum, **457-460**, 1369, (2004)

T. Seyller, N. Sieber, K. V. Emstev, R. Graupner, L. Ley, A. Tadich, D. James, J. D. Riley, R. G. C. Leckey and M. Polcik
The atomic structure of hydrogen saturated a-planes of 4H-SiC
Material Science Forum, **457-460**, 395, (2004)

A. Shaporenko, K. Adlkofer, L. S. O. Johansson, A. Ulman, M. Grunze, M. Tanaka and M. Zharnikov
Spectroscopic characterization of 4-substituted aromatic self-assembled monolayers on GaAs (100) surfaces
Journal of Physical Chemistry B, **108**, 17964-17972, (2004)

A. Shaporenko, M. Brunnbauer, A. Terfort, M. Grunze and M. Zharnikov
Structural forces in self-assembled monolayers: Terphenyl-substituted alkanethiols on noble metal substrates
Journal of Physical Chemistry B, **108**, 14462-14469, (2004)

A. M. Shikin, A. Varykhalov, G. V. Prudnikova, V. K. Adamchuk, W. Gudat and O. Rader
Photoemission from stepped W(110): Initial- or final-state effect?
Physical Review Letters, **93**, 146802, (2004)

S. Siebentritt, P. Walk, U. Fiedeler, I. Lauermann, K. Rahne, M. C. Lux-Steiner, T. P. Niesen and F. Karg
MOCVS as a dry deposition method of ZnSe buffers for Cu(In,Ga)$(S,Se)_2$ solar cells
Progress in Photovoltaics: Research and Applications, **12**, 333-338, (2004)

F. Siewert, T. Noll, T. Schlegel, T. Zeschke and H. Lammert
The Nanometer Optical Component Measuring Machine: A New Sub-nm Topography Measuring Device for X-ray Optics at BESSY
Eighth International Conference on Synchrotron Radiation Instrumentation, AIP Conference Proceedings, San Francisco, California, (2004)

F. Siewert, T. Noll, T. Schlegel, T. Zeschke and H. Lammert
The BESSY-NOM (Nanometer Optical component measuring machine): Non contact Deflectometry Sub-nm Topograpphy measuring Device for X-ray Optcs. Second International Workshop on Metrology for X-rax Oprics.
Second International Workshop on Metrology for X-rax Oprics, Oliver Hignette, Grenoble, (2004)

E. J. Singley, M. Abo-Bakr, D. N. Basov, J. Feikes, P. Guptasarma, K. Holldack, H. W. Hübers, P. Kuske, M. C. Martin, W. B. Peatman, U. Schade and G. Wüstefeld
Measuring the Josephson plasma resonance in Bi2Sr2CaCu2O8 using intense coherent THz synchrotron radiation
Physical Review B, **69**, 92512, (2004)

E. J. Singley, M. Abo-Bakr, D. N. Basov, J. Feikes, K. Holldack, H.-W. Hübers, P. Kuske, M. C. Martin, W. B. Peatman, U. Schade and G. Wüstefeld
New scientific opportunities with intense coherent THz synchrotron radiation: Measuring the Josephson plasma resonance in $Bi_2Sr_2CaCu_2O_8$
Physical Review B, **69**, 092512, (2004)

W.-H. Soe, K.-H. Rieder, A. M. Shikin, V. Mozhaiskii, A. Varykhalov and O. Rader
The surface phonon and valence band dispersions in graphite overlayers formed by solid-state graphitization of 6H-SiC(0001)
Physical Review B, **70**, 115421, (2004)

T. Sorensen, J. V. Moller and P. Nissen
Phosphoryl transfer and calcium ion occlusion in the calcium pump
Science, **304**, 1672, (2004)

C. Sorg, N. Ponpandian, A. Scherz, H. Wende, R. Nünthel, T. Gleitsmann and K. Baberschke
The magnetism of ultrathin Ni films grown with O surfactant
Surface Science, **565**, 197, (2004)

A. A. Sorokin, I. L. Beigman, S. V. Bobashev, M. Richter and L. A. Vainshtein
Total electron-impact ionization cross sections of helium
Journal of Physics B, **3226**, (2004)

A. A. Sorokin, S. V. Bobashev, J. Feldhaus, C. Gerth, A. Gottwald, U. Hahn, U. Kroth and M. Richter
Gas-monitor detector for intense and pulsed VUV/EUV free-electron laser radiation
AIP Conference Proceedings, **560**, (2004)

S. Stepanow, T. Strunskus, M. Lingenfelder, A. Dmitriev, H. Spillmann, N. Lin, J. V. Barth, C. Wöll and K. Kern
Deprotonation-driven phase transformations in terephthalic acid self-assembly on Cu(100)
Journal of Physical Chemistry B, **108**, 19392 - 19397, (2004)

T. Strunskus, O. Fuchs, L. Weinhardt, C. Heske, M. Guraya, M. Muhler, V. Staemmler and C. Wöll
The valence electronic structure of zinc oxide powders as determined by X-ray emission spectroscopy: Variation of electronic structure with particle size
Journal of Electron Spectroscopy and Related Phenomena, **134**, 183-189, (2004)

S. Swaraj, U. Oran, A. Lippitz, R. D. Schulze, J. F. Friedrich and W. E. S. Unger
Surface analysis of plasma-deposited polymer films, 2: Analysis of post-plasma air reacted plasma polymerized styrene by X-ray photoelectron spectroscopy and X-ray absorption spectroscopy
Plasma Processes and Polymers, **1** (2), 134-140, (2004)

Y. Tai, A. Shaporenko, W. Eck, M. Grunze and M. Zharnikov
Depth distribution of irradiation-induced cross-linking in aromatic self-assembled monolayers
Langmuir, **20**, 7166-7170, (2004)

Y. Tai, A. Shaporenko, W. Eck, M. Grunze and M. Zharnikov
Abrupt change in the structure of self-assembled monolayers upon metal evaporation
Applied Physics Letters, **85**, 6257-6259, (2004)

Y. Tai, A. Shaporenko, H. T. Rong, M. Buck, W. Eck, M. Grunze and M. Zharnikov
Fabrication of thiol-terminated surfaces using aromatic self-assembled monolayers
Journal of Chemical Physics B, **108**, 16806-16810, (2004)

J. Thompson, V. Arima, Y. Zou, R. Fink, E. Umbach, R. Cingolani and R. I. R. Blyth
Systematics of the 4f energies in a series of rare-earth organic complexes determined by resonant photoemission
Physical Review B, **70** (15), 153104, (2004)

P. Thomsen-Schmidt, K. Hasche, G. Ulm, K. Herrmann, M. Krumrey, G. Ade, J. Stümpel, I. Busch and S. Schädlich
Realisation and metrological characterisation of thickness standards below 100 nm
Applied Physics A, **649**, (2004)

T. Tolinski, K. Lenz, J. Lindner, E. Kosubek, C. Sorg, M. Bernien, A. Scherz, H. Wende and K. Baberschke
Interlayer exchange coupling and damping processes in coupled trilayer systems
Molecular Physics Reports, **40**, 164, (2004)

S. Török, J. Osán, B. Beckhoff and G. Ulm
Ultratrace Speciation of Nitrogen Compounds in Aerosols Collected on Silicon Wafer Surfaces by means
Powder Diffraction Journal, **86**, (2004)

G. Tzvetkov, G. Koller, Y. Zubavichus, O. Fuchs, M. B. Casu, C. Heske, E. Umbach, M. Grunze, M. G. Ramsey and F. P. Netzer
Bonding and structure of glycine on ordered Al_2O_3 film surfaces
Langmuir, **20** (24), 10551-10559, (2004)

W. Unger
Haftung im Verbund
Metalloberfläche, **57** (7-8), 26-31, (2003)

E. Ünveren
Characterization of Cr_2O_3 catalysts for Ci/F exchange reactions, Doctoral Thesis
Humboldt University of Berlin, (2004)

E. Ünveren, E. Kemnitz, S. Hutton, A. Lippitz, A and W. Unger
Analysis of highly resolved X-ray photoelectron Cr 2p spectra obtained with a Cr_2O_3 powder sample prepared with adhesive tape
Surface and Interface Analysis, **36** (1), 95, (2004)

S. Valencia, H.-C. Mertins, D. Abramsohn, A. Gaupp, W. Gudat and P. M. Oppeneer
Interference effects in the X-ray Kerr rotation spectrum at the Fe 2p edge
Physica B: Physics of Condensed Matter, **345**, 192, (2004)

J. Viefhaus, S. Cvejanovic, B. Langer, T. Lischke, G. Prümper, D. Rolles, A. V. Golovin, A. N. Grum-Grzhimailo, N. M. Kabachnik and U. Becker
Energy and Angular Distributions of Electrons Emitted by Direct Double Auger Decay
Physical Review Letters, **92**, 083001, (2004)

J. Viefhaus, A. N. Grum-Grzhimailo, N. M. Kabachnik and U. Becker
Electron-Electron Coincidence Study of Double Auger Processes in Atoms
Journal of Electron Spectroscopy Relatated Phenomena, **141**, 121, (2004)

J. Vogel, W. Kuch, J. Camarero, K. Fukumoto, Y. Pennec, M. Bonfim, S. Pizzini, F. Petroff, A. Fontaine and J. Kirschner
Time and layer resolved magnetic domain imaging of FeNi/Cu/Co trilayers using x-ray photoelectron emission microscopy
Journal of Applied Physics, **95** (11), 6533-6536, (2004)

L. Vogeley, O. A. Sineshchekov, V. D. Trivedi, J. Sasaki, J. L. Spudich and H. Luecke
Anabaena Sensory Rhodopsin: A Photochromatic Color Sensor at 2.0 A
Science, **306**, 1390, (2004)

J. Wang, W. Kuch, F. Offi, L. I. Chelaru, M. Kotsugi and J. Kirschner
Exchange coupling between ferro- and antiferromagnetic layers across a non-magnetic interlayer: Co/Cu/FeMn on Cu(001)
Journal of Physics: Condensed Matter, **16**, 9181-9190, (2004)

J. Wang, W. Kuch, F. Offi, L. I. Chelaru, M. Kotsugi and J. Kirschner
Magnetic domain investigation in Co/Cu/FeMn trilayers
Journal of Applied Physics, **95** (11), 7504-7506, (2004)

R. Weber, B. Winter, P. M. Schmidt, W. Widdra, I. V. Hertel, M. Dittmar and M. Faubel
Photoemission from aqueous alkali-metal-iodide salt solutions using EUV synchrotron radiation
Journal of Physical Chemistry B, **108** (15), 4729-4736, (2004)

W. A. Weihofen, J. Liu, W. Reutter, W. Saenger and H. Fan
Crystal structure of CD26/dipeptidyl-peptidase IV in complex with adenosine deaminase reveals a highly amphiphilic interface
Journal of Biological Chemistry, **279** (41), 43330-43335, (2004)

U. Weiler, T. Mayer, W. Jaegermann, C. Kelting, D. Schlettwein and D. Wöhrle
Electronic Energy Levels of Organic Dyes on Silicon: A Photo Electron Spectroscopy Study of ZnPc, F_{16}ZnPc and ZnTPP on p-Si(111):H
Journal of Physical Chemistry B, **105** (50), 19398-19403, (2004)

H. Wende
Recent advances in x-ray absorption spectroscopy
Reports on Progress in Physics, **67**, 2105, (2004)

P. Wernet, D. Nordlund, U. Bergmann, M. Cavalleri, M. Odelius, H. Ogasawara, L. A. Näslund, T. K. Hirsch, L. Ojamäe, P. Göatzel, L. G. M. Petterson and A. Nilsson
The Structure of the first coordination shell in liquid water
Science, **304**, 995, (2004)

P. Wernet, D. Nordlund, U. Bergmann, H. Ogasawara, M. Cavalleri, L. Å. Näslund, T. Hirsch, L. Ojamäe, P. Glatzel, M. Odelius, L. G. M. Pettersson and A. Nilsson
The structure of the first coordination shell in liquid water
Science, **304**, 995-999, (2004)

E. Weschke, H. Ott, E. Schierle, C. Schüßler-Langeheine, G. Kaindl, V. Leiner and H. Zabel
Resonant magnetic x-ray scattering at the lanthanide M5 edges
Physica B, **in press**, (2005)

E. Weschke, H. Ott, E. Schierle, C. Schüssler-Langeheine, D. V. Vyalikh, G. Kaindl, V. Leiner, M. Ay, T. Schmitte, H. Zabel and P. J. Jensen
Finite-size effect on magnetic ordering temperatures in long-period antiferromagnets: Holmium thin films
Physical Review Letters, **93** (15), 157204, (2004)

E. Weschke, H. Ott, C. Schüssler-Langeheine, A. Y. Grigoriev, R. Meier and G. Kaindl
Probing Complex Magnetic Structures in Thin Films: Resonant Soft X-ray Scattering at the Lanthanide M_5 Edges
Synchrotron Radiation News, **17** (6), 11, (2004)

B. Winter, R. Weber, P. M. Schmidt, I. V. Hertel, M. Faubel, L. Vrbka and P. Jungwirth
Molecular structure of surface-active salt solutions: Photoelectron spectroscopy and molecular dynamics simulations of aqueous tetrabutylammonium iodide
Journal of Physical Chemistry B, **108** (38), 14558-14564, (2004)

B. Winter, R. Weber, W. Widdra, M. Dittmar, M. Faubel and I. V. Hertel
Full valence band photoemission from liquid water using EUV synchrotron radiation
Journal of Physical Chemistry A, **108** (14), 2625-2632, (2004)

D. P. Woodruff
Understanding adsorbate bonding through quantitative surface structure determination
Applied Surface Science, **237**, 13-20, (2004)

R. Würz, A. Meeder, D. F. Marron, T. Schedel-Niedrig, A. Knop-Gericke and K. Lips
Native oxidation of CuGaSe[sub 2] crystals and thin films studied by electron paramagnetic resonance and photoelectron spectroscopy
Physical Review B, **70** (20), 1-10, (2004)

L. Zhang, R. Szargan and T. Chassé
Photoemission study of Cu deposition on molecular-beam-epitaxy-grown ZnS(001)
Journal of Applied Physics, **95**, 743-748, (2004)

L. Zhang, R. Szargan and T. Chassé
Electron-diffraction and spectroscopical characterisation of ultrathin ZnS films grown by molecular beam epitaxy on GaP(001)
Applied Surface Science, **227**, 261-267, (2004)

A. Zimina, S. Eisebitt, M. Freiwald, S. Cramm, W. Eberhardt, A. Mrzel and D. Mihailovic
Electronic Structure of Subnanometer Diameter MoS2-Ix Nanotubes
Nano Letters, **4**, 1749, (2004)

B. Zimmermann, K.-H. Schartner, O. Wilhelmi, S. Kammer, H. Liebel, A. Ehresmann and H. Schmoranzer
Experimental high resolution study of the photoproduction of Ne+ 3p satellites in the threshold energy range
Journal of Physics B: Atomic, Molecular and Optical Physics, **37** (2), 511-523, (2004)

B. Zimmermann, K.-H. Schartner, O. Wilhelmi, S. Kammer, H. Liebel, A. Ehresmann and H. Schmoranzer
Experimental study of the photoproduction of Ne+-3p satellites in the threshold energy range
Journal of Physics B: Atomic, Molecular and Optical Physics, **37**, 511-23, (2004)

Y. Zubavichus, M. Grunze, O. Fuchs, L. Weinhardt, C. Heske, E. Umbach and J. D. Denlinger
Soft X-ray induced decomposition of amino acids: a time-resolved XPS, mass-spectrometry, and NEXAFS study
Radiation Research, **161**, 346, (2004)

Y. Zubavichus, Y. Yang, M. Zharnikov, O. Fuchs, T. Schmidt, C. Heske, E. Umbach, G. Tzvetkov, F. Netzer and M. Grunze
Local structure of amorphous ice as revealed by O K-edge EXAFS
ChemPhysChem, **5**, 509-514, (2004)

Y. Zubavichus, M. Zharnikov, A. Shaporenko and M. Grunze
NEXAFS study of glycine and glycine-based oligopeptides
Journal of Electron Spectroscopy and Related Phenomena, **134**, 25-33, (2004)

Y. Zubavichus, M. Zharnikov, A. Shaporenko, M. Grunze, O. Fuchs, L. Weinhardt, C. Heske, E. Umbach and J. D. Denlinger
Soft X-ray induced decomposition of phenylalanine and tyrosine: a comparative study
Journal of Physical Chemistry A, **108**, 4557-4565, (2004)

Y. Zubavichus, M. Zharnikov, Y. J. Yang, O. Fuchs, C. Heske, E. Umbach, A. Ulman and M. Grunze
XPS and NEXAFS study of water adsorption on the pyridine-terminated thiolate self-assembled monolayer
Langmuir, **20**, 11022-11029, (2004)

Y. Zubavichus, M. Zharnikov, Y. J. Yang, O. Fuchs, E. Umbach, C. Heske, A. Ulman and M. Grunze
X-ray photoelectron spectroscopy and near-edge X-ray absorption fine structure study of water adsorption on pyridine-terminated thiolate self-assembled monolayers
Langmuir, **20** (25), 11022-11029, (2004)

Keyword Index

(click on page number to open selected page)

Authors Index

(click on page number to open selected page)